

ECIO 2007

European Conference on Integrated Optics

Collected Manuscripts

(c) Copyright 2007 The ECIO Board. All rights reserved.

Contents

ID	Author	Title
WPT1	Serge Valette, CEA-LITEN, France	Integrated Optics: The history and the future (plenary talk)
WA0	Jesper Mørk	Nanomaterials (invited paper)
WA1	E.T. Aw1, H. Wang1, Y. Chu1, S,	Monolithic 2×2 Quantum Dot Switch for Optical Interconnect Networks
WA2	L. Xu, X.J.M. Leijtens, M.J.H. S	InP based Polarization Insensitive Tunable duplexer and Integrated Reflective Transceiver
WA3	L.M. Augustin, J.J.G.M. van der	A compact passive polarization converter optimized for active-passive integration on InP/InGaAsP
WA4	Hideki Ohe1,3, Hiromasa Shimizu2	Carrier-depletion-type multiple quantum well optical phase modulators operating at the 1.55 μm wavelength range
WB0	R.G.Heideman1, D. Geuzebroek1, A	Low loss, high contrast optical waveguides based on CMOS compatible LPCVD processing (invited paper)
WB1	S. Taccheo1, G. Della Valle1, A.	Single-pump high-power robust single-frequency waveguide lasers fabricated by ion-exchange techniques
WB2	F.R. Mahamd Adikan, J.C. Gates,	Recent Developments in Direct-UV-Written Planar Waveguides, Gratings, Sensors, and Substrates
WB3	Haiyan Ou1, Karsten Rottwitt1 an	Ultra-compact silica-on-silicon micro-resonators by etching deep trenches
WB4	E. Jordana1, J.-M. Fedeli1, L. E	Deep-UV Lithography Fabrication of Slot Waveguides and Sandwiched Waveguides for Nonlinear Applications
WC0	Martin Hill	Micro and nanolasers for digital photonics (invited paper)
WC1	D. J. H. C. Maas, A.- R. Bellanc	MIXSELs – a new class of ultrafast semiconductor lasers
WC2	Yousefi M.1, Beri S.1, Barbarin	Towards a compact laser for chaos encryption
WC3	Hitoshi Kawaguchi1,2,3, Takashi	Optical Buffer Memory Using Polarization Bistable Vertical-Cavity Surface-Emitting lasers
WD0	Lars Samuelson	Fabrication and applications of semiconductor nanowires (invited paper)
WD1	R. Martinez Vazquez, R. Osellame	Femtosecond laser fabrication of integrated optical waveguides and microfluidic channels for lab-on-chip devices
WD2	Davide D. Janner1, F. Lucchi2, P	Electric-field poling of Ti indiffused z-cut LiNbO3 wafers without surface grinding
WD3	José Olivares1, Fernando Agulló-	Novel and nanostructured optical waveguides by means of using electronic damage of swift heavy ions
WE0	Kerry Vahala California Institut	Applications of High Q Microresonators: Photonic Clocks, cQED and New laser sources on Silicon (invited paper)
WE1	C. Vannahme, H. Suche, S. Reza,	Integrated Optical Ti:LiNbO3 Ring Resonator for Rotation Rate Sensing
WE2	Edwin J. Klein1, Gabriel Sengo1,	Densely integrated photonic devices based on microring resonators for use in access networks
WE3	Michael Först1, Jan Niehusmann1,	Oxygen-ion implanted silicon microring resonator for high-speed all-optical switching
WF0	Stefan A. Maier	Plasmonics: Engineering of highly confined electromagnetic modes (invited paper)
WF1	Laurent Fulbert1, Roel Baets2, A	MONA – Merging Optics and Nanotechnologies: The Nanophotonics Technology Roadmap

WF2	Stijn Scheerlinck, Frederik Van	Gold Grating Coupler for Silicon-on-Insulator Waveguides with 34 % Coupling Efficiency
WF3	Tiberiu Rosenzveig1, Kristjan Le	Metal nanowires – a new class of plasmonic waveguides
WG1	Chyng Wen Tee1, Kevin Williams1,	Compact Vertically-coupled Microring Laser Array Dual-Wavelength Source for Terahertz Mode Beating
WG2	S. Maine1, D. Marris-Morini1, L.	High Q-factor microrings using slightly etched rib waveguides
WG3	Maxim Fadel and Edgar Voges	Low-Loss SiON Ring Resonators on Silicon for 1.55 μm Wavelength
WG4	R. Nouroozi, Y. H. Min, W. Grund	Efficient Second Harmonic Generation in Matched Ti:PPLN Waveguide Resonators
WG5	Tleyane J. Sono1, Christos Rizio	Second harmonic generation via total internal reflection quasi-phase-matching in a hexagonal nonlinear optical microresonator
WH1	Katarina Grujic and Olav Gaute	Assembly of microsphere chains by counter propagating, guided waves
WH2	A. Ghasempour1,2,4, D. Alexandre	Integrated optic beam combiners for astronomic interferometry: rapid prototyping of hybrid sol-gel devices
WH3	Nikolai Lyndin2, Nathalie Destou	Zero transmission narrow band laser mirror using a waveguide grating under normal incidence
WH4	Curtis W. Neff, L. Mauritz Ander	Enhanced Transmission in Dynamically Tuned Optical Microresonator Possessing Highly Dispersive Media
WH5	Hugo J.W.M. Hoekstra, Paul V. La	Noise and resolution in IO interferometric sensing
ThPT1	Roel Baets, Peter Bienstman, Wim	Progress in high index contrast integrated optics (plenary talk)
ThPT2	Meint Smit, Martin Hill, Roel Ba	How complex can integrated optical circuits become? (plenary talk)
ThA1	H. Herrmann, D. Büchter, R. Rick	Integrated Electro-optic Wavelength Filter With Programmable Spectral Response
ThA2	Davide Janner1, Michele Belmonte	Domain engineering in LiNbO3 for tailoring the electro-optic response of waveguide modulators
ThA3	A. Melloni1, F. Morichetti1,2, R	TriPleX: a new concept in optical waveguiding
ThA4	M.J.R. Heck1, E.A.J.M. Bente1, Y	Integrated Optical Waveguide Device for Picosecond Pulse Compression
ThA5	Wouter Van Parys1, Dries Van Tho	Amplifying Waveguide Optical Isolator with Integrated Electro-magnet
ThA6	Jiro Ito and Hiroyuki Tsuda	A compact arrayed-waveguide grating with a locally enhanced optical confinement structure using trenches filled with low-refractive index materials
ThB0	Kohroh Kobayashi	Innovation for new-genera-tion optical communications based on photonic device break-through (invited paper)
ThB1	Lech Wosinski1, Liu Liu2, Matteo	Amorphous Silicon in Nanophotonic Technology
ThB2	S. Pezzagna1,2, J. Brault1, M. d	GaN, a new material for integrated nonlinear optics
ThB3	Paolo Navaretti1, Andreas Rutz1,	Modelocking of a GaInNAs VECSEL using a GaInNAs SESAM for 1.3 μm applications
ThB4	Jonathan Schrauwen, Frederik Van	Focused-ion-beam fabrication of slanted fiber couplers in silicon-on-insulator waveguides
ThC0	Michal Lipson	High speed silicon photonics (invited paper)
ThC1	Ronald Dekker1, Jan Niehusmann2,	Ultrafast All-Optical Switching by Cross Phase Modulation Induced Wavelength Conversion in Silicon-on-Insulator Waveguides and Ring Resonators
ThC2	K. Voigt, L. Zimmermann, G. Winz	Silicon-on-Insulator (SOI Delay-Line Interferometer with Low Polarization-Dependent Wavelength Shift
ThC3	Raffaella Costa1, Giuseppe Cusma	TE-TM coupling of a standard fiber to a Si-wire waveguide

ThD0	A. Neyer, S. Kopetz, E. Rabe and	Polymer Waveguide Technologies for Optical Interconnects (invited paper)
ThD1	Henry Kelderman, Mart B.J. Dieme	Bends in Polymeric Multimode Waveguides
ThD2	N. Keil, H. H. Yao, C. Zawadzki,	Polymer Optical Motherboard Technology
ThD3	Uwe Hollenbach1, Hans-Jürgen Böh	UV Light Induced Single Mode Waveguides in Polymer for Visible Range Applications
ThE0	Alwyn Seeds University College L	RF over Fibre Systems (invited paper)
ThE1	W. Tittel1, M. Afzelius2, P. Bal	Waveguide Quantum Memories (invited paper)
ThE2	Toshiaki Suhara, Hiroaki Okabe a	Generation of Polarization-Entangled Twin Photons by Type-II QPM Waveguide NLO Device
ThF0	T.L. Koch	Silicon photonics (invited paper)
ThF1	Filip Öhman and Jesper Mørk COM•	Frequency Response of Slow and Fast Light in Integrated Semiconductor Waveguide Amplifiers and Absorbers
ThF2	U. Khalique1, J.J.G.M. van der T	Realization of Polarisation based Integration Scheme (POLIS) for Active and Passive Components
ThF3	B.Han1, R.Orobtchouk1, T.Benyatt	Comparison of optical passive integrated devices based on three materials for optical clock distribution
ThG01	K. Leosson1,2, M.H. Sørensen3, T	Evanescent-wave fluorescence excitation in aqueous solutions using symmetric planar waveguides
ThG02	Nina Skivesen1, Amélie Têtu1, Ma	Planar photonic crystal waveguide biosensor
ThG03	D. Pietroy, A.V. Tishchenko, M.	Waveguide grating spectral phase-shifter for temporal femtosecond pulse splitting
ThG04	N. Bamiedakis1, J. Beals1, F. Ya	Low-Loss, High-Uniformity 1×2, 1×4 and 1×8 Polymer Multimode Y-Splitters Enabling Radio-over-Fibre Multicasting Applications
ThG05	Gabriel Sengo, Henk A.G.M. van W	Optimized Deep UV hardbake process for metal-free dry-etching of integrated optical devices
ThG06	Florent Pigeon1, Marwan Abdou Ah	Waveguide grating for microchip-laser polarization control
ThG07	Y. Barbarin1, E.A.J.M. Bente1, M	18GHz Fabry-Pérot integrated extended cavity passively modelocked lasers
ThG08	N. Grossard, J. Hauden and H. Po	Low-loss and stable integrated optical Y-junction on lithium niobate modulators
ThG09	Michael J. Connelly1, Aisling Cl	Numerical Analysis of Picosecond Pulse Propagation in a Tensile-Strained Semiconductor Optical Amplifier with Parameter Ex-traction using Frequency Resolved Optical Gating
ThG10	A. Kaplan, A. Greenblatt, G. Har	Fully Tunable LiNbO3 Ring Resonator Cavity for Frequency Comb Generator (FCG)
ThG11	J. V. Galán, P. Sanchis and J. M	Low-loss coupling technique between SOI waveguides and standard single-mode fibers
ThG12	N.Cioffi4, D. de Ceglia1,2, M. D	Metallo-Dielectric Multilayer Sensor for Hydrogen Detection in Exhaled Breath
ThG13	Davide Castaldini1,2,3, Paolo Ba	Segmented waveguide tapers for low insertion loss, high performance SPE:LiNbO3 integrated circuits
ThG14	J. Jágerská1, F. Ondrácek1, L. S	Er/Yb Waveguide Amplifiers in Novel Silicate Glasses
ThG15	Damian Kasprzak and Marek Blahu	Polarization effects in gradient index MMI structures made by K+-Na+ ion exchange in glass
ThG16	G. Lifante1, P.L. Pernas2, E. Ca	Integrated electro-optic Mach-Zehnder modulators based on Zn-diffused LiNbO3 waveguides
ThG17	Robert Halir1, Íñigo Molina Fern	High performance, single etch step MMI design on SOI
ThG18	A.V. Tsarev, I.E. Kalabin and V.	High-temperature phases with increased refractive index in HxLi1-xTaO3

		waveguide layers
ThG19	Elena Romanova1, Andrey Konyukho	Energy deposition and heat diffusion in the process of chalcogenide glass modification by femtosecond laser pulses
ThG20	B. Docter, E.J. Geluk, F. Karout	Deep echted DBR gratings in InP for photonic integrated circuits
ThG21	Federica Poli, Matteo Foroni, Si	Surface Modes in Antiresonant Reflecting Optical Waveguides with Rectangular Hollow Core
ThG22	Francesco Dell’Olio and Vi	Silicon-on-Insulator Slot Waveguides for Integrated Optical Sensing
ThG23	Andrei Tsarev	Peculiarity of multi-reflector filtering technology
ThG24	Francesca Magno1, Vittorio M. N.	Investigation of Silicon Slot-based Directional Couplers
ThG25	Kehinde Latunde-Dada and Frank P	An optimal design strategy for MMI splitters
ThG26	Ziyang Zhang, Min Yan and Min Qi	Numerical Studies on Silica Wire Directional Couplers
ThG27	Andrei Tsarev	The New Design and Numerical Simulation by 3D BPM of New Compact Polarisation Rotator in Anisotropic LiNbO3 Graded Index Waveguide
ThG28	Thomas Kamalakis, Thomas Sphicop	A Semi-Analytical Propagation Equation Model for the Study of Signal Propagation in Kerr Nonlinear Nanophotonic Waveguides
ThG29	Eric Cassan, Damien Bernier, Gui	Design of photonic crystal directional couplers for electro-optical wavelength switching
ThG30	Igal Bayn and Joseph Salzman	Photonic crystals in diamond: Cavity Q ¬ Mode volume influence on the design
ThG31	Boris Usievich1, Jamil Nurligare	Excitation of Leaky modes in the System of Coupled Waveguides
ThG32	Michael Bergmair and Kurt Hinger	Band Structure and Coupled Surface Plasmons in one dimensional Photonic Crystals
ThG33	Nikolaos Avaritsiotis, Thomas Ka	A Semi-analytical Model for Estimation of the Transfer Function of a Coupled Resonator Optical Waveguide Based on Coupled Mode Theory
ThG34	K.A. Rutkowska, T.R. Wolinski, P	Light propagation in a highly birefringent photonic crystal fiber infiltrated with a nematic liquid crystal
ThG35	Min Yan and Min Qiu	Finite-element analysis of -wedge plasmon polariton guide
ThG36	G. Kozyreff1,2, J.L. Dominguez J	Whispering Gallery Mode for Second-Harmonic Generation in Microresonators
FPT1	Klaus B. Mogensen, Detlef Snaken	Lab-on-a-chip systems with integrated optics for biochemical applications (plenary talk)
FPT2	Laura M. Lechuga	New frontiers in optical biosensing (plenary talk)
FA0	Thomas F. Krauss	Slow light: perspective and applications (invited paper)
FA1	Wico C.L. Hopman1, Feridun Ay1,	Focused Ion Beam Milling Strategies of Photonic Crystal Structures in Silicon
FA2	A. Talneau, K.H. Lee, S. Guilet	Efficient coupling to W1 Photonic crystal waveguide on InP membrane through thinly supported access guides
FA3	Damien Bernier, Eric Cassan, Gui	Self-collimated superprism effect using a photonic crystal with parallelogram lattice
FA4	René M. de Ridder, Wico C.L. Hop	Mapping the field distribution of a resonator in a photonic crystal slab, using transmission SNOM
FB0	Heinz-Günter Bach	Ultra high-speed photodetectors and photoreceivers for telecom and datacom also aiming at THz applications (invited paper)
FB1	L. D. A. Lundeberg and E. Kapon	Controlling Modes using VCSEL-Based Photonic Crystal Heterostructures
FB2	Toke Lund-Hansen, Jeppe Johansen	Detailed investigation of spontaneous emission decay rates of self-assembled InAs quantum dots
FB3	Mike van der Poel1, Markus Beck2	Surface acoustic wave driven light modulation
FB4	Kenji Kintaka1, Junji Nishii1, S	Different-Guided-Mode-Coupling DBR for WDM Optical Interconnection Board

		Using Channel Waveguides
FC4	Günther Roelkens, Dries Van Thou	SOI grating structure for perfectly vertical fiber coupling
FC5	Mariangela Gioannini and Ivo Mon	Spatial and Spectral Distributed Multi Population Rate Equations Model for Quantum Dot Superluminescent Diodes
FC6	Wolfram H.P. Pernice1, Dominic F	Full-vectorial time-domain modelling of photonic crystal semiconductor lasers
FPD1	H.P. Uranus, L. Zhuang,, C.G.H.	Direct Experimental Observation of Pulse Temporal Behavior in Integrated-Optical Ring-Resonator with Negative Group Velocity
FPD2	A. Melloni1, F. Morichetti1,2, C	2 bit Continuously Tunable Slow Wave Delay Line at 2.5 Gbit/s
FPD3	B. Julsgaard1, S. Stobbe1, J. Jo	Probing the local density of optical states in 2D-photonic crystal membranes
FPD4	P.R.A. Binetti1, J. Van Campenho	An Optical Interconnect Layer on Silicon
FPD5	David Yevick and Michael Reimer	Transition Matrix Methods

Integrated Optics: The history and the future

Serge Valette

CEA-Grenoble
17 rue des Martyrs 38054 Grenoble cedex 9
serge.valette@cea.fr

pôle **O**ptique **R**hône-**A**lpes **ORA**
10 rue Professeur Benoit Lauras 42000 St Etienne
s.valette@pole-ora.com

Abstract: *The continuous improvement of microtechnologies and the recent and very fast development of nanotechnologies have drastically modified technical and economical landscapes in many fields of activities. It's particularly true in optics because of the special position of the visible and near infrared optical wavelengths at the border of the micrometric and the nanometric world.*
Integrated optics which is now almost 30 years old is one of the more relevant fields to illustrate this double impact. This presentation will try to summarise the long and attractive way followed since the end of the 60's by one of the more fruitful branch of optics and to foresee some of its future developments.

Introduction

It is now 28 years since the Bell System Journal published a special issue on integrated optics and opened the way to one of the largest field of scientific investigation in optics. Many very attractive things have been done both in integrated light sources, detectors, optical components and systems and have led to a lot of technical breakthroughs.
One of the encountered difficulties which explains the wealth of integrated optics as well, was the strong diversities of materials and technologies studied and used in this field always balancing between the dream of monolithic integration and the more pragmatic approach offered by heterogeneous assemblies.
It's however clear that the huge diversity of functions and the high level of performances required to achieve an all integrated optical circuits especially in the field of optical communications increase drastically the difficulties to find an ideal substrate.
From the end of 90's, many laboratories, on the track of NTT and LETI, investigated hybrid solutions based on silicon. This hybrid approach associating sometimes both integrated optics and micro-optics became more and more developed around the world.
Curiously, the internet revolution which have been allowed by optical fibres and for a large part by integrated optics components, instead of marking the 'triumph' of integrated optics, has led to one of the worst technical crisis and to a drastic change in research orientations: silicon could once again be the winner of the battle.
I am now going to tell you this history which can be seen like a saga and to give you some indications to foresee the next episode.

Infancy and childhood

I believe that the real beginning of integrated optics is associated with the Bell System Journal issue of September 1969 where one can find some of the basic publications of E.A.J.Marcatili, D.Marcuse, P.K Tien, R.Ulrich, H.Kogelnik or I.P.Kaminow who can be considered, together with A.Yariv, as the fathers of this field.
At this time, all the dreams were allowed and nobody had an objective idea about both attainable performances and practical limitations [1].
At the end of the 60's, the best optical fibres exhibit typical propagation losses of about 20dB/km and laser diodes working at room temperature did not yet exist.
One of the main events was the patent of the Russian team led by Z. Alferov at Ioffe Institute concerning the semiconductor laser heterostructures. It was really the start of the laser diodes development with all the applications you know today.
At this time and during several years, the best wavelengths for optical fibres was not yet in the range 1.3-1.7µm but around 0.8µm. Fortunately, the easier heterostructures which can be achieved with a III-V direct gap semiconductor were founded in the ternary family GaAs/GaAlAs emitting in this spectral range. However during several years many laboratories worked hard to improve the reliability of the diodes, to increase their lifetime and to understand some of physical phenomena well controlled today. Of course all these works have been a good appetizer for mastering more complex heterostructures like quarternary heterostructures on InP [2].
In 1973, I was 25 years old and I begun a Ph.D. thesis at LETI on ion implanted waveguides on zinc telluride, a II-VI semiconductor which exhibited high

electro-optics coefficients and could be a candidate for efficient modulators [3].

Early in the 70's, many laboratories began to achieve optical waveguides on lithium niobate by different approaches including the now well known titanium in-diffusion or proton exchange techniques and to propose different schemes of modulators based on coupled mode theory. I remember the name 'COBRA', then 'BOA' and a little bit later 'timed COBRA' with alternate electrodes configuration which became the reference structure for modern modulators[4]. At the same time appeared the first publications showing the strong advantage of integrated optics and optical confinement to achieve non-linear optics devices [5].

For my part, it appeared clearly that ZnTe was not a good choice and after many efforts and fights with II-VI compounds technology very far from the maturity, I became to think that silicon could be a better way. This idea was not really surprising if one remembers that LETI is at first a microelectronics laboratory.

Between 1980 and 1987, two basic technologies were experimented in my laboratory: IOS1 and IOS2 using respectively silicon nitride and doped silica waveguides. Several basic devices were realised by CVD techniques with a good level of performances [6]. It was the first step of the silicon based technology developments extensively studied around the world some years later. At the same time, the laboratory of M.Kawachi at NTT published the first flame hydrolysis silica waveguides [7]. In both cases, it's the first time that propagation losses could be given in dB/m and not in dB/cm offering a lot of possibilities for new devices in the field of communications and in the field of sensors as well [8].

Few years earlier, ion exchange on glass developed by glass manufacturers in Japan were applied to integrated optics by Pr Chartier and led to a large interest around the world because of the greater simplicity and the lower cost of the fabrication process [9].

Some attractive developments have been done on polymer waveguides for passive and active devices as well [10].

On the other hand, many progresses were done in integrated lasers: towards longer wavelengths to take advantage of the new performances of optical fibres and their propagation losses less than 0.2dB/km, towards smaller wavelengths to join the need of new application fields as optical storage. That meant new III-V semiconductor materials, new type of heterostructures involving quantum wells, strained layers and new concepts of light sources illustrated by VCSEL[11].

Adulthood and maturity

At the end of 80's and at the beginning of the 90', integrated optics becomes a mature technology and optical communications were more and more the motor of its development. All big industrial groups made strong efforts both in silicon based, lithium niobate, III-V or even glass technologies.

A lot of attractive components and devices have been proposed showing the wealth and the maturity of integrated optics [12].

On the other hand, the possibilities to fabricate very long waveguides with low attenuation give new possibilities in the field of sensors and many demonstrations have been done during this period.

One of the best demonstrations of this teaming of ideas is probably the so called 'phasar' invented by Meint Smit which perfectly illustrated both the maturity of the field and showed that there was always the place for innovation [13].

Another smart demonstration of the potential of integrated optoelectronics has been given by the optical fibre gyro. This device combined a lot of progresses including low loss maintaining polarization fibres, super radiant light sources, lithium niobate phase modulators to optimize both sensitivity and low drift in a Sagnac loop [14]. At this time, I was in charge of different training sessions on optoelectronics in University and high school and fibre gyro was my favourite example to illustrate the diversity and the potential of optoelectronics and the scientific process of thinking.

Combination of integrated optics and MEMS technologies brought also new attractive devices, for instance in the fields of sensors [15].

However, in spite of these huge developments in laboratories and in industrial companies, the connection between all these heterogeneous components remains the stumbling block of integrated optics.

Several attempts tried to overcome this difficulty or to give technical solutions able to integrate this step in the component fabrication process. In silicon based technologies, U-groove techniques have been proposed for efficient optical coupling between fibres and silica waveguides [16].

Hybridization approaches derived from flip-chip techniques has been developed to align the different components required to build a complete optoelectronic module [17]. All these attempts have demonstrated interesting possibilities; however they generally led to additional steps in the process which of course penalized the economic balance.

In parallel, segmented waveguides have been demonstrated as one of the more attractive approaches to adapt locally different mode structures and reduce the connection losses [18].

Glory and fall

The beginning of the internet revolution at the end of the 90's can be considered as the hour of glory for optical communication and for integrated optics technologies.

It is interesting to note that among the large panel of studied technologies, all of them have led to industrial developments and to commercialized devices. Silica based technologies mainly for phase array mux-demux, ion exchange on glass for power splitters, lithium niobate for modulators and of course semiconductors for light generation and detection [19].

So there were no losers, but as we know no real winner as well.

All big industrial groups have invested a lot of money to respond to the large demand for long haul communications. Many start-ups have been created to anticipate the appetite of high rate transmissions needed in metro and access areas which were the expected following markets.

All actors which have lived this period have a lot of incredible anecdotes to tell, and it could be interesting to understand what happened during these few years and why many people among the more pragmatic one, scientists, industrials, economists lost the sense of reality.

The crisis had of course several explanations.

I guess that the first one is the extraordinary jump brought by optical communications and optical fibres. It was maybe the first time that a given technology gave the possibility to increase the existing state of art by several decades, leading of course to a strong shift between the social needs and the technical capacity. In microelectronics, the evolution was graduated and the power of the processor grew step by step with the decrease of the transistor size: so the technology has followed the market demand. In optical communications the technical jump was too high and arrived too suddenly.

I think also that there was a common blindness between scientists, which dreamed of optical communication for more than 30 years, and economists who have overestimated the social acceptance and have made subjective analyses.

Finally, the shift lasted maybe less than ten years but for an economical point of view it was extremely long.

The revival

At the end of the crisis, as in the fable, all don't die but all were damaged.

The good side of the medal is maybe the complete calling into questions of the integrated optics field with in many cases the birth of new concepts.

Even if traditional technologies can always be improved, the silicon nanophotonics seems the new way to follow but with very different approaches compared to those developed at the beginning of 80's.

High index contrasts are now the basic structures and SOI substrates seem to be the new materials of optoelectronics. New companies are now in the race, mainly in the field of microelectronics where integrated optics may bring a smart solution to break the deadlock of interconnects [20].

It is curious to see the shift of performance requirements compared with those of previous fields. Losses can be expressed in dB/mm and no longer in dB/m, but the level of integration will be probably ten or hundred time higher.

That suppose of course a very high control of the technological level but advanced microelectronics seems able to bring that. In the same time, the problems of connection are changing ever drastically by the systematic use of hybridization technique or by the integration of all components including light sources in the silicon itself. The complete compatibility with CMOS approach is the new Grail to reach; it can lean on very efficient tools and on some high volume market applications.

Intel and all microelectronics actors are the new leaders of this new optoelectronics field but, by the way, is that optoelectronics yet? [21]

In Rhône-Alpes region we have the chance to work with two of the main actors of this revolution as ST Microelectronics and SOITEC, the world leader of SOI substrate.

So good luck to integrated nanophotonics; I would only like to wish to the new actors to have as many dreams as we have had.

PS: Many information and analyses on this evolution can be available on the website MONA: www.ist-mona.org.

References

1 See for example:

A.Yariv, Integrated optics, International Electron Devices Meeting, vol.18, 1972

D.Marcuse, Theory of Dielectric Waveguides, New York, Academic Press, 1974

A. Yariv, Quantum Electronics, New York, Wiley, 1975.

H. Kogelnik, An introduction to Integrated Optics**,** IEEE Transaction on Microwave Theory and Techniques, 23, n°1, pp 2-16, Jan.1975.

2 See for example:

H.Kressel and K.Butler, Semiconductor lasers and Heterojunction LEDs, Academic Press, New York, 1977

H.C.Casey Jr and M.B Panish, Heterostructures lasers, Academic Press, Orlando,1978

P.Thioulouse, A.Carenco, R.Guglielmi, High-speed modulation of an electrooptic directional coupler,

IEEE Journal of Quantum Electronics, vol.17, n°4, pp.535-541, April 1981.
J.R.Nelson, N.K. Dutta, Review of InGaAsP/lnP laser structures and comparison of their performances, in Semiconductors and Semimetals, edited by W.T. Tsang, Academic Press 1985, Orlando, San Diego, New-York, Londres, Toronto, Montreal, Sydney, Tokyo.
A.Carenco, Semiconductor waveguides in III-V materials for integrated optics, Proceedings of the Fourth European Conference on integrated Optics, pp.1-7, ECIO 87, Glasgow, 11-13 may 1987.

3 See for example:
S.Valette, G. Labrunie, J.Lizet, Optical waveguides in ion implanted ZnTe, J. of Applied Physics, 46, 265H, June 1975
S. Valette, G. Labrunie, J.C. Deutsch, J. Lizet, Planar optical waveguides achieved by ion implantation in zinc telluride: general characteristics, Applied Optics, 16, p. 1289, May 1977

4 See for example:
R.V.Schmidt, I.P Kaminov, Metal diffused optical waveguides in $LiNbO_3$, Appl. Phys. Lett., 25, n°8, 458-460, Oct.1974.
W.K.Burns and A.F.Milton, Mode conversion in planar-dielectric separating waveguides, IEEE J. Quantum Electron., Vol.11, no.1, pp. 32-39, January1975.
M.Papuchon, Y.Combemale, X.Mathieu, DB.Ostrowsky, L.Reiber, A.M.Roy, B.Sejourne and M.Werner, Electically switched optical directional coupler COBRA, Applied Physics Letters, Vol.27, n°5, pp.289-291, 1 September 1975.
M.Papuchon, A.M.Roy, Electically active optical bifurcation BOA, Applied Physics Letters, Vol.31, n°4, pp.266-267, 15 August 1977.
G.L.Destefanis, J.P.Gailliard, E.L.Ligeon, S.Valette, B.W.Farmery, P.D.Townsend, A. Perez, The formation of waveguides and modulators in $LiNbO_3$, by ion implantation, J. Appl Phys, 50, p.78, 1979.
R.C.Alferness, Efficient waveguide electro-optic TE-TM converter, Appl. Phys. Lett., Vol.36, pp.513-515, 1980.
R.C.Alferness and L. L. Buhl, Electro-optic waveguide TE-TM mode converter with low drive voltage, Opt, Lett., Vol. 5, pp. 473-475, 1980.
R.C.Alferness**,** Waveguide Electrooptic Modulators**,** IEEE Transactions on Microwave Theory and Techniques, Vol. MTT-30, pp. 1121-1137, August 1982.
J.L.Jackel, C.E.Rice and J.J Veselka, Proton exchange for high index waveguides in $LiNbO_3$, Appl.Phys. Lett., 41, 607, 1982.
D.B.Ostrowsky and M.Papuchon, Fabrication and Characterization of Titanium Indiffused Proton Exchanged (TIPE) waveguides in Lithium Niobate, Opt.Comm., 42, 101, 1982.
S**.**K.Korotky and R. C. Alferness, Time and frequency domain response of directional coupler traveling-wave optical modulators, J. Lightwave Technol., Vol. LT-1, pp. 244-25 1, 1983.
M. N. Armenise, Fabrication techniques of lithium niobate waveguides, IEE Proc., Part J, Vol. 135, n°. 2, pp. 85-91, April 1988.

5 W.Sohler and H.Suche, Second harmonic generation in Ti-diffused $LiNbO_3$ optical waveguides with 25% conversion efficiency, Applied physics Letters, Vol.33, n°6, pp.518-520, 15 September 1978.

6 See for example
S.Valette,A. Morque, P. Mottier, High performances integrated Fresnel lenses on oxidized silicon substrate, Electron Lett. 18, 2, January 1982.
S.Valette, J.L.Lizet, P.Mottier, J.P.Jadot, S.Renard, A.Fournier, A.M.Grouillet, P.Gidon, H.Denis, Integrated Optical Spectrum Analyser using planar technology on oxidized silicon substrate, Electron Lett. 19, p.883, 13 october 1983
G.Grand, S.Valette, Optical polarisers of high extinction ratio integrated on oxidized silicon substrate, Electronic Letters, 20, p.730, 1984
P.Gidon, S.Valette, P.Mottier, Integrated lenses on silicon nitride waveguides, Optical engineering, 24, p.235, 1984
S.Valette, J.Lizet, P.Mottier, J.P. Jadot, P.Gidon, S.Renard, Integrated optical circuit achieved by planar technology on silicon substrate: application to the optical spectrum analyser, IEEE Proceedings, 131 part H, p.325, 1984

7 See for example:
M.Kawachi, M. Yasu, M. Kobayashi, Flame hydrolysis deposition of Si02-TiO2 glass optical waveguide on silicon, Japanese Journal of Applied Physics, Vol. 22, p.1932, 1983.
N. Takato, M. Yasu, M. Kawashi, Low-loss high silica single mode channel waveguides, Electronics Letters, Vol.22, pp. 321-322, 1986.
M.Kawachi, M.Kobayashi, T.Miyashita, Integrated micro-optic components based on silica waveguides, Proceeding of European Conference on Optical Communications, ECOC 87, pp. 53-58, Helsinki, September 1987.

8 See for example:
T.Suhara, H.Nishihara, Integrated optics components and devices using periodic structures, IEEE Journal of Quantum Electronics, 22, n°6, pp. 845-867, June 1986.
S.Valette, P.Gidon, J.P.Jadot, S.Renard, New integrated optics structure on silicon substrate:

application to optical communications and optical interconnects, Proceedings SPIE 862, Optical Interconnections, Cannes, November 1987.
S. Valette, D. Gidon, J.P. Jadot, New Integrated Optical Multi/Demultiplexer realized on Si Substrate, Proceedings of the Fourth European Conference on Integrated Optics, ECIO 87, p.145, Glasgow, May 11-13 1987, C.D.W. Wilkinson and J. Lamb editors.
J.Lizet, P.Gidon, S.Valette, Integrated Displacement Sensor Achieved on Si Substrate", Proceedings of the Fourth Conference on Integrated Optics, ECIO 87, Glasgow, p.206, 11-13 may 1987, C.D.W. Wilkinson and J. Lamb Editors.
E.E.L.Friedich, S.Valette, P.Gidon, Optical Interconnections for WSI, proceedings of the SPIE, Vol. 963, Optical Computing 88, pp.264-269, 1988

9 R.V. Ramaswamy, R. Srivastava, Ion exchange glass waveguide : a review, Journal of Lightwave Technology, Vol.6, n°6, pp. 984-1002, June 1988.

10 See for example:
R. Lytel, G.F. Lipscomb, M. Stiller, J.I. Thackara, A.J. Ticknor, Organic Integrated Optical Devices, in Nonlinear Optical Effects in Organic Polymers", Edited by J. Messier, F. Kajzar, P. Prasad, D.Ulrich, Academic Publishers Dordrech, Boston, London 1989, NATO Series vol. 162.
G.R.Mohlmann, Polymer electro-optic devices, Proceedings of ECOC 90, Amsterdam, pp.833-840, Sept.1990.

11 See for example:
F.J.Leonberger and J.P.Donnelly, Semiconductor integrated optic devices, in Guided-Wave Optoelectronics, T.Tamir, Ed. Berlin, Germany:Springer-Verlag, pp.317-396,1990.
K.Iga, F.Kay Ama and S.Kinoshita, Surface emitting semiconductor lasers, IEEE Journal of Quantum Electronics, 24, pp 1845-1855, September1988.
L.Jewell, P.Harbison, ASherer, YH. Lee and L.T.Florez, Vertical cavity surface emitting lasers: design, growth, fabrication, characterization", IEEE Journal of Quantum Electronics, 27, pp. 1332-1346, June 1991.
L.Jewell, G.R.Olbright, R.R.Bryan and AScherer, Surface emitting lasers break the resistance barrier, Photonic spectra, pp 126-130, November 1992.
R.A.Morgan, Vertical cavity surface emitting lasers: the next generation, SPIE proceeding Vol. 1992, Miniature and micro-optics and micromechanics, pp. 64-69, 1993.
G.R.Olbright, VCSEL's could revolutionize optical communication, Photonic Spectra, pp 98 - 101, February 1995.

12

A.Donaldson, Candidate materials and technologies for integrated optics: fast and efficient electro-optic modulation, J. Phys. D: Appl. Phys. 24, pp.785-802, 1991.
M.Lawrence, Lithium niobate integrated optics, in Reports on Progress in Physics, pp.363-429, 1993.
E.L.Wooten, K.M.Kissa, A.Yi-Yan, E.J.Murphy, D.A.Lafaw, P.F.Hallemeier, D.Maack, D.V.Attanasio, D.J.Fritz, G.J.McBrien, and D.E.Bossi, A review of lithium niobate modulators for fiber-optic communication systems, IEEE J. Select. Topics Quantum Electron., Vol. 6, no. 1, pp. 69-82, Jan. 2000.
S.Valette, S.Renard, J.P.Jadot, P.Gidon and C.Erbeia, Silicon based integrated optics technology for optical sensor applications, Sensors and Actuators, A21-A23, pp.1087-1091, 1990.
J.Bismuth, P.Gidon, F.Revol, S.Valette, Low losses rings resonators using integrated optics on silicon (IOS) technologies, Electron. Letters, 27, pp.722-724, April 1991.
S.Valette, J.P.Jadot, P.Gidon, S.Renard, G.Grand, A.Fournier, A.M. Grouillet, P.Philippe, H. Denis, E.Desgranges, L.Mulatier, C.Erbeia, Integrated Photonic Circuits on silicon, edited by R.A. Levy, Novel Silicon Based Technology, pp.173-240, Kluwer Academic Publishers, Nevertheland, 1991.
H.Nishihara, Recent studies of miniaturization of optical disk pick-ups in Japan, Proceeding of the SPIE, Vol 1248, Storage and Retrieval Systems and Applications, pp 88-95, Santa-Clara, 13-15 February 1990.
S.Renard and S.Valette, Integrated reading and writing optical heads: a way to a multigigabyte multirigid-disk drive, Topical Meeting on Optical Data Storage, Colorado Springs, pp.25-27, February 1991.
R.A.Soref, Silicon-based optoelectronics, Proc. IEEE 81, 1687-1706, 1993.
S.Valette, Integrated Optics on Silicon: IOS technologies, in Advances in Integrated Optics, edited by AN. Chester and S. Martellucci, p. 151-163, Plenum Press, New York et Londres, 1994.
C.G.M. Vreeburg, T. Uitterdijk, Y.S. Oei, M.K. Smit, F.H. Groen, E.G. Metaal, P. Demeester and H.J. Frankena, First InP-based reconfigurable integrated add-drop multiplexer, Photonics Technol. Lett., Vol. 9, No. 2, pp. 188-190, Feb. 1997.
P. Baldi, M.P. De Micheli, K. El Hadi, S. Nouh, A.C. Cino, P. Aschieri and D.B. Ostrowsky, Proton exchanged waveguides in $LiNbO_3$ and $LiTaO_3$ for integrated lasers and nonlinear frequency converters, in Spe. Issue of Opt. Engineering in Integrated Optics, Vol. 37, n° 4, pp.1193-1202, April 1998.
R. G. Hunsperger, Integrated Optics: Theory and Technology 5th Ed., Springer, 2002

13 M.K.Smit: “New focusing and dispersive planar component based on an optical phased array”, Electronics Letters, Vol. 24, pp. 385-386, 1988.

14 See for example:
H.J.Ardity and H.C.Lefevre, Sagnac effect in fiber gyroscopes, Optics Letters, Vol. 6, n°8, pp.401-403, 1981.
R.A.Bergh, H.C.Lefevre and H.J.Shaw, All-single-mode fiber-optic gyroscope, Opt.Lett.., Vol. 6, pp.198-200, 1981,
R. A.Bergh, H. C.Lefevre and H. J. Shaw, All single-mode-fiber-optic gyroscopes with long term stability, Opt. Lett., Vol. 6, pp. 502-504, 1981.
R. A. Bergh, H. C. Lefevre, and H. J. Shaw, An Overview of Fiber-optic Gyroscopes, IEEE Jour.
Light. Tech., Vol. LT-2, pp.91-107, 1984.
Fiber-Optic Rotation Sensors and Related Technologies, edited by S.Ezekiel and H. J.Arditty, Springer-Verlag, Berlin, 1982.

15 See for example:
F.Merat and M.Mehregany, Integrated micro-opto mechanical systems, Proceedings of SPIE, Vol. 2383, pp 88-98, San Jose, February 1995.
S.Valette, Advances in optical microsystems combining microtechnologies and batch processing fabrication, in Diffractive Optics and Optical Microsystems" edited par S. Martellucci et A. Chester, Plenum Press, New York, Washington et Boston, 1997
E.Ollier, P.Labeye, F.Revol, Micro-opto-mechanical switch integrated on silicon, Electronics Letters, Vol.l3, pp. 2003-2005, November 1995.

16 G.Grand, H.Denis, S.Valette, New Method for low cost and efficient optical connexion between singlemode fibers and silica waveguides, Electron. Lett., 27, pp.16-17, January 1991.

17 See for example:
S.Valette, P.Gidon, S.Renard, J.P.Jadot, Silicon based Integrated Optics Technology: an attractive hybrid approach for optoelectronics, SPIE Proceeding Vol. 1128: glass for optoelectronics, Paris, 24-28 April 1989.
C.H.Henry, G.E.Blonder, R.F.Kazarinov, Glass waveguides on silicon for hybrid optical packaging", J. of lightwave technology, LT 7, pp. 1530-1539 (1989).
E.E.L. Friedrich, M.G.Oberg, B.Broberg, S.Nilsson, S.Valette, Hybrid integration of semiconductor lasers with Si-based single mode ridge waveguides, Journal of lightwave technology, 10, n°3, pp.336-340, March 1992.

18 See for example:
F.Dorgeuille, B.Mersali, S.Francois, G.Herve-Gruyer, and M.Filoche, Spot size transformer with a periodically segmented waveguide based on InP, Optics Letters, Vol. 20, pp. 581-583, 1995.
Z.Weissman and I.Hendel, Analysis of periodically segmented waveguide mode expanders, IEEE Journal of Lightwave Technology, Vol. 13, pp. 2053-2058, 1995.
M.M.Spauhler, B.J.Offrein, G.-L.Bona, R.Germann, I.Massarek, and D.Erni, A very short planar silica spot-size converter using a nonperiodic segmented waveguide, IEEE Journal of Lightwave Technology, Vol. 16, p.1680, 1998.
F.Fogli, N.Greco, P.Bassi, G.Bellanca, P.Aschieri, and P.Baldi, Spatial harmonics modeling of planar periodic segmented waveguide, Optical and Quantum Electronics, Vol. 33, n°. 45, pp. 485-498, 2001.

19 See for example:
A.Sugita, M.Kotoku,Y.Inoue, hybrid integrated photonic devices and planar ligthwave circuits technology, Proceedings of the 12th European Conference on Integrated Optics, pp 22-25, Grenoble, 6-8 April 2005.
Chris Door, Progress in silica PIC’s, Proceedings of the 12th European Conference on Integrated Optics, pp 93-95, Grenoble, 6-8 April 2005.

20 See for example:
D.A.B.Miller, Rationale and Challenges for Optical Interconnects to Electronic Chips, Proc. IEEE, vol.88, pp. 728-749, 2000.
Edwin J. Klein, Gabriel Sengo, Lucy T. H. Hilderink, Marcel Hoekman, Rudy Pellens, Paul van Dijk, and Alfred Driessen, Densely integrated photonic devices based on microring resonators for use in access, proceedings of the 13th European Conference on Integrated Optics, Copenhagen , 25-27 April 2007: to be published.
Ronald Dekker, Jan Niehusmann, M. Först and Alfred Driessen, Ultrafast All-Optical Switching by Cross Phase Modulation Induced Wavelength Conversion in Silicon-on-Insulator Waveguides and Ring Resonators, ibid.

21 See for example the following website http://www.intel.com/research/platform/sp/#anchor1

Nanomaterials

Quantum dots for optoelectronics

Jesper Mørk,

COM•DTU Department of Communications, Optics & Materials, NanoDTU,
Technical University of Denmark, Building 343, DK-2800 Kgs. Lyngby, Denmark, jm@com.dtu.dk.

Abstract: We review the the development of nanostructured materials for exercising control over and improving the properties of materials for optoelectronic devices. In particular, the use of quantum dots as the active element of amplifiers and lasers is discussed as well as the new opportunities arising from the discrete level structure of quantum dots.

Technological developments within crystal growth and processing have made it possible to fabricate structures in which the available electronic as well as photonic states can be controlled. This is achieved by modifying the material composition on the micro- to nanometer scale. Thus, a photonic crystal structure incorporated into the material by a periodic modulation of the refractive index, in 1, 2 or 3 dimensions with periodicity on the order of the optical wavelength in the material, allows realizing a forbidden frequency gap as well as engineering the dispersion of electromagnetic wavepropagation in the structure. Line defects in the crystal can be used to create optical waveguides, while point defects realize optical cavities, which may reach very high quality factors corresponding to long storage times of the photons.

Photonic crystal structures allow smaller and more densely integrated structures compared to conventional wavguide technology, but minimum dimensions are still on the order of a wavelength. The use of surface plasmon polaritons bound to the interface of a metal and a dielectric is another way of guiding electromagnetic excitations, and allows allows a reduction of the minimum characteristic length scale [1], with a corresponding increase of the attainable integration density. The use of nanostructuring of the surface provides additional possibilities for engineering the properties and various kinds of integrated optical components have been realized, such as Bragg gratings [2].

Photonic crystal as well as nanoplasmonic structures may be said to belong to the class of metamaterials, i.e., materials that gain their properties from their structure rather than directly from their composition. They are emerging as important technologies for modifying and engineering the passive properties of materials, e.g for application in optical signal processing and sensing. A further development in the field is the structuring of the electromagnetic properties to achieve a negative effective permittivity and negative effective permeability. These double negative or negative index materials, as they are denoted, allow achieving fundamentally different characteristics, that break with conventional wisdom, such as a perfect lens [3]. However, it is not yet clear how to structure the materials in order to achive double-negative characteristics at optical frequencies.

In order to generate or amplify light, active elements are needed and the only developed technology compatible with optoelectronic integration is based on III-V semiconductors. The possible choices of materials within group III and V is limited and the quasi-continuous nature of the electronic states in the conduction and valence band implies the equivalent of a material with a strong degree of inhomogeneous broadening. However, by exploiting quantization effects in structures with size on the order of the electron wavelength the energy level structure can be rendered discrete and the absolute values of the energy levels can be controlled. In this way the optical transition frequencies of the material can be modified. In semiconductors, 3-dimensional quantum confinement is realized by small protrusions, referred to as quantum dots, with a typical diameter of 10-20 nm and a height of a few nm, on top of a thin (wetting) layer. The low-dimensional quantum dot structures, depending on growth conditions, may also be in the form of truncated quantum wire structures, so-called quantum dashes [4]. Besides modifying the energy spectra, the quantum dots strongly alter the dynamics of the medium with important consequences for device properties.

By utilizing the the characteristics of quantum dots and photonic crystals to control both the energy levels and the dispersive properties, a number of new possibilities arise, e.g. within single-photon generation [5] as well as advanced nonliear switches [6].

In the talk we will mainly focus on the properties of quantum dots with respect to their application in lasers and amplifiers as well as examples of novel functionalities that they may enable.

It has been experimentally demonstrated that quantum dot SOAs enable very high saturation output power as well as operation over a broad range of wavelengths [7]. The saturation and noise properties of SOAs will be discussed based on a detailed theo-

retical model of the SOA [8]. The ultrafast dynamics of QD and quantum dash SOAs has been studied by pump-probe techniques [9,10] and is important in understanding the potential of QD SOAs for all-optical signal processing. In particular, reservoir effects associated with excited and wetting layer states of the SOA may profoundly influence the dynamics [11,12].

The discrete states of QD materials also open up the possibility of carrying out fundamental experiments sofar only performed in atomic gasses. For instance, electromagnetically Induced Transparency (EIT) was shown to enable a very spectacular slow-down of light in an ultracold atomic gas [13], but it is speculated that the same phenomenon could be observed in a QD waveguide [14]. If demonstrated experimentally this may pave the way for practical applications of slow-ligh effects, e.g. as microwave phase shifters. We will discuss the requirements to realize the regime of EIT in QD waveguides as well as alternative techniques [15,16] for controlling the speed of light.

Acknowledgments

This work was supported by the Danish Research Council for Technology and Production Sciences through the SCOOP and QUEST projects as well as through the EU IST 6th framework projects Bigband and QPhoton. The author gratefully acknowledges collaboration with a number of colleagues from the Nanophotonics area at COM•DTU.

References

1. W. Barnes, et al., "Surface plasmon subwavelength optics", Nature, vol. 424, pp. 824 (2003).
2. A. Boltasseva et al., "Compact Bragg gratings for long/range surface plasmon polaritons", J. Lightwave Technol., vol. 24, pp. 912 (2006).
3. J. B. Pendry, "Negative refraction makes a perfect lens", Physical Review Letters, vol. 85, pp. 3966 (2000).
4. J.P. Reithmaier et al., "Semiconductor quantum dots devices: Recent advances and application prospects", phys. stat. sol. (b), 243, No. 15, 3981–3987 (2006).
5. K. Hennessy et al., "Quantum nature of a strongly coupled single quantum dot-cavity system", Nature, vol. 445, pp. 896 (2007)
6. K. Asakawa et al., "Photonic crystal and quantum dot technologies for all-optical switch and logic device", New Journal of Physics 8, pp. 208 (2006).
7. T. Akiyama, et al., "An Ultrawide-Band (120nm) Semiconductor Optical Amplifier Having an Extremely-High Penalty-Free Output Power of 23dBm Realized with Quantum-Dot Active Layers", OFC Proceedings, paper PDP12 (2004).
8. T. W. Berg and J. Mørk, "Saturation and Noise Properties of Quantum Dot Optical Amplifiers", IEEE J. Quantum Electron., vol. 40, pp. 1527-1539, Nov. 2004.
9. P. Borri et al., "Ultrafast Gain Dynamics in InAs-InGaAs Quantum-Dot Amplifiers", IEEE Photonics Technol. Lett., vol. 12, pp. 594 (2000)
10. M. van der Poel et al., "Ultrafast gain and index dynamics of quantum dash structures emitting at 1.55 μm", Applied Physics Letters, vol. 89, pp. 081102 (2006).
11. T. W. Berg et al., "Ultrafast Gain Recovery and Modulation Limitations in Self-Assembled Quantum Dot Devices", Photon. Technol. Lett., vol. 13, pp. 541 (2001)
12. S. Dommers et al., "Complete ground state gain recovery after ultrashort double pulses in quantum dot based semiconductor optical amplifier", Appl. Phys. Lett., vol. 90, pp. 33508 2007).
13. L. V. Hau et al., "Light speed reduction to 17 meters per second in an ultracold atomic gas." Nature 397, pp. 594 (1999).
14. C. Chang-Hasnain et al., "Variable optical buffer using slow-light in semiconductor nanostructures." Proc. IEEE 91, pp. 1884 (2003).
15. M. S. Bigelow et al., "Observation of ultraslow light propagation in a ruby crystal at room temperature." Phys. Rev. Lett. 90, 113903-1-4 (2003).
16. J. Mørk et al., "Slow light in a semiconductor waveguide at gigahertz frequencies." Opt. Express, vol. 13, pp. 8136 (2005).

Monolithic 2x2 Quantum Dot Switch for Optical Interconnect Networks

E.T. Aw, H. Wang, Y. Chu, S, Liu, M.G. Thompson, A. Wonfor, R.L. Sellin, R.V Penty, I.H. White (1)
A.R. Kovsh (2)
1) Engineering Department, Cambridge University, Cambridge CB2 1PZ, United Kingdom, eta22@cam.ac.uk
2) NL Nanosemiconductor GmbH, Konrad-Adenauer-Allee 11, 44263 Dortmund, Germany

Abstract: *The design, fabrication and performance of an integrated 2x2 Quantum Dot SOA based switch is reported. Low penalty performance and a large dynamic range opens the potential for the 2x2 switch to be cascaded as a building block for multi-stage, high capacity optical networks.*

Introduction

Recent studies of quantum dot (QD) semiconductor optical amplifiers (SOAs) have demonstrated properties of broad gain bandwidth, low noise performance, ultra-fast gain recovery, high saturation output power and low crosstalk performance [1-6]. These characteristics are of potential importance in a wide range of prospective applications such as power boosters, in-line repeaters, optical cross connects and optical add/drop multiplexers. The use of active components as add/drop multiplexers are of great interest because of their inherent gain, potentially removing the need for additional amplification in cascaded applications. However, the noise of such systems has limited their potential cascadability, even when using quantum well devices [7]. In this paper we report the operation of quantum dot components which have the potential for greater cascadability [5,6]. Following an investigation of the static performance and noise properties, a dynamic study is presented and the potential of the quantum dot switch for interconnect networks is discussed.

Device Details

The structure of the 2x2 QD switch is presented in Figure 1. It has an overall chip area of only 2.55x0.85 mm^2. The switch incorporates a QD active structure which is grown on a GaAs (100) substrate using molecular beam epitaxy. The active layer comprises a ten-fold stack of $In_{0.15}Ga_{0.85}As$ QDs, separated by 38nm GaAs buffer layer and embedded in a GaAs waveguide. The active layer is sandwiched between two $Al_{0.35}Ga_{0.65}$ layers which form the cladding layers. Standard photolithography and ICP dry etch processes are used to fabricate the ridge waveguide structures. Each of the four input ridge waveguides has a width of 3 µm which expands linearly to a 6 µm width, over a length of 150 µm, to the integrated beamsplitter, before connecting to perpendicular SOA gates. The integrated beamsplitters (see Figure 1 inset) contain a 45° totally internal reflecting (TIR) mirrors to route the light to the drop and through paths. The TIR mirrors are formed by focused ion beam etching vertical slots through the active layer. Patterned p-type electrodes allow individual addressing of the amplifier gates and splitters. The isolation between the electrodes exceeds 5kΩ for all electrode combinations.

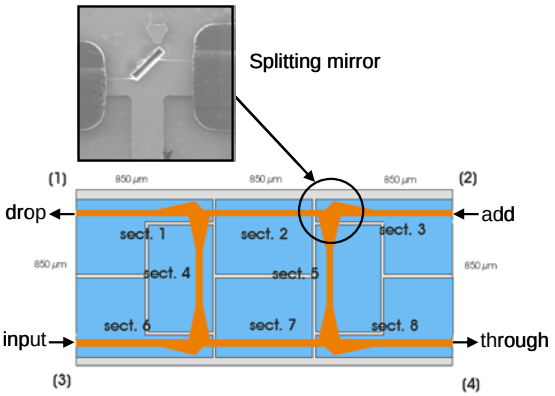


Fig. 1: Schematic of switch structure showing the inputs, outputs, waveguides, splitters and SOA sections. The totally internally reflecting mirror is shown as an inset.

As can be seen from Figure 1, there are eight individually addressable QD SOAs, each connected by the four integrated beamsplitters. The SOAs in sections 1,3,6,8 gate the I/O ports of the switch, while the SOAs in sections 2,3,7,8 gate the splitting stages within the switch. Through the use of an electronic control scheme, the switch operates on a broadcast and select basis to realise a full non-blocking 2x2 switching capability.

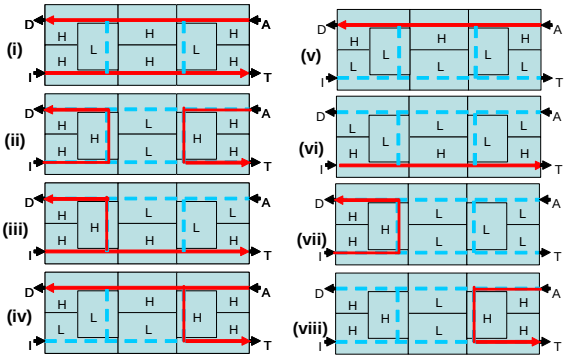


Fig. 2: Monolithic add drop multiplexer mode of operation. Switch bias levels for gates in section 1 to 8 as defined in Figure 1. Abbreviation: Input (I), Through (T), Add (A), Drop (D), On (H), OFF (L). The different operations are as follow: i) bar state (I to T, A to D), ii) cross state (I to D, A to T), iii) broadcast I (I to T and D), iv) broadcast A (A to T and D), and single mode operation: v) A to D, vi) I to T, vii) I to D, and viii) A to T

Mode of Operation

The combination of 'on' and 'off' SOAs for switch-

ing is shown in Figure 2. For the 'off' state a low bias current of less than 20mA is applied, such that the loss in the SOA gate will block any input signal from the 'add' or 'drop' ports, but will still allow fast switching to the 'on' state. For the 'on' state a bias current of between 50mA and 100mA can be applied to provide a net gain out of the SOA. Figure 2 presents the full range of add, drop and broadcast functionalities are avaialbe from this desing. Figure 3 demonstrates the switching operation of a data signal, where the input data is routed to the 'through' and 'drop' paths with the electronic control schemes shown in Figure 2 (vi) and (vii).

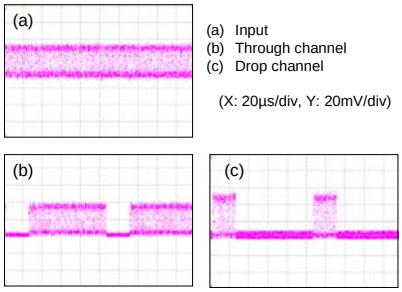


Fig. 3: Oscilloscope capture of 2x2 switch in switching application, showing data switching between the through and drop paths.

DC Characteristics

Continuous wave measurements have been carried out to investigate the DC characteristics of the 2x2 QD switch. Both the through and the drop channels have been investigated for gain saturation, power gain and noise figure. The gain saturation characteristics of the switch are measured for a drive current of 100mA and at a wavelength of 1290nm. The gain dependance on drive current is plotted for a wavelength of 1270nm with an input power of -15dBm, and the gain dependence on wavelength is plotted for a drive current of 100mA with the same input power. Noise figure measurements are performed by directly comparing the optical signal to noise ratio before and after the 2x2 switch. The coupling loss in these devices has been measured by the photocurrent technique to be 3.1dB. At 1290nm, gain saturation is found to occur at on-chip output powers of 6.8dB for the drop path and 10.5dB for the through path. The maximum peak on-chip gain, which occurs at a wavelength of 1275nm, is measured to be 12.1dB for the through path and 9.3dB for the drop path. The 2.8dB difference in on-chip gain between through and drop paths is attributed to the excess loss of the two TIR mirrors in the drop path (the low mirror loss being the result of optimisation of the offset of the mirror at the crosspoint). Minimum noise figures of 7.4dB for the through path and 8.0dB for the drop path are measured at a wavelength of 1275nm. Improved input and output coupling designs, such as expanded mode waveguides, are expected to reduce the system noise figures.

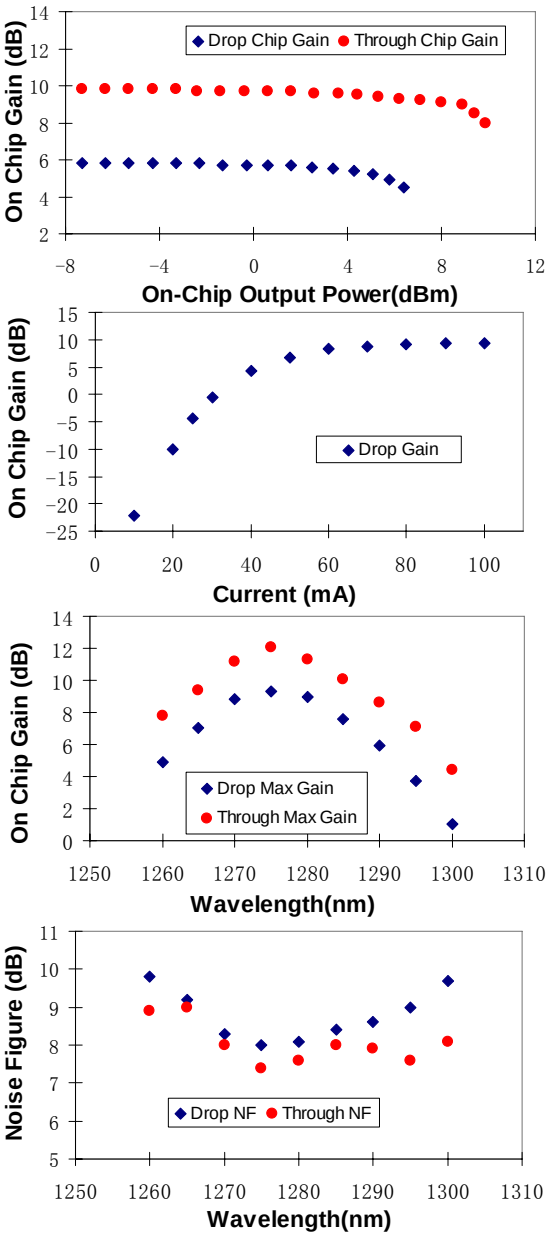


Fig. 4: (a) On-chip gain vs input power of the 2x2 switch at 1290nm, 100mA bias current. (b) Un-saturated on-chip gain vs drive current at 1270nm. (c) On-chip gain and (d) noise figure as the function of wavelength at a bias current of 100mA and -15dBm input power

Dynamic Operation

To investigate the dynamic operation of the 2x2 switch, a complete transmission and reception test-bed is constructed. The input into the switch is sourced by a single frequency laser of 1290nm wavelength, and is modulated at a data rate of 10Gb/s with a PRBS sequence of 2^{31}-1. As the current chip exhibits high polarization dependent gain (inexcess of 20dB), a polarization controller is used prior to the chip's input to ensure a TE input polarisation state. Isolators are used to prevent reflections into the SOAs while a filter is used before the receiver to filter the contributed amplified spontaneous noise from the amplifiers. A commercial multi-quantum

well SOA is placed before the receiver to provide the necessary power budget to perform the input power dynamics range (IPDR) measurement. The BER as a function of the switch input power for the 'through' and 'drop' paths is measured to characterise the dynamic performance.

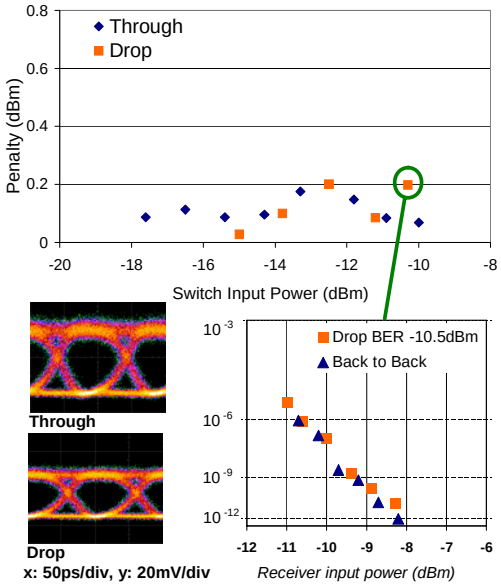


Fig. 5: Receiver power penalty as a function of switch input power along with representative BER curve and eye diagrams for the 'through' and 'drop' paths.

The results of the experiment are presented in Figure 5, showing the received power penalty as a function of input power into the 2x2 quantum SOA switch. These results show that this device has a potential of more than 8dB dynamic range for the through path and 5dB dynamic range for the drop path, for a power penalty of 0.2dB and below. The measurements are only performed for input powers from around -10dBm to -18dBm for the through path, and from -10dBm to -15dBm for the drop path, limited by the available power budget into the switch and receiver. The sensitivity of the receiver limits the measurements for lower input powers into the switch, whilst the input powers above -10dBm are limited by the output power of the tunable laser. The discrepancy between the minimum measurable input power of the through path and the drop path is due to the smaller on-chip gain attainable for the drop path. The gain difference between the through and drop path is around 2.8dB owing to the differences in splitting ratios of the TIR mirrors, as explained previously This accounts for the 3dB difference in dynamic range measurement for the two paths.

Discussion

High port-count switch architectures can be built up from cascades of 2x2 switches. For example, a 16x16 Benes network would comprise 56 2x2 switches arranged in 7 cascading stages. With a gain maximum of 12.1dB for the through path and 9.3dB for the drop path at a 100mA switching current, this 2x2 switch is able to provide enough power budget to overcome the losses from filters and isolators that may be required between switching stages. Large input power dynamic ranges relax the power margin for switch operation, giving the potential to support additional splitting stages prior to the switch fabric. This is important when additional intelligent control circuitry is built around the switch fabric. Examples of intelligent switch controls include the use of out-of band headers for switching time slots allocation [8], power equalization [9] and fault detection & restoration [10]. The low penalty operation suggests acceptable performance after cascades of the 2x2 switch [11][12].

Conclusion

This paper presents the design, fabrication, and system performance of a 2x2 quantum dot SOA based switch. Full, non-blocking 2x2 switching is achieved by biasing the appropriate QD SOAs in the switch. The maximum on-chip gain is 12.1dB, with power penalty of less than 0.2dB observed over an input power range of 8dB, and noise figure of 7.4dB. The high gain characteristics, low noise performance and extremely low penalty makes this novel integrated QD switch an ideal candidate for large scale high speed optical switching applications.

References

1 T Takiyama et al, IEEE Photon. Technol. Lett., Vol 17, p1614-p1616, No 8 August 2005
2 M. Sugawara et al J. Phys. D: Appl. Phys Vol 38, pp 2126-2134, 2005
3 T. Akiyama, et al, IEEE J of Quantum Electronics, vol.37, no.8pp.1059-1065, Aug 2001
4 A.V. Uskov, et al, IEEE Photon Technol Lett, vol.16, no.5pp. 1265- 1267, May 2004
5 S Liu et al, ECOC 2007, Th 4.5.6, Postdateline
6 X Hu et al, OFC 2007, accepted
7 K.A. Williams et al, IEEE J. of Selected Topics in Quantum Electron., vol.11, pp 78-85, 2005
8 T. Lin et al, OFC 2005, OWK5
9 ET Aw et al ECOC 2006, Th1.2.5.
10 ET Aw et al OFC 2007, accepted
11 O. Liboiron-Ladouceur, et al, J. of Lightwave Technology, vol.24, no.1 pp. 262- 270, Jan. 2006
12 S Liu et al, CLEO 2006, CTuM4

InP based Polarization Insensitive Tunable Duplexer and Integrated Reflective Transceiver

L. Xu, X.J.M. Leijtens, M.J.H. Sander-Jochem, T. de Vries, Y.S. Oei, P.J. van Veldhoven, R. Nötzel and M.K. Smit
COBRA Research Institute, Technische Universiteit Eindhoven
Postbus 513, 5600 MB Eindhoven, The Netherlands
l.xu@tue.nl

Abstract: *In this paper, a transceiver is presented which monolithically integrates a tunable wavelength duplexer, a reflective SOA (RSOA) and a detector. The first characterization shows that the tunable wavelength duplexer has less than 2 dB excess loss, better than $-15\,dB$ optical isolation between the upstream and downstream signals, and can be tuned efficiently by electro-optical ($V_\pi = 2.5\,V$) and thermal ($I_\pi = 15\,mA$) effects, independent of the input polarization state. A 750 µm long RSOA achieves around 20 dB on-chip gain, and a 30 µm long photodetector shows good responsivity of 0.4 A/W at $-2V$ bias voltage.*

Introduction

The single mode optic fiber has been adopted as the workhorse for the core and metropolitan networks, and is also increasingly penetrating the access domain to meet the rapidly growing bandwidth requirement for different communication services from the subscribers [1, 2]. The Dutch Broadband Photonics Access project is dedicated to providing the users with a congestion-free (first up to 1 Gbit/s, later up to 10 Gbit/s) optic fiber access network, whose capacity can be adapted according to the instantaneous and temporal user needs. In this access network, the local exchange, fig. 1, distributes two wavelengths spaced 500 GHz for each user, one for the downstream data, and the other one (CW) for later carrying the upstream data, while the spacing between the different channels in the network is 50 GHz. Thus, a transceiver (ONU) at the user site is needed not only to separate these two wavelengths, but also to detect the optical downstream data required by the user, and transmit the upstream data from the user. Since the wavelengths are decided by the local exchange, the transceiver has to be wavelength agnostic, which is why a reflective semiconductor amplifier is chosen as a transmitter. In this way, the wavelength specified by the local exchange could be amplified, modulated and reflected at the user site. Previous research [3] has demonstrated a transceiver up to 1.25 Gbit/s by using discrete components: a wavelength duplexer, a RSOA as transmitter, and a photodetector. However, due to the cost, it is not practical to deploy such a transceiver at the user site.

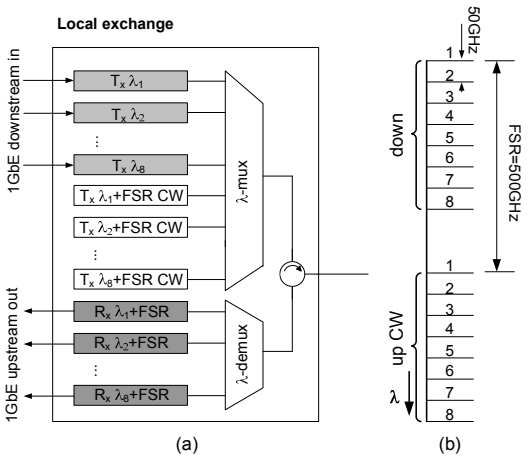


Figure 1: (a) Wavelength allocation scheme at the local exchange. (b) The spacing between the upstream and downstream channels is 500 GHz, while the spacing between the different channels in the network is 50 GHz.

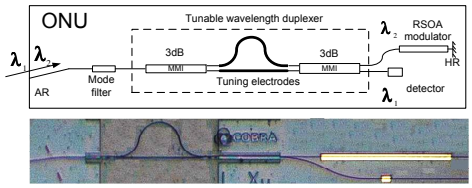


Figure 2: (Up) The layout of the integrated transceiver consisting of a wavelength duplexer, a reflective SOA modulator and a detector. (Below) The fabricated transceiver used for characterization.

In this paper, we present a reflective transceiver which monolithically integrates all above discrete components within one chip based on butt-joint regrowth on InP, fig. 2. The wavelength duplexer is a Mach-Zehnder (MZ) interferometer, composed of two 3 dB MMIs, connected by two waveguides with different length. The length difference between two MZ-arms is 85 µm, to match the 500 GHz band spacing between each upstream and downstream channel-pair. To maximize the transmission for the upstream/downstream

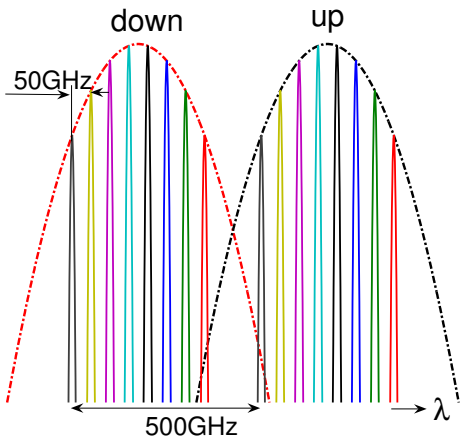


Figure 3: Incoming wavelengths from the local exchange with the passbands of the wavelength duplexer.

channel-pair selected by the local exchange, the wavelength duplexer of the transceiver has to be able to tune the proper wavelength, fig. 3. In order to tune this interferometer, both arms have been provided with 2 mm tuning electrodes. The RSOA is realized by applying a high reflectivity coating (HR) at one side of the chip. To avoid lasing, the other facet of the chip, where the light is coupled into and out of the device, is provided with an anti-reflection coating (AR). To further reduce any residual reflections, the input waveguide is placed at an angle with the chip facet, and a mode filter is inserted to filter first-order modes.

The device works as follows. Two wavelengths (λ_1 and λ_2) come from the network into the transceiver from the left side. They are spatially separated by the tunable wavelength duplexer and guided to the photodetector (λ_1) and the reflective SOA modulator (λ_2). The downstream data, carried by λ_1, is detected by the photodetector, while λ_2 is a continuous wave (CW) light and is guided to the RSOA where it is modulated, amplified and reflected back to the network. Since the polarization state of the incoming light varies with time, the device should be polarization insensitive.

Below, we present the fabrication and measurement results of the transceiver. The tunable duplexer was tuned by both the electro-optic effect and the thermal effect for TE and TM polarization. The saturation power of the RSOA was measured at different injection currents, and the gain of the RSOA was obtained. The dependence of the photodetector responsivity on the wavelength and on the input optical power were investigated.

Fabrication and Characterization

The devices were fabricated in material grown on an N-type InP substrate by three-step low pressure metal-

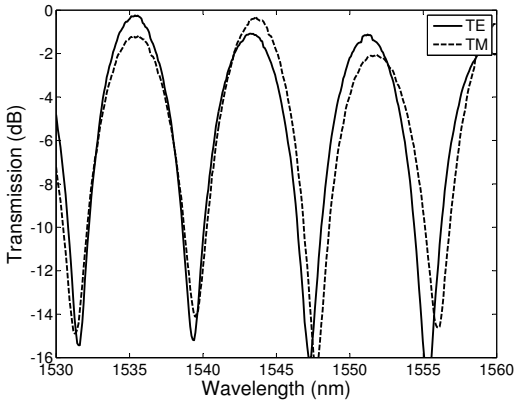


Figure 4: A polarization insensitive duplexer with 500 GHz channel spacing. Shown is the measured transmission as a function of the wavelengths.

organic-vapor-phase epitaxy (MOVPE). The first epitaxy finished with a 120 nm thick SOA active InGaAsP layer (Q1.55, $\lambda_{gap} = 1.55\,\mu$m), embedded between two quaternary confinement layers (Q1.25) with different doping levels, covered by a 200 nm thick p-InP layer. Next, the active sections were defined by lithography and reactive ion etching (RIE) using a SiN_x layer as etching mask. In the second epitaxy step, a n-Q1.25 InGaAsP layer and a 200 nm non-intentionally-doped (n.i.d) InP buffer layer were selectively grown for the passive sections with the SiN_x mask protecting the active sections[4]. In the third epitaxy step, the p-doped InP cladding layers with graded doping level and the p-InGaAs contact layer were grown with a total thickness of 1300 nm.

All the waveguides were fabricated by RIE. Polyimide was spun for passivation and planarization. By etching back the polyimide, the p-InGaAs contact layer was exposed and Ti/Pt/Au metal layers were evaporated to form the electrodes on the top and the ground (n-InP) at the backside. After annealing and cleaving, the chip was soldered on a copper chuck with a Peltier cooler for the characterization.

For measuring the transmission of the duplexer, we used the spontaneous emission spectrum from an EDFA to couple light into the device. The spectral response was recorded with an optical spectrum analyzer. The result of the measurement is shown in fig. 4. The vertical axis shows the transmission of the duplexer, normalized to a shallowly etched straight waveguide. From the figure, we can see that the excess loss is less than 2 dB; the isolation between two datastreams is better than 15 dB; the peak transmission is insensitive to the polarization state of the light.

When a voltage is applied in reverse bias over the 2 mm long electrode on one of the MZ-arms, a change in the effective refractive index (N_{eff}) is induced by the electro-optical effects [5]. The measured values are shown in fig. 5, from which we also see a polarization insensitivity over a 5 V range. According to

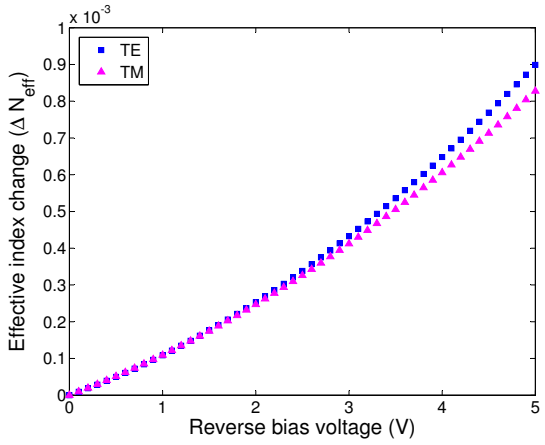


Figure 5: The extracted effective index change due to electro-optical effects as a function of the reverse bias voltage, for TE and TM polarization.

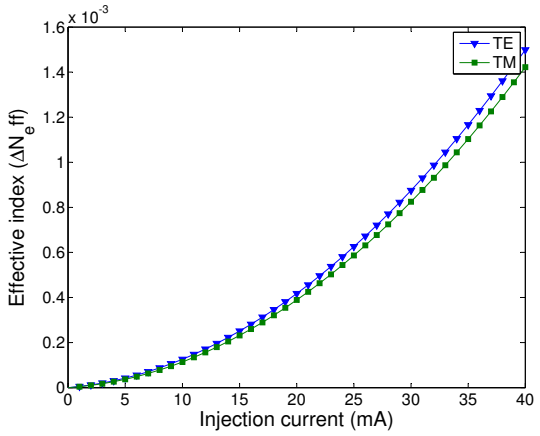


Figure 6: The extracted effective index change due to thermal effect as a function of the injection current for TE and TM polarization.

the equation $\Delta\phi = \frac{2\pi}{\lambda}\Delta N_{\text{eff}} L$, a value for $V_\pi \simeq 2.5\,\text{V}$ is obtained, for both TE and TM polarization. The polarization insensitive tuning with high efficiency under electro-optical effects are mainly due to the carrier induced effects [6], the high field confinement due to the deep etch, and a thin depletion buffer layer above the waveguide film [7].

Instead of applying a tuning voltage, we can also inject a current through the electrode, to generate heat to change the refractive index. The result, fig. 6, shows that the thermal tuning is polarization insensitive, and the tuning current for obtaining π phase shift, I_π, is about 15 mA for a 2 mm long gold electrode. The measurement results show that the refractive index change is linear with the injected electric power (i.e. quadratic with the injected current).

We measured the saturation power and gain of the RSOA for a device with 750 μm length. Fig. 7 shows the fiber-fiber gain for different injections currents. At the highest injection current (80 mA), the gain starts to saturate at an injection power level of -15 dBm, shifting to -10 dBm at lower injection currents. The

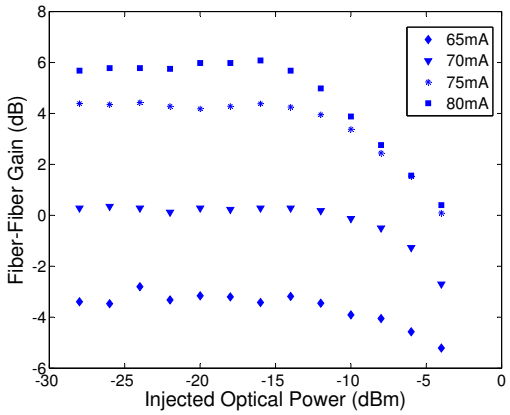


Figure 7: Fiber-fiber gain as a function of the input optical power for $\lambda = 1524\,\text{nm}$ at different injection currents.

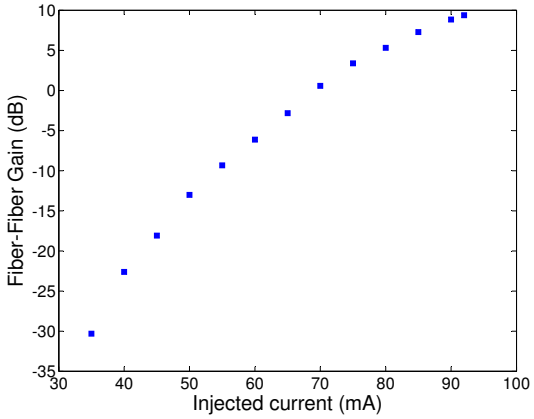


Figure 8: Small signal fiber-fiber gain (before saturation) as a function of the injection current for $\lambda = 1524\,\text{nm}$. The input optical power is $-18\,\text{dBm}$.

fiber-fiber gain for a fixed input injection power of -18 dBm is shown in fig. 8 . Near the peak wavelength (1524 nm) a gain of more than 8 dB can be obtained, which is sufficient for our application. The maximum injection current is limited by the the lasing threshold of the RSOA, and the measured threshold current is about 100 mA. We believe that this can be improved by further removing residual reflections.

The modulation speed of the RSOA is limited mostly by the carrier lifetime, which is shortened with higher injection current. For an InP based SOA the carrier lifetime is on the order of hundreds of picoseconds, thus corresponding to GHz modulation rates. Koren et al. [8] have measured the modulation bandwidth of a single SOA at different injection currents, up to 3 GHz when SOA was saturated.

The photodetector has the same layer structure as the RSOA, but works under reverse bias. We fabricated detectors with lengths ranging from 30 μm to 60 μm. Here we present the measurements of the 30 μm-long and 2 μm-wide detector. The dark current of the photodetector is less than 50 nA at -5 V reverse bias voltage. The measured responsivity, shown in fig. 9, is ~0.4 A/W at -2 V bias. This corresponds to ~90% in-

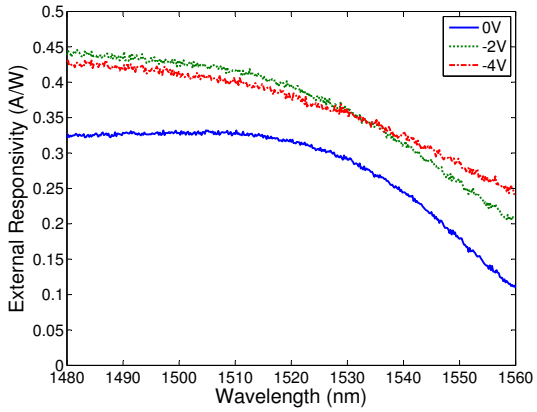


Figure 9: Responsivity of 30 μm long detector as a function of the wavelength at difference reverse bias voltages.

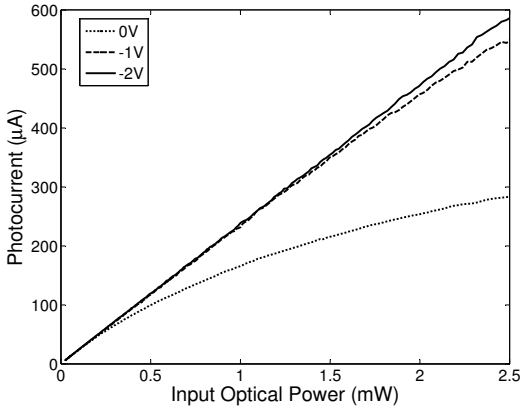


Figure 10: The photocurrent as a function of the input optical power input from the angled input side for a 30 μm long photodetector at $\lambda_{peak} = 1515.18$ nm.

ternal quantum efficiency if the fiber chip coupling loss is estimated at -4.3 dB. The photocurrent increases linearly with the input optical power up to more than 4 dBm (2.5 mW) when the photodetector is reversely biased, shown in fig. 10. The estimated bandwidth for this detector is up to 25 GHz based on RC time and carrier-transit time calculation.

Conclusion

In this paper, we reported a monolithically integrated transceiver that consists of a polarization insensitive tunable duplexer, a RSOA modulator and a photodetector. The tunable duplexer has less than 2 dB excess loss and gives better than 15 dB isolation between the downstream and upstream data channels. Polarization insensitive tuning is realized by employing both the electro-optic effects ($V_\pi \approx 2.5V$) and the thermal effect ($I_\pi = 15$ mA). The transceiver obtained more than 8 dB fiber-fiber gain at 90 mA injection current, and a good responsivity of ~ 0.4 A/W for a 30 μm-long photodetector, at -2 V reverse bias.

Acknowledgment

This work is funded by the Dutch National Broadband Photonics Access project and by the Netherlands Organization for Scientific Research (NWO) through the "NRC Photonics" grant.

References

[1] T. Koonen, "Fiber to the home/fiber to the premises: What,where,and when?" *Proceedings of the IEEE*, vol. 94, no. 5, pp. 911–934, 2006.

[2] H. Shinohara, "Broadband access in Japan: rapidly growing FTTH market," *IEEE Comm. Magazine*, vol. 43, no. 9, pp. 72–78, Sept. 2005.

[3] J. Prat, C. Arellano, V. Polo, and C. Bock, "Optical network unit based on a bidirectional reflective semiconductor optical amplifier for fiber-to-the-home networks," *IEEE Photon. Technol. Lett.*, vol. 17, no. 1, pp. 250–252, Jan. 2005.

[4] Y. Barbarin, E. Bente, C. Marquet, E. Lecère, T. de Vries, P. van Veldhoven, Y. Oei, R. Nötzel, M. Smit, and J. Binsma, "Butt-joint reflectivity and loss in InGaAsP/InP waveguides," in *Proc. 12th Eur. Conf. on Int. Opt. (ECIO '05)*. Grenoble, France, April 6–8 2005, pp. 406–409.

[5] H. Zappe, *Introduction to Semiconductor Integrated Optics*. Boston: Artech House Publishers, 1995, iSBN 0-089006-789-9.

[6] J. Vinchant, J. Cavaillès, M. Erman, P. Jarry, and M. Renaud, "InP/InGaAsP guided-wave phase modulators based on carrier-induced effects: theory and experiment," *J. Lightwave Technol.*, vol. 10, no. 1, pp. 63–69, 1992.

[7] D. Maat, "InP-based integrated MZI switches for optical communications," Ph.D. dissertation, Delft University of Technology, Delft, The Netherlands, 2001, iSBN 90-9014700-4.

[8] U. Koren, B. Miller, M. Young, T. Koch, R. Jopson, A. Gnauck, J. Evankow, and M. Chien, "High frequency modulation of strained layer multiple quantum well optical amplifiers," *Electron. Lett.*, vol. 27, no. 1, pp. 62–64, Jan. 1991.

A compact passive polarization converter optimized for active-passive integration on InP/InGaAsP

L.M. Augustin, J.J.G.M. van der Tol, E.-J. Geluk, M.K. Smit
COBRA Research Institute, Technische Universiteit Eindhoven
Postbus 513, 5600 MB Eindhoven, The Netherlands
l.m.augustin@tue.nl

Abstract: *An improved design for an integrated polarization converter is presented. The device is specially suited for monolithic integration with active and passive components on InP/InGaAsP. A novel simplified fabrication process is shown. Measured polarization conversion > 97% agrees well with simulations.*

Introduction

Polarization handling is of ever greater importance in modern telecommunications networks. First of all a lot of components in the network are highly polarization dependent, furthermore polarization mode dispersion can degrade the transmission in an optical fiber. On the other hand, the polarization can be employed in e.g. polarization multiplexing, and polarization based filtering. In all these cases, polarization converters (PC) are key-elements.

Passive polarization converters that are able to be integrated with both active and passive components are preferred. Polarization conversion can be obtained by periodically loaded waveguide sections [1, 2, 3], by using integrated bends [4], or by using a single waveguide section with a vertical and a slanted sidewall [5, 6, 7].

One problem of these designs is the difficulty to integrate them with passive and specifically active components. The polarization converters and active components (such as semiconductor optical amplifiers (SOAs) and phaseshifters [8]) can be made in the same layerstack, but the optimal thickness of the topcladding differs by more than 1 µm. For polarization converters a large birefringence is needed: hence a thin topcladding is preferred (typically smaller than 300 nm); for SOAs and electro-optic phaseshifters, a thick topcladding (typically 1500 nm) is needed below the contact to avoid optical losses in the contactlayer.

This is clarified in Fig. 1: an SOA, phaseshifter and a conventional polarization converter are shown. Critical lithographical definition is not possible with these height differences which complicates processing and integration of these devices.

A new design is proposed as is shown in the rightmost picture in Fig. 1. This new proposed design uses the same topcladding as an active device and can be easily integrated with the other components. The birefringence with the thicker cladding is only slightly reduced with respect to the thinner cladding. Hence the increase in length for this design is less than 40µm.

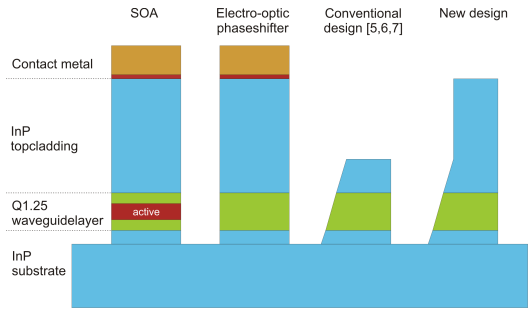


Fig. 1: Cross section of active devices (SOA, phaseshifter), a conventional PC and the new design.

Design

The layer stack consists of an InP substrate, a 500 nm InGaAsP[Q(1.25µm)] waveguide layer and a 1500 nm InP topcladding. Simulations with the commercial waveguide solver FIMMWAVE predict an optimal conversion of TE to TM and vice versa larger than 99% for a width of 0.94 µm and a length of 141 µm. A conversion above 95% is expected for a width deviation of 100 nm.

Deviations from the calculated width and length are expected, because the refractive indices used in the simulations are not accurately known for these materials.

The total device contains an asymmetric waveguide as the converter section, 1.2 µm wide deep input and output waveguides, coupled to 3 µm wide shallow waveguides via 75 µm long tapers (Fig. 2). At the interface of the input waveguides and the polarization converter section a small ridge is present, perpendicular to the waveguide. This is needed to prevent etching of the input waveguide in the wet etch for the slanted sidewall.

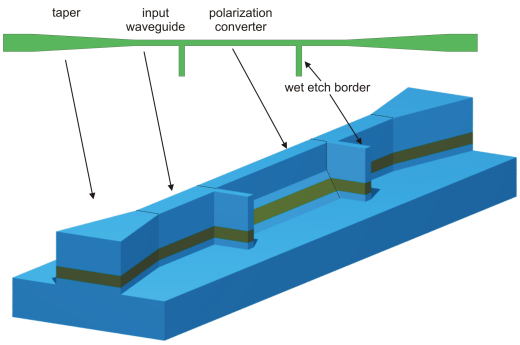


Fig. 2: Overview of the polarization converter including in- and output waveguides and tapers.

Fabrication

The polarization converters have strict tolerances, so the converter sections will be defined using Electron Beam Lithography (EBL). EBL is not suited to write large circuits, therefore all other waveguides will be defined using standard optical lithography. The EBL written parts have to be aligned to the optical waveguides. This can be done by the writefields with alignment marks as shown in Fig. 3.

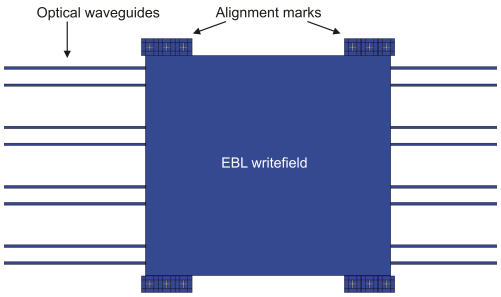


Fig. 3: Optical waveguides and EBL writefields including EBL alignment marks.

The processing scheme of the polarization converter is shown in Fig. 4.

a. First the waveguides and writefields for the EBL, including alignment marks (Fig. 3), are defined optically into a Silicon Nitride (SiN_x) mask. Next the polarization converters are defined in Ti on top of the SiN_x using EBL and a lift-off process.

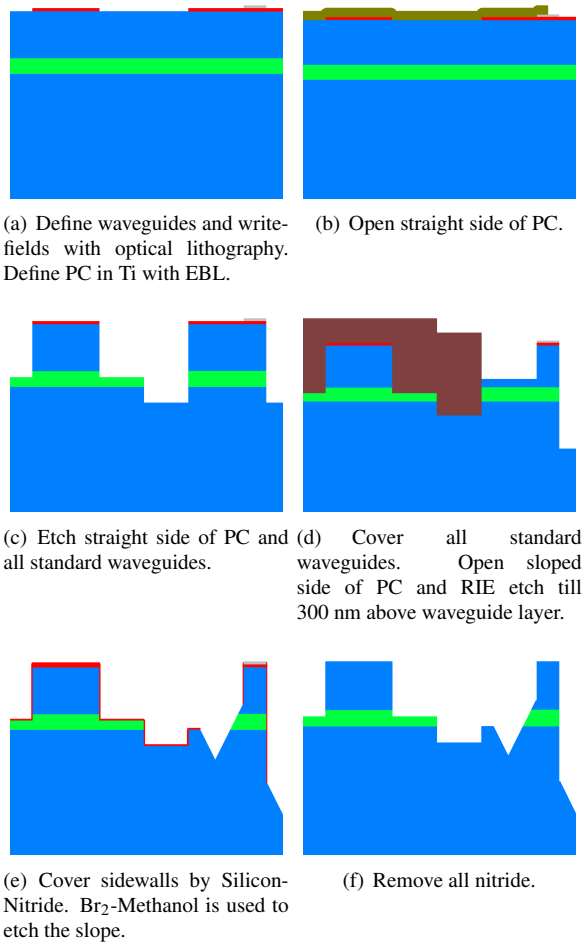
b. Before etching any waveguide, the second EBL step is done to open the straight side of the PC

c. Now the nitride at the straight side of PC is opened. The shallow waveguides and the straight side of the PC are etched with CH_4/H_2 Reactive Ion Etching (RIE).

d. All shallow waveguides are covered with resist, the PC area is opened with a non-critical optical lithography step. The SiN_x at the sloped side of the PC can be openend and RIE etched until 300 nm above the waveguide layer, while etching this side, the straight side is etched even deeper, well below the waveguide layer.

e. Silicon Nitride is deposited on the whole sample and the shallow waveguides are again covered with resist. The SiN_x is etched back using CHF_3 RIE. Because of the directional etching, the etched sidewalls stay covered with SiN_x, which serves as a mask for wet etching.
Br_2-Methanol is used to etch the slope. This etchant etches both InP and InGaAsP with an angle of 54° with respect to the surface.

f. Finally all the nitride is removed using an HF solution.



(a) Define waveguides and writefields with optical lithography. Define PC in Ti with EBL.

(b) Open straight side of PC.

(c) Etch straight side of PC and all standard waveguides.

(d) Cover all standard waveguides. Open sloped side of PC and RIE etch till 300 nm above waveguide layer.

(e) Cover sidewalls by Silicon-Nitride. Br_2-Methanol is used to etch the slope.

(f) Remove all nitride.

Fig. 4: Processing scheme of the integrated Polarization converter.

The fabricated converters are shown in Fig. 5. From these figures it is clear that there is an underetch at the shallow side (the sloped side), but there is no underetch at the deep side. This is most probably caused by stress in the masking material during the wet-etching. The influence of this additional underetch on the conversion performance of the device will be very small as can be understood from Fig. 6. The field is located in the InGaAsP layer, below the sloped side. The width of the polarization converter at the position of the waveguide-layer is not strongly affected and thus the tilt of the modes is still correct. However, because the top of the fieldprofile is influenced, the coupling losses will be increased with respect to the design.

Measurements

The polarization converters are measured using a setup as shown in Fig. 7. The device is excited using an EDFA with a bandpass filter set to 1555 nm as a source. The filter has a 2 nm bandwidth, large enough to prevent Fabry-Pérot resonances. A polarizer at the input of the chip is used to select the input polarization. At the output another polarizer selects the polarization that is measured using the photodiode and the lock-in amplifier.

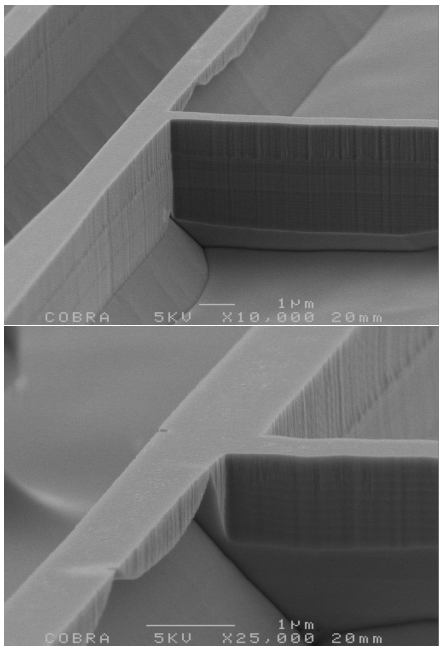


Fig. 5: SEM photographs of the integrated Polarization converter. Top: transition of a straight waveguide to the polarization converter. Bottom: reverse transition.

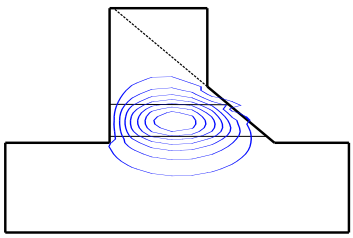


Fig. 6: Field profile of a mode in the polarization converter, the structure is indicated by the solid line, the dashed line shows the etched topcladding caused by the underetch.

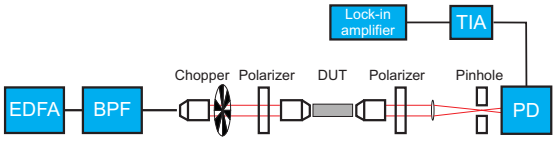


Fig. 7: Setup used for characterization of the polarization converter. BPF: Bandpass filter, PD: Photodiode, TIA: Trans impedance amplifier

The power in both polarizations at the output is measured for both TE and TM polarized light at the input. The conversion is defined as the fraction of the converted polarization in the output power. The conversion C for the two polarizations (i, j = TE, TM) is determined from the following equations:

$$P_{ij} = \alpha_i \alpha_j \, C \, P_j \; ; \quad i \neq j \tag{1}$$

$$P_{ij} = \alpha_i \alpha_j \, (1 - C) \, P_j \; ; \quad i = j \tag{2}$$

where P_j is the input power with polarization j; P_{ij} is the output power in polarization i when the input polarization is j; $\alpha_{i,j}$ are the losses for the two polarizations in the input and output waveguides.
By solving these equations, the propagation losses in the input and the output waveguides for the two polarizations are eliminated and the conversion C is obtained:

$$C = \frac{\sqrt{x}}{1 + \sqrt{x}} \tag{3}$$

where

$$x = \frac{P_{ij} P_{ji}}{P_{ii} P_{jj}} \; ; \quad i \neq j \tag{4}$$

This conversion is plotted as a function of width and length in Fig. 8.

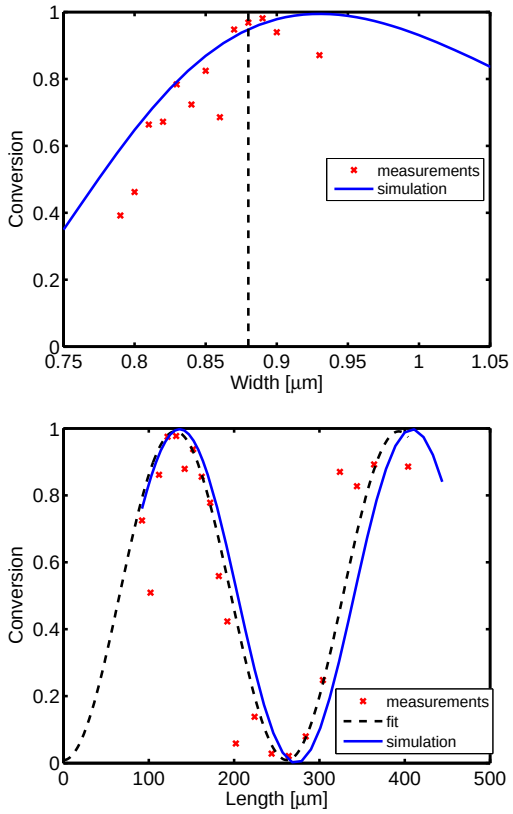


Fig. 8: Measured conversion as a function of width(top) and length(bottom).

The maximum conversion from TE to TM and vice versa occurs at 131 µm length, corresponding to the

half beat length between the modes of the converter section, and back to zero at the full beat length (262 μm). The maximum conversion, for this device is 97.5%.
The large scattering on the measured values is caused by the underetch, this not uniform throughout the whole device. Hence a non-uniform width is obtained along the converter section.
The losses of the polarization converter including input and output tapers are measured to be 2.4±0.3 dB for TE and 2.6 ± 0.3 dB for TM. This value is higher than simulated (less than 0.5 dB), most probably caused by the non-optimal coupling of the waveguide and the converter because of the underetch. This can be optimized by using a more controlled wet etch.

Conclusion

A new type of polarization converter is shown, specially suited for easy integration with other active and passive devices. The device is fabricated and measured. The polarization converter shows a maximum conversion larger than 97%.

Acknowledgments

This research is carried out in the framework of the IST-MUFINS project. The European Commission is gratefully acknowledged for financial support. The Centre for Integrated Photonics in Ipswich, UK is kindly acknowledged for supplying the wafer for this experiment.

References

[1] J.J.G.M. van der Tol et al, "Realization of a short integrated optic passive polarization converter," *IEEE Photon. Technol. Lett.*, vol. 7, pp. 893–895, Aug. 1995.

[2] Y. Shani et al, "Polarization rotation in asymmetric periodic loaded rib waveguides," *Appl. Phys. Lett.*, vol. 59, pp. 1278–1280, Sept. 1991.

[3] H. Heidrich et al, "Passive mode converter with a periodically tilted InP/GaInAsP rib waveguide," *IEEE Photon. Technol. Lett.*, vol. 4, pp. 34–36, Jan. 1992.

[4] C. van Dam et al, "Novel compact polarization convertors based on ultra short bends," *IEEE Photon. Technol. Lett.*, vol. 8, pp. 1346–1348, Oct. 1996.

[5] F.H. Groen et al, "Compact polarisation converter on InP/InGaAsP using an asymmetrical waveguide," in *Proc. 11th Eur. Conf. on Int. Opt. (ECIO '03)*, pp. 141–144, Prague, Czech Republic, April 2–4 2003.

[6] H. El-Refaei et al, "Slanted-rib waveguide InGaAsP-InP polarization converters," *J. Lightwave Technol.*, vol. 22, pp. 1352–1357, May 2004.

[7] U. Khalique et al, "Ultrashort polarization converter on InP/InGaAsP fabricated by optical lithography," in *Technical Digest Integr. Photon. Res. and Apps. (IPRA '05)*, p. IWA3, San Diego, USA, Apr. 11–Apr. 13 2005.

[8] J.J.M. Binsma et al, "InP-based photonic integration technology," in *Technical Digest Integr. Photon. Res. (IPR '04)*, p. IFB1, San Francisco, USA, Jun. 30–Jul. 2 2004. Invited paper.

Carrier-Depletion-Type Multiple Quantum Well Optical Phase Modulators Operating at the 1.55 μm Wavelength Range

Hideki Ohe[1, 3], Hiromasa Shimizu[2, 3] and Yoshiaki Nakano[1, 3]
1) Research Center for Advanced Science and Technology, University of Tokyo, Japan
2) Dept. of Elect. Eng ., Tokyo University of Agriculture and Technology, 3) JST-SORST
hidekiooe@hotaka.t.u-tokyo.ac.jp

Abstract: *We fabricated a carrier-depletion-type optical phase modulator with an InGaAlAs MQW and observed a large modulation efficiency of 87 degree/mm/V without any intensity modulation at the wavelength of 1.58 μm. The modulator has a smaller wavelength dependence than that of the QCSE based devices, and has an almost linear bias dependence. Carrier-depletion-type optical phase modulators are attractive for WDM optical transmission systems and optical signal processing.*

Introduction

Optical cross connects in the future optical networks require optical space switches driven by electronic signals [1]. For long-haul optical transmission systems with bit rates above 10 Gbit/s, Mach-Zehnder modulators are advantageous from their low-chirp characteristics [2]. Most of these optical switching devices utilize phase modulation effect based on the quantum-confined Stark effect (QCSE) under a reverse biased condition, or the carrier injection (plasma effect, band-filling effect) under a forward biased condition. For carrier-injection-type devices, switching time is limited to several nano-seconds by the carrier lifetime, while QCSE based devices have a large wavelength dependence. On the other hand, phase modulators based on a carrier depletion effect [3] are also known. In carrier-depletion-type modulators, depletion of carriers in a reverse-biased pn junction causes a large index change in conjunction with a linear and a quadratic electrooptic effect, and a large modulation efficiency of 96 degree/mm/V at the wavelength of 1.06 μm has been reported [4]. Although much smaller wavelength dependence than QCSE based devices is expected in the carrier-depletion-type modulators, their wavelength dependence hasn't been investigated in detail and there is only a limited number of reports on the 1.55 μm operations [5].

We fabricated carrier-depletion-type InGaAlAs multiple-quantum well (MQW) phase modulators by metal-organic vapour-phase epitaxy (MOVPE) and investigated their modulation characteristics at the 1.55 μm wavelength range under a reverse-biased condition. Efficient phase modulation of 87 degree/mm/V was observed at 1.58 μm and smaller wavelength dependence than QCSE based phase modulators was observed.

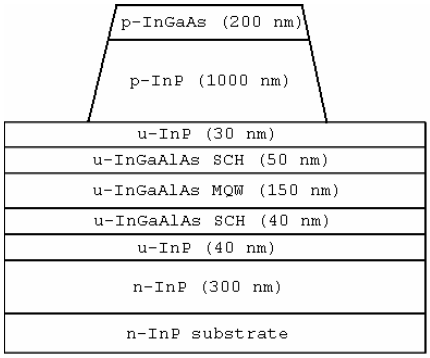


Fig. 1: Schematic illustration of the fabricated InGaAlAs MQW phase modulator with a shallow ridge waveguide structure.

Device Fabrications

Fig. 1 shows the schematic structure of the fabricated modulator. It consists of 10 sets of lattice-matched InGaAlAs MQW (9 nm InGaAlAs wells and 5 nm InAlAs barriers) and has 40 and 50 nm-thick InGaAlAs SCH layers. The overall structure was grown by MOVPE on an n^+InP(100) substrate. The MQW and SCH layers were not intentionally doped, but are of n-type due to residual impurities (mostly oxygen). The impurity density was measured to be $N_D \sim 4 \times 10^{16}$ cm^{-3} by a C-V method. As a result, the total structure constitutes a P-n-N structure in which the pn junction is formed between the p-clad and the upper-SCH layers. Absorption edge of the MQW was measured to be at 1430 nm by the photocurrent spectroscopy. 2 μm wide shallow-ridge waveguide phase modulators were fabricated by wet etching along the [0-11] crystal orientation.

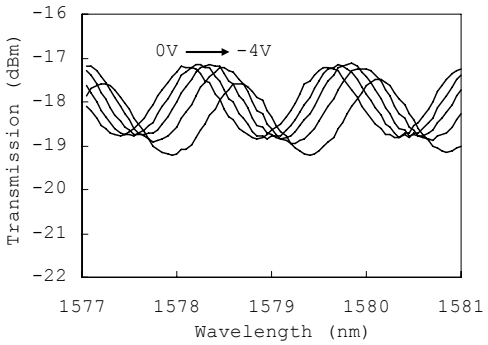


Fig. 2: Measured Fabry-Perot resonance spectra of the 230 μm-long phase modulator at 1580 nm under reverse bias voltages from 0 to -4V for TE mode.

Characterizations

Modulation characteristics of the fabricated devices were measured by the Fabry-Perot method. In this method, cleaved facets of the waveguide form a Fabry-Perot resonator, and the transmission of the resonator was measured as a function of the wavelength. Absorption coefficient was determined from the peak to valley ratio of the transmission spectra, and phase shift was determined from the peak shift $\Delta\lambda$. Fig. 2 shows the measured Fabry-Perot resonance spectra around 1580 nm for TE mode under reverse bias voltages from 0V to -4V. A positive refractive index change was observed without any intensity modulation up to -3V. Fig. 3 shows the phase shift of the modulator determined from the Fabry-Perot spectra. Large phase modulation was observed from +0.5V to -1V, which shows an almost linear bias dependence.

For a comparison, an undoped InGaAsP MQW phase modulator was also measured. It consists of 10 sets of InGaAsP MQW (7 nm InGaAsP wells and 10 nm InGaAsP barriers) with the absorption edge of 1490 nm, and has almost the same structure as Fig. 1. The residual impurity density in the MQW was measured to be $N_A \sim 1\times10^{16}cm^{-3}$. The results are plotted in Fig. 4. On the contrary to the InGaAlAs MQW with a higher impurity density, an almost quadratic phase shift due to the QCSE is observed throughout the measured bias range.

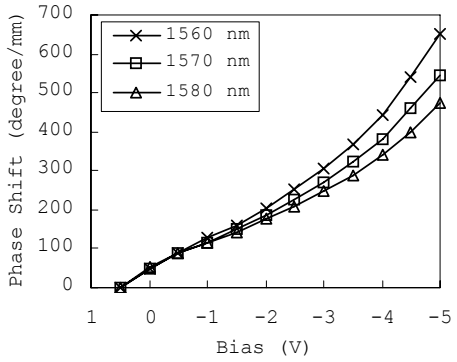


Fig. 3: Measured phase modulation characteristics of the InGaAlAs MQW modulator for TE-mode.

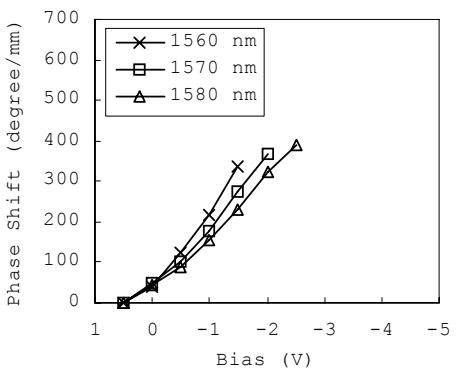


Fig. 4: Measured phase modulation characteristics of the InGaAsP MQW modulator for TE-mode.

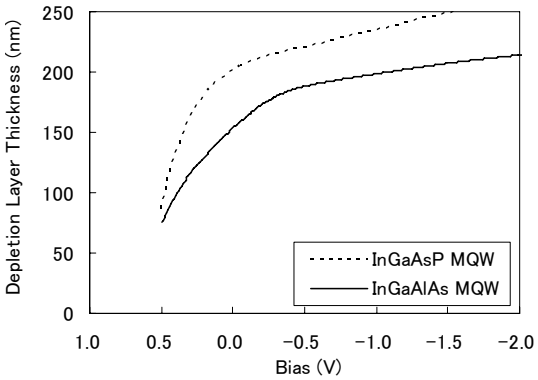


Fig. 5: Measured depletion layer thicknesses of the InGaAsP and InGaAlAs MQWs as a function of the bias voltage.

The reverse bias dependence of the depletion layer thicknesses was determined by measuring the junction capacitances. The results are plotted in Fig. 5 both for the InGaAsP and InGaAlAs MQWs. It shows that for the InGaAlAs MQW with a high impurity density, most of the MQW layer is out of the depletion layer at a bias voltage of +0.5V and the MQW layer is gradually depleted by applying a reverse bias from +0.5V to -0.5V. On the other hand, for the InGaAsP MQW, the MQW is rapidly depleted by applying a reverse bias.

Fig. 6 shows the wavelength dependence of the phase modulation efficiency of the InGaAlAs MQW modulator at 0V for both TE and TM modes. Wavelength dependence is small especially at the longer detuning wavelengths and a large phase modulation efficiency of 87 degree/mm/V was observed at 1580 nm for TE mode.

Fig. 7 shows the wavelength dependence of the modulation efficiencies under reverse bias voltages of 0V and -2V for TE mode. At -2V where the MQW is completely depleted and the QCSE is dominant, wavelength dependence is fairly large and the modulation efficiency quickly drops as the operating wavelength detunes from the absorption edge.

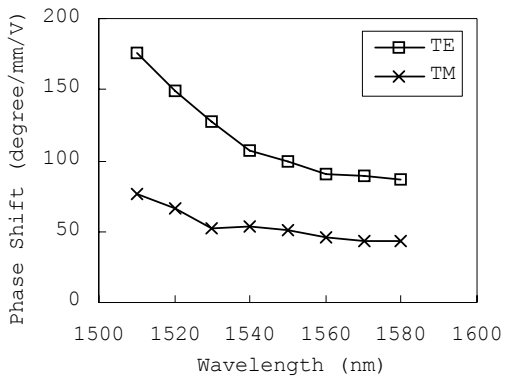


Fig. 6: Wavelength dependence of the phase modulation efficiency of the InGaAlAs MQW modulator at 0V for TE- and TM-mode.

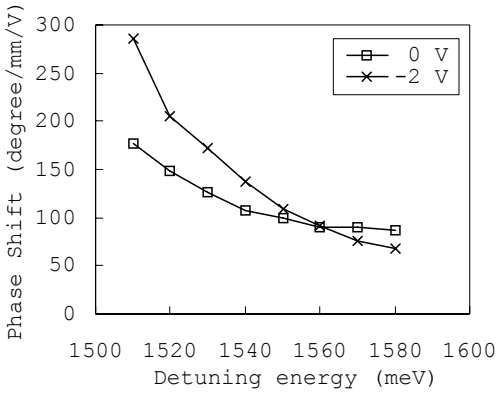


Fig. 7: Wavelength dependence of the modulation efficiency of the InGaAlAs MQW modulator at different bias voltages (0 and -2V) for TE-mode.

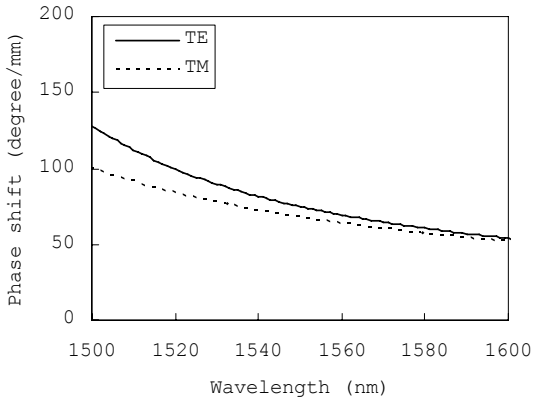


Fig. 9: Calculated phase shift due to the carrier depletion effect in the InGaAlAs MQW for TE and TM mode.

Discussion

The large phase shift observed in the InGaAlAs MQW around 0V is mainly attributed to the carrier depletion effect. For a pn junction with an n-type MQW, part of the MQW is out of the depletion layer at 0V and electrons are accumulated in the conduction subbands of the MQW as shown in Fig. 8 (a). When a reverse bias is applied, the depletion layer thickness increases and the carriers are swept out as shown in Fig. 8 (b). This causes a large positive index change of the MQW by the band-filling effect.

In order to estimate the magnitude of the phase modulation due to the carrier depletion effect, numerical calculations were performed. Here, only the band-filling effect of the MQW was considered. The calculated results are shown in Fig. 9. We assumed that 5 sets of the InGaAlAs MQW (10 sets) are depleted by applying a reverse bias, as schematically shown in Fig. 8. Compared with the measured phase shift shown in Fig. 6, the calculation results are almost consistent with the measurement results for TM mode, whereas for TE mode, measured magnitude of the phase shift and wavelength dependence is larger than those of the calculation. These disagreements are mainly due to the addition of the polarization dependent Pockels effect and some contributions from the QCSE to the actual device. Although carrier effect itself is an almost polarization independent effect, these additional effects render the phase modulator to be polarization dependent. For a polarization independent operation, adoption of a tensile strained MQW is necessary.

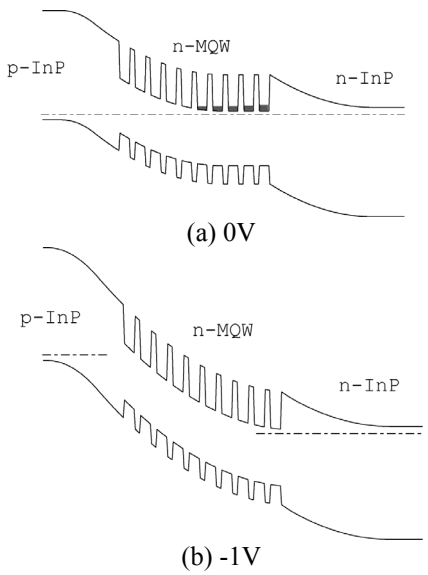
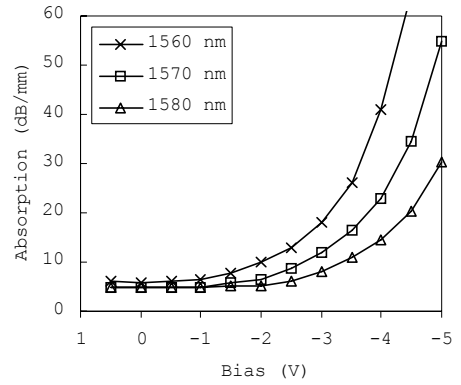


Fig. 8: Schematic illustration of a carrier depletion effect in a pn junction with a shallowly n-doped MQW. Quasi-Fermi levels are depicted by dashed lines.

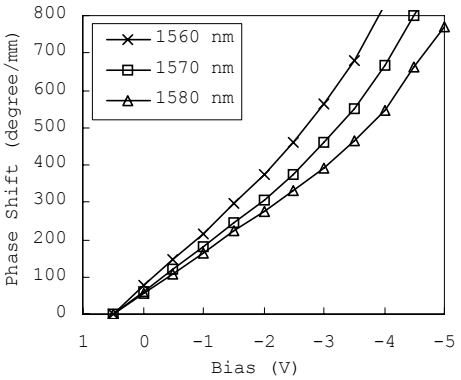
Such polarization insensitive and small wavelength dependent phase modulators are attractive for integrated optical switches with nano-second switching times, which are suitable for optical cross connects and other optical devices for future photonic networks. Carrier-depletion-type optical switches require no current injection, hence no static power consumption is needed.

In the device fabricated, however, carrier depletion effect is observed only in a limited bias range (+0.5V to -1V) because of the relatively low impurity density. Maximum refractive index change will be enhanced to $\Delta n \sim 0.001$ by increasing the impurity density in the MQW. Fig. 10 shows the modulation characteristics of another InGaAlAs MQW modulator (9 nm InGaAlAs well, 5 nm InAlAs barrier, λ_{PL} = 1465 nm) with a higher donor density of $N_D \sim 9 \times 10^{16} cm^{-3}$. As the impurity density is increased, the reverse bias voltage at which the MQW is completely depleted is higher and is about -2V. Consequently, an almost linear phase shift of 109 degree/mm/V without any intensity modulation was observed up to -2V at the wavelength of 1580 nm.

Such linear phase modulation characteristics are advantageous for low-chirp push-pull driven Mach-Zehnder modulators, because nonlinear phase shift results in positive chirpings and bias voltage dependent modulations.



(a) Absorption coefficient



(b) Phase shift

Fig. 10: Modulation characteristics of a highly doped InGaAlAs MQW phase modulator for TE mode.

Conclusion

Carrier-depletion-type MQW optical phase modulators which operate in the 1.55 μm wavelength range were fabricated and a highly efficient phase modulation of 87 degree/mm/V without any intensity modulation was observed at the wavelength 150 nm detuned from the absorption edge. It was shown that these modulators have a small wavelength dependence and a linear bias dependence, which is difficult to be realized in the QCSE based phase modulators. Although there is a trade-off between the modulation efficiency and the frequency bandwidth, carrier-depletion-type phase modulators are useful for optical integrated circuits for future optical networks.

References

1 C. G. P. Herben et al, IEEE Photon. Technol. Lett., no. 12, p. 1599, 1999.
2 S. Akiyama et al, Electron. Lett., no. 1, p. 40, 2005.
3 A. Alping et al, Appl. Phys. Lett., no. 19, 1986.
4 J. G. Mendoza-Alvarez et al, J. Lightwave Technol., no. 6, p. 793, 1988.
5 H. S. Park et al, Jpn. J. Appl. Phys., p. 4378, 2003.

Low loss, high contrast optical waveguides based on CMOS compatible LPCVD processing

R.G.Heideman (1), D. Geuzebroek (1), A. Leinse (1), A. Melloni (2), F. Morichetti (2), C. Roeloffzen (3), A. Meijerink (3), L. Zhuang (3), W. van Etten (3), E. Klein (4) and A. Driessen (4).

1) LioniX bv, P.O. Box 456, 7500 AH Enschede, the Netherlands
2) Dipartimento di Electronica e Informazione, Politechnico di Milano, Via Ponzio 34/5, 20133 Milano, Italy
3) Telecommunication Engineering group, Faculty of Electrical Engineering, MCS, University of Twente, P.O.Box 217, 7500 AE, Enschede, the Netherlands
4) Integrated Optical Micro Systems, MESA$^+$ Research Institute, University of Twente, P.O. Box 217, 7500 AE Enschede, The Netherlands

Abstract: *A new class of integrated optical waveguide structures is presented, based on low cost CMOS compatible LPCVD processing. This technology allows for medium and high index contrast waveguides with very low channel attenuation. The geometry is basically formed by a rectangular cross-section silicon nitride (Si_3N_4) filled with and encapsulated by silicon dioxide (SiO_2). The birefringence and minimal bend radius of the waveguide is completely controlled by the geometry of the waveguide layer structures. Experiments on typical geometries will be presented, showing excellent characteristics (channel attenuation ≤ 0.06 dB/cm, IL ≤ 0.6 dB, PDL ≤ 0.2 dB, Bg «1×10^{-3}, bend radius ≤ 500 μm).*

Introduction

As demand for telecommunication bandwidth increases and the optical fiber networks move steadily towards the customer premises, demand for optical switching and routing components is rising. As a consequence, optical components are replacing electronics for signal processing [1-3]. The adoption rate for optical components is being hampered, however, by their high costs stemming from two major sources: large optical footprint (i.e. high chip real-estate) and high packaging costs. By integrating multiple functions at a higher density on a single optical chip much of these costs can be amortized across several devices. In order to achieve a high density photonic platform, the index contrast and channel attenuation of the waveguide must be sufficiently large and small enough, respectively, to allow for tight curvature and cascading of multiple structures. This opens the pathway to use micro ring resonators as the universal building block in systems capable of providing switching and routing functionality [1,2,4-6].

A new waveguiding technology, designed, developed and patented by by LioniX BV is capable of meeting these demands outlined above. It comprises of alternating CMOS-compatible LPCVD layers which are fully transparent for wavelengths from < 500 nm up to 2 μm and beyond. The technology allows for medium and high index contrast waveguides. In this paper we describe the fabrication and performance of three typical waveguide geometries and give examples of (realized) applications. Both designs exhibit very low waveguide attenuation values but otherwise have totally different characteristics and applications..

Waveguide concept

Stoichiometric silicon nitride (Si_3N_4) fabricated using LPCVD processing is widely used in integrated optics, primarily because of its large refractive index (2.0) enabling very compact devices [2,6,10]. The major drawback of Si_3N_4 is its large internal tensile stress (~1GPa) which limits its layer thickness to ≤350 nm. As a consequence devices fabricated with

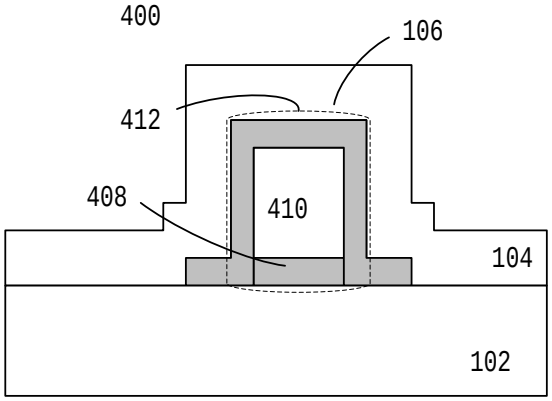


Fig. 1: Cross-section of a typical waveguide structure, with LPCVD Si_3N_4 (in grey) as basic waveguiding layer, filled with and in turn encapsulated by SiO_2 (white). Figure extracted from [7]

Si_3N_4 show a very large polarization dependency, thereby severely limiting their use in telecom applications. By combining it with a second layer that has a very large compressive stress, such as LPCVD SiO_2 (TEOS), however, the total stress of the composite layer stack is strongly reduced. As a result the thickness of the total stack can be considerably larger than the critical layer thickness of Si_3N_4 alone [7,8].

This alternating LPCVD layer stack concept can result in a rectangular channel waveguide structure with outstanding waveguiding characteristics and with strongly reduced polarization effects. The geometry is basically formed by a rectangular cross-section of silicon nitride (Si_3N_4) filled with and en-

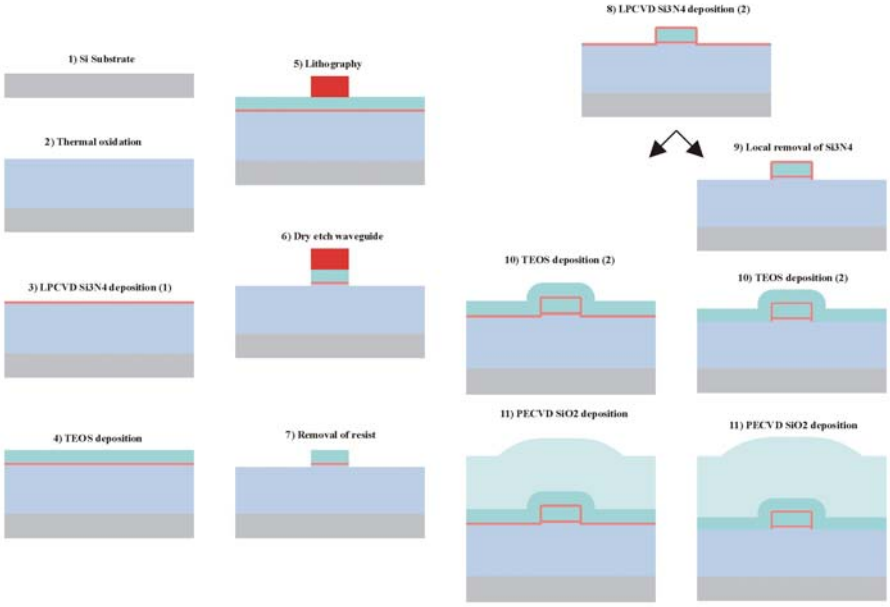


Fig. 2: Flow process scheme as made with Flowdesigner process modeler (PhoeniX BV, Enschede, the Netherlands). Here, the $Si_3N_4$is shown in red, and the (different types of) SiO_2 in blue. For explanation, see text.

capsulated by silicon dioxide (SiO_2) as depicted in figure 1.

The channel geometry approximates a "hollow core" system, as it consists of a low index "inner core" of SiO_2 "cladded" with the high index "outer core" of Si_3N_4. The channel is fabricated on a substrate, e.g. thermally oxidized silicon. The nitride shell has typical outer dimensions in the order of 1 μm^2, with its exact characteristics depending strongly upon the desired application.

Modal characteristics depend only upon the geometry of the structure, as all composing materials are LPCVD end products with very reproducible characteristics. The whole process is CMOS-compatible and very cost effective as only one photo lithographical step is required. In this paper, we will describe three different waveguide geometries based upon this procedure, all going with excellent attenuation values but with strongly deviating modal characteristics. Some applications will be elucidated.

Fabrication

Figure 2 depicts the LioniX fabrication procedure for passive optical channels for two of the three different variations of the waveguide geometry. The fabrication process of all variations starts with thermal oxidation of a 100 mm-diameter silicon wafer (1 and 2) to form the lower cladding. Then LPCVD Si_3N_4 (3) and TEOS SiO_2 (4) are deposited. Photolithography is then performed (5), followed by RIE (6), and photo resist removal (7). After a second deposition of LPCVD Si_3N_4 (8), the top cladding can be deposited with or without local removal of the slab nitride layer (9). Without the local removal of this nitride layer, the fabrication process is simplified but also goes with remaining slab waveguiding effects. Local removal of nitride, although more difficult in fabrication, results in the box-shaped structure going with even further reduction of modal birefringence and, also important, absence of slab waveguides. The last two steps for both options are TEOS deposition and PECVD oxide deposition (10 and 11, respectively) to form the upper cladding. The third geometry -not depicted in figure 2- only deviates in the etching process: in this layout, the bottom nitride layer is only partly etched, see figure 3 (left): this results in a strongly asymmetric waveguide layout going with large modal birefringence.

Although of major importance, the design of the channel waveguides falls beyond the scope of these proceedings and will be described in other publications. Here, we restrict ourselves to three examples of single mode (SM @1550 nm) channel layouts, see figure 3:

1: a non-symmetrical layout with very large modal birefringence (see figure 3, left)

2: an A-shaped layout with strongly reduced modal birefringence (see figure 3, center)

3: a box-shaped layout, with minimal modal birefringence (see figure 3, right and also [9]).

Layout 1 demonstrates the ability to tune to large modal birefringence combined with tight bending radii, at relaxed fabrication tolerances. Here the RIE procedure (which, as explained, is performed before the TEOS deposition) removes approximately only half of the first nitride layer thickness. This layout is used in a tunable true time delay (TTD) application, as described later in this paper (see also [10]). Here the channel waveguide is activated by means of heaters fabricated on the top cladding, exploiting the well-known thermo-optical effect [6].

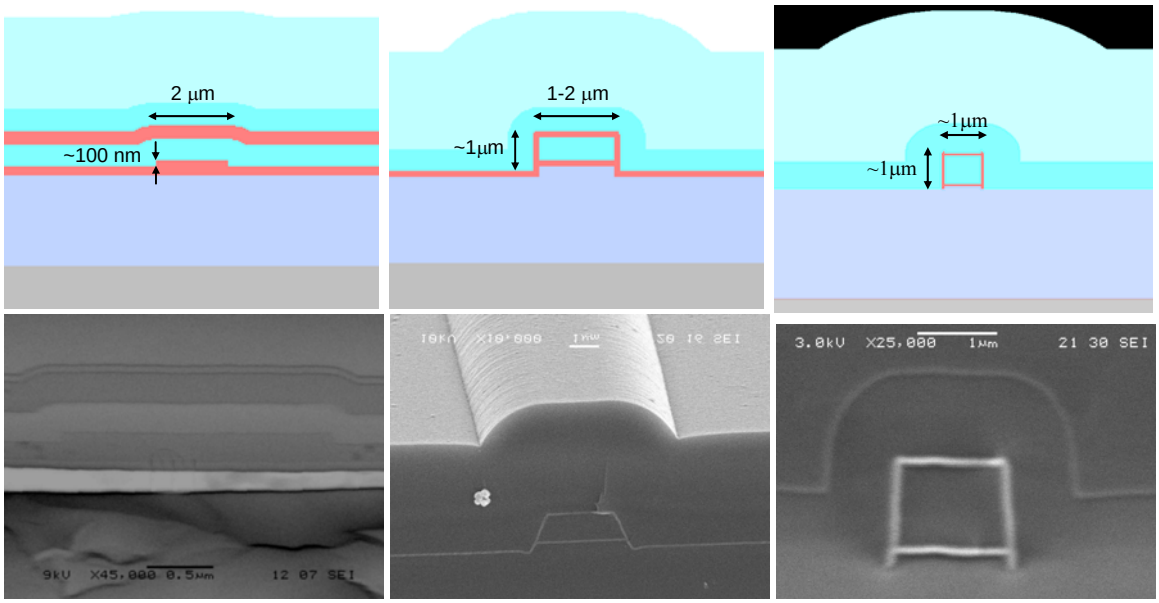


Fig. 3: Schematics (top) and corresponding SEM pictures of realized structures (bottom) of three typical channel layouts: a non-symmetrical layout with very large modal birefringence (left), an A-shaped layout with strongly reduced modal birefringence (center) and a box-shaped layout with minimal modal birefringence (right). The nitride layers are shown in red in the schematic view.

Layouts 2 and 3 show a much reduced polarization dependency, which can be understood in terms of symmetry in the geometry. In both cases, the anisotropic RIE etch step (see figure 2, step 6) completely removes the TEOS and Si_3N_4 layer as well as part of the thermal oxide layer. The following nitride deposition and subsequent top cladding layer deposition therefore results in a more rectangular layout. Both the A-shape (structure 2) as well as the box-shape (structure 3) can be tailored such, that almost no modal birefringence is resulting. Although easier to fabricate, the A-shape has the disadvantage of a remaining nitride slab layer. This is not the case for the third layout, the box-shape, in which the Si_3N_4 layer is locally removed: for telecom applications, this seems to be the most promising layout [9].

Results

The cross-section of the typical waveguides, as fabricated by LioniX, are shown in figure 3, bottom. Clearly visible is the close agreement with the designs of all structures.

The optical characterization is performed using different techniques, including cut-back and phase-sensitive optical low coherence interferometry [9]. These measurements are performed on a variety of differently processed wafers, showing a wide range of parameter settings. Key characteristics as measured on the best samples are given below in Table 1.

Several important conclusions can be drawn from these results. First the optical channel attenuation is very small for all types of geometries, while further improvement in performance is expected. Secondly, the IL is very small for both the A-shaped and (especially) the box-shaped geometries. Thirdly, for the A-shaped and boxed-shaped waveguides, the birefringence can be made very close to zero. Besides, all presented birefringence values are in good agreement with expectations, and therefore perfectly adjustable [9]. Fourth, the PDL is also small. The slightly larger PDL of the box-shaped can be completely attributed to a not-yet optimized fabrication procedure. Finally, all presented structures show reasonably small bending radii, also in line with theoretical predictions.

Two different applications with these waveguide geometries will be discussed hereafter.

Table 1: Measured characteristics on the best samples of the three types of SM channel waveguides.

	Non-symmetrical layout [1]	A-shaped geometry [1]	Box-shaped geometry [2]
Channel attenuation (dB/cm)	0.12	0.10	0.06
Insertion loss (IL) without spot size converter (dB) [3]	8.0	1.4	0.6
Group birefringence (B_g)	$\sim 1\times10^{-1}$	$\ll 1\times10^{-3}$	$\ll 1\times10^{-3}$
Polarization dependent loss (PDL, in dB) [3]	0.20	0.12	0.38
Minimal bend radius (µm)	400	750	500

[1]: chip length 3 cm
[2]: chip length 6¼ cm
[3]: here, small core fibers were used (MFD of 3.5 µm)

Application 1: Beamforming network

Beam forming for broadband RF signals can be achieved by means of a phased-array antenna working with an optical beam forming network (OBFN). This OBFN consists of optical splitting/combining circuitry and delay elements, which need to be continuously tunable in order to achieve continuous beam angle control. Moreover, in order to support relatively broadband RF signals, the delay elements should have a flat magnitude response and a linear phase response in the corresponding frequency range. To meet these requirements, optical ring resonators (ORR's) appear to be good candidates due to their continuous tunability, and well-known advantages of integrated optics [11-15]. Obviously, the waveguide technology used should provide small IL and especially small attenuation values, as substantial optical path lengths are required. Besides, a small bending radius is preferred, as this goes with small optical footprints (eg. reduced costs). In this section the advantages of optical beam forming using integrated ORR's are demonstrated, by explaining its operating principles, and by presenting some measurement results on an actual ORR-based 1x8 OBFN chip. As modal interference should be avoided, a polarization maintaining waveguide layout is preferred. Therefore, the chip is realized in layout 1 of the TriPleX-technology [16].

A single ring resonator shows a periodic bell-shaped group delay response. The peak delay value and its position are determined by the coupling coefficient and the additional round-trip phase shift of the ring, respectively. The bandwidth of the delay element can be increased by cascading multiple ORR sections. As the group delay responses of the individual sections simply add up, the total delay response can be flattened by properly tuning the ORR's [11, 13-15].

When the optical delay elements are integrated together with signal processing circuitry, an OBFN is obtained. In order to reduce the number of tuning elements, a binary tree OBFN topology is considered instead of the straightforward parallel OBFN. An ORR-based 1x8 OBFN has been proposed, consisting of 3 stages with in total 12 ORRs and 7 tunable splitters, as shown in Fig. 4.

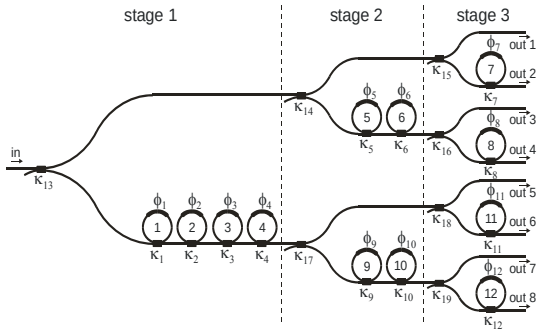


Fig. 4. Binary tree-based 1×8 optical beam forming network for a phased-array transmitter system, consisting of 12 ORR's and 7 tunable splitters.

Thr total size of the corresponding realized optical OBFN chip is only ~5 x 1 cm^2, see figure 5. This small footprint is clearly resulting from the reasonably small bending radius (see section "**Results**").

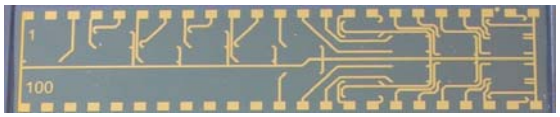


Fig. 5. Photograph of the realized 1x8 OBFN-chip, clearly showing the bondpads and heater electrodes. The chip size is ~5x1 cm^2.

Measurements have been carried out with different settings for the resistive heating elements, manufactured on top of these waveguides (sse section "**Fabrication**"). The measurement results verify the overall waveguide loss to be « 1 dB/cm.

Figure 6 shows the measured group delay responses at the outputs 2 to 8 of the OBFN, which demonstrate the delay generation of one single ring up to 7 cascaded rings. As a 1x8 OBFN, each output is required to give a different delay value over a common frequency band, in order to satisfy the condition of beam forming. Fig. 6 demonstrates linearly increasing delays from outputs 2 to 8 of the 1x8 OBFN chip, considering output 1 as the zero delay reference. The coupling coefficients and round-trip phase-shifts of the rings are tuned such that the delays cover a bandwidth of 2.5 GHz, with the largest delay value of approximately 1.2 ns (corresponding to 36 cm of physical distance in air) and delay ripple of approximately 0.1 ns (3 cm). Since the 1x8 OBFN chip is designed such that each of the 3 stages can be measured separately, in practice the final delay responses at the outputs are achieved by tuning every stage to a flattened delay response over a common frequency band before they add up.

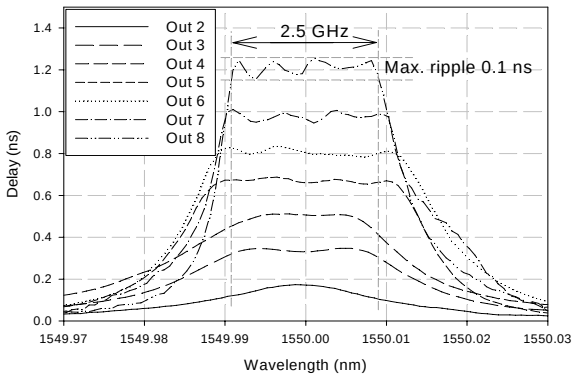


Fig. 6. Measured group delay responses at different outputs of the 1x8 OBFN chip.

Application 2: Microring resonators for telecom

The Microring Resonator (MR) represents a fundamental Planar Lightwave circuit (PLC) building block component. It is an integrated optics filter element with characteristics very similar to those of a

free-space Fabry-Perot filter.

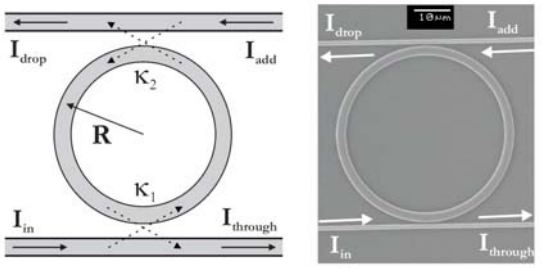


Fig 7. Schematics and picture of a single MR.

The MR offers the advantage, however, that injected and reflected signals are inherently separated into individual waveguides. In addition, since an MR does not require any facets or gratings, it is particularly simple to implement. MR's evolved from the fields of fiber optic ring resonators and micron scale droplets. Their inherently small size (with typical diameters in the range of several to tens of micrometers), filter characteristics, and potential for use in complex and flexible configurations, make these devices attractive for use in many integrated optics and VLSI photonics applications.
A basic schematic drawing of a MR is shown in Figure 7. The structure consists of a ring waveguide of radius R and two straight port waveguides.

The ability to tune a wavelength (MR resonance condition) is a highly desired aspect of the switching or routing function. Wavelength tuning enables better control of a specific wavelength by the network management system. There are several ways to make the MR tunable, but thermal tuning provides a low-cost solution.
Thermal tuning can be implemented by adding a small heater to the MR. When heated, the optical properties of an MR change and, as a result, the center wavelength of the switched wavelength signal is shifted. Thermal tuning is easy to implement with only the addition of a thin film heater on top of the MR.
The small area requirement of an MR enables integration of multiple devices in a limited space. Since they are all fabricated at one time, the cost of integrating tens to hundreds of individual MRs is low. As a result, highly complex system functionality can be provided within a small chip size at low overall cost.

An example of complex system functionality is a photonic switching and routing platform of which some examples are shown in figure 8. A photonic switching and routing platform can be produced by means of dense integration of MR filters. Such a platform enables development of flexible and reconfigurable network components such as optical switches, ROADMS, and dynamic gain equalizing filters.

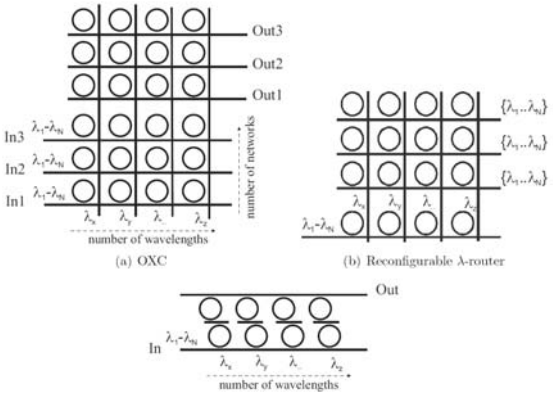


Fig. 8. Possible implementations of the photonic switching and routing platform.

The flexibility of the platform arises from the ability to combine multiple structures of different complexity on a single chip. In addition, individual tuning capability of each MR enables reconfigurability at the individual channel level.
Although MR's seem to be very versatile basic building block elements for VLSI photonic applications, their requirements on waveguiding technology are severe [1-4,18]. As mentioned, to obtain reasonable free spectal range (FSR) values, the MR should have a radius ≤ 50 μm, which can only be obtained using sufficiently high index waveguiding materials. A very suitable material is Si_3N_4, being one of the consisting components of the TriPleX technology. Based upon Si_3N_4, several nicely functioning demonstrators have been reported [18]. It is expected that these results can be improved when based upon TriPleX technology, due to the reported significantly smaller IL values. Currently, several fabrication batches are being processed, based upon MR designs exploiting the box-shaped layout previously described.

Conclusions

The TriPleX technology as been designed, patented and fabricated by LioniX is a CMOS compatible, LPCVD based technology showing very interesting features. Due to its very reproducible consisting materials, e.g. Si_3N_4 and SiO_2, the modal characteristics are determined only by the geometry of the waveguide. This enables a means to carefully control the modal birefringence from very small ($«1\times10^{-3}$) to extremely large values (for non-telecom applications wherein it is desirable to remove one polarization mode). The box-shaped and A-shaped layouts show nice modal overlaps with fiber modes, resulting in very small fiber-to-chip coupling losses (≤0.2 dB per facet). Combined with the small waveguide attenuation values (≤0.06 dB/cm), this results in very small IL values (≤0.6 dB), making the TriPleX technology very interesting for applications that require coupling into and out of the optical fiber network infrastructure. The reasonably small bending radii allow for small footprints, going with reduced cost price. For OBFN applications different demonstrators are fabri-

cated, showing very nice results. For routing and OADM applications, designs based on the box-shaped layout have been completed and batch fabrication is currently in progress. The reported results on the TriPleX technology demonstrate its high potentials for large-scale integrated optics.

Acknowledgments
This work is part of the Freeband BBPhotonics project (http://bbphotonics.freeband.nl). Freeband is sponsored by the Dutch government under contract BSIK 03025. This work is part of the Broadband Photonics beamformer project and the Smart project, Senter Novem project numbers ISO 52081 and ISO 53030, respectively. The Smart project is part of the European PIDEA^{+} project SMART.

References

1 B.E.Little etal , IEEE Photon Technol. Lett., vol.12, pp.323-25, 2000.
2 A.Driessen et al, AIP conf. Proc., Vol. 709, pp.1-8, 2003.
3 C.K.Madsen, IEEE J. Ligthwave Technol., vol. 21, no.10, pp. 2412-20, 2003.
4 D. H. Geuzebroek et al, Wavelength filters for Fiber Optics, H. Venghaus (Ed.), 2006.
5 A.Melloni et al, Proc.Icton 2003(Warsaw), 2003.
6 D.H.Geuzebroek et al,Proc. ECIO 2003, pp. 395-398, 2003.
7 U.S. Patent application nr. 10/756627-001, “Low modal birefringent waveguides and methods of fabrication”, January 2004.
8 M.Melchiorri et al, Applied Phys. Lett., vol.86, pp. 121111-13 (2005).
9 A. Melloni et al, proceedings ECIO 2007, accepted for publication.
10 C.G.H.Roeloffzen, Proc. Leos Benelux Ch., pp 79-82, 2005.
11 G. Lenz, B. J. Eggleton, C. K. Madsen, R. E. Slusher, *IEEE J. Quantum Electron*., Vol. 37, No. 4, April 2001, pp. 525–532.
12 J. E. Heebner, V. Wong, A. Schweinsberg, R. W. Boyd, D. J. Jackson, *IEEE J. Quantum Electron.*, Vol. 40, No. 6, June 2004, pp. 726–730.
13 M. S. Rasras et al., *IEEE Photon. Technol. Lett.*, Vol. 17, No. 4, April 2005, pp. 834–836.
14 L. Zhuang, C. G. H. Roeloffzen, W. van Etten, *Proc. of the 12th IEEE/CVT Symp. in the Benelux*, Enschede, The Netherlands, Nov. 2005.
15 C. G. H. Roeloffzen, L. Zhuang, R. G. Heideman, A. Borreman, W. van Etten, *Proc. of the 9th IEEE/LEOS Symp. in the Benelux*, Mons, Belgium, December 2005, pp. 79–82.
16 R. G. Heideman, A. Melloni, M. Hoekman, A. Borreman, A. Leinse, F. Morichetti, *Proc. of the 9th IEEE/LEOS Symp. in the Benelux*, Mons, Belgium, December 2005, pp. 71–74.
17 L. Zhuang, C. G. H. Roeloffzen, R. G. Heideman, A. Borreman, A. Meijerink, W. van Etten, *Proc. of the International Topical Meeting on Microwave Photonics (MWP’2006)*, Grenoble, France, 3-6 October 2006, p. F1.4.
2005
18 E. Klein, Ph.D. thesis, April 2007.

Single-pump high-power robust single-frequency waveguide lasers fabricated by ion-exchange techniques

S. Taccheo (1), G. Della Valle(1), A. Festa(1), K. Ennser(2), G. Sorbello(3), C.Cassagnettes(4) and D. Barbier(4)
(1): Dipartimento di Fisica Politecnico di Milano and CNISM, Italy, e-mail taccheo@polimi.it
(2): Institute of Advanced Telecommunications, Swansea University, Swansea UK
(3): DIIT, Università di Catania, Italy
(4): Teemphotonics, Grenoble, France

Abstract: *We report on a waveguide laser with output in excess of 20 mW in robust single-frequency operation. The active medium was only 9-mm long. The cavity length was <60 mm including butt-coupled fiber-Bragg-grating mirrors Conditions for robust single-frequency opereation and power scaling to 100 mW are discussed. Preliminary experiments are performed using longer waveguides.*

Introduction

Single-frequency lasers at 1.5 μm are key elements for applications to several fields such as spectroscopy and optical sensing. In many cases, such as free space optical communications [1], laser radar and satellite based remote sensing [2], distribute fiber-optic sensors [3], and frequency domain reflectometry [4], device specifications may become very demanding in terms of power, compactness, insensitivity to environmental disturbance and high temporal coherence. Bulk laser cavities may exploit large modal volumes and are able to provide high output powers. However are generally quite sensitive to technical noise and are not compact devices, despite recently compact large-mode area laser were proposed [5]. On the contrary, short fiber lasers [6] and, in particular, waveguide lasers [7,8] are compact devices with monolithic structures which have the potentialities to satisfy all the requirements previously outlined. However, looking at the literature up to now only few mW output level waveguide laser were demonstrated except few tens of mW power level using Th:Sapphire pumping and large waveguide area [7] or few tens of mW in a not-stable single-frequency cabity were mode-hopping occourred [9].

In order to meet the demand of high-power highly-doped materials are required in order to keep the device length at around a few cm to allow a simple linear cavity structure with large free-spectral range. This requirement make not suitable glass-on-silicon technology. In fact in this case the Erbium concentration is usually limited to avoid quenching effects [10], while other glasses may offer better solubility. In particular phosphate glass offers a far better solubility and efficient codoping with Yb thanks to high phonon energy that optimize energy transfer process [2] and therefore the pump efficiency. The use of Yb is also the key element for high pump absorption over short length. Among several methods to fabricate an active waveguide in a phosphate glass base the most reliable and of highest quality is the ion-exchange techniques [11].

In this paper we demonstrate that optimized laser configuration can produce more than 20 mW robust single-frequency output power by using an Er:Yb-doped phosphate glass waveguide only 9-mm long, corresponding to more that 22 mW/cm. The cavity was formed by two butt coupled fiber-Bragg grating (FBG) mirrors. We also found that single-frequency operation can be obtained by using cavity lengths of up to 60 mm that is, in our opinion, an upper limit value. We believe that 50 mm active waveguides could provide up to 100 mW output power and we report prelimary test. Cavity shortening using integrated mirrors is also discussed.

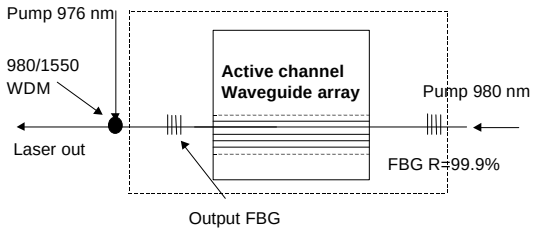


Fig.1: Waveguide laser set-up

Waveguide fabrication and laser set-up.

The ion-exchange method that is a reliable, rugged and low cost technique and was already demonstrated both using Ag-Na [11,12] and K-Na [7]. We used a two-step fabrication technique and a commercial Schott IOG-1 phosphate glass base with Er and Yb concentration of 3.5 10^{20} and 2.6 10^{20} ions/cm^3, respectively. In the first fabrication step the substrate was immersed in fused salts at 330°C for 8 minutes and the Ag concentration was adjusted to produce a maximum refractive index change of 0.02 [13] to ensure single transverse mode operation. In order to reduce the waveguide propagation loss and coupling loss to circular waveguides a second burial step was performed. We obtained a circular mode-field profile compatible with standard SMF-28 telecom fiber. In

total we fabricated a linear array consisting of sixteen 250-μm spaced buried channel waveguides. Fig.1 shows the laser cavity set-up. Two FBGs were butt-coupled to the waveguide by using a suitable index matching fluid. Pump diodes providing up to about 250 mW pump power at 980-nm wavelength were available.

Laser experiment

We first made a set of measurements to evaluate the optimum output coupling. To ensure robust single-frequency opeartion we used a 9-mm waveguide. Figure 2 shows the slope efficiency, pump power threshold and output power for several FBG output couplers centered at 1533 nm and with different reflectivities. The high-reflective FBG was R=99.8% and 125-GHz reflectivity bandwidth (FWHM). During the test the cavity length was of the order of 1 m and the laser was therefore not operating in single-frequency. However the laser bandwith was of few GHz, as defined by FBG transmission spectrum, and only few modes were oscillating within about 1.5 GHz bandwidth. Note that in all cased we used a 976 nm pump diode to enhance absorption by matching the Yb absorption peak.

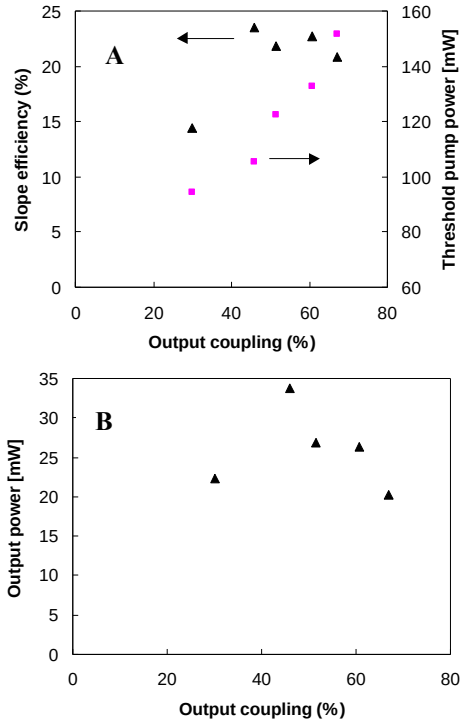


Fig.2: A: slope efficiency (traingles) and pump power threshold (diamonds) vs. output coupling. B: maximum output power. Maximum pump power was 270 mW obtained with 976-nm pump diode.

From Fig.2 the FBG with 54% reflectivity (46% output coupling) gave the best results. However a second consideration is the FBG FWHM. We therefore preferred to use the R=48% FBG because it was narrower with FWHM of about 80 pm (10 GHz) against 100 pm (12.5 GHz) of the R=54% FBG. Once cavity design was defined we made a short cavity by almost butt-coupling the two FBGs to the waveguide. We estimated an overall cavity length of about 55 mm. The 9-mm active material was placed asymmetrically in order to suppress longitudinal mode competition due to spatial-hole burning.

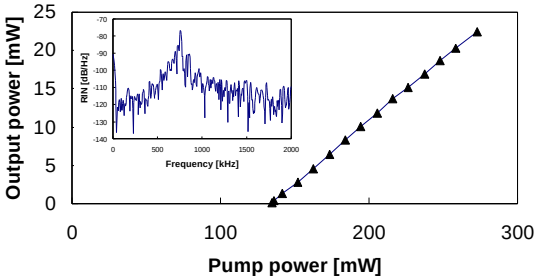


Fig.3: Single-frequency output power. Inset shows RIN spectrum

Figure 3 shows the output power characteristics. We noticed a remarkably stable single-frequency operation at all pump power, even in absence of thermal stabilization. Figure 4 shows the single frequency operation recorde by an high-finesse Fabry-Perot interferometer. This means that 60-mm long cavity ensures only one longitudinal mode can oscillate. Inset shows the relative intensity noise spectrum we measured. The relatively high peak value is due to discrete component cavity. We plan now to bond the two FBG to the waveguide in order to obtain a monolithic structure. Result will be presented at the conference. The final results of 22 mW output power with 17% slope efficiency is quite remarkable and gives a figure of 24 mW/cm as output power per unit length of active waveguide. To the best of our knowledge is the highest output power ever reported for robust single-frequency operation and single-pump scheme. The further work is to evaluate if we can have same figure of merit over a 50 mm waveguide in order to achieve 100 mW output power.

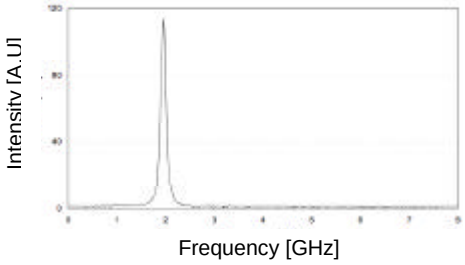


Fig.4: Single-frequency spectrum. Offset shows drift without mode hopping.

Power scaling

Based on the previous results we evaluate power scaling towards 100-mW power level. We observed that 55-mm long cavity was able to ensure stable single-frequency operation without mode-hopping. This means that probably a laser with 40-mm to 50-mm active material is still suitable for single-

frequency operation. Once spatial-hole burning is removed by and very narrow FBGs are used. To evaluate power scaling we made a second waveguide using same active material but 45-mm long. Figure 5 shows the waveguide. We need to use two pump diodes (at 976 nm and at 980 nm) and probably the pump wavelength of 976 nm was not the best solution for such a long waveguide having too short absorption length. The overall test cavity was now long about 1 m. Figure 6 shows the set-up. Still we obtained useful insights. Figure 7 shows results of output power versus pump power. We tested several FBG reflectivity and using 21.5% reflectivity we obtained 164 mW output power with 500 mW pump power. In this case the single-frequency operation was quite unstable and usually at least two modes were oscillating so data refer to multi-longitudinal mode operation.

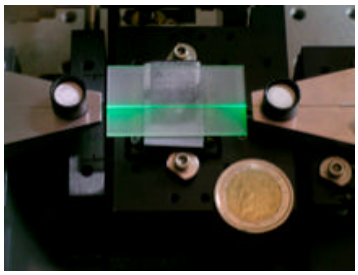


Fig. 5: 45-mm long waveguide.

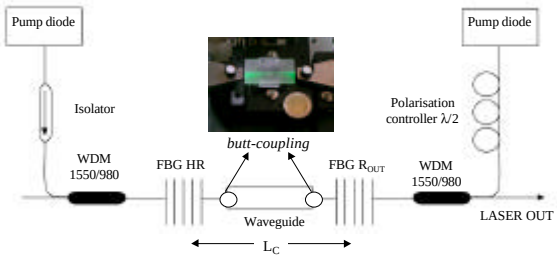


Fig. 6: Set-up for 45-mm long waveguide.laser

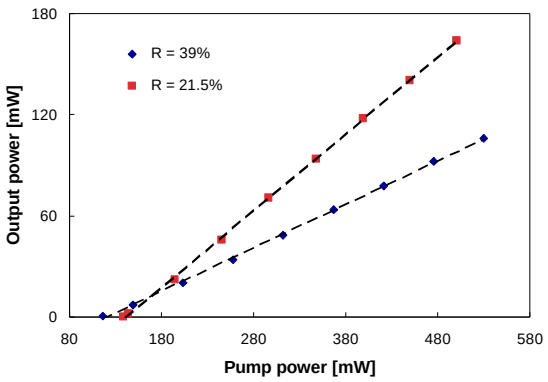


Fig.7: Output power vs. pump power for 45-mm long waveguide

Nevertheless if we now consider the figure of merit defined as output power/active material length at 270 mW pump power we obtain about 15 mW/cm. The lower value compared with 9-mm long waveguide is due to not optimized pump wavelength. In addition our longer waveguide needed for a two-pump scheme that is not suitable for compact devices. To evaluate sinlge-pump longer waveguide we test a 50-mm long waveguide made by Teemphotonics by ion exchange. The waveguide was optimised for single-pump scheme and has Er and Yb concentration of 2% and 4% respectively.

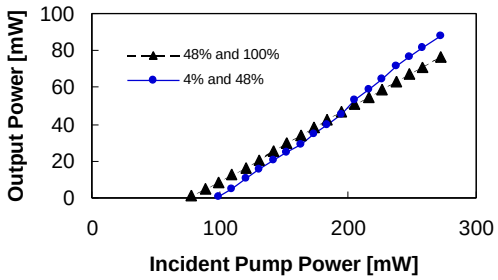


Fig.8: Output power vs. pump power for 50-mm long waveguide

Figure 8 shows the output power we obtained with preliminary measurements. We used the narrow 48% FBG and as second mirror both 100% 125-GHz FWHM mirror end 4% Fresnel reflection from glass/air inferface. Despite the non-optimised coupling we obtained over 80 mW in almost single-frequency operation. In the case of 4% coupler the cavity was 10-cm long but still only one longitudinal mode oscillates carrying over 85% of total power. Residual power was due to transverse mode oscillation. Slight mode-hopping also occured due to long cavity. We believe that use of single transverse mode cavity and a shorter cavity will allow to chieve the 100-mW output power level cavity. A single-transverse mode waveguide is under development -
A further step towards compact cavity is the integration of grating mirrors into the waveguide structures. Surface pattern by mask litography or by laser irradiation [14] could achieve the desired results and test are planned.

As last investigation we evaluated possible competition by glass on silicon technology for waveguide laser. We evaluated the figure of merit of a silica fiber with 0.6% Erbium concentration (no Yb codoping) that reasonably simulates performance of glass-on-silicon waveguide devices. We obtained about 2 mW/cm in multi-longitudinal mode operation with 15 mW from a laser using a 7 cm length active fiber. We believe that probably no more that 3 mW/cm in single-frequency operation can be achieved even considering to double the doping concentration. Waveguide laser based on glass on silicon technology will need to improve Er solubility in glass host to compite with phosphate glasses.

Conclusions

We reported on a stable single-frequency operation waveguide laser able to provide more than 20 mW

output power using only 9-mm long active element. We also evaluated that output power scaling to 100 mW is achievable using phosphate glasses while silica glass, and therefore glass on silicon waveguide technology, will probably not able to reach same performance. We therefore conclude tha ion-exchange technique is a promising solution to achieve 100-mW output power out of a waveguide lasers.

Acknowledgments
Authors acknowledge partial support from MIUR project #2005099872.

References

1. H. Willebrand and B. S. Ghuman, *Free-Space Optics: Enabling Optical Connectivity in Today's Networks*, (Sams Publishing, Indianapolis, In., 2002).
2. C. J. Karlsson et al., Appl. Opt. **39**, 3716-3726, 2000
3. F. T. S. Yu and S. Yin, *Fiber Optic Sensors*, (Marcel Dekker, Inc., New York – Basel, 2002
4. J. Geng et al., Photon. Technol. Lett. **17**, 1827-1829, 2005
5. A. Schülzgen et al., Opt. Express, **14**., N.16, p.7087, 2006
6. C. Spiegelberg et al. J. Lightwave Technol. **22**, 57-62, 2004
7. D. L. Veasey et al., J. Non-Cryst. Solids **263** and **264**, 369-381, 2000
8. S. Blaize et al. IEEE Photon. Technol. Lett. **15**, 516-518, 2003
9. G. Della Valle et al., Opt. Express, **14**., in press 2007
10. A E. Snoeks et al., J. Opt. Soc. Am. B **12**, 1468 , 1995
11. S. Blaize et al. CLEO/Europe 2000, paper CFGZ, Nice, France 2000
12. G. Sorbello et al, Electron. Lett., **37**, 1014-1015, 2001
13. G. Jose et al., Opt. Material, **24** p. 372, 2003
14. S. Yliniemi et al., Opt. Express, **14**, N.7, p. 2898, 2006

Recent Developments in Direct-UV-Written Planar Waveguides, Gratings, Sensors, and Substrates

F.R. Mahamd Adikan, J.C. Gates, A.S. Webb, H.E. Major, C.H. Holmes, M. A. G. Ramirez, B. D. Snow, D. Kundys, C.B.E. Gawith, P.G.R. Smith
Optoelectronics Research Centre, University of Southampton, Highfield SO17 1BJ United Kingdom

Abstract: *We present our recent developments in direct-UV-written integrated optical devices, based on applications in telecommunications, material characterisation, and optical sensing. The inherent advantages of this channel definition technique over traditional etching based approaches are reiterated and demonstrated in the production of small angle, low loss X-couplers with negligible polarisation dependence. Interfering two focussed UV spots also provides us with the capability to simultaneously define a channel waveguide and Bragg grating, opening new device and application opportunities. Such structures provide a method to quantify the photosensitivity effects observed in conventional multilayer substrates, and assess the core uniformity of a novel 'flat-fibre' format recently developed within the ORC. We will also discuss electrically tuned Bragg gratings via liquid crystal overlayers, displaying a dynamic range in excess of 100GHz for use in dynamic optical networks.*

Introduction

Direct UV writing is planar lightwave circuit fabrication technique with enormous potential for the development of novel integrated optical devices and applications. Based on the refractive index change induced by a scanning UV beam, this technique allows channel waveguide structures to be literally 'drawn' into photosensitive materials without the need for photolithography, etching, or expensive cleanroom processing.

Historically, the concept of UV-based waveguide definition was introduced by Chandross et al. in 1974 [1], who produced 4µm optical waveguides in doped polymer films with a 364nm laser. Referring to the process as 'photolocking', Chandross commented that the 'smooth interfaces and low optical losses' would provide a route to avoid the characteristic edge roughness induced by solvent development or sputtering. For integrated optical applications, direct UV writing in silica-on-silicon was first reported by Svalgaard et al. in 1994 who demonstrated buried single-mode channel waveguides in germanium-doped silica films with a refractive index increase of 10^{-3} [2]. This was followed by work on practical devices such as directional couplers and power splitters in 1997 [3, 4] displaying losses of ~0.2dB.

The first reported experimental work from the Smith group at the ORC of Southampton University was in 2002 when Gawith reported direct-UV-written buried channel waveguide lasers in direct-bonded glass [5]. This was quickly followed by Emmerson, who described a more advanced 'Direct Grating Writing' technique for the simultaneous definition of channel waveguides and Bragg gratings via the interference of two focussed UV spots (Fig.1) [6]. Since then, direct UV writing at the ORC has primarily developed towards the realisation of planar Bragg-grating-based devices for real-world integrated optical applications, such as telecommunications and bio/chemical sensing.

Presented here is an overview of some of our recent developments in direct UV writing, and the many emerging applications discovered from this versatile technology. Specific examples include X-couplers for dense optical networks, and a subsequent study on photosensitivity and local control of refractive index. The use of direct UV writing as a characterisation tool is discussed during the introduction of a novel 'flat-fibre' extended-length planar substrate material developed for distributed lab-on-a-chip applications. Also described is a new Bragg grating device that can be electrically tuned over more than four 25GHz-spaced wavelength division multiplexed (WDM) channels by means of index modification of a liquid crystal layer. Finally, we aim to highlight UV writing technologies that we believe may benefit other areas, such as bio/chemical sensing and the automotive industry.

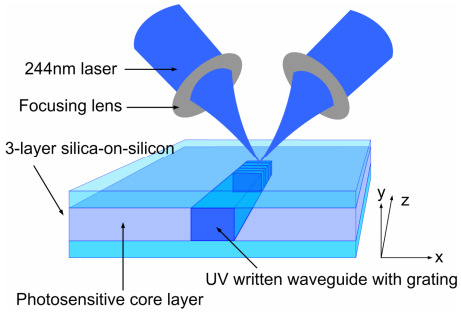
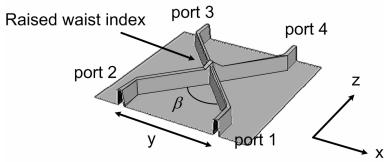


Fig: 1 Schematic diagram of simultaneous channel and grating definition via Direct Grating Writing



Launch port	Measured power	
	Through, $P_=$	Coupled, P_x
port 1	port 3	port 4
port 2	port 4	port 3

Fig: 2 Schematic diagram of an X-coupler showing the UV induced refractive index structure. Note the raised index close to the overlap region (β = crossing angle; y=100µm)

Towards Dense Form-Factor Integrated Optics:
i) Small Angle X-couplers

Price competition and miniaturisation provide powerful incentives for engineers to seek higher device densities in integrated optics. The ability to cross and overlap channel waveguides with minimal loss or distortion of the guided mode is one route towards achieving this, and a process for which direct UV writing is ideally suited. One such structure, the X-coupler (Fig. 2), comprises of two channel waveguides that intersect at a given angle. They are found in many functional integrated optical devices such as switches, power dividers and wavelength selective splitters. Fabrication of small angle (<5°) ridge-style X-couplers in silica-on-silicon using photolithography and etching are prone to under-etching and step coverage problems. This tends to result in high insertion loss and polarisation sensitivity.

In recent work, we have demonstrated small-angle (0.8°-5°) direct UV-written X-couplers with maximum and minimum coupling ratios of 95% (±0.8%) and 1.9% (±1%) respectively. These structures display very low polarisation and wavelength dependence with typical excess loss of 1.0dB (±0.5dB). Device modelling using BPM and an analytical model showed good agreement with experimental results over a broad crossing angle and wavelength range. Such performance owes itself to UV writing overcoming the aforementioned fabrication issues by allowing smooth crossings with arbitrarily small angles. However, the most significant advantage of our technique is the ability to achieve an index increase in the waist region due to repeated illumination. This additional control over the localised index is necessary to produce a raised waist index for near lossless X-coupler operation [7]. This is graphically represented in Fig. 2.

Fig. 3 shows the coupling ratio behaviour of the X-couplers as a function of crossing angle, wavelength and polarisation. Coupling ratio is defined as the ratio between the coupled power and total output power. These results highlight the advantages of UV multi-exposure in fine-tuning device performance. However, little is known about the photosensitivity behaviour of regions within the immediate vicinity of an earlier UV exposed area, a feature known as the 'proximity effect'. In the following section, we will present the use of planar Bragg gratings in quantifying this proximity effect and also in determining core layer flatness of a novel flat fibre sample.

Planar Bragg Gratings as an Assessment Tool:
i) Quantification of the Proximity Effect

When a channel waveguide structure is defined into a photosensitive substrate using a UV beam, the photosensitive area around the channel can also be affected. As such, an accurate understanding of these local proximity effects in UV writing is critical for development of both complex coupling structures and high density devices.

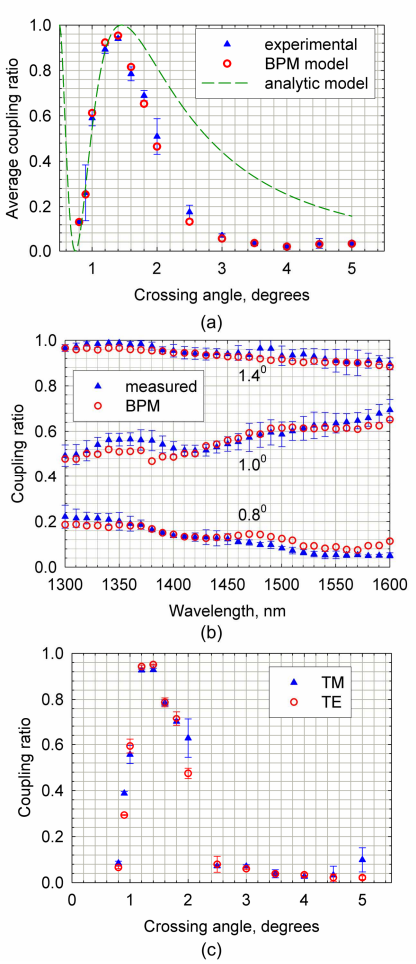


Fig: 3 (a) Coupling ratio against crossing angle (the analytical model is only valid for angles < 1° [7]); (b) Wavelength dependency of X-couplers for 3 different crossing angles showing low dependence over 300nm; (c) Low polarisation dependence of the X-couplers

In current work we have discovered that local photosensitivity increase is evident for regions within 9µm away from the initial exposure with a maximum effective index increase of 8.3×10^{-4}. This quantitative data was achieved through series of experiments, each using sets of three 1mm long Bragg gratings with three different periods (Λ_1=529.3, Λ_2=534.5, Λ_3=539.6nm) defined at a fixed spacing from a set of earlier UV exposed regions. This experimental layout is illustrated in Fig. 4(a), where 'fluence' is the expression for the energy exposed to the sample during the UV writing process.

Reflection spectra of the gratings were recorded, allowing calculation of the average effective index of the waveguide, as depicted in Fig. 4(b). It can be seen that an increase in index is obtained in regions up to 9µm away, highlighting the proximity effect, and with a maximum increase obtained when the same region is multi-exposed (0µm spacing). Effective index increases as large as 8.3×10^{-4} (with respect to the reference gratings) were recorded. We believe

that the behaviour exhibited is either due to non-localised heating effects or more likely a result of diffusion of hydroxyl (OH) species resulting in redistribution of oxygen deficient defects, and therefore an increase in photosensitivity.

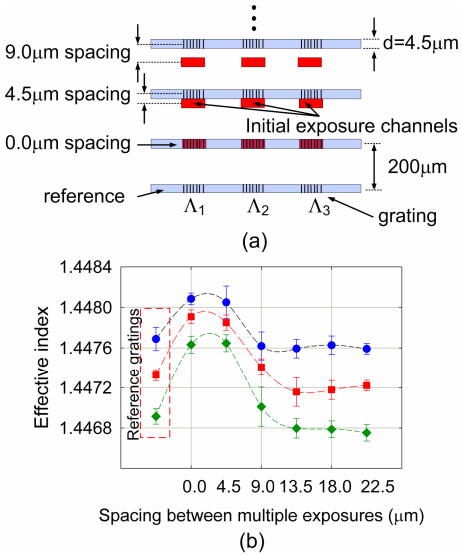


Fig: 4 (a) UV-written Bragg gratings and earlier defined channels for proximity effect characterisation (d: waveguide width); (b) Effective index at various spacing and fluence values (●: Fluence, F = 22kJcm^{-2}, ■ : F = 14kJcm^{-2}, ◆ : F = 9kJcm^{-2})

ii) Assessment of Flat-Fibre Core Layers

While integrated optical devices in silica-on-silicon offer dense functionality in a robust package, they are rarely considered compatible with the fields of remote or distributed sensing or long-haul one-dimensional fibers. At the ORC we aim to change that with the development of new 'flat-fibers' that combine the advantages of existing low-cost fiber drawing with the functionality of planar lightwave circuits in a novel hybrid format (Fig.5). Adapted from MCVD fiber fabrication, our preforms are deposited and collapsed into a rectangular geometry before drawing, resulting in extended lengths of mechanically flexible flat-fiber material with a photosensitive germanium-doped planar core. By taking this approach, we hope to extend beyond the centimeters-length limitations of traditional planar substrates to allow exotic material compositions, integrated optical device layouts, and local sensing functions to be distributed over extended distances with no coupling or compatibility concerns.

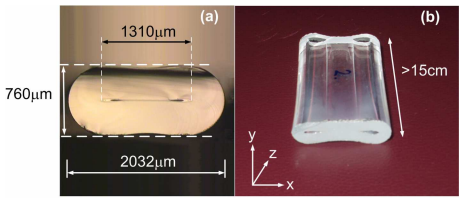


Fig: 5 (a) Cross section; and (b) perspective views of the novel flat fibre sample

In order to optimise the flat-fibre substrates for use in integrated optics, physical and optical assessment in terms of layer flatness and waveguide birefringence must be performed. UV writing again provides a useful approach to this problem, allowing a series of identical Bragg gratings to be inscribed and assessed across the sample profile. Using direct grating writing through the ~350μm thick cladding layer of early samples, a series of Bragg gratings were written into the core of the planarised fibre at 100μm spacing to allow comparative assessment across the flat core region. Inherently, maintaining the overlap and interference pattern of the two focussed 4μm spots places a stringent need for the core layer to be flat and uniform if channel waveguides and Bragg gratings are to be properly defined. Despite the 'bow-tie' profile of our early samples, planar gratings have been successfully demonstrated to prove that the core layer is uniform along the direction of propagation. The reflection spectrum from the first flat-fibre sample with integrated planar Bragg grating developed at the ORC is shown in Fig.6, as was recorded using an ASE source and optical spectrum analyser via a 3-dB coupler. The inset shows the grating reflection and the ASE spectra from the source.

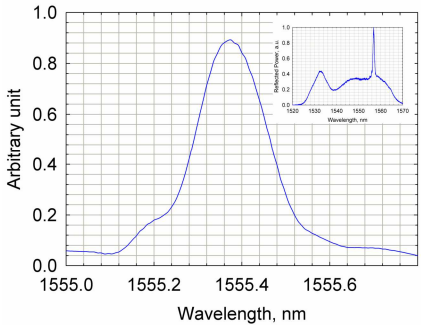


Fig: 6 First demonstration of Bragg reflection in flat fibre sample. The inset shows the ASE spectra of the input light and the Bragg gratings reflection

Following this initial success we proceeded to fabricate identical gratings along the cross section of various flat fibres, allowing us to determine the lateral surface uniformity of each sample. Here, any thickness variation will affect the effective index value of the fabricated structure with a resultant shift in Bragg wavelength. This process also allows us to derive the birefringence of the sample by successively launching TE and TM polarised light. Fig. 7 shows the effective index of the fabricated gratings along the sample profile along with the position of each grating.

In this case, Bragg gratings 6 and 7 display multi-mode behaviour, attributed to the increase in core thickness as we approach the edge of the sample. We have obtained an average birefringence of 3.3x10^{-4} from the same experiment and we believe this low birefringence is due to the reduced level of inter-layer stress-induced birefringence, which is common

in conventional silica-on-silicon samples. Using direct UV writing and planar Bragg gratings in this way highlights the applicability of this process as a material assessment and design tool.

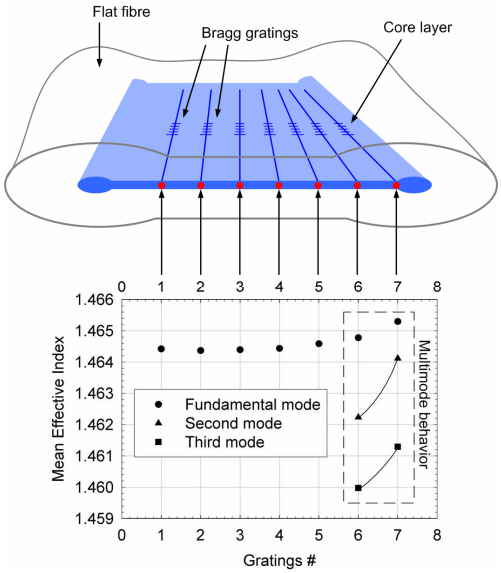


Fig: 7 Mean effective refractive index variation across the cross section of the sample core layer. Gratings 6 and 7 exhibit multi mode behaviour as the core layer thickness increases approaching the edge (solid lines are for indicative purpose only)

Application-based Devices:

i) Tunable Liquid Crystal Gratings

Reconfigurable integrated optical devices are essential in today's dense and complex telecoms meshes. A commonly employed component to fulfill this requirement on the silica platform is a planar Bragg grating, where the ability to tune the reflection peak represents a key enabler towards realizing an all-optical dynamic network. Our approach to this important area of commercial interest has been the development of a series of electrically tunable liquid crystal Bragg gratings devices, which offer up to 114GHz of tunability at just 170Vpp voltage.

Based on a direct-UV-written channel waveguide with an etched window above a planar Bragg grating, these devices operate by use of evanescent coupling into an electrically tuned nematic liquid crystal. Such electrically tunable devices work on the principle of shifting the Bragg wavelength by modifying the effective index of a waveguide in a multilayer substrate. This is achieved by overlaying the grating with a liquid crystal that features a refractive index anisotropy that can be electrically manipulated. Modifying the liquid crystal refractive index subsequently alters the effective index of the waveguide, leading to Bragg wavelength shift. Fig. 8 depicts the schematic diagram of the assembled device and an example Bragg tuning curve.

The demonstrated Bragg wavelength tuning over multiple telecoms channel spacing electrically is encouraging, and our development of a cascaded architecture of such integrated liquid crystal devices operating at different Bragg wavelengths could pave the way towards true colorless add/drop modules for dynamic dense optical networks.

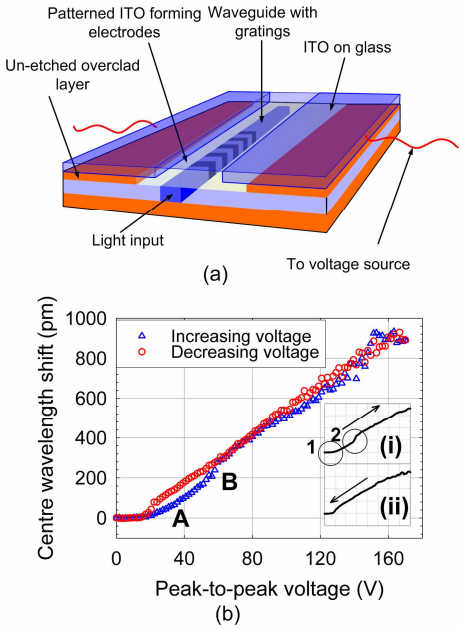


Fig: 8 (a) Schematic diagram of liquid crystal Bragg grating configuration; (b) Tuning curve with insets showing the threshold points

Conclusions

Discussed are our most recent activities in the field of novel direct-UV-written integrated optical devices. The use of direct-UV-written planar Bragg gratings in assessing important physical and optical parameters of various material structures, such as photosensitivity proximity effects and core layer thickness, is presented along with a novel flat optical fibre geometry designed for distributed lab-on-a-chip applications. Ongoing work in the design and optimization of UV-written electrically tunable Bragg gratings for use in reconfigurable optical networks will also be presented.

References:

[1] E. A. Chandross et al *Applied Physics Letters*, vol. 24, pp. 72-4, 1974.

[2] M. Svalgaard et al *Electronics Letters*, vol. 30, pp. 1401-3, 1994.

[3] M. Svalgaard and M. Kristensen *Electronics Letters*, vol. 33, pp. 861, 1997.

[4] M. Svalgaard *Electronics Letters*, vol. 33, pp. 1694-5, 1997.

[5] C. B. E. Gawith et al *Applied Physics Letters*, vol. 81, pp. 3522-4, 2002.

[6] G. D. Emmerson et al *Electronics Letters*, vol. 38, pp. 1531-2, 2002.

[7] F. Durr and H. Renner *Journal of Lightwave Technology*, vol. 23, pp. 876, 2005.

Ultra-compact silica-on-silicon micro-resonators by etching deep trenches

Haiyan Ou(1), Karsten Rottwitt(1), and Hugh Philipp(2)
1) COM.DTU, Technical University of Denmark, 2800, Kgs. Lyngby, Denmark, ho@com.dtu.dk 2) Cornell University, LASSP, Clark Hall, Ithaca, NY 14850

Abstract: *Ultra-compact silica-on-silicon micro-resonators were achieved by etching deep trenches surrounding the waveguides to increase the lateral index contrast. Four types of structures: 1 micro-ring, 2 microrings, 1 micro-disk and 2 microdisks, were fabricated and characterized. Micro-resonators with radius of as small as 25 µm show a free spectral range of 9.1nm. A two-disk optical drop filter was demonstrated. Such structures can be used as fundamental building blocks in more sophisticated optical signal process devices.*

Introduction

Silica-on-silicon waveguide components are important members in the family of integrated optics platform, due to its low propagation loss and low coupling loss with standard fibers [1]. Most commercial passive waveguide components, such as arrayed-waveguide gratings (AWG), splitters et al, widely used in the optical telecommunication system, use this technique. However, components integration density in this technology is limited because the index contrast (index difference between core and the cladding) is small in this technology. The index difference is ~0.02 between Ge doped glass and pure glass, while it is 0.6 for high index contrast material like silicon rich silicon nitride (SRSN) [2]. This low index contrast results very large bending radius of 6 mm to make the bending loss negligible, which seriously limit the size of the components [3]. By etching deep trenches [4] along the waveguide, the lateral index contrast could be increased dramatically from ~0.02 to 0.5. Travelling-wave micro-resonators in the form of disks and rings serve as versatile elements in lasers, narrow-band channel-dropping filters, and low capacitance modulators [5, 6]. In this paper, ultra-compact side-coupled micro-resonators in the form of both rings and disks were fabricated by combining standard silica-on-silicon waveguide fabrication processing with deep glass etching.

Fabrication

The fabrication of the silica-on-silicon ultra-compact structures consists of two main steps. The first step is the deposition of three waveguide layers: buffer, the core and the top-cladding. The process starts with a 4 inch silicon wafer. The buffer layer is a 6 µm thick layer of pure silicon dioxide, grown by thermal oxidization of the silicon substrate. The core is a 3.5 µm thick Ge-doped glass ($Ge:SiO_2$) layer, deposited by plasma enhanced chemical vapour deposition (PECVD). The refractive index of the core (n_c) is 1.465 at the wavelength of 1550nm. Since the refractive index of pure glass (n_b) is 1.445 at 1550nm, the index contrast (n_c-n_b) between the core and buffer is 0.02. The top–cladding is Boron and Phosphorus co-doped glass (BPSG) deposited also by PECVD. The refractive index and thickness of the top-cladding, 1.445 and 6 µm respectively, are matched to that of the buffer.

The second major fabrication step is deep glass etching. The pattern was transferred from the mask to the wafer by using standard optical lithography. It is fast, cheap and avoids using e-beam lithography. The present of micro-resonators (rings or disks) and the 'bus' straight waveguides on the same mask, simplifies the process. Placement of the micro-resonators with respect to the waveguides is precisely controlled eliminating an additional alignment step necessary with schemes using vertically coupled ring resonators and multiple masks [7]. The etching goes through three layers of the waveguide, and the total etching depth is 15.5 µm. Burned resist was used as the mask material of deep glass etching instead of polysilicon [4]. Using burned resist as a mask material is a standard waveguide fabrication technique in the cleanroom of Danchip, DTU. As a result, the sidewalls of the waveguide are angled (82°) instead of vertical.

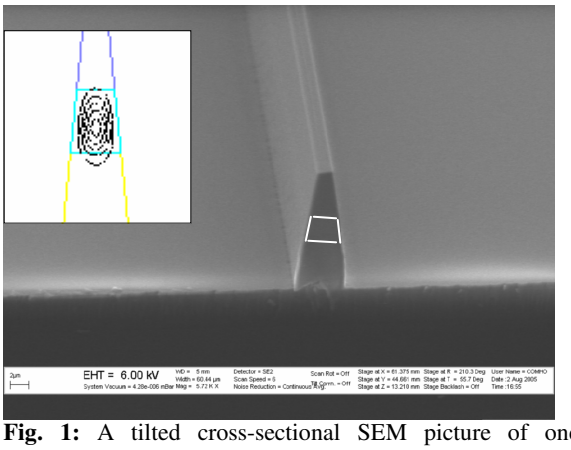
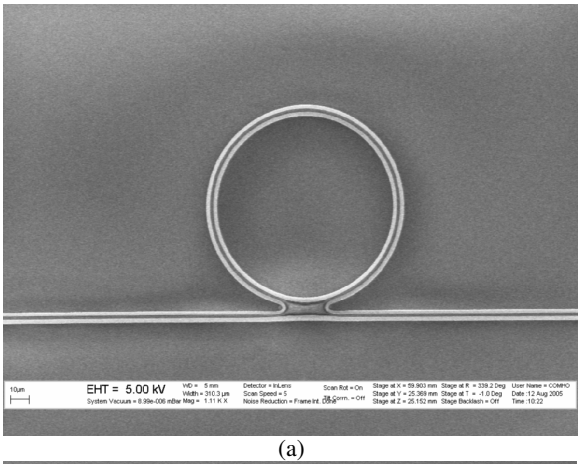


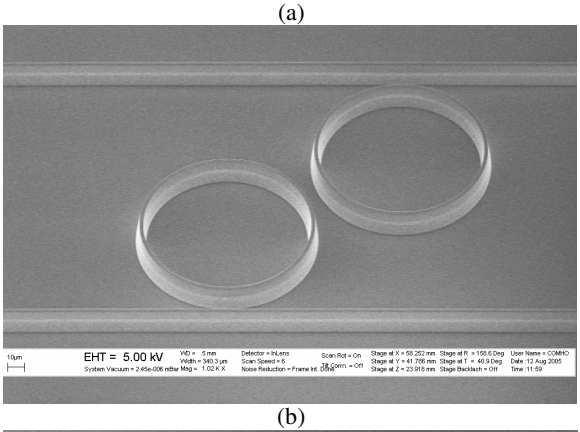
Fig. 1: A tilted cross-sectional SEM picture of one waveguide after the deep etching. The total etching depth is 15.5µm, including three layers of the waveguide: top-cladding, core and buffer layer. A trapezoidal core layer is highlighted. The widths for the top and bottom of the core layer are 3.4 µm and 3.9 µm respectively. The thickness of the core layer is 3.5 µm. The inset is the fundamental mode field distribution in the core simulated by the commercial software Olympios.

Fig.1 shows a tilted cross-sectional SEM picture of a waveguide. As seen from Fig.1, in the horizontal direction, the index contrast of the waveguide is increased from 1.465:1.445 to 1.465:1 after the trench

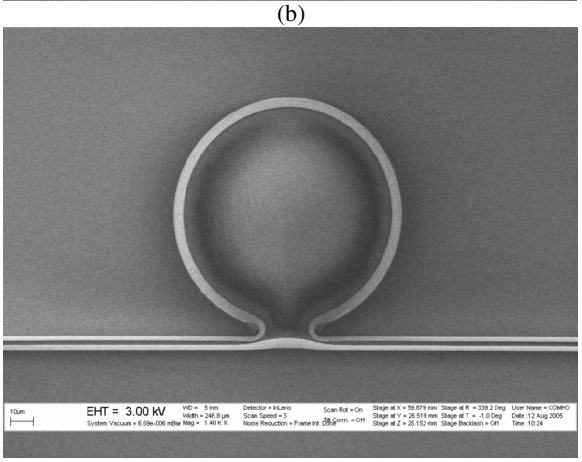
etching. This contrast is comparable to the other high index contrast materials like Si_3N_4. The relative refractive index difference [8], $\Delta = (n_{c2} - n_{b2})/(2n_{c2})$, for Silicon rich Silicon Nitride (SRSN) with a silica cladding is 0.254, while it is 0.267 for the glass-air interface. The tight confinement of the horizontal optical mode enables low-loss small radii bends in the plane of the wafer. The inset of Fig. 1 shows the fundamental propagating mode of the waveguide as calculated by the commercial software Olympios. The mode confinement is tighter in the horizontal direction because of the higher index contrast at the core-air interface as compared to the core cladding interface. Top-view scanning electron microscope (SEM) pictures of a single ring, 2 rings, a single disk, two disks are shown in Fig.2 (a), (b), (c) and (d) respectively.



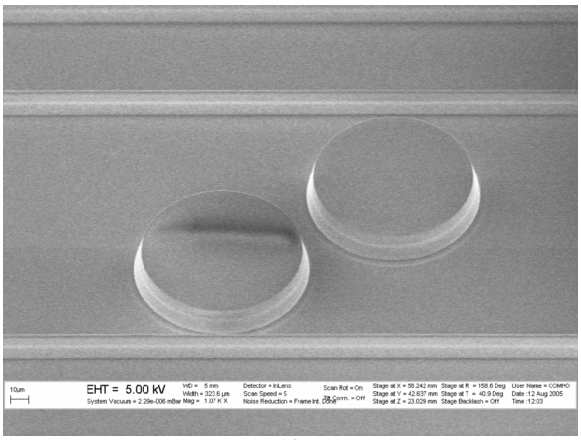
(a)



(b)



(c)



(d)

Fig. 2: SEM pictures of (a) a top-view of a single ring and a straight 'bus' waveguide, (b) a tilted top-view of two rings and two straight 'bus' waveguides, (c) a top view of a single disk and a straight 'bus' waveguide, and (d) a tilted top-view of two disks and two straight 'bus' waveguides.

As shown in Fig. 2 (a) and (c), the straight waveguide and the ring (or disk) are fused together in the coupling region. In Fig.2 (b) and (d). the bus straight waveguides and the resonators are separated by the air trenches in the coupling regions. When these structures were designed, different distances between ring/disk and waveguide were chosen. Very thick photoresist mask made small gaps between ring/disk and waveguide unresolvable. At the mean time, the line-width reduction during the deep glass etching made the large gaps too large for coupling. Therefore, all the structures measured have a fused coupling area like (a) and (c). The coupling area between two rings that are separated is shown in Fig. 3.

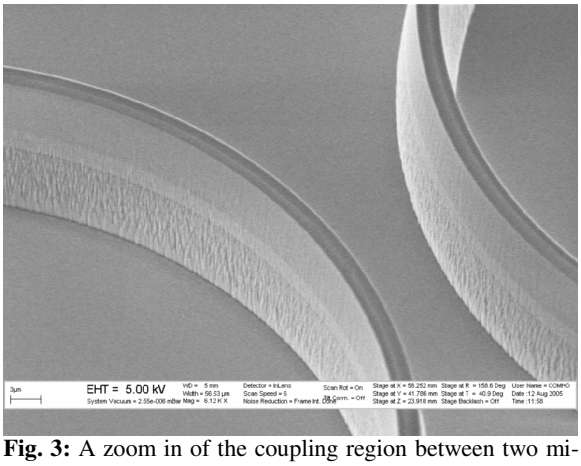


Fig. 3: A zoom in of the coupling region between two micro-rings in Fig. 2 (b).

In Fig. 3, the three layers of the waveguide (top-cladding, waveguide core and thermal oxide buffer) can be seen. The buffer layer shows more sidewall roughness when compared to the top-cladding and core layers.

Results and discussions

Transmission of a straight waveguide, coupled to 1

ring, 1 disk, 2 rings and 2 disks were measured using an optical spectrum analyzer (OSA) synchronised with a tunable laser source (TLS). Before the wavelength was scanned from 1520nm to 1620nm, the coupling of the bus waveguide to standard fibers was optimized at a fix wavelength of 1550nm. The polarization was adjusted to get maximum output power at the same wavelength as well. The transmission spectra of resonators with radius of 25 μm are shown in Fig.4.

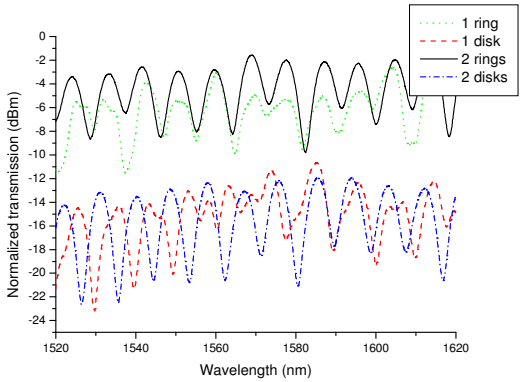


Fig. 4: Transmission spectra of micro-resonators with a radius of 25 μm

The free spectral range (FSR) of the collected transmission spectra. is 9.1nm. A relationship between the radius of the ring R, the effective group index n_g, and the FSR is given by the formula: $$FSR = \frac{\lambda^2}{2\pi R n_g}$$, where λ is wavelength. Using the value of $FSR = 9.1nm$ the radius of the ring $R = 25\mu m$ and a wavelength of $\lambda = 1550nm$, the effective group index of the resonant mode was found to be $n_g = 1.7$. This value is in good agreement with the theoretically expected effective group index of the waveguide structured used.

The spectra collected from double disk/ring resonators show larger out-of-band signal rejection when compared to single ring/disk resonators, which agrees with the theoretically expected results of ref. [9] and the experimental results shown with silicon rich silicon nitride waveguide in reference [2].

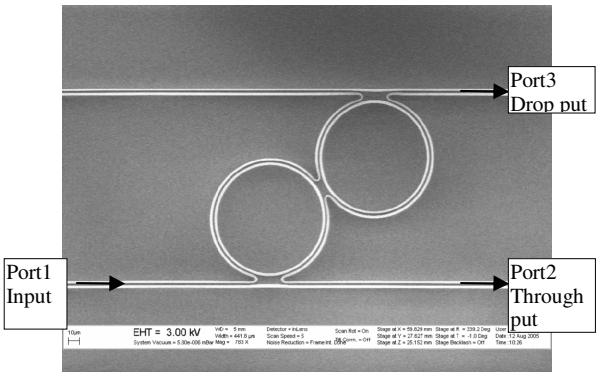


Fig. 5: A SEM picture of 2-ring resonators illustrates different ports for transmission and drop spectra collection.

Double-ring and double-disk resonators are versatile structures that are capable of functioning as channel dropping filters, switches, or add-drop multiplexers. A SEM picture of a double ring resonator with three labelled ports is shown in Fig. 5. The 'through' spectra of the double resonator were obtained by measuring the transmission between ports 1 and 2. The 'drop' spectra was obtained by measuring the transmission between ports 1 and 3. One pair of such spectra from a 2-disk resonator are shown in Fig.6. As a proof of concept, the corresponding peaks and dips appear as expected.

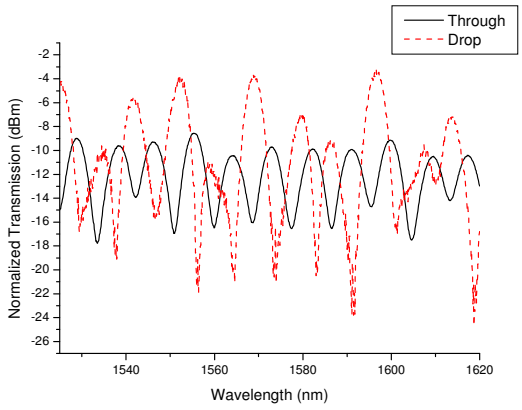


Fig. 6: 'Through' and 'across' spectra of a 2-disk resonator with a radius of 25 μm.

Conclusions

Micro-resonators in the form of rings and disks with a radius as small as 25 μm were fabricated by combining standard silica-on-silicon planar waveguide technology with deep glass etching technology. FSR as large as 9.1nm was achieved. A double disk optical channel dropping filter was demonstrated. This deep etching technology reduces the bend radius from 6mm to 25 μm. More sophisticated optical devices and sub-system are emerging based on it. These novel deep etched micro-resonators add significant functionality to a mature silica-on-silicon waveguide platform.

Acknowledgements

The Danish Technical Research Council is thanked for financial support for this work.

References

1 K. Okamoto, Optical and Quantum Electron., no.31, p.107, 1999.
2 H. T. Philipp, et al, Electron. Lett., no.7, p. 419, 2004.
3 H. Ou, Electron. Lett., no.2, p.212, 2003.
4 H. Ou, IEEE Photon. Technol. Lett., no.5, p. 1334, 2004.
5 B. E. Little et al, IEEE Photon. Technol. Lett., no.10, p2263, 2004
6 P. Rabiei, et al, J. Lightwave Technol., no.11, p. 1968, 2002
7 B. E. Little et al, IEEE Photon. Technol. Lett., no.2, p. 215, 1999.
8 K. Okamoto, Fundamentals of optical waveguides, p.4, Academic Press, 2000.
9 B.E. Little et al, J. Lightwave Technol., no.6, p. 998, 1997.

Deep-UV Lithography Fabrication of Slot Waveguides and Sandwiched Waveguides for Nonlinear Applications

E. JORDANA (1), J.-M. FEDELI (1), L. EL MELHAOUI (1), P. LYAN (1), J.P. COLONNA (1), N. DALDOSSO (2), L. PAVESI (2), P. PELLEGRINO (3), B. GARRIDO (3), ANNA VILÀ (3), Y. LEBOUR (3)
1) Léti-MINATEC, 17 rue des Martyrs, 38054 Grenoble Cedex 9, France, emmanuel.jordana@cea.fr
2) Laboratorio Nanoscienze, Dipartimento di Fisica, Università di Trento, via Sommarive 14, I-38050 Povo, Trento, Italy, daldosso@science.unitn.it
3) EME, Departament d'Electrònica, Universitat de Barcelona, Martí i Franquès 1, 08028 Barcelona, Spain, blas@el.ub.es

Abstract: *Associated to silicon nanocrystals, slot waveguides are promising components for the fabrication of fast optical switches. We report here on the fabrication of slot waveguides with industrial microelectronic tools, especially DUV lithography. The filling of slot waveguides with silicon nanocrystals within SiO_2 by PECVD and LPCVD deposition results in almost filled waveguides owing to incorrect silicon etching profiles. We also report on slot waveguide alternative structure: the sandwiched waveguide. This structure eliminates the slot filling step and allows slot thickness as thin as desired. The association of silicon nanocrystals and slot waveguides, if used in a Mach-Zender Interferometer structure, will pave the way to the first compact all-optical XOR logic gate entirely fabricated with CMOS tools.*

Introduction

Optical interconnections are one of the alternatives to overcome the main limitations (limited bandwidth, increasing resistance and dissipated power) encountered by electrical interconnections for short-distance communications. In particular, for CMOS circuits 2km/cm^2 interconnections density and almost 4x10^6 A/cm^2 current density are expected for 2009 according to the ITRS roadmap [1].

Using silicon as a photonic material is of great interest since this would allow a coherent continuity between electrical and optical circuits since its full CMOS compatibility. Moreover the Si/SiO_2 system is very well known chemically, thermally and mechanically. Furthermore it would be possible to develop low cost and all-optical communication networks without bottlenecks induced by electrical/optical converters.

Unfortunately silicon is a poor light emitter since it is an indirect gap semiconductor, which results in a great difficulty to obtain a 1.55µm wavelength emitting and electrically-pumped silicon laser. But the demonstration of a continuous-wave Raman silicon laser [2], despite being optically-pumped and emitting at 1.686µm wavelength, has greatly increased the interest in silicon light sources and silicon photonics.

Passive devices (filters, couplers, multiplexers…) have already been demonstrated using silicon-based waveguides and materials exhibiting nonlinear optical properties. Contrary to bulk silicon which presents poor nonlinear properties, silicon nanocrystals embedded in SiO_2 are considered as a very promising material for nonlinear applications as its Kerr coefficient was reported to be in the range of two and four orders of magnitude higher than that of bulk Si and SiO_2, respectively (n_2~10^{-16}m^2/W) [3]. Fabricated by high temperature annealing of LPCVD or PECVD deposition of non-stoechiometric SiO_x layers, nonlinear properties can be tuned according to nanocrystallites size and density [4,5].

As silicon nanocrystals within SiO_2 have a relatively low refraction index, their use in conventional strip waveguides would result in a large cross-section and weak light confinement. So a new waveguide architecture, using E-field discontinuity at the interfaces and where light propagates mostly in the low-index medium, has been proposed: the slot waveguide [6]. It is based on the fabrication of a 100nm-150nm (W_s) wide slot in a monocristalline silicon waveguide with a width (W) of approximately 500nm and a height (h) of 200-300nm. For nonlinear applications the slot is filled with SiO_x. After high temperature annealing all the structures are finally covered by stoechiometric SiO_2. A schematic of a slot waveguide without cladding layer is shown on Fig. 1.

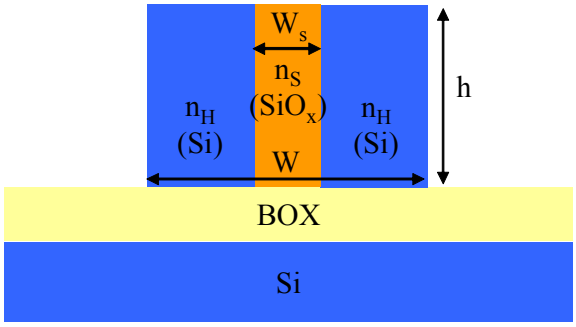


Fig. 1: View of a slot waveguide (W_s=100-150nm, h=200-300nm, W=500nm, n_H ⇔ high index medium : silicon, n_S ⇔ small index medium : silicon nanocrystals within SiO_2).

Strong index contrast and geometrical confinement enables fabrication of highly scalable optical logic gates with reduced optical power and dimensions.

Enhancement of the efficiency of nonlinear processes by a factor $(c/v_G)^2$ is also possible by using slow wave structures concept [7] reducing the group velocity of the light in resonant structures, like slot waveguide-based ring resonators.
Slot waveguides and slot waveguide-based ring resonators have already been fabricated using electron-beam lithography [8-10] but, due to low temperature, PECVD SiO_2 deposition did not fill the slot [10]. Furthermore electron-beam lithography is not compatible with CMOS mass-manufacturing.

This paper is divided into three parts. The first one deals with the fabrication of slot waveguides with almost complete filled slot after e-beam lithography. The second part demonstrates the fabrication of slot waveguides and ring resonators using CMOS compatible 193nm Deep-UV lithography. Slot filling with SiO_x by low temperature deposition process is possible but difficult due to SiO_x deposition method conformality and silicon etching profiles. Then in the last part, we will introduce the fabrication of an alternative slot waveguide structure: the sandwiched waveguide. This structure eliminates the slot filling step and allows the reduction of the slot dimension.

Slot waveguides defined with e-beam lithography

E-beam defined slot waveguides were fabricated on 200mm SOI wafers (400nm Si and 1µm SiO_2). A 110nm thick SiO_2 layer was used as hard mask for silicon etching. The e-beam lithography equipment is a LEICA VB6. After silicon etching a 500nm SiO_2 TEOS cladding layer was deposited.

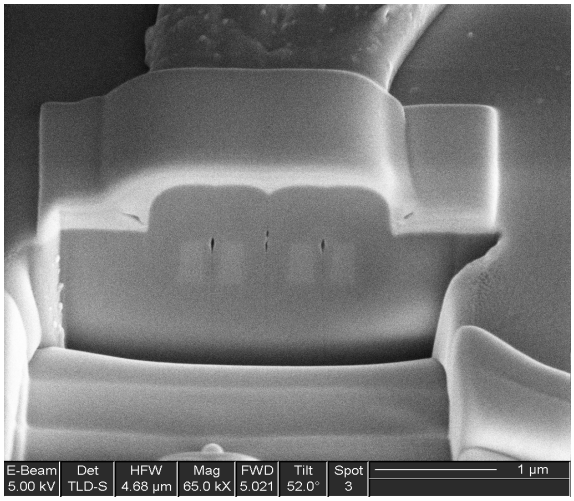


Fig. 2: FIB-SEM cross-section view of 520nm wide slot-waveguides with 110nm wide slots and their associated ring resonators.

As 500nm wide slot waveguides with 120nm slot were expected, the effective dimensions are a guide width of 520nm, a guide thickness of 380nm, and a slot width of 110nm.
As can be seen on Fig. 2, a little air bubble appears on the top of each slot whatever its width is. Their sizes are estimated as 10-15nm for 120nm slots and 20-25 for 160 and 200nm slots. The bubbles sizes are small compared to slot dimensions; thus consequences on waveguiding properties and propagation loss might be not significant.
Propagation losses were measured on basic blocks such as MMI, 90° bends and MZI by coupling in TE and TM polarized light. Two micron width guides with taper section were fabricated on the chip for allowing light injection and collection. Light at 1550nm from a tunable laser is injected by butt coupling through a single-mode-tapered polarization-maintaining fiber. The output was monitored by an infrared camera and the signal collected by an Ge detector.
Table 1 reports the optical losses of the different devices.

Devices	TM	TE
Straight WG	6-8dB/cm	6-8dB/cm
1→2 MMI	2dB	1dB
90° bend with R=30µm	0.02dB/bend	0.02dB/bend

Table 1: Optical losses on basic building blocks measured on slot waveguides devices.

As can be observed propagation losses are not so high (and quite comparable to losses of SOI with similar sizes, which are about 4 dB/cm) although the slot is not entirely filled. Propagation losses should be further reduced once slot waveguides will be fabricated without air bubble in the slot.

Slot waveguides defined with DUV lithography

DUV lithography either at 248nm or 193nm on ASML equipement were used for the purpose of future mass manufacturing. Starting on wafers with 380nm silicon thickness, 150nm thick SiO_2 was deposited as hard mask. After definition of the patterns and hard mask etching, silicon was etched to the buried oxide. Finally a non-stoechiometric SiO_x layer was deposited by LPCVD or PECVD and annealed at 1100°C in a RTP furnace to induce silicon nanocrystals formation. The fabrication process of these slot waveguides was done on a CMOS fabrication line. The slots are 120, 140, 160, 180 and 200nm wide with different guide widths of 500, 520, 540 and 560nm.
Deep-UV 248nm lithography on ASM300 has been successfully used to achieve 120nm slot waveguides. Slot waveguide definition increases with the exposition dose but slot definition is insufficient and rough. If the dose still increases all patterns disappear. Some slots waveguides were successfully defined but the process margins were too low for a reliable fabrication as critical dimensions are above Deep-UV 248nm lithography limits.

For mass manufacturing with acceptable fabrication margins, Deep-UV 193nm lithography on ASM1100 scanner was experimented with different exposition doses (Fig 3).



Fig. 3: SEM top view of slot waveguides just after DUV193nm lithography. W_s=100nm.

Slot waveguides with slots as thin as 120 and 100nm were successfully defined with high reproducibility. So deep-UV 193nm lithography is the right tool for slot waveguides fabrication.
In order to achieve silicon etching, HBr chemistry has been chosen since HBr plasma provides excellent anisotropic etching with a very good selectivity to the oxide [11].

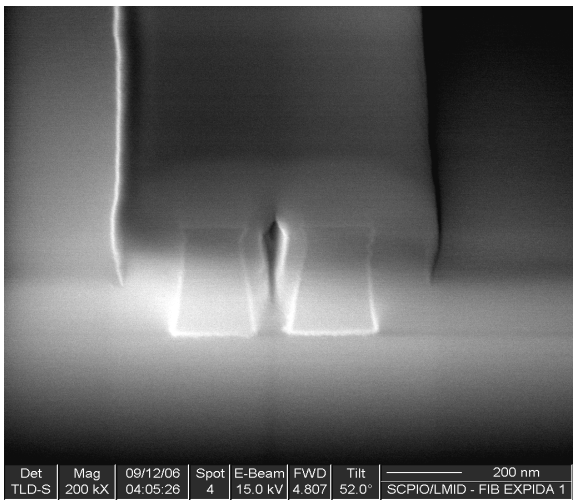


Fig. 4: SEM cross-section view of a 500nm wide slot waveguide (W_s=120nm) just after SiO_x cladding deposition by LPCVD.

On Fig. 4 is reported a FIB-SEM cross-section view of a 500nm wide slot waveguide with a 120nm wide slot which has been covered with SiO_x LPCVD. It is obvious that slot waveguide is not filled even if LPCVD deposition shows a better filling ability than PECVD deposition (not showed) since it is more conformal. But the main reason why air bubble is present in the slot comes from the silicon etching step: silicon profiles bowing phenomena occurs and a significant hard mask layer still remains after etching that, in addition, increases the aspect ratio of the slot and could induce sidewalls roughness. The combination of aspect ratio increase and deposition accumulation at the top of the silicon results in air bubble formation especially if the deposition process is not very conformal such as PECVD.
Thus control of the slopes of the silicon waveguide is one of the key parameters to a good filling of the slot. Further refinements on the etching process and the hard mask optimization should lead to slot waveguides filled with silicon nanocrystals with mass manufacturing process.

Sandwiched waveguides fabrication

In order to reduce processing difficulties encountered above such as defining slot waveguides with lithography, silicon edges control, and slot filling with SiO_x, an alternative process was developed: On 200mm SOI wafers with 205nm Si and 1µm BOX, SiO_x deposition was achieved with a thickness between 50nm and 120nm either by LPCVD or PECVD. The silicon nanocrystals we formed after 1000°C RTP annealing in N_2 atmosphere. Then low loss hydrogenated amorphous silicon [12] was deposited followed by 300nm TEOS SiO_2 deposition acting as hard mask (Fig. 5).

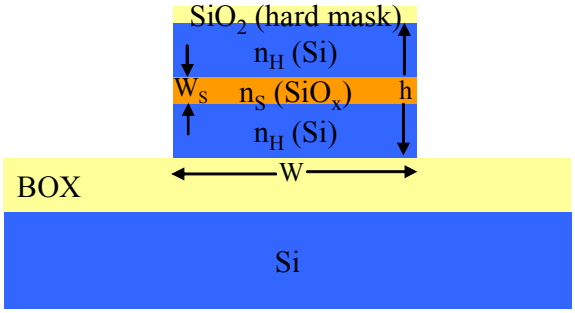


Fig. 5: View of a sandwiched waveguide without SiO_2 cladding layer.

After 248nm Deep-UV lithography and hard mask etching, the three layers (amorphous silicon, SiO_x and monocristalline silicon) were etched sequentially down to the buried oxide. Finally a SiO_2 TEOS cladding layer was deposited by PECVD (Fig. 5). Sandwiched waveguides of 300 and 500nm width were obtained.
On Fig. 6 is reported a SEM cross-section of a sandwiched waveguide. As can be seen, due to fabrication error, almost 300nm amorphous silicon was deposited instead of 200nm. It results in a decrease of the confinement of the light and a shift of the propagating mode towards amorphous silicon. Moreover lateral etching of the amorphous silicon can be ob-

served just above the SiO_x layer. Neverheless, the thin SiO_x layer, obtained by LPCVD, leads to strong confinement of the light.

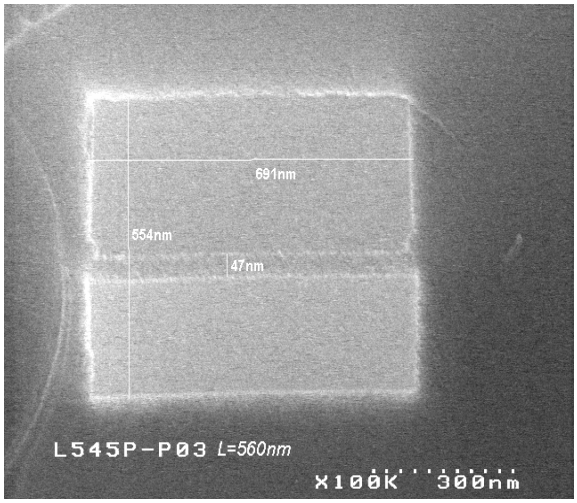


Fig. 6: SEM cross-section of a sandwiched waveguide with 47nm SiO_x. Waveguide width and heigth are respectively 691nm and 554nm.

Propagation losses of the waveguide reported in Fig. 6 were extracted: by injecting light at 1550nm in a 1mm long waveguide, the output of this waveguide was monitored for TE and TM polarization. As low as 4dB/cm propagation losses were measured for the two polarizations. Reduced propagation loss may be obtained with 200nm amorphous silicon instead of 300nm as well as improved etching profiles.

Conclusion

Different slot waveguides fabrications were presented in this paper. The first fabrication of almost filled slot waveguides with a low temperature SiO_2 TEOS deposition was obtained with ebeam lithography. Although a very small air bubble is present in the slot, characterization results showed less than 10dB/cm propagation loss for this kind of waveguide. Improvement in the filling of the slot will be obtained with a very conformal deposition such as LPCVD. Using CMOS compatible 248 & 193nm Deep-UV lithography, first demonstration of the fabrication of slot waveguides and slot waveguide-based ring resonators with mass manufacturing process was shown. DUV 193nm lithography and HBr silicon etching were used to reliably form the slot waveguides. With optimization of the silicon edges of the waveguides, perfect filling with silicon nanocrystals should be obtained. A new alternative process was discussed which leads to the fabrication of sandwiched waveguides. With this process, SiO_x slots as thin as 10nm can be obtained, leading to an increase of the light confinement. The fabricated sandwiched waveguides show propagation loss as low as 4dB/cm which should be reduced with an optimized fabrication process. These first results are thus the first step toward the low-cost CMOS compatible manufacturing of all optical silicon-based logic gates.

Acknowledgments

Financial support by EC under project 017158-PHOLOGIC is acknowledged.

References

[1] http://www.itrs.net/Links/2005ITRS/Home2005.htm

[2] H. Rong, R. Jones, A. Liu, O. Cohen, D. Hak, A. Fang, and M. Paniccia, "A continuous-wave Raman silicon laser", Nature 433, pp725-728, 2005

[3] G. Vijaya Prakash, M. Cazzanelli, Z. Gaburro, L. Pavesi, F. Iacona, G. Franzò, F. Priolo, "Linear and nonlinear optical properties of plasma-enhanced chemical-vapour deposition grown silicon nanocrystals", Journal of Modern Optics, 49, pp719-730, 2002

[4] R. Spano, M. Cazzanelli, N. Daldosso, Z. Gaburro, L. Ferraioli, L. Tartara, J. Yu, V. Degiorgio, S. Hernandez, Y. Lebour, P. Pellegrino, B. Garrido, E. Jordana, J. M. Fedeli, and L. Pavesi, "Non-linear Optical Properties of Si Nanocrystals", Materials Research Society Fall Meeting 2006

[5] M. Cazzanelli, R. Spano, N. Daldosso, S. Hernandez, Y. Lebour, P. Pellegrino, B. Garrido, E. Jordana, J. M. Fedeli, and L. Pavesi, "Non-linear Optical Properties of Si Nanocrystals", Group IV Photonics 2006

[6] C.A. Barrios, "High-performance all-optical silicon microswitch", Electronics Letters, 40 (14), 2004

[7] Y. Chen, S. Blair, "Nonlinearity enhancement in finite coupled-resonator slow-light waveguides", Optics Express, 12(15), pp3353-3366, 2004

[8] T. Baehr-Jones, M. Hochberg, G. Wang, R. Lawson, Y. Liao, P.A. Sullivan, L. Dalton, A.K.Y. Jen, A. Scherer, "Optical modulation and detection in slotted Silicon waveguides", Optics Express, 13(14), pp5216-5226, 2005

[9] T. Baehr-Jones, M. Hochberg, C. Walker, A. Scherer, "High-Q optical resonators in silicon-on-insulator based slot waveguides", Applied Physics Letters 86(8), 081101, 2005

[10] Q. Xu, V.R. Almeida, R.R. Panepucci, M. Lipson, "Experimental Demonstration of Guiding and Confining Light in Nanometer-Size Low-Refractive-Index Material", Optics Letters 29, pp1626-1628, 2004

[11] L. Guo, K. Li, D. Liu, Y. Ou, J. Zhang, Q. Yi, S. Xu, "Reactive ion etching of $Si_{1-x}Ge_x$ alloy with hydrogen bromide", Journal of Crystal Growth, 227-228, pp801-804, 2001

[12] R. Orobtchouk, S. Jeannot, B. Han, T. Benyattou, J.-M. Fedeli, "Ultra compact optical link made in amorphous silicon waveguide", Proceedings- Spie The International Society For Optical Engineering, Vol 6183, p618304, 2006

Micro and Nanolasers for digital photonics

Martin T. Hill (1)
1) COBRA Research Institute, Eindhoven University of Technology, P.O. Box 513, 5600 MB Eindhoven, The Netherlands. Email: m.t.hill@ieee.org

Abstract: *There is an increasing need for high speed digital like processing of signals in integrated optics. The use of current micro and nano lasers to address this issue is examined. Further developments in nano laser technology will improve the case for their use in digital systems. Some of the directions of these further developments in nano lasers are also examined.*

Introduction

The explosive growth of fibre-optic based telecommunications has focused attention again on all-optical digital processing of information encoded in an optical format. Optical signals do not suffer capacitive loading, as in electronics. So optical signal processing systems could in theory be superior to electronics in terms of bandwidth.

Furthermore, the complexity of photonic integrated circuits (PIC) is now being limited due to the lack of signal regeneration and manufacturing tolerances, similar to the situation of analog electronics in the 1960's. There is an urgent need to move to digital processing of optical information in order to achieve VLSI complexity.

To be truly successful all-optical digital information processing systems require: a component or set of components that are boolean complete and can be cascaded to make any digital function, the component(s) must be of microscopic size and able to be densely integrated and interconnected using integrated circuit technology (which also implies that the components have low power requirements), finally the components must operate at very high speed, to be competitive with electronics.

A good review of the requirements for a digital logic device to be used as a building block for larger systems is given in [1]. Some important requirements relevant to optical systems are that device inputs are isolated from the device outputs and visa versa. Furthermore there should be no reflection of energy form the gate output back into the gate. Or if there is reflection then it shouldn't affect the gate operation.

Over the past 40 years significant research has gone into trying to make components that fulfil the above requirements. However, the lack of materials with fast, strong, low power optical non-linearities [2] has meant that high speed, complex, integrated digital optical processors have not been achieved.

Most recent work has concentrated on passive bistable systems which employ micro or nano resonators [3-6]. However these attempts have been remarkably unsuccessful in obtaining high speed low power digital elements. A number of issues have frustrated progress in this direction:

1) High power optical fields are required inside the resonator, and the field levels change dramatically for different states. Absorption leads to heating of the resonantor, and slow thermal effects dominate the device response.

2) It is difficult to build high quality factor (Q) resonators and furthermore there is a trade-off between Q and device speed, leading to fast devices requiring high optical power.

Lasers as digital elements

Lasers have a non-linear optical characteristic suitable for digital operations, and also they are a light source for the optical signals. So it is not suprising that the proposal of using lasers as a digital element has a long history [7-8]. However, these large conventional laser devices consumed considerable power, had limited speed, and finally the passive waveguide technology to interconnect such active devices has only recently been widely available.

Employing micro or nano lasers for digital elements can address some of the disadvantages of larger conventional lasers and also passive bistable systems. Micro-ring lasers have been shown to operate at very low powers [9], [10], this is because there is only a small amount of gain material in the cavity. Even when the laser gain material is pumped hard or far above threshold, the power level is still manageable. Furthermore as the laser size decreases, the ratio of surface area to volume increases, allowing better heat dissipation.

A high Q cavity is not required to build up a large optical field, as the gain medium compensates for losses, thus permitting high speed operation [11]. When light is injected into the laser at a resonant frequency of the laser cavity, only a small amount of input light may be needed to switch the laser light from one mode to another. Thus the amount of light in the laser cavity does not change greatly. Hence, laser based logic gates will not suffer from slow thermal effects caused by the input signals, as occurs in passive systems.

Finally, the recovery time of the laser can in theory be arbitrarily fast, by simply pumping the laser further above threshold [11] (For optical signal modulation, where non-linear gain suppression effects do not limit modulation bandwidth, as is the case in electrical modulation [12].)

Unfortunately micro and nano lasers tolerate only limited coupling to the external environment. So inorder to switch the lasers on and off efficiently, light needs to be injected at a wavelength which is resonant in the laser cavity, i.e. injection locking [13]. We have shown that via injection locking microlasers are able to switch each other, and can form a simple digital systems [14].

However more is required than the system presented in [14] for a digital building block (such as a 2 input NOR gate), that can be used to make arbitrarily large and complex digital systems. In particular the basic requirements of isolating inputs from outputs in the device and avoiding reflections need to be satisfied. To achieve input/output isolation requires at least three orthogonal cavity modes in the micro/nano laser, two for the inputs and one for the output. Furthermore some filtering is required on the device output to block inputs propagating to the outputs and visa versa. Systems using differences in wavelength to obtain orthogonality have been been demonstrated in integrated systems [15], albeit with large lasers.

Ring lasers coupled with a passive ring resonator can have orthogonal modes and provide isolation between inputs and outputs by using modes one free spectral range of the resonator away from each other. The operation of such a gate which can be implemented in active/passive photonic integrated circuit technology is examined in [16]. Additionally the problem of reflections is solved, as in theory no reflections occur in such ring systems.

Single defect photonic crystal lasers [17] offer the possibility of even smaller laser devices, with possibly lower power consumption. Furthermore very high speed operation has been demonstrated in these devices [11]. Photonic crystal cavities also posses a large variety of resonant modes. In such cavities spatial orthogonality can be used to separate the input and output modes.

Consider a modified single defect cavity in a triangular air hole photonic crystal [17] fig. 1. Here just the hexapole mode and doubly degenerate quadrapole modes are considered, a total of three modes. These three modes have a high Q and the resonant frequencies can overlap and be tuned independently by modifying the surrounding air-holes. Remarkably, there exists waveguides with a particular direction and end point, which will couple strongly to one cavity mode and only weakly to the other modes. By choosing an output waveguide which only couples to the main lasing mode and not the two input modes, optical isolation of the output from the inputs is achieved. Furthermore, the inputs can be isolated from the output by choosing input waveguides which only couple to the input modes. Fig. 2 shows this selective excitation for two of the modes.

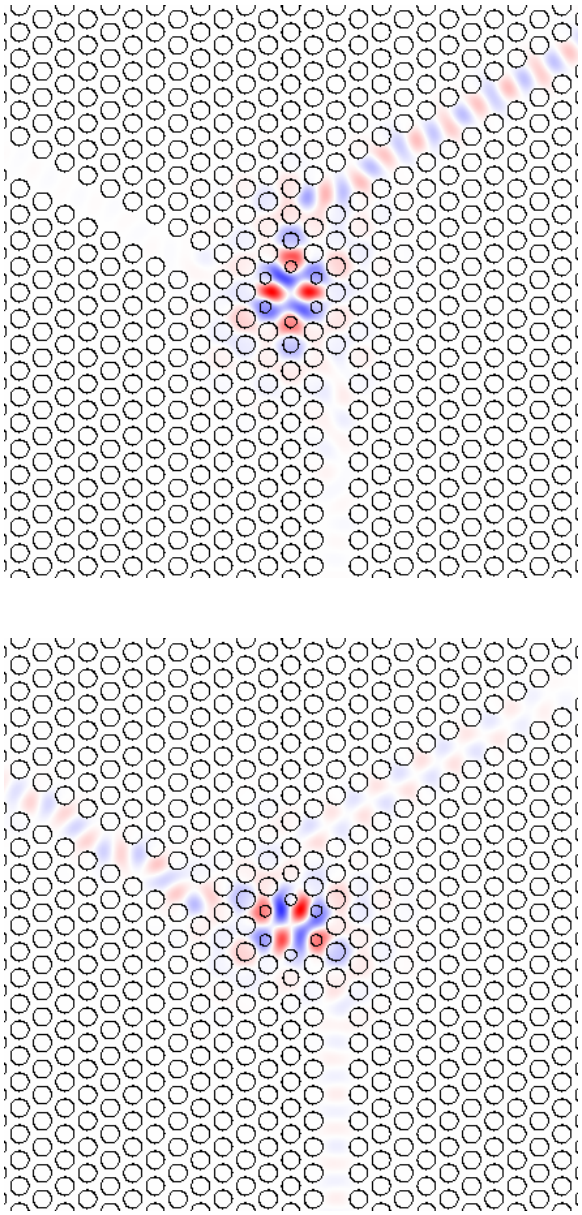


Fig. 1: Finite difference time domain simulation showing selective coupling of cavity modes to just one particular waveguide. The vertical H field is shown in color. Top: even quadrapole mode of single defect cavity. Bottom: odd quadrapole mode.

However, reflections of the output signal back into the driving laser is a difficult problem to solve with single defect cavities, although some solutions exist. This lack of reflections is one area where ring lasers excel, as in theory there is no reflection of light injected into a ring laser.

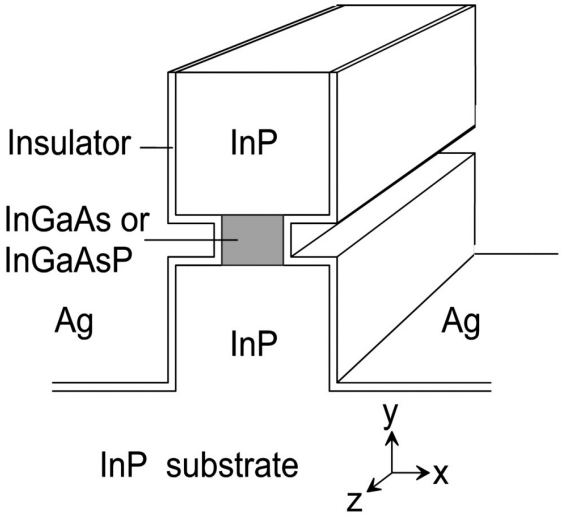


Fig. 2: Structure of an active surface plasmon polariton gap waveguide. Lithography, dry etching and selective wet etching can be used to form the three dimensional nano structure. Metal can be deposited by evaporation around the form to complete the waveguide and provide a top electrical contact.

Further miniturization of lasers

With dielectric cavities there is a fundamental limit to how small the cavity modal volume can be [18]. Furthermore, even in the dielectric cavities with the smallest modal volumes, a much larger structure is required to confine the light to the central region of the device. However, in metallic structures light can be confined and guided to below the diffraction limit. Of particular interest are the surface plasmon polariton gap waveguides (SPGW) [19-20]. Such structures have been shown in theory to confine light in two dimensions to below the diffraction limit.

A method to construct such a waveguide would be to employ a semiconductor heterostructure as shown in Fig 2. Here lithography, dry etching, and selective chemical etching [21] can be used to create a three dimensional form. A thin layer of insulator can be deposited on the form. Finally metal such as gold or silver can be deposited over the form to create a SPGW. The optical mode of the waveguide is strongly confined to the InGaAs region [19-20]. The InGaAs region may be shrunk in the x and y dimensions to several tens of nanometers, while still effectively guiding wavelengths in the 1550nm range.

Such a structure can also serve as an active waveguide offering gain to signals passing along it. This is possible because the central InGaAs region can be electrically pumped with carriers. The top of the InP pillar which is is contact with the metal cladding can form one electrical contact. The other electrical contact is connected to the InGaAs region via the InP substrate.

Resonant cavities suitable for lasers could be constructed from these waveguides by employing Bragg grating reflectors [22]. Or by simply having a section of waveguide an integer number of half wavelengths long, encapsulated in metal. Finite difference time domain (FDTD) simulations of such a cavity are shown in Fig. 3. Here the InGaAs region is 26nm x 26nm x 82nm in size. For simplicity, the insulating layer wasn't present. The surrounding metal was silver.

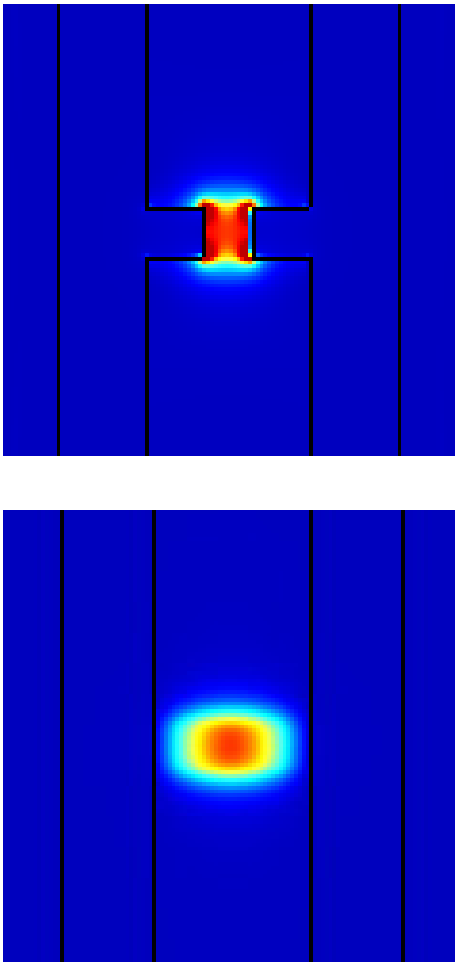


Fig. 3: Results of FDTD simulation of section of SPGW one half wavelength long, and terminated by metal ends. The size of the InGaAs region is 26x26x82nm. Shows the electric field intensity of the resonant mode. Top: E^2 through the x-y plane. Bottom: E^2 through the y-z plane

The simulation results show the resonant mode of the cavity is tightly confined to the InGaAs region, Fig 3. From the simulation the resonant wavelength of the cavity is found to be 1380nm, the quality factor (Q) is 53, and the overlap of the optical mode with the active region, the confinement factor Γ [23] is 0.43. The material gain g required to overcome losses in the cavity can be found from these cavity parameters: $g=2\pi/(\lambda\Gamma Q)$, to be approximately 2000 cm^{-1}. Such gain can be in theory be achieved with

bulk InGaAs lattice matched to InP. Quantum confinement may also increase the material gain [24] in such small structures, making it easier to achieve lasing threshold.

The volume of active material is so small in such a laser structure, that it is possible to achieve intrinsic modulation bandwidths in the terahertz region, with only a few tens of microamps of current. Furthermore with such a small device encapsulated in metal, the problems of device self heating can be minimized.

Conclusions

The rapid progress in integrated optics and laser technology in recent years means that micro and nanolasers are a potential solution for digital photonics. In theory it is possible to satisfy all the requirements for a digital system using micro and nanolasers and passive integrated optics components. Thus providing medium scale integration digital systems with moderate performance. However to truly exploit the high bandwidth potential of optics, and also achieve high integration levels will require further progress in the miniturization of lasers. A method that this can in theory be achieved is via metallic nano structures.

Acknowledgments

This work was supported by the Netherlands Organization for Scientific Research (NWO) through the "NRC photonics" grant.

References

1 R. W. Keyes, Science, vol. 230, p. 138, 1985.
2 A. M. Glass, Science, vol. 226, no. 10, p. 657, 1984.
3 V. R. Almeida, M. Lipson, Optics Letters, vol. 29, no. 20, p. 2387, 2004.
4 M. F. Yanik et al, J. Lightwave Technol., vol. 22, no. 10, p. 2316, 2004.
5 V. Van et al, IEEE J. Sel. Topics Quantum Electronics, vol. 8, no. 3, p. 705, 2002.
6 T. A. Ibrahim et al, IEEE Photon. Technol. Lett., vol. 15, no 10, p. 1422, 2003.
7 G. J. Lasher, A. B. Fowler, IBM Journal, no. 8, p. 471, 1964.
8 W. J. Grande, C. L. Tang, Applied Physics Letters, vol. 51, no. 22, p. 1780, 1987.
9 T. Baba, IEEE J. Sel. Topics Quantum Electronics, vol. 9, p. 1340, 2003.
10 A. Polman, Applied Physics Letters, vol. 84, p. 1037, 2004.
11 H. Altug, D. Englund, J. Vuckovic, Nature Physics, vol. 2, p. 485, 2006.
12 S. L. Chuang, Physics of Optoelectronic Devices, John Wiley & Sons, New York, 1995.
13 C. J. Buczek, R. J. Freiberg, M. L. Skolnick, J. Appl. Phys. Vol. 42, p. 3133, 1971.
14 M. T. Hill et al, Nature, vol. 432, p. 206, 2004.
15 M. T. Hill et al, IEEE Photonics technology Letters, vol. 17, no. 5, p. 956, 2005.
16 M. T. Hill, Frontiers in Optics, paper FThk5, 2006
17 H-G. Park, et al, IEEE J. Quantum Electron., vol. 38, p. 1353, 2002.
18 R. Coccioli, et al, IEE Proceedings Optoelectronics, vol. 145, p. 391, 1998.
19 F. Kusunoki, T. Yotsuya, J. Takahara, T. Kobayashi, Applied Physics Letters, vol. 86, p. 211101, 2005.
20 K. Tanaka, M. Tanaka, Applied Physics Letters, vol. 82, p. 1158, 2003.
21 G. A. Ferrante, J. P. Donnelly, C. A. Armiento, J. Electrochem. Soc.: Solid-State Science and technology, vol. 130, no. 5, p. 1222, 1983.
22 Z. Han, E. Forsberg, S. He, IEEE Photonics Technology Letters, vol. 19, no. 2, p. 91, 2007.
23 G. P. Agrawal, N. K. Dtta, Semiconductor Lasers, second edition, (Van Nostrand Reinhold, New York, 1993.
24 M. Asada, Y. Miyamoto, Y. Suematsu, IEEE J. Quantum Electron., vol. QE-22, p. 1921, 1986.

MIXSELs - a new class of ultrafast semiconductor lasers

D. J. H. C. Maas, A.- R. Bellancourt, B. Rudin, M. Golling, H. J. Unold, T. Südmeyer, and U. Keller
Department of Physics, Institute of Quantum Electronics, ETH Zurich, Wolfgang-Pauli-Str. 16, 8093 Zurich, Switzerland

Abstract: *We have demonstrated for the first time a passively modelocked vertical external cavity surface emitting semiconductor laser with an integrated saturable absorber within the same growth run. This ultrafast surface emitting semiconductor laser is power scalable at high pulse repetition rates and suitable for cost-effective high-volume wafer-scale fabrication for telecommunications or optical clocking applications.*

Introduction

Since the first demonstration of a passively modelocked vertical-external-cavity surface-emitting semiconductor lasers (VECSEL) in 2000 [1], pulse durations, average powers and pulse repetition rates have dramatically improved [2]. Today, the performance of these ultrafast laser sources is competitive to diode-pumped solid-state lasers: high average output powers of up to 2.1 W [3], short pulse durations of <500 fs [4], and high pulse repetition rates of up to 50 GHz has been achieved [5]. These lasers, however, were based on a separate intracavity semiconductor saturable absorber mirror (SESAM) in folded cavity geometries [6] (Fig. 1a and b).
The integration of the absorber and the gain in a single semiconductor device enables modelocking with the simplest cavity – a straight cavity (Fig. 1c). This will ultimately offer the potential for wafer-scale fabrication and operation at even higher repetition rates. In this work, we have successfully demonstrated such a device for the first time and refer to it as the modelocked integrated external-cavity surface emitting laser (MIXSEL). Such lasers could become an enabling technology basis for ultra-compact high-repetition-rate laser devices suitable for cost-efficient high-volume fabrication.

Integration Concept

The first modelocking experiments were based on quantum well (QW) SESAMs and VECSELs. With semiconductor lasers we have to take into account dynamic pulse-to-pulse gain saturation. Therefore, the saturable absorber has to saturate and recover faster than the gain for stable modelocking. With the same QW material and therefore similar saturation fluence in both the gain and the absorber, this only can be achieved with a smaller cavity mode size on the SESAM (Fig. 1a). Such cavities are not ideal for high power or high repetition rate scaling. More important, this concept is not applicable for wafer-scale integration (Fig. 1c) because of the different mode sizes on gain and absorber.
We were able to lower the saturation fluence and reduce the recovery time of the absorber with quantum dot (QD) SESAMs grown at low temperatures and successfully demonstrated passive modelocking with the same mode size on gain and absorber (Fig. 1b), which we referred to as 1:1 modelocking [7]. This was an important milestone towards our integration goal and also relaxed the constraints on cavity design. This resulted in higher output powers at repetition rates of up to 50 GHz [5].
For the first integration demonstration, however, many more challenges needed to be solved. The acceptance for growth errors is much lower for an integrated structure than for separate gain and absorber, since both electric field enhancements and dispersion depend critically on layer thickness and layer material composition. Another difficulty is the lower growth temperature for the quantum dot section than for the rest of the structure, which leads to annealing of the dots during the continuation of the growth.

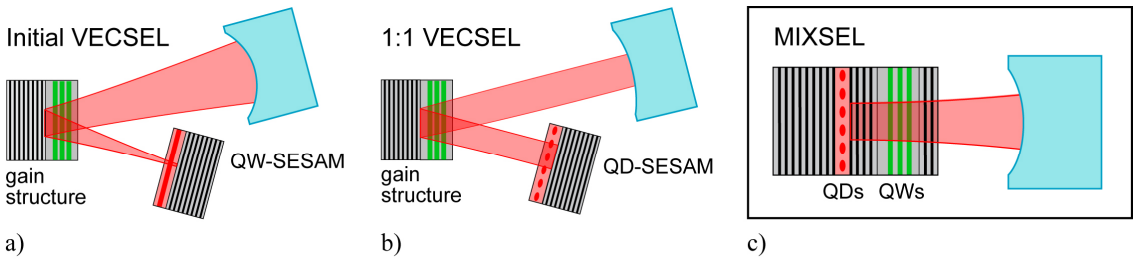


Fig. 1: Three step integration scheme from VECSEL-SESAM modelocking with a) large mode area ratios, b) to identical mode areas and c) to absorber gain integration in a MIXSEL.

MIXSEL Design

The MIXSEL-structure was grown with molecular beam epitaxy (MBE) in a single growth run and consists of five sections (Fig. 2):
1) a highly reflective AlAs/GaAs distributed Bragg reflector (DBR) for the laser wavelength at 960 nm;
2) a low temperature grown absorber section composed of a layer of self-assembled InAs quantum dots embedded in GaAs layers;
3) an intermediate AlGaAs/AlAs DBR for the pump wavelength at 808 nm which prevents the absorption of the pump light in the absorber section;
4) a gain section with 7 InGaAs QWs;
5) an antireflection coating to achieve the required electric-field enhancements for the gain and absorber sections.

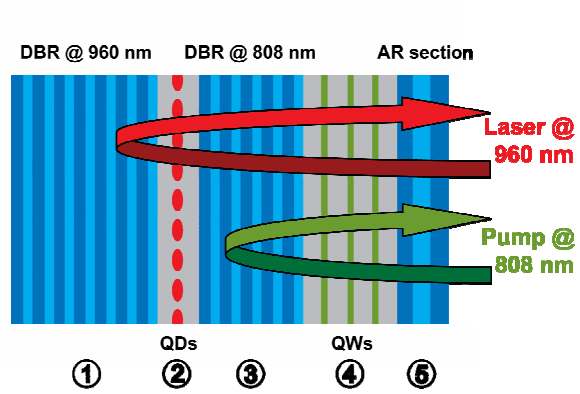


Fig. 2: Schematic MIXSEL-structure (not to scale) with five sections: High reflector at 960 nm, absorber section with self-assembled InAs quantum dots, an intermediate mirror at 808 nm, gain section with InGaAs quantum wells and an antireflection section.

The gain region contains seven InGaAs quantum wells placed in the maxima of the standing-wave pattern and separated by spacer layers of GaAs. The pump light is absorber in the spacer layers around the QWs, giving high pump absorption.
The structure is designed to reduce the influence of growth errors and to minimize the group delay dispersion (GDD) for better modelocking conditions.

Characterization

The grown structures are analyzed with an optical reflectivity measurement in combination with scanning electron microscopy (SEM). Moreover, the GDD is characterized by white light interferometry. The quantum dot properties (absorption and saturation) have been optimized with a nonlinear reflectivity measurement setup using a conventional ML-VECSEL as laser source. The advantage of this laser source is that we operate at similar wavelengths and pulse durations as the MIXSEL. The setup was optimized for high precision: for a variation of three orders of magnitude in pulse energy, the reflectivity is measured with an accuracy of below 0.1%. This enabled us to optimize the saturation fluence and the modulation depth (the difference between an unsaturated and completely saturated SESAM).

Experiment and Results

After growth, the MIXSEL-structure was soldered to a copper heatsink, which is temperature-stabilized using peltier elements and a water-cooled mount. The laser cavity is linear, 5.3 cm long, with the MIXSEL-structure as the end-mirror and a 0.35% output coupler with 60-mm radius of curvature, see Fig. 3. The laser mode size on the MIXEL-structure was 80 µm. We pumped the structure optically at an angle of 45º and at a wavelength of 808 nm. An intracavity 25-µm thick fused silica etalon was used for wavelength tuning and dispersion management.
Modelocking was achieved for lasing wavelengths of 953 – 956 nm. The MIXSEL delivered 40 mW output power at a repetition rate of 2.8 GHz in 35 ps pulses (Fig. 3). The spectral width was 0.11 nm, leading to a time bandwidth product of 4 times the transform limit, indicating that shorter pulses should be possible with these quantum dots.
In this first demonstration of a MIXSEL, the maximum achievable output power was limited by thermal effects due to the high thermal impedance of the 600-µm thick GaAs substrate on which the structure was grown. This can be improved by growing the structure in reverse order ("up-side-down" structure) with etch-stop layers and removing the substrate using selective etching. This has previously been demonstrated with the former VECSEL-SESAM modelocking approach [2, 8]. The low thermal impedance results in a quasi-one-dimensional heat flow, thus the output power can be increased by enlarging the mode sizes on the gain accordingly and operating at the same pump intensity.

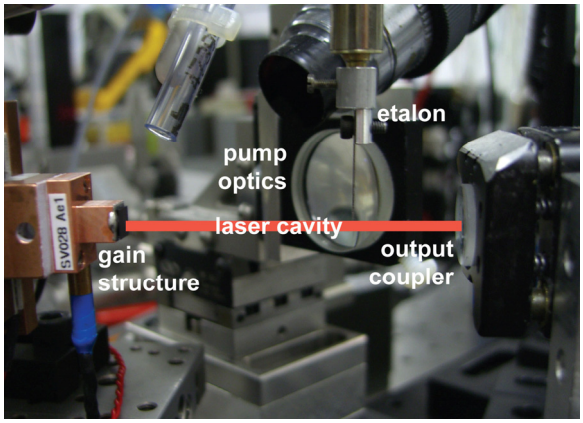


Fig. 3: Laser cavity, the red line indicates the cavity-mode. The large lens in the middle of the picture focuses the pump beam on the gain structure.

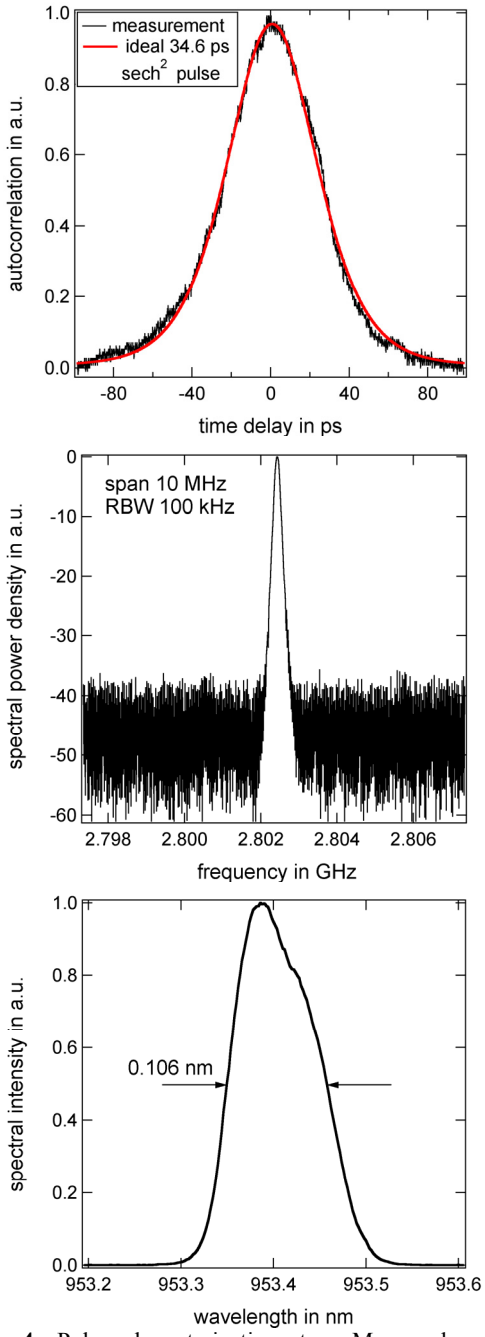


Fig. 4: Pulse characterization; top: Measured autocorrelation fitted with autocorrelation of an ideal 34.6 ps sech2 pulse, center: RF spectrum at pulse repetition rate, bottom: optical spectrum.

Conclusions and Outlook

We have successfully demonstrated the first passively modelocked VECSEL for which the gain and absorber were integrated into single semiconductor structure. Modelocking was achieved with a simple straight cavity with 40 mW average output power at a pulse repetition rate of 2.8 GHz. The pulse width was 34.6 ps and the central wavelength was tunable between 953 nm and 956 nm. This new-class of passively modelocked semiconductor lasers (MIXSELs) will potentially enable the realization of robust, ultra-compact multi-GHz sources. Furthermore this structure is amenable for cost-efficient wafer-scale mass production. The simple cavity geometry should allow record-high repetition rates. Moreover, advanced heat management with an "up-side-down" structure and substrate removal should result in multi-Watt average output powers as previously demonstrated in the former VECSEL-SESAM modelocking experiments [2]. The last step towards even cheaper and more compact ultrafast semiconductor surface emitting lasers will be electrical pumping. This would result in devices ideally suited for many applications such as RGB systems, telecommunications, optical clocking, microscopy – anywhere where the current ultrafast laser technology is considered to be too bulky or expensive.

Acknowledgements

This work was supported in part by the Intel Corporation through a university sponsored research agreement, the European Network of Excellence "ePIXnet," and ETH Zurich.

References

[1] S. Hoogland, S. Dhanjal, A. C. Tropper, S. J. Roberts, R. Häring, R. Paschotta, and U. Keller, "Passively mode-locked diode-pumped surface-emitting semiconductor laser," IEEE Photon. Technol. Lett., vol. 12, pp. 1135-1138, 2000.

[2] U. Keller, A. C. Tropper, "Passively modelocked surface-emitting semiconductor lasers," Physics Reports, vol. 429, pp. 67-120, 2006.

[3] A. Aschwanden, D. Lorenser, H. J. Unold, R. Paschotta, E. Gini, and U. Keller, "2.1-W picosecond passively mode-locked external-cavity semiconductor laser," Opt. Lett., vol. 30, pp. 272-274, 2005.

[4] A. Garnache et al., "Sub-500-fs soliton-like pulse in a passively mode-locked broadband surface emitting laser with 100 mW average power," Appl. Phys. Lett., vol. 80, pp. 3892-3894, 2002.

[5] D. Lorenser et al., "50-GHz passively mode-locked surface-emitting semiconductor laser with 100-mW average output power," IEEE J. Quantum Electron., vol. 42, pp. 838-847, 2006.

[6] U. Keller et al., "Semiconductor saturable absorber mirrors (SESAM's) for femtosecond to nanosecond pulse generation in solid-state lasers," IEEE J. Sel. Top. Quantum Electron., vol. 2, pp. 435-453, 1996.

[7] D. Lorenser et al., "Towards wafer-scale integration of high repetition rate passively mode-locked surface-emitting semiconductor lasers," Appl. Phys. B, vol. 79, pp. 927-932, 2004.

[8] R. Häring, R. Paschotta, A. Aschwanden, E. Gini, F. Morier-Genoud, and U. Keller, "High–power passively mode–locked semiconductor lasers," IEEE J. Quantum Electron., vol. 38, pp. 1268-1275, 2002.

Towards a compact laser for chaos encryption

Yousefi M., Beri S., Barbarin Y., Bente E.A.J.M, de Vries T., Smalbrugge E.,
Van Veldhoven P. J., Oei S., Smit M.K., Nötzel R., Lenstra D. (1)
COBRA Research Institute, TU/e, Postbus 513, 5600 MB Eindhoven, The Netherlands;
1) Delft University of Technology, Faculty of EEMCS, P.O.Box 5031, Delft, The Netherlands;

Abstract: *We demonstrate an integrated laser device that shows well-defined and controllable nonlinear dynamics and even chaos. This makes our laser suited for encryption of data that has to be transmitted in a secure way, using chaos encryption.*

Introduction

As the world becomes more dependent on optical telecommunication, the issue of the security of the transmitted information takes a more prominent role. Since today virtually all information and most transactions are performed using contemporary telecommunications infrastructure, sensitive information such as bank transactions, patient information and government secrets require additional security measure, as compared to for instance a streaming video.

Software level encryption scheme have existed since the birth of information technology, but they are prone to human errors, i.e. the user may forget to encrypt the sensitive data or the encryption key may become public. More reliable hybrid software-hardware level encryption schemes have also been devised, among which the most prominent is the Quantum encryption scheme [1]. This scheme relies on the fundamental properties of quantum mechanical systems to transmit a software encryption key. This key is then used to encrypt the data, which is thereafter transmitted over a conventional line.

Recently the feasibility of a purely hardware level encryption scheme based on chaos was demonstrated over the metro fiber-network of Athens, Greece [2]. The optical data signal was hidden in the chaotic output of a semiconductor laser with electro-optical feedback and thereafter transmitted over a conventional fiber link. At the receiver side, an identical chaos generator was employed to generate a chaotic signal, which was subtracted from the incoming signal and the original data message was recovered. The key factor in this hardware level encryption scheme is that the chaos on the transmitter side and the receiver side must be identical. Once that is achieved, the two chaotic oscillators will synchronize, resulting in identical chaotic signals on the receiver and transmitter sides [3].

Nonlinear dynamics and chaos in the output of semiconductor lasers appear because of the resonant interplay between the field and matter in the laser [4]. These dynamics are generally damped, meaning that if the laser is left alone, any perturbation will die out after a few cycles. If the laser is perturbed, say by external resonant optical injection, then it will display nonlinear dynamics, which can evolve into fully blown chaos. This has been the focus of the field of laser dynamics for the past three decades and researchers have gained substantial insight into the underlying fundamental physics [4]. The workhorse of the field has been table-top setups, consisting of semiconductor lasers in various configurations, including semiconductor lasers with external optical injection and lasers subject to optical or opto-electronic feedback [4]. The large sizes of these setups (~ 1m) make them impractical for applications and also handicaps the systems when it comes to alignment and synchronization issues. Moreover, since the complexity of the chaos, i.e. the bandwidth of the chaotic signal, is proportional to the time and lengthscales of the chaos generating system, table-top setups tend to exhibit ‘slow’ (a few GHz) chaos as compared to comtemporary telecommunications standards (a few tens of GHz). It is therefore natural to look towards Photonic Integrated Circuits (PIC) for a fast, compact and controllable chaos generator.

A first step towards such Chaotic Photonic Integrated Circuit (C-PIC) is the demonstration of the existence of chaos in PICs. For this purpose we choose a device that has been fabricated using InGaAsP/InP based COBRA-integration technology: the Colliding Pulse Mode Locked Laser (CPMLL). This device consists of two front-to-front coupled ridge-type Semiconductor Optical Amplifiers (SOA), which are coupled through a ridge Saturable Absorber (SA). The small reflection off the absorber will result in each SOA section having its own modecomb and the CPMLL having a complex compound-cavity modecomb. The form of the CPMLL-modecomb will change with the operation conditions of the CPMLL and for certain values of the parameters (pump current and absorber voltage) the two modecombs will be resonant and the two SOAs will resonantly inject eachother. This is an ideal scenario for the generation of nonlinear dynamics and chaos.

Using a novel method, we demonstrate structured nonlinear dynamics in the output of the CPMLL by constructing a phase space for this system and identifying and reconstructing the attractors on which the system operates. Moreover, as a function of the common pump current over the SOAs, we can identify a Hopf-bifurcation [5], evolving into a period-doubling sequence (Feignbaum-sequence) [5], which eventually evolves into fully-blown chaos [5].

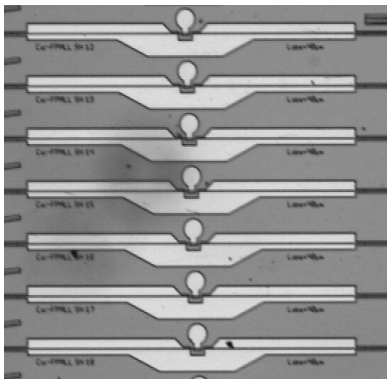


Figure 1: A picture of an array of seven CPMLL's. The SOA's have a common contact and the (round) pad contacts the 40 µm long SA, which is surrounded by 15 µm long isolation sections. The whole chip-width (facet-to-facet) is 1985 µm

These are typical characteristics of a dynamical system and we can therefore claim the existence of C-PICs [5].

In the next section the fabrication of the device and the experimental setup are described. Thereafter we present the nonlinear dynamics of the system and end with a conclusions and outlook section.

The device and experimental setup

The material for the device was epitaxially grown by the PSN-group of the COBRA institute, and consists of a 350 or 400 nm thick n-type InP substrate, on which a 120 nm thick λ = 1.5 µm bulk InGaAsP layer has been grown between two 190nm thick λ = 1.25 µm InGaAsP layers. The film is capped by 1500nm gradually doped layers of InP ending with a 200 nm thick highly doped InGaAs layer for contacting purposes. The material was MOVPE grown using all metal-organic precursors.

Five mask sets were used for the processing. The sample was coated with 70 nm SiN_x using Plasma Enhanced Chemical Vapor Deposition (PECVD), after which the first waveguide mask pattern was etched into the SiN_x using a Freon Reactive Ion Etching (RIE) process. The pattern was then transferred to the wafer using a second step of Methane-Hydrogen based RIE [6]. Since both shallow and deep etched ridge waveguides were present on the mask, the RIE etch of the total InP structure was performed in several steps, using 2 other masks (deep regions and isolation section) to achieve the desired surface topology. Next, the sample was passivated and planarized by spinning and curing six layers of polyimide (PI-2737) on the sample. The polyimide was then etched back to open the contact openings, resulting in a surface suitable for self-aligned metallization. Next, the metallization mask was used to define the contact regions, where 65/70/400 nm of Ti/Pt/Au was evaporated to create the contacts. Finally, a 500 nm thick plating gold layer was grown using electro plating techniques. At this stage a 65/70/500 nm of Ti/Pt/Au was deposited on the backside of the sample to achieve an n-contact. The sample was then annealed to create the Ohmic contacts and the different components were cleaved apart for characterization.

The device under study is part of a series of Colliding Pulse Mode Locked Lasers (CPMLL), an array of which are depicted in Figure 1. The design consists of 2 µm wide ridge-Semiconductor Optical Amplifier (SOA) terminated by cleaved facets (R=0.35) at the two ends. With our layer stack, the 2 µm wide ridge is designed to sustain the fundamental transverse mode in the structure, while the first order mode is cut-off. Through removal of the contact layer and ~700 nm InP, a short section (20 or 40 µm long) located around the centre of the device is isolated from the SOAs. This section is electrically contacted and by setting a reverse bias a Saturable Absorber (SA) is realized. Both the amplifier sections are connected to the same contact for the current supply. The chip is 1985µm long in order to obtain 39.8 GHz repetition rates for mode-locking operation [7]. The locations of the 40µm long SAs are varied gradually from the centre over the series of lasers. This guarantees that after cleaving we have at least one laser where the SA is centered symmetrically between the two SOAs and which will be well suited for mode-locking operation. Two separate batches of devices were produced with material gain centered at 1520 and 1550 nm, respectively. Each batch contained 20 CPMLLs with 40 µm long SA sections and 20 CPMLLs with 20 µm long SA sections. Also, each of the device sets was produced with both deep and shallow etched ridge waveguides. The deep etched devices were quite stable and did not show nonlinear dynamics and will therefore be disregarded in the current analysis. Of the 40 shallow etched CPMLLs, the ones with long absorber sections showed strongest nonlinear dynamics in the ~ 1 GHz range. The work presented in this paper is from the most asymmetric of the shallow etched devices with a 40 µm long SA section, surrounded by 15 µm of isolations on both sides and the SA is ~ 40µm off from the center. In what follows, this device will be refereed to as the CPMLL.

Under normal operation conditions, the symmetric device is expected to show mode-locking operation at 39.8 GHz repetition rate with 2.4 ps wide pulses [7]. The asymmetric devices are not expected to show optimal mode-locking and generally show nonlinear dynamics in the ~1 GHz range. The most prominent cause of these nonlinear dynamics is the asymmetry in the mode spacing of the two gain section, which due to the low reflectance off the absorber section, form two cavities with slightly different optical path lengths, resulting in slightly different mode-combs. As the index is varied, by for instance changing the pump current, the optial path lengths in the device changes and a resonant injection scenarion may be

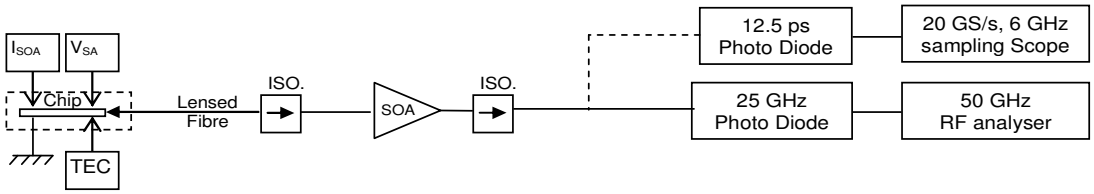


Figure 2: The experimental setup. The chip (left) was mounted on a (grounded) temperature mount and contacted. The light was collected by a lensed fiber and passed trough a SOA between two isolators. Thereafter two 25 GHz photodiodes were used to detect the light and pass it into an RF analyzer and a sampling scope

achived. Intuitively, the device can therefore be seen as two front-to-front coupled lasers with mutual injection, where the nonlinear dynamics are caused by the beating between of the longitudinal modes of the unequal mode combs.

The CPMLL chip was glued on a temperature controlled copper mount, which was attached to a heat reservoir that was kept at constant temperature of 14°C using a (cooled) water pump to facilitate constant alignment of the facet into a fiber (Figure 2). The current to the two amplifier sections and the reverse bias voltage of the saturable absorber were applied through two probes, using an ILX Lighwave LDX-3900 laser deriver and a Keithly Model 2400 stabilized voltage source, respectively. Light from the laser output waveguides was collected using a lensed fiber. The signal of the 1520 nm gain centered chip was amplified using a SOA between two optical isolators in order to avoid feedback into the laser, while the signal of the chip with gain centered at 1550 nm was amplified using an EDFA between two optical isolators. The extracted light was analyzed using a 25 GHz bandwidth NewFocus-photodiode connected to a 50GHz electrical spectrum analyzer [Agilent E4448A], or to a 20 GS/s oscilloscope with 6 GHz bandwidth and 8 MegaSamples per channel memory [LeCroy WaveMaster 8160].

It is quite clear, already from a quick overview of the data (see for instance Figure 3, right column) that the CPMLL operates on many dynamical attractors, including some chaotic ones. We found that for a reverse bias of –1.6 V on the absorber the device shows nonlinear dynamics which are characteristic for a large number of devices in the series. The common pump current of the device was used as the bifurcation parameter. It is essential from a bifurcational theoretical point of view that a single bifurcation parameter is used for the analysis, in order to be able to conclude on specific routes in parameter space that cause certain sequence of bifurcations, or phase transitions [5]. The threshold of the CPMLL was at 128 mA and the current was varied between 137 and 150 mA in this work.

Data analysis

Using the method of Ref [8], we constructed a three dimensional phase space **Σ** for the system and analyzed the phase space trajectory, consisting of $\vec{X}(t) = (P(t+\tau), P(t), dP(t)/dt)$. Here $P(t)$ is the detected output power of the CPMLL. Analogous to [8], the full three dimensional phase space is used for the analysis, while for the sake of simplicity only the two dimensional projections of the phase space trajectory on the $(P(t+\tau),P(t))$ and $(P(t), dP(t)/dt)$-planes are displayed.

Figure 3 shows one bifurcation sequence of the CPMLL as a function of the pump current. The left column shows the $(P(t+\tau),P(t))$-plane, the middle column is the $(P(t),dP(t)/dt)$-plane and the right column shows the RF-spectrum on a 0 to 3 GHz scale.

Above a pump current of 148.4 mA, the CPMLL operates on a fixed-point, i.e. CW-operation (not shown). It is in this region that one should search for mode locking behaviour. At 148.4 mA, the fixed point has already destabilized slightly and any deviation from the fixed point results in a spiraling trajectory towards the fixed point value. Due to the presence of noise in the system, the bifurcations i.e. the transitions between various kinds of dynamics, are not very clear. It is therefore not possible to distinguish the spiraling behaviour exhibited in Figure 3, top row, from a very low amplitude limit cycle (self-oscillations). As the pump is decreased to 145.2 mA, the Hopf-bifurcation (appearance of self-oscillations) becomes more stable and a clear limit cycle with an oscillation frequency of ~ 1.25 GHz appears in the output. This limitcycle undergoes a period-doubling cascade wich eventually results in chaotic behaviour at I=140.4 mA. The noise-like RF-spectra at 140.4 mA clearly identifies the chaotic nature of the dynamics. This pocket of chaos is exited through a quasi-periodic attractor (torus) at I=139.7 mA and the torus eventually changes into a period-2 limitcycle at I=137.2 mA. This is a scenario which occurs in many dynamical systems. We have also performed similar analysis on other device in both the batches that were fabricated and they all show similar nonlinear dynamical scenarios.

For chaos encryption applications, it would be desireable to be able to follow the period doubling sequence leading to the chaos at I=140.4 mA. This will allow one to draw conclusions on the exact nature of the chaotic attractor at I=140.4 mA and thus

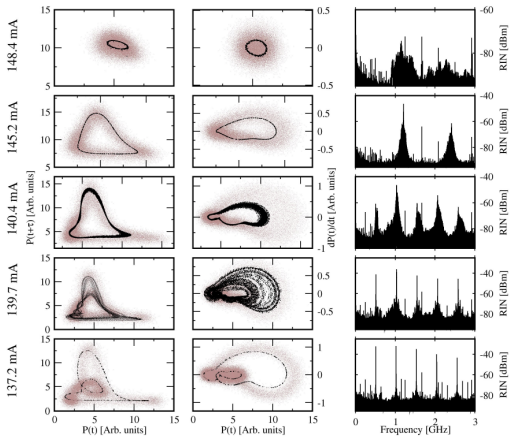


Figure 3: Left column shows the $(P(t+\tau),P(t))$-plane, the middle column is $(P(t),dP(t)/dt)$ projection and the right column shows the RF-spectra up to 3 GHz scale. (Top to bottom) In the top row the fixed point operation has just destabilized and is followed by a limitcycle in row 2, which evolves into chaotic dynamics in row 3 which is then exited through a torus in row. Finally the CPMLL ends up on a period-2 limit cycle attractor. The narrow peak at ~1.7 GHz in the RF-spectra is from the oscilloscope or photodiode and should be disregarded. Black dots are the reconstructed trajectory and gray are the experimental data points.

facilitate synchronization of two chaos generators. Unfortunately, the parameter range over which the CPMLL shows nonlinear dynamcis is very small. This is because the CPMLL was originally designed for mode locking applications and thus does not have any specific built-in control mechanism with which one can vary the interaction between the two SOAs. Future C-PIC designs, consisting of coupled lasers, must therefore contain mechnaims for the control of the coupling between the lasers. At COBRA, we are currently fabricating integrated laterally coupled ridge lasers and laterally coupled tunable ridge lasers (with built-in phase shifters) for chaos encryption purposes. Furthermore, our future devices will be fabricated on COBRA-Active/Passive platform, allowing us separate control of the spectral and gain properties and thus further increasing the impact of the control parameters on the chaotic output.

Conclusions and outlook

We have fabricated a set of Colliding Pulse Mode-Locked semiconductor Lasers, on a photonic integrated circuit. The device, originally intended for mode locking applications, show well-structured nonlinear dynamics in its most asymmetric form, i.e. when the absorber is placed about 40 µm away from its symmetri point.

Using a novel method of analysis, we were able to visualize the attractors and show a clear transition in and out of chaos as a function of a single bifurcation parameter, namely the pump current. From a dynamcial system point of view, this is strong evidence of well-structured nonlinear dynamics in the CPMLL. Unfortunatelty, the small current range over which all these transitions occur make the CPMLL a bad candidate for chaos encryption. For this purpose, we at COBRA are fabricating novel Active/Passive based C-PICs with higher level of control over the nonlinear dyanmcis.

One aspect most PICs have in common is that they consist of networks of monolithically coupled components. In this respect, the CPMLL analyzed here is not unique at all and confronts us with the fact that photonic integrated devices will inevitably exhibit deterministic nonlinear dynamics. This is good news, since the nonlinear dynamics exhibited by the CPMLL are stable over the life time of the device, reproducible from batch to batch and generally faster than their table-top counterparts.

Acknowledgments

The authors acknowledge financial support by the Dutch Science Foundation (NWO) through the Dutch Technology Foundation (STW) and the NRC-Photonics program, and by the *Towards Freeband Communication Impulse* program of the Dutch Ministry of Economic Affairs and the EU-COST288 action. M.Y. is funded through the STW-TWICE project.

References

1 D Stucki *et al* 2002 *New J. Phys.* **4** 41, 2002.
2 A. Argyris *et al.*, *Nature* **438**, 04275, 2005.
3 G. D. van Wiggeren and R. Roy, *Science* **279,** 1198, 1998.
4 D.M. Kane, K.A. Shore, Ed. *Unlocking Dynamical Diversity: Optical Feedback Effects on Semiconductor Lasers*, Wiley, New New York, 2005.
5 E. Ott, *Chaos in Dynamical Systems*, Cambridge Univ. Press, Cambridge, 1993.
6 Y.S. Oei et.al., Proc. 7th Eur. Conference on Intergr. Opt. (ECIO '95) p. 205, 1995.
7 Y. Barbarin, et al., *Proc. ECOC 2005 Glasgow Scotland Vol 3 We4.P.086*, p. 673, 2005.
8 Yousefi et. al., "New role for nonlinear dynamics and chaos in integrated semiconductor laser technology", Phys. Rev. Lett., 2007, in print.

Optical Buffer Memory Using Polarization Bistable Vertical-Cavity Surface-Emitting Lasers

Hitoshi Kawaguchi (1), (2), (3), Takashi Mori (1), (2), and Yuuki Sato (2)
1) Graduate School of Materials Science, Nara Institute of Science and Technology,
8916-5, Takayama-cho, Ikoma-shi, Nara-Pref. 630-0192, Japan
2) CREST, Japan Science and Technology Agency (JST)
3) Optoelectronic Industry and Technology Development Association (OITDA)
e-mail: khitoshi@ms.naist.jp

Abstract: *A novel optical buffer memory with shift register function is proposed. The buffer consists of a two-dimensional array of polarization-bistable vertical-cavity surface-emitting lasers (VCSELs), in which the bit state of the optical signal, "0" or "1" is stored as a lasing linear polarization state of 0 or 90°. Two-bit optical buffering is experimentally demonstrated using two 980 nm polarization-bistable VCSELs having a mesa structure.*

Introduction

Optical packet switching is emerging as a potentially important technology in optical networks. To handle the contention of output ports at an optical packet-switching node, a high-speed, low-power optical memory for buffering data is required. A fiber-loop-type buffer equipped with a gate has been proposed[1]. However, these all-optical buffers are unable to access the data randomly at an arbitrary timing. Optical flip-flop memories, in which one bistable device acts as a one-bit memory, are also potentially applicable to this scenario[2]. Two configurations for achieving fast and low-power bistable optical devices have been reported: a polarization-bistable vertical-cavity surface-emitting laser (VCSEL)[3], and a coupled micro-ring laser[4]. Optical shift registers have received considerable attention and several approaches have been explored, including an optical shift register based on cascaded optical flip-flop memories driven by common optical clock pulses[5]. This concept has also been realized using coupled self electrooptic effect devices (SEEDs) driven by changes of the driving voltage[6].

The existence of pitchfork bifurcation bistability through gain saturation in laser diodes has been predicted theoretically[7], and has been observed experimentally as polarization bistability in VCSELs[8]. The polarization bistable operation in a VCSEL is shown schematically in Fig. 1. The VCSEL with square mesa structure exhibited bistable polarization switching between 0° polarization and 90° polarization[8]. The VCSEL initially oscillated with 90° linear polarization, but switched permanently to 0° linear polarization upon injection of a 0° polarized optical trigger pulse. The polarization switch was reversible upon injection of a suitable 90° polarization trigger pulse. The polarization state did not change upon injection of an optical trigger input with the same polarization as the current VCSEL state. This polarization-bistable VCSEL is thus usable as an AND or OR gate. In previous experiments using VCSELs[9], ultrafast polarization switching with 7 ps switching-time was successfully demonstrated in all-optical flip-flop operation[3]. Switching energy of just 0.2 and 0.3 fJ has also been achieved for the set and reset optical pulses, and a switching frequency of 10 GHz has been demonstrated in flip-flop operation[10].

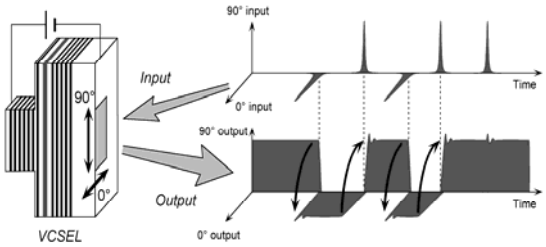


Fig. 1: Bistable polarization operation in a VCSEL

In this presentation, a novel optical buffer memory with shift register function is discussed. The buffer is based on a two-dimensional (2D) array of polarization-bistable VCSELs, and is experimentally demonstrated to realize optical buffering, involving the sequence of selective storage of signal bits from a four-signal-bit train, readout of the stored signals with an appropriate time delay, and finally erasure of the stored signals.

Principle of optical buffer memory

Using a 2D array of polarization-bistable VCSELs, a novel optical buffer memory can be constructed, as shown in Fig. 2[11,12]. The polarizations of the VCSELs in the first column (M_{1x}) are reset to 0° by injection of an optical reset pulse with 0° polarization. The ultrafast optical signal is converted to spatially parallel signals by a time-to-space converter, and the parallel set of signals is injected into the VCSELs together with optical set pulses. The power of the optical signals "1" and the optical set pulse are weaker than the polarization switching threshold, but the sum of the powers of the two inputs exceeds the threshold. Thus, the VCSELs only change polarization (from 0 to 90°) when the optical signals "1" and the optical set pulses are injected simultaneously into the VCSELs (i.e., AND gate operation). The output of each VCSEL of the first column is thus polarized depending on the bit state ("0" or "1") of the input signal which is injected with the set pulse simultaneously. The optical gates

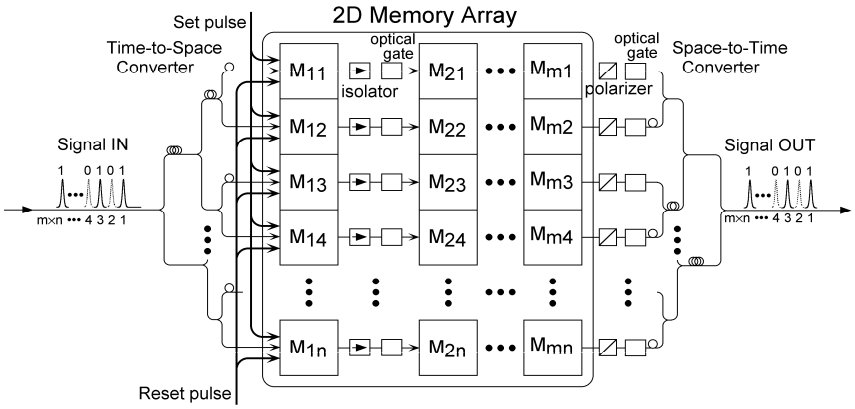


Fig. 2: Proposed optical buffer memory with shift register function

between the first column (M_{1x}) and the second column (M_{2x}) are then opened, and the optical outputs of M_{1x} are injected into M_{2x} via optical isolators. The data stored in M_{1x} are transferred to M_{2x} and held as memory, since the polarizations of the M_{2x} array switch to match those of M_{1x}. Only the 90° outputs from the VCSELs of the last column (M_{mx}) transmit through polarizers. The output signal pulses are created from the CW outputs of the VCSELs using optical gates, and are converted to an ultrafast optical signal by a space-to-time converter. This circuit thus provides an optical buffer memory with shift register function. This shift register function allows continuous and long data to be stored, and simplifies the design of the time-to-space and space-to-time converter, both of which can now be constructed using optical fibers of appropriate lengths and 3 dB couplers. This makes it possible for the converters to be integrated into silicon-based planar lightwave circuit (PLCs) or semiconductor integrated waveguides. As optical gates that are inserted between columns and at the output of the VCSEL, $LiNbO_3$ modulators were used in the present experiments. However, ultrafast all-optical switches should be used for higher signal bit rates. These features provide advantages such as the potential for large-scale 2D VCSEL arrays.

Polarization bistable VCSEL

A 980 nm VCSEL was used as the memory element (Fig. 3). This VCSEL has InGaAs active layers and AlGaAs distributed Bragg reflectors (DBRs)[13]. The p-type DBR was processed to a 5×4.5 μm^2 rectangular post-structure and was buried with a polyimide layer. The VCSEL lased in the lowest-order transverse mode. The lasing polarization was one of the two linear polarizations of 0 and 90°, and polarization switching was observed at approximately 6.7 mA with hysteresis of about 0.6 mA in operation at 15 °C. The typical side-mode suppression ratio (SMSR) determined from the measured polarization resolved spectra was 34 dB, indicating stable laser oscillation in the lowest-order transverse mode. The typical value of the orthogonal

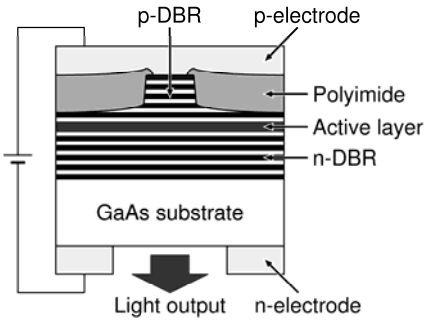


Fig. 3: Schematic structure of VCSEL as a memory element

polarization suppression ratio (OPSR) was 23 dB. All-optical flip-flop operation was obtained with injection of a 9.6 μW set pulse and 9.2 μW reset pulse.

One-bit optical buffering

The circuit described above was successfully used to perform one-bit optical buffering in experiments. A timing chart for the optical buffering is shown in Fig. 4 for both "1" and "0" signals. The injection power of the data signal and set pulse is set less than the polarization switching threshold in order to obtain AND gate functionality. In the case of "1" signals, when both the data signal and set pulse are injected simultaneously, the injection power exceeds the polarization switching threshold and the lasing polarization of the VCSEL is switched from 0 to 90°. Thus, b_1 of the data signal is stored as the polarization state of the VCSEL. The 90° polarization component of the VCSEL output is read as the readout signal by opening an optical gate. A reset pulse is finally injected, and the lasing polarization of the VCSEL returns to 0°. In the case of "0", the sum of b_1 and the set pulse power does not exceed the threshold, causing the lasing polarization of the VCSEL to remain at 0°. A "0" signal is then readout by applying a gate pulse.

Figure 5 shows the setup. The injection lights for the data signal, set pulse and reset pulse were generated by tunable external cavity laser diodes (EC-LDs) and $LiNbO_3$ modulators, and were polarized to 90 or 0° by polarization controllers (PCs). The VCSEL was

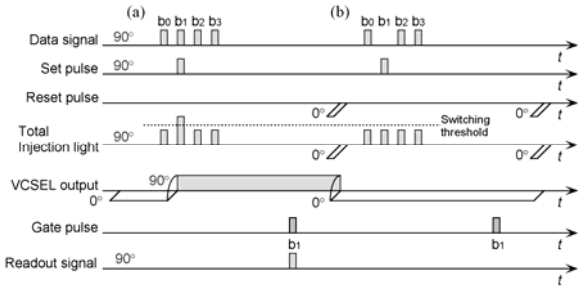


Fig. 4: Timing chart for one-bit optical buffering

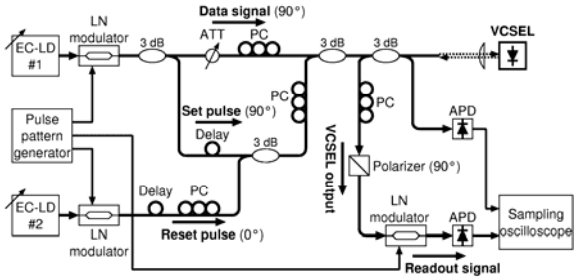


Fig. 5: Experimental setup for demonstration of one-bit optical buffering

operated at an injection current of 5.8 mA, output power of 28 μW, and temperature of 20 °C. A readout signal was created from the 90° component of the CW output of the VCSEL by a $LiNbO_3$ modulator.

The experimental results are shown in Fig. 6. Due to limitations with respect to pattern generation, the injection lights include unnecessary pulses, but these do not affect the operation of the optical buffer memory. The data patterns were set to "1111" in the first half and "1011" in the later half of the run. The timing of the set pulse was adjusted to that of the 2nd bit of the data signal. The lasing polarization of the VCSEL was switched from 0 to 90° only in the first half, remaining at 0° in the later half. Readout signals corresponding to the 2nd bits of the data signal were obtained, demonstrating one-bit optical buffering.

Two-bit optical burning

Principle of the two-bit optical buffer memory is shown in Fig. 7. A data signal and a set pulse are a linear polarization of 90°. The data signal is devided into two (data signal (bit 1) and data signal (bit 2)) and data signal (bit 1) is delayed for one-bit priod. The data signal (bit 1) and the data signal (bit 2) are injected into VCSEL 1 and VCSEL 2, respectively, together with the set pluse. Each injection power of the data signal and the set pulse are set to be less than the polarization switching threshold of the VCSEL. When both of the data signal and the set pulse are injected simultaneously, the injection power exceeds the polarization switching threshold and the lasing polarization of the VCSEL is switched from 0° to 90°. Therefore, b1 and b2 of the data signal are stored as the polarization states of VCSEL 1 and VCSEL 2,

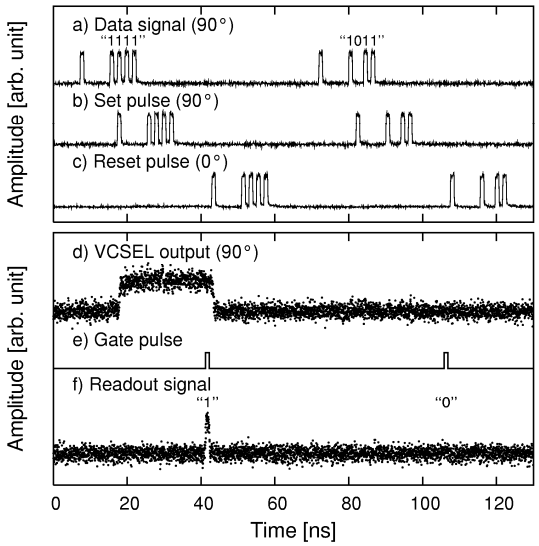


Fig. 6: Experimental results of one-bit optical buffering

respectively. Then, 90° polarization component of the VCSEL outputs are gated and are multiplexed for the memory output. Finally a reset pulse of 0° polarization is injected, and the lasing polarizations of the VCSELs return to 0°.

Figure 8 shows the experimental setup of 2-bit optical buffering. The data signal was devided into two parts and one data signal was delayed for one-bit period. In order to perform the polarization switching of two VCSELs using the injection lights with the same wavelengths, the lasing wavelengths of the VCSELs were tuned by controlling the device temperature. To construct a serial data stream, one VCSEL output was combined with another VCSEL output with one bit period delay. Other parts were the same as the experiment shown in Fig. 5.

Experimental results are shown in Fig. 9[14]. The data sequences were set to four patterns of "1001," "1011," "1101" and "1111." The 2nd and 3rd bits of the data sequences were stored as the polarization states of VCSEL 1 and VCSEL 2, respectively. The memory output signal had four bit patterns of "00," "01," "10" and "11" that correspond to 2nd and 3rd bits of the data sequences. Therefore 2-bit optical buffering has been successfully demonstrated.

Assuming the development of key technologies such as appropriate time-to-space and space-to-time converters, the number of bits that can be stored in this buffer memory is ultimately limited by the electrical power consumption of the VCSEL. If the bias current can be reduced to 1 mA, a single VCSEL consumes 1 mW at 1 V. Thus, a single 1000 × 100 2D array of VCSELs provides 100 kbits of optical memory, but requires 100 W of power. Arrays of this size will be required for all-optical routers with small integrated optical buffers as small as 10-20 packets (80-160 kbits)[15]. Substantial improvements in the buffer memory are considered possible. The VCSELs of the first column (M_{1x}) should operate

with high-speed. For the other VCSELs (M_{2x} ~ M_{m-1x}), low power consumption is the most important factor. Optical output of the VCSELs of the last column (M_{mx}) should be high. For low power consumption, photonic bandgap defect cavity lasers having an optical mode size as small as 0.5 μm in diameter[16] can be used.

Conclusion

A novel optical buffer memory consisting of a 2D array of polarization-bistable VCSELs and providing shift register functionality was proposed. One-bit optical buffering was experimentally demonstrated, involving selective storage of a signal bit from a four-signal-bit train, readout of the signal with an appropriate time delay, and erasure of the stored signal. 2-bit optical buffering has also been experimentally demonstrated using two polarization bistable VCSELs. These experimental results, therefore, showed a technological feasibility of a multi-bit optical buffer memory.

The authers have also demonstrated experimentally shift register function very recentry. Input data stored as the polarization states of the first VCSEL were transfered to the polarization states of the second VCSEL by injection of the output from the first VCSEL to the second VCSEL.

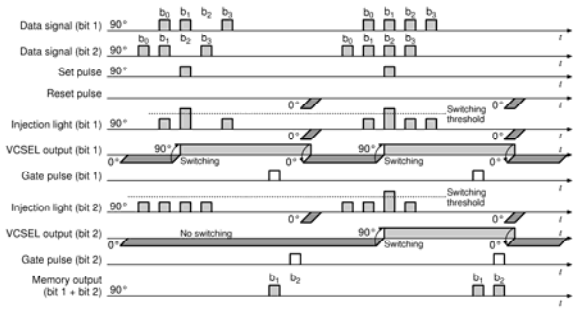


Fig. 7: Timing chart for 2-bit optical buffering

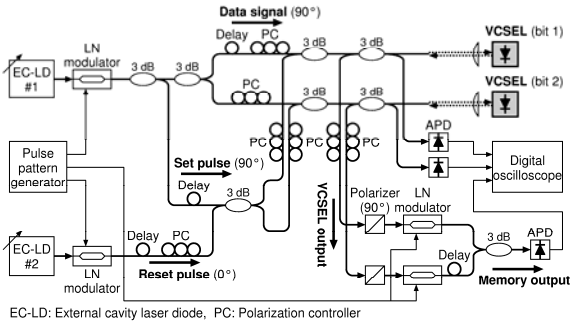


Fig. 8: Experimental setup for 2-bit optical buffering

Acknowledgments

This research was supported in part by Grant-in-Aid for Scientific Research on Priority Areas, 17068003, 2005, the Ministry of Education, Culture, Sports, Science and Technology and the International Communications Foundation.

References

1 R. Langenhorst et al, J. Lightwave Technol., no 3, p. 324, 1996.
2 H. Kawaguchi, Bistabilities and Nonlinearities in Laser Diodes, Artech House, London, 1994.
3 H. Kawaguchi, IEEE J. Sel. Top. Quantum Electron., no. 5, p. 1254, 1997.
4 M. T. Hill et al, Nature, no. 7014, p. 206, 2004.
5 S. Zhang et al, Opt. Express, no. 24, p. 9708, 2005.
6 B. Tian et al, IEEE J. Sel. Top. Quantum Electron., no. 3, p. 722, 2002.
7 H. Kawaguchi et al, Opt. Lett., no. 2, p. 130, 1992.
8 H. Kawaguchi et al, Electron. Lett., no. 2, p. 109, 1995.
9 T. Yoshikawa et al, Appl. Phys. Lett., no. 8, p. 908, 1995.
10 T. Mori et al, Appl. Phys. Lett., no. 10, p. 10112, 2006.
11 H. Kawaguchi, PS, Paper TuB3, 2002.
12 H. Kawaguchi et al, Jpn. J. Appl. Phys. Express Lett., no. 34, p. L894, 2006.
13 Y. Sato et al, Jpn. J. Appl. Phys., no. 16, p. L438, 2006.
14 T. Mori et al, LEOS, Paper WJ2, 2006.
15 M. Enachescu et al, ACM SIGCOMM Computer Communication Review, no. 3, p. 83, 2005.
16 For example, O. Painter et al, Science, no. 5421, p. 1819, 1999.

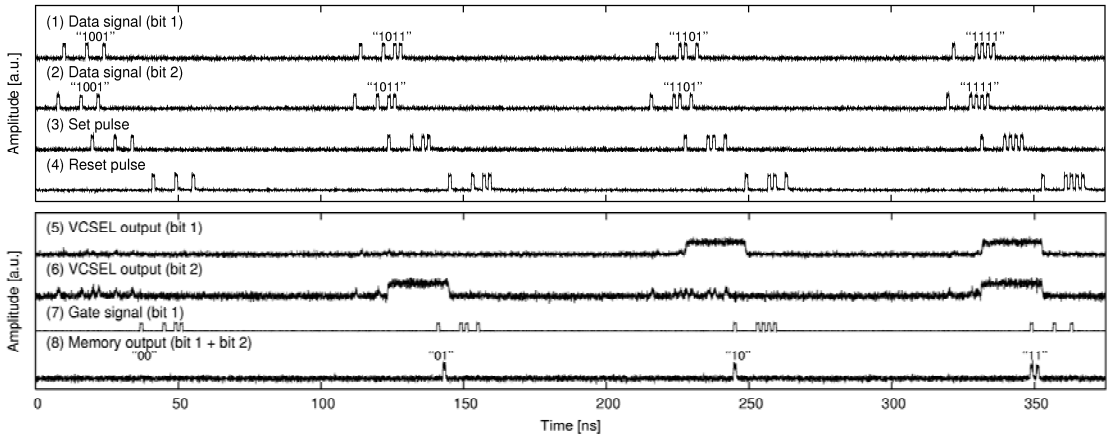


Fig. 9: Experimental results of 2-bit optical buffering

Fabrication and applications of semiconductor nanowires

Lars Samuelson
Lund University, Solid State Physics / the Nanometer Structure Consortium, Box 118, S-221 00 Lund, Sweden
Email: lars.samuelson@ftf.lth.se; Web: http://nano.lth.se

Abstract: *In this talk I will give examples of the rapid development in the areas of growth, processing and applications of semiconductor nanowires. The approach employed is based on the combination of top-down patterning and self-organized growth, sometimes called guided self-assembly. I will describe the state-of-the-art in materials properties, in control of dimensions and positions as well as give examples of the use of semiconductor nanowires in different quantum device applications.*

Introduction

Optoelectronic as well as high-speed electronics has for decades been based on the ability to create ideal two-dimensional heterostructures, like quantum wells and two-dimensional electron gas structures. This field was rewarded the Nobel-prize in physics in the year 2000. The value of employing as active materials semiconductors of even lower dimensions, like quantum dots and nanowires, has been anticipated for a long time and many approaches for creation of such structures have been proposed. It was, however, with the event of self-assembled growth of locally catalyzed one-dimensional nanowires that such structures became realistic and could be seen as a complement to conventional device and circuit technology. In the following I will first describe principles of growth of epitaxially nucleated semiconductor nanowires, including the formation of ideal axial as well as radial heterostructures, and will give examples of physical properties and families of quantum devices realized in this way. Then I will describe the processing methods by which ideal arrays of such nanowires can be formed and will present recent progress in realization of ideal, high-performing wrap-gate field-effect transistors. Finally, I will describe visions for where I think this technology is going for electronics, photonics and other applications.

Growth of semiconductor nanowires

Catalytically induced growth of whiskers has been known for a very long time and much fundamental studies were performed in the 1960's, however mainly for μm and mm dimensions [1]. It was with the work of Hiruma and coworkers at Hitachi Central Research Labs, in the late 1980's to mid 1990's, that growth and properties of wires with nm-scale dimensions were explored [2]. From the end of 1990's the field grew very rapidly, with early contributions from Lieber et al. performed at Harvard University. Our own research started around the year 2000.

The mode of growth of nanowires has traditionally been described as a vapor-liquid-solid (VLS) growth mode, with a (liquid) metal droplet interfacing on one side with the growing (solid) wire and on its open surface interacting with the vapor-phase environment with its supply of the active precursor molecules by which necessary super-saturation is maintained. For many systems this appreas as a valid model, although we, as well as others, have found that in many cases the metal is indeed in a solid, and even crystalline, phase during growth [3.4]. It can be debated if, also in this case, a very thin interface layer between the nanowire and the metal is indeed quasi-liquid and providing a highly activated interface and an efficient supply of the atoms to be incorporated at the end of the nanowire.

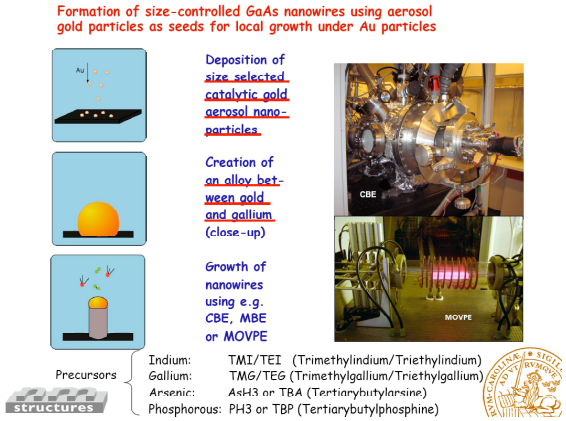


Fig. 1: Schematic of how nanowires are grown from Au-particles, either by CBE (Chemical Beam Epitaxy) or MOVPE (Metal-Organic Vapor-Phase-Epitaxy) growth.

Formation of heterostructures and 3D-structures

A homogeneous nanowire can offer 1D-transport behaviour as well as lateral confinement characteristics, but for most applications in opto-electronics or in applications involving tunnelling characteristics, a technology for heterostructure formation in nanowires would be required. About five year ago, several groups made strong progress in this respect by demonstrating the ability to combine different semiconductors in the length (axial) dimension of nanowires [5-7]. For the InAs/InP heterostructure system, even atomically abrupt heterointerfaces where demonstrated and structural as well as electronic properties were explored [5]. Figure 2 shows an examples of such abrupt heterostructures with two InP tunnelbarriers surrounding an InAs quantum dot.

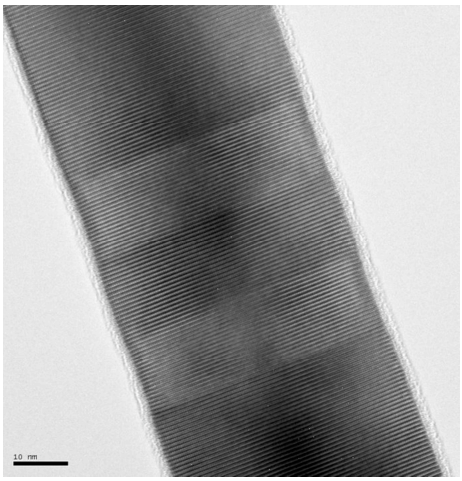


Fig. 2: High-resolution TEM-image of an InAs NW with a central InAs QD surrounded by two InP tunnelbarriers, as grown by Linus Fröberg at Lund University.

One of the most remarkable opportunities of the NW growth is the tolerance for combinations of non lattice-matched materials, also to be seen in Fig. 2 with the free radial expansion absorbing the lattice mismatch. More recently, we have developed also radial growth of core-shell heterostructures, by which it is possible to form an ideal passivation of the core, as exemplified by recent work by Niklas Sköld in my group [8,9], with increase in the optical emission efficiency by 2-3 orders of magnitude for a GaAs core surrounded by a GaInP shell.
3D-structures resembling trees have also been developed [10], by a process where a secondary set of catalytic gold-particles are allowed to absorb on the first grown wire (trunk). In this case, the original vertical NW serves as the substrate for the nucleation and growth of directionally controlled branches, with these branches either being of the same material or from a different semiconductor. Beside the beauty of these monolithic tree-structures they may find novel applications in areas ranging from photovoltaics to inter-connected self-assembling networks resembling neural-net systems [11]. An example is shown in Fig. 3, taken from a recent publication from the research of Kimberly Dick in my group.

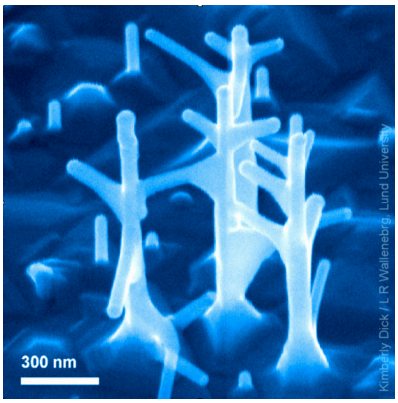


Fig. 3: Example of interconnected InAs vertical NWs where branches are directed to hit nearest neighbor trees.

Lithographic patterning for NW growth
Fig. 3 showed an example of how pre-patterning of the catalytic seed particles allows good control of the actual positions of the vertical, epitaxially nucleated nanowires. In most cases we use electron-beam lithography for this patterning, as also described in earlier publications [12,13]. A more production-friendly procedure is that of nanoimprint lithography (NIL), by which a pre-fabricated stamp is used to define all the seeding points in a single, parallel, lithographic step [14]. An example of this method, (from Thomas Mårtensson), is shown in Fig. 4.

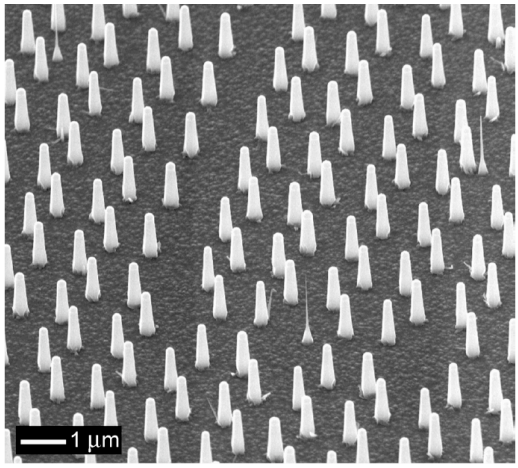


Fig. 4: SEM micrograph of a NIL-definced InP NW array. The wires are ≈1.5 µm long with a diameter of ≈290 nm, chosen for a photonic structure at wavelengths of 1 µm.

In order to describe the compatibility of NW-technology with mainstream silicon technology, I will present the state-of-the-art in III-V NW growth on silicon substrates [15] as well as different approaches towards gold-free methods for NW growth.

Examples of quantum devices realized by NWs
Soon after the technology break-through for formation of atomically abrupt heterostructures in NWs we demonstrated resonant tunneling diodes (RTD) [16] as well as single-electron transistors (SET) [17] showing ideal (low-temperature) device characteristics. Examples are reproduced in Fig. 5, for the single-electron (Coulomb blockade) characteristis as observed for a 100 nm long Coulomb island surrounded by about 5 nm thick InP tunnel-barriers.

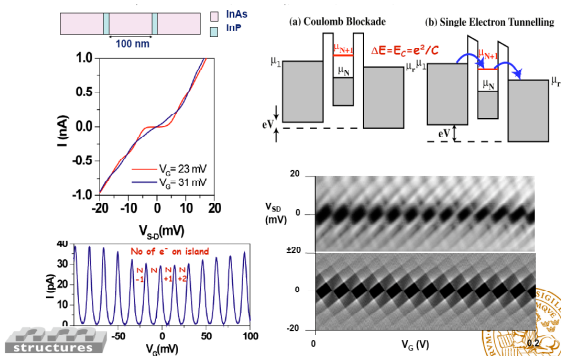


Fig. 5: Data for an InAs/InP single-electron transistor.

During the last two years much progress has been made in the area of nanowire-based transistors using a technology, which we have named wrap-insulator-gate field-effect transistors (WIG-FETs). In this cylindrical geometry, the most ideal electro-statics is achieved and continued down-scaling is readily done [18]. In this geometry it is also possible to enhance the device performance further by incorporating hetero-structures in the active region of the transistor [19], offering more efficient suppression of the off-current of the transistors.

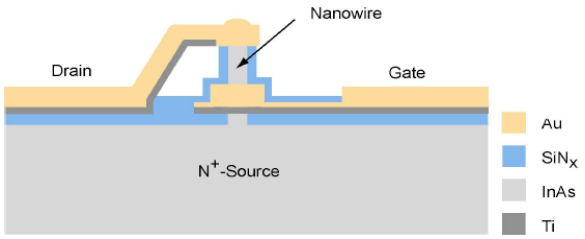


Fig. 6: Principle lay-out of an InAs WIG-FET transistor.

These devices also constitute the focus of a major EU-project, an Integrated Project called NODE (Nanowire-based One-Dimensional Electronics), with participation from leading European electronics industries (Philips, NXP, Infineon/Quimonda, IBM-Zürich and our start-up company QuMat Technologies AB), research institutes (Max-Planck, IMEC, CEA-Grenoble) and strong academic partners (Delft, Wurzburg, Pisa and Lund), all coordinated from us in Lund. I will present the status of this exciting research effort [20].
For applications in the opto-electronics areas one may expect that surface-emitting LEDs (or lasers) based on ordered arrays of nano-LEDs, grown on Si-substrates, may become of significant importance in the future. Also, nanowires offer exciting opportunities for use as sensors, either in a chemical-FET mode or as nano-mechanical detectors.

Conclusions

In this paper I summarize the development and the status of epitaxially grown semiconductor nanowires, from the point of view of materials science, processing technology and device opportunities. As judged from the great interest in this technology, and the opportunities to combine nanowire-devices with main-stream silicon technology, it seems reasonable to expect that nanowires may come to influence many areas of electronics, photonics and sensors.

Acknowledgments

The research presented here has come out of research made by many students, post-docs and senior scientists, who are all acknowledged for excellent contributions. This work has also benefited from interactions with QuMat AB in the field of electronics and with QuNano AB in the area of opto-electronics.

References

1 R. Wagner et al, in *Whisker technology*, 47, 1970
2 K. Haraguchi et al, Appl Phys Lett 60, 745, 1992
3 A. Persson et al, Nature Mat 3, 677, 2004
4 K. Dick et al, NanoLett 5, 761, 2005
5 M. Björk et al, NanoLett 2, 87, 2002
6 Y. Wu et al, NanoLett 2, 83, 2002
7 M. Gudiksen et al, Nature 415, 617, 2002
8 N. Sköld et al, NanoLett 5, 1943, 2005
9 N. Sköld et al, NanoLett 6, 2743, 2006
10 K. Dick et al, Nature Mat 3, 380, 2004
11 K. Dick et al, NanoLett 6, 2842, 2006
12 T. Mårtensson et al, Nanotechn 14, 1255, 2003
13 L Jensen et al, NanoLett 4, 1961, 2004
14 T. Mårtensson et al, NanoLett 4, 699, 2004
15 T. Mårtensson et al, NanoLett 4, 1987, 2004
16 M. Björk et al, Appl Phys Lett 81, 458, 2002
17 C. Thelander et al, Appl Phys Lett 83, 2053, 2003
18 T. Bryllert et al, IEEE-EDL 27, 323, 2006
19 E. Lind et al, NanoLett 6, 1842, 2006
20 C. Thelander et al, Materials Today 9, 28, 2006

Femtosecond laser fabrication of integrated optical waveguides and microfluidic channels for lab-on-chip devices

R. Martinez Vazquez, R. Osellame, V. Maselli, R. Ramponi, G. Cerullo
Istituto di Fotonica e Nanotecnologie, Consiglio Nazionale delle Ricerche,
National Laboratory for Ultrafast and Ultraintense Optical Science – INFM,
Dipartimento di Fisica, Politecnico di Milano, Piazza Leonardo da Vinci 32, 20133 Milano, Italy
rebeca.martinez@.polimi.it

Abstract: *We use a femtosecond laser to fabricate on a glass substrate both microfluidic channels and high quality optical waveguides, intersecting each other. Waveguide-channel integration opens new prospects for in-situ sensing in lab-on-chip devices.*

Introduction

A lab-on-chip (LOC) is a device that squeezes onto a single glass substrate the functionalities of a biological laboratory, by incorporating on it a network of microfluidic channels, reservoirs, valves, pumps and micro-sensors [1,2]. It offers the capabilities of preparation, transport, reaction and analysis of very small volumes (nano- to picoliters) of biological samples. Its main advantages are high sensitivity, speed of analysis, low sample and reagent consumption and the possibility of measurement automation and standardization. This novel concept promises dramatic advances both in basic research and in clinical applications as a low-cost diagnostic tool. The next technological challenge of LOCs is direct on-chip integration of photonic functionalities, by manufacturing optical waveguides for sensing of biomolecules flowing in the microchannels. Such integrated approach has many advantages over traditional free-space optical sensing, including compactness and portability, enhanced sensitivity and possibility of parallel excitation at multiple points in the channel.

The microfluidic channels in commercial LOCs are currently fabricated using technologies borrowed from semiconductor processing, such as micro-sandblasting, wet chemical etching and deep reactive ion etching. These are intrinsically two-dimensional techniques, creating surface channels that need to be covered by a glass slab; multilayer processing is required to produce three-dimensional structures. Standard waveguide fabrication methods (ion exchange, silica-on-silicon, polymers, …) are also two-dimensional multistep processes and their integration with microchannel fabrication is very complicated, strongly limiting its application [3].

Femtosecond-laser induced refractive index modification is a powerful technique enabling single-step, three-dimensional fabrication of optical waveguides in glass [4-8], and appears to be particularly suited for their integration into LOCs. In addition, femtosecond-laser irradiation of fused silica followed by chemical etching in HF solution allows also the manufacturing of microfluidic channels, due to the enhanced (by up to two orders of magnitude) etching rate of the irradiated material with respect to the pristine one [9-12]. This opens the intriguing possibility of using a single laser system for the fabrication of both microfluidic channels and optical waveguides and also gives the capability of a real three-dimensional integration of the two structures.

In this work we demonstrate the fabrication, by femtosecond laser irradiation, of both high-quality microfluidic channels and optical waveguides on the same fused silica glass substrate. The waveguides are fabricated in order to cross perpendicularly the microfluidic channel in several points. The microchannel is filled with a fluorescent solution to verify the capability of selectively addressing its contents by coupling light into the waveguides. The results demonstrate the possibility of an *in-situ* sensing with a very good spatial selectivity and extremely high signal to noise ratio.

Experiment and Results

The experimental setup used for the fabrication process is presented in Fig.1. It starts with a regeneratively amplified Ti:sapphire laser (model CPA-1 from Clark Instrumentation), generating 150-fs, 500-μJ pulses at 1-kHz repetition rate and 790 nm wavelength.

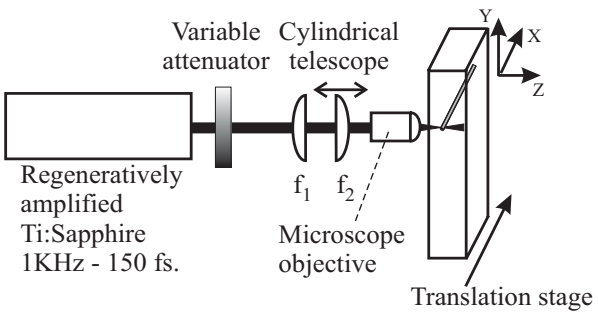


Fig.1 Schematic setup, employing astigmatig beam shaping, for writing the waveguides and the channels to be etched.

In our experiments the sample is translated perpendicular to the beam propagation direction, since it provides a superior flexibility and it allows to define structures of arbitrary length and shape. This geometry has the disadvantage of creating laser affected zones (LAZ) with highly asymmetric cross section [8,12]. In fact, the size of the LAZ cross-section perpendicularly to the translation direction is given by the beam focal diameter $2w_0$ and by the confocal parameter $b = 2\pi w_0^2/\lambda$ (see Fig.2).

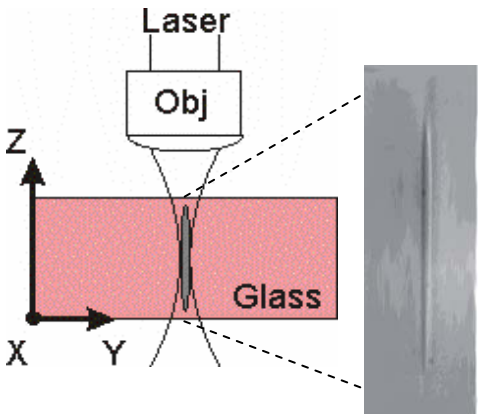


Fig. 2. Schematic of the asymmetric cross-section of the modified region in the transversal writing configuration. The blow-up is a microscope image of a waveguide cross-section fabricated with a laser beam waist w_0=3μm.

For typical focused beam sizes this results in modifications with profile dimensions markedly different along the two directions, making the waveguides and channels cross section strongly elliptical. Instead it is important to produce laser affected zones with circular cross-section, which is quite useful both for the microfluidic channels and the optical waveguides [12]. The beam, initially circular is made astigmatic by passing it through a cylindrical telescope (f_1 =50 mm, f_2=150 mm) that provides a demagnification by a factor 3 in the y direction (see Fig.1). The distance between the cylindrical lenses is finely controlled by a translation stage so as to vary the position of the focal plane in the y direction and thus to control the astigmatic difference [8, 13].

The beam is then focused by either a 20× (NA = 0.3) or a 50× (NA = 0.6) microscope objective. Typically, the focus is located from 100 μm to 300 μm below the surface of the sample, to minimize spherical aberrations of the focused beam by the glass path. The samples are translated by a precision translation stage (Physik Instrumente model M-511.DD).

The channels are manufactured by laser irradiation with pulse energy of 4 μJ through a 50× objective, and translating the sample at a speed of 20 μm/s. A subsequent etching for 3 h in an ultrasonic solution of 20% HF in water provides long and smooth channels. Etching from a single side gives channels 1.8 mm long with an entrance diameter of 85 μm (Fig.3a).

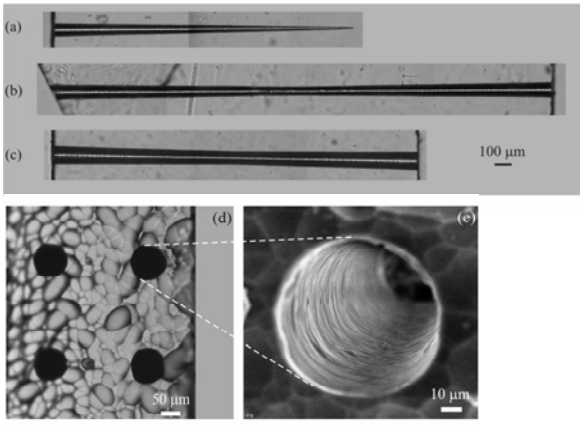


Fig. 3. Microscope images of microfluidic channels fabricated by laser irradiation plus chemical etching (see text for details). Top view (a,b,c); end view (d); SEM image (e).

By using samples of suitable lengths it is possible to etch the channels from both sides with good overlap. According to the degree of overlap different channel shapes can be obtained, such as a long one with a narrow passage in the middle (Fig.3b) or a short one with an almost uniform cross section (Fig.3c). The former has a 3 mm length with an entrance diameter of 90 μm and a waist diameter of 50 μm, while the latter has a 2.2 mm length with 110 μm diameter at the ends and 90 μm at the waist. Both shapes can find applications, for example the one with a bottleneck in the middle, besides giving the longest channel, can align in a single row the cells flowing through it, with advantages in flow cytometry and single cell fluorescence measurements.

One of the main advantages of femtosecond laser processing for microchannel manufacturing is the possibility of easily exploiting the volume of the substrate. As an example Fig.3d shows a square 2 × 2 matrix of microchannels that has been fabricated inside the substrate at depths of 100 and 350 μm, respectively, for the first and second columns. As for a single channel the matrix has been fabricated by a two step process, first each channel is inscribed by the femtosecond laser with the same irradiation parameters and changing the focus depth. After this the four channels are etched at the same time. The size and shape of the channels are well reproducible and smoothly round even for rather different focusing depths. The quality of the channels is very high, as shown in the SEM image of one of them (Fig.3e).

This result, which is rather straightforward with this technology, would require a complicated multi-step process with standard technology.

The optical waveguides are fabricated using a 20× objective, 4 μJ pulse energy and a 7.5 μm/s scanning rate. These waveguides are very smooth and uniform with almost circular cross section and excellent optical properties. The peak refractive index change is 2×10^{-3}. These waveguides support guided modes at 633 nm and 543 nm. The mode profile at 543 nm, measured with a Vidicon camera (Hamamatsu C2400) is shown in Fig. 4. Propagation losses in the green are extremely low. A first estimation by out-of-plane scattering resulted in propagation losses below the sensitivity of our set-up which is 0.5 dB/cm.

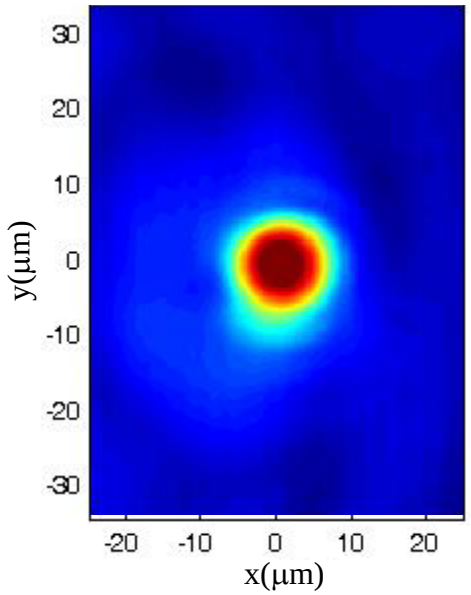


Fig. 4. Experimental near field of the fundamental guided mode at 543 nm.

In order to demonstrate the integration capabilities, three waveguides spaced by 200 μm have been fabricated crossing the central region of the 2.2 mm microchannel, according to the scheme depicted in Fig.5a.
The microfluidic channel is filled with a solution of rhodamine in ethylene glycol. When coupling green light in the waveguides by means of an optical fiber, yellow fluorescence is visible from the microfluidic channel (Fig.5b). The very good signal to noise ratio of the fluorescence is a demonstration of the high waveguide quality, in fact no stray light coming from waveguide scattering reaches the microfluidic channel, thus the excitation is very selective in space. Moreover, this fabrication technique allows an easy implementation of multiple point excitation. In Fig.5 an example of a three point excitation of the microfluidic channel is shown. This would be very useful for the realization of a device capable of measuring the velocity of a particle flow [14].

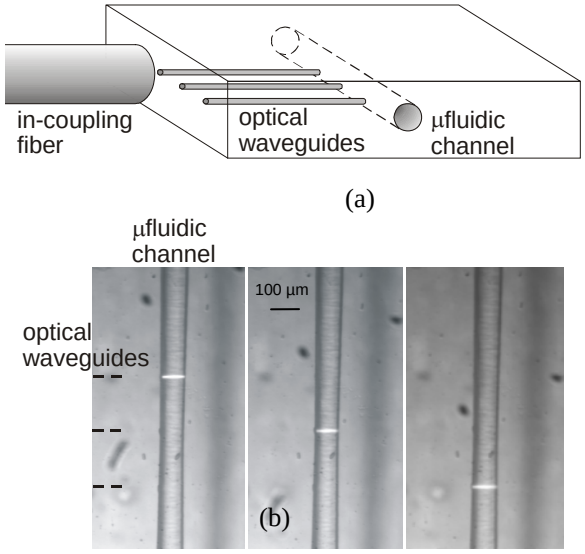


Fig. 5.(a) Schematic of the waveguides crossing the microfluidic channel; (b) microscope image of the microfluidic channel with the fluorescence excited by the optical waveguides, which are not visible due to the low refractive index change and scattering losses.

The next step will be the integration of optical detection methods, and not only excitation waveguides, in order to create lab-on-a-chip devices with integrated optical sensing functionalities.

Conclusions

In this work we presented a two-step method, laser irradiation plus chemical etching, to create microchannels with circular cross section in fused silica substrates. The reproducibility and the three-dimensional capabilities of the process have been demonstrated. The same technique has been used to produce optical waveguides in the same substrates, with excellent optical properties.
We can envisage a single production machine for the biophotonic chips, based on a high-power femtosecond laser, that can manufacture both the microfluidic channels and the optical waveguides for lab-on-chip devices.

Acknowledgements

This work was supported by the European Union within contract IST-2005-034562 (Hybrid integrated biophotonic sensors created by ultrafast laser systems - HIBISCUS).

References

1 R. D. Reyes et al, Anal. Chem., no. 74, p. 2623, 2002
2 S.C. Jakeway et al, Fresenius' J. Anal. Chem., no. 366, p 252, 2000
3 P. Friis et al., Applied Optics, no 40, p. 6246, 2001
4 K. M. Davis et al., Opt. Lett., no 21, p. 1729, 1996
5 K. Minoshima et al., Opt. Express, no 10, p.645, 2002
6 S. Nolte et al., Appl. Phys. A: Mater. Sci. Process., no 77, p. 109, 2003
7 C.B. Schaffer et al., Opt. Lett., no 26, p. 93, 2001
8 R. Osellame et al, J. Opt. Soc. Am. B, no 20, p 1559, 2003
9 Y. Cheng et al, Optics Letters, no. 26, p.277, 2001
10 K. Sugioka et al, Applied Physics A: Mater. Sci. Process., no. 79, p.1815, 2004
11 Y. Bellouard et al, Optics express, no 12, p. 2120, 2004
12 V. Maselli et al, Applied Physics Letters, no 88, p. 191107, 2006
13 G. Cerullo et al., Optics Letters, no 27, p 1938, 2003
14 K.B. Mogensen et al., Analytical Chemistry, no75, 4931, 2003

Electric-field poling of Ti indiffused z-cut $LiNbO_3$ wafers without surface grinding

D. Janner (1), F. Lucchi (2), P. Vergani (2), S. Giurgola (2), and V. Pruneri (1,3)

1) ICFO -Institut de Ciencies Fotoniques, Mediterranean Technology Park. Av. del Canal Olimpic s/n 08860 Castelldefels, Barcelona, Spain. valerio.pruneri@icfo.es 2) Avanex Corporation Sede Secondaria, San Donato Milanese (MI), Italy 3) ICREA -Institució Catalana de Recerca i Estudis Avançats, 08010, Barcelona, Spain

Abstract: *We have achieved domain inversion in Ti indiffused z-cut $LiNbO_3$ substrates through electric field poling without the need of any grinding process after Ti indiffusion. This allows a simplified, high yield and inexpensive production of domain engineered electro-optic and nonlinear optical devices, which is needed for an industrially viable processing over the full wafer scale.*

Introduction

In ferroelectric materials (e.g. $LiNbO_3$), the second-order nonlinear optical properties (including electro-optic and nonlinear optic properties) are intrinsically related to the crystal orientation (also called poling orientation or domain) [1]. In particular one can purchase $LiNbO_3$ substrates up to 5" in diameter which are already poled during or after the crystal growth. These wafers thus present a single domain structures, i.e. the same c- or z-axis orientation over the whole volume. It is also known that by applying high electric fields (>20kV/mm) through appropriate electrodes across single domain $LiNbO_3$ crystals, one can achieve domain inversion [2]. Electric-field domain inversion is widely exploited in, for example, quasi-phase-matched nonlinear optical frequency conversion processes, such as second-harmonic generation [3], optical parametric oscillation [4] and wavelength switching [5]. More recently, domain inversion has been used in integrated electro-optics, both in a periodic [6] and not periodic fashion [7], to produce high frequency narrow band modulation and low driving voltage, respectively.

For both integrated nonlinear frequency conversion and electro-optic devices one needs also a suitable means to produce waveguides. The two most common techniques to produce waveguides in $LiNbO_3$ are proton exchange and Ti indiffusion. Both of them are used for nonlinear frequency conversion devices while Ti indiffusion in fact is the preferred one to be used in high frequency (>1 GHz) electro-optics, mainly thanks to its superior microwave performance. The worldwide market for integrated electro-optic modulators in $LiNbO_3$ is steadily increasing and >50000 units are produced each year. It has been recently shown that the performance of integrated electro-optic modulators in Ti indiffused z-cut $LiNbO_3$ can be significantly improved by making use of domain inversion. In particular, modulators with driving voltage well below 3 V [7,8] for inexpensive electro-absorption drivers as well as chirp free modulators [9] can be produced. It becomes crucial that Ti indiffusion is fully compatible with electric-field poling for an industrially viable production of wafers with a sufficiently large quantity of chips. In this paper we provide a receipt for Ti indiffusion which allows subsequent poling without the need of grinding one of the crystal surfaces after waveguide fabrication. In particular we show how the setting of Ti indiffusion temperature and atmosphere is critical to avoid the grinding process, which is unpractical for industrial wafer processing, time consuming and introduces high risks of breakage.

Experimental results

It is known that Ti indiffusion is accompanied by Li_2O outdiffusion from the crystal surface [10]. If ad-hoc measures are not taken to prevent Li_2O outdiffusion, domain inversion on the z+ crystal surface may occur: the result is usually a thin (up to a few tens of μm) domain inverted layer, which is oppositely oriented with respect to the initial crystal domain structure. The closer the temperature to the Curie point (1145 °C) the more significant the formation of the thin domain layer on the z+ surface [11]. On the contrary Li_2O outdiffusion does not cause any domain reversal in proximity of the z- surface and this is why Ti indiffused waveguides are produced on the z- surface.

So far it has been shown that, after the Ti waveguide is made, the thin domain inverted layer usually prevents domain inversion [12]. This is most likely related to the fact that the thin layer functions is an insulating layer for the poling. In

fact during poling the internal polarization switching current is compensated by the external ohmic current which has to reach the surfaces of the crystal portion that is to be inverted. The presence of a thin layer which is already oriented as the applied field and at the same time insulating does not allow any current to reach the z+ surface of the initial crystal, which thus does not invert. An obvious method to solve the problem is grinding of the z+ surface to remove the thin domain inverted layer and bring the crystal to a thinner single domain structure with optical waveguides on the z-surface [5,12]. After removal of this thin layer the crystal can be poled. Beside being time consuming and expensive the grinding can be detrimental for the mechanical resistance of the crystal, in particular when most of the processing is performed at a wafer level before dicing into chips. Any crystal weakness introduced by grinding may result in breakage of the wafer during subsequent processing steps and loss of all the chips.

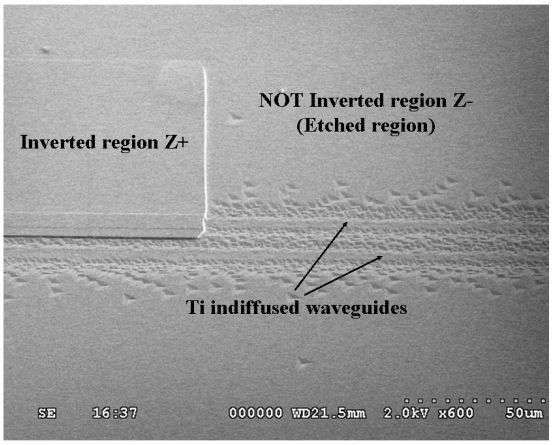


Fig. 1: Domain inversion in a Ti indiffused $LiNbO_3$ crystal revealed by etching: the domain inversion boundary is clearly in the middle of two optical waveguide Mach-Zehnder arms.

Contrary to what has been reported in the literature so far, our waveguide fabrication process does not prevent subsequent poling. After deposition of Ti metal strip on the z- face of a 0.5 mm 3" wafer, Ti indiffusion is performed at 1030ºC for 9 hrs under an O_2 flow of 1.3 l/m. During the indiffusion dummy $LiNbO_3$ wafers are added to enrich the atmosphere with Li. Without any grinding process the wafer was then patterned with an appropriate insulating masked layer and poled using 10.5 kV pulses. The regions where LiCl water electrodes are in contact with the free crystal surface were domain inverted without any significant difference with respect to wafers as received (not indiffused with Ti). Fig. 1 shows a typical result of a structure with Ti indiffused waveguides and domain inversion obtained by the above procedure.

Our belief is that the simultaneous use of low temperature (1030 °C) and O_2 atmosphere avoids the need of any grinding. The low temperature itself and O_2 enriched atmosphere prevent Li_2O out-diffusion. At the same time a lower temperature (i.e. a temperature further from the Curie point) reduces local domain inversion at the z+ surface (the lower the temperature the higher the required local coercive field to invert the crystal). The final result is an insignificant domain inverted layer on the z+ face. These conclusions are supported by poling measurements carried out on 4 different samples from the same wafer: (#1) crystal as received, no Ti indiffusion; (#2) crystal with Ti indiffusion at 1030ºC, 9 hrs, 1.3 l/min O_2 flow and Li enriched atmosphere; (#3) crystal with Ti indiffusion at 1030ºC, 9 hrs, 1.3 l/min N_2 flow and Li enriched atmosphere; (#4) crystal with Ti indiffusion at 1100ºC, 9 hrs, 1.3 l/min O_2 flow and Li enriched atmosphere.

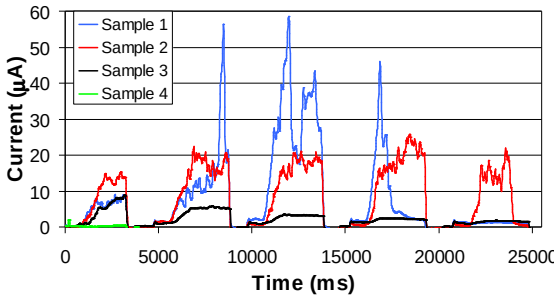


Fig. 2: Current during poling for samples: #1 (as received), #2 (1030ºC, O_2 flow), #3 (1030ºC, N_2 flow) and #4 (1100ºC, O_2 flow).

The 4 samples have a quite different poling behavior (figs. 2-3). Fig. 2 shows the poling current dynamics for #1, 2 and 3 subjected to subsequent 10.5 kV, 4 s pulses. It is evident that #1 (as received) and #2 (1030ºC, O_2 flow) show a faster dynamic than #3 (1030ºC, N_2 flow) which is unable to complete poling. In particular #1 also finishes poling before #2 (due to higher poling current) and #3 shows a decreasing poling current (negligible already after 5 pulses). The difference is also highlighted in fig. 3 where it is evident that #1 completes poling (reaches total charge of about 190-200 µC) before the end of 4th pulse, #2 before the end of 5th pulse while for #3 the cumulative

charge is saturating at about 50 µC, i.e. 25% of the total charge requested to invert the whole area (same as #1 and 2).

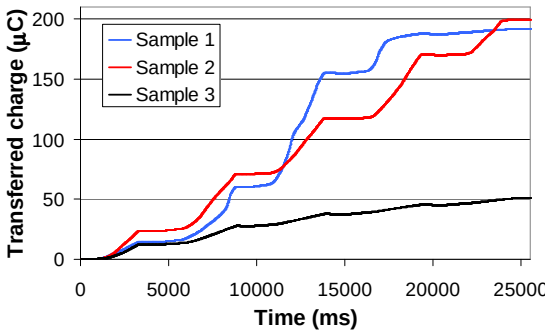


Fig. 3: Cumulative poling charge for #1, 2, 3.

Sample #4 (1100ºC, O_2 flow) shows already a very low poling current (<0.5 µA) during first poling pulse at 10.5kV (fig. 2). To see whether poling efficiency could be increased at higher voltage pulses subsequent poling was performed at 10.7, 10.8, 10.9, until breakdown occurred at 11 kV. Even for these higher voltages the poling current was always limited to <3 µA, showing the impossibility to get significant poling in this sample (see fig. 4). Note that also, similarly to #4, also #2 above was subjected to higher voltage poling after the 5th pulse at 10.5kV without getting any significant increase in current (cumulative charge).

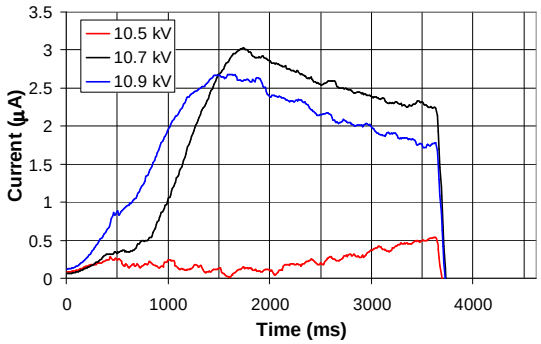


Fig. 4: Poling current of # 4 at increasing applied voltages where it is evident the negligible poling current even for higher voltages (before breakdown).

Conclusions

A Ti indiffusion in $LiNbO_3$ process has been found which allows subsequent electric field poling with a dynamic similar to that achievable in as received material, without the need of any crystal surface grinding. Our experiments also show that if Ti indiffusion were to be performed at higher temperatures in the same atmosphere or at the same temperature in a different atmosphere, subsequent poling would have a significantly different dynamic and cannot be completed. These findings are in agreement with the formation of an insulating thin domain inverted layer during Ti indiffusion which prevents subsequent poling. The proposed technique is crucial for high yield wafer processing of integrated electro-optic modulators and frequency converters.

References

1. R. S. Weiss and T.K. Gaylord, “Lithium niobate: summary of of physical properties and crystal structure”, Appl. Phys. A **37**, 191 (1985).

2. M. Yamada, N. Nada, M. Saitoh and K. Watanabe, “First-order quasi-phase-matched $LiNbO_3$ waveguide periodically poled by applying an external electric field for efficient blue second harmonic generation”, Appl. Phys. Lett. **62**, 435 (1993).

3. V. Pruneri, R. Koch, P.G. Kazansky, P.St.J. Russell and D.C. Hanna, “49 mW of cw blue light generated by first-order quasi-phase-matched frequency doubling of a diode-pumped 946 nm Nd:YAG laser”, Opt. Lett. **20**, 2375 (1995).

4. L.E. Myers, R.C. Eckardt, M.M. Fejer, R.L. Byer, W.R. Bosenberg and J.W. Pierce, “Quasi-phase-matched optical parametric oscillators in bulk periodically poled $LiNbO_3$”, J. Opt. Soc. Am. B **12**, 2102 (1995).

5. G. Schreiber, H. Suche, Y.L. Lee, W. Grundkötter, V. Quiring, R. Ricken and W. Sohler, “Efficient cascading difference frequency conversion in periodically poled Ti:$LiNbO_3$ waveguide using pulse and cw pumping”, Applied Physics B **73**, 501 (2001).

6. J.H. Schaffner, “Periodic domain reversal electro-optic modulator”, US patent 5,278,924 (1994).

7. V. Pruneri and A. Nespola, “Coplanar integrated optical waveguide electro-optical modulator”, US patent 6,760,493 (2004).

8. S. Oikawa, F. Yamamoto, J. Ichikawa, S.

Kurimura and K. Kitamura, "Zero-chirp broadband *z-c*ut Ti:$LiNbO_3$ optical modulator using polarization reversal and branch Electrode", J. Lightwave Tech. **23**, 2756 (2005).

9. N. Courjal, H. Porte, J. Hauden, P. Mollier and N. Grossard, "Modeling and optimization of low chirp LiNbO3 Mach-Zehnder modulators with an inverted ferroelectric domain section", J. Lightwave Tech. **22**, 1338 (2004).

10. S. Thaniyavarn, T. Findakly, D. Booher and J. Moen, "Domain inversion effects in Ti-$LiNbO_3$ integrated optical devices", Appl. Phys. Lett. **46**, 933 (1985).

11. K. Nakamura, H. Hando and H. Shimizu, "Ferroelectric domain inversion caused in $LiNbO_3$ plates by heat treatment", Appl. Phys. Lett. **50**, 1413 (1987).

12. J. Amin, V. Pruneri, J. Webjörn, D.C. Hanna, P.St.J. Russell and J.S. Wilkinson, "Blue light generation in a periodically poled Ti:$LiNbO_3$ channel waveguide", Optics Communications **135**, 41 (1997).

Novel and nanostructured optical waveguides by means of using electronic damage of swift heavy ions.

José Olivares (1), Fernando Agulló-López (2), Gastón García (3), Angel García-Cabañes (4) and Mercedes Carrascosa (4).
1) Instituto de Óptica, CSIC, Serrano 121, 28006-Madrid, Spain. j.olivares@io.cfmac.csic.es
2) Centro de Microanálisis de Materiales, UAM, Cantoblanco, 28049-Madrid, Spain. fal@uam.es
3) CELLS, 08193 Bellaterra, Spain.
4) Depto. Física de Materiales, UAM, Cantoblanco, 28049-Madrid, Spain.

Abstract: *We present a review and the new results regarding a new and very efficient method for the fabrication of novel optical waveguides in crystalline materials by means of using the processing capability of the high electronic excitations provided by high-energy (~ 2-50 MeV) heavy (A > 8) ions. The control of the electronic damage both in intensity (i.e. keV/nm) and in spatial distribution (depth and lateral in single nano-track regime) allows the fabrication of new optical structures at moderate (~10^{14} cm^{-2}) or even ultra-low fluences (~10^{12} cm^{-2}). It is a clear alternative to the standard procedure (based on using the nuclear damage caused by light ions) which requires excessively high fluences (10^{16} – 10^{17} at/cm^2). Moreover new nanostructured waveguides are feasible with potential for size-controlled nanopores integrated in waveguides for novel optical devices.*

Introduction

Optical waveguides are fundamental elements of many photonic devices. Various crystalline materials have been intensively studied for such broad field depending on the particular application. Ion-beam irradiation offers a general and flexible method to modify the structure and properties of materials with several advantages over other physical or chemical methods. So far, the technological applications of ion irradiation mostly rely on the effects caused by nuclear collisions and ion implantation. In particular, ion implantation of transparent materials with light ions (H and He) of a few MeV´s energy has allowed for the fabrication of optical waveguides and a variety of integrated optics devices [1]. Particular attention has been given to lithium niobate ($LiNbO_3$) due to its excellent electrooptic and nonlinear optical properties and that large good quality crystals can be routinely grown at a reasonable cost. Essentially, the mechanism proposed to account for the generation of the waveguiding layer is the amorphization of the region at the end of the ion range as a consequence of nuclear collisions and ion implantation. It presents a markedly reduced refractive index in comparison to the unirradiated material and behaves as an optical barrier. However, this is at the expense of using quite high fluences (10^{16}-10^{17} cm^{-2}) that strongly hinders the practical usefulness of the method.

Recently, the use of heavier ions and higher energies to cause structural damage and modify the physical response is starting to be explored. A variety of ions at energies ranging from 3 MeV to 50 MeV have already been investigated in $LiNbO_3$ [2-3]. Under these irradiation conditions the electronic stopping power becomes dominant over the nuclear stopping power. As a consequence of these studies it has been ascertained that the induced damage is mostly related to electronic excitation mechanisms. The features associated to these processes markedly differ from those applying to nuclear collisions. In particular, full amorphization of the lattice can only be achieved when the electronic stopping power is above a certain threshold (*thresholding behavior)* [4].
So far, most studies have dealt with the generation of latent (amorphous) tracks by single swift-ion (energies ≥ 0.1-1 MeV / amu) impacts in insulating materials which is well-documented [5-8]. Amorphous tracks with nanometric radius are generated along their trajectory when the electronic stopping power S_e is above a certain threshold S_{th} (~ 5 keV/nm for $LiNbO_3$). The radius of the track is a growing function of S_e and so it can be varied through the irradiation conditions.

Here we present a review and some new results regarding the electronic excitation damage by swift ions and its potential application to Photonics [4,7,8,10-15]. In particular, irradiation with high-energy (~ 2-50 MeV) medium-mass (A > 8) ions has been shown to be a very efficient method for the modification of crystalline materials and fabricating novel optical waveguides. This results from the processing capabilities of the high electronic excitations provided by swift ions through the control of beam energy and intensity or better the electronic stopping profile inside the crystal. At variance with the classical implantation method the new optical structures can be produced at moderate (~10^{14} cm^{-2}) [10] or even ultra-low fluences (~ 10^{12} cm^{-2}) [13]. Most results (experimental and detailed analysis) have been obtained with $LiNbO_3$ and the potential of universal applicability to other crystalline materials has been explored with $KGd(WO_4)_2$ (KGW) [11].

Experimental

Ion irradiations were performed with the 5 MV tandem accelerator recently installed in the Centro de Microanálisis de Materiales (CMAM) at University Autónoma of Madrid [9]. Maximum ion beam cur-

rents were in the range 10-50 nanoamps to prevent excessive charging and heating. Samples were tilted 9º with respect to beam direction to avoid ion channeling. The ion beam was overfocused and expanded so that, by means of a mask, only the central homogeneous part of the beam is used. The dimensions of the irradiated area were typically 6x6 mm^2. The beam homogeneity, better than 10 % , was checked by means of measuring the ion induced luminiscence in a SiO_2 glass sample with a sensitive CCD camera. The main material studied has been congruent $LiNbO_3$ having integrated optics quality purchased from PHOTOX and CASIX. KGW slides were purchased from Passat Ltd., Ontario, Canada.

The prism coupling dark m-lines method has been used to determine the refractive index profiles induced by the irradiations. By proper selection of TE and TM mode coupling and sample orientation under the prism, all the main refractive indices can be measured separately (two for the birrefringent $LiNbO_3$ and three for the biaxial KGW).

Buried amorphous layers: High index jump optical waveguides

The novel strategy followed in these experiments is illustrated in Fig. 1. One looks for irradiation conditions where the maximum of the electronic stopping power $S_e(z)$ curve, lies at a certain depth inside the crystal (well separated from the peak value of the nuclear stopping power $S_n(z)$) and reaches a value close to the intrinsic threshold ($S_{th} \approx 5$ keV/nm). Our irradiation conditions F at 22 MeV, O at 20 MeV and Mg at 28 MeV fulfill this requirement as illustrated in Fig. 1a), derived from SRIM 2003 calculations. Then, it is expected that, after some *incubation fluence*, amorphization at every single ion trajectory starts at the location of the maximum of $S_e(z)$ so that the process would proceed as illustrated in Fig. 1b: When the fluence guarantees full overlapping of the individual latent tracks (~10^{13} cm^{-2}) a low refractive index homogeneous layer is formed inside the crystal and consequently a surface planar optical waveguide is generated at the surface.

For sufficiently high fluences the profile approaches a step-like shape, whose bottom level reaches a limit value, $n = 2.10$, approximately independent of the investigated ion as well as of light polarizations and coincides with the refractive index of amorphous $LiNbO_3$.

Another interesting feature of those waveguides is the low level of propagation losses (~ 1 dB/cm), quite comparable to that measured for conventional implanted waveguides [10].

Nanostructured optical waveguides at ultralow fluences

Next, we address the processing of $LiNbO_3$ by means of swift-heavy ions in the very low fluence regime where single-track are not overlapping. In this case

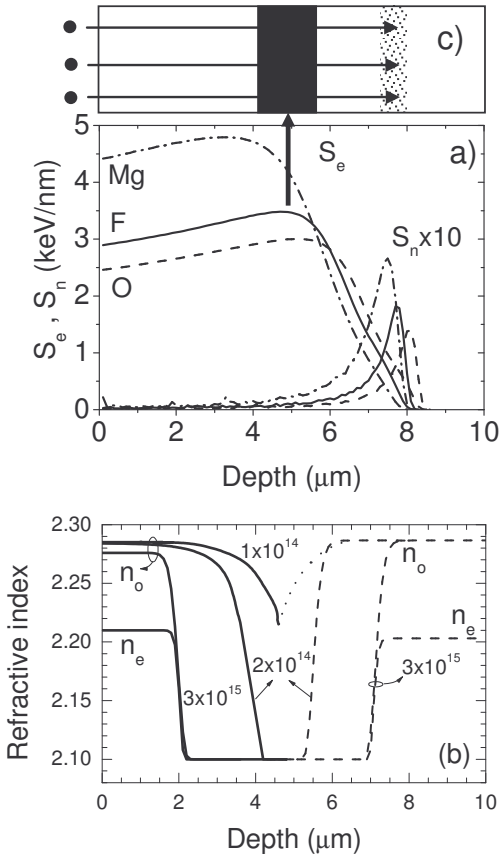


Fig. 1: (a) Plot of the electronic and nuclear stopping power for F at 22 MeV (continuous line), O at 20 MeV (dashed line) and Mg at 28 MeV (dashed-dotted line); (b) Ordinary (n_o) and extraordinary (n_e) refractive index profiles obtained from the dark-mode data (solid lines) for some representative fluences. The estimated refractive index profile (using the low index optical resonances and RBS/channeling data) corresponding to the back amorphous-crystalline boundary is also shown with dashed lines (c) scheme, considering the F 22 MeV case for the illustration, of the generated buried amorphous layer (black strip) near the maximum of the electronic stopping curves. The dotted strip indicates the region of nuclear damage and implantation.

uniform layers are not formed but instead a nanostructured heterogeneous medium is achieved. By using optical methods (waveguide dark-mode analysis) we have learned about the depth morphology of the tracks and about the potential for tailoring the optical response of the irradiated region and lead to optical waveguide fabrication. The strategy of our method is illustrated in Fig. 2 where the stopping power S_e (z) for Cl (46 MeV) calculated with SRIM 2003 is plotted as a function of z, Fig. 2a, together with a qualitative illustration of the (average) expected track profile, Fig. 2b. It includes a low-index amorphous core ($n_a = 2.10$ *at* $\lambda = 633$ *nm*) and a defective surrounding halo. Following the S_e (z) curve the track radius should increase with depth up to a maximum and then decrease with increasing z. In Fig

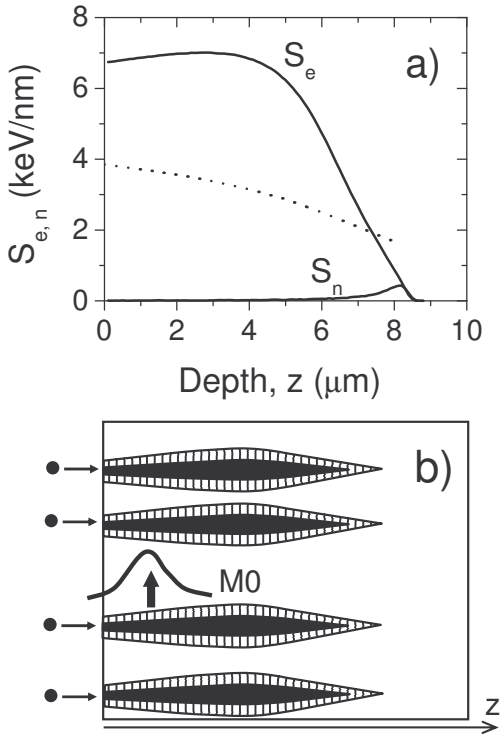


Fig. 2: a) Electronic, S_e, and nuclear, S_n, stopping power curves for Cl 46 MeV in $LiNbO_3$ calculated with SRIM2003. The dotted line shows the corresponding "amorphization" threshold curve. b) Schematic depth morphology of the tracks, showing the core (black) and the surrounding halo (dashed). An schematic light profile (M0) illustrates waveguiding behavior.

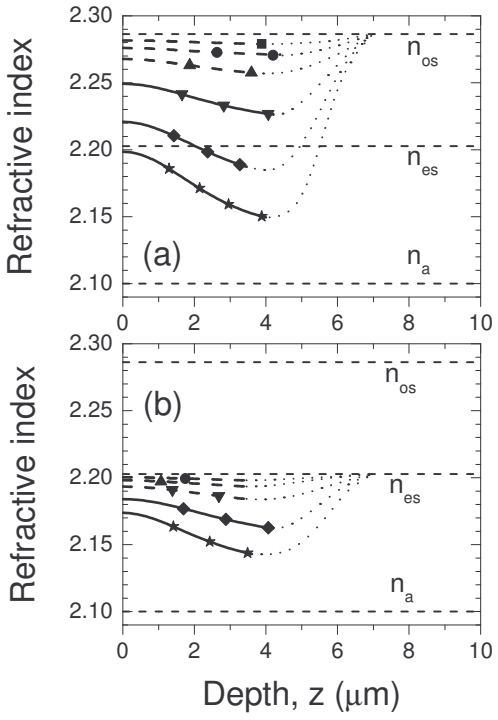


Fig. 3: Ordinary, a), and extraordinary, b), refractive index profiles (solid lines) at λ = 633 nm for X-cut $LiNbO_3$ samples irradiated with Cl 46 MeV ions at the fluences (at/cm^2) of: 5x10^{11} (squares), 1x10^{12} (circles), 2x10^{12} (up triangles), 4x10^{12} (inverted triangles), 8x10^{12} (rhombi), and 1x10^{13} (stars). Horizontal dashed lines show the refractive index values for the crystal (n_{os} and n_{es}) and amorphous (n_a) regions. A guess of the expected refractive index profiles behind the minimum is also plotted with a dotted line.

2a) the dotted line shows the predicted ("amorphization") threshold according to recent data, that include the effect of ion velocity. The measured ordinary and extraordinary refractive index profiles, $n_0(z)$ and $n_e(z)$ induced by the Cl (46 MeV) irradiations are shown in Fig. 3a and Fig. 3b, respectively. It has been found that tracks are composed of an amorphous core surrounded by a *damaged (pre-amorphous) halo*. The measured radius of the track core at the surface shows a reasonable accordance with previously reported data.

The functionality of this novel waveguides made by partial amorphization of the $LiNbO_3$ crystal is a matter of concern. The measured SH coeficient (d_{33}) vs. fluence is shown in Fig. 4. It is normalized to a virgin substrate. A remarkable high activity (> 60%) is still preserve at the fluences where optical waveguides are obtained. The gradual decrease of the d_{33} coefficient is logical following the increase in the amorphous fraction at the surface.

Conclusions

By using the electronic excitation provided by high-energy medium-mass (i.e. A > 8) ions it is possible to produce various novel optical waveguides, by playing with the shape of the electronic stopping curve. By using curves with a maximum stopping value inside the crystal, buried amorphous layers are generated which produce good quality high index-jump step-like optical waveguides. This method requires the use of moderate fluences (~ 10^{14} cm^{-2}) to generate overlapping individual amorphous tracks. Using the same strategy but ultra-low fluences of ~ 10^{12} cm^{-2} , i.e. in the isolated tracks regime, a nanostructured optical medium with an effective gradually decreasing refractive index profile is produced. This profile

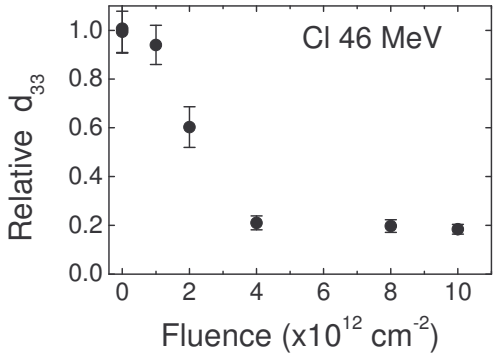


Fig. 4: Fluence evolution of the second order non-linear optical coeffient d_{33} relative to the one of virgin $LiNbO_3$ for the $LiNbO_3$ samples irradiated with Cl 46 MeV ions.

supports waveguide modes and shows a high second order optical nonlinerity. Note that in all cases the fluences required are several orders of magnitude below those ones needed in standard implantation with light ions. The physical mechanisms and theoretical basis for the observed behavior have been summarily described.

Acknowledgments
We acknowledge funding from the Spain´s MEC project: MAT2005-06359.

References

1 1 P.D. Townsend, P.J. Chandler and L. Zhang, *Optical Effects of Ion Implantation,*Cambridge University Press, Cambridge (1994).
2 Hui Lu et al, J. Appl. Phys. **89**, 5224, 2001.
3 G.G. Bentini et al, J. Appl. Phys. **92**, p. 6477, 2002.
4 J. Olivares et al, Appl. Phys. A 81, p. 1465, 2005.
5 M. Toulemonde et al, Nucl. Instrum. Meth. B 216, p. 1, 2004.
6 G. Szenes, Phys. Rev. B 51, 8026, 1995.
7 F. Agulló-López et al, J. Appl. Phys. (97) 093514, 2005.
8 G. García et al, J. Appl. Phys. (99) 053504, 2006.
9 www.uam.es/cmam
10 J. Olivares et al, Appl. Phys. Lett. (86), 183501, 2005.
11 A. García-Navarro et al, NIMB 249, p. 177, 2006.
12 A. García-Navarro et al, NIMB 249, p. 172, 2006.
13 J. Olivares et al, Appl. Phys. Lett. (89), 071923, 2006.
14 G. García et al, Europhysics Letter 76 (6), p. 1, 2006.
15 F. Agulló-López et al. Phys. Rev B. (74), 174109, 2006.

Applications of High-Q Optical Micro-resonators: Photonic Clocks, Cavity-QED and New Laser Sources on Silicon

Kerry Vahala
California Institute of Technology, Pasadena, CA 91125
vahala@caltech.edu

Abstract: *After a brief discussion of nonlinear optical sources (Raman and Parametric) based on microtoroid resonators, recent results which use radiation pressure in these devices either to: (1) create micro-wave-rate mechanical oscillations or (2) cool the mechanical degree of freedom to cryogenic temperatures are overviewed. The implication of these results for new science is discussed. Also, the recent application of toroids for cavity QED on-a-chip experiments is briefly described.*

Micro-toroid optical resonators on silicon [1] are finding a range of applications in basic science. Besides providing optical modes having Q factors as high as 500 million, these devices also exhibit high-Q mechanical modes. This added feature has provided access to a range of new opto-mechanical phenomena which are driven by radiation pressure. After describing the processing and passive optical properties of these devices, the consequences of resonant energy buildup in a microscale, ultra-high-Q system will be described. Beyond laser sources based on Raman and parametric oscillation [2], radiation pressure created by the high circulating power within the resonator couples the optical and mechanical degrees of freedom. Under appropriate conditions, this coupling leads to regenerative, mechanical-oscillation, up to microwave rates, which is driven solely by radiation pressure from a continuous-wave optical pump [3,4,5]. This phenomenon is a manifestation of a more general physical principle of dynamic back action [6], and has a counterpart in which cooling of the mechanical mode is possible [4,6]. Along with recent demonstrations in cantilevers [7,8], demonstration of radiation pressure cooling of a mechanical mode from room temperature to 11°K using a microtoroid resonator will be discussed [9]. Finally, the use of fiber-based couplers in these toroidal devices enables high coupling efficiencies [10]. This feature as well their high Q, low mode volume and wafer-based design make them interesting cavities for study of strong-coupling physics. We will describe the recent observation of strong coupling in collaboration with the Kimble group at Caltech [11].

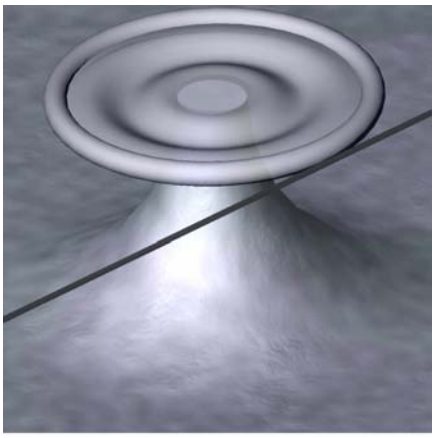


Figure: Rendering of a toroidal optical resonator exhibiting mechanical oscillation driven by radiation pressure. Black line is fiber taper waveguide used to couple the CW pump wave.

References

[1] D. K. Armani, T. J. Kippenberg, S. M. Spillane and K. J. Vahala, Nature, **421**, pp. 925-929, 27 February 2003.
[2] Kippenberg, T. J., Spillane, S. M. & Vahala, K. J. Physical Review Letters, **93**, no. 8, August (2004).
[3] T. Carmon, H. Rokhsari, L. Yang, T. J. Kippenberg, and K. J. Vahala, Physical Review Letters, **94**, 223902, June 2005.
[4] T. J. Kippenberg, H. Rokhsari, T. Carmon, A. Scherer, and K. J. Vahala, Physical Review Letters **95**, 033901, 2005.
[5] H. Rokhsari, T. J. Kippenberg, T. Carmon, and K. J. Vahala, Optics Express, **13**, No. 14, July 2005.
[6] V. B. Braginsky, S. P. Vyatchanin, Phys. Lett. A, **293**, 228 (2002).
[7] S. Gigan, H.R. Boehm, N. Paternostro, F. Blaser, G. Langer, J. B. Hertzberg, K. C. Schwab, D. Baeuerle, M. Aspelmeyer, and A. Zeilinger, Nature (London) **444**, 67 (2006).
[8] O. Arcizet, P. F. Choadon, T. Brinat, M. Pinard, and A. Heidmann, Nature (London) **444**, 71 (2006).
[9] A. Schliesser, N. Nooshi, P. Del'Haye, K. Vahala, T.J. Kippenberg, Physical Review Letters, 97, 243905, Dec 15, 2006
[10] S. M. Spillane, T. J. Kippenberg, O. J. Painter, and K. J. Vahala, Phys Rev Lett, **91**, 2003.
[11] Aoki, Dayan, Wilcut, Bowen, Parkins, Kippenberg, Vahala, Kimble, Nature, **443,** 05147, Oct 12, 2006

Integrated Optical Ti:$LiNbO_3$ Ring Resonator for Rotation Rate Sensing

C. Vannahme, H. Suche, S. Reza, R. Ricken, V. Quiring, and W. Sohler

Angewandte Physik, Universität Paderborn, Warburger Str. 100, 33098 Paderborn, Germany
email: sol_cv@physik.uni-paderborn.de

Abstract: *Design, fabrication, packaging, and characterization of a high finesse Ti:$LiNbO_3$ integrated optical ring resonator are reported. First results of rotation rate sensing are presented.*

Introduction

Optical rotation rate sensors utilizing the Sagnac effect are attractive devices, which - in contrast to their mechanical counterparts - have no moving parts [1]. Active ring laser gyroscopes and passive fiberoptic gyroscopes of high resolution are already used successfully for navigation of aircrafts and ships. However, for consumer needs with low and medium resolution like in car navigation and robotics, less complex and cheaper sensors systems are needed suited for volume production. Integrated optical ring resonators based on planar microfabrication technologies have the required potential. If fabricated on an electrooptic substrate like $LiNbO_3$ (LN), even optical signal processing components can be monolithically integrated. In contrast to ring resonators for wavelength filtering, devices for rotation rate sensing must have a much larger diameter as the Sagnac effect is proportional to the area enclosed by the ring.
Up to now, only a few integrated optical ring resonators have been reported for rotation rate sensing. They have been fabricated by chemical vapour deposition of silica on silicon [2-4].
In this paper we report the design, fabrication, packaging, and characterization of the first ring resonator fabricated in LN for rotation rate sensing with a diameter of 60 mm.

Theoretical modelling and design

The overall waveguide structure to be investigated is shown in Fig. 1. It consists of a single mode (at $\lambda \sim$ 1550 nm), Ti:LN ring resonator of 60 mm diameter.

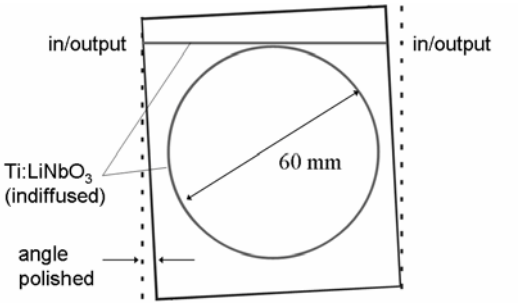


Fig. 1: Scheme of the integrated ring resonator connected with an adjacent straight waveguide via a directional coupler.

Light can be coupled to the ring via a directional coupler connecting a straight waveguide and the resonator.
The directional coupler determines to a large degree the properties of the resonator and – as a consequence – the properties of the rotation rate sensor. It is formed by the straight and the curved waveguides approaching each other. As the Ti:LN waveguides are anisotropic with polarization dependent mode field dimensions also the properties of the directiononal coupler will be polarization dependent. Nevertheless, we will consider in the following the TE-polarization only as the corresponding waveguide losses are smaller than those of the TM-mode. Therefore, for a given polarization (and wavelength) there is only one parameter to be adjusted, namely the smallest gap d between both guides (see Fig. 2).

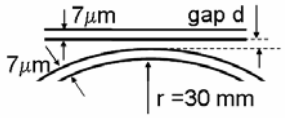


Fig. 2: Directional coupler formed by straight and curved channel guides.

In a first step a power coupling coefficient K is calculated as function of d at the wavelength λ = 1550 nm (see Fig. 3 on the left). K is equivalent to the reflectivity of one of the two mirrors of a conventional Fabry-Perot cavity with a second mirror of reflectivity 1. Moreover, the dependence of K on the wavelength is analyzed and presented on the right of Fig. 3 for d = 4.9 μm as fixed parameter. This result shows that the coupling can be fine tuned even after fabrication by selecting the right wavelength.

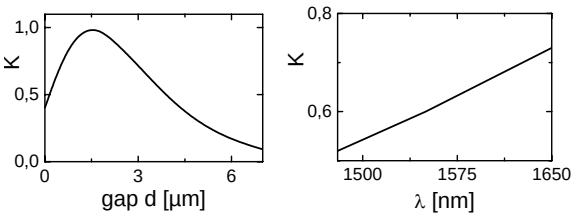


Fig. 3: Left: power coupling coefficient K as function of the minimum gap d of the directional coupler at λ = 1550 nm. Right: K versus wavelength for d = 4.9 μm.

Knowing the power coupling coefficient K the resonances of the ring cavity can be modelled using waveguide propagation losses α of 0.03 dB/cm as measured in straight channel guides for TE-polarization.

Bending losses can be neglected for a radius of curvature larger than about 25 mm. Fig. 4 shows two resonances of the transmission through the straight guide versus the optical frequency change. The free spectral range of the ring cavity is 830 MHz with a halfwidth of the resonances of 80 MHz. The diagram allows a direct comparison with experimental results (see Fig. 9). An equivalent representation is the transmission versus phase, which is used to analyze the rotation rate sensitivity.

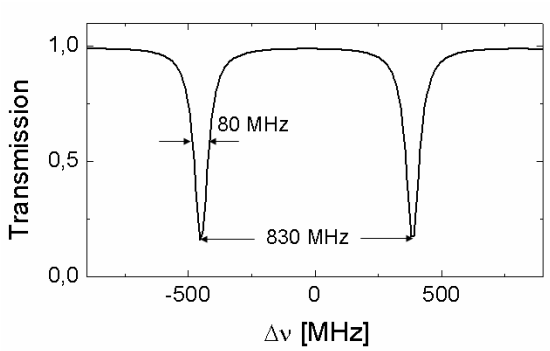


Fig. 4: Calculated straight waveguide transmission (see Fig. 1) versus a change $\Delta\nu$ of the optical frequency for α = 0.03 dB/cm and K = 0.3.

To determine the optimum gap d_{opt} of the directional coupler (for λ = 1550 nm) the steepest slope of the ring resonances is calculated as function of the power coupling coefficient K and as function of the propagation loss coefficient α. The steepest slope determines the operation point of maximum sensitivity for rotation rate sensing. The results are presented in Fig. 5 yielding an optimum K of about 0.3 nearly independent on the waveguide losses. As a consequence, the optimum gap should be d_{opt} = 4.9 µm (see Fig. 3).

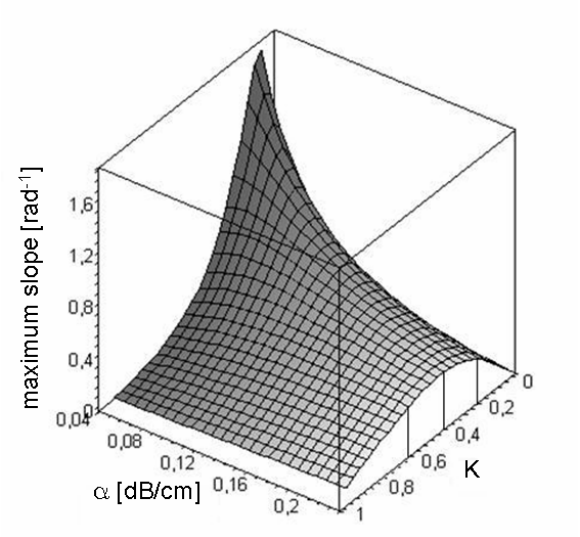


Fig. 5: Steepest slope of the ring resonances as function of the waveguide propagation losses α and of the power coupling coefficient K of the directional coupler.

The ultimate sensitivity of the integrated ring resonator operated as optical gyroscope is determined by the quantum noise limit. The minimum rotation rate is given by [1]:

$$\Omega_{min} \approx \frac{\lambda_0}{2R} \frac{\Gamma}{\sqrt{n_{ph}\eta_D\tau}}$$

with R: ring radius; λ_0: vacuum wavelength; Γ: halfwidth of the cavity resonance; n_{ph} : number of photons/sec; η_D: quantum efficiency of the photodiode; τ: averaging time.
Using the parameters of our sample (R = 3 cm; τ = 1 s; η_D = 0,5; λ_0 = 1550 nm; Γ =80 MHz; $n_{ph} = 8*10^{15}s^{-1}$) a minimum rotation rate of

$$\Omega_{min} = 6,7\,°/h = 0,45\,\Omega_E$$

can be expected; Ω_E is the angular velocity of the earth.

Sample fabrication and experimental setup

According to the modelling results a sample has been designed and fabricated in a Z-cut LN substrate of 75 mm x 75 mm dimensions. By an indiffusion (1060 °C; 8.5 hrs) of photolithographically defined 7µm wide, 100 nm thick Ti-stripes the waveguide structure has been formed with a ring cavity of 60 mm diameter and a minimum gap width of the directional coupler of 4.9 µm (see Fig. 1). The two end faces of the straight waveguide have been angle polished to avoid back reflections. Afterwards, the sample has been pigtailed with polarization maintaining fibers and glued on a copper base plate on a thermoelectric cooler/heater to enable temperature stabilization. Finally, it has been mounted in a rotatable aluminium box (see Fig. 6).

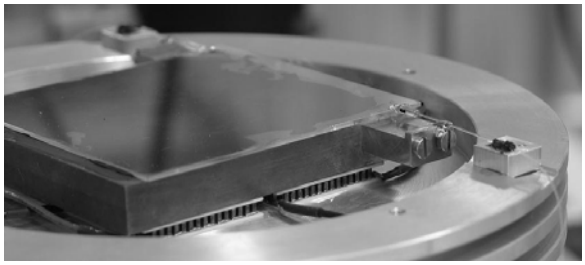


Fig. 6: Opened aluminum box with pigtailed ring resonator on a copper base plate, which can be temperature stabilized by a thermoelectric cooler/heater.

The packaged ring resonator is driven via an excentric as shown in Fig. 7; it can be rotated back and forth with a time dependent rotation rate. Depending on the speed of the driving electric motor the amplitude of the angular velocity of the sample can be adjusted up to about 3 rad/sec.

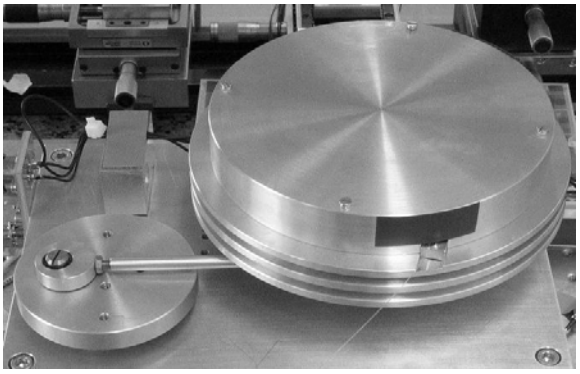


Fig. 7: Electromechanical drive to rotate the packaged ring resonator.

The experimental setup to investigate the resonator and to study the Sagnac effect is shown in Fig. 8. A semiconductor extended cavity laser (ECL) is used as tunable coherent source of about 150 kHz instantenous linewidth in the wavelength range around 1550 nm; it can be frequency modulated by an external function generator. The light is coupled to a standard single mode fiber and routed via 3 dB coupler, polarization controller and circulator either to one or to both inputs of the sample to allow an uni- (solid lines) or bidirectional (solid and dotted lines) mode of operation. The transmitted light is routed via the circulator(s) to the photodiode(s). Their signals are processed by lock-in amplifiers to allow laser frequency control and measurement of the rotation rate.

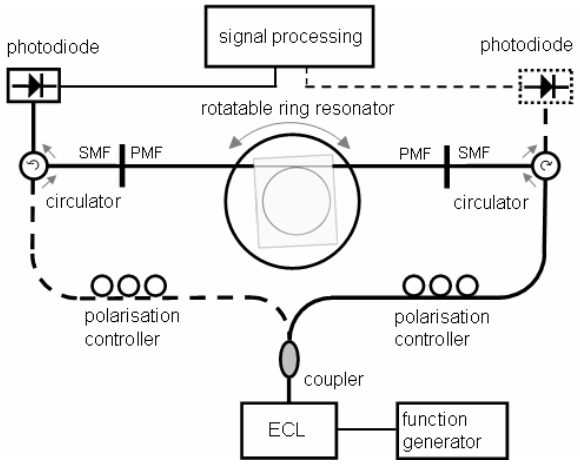


Fig. 8: Experimental setup to investigate the ring resonator and to study the Sagnac effect in uni- or bidirectional (dotted) operation. ECL: tunable extended cavity laser. PMF: polarization maintaining fiber. SMF: single-mode fiber

In the unidirectional mode the transmission resonances can be measured either for clockwise or counterclockwise propagating light. In the bidirectional mode of operation both resonances can be measured simultaneously.
To observe the Sagnac-effect and to measure a rotation rate in the unidirectional mode of operation the laser frequency is periodically modulated around a cavity resonance (transmission minimum). The amplitude of this sinusoidal modulation of frequency Ω should correspond to about half of the halfwidth of the resonance (i. e. about 40 MHz for the modelling example presented in Fig. 4). As result the detector signal consists of even multiples of the modulation frequency only. If the Sagnac effect shifts the resonance also odd multiples arise and the first harmonic can be detected with the help of the lock-in amplifier. However, this mode of operation requires a stabilized ring resonator and a laser center frequency stabilized to a ring resonance (at zero rotation rate). All drift effects and resulting phase shifts, which are not caused by the Sagnac effect, give rise to a signal at the first harmonic as well. Therefore, the bidirectional mode of operation is preferable. As result the difference of the two photodiode signals is proportional to the rotation rate. Only phase shifts caused by the Sagnac effect change the differential signal; reciprocal phase shifts will be eliminated automatically as long as the laser frequency is close to the point of operation at the steepest slope of the resonance.

Experimental results and discussion

Fig. 9 shows both, the clockwise and counterclockwise resonances measured simultaneously using the bidirectional setup (see Fig. 8). According to the ring parameters the free spectral range is 830 MHz. The halfwidth and depth of the cavity resonances are 85 MHz and 92%, respectively, in excellent agreement with the modelling results (see Fig. 4). The resulting finesse of the resonator is 10 corresponding to a Q of $2.4*10^6$. Some small oszillations can be observed mainly for ccw propagation in the bidirectional mode

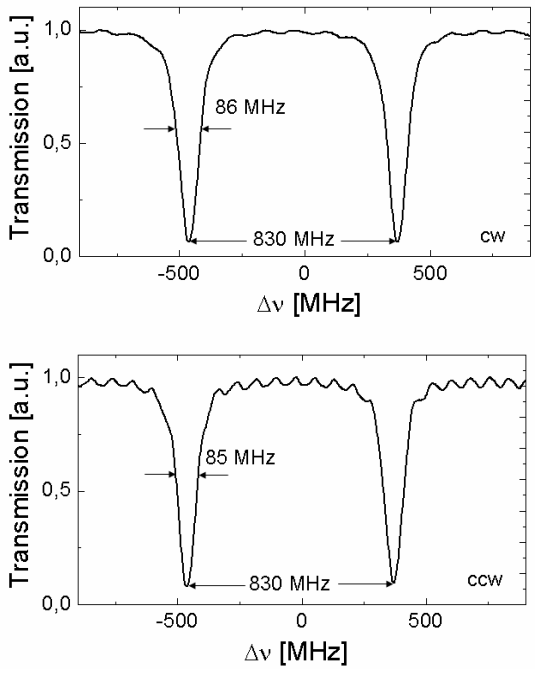


Fig. 9: Cw and ccw resonance curves of a ring resonator in bidirectional operation.

of operation only. They are due to interference effects caused by unidentified residual reflections at fiber connectors.

Unfortunately, due to instabilities of the laser frequency it was not yet possible to unambigously measure the Sagnac effect and in this way the rotation rate using the method sketched above for bidirectional operation. Only for unidirectional operation, an output signal of the lock-in amplifier could be observed proportional to the rotation rate of the sample as a whole. In Fig. 10 the angular position of the sample is plotted versus time; therefore, its first derivative is the time dependent rotation rate. Though the amplitude of the lock-in amplifier output is not stable due to a drift of the laser frequency the signal shows the expected behaviour. From the experimental results a minimum rotation rate of Ω_{min} = 10 °/s can be derived more than three orders of magnitude larger than the theoretically expected minimum rate.

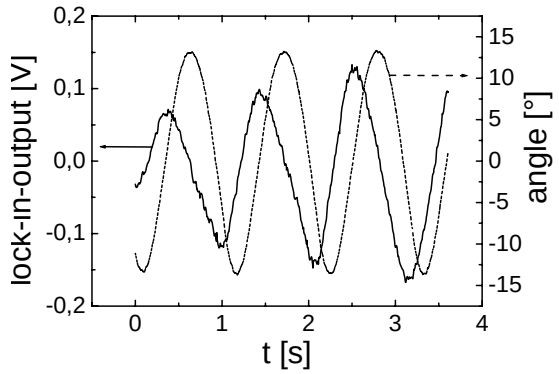


Fig. 10: Angular position of the ring resonator (right ordinate) and output signal of the lock-in amplifier (left ordinate) versus time. 0.1 V correspond to a rotation rate of about 100 °/s.

Conclusions

We have reported the first successful demonstration of the Sagnac effect in a Ti:$LiNbO_3$ waveguide ring resonator of 60 mm diameter and a Q of $2.4*10^6$. The ring cavity has been designed to yield the steepest slope of the transmission at the turning point of a cavity resonance. By dithering the laser frequency and using a lock-in technique the non-reciprocal Sagnac shift of a resonance as function of the rotation rate has been demonstrated. Drift effects of the mean laser frequency with respect to the ring resonance did not yet allow a stable measurement of better accuracy.

In the future, a slow feedback loop will be introduced to lock the laser frequency to a ring resonance. Moreover, an advanced lock-in technique for bidirectional operation of the ring cavity will allow to measure the non-reciprocal resonance frequency splitting separately.

References

1 Ezekiel, S., Arditty, H. J.: *Fiber-Optic Rotation Sensors and Related Technologies*, Springer Verlag, Berlin Heidelberg New York, 1982

2 Suzuki, K., Takiguchi, K., Hotate, K.: *Monolithically Integrated Resonator Microoptic Gyro on Silica Planar Lightwave Circuit*, J. Lightwave Technol. **18** (1), pp. 66-72, 2000

3 Monovoukas, C., Swieki, A. K., Maseeh, F.: *Integrated optical gyroscopes offering low cost, small size and vibration immunity*, Proc. SPIE **3936**, pp. 293-300, 2000

4 Ma, H., Zhang, X., Jin, Z., Ding, C.: *Waveguide-type optical passive ring resonator gyro using phase modulation spectroscopy technique*, Opt. Engineering, **45** (8), Article 080506, 2006

Densely integrated photonic devices based on microring resonators for use in access networks

Edwin J. Klein[1], Gabriel Sengo[1], Lucy T. H. Hilderink[1], Marcel Hoekman[1], Rudy Pellens[2], Paul van Dijk[2], and Alfred Driessen[1]

[1]Integrated Optical MicroSystems Group, MESA+ Research Institute, University of Twente, P.O.Box 217, 7500 AE Enschede, The Netherlands (email: e.j.klein@utwente.nl)

[2]ASML, The Netherlands (email: Paul.van.Dijk@asml.com)

Abstract: A reconfigurable optical add-drop multiplexer as well as a 1x4x4 reconfigurable λ router, designed for use in the second telecom window, are demonstrated. The devices that each have a footprint less than 2 mm^2 are based on thermally tunable vertically coupled microring resonators fabricated in Si_3N_4/SiO_2.

Keywords: optical networks, optical add-drop multiplexer, optical cross-connect, integrated optics, thermally tunable, microring resonator, Si_3N_4

Introduction

The application of optical fibers has led to virtually loss-less point to point data links in the core network with practically unlimited bandwidth. In response to the ever increasing bandwidth demands of consumers the optical techniques employed in these networks are now gradually extended towards the consumers premises with the ultimate goal of enabling ubiquitous high-speed network access for everyone. At the access network level, where equipment is shared by a few users at the most, cost is the major issue. In addition the demand of optical transparency at the nodes and hubs, requiring no conversion between the optical and electrical domains, results in a high degree of complexity of the devices.

In our opinion, the answer to the challenges of cost and complexity will be mass-produced very large scale integrated (VLSI) photonics [1]. Promising building blocks in these devices are Microring Resonators (MRs) [2,3] built using high refractive index waveguides which can be used to create densely integrated wavelength filters as well as more complex functionality [4-7]. The high degree of integration that can be achieved with these micro-resonators is demonstrated by the mask layout in figure 1. This mask layout, which was created from the overlay of multiple stepper reticle images, defines a wafer area of only 1 x 1 cm^2 yet contains five 4-channel WDM routers and several test structures. In fact, the minimum size of the components shown in this layout was not limited by the size of the micro-resonators, but rather the size of the electrodes used to tune the resonators and the 250 µm spacing between the in- and output waveguides required for the fiber-chip coupling for these devices.

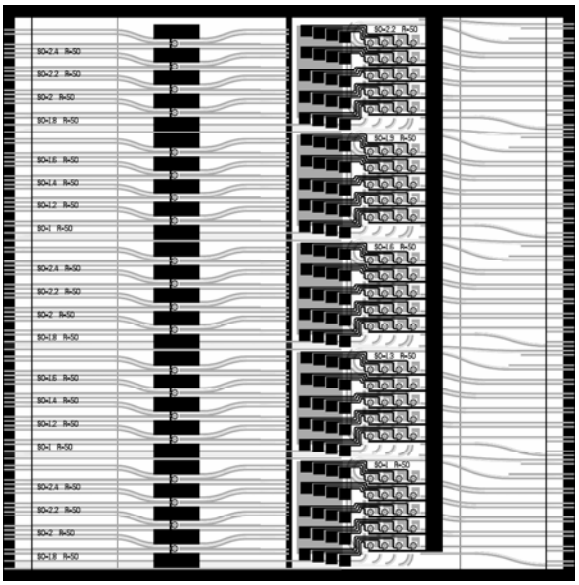


Figure 1. Mask lay-out of 5 WDM routers (right) and a number of test structures (left); the layout is equivalent to an on-wafer area of 1 x 1 cm^2.

The design, fabrication and measurements of the densely integrated WDM router [5] shown in figure 1 as well as a less complex 4-channel reconfigurable Optical Add Drop Multiplexer (ROADM), both intended for use in the second telecom window, will be presented in this paper.

Design and fabrication

The schematic layouts of the OADM and the router are given in figure 2. The OADM consists of a central bus waveguide along which four resonators are placed. These resonators can be used to add or drop channels to and from the eight port waveguides. The router consists of a single de-multiplexer and a routing matrix. The de-multiplexer consists of four resonators that de-multiplex up to four channels from the input port. These channels can then be combined in any combination by the routing matrix and sent to any of the four drop ports. Both devices have been designed using the same basic resonator building block. The resonator building blocks in the OADM are vertically spaced at 250 µm. Although a smaller spacing is possible, this is not practical since the device has been designed to interface with a fiber array with a fiber pitch of 250 µm. For the router the vertical spacing between the drop-port waveguides is 300 µm due to electrode wiring requirements. The resonator building block in both devices uses a cross-grid waveguide approach [5], in which the two waveguides that couple to the MR cross each other. All of the resonators are made thermally tunable using a thin-film omega-shaped chromium heater. A 3D geometry and cross-section of the 3D MR are shown in figure 3. The resonator has a radius of 50 µm and is implemented using a ridge waveguide with a total thickness of 180 nm. The port waveguides also consist of a ridge waveguide having a total thickness of 140 nm. The microring resonators have been designed to work exclusively with the TE polarization.

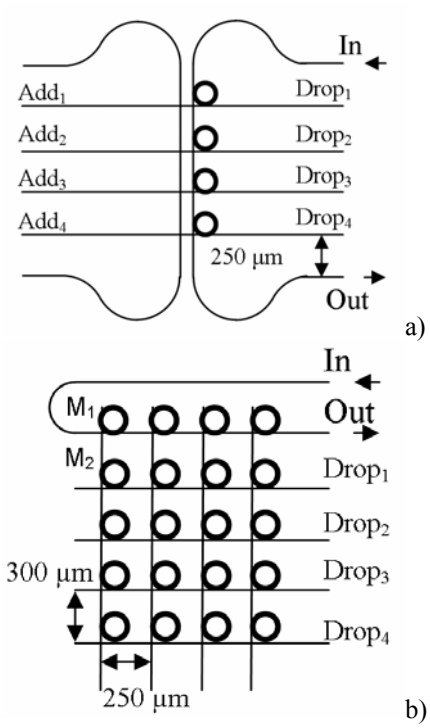


Figure 2: Schematic layout of an OADM a) and b) 1x4x4 λ- router.

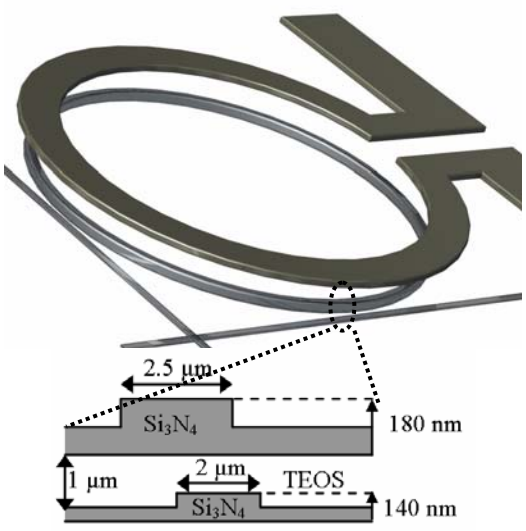


Figure 3: MR top view and coupling region cross-section.

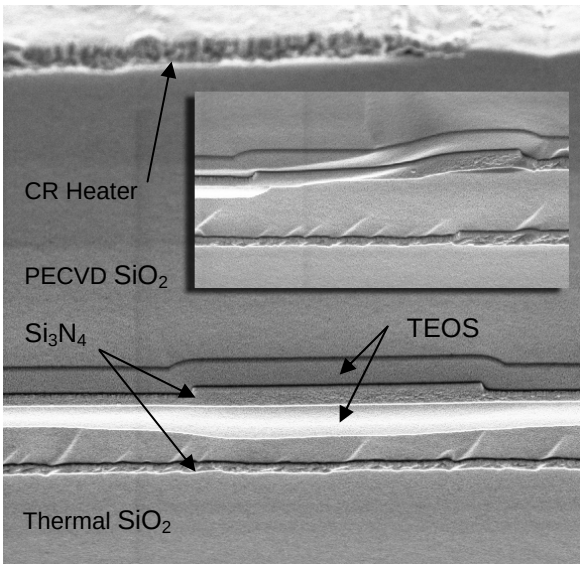


Figure 4:SEM micrograph of the cross-section of a MR. The inset shows the cross-section of a MR fabricated without using CMP. The resonator is" lifted up" due to the waveguide underneath.

A major concern in the fabrication of vertically coupled micro-resonators [8] is the correct alignment of the resonator to the port waveguides. In previously demonstrated devices [6,7], fabricated using contact lithography, the alignment was improved by using a nonius-type approach of built in deviations in the alignment. This, however, significantly lowered the yield. A combination of stepper and contact lithography was therefore used in these new devices to improve yield and increase the alignment accuracy. Contact lithography was used to define

the non-critical layers, such as the electrodes, while the critical resonator and port waveguide layers were defined using an ASML PAS-5500/275 stepper tool. With this tool these layers could be aligned with an accuracy better than 100nm. To facilitate the use of the stepper, alignment markers were first etched into a bare silicon wafer. This wafer was then thermally oxidized to a thickness of 6 µm after which a 140 nm thick layer of LPCVD Si_3N_4 was grown on top [9]. After exposure using the stepper the port waveguides were then etched in this layer using reactive ion etching (RIE). A 1 µm TEOS separation layer was deposited next. Because the TEOS layer closely follows the topography of the underlying layers this layer was chemically mechanically polished (CMP). This is important because without it the "lifting up" of the resonator that occurs when the resonator lies on top of a port waveguide, as shown in the inset in figure 4, can significantly increase the roundtrip losses in the resonator. After the CMP the Si_3N_4 resonator layer was deposited, exposed with the stepper and etched using RIE. A passivation layer consisting of 0.5 µm TEOS and 3.5 µm PECVD SiO_2 were deposited next after which the device was annealed at 1150°C. On top of this layer stack, of which a cross-section is shown in figure 4, 200 nm thick chromium heaters and gold leads were created using contact lithography in combination with lift-off.

Measurement results and discussion

The realized OADM, of which a picture is shown in figure 5, was measured using a broadband source and an optical spectrum analyzer with a resolution of 0.05 nm. Figure 6 shows the normalized responses measured for the four drop ports when the broadband source was connected to the "In" port of the OADM (see figure 2a). To demonstrate the dropping of four different channels to these ports the resonance frequency of each resonator in the OADM has been tuned to a different wavelength. In the drop port responses the effects of channels dropped by adjacent MRs can be observed, for instance in the response at the fourth drop port. The three dips in the response of this port are the through responses of the three preceding resonators. For the drop port responses shown the filter rejection ratio of the individual resonators is ≈16.7 dB. From the measurements the amplitude coupling constants of the individual resonators were determined to be $\kappa_1=\kappa_2=0.40 \pm 0.01$ and the resonator losses 33 ±3 dB/cm. The FSR and Finesse are 3.0 nm and 10.6 respectively, giving a FWHM of 0.28 nm (=46 GHz @1310 nm). The channel crosstalk for channels spaced at 100 GHz (0.6 nm @1300 nm) is ≈-12dB. The considerable losses in the resonator are due to ridge height of the resonator, which was not etched deep enough. These losses also resulted in relatively high on-chip insertion losses of the resonators of ≈5 dB.

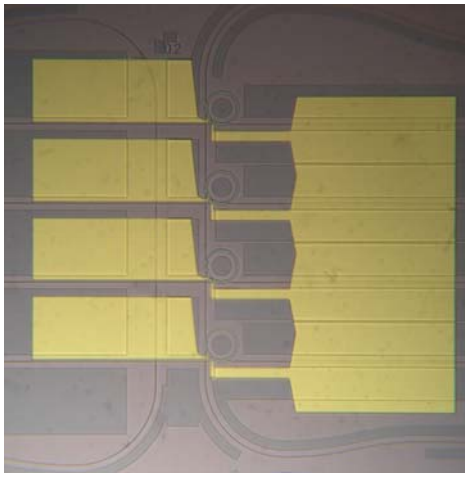


Figure 5: Realized OADM.

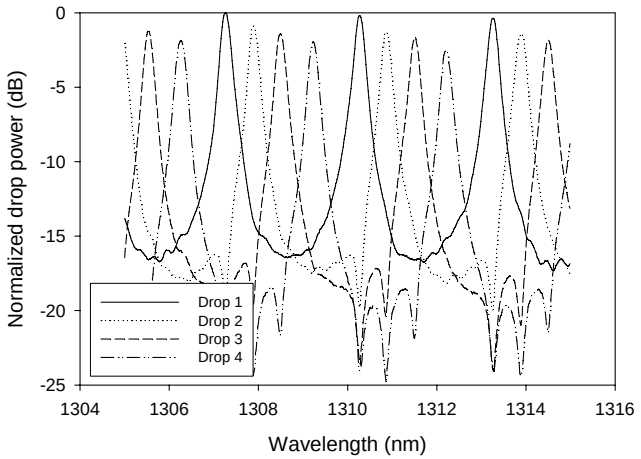


Figure 6: Drop Responses of $Drop_1$-$Drop_4$ for a broadband source connected to the "In" port.

The λ-router, shown in figure 7, has also been characterized using the broadband source at the input and the OSA to measure the wavelength response of the first drop port (see figure 2b). In figure 8 the responses measured at this port are given for three different "tuning" configurations of the router. In the first configuration the heaters on all resonators are switched off and all resonators are in resonance at the same wavelength. The spectral response of this configuration shows a single broad peak, with a FSR of 3 nm. This peak is predominantly the result of the power dropped by the first resonator in the de-multiplexer section of the router (M1 in figure 2b). The minor dip in the center of the peak is due to the interaction with the (smaller) power fractions dropped by subsequent resonators in the de-multiplexer. For the second configuration the first resonator was tuned half a FSR. The power dropped by this resonator shows up as the minor peak in the response. The major peak is now the result of the power dropped by the second resonator in the de-multiplexer and the interactions with the third and fourth resonators. For the third and final router configuration resonator M2 was

tuned to the same wavelength as M1. This causes the channel selected by M1 to be dropped by M2 onto the first drop port. The channel is therefore effectively switched "on" on this port for this configuration as is shown by the large peak in the response measured for this configuration. A comparison with the response of the second configuration shows that the "on" / "off" switch ratio that can be obtained for this router is ≈15 dB. Also the FWHM of the dropped channel is 0.22 nm (=37 GHz @1310 nm), making it suitable for use in next generation access networks that require bandwidths of up to 10 GHz.

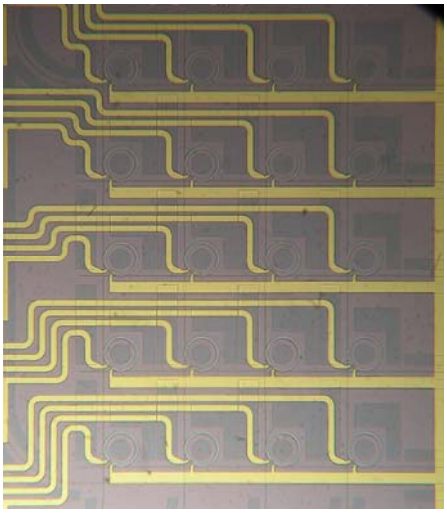


Figure 7: Realized 1x4x4 λ-router.

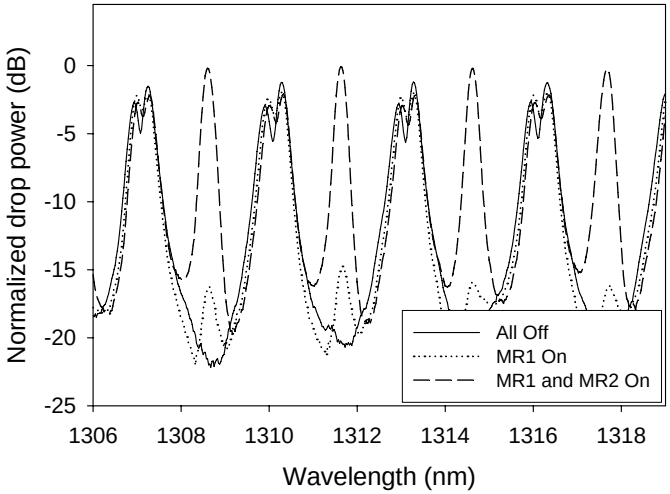


Figure 8: Switching of a single channel in the router

Conclusions

We have presented a reconfigurable 4-channel OADM and a 1x4x4 channel λ-router based on Si_3N_4/SiO_2. Due to the use of microring resonators these devices are able to combine a large functionality with a small footprint: less than 2 mm^2 for the devices discussed here. These devices therefore have the potential to enable more cost effective solutions for bringing fiber based networks all the way to the consumer. In addition, to our knowledge basic routing functionality of a micro-resonator based reconfigurable router has been demonstrated for the first time.

Acknowledgements

The authors would like to thank LioniX B.V for their contributions to the fabrication of the OADM and router devices. The work has been carried out with the financial support of the Dutch Freeband Communication Project "Broadband Photonics".

References

1) B.Little et al., 'Microring resonator arrays for VLSI photonics', IEEE Phot. Techn. Letters, vol. 12, pp. 323-325, 2000
2) S.Suzuki et al., 'Integrated –optic ring resonators with two stacked layers of silica waveguide on Si', IEEE Phot. Techn. Letters., vol. 4(11), pp. 1256-1258, 1992
3) F.C. Blom et al., 'Experimental study of integrated-optics microcavity resonators: Toward an all-optical switching device', Appl. Phys. Letters, vol. 71, pp. 747-749, 1997
4) B.Little et al., 'Microring resonator channel dropping filters', J. of Lightw. Technology, vol. 15, pp. 998-1005, 1997
5) R. A. Soref et al. 'Proposed N-Wavelength M-Fiber WDM Crossconnect Switch Using Active Microring Resonators', IEEE Phot. Techn. Letters, vol. 10, no. 8, 1998.
6) E.J.Klein et al., 'Reconfigurable add-drop multiplexer using microring resonators', IEEE Phot. Techn. Letters, vol. 17, no. 11, pp. 2358-2360, 2005
7) D.H.Geuzebroek et al., 'Compact wavelength-selective switch for gigabit filtering in access networks', IEEE Phot. Techn. Letters, vol. 17, no. 2, pp. 336-338, 2005.
8) D.Klunder et al., 'Vertically and laterally waveguide-coupled cylindrical microresonators in Si_3N_4 on SiO_2 technology', Appl. Phys. B, vol. 73, pp. 603-708, 2001
9) K.Worhoff et al., 'Silicon oxinitride – a versatile material for integrated optics applications', J. Electrochemical Society, vol. 149(8), pp. F85-F91, 2002

Oxygen-ion implanted silicon microring resonator for high-speed all-optical switching

Michael Först(1), Jan Niehusmann (1), Tobias Plötzing (1),
Thorsten Wahlbrink (2), Christian Moormann(2), and Heinrich Kurz (1,2)
1) Institut für Halbleitertechnik, RWTH Aachen University, 52074 Aachen, Germany,
Email: foerst@iht.rwth-aachen.de
2) Advanced Microelectronic Center Aachen (AMICA), AMO GmbH, 52074 Aachen, Germany

Abstract: *Ultrafast all-optical switching is demonstrated in an oxygen-ion implanted silicon-on-insulator microring resonator. The spectral response of the device is rapidly modulated via femtosecond optical excitation and subsequent recombination of charge carriers at artificially introduced ultrafast recombination centers. At an implantation dose of* 1×10^{12} *cm*$^{-2}$ *the carrier lifetime is reduced to 55 ps which facilitates optical switching of signal light in the 1.55 μm wavelength range at modulation speeds larger than 5 Gbit/s.*

Introduction

Silicon-on-insulator (SOI) technology is a promising platform to realize cost-efficient CMOS-compatible integrated photonic on-chip components. Among a variety of passive and active photonics devices demonstrated in recent years (see, e.g., Ref. 1 for an overview), compact microring resonators fabricated from Si strip waveguides have gained noticeable attention [2, 3]. They appear specifically attractive for active photonic switching, since their spectral transmission characteristics are very sensitive to minimal modifications of the optical phase [4].

In the case of all-optical switching, the transmission of a photonic device can be modulated by the optical Kerr effect or by photoexcitation of electron-hole pairs where the latter modify the silicon dielectric function based on the plasma dispersion effect [5]. All-optical carrier-based switching in a silicon microring resonator has been demonstrated via vertical out-of-plane optical excitation and via resonantly in-plane coupled excitation upon linear absorption and nonlinear two-photon absorption, respectively [6, 7]. The switching speed of this approach is determined by the effective free carrier lifetime. Bulk and surface recombination processes in the silicon waveguide and at sidewalls as well as carrier diffusion out the modal area are the dominating processes [8]. They limited the switching time to approximately 450 ps in both experiments.

An increase of switching speed requires the artificial reduction of the effective free carrier lifetime in the photonic device. One alternative is the incorporation of lateral p-i-n structures to the silicon waveguides for electrical carrier sweep out [9, 10, 11]. By this means, the modulation time of a microring resonator could be decreased to about 120 ps [12]. On the other hand, ion-implantation is a well known process to reduce effective free carrier lifetimes in semiconductors. Defect states artificially introduced into the crystalline semiconductor act as trapping centers for fast electron-hole pair recombination [13]. It was recently shown that He-ion implantation can decrease the free carrier lifetime in large area Si rib waveguides down to the nanosecond scale [14]. The result was an enhancement Raman amplification in that experiment.

In this contribution, we demonstrate that O^+-ion implantation of silicon waveguides is an extremely valuable approach for high-speed switching applications in SOI microring resonators. Compared to incorporating p-i-n junctions to the resonator waveguide, the fabrication of the final device benefits from relaxed processing requirements – since only one sort of ions has to be implanted and masking issues require less accuracy. Even higher switching speeds appear feasible via the implantation approach, since the free carrier lifetime can be precisely tailored down to the few-picosecond range via the chosen implantation dose.

Device fabrication

The investigated device is a waveguide bus-coupled silicon microring resonator fabricated from an SOI substrate. All waveguides are 300 nm high and 400 nm wide, the resonator radius is 5 μm, and the coupling gap between resonator and adjacent straight waveguides is 300 nm. The photonic structure was defined by electron beam lithography (EBL) using hydrogen silsesquioxane (HSQ) as resist. Pattern transfer is achieved by HBr inductive coupled reactive-ion etching.

To reduce the free carrier lifetime in the microring resonator, the device was implanted with O^+ ions at an energy of 120 keV and a dose of 1×10^{12} cm^{-2}. These parameters were chosen for the following reasons: (i) Taking into account the residual 100 nm thick HSQ EBL resist layer on top of the waveguide, the depth profile of defect states is calculated to be centered midway the waveguide height. (ii) According to previous studies on the implantation of bulk silicon, an implantation dose in the range of 1×10^{12} cm^{-2} should result in carrier lifetimes clearly below 100 ps [13]. To protect the several millimeter long bus waveguides from implantation, the sample was covered by an additional 900 nm thick SiO_2 layer prior to this process except of a 50×50 μm^2 rectangular mask centered at the microring.

Linear characterization

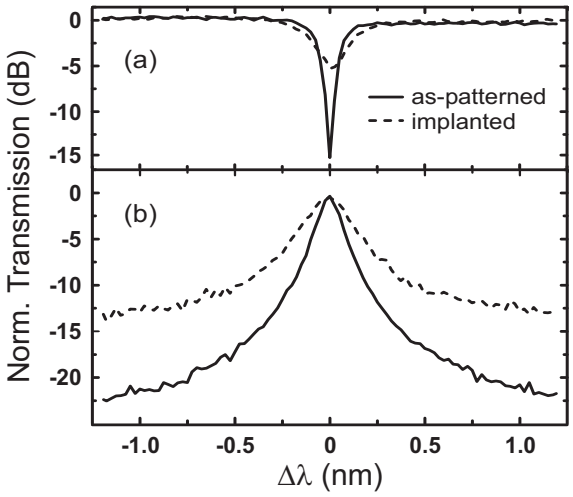


Fig. 1: Transfer function of the investigated microring resonator after EBL patterning (solid lines) and after additional O^+ ion implantation at energy of 120 keV and dose of 1×10^{12} cm^{-2} (dotted lines). (a) drop port and (b) through port. $\Delta\lambda = \lambda - \lambda_0$, with λ_0 the resonance wavelength.

The linear spectral response of the fabricated device was measured before and after the implantation process. Transmitted light at the through channel (Figure 1(a)) and resonator-coupled light at the drop channel (Figure 1(b)) were measured for TM-polarization (for details of the experimental setup see Ref. 3). The transmission spectrum (through port) of the unimplanted device exhibits a sharp dip of approximately −15 dB at the resonance wavelength λ_0=1567.72 nm. The quality factor of this resonance, defined as $Q = \lambda_0/\Delta\lambda_{3dB}$, is 11450. In comparison, the transmission spectrum of the implanted microring shows an increase in spectral width and a concomitant decrease in modulation depth. The corresponding Q-factor is about 6200, and in resonance the transmission drops only by about −5 dB. The corresponding maxima measured at the drop channels (Figure 1(b)) exceed the background level by about 22.5 dB and 13 dB for the as-patterned and implanted device, respectively.
Implantation induced defects in the resonator waveguide are assumed to increase the waveguide propagation losses by providing additional light scattering centers. To gain detailed insight into the observed Q-factor decrease, we quantify the microring's photon losses per roundtrip before and after ion implantation. To this end, we fit the analytical transfer function

$$|S_{21}|^2 = \frac{t^2 + t^2\tau^2 - 2t^2\tau\cos\phi}{1 + t^4\tau^2 - 2t^2\tau\cos\phi}, \qquad (1)$$

to the respective transmission spectra measured at the through port of the device. Here, t is the symmetric field transmission coefficient at the coupling gaps between resonator and bus waveguides at through and drop channel, τ the field transmission per resonator roundtrip, and $\phi = 2\pi n_{eff} L/\lambda$ the phase shift per round trip with effective refractive index n_{eff} and resonator length L [15]. The coupling coefficients obtained from these numerical fits are t_1 =0.9962 and t_2 =0.9958 before and after implantation of the device, respectively. Hence, the the implantation process affects the coupling strength between the waveguides and the resonator only marginally. In contrast, the transmission coefficient drops from τ_1 =0.9987 to τ_2 =0.9908 as consequence of the implantation process. The corresponding waveguide losses in the resonator $\alpha = -2\ln(\tau)/L$ increase from 3.6 dB/cm to 25.6 dB/cm – an effect which is expected from additional scattering centers for the light wave propagating in the implanted microring. Nonetheless, the Q-factor of the implanted device is sufficiently large, to allow for optical switching at reasonable carrier densities [6, 7].

Time-resolved switching characteristics

All-optical switching characteristics of the implanted device are investigated in a pump-probe setup which allows for a spectral analysis of the switching process with sub-picosecond resolution (see Fig. 2).

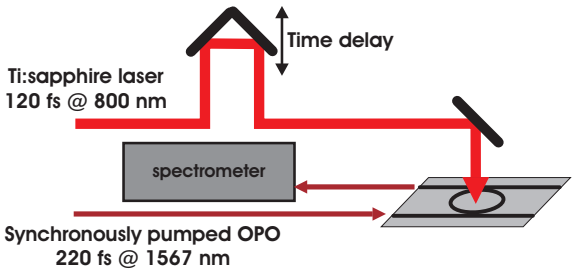


Fig. 2: Schematic illustration of the experimental setup for the time-resolved investigation of the switching process.

For optical excitation, laser pulses of 120 fs duration are derived from a Ti:sapphire oscillator at 800 nm wavelength. These are focussed onto the microring to photogenerate electron-hole pairs in the resonator waveguide by linear absorption. The spectral response of the device is probed with infrared pulses from a synchronously pumped optical parametric oscillator. The pulse length is 220 fs, the central wavelength is adjusted close to the resonance of the microring at 1.567 μm, and the spectral bandwidth is about 15 nm. These probe pulses are coupled to the device waveguides by a polarization maintaining singlemode fiber. A second singlemode fiber guides the output at the drop channel to a sub-nanometer resolution optical spectrum analyzer. A motorized translation stage provides an adjustable time delay between excitation and probe pulses to temporally resolve the switching dynamics.
Figure 3 shows the temporal evolution of the spectrally resolved intensity measured at the drop channel

of the implanted microring resonator. The spot diameter and pulse energy of the excitation laser are 20 μm and 0.75 nJ. At zero time delay, the resonance of the device clearly shifts to shorter wavelength followed by a red-shift to its initial position within 200 ps after optical excitation. The resonance shift at $\Delta t = 0$ is accompanied by a decrease of the resonance amplitude and, again, subsequent relaxation to approximately the initial value within the measured time window. Both observations are ascribed to the optical excitation of electron-hole pairs and their fast recombination dynamics. As long as photogenerated free carriers are present in the microring waveguide the resonance wavelength shifts out of equilibrium via the plasma dispersion effect, while the drop port intensity decreases due to an increased free carrier absorption at the infrared probe wavelength.

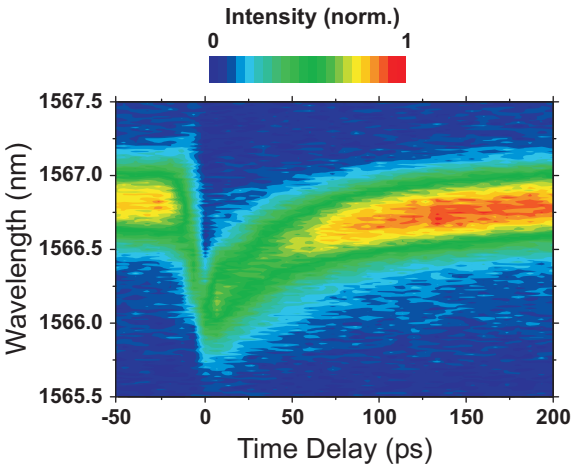


Fig. 3: Spectral response (intensity plot) of the implanted microring resonator measured at the drop channel after optical excitation.

The temporal evolution of the resonance wavelength shift, plotted in Fig. 4(a), is determined by the intrinsic response time of the resonator and the lifetime of photogenerated electron-hole pairs [7, 12]. Although charge carriers are optically excited within a 120 fs pulse duration, the temporal evolution of the wavelength shift out of resonance at zero time delay is governed by the photon cavity lifetime τ_{cav}. For the investigated resonance of the device, we calculate $\tau_{cav} = \lambda_0/(2\pi cQ) = 5.2$ ps, where c is the vacuum speed of light. A monoexponential numerical fit to the wavelength shift for negative time delays (not shown in Fig. 4(a)) results in $\tau_{cav} = 6.2$ ps which is in close agreement with the cavity photon lifetime calculated from the quality factor. Note here, that $\Delta t = 0$ is defined at the time delay of maximum wavelength shift.
At positive time delays, the peak wavelength of the resonance shifts back to its equilibrium position. In this case, the corresponding time constant is determined by the free carrier lifetime $\tau_{e,h}$ in the waveguide. From a monoexponential fit to these data (grey solid line in Fig. 4(a)), $\tau_{e,h}$=55 ps is obtained which clearly demonstrates the capability of O^+-ion implantation to drastically reduce the effective free carrier lifetime in the silicon waveguide. Noteworthy, the free carrier lifetime – measured in the investigated microring device at the chosen implantation dose of 1×10^{12} cm^{-2} – corresponds well to published data of O^+-implanted bulk Si [13]. Note, that an increase of the ion implantation dose is expected to result in a further reduction of the free carrier lifetime where values below 10 ps are predicted at an implantation dose of about $1{\times}10^{13}$ cm^{-2}. In this case, careful attention will have to be paid to a further increase of waveguide propagation losses which will, in turn, decrease the resonator Q-factor and concomitantly increase required switching powers [16].

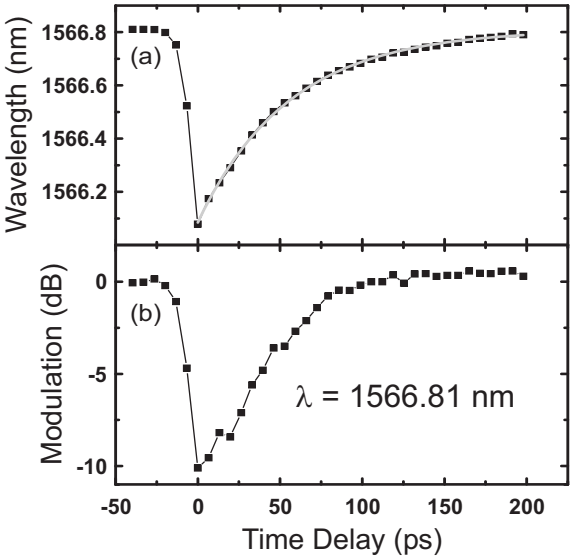


Fig. 4: (a) Time resolved shift of the peak resonance wavelength at the drop waveguide (squares). The grey solid line is an exponential fit to the data for positive time delays. (b) Normalized drop waveguide intensity at the resonance wavelength λ=1566.81 nm.

For a quantitative spectral analysis of the induced wavelength shift, Fig. 4(a) depicts resonance peak wavelength as a function of time delay. The maximum resonance shift at zero time delay is $\Delta\lambda = -0.74$ nm. Considering an effective refractive index $n_{eff} = 2.27$ of the resonator waveguide, this wavelength shift corresponds to a carrier-induced effective refractive index change $\Delta n_{eff} = 1.07{\times}10^{-3}$ or a silicon refractive index change $\Delta n_{Si} = 0.97 \times 10^{-3}$, respectively. A photogenerated charge carrier density of $\Delta N_{e,h} = 2.7{\times}10^{17}$ cm^{-3} is required to induce this refractive index change in an unimplanted silicon microring [5]. From the experimental parameters, i.e. laser spot size, pulse energy, and microring dimensions, and the silicon absorption coefficient $\alpha_{Si} = 1500$ cm^{-1} at 800 nm wavelength, we estimate an optical excitation density of $\Delta N_{e,h} = 5.5 \times 10^{17}$ cm^{-3} in the resonator waveguides.

The equivalent optical energy absorbed in the microring amounts to 0.75 pJ which corresponds to about one per mill of the laser power incident on the sample. The calculated and experimentally obtained carrier densities differ by only a factor of 2, thus showing good quantitative agreement.
To demonstrate the applicability of the fabricated device as an all-optical switch for a continous-wave signal beam, Fig. 4(b) shows the temporal evolution of the normalized drop port intensity at the resonance wavelength λ_0 = 1566.81 nm. At zero time delay, the intensity drops by approximately −10 dB and completely recovers within the following 100 ps. This dynamic response facilitates optical switching at data rates beyond 5 Gbit/s.

Conclusion

In conclusion, we demonstrated the capability of O^+-ion implantation to reduce the free carrier lifetimes in a silicon strip waveguide device. High-speed all-optical light modulation was observed in an SOI microring resonator at a moderate implantation dose. A further increase of the optical modulation frequency, which is essential for future silicon photonic circuits, appears feasible by reducing the free carrier lifetime at higher implantation doses.

Acknowledgments

We thank F. Merget for assistance in sample fabrication. This work has been financially supported by the European Commission within the STREP project "Circles of Light" (Contract No. FP6-034883) and in part within the European Network of Excellence "ePIXnet".

References

[1] L. Pavesi and G. Guillot (Eds.) "Optical Interconnects: The Silicon Approach", Springer Series in Optical Sciences **119**, (Springer Verlag, Berlin, 2006).

[2] T. Baehr-Jones, M. Hochberg, C. Walker, and A. Scherer, Appl. Phys. Lett. **85,** 3346 (2004).

[3] J. Niehusmann, A. Vörckel, P. Haring Bolivar, T. Wahlbrink, W. Henschel, and H. Kurz, Opt. Lett. **29,** 2861 (2004).

[4] B.E. Little, S.T. Chu, H.A. Haus, J. Foresi, and J.-P. Laine, IEEE J. Lightwave Technol. **15,** 998 (1997).

[5] R. Soref and B. Bennett, IEEE J. Quantum Electron. **23,** 123 (1987).
Phys. Lett. **59**, 3276 (1991).

[6] V.R. Almeida, C.A. Barrios, R.R. Panepucci, M. Lipson, M.A. Foster, D.G. Ouzonov, and L. Gaeta, Opt. Lett. **29,** 2867 (2004).

[7] V.R. Almeida, C.A. Barrios, R.R. Panepucci, and M. Lipson, Nature **431,** 1081 (2004).

[8] R. Claps, V. Raghunathan, D. Dimitropoulos, and B. Jalali, Opt. Express **12,** 2774 (2004).

[9] H. Rong, A. Liu, R. Jones, O. Cohen, D. Hak, R. Nicolaescu, A. Fang, and M. Paniccia, Nature **433**, 292 (2005).

[10] D. Dimitropoulos, R. Jhaveri,R. Claps, J.C.S. Woo, and B. Jalali, Appl. Phys. Lett. **86**, 071115 (2005).

[11] Q. Xu, B. Schmidt, S. Pradhan, and M. Lipson, Nature **435,** 325 (2005).

[12] S.F. Preble, Q. Xu, B.S. Schmidt, and M. Lipson, Opt. Lett. **30,** 2891 (2005).

[13] F.E. Doany, D. Grischkowsky, and C.-C. Chi, Appl. Phys. Lett. **50,** 460 (1987).

[14] Y. Liu and H.K. Tsang, Opt. Lett. **31,** 1714 (2006).

[15] A. Vörckel, M. Mönster, W. Henschel, P. Haring Bolivar, and H. Kurz, IEEE Photon. Technol. Lett. **15,** 921 (2003).

[16] Q. Xu, V.R. Almeida, and M. Lipson, Opt. Lett. **30,** 2733 (2005).

Plasmonics: Engineering of highly confined electromagnetic modes

Stefan A. Maier
Centre for Photonics and Photonic Materials, Department of Physics,
University of Bath, Bath BA2 7AY, UK, S.Maier@bath.ac.uk

Abstract: *This conference proceedings paper presents a brief discussion of sub-wavelength electromagnetic energy localization using engineered coupled surface plasmon polariton modes occurring at metal/dielectric/metal three-layer stacks. Using a simple analytical model taking the energy in the metallic cladding layers into account, it is demonstrated that such heterostructures allow out-of-plane energy confinement below the diffraction limit. An application in the form of a metal nanoparticle plasmon waveguide operating via evanescent coupling of gap modes is presented, and conclusions for the general trade-off between localization and loss in plasmonic waveguiding drawn.*

A condensed history of plasmonics

Plasmonics [1] is currently one of the major driving forces of the fascinating field of *nanophotonics*, which explores how electromagnetic fields can be confined over dimensions on the order of or smaller than the wavelength of light. It is based on interaction processes between electromagnetic radiation and conduction electrons at metallic interfaces or in small metallic nanostructures, leading to an enhanced optical near field of sub-wavelength dimension.

Research in this area demonstrates how a distinct and often unexpected behaviour can occur even with in bulk form well-characterized materials such as metals if discontinuities or sub-wavelength structure is imposed.

Another beauty of this field is that it is firmly grounded in classical physics, so that a solid background knowledge in electromagnetism is sufficient to understand main aspects of the topic.

However, history has shown that despite the fact that the two main ingredients of plasmonics - *surface plasmon polaritons* and *localized surface plasmons* – have been clearly described as early as 1900, it is often far from trivial to appreciate the interlinked nature of many of the phenomena and applications of this field. This is compounded by the fact that throughout the 20th century, surface plasmon polaritons have been rediscovered in a variety of different contexts.

The mathematical description of these surface waves was established around the turn of the 20th century in the context of radio waves propagating along the surface of a conductor of finite conductivity [2, 3]. In the visible domain, the observation of *anomalous* intensity drops in spectra produced when visible light reflects at metallic gratings [4] was not connected with the earlier theoretical work until mid-century [5]. Around this time, loss phenomena associated with interactions taking place at metallic surfaces were also recorded via the diffraction of electron beams at thin metallic foils [6], which was in the 1960s then linked with the original work on diffraction gratings in the optical domain [7]. By that time, the excitation of Sommerfeld's surface waves with visible light using prism coupling had been achieved [8], and a unified description of all these phenomena in the form of surface Plasmon polaritons was established.

From then on, research in this field was so firmly grounded in the visible region of the spectrum, that several rediscoveries in the microwave and the terahertz domain took place at the turn of the 21st century, closing the circle with the original work from 100 years earlier. The history of *localized* surface plasmons in metal nanostructures is less turbulent, with the application of metallic nanoparticles for the staining of glass dating back to Roman times. Here, the clear mathematical foundation was also established around 1900 [9].

While there exist many recent reviews and introductions to the field, for example [10, 11], it is the purpose of this conference communication paper to briefly elucidate the general trade-off between localization and loss in plasmonics - highermode confinement implying larger fraction of the mode energy inside the metallic media, and therefore higher Ohmic losses. As an example, it is shown how the engineering of surface plasmon modes in metal/dielelectric/metal heterostructures allows the excitation of gap-modeswitch good field confinement [12] while at the same time trying to keep losses due to Ohmic heating to a minimum. For this purpose, after a brief

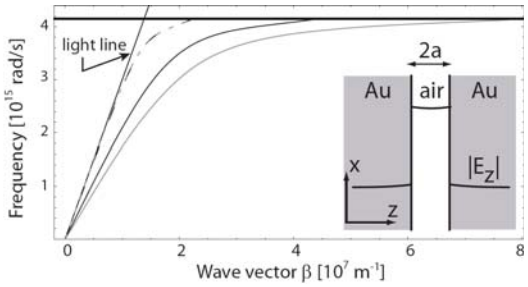


FIG. 1: Dispersion relation of the odd plasmon-polariton gap mode sustained by two infinite Au half spaces separated by an air gap 2*a* (inset) for: 2*a* = 1μm (broken black line), 100 nm (black line), and 50 nm (gray line). Also shown is the dispersion for a single interface (broken gray line). For large wave vectors, the frequency of the mode approaches the Au/air surface plasmon frequency (horizontal line).

discussion of how to assess subwavelength energy confinement, the specific example of a metal nanoparticle waveguide sustaining a mode preferentially localized in inter-particle gaps will be discussed. It is hoped that this will inspire more detailed investigations of the optimization between confinement and loss in a context of waveguiding using surface plasmons.

The trade-off between localization and loss and gap-mode engineering

In order to investigate the ability of surface plasmons for sub-wavelength energy localization, we will as a didactic example study one of the simplest geometries of a multilayer structure, a thin dielectric layer (air) sandwiched between two metallic claddings (Fig. 1, inset).

As is well known, such a heterostructure can support two surface modes propagating in the *x*-direction parallel to the interfaces that are set up by coupling of the surface plasmon-polariton modes of the individual air/metal boundaries [13]. Here the focus will be on the mode of odd *vector* parity, which does not have a cut-off gap size and shows a symmetric scalar field distribution of the dominant electric field component, E_z, with respect to the symmetry plane, as depicted in the inset of Fig. 1. The dielectric response of the metallic half-spaces is modelled using a Drude fit to the dielectric function $\varepsilon(\omega)$ for gold (Au) at visible and near-infrared frequencies [14]. More details regarding these and all subsequent calculations can be found in [12].

Fig. 1 shows the dispersion relation of the coupled mode for varying gap size 2*a*. The dispersion for a single interface is also shown (broken gray line), which is seen to coincide with the dispersion for large gap sizes.

An important point to note here is that large propagation constants β can be achieved even for excitation significantly below the bulk metal plasma frequency provided that the gap width is chosen sufficiently small.

The ability to access such large wavevectors by adjusting the geometry indicates, as has been pointed out in previous work on sub-wavelength guiding structures [15], that localization effects that for a single interface can only be sustained at excitations near the material plasma resonance, can for this gap structure also be attained for excitation out in the mid- and far-infrared.

As will be seen below, this highly dispersive region of the bandstructure has a significant impact upon the effective size of the guided mode. Fig. 2(a) shows the evolution of both the real and imaginary parts of β with varying gap size for excitation at a free space wavelength of λ_0 = 850nm. Both parts are seen to increase with decreasing gap size, suggesting that the mode is becoming more electron-plasma in character, and that the electromagnetic energy is residing increasingly in the metal half-spaces. A plot of the fractional amount of energy inside the metal regions is shown in Fig. 2(b) for excitation at wavelengths λ_0 = 600 nm, 850 nm, 1.5 μm, 10 μm, and 100 μm (= 3THz), reaching e.g. 40% for a gap of 20 nm at λ_0 = 850 nm. For this and the following figure, the gap size is normalized to the

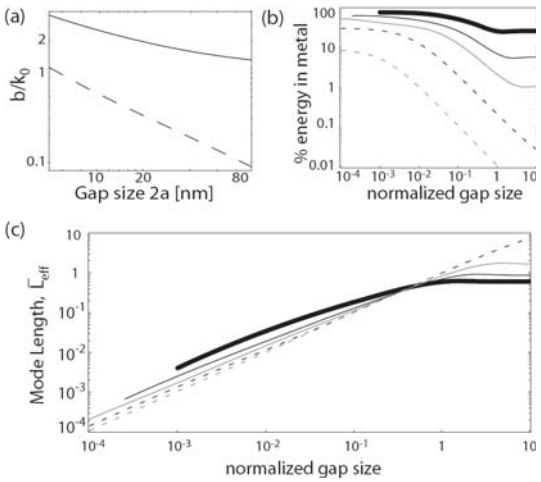


FIG. 2: (a) Normalized propagation constant β versus gap size at λ_0 = 850nm. Both the real (solid curve) and the imaginary (broken curve, 10x) part of β are seen to increase for decreasing gap. (b) Fractional electric field energy residing inside the metallic half spaces as a function of normalized gap size for excitation at λ_0 = 600 nm (thick line), 850nm (black line), 1.5 μm (gray line), 10 μm (broken black line), and 100 μm (broken gray line). (c) Effective mode length L_{eff} normalized to free space wavelength λ_0.

respective free space wavelength, and the results for each wavelength are plotted over the range of convergence of the analytical model.
It can be seen then, that along with the increased localization of the field to the metal/air interface, either via small gap sizes or excitation closer to the surface plasmon frequency, comes a shift of the energy into the metal regions.

Electromagnetic energy density and the effective mode volume in plasmonics

It seems a natural question to ask if the effective size of the mode perpendicular to the metal/air interfaces drops below the diffraction limit if the energy pushed into the metallic half spaces with closing gap is considered properly. In order to get a better handle on the consequences of increasing fractions of the total energy of the mode entering the metallic cladding upon decreasing size of the dielectric gap, and to determine the overall effect on the scaling of the electric field strength per plasmon-polariton excitation in the air gap as a function of the gap size, one can define in analogy to the effective mode *volume* V_{eff} of cQED [16], an effective mode *length* L_{eff} for this one dimensional stack,

$$L_{\mathrm{eff}}(z_0)u_{\mathrm{E}}(z_0) = \int u_{\mathrm{E}}(z)dz. \qquad (1)$$

Here $u_{\mathrm{E}}(z)$ represents the electric field energy density at position z, with z_0 corresponding to a position of interest within the cavity (usually the point of highest electric field strength). For the structure of Fig. 1, z_0 resides in the air gap where an object may be placed to interact with the field. Fig. 2(c) shows the variation of $\bar{L}_{\mathrm{eff}}$ (normalized to the free space wavelength λ_0) with normalized gap size for the capacitor mode.
As can be seen, the mode lengths dropwell below $\lambda_0/2$, demonstrating that plasmonic metal structures do indeed sustain *effective* as well as *physical* mode lengths below the diffraction limit of light. The trend in L_{eff} with gap size tends to scale with the physical extent of the air gap. For large normalized gap sizes and low frequencies, this is due to the delocalized nature of the surface plasmon, leading to smaller mode lengths for excitation closer to the surface plasmon resonance frequency for the same normalized gap size. As the gap size is reduced to a point where the bandstructure of the capacitor mode turns over (see Fig. 1) and energy begins to enter the metallic half spaces, the continued reduction in mode length is due to an increase in field localization to the metal-air surface. In this regime, excitations with lower frequencies show smaller mode lengths for the same normalized gap size than excitations closer to the plasmon resonance, due to the fact that more energy resides inside the metal for the latter.
This simple analysis of field confinement of surface plasmon modes can also be applied to surface plasmon polaritons propagating at a single interface, where confinement below the diffraction limit is possible only for frequencies that are a substantial fraction of the intrinsic surface plasma frequency of the conductor, and also for localized plasmons in metal nanoparticles.

Waveguiding via interparticle gaps in linear nanoparticle chains

In the following, the concept of surface plasmon modes coupled via nanoscale dielectric gaps will be applied to a metal nanoparticle chain. Recently, there has been a huge amount of interest into the optical properties of metallic nanoparticles, due to the possibility of creating subwavelength modalities for confining and guiding light below the diffraction limit via the excitation of localized surface plasmons [11]. Specifically, it has been shown that one-dimensional arrays of closely spaced metallic nanoparticles can act as waveguides when excited at the dipole plasmon resonance frequency of the constituent particles [17]. The tight confinement offered by resonant excitation fundamentally implies substantial losses due to energy penetration into the metal and subsequent ohmic heating, leading to 1/e energy attenuation lengths below 1 μm. Metal nanoparticle plasmon waveguides have thus far been analyzed via quasistatic models using generalized Mie-theory [18], point-dipole [19] and tight-binding [20] calculations, and by fully retarded models [21, 22] as well as finite-difference time-domain (FDTD) simulations [23]. Using these models, typical 1/e energy attenuation lengths between 750 and 900 nm have been estimated for arrays of 50 nm Ag spheres in air spaced by 25 nm gaps excited at the dipole particle plasmon frequency (corresponding to a free-space wavelength λ = 380 nm). Nanoparticle plasmon waveguides operating using this principle have been fabricated and their guiding properties characterized using near-field optical microscopy [17]. The high confinement of optical energy offered by metal nanoparticle plasmon waveguides suggests applications for channelling energy to nano- and molecular scale detectors over modest distances, for example in a context of highly integrated optical sensing. However, tight confinement of the energy requires excitation at the dipole plasmon frequency of the constituent

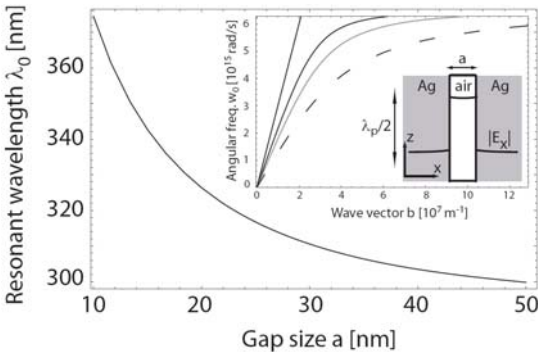


FIG. 3: Evolution of the wavelength of the fundamental gap resonance with gap width *a* for a Ag/air/Ag heterostructure (inset) calculated using a one-dimensional analytical model assuming perfect cavity mirrors confining the mode to a lateral size of 50 nm in the z-direction. The inset shows the dispersion relation of the coupled plasmon mode propagating in the z-direction for *a*=50 nm, 25 nm, and 10 nm (black, grey and broken line, respectively).

particles, for which most of the energy of the mode resides in the particle itself, leading to high attenuation and only limited field accessibility. Additionally, resonant particle excitation constrains the tunability to longer wavelengths, which can only be achieved via increasing particle size or aspect ratio, or the refractive index of the surrounding host. For Ag nanoparticles, this leads to a broadening of the dipole resonance due to retardation effects and radiative losses, adversely affecting the guiding properties. While waveguides operating on this resonant particle principle have been successfully fabricated and characterized [17], this guiding mechanism cannot readily explain the experimental observation of a lower electric field distribution above the particles compared to the interparticle gaps obtained using collection mode near-field optical microscopy [24].

To overcome this discrepancy and enlarge the versatility of plasmon waveguides, here a new design principle for metal nanoparticle plasmon waveguides is presented that overcomes the requirement of resonant excitation of the particle plasmon while additionally maximizing the amount of energy outside the particles themselves. High confinement of the electromagnetic energy is assured via the excitation of evanescently coupled resonant modes in the gaps between adjacent particles. Adjustment of the gap dimensions (width and lateral size) allows for a tuning of the guiding frequency, mode size as well as attenuation length (via the quality factor of the fundamental gap resonance). Regarding the later,

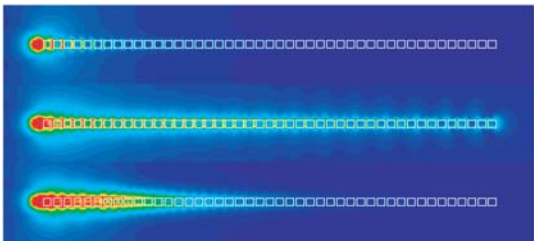


FIG. 4: Electric field distribution around nanoparticle plasmon waveguides excited using a longitudinally polarized point-dipole located to the left of the waveguide at λ0=500 nm (top), 429 nm (center), and 390 nm (bottom). In the case of resonant excitation at 429 nm, the energy is efficiently guided along the array. The color scale spans 5 orders of magnitude in the absolute value of the electric field

the amount of energy inside the metal particles and thus the attenuation is determined by the size of the gap, allowing relatively low-loss operation via careful tuning of the ratio between the evanescent coupling in the air and metallic regions, respectively.

In the following, Ag cubes of dimensions 50 × 50 × 50 nm3 in air spaced by a gap of size *a* will be considered as the fundamental building blocks of a plasmon waveguide. Before presenting results obtained from three-dimensional FDTD simulations, the nature of the fundamental mode squeezed in the nanometric space between two metal particles can best be analyzed using the simple, one-dimensional analytical model of a metal/air/metal heterostructure presented above employing a straightforward boundary condition analysis.

The inset of Fig. 3 shows the dispersion relation for this mode for gap sizes of 50 nm (black line), 25 nm (grey line) and 10 nm (broken line), respectively. As can be seen, the real part of the propagation constant of the mode along the interfaces increases for decreasing gap size, leading to a reduced wavelength of the propagating plasmon $\lambda_p = 2\pi/\beta$. Thus, the wavelength of the propagating plasmon can be tuned via the size of the gap, which additionally controls the amount of dissipation due to the fact that upon decreasing gap the fraction of the energy of the mode inside the metallic half-spaces increases.

This structure can be converted into a Fabry-Perot type resonator by inserting perfectly reflecting cavity walls perpendicular to the direction of propagation. Thus, the fundamental mode will be excited when the cavity length *d* equals $\lambda_p/2$. Figure 3 shows the evolution of the corresponding free-space wavelength of excitation λ_0 with gap

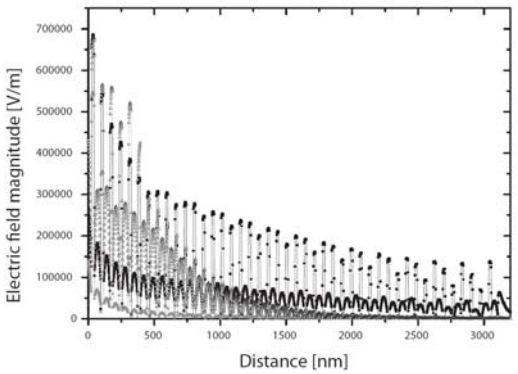


FIG. 5: Magnitude of the electric field along the waveguide axis for excitation at 500 nm (grey circles), 429 nm (black squares), and 390 nm (open triangles). After a fast initial decay due to transient effects, relatively low-loss guiding with a 1/e field decay of α_F^{-1} = 2200 nm occurs for resonant excitation at 429 nm.

size for a fixed cavity length d=50nm. As expected, λ_0 increases for decreasing gap size due to the increase in the wave vector β of the fundamental mode. Thus, there exists an intricate interdependency between gap size, cavity length, resonant wavelength and attenuation of the two-dimensional cavity.

The proposed plasmon waveguide relies on the evanescent coupling of adjacent gaps separated by a metallic nanoparticle, which was analysed using FDTD simulations of a chain of 45 Ag nanoparticles spaced by a gap of size a=20 nm. The first particle was excited using a dipole oriented along the waveguide axis. Using pulsed excitation, the resonant frequency of the fundamental gap mode was determined to 7×10^{14} Hz, corresponding to λ_0 = 429 nm. The resonant wavelength is longer than that predicted (325 nm) using the simple one-dimensional model with perfectly reflecting cavity boundaries, which is due to the field penetration into the air-space surrounding the particles, thus increasing the resonant wavelength. Fig. 4 shows the absolute value of the electric field on a linear color scale for excitation at 500 nm (top), 429 nm (center), and 390 nm (bottom). Clearly, significant guiding along the waveguide takes place upon resonant excitation only. Additionally, the field is seen to be tightly confined inside the gap regions in agreement with the squeezed near-field observed in [25], while in the particles themselves the electric field is confined to the surfaces, as opposed to the homogeneous polarization sustained during dipole particle plasmon excitation of spherical nanoparticles. In the latter case, excitation of longitudinally coupled dipolar modes show some resemblance to the gap modes presented here for cubic particles, however with larger penetration of the electromagnetic fields inside the metal nanoparticles.

Fig. 5 shows the absolute value of the electric field along the waveguide axis through the particle centers for the three wavelengths of interest. While nonresonant excitation is characterized by a rapid decrease in field amplitude after only a small number of gaps, for resonant excitation relatively low-loss guiding is seen to be possible. In this case, a number of interesting features are apparent. Firstly, at the beginning of the waveguide close to the excitation source, an initial fast decay of the field over the first 6 gaps is apparent, which can be attributed to transient effects and direct excitation from the source at a distance. The same phenomenon was previously seen in plasmon waveguides excited at the particle plasmon resonance frequency [21]. Additionally, towards the end of the waveguide modulating effects due to the reflection of the guided wave at the impedance mismatch after the last particle are discernable. Incorporating the effects of this reflection, an exponential decay of the electric field amplitude along the waveguide with a decay constant α_F^{-1} = 2200 nm was determined, corresponding to a 1/e energy attenuation length α_E^{-1} = 1100 nm. To verify the exponential decay fits, waveguides with varying number of particles have been simulated, yielding close agreement in their attenuation lengths.

Thus, metal nanoparticle plasmon waveguides guiding electromagnetic energy via coupled gaps compare reasonably favourably to the dipole particle plasmon case in terms of field accessibility and also energy attenuation. Additionally, the number of variables available (particle size, gap size, gap width) for tuning the excitation wavelength should allow for the design of plasmon waveguides tailored for particular applications. From a practical standpoint, gap widths on the order of 20 nm are possible using top-down fabrication techniques such as electron beam lithography or ion-beam milling.

Results obtained for the influence of substrates and dielectric hosts will be presented elsewhere, together with an extended study of the dependency of the energy attenuation length on particle and gap size.

Conclusion

In summary, the ability to confine electromagnetic energy to mode sizes well below the diffraction limit has been elucidated via a discussion of gap

modes in metal/dielectric/metal heterostructures. This concept can be applied in a context of waveguiding using arrays of closely spaced metallic nanoparticles. The excitation of resonant gaps instead of particles increases the amount of tunability of plasmonic waveguides and compares favourably in terms of energy attenuation while at the same time providing highly localized and accessible fields, promising useful applications for a subwavelength photonic sensing and guiding infrastructure.

Clearly, the examples presented in this paper can serve only as a starting point for detailed investigations into waveguide geometries with themost favorable confinement/loss trade-off. A more detailed investigation of this issue will be necessary in order to assess the potential of plasmonics to be of importance for emerging technologies of highly minituarized optical circuits or on-chip data communication.

Acknowledgements

This work was sponsored by the Engineering and Physical Sciences Research Council EPSRC.

References

[1] S. A. Maier, M. L. Brongersma, P. G. Kik, S. Meltzer, A. A. G. Requicha, and H. A. Atwater, Adv. Mat. **13**, 1501 (2001).
[2] A. Sommerfeld, Ann. Phys. und Chemie 67, 233 (1899).
[3] J. Zenneck, Ann. d. Phys. 23, 846 (1907).
[4] R. W. Wood, Proc. Phys. Soc. London 18, 269 (1902).
[5] U. Fano, J. Opt. Soc. Am. 31, 213 (1941).
[6] R. H. Ritchie, Phys. Rev. 106, 874 (1957).
[7] R. H. Ritchie, E. T. Arakawa, J. J. Cowan, and R. N. Hamm, Phys. Rev. Lett. 21, 1530 (1968).
[8] E. Kretschmann and H. Raether, Z. Naturforschung 23A, 2135 (1968).
[9] G. Mie, Ann. Phys. 25, 377 (1908).
[10] W. L. Barnes, A. Dereux, and T. Ebbesen, Nature 424, 824 (2002).
[11] S. A. Maier and H. A. Atwater, J. Appl. Phys. 98, 011101 (2005).
[12] S. A. Maier, Opt. Express 14, 1957 (2006).
[13] B. Prade, J. Y. Vinet, and A. Mysyrowicz, Phys. Rev. B44, 13556 (1991).
[14] P. B. Johnson and R. W. Christy, Phys. Rev. B 6, 4370 (1972).
[15] J. Takahara, S. Yamagishi, H. Taki, A. Morimoto, and T. Kobayashi, 22, 475 (1997).
[16] L. C. Andreani, G. Panzarini, and J.-M. G´erard, Phys. Rev. B 60, 13276 (1999).
[17] S. A. Maier, P. G. Kik, H. A. Atwater, S. Meltzer, E. Harel, B. E. Koel, and A. A. G. Requicha, Nat. Mat. 2, 229 (2003).
[18] M. Quinten, A. Leitner, J. R. Krenn, and F. R. Aussenegg, Opt. Lett. 23, 1331 (1998).
[19] M. L. Brongersma, J. W. Hartman, and H. A. Atwater, Phys. Rev. B 62, R16356 (2000).
[20] S. Y. Park and D. Stroud, Phys. Rev. B 69, 125418

MONA - Merging Optics and Nanotechnologies: The Nanophotonics Technology Roadmap

Laurent Fulbert (1), Roel Baets (2), André Scavennec (3), Ulrich Fotheringham (4), Rainer Beccard (5) Krassimir Krastev (6), Dirk Holtsmanspötter (7), Eric Mounier (8), Bertrand Noharet (9), Thomas Pearsall (10) and Suvi Haukka (11)

1) CEA-LETI Minatec France, Laurent.fulbert@cea.fr 2) IMEC, Belgium, Roel.Baets@intec.UGent.be 3) Alcatel-Thales 3-5 Lab, France, andre.scavennec@alcatel.fr 4) Schott, Germany ulrich.fotheringham@schott.com 5)Aixtron, Germany R.Beccard@aixtron.com 6) Optics Valley, France k.krastev@opticsvalley.org 7) VDI-TZ, Germany holtmannspoetter@vdi.de 8) YOLE Développement, France mounier@yole.fr 9) Acreo, Sweden Bertrand.Noharet@acreo.se 10) EPIC France pearsall@epic-assoc.com 11) ASM, Netherlands suvi.haukka@asm.com

Abstract: *The MONA project has three principal objectives:*

- *Create a common site for the exchange of information concerning research, networks of excellence, and integrated projects in photonics and nanotechnologies.*
- *Promote the timely exchange of scientific results, market development, and technology needs through MONA-developed workshops.*
- *Develop a European roadmap for photonics and nanotechnologies.*

MONA, both through its expected outcomes and the collective process implemented, will help the future European research be more competitive through the development of the Nanophotonics Technology Roadmap. The MONA Roadmap will provide an essential decision-supporting instrument for the Community at a broad and international level. The results will directly feed into the European Technology Platform Photonics21.

Introduction

The goal of the MONA project (Merging Optics and Nanotechnologies) is to leverage synergies in photonics and nanotechnologies, seeking to increase the impact and efficiency of investment on European research.

There are three principal objectives for the MONA project:

- Create a common site for the exchange of information concerning research, networks of excellence, and integrated projects in photonics and nanotechnologies.
- Promote the timely exchange of scientific results, market development, and technology needs through MONA-developed workshops.
- Develop a European roadmap for photonics and nanotechnologies.

MONA will foster collaborations between photonics and nanotechnologies stakeholders and will help preparing future research activities. A major outcome of MONA will be a consolidated scenario (time horizon 5-10 years), setting out development and technology road maps.

The MONA project contributes directly to the development of synergies between photonics/nanophotonics and nanomaterials/nanotechnologies. The challenge of mastering nano-electronics and nano-photonics science and technologies at an industrial scale (i.e. aiming at low cost mass production capability) is of utmost strategic importance for the competitiveness of the European industry in a global context. Through the cooperative work between equipment manufacturers, nanotechnologies and photonics experts, MONA will help to identify and address the most critical manufacturing issues. This will ensure the building of a strategic comprehensive approach for the key technologies in order to profit from this highly important area for the European Union

Development of a roadmap: starting point

During the first part of the project, a frame of reference summarizing the state of the art in the fields of nanostructuring technologies and nanophotonics has been established. Each of these two fields have been analysed with respect to:

- Materials and technologies
- Equipment and processes.

The main result is a report that analyses and assesses the various technologies with respect to their potential for volume production. In particular, the compatibility with CMOS processes will be investigated.

The main topics addressed in the report are:

- Current Production Technologies in Photonics
- Nanostructuring Technologies
  - Top-Down Technologies
  - Bottom-Up Technologies
- Photonics
  - New Approaches in Nanophotonics
  - Nanotechnology in Photonic Devices
- Equipment
- Projects and Networks of Relevance

The MONA consortium adopted the following definition for Nanophotonics: Optics and Nanotechnologies merge, where lateral structures, layers, molecular units, inner boundary layers and surfaces with

critical dimensions or production tolerances that extend from about 100 nanometers down to atomic orders of magnitude are produced, studied and utilized for the generation, transmission, manipulation, detection, and utilization of light.
In addition to this definition, the MONA consortium decided to study in the roadmap only 2D and 3D structures. 1D structures such as Quantum Wells for instance are already well known and used and have not been investigated in depth.

Development of a roadmap: methodology

For the Mona roadmap, we have considered both **a market-pull perspective and a technology-push approach** (see *Fig 1*)**:** In one hand, we have considered the applications with potential market volume. Then we have identified what photonic products will be used and where nanotechnologies can be used to improve performances, add new functionalities and/or reduce costs. However, for technologies such as nanophotonics which can be considered as "disruptive" technologies (in the sense that it is still difficult to imagine markets for functions and materials which have not yet an industrial reality), one can miss out interesting technologies. Then we have considered a technological approach as well.

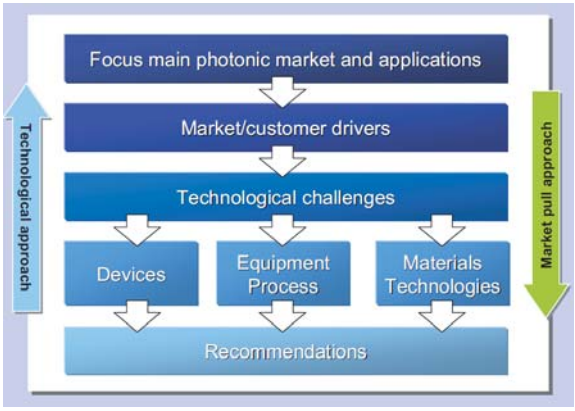


Fig 1*: the Mona methodology*

Based on the first MONA workshop, on the work done the frame of reference, as well as on different market studies, the consortium members has made a selection of the most promising applications area of Nanophotonics devices. These applications areas are:

- Optical Interconnects
- Datacoms/Telecoms
- Lighting
- Data storage
- Imaging
- Sensors
- Displays
- Photovoltaics
- Instrumentation/metrology

As already mentioned, we have also followed a bottom-up methodological approach that leads us to identify the following families of nanostructures/nanomaterials:

- Semiconductor quantum dots&wires in silicon including colloidal nanostructures
- Semiconductor quantum dots&wires in III-V including colloidal nanostructures
- Semiconductor quantum dots&wires in II-VI including colloidal nanostructures
- Plasmonics/metallic nanostructures including colloidal nanostructures (metal)
- Photonic Crystals/High index contrast nanostructures in silicon
- Photonic Crystals/High index contrast nanostructures in III-V
- Photonic Crystals/High index contrast nanostructures in other materials
- Organic nanostructures
- Carbon Nanotubes (CNT)
- Integration of nanophotonic materials/structures with electronic ICs/Silicon Photonics
- Nanoparticles in glass or polymer
- Left-handed metamaterials

A separate roadmap has then been established for each class of material that could be used for each application identified. A final set of more than 50 roadmaps have been created. Each of these roadmaps drafts describes the nano technology, the application, the manufacturing process and required processes/equipments, as well as the timeline of technological development.
As far as equipment are concerned, the major equipment and processes classes have been identified and some issues have been raised. For example, high resolution / high throughput lithography is still a challenge, or metrology for in-situ process control is identified as one of the major key issues for transfer to industrial scale
A final consolidation and synthesis will be made in 2007 to obtain a comprehensive document that could be used by the whole photonics and nanophotonics community.

Development of a roadmap: assessment and feedback

For successful roadmapping, the process is as important as the technical quality. That means that the two following points are essential:

- Real involvement of the right players in set-up and propagation of the roadmap
- Endorsement of its strategic relevance by the wider photonics community including industry

The MONA consortium has organised three different workshops to implement the roadmapping process. As an example, the second workshop gathered more than 100 experts from 13 European countries, including more than 40% of industrial participants. During

this event, the draft versions of the roadmaps have been discussed and improved.
The third workshop has been organized during one of the major international conference in photonics in the US. This workshop has included comparison of roadmapping activities in Japan, Korea, Taiwan, US and Europe.
A continuous updating of the documents is expected during the first half of 2007. Feedback from the wider nanophotonics community as well as industrial players will be encouraged.

Dissemination and intention for use
Dissemination of the results and communication with other nanotechnologies and photonics activities are key objectives of MONA. The following actions have already been made:

- Launch of the MONA web site http://www.ist-mona.org.
- Press release on the launch of MONA disseminated to general public and branch press in Europe and US.
- Organization of a symposium collocated with the second workshop with more than 100 particpants
- Publication and dissemination of the electronics newsletter.
- Edition and dissemination of a CD-ROM on the Frame of Reference. This CD-ROM was distributed at conference exhibitions. The report could also be downloaded on the MONA website.
- Exhibition in conferences
- Exchange mission to several Asian countries with extensive two-way exchanges of information on nanotechnologies and photonics activities in European and in Asia. CD-ROMs have been edited and disseminated afterwards.
- Links have been established with other European projects related to nanophotonics/nanotechnologies. It has been decided to line up the activities and make a combined effort in order not to duplicate efforts and come up with the best possible outcome.

It is intended to broadly disseminate the results of MONA to the industrial, R&D and education communities through conferences and the media.
The project MONA is strongly contributing to the European Technology Platform Photonics21. One of the objectives of the platform is to pave the way for Europe's scientific, technological and economic leadership in Photonics and, in the long run, to make Europe the number one knowledge-based economic area in the world.
The MONA consortium will participate to the roadmapping activities of the platform and thus is expected to shape nanophotonics in European and national research programmes.

Conclusion
MONA will produce tangible results for the benefit of the European Community. The main end results will be roadmaps of technologies / processes / applications / research.
The real involvement of the right players in set-up and propagation of the roadmap, as well as the endorsement of its strategic relevance by the wider photonics community are essential. The outcomes of MONA should be used to shape the future national and European research programmes in the field of nanophotonics.

Acknowledgments
Financial support by EC under project 017255-MONA is acknowledged

Gold Grating Coupler for Silicon-on-Insulator Waveguides with 34 % Coupling Efficiency

Stijn Scheerlinck, Frederik Van Laere, Jonathan Schrauwen, Dirk Taillaert, Dries Van Thourhout and Roel Baets
Photonics Research Group, IMEC-Ghent University, Belgium, stijn.scheerlinck@intec.ugent.be

Abstract: *Gold gratings are proposed for efficient coupling between optical fibers and silicon-on-insulator (SOI) waveguides. They are compact and very easy to fabricate using a processing scheme based on lift-off. In this paper, a gold grating coupler is demonstrated with 34 % coupling efficiency at a wavelength of 1.55 μm. The measurement results are in good agreement with simulation results.*

Introduction

Silicon-on-Insulator (SOI) is emerging as a very interesting platform for integrated nanophotonics due to the high refractive index contrast between the silicon core and the oxide cladding. One of the drawbacks of the high index contrast is the large mismatch in mode size and shape between the fundamental mode of SOI waveguides and the mode of optical fibers. This makes efficient coupling from fiber to waveguide difficult to achieve. Grating couplers defined by etching a grating a few tens of nanometer into the high index silicon waveguide layer offer a very elegant solution to this problem [1]. Their compactness (10 μm x 10 μm), efficiency, large optical bandwidth and very good alignement tolerances make them suitable for many applications such as rapid testing of photonic circuits on wafer-scale and packaging of photonic circuit chips with optical in- and outputs.

With conventional SOI grating couplers, a coupling efficiency of 33 % [2] from fiber to waveguide has been demonstrated and several approaches are being investigated to improve this value. In particular, introducing a bottom gold mirror has been proven to improve the coupling efficieny up to 69 % [3] and apodizing the grating in combination with local deposition of a poly-silicon overlay is expected to improve the coupling efficiency even more [4]. However, all of these approaches require a number of extra processing steps and make fabrication rather challenging. In contrast, the metal grating couplers proposed here are very easy to fabricate and demonstrate high efficiencies comparable to the coupling efficiencies of current state-of-the art SOI grating coupler devices.

Device layout and operation principle

A scheme of the metal grating coupler for SOI waveguides is depicted in Fig. 1. It consists of a metal grating on top of the silicon waveguide layer of an SOI layer structure. The optical fiber is slightly tilted with respect to the vertical axis in order to prevent a large second order reflection.

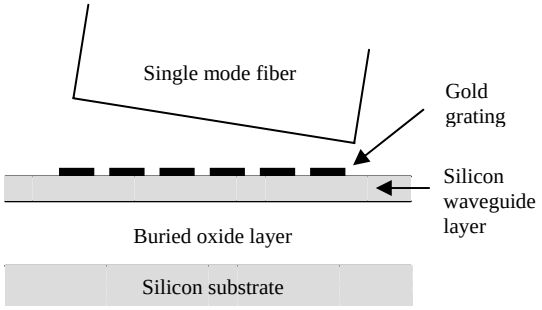


Fig. 1: Device layout and principle: gold grating on top of an SOI waveguide. Light from the single mode fiber incident on the grating is diffracted by the grating into the silicon waveguide layer.

At a wavelength of 1.55 μm, there is a very high refractive index contrast between the metal teeth and their surroundings. In the case of gold, the refractive index contrast between gold and silicon equals $\Delta n = n_{Si}-n_{Au} = 2.9 + 10.8j$. Thus, light incident on the grating is strongly scattered. This property can be exploited for the design of efficient, broadband and compact grating couplers. Moreover, due to the very high index contrast, only a very thin layer of gold suffices to achieve high coupling efficiency, as will be shown in the next section.

Simulation Results

For the design of gold grating couplers, we use CAMFR, a two-dimensional fully vectorial simulation-tool based on eigenmode expansion and mode propagation with perfectly matched layer (PML) boundary conditions [5]. We consider 1-D gratings in 2-D simulations and concentrate on TE polarization (electric field parallel to the grating lines).

Simulation is performed for an SOI layer structure with 220 nm top silicon layer and 2 μm buried oxide layer thickness. The refractive index data for gold is taken from [6]. An index matching glue is present between the optical fiber and the grating coupler so that reflections at the fiber facet are avoided. The waveguide mode is incident from the left and is normalized to the input power. The top and bottom boundaries of the simulation area have PML to avoid parasitic reflections.

In a first step reflection and transmission of the entire structure is calculated. Afterwards, the diffracted field is calculated from which the power flux and overlap with a fiber mode can be calculated. The fraction of the input power that couples to the fiber mode is defined as the coupling efficiency. To this end, the fiber mode is modelled as a Gaussian distri-

bution with a full width at half maximum (FWHM) of 5.2 μm.

Fig. 2 plots the coupling efficiency as a function of wavelength for a gold grating with period 610 nm, filling factor 50 % and thickness of the metal layer 20 nm. The coupling efficiency is 40 % and the 1dB bandwidth exceeds 40 nm. A field plot illustrates the strong diffraction by the grating in the direction of the fiber. This is shown in Fig. 3. We note that the coupling efficiency can be further improved by optimizing the grating parameters and the parameters of the SOI layer structure. However, the above mentioned values were taken as they correspond to the geometric parameters of the prototype device that was fabricated. Fabrication is discussed in the next section.

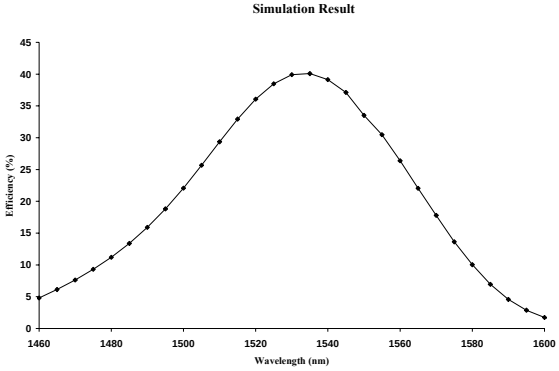


Fig. 2: Simulation of coupling efficiency as a function of wavelength of a gold grating coupler with the following grating parameters: period = 610 nm, filling factor = 50 %, height = 20 nm.

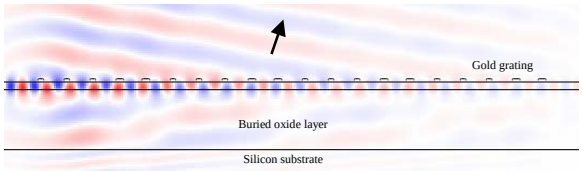


Fig. 3: Field plot of a gold grating coupler on top of an SOI waveguide. The mode guided by the top silicon layer from is incident from the left and is diffracted in the direction of the fiber.

Fabrication

Gold grating couplers are very easy to fabricate. We fabricated a prototype as follows. First, PMMA was spun on an SOI sample containing 10 μm wide and 7 mm long SOI waveguides with standard SOI grating couplers at both ends of the waveguides. The waveguides and couplers were fabricated using Deep UV-lithography (DUV) and inductively coupled plasma etching (ICP). With the electron beam of a Nova 600 Dualbeam (FEI) system, a 610 nm period grating was defined in the PMMA on top of the SOI waveguides. Then, gold was evaporated followed by a lift-off in acetone. A SEM-picture of a fabricated gold grating coupler device is depicted in Fig. 4. The final device is 12 μm x 10 μm.

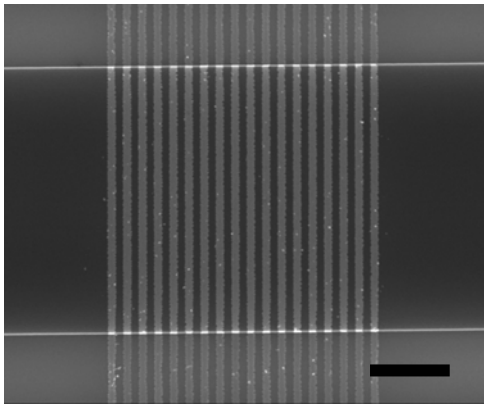


Fig. 4: Top view of the fabricated gold grating coupler on top of an SOI waveguide. Reference bar length = 3 micron.

Measurement results

The fabricated gold grating coupler was optically characterized using the following experimental set-up. An input single mode fiber connected to a tuneable laser source was positioned over the gold grating coupler. An output single mode fiber connected to a photodetector was positioned over the SOI grating coupler. Polarization wheels were used to control polarization. After an active alignation procedure whereby the fiber positions were optimized in order to obtain maximal transmission at a wavelength of 1.55 μm, the tuneable laser source was swept from 1.5 μm to 1.6 μm and the photodetector data were recorded. The same procedure was followed for a reference measurement in which the SOI grating couplers on both ends of a waveguide were used both for incoupling and outcoupling.

From these measurements, the fiber-to-waveguide coupling efficiency of the gold grating coupler can be calculated. The result is plotted in Fig. 5. To this end, a fiber-to-waveguide coupling efficiency of 34 % has been measured at a wavelength of 1.55 μm and a 1dB bandwidth of 35 nm. This result is in good agreement with the simulation results plotted in Fig. 2.

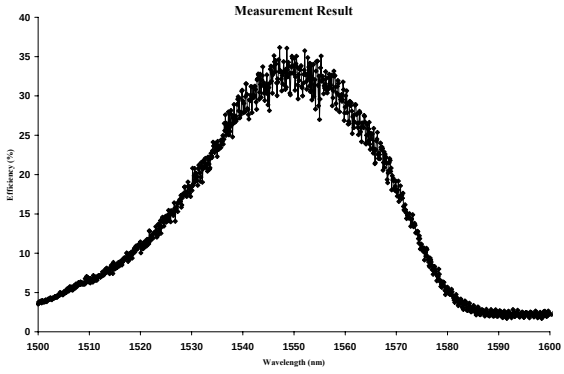


Fig. 5: Experimentally obtained coupling efficiency of a gold grating coupler on top of an SOI waveguide as a function of wavelength.

Conclusion

In this paper, a gold grating coupler was introduced for efficient and broadband coupling between SOI waveguides and optical fibers. A compact gold grating coupler was designed by simulation using eigenmode-expansion and fabricated using an easy processing scheme based on e-beam writing and lift-off. The fabricated device demonstrated 34 % coupling efficiency at a central wavelength of 1.55 μm. The measurement results are in good agreement with the simulation results for the fabricated structure.

Acknowledgments

This work was supported by Ghent University, the Belgian IAP-PHOTON Network and the European Union through the IST-ePIXnet Network of Excellence. S. Scheerlinck and F. Van Laere thank the Institute for the Promotion of Innovation through Science and Technology in Flanders (IWT-Vlaanderen) for a specialization grant. D. Taillaert thanks the Institute for the Promotion of Innovation through Science and Technology in Flanders (IWT-Vlaanderen) for a post-doctoral grant.

References

1 D. Taillaert et al., Jap. J. Appl. Phys., Vol. 45, p. 6071-6077, 2006.
2 D. Taillaert et al., Proc. of IEEE/LEOS Workshop on Fibers and Optical Passive Components, p 115-120, 2005.
3 F. Van Laere et al., J. Lightwave Technology (accepted, to be published).
4 G. Roelkens et al., Optics Express, Vol. 14 (24), p. 11622-11630, 2006.
5 P. Bienstman and R. Baets, Opt. Quantum Electron., Vol. 49, p. 349-354, 2001.
6 P.B. Johnson and R.W. Christy, Phys. Rev. B, Vol. 6 (12), p. 4370-4379, 1972.

Metal nanowires - a new class of plasmonic waveguides

Tiberiu Rosenzveig (1), Kristjan Leosson (2) and Alexandra Boltasseva (3)
1) Science Institute, University of Iceland, IS-107 Reykjavik, Iceland, jptibirosen@raunvis.hi.is
2) Science Institute, University of Iceland, IS-107 Reykjavik, Iceland, k.leosson@raunvis.hi.is
3) COM•DTU, Technical University of Denmark, Building 345v, DK-2800 Kgs. Lyngby, aeb@com.dtu.dk

Abstract: *We present results of transmission measurements and mode analysis for metal nanowire waveguides with close-to-symmetric cross-sections, supporting propagation of long-range surface plasmon polariton waves. In contrast to conventional plasmonic waveguides, the waveguide structures presented here are polarization-insensitive due to the cross-sectional symmetry. At a free-space wavelength of 1064 nm, we measure a propagation loss of 0.43 dB/mm for two orthogonal polarization states. Transmission measurements at high input powers suggest that only a small part of this propagation loss can be attributed to ohmic loss in the metal.*

Introduction

The practical use of surface plasmon polariton (SPP) waveguides in integrated optical devices is hampered mainly by two factors, large propagation loss and strong polarization dependence. Two approaches have been followed in order to address the former issue; first, reducing the size of functional components to minimize propagation lengths and, consequently, the total insertion loss [1] and, second, a lowering of the propagation loss by reduction of the field-metal overlap, e.g. through the use of long-range surface plasmon polariton (LRSPP) thin-stripe waveguides as initially suggested by Berini [2]. Single-mode LRSPP waveguides with mode sizes close to that of a standard telecom fiber (e.g. SMF28) have been reported in the literature and novel integrated optical devices have been demonstrated [3-7].

The issue of polarization dependence, however, has remained largely unaddressed. A planar metal-dielectric interface only supports a TM-polarized wave having the main electric field component perpendicular to the interface, which seriously limits the applicability of devices based on conventional plasmonic waveguides, e.g. in optical networks. To circumvent this problem, a waveguide structure with a square cross-section consisting of a metallic nanowire embedded in a dielectric was proposed by Berini [8]. Transmission through such waveguides was recently demonstrated at 1550 nm wavelength in Ref. [9], where it was also shown that the effective index of the waveguide mode could be decreased by resistive heating of the waveguide core due to the negative *dn/dT* of the cladding polymer, enabling the design of a simple LRSPP-based variable optical attenuator. In the present paper, we report transmission measurements on nanowires designed to work at shorter wavelengths. We test also the nonlinear transmission of the metallic waveguides, related to heating caused by absorption of light in the core.

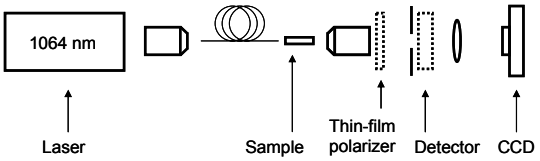


Fig. 1: Experimental set-up for waveguide transmission measurements and mode analysis.

Sample preparation and experimental set-up

Nanowire waveguides were fabricated in the following fashion: A 4" silicon wafer was coated with a 10-µm layer of a transparent polymer material (benzocyclobutane/BCB). The BCB was spin-coated with a 120-nm layer of electron-beam resist (PMMA). A series of 70-mm long stripes with nominal widths ranging from 92 nm to 108 nm was exposed in the resist using an electron beam writer (JEOL JBX 9300FS). 100-nm thick gold nanowires were fabricated by electron-beam deposition and lift-off and subsequently covered with a second layer of BCB. The wafer was diced into individual samples with waveguide lengths ranging from 2 mm to 20 mm.

The experimental set-up is illustrated in Fig. 1. Insertion loss measurements were made using 1064 nm light from a diode-pumped Nd:YAG laser (Coherent Inc.). The polarized laser light was coupled into an HB1000 polarization-maintaining optical fiber (Fibercore Ltd.). The light was transmitted to the waveguide by end-fire coupling. Fiber rotation or a waveplate in the beam path were used to generate different polarization states for the input light. The light at the output facet was picked up by a microscope objective, spatially filtered through a pinhole placed in the intermediate image plane and measured using calibrated Ge and Si photodetectors. For mode analysis, the output facet was imaged onto a CCD camera (Thorlabs Inc.) using a 10× microscope objective. A thin-film polarizer was used to distinguish between different polarizations at the output facet. High-resolution mode images were obtained by using a 100× infra-red microscope objective (Olympus MPlan IR) for imaging directly onto the CCD camera, omitting the intermediate lens and pinhole. The spatial resolution of the imaging system in this case is given by $0.6\ \lambda$ / N.A. ~ 0.7 µm. For high-power transmission measurements, we used the intensity of scattered light from the input facet as a measure of the input power, in order to avoid errors due to variations in laser-to-fiber coupling efficiency.

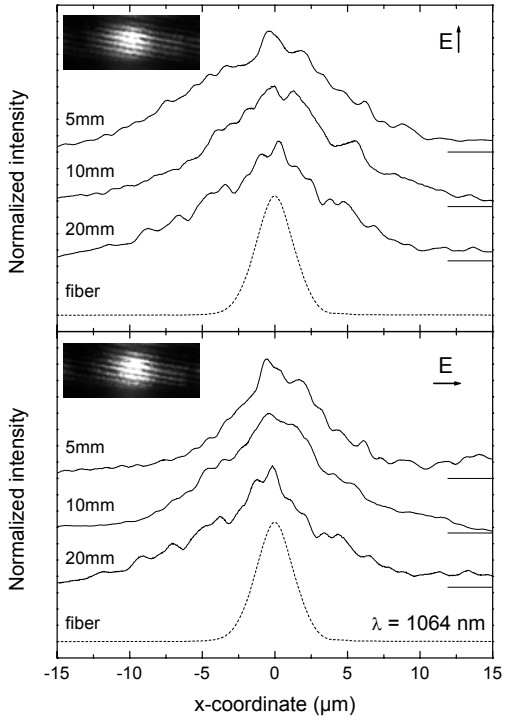


Fig. 2: Mode profiles recorded of at the output facets of nanowire waveguides samples of different lengths for orthogonal input polarizations. Irregularities in the intensity plots are due to dicing marks on the facet, as seen in the inset figures. The fiber mode is shown for reference.

Results

Images of waveguide modes at the output facet obtained using a 100× objective for horizontal and vertical input polarization are shown in Fig. 2 and the corresponding mode profiles along the x-direction (parallel to the cladding layers) are plotted for different sample lengths. The mode field diameter is approximately 20 μm for both polarizations and we do not observe significant changes in the mode shape with increasing sample length. Similar mode profiles were observed for 150 × 150 nm wires excited at 1550 nm wavelength [9].

Cutback measurements were performed using 4 sample lengths as shown in Fig. 3. A set of 15 waveguides was measured on each sample, consisting of 5 groups of 3 nominally identical nanowires. The width of the wires in the exposure file varied from 92 nm to 108 nm in steps of 4 nm. All waveguides transmitted both polarizations and no systematic difference in insertion loss for different waveguide widths was observed. Each data point in Fig. 3 therefore represents an average over several waveguide widths. A propagation loss of 0.43 dB/mm is observed for both polarizations. A 1.5-dB coupling loss from fiber to waveguide is measured. It should be emphasized, however, that this value is obtained by collecting light from the whole output facet and fiber-to-fiber loss measurements have yet to be conducted.

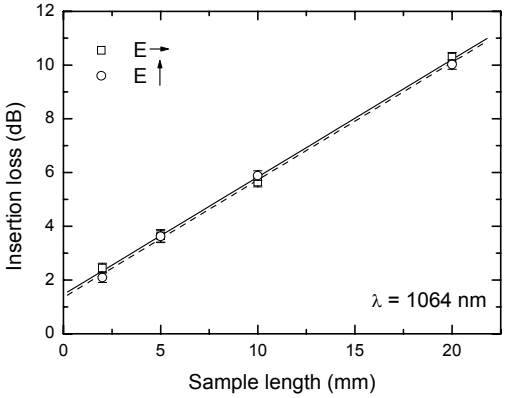


Fig. 3: Cutback measurements on nanowire waveguides for different input polarizations. The solid and dashed lines show the least-squares fit to the data points for horizontally and vertically polarized input fields, respectively, giving a propagation loss of 0.43 dB/mm for both polarizations.

It has previously been established that absorption in LRSPP waveguides can lead to a measurable heating of the waveguide core [5]. Furthermore, a lowering of the effective index of LRSPP waveguides induced by a temperature increase in the polymer cladding obtained by driving electrical current through the waveguide core has been used to efficiently reduce waveguide transmission [4,9]. It is clear, therefore, that sufficiently high input power will result in reduced waveguide transmission due to absorptive heating of the waveguide core. In order to investigate this effect we measured transmission through a 5-mm long waveguide for input powers up to 325 mW, as shown in Fig. 4. At input powers above 200 mW, the transmission starts to deviate significantly from linear behavior, reaching a 0.5 dB (10%) extinction at 350 mW input power. We did not observe a significant change in the mode profile at the output of the waveguide when the input power was increased, consistent with the fact that the absorbed power decreases along the length of the waveguide and the weakening of the confinement should therefore be most pronounced close to the input end of the waveguide.

Discussion

Although the propagation loss in LRSPP waveguides is low compared to other SPP configurations, it is still much higher than in typical dielectric waveguides with the same degree of field confinement. The propagation loss can be partly accounted for by absorption in the metal film and in comparatively thick (>15 nm) stripe waveguides transmitting light at 1550 nm, this contribution has been shown to be dominating [7]. For thinner (<15 nm) stripe waveguides [7] and, in particular, for nanowire waveguides [9], the loss measured at 1550 nm is larger than expected. It is plausible to assume that the propagation loss in this case is limited by scattering

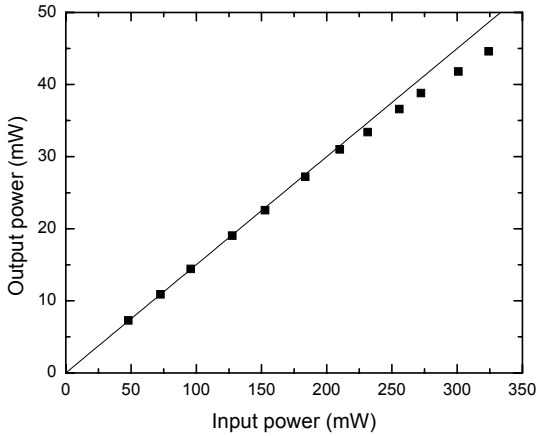


Fig. 4: Non-linear transmission through a 5-mm long nanowire waveguide. At high input powers, absorption in the waveguide core results in a heating of the waveguide which lowers its effective index and reduces the transmitted power.

due to structural imperfections in the waveguide core, absorption and scattering in the cladding layers, and coupling to the substrate and the top surface due to the finite thickness of the cladding layers. For shorter wavelengths, contributions from scattering as well as metal absorption should be more pronounced. Conversely, propagation loss in BCB is lower at 1064 nm wavelength (0.05 dB/mm) than at 1550 nm (0.2 dB/mm) [11].

We can make a rough comparison between the results plotted in Fig. 4 and data for extinction modulators based on nanowire waveguides operating at 1550 nm wavelength, reported in Ref. [9]. The confinement of the LRSPP mode is similar in the two cases due to the different wire geometries. In the case of the extinction modulator, 1.2 mW of electrical power passed through 1 mm of the waveguide is sufficient to reduce transmitted power by 10%. Taking into account 1.5 dB of coupling loss, we need only 0.02 dB/mm of propagation loss due to metal absorption to account for the observed decrease in transmission in Fig. 4. This value is similar to the theoretically predicted propagation loss for 150 × 150 nm gold nanowires embedded in SiO2 [8].

In spite of the differences in geometry and wavelength between the two cases, the above comparison strongly suggests that significantly lower propagation losses can be obtained by improving the structural quality of the metallic waveguides. Recent measurements on short (10's of μm) silver nanowires showed a dramatic difference in the optical quality of single-crystalline and polycrystalline wires in the wavelength range 600–800 nm [12]. Fabricating centimeter-long single-crystal metallic nanowires with a symmetric cross section remains a technical challenge but advances in this field will certainly have a strong impact on applied plasmonics.

Conclusions

We have reported measurements on a new class of plasmonic waveguides based on metal nanowires embedded in a transparent polymer. We have demonstrated that waveguides with symmetric cross-sections are polarization insensitive which makes them particularly interesting for practical applications. The observed propagation loss is among the lowest reported for any SPP-based waveguide and high-power transmission measurements indicate that this can be further reduced if the structural quality of the waveguides can be improved.

Acknowledgments

TR and KL acknowledge the support of the Eimskip Research Fund at the University of Iceland and Icelandic Equipment Fund (grant no. 061051).

The authors wish to thank Peixiong Shi at Danchip for e-beam lithography and Michel Hansen at Lumiscence A/S for assistance with sample processing.

References

1 W.L. Barnes, A. Dereux, and T.W. Ebbesen, Nature **424**, p. 824, 2003.

2 P. Berini, Opt. Lett. **24**, p. 1011, 1999.

3. R. Charbonneau, et al., Opt. Lett. **25**, p. 844, 2000.

4 T. Nikolajsen, K. Leosson, and S. I. Bozhevolnyi, Opt. Commun. **244**, p. 455, 2005.

5 S.I. Bozhevolnyi, T. Nikolajsen, and K. Leosson, Opt. Commun. **255**, p. 51, 2005.

6 R. Charbonneau, et al., Opt. Express **13**, p. 977, 2005.

7 A. Boltasseva, et al., IEEE J. Lightwave Technol. **23**, p. 413, 2005.

8 P. Berini, US patent number 6,741,782.

9 K. Leosson, et al., Opt. Express **14**, p. 314, 2006.

10 T. Nikolajsen, et al., Appl. Phys. Lett. **82**, p. 668, 2003.

11 A. Boltasseva and S.I. Bozhevolnyi, JSTQE, *in press,* 2006.

12 Ditlbacher et al., Phys. Rev. Lett. **95**, 257403, 2005

Compact Vertically-coupled Microring Laser Array Dual-Wavelength Source for Terahertz Mode Beating

Chyng Wen Tee(1), Kevin Williams(1, 2), Richard Penty (1), Ian White (1),
Michael Hamacher (3), Ute Troppenz (3), Helmut Heidrich (3),
Viorel Dragos (4), Marin Alexe (5),
Dimtris Alexandropoulos (6), Spiros Mikroulis (6), Hercules Simos (6), Dimitris Syvridis (6),
Mihai Kusko(7), Dana Cristea (7).

1) Cambridge University Engineering Department, 9 JJ Thompson Avenue, Cambridge, CB3 0FA, U.K.
2) Eindhoven University of Technology, The Netherlands.
3) Fraunhofer Institute for Telecommunications, Heinrich-Hertz-Institute.
4) EV Group, E. Thallner GmbH, A-4780 Scharding, Austria.
5) Max Planck Institute for Microstructurephysics, Germany.
6) University of Athens, Faculty of Science, Department of Informatics, Greece.
7) National Institue for R&D in Microtechnologies, Laboratory of Microphotonics, Romania.
(Email: cwt23@cam.ac.uk)

Abstract: *Continuous-wave operation of a fully tunable compact microring twin-laser array is demonstrated for the first time. The two active microrings, with radii of 70μm and 74μm, are vertically-coupled to a single passive waveguide. Tuning of the current facilitates a wavelength separation from 4.9nm to 6.3nm.*

Introduction

Microring lasers based on III-V semiconductor material are an attractive candidate as future ultra-compact light sources. They are expected to play a crucial role in the future large scale monolithic integration of photonic integrated circuits as they do not require cleaving to form edge mirrors.

However, while significant advances have been made using sophisticated passive microring topologies for dispersion compensation and filtering [1], the integration of multiple active components has been frustrated by the need for an integration technology which allows the close coupling of active devices with low loss bus waveguides.

One promising method for allowing effective integration has been the use of vertical-coupling, and several III-V microring devices involving active-passive integration have been studied for potential applications in telecommunications [1]. By implementing the active microring resonator and the passive bus waveguide on a different epilayer plane, one can achieve a greater flexibility in device design (allowing separate optimisation of ring and bus guides) and minimise the area of pumping in the device by using the minimum areas of active region waveguide. Closely spaced active and passive waveguides with controlled coupled coefficients may be realised by exploiting wafer-bonding technology [2]. A part-processed wafer may be inverted and wafer bonded to a transfer wafer, which provides mechanical support while the second face is etched back and processed. This enables the intergation of passive bus waveguides with active photonic components through 3-D interconnection. This approach has allowed active, vertically-coupled microdisk devices for switching and routing [3], demultiplexing [4] and microresonator arrays [5]. Vertically coupled active microrings have also been developed, where pulse-operated laser oscillation with a 13mA threshold current had recently been reported [6].

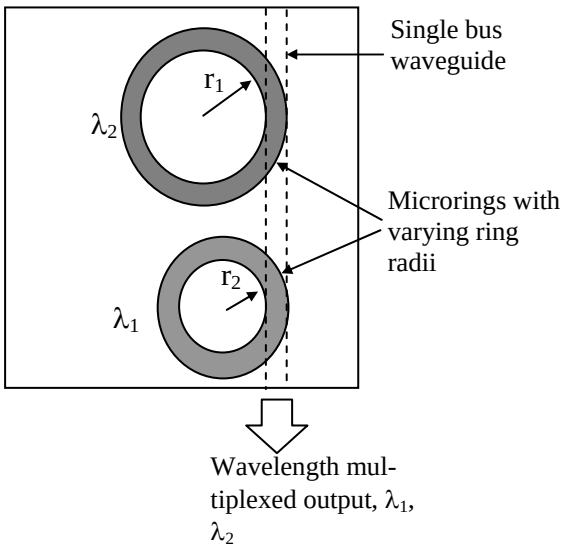


Fig. 1: Schematic of vertically-coupled microring laser array architecture.

In this paper, we demonstrate, for the first time to our knowledge, a CW-operated vertically-coupled microring dual-laser array. The twin lasers, as shown in the schematic in figure 1 above, are set to generate different wavelengths, this proving the feasibility of a compact and robust dual-wavelength light source for applications for example in terahertz generation.

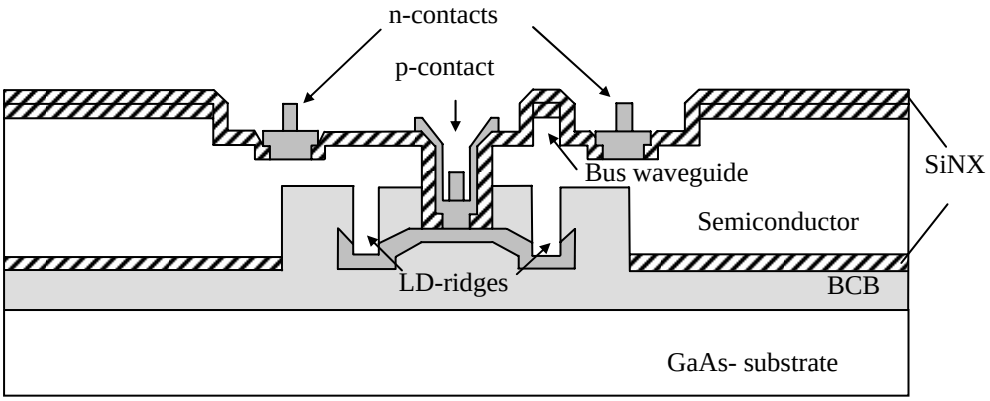


Fig. 2: Epitaxial layer structure of the microring laser.

Design

Two microring laser cavities with an offset resonance, integrated onto a single bus waveguide, can lase independently while coupling their output to the same passive bus waveguides. The resonance condition in a microring cavity is given by:

$$m\lambda_{res} = 2\pi n_{eff} R, \qquad (1)$$

where m is an integer indicating the longitudinal mode number, λ_{res} is the resonance wavelength, n_{eff} is the effective index of the optical mode and R is the ring radius. By selecting two microrings with different ring radii, an offset can be introduced to the resonance wavelength of the two microring lasers. The effective index in a laser cavity is a function of the injection current, temperature distribution and cavity geometry. The effective indices in the two microring lasers exhibit different sensitivity against injection current, an effect which can be exploited in order to tune the separation in the resonance wavelength by simply varying the injection current to the two laser cavities.

Device Structure

Previous studies of vertically coupled microring lasers using a wafer-bonded transfer substrate [7] have defined the bus waveguide prior to inverting the wafer. The microring resonators are therefore processed on the bonded wafers. However this approach may become susceptible to tight alignment tolerances resulting from run-out in the mask alignment features or warping in the composite wafer. This becomes increasingly important for active laser structres where multiple photolithographic steps are performed. To avoid this possibility, the laser structures are defined on the first face, prior to wafer bonding. The complete epitaxial structure is grown, the laser waveguides are defined and the p-type metal is deposited prior to wafer bonding to the transfer wafer. The substrate is removed by etching prior to the formation of bus waveguides and the opening of via holes to the p-metal at the transfer wafer. This results in a buried active microring waveguide structure, with the additional advantage that the laser is well protected during wafer dicing process.

Furthermore, this enables a standard laser epitaxial growth processes prior to wafer bonding. Figure 2 shows the layer structure of the vertically-coupled microring laser. The buried microring structure is clad by low index benzo-cyclo-butene (BCB) material applied during the wafer-bonding process, where the high index difference ensures a good modal confinement within the waveguide.

The passive bus waveguides are formed on top of the active microring structure. Both p and n contacts are implemented on the top surface of the fabricated device. The width of both the passive bus waveguide and active microring are 1.8μm. The active region of the microring laser comprises of six InGaAs quantum wells, with a bandgap of Q_{ring} = 1.55μm, and is clad by a confinement layer with a thickness of 0.43μm. The InGaAsP bus waveguide has a bandgap of Q_{bus} = 1.44μm, and a thickness of 0.35μm. The serially cascaded microring lasers with ring radii of 70μm and 74μm are vertically-coupled to the same bus waveguide.

Experiment

Measurements are performed to assess the lasing performance of the fabricated devices in terms of light-current (LI) characteristics, wavelength spectrum and wavelength separation between lasing modes of the two cascaded lasers.

Figure 3 shows the LI characteristics for both clockwise and counter-clockwise oscillating modes for the two cascaded microring lasers.

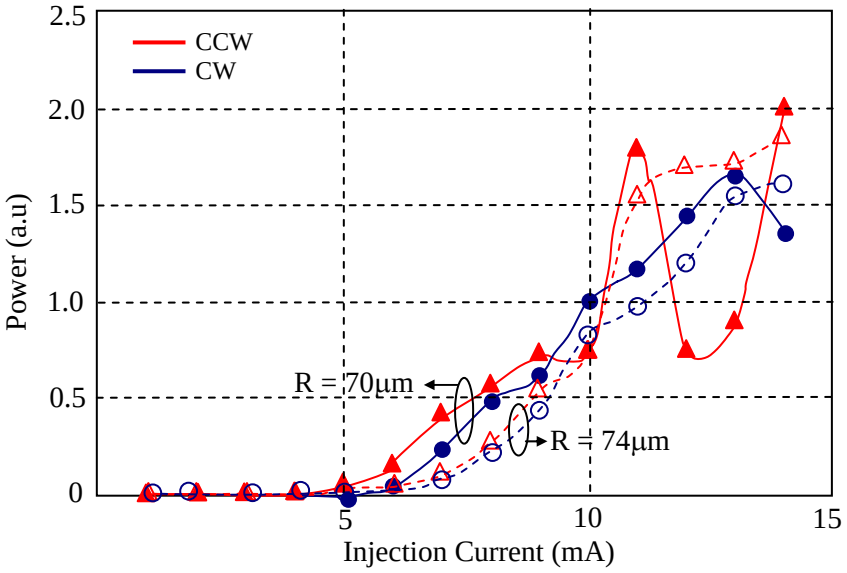


Fig. 3: Clockwise and counter-clockwise light-current characteristics of microring lasers.

The threshold currents for the two devices are 6mA, which corresponds to a threshold current density of 720A/cm^2. Thermal roll-over in the LI characteristic occurs at an injection current of 14mA.
Figure 4 plots the output spectra for the clockwise propagating modes of the two lasers as well as the combined power against wavelength under a bias current of 8mA, 10mA and 12mA, respectively. The lasing wavelength of the cascaded microring laser is centred in the 1575nm window, where a current range of 4mA gives rise to a wavelength variation from 1573.9nm to 1580nm for the 70μm-radius device, and 1580.2nm to 1584.9nm for the 74μm-radius device. This corresponds to a wavelength-current sensitivity of 1.5nm/mA and 1.15nm/mA, respectively. Side-mode suppression-ratio is observed to be in excess of 20dB, demonstrating excellent single-mode operation.

In order to provide a graphical illustration of the fine-tuning mechanism of the wavelength separation Δλ between the two microring lasers, figure 5 plots the wavelength separation as a function of injection current. The wavelength difference is observed to vary from 6.3nm at an injection current of 8mA to 4.9nm at an injection current of 12mA, corresponding to an overall wavelength difference tuning characteristics of 0.35nm/mA.

The result presented here highlights the potential of cascaded microring laser as compact and robust tunable dual-wavelength light source suitable for applications in terahertz mode-beating.

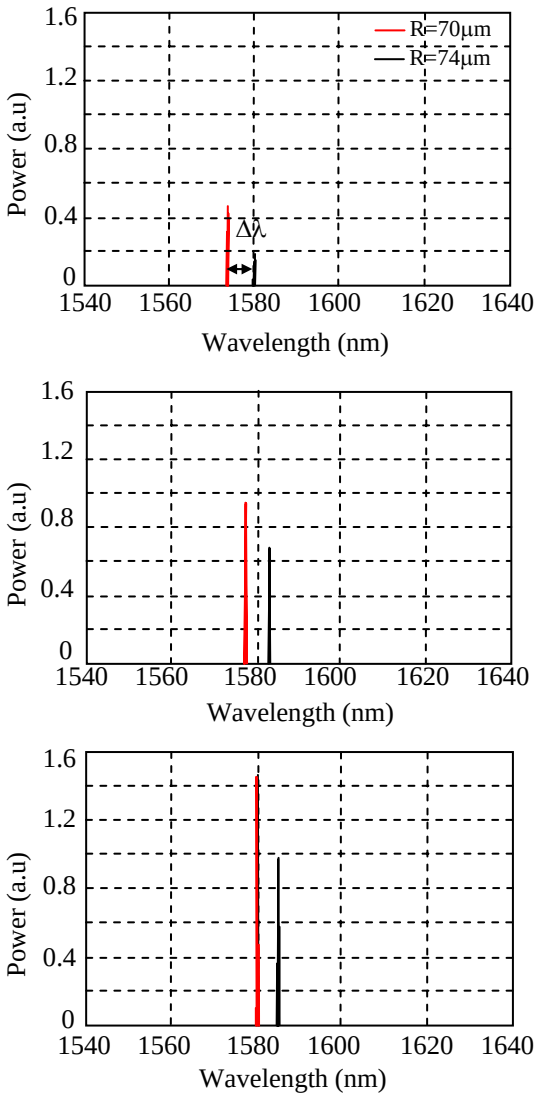


Fig. 4: Spectra of the dual-wavelength cascaded device at an injection current level of 8mA (top), 10mA (middle and 12mA (bottom).

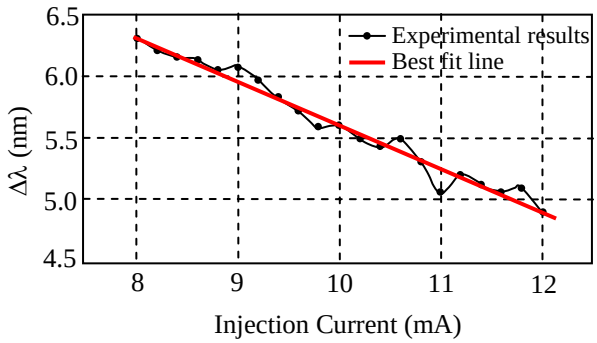


Fig. 5: Wavelength separation between the two lasing modes from the microring laser array.

Conclusions

A novel serially-cascaded vertically-coupled microring laser array, constructed using wafer-bonding technology, is demonstrated. CW operation of the lasers is demonstrated for the first time. The cascaded devices have threshold current of 6mA and oscillate with side mode suppression of greater than 20dB up to 12mA. The wavelength-current sensitivity of the two lasers is measured to be 1.5nm/mA and 1.15nm/mA. This corresponds to a tunable wavelength difference of 1.4nm across a current range of 4mA, highlighting its potential as compact and robust dual-wavelength light source suitable for broadband continuous tuning with a device footprint as small as 100×150μm².

Acknowledgments

The authors would like to gratefully acknowledge financial support from the European Committee through the research project WAPITI (Wafer-bonding and Active Passive Integration Technology and Implementation, FP6-2003-IST-2-004073), and ePIXnet (European Network of Excellence on Photonic Integrated Components and Circuits, Project no 004525).

References

1 R. Grover et al, Summer School, Int. Sch. Quantum Electron., 18-25 October, 2003.
2 C. W. Tee et al, J. Sel. Top. Quantum Electron., vol. 12, pp. 108, 2006.
3 K. Djordjev et al, Photon. Technol. Lett., vol. 14, pp. 1115, 2002.
4 S. J. Choi et al, Photon. Technol. Lett., vol. 16, pp. 2517, 2004.
5 S. J. Choi et al, Photon. Technol. Lett., vol. 16, pp. 356, 2004.
6 K. Amarnath et al, Photon. Technol. Lett., vol. 17, pp. 2280, 2005.
7 C. W. Tee et al, Photon. Technol. Lett., vol. 18, pp. 2129, 2006.

High Q-factor microrings using slightly etched rib waveguides

S. Maine(1), D. Marris-Morini(1), L. Vivien(1), E. Cassan(1), D. Pascal(1), S. Laval(1),
B. Han(2), R. Orobtchouk(2), T. Benyattou(2),
L. El Melhaoui(3) and J-M. Fédéli(3)
1) Institut d'Electronique Fondamentale, UMR 8622, Université Paris-Sud, 91405 Orsay, France
2) Laboratoire de Physique de la Matière, UMR 5511, INSA de Lyon, 7, avenue Jean Capelle 69621 Villeurbanne, France
3) Laboratoire d'Electronique de Technologie, de l'Information LETI-Minatec, CEA-G 17 Rue des Martyrs F38054 Grenoble

Abstract: *The paper reports the design, fabrication and characterization of silicon on insulator (SOI) microring resonators using shallow etched rib waveguides. The variation of the Q-factor of the microring resonators as a function of coupling gap between the input waveguide and the ring is studied. Such structures are fabricated using e-beam lithography and reactive ion etching steps. Propagation loss of such rib waveguide has been evaluated lower than 0.8 dB/cm for wavelengths around 1550nm. With a ring diameter of 50µm and a coupling gap of 450nm, the measured Q-factor and finesse are up to 21900 and 28, respectively. The results are matched by numerical optical simulations.*

Introduction

Silicon-on-insulator substrates (SOI) have generated an increasing interest in the recent years, for both microphotonic and microelectronic applications. The thin crystalline silicon film which is separated from the silicon substrate by a buried oxide layer constitutes a high quality optical waveguide at telecommunication wavelengths (from 1.3 µm to 1.6 µm) where silicon is transparent. A very strong light confinement is obtained with SOI structures, due to the large refractive index difference between silicon and its oxide ($\Delta n \approx 2$). This allows the realization of ultra-compact nanophotonic devices and circuits. Among passive structures, waveguides, 90°-turns and beam splitters have been widely studied using either strip or rib waveguides(1).

One of the main optoelectronic devices necessary to realize a high speed optical link is the optical modulator. For few years, several optical modulators integrated in submicron rib SOI waveguides have been proposed (2-4). These structures provide a phase modulation which has to be transformed into an intensity modulation using interferometers such as microring resonators, Fabry-Perot cavity and Mach Zehnder.

We report the design, realisation and characterisation of microring resonators in accord with the constraints established by the proposed modulator devices (5). The characteristics like optical losses, light coupling, and Q-factors are numerically studied and then compared with experimental results for microring resonators on SOI substrates.

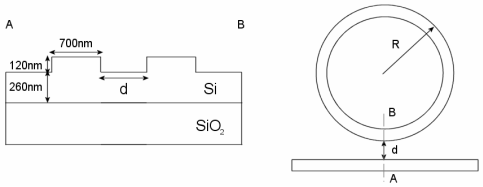


Fig. 1: (a) Cross section schematic view of the designed rib waveguide etched in the silicon layer of SOI. (b) The ring resonator is formed by a ring separated from a waveguide by a distance *d*.

Theory and design

Fig. 1 presents the schematic view of rib waveguide and microring resonator. The waveguide height and width are fixed to 380 nm and 700nm, respectively and the etching depth to 120nm. This rib waveguide ensures single mode propagation for the considered wavelengths: λ=1.3-1.5µm.

A ring resonator is a photonic component composed by a microring waveguide (radius *R*) coupled to an input/output bus waveguide, separated by a distance *d*. The optical transmitted power can be written as:

$$I_t = I_0 \frac{(K+T)^2\tau^2 + T - 2\tau(K+T)|t|\cos(\phi)}{1 + T\tau^2 - 2|t|\tau\cos(\phi)}$$

where I_0 is the incident optical power, *K* the fraction of optical power coupled between the waveguide and the microring, *T* the transmitted optical power coefficient, $|t| = \sqrt{T}$ the field transmission coefficient, P=1-T-K the fraction of lost optical power, $\phi = k_0 n_{eff} L_{eff} = k_0 n_{eff} 2(\pi R)$ the phase shift for a roundtrip along the resonator, $\tau = e^{-\frac{\alpha L_{eff}}{2}} = e^{-\alpha\pi R}$ the attenuation of the field for a roundtrip and α the loss coefficient of the microring. The fraction of optical power coupled in the microring depends on the geometry of the waveguide, which is fixed, on the radius of the microring and on the distance between the microring and the input waveguide *d*.

The quality of the microring resonator is represented by the *Q* factor which depends mainly on two parameters: τ the attenuation of the field and $|t|$ the field transmission coefficient.

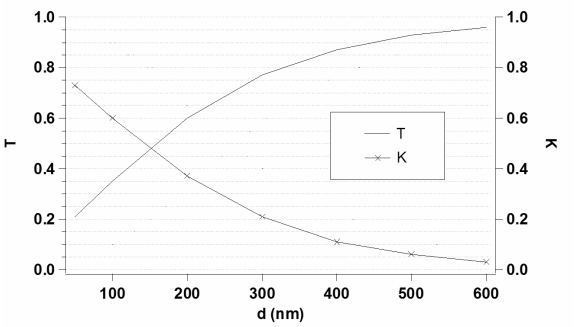


Fig. 2: Fraction of power coupled in the microring (K) and transmitted (T) as a function of the gap d at λ=1.52µm.

Simulation of the coupling between the ring and the waveguide

To numerically study the influence of the gap d (between the waveguide and the microring) on the coupling coefficient, the structure is simulated by a straight waveguide and a portion of a microring resonator with a radius of 50µm. The gap d between the waveguide and the portion of ring is varied from 100nm to 600nm.

The numerical tool was a three-dimensional finite-difference time-domain (FDTD) (6) method with perfectly matched layers as absorbing boundary conditions. The wavelength is fixed to 1.52µm.

From these simulations the fractions of optical power coupled in the microring K and transmitted in the straight waveguide T are determined (Fig. 2). The coupling coefficient K decreases as the gap widens and covers a 3-73% range while T increases from 21% to 96%. Coupling loss, without considering the rib roughness is smaller than 4%.

To validate these simulations, devices with microring resonators were fabricated. The radius of the microrings is fixed to 50µm. To cover a large range of value for the coupling coefficient and taking into account technological constraints, three values of gaps are considered: 200, 300 and 450nm.

Fabrication and measurements

The devices are fabricated on SOI wafers, which have a 400nm thick silicon device layer on a 1µm thick buried silicon oxide (BOX) layer. The thickness of the silicon layer is decreased to 380nm by thermal oxidation. High thermal oxide is deposited to form a hard mask. Electron-beam lithography with negative resist is used. The hard mask is etched down to the silicon layer, followed by a partial etching to 120nm of the silicon to create the rib waveguide. Devices are encapsulated by 500nm of SiO_2 and cleaved into 4.5×9mm dies.

Fig. 3 shows an optical microscope view of the ring resonator device. Input light is split to obtain two balanced branches. The first branch is coupled with a microring and the other one is taken as a reference.

A laser beam from a tuneable laser source with 1530µm centre wavelength is used at TE polarization. Light is coupled to the cleaved facet of the input

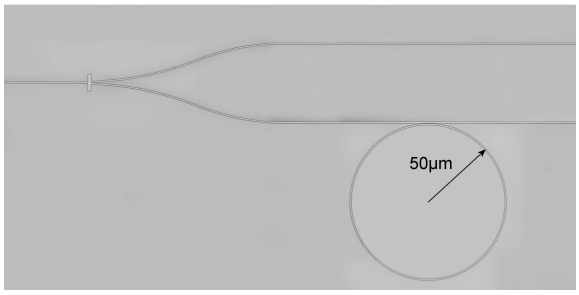


Fig. 3: Optical micrograph of one fabricated microring.

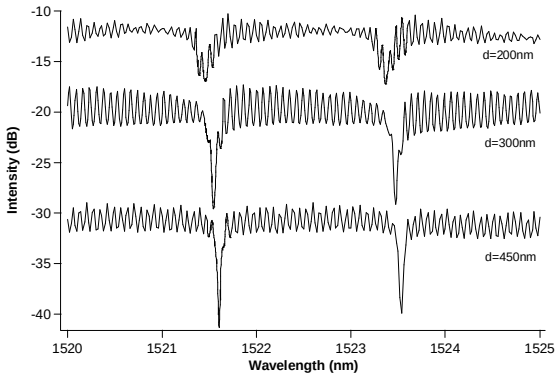


Fig. 4: Measured transmission spectra of microring resonators for gaps of 200, 300 and 450nm and for a radius of 50µm.

waveguide using a lensed fibre. The output beams are collected by a microscope objective and sent on a photodetector. For each device, output power is recorded (Fig. 4) for wavelengths from 1520nm to 1525nm.

The intensity spectrum shows dips which are the consequence of the presence of the microring. The resonant wavelengths and the contrasts depend on the characteristics of the system. Among these: the effective index of the microring, the coupling coefficient and the losses. When the gap varies, the shape of the dip created by the microrings varies as the coupling coefficients change. For a given radius, the losses of the microrings are fixed. So the extinction ratio variation is only due to the gap size variation. The extinction ratio is about 2.5dB for a gap of 200nm and increase to 8dB for d=450nm. So the gap has an important influence on the quality of the resonance.

In addition to the dips created by the microring resonators, small oscillations due to Fabry-Perot resonances between the cleaved ends of the waveguides are clearly observed. In order to dissociate the characteristics of the microrings from Fabry-Perot oscillations, regressions are realized on the measurements. A mathematical function taking into account the parameters of the microring resonator, the Fabry-Perot cavities and the splitter is used. The parameters are the transmission coefficient of the ring t_r, the ring losses τ_r, the group index in the ring n_{gr}, the losses of the straight waveguide τ, the group index of the waveguides n_g, the transmitted fraction of intensity through the cleaved facet T and the losses of the

splitter τ_d. The splitter is supposed to be well balanced.

From theses simulations the values of the parameters are extracted. Concerning the microring itself, the group index n_{gr} is evaluated to 3.79 and the losses to 0.5dB per roundtrip. The interaction between the straight waveguide and the microring is also described. The transmitted intensity coefficient T_r is deduced and is compared to the Finite Difference Time domain (FDTD) simulations (Fig. 5). Measurements are in good agreement with the FDTD calculations previously realized. Both the shape and the values are close to the predicted results.

To evaluate the quality of the microrings independently of the Fabry Perot cavities, the Q-factors are evaluated with the parameters extracted from the measurements. To calculate the Q factor and the finesse of the microrings the following expressions are used:

$$Q = \frac{\lambda_0}{(\Delta\lambda)_{3dB}} = \frac{2\pi n_{gr} L_{eff}}{2\lambda_0 \arccos\left(\frac{2|t_r|\tau_r}{1+|t_r|^2\tau_r^2}\right)}$$

$$\mathcal{F} = \frac{(\Delta\lambda)_{FSR}}{(\Delta\lambda)_{3dB}} = \frac{\pi}{\arccos\left(\frac{2|t_r|\tau_r}{1+|t_r|^2\tau_r^2}\right)}$$

Table 2 gives the values deduced from these expressions. Measured Q-factors as high as 21900 are obtained for a radius of 50µm and a gap of 450nm. For smaller gaps, the Q-factor is lower. This variation can be explained as follow.

For a given radius, the length L_{eff} and the attenuation factor $\tau_r = e^{-\frac{\alpha_r L_{eff}}{2}} = e^{-\alpha_r \pi R}$ are constant.The increase of the Q-factor with the gap is the consequence of the decrease of the coupling coefficient between the microring and the straight waveguide which corresponds to an increase of the transmission coefficient t_r. As the gap is widening, t_r and so the Q-factor, get higher. However to determine an optimum structure, the Q-factor must be considered in parallel with the extinction ratio or contrast of the modulator which tends to zero as t_r tends toward 1.

Conclusions

Microring resonators integrated on SOI substrates using slightly etched rib waveguides have been designed, fabricated by electron beam lithography and characterized. The experimental results on the coupling coefficients between the straight waveguide and the ring are in good agreement with the FDTD simulations. The finesse and quality factor of the microrings have been extracted and Q-factors as high as 21900 have been obtained for 50µm radius microrings and gaps of 450nm.

The small size of microring resonators and high attainable quality factors make them attractive for highly integrated components. Such microrings are especially interesting for the realization of integrated compact modulators.

Table 2: Summary of Q factors and finesses extracted from the measures.

d (nm)	Q-Factor	Finesse
200	8100	10.4
300	13000	16.6
450	21900	28.0

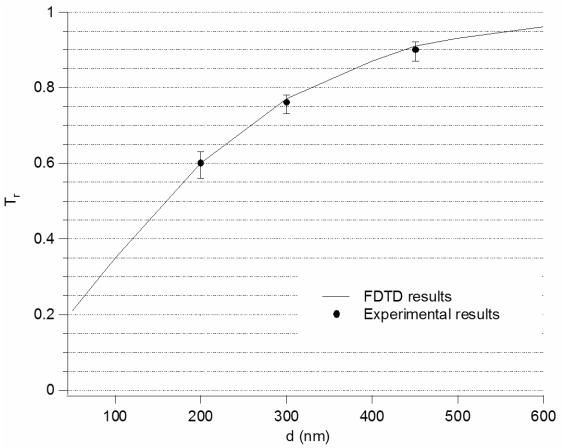


Fig. 5: Comparison between the experimental measurements of the coefficient of transmitted intensity versus the gap for the microring of radii 50µm and 100µm.

Acknowledgments

This work was supported by the French RMNT project "CAURICO" in the frame of collaboration between Institut d'Électronique Fondamentale (CNRS/UPS Orsay), CEA-LETI (Grenoble), Laboratoire de Physique de la Matière (INSA Lyon) and ST-Microelectronics (Crolles). The authors acknowledge the staff of the 200nm cleanroom of the LETI for fabrication of high quality optical structures.

References

1 D. Marris et al, Applied Physics Letters, no 87, 2005.
2 L. Liao et al; Optics Express, no 13, p. 3129, 2005.
3 Q. Xu et al, Nature, no 435, p. 325, 2005.
4 D. Marris et al, J. of Selected Topics in Quant. Elec., no 9, p 747, 2003.
5 S. Maine et al, Proc SPIE 6183, 618360D1-6, 2006.
6 PhotonDesign software, www.photond.com

Low-Loss SiON Ring Resonators on Silicon for 1.55 µm Wavelength

Maxim Fadel (1) and Edgar Voges (2)
High Frequency Institute, University of Dortmund, D-44221 Dortmund, 1) maxim.fadel@udo.edu 2) edgar.voges@udo.edu

Abstract: *Low-loss (0.05 - 0.2 dB/cm) and low-birefringence (-3·10^{-5}) silicon-oxynitride waveguides for $\lambda \cong 1.55$ µm are fabricated by plasma-enhanced chemical vapour deposition. A combination of high-index contrast and a compact core dimension allow the realization of small bending radii. Tunable IIR-filters with ring resonators are fabricated. We show an evaluation of the waveguide losses and polarisation dependence by measuring the transmission spectra of the ring resonators.*

Introduction

Common optical components made by doped silicon oxide on silicon are mode-matched to telecom fibre systems. The waveguide could have large core dimensions with a low-index contrast [1] or a high-index waveguide with a thin core [2]. However, it is not possible to fabricate compact optical circuits with this kind of waveguide because of high radiation losses for small bending radii. So we investigate in this paper a waveguide design that combines a thick core layer with a high index contrast [3][4]. Then, the bending losses can be reduced strongly. In order to determine the optical circuit losses, tolerable bending radii and the polarisation dependence of the waveguide we measure the spectral transmission of ring resonator structures.

Waveguide technology and components

A PECVD-system (Plasma Enhanced Chemical Vapour Deposition, Oxford PS100) with the process gases SiH_4, N_2O and NH_3 is used for the deposition of the SiO_2 and silicon-oxynitride (SiON) layers on 4 inch silicon {100}-wafers. The deposition parameters were optimized for homogenous and low-loss optical layers to suit the high requirements for optical applications. The hydrogen content in the layers, which will cause optical losses, is thereby reduced. Nevertheless, a high temperature annealing at about 1150 °C is still necessary to break the hydrogen bonds and to achieve low-loss devices. At the same time the stress caused by the different thermal expansion coefficients of the material systems SiO_2/Si could lead to layer cracking at high temperature. To avoid this, the stress and the hydrogen content of the deposited layer should be controlled within the given parameter range. With the parameters of Fig. 1a robust and low-loss optical layers are deposited. A very reproducible and homogeneous layer thickness and refractive index are achieved with standard deviations σ_d = 1 nm and σ_n = 0.0005, respectively. One great advantage of the SiON technology is the ability to adjust the refractive index of the deposited layer in a wide range, which starts at the undoped oxide at 1.45 and ends at Si_3N_4 with a refractive index of about 2. In this work the refractive index difference between the core and the undoped cover layer can be tuned from 0 to 0.08 as shown in Fig. 1b. In order to do this the NH_3-flow is changed. Appropriate deposition parameters must include the subsequent annealing process. The SiON densifies during annealing. Therefore, the refractive index is increased and the effective deposition rate is reduced.

parameter	SiON	SiO_2
N_2O/SiH_4	55	135
NH_3 [sccm]	0-80	0
power [W]	50	70

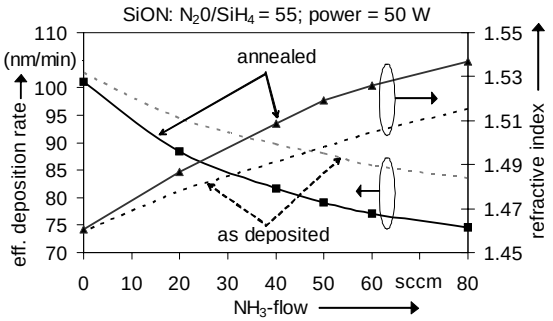


Fig. 1: a) Deposition parameters for SiON- and SiO_2-layers; b) refractive index and deposition rate before and after 1150°C annealing in dependence on the NH_3-flow

Waveguide devices are fabricated on 4 inch silicon wafers with 10 µm thermal oxide as a buffer layer. The core layer of 2 µm thickness is deposited and annealed. A negative resist is structured by UV photolithography and used as a mask for a dry reactive ion etching (RIE) step with CHF_3. Finally, the SiO_2 cover layer is deposited. Fig. 2 shows the typical geometry of the fabricated waveguides.

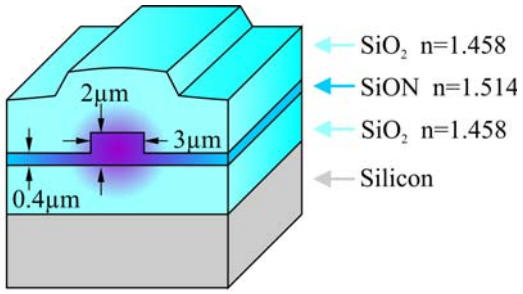


Fig. 2: Geometry and parameters of SiON-waveguides

The facets of the waveguides are prepared with a special polishing saw disc with a grit size of about 3 µm. The residual roughness of the waveguide fac-

ets is lower than 3 µm and has no effect when using an index-matched fluid or adhesive during butt coupling. The mode shape of the high-guidance waveguide is much smaller than that of the standard fibre, so that high coupling losses (≈ 3.5 dB) are expected (see Fig. 3b).

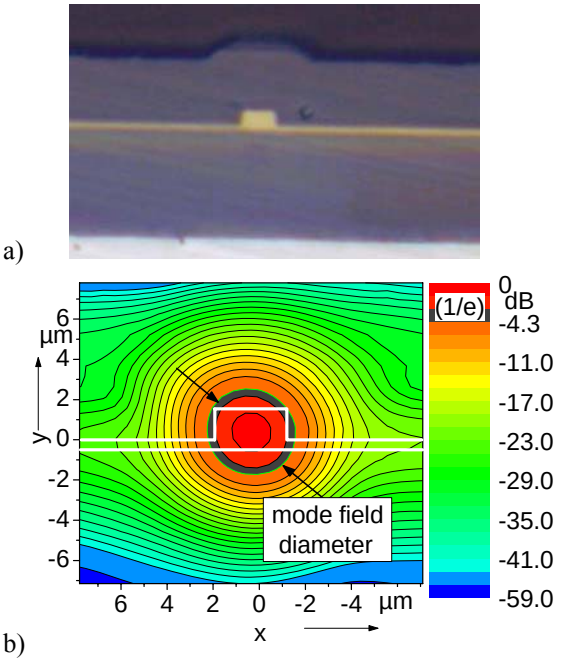


Fig. 3: a) Microphoto of waveguide facet with injected white light; b) near field distribution obtained by scanning with a high-aperture fibre

Therefore, we use a high numerical aperture fibre (UHNA) with a small mode field diameter allowing low coupling losses below 0.15 dB/facet to the waveguides.

The high-aperture fibre can be spliced to standard fibres with low losses of about 0.2 dB by using appropriate splicing parameters.

Furthermore, the thermo-optic effect of silica offers an effective way to locally control the refractive index by positioning Cr-heaters on the top of the waveguide. The width of the Cr-electrodes with 0.4 µm thickness is between 4 and 8 µm; a typical length is between 2 and 5 mm. These tunable phase-shifters allow an adaptive control of the device-response, which can be used in many applications. A basic device, which employs the thermo-optic phase-shifter, is shown in Fig. 4. The optical coupling ratio of a Mach-Zehnder interferometer (MZI) is electrically changed by heating one path. A heating power of 0.6 W yields a phase shift of 2π. This could be reduced by etching grooves for thermal isolation. The tunable MZI can be used in more complex optical devices. A finite impulse response filter (FIR) is achieved by cascading a number of MZI separated by optical delays [5]. We utilize the MZI-coupler for IIR-filters (Infinite Impulse Response) with ring resonators [6].

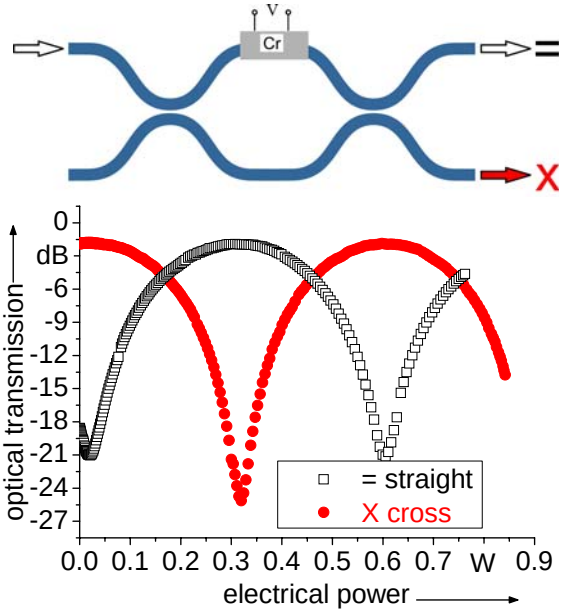


Fig. 4: Thermo-optic control of a tunable MZI-coupler

A simple ring resonator basically consists of a straight waveguide that is coupled to a ring as seen in Fig. 5a. Fig. 5b shows such a fabricated ring resonator. The resonance occurs when the phase delay between light in the ring and light passing through the straight waveguide are a multiple of half a wavelength. The spectral transmittance of a ring resonator is shown in Fig. 5c, with a Free Spectral Range (FSR) of 25 GHz. The width Δf and height T_{max}-T_{min} of the resonance depends on the coupling ratio between straight waveguide and ring and on the ring losses. It does not depend on the fibre-to-chip coupling losses.

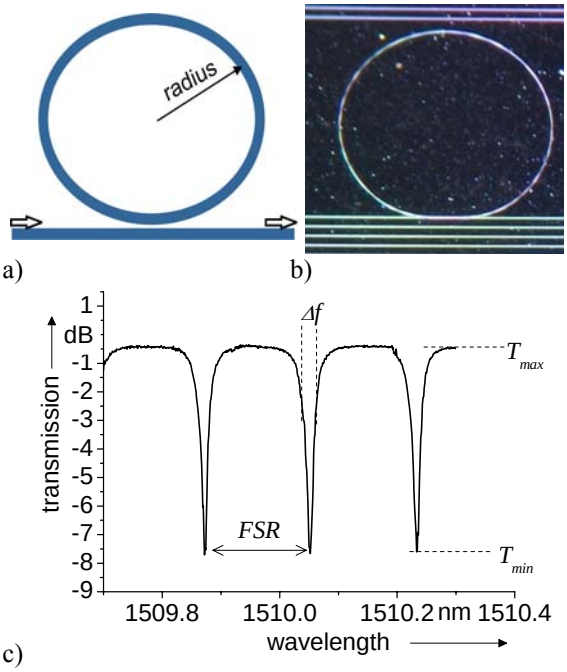


Fig. 5: a) Ring resonator scheme and b) Microphoto; c) Typical transmission spectra of a single ring resonator

We fabricate also fully tunable ring resonator filters by using a thermo-opticaly controlled MZI-coupler instead of the simple coupler [6]. The basic design is shown in Fig 6, where the phase shifters are tuned to control the transmission behaviour of the ring. In the upper part of the figure the phase shifter of the MZI in one of the four cascaded rings is heated. This decreases the coupling ratio and causes basically only an increase of the resonance depth. The independent heating of the phase shifter in the feedback path of ring 1 leads to a shift of the resonance. A combined tuning of both phase shifters can be used to set a filter response, which is desired to e.g. equalize an input signal.

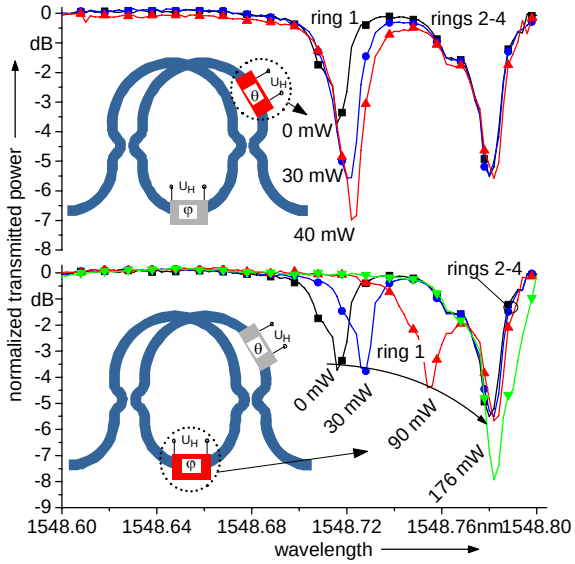


Fig. 6: Tuning the phase shifters of one of four ring resonators, which are based on a tunable MZI. The resonance depth is controlled by the MZI-phase. The resonance wavelength is shifted by the thin-film heater in the feedback path.

Optical losses and birefringence

After the annealing treatment at about 1150°C the losses of straight waveguides are determined by measurements of the transmission for different lengths of the waveguides. Attenuation constants between 0.2 dB/cm (at λ = 1530 nm) and 0.05 dB/cm (at λ = 1550 nm) are obtained. We take here into account that the losses due to fibre-to-chip coupling are 0.12 dB/facet.

As already mentioned it is possible to calculate the ring losses from a spectral measurement by evaluating the resonance behaviour [7]. We investigate ring resonators of about 2 mm diameter and different coupling factors. We use two wavelength regions around 1542 nm and 1510 nm to prove the expected difference due to the N-H-bonds. A residual amount of these bonds in the core layer increases the attenuation toward the shorter wavelength that reaches his maximum of 0.6 dB/cm at about 1510 nm.

Fig. 7 shows the results for the ring losses and the coupling ratio κ at both wavelengths over the coupling length of the coupler. As expected, the coupling ratio increases with a longer coupling length. For comparison a direct measurement of separated couplers is inserted.

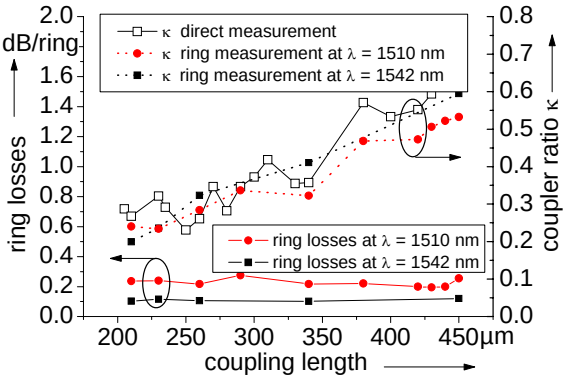


Fig. 7: Ring losses and coupling ratio at both wavelengths over the coupling length

As expected, the attenuation increases at 1510 nm. The attenuation average at 1542 nm is about 0.1 dB/ring. Taking into account the direct measurement results of the straight waveguide above, there is only 0.06 dB bending loss left. Therefore, a further reduction of the ring radius using this waveguide technology is possible. The attenuation average at 1510 nm is about 0.3 dB/ring. If we subtract the radiation losses of 0.06 dB, 0.24 dB of pure waveguide losses remain. This value is about half of the value of the direct measurement above.

Because the effective refractive indices of the TE- and TM-modes are different there will be a shift in the ring resonance in dependence on the polarisation. Determining the polarisation dependence of the waveguide with a ring resonator is much easier than the commonly used complex measurement setups where an accuracy better then 10^{-4} is difficult to achieve.

The causes of the birefringence in our waveguides are mainly the geometry of the core and the mechanical stress in the layers. The geometrical effect and the stress effect may have opposite signs so they can compensate each other for proper fabrication parameters. This issue will be pursued in further works.

The birefringence causes a wavelength shift in the spectral behaviour of interferometric devices. This is also valid for a ring resonator with the advantage of a sharp resonance, which allows an accurate detection.

In our experiment a fibre-based polarisation controller (see Fig. 8a) launches TE, TM mode and a combination of both into the ring. The controller scrambles the polarisation for every wavelength in a given time, for example 100 seconds and covers almost the entire Poincaré-sphere. The resonance condition will be fulfilled for a given wavelength only, for either the TE or the TM mode.

If we measure the minimum of the transmitted

power, a curve as in Fig. 8b will result. The wavelength difference between the TE- and TM-dips is the Polarisation Wavelength Dependence (PWD). The birefringence B is then:

$$B = n_{eff} \cdot (PWD/\lambda)$$

where n_{eff} is the effective refractive index.
In this experiment we measure a birefringence below $-3 \cdot 10^{-5}$ (see Fig. 8b), which is a good result concering high-guidance SiON-waveguides because the published values are between -10^{-3} [8] and -10^{-4} [3].

Conclusions

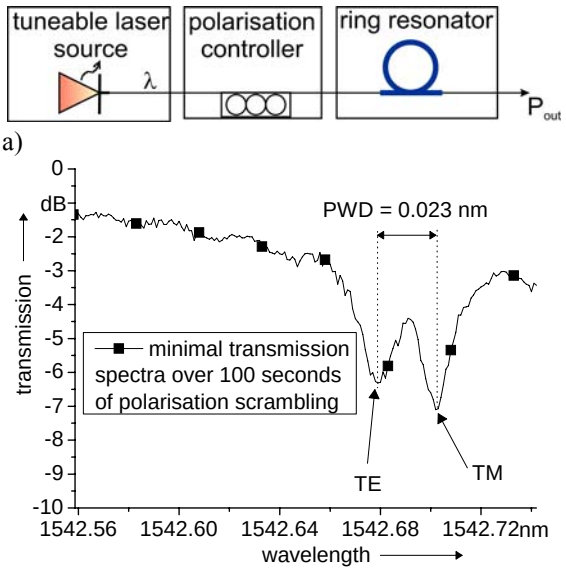


Fig. 8: a) Measurement setup of the polarisation wavelength dependence; b) shift of the resonance dips over the wavelength in dependence of the polarisation state

With a high-index SiON waveguide technology combined with a compact and thick core design low-loss and small bending radii are realized. The total ring losses for a ring resonator with a radius of about 1 mm are below 0.15 dB. Tunable IIR-filters with ring resonators and thermo-optic phase shifters are fabricated. The determined birefringence is $< -3 \cdot 10^{-5}$ and there is a high potential of its further reduction by optimizing the layer stress to compensate the geometrically induced birefringence.

References

1 M. Yasu et al, Trans. Inst. Electron Comm. And Eng. of Japan, no. J68-C, p. 454-461, 1985
2 M. Hoffmann et al, IEEE Photonics Technol. Letters, no. 9, p. 1238-1240, 1997
3 G.L. Bona et al, Microsystem Technologies, no. 9, p. 291-294, 2003
4 M. Fadel et al, Electrochem. Soc. 501, Paper 389, 2006.
5 K. Takiguchi et al, J. Lightwave Technol., no. 9, p. 1647-1656, 1998
6 C.K. Madsen et al, Photonics Technol. Letters, no. 12, p. 1623-1625, 1999
7 R. Adar et al, J. Lightwave Technol., no. 8, p. 1369-1372, 1994
8 K. Wörhoff et al, J. Lightwave Technol., no. 8, p. 1401-1407, 1999

Efficient Second Harmonic Generation in Matched Ti:PPLN Waveguide Resonators

R. Nouroozi, Y. H. Min, W. Grundkötter, V. Quiring, R. Ricken and W. Sohler

Angewandte Physik, Universität Paderborn, Warburger Str. 100, 33098 Paderborn, Germany
email: sol_rn@physik.uni-paderborn.de

Abstract: *Second harmonic generation in Ti:PPLN waveguide resonators is investigated as a means of enhancing the conversion efficiency. Using a matched resonator of 65 mm length a record conversion efficiency of 10.3 %/mW is achieved with 0.5 mW fundamental power at λ_f = 1531 nm.*

Introduction

Second harmonic generation (SHG) in waveguide resonators has been investigated in detail many years ago [1,2]; at that time phase matching was usually achieved by exploiting the birefringence of the waveguide material. This was a strong limitation for the possible wavelength combinations of a three wave nonlinear second order interaction. Moreover, it was not possible to exploit the largest nonlinear coefficient. With the advent of periodically poled substrate materials quasi phase matching became possible. It proved to be a very versatile method allowing nearly arbitrary wavelength combinations and the exploitation of the largest nonlinearity. In the meantime single pass SHG and other parametric interactions have been demonstrated in periodically poled materials with excellent efficiencies for wavelengths in different spectral ranges from the UV to the infrared [3,4]. Moreover, quasi phase matched SHG is exploited in a number of devices using cascaded $\chi^{(2)}$:$\chi^{(2)}$ interactions for all-optical signal processing such as wavelength conversion and optical time-division multiplexing [5,6].

It is surprising that up to now SHG in periodically poled waveguide resonators has not yet been studied though power enhancement and the higher nonlinearity promise a significant enhancement of the conversion efficieny.

Several nonlinear substrate materials can be used to develop periodically poled waveguide resonators. Among them ferroelectric crystals such as Potassium Titanium Oxide Phosphate (KTP), Lithium Tantalate, and Lithium Niobate (LN) are the preferred candidates. We are using the standard Ti-indiffusion technique to fabricate optical channel guides of excellent quality in Periodically Poled Lithium Niobate (PPLN). Very good homogeneity of all waveguide properties can be achieved over a length of up to 95 mm enabling quasi phase matched nonlinear interactions of high efficiency. Moreover, the low propagation losses of Ti:PPLN guides (down to 0.05 dB/cm around λ = 1550 nm) allow the development of high Q waveguide resonators as already exploited e.g. in different types of optical parametric oscillators [7].

In this contribution SHG in matched Ti:PPLN waveguide resonators for the fundamental wave is reported. The realization of this concept, which leads to the maximum intracavity power enhancement and, therefore, to the maximum conversion efficiency, is experimentally demonstrated. A record conversion efficiency of 10.3 %/mW has been achieved with 0.5 mW fundamental power at λ_f = 1531 nm.

Modelling

The theory of SHG in (Fabry-Perot-type) waveguide resonators has been presented long time ago [2]. Only resonances of the fundamental wave have been considered up to now. The key results will be mentioned here again, to highlight the advantages of SHG in waveguide resonators. The main advantage is the large intracavity enhancement of the fundamental power, if low loss waveguides and appropriate mirrors are used. This enhancement can be described by a resonance factor f with:

$$f = \frac{1 - R_f}{\left[1 - (R_f R_r)^{1/2} \exp(-\alpha_\omega l)\right]^2} \qquad (1)$$

R_f and R_r are the reflectivities of the front and rear mirror of the resonator, respectively; α_ω is the loss coefficient describing the propagation loss of the fundamental wave; l is the sample length.

If no transmitted fundamental power is needed R_r can be set to 1. Then R_f is determined by the condition for maximum power enhancement or maximum f yielding:

$$R_{fm} = R_r \exp(-2\alpha_\omega l) \qquad (2)$$

Such a front mirror reflectivity leads to zero reflectivity at maximum resonance; all the input power is used for intracavity power enhancement limited by (scattering) losses alone. The maximum enhancement factor of such a "matched" resonator is given by:

$$f_m = \frac{1}{1 - R_{fm}} \rangle 1 \qquad (3)$$

This power enhancement leads in the nondepleted pump approximation to a corresponding enhancement of the conversion efficiency for SHG:

$$\eta_{res} = \eta f^2 \qquad (4)$$

with the single pass, nonresonant efficiency η.

As shown in [2], η_{res} is only weakly dependent on the length of a matched resonator, but strongly on the propagation losses α_ω. Fig. 1 shows this dependence

as f^2 versus α_ω for parameters as used in our experiments (λ = 1550 nm; l = 65 mm); note, that the reflectivity of the front mirror is continuously adjusted according equation (2). It is seen that an improvement of the conversion efficiency for SHG of more than 100 can be expected low loss waveguides assumed! Therefore, matched waveguide resonators are most attractive devices for efficient second harmonic generation.

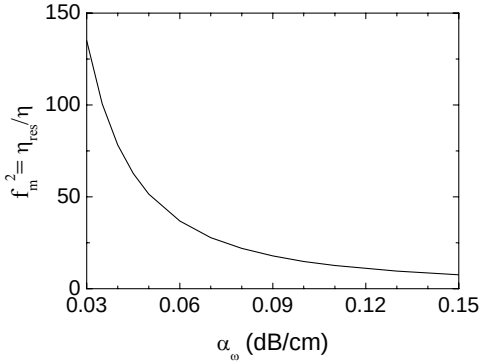


Fig. 1: Calculated ratio of SHG efficiency η_{res} in a matched resonator and efficiency η of a single pass nonresonant device as function of waveguide propagation losses α_ω at the fundamental wavelength.

Fabrication and experimental setup

In a first step 65 mm long single mode channel waveguides have been fabricated in a 0.5 mm thick Z-cut LN substrate. Photolithographically defined, 7 µm wide, vacuum-deposited Ti-stripes of 98 nm thickness have been indiffused (8.5 h @ 1060°C) to form the optical waveguides. They have been aligned parallel to the X-axis of the crystal. In the second step, the sample has been periodically poled by the electric field assisted poling technique using liquid electrodes. The periodicity of the microdomain structure is 16.6 µm allowing quasi-phase-matched SHG at 1531 nm fundamental wavelength. In the third step, the end faces of the waveguides have been polished perpendicular to the waveguide axis. Finally, dielectric end face mirrors of special properties have been prepared by vacuum-depositing. On one hand, both, input and output mirrors, should have a negligeable reflectivity at 765 nm wavelength, but a high reflectivity at 1530 nm. To be specific, according to theoretical results the reflectivity of the input (output) mirror should be 76% (> 99%) to get a matched resonator for most efficient SH-generation by maximum intracavity fundamental field enhancement. Modelling calculations show that 5 (6) pairs of SiO_2 and TiO_2 layers will form dielectric multilayer mirrors of the required spectral properties. Fig. 2 presents the measured transmission of input and output mirrors. The resulting reflectivities are 3% (at λ = 765 nm) and 74% (at λ = 1530 nm) for the input mirror; the corresponding data for the output mirror are 3% and 99%.

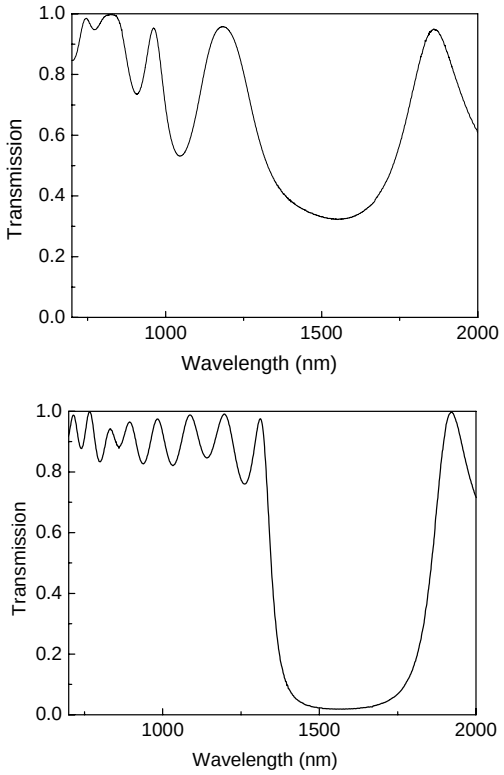


Fig. 2: Simulated and measured transmission spectra of the input (above) and output mirror (below) of the matched waveguide resonator.

The experimental setup to investigate SHG in the matched Ti:PPLN waveguide resonators is shown in Fig. 3. The sample is mounted on a thermoelectric cooler/heater, which allows a temperature stabilisation of about ± 1°C. A semiconductor Extended Cavity Laser (ECL) is used as tuneable coherent light source of about 150 kHz instantaneous linewidth. It can be continuously tuned in a small wavelength range enabling to sweep over some cavity resonances. The light is fed into the sample via a 10/90 fiber coupler to monitor the reflected fundamental power by a Ge-photodiode. The generated SH output power is measured by a Silicon photodiode, which is sensitive at the SH-wavelength only.

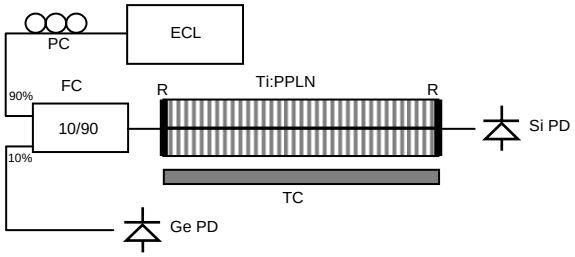


Fig. 3: Experimental Setup: ECL-tuneable, semiconductor Extended Cavity Laser; PC-polarization controller; FC-fiber coupler; R_1 and R_2-dielectric end face mirrors; TC-thermoelectric cooler/heater; PD-photo diode.

Results and discussion

Fig. 4 presents the measured reflected fundamental power versus wavelength around the expected phase match wavelength of 1531 nm; the input power was 0.5 mW. Using experimentally determined waveguide parameters (R_{in} = 74%, R_{out} = 98.6%, α = 0.084 dB/cm, l = 65 mm) also simulated results are given. As predicted for matched resonators the reflected power nearly drops to zero in a resonance due to maximum fundamental power enhancement. The agreement of theoretical and experimental results is relatively good; only the measured drop in the resonances is somewhat smaller than calculated.

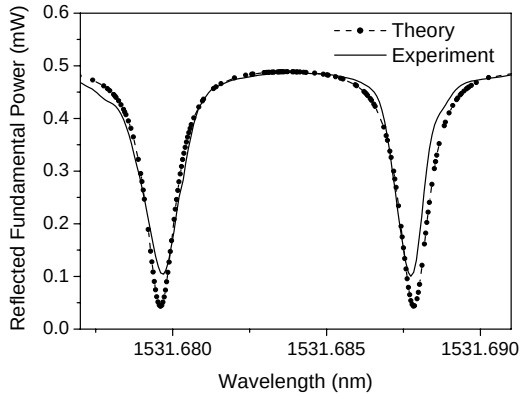


Fig. 4: Measured and calculated reflected fundamental power versus wavelength for an input power of 0.5 mW

In Fig. 5 the generated SH-power (at $\lambda \sim 765$ nm) is shown as function of the wavelength of the fundamental radiation. Again, the fundamental power in front of the waveguide resonator is 0.5 mW. SHG can be observed in a large number of cavity resonances (not completely resolved). The envelope of the SH-power reflects the phase match properties of the waveguide. Due to inhomogeneities, which might be arise from inhomogeneities of the substrat or /and of the fabrication process, not a $sinc^2$-response is observed. The wavelength of the laser can be stabilized to a single resonance by a proper feedback to the laser power supply.

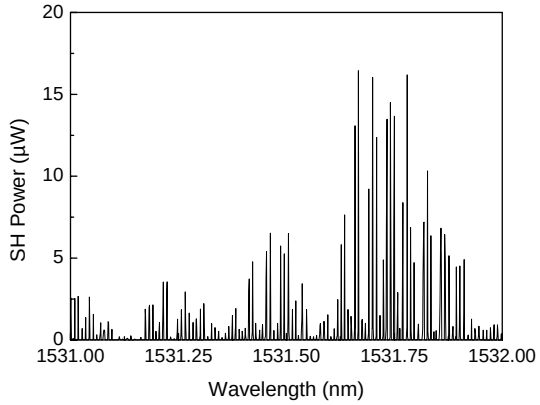


Fig. 5: Measured SH-power emitted in forward direction from a matched Ti:PPLN waveguide resonator versus fundamental wavelength around phase matching. Fundamental power is 0.5 mW.

The results of SHG in the two neighbouring resonances of highest efficiency are presented in Fig. 6. With only 0.5 mW of fundamental power, measured in front of the waveguide resonator (not coupled), a SH power of 25.8 μW was generated in forward direction. This corresponds to a record conversion efficiency of the device of 10300 %/W or 10.3 %/mW in reasonable agreement with the theoretical simulation. This impressive efficiency can even be doubled by using an appropriate input mirror of high reflectivity and appropriate phase for the SH-wave. A further improvement should be possible with a doubly resonant device, which is currently fabricated and investigated in our lab.

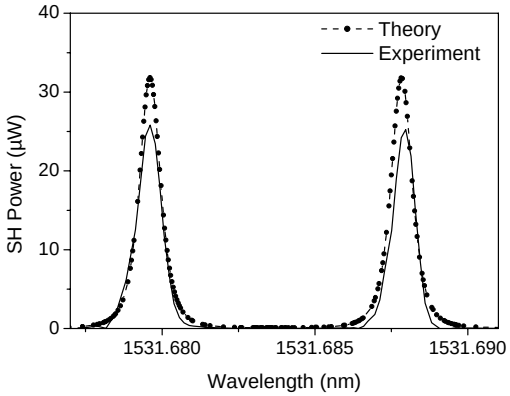


Fig. 6: Measured SH-power emitted in forward direction from a matched Ti:PPLN waveguide resonator versus fundamental wavelength around the two resonances of highest efficiency. Fundamental power is 0.5 mW.

Conclusions

In conclusion, SHG in Ti:PPLN waveguide resonators for the fundamental wavelength has been investigated. Theoretical modelling helped to identify matched resonators as optimum devices for maximum conversion efficiency. Based on these results corresponding Ti:PPLN resonators with appropriate dielectric mirrors have been developed. In a device of 65 mm length a record conversion efficiency of 10.3 %/mW has been achieved with 0.5 mW fundamental power at λ_f = 1531 nm.

A further improvement of the efficiency can be expected by devices, which are doubly resonant for fundamental and SH-waves simultaneously.

Acknowledgments

This work has been supported by the DFG (Deutsche Forschungsgemeinschaft) within the frame of the research unit "Integrated Optics in Lithium Niobate: New Devices, Circuits and Applications". The authors would like to acknowledge helpful discussions with H. Suche and S. Orlov.

References

1 R. Regener et al., *Digest of 1st European Conference on Integrated Optics* (ECIO), p. 19, 1981
2 R. Regener et al., J. Opt. Soc. Am. B, Vol. 5, No. 2, p. 267, 1988.
3 K. R. Parameswaran et al., Opt. Lett. Vol. 27, No. 3, p. 179, 2002
4 M. Fujimura et al., Electron. Lett., Vol. 28, No. 20, p. 1868, 1992
5 S. L. Jansen et al., J. Lightwave Technol., Vol. 24, No. 1, p. 54, 2006
6 C. Langrock et al., J. Lightwave Technol., Vol. 24, No. 7, p. 2579, 2006
7 G. Schreiber et al., Proc. SPIE, Vol. 4277, p. 144, 2001

Second harmonic generation via total internal reflection quasi-phase-matching in a hexagonal nonlinear optical microresonator

Tleyane J. Sono*[a], Christos Riziotis[b], Sakellaris Mailis[a], Robert W. Eason[a]
*tjs@orc.soton.ac.uk

a. Optoelectronics Research Centre, University of Southampton, Highfield, Southampton, SO17 1BJ, U.K.
b. Department of Telecommunications Science and Technology, University of Peloponnese, 22100, Tripoli, Greece

Abstract: *We propose the enhancement of the second harmonic generation process in an optical hexagonal microcavity, consisting of a nonlinear material, via total internal reflection quasi-phase-matching technique. We present preliminary numerical simulation results showing resonance operation in a suitably designed hexagonally shaped optical microresonator, which demonstrates the operating feasibility of the proposed scheme. The SHG efficiency was calculated using lithium niobate as the nonlinear material. High optical quality hexagonal superstructures can be manufactured routinely by chemical etching of inverted ferroelectric domains in this material.*

Introduction

Quasi-phase-matching (QPM) is a technique commonly used to enhance the efficiency of nonlinear interactions, such as second harmonic generation, (SHG), in cases where full phase-matching cannot be applied. One example of QPM SHG is by periodic poling in lithium niobate or KTP where the sign of the relevant nonlinear *d* coefiecient is inverted every coherence length ($l_c = \pi / \Delta k$) to compensate for the phase error between the fundamental wave (FW) and the second harmonic (SH) wave caused by the dispersion of the nonlinear medium. Another way to achieve quasi-phase-matching is by utilising the relative Fresnel phase shift ($\Delta\Phi_F$) between the FW and SH, induced upon total internal reflection (TIR) of the two waves at the medium-air interface to compensate for the dispersion phase mismatch (Δkl) as reported in ref[1]. The phase shift $\Delta\Phi_F$ in TIR-QPM, depends on: (1) the reflection angle, which always exceeds the critical angle, (2) the refractive indices of the propagation and surrounding media and (3) on the input/output polarization of the propagating waves [2]. The effective nonlinear *d* coefficient (d_{eff}) can also change sign after reflection depending on the selection of the input/output polarization which will result in an extra phase shift ($\xi\pi$) with ξ being 1 or 0 depending on the inversion of d_{eff}. Above the critical angle, the combination of $\Delta\Phi_F$ and $\xi\pi$ can take any value between 0 and 2π allowing for more flexibility for the propagation length between adjacent reflections as compared to the periodic poling case where the $2l_c$ period constraint is strict. TIR-QPM has been demonstrated and analysed in planar geometries for semiconductor materials.[2, 3] In this contribution we propose TIR-QPM in a hexagonal nonlinear optical microcavity where the FW is resonantly enhanced which subsequently increases the efficiency of the non-linear process while maintaining the small device size.

Micro-cavities have attracted much attention due to their wide range of functionalities and their small size which enables dense integration. Hexagonal microcavities in particular exhibit advantageous long input/output-coupling lengths, hence the coupling gap is not limited to the sub-micron bottleneck imposed on other geometries e.g. micro ring resonators. Most of the work on resonators demonstrated to date is focussed however on filtering applications such as add-drop filters. However this paper considers nonlinear phenomena with the principal aim to demonstrate the use of the hexagonal microcavity for an efficient SHG process by utilising the power build-up in an optical resonator. The choice of the hexagonal geometry is due to the fact that hexagonal optical cavities of superior optical quality can be fabricated by differential etching of inverted ferroelectric domains in lithium niobate.[4] Additionally, lithium niobate possesses a large d_{33} coefficient and hence, along with the fabrication argument constitutes a good candidate for the demonstration of TIR-QPM in this microcavity geometry.

Ma *et. al.*[5, 6] have studied the incident angle dependence of the optical power build-up in a hexagonal cavity showing an increase of number of cavity round trips resulting in sharp resonance for a reflection angle of 60°. Only at this angle can the length between subsequent reflections be constant and support long lived resonances with high Q. This restriction is also critical for QPM operation inside the cavity, as in the studied technique here. As shown in fig.1 the FW is being launched within the cavity (at the "source" position) in order to maintain the 60° reflection angle. We followed this launching approach instead of the side evanescent wave coupling in order to focus this initial work on the operational principle rather than on technical issues such as the design of side coupling sections. At this reflection angle, we avoid open-loop trajectories which although they also lead to cavity resonance

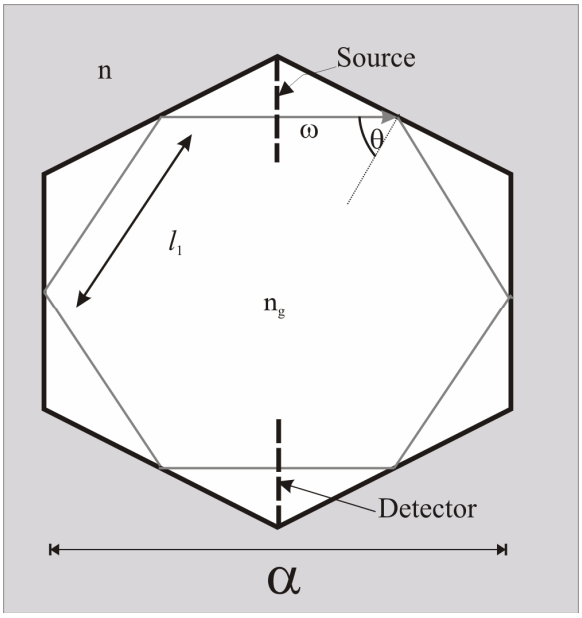


Fig. 1: Regular hexagonal optical cavity showing the optical path of the fundamental wave ω. α is the distance between opposite walls and l_1 is the propagation length between sequential reflections.

modes (provided they are waterfront-matched after each cavity round-trip) , they however have a short cavity life-time.[5, 6] A reflection angle of 60° also guarantees that the length (l_1) between subsequent TIRs in the regular hexagonal cavity is equal, which simplifies the expression for phase compensation.

The first step of the analysis will be to determine by a simplified but effective analytical model the optimal cavity size which supports both a resonance for the FW and provides TIR-QPM for second harmonic generation.

Theoretical Approach

The condition for TIR-QPM is given by the following expression[7]:

$$\phi = \Delta k l_1 + \Delta\Phi_F + \xi\pi = 0 \bmod 2\pi \text{ . Eq. 1}$$

Simultaneous resonance of the FW and SH wave is possible provided that the following conditions are satisfied[7]:

$$k^{\omega} l_1 + \Phi^{\omega} = 0 \bmod \pi \quad \text{Eq. 2}$$

$$k^{2\omega} l_1 + \Phi^{2\omega} = 0 \bmod \pi \quad \text{Eq. 3}$$

Φ^{ω} ($\Phi^{2\omega}$) and k^{ω} l_1 ($k^{2\omega}$ l_1) are the Fresnel and dispersion phase shift of FW (SH wave) on reflection. Upon propagation of FW along l_1, SH signal is generated, with optimum efficiency provided that the TIR-QPM condition is satisfied. To satisfy both the resonance of FW and SH waves and TIR-QPM condition,

Table 1: Results of the cavity dimension at different values of λ_{ω}

λ_{ω}/μm	α/μm	l_c/ μm
0.900	3.369	1.956
1.000	5.133	2.788
1.064	5.973	3.401
1.200	8.978	4.899
1.550	17.47	9.512

a suitable cavity size is determined by identifying an appropriate l_1 that simultuneously satisfies all eqs (1-3) for a given wavelength (λ).

The intensity of the generated SH ($I_{2\omega}$), (assuming no depletion of the FW), can be written as[3]

$$I_{2\omega} = \frac{8\pi^2 d_{eff}^2}{n_{\omega}^2 n_{2\omega} \lambda_{\omega}^2 \varepsilon_0 c} I_{\omega}^2 l_1^2 \left[\frac{\sin(\Delta k l_1/2)}{\Delta k l_1/2}\right]^2 \times \left[\frac{\sin(N\phi/2)}{\sin(\phi/2)}\right]^2 \text{ . Eq. 4}$$

where N is the number of TIR reflections within the cavity, I_{ω} is the FW intensity and λ_{ω} is the wavelength of the FW. Here, unlike the case of resonant TIR-QPM, l_1 does not have to be an exact odd multiple of the coherence length.[2] The value of l_1 is determined by the balance between the dispersion and the relative Fresnel phase shift.
The results of the numerical calculations for the determination of a suitable cavity size and the cavity characteristics showing the resonance of FW for lithium niobate are shown below. Also we show numerical results for the SHG efficiency.

Results

A suitable cavity size was determined by combining the phase matching condition (equation (1)), and wave propagation conditions for FW and SH wave (equations (2-3)) resulting in the following equation[7].

$$\cos(0.5(\Delta k l_1 + \Delta\Phi_f + \xi\pi)) \times \cos(k^{\omega} l_1 + \Phi^{\omega}) \times \cos(k^{2\omega} l_1 + \Phi^{2\omega}) = \pm 1 \quad \text{Eq. 5}$$

In the cavity geometry as shown in figure 1 the z axis of the $LiNbO_3$ crystal is normal to the page and each side of the cavity is along a y-axis of the

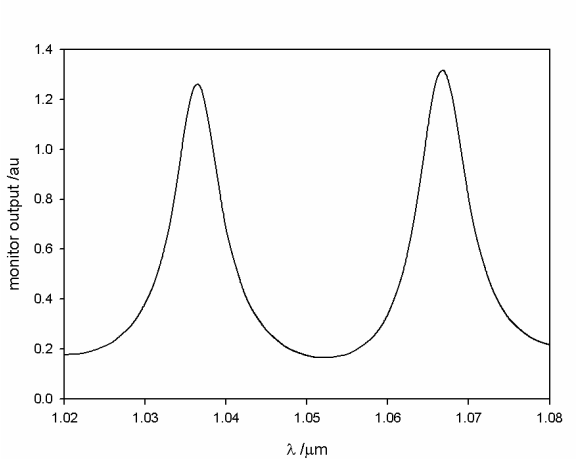


Fig. 2: FSR for FW in a z-cut $LiNbO_3$ regular hexagonal micro-cavity when $\alpha = 5.973$ μm.

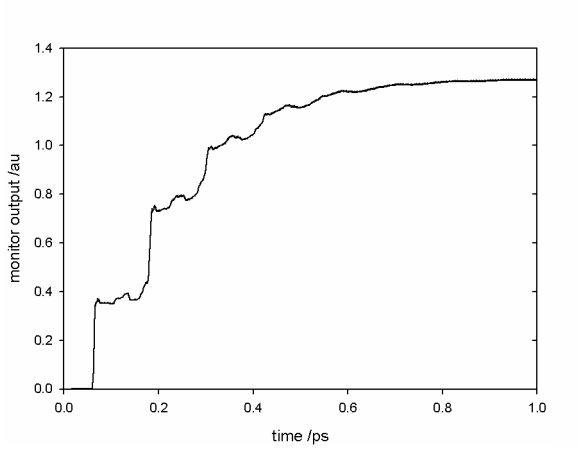


Fig. 3: Cavity build-up for FW in a z-cut $LiNbO_3$ regular hexagonal micro-cavity for $\lambda_\omega = 1.064$ μm.

crystal. In this particular z-cut $LiNbO_3$ cavity geometry, $d_{eff} = d_{33}$ and does not change sign when both FW and SH wave have a polarization parallel to the plane of incidence. Here we consider the first order TIR-QPM as corresponding to the smallest cavity size which satisfies eq (5). Solving eq (5) using the dispersion and Fresnel parameter for a z-cut lithium niobate crystal at a given λ_ω and an incidence angle $\theta = 60^o$ determines the values of l_1 and subsequently the cavity size ($\alpha = 2l_1$) that simultaneously satisfies the FW and SH wave propagation and TIR-QPM conditions. Table 1 contains the cavity dimensions and the coherence lengths determined for the first-order TIR-QPM for a cavity at different values of λ_ω.

A 2-D FDTD simulation tool was employed to carry out the simulation work. Steady-state solutions were obtained for the cavity free spectral range (FSR) and optical power build-up for the FW and SH. The following parameters were employed in this calculation: A c.w. beam at λ_ω (TM polarized, $n_g = n_e(\lambda_\omega)$ and n = 1) was launched from the "source" position in a microcavity and detected by an overlap monitor as shown in fig. 1. Fig. 2 shows the FSR for FW in the micro-cavity with $\alpha = 5.973$μm which corresponds to a solution of eq (5) optimised for TIR-QPM and propagation of both FW and SH wave at $\lambda_\omega = 1.064$ μm. This numerical result was achieved by varying the exciting wavelength for this cavity. The values in fig. 2 are measured after 1ps, (which is long enough to allow steady state to be reached. The FSR is ~ 30 nm which is in good agreement with the theoretical estimate $FSR \approx \lambda^2/3n_g\alpha$ for $\theta = 60^o$.[5] Fig. 3 shows the optical power build-up in the cavity for $\lambda_\omega = 1.064$ μm which reaches a steady state after approximately five round trips (0.8 ps) after which the signal loss balances the input source. The steady state power of the FW can be used to calculate the power of the SH wave. Each cavity round-trip equals six reflections. The FW power in the cavity is maximum after five round-trips which implies N= 30. This N value was used in equation (4) to estimate SHG yield and conversion efficiency. Fig.4 shows a plot of the normalized SH signal growth per round-trip in the cavity. Each curve in the plot of fig. 4 shows the power of the SHG as a function of the reflection angle after a specific round trip. The SH signal growth is about 80% of the maximum obtainable SHG efficiency for $\theta = 60^o$ after five round trips.

Discussion

Microresonators form a very favourable solution for high density integrated optics suitable for a variety of applications, from sensing, to high channel count optical filters for DWDM systems. The integration of additional nonlinear functionalities, such as second harmonic generation will strengthen their role and make more compatible the use of microresonators in integrated optics circuitry. The proposed scheme for SHG via TIR-QPM in a hexagonal microcavity can improve the efficiency and also the compactness of SHG devices compared to traditional linear-type based devices. Based on a simple theoretical model the optimal cavity size could be easily determined. Furthermore numerical simulation results based on Beam Propagation analysis confirmed the solutions obtained by demonstrating resonant operation of the microcavity first in the FW and also in the SH wave produced by TIR-QPM. These results suggest the feasibility of this proposed scheme that could also be extended to higher order polygons.

Although it is evident from the simulation results that the hexagonal optical cavity considered here is a lossy optical structure, this is due to the sharp corners of the cavity. This is a common problem in polygonal resonators and can degrade also the performance of passive devices such as add-drop filters. Lately the use of smoothed round cornered polygonal microresonators has shown the improvement in the Q factor and finesse in such devices[8]. This rounding

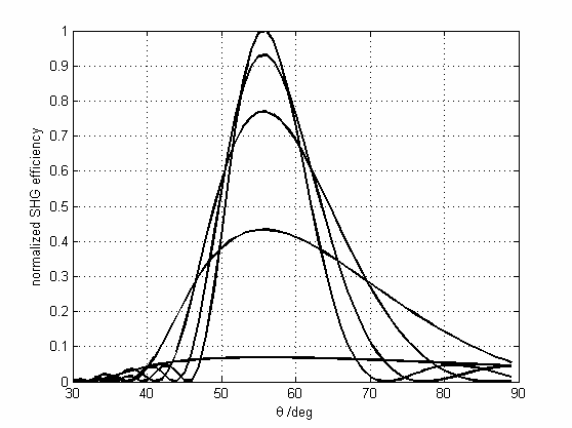


Fig. 2: Growth of the SH wave per round trip in the cavity as a function of the reflection angle. The curve with the highest peak value coresponds to the 5th successive roundtrip.

improved in turn, drastically the actual filtering characteristics of those devices.

However it should be stressed here that the sole purpose of this work is to introduce and demonstrate the concept of SHG via TIR-QPM inside a resonant cavity. Further work is currently in progress in order to consider improved and more realistic implementation of this scheme with hexagonal cavities, or even circular cavities, with the expectation of improving the SHG efficiency. We will further discuss the optimization of such a scheme based on these preliminary results.

Conclusions

We have numerically demonstrated the enhancement of SHG efficiency via TIR-QPM by utilising the resonance of the fundamental beam within a hexagonal micro-cavity with suitable dimensions. Lithium niobate can serve as a useful platform to demonstrate and implement effectively the proposed process because of its high non-linearity and its preferred hexagonal shaped which results during chemical etching of the inverted ferroelectric domains.

Acknowledgment
The authors would like to thank the commonwealth Scholarship for T. J. S, the University of Southampton alleviation fund, the EPSRC Portfolio Partnership in Photonics EP/C515668/1 and the EU STREP 3D-DEMO for financial support.

References

1 J. A. Armstrong, N. Bloembergen, and J. D. P. S. Pershan, Phys. Rev. **127**, 1918 (1962).
2 R. Haidar, N. Forget, P. Kupecek, and E. Rosencher, J. Opt. Soc. Am. B **21**, 1522 (2004).
3 H. Komine, W. H. long, J. W. Tully, and E. A. Stappaerts, Opt. Lett. **23**, 661 (1998).
4 C. L. Sones, S. Mailis, W. S. Brocklesby, R. W. Eason, and J. R. Owen, J. Mater. Chem. **12**, 295 (2002).
5 N. Ma, F. K. L. Tung, S. F. Lui, and A. W. Poon, in *Proc. SPIE*, Photonics West Conference, San Jose, California, 2003), Vol. 4986.
6 N. Ma, in *Dept. Elec. and Electron. Eng.* (The Hong Kong Univ. of Science and Tech., 2004), Vol. MPhil.
7 R. Haidar, Appl. Phys. Lett. **88**, 211102 (2006).
8 C. Li and A. W. Poon, Opt. Lett. **30**, 546 (2005).

Assembly of microsphere chains by counter-propagating, guided waves

Katarina Grujic (1) and Olav Gaute Hellesø (2)
Department of Physics and Technology, University of Tromsø
1) Katarina.Grujic@phys.uit.no 2) ogh@phys.uit.no

Abstract: *Microspheres can be trapped in the evanescent field of an optical waveguide and guided along it. In this work we show how counter-propagating waves in the waveguide can be used to assemble chains of microspheres of arbitrary length.*

Introduction

For light propagating in a dielectric waveguide, a part of the field extends into the cover medium. This evanescent tail can be used to manipulate microparticles suspended in water, provided that the refractive index of the particle is higher than that of the cover medium and the size of the particle is less than about 15µm [1]. The optical forces due to the evanescent field act to guide the particle along the waveguide. The use of waveguides to trap particles combines the possibilities of optical tweezers with the techniques employed in integrated optics. This technique can be used to make a Lab-on-a-Chip for manipulation and sorting of nano- and microparticles [2,3]. We have previously shown that chains of two and more particles are readily formed, and that these chains travel faster than single particles [4]. In this work we have used counter-propagating waves from a high-power laser to move particles both ways and hold it at a fixed position on the waveguide surface. We will show how counter-propagating waves can be used to form chains of arbitrary length in a controlled way.

Experimental configuration and procedure

Channel waveguides were formed in soda-lime glass, using an Al mask with 4 µm wide openings, by Cs^+ ion-exchange in a molten $CsNO_3$ salt at 450ºC for a duration of 24 hours. The resultant waveguides were monomode at 1083nm, which is the wavelength of the laser used. The output power from the laser was in the range 0.5 to 1 W. A directional coupler was used to split the light from the laser 50:50 in two fibres. Light was coupled from the fibres to each end of the waveguide by direct butting. Polystyrene beads (n=1.59) of 7 µm diameter were used. The microspheres were diluted in de-ionized water (n=1.33). The particle solution was confined on top of the waveguide in a volume (usually 20mm × 20mm × 0.1mm) defined by spacers made of PDMS and a glass cover slip on top. Particles were observed with an optical microscope with bright field illumination and a ×50 microscope objective. A digital CCD camera was mounted on top of the microscope, and images were recorded on a computer.

Particles migrate onto the waveguide due to Brownian motion, get trapped in the evanescent field of the waveguide and are guided along it when only one fibre is present. With two fibres and equal power going both ways in the waveguide, the particles should stop. In this work, the fibres were positioned laterally to adjust the power injected into the waveguide. By doing so, particles could be moved both ways along the waveguide, and also stopped at a given location. However, there is some propagation loss in the waveguide, and the power in the two directions will thus be equal over a limited length of the waveguide. Particles moved towards this section from both sides and chains are thus formed. The process is speeded up by adjusting the power in the fibres and moving the growing chain back and forth to sweep up single particles. It also helps that chains tend to move faster than single particles [4] so that the chain will catch up with single particles.

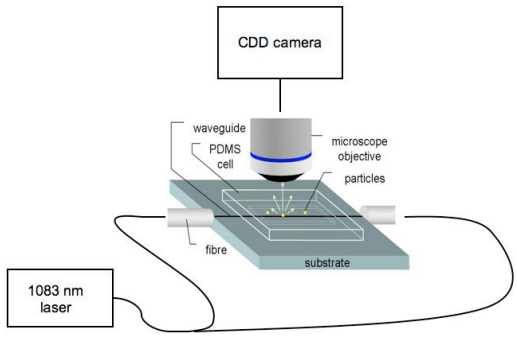


Fig. 1: Set-up with counter-propagating waves in waveguide and microparticles suspended in water in PDMS cell.

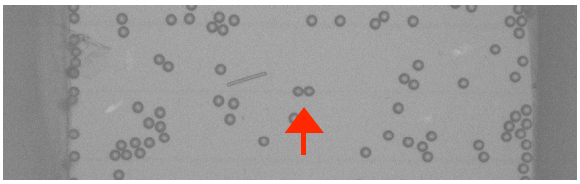


Fig. 2: Two microspheres brought together with counter-propagating waves

Results

In order to show that chains of arbitrary length can be formed, we started by making a chain of only two particles. For this we used a relatively low particle concentration and a short PDMS-cell. A single particle migrated onto the waveguide by Brownian motion and was trapped on the waveguide. It was moved back and forth on the waveguide until a second particle was trapped on the waveguide and eventually was caught up by the first due to a difference in velocity. A single chain of two particles was thus formed, as

shown in fig. 2.

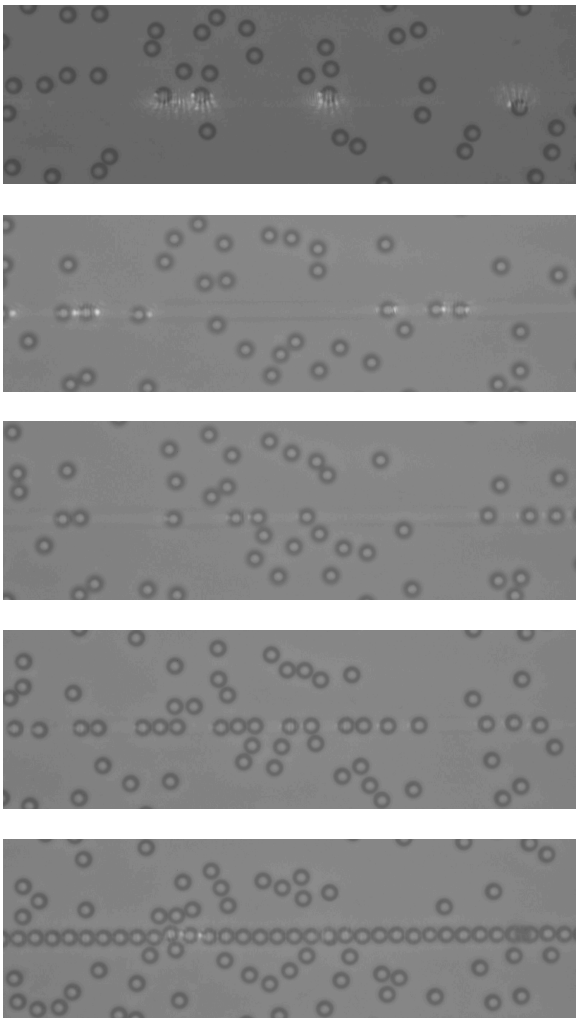


Fig. 3: Sequence of images showing the formation of a chain of microspheres. The upper image is taken with low power in the waveguide, but no IR-filtre. The others are taken when moving the particles back and forth with higher power and an IR-filtre.

By using a higher concentration and a longer PDMS-cell, many particles can be trapped along the waveguide. Some of the particles will form chains at random. By starting out with such a chain and move it back and forth, it will catch up with other particles and thus grow into a long chain. Some images of this sequence are shown in fig. 3. As explained previously, the formation of a chain in this way is both due to chains travelling faster than single chains and due to particles moving from both sides towards the point of equal intensity. Figure 4 gives the velocity of particles at different points along the waveguide. The velocity decreases and eventually changes sign, meaning that the particles move in the opposite direction. This shows that the particles are moving from both sides towards the point of equal intensity. For this measurement, input power was not adjusted, while the microscope was moved along the waveguide.

The velocity of the particle should be approximately proportional to the difference in intensity impinging on the particle from the left versus from the right. The amount of light scattered by the particle is also linear with the incident intensity. The velocity should thus be linearly related to the difference in scattered light on the two sides of the particle, and figure 5 shows this relationship. The intensity of the scattered light was measured by summing up the intensity in an area on each side of the particle, from images like no. 2 in figure 3. This measurement was done for a single particle while adjusting the power in one direction. It is close to a linear relationship between velocity and difference in intensity, as anticipated.

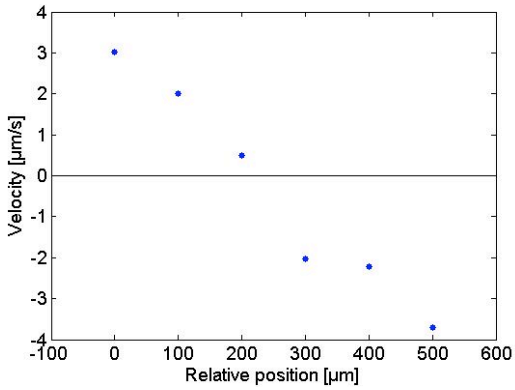


Fig. 4: Velocity of particles vs. relative position along the waveguide.

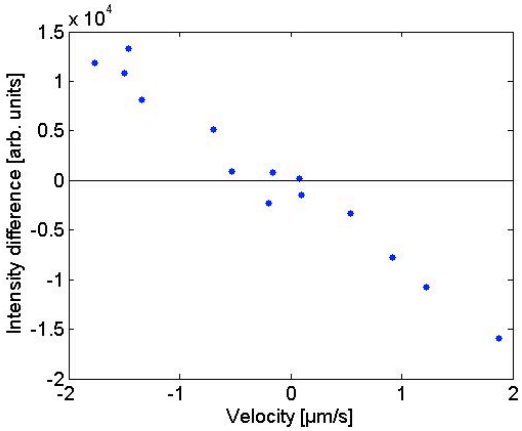


Fig. 5: Difference in intensity of scattered light on two sides of particle, versus velocity of particle.

The laser was linearly polarised, but we did not adjust the fibre output to any particular polarisation. Interference effects were not observed, possibly due to different polarisation for the two beams and also due to the large size of the spheres.

Conclusions

We have shown how counter-propagating waves in an optical waveguide can be used to assemble chains of microspheres. Chains consisting of any number of spheres, from just two up to more than 50, can be assembled in this way. We have also shown that the velocity of the microspheres depends on the position

along the waveguide due to propagation losses, and again that the velocity is linearly dependent on the amount of light scattered by the particle.

Acknowledgements
Support from the NANOMAT-program of the Research Council of Norway is acknowledged.

References

1 K. Grujic, O.G. Hellesø, J.S. Wilkinson, J.P. Hole, 'Optical propulsion of microspheres along a channel waveguide produced by Cs^+ ion-exchange in glass', Optics Comm. **239** 227 2004.
2 K. Grujic, O.G. Hellesø, J.P. Hole & J.S. Wilkinson, Optics Express **13** 1 (2005)
3 S. Gaugiran et al., Optics Express **13** 6956 (2005).
4 K. Grujic, O.G. Hellesø, J.S. Wilkinson, J.P. Hole, 'Microsphere chain formation in the evanescent field of an optical waveguide' ECIO 2005.
5 M. Guillon, 'Field enhancement in a chain of optically bound dipoles', Optics Express **14** 3045 2006.
6 C.D. Mellor and C.D. Bain, 'Array formation in evanescent waves', ChemPhysChem **7** 329 2006.

Integrated optic beam combiners for astronomic interferometry: rapid prototyping of hybrid sol-gel devices

A. Ghasempour[1,2,4], D. Alexandre[1,2,3], C. Brites[1,2], P.J. Moreira[1,4], P.J.V. Garcia[4,5], J. L. Santos[1,2], P.V.S. Marques[1,2] and A.M.P Leite[2]

[1]Unidade de Optoelectrónica e Sistemas Electrónicos – INESC Porto, Portugal
[2]Departamento de Física da Faculdade de Ciências da Universidade do Porto, Portugal
[3]Departamento de Física da Universidade de Trás-os-Montes e Alto Douro, Portugal
[4]Centro de Astrofísica da Universidade do Porto, Portugal
[5]Departamento de Engenharia Física da Faculdade de Engenharia da Universidade do Porto, Portugal

Abstract: *Results concerning the design, fabrication and characterization of a multiaxial two beam combiner for astronomical interferometry are presented. The devices were fabricated in hybrid sol-gel materials in conjunction with laser direct writing techniques.*

1. Introduction

Long baseline optical (1μm<λ<10μm) astronomical interferometry is an emerging technology allowing angular resolutions an order of magnitude larger than the largest available telescopes [1]. Existing arrays, with telescopes separated by 200m baselines, are able to reach angular resolutions in the near infrared (λ~1μm) of the order of 5 pico-radians. In contrast, the largest telescopes (10m diameter) only reach 0.1 μradians. As the technology matures the number of telescopes in the arrays increases and instruments are now under design to combine up to 8 telescopes [2]. Single mode guided wave optics has a great potential for the implementation of several critical functions (e.g. beam transportation, equalization, combination and metrology) for these broadband single mode interferometers both in ground [3] and space [4]. Integrated optics beam combination devices can be implemented using different basic schemes [3]. The coaxial combination arrangement (similar to the configuration of the Michelson interferometer) can be implemented with cascaded Y-junctions [5], for field splitting and combination. The multiaxial combination scheme (similar to that of the classical Young's interferometer) can be constructed through angularly coded propagation of nearly collimated guided waves in planar waveguide sections [6], as discussed below. Photometry channels can be included to allow for the correction of the interferometric raw signals in terms of unequal beam powers due to atmospheric thurbulence. The interferometer arrangements can vary from "pair-wise" to "all-in-one" combination [10]. Fundamental aspects, such as preservation of polarization and broadband response have to be taken into account in the guided wave designs.

Co-axial beam combiners demonstrators at H (λ~1.6μm) and K (λ~2.2 μm) astronomical bands have been fabricated with ion-exchange in glass and silica-on-silicon technologies [5, 7, 8], some including metrology functions integrated with the science beam combiner [9]. In this paper we focus on the fabrication of a multi-axial beam combiner using hybrid sol-gel technology for the J astronomical band (λ~1.2 μm).

2. Hybrid sol-gel technology

The hybrid sol-gel technology offers an interesting potential for simplified fabrication and rapid prototyping of integrated optic devices [11], as low temperature processing is used, thick optical layers can be achieved in a single deposition and no reactive ion etching is needed. Using the MAPTMS-ZrO_2 material system and UV laser patterning, channel waveguides and devices have been demonstrated, without recourse to photoinitiator [12]. As this material system allows direct photopatterning, it is quite suitable for testing of designs and verification of concepts.

A laser photopatterning system has been developed which can produce masks on special plates with a focussed laser beam (532 nm), or write directly the integrated optic hybrid sol-gel device using a UV laser (244 nm). The laser writer is computer controlled, uses the output CAD files from an integrated optics simulation package, and the pattern is written by X-Y displacement of crossed precision translation stages (2nm resolution) under the dynamically focussed laser beam. Figure 1 shows the laser direct writing machine developed and the multiaxial two beam combiner produced.

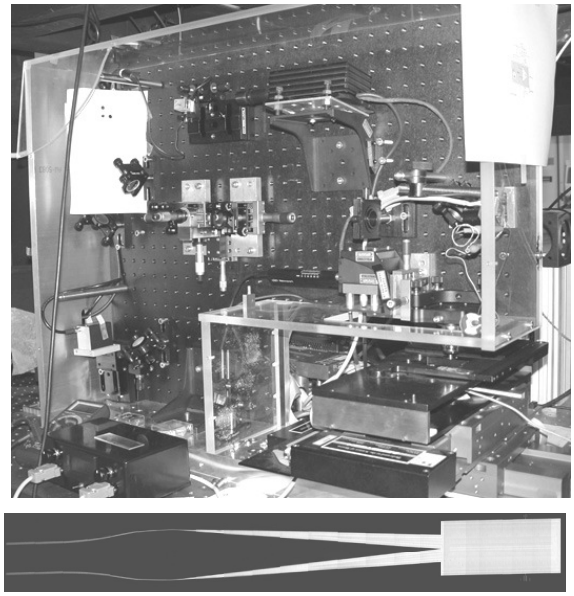


Figure 1 – Photograph of the laser direct writing unit and picture of the multiaxial two beam combiner written in mask photoblanks

Loss levels measured on single mode sol-gel channel waveguides are 0.4dBcm^{-1} @ 1300 nm, which are acceptable from the point of view of rapid prototyping. High performance devices should, however, employ lower loss silica waveguides, but their design follows very similar rules to those applied in the sol-gel case.

3. Design of integrated optics beam combiners

The design of the prototypes of several configurations of coaxial and multiaxial beam combiners for the J band used a BPM-CAD commercial software package (Optiwave). Channel waveguides were designed with a square core (typically $4\times4\,\mu m^2$) to guide a single mode and couple efficiently to single mode fibres. Elements such as S-bends, X-crossings, Y-junctions and waveguide tapers were individually studied and optimized. Figure 2 shows the amplitude of the field in a coaxial two beam combiner with photometry outputs, based on Y-junctions.

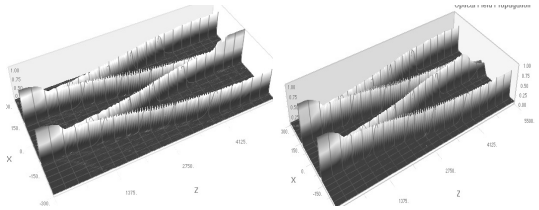


Figure 2 – Field amplitude along the two beam combiner for inputs in phase and π out of phase.

For an even number N of input beams, the design of a coaxial all-in-one beam combiner follows almost directly from the design for N=2. However, in the case of N odd, the design is slightly more complex, as it is of fundamental importance to ensure that all interfering optical paths have the same length for correct broadband operation.

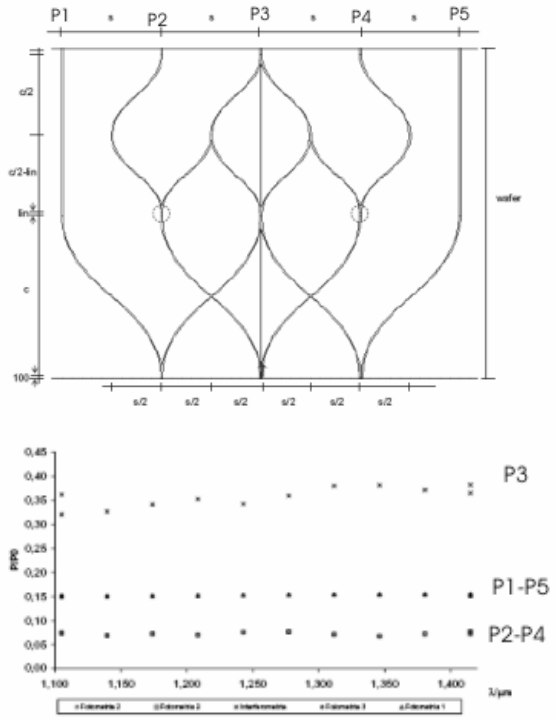


Figure 3 – (a) Schematic layout of a three beam combiner and (b) power output as a function of wavelength.

Figure 3 shows the layout for a N=3 device with photometry outputs, and the results of its simulation.

The design of multiaxial combiners was also addressed, and Figure 4 displays a configuration for N=3. Waveguide tapers are employed to achieve adiabatic expansion of the square core channel waveguide field to the fundamental mode of a rectangular core waveguide at the taper end ($150\times4\mu m^2$), in order to ensure nearly collimated beams in the planar waveguide section. The taper axis angles δ_i must be chosen carefully in order to result in interference fringe patterns with different periods for each beam pair combination, in order to discriminate between the interferometric spatial patterns. The radius R of the planar waveguide region and the angular separation of the taper ends must ensure that no coupling occurs between neighbour waveguides.

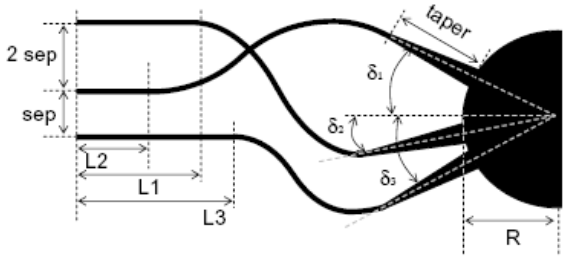


Figure 4 – Schematic representation of a multi-axial beam combiner (in this case, $\delta_1 > 0, \delta_{2,3} < 0$).

The spatial frequency f_{ij} of the pattern for the (i, j) beam pair is given by

$f_{ij} = C\left|\sin\delta_i - \sin\delta_j\right|$, where $C = n_{eff} / \lambda_0$, n_{eff} is the effective index of the fundamental mode in the planar region and λ_0 is the vacuum wavelength. The spatial frequencies can be arranged in a $1f_0$, $2f_0$, $3f_0$ series, where f_0 is the lowest frequency (which depends on the specification of the transverse magnification M_T of the optical system used for fringe detection, and on the CCD detector pixel period d_{pixel}; the maximum frequency $3f_0$ should be $M_T / 2d_{pixel}$ in order to achieve accurate recording of the pattern). Additional information is necessary to calculate a unique solution; the criterion used was to specify a symmetric angular aperture to cover all taper axes (in this example, $\delta_1 = -\delta_3$), resulting in

$$\delta_1 = -\delta_3 = \arcsin\left[\frac{3\lambda_0 f_0}{2n_{eff}}\right]; \delta_2 = -\arcsin\left[\frac{\lambda_0 f_0}{2n_{eff}}\right]$$

Figure 5 shows the layout of a 2 beam combiner and respective field distribution in the interference region. Photometry outputs were not included, but were used in other designs. Particular care was taken in the design of S-bends to avoid field distortion at the tapers inputs.

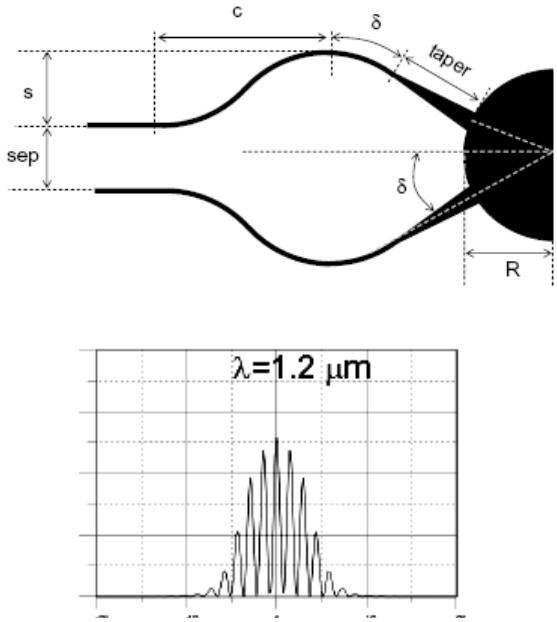


Figure 5 – Schematic representation of a two beam combiner and intensity distribution at the output plane.

The modal field amplitudes have a distribution which causes modulation of the fringe pattern, as shown in Figure 5. This implies a certain spatial frequency bandwidth for each interference pattern, thus forcing a minimum separation between the centre frequencies ($n\times f_0$) of the fringe patterns in order to separate them in the signal processing stage, for N>2.

The N=3 combiner design presents more problems, as the channel waveguides feeding the tapers must provide optical path equalization over the specified radiation bandwidth in order to keep the white-light fringe well centred and maximum for equal input

phases. This resulted in the design of Figure 4, which employs an X-crossing and adjustment of the input fibre positions.

4. Experimental results

The production of a master mask used a Canyon Materials Inc photomask blank and laser direct writing (532nm). Amplitude masks were subsequently replicated on fused silica substrates, using standard lithography techniques.

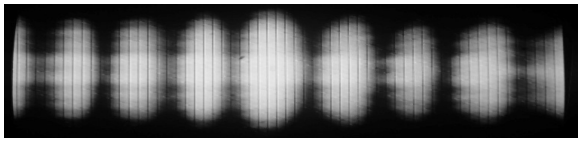


Figure 6 – Experimental intensity pattern at device output imaged in the sensor of a vidicon camera using a 4× microscope objective lens, using a semiconductor laser at 1.3μm. The spatial period is ≈ 20.5μm, in good accordance with the expected value (20.0μm). The vertical lines are an artefact of the image.

The sol-gel core layer is 4 μm thick, and was deposited on soda-lime substrates using spin coating (n_{core}=1.5076.@ λ_0=1302 nm). The cladding layer (n_{clad}=1.4976.@ λ_0=1302 nm) was also deposited by spinning, and has a thickness of 15μm. The detailed fabrication procedure is described in [12].

Coaxial all-in-one two and three beam combiners, and a two beam multiaxial device, were fabricated and tested for their basic functionality. Figure 6 shows the example of the output fringe pattern obtained from the multiaxial device at λ=1.3μm, as captured using a 4× microscope objective at a distance of 138 cm from an infrared camera linked to an image processing system. The spatial period measured is 20.5 μm, in good agreement with the calculated value. Further tests are under way in this and other devices, in order to extract data on polarization and chromatic performance.

5. Conclusions

We presented the first fabrication of multiaxial beam combiners using hybrid sol-gel technology. Their optical properties open the possibility of using these devices in the J astronomical band. The combination of an integrated optics simulation-CAD package with a laser writing machine, linked to the use of hybrid sol-gel technology, provides a useful solution to rapid prototyping of complex integrated optic devices, such as beam combiners used in astronomic interferometry. Design considerations were adressed and experimental results of a multiaxial two beam combiner were presented. Other implementations are presently under investigation.

Acknowledgments

AG is supported by a doctoral fellowship SFRH/BD/24493/2005 approved by FCT and POCI, with funds from the European community programme FEDER. This work was partially supported by the EU FP6 under contract number RII3-Ct-2004-001566 (OPTICON).

References

1. Monnier J.D., Rep. Prog. Phys. **66**, 789-857 (2003).
2. Malbet, F. et al., in proceedings of SPIE **5491**. Edited by Wesley A. Traub, pag. 439 (2004)
3. Malbet F., et al, Astron. Astrophys. Suppl. Ser. 138, 135-145 (1999).
4. Olivier S., et al, J. Opt. A: Pure Appl. Opt. **7**, 660-662 (2005).
5. Berger J.P., et al, Astron Astrophys. Suppl. Ser. **139,** 173-177 (1999).
6. Schanen-Duport I., et al, Appl. Opt. **33,** 5954-5958 (1994).
7. LeBouquin J.-B., et al, Astron. Astrophys. **424**, 719-726 (2004).
8. LeBouquin J.-B., et al, Astron. Astrophys. **450**, 1259-1264 (2006).
9. Collomb V., et al, ECIO'05, post-deadline paper (2005).
10. LeBouquin J.-B., Proc. SPIE **5491**, 1362-1369 (2004).
11. Andrews M.P., Najafi S.I., (eds), SPIE **CR-68** (1997).
12. Moreira P.J., et al, Phot. Technol. Lett. **17**, 399-401 (2005).

Zero transmission narrow band laser mirror using a waveguide grating under normal incidence

Nikolai Lyndin (2), Nathalie Destouches (1), Tina Clausnitzer (3), Svetlen Tonchev (4), Olivier Parriaux (1)

1 Laboratoire Hubert Curien UMR 5516 (formerly LTSI), Université Jean Monnet, F-42000 Saint-Etienne, parriaux@univ-st-etienne.fr
2 Institute of General Physics, Vavilova 38, 117942 Moscow, Russian Federation
3 Institut für Angewandte Physik, Friedrich-Schiller Universität, Max-Wien Platz 1, 07743 Jena, Germany
4 On leave from the Institute of Solid State Physics, Sofia, Bulgaria

Abstract: *A resonant grating mirror comprizing a multilayer submirror and a grating waveguide submirror exhibiting constructive mutual reflection is shown experimentally to provide zero transmission at resonance. Its reflection line width of less than 2 nm, its polarization selectivity and low overall loss make the device useable as a longitudinal mode filter in a disk laser in the 1000-1100 nm wavelength range.*

Introduction

Waveguide grating mirrors based on the excitation under normal incidence of a guided mode of a high index layer belonging to a multilayer mirror have been shown to induce into said multilayer mirror a dichroic character [1]. This resonant effect can be used in multilayer laser mirrors to monolithically control the polarization of the emission. The direction of linear polarization is controlled by means of a rectilinear grating [2] whereas a circular grating permits the generation of the radially polarized mode as shown in a high power Nd:YAG laser [3]. The resonance is designed to be broad so as to cover the entire gain bandwidth of the laser active medium.

The present paper reports on a different application of a waveguide mirror to the control of laser emission. The objective is here to achieve very close to 100% resonant reflection under normal incidence and the narrowest possible reflection peak in order to select a single longitudinal laser mode. Such function is needed in interferometry and for second harmonic generation for instance.

Operation principle of a narrow band waveguide laser mirror.

The principle is the same as in the polarization filtering resonant mirror exhibiting constructive interference between the broad band ground reflection provided by a multilayer submirror and that provided by the waveguide resonance [2].

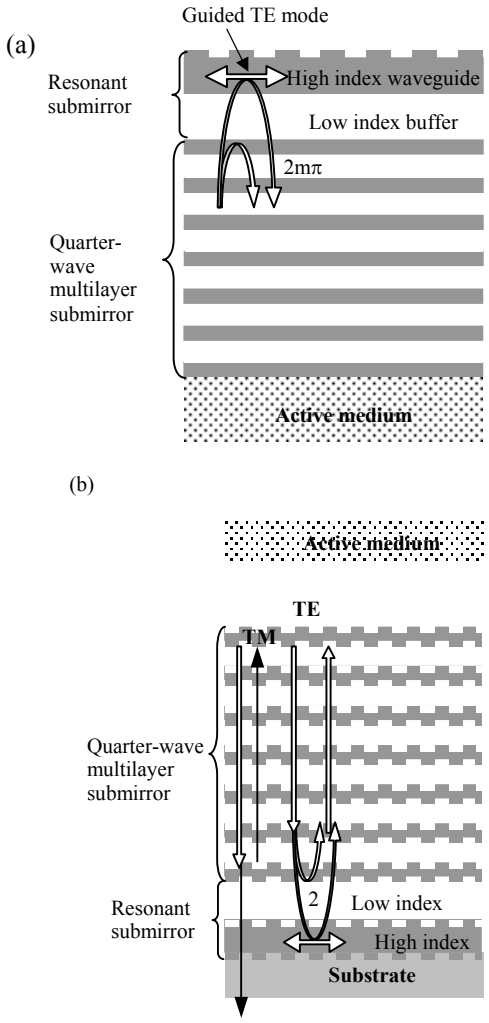


Fig. 1: (a) Operation principle of a polarizing mirror integrated to the active medium [2], (b) of a longitudinal mode filter. In both structures light experiences constructive interference between multilayer and resonant submirrors.

Figure 1a) is the sketch of the corresponding polarizing resonant mirror. The mirror in the present application is the stand alone rear mirror of an extended cavity laser. As a consequence, the reflection threshold provided by the very low loss multilayer submirror must be as high as possible, leaving only a few percents of reflection to the highly selective waveguide submirror, the only concern being that the spectral components outside the reflection peak do not lase. It must be looking at the inside of the laser cavity, its substrate being outside the cavity. Consequently, the resonant submirror must be located past the multilayer submirror on the way of the incident wave. This imposes the somewhat unusual configuration sketched in Figure 1b) where the mirror substrate gets first corrugated, then the resonant waveguide submirror layers are deposited as well as the layers of the multilayer submirror at once in the said order. It is important to point out that we are making use here of a resonant diffraction mechanism where the field in the waveguide is so large that a very shallow corrugation of hardly 15 nm depth is sufficient to give rise to high reflection. The layer deposition technology will be that of ion plating [4] which ensures a conformal reproduction of the corrugation amplitude up to a large number of layers.

The most important element in the multilayer system is the grating waveguide placed on top of the corrugated substrate. The whole synthesis of this element is made on the basis of the physical understanding of waveguide grating resonances first developed by Sychugov and team in the mid eighties [5]. The grating waveguide is well isolated from the multilayer by the thick low index buffer layer. It is symmetrical (double corrugation and cover and substrate index nearly identical). In addition, the waveguiding layer with its 240 nm thickness of Ta_2O_5 of 2.18 index is very close to a half wave layer. This implies that the modulus of resonant reflection shows as a single peak with zero offset and no side dip; as a consequence, the resonant reflection can be simply placed as a quasi symmetrical peak on top of the multilayer ground reflection. Fig. 2 shows that the transmission dip of the sole high index corrugated waveguiding layer surrounded by SiO_2 at both sides in the described conditions is symmetrical. The transmission falls from quasi 100% to zero as expected. The grating has a 559 nm period and a 21.6 nm deep sinusoidal corrugation. The transmission of the complete multilayer structure is represented by the dotted line of Fig. 2; it confirms that the two submirror reflections superpose constructively.

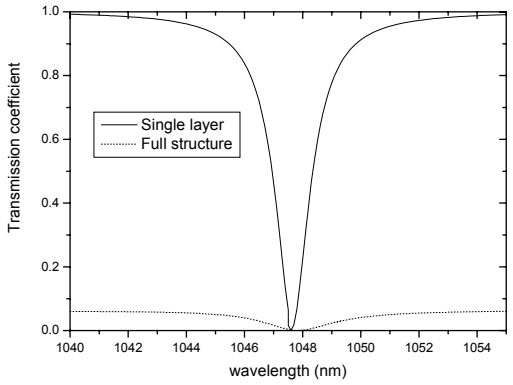


Fig. 2: Calculated transmission coefficient of the complete resonant mirror (doted line) and of the sole waveguide submirror (full line) versus wavelength in the resonance neighbourhood.

Figure 3 is the optimised reflection spectrum of the TE polarization, assuming plane wave incidence and infinite grating length; it extends to the green region because the mirror has the additional function of reflecting the second harmonics as well. The optimization was made by means of Lyndin's code using the C-method [6].

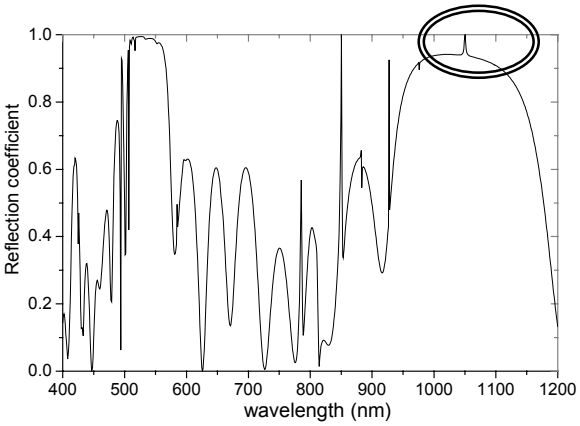


Fig. 3: Reflection coefficient of the optimised structure versus wavelength in the visible and IR regions with a peak at 1050 nm.

As shown in Fig. 4, the TE_0 waveguide mode field at resonance is well concentrated in the bottom high index layer.

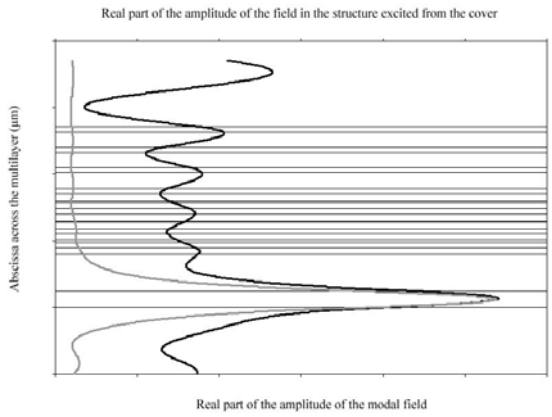


Fig. 4: Transverse electric field profile in the multilayer. Grey curve: TE_0 modal field, Black curve: field profile upon excitation from the air side. The horizontal lines show the different layers of the stack.

Experiment

The grating corrugation in the fused quartz substrate is obtained by first exposing a 300 nm thick positive resist layer to an interferogramme at the HeCd laser wavelength of 442 nm, then by reactive ion beam etching into the silica surface. The obtained depth is 17 nm. The multilayer is then deposited by ion plating [4]. The AFM scan of the surface after the deposition of the 2706 nm thick multilayer is also essentially binary with a depth of 23 nm.

Figure 5 is the spectral measurement of the TE polarized transmission of the complete structure around 1050 nm wavelength. It reveals under normal incidence a sharp and deep dip on a wide band transmission background. The measurements were made by using an optical fibre white light supercontinuum and a spectrometer of the type ANDO AQ-6315A Optical Spectrum analyzer ensuring a spectral resolution of 0.1 nm. The high spatial coherence of the source permits the separation between the angular and spectral effects. The beam diameter is about 1 mm. Index matching a prism at the backside of the grating substrate with glycerol (insert of Fig. 5), whose refractive index matches that of the silica substrate, reduces the oscillations due to the backside reflection and the resulting interference. This leads to the spectacular transmission spectra of figure 5 revealing that the TE line width is as small as 2.2 nm and that the transmission is practically cancelled. The transmission at resonance is two orders of magnitude below the off-resonance transmission. It is at the detection limit of the detector. Remarkable also is the fact that the resonance wavelength is only 1 nm away from the expected nominal resonance wavelength taking into account the experimental values of the grating period and depth in the calculations. This is a result of the good control which ion plating ensures on the layer index and thickness. The experimental transmission curve exhibits a double dip which infers that the incidence is not exactly normal. Experimentally, the autocollimation reference is defined at a resolution better than 0.02 degree. This is confirmed by calculating the theoretical transmission coefficient of the structure if illuminated under an incidence angle of 0.015°: the resulting spectrum (dashed curve in Figure 5) exhibits the same feature as the experimental curve with exactly the same 0.6 nm distance between the two dips. The line width under oblique incidence is proportional to the radiation coefficient α of the grating waveguide; in other words it scales as the square of the grating depth for small depths [7].

Figure 6 refers to a transmission measurement. Nothing presently tells that zero transmission amounts to exactly 100% reflection at resonance. Reflection measurements are very difficult to make with high precision. This will be the subject of further experimental studies.

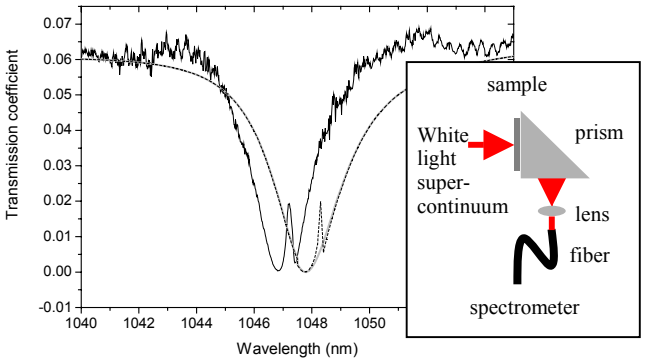


Fig. 5: Transmission coefficient of the structure around 1050 nm after suppression of backside reflection (insert). The grey curve is the theoretical transmission coefficient taking into account the measured grating parameters (period of 559.1 nm and depth of 17 nm). The dashed curve is the theoretical spectrum obtained under an incidence angle of 0.015°

Conclusion

The present paper reports on the demonstration of a further optical function that a waveguide grating can

perform for laser control: line narrowing leading to longitudinal mode filtering. It is demonstrated that the constructive association between a broadband multilayer and a waveguide grating permits to fully benefit from the narrow filtering property of waveguide grating resonant reflection without the penalty of its absorption and scattering losses. The design of the resonant mirror is made via an intelligible synthesis process based on field diffraction and interference, only the optimisation step being left to numerical modelling. A line as narrow as 2 nm is obtained at 1050 nm wavelength for a beam of 400 nm diameter by an embedded binary grating of 17 nm depth. A remarkable feature is the achievement of practically zero transmission at resonance by means of a multilayer structure having all interfaces corrugated.

Acknowledgement
The authors want to thank J.Cl Pommier for performing the RIB-etching of the quartz grating and S. Reynaud for the AFM scans. This work is part of an initiative on resonant gratings within the European network of excellence on microoptics NEMO.

References

1. F. Pigeon et al., IEEE Photon.Technol. Lett., vol. 12, p. 648, 2000.
2. J.-F. Bisson et al., Appl. Phys. B, vol. 85, p. 519, 2006.
3. T. Moser et al., Laser Phys. Lett., vol. 1, p. 234, 2004.
4. S. Schlichtherle et al., Vakuum in Forschung und Praxis, vol. 17, p. 210, 2005.
5. G.A. Golubenko et al., Sov. J. Quantum Electron., vol. 15, p.886, 1985.
6. A.V. Tishchenko et al., Workshop on grating theory, Clermont-Ferrand, France, June 2004.
7. I.A. Avrutsky et al., J. Mod. Opt., vol. 36, p. 1527, 1989.

Enhanced Transmission in Dynamically Tuned Optical Microresonator Possessing Highly Dispersive Media

Curtis W. Neff (1), L. Mauritz Andersson (2) and Min Qiu (3)
Laboratory of Optics, Photonics and Quantum Electronics
Department of Microelectronics and Applied Physics, Royal Institute of Technology (KTH)
Electrum 229, 164 40 Kista, Sweden
1) curtisn@kth.se 2) mauritza@kth.se 3) min@kth.se

Abstract: *We present a theoretical study of an optical microresonator system which contains a electromagnetically induced transparency medium within the resonator. We find that a time-dependent tuning of the dispersive properties of the resonator medium results in an enhanced transmission spectrum.*

Introduction

Many interesting optical phenomena, such as electromagnetically induced transparency (EIT) and ultraslow light propagation have been observed in highly dispersive media [1, 2]. Additionally, the introduction of a highly dispersive media into an optical cavity results in dramatic narrowing of spectral features as well as enhancing cavity lifetimes [3, 4, 5].

At the heart of EIT is a resonance condition established by a quantum interference effect known as coherent population trapping [6]. Figure 1 is a schematic of one such atomic arrangement known as the Λ scheme which exhibits EIT. The system consists of three atomic energy levels *a*, *b* and *c*, where *b* and *c* are long-lived lower levels. EIT in this system is observed by applying two electromagnetic fields to the medium, a control field E_c and a probe field E_p. When the control field is tuned to the resonance frequency of the *ac*-transition, a transparency window opens for the probe field if the two-photon resonance condition is fulfilled. (Throughout this work we assume that the probe pulse is weak in comparison to the control field.) When two-photon resonance is satisfied, the single absorption peak in Im$\{\varepsilon\}$ splits into two peaks, dashed and solid line respectively in Figure 2(b), that are separated symmetrically on the *ab*-transition resonance frequency, ω_{ab}. The two peaks are also separated spectrally in a magnitude equal to the control field Rabi frequency, $\Omega_c = p_{ac}E_c/\hbar$, where p_{ac} is the dipole moment of the *ac*-transition. Since the absorption is near zero around ω_{ab}, a probe field with that frequency is not absorbed as it propagates through the EIT medium. However, the frequency region around the transmission window is highly dispersive as shown by the solid line in Figure 2(a). It is this extreme dispersion which accounts for the line-width narrowing and enhanced lifetimes in a resonator cavity which contains this type of medium. In fact, as the dispersion increases, the line-widths increasingly narrow and the cavity lifetimes lengthen. However, simultaneously, the system becomes bandwidth limited as the absorption peaks move closer together. To circumvent this effect, one could imagine that a dynamic change in Ω_c could allow an increased performance of the resonant cavity system.

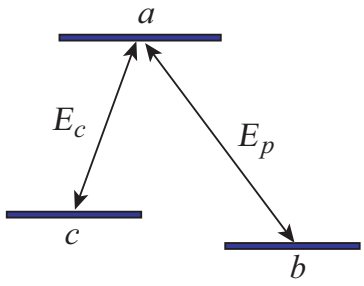


Fig. 1: Schematic of the energy levels in a three level Λ system.

Calculation method

Recently, we described a finite-difference time-domain (FDTD) technique capable of modelling EIT [7] and incorporating a dynamic control field Rabi frequency . The algorithm utilized an implementation of the auxiliary differential equation (ADE) method [8] and a representation of the dielectric constant which is connected to experimental parameters, such as Ω_c. Such an implementation of the FDTD method allows EIT media and arbitrary dielectric structures to occupy the same computational domain, a task not easily realizable in other calculations methods, such as the Maxwell-Bloch algorithm [9].

The susceptibility of a three-level EIT medium can be expressed as [10]

$$\chi(\Delta) = -\frac{N|p_{ab}|^2}{\varepsilon_0\hbar}\frac{\Delta + i\gamma_{bc}}{(\Delta + i\gamma_{bc})(\Delta + i\gamma_{ab}) - \Omega_c^2/4}, \quad (1)$$

where $\Delta = \omega - \omega_{ab}$ is the probe beam detuning from the resonance frequency ω_{ab} of the *ab*-transition, γ_{ab} is the loss due to the *ab*-transition, Ω_c is the Rabi frequency of the control field, γ_{bc} is the decoherence rate, N is the density of excitation centers, and the p_{ab} is the dipole moment of the *ab*-transition. Assuming $\chi \ll 1$, we used a pole expansion to arrive at an exact, complex two-pole representation of the relative permittivity:

$$\varepsilon = \varepsilon_b + \sum_{l=1}^{M}\left(\frac{A_l}{B_l + i\omega}\right), \quad M = 2, \quad (2)$$

where ε_b is the background dielectric constant and A_l

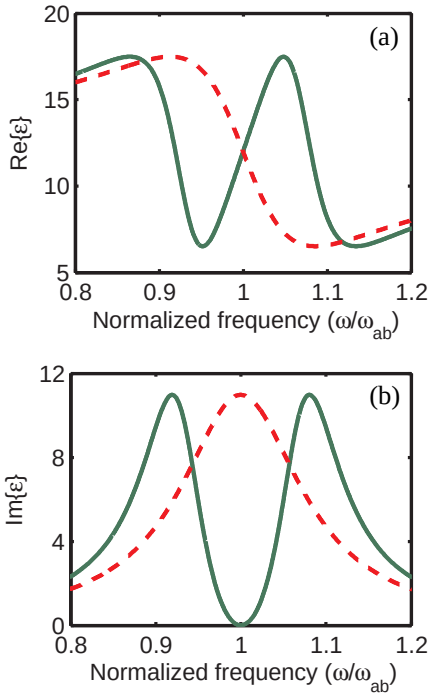


Fig. 2: (a) Real and (b) imaginary parts of the permittivity of an EIT medium when the control field is on (solid) or off (dashed).

and B_l are complex coefficients given by

$$A_l = \frac{iN|p_{ab}|^2}{2\varepsilon_0\hbar}\left\{-1 + i^{(2l)}\frac{(\gamma_{bc}-\gamma_{ab})}{\left[(\gamma_{bc}-\gamma_{ab})^2-\Omega_c^2\right]^{1/2}}\right\}, \quad (3)$$

and

$$B_l = -i\omega_{ab} + \frac{1}{2}\left\{\gamma_{bc}+\gamma_{ab} + \right.$$
$$\left. + (-1)^l\left[(\gamma_{bc}-\gamma_{ab})^2-\Omega_c^2\right]^{1/2}\right\}. \quad (4)$$

The standard FDTD implementations are then performed in combination with the ADE method [8] to derive the field-update equations. In all, the update algorithm involves only one extra step since a polarization current term was introduced into the equations to link the frequency dependence of ε into the algorithm. Thus, the performance of the FDTD calculations do not suffer severely from the inclusion of dispersive media. For convenience, we normalize frequencies by ω_{ab} since the FDTD calculations are performed with a unit length that is normalized by the wavelength of interest.

Microresonator structure

To study the impact of a dynamically changing EIT medium inside of a optical resonator, we used our EIT FDTD code to perform two-dimensional calculations on the corrugated waveguide microcavity system shown in Figure 3. Previous studies found that the introduction of a highly dispersive medium in the cavity of this system had the effect of increasing the *Q*-factor while decreasing the transmission line-width of

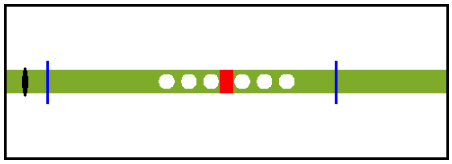


Fig. 3: Geometry of the microcavity waveguide system used for calculating the effect of a dynamically changing EIT medium inside of a optical resonator. The shaded region indicates the area that contained the EIT medium.

the waveguide [5]. However in those calculations, the EIT region was under a static Rabi frequency configuration, e.g. the permittivity of the EIT did not change as a function of time.

As shown in Figure 3, a silicon waveguide was defined in an air background in the center of the computational domain. A periodic arrangement of three air holes, lattice spacing a and radius $0.35a$, were positioned on each side of an EIT region in the waveguide to form a resonator cavity. The holes act as partially transmitting Bragg mirrors, and the cavity was $1.4a$ in width. The source pulse was TE-polarized (E-field within the plane of the paper) and propagated from left to right starting from the black vertical line on the far left of the waveguide. Detectors were located at the vertical lines on either side of the microcavity as indicated. Only the material in the cavity of the waveguide was an EIT medium, as indicated by the darker color in Figure 3, with a permittivity given by Equation (2). The computational domain is terminated on all sides by a perfectly-matched-layer absorbing boundary condition to avoid reflections from the domain boundaries. The EIT material was designed such that the *ab*-transition frequency coincided with the resonance frequency of the cavity.

At the beginning of the calculation, the control field Rabi frequency Ω_c/ω_{ab} was set to 0.1612. The permittivity of the EIT in this state is given by the solid line in Figure 2. Then, after the resonance of the cavity was allowed to establish, Ω_c/ω_{ab} was linearly decreased to 0.0 (the 'off' state which is given by the dashed line in Figure 2) over the period of 1000 time steps. The Rabi frequency was left in the off state for the remainder of the calculation.

Results

Figure 4 shows the power spectrum of the input pulse (dashed line) and of the resonator cavity (solid line) after the control field is turned off. As shown, the power increased almost an order of magnitude due to the dynamic tuning of Ω_c. The total power in the cavity was calculated from the data collected by the two detectors and was found to be slightly less than that of the input pulse. Thus, the increase of power at the ω_{ab} is not in violation of the conservation of energy. Physically, one can understand this as a squeezing of the energy

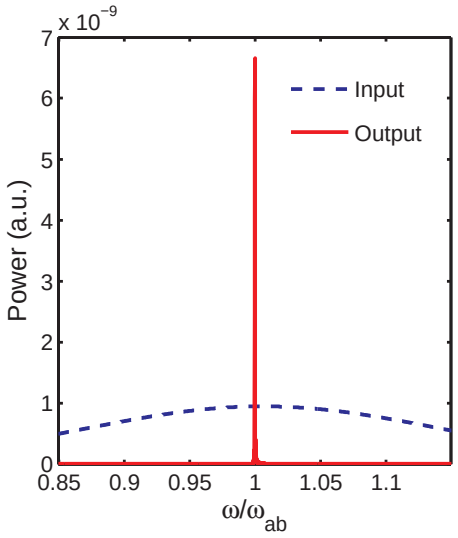


Fig. 4: Power spectrum of the input pulse (dashed) and of the cavity (solid) after the control field was turned off.

of the cavity resonance into the single frequency of the *ab*-transition by the dynamic change in the steep dispersion of the EIT. Since we have assumed a zero decoherence rate, the dominating limitation of this system is the radiation of the cavity to the surroundings above and below the cavity region.

Conclusion

We modelled a microcavity resonator system which possesses a dynamic, highly dispersive medium (such as an EIT medium) inside of the resonator cavity. We showed that the dynamic tuning of such a microresonator cavity shows a response where the power of the cavity mode is channelled into a single frequency, increasing the power output and the lifetime of the cavity dramatically.

Acknowledgments

Funding for this work was through the Swedish Foundation for Strategic Research (SSF) under the INGVAR program, the SSF Strategic Research Center in Photonics, and the Swedish Research Council (VR).

References

[1] K.-J. Boller et al, Phys. Rev. Lett., no. 66, p. 2593, 1991.

[2] L. V. Hau et al, Nature, no. 397, p. 594, 1999.

[3] G. Müller et al, Phys. Rev. A, no. 56, p. 2385, 1997.

[4] M. D. Lukin et al, Opt. Lett., no. 23, p. 295, 1998.

[5] M. Soljačić et al, Phys. Rev. E, no. 71, p. 026602, 2005.

[6] G. Alzetta et al, Nuovo Cimento B, no. 36, p. 5, 1976.

[7] C. W. Neff et al, submitted for publication, 2006.

[8] A. Taflove and S. C. Hagness, *Computational Electrodynamics: the Finite-difference Time-domain Method* (Artech House, Boston), Chap. 9., 2000.

[9] P. Arve et al, Phys. Rev. A, no. 69, p. 063809-1, 2004.

[10] M. O. Scully and M. S. Zubairy, *Quantum Optics* (Cambridge University Press, Cambridge), 1997.

[11] D. F. Phillips et al, Phys. Rev. Lett., no. 86, p. 783, 2001.

[12] M. Okoniewski et al, IEEE Micro. Guided Wave Lett., no. 7, p. 121, 1997.

[13] P. Jänes et al, J. Lightwave Technol., no. 23, p. 3893, 2005.

Noise and resolution in IO interferometric sensing

Hugo J.W.M. Hoekstra, Paul V. Lambeck, Ton M. Koster and Henri P. Uranus
IOMS group, MESA Research Institute, University of Twente; e-mail: h.j.w.m.hoekstra@ewi.utwente.nl

Abstract: *The paper presents a general theory for sensing devices, relating noise and device parameters to resolution of modal index changes. The theory is applied to optimise the length of a few integrated optics sensing devices, being a Mach-Zehnder interferometers and two Fabry-Perot implementations. The results enable the determination of the maximum attainable resolution, and show the crucial importance of loss.*

Introduction

Integrated optics (IO) refractometric sensors are suitable candidates for the accurate detection of parameters like index changes, layer thickness changes and displacements. The advantages of such sensors are the following:

- Diffractionless propagation,
- The possibility for in-situ detection,
- The possibility for compact integration of all kind of functions, and also of
- Multi-sensing arrays for multi-parameter detection,
- The possibility for sensor set-ups that can not or hardly be realized with classical optics components.

Related to the latter item we note that indeed a large number of different typically IO sensing devices have been proposed and realized, based on for example mode coupling [1], modal field changes [2], grated waveguides (WGs) [3], photonic crystals [4] or surface plasmon resonance (SPR) [5,6]. In addition quite a number of IO implementations of classical optics instruments have been studied in detail, like Mach-Zehnder [7], Young [8,9] and Fabry-Perot interferometers [10,11], abbreviated by MZIs, YIs and FPIs, respectively. An overview can be found in [12].

It is the aim of this paper to present a theoretical frame work describing the relation between device parameters, including propagation loss, and modal index resolution, in the presence of detection noise. For parameter reduction it appears to be convenient to introduce the so-called normalized specific resolution (NSR). The presented theory is used for parameter optimization of a number of IO implementations of classical optics devices, being a balanced MZI, a symmetric and an asymmetric FPI. The crucial role of modal propagation loss for the attainable resolution will be shown. The paper ends with conclusions.

Effect of noise on the effective index resolution

We consider sensing set-ups in which the change of the modal index *N*, which results from an index change in the sensing section is derived from the measured transmittance, *T*. *T* is measured as a function of some scanning variable *s*, which varies in time with a modulation frequency. Such a variable could be the angle of incidence in SPR, the modulation voltage applied in both branches of an MZI [7], a spatial coordinate along which the power distribution is monitored, in a YI [8,9], or the wavelength in an FPI. The advantages of utilizing such a scanning variable is that large amount of data points at one scan enable to correct for drift, being defined as the effect of disturbing factors with frequencies appreciably lower than the modulation frequency and reduces the effects of noise (frequencies appreciably higher than the modulation frequency) in the output power by fitting the response curve. On fitting the analytical expression of the response curve (in terms of *s* and the modal index *N*) should be known, by theoretical or experimental means, except possibly for a few adjustable parameters (next to *N*).

In the paper we will focus on two types of noise:

1. noise which is proportional to the output power , such as noise resulting from fluctuations in source power, noise introduced by mechanically unstable parts of the device like fiber to chip couplers or noise corresponding to scattered light in the output signal.
2. noise of which the value is independent of the output power such as detector dark current noise.

Hence, the assumed noise in the output power, P_{out}, is given by:

$$\delta P_{out}^{total} = \delta P_{out} + \delta P_{dark} . \qquad (1)$$

The first term at the right hand side of equation 1 is proportional to P_{out}, which may consist of contributions from both functional output and re-captured stray light. The second term at the right hand side of equation 1 denotes noise related to the dark current, which is assumed to be independent of the output power. The first term in the above is usually the largest unless the output power is relatively low, in for example devices with large losses.

Rewriting equation 1 in terms of the dimensionless quantity transmittance defined by

$$T \equiv P_{out} / \overline{P}_{in} ,$$

with $\overline{P}_{in}$ the time-averaged input power, it follows:

$$\delta T^{total} = \delta T + \delta \tilde{T} \equiv (\delta P_{out} + \delta P_{dark}) / \overline{P}_{in} . \qquad (2)$$

In the below normal (Gaussian) distributions of the noise around zero is assumed, with standard deviations of $T\sigma_T$ and $\tilde{\sigma}_T$, corresponding to the terms δT and $\delta \tilde{T}$, respectively, in equation 2. Note that

$\tilde{\sigma}_T$ decreases if P_{in} increases. In most practical situations things can be arranged such that $\tilde{\sigma}_T \ll \sigma_T$.

In case that inaccuracy in the scanning parameter plays a relevant role (which should of course possibly be avoided) a term $\delta T^s = (\partial T / \partial s)\delta s$ has to be added to equation 2. In the below it is assumed that the accuracy of the set-up is such that its effect on the modal index resolution can be neglected, as well as effects of the drift.

The measured transmittance on varying *s* is given by:

$$T_{m,l} = T_{c,l} + \delta T_l \,, \qquad (3)$$

where T_c indicates the correct curve, corresponding to a measurement with zero noise, δT denotes the noise and the subscripts l indicate the sampling points corresponding to *s*. The total number of data points is *Q*. In the below it is assumed that, from the measurements, only the modal index, *N*, has to be obtained. In practical situations generally more parameters have to be determined, in order to correct for drift, in for example laser power. It can be made plausible that theses additional fitting parameters hardly affect the error in the fitting of *N*.

For the obtained fitted response curve, T_f, the following holds:

$$T_{f,l} = T_{c,l} + \left(\partial T_{c,l} \Big/ \partial N_f \right) \Delta N_f \qquad (4)$$

where ΔN_f is the error as a result of noise. The fitting procedure is assumed to consist of minimizing the following function of N_f:

$$F(N_f) = \sum_{l=1}^{Q} (T_m - T_f)_l^2 \,. \qquad (5)$$

Equation 5 can be re-written by substitution of equations 3 and 4, leading to:

$$F = \sum_{l=1}^{Q} \left[\delta T_l - \left(\partial T_{c,l} \Big/ \partial N_f \right) \Delta N_f \right]^2 . \qquad (6)$$

The minimum of *F* as a function of N_f follows from:

$$F'(N_f) = \sum_{l=1}^{Q} 2 \left(\frac{\partial T_{c,l}}{\partial N_f} \right) \left(\left(\frac{\partial T_{c,l}}{\partial N_f} \right) \Delta N_f - \delta T_l \right) = 0 \,. \qquad (7)$$

From equation (7) it follows (omitting the subscripts *c* and *f* in the derivatives, for simplicity):

$$\Delta N_f = \sum_{l=1}^{Q} (\partial T_l / \partial N) \delta T_l \Big/ \sum_{l=1}^{Q} (\partial T_l / \partial N)^2 \,. \qquad (8)$$

For an ensemble of such N_f determinations the standard deviation is given by:

$$\sigma_N = \frac{\sqrt{\sum_{l=1}^{Q} (T_l^2 \sigma_T^2 + \tilde{\sigma}_T^2)(\partial T_l / \partial N)^2}}{\sum_{l=1}^{Q} (\partial T_l / \partial N)^2} \,. \qquad (9)$$

Here we have used equation 2 and repeatedly the fact that the resulting standard deviation on adding two stochastic quantities is given by the square root of the sum of the two squared standard deviations involved. Neglecting the effect of variations in the terms under the summations in equation 9 one can state roughly that the resulting standard deviation is proportional to $1/\sqrt{Q}$, and that on adding data points the value of σ_N is always reduced, even if $|\partial T / \partial N|$ is small. It is also clear from equation 9 that in general the inclusion of data corresponding to large values of $|\partial T / \partial N|$ will lead to a strong decrease in the standard deviation. Note that the standard deviation σ_N does not depend implicitly on the scanning variable *s*. The advantage of using a scanning variable lies mainly in the fact that data points with large $|\partial T / \partial N|$ values are part of the response curve.

Using equation 9 we can now define the modal index resolution quantitatively by $\rho \equiv 1/\sigma_N$.

Device optimization for a number of integrated optics sensing devices

In this section the optimization of a few IO sensing devices will be discussed. The considered devices are a balanced, modulated MZI, a symmetric and asymmetric FP-cavity. A general approach to optimize the resolution of these devices is presented. It is assumed that only functional device output is captured by the detector (i.e., no stray light), propagation loss is taken into account and, for simplicity, only a single data point, corresponding to the maximum value of $|\partial T / \partial N|$, is assumed in the expressions for the modal index resolution. The true resolution can be determined roughly from it by multiplication with $\sqrt{Q}$, with *Q* the number of sampling points.

In the *balanced MZI* it is assumed that the loss in both branches is equal. The transmittance of the device is given by:

$$T_{bMZI} = 0.5[1 + \cos(\varphi_N + \varphi_s)] e^{-\alpha L} , \qquad (10)$$

with $\alpha \equiv 2k_0 N_{im}$, N_{im} being the imaginary part of the modal index, $\varphi_N \equiv k_0 (N - N_r) L$, with k_0 the wavenumber, N_r the modal index of the reference branch, and *L* is the length of the sensing section. The phase shift φ_s is due to electro-optic modulation (see inset of figure 1), and can for example be varied between 0 and 2π. In the above we neglected the assumed small losses in splitting and modulation sections. With equation 9, and using a single data point (at $\varphi_N + \varphi_s = \pi/2$) it follows:

$$\sigma_N = \frac{1}{k_0 L} \sqrt{\sigma_T^2 + (2\tilde{\sigma}_T)^2 e^{2\alpha L}} \,. \qquad (11)$$

In the below we will introduce the so-called normalized specific resolution (NSR), η, defined via:

$$\rho (\equiv 1/\sigma_N) = \eta k_0 / (\alpha \sigma_T) \,. \qquad (12)$$

It can be shown that η, which is device specific, depends generally only on the normalized length, αL (rather than on both α and *L*), other device parameters (if any; like reflectance in a FP cavity), the ratio

$\sigma_T / \tilde{\sigma}_T$ and the used data points of the response curve.

From equation 11 it follows that minimum of σ_N, as a function of the device length, occurs at a normalized length αL_{opt} defined by:

$$(\sigma_T / \tilde{\sigma}_T)^2 = 4(\alpha L_{opt} - 1)e^{2\alpha L_{opt}}, \qquad (13)$$

leading, after substitution into equation 11, to

$$\sigma_N = \frac{\alpha \sigma_T}{k_0 \eta_{opt}}, \quad \eta_{opt} = \sqrt{\alpha L_{opt}(\alpha L_{opt} - 1)}\,. \qquad (14)$$

In figure 1 plots as a function of $\sigma_T / \tilde{\sigma}_T$ are given of αL_{opt}, obtained from equation 13 by taking the inverse function (Matlab function *lambertw*), the NSR, η_{opt}, according to equation 14, and the transmittance (for the considered single data point).

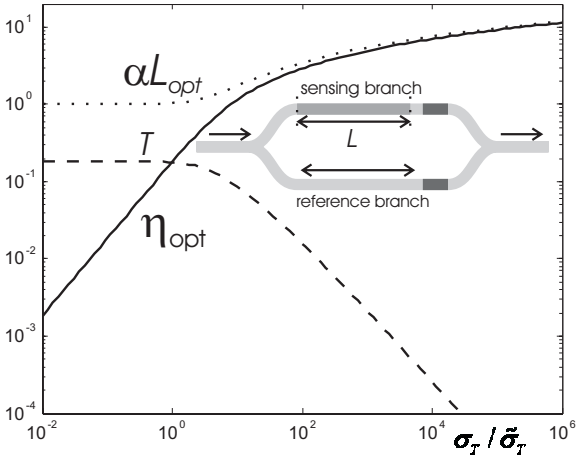


Fig. 1: Optimized NSR, transmittance and optimised nomalised length of a balanced MZI as s function of the ratio $\sigma_T / \tilde{\sigma}_T$ (see text). The inset shows a schematic lay out, including modulator sections [7].

For large $\sigma_T / \tilde{\sigma}_T$ values the exponent in equation 13 dominates, i.e., $\alpha L_{opt} >> 1$, and the optimum length can be approximated as follows:

$$\alpha L_{opt} = \ln\left[\frac{\sigma_T}{2\tilde{\sigma}_T\sqrt{\alpha L_{opt} - 1}}\right] \approx \ln\left(\frac{\sigma_T}{2\tilde{\sigma}_T}\right). \qquad (15)$$

From the above and equation 13 it follows:

$$\eta = \sqrt{\alpha L_{opt}(\alpha L_{opt} - 1)} \approx \alpha L_{opt} \approx \ln[\sigma_T / (2\tilde{\sigma}_T)]\,, \quad (16)$$

where use was made of the fact that $\alpha L_{opt} >> 1$.

The transmittance of a *symmetric FPI* is given by:

$$T_{sFP} = \frac{(1-R)^2 e^{-\alpha L}}{(1-R')^2(1 + F' \sin^2 \varphi_{N,\lambda})}, \qquad (17)$$

with L the cavity length, $\varphi_{N,\lambda} \equiv k_0 L N$, R the modal reflectance at the end-faces, $R' \equiv R \cdot \exp(-\alpha L)$ and $F' \equiv 4R'/(1-R')^2$. It is assumed in the above that there is no power loss at the end-faces, which are both assumed to be equal. Without losing generality, it is assumed that the wavelength is the scanning variable. Note that the above expression applies equally well to a ring resonator, with a circumference of 2*L*, coupled symmetrically to two WGs (see inset of figure 2).

Device optimization has been done numerically in the following way. It is assumed, for the moment, that noise due to the dark current can be neglected, i.e., the term with $\tilde{\sigma}_T$ in equation 9 is assumed to vanish. From the results presented below it appears that things can be arranged such that it plays only a minor role for the obtainable resolution in both symmetric and asymmetric FPIs. For a given reflectance, *R*, the value of $\varphi_{N,\lambda}$, for which $|\partial T / \partial N|$ has a maximum, is determined numerically using equation 17. Next, the normalized optimum device length, αL_{opt}, has been calculated numerically by maximizing the NSR, η_{opt}, with the Matlab *fminsearch*-function. The resulting values of αL_{opt}, η_{opt} and the transmittance, *T*, as functions of the reflectance are given in figure 2.

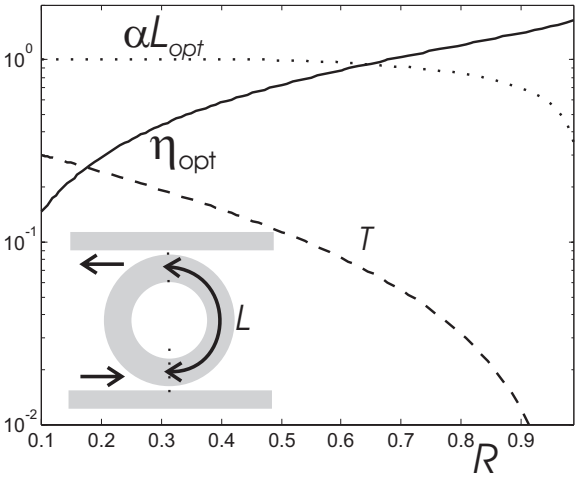


Fig. 2: η_{opt}, transmittance and optimised nomalised length of a symmetric FPI as s function of the reflectance. The inset shows a schematic lay out of the device.

The modal transmittance of the considered *asymmetric FP cavity*, with one fully reflecting end facet, is given by:

$$T_{aFP} = \frac{R - 2r\cos(2\varphi_{N,\lambda})e^{-\alpha L} + e^{-2\alpha L}}{1 - 2r\cos(2\varphi_{N,\lambda})e^{-\alpha L} + Re^{-2\alpha L}}, \quad (18)$$

where L is the cavity length, $\varphi_{N,\lambda} \equiv k_0 L N$, $\alpha \equiv 2k_0 N_{im}$, $R(\equiv r^2)$ the modal reflectance at the input of the device and r is the corresponding reflection coefficient. Proceeding as above for the symmetric FP cavity, also assuming that there is no dark current noise and a single data point (corresponding to the maximum of $|\partial T / \partial N|$), the parameters αL_{opt}, η_{opt} and T have been determined numerically as a

function of the reflectance. The result is given in figure 3.

Note that the considered structure is functionally

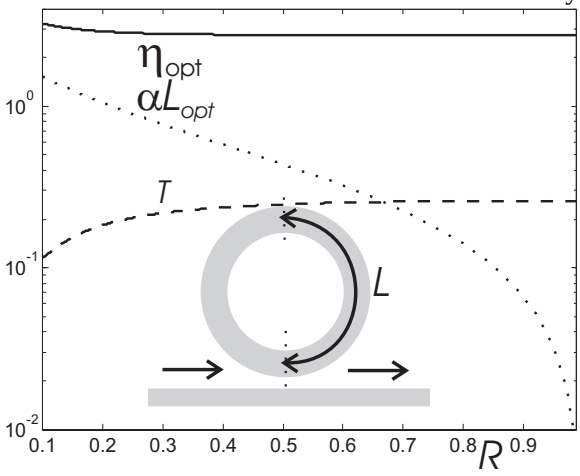


Fig. 3: η_{opt} , transmittance and optimised nomalised length of an asymmetric FPI as s function of the reflectance. The inset shows a schematic lay out of the device.

equivalent to a ring resonator, coupled to a single WG (see inset of figure 3).

Considering the graphs of the three considered devices the following main conclusions can be drawn:

- the length-optimized NSR, η_{opt} , for a MZI is determined by the ratio $\sigma_T / \tilde{\sigma}_T$, and can take on large values if this ratio is large, whereas
- its value is limited in both symmetric and asymmetric FPI to values of η_{opt} ~1 and 3, respectively.
- In the considered FPIs the effect of dark current noise is relatively small if $\sigma_T / \tilde{\sigma}_T \gtrsim 100$ and $T \gtrsim 0.01$ (for example), as can be seen with equation 9. The latter leads to the requirement $R \lesssim 0.9$ for the symmetric FPI (see figure 2).

The length-optimized resolution can be calculated from the presented η_{opt} curves with equation 12. Note, that, quite general, the absorption α plays a crucial role for this quantity

Concluding remarks

The paper presents theory of the relation between the resolution for modal index changes and noise and device parameters for a number of IO sensing devices, assuming a scanning variable, like the wavelength. The theory is applied on a balanced MZI, and a symmetric and asymmetric FPI, to calculate the length-optimised so-called normalised specific device resolution (NSR), η_{opt} , assuming that only a single data point of the response curve is used in the measurement. The NSR depends on device parameters, but not explicitly on α, the power loss coefficient, and k_0 , the wavenumber. From the NSR the resolution for modal index changes, ρ, can be calculated according to $\rho(\equiv 1/\sigma_N) = \eta k_0 /(\alpha\sigma_T)$, with σ_T the standard deviation in the transmittance and σ_N is the resulting standard deviation in the effective index.

From the results the following can be concluded:

- Loss is a crucial factor for the maximum attainable device resolution,
- The maximum attainable NSR of the balanced MZI can be large and limited by the presence of so-called dark current noise, whereas,
- Its value is always limited to η ~1-3 for considered FPIs.

As mentioned, for simplicity only a single data point of the device response curves was considered in the presented results. But, it is expected that the general features of the presented graphs, and also the main conclusions hold as well in case of considering a (much) larger number of data points (leading normally to higher resolution).

The presented results may be of help to select an IO sensing device for a certain application, although other properties may also be quite relevant, such as:

- Compactness,
- Sensitivity for temperature fluctuations,
- Robustness against technological errors, and
- Accuracy and range of the scanning variable.

Acknowledgments

Part of presented work has been performed in the framework of STW Technology Foundation project TOE.6596 and a SenterNovem project.

References

1 R.E. Kunz et al, Sensors and Actuators A no. 47, p. 482, 1995.
2 P.V. Lambeck et al, J. Nonlinear Opt. Phys. Mater. No. 13, p. 209, 2004.
3. W.C.L. Hopman et al, IEEE J. Sel. Top. Quantum Electron., no. 11, p. 11, 2005
4 H.M.H. Chong et al, IEEE Photon. Tecnol Lett., no. 16, p. 1528, 2004
5 J. Homola et al, Biosensors, no. 37, p. 26, 2005
6. P.I. Nikitin et al, Sensors and Actuators A no. 81, p. 189, 2000.
7. R.G. Heideman et al, Sensors and Actuators B no. 61, p. 100, 1999
8. A. Ymeti et al, Appl. Opt., no. 42, p. 6549, 2003
9. A. Brandenburg, Sensors and Actuators B, no. 38-39, p. 266, 1997
10. E. Krioukov et al, Opt. Lett., no. 27, p. 512, 2002
11. C-Y Chao et al., J. Lightw. Technol., no. 24, p. 1395, 2006
12. P.V. Lambeck, Meas. Sci. Technol., no. 17, p. 93, 2006

Progress in high index contrast integrated optics

Roel Baets, Peter Bienstman, Wim Bogaerts, Joost Brouckaert, Peter De Backere, Pieter Dumon, Gunther Roelkens, Stijn Scheerlinck, Meint Smit, Dirk Taillaert, Joris Van Campenhout, Frederik Van Laere, Dries Van Thourhout

Ghent University - IMEC
INTEC department
Photonics Research Group
Sint-Pietersnieuwstraat 41
B-9000 Gent, Belgium
roel.baets@ugent.be

Abstract: *A large fraction of the recent innovation in integrated optics is enabled by the use of high index contrast structures and devices. The strong confinement achievable in such devices allows for dramatic performance benefits and downscaling. In this paper the progress in this field is reviewed.*

Introduction

Photonic components with a high refractive index contrast in their device structure have gained strong interest over the past decade. High index contrast does not have a strict definition but roughly speaking the ratio of the difference between the highest and the lowest refractive index in a device to their sum should be of the order of 50% or more before one can truly exploit the benefits of this high contrast. This ratio is a measure for the field reflectivity of the high contrast interface under normal illumination. More precisely the absolute value of this ratio should be of the order of 50% or more. With this definition one can include media with complex refractive index, such as metals, and hence plasmonic devices also belong to the class of high index contrast devices.

High index contrast allows for strong confinement and ultra-compact devices. Strong confinement is important both for linear and non-linear devices. In linear devices it allows to control the propagation of light from a small volume of material. This is important in sensors as well as in low-power and /or high speed active components. In non-linear devices strong confinement allows to achieve all-optical functions at moderate power levels. The strong confinement can be achieved either by waveguide confinement or by cavity confinement or by a combination of both. In case of cavity confinement high index contrast allows to realize small cavities with high quality factor. This implies that one can realize very selective filters with a high free spectral range, which is important in many applications. In particular photonic crystal devices have led to spectacular progress in this field.

High index contrast also allows to realize compact beam or mode conversion devices both for situations with and without change of direction. In-plane bends can be very compact and the same holds for out-of-plane couplers. High index contrast allows to implement very short adiabatic tapers and even shorter non-adiabatic mode conversion devices.

In this paper a number of developments in high index contrast devices will be reviewed. First the major material systems for high index contrast devices will be described. Then the progress in waveguide confinement, mode conversion and cavity confinement will be described. Finally we describe some of the challenges this research field faces.

Materials

High index contrast can most easily be achieved by using a combination of a semiconductor material with a low-index dielectric or by a combination of a metal with a semiconductor or a dielectric.

The most popular material system for high index contrast devices is definitely the silicon-on-insulator (SOI) system. High quality 200 and even 300 mm SOI-wafers are manufactured industrially today. For photonic purposes these wafers typically consist of a crystalline silicon layer with a thickness of a few 100 nm on a buffer layer of silica of a few micrometer on a silicon substrate. Alternatively one can use polycrystalline or amorphous silicon layers, which provides a great flexibility in the underlying substrate. The fact that SOI photonic devices can often be manufactured by means of CMOS-oriented technologies is a major driver for this material choice [1-2].

Next in importance is the use of high index III-V semiconductor layers in combination with dielectrics. The fabrication of thin III-V layers on a dielectric involves the use of a bonding step between the III-V substrate and the host substrate, followed by substrate removal of the III-V substrate. In recent years there has been considerable progress in the development of wafer-to-wafer and die-to-wafer bonding methods, either by exploiting molecular bonding [3] or by using adhesive bonding, for example by using BCB as bonding agent [4].

An important development in this context is the combination of a III-V high index contrast layer above an SOI high index contrast layer. This allows for the integration of III-V active devices (lasers, detectors...) with passive SOI waveguides [5-7].
In the specific case of the GaAs/AlGaAs system the bonding step can be avoided by oxidising a high Al-content AlGaAs-layer beneath a GaAs-layer. While this is an elegant approach, technologically speaking, the range of device functionalities it offers is relatively limited.
Plasmonic devices are typically based on modes propagating at the interface of noble metals and dielectrics or semiconductors. In terms of layer structure these devices are very simple to make. However they always suffer from losses due to the metal absorption. Therefore to make practical use of plasmonic devices it will generally be necessary to combine (compact) plasmonic device structures with waveguide structures based on dielectrics and semiconductors.

Waveguide confinement

In a waveguide structure the propagating mode can be confined to a very small cross-section when high index contrast is exploited. In a simple stripe waveguide with real refractive index the mode can be confined to an area of the order of a square wavelength. In a plasmonic structure the field can be confined further to sub-wavelength dimensions. The same holds for slotted real-index waveguides where the low index slot can have a very high confinement factor.
The strong confinement is not only important for passive functions such as bends, as described below, but also to optimize the efficiency or sensitivity of certain functions. In the case of active functions – functions whereby the mode propagation is influenced somehow by something over time – it can be of key importance that the active part of the structure is as small as possible. This allows to make active devices power efficient and/or fast and it allows to make sensors - that sense the presence of an adlayer - sensitive.
As an illustration the potential of various high index contrast SOI waveguide structures for sensing applications is shown. In Fig. 1 we have plotted the change in effective index of the guided modes as a function of the thickness of a thin adsorbed layer (n=1.45) at the waveguide surface ($\partial n_{eff} / \partial t_{adlayer}$ [1/µm]). By using different transduction principles (interference, resonance, mode coupling) the effective index of the guided modes can be read out as a power difference, thus enabling sensing action. Comparison between three different waveguide geometries, the surface plasmon interferometer geometry on SOI [8] with an adsorbed layer on top, a single mode SOI waveguide (220 nm thick, 450 nm broad) with an adsorbed layer on top and a slotted waveguide (same single mode waveguide but with a slot of 50 nm and the adsorbed layer on the slot walls) show the enormous potential of the TE mode of slotted waveguides for sensing applications.

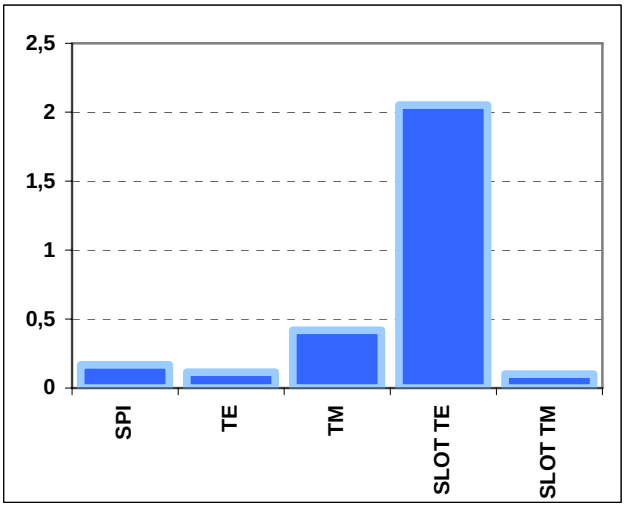


Figure 1: Comparison of different waveguide geometries for sensing applications. $\partial n_{eff} / \partial d_{thickness}$ [1/µm] for surface plasmon modes (SPI), single modes SOI waveguides (TE and TM) and slotted single mode SOI waveguide (SLOT TE and SLOT TM)

Mode conversion

Mode conversion – both in terms of mode size and mode propagation direction - is important in guided wave optical systems.
The most obvious example is given by bends, which are ubiquitous in integrated optical circuits. High index contrast allows to make very sharp bends with radii of curvature down to the scale of the wavelength [9-10]. Bend losses were measured using spiral waveguides with up to 600 bends, allowing for an accurate fit. As expected, bend losses increase for smaller radii, but we can see that even for a 2µm bend radius the excess bend loss is manageable for a small number of bends per circuit. For more extensive circuits with many bends, a radius of at least 3µm is recommended.

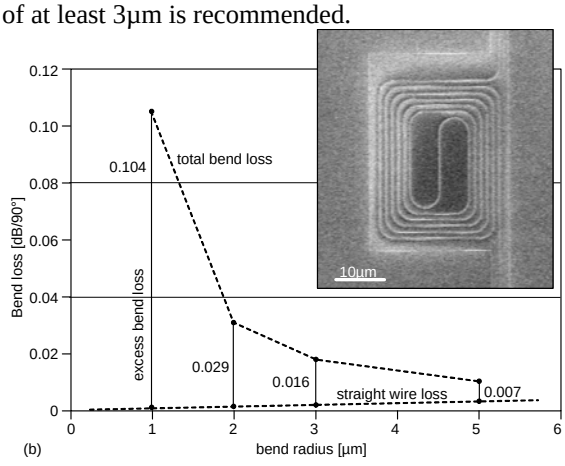


Figure 2: Bend losses for various bend radii measured through spiral waveguides

The next important example is given by fiber coupling between a photonic chip and an optical fiber. The tight confinement in high index contrast waveguides was often seen as a disadvantage given the difficulty to couple light efficiently to low index contrast optical fibers. However it has turned out to be relatively easy to convert a mode tightly confined in a high index contrast waveguide into a fiber matched mode and to do so on-chip, thereby alleviating the alignment tolerances of the packaging process.

In a first approach, the waveguide is adiabatically tapered down until the guide no longer confines the optical field and the light is pushed upwards to a polymer or SiN overlay. This approach has been demonstrated by several groups [1, 11-12], with coupling losses below 1dB, has a large bandwidth and does not require complicated processing. However, this approach does not allow for wafer testing, it requires the definition of very narrow silicon lines (<80nm) and in most cases the overlaying waveguide is coupled to a lensed fibre or a high numerical aperture fibre, which results in smaller alignment tolerances.

In a second approach, a diffraction grating is used to couple light between the planar waveguides and an out-of-plane butt-coupled standard fiber. Thanks to the high refractive index contrast, the grating can have a short coupling length. A typical SOI grating coupler consists of roughly 20 grating periods and consequently has a relatively large bandwidth. A basic grating coupler on a standard SOI wafer with an experimental coupling efficiency > 30% and a 1dB bandwidth of 40nm was presented in [13]. An advantage of the grating coupler approach is that standard single mode fibers are used and consequently the alignment tolerances are more relaxed. The efficiency can be improved by using more advanced designs and custom layer stacks. Using a silicon overlay layer, the efficiency can be increased to 78% theoretically.[14] An efficiency of 70% was demonstrated in [15] by adding a gold bottom mirror using wafer bonding technology.

Cavity confinement

Cavity mode volume and cavity Q-factor are the key parameters that determine the performance of cavity-based devices. High index contrast allows to reduce the cavity mode volume while keeping the Q-factor high. This is important for low power and/or high speed operation of microlasers, tunable filters, modulators, switches and all-optical nonlinear functions. It is also important for adlayer sensing devices in that it makes these devices sensitive to very small volumes of the adlayer material.

The two most prominent types of cavities, based on high index contrast, are the microring (or disk) resonator and the photonic crystal cavity.

Several high-Q ring resonators were demonstrated. For optical channel drop filters, the transmission should be maximized. The internal losses limit the Q due to trade-off between external coupling and transmission. Ring resonators based channel drop filters with 5µm radius have been demonstrated with Q values in the range of 5 000 - 20 000 [10, 16]. These resonators have single-mode waveguides with an effective mode area of around $0.25\mu m^2$. For applications such as sensors, obtaining a high Q is more important, and external coupling can be decreased. With current fabrication technology, waveguide losses are low enough to increase the ring circumference, which decreases the free spectral range and in this way further decreases the 3dB bandwidth and increases the Q factor. Q factors as high as 45000 to 139000 were shown with ring resonators with a radius of 20-30µm, coupled to a single waveguide [17-18]. However, useful Q factors for sensing can already be obtained with much smaller rings with 3-5µm radius.

As far as photonic crystal cavities are concerned, two routes to achieve high Q are popular. One design is based on point defects where the local neighbourhood is deformed in such a way as to minimise leaking Fourier components [19] or create a gentle Gaussian-like field profile [20]. In that last publication, Q-factors of 100 000 were experimentally observed in an SOI material system with a model volume of 0.7 cubic wavelengths.

Even higher performance can be achieved by a design based on locally perturbed line effects. By modulating a line defect, Notomi experimentally showed a Q-factor of 800 000 with a volume of 1.4 cubic wavelengths [21]. Noda proposed a double heterostructure design, also in SOI, which led to observed Q-factors over almost one milion, still with very small modal volumes of 1.2 cubic wavelengths [20].

The Q-factors which are currently achieved in active materials like InP by e.g. the Caltech group are lower than their SOI counterparts, but still reach a respectable 13 000 in laser cavities [22].

Challenges

While the potential of high index contrast devices is large, the challenges are also very large.

At the conceptual level, one of the major challenges is polarisation independence. For devices with input light coming from an optical fiber, the behaviour should preferably be polarisation independent. Theoretically speaking it may be possible to design waveguides and cavities with a polarisation independent behaviour but this leads to a very drastic reduction of the design freedom in relationship to other performance aspects and it will be extremely challenging from a technological point of view. Therefore the better option may be to make sure

that the application is not critically dependent on polarisation independence or to make use of polarisation diversity approaches. The fiber grating couplers described earlier can be extended to polarisation splitting functionality and thereby offers an elegant solution for polarisation diversity. This has been demonstrated for the case of wavelength demultiplexers [23].

A second challenge relates to design and modelling. In low index contrast photonic devices, one is used to a situation where a collection of theoretical models and approximations in conjunction with a range of CAD tools allows to design these devices accurately and efficiently. In high index contrast devices on the contrary, it is often necessary to make use of rigorous vectorial simulation methods in three dimensions. This often means that the computing times are very large and/or the accuracy is low. What makes things worse is the fact that it is much more difficult to use intuition as part of the design process when dealing with high index contrast.

The major challenges of high index contrast photonics have to do with technology however. The geometrical accuracy of high index contrast structures needs to be extremely good. The dimensions of the smallest features – with dimensions of a few 100 nm or even less – should typically be correct down to the 1-10 nm range. An error of 10 nm on a critical wavelength scale dimension (waveguide width or thickness, cavity length...) will typically lead to a shift of the order of 10 nm in the spectral behaviour of the component. Short range geometry deviations – roughness – should also be extremely small. Roughness is still considered to be the major cause of loss mechanisms in most high index contrast devices.

A further technological (and conceptual) challenge is presented by active devices involving a pn-junction. Given the compactness of high index contrast devices, it is far from trivial to design (and fabricate) these devices in such a way that the current flow is used effectively while the doped areas do not lead to loss penalties. Something similar holds for the problem of heat removal, especially since most high index contrast devices involve bonding layers with a low heat conduction capability.

A final challenge is present in the transition from research to industrial deployment. With the technology issues in high index contrast photonic components being so demanding, it is unlikely that many companies can afford to own their own fab. This is definitely true at the prototyping level and as long as the market size is modest. Even for many research groups it will become increasingly difficult to have all technological tools in house. Therefore there is a need for an approach whereby research, prototyping and small volume production is possible in an open access fab, which can serve many actors. For the case of silicon-on-insulator, such an open access structure is already operational in the form of a silicon photonics technology platform [24]. This is possible because (and *only* because) silicon photonics can rely on an existing CMOS-technology base. The fact that the CMOS world is at present trying to diversify with a “More than Moore” vision may well offer a unique win-win opportunity.

This platform, set up in the framework of the European network of excellence ePIXnet, provides a facility access service in which users can have designs fabricated in the form of a multi-project wafer run, where as many contributions as possible are grouped together to bring down the cost to a level acceptable for research groups. Actual fabrication is handled in an advanced CMOS research facility [2, 24].

Conclusion

High index contrast photonic components and integrated circuits have a great potential but do also present important challenges. However in the past 5-10 years there has been an enormous progress in this field at the level of proof-of-principle devices. It is realistic to expect that the next 10 years will bring deployment in the form of products with unique performance and/or lower cost as compared to their lower index contrast counterparts. To what extent this will happen will strongly depend on the way the research and industrial photonics community organizes itself. A foundry-oriented model will be a key ingredient and may well make the difference between niche and large volume deployment.

Acknowledgements

The authors acknowledge partial support from the EU-FP6 Network of Excellence ePIXnet as well as from the Belgian IAP projects PHOTON and photonics@be, from IWT and from FWO for doctoral and post-doctoral grants.

References

[1] Vlasov and S. McNab, "Losses in single-mode silicon-on-insulator strip waveguides and bends," Opt. Express 12, 1622-1631 (2004)

[2] W. Bogaerts, R. Baets, P. Dumon, V. Wiaux, S. Beckx, D. Taillaert, B. Luyssaert, J. Van Campenhout, P. Bienstman, D. Van Thourhout, Nanophotonic Waveguides in Silicon-on-Insulator Fabricated with CMOS Technology,Journal of Lightwave Technology (invited), 23(1), p.401-412 (2005)

[3] M. Kostrzewa, L. Di Cioccio, M. Zussy, J. C. Roussin, J. M. Fedeli, N. Kernevez, P. Regreny, Ch. Lagahe-Blanchard, B. Aspar , “InP dies transferred onto silicon substrate for optical interconnects application”, Sensors & Actuators A 125 411-414(2006)

[4] G. Roelkens, J. Brouckaert, D. Van Thourhout, R. Baets, R. Notzel, M. Smit, “Adhesive Bonding of InP/InGaAsP Dies to Processed Silicon-on-

Insulator Wafers using DVS-bis-Benzocyclobutene", Journal of Electrochemical Society, 153(12), p.G1015-G1019 (2006)

[5] W. Fang, R. Jones, H. Park, O. Cohen, O. Raday, M. J. Paniccia, and J. E. Bowers, " Integrated AlGaInAs-silicon evanescent race track laser and photodetector," Opt. Express 15, 2315-2322 (2007)

[6] G. Roelkens, D. Van Thourhout, R. Baets, R. Notzel, M. Smit, "Laser emission and photodetection in an InP/InGaAsP layer integrated on and coupled to a Silicon-on-Insulator waveguide circuit", Optics Express, 14(18), p.8154-8159 (2006)

[7] Rojo Romeo, P., J. Van Campenhout, Regreny, P., Kazmierczak, A., Seassal, C., Letartre, X., Hollinger, G., D. Van Thourhout, R. Baets, Fedeli, J.M., Di Cioccio, L., "Heterogeneous integration of electrically driven microdisk based laser sources for optical interconnects and photonic ICs", Optics Express, 14(9), p.3864-3871 (2006)

[8] P. Debackere, S Scheerlinck, P. Bienstman, R. Baets, Surface plasmon interferometer in silicon-on-insulator: novel concept for an integrated biosensor, Optics Express, 14(16), p.7063-7072 (2006)

[9] P. Dumon, W. Bogaerts, V. Wiaux, J. Wouters, S. Beckx, J. Van Campenhout, D. Taillaert, B. Luyssaert, P. Bienstman, D. Van Thourhout, R. Baets, Low-loss SOI Photonic Wires and Ring Resonators Fabricated with Deep UV Lithography,IEEE Photonics Technology Letters, 16(5), p.1328-1330 (2004)

[10] W. Bogaerts, P. Dumon, D. Van Thourhout, D. Taillaert, P. Jaenen, J. Wouters, S. Beckx, R. Baets, Compact Wavelength-Selective Functions in Silicon-on-Insulator Photonic Wires,J. Selected Topics in Quantum Electronics, 12(6), p.1394-1401 (2006)

[11] Tsuchizawa, T.; Yamada, K.; Fukuda, H.; Watanabe, T.; Jun-ichi Takahashi; Takahashi, M.; Shoji, T.; Tamechika, E.; Itabashi, S.; Morita, H.; "Microphotonics devices based on silicon microfabrication technology" IEEE Journal of Selected Topics in Quantum Electronics, Vol 11, Issue 1, p.:232 – 240 (2005)

[12] G. Roelkens, P. Dumon, W. Bogaerts, D. Van Thourhout, R. Baets, "Efficient Silicon-on-Insulator fiber coupler fabricated using 248nm deep UV lithography", Photonics Technology Letters, 17(12), p.2613-2615 (2005)

[13] D. Taillaert, F. Van Laere, M. Ayre, W. Bogaerts, D. Van Thourhout, P. Bienstman, R. Baets, "Grating Couplers for Coupling between Optical Fibers and Nanophotonic Waveguides," Japanese Journal of Applied Physics, vol. 45(8A), pp.6071-6077, (2006)

[14] G. Roelkens, D. Van Thourhout, R. Baets, R. Noetzel, M. Smit, "High efficiency Silicon-on-Insulator grating coupler based on a poly-Silicon overlay," Optics Express, vol. 14(24), pp.11622-11630, (2006)

[15] F. Van Laere, G. Roelkens, J. Schrauwen, D. Taillaert, P. Dumon, W. Bogaerts, D. Van Thourhout, R. Baets, "Compact grating couplers between optical fibers and Silicon-on-Insulator photonic wire waveguides with 69% coupling efficiency," OFC 2006, United States, pp .PDP15, (2006)

[16] T. Tsuchizawa, K. Yamada, H. Fukuda, T. Watanabe, J. Takahashi, M. Takahashi, T. Shoji, E. Tamechika, S. Itabashi and H. Morita: IEEE J. Sel .Topics Quantum Electron 11, 232 (2005)

[17] J. Niehusmann, A. Vorckel, P. H. Bolivar, T. Wahbink, W. Henschel and H. Kurz: 2861.Ultrahigh-quality-factor silicon-on-insulator microring resonator., Opt. Lett. 29 (2004)

[18] T. Baehr-Jones, M. Hochberg, C.Walker and A. Scherer: High-Q ring resonators in thin silicon-on-insulator, Appl. Phys. Lett. 85, 3346 (2004)

[19] K. Srinivasan, O. Painter, Fourier space design of high-Q cavities in standard and compressed hexagonal lattice photonic crystals, Optics Express 11 (6): 579-593 (2003)

[20] Asano T, Song BS, Akahane Y, Noda S, Ultrahigh-Q nanocavities in two-dimensional photonic crystal slabs, IEEE Journal of Selected Topics in Quantum Electronics 12 (6): 1123-1134 Part 1, (2006)

[21] Kuramochi E, Notomi M, Mitsugi S, Ultrahigh-Q photonic crystal nanocavities realized by the local width modulation of a line defect, Applied Physics Letters 88 (4): Art. No. 041112 (2006)

[22] K. Srinivasan, P.E. Barclay, O. Painter, Chen J, Cho AY, "Fabrication of high quality factor photonic crystal microcavities in InAsP/InGaAsP membranes," Journal of Vacuum Science and Technology B, Vol. 22, No. 3, pp. 875-879, (2004)

[23] W. Bogaerts, D. Taillaert, P. Dumon, D. Van Thourhout, R. Baets, A polarization-diversity wavelength duplexer circuit in silicon-on-insulator photonic wires, Optics Express, 15(4), p.1567-1578 (2007)

[24] ePIXnet silicon photonics technology platform: www.siliconphotonics.eu

How complex can integrated optical circuits become?

Meint Smit, Martin Hill, Roel Baets, Erwin Bente, Harm Dorren, Fouad Karouta, Paul Koenraad, Ton Koonen, Xaveer Leijtens, Richard Nötzel, Siang Oei, Huug de Waardt, Jos van der Tol, Djan Khoe.

COBRA Research Institute, Technische Universiteit Eindhoven
Postbus 513, 5600 MB Eindhoven, the Netherlands
m.k.smit@tue.nl

Abstract: *The integration scale in Photonic Integrated Circuits will be pushed to VLSI-level in the coming decade. This will bring major changes in both application and manufacturing. In this paper developments in Photonic Integration are reviewed and the limits for reduction of device dimensions are discussed*

Introduction

Photonics is a rapidly growing sector in the global economy. Optical communications, optical disks, digital cameras, lighting, lasers and optical sensors are just a few examples. In comparison to electronics, most photonic equipment is still large and expensive. Just like in micro-electronics, many applications can be realized in a much more compact and cost-effective way by integrating the required functionality in a single chip.

So far, the progress in photonic integration has been hampered by the large variety in photonic devices and technologies, and the fact that most integration technologies are specific for the applications for which they have been developed. As a result the market for integrated photonics is too fragmented to justify the investments for developing an integration technology to a level that really leads to substantial cost reductions, and this, in turn, prevents rapid growth of the applications.

The way to break out of this cycle is by developing a generic integration technology with a level of functionality that can address a broad range of applications. Such a technology, which should be made accessible via foundries, can address markets that are sufficiently large to pay back the development costs. This is quite similar to what happened in microelectronics.

The power of micro-electronic integration technology is that a broad class of electronic functionalities can be synthesized from a small set of elementary components, such as transistors, resistors and capacitors. A technology that supports wafer-scale integration of these elementary components can, therefore, be used for a broad class of applications, and investments made in its development are paid back by a large market.

In a similar way, the key for the success of integration in photonics is to realize a broad range of optical functionalities with a small set of elementary components, and to develop a generic wafer-scale technology for integration of the elementary components, thereby reducing the variety in components and technologies, and to make this technology available through a fabless approach using a foundry model, and set up libraries and a proper design and training environment to support potential users of the facilities.

In this way the development of photonic integration technology can gain sufficient momentum to achieve the substantial cost reductions that are necessary to penetrate in mass markets. The rapidly emerging market for broadband access (FTTH) is such a market. Once this happens photonic integration can enter into a similar dynamics as we are seeing now for more than three decades in microelectronics, i.e. a steady increase in functionality at an essentially constant price, a development which can only be sustained by a steady innovation of the integration technology.

Just like in electronics, where CMOS doesn't provide the answer for all problems, a single generic technology will not be able to cover all applications, if it were only because of the quite different wavelength windows required by different applications. So we will need a few technologies to cover the whole field. But it will be a small (but powerful) subset of the multitude that we have today, and some of them may eventually merge into a technology that combines the best of photonics and electronics into a hybrid or heterogeneous integration platform.

In the present paper we will focus on semiconductor-based integration technology (InP), which is a key technology for large scale photonic integration. In the last section we will pay some attention to other technologies.

Moore's law in Photonics

The field of Information and Communication Technologies is showing a development speed which is unprecedented in history. Over a period of more than thirty years key features like processor speed and memory size are roughly doubling each 18 months. It is known as Moore's law [2] and enabled by the developement of micro-electronic integration technology. There have been several attempts to map the development of Photonic Integration on a Moore-like plot, with circuit complexity or integration density mapped logarithmically against time. However, due to the large variety in components and technologies, one ends up with a

scattered cloud of data points that provides little insight.

If we restrict ourselves to devices realised in a similar technology, which is actually also the case in the famous Intel plot [2], a clear trend becomes visible as shown in ***Figure 1*** for InP-based WDM-PICs [3]. This plot, of which we presented the first version in 1995 (IEEE/LEOS Annual Meeting), appears to be surprisingly valid today, more than ten years later and it is very useful for explaining trends in photonics. The plot shows an increase in integration density of around two orders per decade, which is roughly the slope of Moore's law. It should be noted that the vertical axis does not refer to circuit complexity, but to the number of (basic) components that fit on 1 cm^2, which is about the maximum size of a chip. So they are indicative for the maximum achievable circuit complexity, but practical circuits are usually smaller. The main drivers of the size reduction are increasing lithographical resolution and increasing refractive index contract, as explained bij Baets in [4].

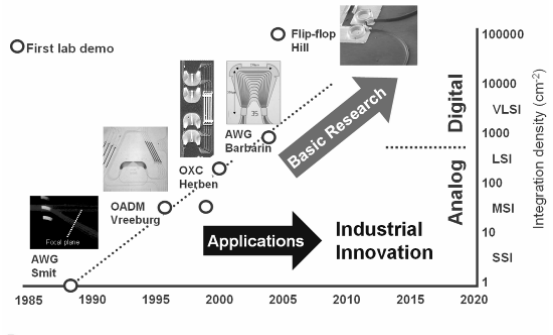


Figure 1 Moore's law in photonics for PIC's developed at COBRA.

The data points shown are first laboratory demonstrators. Early commercial realisations follow the line with a delay in the order of 5 years. The most recent example is the 10-channel WDM transmitter chip with a capacity of 100 Gb/s (10x10 Gb/s), that is applied by Infinera in its WDM systems [5]. It integrates over 40 components in a single chip: 10 tunable DFB-lasers, 10 EA-modulators, 10 VOAs, 10 monitor-diodes and a 10-channel AWG. Although Infinera does not reveal the chip size the density is probably around 500 components per cm^2, which fits well into the metrics of ***Figure 1***.

Analog PICs

An interesting question is how long this increase in density and complexity will continue. Infinera announced already a chip with over 200 components per chip, by increasing the channel count of its device from 10 to 40 [5]. On a longer term even larger channel counts will appear, but it is unlikely that in this way, by increasing parallellism, the complexity will exceed a component count of 1000 per chip.

The alternative is serial integration, but also along this line it is improbable that the 1000 components/chip barrier will be broken. The main reason for this is that todays PICs, although they usually carry digital signals, operate essentially in an analog mode. As a result, errors generated by the components will cumulate and, after having passed a number of components, the signal will be degraded so strongly that it has to be regenerated. On-chip signal regeneration is possible, but full regenerators are complex and they also require a significant amount of chip space. Breaking the 1000 components/chip barrier by serial integration is, therefore, also unlikely. A combination of serial and parallel integration may bring us close, but we expect that for analog PICs the increase in complexity will saturate around or below 1000 components/chip. But this is not the end of Moore's law for Photonics.

Towards Digital PICs

In the early days of micro-electronics analog circuits, such as operational amplifiers, formed an important market. Their complexity was typically limited to a few hundred components per circuit. Signal integrity was maintained by the application of feedback, but this limits the circuit complexity because feedback over too long distances reduces the speed and may cause instabilities. A real breakthrough towards VLSI required, therefore, digital circuits that operate essentially with only two levels, so that the signal is inherently regenerated after each operation and cascading of hundreds of signal operations becomes possible with virtually no signal degradation.

In photonics digital signal processing is still in an embryonic stage. A number of papers on flip-flops or logical gates have been published, but their size, speed and power consumption is such that they allow only for very small integration levels and they are by far not competitive with modern electronics.

Recently a breakthrough in digital photonic signal processing has been reported by Hill [6]: a photonic flip-flop based on two coupled microring lasers with dimensions of 20x40 μm^2, a switching time of 15 ps and a switching energy of a few femtojoules. Allthough the device is still considerably larger than an electronic flip-flop, its dimensions allow for integrating hundred thousands of these components on a single chip, which is an integration complexity far beyond todays imagination. Its switching speed is comparable to that of high-speed electronic transistors, its switching energy is smaller by more than three orders. With some modifications (adding addiational input waveguides) the device can also be used as a logical gate, so that the coupled microlasers form a basic building block for both digital photonic signal processing and storage.

From ***Figure 1*** it is seen that this device does not fit into the Moore's law metrics, it is more than a dec-

ade ahead. This is due to the fact that, although it is realised in a similar technology as the other devices in the plot, the flip-flop element is much smaller than the basic elements (AWGs, switches) used in the other devices. This underlines the potential of this kind of technology for VLSI.

An important issue for digital photonics is the competition with electronics. Analogue photonics brings a number of functionalities that are difficult to realise with electronics, especially for high speed signal processing. But as soon as we go to digital signal processing we will have to beat electronics in a field where it is extremely strong. Allthough the whole field is still very young a few applications where digital photonics will become competitive are already visible. An important one is header processing in all-optical packet switched networks, where huge electronic routers are required to switch the Terabit datastreams that occur in high-level networks. In such networks digital photonic header processing may lead to a substantial reduction of the amount of high speed electronics that is required in the routers. But when the performance of digital photonics increases more applications can be envisaged and also operations like high-speed Optical Time Domain Demultiplexing, which are now performed by rather sensitive analog optical circuitry, may be performed by digital photonic circuits.

Where are the limits?

It is clear that the device reported in [6] is only a first step into a new field of photonics, and it is an interesting question how far we can get before we encounter the fundamental limits of digital photonic signal processing.

An advantage of photonics over electronics is that it does not incur the charge displacements which form the speed bottleneck in electronic switching. Photonics can, therefore, operate at a higher speed than electronics, in principle, its switching speed is limited by the time that light needs for effective interaction in the switching structure. In nanocavities this time can be far into the subpicosecond domain. Electronics has the advantage that it can store information (charge) with virtually no power consumption. This is not possible in coupled lasers, they consume the same power in static and dynamic operation. We expect, therefore, that for ultrafast processing, including some short term memory functions, photonics may turn out to be superior to electronics, but for longer-term storage electronics will remain superior.

Whether photonics will really become an option for digital signal processing depends on how far features like component size and power consumption can be reduced. The microring lasers used in [6] had a ring diameter of 16 μm, and a threshold current of 30 mA. Much smaller lasers have been reported, such as the Photonic-Crystal micro-cavity lasers by Park [7], which have dimensions of a few micrometers and a threshold current of 260 μA. Logical gates based on such a laser will combine sub-ps switching times with sub-femtoJoule switching energies. Although the required injection currents are still prohibitive for integrating millions of such lasers, results reported on other microcavity lasers suggest that threshold currents can become so small (a few microamps) that integrating a million lasers on a chip may become reality. This is still much less than the transistor count in a modern pentium, but if the memory and other “slow” functions are provided by electronics it would allow for the design of powerful processors.

Research reported by Hill at this conference [8] indicates that by using metallic cavities the size of lasers can become comparable with that of modern transistors. Due to their small size, these lasers would operate at very low powers, and their predicted operation speeds are well into the THz domain. Research on nanostructuring of materials and components should make it possible for these devices to operate at room temperature. Such lasers would pave the way for VLSI digital photonic ICs, containing millions of lasers, and operating at multi-TeraHz clock rates.

Integration Technologies

So far we have focused on InP-based integration technology, which is the obvious choice for complex circuits with a broad range of photonic functionalities: passive functions like coupling and filtering, signal generation, modulation, detection, and non-linear functions like wavelength conversion. It is the only technology that can support digital photonic VLSI.

For low-cost circuits with a low complexity level InP is a less obvious choice, however. For such applications silicon photonics, a rapidly emerging technology that uses mature CMOS-technology for fabrication of photonic ICs, is a promising candidate, and might become the dominant technology for circuits like low-cost transceivers for broadband access networks.

Both technologies use high-index semiconductors as waveguide material. High index waveguides allow for very small device dimensions, but the propagation losses in these materials are relatively high. For functions like high-Q filtering and time delay much lower losses are required. In the future photonic landscape there is room, therefore, for a third technology based on low-loss dielectric waveguides with a lower index contrast.

Another advantage of dielectric waveguides is that they can also be used at wavelengths outside the telecom windows, for example in the visible region. This makes them suitable as a hybrid platform for integration of passive functions (such as filtering and time delay) with active semiconductor based functions, such as light generation and amplifica-

tion, from the visible to the infrared region. Further, because of their favourable fibre coupling properties, they might act as an intermediary between semiconductor PICs and fibres.
The photonic functionality described above should be integrated in a compact and low-cost manner with the electronic functions that are required in almost any application. Ultimately we will end, therefore, with a package in which photonic functions are intimately integrated with electronic functions. This will start with todays hybrid integration technology, become more and more compact using advanced 3D integration technologies, and develop towards a VLSI photonic layer which is heterogeneously integrated onto a CMOS wafer.

Conclusion

After a long time of development and struggling with market economics, photonic integration is becoming commercial reality. Costs are still high, however, because no large scale low-cost manufacturing facilities are available. For complex analog photonic circuits to penetrate mass markets, convergence in technologies will be mandatory, and here InP-based technology is a powerful candidate. Most probably in a hybrid technology platform that combines the power of InP-based technology with the power of CMOS. Such a technology is the subject of a number of research projects today.
For low-cost devices with a limited complexity silicon photonics will become a viable alternative, because of its compatibility with mature CMOS technology. For high complexity, involving light generation and amplification, and strong non-linear functionality, InP-based technology has a better potential and for large scale digital photonics it has no real competitor.
However, digital photonics is a dream so far. And so is much of what has been presented here. Many major issues have to be solved yet, such as thermal issues, developing a massive photonic interconnect layer, and finding proper ways of making the digital photonic circuits uni-directional, which is not trivial because of the strong preference of photonic circuits for reciprocal operation. But is a fascinating dream, and one that may come true.

References

[1] G.E. Moore, “Cramming more components onto integrated circuits”, Electronics, Vol. 38, pp. 114-117, Apr. 1965.

[2] www.intel.com/technology/mooreslaw

[3] Smit, M.K. et al., “Photonic integrated circuits: where are the limits?”, Proc. IPRA/NPIS 05, San Diego, CA, 11-13 April 2005, paper IWB1.

[4] R. Baets, “Progress in high index contrast integrated optics”, ECIO 2007, this issue.

[5] R. Nagarajan et al., “Large-scale photonic integrated circuits for long haul transmission and switching”, J. of Opt. Networking, Vol. 6, No. 2, Feb. 2007, pp. 102-111.

[6] M.T. Hill et al., “A fast low-power optical memory based on coupled micro-ring lasers”, Nature 432, nr. 7014, 2004, pp. 206-209.

[7] H.-G. Park et al., “Electrically Driven Single-Cell Photonic Crystal Laser”, Science, Vol. 305. no. 5689, pp. 1444 – 1447, September 2004.

[8] M.T. Hill, “Micro and nanolasers for digital photonics”, ECIO 2007, this issue.

Integrated Electro-optic Wavelength Filter With Programmable Spectral Response

H. Herrmann, D. Büchter, R. Ricken, and W. Sohler

Angewandte Physik, Universtät Paderborn, Warburger Str. 100, 33098 Paderborn, Germany,
e-mail: h.herrmann@physik.uni-paderborn.de

Abstract: *An integrated optical circuit in $LiNbO_3$ consisting of a sequence of electro-optic polarization converters is operated as wavelength filter with a programmable spectral response. Bandpass filter operation with strong sidelobe suppression, with flat-top filter response and tuneabilty are demonstrated.*

Introduction

Wavelength filters are key components for many applications in optical communications and instrumentation with different demands on the filter characteristics. For instance, some applications require band pass characteristics with strong suppressions of sidelobes, others require tuneabilty and/or an especially tailored spectral response.

In recent years several types of integrated optical filters have been demonstrated. Among them are integrated electro-optic filters in $LiNbO_3$ which take advantage of the wavelength-selective polarization conversion induced by a periodic electric field [1,2]. These filters use a constant voltage applied to all converter electrodes and, hence, have a fixed $sinc^2$-like spectral filter response. In this contribution we demonstrate for the first time a new mode of operation of such a filter which allows to obtain a programmable spectral response. The filter consists of a series of electro-optic polarization converters which enable to tailor the spectral response by individually addressing the different electrodes. Such a device has already been used for polarization mode dispersion compensation [3,4].

Device structure and principle of operation

In a Ti-indiffused optical waveguide in X-cut, Y-propagating $LiNbO_3$ a periodic electric field parallel to the Y-axis can induce a polarisation conversion, i.e. a coupling between TE- and TM-polarized modes via the r_{51} component of the electrooptic tensor [1]. This coupling along the propagation direction z can be described using the coupled-mode theory with amplitudes A_{TE} and A_{TM} of the TE- and TM-polarized modes:

$$\frac{\partial A_{TE}}{\partial z} = i\kappa A_{TM}\exp(-i\Delta\beta z)$$
$$\frac{\partial A_{TM}}{\partial z} = i\kappa A_{TE}\exp(+i\Delta\beta z) \qquad (1)$$

with $\Delta\beta = \beta_{TM} - \beta_{TE} - 2\pi/\Lambda$. β_{TE} and β_{TM} are the wave numbers of the TE- and TM-polarized modes, respectively. κ is the coupling coefficient depending on the applied voltage U and Λ is the periodicity of the electrode pattern.

An efficient conversion requires phase-matching and therefore $\Delta\beta \approx 0$, i.e. the difference of the wave numbers of the TE- and TM polarized modes must be compensated by the periodicity of the electric field. The period of the comb-like electrode pattern (Fig. 1) on top of the waveguide determines the wavelength at which phase-matching is fulfilled.

If the coupling strength along the interaction is constant, the spectral response is given by a $sinc^2$-like function; it is approximately given by the square of the Fourier transform of the position dependent coupling coefficient $\kappa(z)$. This means that via a proper design of the coupling strength a tailoring of the spectral characteristics is possible. Similar schemes for tailoring a spectral response have already been demonstrated for instance to design integrated acoustooptical filters [5,6] or Bragg-type reflectors [7].

The idea of this work is to realize a programmable spectral response by using a sequence of electrode sections which can be individually addressed with different voltages. To have full freedom in the design of $\kappa(z)$, each electrode section consists of in-phase and quadrature interdigital electrodes, i.e. a section contains two interleaved electrodes with finger pairs which are shifted by a quarter of a period. One side is always grounded. The detailed structure of an electrode section is plotted in Fig. 2. A section is about 1.2mm long. In-phase and quadrature interdigital electrodes alternate after 6 or 7 finger pairs.

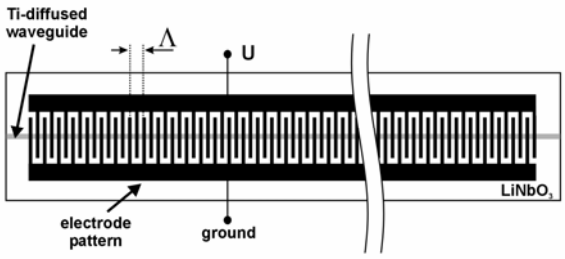


Fig. 1: Electrooptic polarisation converter with homogeneous coupling.

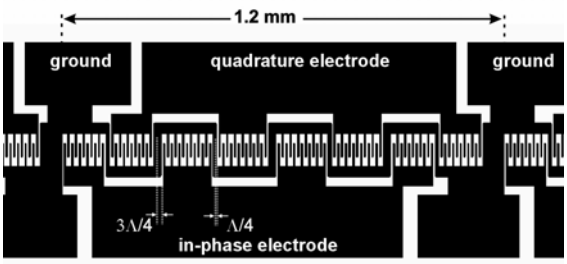


Fig. 2: Details of an electrode section with in-phase and quadrature electrodes.

The overall device consisting of *N* electrode sections is driven by the voltages $U_{i1}\ldots U_{iN}$ and $U_{q1}\ldots U_{qN}$ applied to the in-phase and quadrature electrodes, respectively.

Modelling

For a given spatial dependence of the coupling coefficient the coupled-mode equations (1) must be solved to calculate the spectral response. They can be solved analytically for homogenous coupling. From this result a Jones matrix can be determined [1]. Each electrode section of the filter can be treated as an electro-optic converter with homogeneous coupling. The in-phase and the quadrature parts are taken into account by assuming an effective drive voltage $U_{eff} = \sqrt{U_i^2 + U_q^2}$ and an additional relative phase-shift $\Phi = \arctan\left(U_q / U_i\right)$ of the coupling strength with U_i and U_q being the in-phase and the quadrature drive voltages. The spectral response of the overall device can be calculated from the product of the Jones matrices of each section.

To obtain a desired spectral response the corresponding coupling strength function $\kappa(z)$ must be determined and this function has to be discretized in order to find a proper set of voltages to be applied to the electrode sections. For a given spectral response $\kappa(z)$ can be determined using an inverse scattering formalism [8]. However, this method is rather difficult. Therefore, we used the reverse way and started with trial functions for the coupling strength and optimized them until we achieved the desired result.

One example is the development of a filter with strong sidelobe suppression. We used some well-known window functions [7] for the shape of the coupling strength. In Fig. 3 the calculated spectral response is shown for a Kaiser-type window function [7] discretized into 20 sections (see also Fig. 7). For comparison, the spectral response for homogenous coupling is shown as well with sidelobes of about -10 dB below the maximum transmission. In contrast, a coupling strength which approximates a Kaiser-type window function leads to a filter response with sidelobe suppression better than 40 dB.

Wavelength tuning of the filter is possible if a phase-shift of the coupling strength between subsequent sections of the filters is imposed [1]. With such an additional phase-shift the wavelength of maximum conversion is shifted. This tuning can be realized by

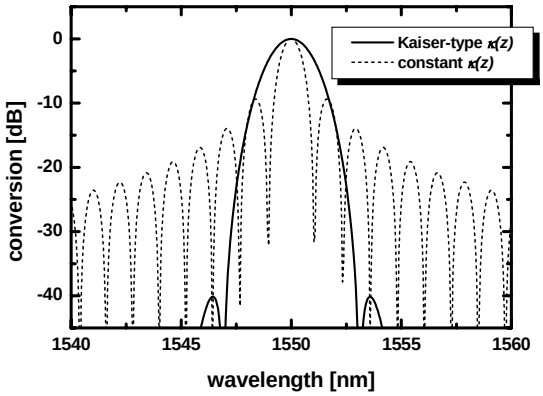


Fig. 3: Calculated spectral responses assuming a coupling strength function according to a Kaiser type window function discretized into 20 sections. For comparison the dashed line shows the response assuming a homogeneous coupling strength.

a proper adjustment of the in-phase and quadrature voltages. In Fig. 4 calculated spectral responses are shown assuming a Kaiser-type window function discretized to 16 sections for various relative phase shifts between subsequent sections. With increasing phase-shift satellite peaks occur which are about 25 nm separated from the central peak. This separation increases with shorter length of the electrode sections. However, within a spectral range of about 10 nm the filter can be tuned without getting satellite peaks of more than -10 dB height.

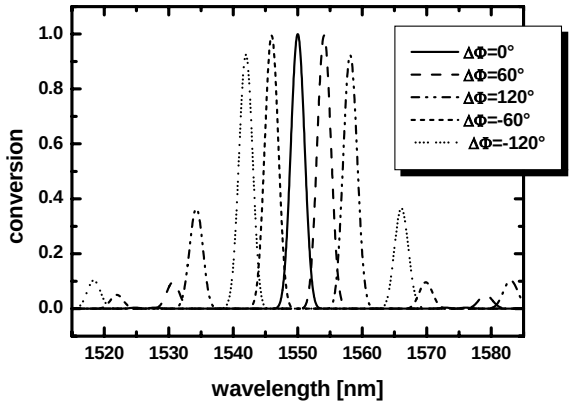


Fig. 4: Calculated tuning characteristics of a filter with 16 sections (Kaiser-type window). Between subsequent sections a relative phase-shift of $\Delta\phi$ is imposed.

Sample fabrication

Optical waveguides were fabricated by an indiffusion of 7 µm wide and 100 nm thick Ti-stripes into X-cut $LiNbO_3$. The diffusion was performed at 1060°C for 9h. Prior to the electrode fabrication an about 500 nm thick SiO_2 buffer layer was deposited on the surface. Subsequently, about 500 nm thick gold electrodes according to the structure shown in Fig. 2 were evaporated. The overall sample has a length of 50 mm with 30 electrode sections; their period is Λ=21.7 µm. To suppress spurious reflections at the



Fig. 5: Photograph of the sample.

end faces an AR-coating for the 1.55 µm spectral region was deposited directly on the end faces.
Investigation of the waveguides in the spectral range around 1.55 µm revealed that they are monomode and the losses are 0.1 dB/cm (TM polarization) and 0.4 dB/cm (TE), respectively.
Fig. 5 shows a photograph of the sample. It is mounted on a temperature stabilized copper holder in order to control the temperature during operation with about 0.1°C accuracy. The electrodes are contacted with thin wires to small strips of a printed circuit board beside of the sample.

Experimental results
In the optical setup the amplified spontaneous emission from an Erbium-doped fiber amplifier is used as light source. The sample is mounted between crossed (external) polarizers. Butt-coupling using lenses with 10 mm focal length is used at the input and output sides of the sample. The transmitted light behind the rear polarizer is fed to an optical spectrum analyser with 0.1 nm resolution.
A computer controlled programmable voltage supply with up to 32 channels delivering -50V… +50V was used to drive the electro-optic converter sections.
In a first experiment a constant voltage of 11.2 V was applied to the in-phase electrodes of 20 sections. This gives rise to a complete conversion at the phase-match wavelength of 1553.4 nm. The corresponding measured spectral response is shown in Fig. 6. Due to inhomogeneities of the waveguide structure the shape of the spectral characteristics differs from the ideally expected $sinc^2$-function which is also plotted in the diagram. The spectral bandwidth of the measured curve is 1.1 nm and the largest sidelobe is 7.9 dB below the maximum transmission.
In order to suppress the sidelobes, the voltages applied to the in-phase electrodes where modified to approximate a Kaiser-type window function. In the upper diagram of Fig. 7 the corresponding voltages applied to the 20 electrodes are shown. The lower diagram presents the resulting measured and calculated spectral responses. It can be seen that the sidelobes are now strongly suppressed. The largest sidelobe of the measured characteristic is about 20.3 dB below the maximum transmission. On the other hand, the spectral 3dB-band width increases to 2.3

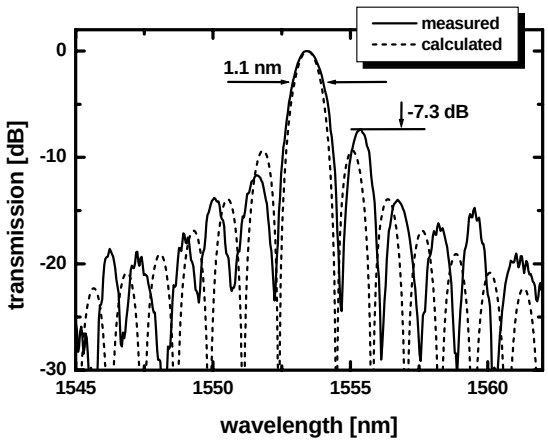


Fig. 6: Measured (solid line) and calculated (dashed line) spectral response of the filter with homogenous coupling.

nm.
Tuning of the filter as discussed in the section on modelling could be verified as well. We operated the device with 16 sections. In Fig. 8 the measured filter characteristics are shown for various relative phase shifts between subsequent sections. It can be seen that the filter is tunable as predicted from the theoretical results.
Another example of a tailored spectral response obtained with the programmable filter is shown in Fig. 9. The device has been programmed to give a (nearly) rectangular response, i.e. a flat-top characteristic. The corresponding coupling strength approximates a seventh-order Butterworth function. Due to

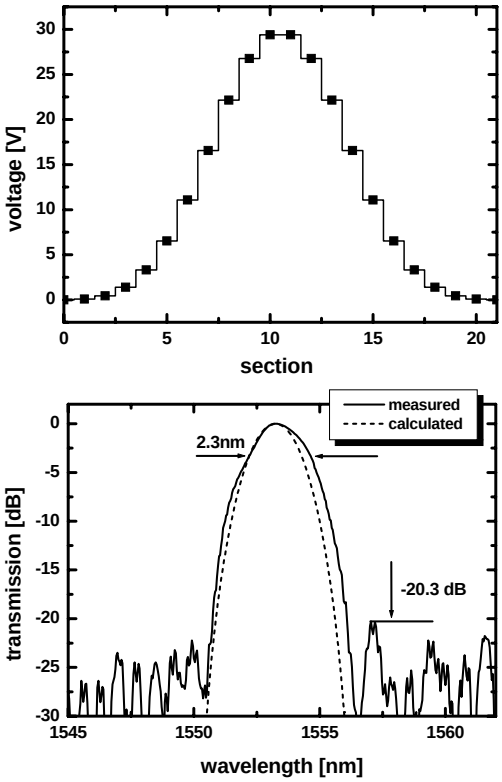


Fig. 7: Filter with strong sidelobe suppression. Voltages applied to the in-phase electrodes of the 20 sections (top diagram) and measured and calculated corresponding spectral responses.

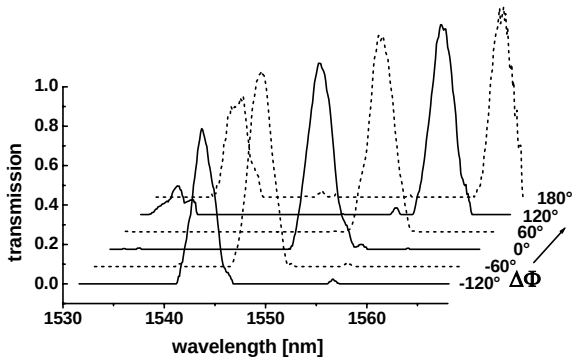


Fig. 8: Measured tuning characteristics of a 16 sections filter with Kaiser-type coupling strength. The different curves are obtained by imposing a phase-shift of ΔΦ between subsequent sections.

the limited voltages available from our signal source, we could not obtain complete conversion. Maximum conversion is about –2.9 dB. The spectral 3dB-width is about 4.3 nm and the highest sidelobe 14.8 dB below the maximum conversion.

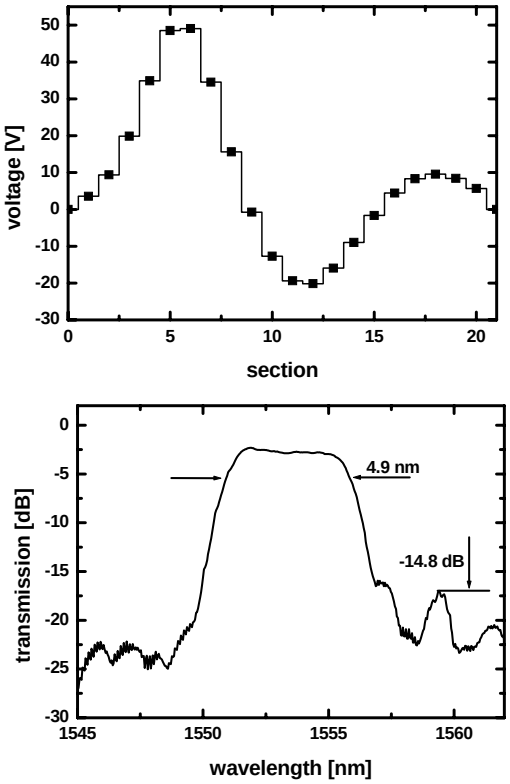


Fig. 9: Flat-top operation of the filter: Voltages applied to the in-phase electrodes of the 20 sections (top diagram) and measured corresponding spectral response.

Conclusions

We have demonstrated for the first time an integrated electrooptic wavelength filter with a programmable spectral response. Bandpass filter characteristics with high sidelobe suppression and flat-top response have been experimentally demonstrated as well as tuneability of the filter. The results are in good agreement with theoretically predicted results.

Further work will concentrate on the improvement of the filter performance. Of particular interest will be a polarization independent operation. This might be achieved by using a polarization diversity scheme. Furthermore, the integration of polarizers or polarization splitters (for the polarization independent device) to form a complete integrated optical circuit would be of great importance.

References

1 F. Heismann, R. Alferness, *IEEE J. Quantum Electron.* QE-24, pp. 83-93 (1988)

2 W. Warzanskyj et al. Appl. Phys. Lett. vol. 53, pp. 13-15 (1988)

3 R. Noé et al., *Electronics Letters*, vol.35, pp.652-4 (1999)

4 R. Noé et al., *J. Sel. Top. Quantum Electron.*, vol. 10, pp. 341-355 (2004)

5 H. Herrmann et al., *J. Lightwave Technol.*, vol. 13, pp. 364-374 (1995)

6 D.A. Smith, J.J. Johnson, APL, vol. 61, pp.1025-1027 (1992)

7 P.S. Cross, H. Kogelnik, Opt. Lett, vol. 1, pp. 43-45 (1977)

8 G.-H. Song, S.-Y. Shin, J. Opt. Soc. Am. A, vol. 2, pp. 1905-1915 (1985)

Domain engineering in $LiNbO_3$ for tailoring the electro-optic response of waveguide modulators

Davide Janner (1) , Michele Belmonte (2) and Valerio Pruneri (1, 3)

1) ICFO -Institut de Ciencies Fotoniques, Mediterranean Technology Park. Av. del Canal Olimpic s/n 08860 Castelldefels, Barcelona, Spain. valerio.pruneri@icfo.es 2) Avanex Corporation Sede Secondaria, San Donato Milanese (MI), Italy 3) ICREA -Institució Catalana de Recerca i Estudis Avançats, 08010, Barcelona, Spain

Abstract: *A general approach is proposed to achieve a predefined electro-optic response in domain inverted $LiNbO_3$ modulators. In particular an apodised domain inversion profile is used in a non-velocity matched configuration to obtain modulation with intrinsic third-order Bessel optical filtering for duobinary transmission.*

Introduction

With the increasing demand for broadband communication, optical networks play a crucial role as the primary carrier of the data stream. In this context, high-speed optical modulators are essential for optical transmission systems and external $LiNbO_3$ modulators are still extremely effective [1], in particular for long haul and metro applications, as it is shown by their recent increasing commercial demand. With respect to semiconductor materials, $LiNbO_3$ based modulators market share could even become larger if performance, integration and cost effectiveness further improve.

The basic scheme of an interferometric Mach-Zehnder amplitude modulator in a single domain crystal produces a frequency response which has a cardinal sine shape and a limited bandwidth inversely proportional to the length [1]. This feature represents a drawback in the picture of actual needs for broadband modulation because of the restriction of the bandwidth and because the ripples in the electro-optic (EO) response may negatively affect some transmission formats, e.g. duo-binary.

Domain inversion (DI) in ferroelectrics, such as $LiNbO_3$, produces a sign reversal of the second-order nonlinear optical properties, including the nonlinear optical coefficient and electro-optic coefficient [2]. So far its use in electro-optics, where one of the interacting fields is at low frequency or a microwave, has been mostly limited to quasi-velocity-matching devices using periodic structures to produce narrow band modulation at high frequency [3,4]. More recently domain inversion has been used to produce large bandwidth and low driving voltage modulation [5, 6], a desired chirp value for the output electro-optic modulated optical wave [7] and to realize single-side-band modulators [8]. When DI (also called poling) is used in a periodic fashion it allows centering the EO frequency response of interest by simply changing the periodicity of the poling. In this case a quasi velocity matching condition is reached and the center of the cardinal sine is shifted from DC of the single domain (unpoled) modulator to the desired frequency, while its shape remains qualitatively the same. In the attempt of keeping the advantages of periodically poled modulators while broadening the bandwidth, multi period structures, constituted by a sequence of different period periodically poled zones, have been employed with promising results [9].

Using a new approach and considering general aperiodic poling profiles, we propose a DI configuration to tailor the EO response to a predefined one. In particular, we design an apodised longitudinal poling profile in non velocity matched (NVM) modulators to achieve a desired electro-optic response using an apodisation technique similar to that of fibre Bragg Gratings. As an example, we demonstrate the possibility to induce a predefined EO frequency response by reporting the synthesis of a third-order Bessel type modulation. This Bessel type modulator, embedding a filter at optical level, is suitable for duobinary transmission [10], without the need of any additional electrical filter in the transmitter.

Precise electro-optic response modulator

Let us consider a travelling wave z-cut $LiNbO_3$ modulator in NVM configuration, with straight electrodes and perfectly impedance matched [1]. In such a modulator the driving voltage is described by

$$V(x,t) = V_0 \sin\left(k_m \cdot \delta \cdot x - 2\pi f_m t_0\right) \quad (1)$$

where V_0 is the amplitude of the wave, $k_m = 2\pi n_m / \lambda_m$, is the microwave wave-number, $\delta = 1 - n_o / n_m$ is the relative mismatch between the refractive index of the microwave (n_m) and optical (n_o) waves, f_m is the microwave frequency corresponding to the wavenumber k_m and t_0 accounts for an initial phase. Driven by this wave, the phase change which the optical wave accumulates at the end of the modulator arms can be written as

$$\Delta\phi(t_0) = \int_0^L -\frac{2\pi}{\lambda}\frac{n_0^3}{2} r \frac{\Gamma}{G} \cdot \cdot \{p(x)\cdot V_0 \sin[k_m \cdot \delta \cdot x - 2\pi f_m t_0]\} dx \quad (2)$$

where L is the length of the arms, λ is the optical wavelength, n_o is the optical refractive index, r is the electro-optic coefficient (in our case, $r=r_{33}$), G is the spatial gap between the two electrodes and Γ is the overlap integral between the optical and microwave electric fields.

If we consider the following identity

$$P(f) = e^{j2\pi fx}\int_{-\infty}^{+\infty} p(x)\cdot e^{-j2\pi fx}dx = \quad (3)$$

$$= \int_{-\infty}^{+\infty} p(x)\cdot\cos(2\pi fx - 2\pi ft_0) - j\int_{-\infty}^{+\infty} p(x)\cdot\sin(2\pi fx - 2\pi ft_0)$$

we note that its imaginary part is very similar to Eq. 2 provided we extend the integration domain to infinity and introduce a rectangular window function to account for the finiteness of the poled region. Thus, we may write the phase change in Eq. 2 in terms of the Fourier transform of the poling function as

$$\Delta\phi'(t_0) = \frac{2\pi}{\lambda}\frac{n_0^3}{2} r \frac{\Gamma}{g} V_0 \cdot \mathrm{Im}\left\langle F[p(x)]\cdot e^{j2\pi ft_0}\right\rangle \quad (4)$$

in which the constants have the same meaning as in Eq. 2 and the symbol F denotes the Fourier transform of the windowed poling function $p(x)$. In this way, the response of the modulator can be obtained numerically via a simple Fast Fourier transform (FFT) of the poling function, and the relationship between the modulation frequency and the computed frequency of the FFT is given by:

$$k_m \cdot \delta = 2\pi f \rightarrow f_m = \frac{c}{N\cdot\Delta x\cdot\Delta n} l, \Delta f = \frac{c}{N\cdot\Delta x\cdot\Delta n}, \quad (5)$$

where N is the number of discrete samples into which is divided the poling function $p(x)$, Δx is the width of one sample, l is an integer number ranging from 0 to N-1, $\Delta n = n_m - n_o$ is the index mismatch, and Δf is the frequency step.

We also note that electrical losses of the modulating wave may be easily included in the computation by the substitution $p(x) \rightarrow e^{-\alpha x} p(x)$ in Eq. 4. Here, we assume the loss parameter to be $\alpha(f) = k\sqrt{f}$ with k=0.51 (cm GHz)$^{-1/2}$. This value is obtained by fitting the losses of a typical modulator up to 40GHz computed using FEM techniques.

The advantage of the formulation of Eq. 4 for the modulator response is that a straightforward inversion could be obtained by the simple relation:

$$h(x) = \mathrm{Re}\left\langle F^{-1}[\Delta\phi_0(f)]\right\rangle, \quad (6)$$

where F^{-1} is the inverse Fourier transform and $\Delta\phi_0(f)$ is the desired frequency response of the modulator so that we may recover a continuous poling function from a desired frequency response. Also in this case a common FFT algorithm can be employed, and with analogous consideration as in the direct case, the following relationships can be obtained:

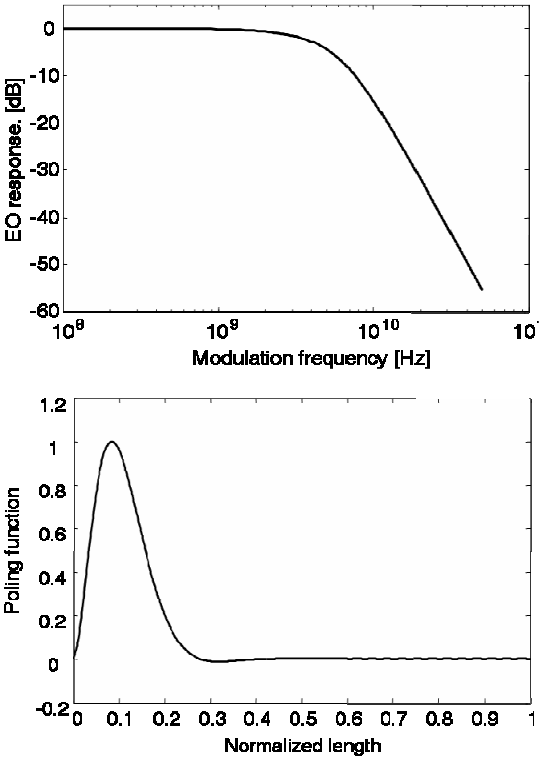


Fig. 1: Desired electro-optic response for a third order Bessel filtering modulator with a -3 dB frequency of 4.5 GHz (top). Reconstructed poling function $h(x)$ which produces the desired Bessel filter response. (bottom)

$$\Delta x = \frac{c}{N\cdot\Delta f\cdot\Delta n} \quad L = N\Delta x = \frac{c}{\Delta f\cdot\Delta n} \quad (7)$$

where Δx is the spatial step into which the poling function $h(x)$ is sampled, N is the number of discrete samples considered, Δf is the step in frequency, Δn is the index mismatch, and L is the total length of the modulator.

The function $h(x)$ in Eq. 6 is a continuous function assuming values ranging from -1 to +1. For this reason, in order to recover the real apodised poling profile $p(x)$ which assumes only two discrete values (-1 or +1), we must provide an algorithm to quantize the continuous function $h(x)$. The procedure is analogous to the apodisation technique used in fiber Bragg grating design.

Let us divide the domain of the function $h(x)$ into a large number of sections of length L_s and consider also the target poling function $p(x)$ composed by equally spaced sub-domains each of size L_s/N, where N>1 is an integer. After computing $\bar{h}_i$, the average of $h(x)$ on the i-th section, we can convert it in terms of

the poling function $p(x)$ by letting the average value of $p(x)$ on that section coincide with $\bar{h}_i$. For example, if we assume for a single section that $\bar{h}_i$ = -0.4, this means that 30% of the sub-domains comprised by $p(x)$ in that section must be set to +1 and the other 70% of the poling sub-domains must be set to -1, so that 0.3·1 + 0.7· (-1) = -0.4. In this way, the mean value $\bar{h}_i$ of the continuous function $h(x)$ is easily reported to the poling function $p(x)$ by simply imposing a length $L_p^- = 0.7L_s$ of the section to -1 and a length $L_p^+ = 0.3L_s$ to +1.

This approximation is valid since we assumed the section length L_s much smaller compared to the coherence length ($\lambda_m/2\Delta n$, about 750 μm at 10 GHz), of the microwave and the phase modulation in this case has an almost linear response with no sensitivity on the order of the sub-domains of $p(x)$ in the single section.

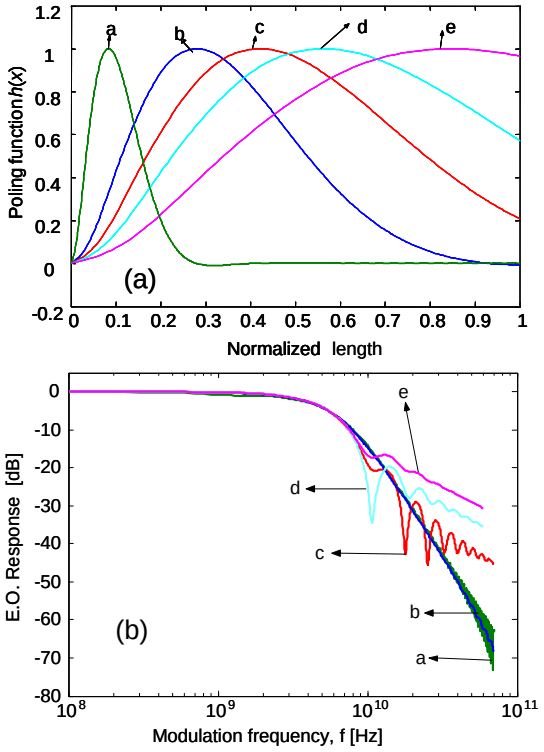


Fig. 2: Comparison of the different poling functions (fig. a) and their E. O. response (fig. b) for the a) ideal case (V_π=99 V·cm) or truncated to b) the first lobe (V_π=30 V·cm); c) 2/3 of the first lobe (V_π=21 V·cm); d) ½ of the first lobe (V_π=18.6 V·cm); e) 1/3 of the first lobe (V_π=20.1 V·cm).

To illustrate the potential of this technique, we report here, as an example, a modulator having an EO response of a third order Bessel filter with a -6 dB frequency of 6 GHz. This kind of filter is very useful in the duobinary format transmissions where the tails of the typical cardinal sine response of normal modulators has negative effects and an electrical filter is usually needed to cut them off [10]. Starting from the desired EO response and applying the inverse Fourier transform algorithm of Eq. 6, we obtain the continuous poling profile $h(x)$ as reported in figure 1. The poling function here is plotted against a normalized length $L' = \Delta n \cdot L$ since, in this first stage of the design, we neglect the microwave losses and assume that the EO response does not depend on the length by keeping the product $\Delta n \cdot L$ constant. In such a way, we can consider the length L and the index mismatch Δn design parameters to be decided *a posteriori* depending on the EO response and including the microwave losses. Observing the recovered poling function in figure 1, we note that the longest part of it is nearly zero, almost not influencing the modulation of the phase. Moreover, the average of the function $h(x)$ over the domain can be used to estimate $V_\pi = 99$ V·cm which is extremely large. Thus, from these considerations we can argue that the last part of the poling function which is nearly zero could be disregarded in the modulator design and dropped.

To address this point in figures 2(a)-(b) we report the comparison of the ideal and some poling functions obtained by truncation of the ideal one and their respective EO responses. We note that the switching voltage is inversely proportional to the area under the poling curve and moreover the more truncated the poling function the worse the EO response (ripples). From figure 5(b) we may also note that the closest response to the ideal case of the third order Bessel filter is the function truncated at the first lobe differentiating its response from the ideal one only by negligible ripples at higher frequencies. Moreover, this profile has a much lower $V_\pi = 30$ V·cm.

Once chosen the single lobe function as our poling function, we may account for electrical losses. If we compare the EO responses with and without microwave loss, for a constant $\Delta n \cdot L$, we note that they depend on the device length. Indeed, with respect to the ideal (no microwave loss) EO response, the behaviour that accounts for the loss (α=0.49 $\sqrt{f}$ dB/cm) for a modulator of length L=45 mm and Δn=1.32 remains qualitatively the same with the exception of the cut-off frequency that, from the 6 GHz ideal case, is reduced to about 5.25 GHz. However, the 6 GHz bandwidth could be achieved by initially designing the ideal structure (no losses) having a larger cut-off frequency, so that, after accounting for microwave loss, the EO response becomes the desired one.

The final apodised poling profile $p(x)$ for the designed Bessel type modulator with a cutoff frequency at -6 dB of 6 GHz is reported in figure 3 and compared with the continuous poling function $h(x)$. Such a modulator has a switching voltage of 6.6 V and the EO response for the poling profile calculated is com-

pared to the ideal case of a Bessel third order filter in figure 4 showing a good agreement and the effectiveness of the method.

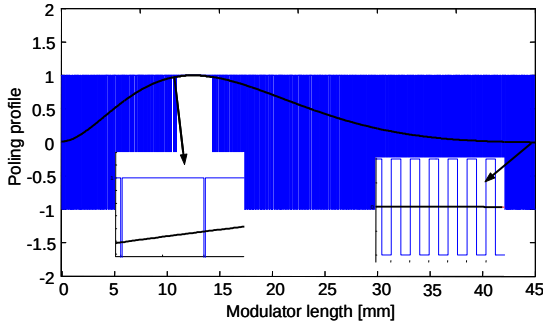


Fig. 3: Continuous poling function (black solid) and reconstructed discrete valued profile function (blue line).

The proposed design is for a modulator that can be used for a 10 Gb/s transmission. The common approach consists in 3rd order Bessel type electrical filtering of a standard 10Gb/s modulator (>10GHz bandwidth) which results in a typical driving voltage in the 4 to 5 V range. Note that, in comparison, the driving voltage in our case is higher but could be reduced by increasing the transverse overlap (Γ) which, in the case of classical modulators, would not be possible because the VM condition imposes severe geometrical constraints.

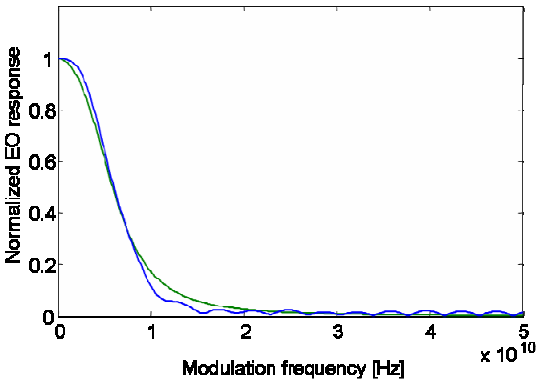


Fig. 4: Comparison of the normalized EO response of the ideal (green) and truncated (blue) poling function

Conclusions

The DI engineering procedure we proposed for precise EO response design is general and straightforward, requiring only simple numerical operations as an inverse Fourier transform and a small number of empirical tries providing precise results. No particular geometry of the electrodes is required, only straight lines, thus avoiding curvatures which cause reflections or the modification of the Γ coefficients; effects that can induce different phase changes in the two branches of the modulator producing residual chirp. Moreover, the possibility of tailoring the desired EO response and integrate optical filtering (such as 3rd order Bessel) makes this technique powerful for design of commercial modulators.

References

1. E. L. Wooten, K. M. Kissa, A. Yi-Yan, E. J. Murphy, D. A. Lafaw, P. F. Hallemeier, D. Maack, D. V. Attanasio, D. J. Fritz, G. J. McBrien, D. E. Bossi, IEEE J. Select. Topics Quant. El., vol. 6, no. 1, pp. 69-81, Feb. 2000
2. R. S. Weiss and T.K. Gaylord, Appl. Phys. A, vol. 37, no. 4, pp. 191-203, 1985.
3. J.H. Schaffner, US patent 5,278,924 (1994).
4. Y. Lu, M. Xiao and G. J. Salamo, Appl. Phys. Lett., vol. 78, no. 8, pp. 1035-1037, 19 Feb 2001
5. V. Pruneri and A. Nespola, US patent 6,760,493, year 2004.
   F. Lucchi, M. Belmonte, S. Balsamo, M. Villa, L. Trevisan, S. Pensa, G. Consonni, C. Emanuele, P. Vergani, M. Sottocorno, V. Pruneri, paper OWH3, to be presented at OFC 07.
6. S. Oikawa, F. Yamamoto, J. Ichikawa, S. Kurimura, K. Kitamura, J. Light. Tech., vol. 23, no. 9, pp. 2756-2760, Sep. 2005
7. N. Courjal, H. Porte, J. Hauden, P. Mollier and N. Grossard, J. Lightwave Tech., vol. 22, no. 5, pp. 1338-1343, May 2004.
8. H. Murata and Y. Okamura, in Photonics Based on Wavelength Integration and Manipulation, pp. 213-224, IPAP Books 2, 2005
9. Chen XF, Zeng XL, Chen YP, Xia YX, Chen YL, Journal. of Opt. A-Pure and applied optics, vol. 5, no. 3, pp. 159-162, May 2003
10. P. Bravetti, L. Moller, IEEE Phot. Tech. Lett., vol. 16, no. 9, pp. 2159 – 2161, Sept. 2004

TriPleX: a new concept in optical waveguiding

A. Melloni (1), F. Morichetti (1,2), R. Costa (2), G. Cusmai (2),
R.G. Heideman (3), R. Mateman (3), D. H. Geuzebroek (3), and A. Borreman (3)
1) *Dipartimento di Elettronica e Informazione, Politecnico di Milano,*
Via Ponzio 34/5, 20133 Milano – Italy, melloni@elet.polimi.it
2) *CoreCom, Via G. Colombo 81, 20133 Milano, Italy, morichetti@corecom.it*
3) *LioniX BV, P.O. Box 456, 7500 AH, Enschede, the Netherlands*

Abstract: A novel optical waveguide, consisting of a thin high-index coating boxing a low-index inner material, is presented. Details on waveguide design, fabrication and experimental results are shown, demonstrating high potentialities for CMOS-compatible large-scale integrated optics.

Introduction

In optical fibers, the radial refractive-index profile is the most suitable and exploited mean to manage most of the propagation characteristics. Apart from the attenuation of the fiber, mainly dependent on the technological fabrication process, the radial index profile and contrast can be designed to tailor dispersion characteristics, mode shape and dimension, effective area and hence nonlinearities, bending capability and so on. In integrated optics, contrary to optical fibers, the shape of the waveguide is inflexibly connected to the technological process for the realization of the guiding structure and the transverse profile is typically a step function. Moreover, the restricted variety of available materials forces the index contrast to few fixed values, thus limiting the possibility to fully exploit such a parameter to optimize the trade-off between optical properties and technological implications.

Waveguides composed by a combination of layered materials, such as SiO_2, Si_3N_4, Si, and also Tellurium and Polymide, usually known as Multi-Layer Waveguides (MLWs), possess many intriguing characteristics and represent promising alternatives to overcome the previously described limitations. Optical waveguiding in MLWs or waveguides confined by multilayers has been recently widely investigated [1] for high power transmission, tight turning radii, dispersion compensation, hollow waveguide applications, sensors and so on. One of the main disadvantages of these confinements (hollow-core ARROW waveguides [2] and Bragg cladding waveguides [3]) is the large number of layers required for achieving low radiative losses, resulting in complex technological processes and low reproducibility.

In this contribution non-conventional waveguides, consisting of overlapped layers of dielectric media with different thickness and refractive index, are proposed as a way to merge the advantages of low index-contrast waveguides (low loss, low polarization dependent loss, low birefringence) to the potentialities of higher index ones (high curvature and devices' compactness). With respect to conventional structures, in the proposed waveguide additional degrees of freedom can be exploited for the optimization of the waveguide, whose effective index-contrast can be tailored by using only few (typically two) standard materials. Morover, the low-cost, simple and CMOS compatible technology makes the proposed waveguide an interesting candidate for highly integrated optical circuit applications.

The transversal profile of the proposed waveguide is shown in Fig. 1. It is made of a thin high-index box layer (50-150 nm) of Silicon Nitride (refractive index 1.99) surrounding and encapsulating a low-refractive-index material (SiO_2). This technology has been designed, patented and set up at LioniX – the Netherlands [4 - 7] and it is named TriPleX. Both the technological realization and the theoretical study of the propagation in TriPleX waveguides are challenging tasks, but the flexibility and the advantages of such a new composite structure are remarkable, as already demonstrated through the realization of several devices [8-10].

The paper is organized in three sections explaining the waveguide properties and design, the technological process for the waveguide fabrication and the experimental characterization.

Waveguide design

LPCVD Silicon nitride (Si_3N_4) is a widely used material in integrated optics, primarily because of its large refractive index (1.99 at 1.55 μm) enabling the realization of very compact devices [11]. Unfortunately, its large internal tensile stress limits the maximum layer thickness to < 350 nm, not

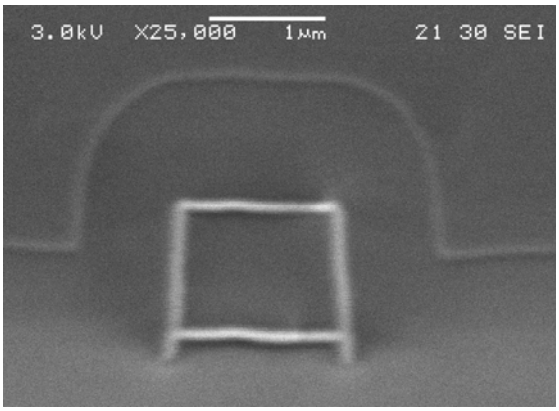


Fig. 1: Photograph of a box-shaped waveguide realized with TriPleX technology. The clear box is Si_3N_4 65nm thick; the gray surrounding is SiO_2.

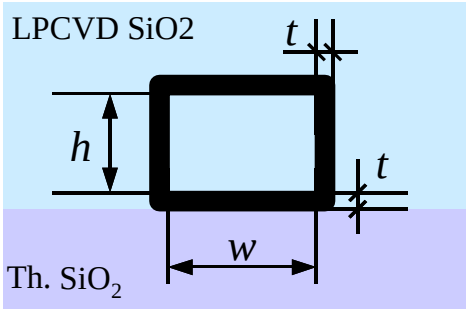


Fig. 2: Transverse shape of the realized waveguide

Table 1: Characteristic dimensions and properties of two box-shaped TriPleX waveguides for null birefringence

	t = 65 nm	t = 150 nm
$w = h$ [μm]	1.10	0.60
R_{min} [μm] (FSR [GHz])	500 (60)	60 (530)
η (UNHA) [dB]	0.13	4.5
PDL η [dB]	<0.02	<0.05
n_{eff} (TE, TM)	1.465	1.521

sufficient to realize optical waveguides able to support single mode operation of both TE and TM modes. As a consequence, silicon nitride waveguides are typically designed as strip waveguides.

The effective thickness of the waveguide can be increased by overlapping parallel strips of Si_3N_4 and SiO_2. The SiO_2 layers sandwiched between the nitride layers relax material stresses and several layers can be deposited, as shown in Ref [12]. In this way also the TM mode can be brought to full propagation still keeping the TE in the single mode regime. However, in this way, the birefringence increases to values higher than 10^{-2}. As a further disadvantage, in a MLW waveguide the TE and TM modes assume different dimensions and shape, leading to different coupling efficiency with optical fibers, bending capabilities, losses and PDL.

On the contrary, the presence of vertically oriented high-index layers, such as in the case of the "box-shaped" waveguide of Fig. 1, is found to add interesting features with respect to MLWs barely made of horizontally overlapped parallel strips. The transverse section of the proposed waveguide is shown in Fig. 2, where t is the thickness of the nitride layer, w is the inner width and h the inner height of the low index core. The optimal relationship between these dimensions guarantees the null birefringence condition in single mode regime, good bending capabilities and fiber coupling efficiency with very a very low PDL.

Following several numerical simulations and technological feasibility evaluations, the optimal dimensions has been found and reported in Table 1 for two different thickness values of the nitride layer.

Even though the square shape is the best one to reduce form birefringence, in practice a slightly wider box is required to compensate for the small anisotropy of the vertical nitride walls. Waveguide dimensions, minimum bending radius (to get radiation losses of 0.1 dB/rad), coupling efficiency η with a small core optical fiber with NA=0.38 (UHNA - Nufern, 3.6 μm spot size), PDL and effective refractive index are reported in Table 1. These results were obtained with a simulator based on the eigenvalue expansion method and validated by a BPM tool. Both waveguides have a null birefringence at a wavelength of 1550 nm. A thicker nitride layer allows a much tighter bending radius, because of the higher mode confinement, and hence a low coupling efficiency with optical fibers. In brackets it is shown the maximum Free Spectral Range attained by a ring resonators realized with the corresponding waveguide. The FSR can be increased up to 2 THz for a nitride thickness t = 250 nm. The fiber coupling efficiency is excellent for the t = 65nm waveguide, while lensed or tapered fibers or mode matching adapters should be used if thicker nitride layers are used. Note, in both cases, the almost null PDL that, furthermore, remains below 0.05dB per facet in the wide range from w = 0.5 to 2 microns.

An interesting feature is the low effective refractive index of the guided modes, despite of the small minimum bending radius. As shown Fig 3a) and b), the optical field is not strictly confined into the nitride layers, but widely spreads over the whole cross section. The shapes of the two modes are very similar, but rotated by 90 deg. The field of the quasi-TE mode is mainly confined by the horizontal layers

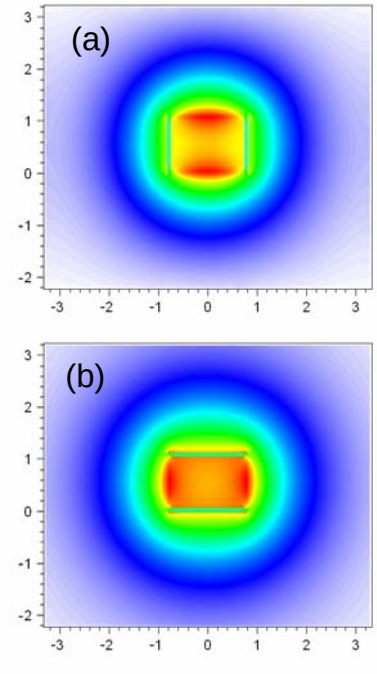


Fig. 3: Electric field transverse intensity of TE (a) and TM (b) modes.

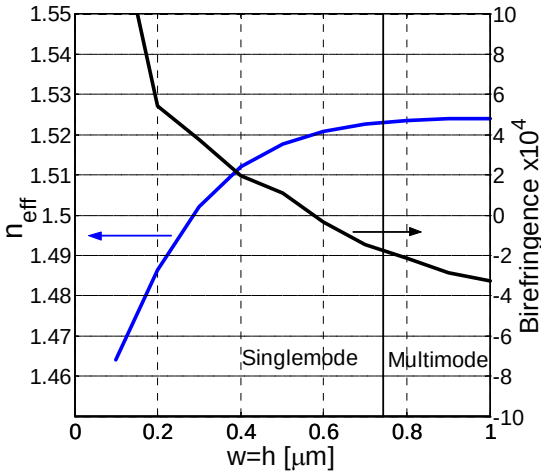


Fig. 4: Refractive index and birefringence of a box-shaped waveguide with t = 150 nm.

of the box, while the quasi-TM mode is confined by the vertical layers. This shape guarantees an excellent compromise between minimum bending radius, fiber coupling efficiency and technological feasibility, allowing accessing to effective index contrasts otherwise not available with standard materials. Moreover, it can be efficiently exploited to design polarization independent or strongly polarization sensitive devices (like directional couplers).

Fig. 4 shows the effective refractive index and birefringence of the square waveguide with t = 150 nm vs waveguide dimensions. Differently from classical buried waveguides, the n_{eff} tends to saturate rapidly and, in the multimode region, even to decrease. With respect to the waveguide width (with fixed height and vice versa), the TE and TM effective indexes, have opposite behaviours. As one can perceive from mode shapes of Fig. 3, by increasing w the TE confinement increases, while the TM confinement decreases and n_{eff} varies accordingly. The opposite holds for the h dependency. This unusual property can be conveniently exploited to easily get the zero birefringence point, tune the propagation characteristics in bends and in general de-couple the TE and TM behaviour.

Technology and realization

The box-shaped waveguide is based on alternating LPCVD Si_3N_4 and LPCVD SiO_2 layers. The latter is called TEOS SiO_2. Figure 5 depicts the schematics of the LioniX fabrication procedure for the square shaped waveguides. The process starts with thermal oxidation of a 100 mm-diameter silicon wafer (1 and 2) to form the lower cladding. Then LPCVD Si_3N_4 (3) and TEOS SiO_2 (4) are deposited. Then photolithography is performed (5), followed by RIE (6), photo resist removal (7) and a second LPCVD Si_3N_4 deposition (8). Finally, the Si_3N_4 is locally removed to obtain the box-like waveguide geometry (9), followed by the deposition of the passivating top cladding layer (10).

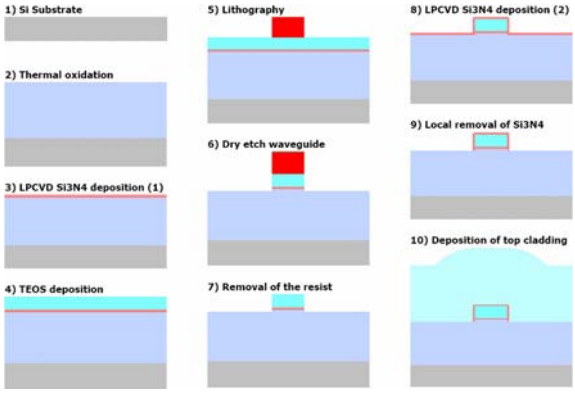


Figure 5: Flow process scheme for the box- shaped waveguides as made with Flowdesigner process modeller (PhoeniX BV, Enschede, the Netherlands).

Waveguide characterization

Several wafers were produced and characterized both at structural and optical level. Samples were prepared as usual, by cutting the wafers with a circular saw and no particular difficulties arose from the layered structure. Waveguides were characterized in butt coupling, without facet polishing, with a small core fiber (UHNA) with a measured MFD = 3.6 μm. All the results reported in this contribution refer to waveguides with t = 65nm on chips 6.25 cm long.

Fig. 6a) shows the measured fiber-to-fiber insertion losses of the TE mode versus the waveguide width and also the simulated fiber to waveguide total coupling efficiency (two facets). Apart from the damaged 3.5 and 0.5 μm wide waveguides, the insertion loss is very low and the attenuation ranges from 0.06 to 0.08 dB/cm over the whole third telecom window. Also the overall PDL, shown in Fig. 6b), partially due to the fiber coupling efficiency and partially to the higher TM attenuation (estimated around 0.17dB/cm for every waveguide width), keeps very low levels. At present the reasons of the higher TM insertion loss is under investigation and cut-back measurements will be carried out. Note that the PDL due to the fiber coupling can be reduced by properly tapering the waveguide near the chip edges.

The second important parameter experimentally and theoretically investigated is the group refractive index of the two modes, and hence the group birefringence. The simulated and the measured TE and TM group refractive index of the same waveguides are reported in Fig. 7. Measurements were carried out with a phase sensitive optical low coherence interferometric technique [13]. Group index and also birefringence are in very nice agreement with simulations for waveguide widths larger than 1.5 μm. In the narrower waveguides, the TM mode group index is slightly lower than expected. The zero group birefringence point is very close (about 100 nm in width) to the expected one. A possible explanation is that material dispersion and material anisotropy are neglected in these simulations.

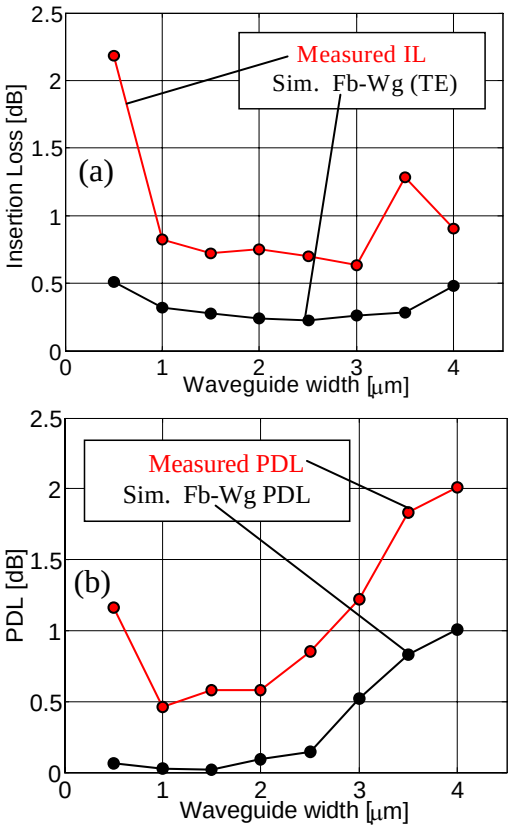


Fig. 6: Measured insertion loss, simulated coupling efficiency and PDL of the waveguide with t = 65nm.

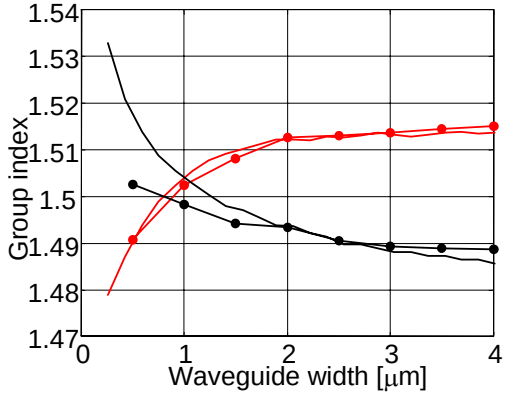


Fig. 7: Simulated (lines with marks) and measured TE and TM group refractive index (t = 65 nm).

To investigate the bending capabilities of the TriPlex waveguides, the insertion loss of several waveguides with radii ranging from 3mm to 250μm were measured with a polarimetric set up. As shown in Fig. 7, where the attenuation of the TE mode in the bends is reported, minimum bending radii down to 750 and even 500 μm with negligible radiation losses were obtained, in agreement with numerical predictions (Tab. 1). By increasing the channel width, the bending loss for the TE polarization reduces. However, one has to take care of PDL that increases with the channel width because the TM mode suffers from waveguides widening, as suggested by the effective index reduction shown by

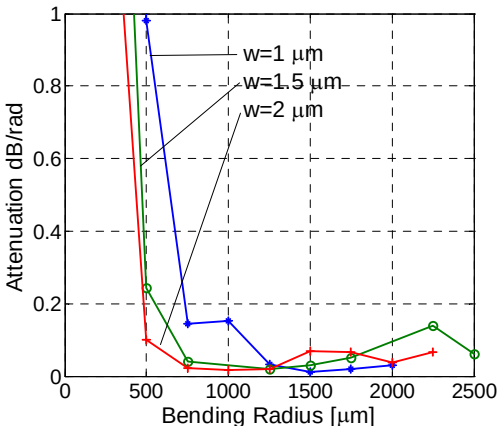


Fig. 8: Measured TE bending losses (t = 65 nm).

Fig. 6. PDL remains however unaffected respect the straight waveguide down to 1.25mm bending radius. Waveguides with a thicker nitride layer should are expected to support even tighter bends, as predicted by Table 1.

Conclusions

A new class of optical waveguides, combining enhanced design flexibility, advanced optical properties and a simple, fully CMOS-compatible technology, has been presented. Experimental results show values of attenuation, PDL, birefringence and fiber-to-waveguide coupling loss comparable to conventional low-index contrast waveguides, but with significantly increased bending capabilities. These results demonstrate that the TriPleX technology can fulfil the requirements of large scale integrated optics, with promising applications in the field of optical communications and sensors.

Acknowledgments

The authors want to thank Arjan Hoekman, Robert Wijn and Rik de Boer for their support in the fabrication of the waveguides.

References

1 M.Ibanescu et al, Science, no. 5758, p. 415, 2000.
2 D.Yin et al, Optics Express, no. 23, p. 9331, 2005.
3 Y.Yi et al, Optics Express, no. 20, p. 4775, 2004.
4 R.G.Heideman et al, Photonic West, 2006.
5 R.G.Heideman et al, Leos Benelux Chapter, 2005.
6 R.G.Heideman et al, US Patent US 7,146,087 B2.
7 R.G.Heideman et al, US Patent US 7,142,759 B2.
8 C.G.H.Roeloffzen et al, LEOS Benelux Chapter, p. 71, 2005.
9 A. Meijerink et al, Symp.on Comm.and Vehicular Techn. in the Benelux, p. 7, 2006.
10 L. Zhuang et al, LEOS Benelux Chapter, p. 45, 2006.
11 S. Zheng et al, Sel. Topics in Quant. Electron., no. 6, p. 1380, 2006.
12 M.Melchiorri et al, Appl. Phys. Lett. 86, 121111, 2005.
13 F.Morichetti et al, ECIO, Paper WeB3-2, 2005.

Integrated Optical Waveguide Device for Picosecond Pulse Compression

M.J.R. Heck (1), E.A.J.M. Bente (1), Y. Barbarin (1), H.D. Jung (1), Y.S. Oei (1), R. Nötzel (1), D. Lenstra (2) and M.K. Smit (1)

1) COBRA Research Institute, Technische Universiteit Eindhoven, Postbus 513, 5600 MB Eindhoven, the Netherlands, m.heck@tue.nl

2) Dept. of Electrical Engineering, Mathematics and Computer Science, Technische Universiteit Delft, the Netherlands

Abstract: *We report on the fabrication and characterization of a new device, named IRIS. It is designed to increase the coherent optical bandwidth of a picosecond pulse train for subsequent pulse compression. The IRIS device consists of a concatenated array of semiconductor optical amplifiers and saturable absorbers. It is realized in the InP/InGaAsP material system for the 1550 nm range.*

Measurements on the realized IRIS devices show increased broadening of the pulse spectrum as compared to an SOA of equivalent length and a smoother optical power spectrum. Consequent compression of the chirped pulses using standard single mode fiber shows decreased pulse pedestals as compared to an SOA, indicating increased linearity of the chirp. Pulse compression up to 50 % is observed.

Introduction

Trains of picosecond optical pulses with wavelengths around 1550 nm generated by semiconductor lasers have many applications, most notably in high-speed optical time division-multiplexed multiplexed (OTDM) systems [1]. Future 640 Gbit/s and Tbit/s systems will even require pulses with sub-picosecond duration. Integrated mode-locked semiconductor laser sources (MLLs) are typically able to generate transform limited pulse trains with durations down to a few picoseconds [2]. Further pulse compression can for example be obtained using soliton effects in fiber amplifiers and the subsequent use of dispersive fibers [3]. However these are bulk components.

For reasons of compactness, stability and cost, integration of a pulse compressing system with the pulse source is preferable. Several options have been proposed as an integrated optical pulse compressor. In [4] a waveguide device with concatenated semiconductor optical amplifiers (SOAs) and saturable absorbers (SAs) has been simulated and it was shown to be able to compress initially transform limited picosecond pulses. Chirped, or non-transform limited, pulses can be compressed further using integrated pulse compressing devices [5, 6].

Chirping or adding bandwidth to an initially transform limited pulse can be done using SOAs, though the amount of spectral broadening is limited and the power spectrum shows a modulation [7]. The latter will result in pulse pedestals or even satellite pulses when the pulses are compressed. In [7] we showed experimentally that an integrated optical waveguide device consisting of multiple equal SOA/SA pairs, which we named IRIS (Integration of Regeneration, Isolation and Spectral Shaping), seems promising for abovementioned application. Compared to a single SOA the obtained bandwidth after picosecond pulse propagation through the device is larger and showed significantly less modulation in the spectrum for specific operation conditions.

In this work we study this IRIS device with respect to both its temporal pulse shaping and spectral shaping effects on a picosecond pulse train. A number of configurations of IRIS devices have been realized by us. We experimentally compare the performance of these devices with an SOA of the same length.

IRIS device design and realization

The IRIS device consists of a series of equal pairs of one SOA section and one SA section, as schematically depicted in Fig. 1(a). Its most important feature is that the saturation energy of the SA is lower than the saturation energy of the SOA. As a result a picosecond pulse that is being amplified by the device will first saturate the SA and only after that the SOA, much like in passive mode-locking.

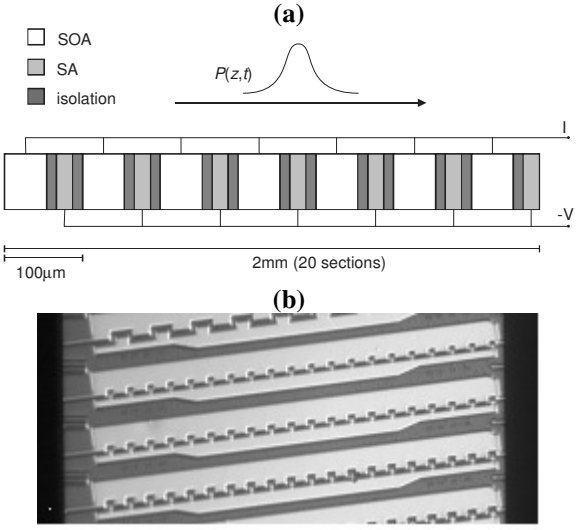


Fig. 1: (a) Schematic overview of the IRIS configuration. An input pulse (denoted by $P(z,t)$) enters from the left side, entering an SOA and exiting from the right-hand side. The ratio of the SOA and SA length within the 100 µm section (only 7 out of 20 shown) is varied. Common contacts are used for applying the injection current I and the reverse bias V. **(b)** Photograph of a number of realized devices, showing different configurations.

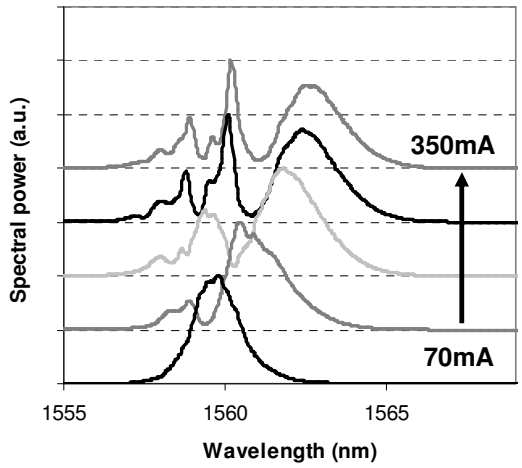


Fig. 2: Optical pulse spectra obtained after propagation through a 2 mm SOA, using a 10 GHz input pulse train with 2.0 ps duration and 0.1 W peak power. Spectra for different SOA injection currents are given.

Such devices have been realized using InP/InGaAsP bulk gain material, operating at wavelengths in the region of 1.55 µm. The sequence of SOAs and SAs is fabricated by first etching a shallow ridge waveguide of 2 µm width in the bulk gain material. To suppress lasing, the waveguide is oriented at the Brewster angle for the fundamental waveguide mode with the facets. The facets have also been antireflection coated. To create electrical isolation between the SOAs and SAs, the most highly doped part of the p-cladding layers is etched away using a dry RIE etch process. The isolation section between the SOA and SA has a length of 10 µm to 15 µm. Two gold metal pads alternately contact the waveguide sections to create two common contacts for the SOAs and SAs respectively as can be seen in Fig. 1(b). Amplification and absorption are realized by a forward or reverse electrical bias of the diodes respectively.
We have designed and realized a number of different device configurations with 20 SOA/SA pairs and varying length ratio between the SOA and SA, with the SA length increasing from 10 µm up to 20 µm. We have added 2 mm long SOAs on the same chip for reference purposes. The fabrication technology of the IRIS device is compatible with the technology to fabricate MLLs [8] or pulse shapers [5]. This allows for further integration of these components with the IRIS device.

Experimental results

A picosecond pulse train propagating through an SOA or SA experiences a self-phase modulation (SPM) due to the effects of gain saturation, carrier heating and other ultrafast nonlinear refraction [9]. The result of this SPM is a change in the optical spectrum of the pulse train. This effect increases the bandwidth of the spectrum of a pulse train, effectively chirping it. Depending on the shape of the chirp profile, the pulses can be compressed consequently by a dispersive element.

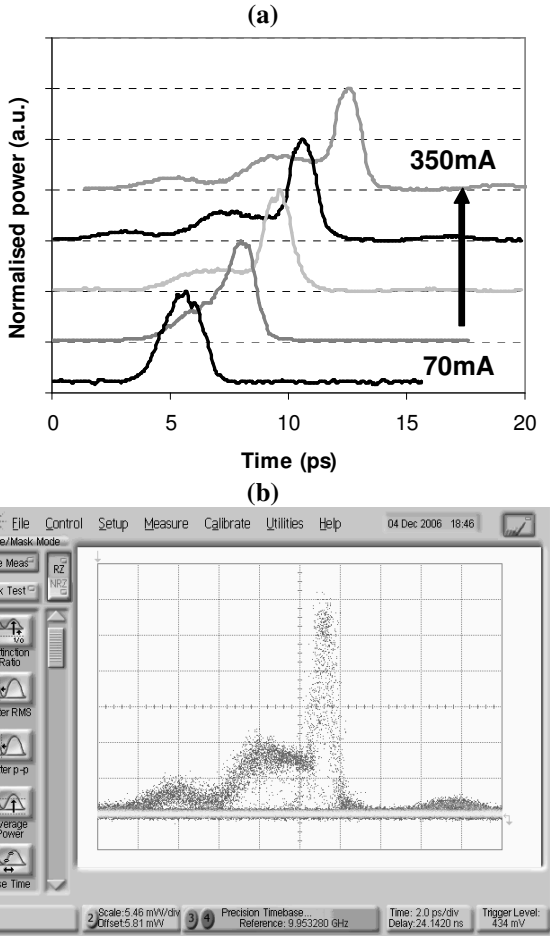


Fig. 3: (a) Temporal pulse profiles, corresponding to the spectra shown in Fig. 2, after propagation through 15 m of SMF. Profiles have been horizontally shifted for easy comparison. The temporal profiles have been obtained with a 700 GHz optical sampling oscilloscope. In **(b),** a trace obtained at 350 mA injection current is shown. The zero level (horizontal) trace is due to the pulsed injection current. Jitter in the pulsed laser and sampling laser in the oscilloscope cause the broadening of the pulse profile trace.

We have measured spectra of short optical pulses that have propagated through IRIS devices with SA lengths of 10 µm and 20 µm (see Fig. 1(a)). A 10 GHz pulse train, with pulse durations of 2.0 ps and a peak power of 0.1 W is used for the input. Also we have measured temporal pulse profiles exiting from the IRIS devices. For this we use a 700 GHz bandwidth optical sampling oscilloscope. A lensed fiber tip is used for coupling the pulse train in and out of the IRIS device and a total of 15 m of standard single mode fiber (SMF), with a dispersion of 18 ps/nm/km, is used in between the device and the sampling oscilloscope. For comparison spectra and pulse shapes are also obtained for pulse train propagation through a 2 mm SOA, i.e. with an equivalent total length to the IRIS device. Pulsed injection current (300 ns pulses, 1 % duty cycle) is used to prevent heating of the device.

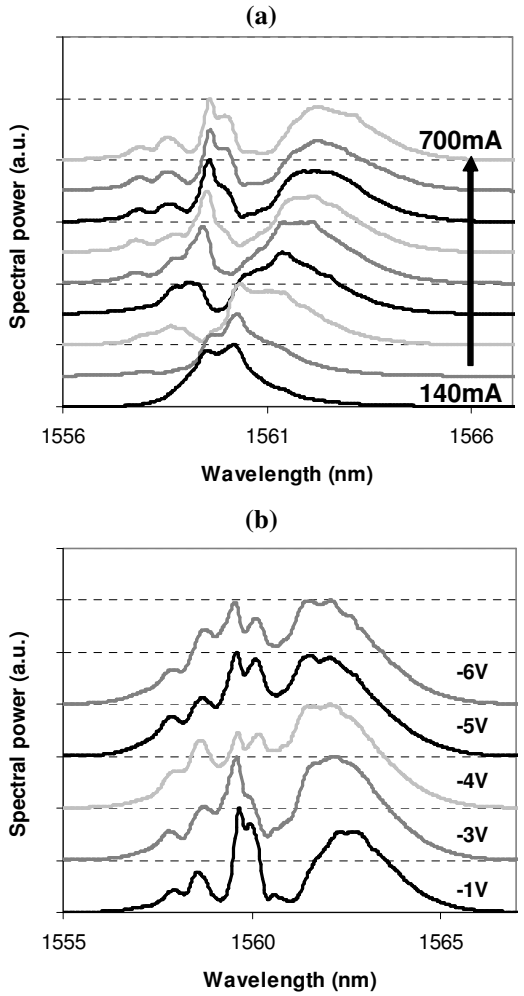


Fig. 4: Optical pulse spectra obtained after propagation through an IRIS device with 10 µm SAs, using a 10 GHz pulse train with 2.0 ps duration and 0.1 W peak power. **(a)** Total injection current for the 20 SOAs is varied. The SA reverse bias voltage is -1 V. **(b)** Injection current is fixed at 700 mA, SA bias voltage is varied from -1 V down to -6 V.

In Fig. 2 pulse spectra after propagation through a 2 mm SOA are presented for different injection currents. As can be seen, increasing the injection current introduces a shift of the spectrum towards longer wavelengths, as can be expected from the gain saturation [9]. However the spectral profile shows much structure, with peaks around the wavelength of the input pulses at 1560 nm. This indicates that the induced chirp profile over the pulse train is not linear. Therefore pulse compression using mainly second order dispersion, as introduced by e.g. SMF, is not optimal. We have measured the temporal output pulse shapes after propagation through 15 m of SMF, with a total dispersion of 0.34 ps^2. This corresponds approximately to a pulse broadening (or compression) value of 0.3 ps per nanometer optical bandwidth, assuming linear chirp profiles. Given the optical bandwidths as mentioned in Fig. 2, this value of the dispersion will clearly show either pulse compression or broadening, depending on the sign of the chirp of the pulses. As a result, applying this amount of dispersion gives qualitative insight in the shape of

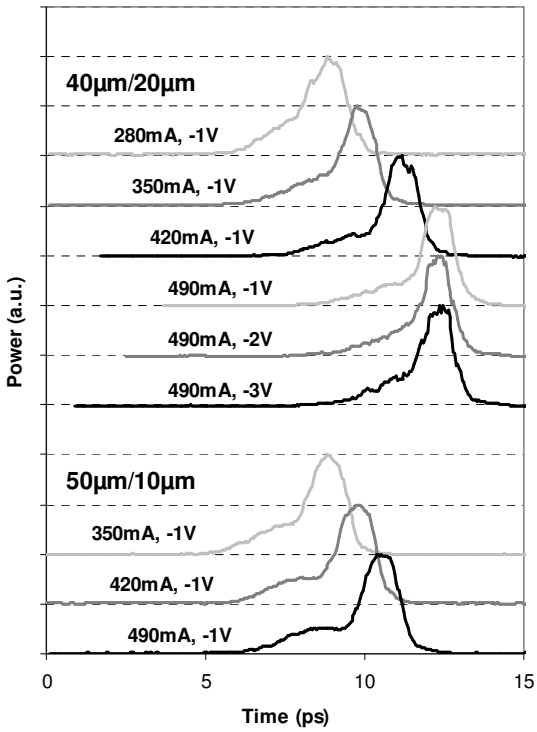


Fig. 5: Normalized temporal pulse profiles after propagation through 15 m of SMF, obtained with a 700 GHz optical sampling oscilloscope. Profiles have been horizontally shifted for easy comparison. Pulse profiles for IRIS devices with 20 µm SAs (40 µm SOAs) and 10 µm SAs (50 µm SOAs) are given, for various SOA injection currents and SA bias voltages.

the phase profile over the pulse. We note that a full phase characterization of the pulse can be made using the method mentioned in [10], using only the temporal pulse profile and the optical power spectrum.

Fig. 3 shows the obtained temporal pulse shapes. As can be seen the pulse is only partially compressed at the higher injection currents, with one or two weaker and longer pulses preceeding the compressed part.

In conclusion it can be said that the SOA is not a suitable device for chirping an optical pulse with the aim of further pulse compression. As the chirp profile is not linear, using only second order dispersion, e.g. by a SMF, will only partially compress the pulses. Also, due to the modulation in the optical spectrum, even more advanced pulse compressors, e.g. as mentioned in [5], can not avoid the generation of satellite pulses when trying to fully compress the pulse.

In Fig. 4(a) spectra observed from pulses after propagation through an IRIS device with 10 µm SAs are given. As the 20 SOAs have a common contact, the total injection current is given. The SAs are reversely biased with a voltage of -1 V. As can be seen, the spectrum is still heavily modulated at the higher injection currents. However, increasing the voltage over the SAs severely decreases this modulation depth, as can be seen in Fig. 4(b). Again, because of the 15 m SMF, a second order dispersion of 0.34 ps^2 is applied to the pulse train after propagation through the IRIS devices. Fig. 5 shows the obtained temporal

pulse profiles. Comparing the pulse profiles obtained with IRIS devices with those obtained by an SOA (Fig. 3) shows that the pulse pedestal and preceeding pulses decrease. This effect is more pronounced for the IRIS devices with 20 µm SAs as compared to those with 10 µm SAs. Also, increasing the bias voltage over the SAs decreases the pedestal even more. The obtained compression is almost 50%, with output pulse durations down to 1.1 ps for IRIS devices with 20 µm SAs at higher injection currents. This value of the pulse duration is close to the measurement limitation of the 700 GHz sampling oscilloscope due to the limited risetime.

The spectral bandwidth of over 4 nm (Fig. 4(b)) allows for further pulse compression, either by optimizing the SMF length of by adding higher order dispersion. This depends on the exact shape of the chirp profile of the pulses.

Concluding it can be said that the chirp profile of a train of pulses with a duration of 2.0 ps after propagation through an IRIS device makes it possible to compress these pulses further using second order dispersion. A total dispersion of 0.34 ps^2 compresses these pulses down to 1.1 ps, i.e. almost 50%.

Conclusion

We have fabricated a device, named IRIS that is able to chirp a train of picosecond pulses. Measurements show that pulses with an initial duration of 2.0 ps can be compressed down to 1.1 ps after propagation through the device, using only second order dispersion, without the appearance of leading or trailing pulses. This indicates a good linearity of the chirp over the pulses. Such compression is not possible using an SOA of the same length as the obtained chirp profile is less linear and only partial compression of the pulses occurs. This is an important result as second order dispersion is the dominant dispersion term in SMF, but also in integrated dispersive components [6].

The shape of the spectrum obtained has a more smooth structure as compared to that from an SOA. This makes the IRIS device more suitable for use in combination with an arbitrary pulse shaper [5] as the spectrum needs less power equalization.

As the fabrication technology of the IRIS device is compatible with both MLLs [8] and pulse shaping devices [5], it is a promising candidate for further integration to create monolithically integrated (sub-) picosecond or arbitrarily shaped pulse sources.

Acknowledgments

This research is supported by the Towards Freeband Communication Impulse of the technology programme of the Dutch Ministry of Economic Affairs and by the Dutch NRC-Photonics programme.

References

1 L.A. Jiang et al., J. Opt. Fiber. Commun. Rep. 2, pp. 1-31, 2005
2 R. Kaiser et al., IEEE Photon. Technol. Lett., vol. 15, no. 5, p. 634, 2003.
3 J.T. Ong et al., IEEE J. Quant. Electr., vol. 29, no. 6, p. 1701, 1993
4 Shimizu et al., Jpn. J. Appl. Phys., vol. 39, p. 475, 2000
5 M.J.R. Heck et al., ECIO, p. 351, 2005
6 Y. Lee, Appl. Phys. Lett., vol. 73, no. 19, p. 2715, 1998
7 M.J.R. Heck et al., IEEE/LEOS Benelux, p. 41, 2006
8 Y. Barbarin et al., Opt. Expr., vol. 14, p. 9716, 2006
9 J.M. Tang and K.A. Shore, IEE Proc.-Optoelectron., vol. 146, p. 45, 1999
10 M. Hacker et al., Opt. Expr., vol. 9, no. 4, p. 191, 2001

Amplifying Waveguide Optical Isolator with Integrated Electromagnet

Wouter Van Parys, Dries Van Thourhout, Roel Baets (1) Beatrice Dagens, Jean Decobert, Odile Le Gouezigou, Dalila Make (2) and Liesbet Lagae (3)
1) Department of Information Technology, Ghent University - IMEC, St-Pietersnieuwstraat 41, 9000 Gent, Belgium (wouter.vanparys@intec.ugent.be) 2) Alcatel Thales III-V Lab, Route Départementale 128, 91767 Palaiseau, France (beatrice.dagens@3-5lab.fr) 3) Interuniversitair Micro-Elektronica Centrum, IMEC vzw, Kapeldreef 75, 3001 Leuven, Belgium (liesbet.lagae@imec.be)

Abstract: *We have demonstrated an amplifying waveguide optical isolator with integrated electromagnet. This provides a solution to the generally poor magnetic remanence of this type of isolator. The proof of principle is presented and optimization routes are discussed.*

Introduction

An optical isolator is indispensable in an optical telecom link to protect semiconductor lasers from optical feedback. A planar, waveguide version of the optical isolator is highly desirable as it would greatly reduce the packaging cost – hence the overall cost – of a laser diode module, because it avoids the expensive alignment required with current commercial bulk isolators.

An integratable isolator configuration that is getting a lot of attention recently is the amplifying waveguide optical isolator [1-4]. The device basically is a semiconductor optical amplifier (SOA) with a transversally magnetized ferromagnetic film close to the guiding core. The magneto-optic (MO) Kerr effect causes a non-reciprocal shift of the complex effective index of the guided modes, implying that the modal loss is dependent on the propagation direction. Current injection decreases the overall loss level in the device. As illustrated in the bottom part of figure 1, the result is a device which, being transparent in one direction while providing loss in the opposite direction, is isolating. The main advantage of this isolator concept is that monolithic integration with a semiconductor laser is straightforward, as both components are essentially the same. Configurations operating in TM-polarization [1, 3-4], illustrated in figure 1 (top), and TE-polarization [2] have been demonstrated in recent years.

One of the main issues for this kind of device is the magnetization of the ferromagnetic metal film. The very high aspect ratio of the length of the film to the width results in very low remanent magnetization of the film due to large demagnetizing fields. One of the solutions to this problem is to have a magnet integrated with the isolator. In this paper we demonstrate an amplifying waveguide isolator with an integrated electromagnet. This magnet is a gold stripe deposited along the longitudinal direction of the isolator in close vicinity of the bias contact. Current flowing from one side of the cavity to the other generates a transverse magnetic field causing the magneto-optic Kerr effect.

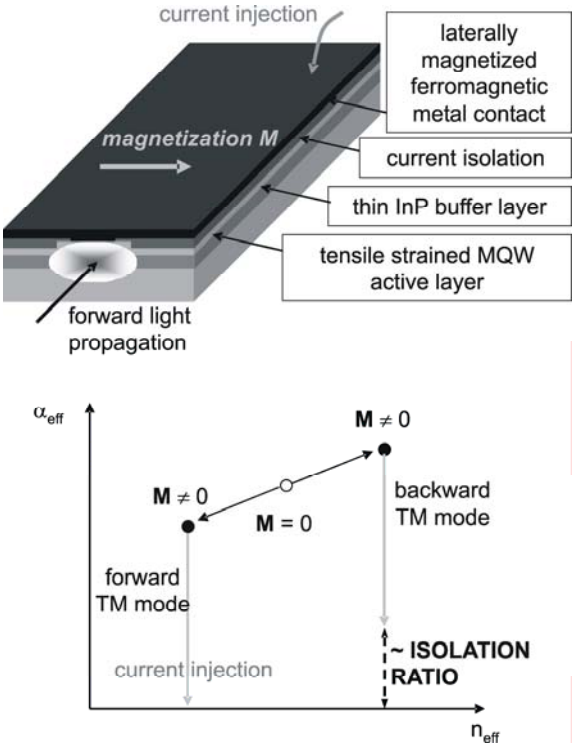


Fig. 1: Lay-out (top) and operation principle (bottom) of the TM-mode amplifying waveguide optical isolator.

Apart from application as an optical isolator, this result is interesting in itself as it is now possible to modify the internal loss of an SOA dynamically and non-reciprocally.

Design

The design of the amplifying waveguide optical isolator and the integrated electromagnet can be considered as two separate parts, which will both be discussed in this paragraph.

The operation of the isolator is determined by the interplay of the source of the non-reciprocal loss shift – the ferromagnetic metal – and the gain that can be provided by the amplifying material to compensate the absorption in the metal film. The optimization of both building blocks has been extensively discussed earlier [4]. The amplifying core is an AlGaInAs (λ_g = 1288nm) tensile strained multiple quantum well

structure, where the built-in tensile strain provides TM-selective material gain while suppressing TE-gain. As was demonstrated by Decobert et al., [5] the gain parameter g_0 can be strongly enhanced by increasing the amount of tensile strain; hence a very large value of -1.6% strain is built-in in the quantum wells. Three Co_xFe_{1-x} compounds have been characterized ($Co_{90}Fe_{10}$, $Co_{50}Fe_{50}$ and Fe) and $Co_{50}Fe_{50}$ was found to be the best compromise between a high MO effect and low absorption [6]. The MO metal film also acts as the electrical contact for the underlying semiconductor optical amplifier. Low contact resistivity combined with minor additional absorption is provided by a hybrid Be p^+-doped $In_{0.81}Ga_{0.19}As_{0.41}P_{0.59}$ / $In_{0.54}Ga_{0.46}As$ bilayer (thickness = 100nm/15nm, $N_{Be} = 2.0\ 10^{19}cm^{-3}$ / $3.0\ 10^{19}cm^{-3}$) [7].

Apart from the two main building blocks the isolator design is a matter of optimization of the thickness of the cladding layers; the two $In_{0.86}Ga_{0.14}As_{0.32}P_{0.68}$ separate confinement heterostructure (SCH) layers surrounding the quantum well core and the InP buffer thickness between the amplifying core and the contact structure. The procedure for the design of these geometric device parameters targets optimization of the practical device specifications. The corresponding figure of merit to be minimized is the total bias current required for transparency in the forward propagation direction corresponding to 1dB of optical isolation. The 1D simulations have been done with an optical mode solver [8] extended with a perturbation-based algorithm for MO waveguide calculation [9]. A steepest-descent algorithm was implemented to obtain the best values for the three geometric parameters. Theoretically, the isolator has a FoM equal to 7.45mA/dB isolation for a ridge width of 2μm, and a cavity length of 155μm/dB isolation.

A schematic cross-section of the amplifying waveguide optical isolator with integrated electromagnet is given in the top part of figure 2. The design parameters for the electromagnet are the width of the gold stripe and the distance between the electromagnet and the ferromagnetic metal film. Other parameters are the thickness of the gold stripe, which influences the current density in the electromagnet but not the strength of the magnetic field, and the variation of the generated magnetic field in the lateral direction (x-direction), which is of only minor importance if the stripe width is much larger than the width of the ferromagnetic film. It is to be noticed that the latter has to be the case for the isolator to ensure that the magnetic field is aligned along the lateral direction (x-direction).

The partial differential equation describing the magnetic field problem was solved with MATLAB. The bottom part of figure 2 shows the result of these calculations. The simulated values of the magnetic flux density (in mT) are plotted for variation of the width of the electromagnet and the distance from the electromagnet per unit (mA) current injection in the gold

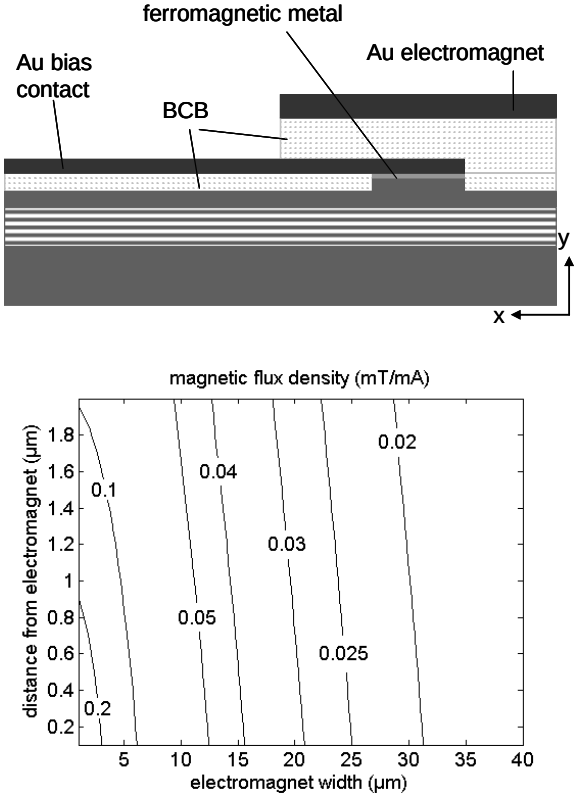


Fig. 2: (top) Schematic cross-section of the amplifying waveguide isolator with integrated electromagnet. (bottom) Simulation of the lateral magnetic flux density (x-direction) as a function of the width of the electromagnet gold stripe and the distance (y-direction) from the electromagnet, expressed in mT per mA of current injection.

stripe. For sufficiently wide stripes the generated magnetic field is quasi-independent of the distance from the electromagnet. This is an advantage for the fabrication because the use of a thick separation layer between bias contact and electromagnet reduces the risk of short-circuiting both metal layers.

With the available lithography mask it was only possible to have an electromagnet gold stripe as wide as 30μm, resulting in a magnetic field that is far from optimized. However, it is suitable for the first demonstration of the principle.

Fabrication

The isolator was grown with metal organic vapor phase epitaxy on an n^+ S-doped InP substrate ($N_S = 3.0\ 10^{18}cm^{-3}$). The layer structure is a Si n-doped ($N_{Si} = 10^{18}cm^{-3}$) InP cladding layer, the non-intentionally doped (n.i.d.) optimized active core, a Be p-doped InP cladding ($N_{Be} = 5.0\ 10^{17}cm^{-3} \rightarrow 2.0\ 10^{18}cm^{-3}$) and the optimized contact structure. The sputter-deposited 50nm thick $Co_{50}Fe_{50}$ film, capped with a 40nm/150nm Ti/Au protective bilayer, was patterned into 2μm wide stripes with standard lift-off. Ridge waveguides were defined with CH_4:H_2 plasma reactive ion etching using these metallic stripes as an etch

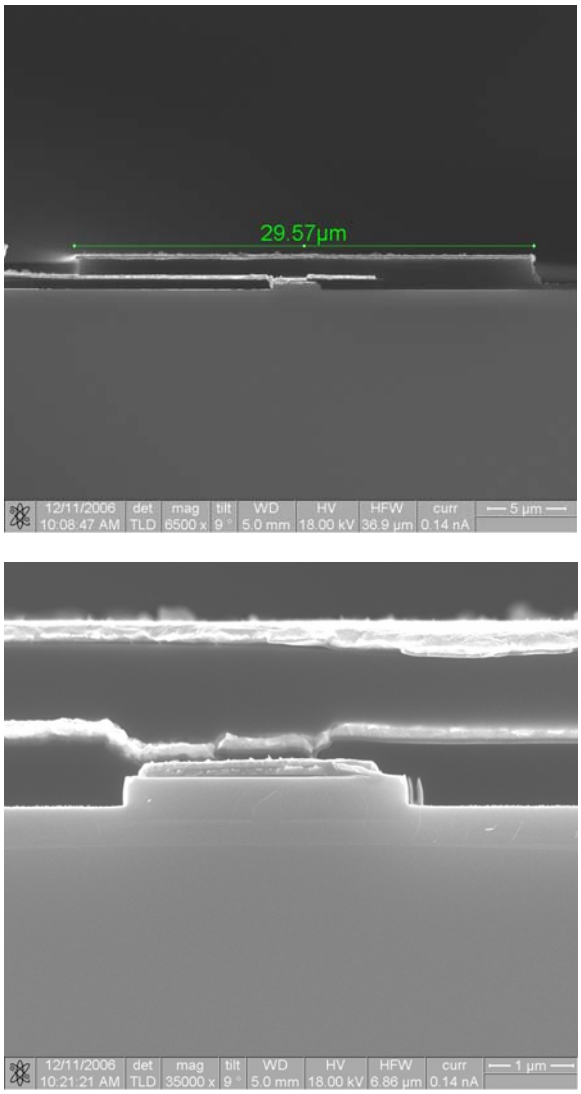


Fig. 3: SEM pictures of the cross-section of the amplifying waveguide optical isolator with integrated electromagnet.

mask. With this technique full covering of the ridge with metal has been achieved. An additional 30µm wide gold stripe is evaporated to enable contacting of the isolator, separated from the semiconductor surface by a benzocyclobutene (BCB) current isolation layer. On top of the isolator bias contact a 30µm wide and 250nm thick gold stripe is deposited, serving as the electromagnet. Both gold stripes are separated by a 1µm thick BCB layer. Isolators with a cavity length of 1.3mm have been cleaved and mounted for characterization.

In figures 3 two scanning electron microscope (SEM) images of a cross-section of the amplifying waveguide optical isolator with integrated electromagnet are given. The top picture shows that the fabricated device is in agreement with the design. When zooming in on the ridge waveguide (bottom part of figure 3) it can be seen that the definition of the ridge is not perfect, with a ridge width that is slightly wider than designed roughness present at the side of the ridge. However, these inaccuracies are not expected to influence the operation of the integrated electromagnet.

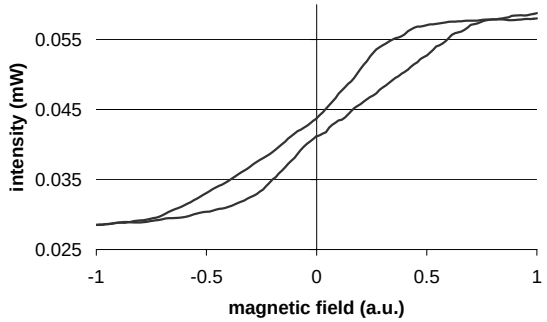


Fig. 4: Optical power emitted by the optical isolator as a function of the externally applied magnetic field at a bias current of 140mA (= above threshold).

Characterization

As was previously elaborated [10] an easy and fast characterization method for the amplifying waveguide optical isolator is to pump as-cleaved isolators above threshold and extract the emitted power as a function of the applied lateral magnetic field – switching the magnetic field direction is equivalent to switching the light propagation direction. Because the material gain is clamped above threshold the non-reciprocal loss shift is independent of the isolator bias current and the optical isolation can be extracted from the ratio of forward to backward intensity – or equivalently the intensity at magnetization in either lateral direction:

$$isolation\,[dB] = \frac{10}{\ln 10}\, 2\, ln(intensity\ ratio) \qquad (1)$$

In order to evaluate the performance of the integrated electromagnet, the amplifying waveguide isolator was initially characterized with an external electromagnet. In figure 4 the emitted power is plotted as a function of the externally applied magnetic field for a bias current of 140mA on a 1.3mm isolator. The corresponding maximal isolation, at saturation magnetization, is 6.1dB. This graph shows that the remanent isolation – at zero magnetic field – is only 8.5% of the maximum value.

Next, the integrated electromagnet was characterized by applying current to the gold strip while pumping the isolator above threshold. To avoid heating, the electromagnet is driven with pulsed current (pulse width 0.3µs, duty cycle 3%). The isolator bias current is continuous wave (CW). The output signal is evaluated on an optical oscilloscope. The measurement is done for both directions of the current flow in the electromagnet, corresponding to a magnetic field in either lateral direction. The bottom part of figure 5 shows the measured intensity time evolution corre-

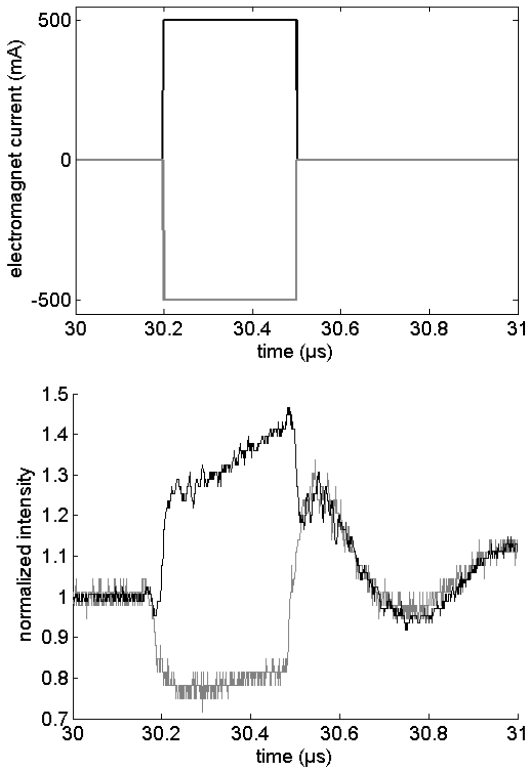


Fig. 5: (top) Time evolution of the injected (pulsed) current in the electromagnet. (bottom) Corresponding (normalized) intensity emitted by the amplifying waveguide optical isolator at a bias current of 140mA (= above threshold).

sponding to the pulsed current of figure 5 (top), where negative current corresponds to reversed current flow direction. The intensity is normalized to compensate for variations in the fiber-to-chip coupling. At the on-set of the current pulse the emitted power rapidly increases or decreases, depending on the current flow direction. This is a clear proof of the on-set of the non-reciprocal loss shift. After the off-set of the pulse, the emitted power quickly becomes identical again in both cases and then slowly recovers from the heating of the device. The ratio of the intensity at "forward" to that at "backward" current injection equals 1.64, which for an isolator of 1.3mm cavity length corresponds to an isolation of 4.3dB, or 70% of what is achieved at saturation magnetization.

We repeated the measurements for different values of the electromagnet current injection. In figure 6 the corresponding evolution of the optical isolation with injected (pulsed) current is plotted. For comparison the optical isolation as a function of the strength of an externally applied magnetic field is also given. From this graph it can be derived that with a current injection of 500mA the achieved magnetic field is about half the value needed to saturate the ferromagnetic film.

The results in figure 6 shows that a very high current of 1.1A is needed to achieve magnetic saturation with the fabricated electromagnet. However, as previously

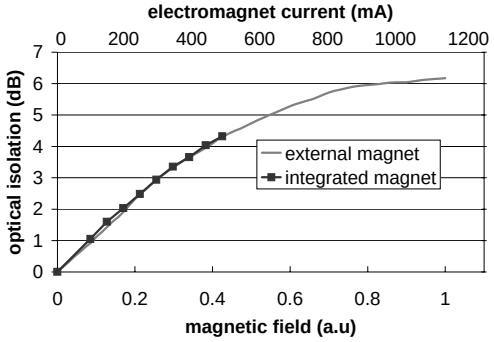


Fig. 6: Evolution of the optical isolation with injection current in the electromagnet and with externally applied magnetic field.

mentioned, due to limitations in the fabrication the demonstrated electromagnet design is far from optimized. Adjusting the width of the gold stripe will decrease the required current by at least a factor of 5. Furthermore, modification of the ferromagnetic film might decrease the magnetic field – hence the current level – required to saturate the film, a point which needs further investigation.

Conclusion

We have developed an optical isolator with integrated electromagnet. While the demonstrated drive current is beyond the acceptable level, possibilities for major improvement have been identified. Decrease of the required current injection should also enable CW operation of the electromagnet.

Acknowledgment

This research was partially performed in the frame of the European Union IST-project ISOLASER.

References

1 M. Vanwolleghem et al., APL, **85**, 3980 (2004).
2 H. Shimizu et al., JLT **24**, pp.38-43 (2006).
3 V. Zayets et al., APL, **86**, 261105 (2005).
4 W. Van Parys et al., APL, **88**, 071115 (2006).
5 J. Decobert et al., J. Crystal Growth **272**, 542 (2004).
6 M. Vanwolleghem et al., JOSA B **24**, p.94-105 (2007).
7 W. Van Parys et al., 2006 LEOS Annual Meeting (Montreal), p.679-680 (2006).
8 P. Bienstman et al., Opt. and Quant. Elect. **33**, 327-341 (2001).
9 K. Postava, et al. JOSA B **22**, 261-273 (2005).
10 W. Van Parys et al., ECIO 2005 (Grenoble), p.33-36 (2005).

A compact arrayed-waveguide grating with a locally enhanced optical confinement structure using trenches filled with low-refractive index materials

Jiro Ito (1) and Hiroyuki Tsuda (2)
1) *Department of Electronics and Electrical Engineering, KEIO University.* jiro-i.23@tsud.elec.keio.ac.jp
2) *Department of Electronics and Electrical Engineering, KEIO University.* tsuda@elec.keio.ac.jp

Abstract: We have reduced the minimum bending radius of a silica waveguide from 2 mm to 200 μm by burying low-refractive index material along both sides of the core. The local lateral relative refractive index difference (Δ) was increased to 9.05%. Moreover, we fabricated both an 8-channel, 100-GHz channel-spacing arrayed-waveguide grating (AWG) and an 8-channel, 12.5-GHz channel-spacing AWG using variations of these new compact bend structures. Compared with conventional AWGs, the relative chip-sizes of these devices were reduced to about 1/2 and 1/4, respectively.

Introduction

Planar lightwave circuits (PLC) are useful devices for realizing large capacity and high-speed photonic networks. In particular, arrayed-waveguide gratings (AWGs) are key devices that can multi/demultiplex a number of wavelength channels with low loss. Optical communication requires multifunctional small-sized PLCs.

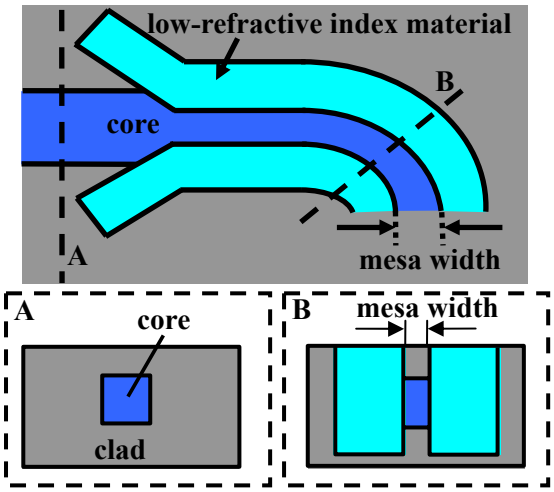


Fig. 1: Schematic of a silica bend waveguide with trenches filled with a low-refractive index material.

However, dense integration is difficult because the minimum bend radii of conventional silica waveguides with high (H)-relative refractive index differences (Δ) of 0.75 % and with super-high (SH)-Δ values of 1.5% are 5 mm and 2 mm, respectively. Semiconductor AWGs [1] and Si photonic wire AWGs [2] with large Δ have been reported. However, the coupling losses of these devices with single mode fibers are large without the use of mode-conversion interfaces. Air trench bend (ATB) technology, which consists of a “cladding taper” and a pair of air trenches along the waveguide bend, can reduce the bend radius, maintaining low loss [3], [4]. We have previously fabricated air-trenched AWGs by this method [5]. However, such trenches can be contaminated by dust and by impurities, and therefore they do not have stable characteristics. On the other hand, we have proposed a locally-enhanced optical confinement structure using trenches filled with low-refractive index resin along the both sides of the core, and we applied this structure to AWGs with H-Δ [6], [7].

In this paper, we have fabricated both a 90-degree bend-type AWG and a triple-arrowhead-type AWG using locally-enhanced optical confinement structures with SH-Δ waveguides. The sizes of these AWGs were reduced to about 1/2 and 1/4 of those of conventional devices, respectively.

Waveguide Design

We used a two-dimensional beam propagation method (2DBPM) to optimize the taper angle of the transition region between a conventional single mode straight waveguide and a narrow-width core sandwiched between low-refractive index material, as shown in Fig. 2.

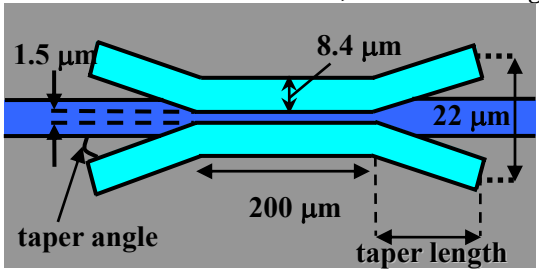


Fig. 2: Straight waveguide for simulations.

The widths of the core, the mesa and the trench were assumed to be 4.3 μm, 2.5 μm and 8.4 μm, respectively. The refractive indices of the core, the cladding and the low-refractive index material were 1.4611, 1.4440 and 1.3335, respectively. The lateral Δ was 9.05%. The simulation results are shown in Fig. 3.

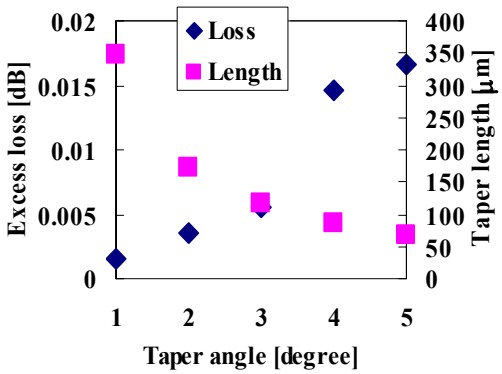


Fig. 3: Excess loss and taper length as a function of taper angle.

The larger taper-angle provides a shorter taper length. However, this leads to higher junction losses because the lateral Δ changes abruptly. Therefore, we determined that the optimum taper angle was 3 degrees, which allows a shorter taper length to minimize losses. The bend radius and the mesa width were optimized by 3D BPM simulation. We used a 90-degree bend to calculate the bend loss, as illustrated in Fig. 4.

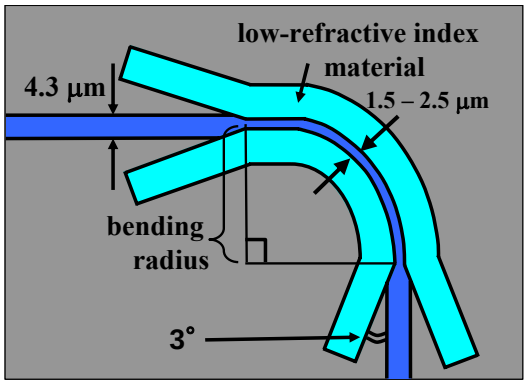


Fig. 4: Schematic of a 90-degree bend waveguide for calculating bending loss.

The taper angle was 3 degrees. The bending radius was changed from 100 to 500 μm. The mesa width was changed from 1.5 to 2.5 μm. The result of the simulation is shown in Fig. 5. For a bending radius of 200 μm, the loss was about 0.1 dB. In addition, the bend loss increased rapidly when the bending radius was less than 100 μm. Hence, we determined that the minimum bending radius for practical applications was 200 μm. The polarization-dependent loss (PDL) was 0.02 dB. Smaller mesa widths provide lower losses, as shown in Fig. 5.

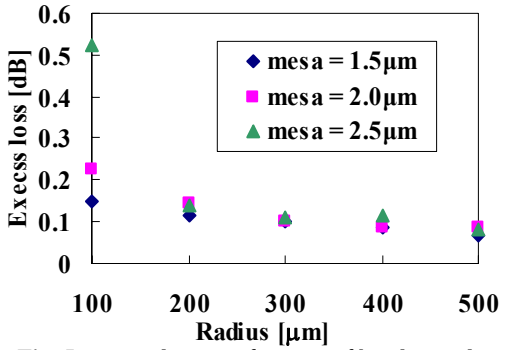


Fig. 5: Excess loss as a function of bending radius.

90-degree Bend-Type AWG

We then applied these small-radius bend structures to an 8-channel, 100-GHz channel spacing, 90-degree bend-type AWG, as shown in Fig. 6. The specifications for this type of AWG are shown in Table I.

Table I: Specifications of a 90-degree bend-type AWG.

Parameter	Value [unit]
number of channels	8
channel spacing	100 [GHz]
FSR	800 [GHz]
number of arrayed waveguides	30
path length difference	252.7 [μm]
diffraction order	237
center wavelength	1552.45 [nm]
taper angle	3 [degree]
minimum bending radius	200 [μm]

We fabricated three kinds of AWGs by changing the mesa width from 1.5 to 2.5 μm. We used Cytop™, which has a refractive index of 1.3335, as the low-refractive index material. The transmission characteristics from the center ports for the three different mesa widths are shown in Fig. 7. The transmission loss includes a coupling loss of 0.9 dB/facet between the single mode fiber and the waveguide, a

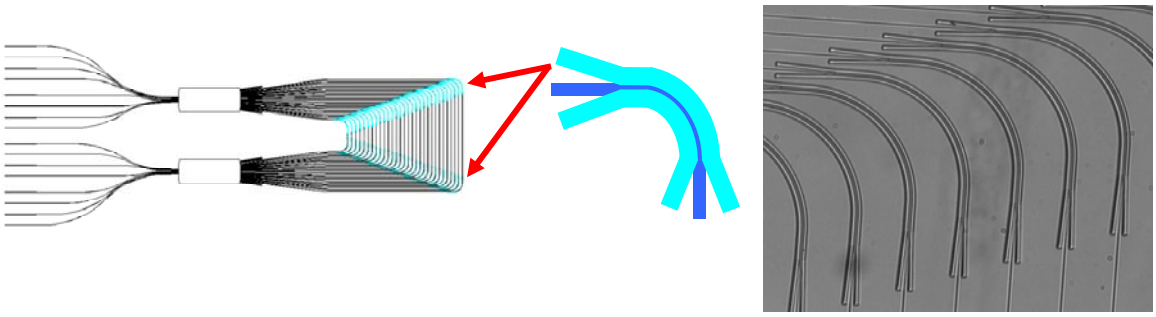


Fig. 6: Schematic of a 90 degree AWG using trenches filled with low-refractive index material.

transition loss of 0.75 dB/slab between the slab waveguide and the array waveguide, and an excess loss due to the bend of 0.1 dB × 2. Contrary to the simulation, the AWG with the mesa width of 2.5 μm had the best characteristics in terms of both loss and crosstalk. These results are attributed to sidewall roughness. Therefore, we determined that the optimum mesa width was 2.5 μm.

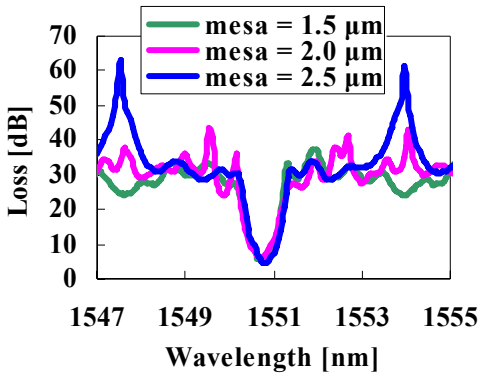


Fig. 7: Transmission characteristics from the center port of a 90 degree bend AWG.

Arrowhead Type AWG

Arrowhead-shaped AWGs using elliptic Ag mirrors have been reported [8]. The size of the chips can be reduced by using multiple arrowhead structures [9]. However, the propagation losses of v-bend waveguides using elliptic Ag mirrors were very large, and the degradation of their characteristics due to fabrication errors was also significant. Therefore, we have fabricated an 8-channel, 12.5-GHz channel spacing, triple-arrowhead AWG using trenches filled with low-refractive index material instead of the elliptic Ag mirrors. The specifications of the fabricated AWG are shown in Table II.

Table II: Specifications of the triple Arrowhead AWG.

Parameter	Value [unit]
number of channels	8
channel spacing	12.5 [GHz]
FSR	100 [GHz]
number of arrayed waveguides	30
path length difference	2021.56 [μm]
diffraction order	1899
center wavelength	1550 [nm]
taper angle	3 [degree]
minimum bending radius	200 [μm]
mesa width	2.5 [μm]

The triple arrowhead AWG configuration is shown schematically in Fig. 8. The bending angle of the small-bend waveguides was 150 degrees. The chip area, including the arrayed-waveguides and the slab waveguides, was 4.33 × 23.43 mm^2. This is about 1/4 of the size of a conventional AWG with a Δ value of 1.5% with the same number of channels, the same diffraction order, the same array number, and the same channel spacing. The transmission characteristics are shown in Fig. 9. The losses included a coupling loss of 1.8 dB between the single mode fibers and the waveguides. The minimum loss at the center wavelength was 8.25 dB. The PDL was 0.27 dB, and the adjacent channel crosstalk was -15.7 dB. The polarization-dependent peak wavelength difference (PDΔλ) was 3.1 GHz.

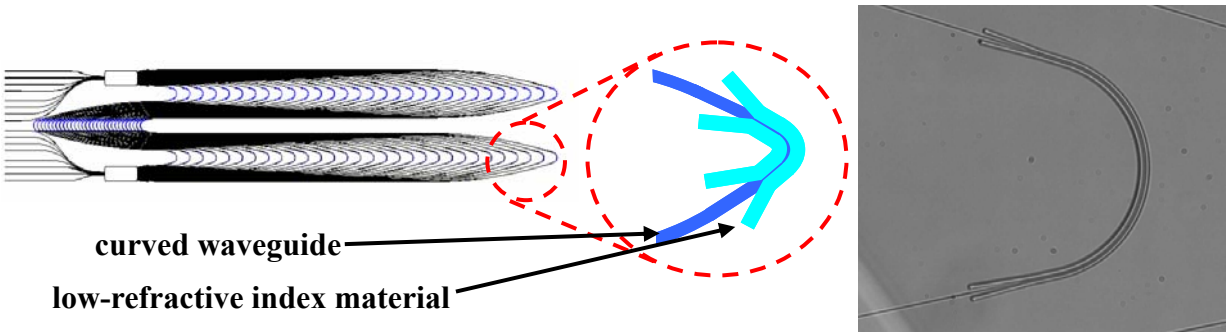


Fig. 8: Schematic of the triple arrowhead type AWG using trenches filled with low-refractive index material.

Conclusion

We proposed two types of AWGs into which we introducing small-bend structures using trenches filled with low-refractive index material. The 90-degree bend-type AWG had 8 channels with a spacing of 100 GHz and the triple-arrowhead AWG had 8 channels with a spacing of 12.5 GHz, respectively. The sizes of the 90-degree bend-type and the triple-arrowhead-type AWGs were about 1/2 and 1/4 of those of conventional AWGs with a Δ of 1.5 % respectively. They exhibited minimum losses of 4.47 dB and 8.25 dB, PDL values of 0.25 dB and 0.27 dB, and adjacent-channel crosstalk of -26.3 dB and -15.7 dB, respectively.

Acknowledgments

We are grateful to Hitachi Cable Ltd. for supporting the fabrication of the devices.

References

1. K. Kohtoku, IPRA, Paper ITuF1, 2005.
2. T. Fukazawa, F. Ohno and T. Baba, Jpn. J. Appl. Phys., vol. 43, no. 5B, pp. L673-L675, 2004.
3. M. Popovic, K. Wada, S. Akiyama, H. A. Haus, and J. Michel, J. Lightwave Technol., vol. 20, no. 9, pp. 1762-1771, 2002.
4. S. Akiyama, M. Popovic, P. T. Rakich, K. Wada, J. Michel, H. A. Haus, E. P. Ippen, and L. C. Kimerling, J. Lightwave Technol., vol. 23, no. 7, pp. 2271-2277, 2005.
5. T. Y. Fan, J. Ito, T. Suzuki and H. Tsuda, IPRA, Paper IMB3, 2006.
6. J. Ito, T. Y. Fan, T. Suzuki, A. Tate and H. Tsuda, OECC, Paper 5B2-2, 2006.
7. J. Ito, T. Y. Fan, T. Suzuki and H. Tsuda, IEICE Electron. Express, vol. 3, no. 23, pp. 499-503, 2006.
8. T. Suzuki and H. Tsuda, IEEE Photon Technol. Lett., no. 4, pp. 810 - 812, 2005.
9. T. Suzuki and H. Tsuda, Jpn. J. Appl. Phys., vol. 45, no. 7, pp. 5575-5581, 2006.

Innovation for New-Generation Optical Communication Based on Photonic Device Breakthrough

Kohroh Kobayashi
Precision & Intelligence Laboratory, Tokyo Institute of Technology
kobayashi.k.ad@m.titech.ac.jp

Abstract: *Activities of a goverment-funded project on optical communication in Japan are introduced. More than 20 professors and researchers from univiersities and national laboratories are involved in the project INGOC, Innovation for New-Generation Optical Communications. The fundamental objects are to create and expand a new area of science and technology of optical communications through the breakthrough of the photonic devices.*

Introduction

Strong increase in the communication traffic has been continuing steadily over recent 10 years, mainly due to the drastic growth of Internet traffic. A high volume contents such as musics, pictures and movies began to distribute over the world through the global networks. The spread of the broadband access such as ADSL and FTTH accelerates the increase in the network traffic. NTT has announced their medium term management strategy claiming that they will accomplish 30 million optical fiber broadband access by 2010[1]. As a result of the strategic efforts, the FTTH subscriber number in Japan exceeded 7 millions in the middle of 2006 and is keeping its growth speed. The distribution of the huge amount of the information data has been supported by the progress of photonic technologies such as direct optical repeater systems with an Er-doped fiber amplifier and dense wavelength multiplexing (DWDM) systems. In addition to the simple increase in the high-volume contents, transition to the higher-quality, including high-density TV (HDTV) and/or Super Hi-vision[2] in a future will induce further strong motivation to realize extraordinary higher-performance network, two or three orders magnitude higher than that of the existing network. To cope with the requirement, extensive research efforts are strongly anticipated.

Project Formation

We have started a new research project under the MEXT(Ministry of Education, Culture, Sports, Science and Technology) Grant-in-Aid for Scientific Research on Priority Areas in the middle of 2005. The project title is ”Innovation for New-Generation Optical Communications (INGOC)”. The project structure is shown in Fig. 1. It consists of three research groups and an executive committee. The research groups are entitled as A01: Function Innovation group, A02: Structure Innovation group and A03: Integration Innovation group. In the research groups, tweleve principal research topics and eleven supporting research topics were selected in 2005-2006 and 2006, respectively. The project aims to

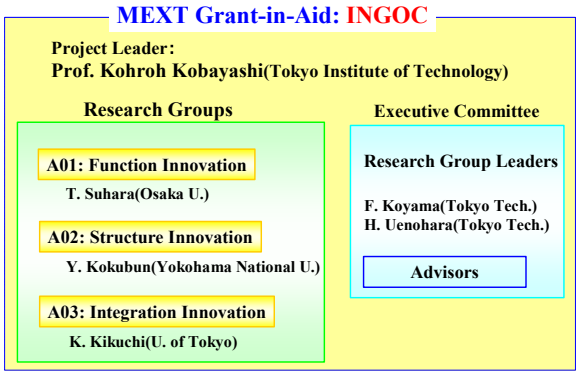


Fig. 1: Configuration of INGOC: Innovation for New-Generation Optical Communication

create a new area of science and technology and to achieve innovation for the transmission as well as for the signal processing for future optical communicaitons through breakthorugh of photonic devices. In order to achieve remarkable progress in the optical communication technology, we would like to explore new functions of light, which have not been yet fully utilized. We call them “higher-order functions of light”. Among them are phase, polarization, quantum state of light, velocity of light, and so on. In other word, we try to make full use of the undeveloped ability of light in this project. The conceptual image is shown in Fig. 2 with the logo mark.

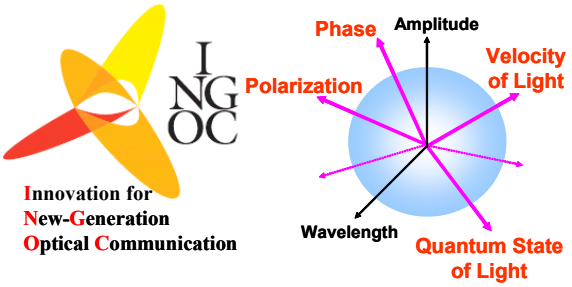


Fig. 2: Conceptual image of the project and the logo mark.

A01: Function Innovation Group

Professor T. Suhara, Osaka University, is a leader of this research group. This group is investigating new principles to conrol light.

Prof. Suhara’s research is aiming to realize various quantum photnic devices[3] for quantum information processing and/or quantum cryptography. He demonstrated sum-frequency generation using a photon

wavelength converter based on the non-linearity of the waveguide quasi-phase matching (QPM). The wavelength conversion from 1.55 μ m to 0.7 μ m enables the use of highly sensitive Si-APD for efficient single photon detection. Domain-inverted grating are formed on Mgo:LiNbO3 crystal by applying high-voltage under high-temperature.
Ti-diffused channel waveguide combined with domain-inverted grating is pumped by a wavelength tunable AlGaAs semiconductor laser as depicted in Fig. 3. As clearly shown in a histogram in Fig. 4, cross-polarized twin-photons were generated for the first time with the waveguide devices.[4] Entangled quantum state was experimentally confirmed with the cross-polarized twin photons.

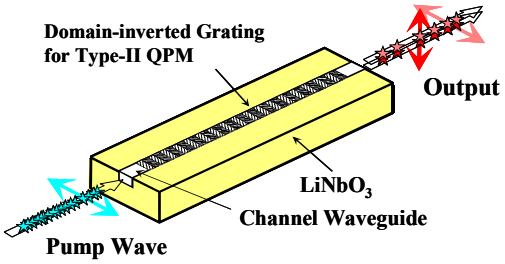


Fig. 3: Cross-polarized twin photon generatin devces.

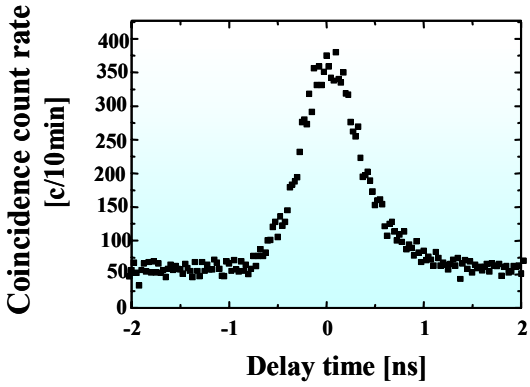


Fig. 4: Measured correlation of cross-polarized twin photons.

Other research topics assigned in this Function Innovation group are single photon and single photon pair generation from single InAlAs/GaAs quantum dot[5] by Prof. I. Suemune, Hokkaido University, light velocity control in a photonic crystal waveguide with a chirped structure and dispersion compensator and their application to an optical buffer memory by Prof. T. Baba, Yokohama National University, optical control of various functions of light using ultrafast optical nonlinearity of optical fibers induced by ultrashort pulse[8] by A. Prof. N. Nishizawa, Nagoya Univiersity and some others.

A02: Structure Innovation Group

The main mission of this group, headed by Prof. Y. Kokubun, Yokohama National University, is to create novel optical devices in collaboration with other groups.
Prof. Y. Kokubun is concentrating on multiwavelenght mutliport wavelength selective switching circuits to apply to a reconfigurable optical add/drop multiplexer (ROADM) based on a hitless wavelength selective switch. The switching element consists of waveguides and double series-coupled ring resonators with a tuning micro heater.[7] A fundamental layout of the multi-port hitless wavelenghth selective switch is depicted in Fig. 5. The switching element structure is also shown in the figure. A Ta_2O_5-SiO_2 core is embedded in SiO_2 cladding on a Si substrate. The multi-layered dielectric material system was found to be suitable than the polymer system from a view point of switching response time. Basic wavelength selective switching characteristics were successfully demonstrated.[8]

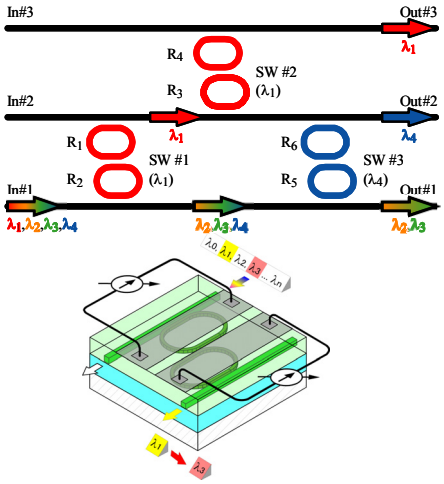


Fig. 5: Multi-port hitless wavelength selective switching circuit layout and a switching element.

Among other research topics in the A02 group are research on propagation characteristics of tunable hollow waveguides[9] and their applications for photonic integrated circuits such as widely tunable dispersion compensator,[10] WDM multiplexer/demultiplexer coupled with vertical cavity devices by Prof. F. Koyama, Tokyo Institute of Technology, investigation of MEMS technologies for highly functional telecommunication devices such as tunable grating optical reflectors[11] and valuable optical attenuation filters by Prof. K. Hane, Tohoku University, research on a ultrafast all-optical switch using intersubband transition of an InGaAs/AlAs/AlAsSb muti-quantum well[12] by Dr. H. Ishikawa, National Institute of Advanced Industrial Science and Technology, and some others.

A03: Integration Innovation Group

This research group takes most system-oriented approach in our project. Prof. K. Kikuchi, University of Tokyo, serves as a leader.
Prof. Kikuchi is tackling an issue of upgrading the

transmission capacity by utlizing multi-level modulation formats. He has been investigating the multi-level demodulation scheme, where a phase diversity homodyne receiver followed by an electronics digital signal-processing (DSP) circuit is utilized. In Fig. 6, a diagram of the phase diversity homodyne receiver and an example of the pattern of 20 Gb/s QPSK demodulation.[13] He has recently succeeded to construct 1000km-20Gb/s QPSK transmission systems using the developed digital coherent optical receivers.[14]

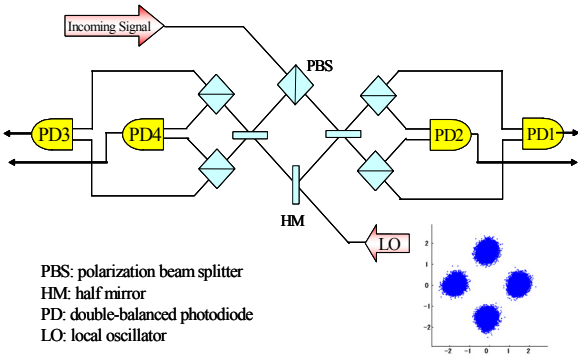


Fig. 6: Schematic diagram of the phase diversity homodyne receiver and a demodulated pattern.

The author (K. Kobayashi) and A. Prof. H. Uenohara, Tokyo Institute of Technology, are involved in the A03 group. They are mainly concentraing on all-optical packet processing/routing to provide solutions to the feasible bottleneck in the network nodes in future. Among the various functions in the packet routing system (Fig. 7), the first bit extraction, the label-payload separation and the label information recognition[15] were experimentally demonstrated with SOA-MZI all-optical 1x2 swithces. Self-switching scheme, where the input signal to the SOA-MZI switch is used as the optical control signal, is utilized to simply realize the avove functions. Four-bit label was extracted from the time sequential bit stream at 20 Gb/s as shown in Fig. 8.[16] Optical buffering was investigated with optical fiber delay lines combined with optical switches and optical wavelength converters.

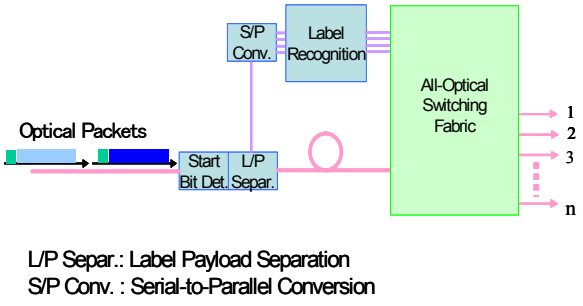


Fig. 7: Schematic diagram of the all-optical packet routing subsystem.

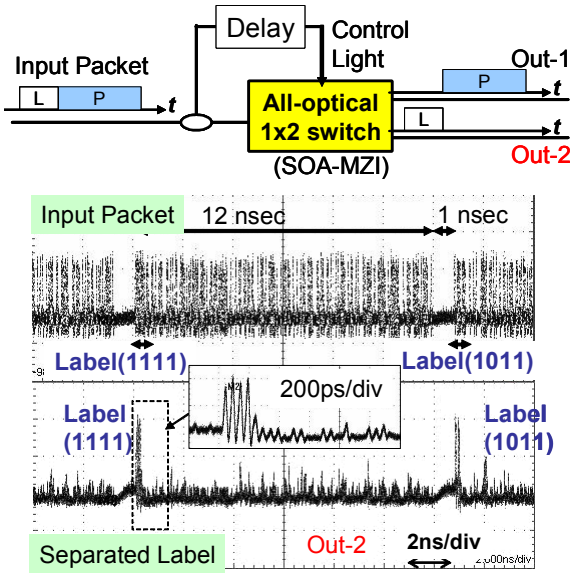


Fig. 8: Experimental result of the label separation by self-switching scheme of SOA-MZI all-optical switch.

All-optical signal processing with a different device and toward a different direction has been doing by Prof. H. Kawaguchi, Nara Institute of Science and Technology. He has been focusing on all-optical technology with polarization bistable VCSELs. He has demonstrated all-optical buffering and its shift resister function using fast polarization switching of VCSEL output light.[17]

Prof. K. Kodate, Japan Women's University, is working wideband optical spectrum processing, in collaboration with Dr. N. Wada, National Institute of Information and Communications Technology, using arrayed waveguide grating with amplitude and phase tunablity.[18] Multiple label generation and processing have been realized by utilizing Fourier transformation[19] of the light signal.

Concluding Remarks

As described above, this project is aming to explore and create a new scienc and technology area which is necessary to future photonic networks. The target area is described in a space defined by three axes, ie. higher-order functions, optical transmission/control and optical signal processing, as depicted in Fig. 9. Although optical communication technologies seem to have reached to fairly high levels, they are still in a very limited space as shown in Fig. 9. So far, only fundamental parameters of light, such as amplitude, intensity, and wavelength have been widely used in optical communications. There remains a wide room to be explored. Signal processing so far has been fully relied on the progress of electronics. With the increase in the signal bitrate, power consumption will become a serious issue. Optical signal processing will be a potentially strong candidate to overcome this problem. We hope that our effort to expand the

conventional sciense and technology area to the wider and fruitful one will contribute to cope with the strong demand for the extremely huge amount of information exchange in the future next generation photonic networks.

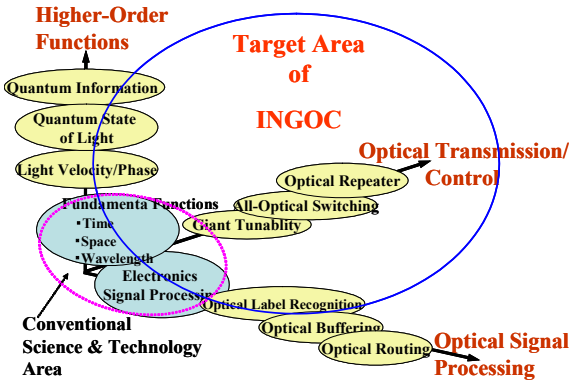


Fig.9: Target area of INGOC.

Acknowledgement

The author appreciates the support by the Misistry of Education, Culture, Sports, Science and Technology Japan under the Grant-in-Aid for Scientific Research on Priority Areas, 17068007: Innovation for New-Generation Optical Communications. The author also would like to express sincere thank to Prof. K. Maruyama, Ritsumeikan University for his kind support and help to the project.

References

1 O. yamaguchi, NTT Research Review, vol. 4, p. 21, 2006.
2 M. Sugawara et al, SMPTE Motion Imaging, vol 112, p. 339, 2003.
3 T. Suhara, Europ. Conf. Integrated Optics, ThP1, p. 73, Prague, 2003.
4. T. Nosaka et al., IEEE Photon. Tech. Lett., vol. 18, p. 124, 2006.
5. H. Kumano et al., J. Nanoelectron. Optoelectron., vol. 1, p. 39, 2006.
6. D. Mori et al., Opt. Express, vol. 13, p. 9398, 2005.
7. Y. Goebuchi et al., IEEE Photon. Tech. Lett., vol. 18, no. 3, p. 538, 2006.
8. Y. Goebuchi et al., MOC'06, C3, Seoul, 2006.
9. T. Miura et al., Jpn. J. Appl. Phys., vol.40, no. 7A, p. L688, 2001.
10. Y. Sakurai et al., Jpn. J. Appl. Phys., vol. 43, no. 8B, p. 5828, 2004.
11. K. Hane et al., Appl. Phys. Lett., vol 88, p. 141109, 2006.
12. S. Sekiguchi et al. OFC2005, OFE04, 2005.
13. S. Tsukamoto et. Al., IEEE Photon. Tech. Lett., vol. 18, no. 10, p. 1131, 2006.
14. K. Kikuchi et al., OFC2007, OtuA2, 2007.
15. J. Kurumida et al., Electron. Lett., vol. 42, no. 23, p. 1362, 2006.
16. J. Kurumida et al., ECOC2006, We2.4.6, Cannes, 2006.
17. H. Kawaguchi et al., Jpn. J. Appl. Phys., Express Lett., vol. 45, no. 34, p. L894m 2006.
18. Y. Komai et al., MOC04, G-4, 2004.
19. F. Morituka et al., ECOC2006, We2.4.2, Cannes, 2006.

Amorphous Silicon in Nanophotonic Technology

Lech Wosinski (1), Liu Liu (2), Matteo Dainese (3), and Daoxin Dai (4)
1) Department of Microelectronics and Applied Physics, Royal Institute of Technology (KTH), Electrum 229, S-164 40 Kista, Sweden, Joint Research Center of Photonics of the Royal Institute of Technology (Sweden) and Zhejiang University (China) and Kista Photonics Research Center, Stockholm, Sweden; e-mail: lech@imit.kth.se, 2) Department of Microelectronics and Applied Physics, Royal Institute of Technology (KTH), Electrum 229, S-164 40 Kista, Sweden, and Joint Research Center of Photonics of the Royal Institute of Technology (Sweden) and Zhejiang University (China); e-mail: liuliu@imit.kth.se, 3) Replisaurus Technologies AB, Isafjordsgatan 22B 5fl, SE-164 40 Kista, Sweden; e-mail: matteo.dainese@replisaurus.com, 4) Centre for Optical and Electromagnetic Research, East Building No. 5, Zijingang Campus, Zhejiang University, Hangzhou, 310058, China, e-mail: dxdai@coer.zju.edu.cn.

Abstract: Silicon-on-insulator nanowire waveguides appear to be the technology for next generation of super compact integrated devices. Due to a very high refractive index contrast and strong light confinement in the core, the waveguide bend radius can be reduced to a few micrometers and the size reduction of the functional integrated circuits can reach several orders of magnitude in comparison to standard integrated optics based on silica-on-silicon technology. Amorphous silicon is an interesting material allowing for more flexibility in nanowire structures. An array waveguide grating multi/demultiplexer that usually occupies several square centimetres in silica-on-silicon technology can be reduced to the size of 320 x 270 μm^2.

Introduction

Highly integrated photonic devices based on materials with high refractive index contrast gain more and more interest when the complexity of photonic structures increases and the integration of photonic and electronic circuits becomes a reality.

High refractive index contrast means strong light confinement in the waveguide core allowing for very small core sizes and sharp waveguide bends and leading to shrinkage of the component size by several orders of magnitude in comparison to traditional low contrast integrated optics.

There ares several possible material structures suitable for realizing complex photonic devices. Those ones, based on III-V semiconductors gained a lot of attention as it is possible to realize almost all important for optical communication building blocks in this technology: passive waveguides and wavelength selective devices, light sources, switches, modulators and detectors. However, for very small structures high index contrast to the air or dielectric overclading is not sufficient as light leaks out of the bends to the buffer or substrate because of the low index contrast between substrate and epitaxial grown materials. III-V semiconductor-based structures suffer also for higher losses and higher material cost. Moreover, their material technology is more complex in comparison to other technologies based on silicon wafer.

Silicon is an inexpensive material and the most widely used semiconductor material in current electronic devices. For photonic applications it is important that silicon has low losses for optical communication window and high refractive index of 3.5 in comparison to silica (n=1.5), which can be used as surrounding media for the light guiding waveguide core. Strong light confinement of such structures allows for very sharp bends and submicrometer core sizes and enables design of nano-scale optical devices and ultra-compact optoelectronic systems.

Additionally, silicon photonic devices can be fabricated using standard silicon processing technology. Compatibility with CMOS techniques allows cheap mass production of monolithically integrated optoelectronic structures.

Silicon components can play different wavelength selective functions and silicon waveguides can serve as connection links guiding optical signals among active and passive elements. Silicon, as an indirect semiconductor, has a very inefficient light emission at room temperature; therefore the active structures for photonics applications are usually based on the III-V materials and are usually not compatible with silicon. Recently a lot of effort is devoted to overcome these shortcomings of silicon.

SOI technology

Most of the fabricated passive nanophotonic devices are formed using silicon-on-insulator (SOI) technology. Here, commercially available SOI wafers are normally used, with thickness of the silica buffer and the top silicon layer optimized to get low leakage to the substrate as well as single mode light guiding at 1.55 μm. One of the commonly used standard SOI wafers has 1 μm silica buffer layer and 220 nm single crystalline high quality silicon layer [1].

With this technology sub-micrometer size waveguides – "nanowire waveguides" can be formed using e-beam or deep UV lithography and high precision plasma etching. Typical parameters of these waveguides are: core size 220 x 500 nm^2, bending radius below 5 μm, straight waveguide losses about 2 dB/cm and coupling losses of order of 7 dB/point, that can be considerably diminished using a specially designed tapers or mode converters.

Main limitation of SOI-based waveguide technology is lack of flexibility in design and material parameters. This flexibility can be offered by alternative technologies, where the different material layers are deposited during the technological process and can be customly adjusted depending on the demands.

Here we describe our optimized amorphous silicon technology that allows to freely adjust the deposited layers thickness and their refractive indices, and makes it possibile to fabricate more complex structures including multi-layer components, vertical cavities and Bragg reflectors [2, 3].

Hydrogenated amorphous silicon

Amorphous silicon is a known from long time ago semiconductor material mainly considered for applications in electronics [4] and solar cells [5]. Unhydrogenated amorphous silicon films, obtained most often by thermal evaporation, sputtering or ion bombardment contain usually a large amount of point defects in form of dangling bonds associated with silicon single- or multivacancy complexes within the disordered amorphous network [6]. These defects degrade electric performance of the semiconductor as well as generate absorption bands at the optical communication wavelengths between 1.3 and 1.6 μm.

Hydrogenated amorphous silicon (a-Si:H) was obtained for the first time in 1969 using glow discharge to generate plasma with silane (SiH_4) as a precoursor. This technique resulted in much lower concentration of dangling bonds, which were saturated by hydrogen atoms. The improvement of electrical parameters of this material as well as observed photovoltaic effect made it very interesting for applications to large area electronic arrays, displays, optical scanners and solar cells. Research was concentrated on the optoelectronic properties of a-Si:H in the visible part of spectrum for a long time, although recently scientists recognized its good optical properties in IR region for optical communication applications [7].

Presently to obtain good quality a-Si:H material for optical applications, Plasma Enhanced Chemical Vapor Deposition (PECVD) technique is commonly used with very low RF power at 13.56 MHz, which is essently the modified glow discharge technique used for the first a-Si:H deposition. Low power prevents ion bombardment that generates defects rather than assists the deposition. Relatively low temperature between 200 °C and 300°C and other process parameters are optimized to incorporate a right amout of hydrogen, that should passivate most of the dangling bonds, but the excess of hydrogen can increase the material porosity and increase scattering losses.

Here we use pure silane (SiH_4) as a gas precursor, RF power 10-20 W and 200 mTorr process pressure.

The low pressure and power levels prevent excessive polymerization of silane radicals in the gas phase. It contributes also to the low deposition rate, but as the film thickness necessary for fabricating waveguides is below 300nm it is of less importance. In Fig. 1 the deposition rate as a function of deposition temperature is shown for an RF power of 10W and 20W.

As it is seen from the graph, the deposition rate is very much dependent on the RF power. It facilitate to adjust this parameter together with silane flow rate to obtain the conditions, where the reacting molecules have short residence time in the chamber preventing unwanted polymerizing reactions in the gas phase.

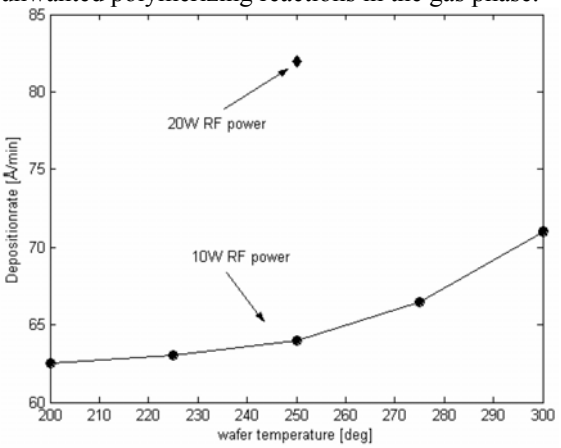


Fig. 1: Deposition rate as a function of the substrate temperature, at a process pressure of 200 mTorr.

The hydrogen can be incorporated into the films either singly, doubly or triply in SiH, SiH_2 or SiH_3 groups. Each of them has absorption bands at around 630 cm^{-1} and 2000 cm^{-1} as shown in Table 1.

Table 1: IR absorption peaks for three SiH_n groups

Group	Bond stretching	Bond bending/rocking
SiH	2000 cm^{-1}	630 cm^{-1}
SiH_2	2090 cm^{-1}	630 cm^{-1}
SiH_3	2140 cm^{-1}	630 cm^{-1}

The optimization of the processs parameters was towards formation of only SiH type of bonds in the film to increase film homogeneity. The ratio of SiH_2 and SiH_3 to SiH groups can be minimized by increasing the substrate temperature and reducing the silane pressure [6]. The absence of SiH_2 and SiH_3 groups was confirmed by taking a FTIR spectrum of prepared samples at around 2000 cm^{-1} and by measuring the correlation of the integrated absorption at 2000 cm^{-1} and at 630 cm^{-1}. FTIR spectrum for the samples with 500 nm a-Si:H film deposited with RF power 10 W, shown in Fig. 2, exhibit lack of absorption peaks characteristic for SiH_2 and SiH_3 groups. Fig. 3 plotted for the same samples shows strong correlation of the integrated absorption at 2000 cm^{-1} and at 630 cm^{-1}.

The optimization of temperature to obtain good quality a-Si:H films is quite complicated. As it was stated, with increasing the temperature the content of the SiH_2 and SiH_3 groups is decreasing, but also the total amount of hydrogen in the film falls down. To find the optimal deposition temperature the deposited material quality was evaluated directly by measurement of propagation loss in optical waveguides patterned on the fabricated samples. Strip loaded waveguides with geometry shown in Fig. 4 and cutback method for loss measurement were used.

The structure consists of 6 μm SiO_2 layer deposited on the silicon substrate, 0.22 μm thick layer of a-Si:H core and a top ridge of the waveguide, made of SiO_2.

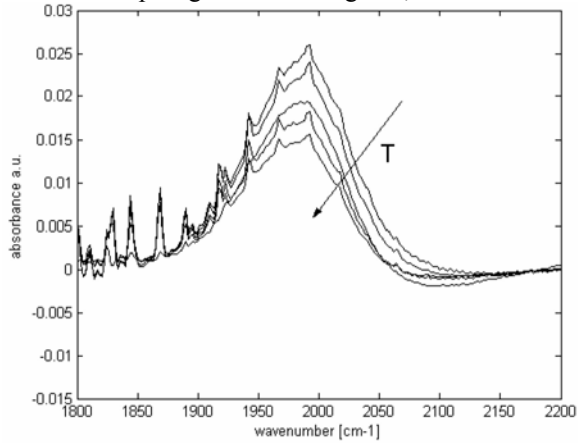


Fig. 2: FTIR spectrum of the a-Si:H film with only SiH band at 2000 cm^{-1} seen. Temperatures as in Fig. 1.

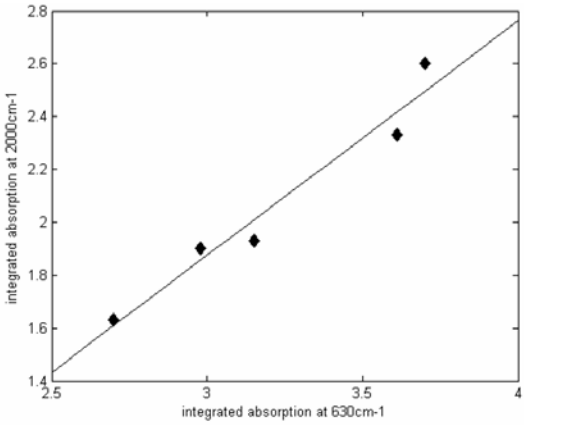


Fig. 3: Integrated absorption correlation between the 630 cm^{-1} and 2000 cm^{-1} bands for the same samples as shown in Fig. 2.



Fig. 4: Cross section of the waveguide structure used for measurements of the material losses.

The ridge is etched to be 3 μm wide and 0.45 μm thick, then there is 0.05 μm thick layer of SiO_2 left to cover underlying core.

According to the simulation this structure gives a single mode waveguiding with propagating light well confined in the a-Si:H layer just under the SiO_2 strip with confinement factor approx. 0.9. In this way we almost eliminated loss originating from surface roughness due to lithography and etching. The measured here loss is mostly due to material quality being tested. Fig. 5 shows the results measured for 1.55 μm. The propagation loss is constant with accuracy of +/-0.5dB within the band 1.52 μm to 1.62 μm of ASE unpolarized source used for measurements. The propagation loss of 1.5dB/cm for the temperature 250°C was measured, therefore this temperature was chosen as optimized deposition temperature for fabrication of amorphous silicon devices. The refractive index of the optimized a-Si:H at 1.55 μm was measured using spectroscopic ellipsometry to be 3.63.

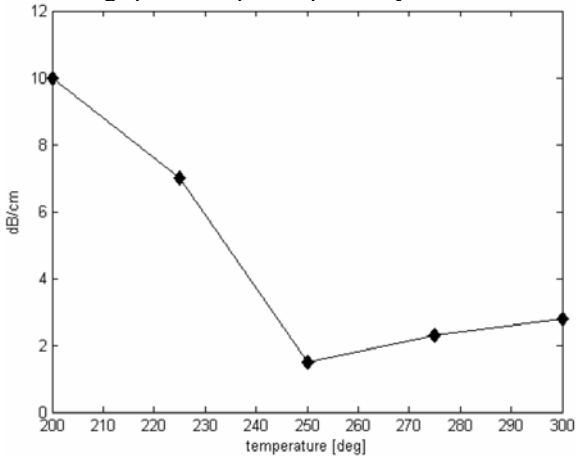


Fig. 5: Propagation loss in a-Si:H strip loaded waveguides, as a function of the deposition temperature.

Silicon nanowire waveguides and devices

5 μm silica buffer layer and 250 nm a-Si:H core layer patterned to 500 nm wide strips is the structure used here for fabrication of single mode nanowire waveguides and waveguide devices. A cross section of this structure is shown in Fig. 6.

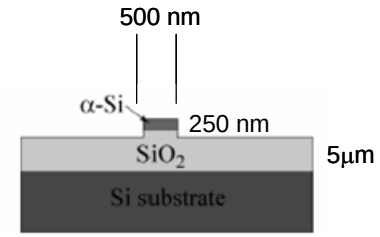


Fig. 6: Structure of the films and patterning used for single mode nanowire waveguides and waveguide devices.

In this technology both layers are deposited with Plasma Enhanced Chemical Vapor Deposition (PECVD), patterned by e-beam lithography and subsequently etched with Inductively Coupled Plasma Reactive Ion Etching.

In these sub-micron size structures the fabrication accuracy has a very critical influence on the performance of the devices. High contrast makes that waveguide losses are very sensitive to scattering at roughness on the core-cladding interface. Especially the sidewall surfaces after etching the waveguide profile are crucial for the final quality of the device. Both, lithography and etching itself can have influence on the sidewall roughness and so both these steps should be optimized. The sidewall roughness can be also improved after etching by slight thermal oxidation of the etched silicon profiles.

As an example for the Si nanowire waveguide components fabricated in amorphous silicon technology a compact arrayed waveguide grating (AWG) is fabricated.

An AWG with 1.6nm channel spacing and a layout of overlapped "free propagation regions" [8] is shown in Fig. 7. This novel layout introduces more flexibility for the design, and the separation between two adjacent arrayed waveguides can be further decreased. Consequently very compact AWG can be achieved. The detailed structural parameters for this AWG are presented in Table 2.

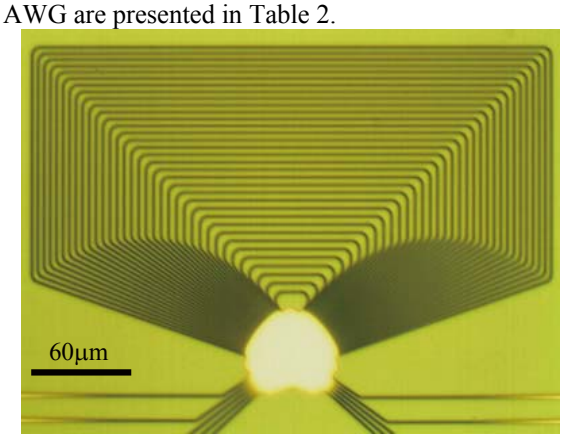


Fig. 7: Picture of the fabricated Si nanowires and AWG.

Table 2: Structural and measured parameters of the AWG.

Designed structural parameters	
waveguide dimension	500 x 250 nm^2
number of arrayed waveguides	34
number of channels	5 x 5
constant length difference ΔL	24.9 μm
diffraction order	42
FPR (focal) length	50 μm
output waveguide width at FPR	1.5 μm
output waveguide spacing at FPR	350 nm
arrayed waveguide width at FPR	950 nm
arrayed waveguide spacing at FPR	50 nm
total size	320 x 3270 μm^2
Measured spectral characteristics (TE polarization)	
channel spacing	1.5 nm
free spectral range	21.7 nm
insertion loss	~- 8.5 dB
Crosstalk	~-7dB

After the deposition the wafer was then cleaved into small samples. The Raith 150 EBL system was used for creating the patterns of Si nanowires and AWGs. To increase the coupling efficiency, the width of each input and output waveguide was tapered from 500nm to 2 μm through a 25 μm long linear taper. The samples were then etched using ICP-RIE with the SF_6 and C_4F_8 gas mixture. The roughness of the sidewall is ~10nm, which is directly measured from the SEM pictures.

Fabricated straight waveguides were measured with the end-fire characterization setup giving the propagation loss of ~4dB/mm using cut-back method. For photonic devices based on Si nanowires, such a loss level is still acceptable.

Fig. 8 shows the spectral responses of the fabricated AWG for the TE polarization. The measured spectral characteristics are listed in Table 2.

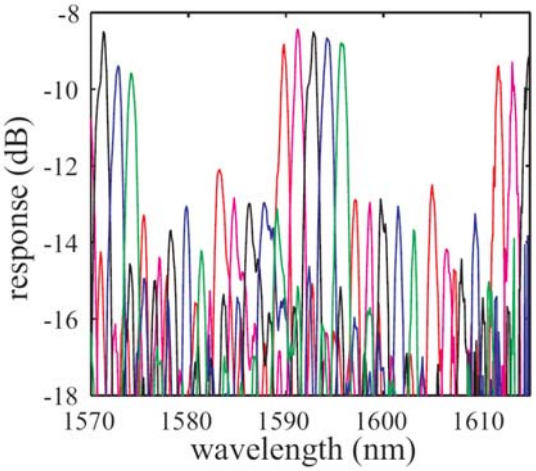


Fig. 7: TE spectral response of the AWG.

We can find that the crosstalk is relatively high here and we attribute this to the phase error induced in the arrayed waveguides due to the width variation in short range (sidewall roughness) and long range (stability of the E-beam during exposure). Due to the high confinement of light in Si nanowires, even a small change in width will cause a large variation in the propagation constant. Improving the fabrication process or introducing a tuning mechanism to each of the arrayed waveguides can decrease or compensate this phase error, and help to achieve a lower crosstalk.

Conclusions

Reduction of dimensions in future highly integrated photonic devices is due to application of materials with high refractive index contrast, where much higher light confinement allows for very small core sizes and sharp bends. Amorphous silicon is proposed as an alternative to SOI technology and used for fabrication of nanowire waveguide-based AWG .

References

1 W. Bogaerts et al, J. Lightwave. Techol., no.23, p. 401, 2005.
2 M. Dainese et al, Opt. Commun., no. 260, p. 514, 2006.
3 M. Dainese et al, ECOC, vol.2, p. 185, 2005.
4 R.A. Street, "Hydrogenated Amorphous Silicon", Cambridge Solid State Science Series, 1991.
5 X. Deng and E. A. Schiff , "Amorphous Silicon Based Solar Cells", in "Handbook of Photovoltaic Science and Engineering", A. Luque and S. Hegedus, ed. John Wiley & Sons, 2003.
6 M.H. Brodsky et al, Phys. Rev, B, vol. 16, no. 8, p. 3556, 1977.
7 G. Cocorullo et al, IEEE J. Of Sel. Topics in QE, vol. 4, no. 6, p. 997, 1998.
8 D. Dai et al, Electron. Lett., vol 42/7 p. 400, 2006.

GaN, a new material for integrated nonlinear optics

S. Pezzagna[1,2], J. Brault[1], M. de Micheli[1,3], P. Vennéguès[1], A. D. Wieck[2], and J. Massies[1]

[1] Centre de Recherche sur l'Hétéro-Epitaxie et ses Applications (CRHEA-CNRS), Sophia Antipolis, rue Bernard Grégory, 06560 Valbonne, France
[2] Lehrstuhl für Angewandte Feskörperphysik, Ruhr-Universität Bochum, D-44780 Bochum, Germany
[3] Laboratoire de Physique de la Matière Condensée, Université de Nice-Sophia Antipolis, Parc Valrose 06108, Nice Cedex 2, France

sp@crhea.cnrs.fr / marc.de-micheli@unice.fr

Abstract

This article presents gallium nitride (GaN) as a new material for integrated nonlinear optics. The GaN optical properties such as refractive indices and nonlinear coefficents were measured. The technique developped to satisfy quasi phase matching with GaN is detailed. The propagation losses in GaN waveguides epitaxially grown on sapphire substrates were determined by prism coupling. The burying of the waveguides is shown to reduce these losses. Finaly, backward propagating nonlinear interactions can be envisaged since we demonstrated submicronic modulations of the sign of the GaN nonlinear coefficient.

*****

Introduction

Gallium nitride, GaN, is a wide bandgap semiconductor (3.4 eV) which possesses a large transparency zone covering the visible and the near and mid infrared domains. GaN and other III-nitrides have been widely studied since the early 90s for their unique optoelectronic properties in terms of light emitters and detectors. The applications such as the first blue laser diodes[1] became possible once the p-type doping problems were solved. Nowadays, the white light emitting diodes[1,2] (based on (In,Ga)N quantum wells) are getting very competitive in terms of power and efficiency and an intensive research is going on for the future general lightening. Many other works on III-nitrides deal with high-power and high-frequency electronics. Nevertheless, very few studies concerned GaN for optics or nonlinear optics. Most of them were dedicated to the measurement or calculation of the nonlinear coefficients $c^{(2)}$ of GaN[3-5]. Indeed, GaN crystallizes in the wurtzite structure which has hexagonal symmetry and therefore is non centro-symmetric. The $c^{(2)}$ published values present a significant discrepancy but they are of the same order as the lithium niobate ones. Therefore, optical frequency conversions can be envisaged over the whole transparency zone of GaN. Recently, the first second harmonic generation (SHG) performed in periodically poled GaN by quasi phase matching (QPM) was realized from 1660 nm to 830 nm by Chowdhury *et al*[6]. Yet, the conversion efficiency was extremely low.

In this paper, we present a different approach to achieve nonlinear interactions with GaN but still based on QPM[7]. This technique which compensates artificially the dephasing introduced along light propagation by the chromatic dispersion requires a periodic modulation of the sign of the nonlinear coefficient. The modulation period L can then be adapted in principle to any nonlinear process. For instance, in the simple case of SHG with a pump wavelength at l_w, the period is given by:

$$\Lambda = \frac{l_w}{2\left|n_{2w} - n_w\right|}$$

where n_w and n_{2w} are respectively the refractive indices at the fundamental and second harmonic wavelengths. This previous equation shows that QPM requires a "perfect" knowledge of the GaN chromatic dispersion. Indeed, the QPM condition is severe *i.e.* spectrally very narrow[8], which means that for the slightest index difference, the constructive interference effect is rapidly lost. In the literature, the GaN index measurements[3,9,10] present a too important discrepancy. Therefore, we have measured the ordinary n_o and extraordinary n_e refractive indices of GaN by prism coupling between 458 and 1570 nm using several laser sources.

First, the GaN chromatic dispersion from a thin film grown on sapphire will be presented. We will also give the nonlinear coefficients measured on the same sample. Then, we will describe the process used to obtain GaN structures dedicated to QPM. We will see that the main problem encountered concerns

the propagation losses. A way to lower these losses will be discussed. Finaly, we will show that it is possible to get GaN structures with submicronic periods, thus opening the way to backward nonlinear optics interactions.

Chromatic dispersion, nonlinear coefficients, and propagation losses

The hetero-structures further presented were all grown by molecular beam epitaxy (MBE) using ammonia as nitrogen precursor. In order to measure the refractive indices of GaN, we grew a 1.9 µm thick GaN film on sapphire. A 25 nm thick low temperature (400°C) buffer layer is primarily grown on sapphire. Then, the GaN film is deposited at 800°C at a growth rate of ~ 1 µm/h under N-rich conditions. This film is an asymmetric planar waveguide which is strongly multimode at visible wavelengths as regards as its thickness and the index contrasts between guide and claddings. A classic prism coupling method is employed to determine the refractive indices by measuring the effective indices of the transverse electric (TE) and transverse magnetic (TM) propagation modes allowed in the waveguide. The experimental dispersion curves are shown in figure 1.

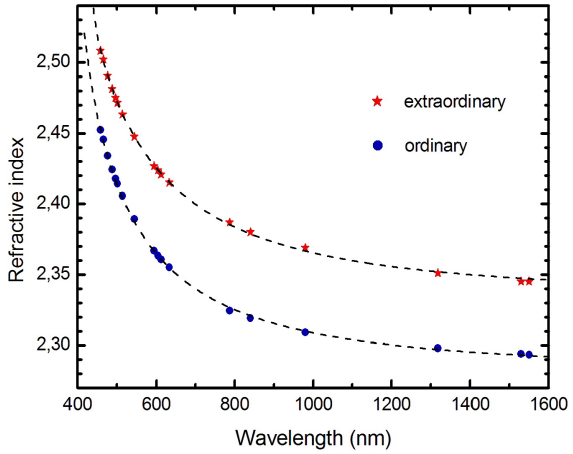


Fig. 1: Ordinary n_o and extraordinary n_e refractive indices of GaN as a function of optical wavelength. The dotted lines represent the experimental data adjustments.

These data are well adjusted with the 2-term Sellmeier-like equations given below:

$$n_o(l) = \sqrt{1 + \frac{0.298\, l^2}{l^2 - (342.0)^2} + \frac{3.909\, l^2}{l^2 - (144.6)^2}}$$

$$n_e(l) = \sqrt{1 + \frac{0.0117\, l^2}{l^2 - (422.5)^2} + \frac{4.437\, l^2}{l^2 - (177.0)^2}}$$

where l is expressed in nm. The refractive indices of several other GaN samples were also measured. Slight differences appeared between all these measurements. Nevertheless, we found out that there was a linear relation between the refractive indices and the stress state of the studied waveguides. Moreover, the ordinary index n_o appears to be more sensitive to stress variations than the extraordinary index n_e. These results, in terms of elasto-optic coefficients, are about to be published.

From the GaN/Sapphire film presented before, the nonlinear coefficients could be determined. They were measured by the rotational Maker fringes method. The pump laser was a pulsed Nd:YAG at 1064 nm. After adjustement of the angle resolved transmitted second harmonic signal generated in the GaN film, we found the following values for the non-zero elements of the $c^{(2)}$ tensor: $c_{33} = -10.6\, pm/V$ and $c_{15} = c_{31} = 5.3\, pm/V$. They are in good agreement with the latest published values by Sanford *et al*[5]. These are about one third of the lithium niobate coefficients.

Planar waveguide structures were grown directly on sapphire. The overall optical properties of these guides such as the effective indices or the propagation losses of the different TE and TM modes, were studied on Ga-polar GaN films. A strong increase of the losses from the fundamental mode (~ 1 dB/cm) to the highest order ones was evidenced. The same behaviour is observed for both the TE and TM modes. This is mainly due to light scattering at the guide interfaces. Indeed, the index contrasts are very high: 1.35 at the GaN/air interface and ~ 0.6 at the GaN/Sapphire interface at 632.8 nm. Figure 2 shows the intensity profiles of the four first TE modes of a GaN waveguide on sapphire. Here, these profiles are superimposed to the section image of such a guide as seen by transmission electron microscopy.

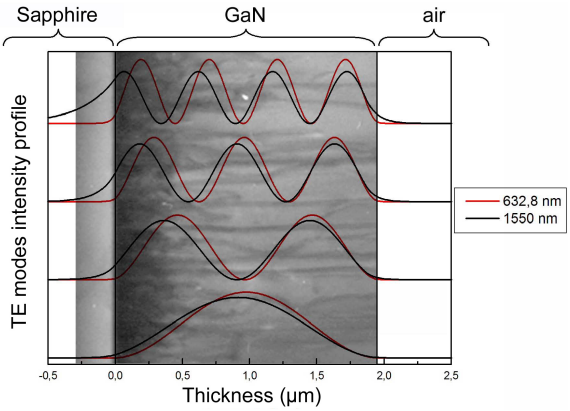


Fig. 2: Intensity profiles of the four first TE modes of a GaN planar waveguide on sapphire, at 632.8 and 1550 nm wavelengths. The guide thickness is 1.9 µm. The backward image is a transmission electron microscopy (cross section) picture of such a GaN film.

The dark lines are threading dislocations which originate from the strong lattice mismatch between GaN and sapphire (-15.9%). Their number decreases with the deposited film thickness. In general, the

GaN films grown by molecular epitaxy on sapphire substrates present a dislocation density of few 10^9 cm^{-2}. Yet, their potential influence on the propagation losses is still unclear. Note that the index variations that may occur along the guide thickness are negligible compared to the index contrasts responsible of the optical confinement.
GaN planar waveguides were also grown with differents inferior cladding layers consisting of AlN, $Al_{0.4}Ga_{0.6}N$, or $Al_{0.1}Ga_{0.9}N$ films. The index contrast between guide and cladding is all the more reduced as the Al composition decreases. In every case, the same behaviour of losses increase with the mode order is still observed. Therefore, its origin is essentially due to scattering at the GaN/air interface. Thus, the surface roughness plays a key role on the optical losses observed.

GaN structures dedicated to quasi phase matching

The QPM technique necessitates a periodic structuration of the sign of the nonlinear coefficient $c^{(2)}$ (with a typical period of few to tens of microns). Yet, the $c^{(2)}$ sign is linked to the crystal orientation. Therefore, the GaN films dedicated to QPM have to present an alternance of (0001) domains (said to be of Ga-polarity) and of $(000\bar{1})$ domains (N-polarity). The process used to get such periodically poled (PePo) structures involves two growth steps[11] and an intermediate etching step in order to define the periodic pattern. These different steps are summarized in figure 3.

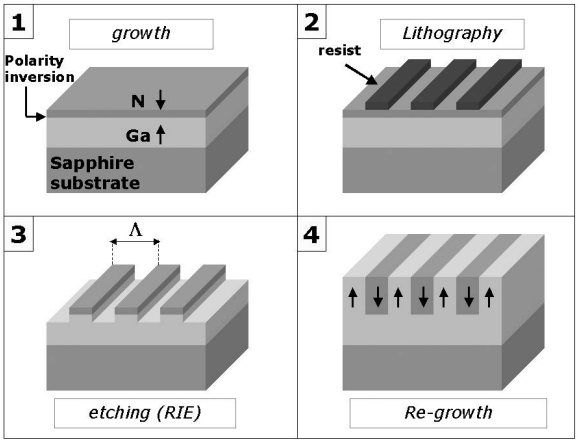


Fig. 3: Realization of periodically poled (PePo) GaN structures. (a) polarity inversion induced during GaN growth by a strong Mg doping. (b) resist deposition and UV lithography of the PePo pattern. (c) etching of the stripes down to the inferior Ga-polarity by reactive ion etching. (d) re-growth of the PePo film.

In our standard growth conditions, the layers naturally exhibit the Ga-polarity. The crystal orientation have first to be reversed. This is now well established by briefly and strongly doping the GaN film with Mg during growth[12]. The inversion process is checked in situ by reflexion high energy electron diffraction (RHEED). The diffraction diagrams are different whether the surface is the one of a Ga-polar or of a N-polar film. Then, the stripes pattern is fixed into some resist by UV lithography. An etching step is driven and the depth is controlled to be around 50 nm so that the inferior Ga-polar film is reached. The resist is further removed and the sample is re-introduced in the MBE chamber for a ~ 1h annealing at 800°C under ammonia flux. The re-growth is driven at a lower temperature, 770°C, which gives the lower roughness for the N-polar domains.

In the case of PePo planar waveguides (with Ga and N-polar domains), the propagation losses are very high (> 20 dB/cm) due to the superior roughness of the N-polar domains. Figure 4 shows a 3 µm thick regrowth of a PePo sample at 770°C. Figure 4a is a scanning electron microscopy (SEM) image of a sample of period 10 µm. The Ga and N-polar domains have almost the same thickness. Figure 4b is centered at the junction between two domains of a PePo pattern of period 40 µm. The surface roughnesses are well visible on this image. The Ga domain is smooth and presents a typical kinetic roughness[13]. The N domain is flat at a large scale but presents a high roughness at low scale. Although small pyramids can be seen, the surface is well smoother than for a regrowth at 800°C.

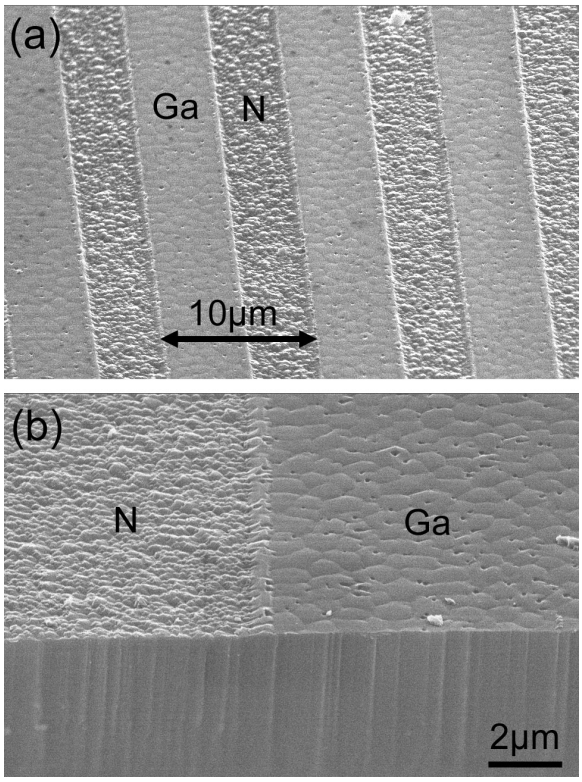


Fig. 4: Scanning electron microscopy images of a same sample (PePo GaN film having a thickness of 3 µm) for different periods. (a) period of 10 µm. (b) period of 40 µm.

The propagation losses should be reduced if the index contrast between guide and cladding (which in this case is air) is lowered. This can be realized by the growth of a superior (Al,Ga)N cladding layer with a low Al content (refractive index slightly inferior to the GaN one). With the deposition of such a film, a significant diminution of the losses has already been observed on Ga-polar waveguides. Works are currently driven towards the realization of PePo symmetric ridge waveguides.

Submicronic periods

Finaly, PePo structures with submicronic periods down to 170 nm have been grown[11]. In that case, the classic UV lithography is replaced by an etching by focused ion beam (FIB). The stripes are directly etched using Ga^+ ions accelerated at 35 kV with doses in the range 10^{16} to 10^{17} cm^{-2}. Before regrowth, no surface treatment is done, but the sample is annealed at 650°C under vacuum during 12h. Figure 5 is a SEM image of a 2 µm thick regrown submicronic PePo sample. It can be seen that the period is well respected. Yet, the Ga and N-polar domains do not have exactly the same thickness. Further work is needed to optimize the growth conditions (growth temperature, V/III ratio,…) in order to have equality of growth rates between the Ga and N-polar domains. Nevertheless, this result is very promising since it makes of GaN a candidate to backward propagating nonlinear interactions which have still not been achieved experimentally. Indeed, actual technological limitations prevent to reach, with the classic and widely used nonlinear materials such as lithium niobate[14], the submicronic periods that are required.

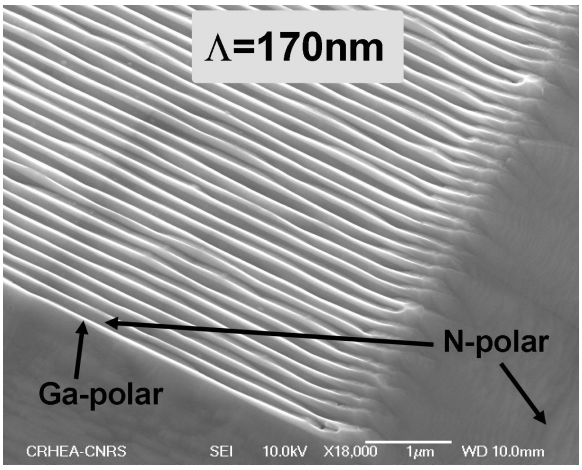


Fig. 5: Scanning electron microscopy images of a PePo film with a 170nm period. The re-grown thickness after focused ion beam process is 2 µm.

Summary

In conclusion, we have presented GaN as a new material for nonlinear optics. Periodically poled GaN structures dedicated to quasi phase matching are obtained by two growth steps with an intermediate etching step. The ordinary and extraordinary refractive indices are now well known on a wide spectral domain as well as their variations with stress. Yet, the propagation losses in periodically poled waveguides are high due to strong light diffusion at the rough N-polar domains surface. The burying of such waveguides with an (Al,Ga)N film should permit a significant reduction of the losses since it is already the case for Ga-polar buried waveguides. On the other hand, periodically poled GaN structures with submicronic periods were realized and backward propagating nonlinear interactions can then be envisaged.

References

[1] S. Nakamura and G. Fasol, " The blue laser diode ", Springer edition, (1997).
[2] B. Damilano, N. Grandjean, C. Pernot, and J. Massies, Jpn. J. Appl. Phys. **40**, L918 (2001).
[3] H. Y. Zhang, X. H. He, Y. H. Shih, M. Schurman, Z. C. Feng, and R. A. Stall, Appl. Phys. Lett. **69**, 2953 (1996).
[4] T. Fujita, T. Hasegawa, M. Haraguchi, T. Okamoto, M. Fukui, and S. Nakamura, Jpn. J. Appl. Phys. **39**, 2610 (2000).
[5] N. A. Sanford, A. V. Davydov, D. V. Tsvetkov, A. V. Dmitriev, S. Keller, U. K. Mishra, S. P. DenBaars, S. S. Park, and J. Y. Han, J. Appl. Phys. **97**, 053512 (2005).
[6] A. Chowdhury, H. M. Ng, M. Bhardwaj, and N. G. Weimann, Appl. Phys. Lett. **83**, 1077 (2003).
[7] J. A. Armstrong, N. Bloembergen, J. Ducuing, and P. S. Pershan, Phys. Rev. **127**, 1918 (1962).
[8] M. M. Fejer, G. A. Magel, D. H. Jundt, and R. L. Byer, IEEE J. Quant. Elec. **28**, 2631 (1992).
[9] Ü. Özgür, G. Webb-Wood, H. O. Everitt, F. Yun, and H. Morkoç, Appl. Phys. Lett. **79**, 4103 (2001).
[10] N. A. Sanford, L. H. Robbins, A. V. Davydov, A. Shapiro, D. V. Tsvetkov, A. V. Dmitriev, S. Keller, U. K. Mishra, and S. P. DenBaars, J. Appl. Phys. **94**, 2980 (2003).
[11] S. Pezzagna, P. Vennéguès, N. Grandjean, A. D. Wieck, and J. Massies, Appl. Phys. Lett. **87**, 062106 (2005).
[12] S. Pezzagna, P. Vennéguès, N. Grandjean, and J. Massies, J. Cryst. Growth **269**, 249 (2004).
[13] S. Vézian, F. Natali, F. Semond, and J. Massies, Phys. Rev. B **69**, 125329 (2004).
[14] A. C. Busacca, C. L. Stones, V. Apostolopoulos, R. W. Eason, and S. Mailis, Appl. Phys. Lett. **81**, 4946 (2002).

Modelocking of a GaInNAs VECSEL using a GaInNAs SESAM for 1.3 µm applications

Paolo Navaretti (1), Andreas Rutz (1), Valeria Liverini (1), Deran J. H. C. Maas (1), Benjamin Rudin (1), Aude-Reine Bellancourt (1), Silke Schön (2) and Ursula Keller (1)

1) ETH Zurich, Physics Department, Institute of Quantum Electronics
Wolfgang-Pauli-Strasse 16, CH-8093 Zürich, Switzerland
2) ETH Zurich, FIRST Center for Micro- and Nanoscience
Wolfgang-Pauli-Strasse 10, CH-8093 Zürich, Switzerland

Abstract: *In this paper we report the results of the first GaInNAs Vertical External Cavity Surface Emitting Laser (VECSEL) modelocked using a GaInNAs Semiconductor Saturable Absorber Mirror (SESAM). The intracavity SESAM provides self-starting of stable modelocking for the optically-pumped VECSEL. Trains of pulses 18.6 ps long with a repetition rate of 6.1 GHz and an average power of 57 mW were obtained at 1308 nm using this system. Operating the VECSEL in continuous-wave (cw) regime we obtained an average output power of 560 mW in single TEM_{00} mode.*

Introduction

Broadband high-speed optical networks require stable short-pulse sources with high repetition rates operating at an optical wavelength of 1.3 µm, where the zero-dispersion in silica fibers occurs.

Passive modelocked VECSELs provide stable pulse trains in the picosecond and sub-picosecond regime with multi-GHz repetition rates and power scaling up to a few watts for optical pumping [1].

Emission in the 1.3-µm wavelength range can be obtained using GaInNAs quantum well (QW) systems, which, in the last few years, proved to be excellent candidates for the active region in laser diodes [2].

Optically pumped VECSELs have been modelocked for the first time in 2000 [3]. Since then the research efforts in this field made it possible to obtain higher repetition rates [4], higher average output power [5] and different wavelengths. However, previously no VECSEL has been modelocked at the wavelength of 1.3 µm.

Before this result, GaInNAs SESAMs were used to modelock solid-state lasers both at 1.3 [6] and at 1.5 µm [7]. Here we report on the modelocking of a GaInNAs VECSEL using a GaInNAs SESAM.

In order to use the same material for both the gain and absorbing media different growth and processing procedures must be applied in order to optimize the material characteristics to the application. Indeed, GaInNAs is very susceptible to different growth and processing conditions, dramatically changing optical properties on slight changes of one of the parameters of its production process. This characteristic, alongside with the lattice compatibility to GaAs and the large wavelength tunability with nitrogen concentration, makes this compound semiconductor an ideal candidate for passive modelocking in the 1.3µm wavelength range.

Since GaInNAs has been proposed by Kondow and co-workers [8] as the gain material for telecommunication lasers, its optical quality has improved substantially. However the optical efficiency is still affected by growth time incorporation of nonradiative defects that have to be cured post-growth with the use of thermal treatments [9].

These non-radiative defects can, on the other hand, be exploited to make saturable absorbers with fast recovery characteristics.

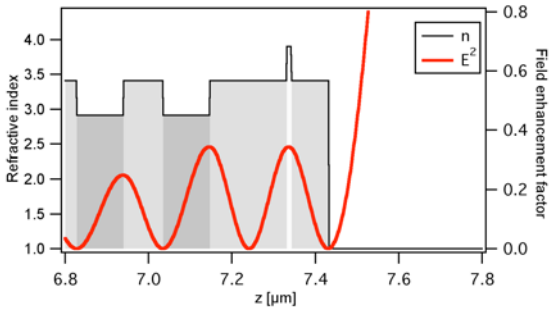


Fig. 1 SESAM design: refractive index (left axis) and electric field enhancement factor (right axis) in the top 0.6 µm of the SESAM device.

Growth and processing of the SESAM and the VECSEL structures

The SESAM structure has been grown entirely by molecular beam epitaxy (MBE) on an undoped (001) GaAs substrate. It consists of a 35-pair AlAs/GaAs distributed Bragg reflector (DBR) centered at 1310 nm, a 90 nm GaAs spacer layer, a 10 nm $Ga_{0.65}In_{0.35}N_{0.016}As_{0.984}$ absorber and finally a 90 nm GaAs cap. This last layer has the function of making the structure antiresonant, thus giving it negligible group delay dispersion at the wavelength at which it is centered [10]. The refractive index and field enhancement factor versus device thickness is shown in figure 1. The indium and nitrogen concentrations were chosen such that the photoluminescence (PL) wavelength occurs around 1310 nm. Since the PL emission wavelength corresponds to the onset of absorption, this choice placed the absorption edge very close to the laser wavelength, thus giving the SESAM low saturation fluence in our laser setup

[11]. The absorption spectrum of this SESAM is plotted in figure 2.

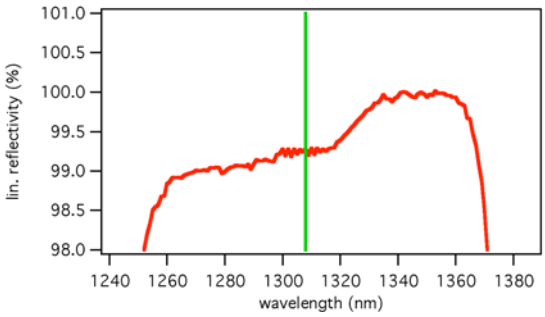


Fig. 2 Reflectivity spectrum of the SESAM. The vertical line indicates the laser wavelength.

No post growth processing was applied to the SESAM.

The VECSEL structure was grown upside-down in order to be able to subsequently remove the substrate from the device for better heat removal during operation [12]. At first an etch stop structure was grown on an undoped (001) GaAs substrate. It consisted of three layers of different materials: $Al_{0.85}Ga_{0.15}As$, GaAs and AlAs. On top of the etch-stop, an antireflection (AR) structure was grown to minimize reflection losses from the VECSEL surface of both the pump wavelength at 45º of incidence and of the laser wavelength normal to the surface. This structure consists of 10 layers of AlAs and $Al_{0.20}Ga_{0.80}As$. Their thicknesses were numerically optimized for an antireflection effect for both wavelengths. The choice of $Al_{0.20}Ga_{0.80}As$ instead of pure GaAs in the DBRs of the VECSEL is to minimize the absorption of the pump outside of the gain region.

After the AR structure, the active region has been grown. This consists of 5 $Ga_{0.65}In_{0.35}N_{0.018}As_{0.982}$ quantum wells (QWs) 8 nm thick. We designed the QWs each at different antinode of the standing wave of the laser electric field and, therefore, designed the GaAs barriers separating them to be 178 nm thick.

The growth of these structures has been conducted using the same MBE used for the the growth of the SESAM. The DBRs of the VECSEL were, instead, grown by metal-organic vapor phase epitaxy (MOVPE). The laser mirror consists of 32 pairs of AlAs/$Al_{0.20}Ga_{0.80}As$ whose thicknesses were chosen to give high reflectivity at 1300 nm under normal incidence. The pump DBR consists of 10 pairs of the same materials designed to reflect at 808 nm under an incidence angle of 45º. The refractive index and field enhancement factor versus device thickness of the top layers after substrate removal are shown in figure 3.

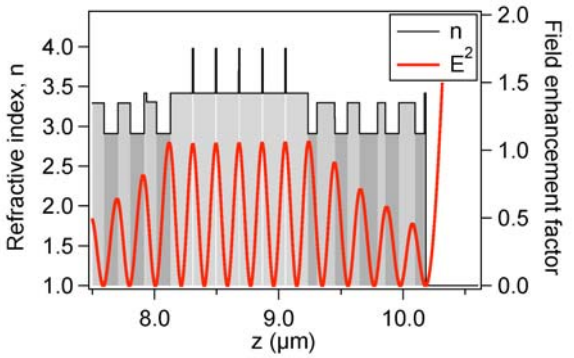


Fig. 3 VECSEL design: refractive index (left axis) and electric field enhancement factor (right axis) as a function of distance in the top 3 µm of the VECSEL device.

Two main characteristics distinguish the GaInNAs material used in the active structure from the one used in the absorber: a slight difference in nitrogen composition and a different growth temperature. The slightly higher nitrogen concentration in the gain material is necessary to compensate for the thermal treatment due to the high-temperature growth of the DBR. This improves the optical quality but also blueshifts the optical emission [13][14]. More nitrogen is, therefore, necessary to obtain lasing at 1300 nm.

The difference in growth temperature is due to the fact that GaInNAs has a higher optical efficiency when grown at lower temperatures and then annealed. These low temperatures, on the other hand, tend to make its recovery time longer. For this reason the active region material has been grown at a lower temperature of 410ºC than the one of the absorbing material, which was of 450ºC.

After growth was completed the VECSEL required further processing steps before it could be used in the laser. First, the surface was metallized with indium and soldered face-down in vacuum to a copper heat sink. Afterwards, the substrate was removed by a combination of mechanical lapping and wet chemical etching. The final surface was etch-pit free and mirror-like, denoting very high quality of the growth and of all the processing steps involved in its preparation.

Characterization of the SESAM and of the VECSEL

The SESAM has been characterized by pump-probe and nonlinear reflectivity techniques in order to assess its recovery time and nonlinear absorption characteristics [15]. This resulted in a low saturation fluence of 6.8 (+/- 0.2) µJ/cm^2, a low modulation depth of 0.76%, nonsaturable losses of 0.12% and a recovery time of about 47 ps, which is suitable for modelocking in the ps-pulse regime [16].

Laser setup and cw results

The cw lasing characteristics of the VECSEL were tested using a similar cavity as for modelocking, simply replacing the SESAM with a high reflectivity DBR mirror. We used an 808 nm free-space diode laser as the pump and a 1.5% output coupler with a radius of curvature of 100 mm. With this configuration we obtained 560 mW of output power in single TEM_{00} mode at a wavelength of 1280 nm.

For modelocking, the laser was built as a V-cavity configuration, with on one arm of the V a 0.7% transmission output coupler with a radius of curvature of 25 mm and on the other one the SESAM (substituted by a DBR in the cw measurements). The VECSEL was positioned at the intersection of the arms. The 808 nm free-space diode laser provided the pump power and was positioned so that it hit the VECSEL under an angle of 45º [17].

The SESAM was placed 8 mm from the VECSEL and the output coupler at approximately 16 mm for a total cavity length of 24 mm. A 25 µm fused silica etalon was inserted between the VECSEL and the output coupler to provide wavelength stabilization.

The VECSEL stage was cooled to 5ºC using peltier elements.

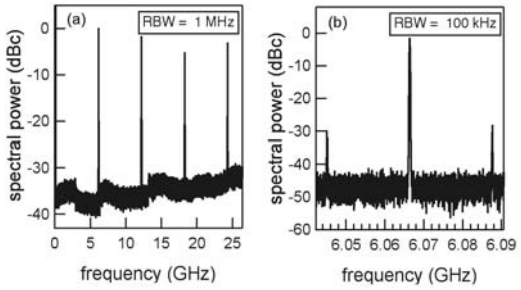


Fig. 4 Microwave spectra: (left) 25 GHz span with a resolution bandwidth of 1 MHz, (right) 50 MHz span with a resolution bandwidth of 100 kHz, centered around the main peak.

Modelocking results

We obtained stable self-starting cw modelocking with a repetition rate of 6.1 GHz. Figure 4 (left) shows the microwave spectrum of the laser with a full span from DC up to 25 GHz. Figure 4 (right) shows the same spectrum but centered to the pulse repetition rate and with a span of only 50 MHz. From the latter it is possible to notice two side peaks around the main peak separated by about 20 MHz from it. These are suppressed by more than 30 dB and we believe they might be due to higher-order mode beating as the cavity length influences their separation from the main peak.

Figure 5 shows the autocorrelation signal of the pulse train generated by our modelocked VECSEL. This has been fitted using a $sech^2$ function and a pulse duration of 18.6 ps was obtained. Figure 6 shows the optical spectrum collected using a 0.1 nm spectrum analyzer.

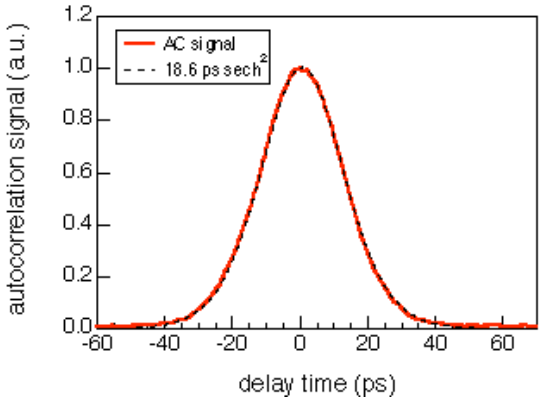


Fig. 5 Autocorrelation signal fitted to a $sech^2$ function.

The average power obtained in the modelocked regime was 57 mW under a pump power of 3 W.

Measurements of the beam profile using a knife-edge beam profiling system yielded an M^2 value of 1.15, which supports the theory of higher-mode beating to explain the side peaks.

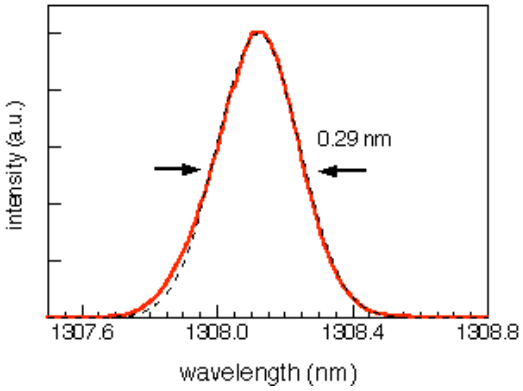


Fig. 6 Optical spectrum of the modelocked VECSEL fitted to a gaussian function.

Conclusions

We have reported the results of the first 1.3 µm VECSEL modelocking. This result has been obtained using GaInNAs in the dilute nitrogen regime for both the gain and absorbing media.

Self-starting modelocking with pulses in the picosecond regime and repetition rates in the GHz range have been demonstrated.

Acknowledgments

We wish to acknowledge NCCR for funding this project under the Quantum Photonics framework.

We also thank Dr. Emilio Gini for the MOVPE growth.

References

1 U. Keller et al., Physics Reports 429 (2) , p. 67, 2006.

2 N. Tansu et al., Appl. Phys. Lett. 83, p. 18, 2003.

3 S. Hoogland et al., IEEE Photon. Technol. Lett. 12, p. 1135, 2000.
4 D. Lorenser et al., Appl. Phys. B 79, p. 927, 2004.
5 A. Aschwanden et al., Opt. Lett. 30, p. 272, 2005.
6 V. Liverini et al., Appl. Phys. Lett. 84, p. 4002, 2004.
7 A. Rutz et al., Elec. Lett. 41, p. 321, 2005
8 M. Kondow et al., Jpn. J. Appl. Phys., Part 1 **35**, p.1273, 1996 .
9 M. Kondow et al, Journal of Physics: Condensed Matter 16, p. S3229, 2004.
10 G. Spühler et al., Appl. Phys. B 81, p. 27, 2005.
11 R. Grange et al., Appl. Phys. Lett 87, p. 132103, 2005.
12 R. Häring et al, Electron. Lett. 37, p. 766, 2001.
13 V. Liverini et al., J. Appl. Phys. 99, p. 113103, 2006.
14 E.-M. Pavelescu, Appl. Phys. Lett. 83, p. 1497, 2003.
15 M. Haiml et al., Appl. Phys. B 79, p. 331, 2004.
16 R. Paschotta et al., Appl. Phys. B 73, p. 653, 2001.
17 A. Aschwanden et al., Appl. Phys. Lett. 86, p. 131102, 2005.

Focused-ion-beam fabrication of slanted fiber couplers in silicon-on-insulator waveguides

Jonathan Schrauwen (1), Frederik Van Laere, Dries Van Thourhout and Roel Baets
1) Photonics Research Group - Department of Information Technology - UGent/IMEC email:jonathan.schrauwen@intec.ugent.be

Abstract: *We have designed and fabricated an efficient grating coupler for silicon-on-insulator waveguides. The coupler consists of 88nm wide slits, under an angle of 58° to the surface normal. They are defined by direct etching with a focused ion beam, using iodine gas and an alumina hard mask. The measured efficiency was 46%.*

Introduction

The silicon-on-insulator (SOI) platform is a promising candidate for future ultra-compact photonic integrated circuits because of its compatibility with CMOS technology [1]. The high index contrast in this material system allows for the fabrication of short waveguide bends and therefore circuits with a high degree of integration. Due to the large size and shape mismatch between the optical mode in a high index contrast waveguide and in an optical fiber, coupling between both is a problem that has to be addressed. Literature proposes adiabatic tapering and out of plane diffraction as candidates to solve this problem. Three dimensional [2] and inverse [3] taper structures can adiabatically transform the optical mode between a silicon waveguide and a fiber with low loss, but need complicated fabrication strategies and are not compatible with waferscale processing. Alternatively, out of plane diffraction gratings can easily be fabricated with completely CMOS compatible technologies [4]. These gratings are very compact, can be one or two dimensional, and couple light from a waveguide to a fiber with a reasonable efficiency. Grating couplers avoid the necessity of polished facets and enable wafer scale testing of integrated circuits. Although 1D gratings are very polarization sensitive, a polarization insensitive approach can be envisaged when one uses 2D grating couplers [5]. Although the basic process for these gratings is completely CMOS compatible, the different approaches that are proposed in literature to enhance the efficiency are more complicated. One approach is the use of a bottom gold mirror, that can be added by wafer bonding [6]; another approach is the deposition of poly-Silicon overlay which needs Chemical Mechanical Polishing (CMP) and the deposition of low-loss poly-Silicon [7].
These were all fabricated with standard lithography so they do not enable in situ analysis of wafer scale optical circuits. Another approach is the direct etching of grating couplers in predefined silicon waveguides. This is feasible with focused-ion-beam (FIB), a common tool for device analysis and modification in electronics. It was shown that shallow grating couplers can be etched with FIB [8]. However, these couplers require a two step etching process and have a moderate coupling efficiency of 24%.

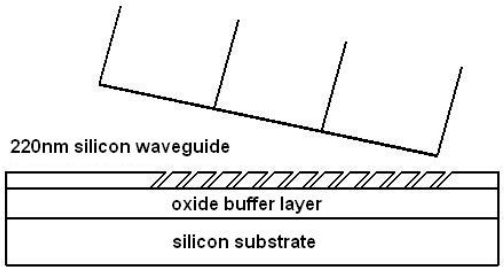


Fig. 1: Schematic drawing of the slanted fiber coupler.

In this paper we discuss the design and fabrication of a slanted grating coupler, combining the flexibility of FIB with a higher efficiency. In the first section we report on the design of a slanted fiber coupler with a theoretical efficiency of 64%. This approach was originally proposed by Ref. [9]. In the next section we discuss the fabrication of the grating with FIB. And in the final section we present the experimental results: a measured fiber-to-chip coupling efficiency of 46%.

Simulation

Regular shallow gratings in SOI have an inherent efficiency limit of around 50% due to diffraction of the first order into the substrate. This limit can be circumvented by a bottom DBR mirror [4], or by a bottom gold mirror [6]. However, these greatly complicate the fabrication of integrated circuits in SOI. Another method to enhance the coupling to the upward first order is the use of slanted facets, in analogy to a blazed grating. Because it is difficult to control the depth of the slanted slits with FIB we have chosen to design a slanted grating with slits through the entire top silicon layer. We use SOI wafers with 220nm top silicon and 2μm oxide buffer. The gratings were simulated in a Finite Difference Time Domain (FDTD) environment. The optimization was done by first scanning the complete parameter space, followed by a local quasi Newton optimization. Although one can in principle couple light upwards by total internal reflection on a single slanted facet, there will be little overlap with the mode in the fiber in that case. To ensure more overlap with the large fiber mode one needs to couple light upwards in a distributed way. This is feasible with - FIB fabricated - sub 100nm slanted slits that allow tunnelling.
The optimum grating for 10° coupling has 87.5nm wide slits under an angle of 58.4°. Our simulations

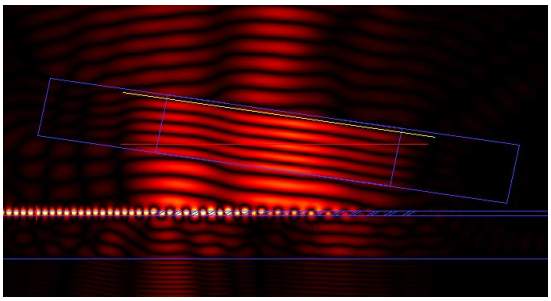


Fig. 2: Part of the FDTD simulation environment of the optimal grating with 64% efficiency. The plot shows the field pattern at 1550nm operation.

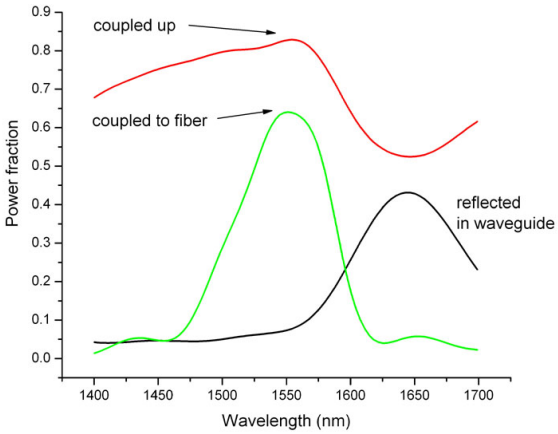


Fig. 3: Result of the slanted coupler optimization with an FDTD simulation. The curves present the power fractions coupled upwards, coupled into the fiber mounted at 10°, and reflected back into the waveguide.

were performed in a 25μm x 14μm base, and converged with a 10nm mesh. A plot of the calculated field pattern for 1550nm operation is shown in Figure 2. The slanted grating coupler has a fiber-to-chip coupling efficiency of 64%, a period of 675nm and a 3dB bandwidth of 100nm. Figure 3 shows the calculated power fractions that are diffracted upwards; coupled into the fiber; and reflected in the waveguide. To ensure a low second order reflection in the waveguide the fiber mounted at 10°. For 1550nm light the back reflection is only 7%. The total amount of power diffracted out of plane is 83% at 1550nm. Although only part of this upward power is coupled into the fiber due to mode mismatch for a periodic grating, the mode mismatch can be decreased by varying slit width. However, due to fabrication complexity of varying slit widths, we have chosen to only design and fabricate periodic slanted gratings.

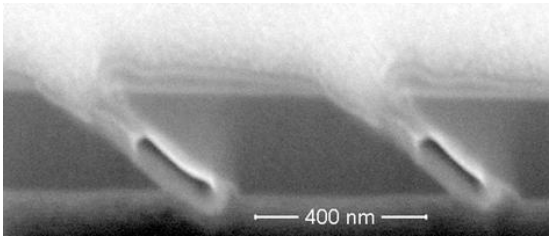


Fig. 4: Cross section of two slits of the slanted grating coupler. There is a good agreement with the FDTD designed grating.

Fabrication with focused-ion-beam

Microfabrication with FIB consists of hitting a substrate locally with high energy ions; in most commercial systems, like our FEI Dualbeam 600, these are gallium ions with energies around 30keV. In crystalline substrates this process induces lattice damage, makes the top layer amorphous, and implants ions deeper into the substrate [10, 11]. Although these effects cause optical losses and make the direct fabrication of low-loss photonic devices non-trivial, there are fabrication strategies to minimize optical losses. When carefully adopting these strategies FIB remains a promising tool due to the flexibility with which we can make photonic devices. In previous work we have for instance demonstrated that low-loss fiber couplers can be fabricated with FIB [8]. By using Al_2O_3 as hard mask and I_2 as selective etchant the loss by crystal damage can be minimized. Al_2O_3 has a very low penetration depth for incident gallium ions and has a very low etch rate under iodine atmosphere.

Therefore 50nm of Al_2O_3 was deposited on predefined SOI waveguides using electron beam evaporation. Simulations and experiments have shown that this thin layer has no influence on the propagation losses of light in the predefined waveguides. That is why we did not incorporate the layer in our simulations. To etch narrow slanted slits we have mounted the sample under 58° relative to the ion beam, and scanned lines under an iodine atmosphere. Both hard mask and silicon are etched in the same run, where narrow slits are formed due to the large etch rate difference between alumina and silicon. The etch dose was optimized to etch down to the oxide buffer layer. We have noticed that the slit width depends strongly on the beam size. The beam current used was 50pA, corresponding to a beam size of about 30nm. A cross section of two grating slits is shown in Figure 4, and a top view is shown in Figure 5. For an etch dose of 1.1 x 10^{13} Ga^+/cm the slits are etched down to the oxide buffer layer and the slit width corresponds to the simulations. The etch time for 15 slits of 10μm wide is about 8 minutes. After fabrication the sample was baked for two hours at 300°C in a nitrogen atmosphere.

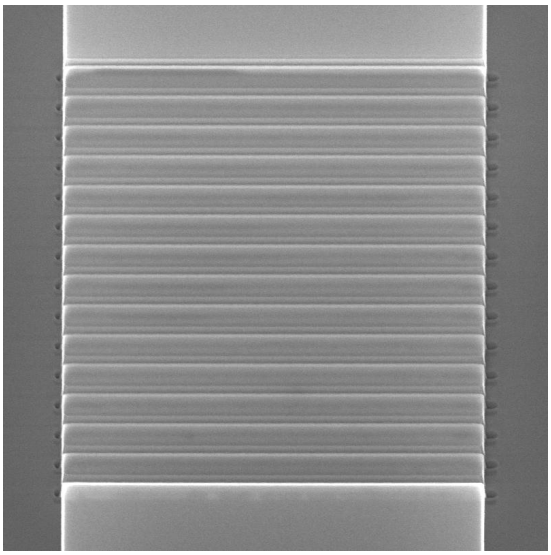


Fig. 5: A top view of the slanted grating coupler.

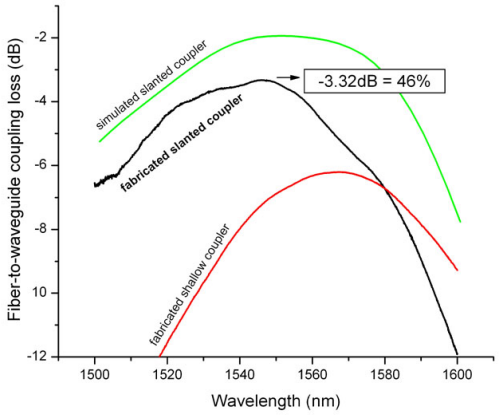


Fig. 6: Coupling spectra of simulated and fabricated slanted fiber coupler, as compared to a shallow grating coupler fabricated with optical lithography.

Measurement and discussion

To determine the coupling efficiency of the fabricated coupling structure we have used a fiber-to-fiber transmission measurement for TE polarized light from a super luminescent LED. The structure consisted of a regular shallow input coupler fabricated with optical lithography, a broad 10μm waveguide, and a slanted output coupler fabricated in situ with FIB. The coupling characteristic of the shallow couplers was measured in a separate setup with identical input and output couplers. The coupling efficiency of the slanted grating coupler is depicted in Figure 6. It is calculated by subtracting - on a logarithmic scale - source spectrum and shallow coupler spectrum from the measured spectrum. We have extracted a maximum fiber-to-waveguide coupling efficiency of 46% and a 3dB bandwidth of about 80nm for the slanted fiber coupler fabricated with FIB.

To evaluate the discrepancy between simulated and measured coupling efficiency we have investigated the fabrication tolerances of the slanted coupler. Period, slant angle, and slot width were varied within the measurement tolerance of the cross section in Figure 4. The observed drop in efficiency was below 5%, therefore bad grating parameters can not fully explain the discrepancy. Instead, we consider the measured loss to be material related. Is is known that FIB etching generates optical losses in silicon [8]. Although the use of alumina as mask and iodine as enhancement gas considerably reduces these losses, we have noticed that an additional baking step at 300°C is necessary to fabricate slanted couplers with efficiencies above 20%. We think that the baking step removes all remaining iodine and silicon iodide from the etched region. However, the damage caused to the silicon crystal remains unaltered after a temperature treatment at 300°C. Therefore we are convinced that silicon crystal damage in the region of the etched slits causes the discrepancy between theory and experiment.

Conclusions

We report on the design and focused-ion-beam fabrication of a slanted grating coupler in a silicon-on-insulator waveguide. The coupler has a maximum coupling efficiency of 46% and can be etched in situ, anywhere on a wafer, in less than 10 minutes.

Acknowledgments

This work was partly supported by the European union through the Network of Excellence ePIXnet, by the Belgian IAP-PHOTON network and the Fund for Scientific Research (FWO).

References

[1] W. Bogaerts, R. Baets, P. Dumon, V. Wiaux, S. Beckx, D. Taillaert, B. Luyssaert, J. Van Campenhout, P. Bienstman and D. Van Thourhout, "Nanophotonic Waveguides in Silicon-on-Insulator Fabricated with CMOS Technology", *Journal of Lightwave Technology*, vol. 23(1), pp. 401-412, 2005.

[2] A. Sure, T. Dillon, J. Murakowkski, C. Lin, D. Putsai and D.W. Prather "Fabrication and characterisation of three-dimensional silicon tapers", *Optics Express*, vol. 11, pp. 3555-3561, 2003.

[3] G. Roelkens, P. Dumon, W. Bogaerts, D. Van Thourhout, R. Baets "Efficient Silicon-on-Insulator fiber coupler fabricated using 248nm deep UV lithography", *Photonics Technology Letters*, vol. 17(12), pp. 2613-2615, 2005.

[4] D. Taillaert, P. Bienstman and R. Baets, "Compact efficient broadband grating coupler for silicon-on-insulator waveguides" ,*Optics Letters*, vol. 29(23), pp. 2749-2751, 2004.

[5] D. Taillaert, H. Chong, P. Borel, L. Frandsen, R.M. De La Rue, R. Baets, "A compact two-dimensional grating coupler used as a polarization splitter" ,Photonics Technology Letters, vol. 15(9), pp. 1249-1251, 2003.

[6] F. Van Laere, G. Roelkens, J. Schrauwen, D. Taillaert, P. Dumon, W. Bogaerts, D. Van Thourhout and R. Baets, "Compact grating couplers between optical fibers and Silicon-on-Insulator photonic wire waveguides with 69% coupling efficiency", *OFC 2006, United States*, p. PDP15, 2006.

[7] G. Roelkens, D. Van Thourhout, R. Baets "High efficiency Silicon-on-Insulator grating coupler based on a poly-Silicon overlay", *Optics Express*, vol. 14(24), pp. 11622-11630, 2006.

[8] J. Schrauwen, D. Van Thourhout and R. Baets, "Focused-ion-beam fabricated vertical fiber couplers in silicon-on-insulator waveguides", *Applied Physics Letters*, vol. 89, pp. 141102, 2006.

[9] B. Wang, J.H. Jiang and G.P. Nordin, "Embedded, slanted grating for vertical coupling between fibers and silicon-on-insulator planar waveguides", *IEEE Photonics Technology Letters*, vol. 17(9), pp. 1884-1886, 2005.

[10] S. Rubanov and P.R. Munroe, "FIB-induced damage in silicon", *Journal of Microscopy-Oxford*, vol. 214, pp. 213-221, 2004.

[11] A.A. Tseng, "Recent developments in micromilling using focused ion beam technology", *Journal of Micromechanics and Microengineering*, vol. 14(4), pp. R15-R34, 2004.

High speed silicon photonics

Michal Lipson
Cornell University, USA, ml292@cornell.edu

Paper not available

Ultrafast All-Optical Switching by Cross Phase Modulation Induced Wavelength Conversion in Silicon-on-Insulator Waveguides and Ring Resonators

Ronald Dekker (1), Jan Niehusmann (2), M. Först (2) and Alfred Driessen (1)
(1) Integrated Optical Micro Systems, Mesa+ Research Institute, University of Twente, P.O. Box 217, 7500 AE Enschede, The Netherlands. E-mail: r.dekker@utwente.nl.
(2) RWTH Aachen University, Institut für Halbleitertechnik, 52074 Aachen, Germany.

Abstract: *We present new results on ultrafast all-optical wavelength conversion in Silicon-on-Insulator waveguides through cross phase modulation. We demonstrate sub-picosecond all-optical switching with 13dB on/off ratio by combining the nonlinear wavelength conversion in the port waveguide with passive filtering using an integrated SOI microring resonator.*

Introduction

Because of its potential for integration with microelectronics silicon photonics is receiving increasingly attention. Figure 1 shows the results of a literature search on the Web of Science, where a search was conducted on article titles with the words 'silicon AND waveguide', or 'silicon AND resonator', or 'silicon AND photonic' in the period from 1988 till October 2006. The bottom bars indicate the number of papers per year that turned out to be relevant with respect to silicon integrated optics. Although this graph does not represent all papers on silicon photonics, it is clear to see that there is an exponential trend in the number of publications on this topic. Furthermore, the shaded areas above the bar chart give an indication about the main contents of the papers.

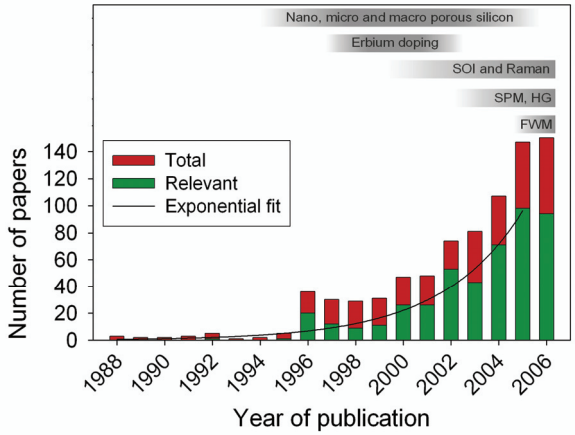


Fig. 1: Web of Science literature search on SOI. Only part of the total search results yielded topics that were relevant with respect to integrated optics. The data for 2006 only includes the months January through October.

It can be seen that in the period 1996 till 2000 there were several groups working on doping silicon with erbium for light emission purposes. In the period from 2000 till 2004 a shift from porous silicon to single crystalline SOI took place. From that moment, Raman gain was studied by many groups and nonlinear processes like self phase modulation and harmonic generation became a topic of particular interest. It can be concluded that there is a clear shift towards active optical nonlinear processing in SOI.

Substantial progress has been achieved, *e.g.*, in the field of Raman amplification, in both continuous-wave [1] and pulsed pump-probe [2, 3] experiments. Further, nonlinear effects like two-photon absorption (TPA) [4], self phase modulation (SPM) [5-7], cross phase modulation (XPM) [8], continuum generation [9], four wave mixing (FWM) [10] and the optical Kerr effect [11] have also been successfully demonstrated and thoroughly investigated. This paper will discuss our recent achievements on ultrafast sub-picosecond all-optical wavelength conversion in Silicon-on-Insulator waveguides through cross phase modulation and explains how we exploit this to achieve modulation with 13dB on/off using an integrated passive microring resonator.

Experimental setup

Figure 2 shows a schematic representation of the pump-probe setup. Both pump and probe pulses with a FWHM pulse duration of ~220fs have some degree of tunability with respect to wavelength and are delivered by an optical parametric oscillator (OPO) with a repetition rate of 80MHz. The time delay between pump and probe pulses is controlled with a free-space optical delay line (ODL) with 6.6 femtosecond accuracy. Both beams are combined using a beam splitter (BS) and coupled into a 10cm piece of a lensed and tapered polarization maintaining fiber (PMF) using a microscope objective (MO) with a magnification of 10X in order to match the numerical aperture of the PMF fiber. The beam shapes are being modified by optical beam formers (OBF) in order to optimize the fiber coupling efficiency. The PMF is used to facilitate the simultaneous coupling of the TM polarized pulses into the waveguide samples. No spectral broadening due to the fiber nonlinearities has been observed at the output of the fiber, prior to entering the waveguide under investigation. After propagation through the planar optical waveguides the transmitted pulses are coupled out using a single mode fiber, which is attached to an optical spectrum analyzer (OSA). By this means, both intensity and spectral characteristics of the transmitted pump and probe pulses can be detected simultaneously. Folding mirrors (FM) are used to tap the pump and probe

signals in front of the waveguide for power level detection using an optical detector (OD). The pump intensity can be controlled using a neutral density filter (NDF). A nonlinear crystal (BBO) is used to determine the zero time delay by detecting the sum frequency of pump and probe with the OSA.

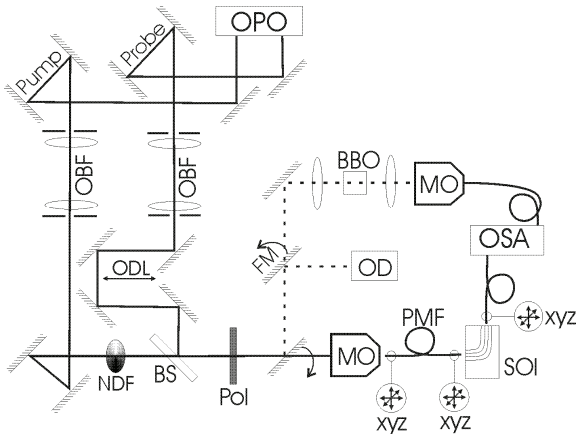


Fig. 2: Schematical representation of the pump-probe setup.

Two photon and free carrier absorption

The pump wavelength was tuned at 1700nm and the probe wavelength at 1550nm. The 220fs pulses were coupled to a 400×300nm SOI waveguide with a length of 7mm using a lensed tapered fiber in order to improve the coupling efficiency. The effect of TPA and FCA on both the pump and probe pulses are shown in Fig. 3 and Fig. 4, respectively. Figure 3 shows the saturation effect of the pump pulses, whereas Figure 4 shows the cross absorption modulation (XAM) of the probe pulses.

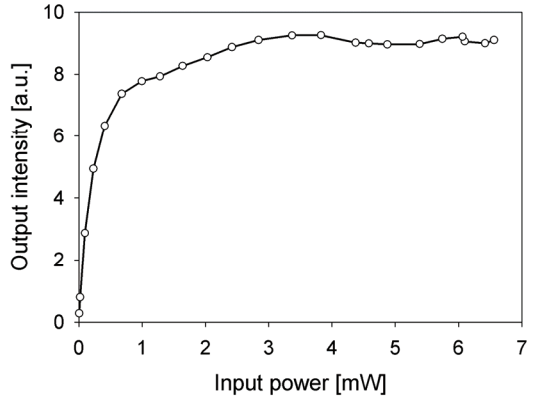


Fig. 3: Pump saturation as function of average coupled input power.

The effect of the free carrier absorption becomes more prominent as the pump power is increased. The saturation in Figure 3 is mainly caused by TPA. In Fig. 4 this TPA is observed at zero time delay. At powers larger than 0.4 mW the resulting free carrier density is large enough to induce FCA for positive time delays.

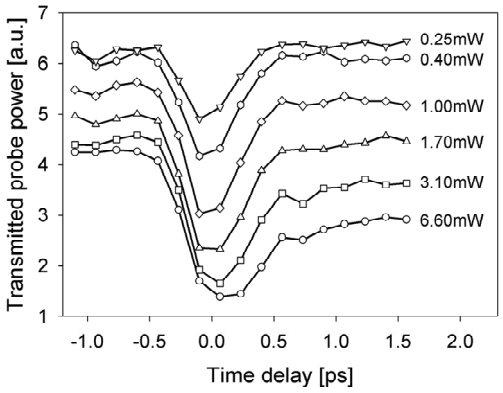


Fig. 4: Cross Absorption Modulation of the probe pulses as function of pump power and delay time.

Cross phase modulation

The probe pulses not only experience losses induced by the pump pulses, but also refractive index changes caused by the Kerr nonlinearity and the generated free carriers. The Kerr induced refractive index change is described by:

$$\Delta n_{Kerr}(t,z) = n_2 . I(t,z) \qquad (1)$$

where n_2 is the intensity dependent refractive index and I is the intensity of the pulses. The free carrier induced refractive index change has an opposite sign and can be described by the well-known accurate empirical relation presented by Soref *et al.* [12]:

$$\Delta n_{FC}(t,z) = -(8.8 \cdot 10^{-22} N + 8.5 \cdot 10^{-18} N^{0.8}) \qquad (2)$$

where N is the free carrier density in units of cm^{-3}. Consider a pump-probe experiment where the delay time between the pulses is such that the probe signal has a temporal overlap with the pump signal on either the rising or trailing edge. In this case, the probe signal will experience a time dependent phase shift $\Delta\phi(t,z)$ which is caused by the temporal change $I(t,z)$ of the pump pulse induced index changes [3]:

$$\Delta\phi(t,z) = \frac{2\pi L_{\text{int}}}{\lambda}\left[\Delta n_{Kerr}(t,z) + \Delta n_{FC}(t,z)\right] \qquad (3)$$

where Δn_{Kerr} and Δn_{FC} are the positive and negative Kerr and free carrier induced refractive index changes, L_{int} is the interaction length, *i.e.* the length over which the pump and probe pulses feel each others presence. This temporal variation in phase will result in a frequency shift of the probe pulses:

$$\Delta\omega(t,z) = -\frac{d}{dt}\Delta\phi(t,z) \qquad (4)$$

resulting in a shifted center wavelength of the probe pulses [8]:

$$\lambda_s = \frac{\lambda_0}{1 - \frac{L_{\text{int}}}{c} \cdot \frac{\Delta n(t,z)}{dt}} \qquad (5)$$

where λ_s is the center wavelength of the frequency converted probe pulse, λ_0 the center wavelength of the original probe spectrum and c is the speed of light in vacuum.

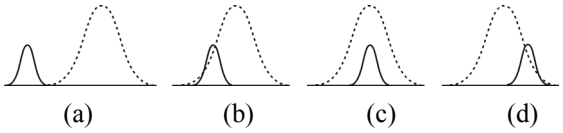


Fig. 5: Schematic representation of pump-probe pulses that overlap in time (a pulse on the right means lagging behind in time). The dashed curve represents the high intensity pump pulse, whereas the solid line represents the much weaker probe pulse.

Figure 5 shows a schematical representation of the time delay. In the case of Fig. 5(a), the probe pulse does not feel any influence of the probe pulse and therefore nothing happens to the spectral distribution of the probe pulse. However, in case (b), when the probe is overlapping with the leading edge of the pump pulse, it is influenced by the positive change in the refractive index as function of time $d(\Delta n)/dt$, which in turn generates a positive phase change $d(\Delta\phi)/dt$. This positive change of the phase induces a decreased carrier frequency, which results in an increase of the center wavelength of the probe. In other words, the probe spectrum gets redshifted. In configuration (c) the probe pulse is exactly centered with the pump pulse and the induced phase changes will more or less compensate each other (depending on the dispersion properties of the waveguide) and the shift of the wavelength will be negligible. In Fig. 5(d) the probe does overlap with the trailing edge of the pump, experiencing a negative refractive index change, resulting in a blue shift of the probe carrier wavelength.

The experimentally determined wavelength shifts as function of delay time and pump power are plotted in Fig. 6. At increasing pump powers the redshift practically remains constant, while the blueshift increases up to 26nm as a result of the contribution of the increasing free carrier density, resulting in a refractive index decrease. The total tunability of the probe pulses that have been obtained in the experiments was 36nm. The asymmetry in the wavelength shift with respect to the shape of the pump pulses can be explained by the refractive index change caused by the free carriers. The negative slope of $d\Delta n/dt$ becomes more dominant as the free carrier concentration increases, *i.e.* when the peak intensity increases or when the pulse lengths increase [8]. The more the probe pulse interacts with this negative change in the refractive index the larger the blueshift will be, which is in agreement with Equation (5).

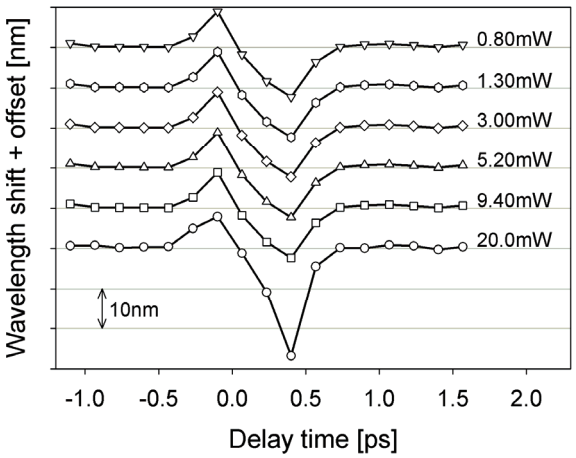


Fig. 6: Cross phase modulation induced wavelength shift exerted on the probe spectrum.

All-optical modulation or switching can be obtained in case the XPM shifted probe pulses are filtered using a passive microring resonator filter, as has been recently proposed [8, 13]. A typical SEM image of the microring resonator filters used for this purpose is shown in Fig. 7. The insets at the left and right of the SEM picture show the filtered probe spectra that have been captured using a spectrum analyzer at the drop and through port, respectively.

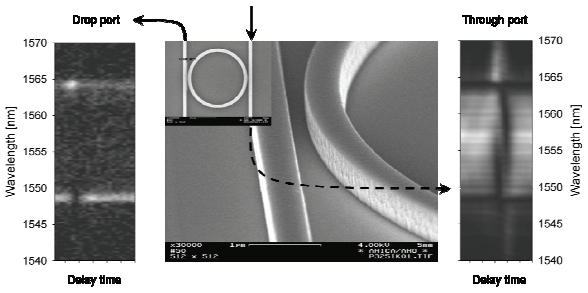


Fig. 7: (b) Scanning Electron Microscope image of a ring resonator in SOI, fabricated via direct e-beam writing. The insets,(a) and (c), show the filtered probe spectra at the drop and through port as function of pump-probe delay time, respectively.

Figure 8 shows the probe spectra at the drop port in more detail. The resonance peaks are shown schematically and reveal a FSR of about 16nm. The center wavelength of the probe spectrum was tuned in between two resonance wavelengths. Part of the wavelength components in the tail of the transform limited pulses are leaking to the drop port. However, when the probe spectrum is all-optically shifted to a larger wavelengths, more power is coupled to the 1564nm resonance and less to the 1548nm resonance peak.

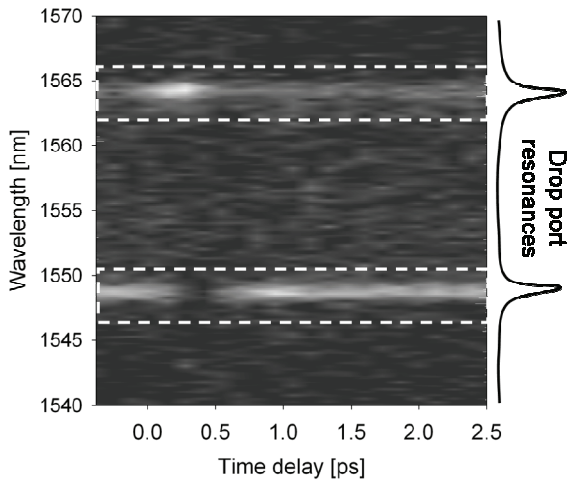


Fig. 8: Filtered probe spectra detected at the drop port of a SOI microring resonator as function of delay time. The resonance peaks of the resonator are schematically drawn at the right side of the plot.

The power of the filtered wavelength components have been integrated for both resonance peaks and are plotted in Figure 9. It can be seen that the signal at the 1564nm resonance is enhanced by 5dB while the power around the 1548nm resonance is decreased by 13dB.

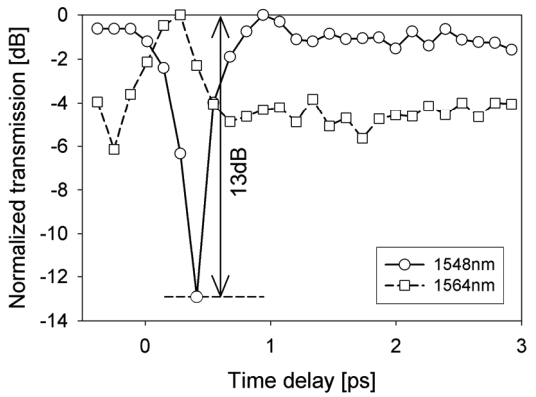


Fig. 9: Normalized integrated power detected at the drop port. Circles represent the power around the resonance wavelength of 1548nm, squares show the power at the wavelength of 1564nm.

The modulation depth is limited by the combination of the width of the probe spectrum and the FSR. The larger the ratio between these two quantities ($FSR_{ring}/FWHM_{probe}$) the higher the modulation depth that can be obtained. The shorter the pulse lengths, the broader the probe spectrum. However, the wavelength shifts are directly related to the pulse intensities, which in turn scale with the pulse lengths. Therefore, it is not a logical choice to increase the pulse duration, since the wavelength shift strongly depends on this parameter. A better choice would be to increase the FSR of the microring resonator. In case a microring with a smaller radius is used the free spectral range can be increased to about 28nm (in case n_{eff}~2.7 and R=5μm), which further enhances the modulation depth.

Conclusions

We have shown that 26nm blue- and 10nm red shifts of probe light are feasible in SOI waveguides by exploiting the ultrafast Kerr-induced and free carrier induced refractive index changes by high intensity 220fs laser pulses. The XPM induced wavelength up- and down-conversion takes place in a sub-picosecond timeframe. We have demonstrated ultrafast all-optical modulation of a probe signal with a modulation depth of 13dB, which can be further improved by employing SOI microring resonators with smaller radii. These results open the way to sub-picosecond all-optical switching and modulation using SOI microring resonators or, alternatively, waveguide gratings.

Acknowledgments

The authors thank T. Wahlbrink and J. Bolten (AMICA, AMO GmbH Aachen, Germany) for device fabrication. R. Dekker and A. Driessen would like to thank the Freeband Impulse technology program of the Ministry of Economic Affairs of the Netherlands. All authors would like to acknowledge the European Network of Excellence on Photonic Integrated Components and Circuits (ePIXnet).

References

1. V. Raghunathan et al, J.Lightwave.Technol, Vol 23 (6), pp 2094-2102, 2005.
2. A. Liu et al, Opt.Express, Vol 12 (18), pp 4261-4268, 2004.
3. Q. Xu et al, Opt.Express, Vol 12 (19), pp 4437-4442, 2004.
4. T. K. Liang et al, Appl.Phys.Lett., Vol 84 (15), pp 2745-2747, 2002.
5. O. Boyraz et al, Opt.Express, Vol 12 (5), pp 829-834, 2004.
6. R. Dekker et al, Symposium IEEE/LEOS Benelux Chapter, Mons, Belgium, ISBN 2-9600226-4-5, pp 197-200, 2005.
7. E. Dulkeith et al, Opt.Express, Vol 14 (12), pp 5524-5534, 2006.
8. R. Dekker et al, Opt.Express, Vol 14 (18), pp 8336-8346, 2006.
9. O. Boyraz et al, Opt.Express, Vol 12 (17), pp 4094-4102, 2004.
10. H. Fukuda et al, Opt.Express, Vol 13 (12), pp 4629-4637, 2005.
11. M. Dinu et al, Appl.Phys.Lett., Vol 82 (18), pp 2954-2956, 2003.
12. R. A. Soref et al, IEEE.J.Sel.Top.Quant.Electr., Vol QE-23 (1), pp 123-129, 1987.
13. R. Dekker, PhD Thesis, ISBN: 90-9021436-8, University of Twente, Enschede, The Netherlands, 2006.

Silicon-on-Insulator (SOI) Delay-Line Interferometer with Low Polarization-Dependent Wavelength Shift

K. Voigt, L. Zimmermann, G. Winzer, M. Schnarrenberger, T. Mitze, J. Bruns, K. Petermann
Technische Universitaet Berlin, HFT 4, Einsteinufer 25, 10587 Berlin, Germany, T:+49 30 314 23809, F:+49 30 314 24626
Karsten.Voigt@tu-berlin.de

Abstract: *A 40 Gbit/s delay-line interferometer realized in SOI rib waveguide technology is presented. Across the C-band we demonstrate high uniformity, low loss, low PDL, and PDF as low as 1 GHz for the SOI interferometer.*

1. Introduction

Silicon photonics has become a vast and quickly growing area of photonics R&D within less than a decade. Most of the attractiveness of the technology stems from the vision of a convergence of electronics and photonics on one substrate, using only Silicon manufacturing tools. The high index contrast of the Silicon-on-Insulator (SOI) material system allows for very compact devices [1], while the integration with CMOS electronics permits the fabrication of photonic integrated circuits [2]. Silicon-on-Insulator (SOI) waveguide technology for optical communications motherboards, on the other hand, has recently attracted attention for different reasons. Devices fabricated in this technology have larger footprints than ultra-compact SOI waveguide devices. However, they feature distinct advantages compared to the latter, such as low-cost fabrication technology, much reduced birefringence, and the possibility to match silicon waveguide mode size to that of III-V active devices.

In course of another work we have previously demonstrated a 4-wavelength CWDM transmitter chip for LX4 applications. The chip comprised a SOI motherboard with an arrayed waveguide grating multiplexer combined with four flip-chip-soldered DFB laser-diodes [3]. Here we present a Mach-Zehnder-Delay Interferometer (MZI) device realized in SOI waveguide technology, which exhibits very low Polarization-Dependent Wavelength / Frequency (PDWL / F) shift. The device is to be integrated with a balanced photodiode pair to implement a DPSK receiver chip for direct demodulation of 40 Gbit/s DPSK signals. Since PDF shift is a major performance issue for all balanced DPSK detection schemes this paper shall demonstrate the potential of SOI waveguide technology, respectively.

2. Device technology and design

The devices were fabricated in rib-waveguide technology on 4 µm commercial BESOI (Bonded and Etched-back SOI) substrates. Waveguides were fabricated using standard contact lithography and reactive-ion etching (RIE), which in our case was based on Fluorine chemistry. The devices received an antireflective coating before measurements.

The MZI layout followed a straight-forward left-in / right-out design that is adapted to the geometry of our measurement setup. We chose 2x2 paired Multi-Mode Interference (MMI) couplers as splitting and combining elements [4], because of their comparatively low sensitivity to process variations. The chip-area was 25 x 25 mm^2, combining 3 MZI devices and some test-structures on a single die. The size of the chip could be further reduced if test-structures and other MZI-devices are omitted. The layout of the actual chip is shown in Fig. 1. The MZI was designed for 40 Gbit/s DPSK demodulation, which corresponds to a free spectral range of 0.32 nm at 1550 nm.

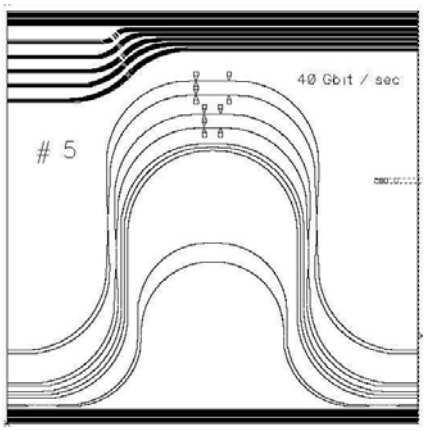


Fig. 1. Layout of the delay interferometer chip (three delay interferometers plus test structures).

3. Experimental results

PDF-specifications for balanced DPSK receivers are in the range of 1 GHz (~ 8 pm at 1550 nm) [5]. To measure such small shifts, polarization and temperature need to be carefully controlled. Our measurement setup is sketched in Fig. 2. A tunable laser source (Agilent 81940A) feeds a programmable polarization controller (8169A), which provides a well defined state of polarization. Light is coupled-in and out of the samples using lensed single-mode fibers with a spot-diameter of ~ 3 µm, corresponding

to typical coupling-loss values of 1 dB per facet. A fiber optical power sensor (81634B) provides the dynamic range and measurement speed required for stable measurements of the MZI transmission characteristics.

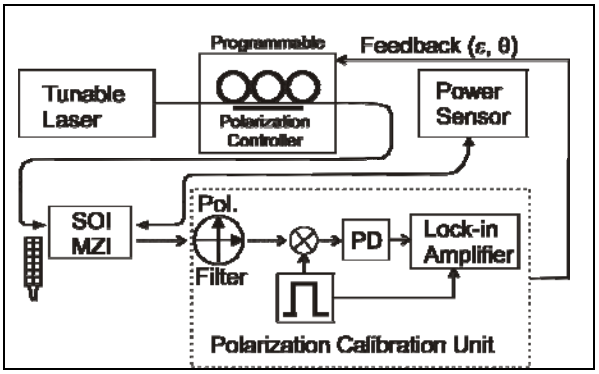


Fig. 2. Setup for PDWL shift measurements. Solid lines correspond to fiber or cable connections, dotted lines represent free space transmission paths. The photodiode (PD) of the polarization calibration unit provides a feedback signal depending on the (ε, θ)-settings of the polarization controller.

During the measurements the samples were temperature-stabilized. To compensate the birefringence properties of the fiber at the coupling-in side, a feedback signal from the polarization calibration unit was used. Only linearly polarized light was employed during the experiments. The stability of the state of polarization delivered by the setup was confirmed by identical polarization calibration curves taken before and after the experiment. In the following, all measurements are presented with respect to the fiber-to-fiber transmission signal.

Wavelength scans were conducted with 1 pm increment for small wavelength ranges (< 10 nm), and with 4 pm resolution for larger ranges. To determine the PDWL shift-value, transmission curves were measured for both polarizations (TE/TM). We observed that within the scanned wavelength window (e.g. 2nm around 1550nm in Fig. 3), PDWL shift-values varied randomly between positive and negative (see the lower part of Fig. 3). It is therefore not sufficient to state a PDWL shift-value measured at a single minimum. To determine an upper limit for the PDWL shift-values we always calculated an rms-shift-value over 10 minima, as shown in the upper part of Fig. 3. In this paper, unless stated otherwise, we shall, thus, always list the rms-value.

The C-band transmission characteristics of a 40 GHz SOI-MZI is depicted in Fig. 4 (TM-polarization, the filter characteristic of the TE-mode is very similar, and is therefore not presented here). Fig. 4 reveals a uniform insertion loss (~ -3 dB) as well as high extinction ratios across the entire C-band (minimum 24 dB).

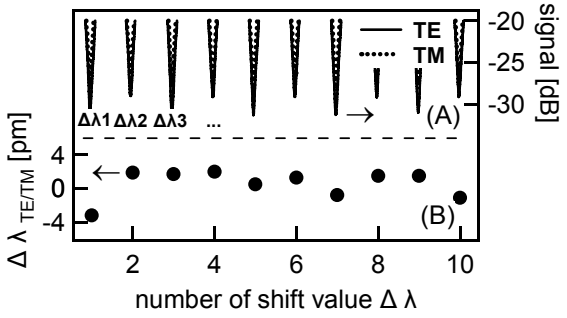


Fig. 3. TE/TM-transmission curve minima (A), and PDWL shift-values (B). The minima in (A) were measured in the range 1550 ± 2 nm . In (B), each Δλ-value was determined from the corresponding pair of TE/TM-minima in (A).

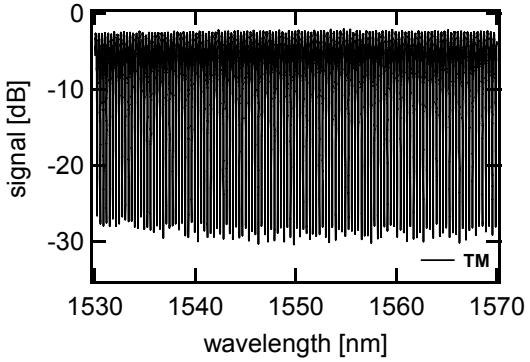


Fig. 4. C-band filter characteristic of a 40 GHz MZI on SOI. The curve represents the measurement in TM-polarization (T= 35 ºC). The signal values were determined with respect to the fiber-to-fiber signal.

We noticed (Fig. 5) a slightly higher insertion loss (~ -4 dB) for the TM-mode, which we attribute to a higher excess loss of the MMI-couplers in the TM-case. Polarization-dependent excess loss of MMI-couplers in this technology has also been reported by others [6]. Slightly higher extinction ratios were observed in case of TM-polarization (minimum 26 dB). Fig. 5 shows that our MMI-couplers exhibit correct splitting ratios and phase relation between the II-port and the X-port.

Polarization-dependent frequency of the demodulator MZI is considered a severe threat to DPSK receiver performance. Specifications for the PDF were discussed previously [5], typical limits are ~1 GHz. Fig. 6. depicts the transmission minima for TE/TM-polarization at the outer limits as well as in the middle of the C-band. The measured polarization-dependent shift never exceeds 1 GHz. We observed shifts staying below 1 GHz also for chip-temperatures up to 70°C. These results are comparable to the best values that have been achieved in other technologies [7]. To the best of our knowledge, such low PDWL / F shift values are shown for the first time in SOI waveguide technology. The polarization-dependent envelope of the transmission characteristic at maximum leads to a Polarization Dependent Loss (PDL) of ~1 dB.

Due to drift and offset, the demodulator will need to be tuned to the laser frequency by temperature control. Linearity of the tuning characteristic is a desirable feature of the demodulator chip. In our setup, we have varied the temperature of the chip (using a Peltier element), to study the tuning characteristic of our SOI MZI. The position of the minimum of the TM-curve at 1550nm relative to an arbitrary zero at 35 ºC is shown in Fig. 7. together with a linear fit of the data.

The shift of the minimum position as a function of chip temperature follows a linear characteristic, with a tuning increment of ~ 80 pm/K, for both, TE and TM polarization.

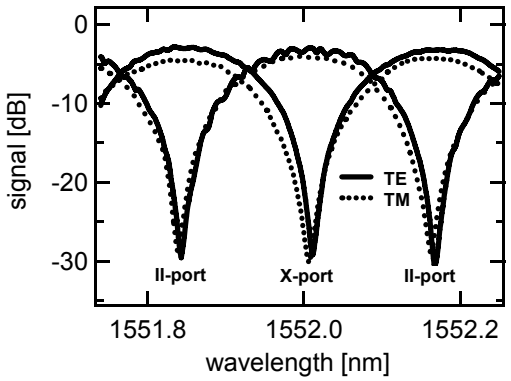


Fig. 5. Signals at the II- and the X-port for both polarizations.

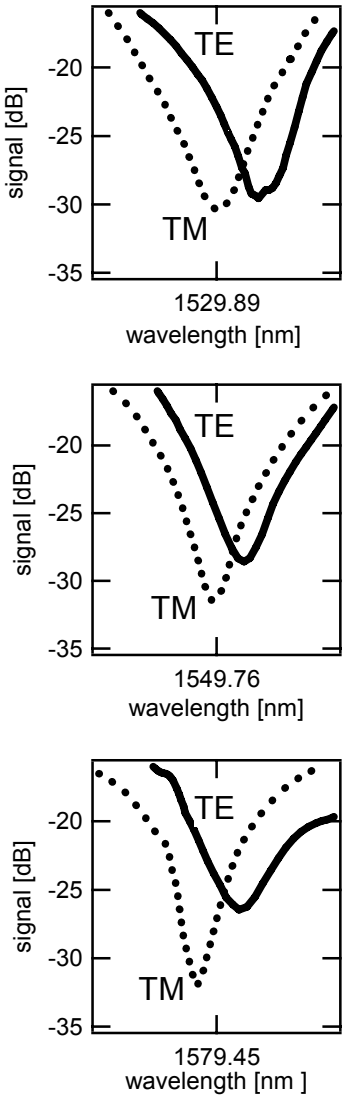


Fig. 6. Polarization dependent frequency shift of the minimum transmission (TE/TM) across the C-band, at 1530 nm, at 1550 nm, and at 1570 nm (each graph depicts a wavelength range of 50 pm). The measured shift in all three cases is ~ 8pm (1 GHz). T = 35 ºC.

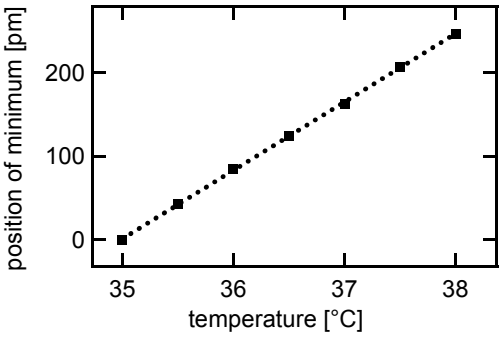


Fig. 7. Position of the minimum of the TM curve as a function of chip temperature. The position is relative to an arbitrary 0 at 35 ºC. Also shown is the linear fit of the data, the increment is ~ 80pm / K.

4. Summary and conclusions

Our MZI devices based on SOI rib waveguide technology exhibit across the entire C-band PDF as low as 1 GHz, extinction ratios substantially exceeding 20 dB, uniform insertion loss, and low PDL. The here presented results demonstrate for the first time the high potential of SOI rib waveguide technology for low-PDF applications, in particular for balanced DPSK reception. A system validation experiment of fiber-optical 40 Gbit/s DPSK transmission using the here presented SOI delay-line interferometer is planned for the near future.

5. References

[1] P. Dumont et al., Low-loss SOI photonic wires and ring resonators fabricated using deep UV lithography, Photonics Technology Letters, Vol. 16 (5), p. 1328, 2004

[2] C. Gunn, CMOS Photonics – SOI learns a new trick, Proceedings IEEE International SOI conference 2005 p. 7, 2005

[3] T. Mitze et al., CWDM transmitter module based on hybrid integration, to appear in issue on Optoelectronic Packaging, Journal of Selected Topics in Quantum Electronics, scheduled for September 2006

[4] L.B. Soldano, E.C.M. Pennings, Optical multi-mode interference devices based on self-imaging: principles and applications, J. Lightwave Technology, Vol. 13 (4), p. 615, 1995

[5] P. Winzer, H. Kim; Degradations in balanced DPSK receivers, Photonics Technology Letters, Vol. 15 (9), p. 1282, 2003

[6] A. House et al., Silicon waveguide integrated optical switching with microsecond switching speed, Proceedings OFC 2003, Vol. 2, p. 449, 2003

[7] J. Gamet, G. Pandraud, C- and L-band planar delay interferometer for DPSK decoders, Photonics Technology Letters, Vol. 17 (6), p. 1217, 2005

TE-TM coupling of a standard fiber to a Si-wire waveguide

Raffaella Costa, Giuseppe Cusmai, Andrea Melloni (*) and Mario Martinelli (*)
Corecom, via G. Colombo 81 - Milano - ITALY
(*) DEI- Politecnico di Milano, via G.Ponzio 34/5 - Milano - ITALY

Abstract: *Light coupling form a standard small core fiber to a Si-wire waveguide is demonstrated for both TE and TM through a vertical coupler. Exhaustive design criteria are presented and experimentally validated. A polarization independent couping is realized as a first trial with an efficiency of 72%.*

Introduction

The Si-wire waveguides realized from a silicon on insulator (SOI) wafer are a promising technological platform for a number of applications in both the communication and the optoelectronic word [1].

Due to the very high index contrast $\Delta n=2$, these tiny waveguides present a very small cross section, of fractions of communications wavelengths, and the effective area of the fundamental mode is as small as a few tenths of micron. This guarantees a miniaturization of the optical circuits, with a bending radius which can be reduced down to few microns, but on the other side this give rise to the detrimental effect of the scattering losses at the sidewalls. Moreover, coupling light to and from the Si-wire waveguides is still an unsettled technological issue which can limit the potentially widespread application of this platform. Contributions to so high coupling losses arise from the mode-size and the effective index mismatch.

Many different approaches have been attempted to solve this problem, blazing a trail, still strongly dependent on a challenging technological quality.

By an inverse nanotaper directly made on the silicon waveguide coupling losses of a few dB can be achieved with lensed fibers, for both the polarizations [2]. Nevertheless these fibers are not reliable for commercial applications. Coupling from a standard fiber has been demonstrated by vertical grating couplers, and the maximum coupling efficiency yet demonstrated is 69% for a single polarization [3]. The most simple and reliable approach on the technological side is the vertical coupling to an intermediate waveguide with low index contrast, having a good mode matching with a fiber. This approach has been demonstrated by different labs for a TE-like polarization coupling [4-6], while a polarization independent coupler still requires a more exhaustive study.

The aim of the present contribution is to demonstrate that an optimum standard fiber-to-Si-wire waveguide coupler can be obtained, optimized for low polarization dependence and low losses, through an exahustive review of the design procedure focousing on the main constraints with the aim of relaxing the technological issues. An experimental study of a preliminary structure is presented as a validation.

Design criteria

The mode adapter consists in a vertical coupler between a Si-wire tapered waveguide and a low index contrast waveguide which can be efficiently coupled to a standard optical fiber, as shown in Fig.1.

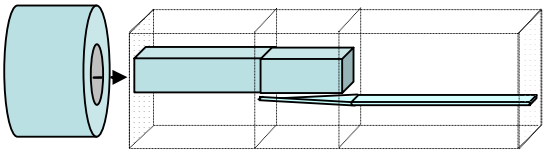


Fig. 1 The fiber to Si-wire coupling through an intermediate waveguide vertically coupled by means of a silicon taper.

The coupling between the lower and the upper waveguide modes requires the phase matching condition to be satisfied in order to obtain a complete power transfer. This is achieved locally by tapering the silicon wire, because the propagation constant scales down with the wire width, as it is shown in Fig.2 by the solid lines, which represent the effective index of the TE-like and the TM-like fundamental modes of the wire. The upper waveguide has a uniform cross section along the coupler and consequently the effective index of the fundamental mode is fixed by the index contrast and is reported on the figure too (dashed line).

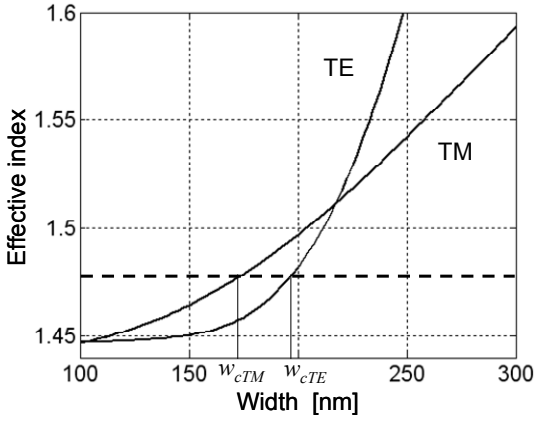


Fig.2 The effective index of the fundamental TE-like and TM-like modes of a Si-wire (solid lines) vs. width. The dotted line is the effective index of the upper waveguide. The phase matching condition between the two waveguides is satisfied in w_c for the two polarization states.

Each dispersion curve crosses the upper waveguide effective index in correspondence of the width w_c of the optimum phase matching condition, in whose surroundings takes place the coupling.

In general, w_c is different for the two polarizations, and depends on the index contrast Δn of the upper waveguide, being large in case of a high Δn, and narrow for a low Δn. The high slope of the effective index of the modes of the Si-wire vs. width, plays an important role in the working principle of the coupler, because it allows the phase matching condition to be fulfilled yust over a very short length along the taper. In fact the taper can be locally modelled over a length dL as a uniform asynchronous coupler with transfer function in the cross condition given by:

$$dP = \frac{\kappa^2}{\delta^2}\sin^2(\delta dL)$$

with $\delta^2 = \kappa^2 + \Delta\beta^2/4$, where κ is the coupling coefficient and $\Delta\beta$ is the difference of the propagation constants of the two isolated waveguides and depends on the taper width w and on the gap g [7]. The ratio κ/δ is unitary for $w=w_c$, and is significant only in a small range of widths between w_0 and w_f, which define the maximum range of the coupling and can be less than *50nm* wide, depending on the vertical gap. This is the main origin of the withstanding functioning of this mode adapter, which results to be very tolerant to fabrication errors both on the waveguide dimensions and on the layers displacement, as it will be experimentally demonstrated in the following.

For an optimum design of the mode adapter, a key point is the right choice of the Δn of the upper waveguide, looking for the best compromise among three limiting factors: the minimum reliable taper width, the impact of leakage losses and the optical fiber *MFD*. In particular, the minimum tip width technologically reliable, is ultimately limited by the lithography resolution and it defines the minimum value of the lower boundary. But a more severe restriction is given by the buffer oxide thickness which is tipically limited to a few micrometers if the silicon on insulator (SOI) technology is used for the realization of the Si-wires. As a consequence, both the waveguides have a limited buffer layer which determs leakage losses to the substrate and an inefficient coupling to the optical fiber. Certainly, the minimum oxide thickness required for a limited impact of the leakage decreases by increasing the Δn, but on the other side as this waveguide has to be efficiently coupled to the optical fiber, it is clear that the index contrast should be kept as low as possible. In order to avoid the use of the lensed fibers, a good compromise is the choice of a standard small core fiber, having a mode field diameter $MFD_f \approx 4\mu m$. This fiber can be efficiently coupled to a square waveguide with $\Delta n=4.5\%$, regular-sized to be monomodal, resulting thus the upper boundary for the usefull range of the Δn that guarantees an efficient and technologically reliable coupling to a standard optical fiber. For all these reasons this was our choice of index contrast.

The minimum oxide thickness required below a waveguide in order to minimize the undesired effects of leakage is found to be mainly dependent on the MFD_{wg} of the waveguide resulting in a condition on the buffer thickness t as $t > 1.25\ MFD_{wg}$, while on the fiber side a good fiber-to-waveguide coupling requires a minimum thickness $t > 0.75\ MFD_f$ [8].

For a waveguide with $\Delta n=4.5\%$, the mode diameter is $MFD_{wg} = 2.6\mu m$, and as a consequence the oxide thickness should be $t \geq 3.5\mu m$.

Once the fiber and the index contrast of the upper waveguide are chosen, there is still a fundamental parameter to be determed, that is the vertical gap between the two waveguides (g). As the strength of the coupler depends on the gap thickness, the minimum working with of the Si-taper (w_0) is consequently influenced by the gap, as it is shown in Fig.4: narrow gaps require very small tips with strong technological requirements [9]. For a minimum tip of $w_0=100nm$, a minimum gap $g=0.6\mu m$ is necessary.

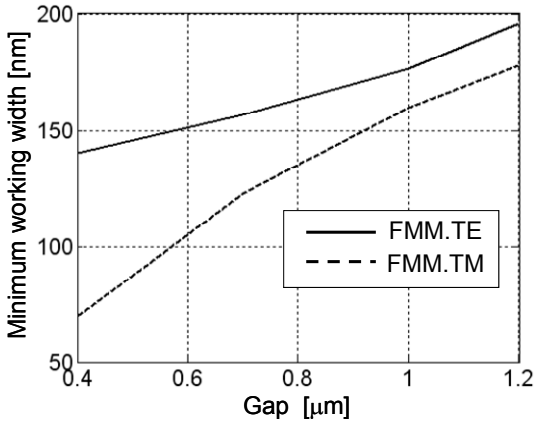


Fig. 4: Minimum working taper with w_0 vs. gap obtained numerically by FMM [10]. The index contrast of the upper waveguide is $\Delta n=4.5\%$.

On the other hand, by increasing the vertical gap, the length of the taper is increased exponentially, as it is shown in Fig.5 for a linear tapering profile. The gap is thus taken as a compromise of minimum reliable tip and device length: a short taper is desirable to limit both the dimension and the losses of the coupler.

The propagation losses in the silicon tip are in fact quite high due to the sidewalls roughness, in particular for the TE-like polarization, wich presents a higher level of losses and also a strong dependence on the wire width.

The taper losses (A_t) are the integral contribution of the wire losses $\alpha(w)$ over the operating range of widths $(w_0\text{-}w_f)$ and in case of a linear tapering function it can be written as:

$$A_t = L_t \frac{1}{w_f - w_0}\int_{w_0}^{w_f}\alpha(w)dw = L_t a \qquad (1)$$

being L_t the taper length. The constant a is in general different for the TE and the TM polarization, as so are the wire losses $\alpha(w)$.

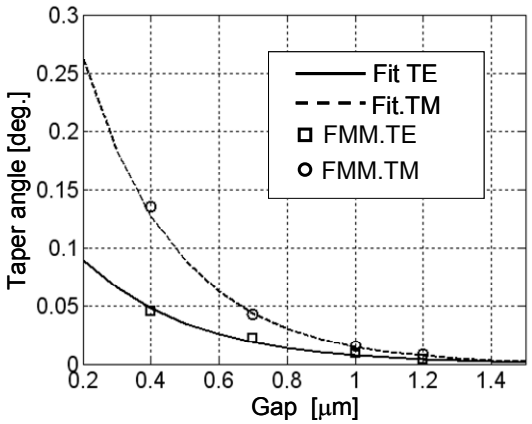


Fig. 5: Si-taper angle vs. gap, calculated by FMM for both the TE-like and the TM-like polarizations.

Experimental results

A set of mode adapters with a linear tapering profile and different lenghts was realized. The upper waveguide has a square-shaped core with $\Delta n=4.5\%$, while the Si-wire core is *220nm* thick and the vertical gap is $g=1.2\mu m$ to ease the integration issues of the two core layers. The minimum taper tip is $w_{tip}=100nm$. The complete structure (Fig.6) consists of an input and an output coupler linked by a Si-wire with $w_N=400nm$, and is realized from a commercial SOI wafer with buffer oxide thickness $t=3\mu m$.

For a best knowledge of all the single elements of the coupler, a number of test patterns was also realized: a family of straight waveguides having $\Delta n=4.5\%$ and different buffer layer thickness t, for quantifying the leakage contribution and the fiber-coupling efficiency, and a few samples of Si-wires having a range of widths for the measurement of the wire losses.

The low index contrast samples, with buffer layer thickness in the range $t=2\text{-}5\mu m$, were characterized by the cut-back method at the wavelength of *1580 nm*. The measured coupling efficiency to a small core fiber with $MFD=4\mu m$ is $A_c=0.2$ *dB* with no polarization dependence for every sample having $t>3\mu m$. Concerning the waveguide loss, the contribution of the material absorption is *0.12 dB/cm* for both polarizations, while the leakage depends exponentially on the substrate thickness and at the working point of the mode adapter, that is $t=4.4\mu m$, the additional leakage losses are *0.25 dB/cm* for the TM polarization and *0.05 dB/cm* for the TE polarization. In Fig.6 a complete set of results on the leakage loss vs. the thickness t is reported. It has to be observed that for a good performance of the mode adapter only a few millimiters of waveguide are required.

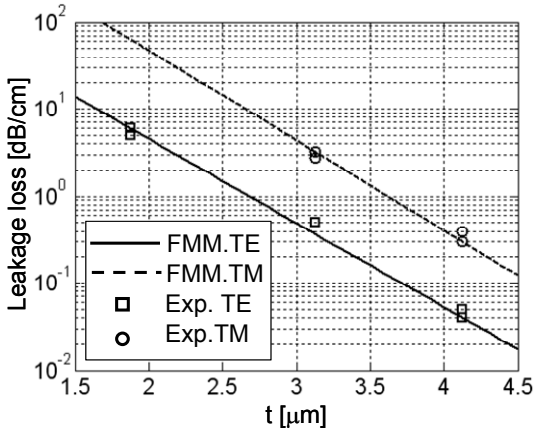


Fig. 6: Leakage loss of the waveguide with Δn=4.5%, versus buffer thickness for both the TE and TM fundamental modes. Solid lines are the numerical results, dots are the experimental ones.

The wire loss $\alpha(w)$ was characterized over a family of Si-wire waveguides with w in the range *150* to *700 nm*. The experimental data are fitted with a partially exponential and partially gaussian model which takes into account of both the leakage and the roughness contribution to the loss:

$$\alpha(w) = A\exp\left(-\frac{w}{B}\right) + C\exp\left(-\frac{(w-D)^2}{E}\right) + F \ .$$

The resulting curves for both the TE-like and the TM-like modes are presented in Fig.7: it is verified that the sidewall roughness mainly affects the TE polarization. The expected propagation loss of a Si taper can be then calculated as in (1) by integrating the experimental curve over the working width range from w_{0TE}=170nm (w_{0TM}=160 nm) to $w_f=w_N=400nm$.

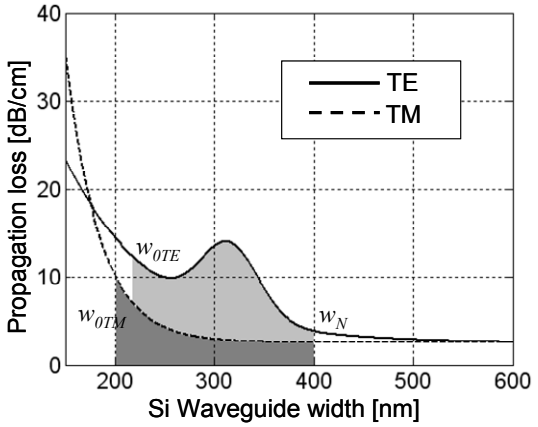


Fig. 7: Propagation loss of a Si waveguide versus waveguide width for both TE and TM polarization states. The grey zone is indicating the widths working range of the coupler.

The resulting loss curves are reported in Fig.8 versus the taper length, and are a reference for the analysis of the experimental results obtained from the characterization of the test structure. The slope of each cur-

ve is the constant *a* calculated as in *(1)* for both the polarizations. As its value is quite different for the TE-like and the TM-like mode it is hard with a linear profile to obtain a polarization independent coupling, unless a very short taper is used.
The experimental points are the loss contribution due to the propagation in the Si taper and also to the vertical coupling efficiency. They are obtained from the insertion loss measurement, by subtracting all the loss contribution given by the fiber to waveguide coupling and by the propagation in the upper waveguide and in the linking wire, previously evaluated.

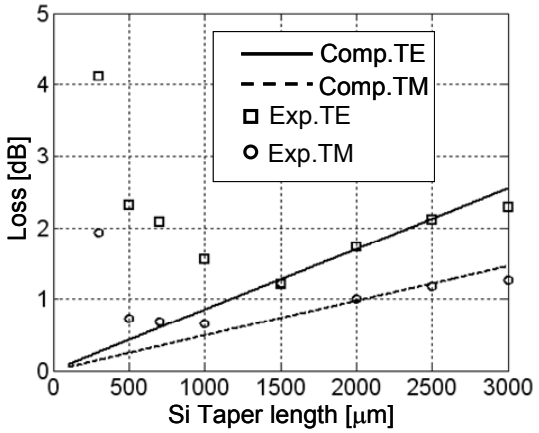


Fig. 8: Computed (solid and dashed line) and measured (squares and dots) losses of the vertical coupling process and the Si linearly tapered waveguide.

If $L_t \geq 1500$ μm the experimental points agree with the straight lines: the taper loss may be high, but the vertical coupling efficiency is close to a unitary value. On the other hand, for $L_t < 1500$ μm the points depart from the calculated lines: the vertical coupling efficiency decreases as L_t is decreased, because the vertical coupler is no longer adiabatic that is the coupling region is too short and the power transfer is not complete. The best result is so far achieved for $L_t=1500\mu m$ representing a good compromise between vertical coupling efficiency and Si taper loss. In this case the measured fiber-to-Si waveguide losses are *1.4* dB for TE and *1.5* for TM.
While the TE loss is completely in accordance to the expected value, the TM loss is about *0.5 dB* higher probably due to experimental tolerances.
A further interesting result is the high tolerance to the layer displacements in case of different taper lengths, which increases with the taper length: for a taper length $L_t=2mm$ a displacement of $0.5\mu m$ doesn't affect the coupling, as shown in Fig.9.

Conclusions
A TE and TM coupling from fiber to Si-wire *220x400nm* waveguide has been exhaustively studied and experimentally demonstrated. Design criteria are presented with the aim of relaxing the technological constraints on the fiber side and on the minimum wire width requided. A prototype of the device according to the discussed design criteria has been fabricated by Pirelli Labs Optical Innovation. As a first trial an almost polarization independent coupling efficiency of 72% was demonstrated experimentally.

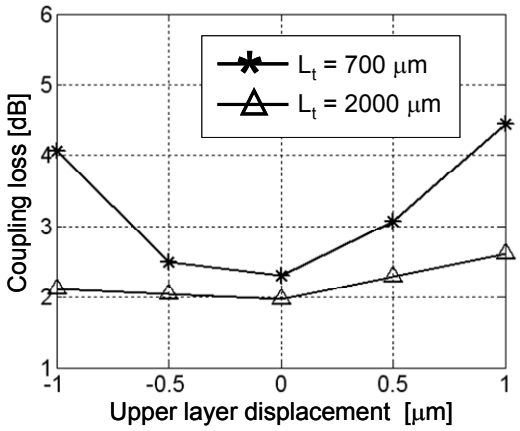


Fig. 9: Eperimental sensitivity of the coupling efficiency to upper layer relative displacement for TE polarization and two taper length L_t.

An optimization of the structure can be obtained either on the technological side by a further reduction of the sidewall roughness of the Si-taper, or on the design side by an opportune choice of the taper prfile or by reducing the vertical gap, in order to reduce the structure length. Further fabrications are in progress.

Acknowledgments
The authors would like to thank the technological staff of Pirelli Labs for the realization of the devices and for the useful technical discussions held with the design group. A special thanks to Dr. M. Artiglia for his useful advice.

References
1. W. Bogaerts et al., Sel. Top. in Q. El., IEEE J. of, Vol.12 No.6, p.1394, 2006.
2. V.R. Almeida et al. Opt.Lett., Vol.28, No.15, p.1302, 2003.
3. F. Van Laere et al., in proc. OFC2006, p.1, 2006.
4. G. Roelkens et al., IEEE Phot. Technol. Lett., Vol.17 No.12, p.2613, 2005.
5. K.K. Lee et al., Opt. Lett., Vol.30, No.5, p.498, 2005.
6. T. Tsuchizawa et al. IEEE J. of Sel. Top. in Q. El., Vol.11 No.1, p.232, 2005.
7. R. Costa et al., proc. OWTNM 2006, p. 42.
8. C.M. Kim, Sel. Top. in Q. El., IEEE J. of, Vol.6 No.1, p.170, 2000.
9. J. Shoji et al., El. Lett., Vol.38 No.25, p.1669.
10. Fimmwave, by Photon Design (www.photond.com).

Polymer Waveguide Technologies for Optical Interconnects

A. Neyer, S. Kopetz, E. Rabe, D. Cai

University of Dortmund
Faculty of Electrical Engineering and Information Technology
Arbeitsgebiet Mikrostrukturtechnik (AG MST)
Otto-Hahn-Str. 6, 44227 Dortmund, Germany
andreas.neyer@uni-dortmund.de

Abstract: *Basic polymer waveguide technologies actually applied for optical interconnects are reviewed with main emphasis on optical waveguide layers for integration in electrical-optical circuit boards. Main part of the paper is devoted to a technology based on Polydimethylsiloxane (PDMS) as low cost, low loss (0.05dB/cm at 850 nm) and high temperature stable (> 260°C) material system. The optical properties of the implemented materials and realized waveguides are discussed as well as a set up for a first industrial production line of electrical-optical circuit boards.*

1. Introduction

Next-generation internet switches and high-end computers are expected to process aggregate data rates in the order of Tbit/s. In consequence, the interconnections between the processing units will have to handle data rates in the order of 10-40 Gbit/s. It is, however, well known from basic physical laws that electrical interconnections will suffer from high transmission losses and severe signal integrity problems at such data rates [1, 2]. In order to overcome the evident high-speed interconnection bottle-neck, optical interconnects are considered the preferred option. In Gbit/s-rack-to-rack interconnections with link lengths in the order of several meters, the widespread solution is the commercial fiber-ribbon cable in combination with high speed parallel OE-modules. If, however, interconnection lengths come down to the order of 1m, e.g. in backplanes, integrated optical waveguides are considered more economical [3].

The integration of optical waveguides in printed circuit boards as well as in backplanes imposes severe requirements on the materials and processes involved. Some of them are: High transparency of the waveguide materials (< 0,1dB/cm) in the standardized interconnect wavelength window of 850 nm, high temperature stability to overcome standard multilayer printed circuit board lamination process temperatures at 180°C for two hours and especially the soldering process temperatures of 260°C, large area processing capability (> 0,5m x 0,5m), and cost effective mass production.

2. State-of-the-art in polymer multimode waveguide technologies

Among the waveguide technologies studied worldwide for the production of electrical-optical circuit boards, photolithography is the most popular to define the multimode waveguide core structure. Both, direct laser writing and mask exposure techniques are being applied (see Fig. 1)

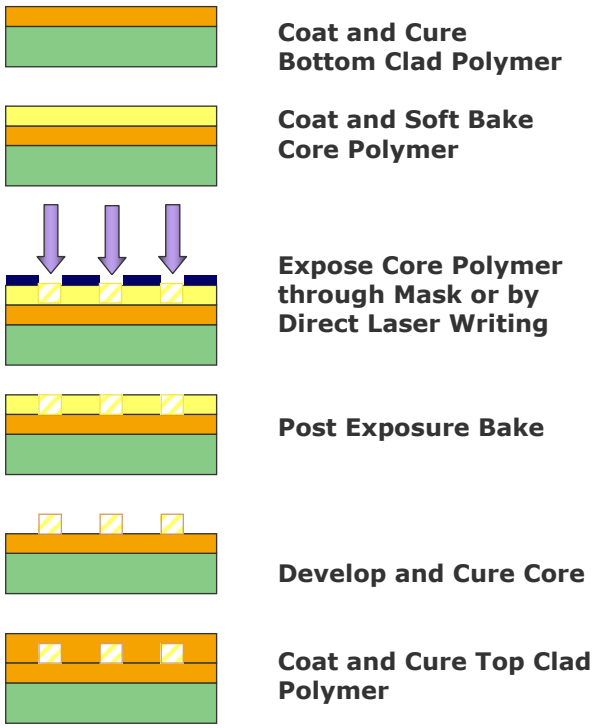


Fig. 1: Polymer waveguide fabrication by photolithography

A considerable variety of temperature stable polymers has been developed for this technology: epoxies [4,5], modified acrylates [6,9], and polysiloxanes [10-13]. Waveguide data obtained with theses techniques and materials are summarized in Table 1.

Material manufacturer	Material	Thermal stability °C	Optical waveguide loss at 850nm dB/cm
Microresist Techn. [4,5]	Epoxy	>200	0,1-0,2
Optical Crosslinks [6,7]	Acrylate	>200	0,08
Exxelis [8,9]	Acrylate	>250	0,04
Dow Corning [10,11]	Siloxane	-	0,04
Rhom & Haas [12,13]	Siloxane	>250	0,03

Table 1: Performance data of reported photopolymer materials and waveguides

Although the photopolymer waveguides reported in Table 1 show excellent performance their industrial implementation in large area boards is critical because of high material costs (>1000 €/l).
Furthermore, hot embossing has been investigated as a suitable technology for multimode polymer waveguide fabrication [14,15]. However, problems may arise from insufficient high temperature stability of optical thermoplastic polymers (for T>200°C) as well as from difficulties with the required high precision at large areas.
In this paper we will focus on a waveguide technology based on casting of thermally curing polysiloxanes which comprises all essential features for a low cost mass production of large area electrical-optical circuit boards.

3. Polysiloxane Waveguide Materials

3.1 Optical loss and thermal stability of bulk PDMS materials

High transparent polysiloxanes are widely used in electronics industries, e.g. to encapsulate LEDs. In addition to the low optical loss, the advantages of polysiloxane for integrated optical waveguide fabrication in printed circuit boards are the high thermal stability, the extreme moulding precision, the large area process ability and especially the low cost (in the order of 50-100€/l). The transmission loss of optical grade polysiloxane bulk samples of different suppliers has been measured to 0.02 – 0.04 dB/cm in the 850 nm wavelength window.

In this paper, two-component room temperature cross linking polysiloxanes of Wacker Chemie GmbH, Burghausen, Germany, have been used. The cladding materials are standard commercial polymers, whereas the core polymer is a special development of Wacker in close cooperation with the University of Dortmund. The transmission spectra of core and cladding materials are almost identical.

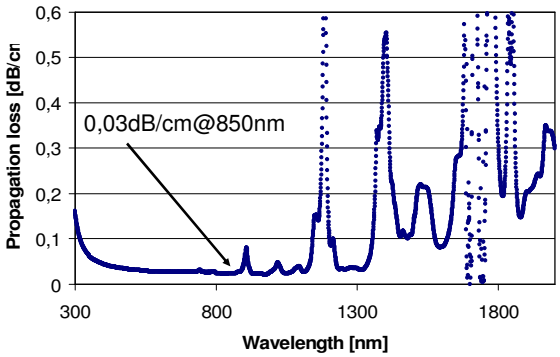


Fig. 1: Spectral transmission of bulk PDMS (Wacker)

The thermal stability of the polysiloxane materials has been studied by comparing the transmission spectra of bulk samples after curing them at room temperature, after a subsequent exposure at 180°C for two hours and after a final exposure at 260°C for five minutes (Fig. 2). This temperature treatment simulates the real process conditions at multilayer board lamination and at reflow soldering. Except in the ultraviolet region (200 nm to 400 nm) there is no significant change in the optical transmission loss. A slight increase in transmission loss is observed only at temperatures above 270°C which makes the material very suitable even for lead free soldering processes.

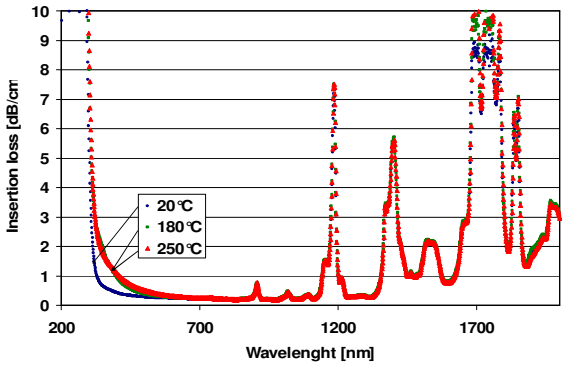


Fig.2: Influence of thermal treatment on transmission loss of bulk PDMS

3.2. Dispersion curves of PDMS bulk materials and their influence on waveguide numerical apertures

The numerical aperture *AN* – resulting from the index difference between core and cladding – is an important parameter in optical waveguides. It defines the optical coupling efficiencies in and out of the waveguides, the bending losses and the trans-

mission bandwidth. To meet an *A*N of about 0,25 by the actual PDMS system, the index of the core material has been tuned to ≈ 1.43 by implementing phenyl groups in the side chain of the PDMS backbone, whereas the cladding material is unmodified PDMS with a refractive index of 1,41. The refractive indices of both components have been measured as a function of wavelength using an "Abbe-Refractometer". In Fig. 3 the dispersion curves of Wacker PDMS cladding and core materials are shown together with Sellmeier fitting curves and respective *A*N values at a temperature of 20 °C. The requirement of an *A*N below 0.26 at 850 nm wavelength results from data transmission rates of 10 Gbit/s over interconnection distances of 1m.

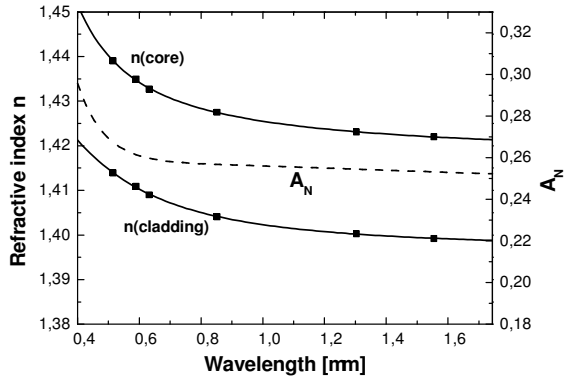


Fig. 3: Dispersion curves of cladding and core material (left axis) and resulting *A*N (right axis) at T = 20 °C.

In Fig. 4, the refractive indices at λ = 589 nm are plotted as a function of temperature including the thermo-optic coefficients (TOC) which are in the order of −3.6×10−4 K−1. From Fig. 4 we conclude that *A*N is almost constant in the temperature range between 20 and 55 °C resulting in a nearly athermal waveguide behavior.

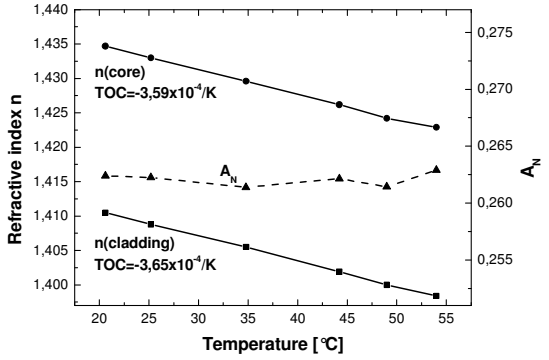


Fig. 4: Refractive indices of cladding and core material at λ = 589 nm as a function of temperature (left axis) and resulting *A*N (right axis).

4 . Fabrication of waveguide layer and board integration

Reactive ion etching and UV-curing have been reported for waveguide fabrication in polysiloxane. We have adopted casting in combination with the doctor blading technique as a new low cost polysiloxane waveguide fabrication method [16,17]. One of the advantages of this technology is that it has the unique feature of simultaneous fabrication of optical waveguides together with integrated micro mirrors for efficient OE-module coupling. Furthermore, casting in combination with the doctor blading technique is well compatible with large area printed circuit board production technologies.

First a casting mould for the waveguide core layer is generated. This is accomplished by SU-8-photolithography and, if required, by subsequent electroplating. In the reported experiments standard 6"-photoresist technology has been applied, but currently extension to larger formats (300mm x 400mm) is under work. In case of large area formats, doctor blading is used instead of spin coating because of the better thickness uniformity of the resist on rectangular substrates. The resist is dried and exposed through a photolithographic mask. After development of the resist the master mould is finished. In order to obtain a mechanical stable mould for mass production an electroplated copy of the resist mould may be realized. The complete production process of the optical layer is shown in Figure 5.

First, the waveguide cores are fabricated by filling the grooves in the mould by the core polymer (n = 1.43). This is accomplished by the doctor blading technique which is easily applicable to large formats. Then the core material is thermally cured.

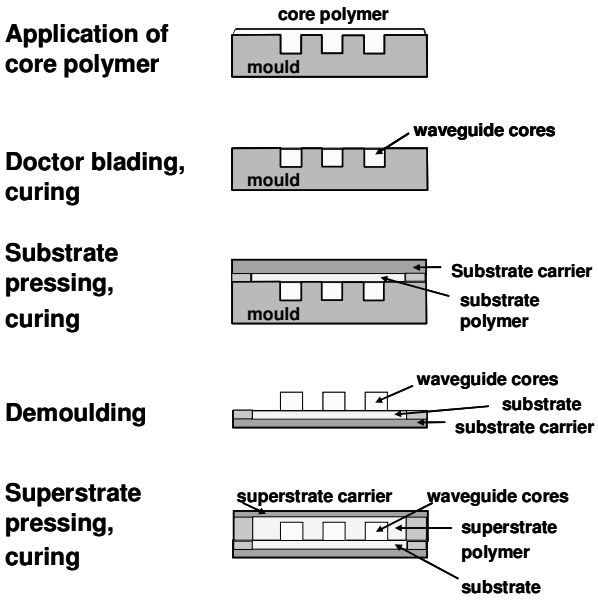


Fig. 5: Scheme of fabrication process of optical waveguide layer embedded between two thin PCB carrier sheets (FR4 or Kapton)

The next step is the preparation of the substrate carrier. One function of this carrier is the mechanical stabilization of the thin optical layer during the subsequent production steps. At the same time, the carrier serves as interface to adjacent PCB layers in case of a multi layer board. It is obvious to use conventional circuit board laminates like FR4 or Kapton. It is advantageous to use copper clad material, since the copper can be structured by standard processes and these structures are well suited to define the thickness of the substrate polymer.
Another function of the copper structures is the prevention of pressure on the waveguide layer during multilayer PCB lamination.
The waveguide substrate layer is fabricated by applying the liquid cladding polymer (n=1.41) to the mould (which still contains the cured cores) and, subsequently, the substrate carrier is pressed against the mould. Now, the copper structures will define exactly the thickness of the waveguide substrate layer. After curing the complete layer comprising cores, substrate layer and carrier is demoulded. Excellent adhesion between the substrate carrier and the PDMS substrate layer could be achieved by using special adhesion promoters.
The production of the superstrate layer is performed by the same technique using identical cladding polymer. Figure 6 shows the cross section of a realized electrical-optical PCB using Kapton ™ (Dupont) substrate carriers. The waveguides have core sizes of 70µm x 70µm and a numerical aperture of 0.26.

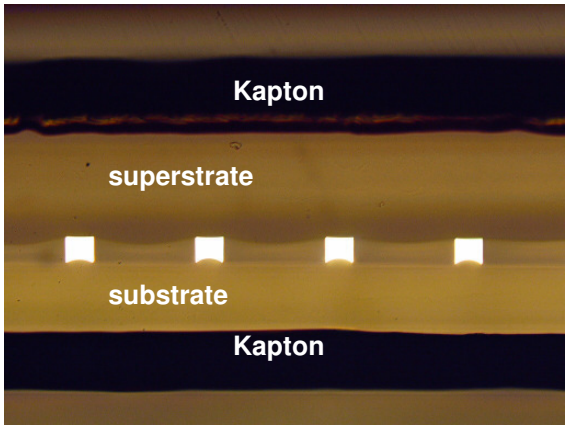


Fig. 6 Cross section of PDMS optical waveguide layer embedded between Kapton™ laminates

4. Optical transmission loss and thermal stability

The waveguide loss has been measured by exciting the waveguides using a 50µm-GI-fibre and collecting the transmitted light by a 200µm-SI-fibre. Typical waveguide loss figures at 850 nm are 0.05 dB/cm measured by the cut back method. The thermal stability has been tested at the PCB-lamination temperature of 180°C for 2 hours followed by an exposure at 220°C and 260°C for 5 minutes to simulate reflow soldering conditions (see Fig. 7)

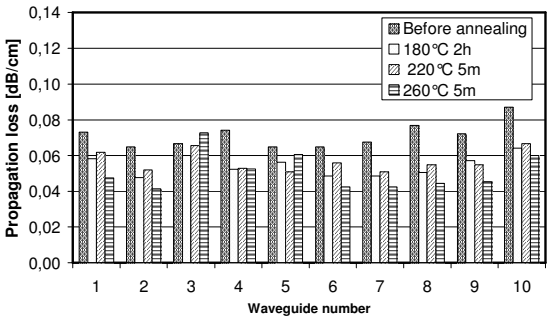


Fig. 7: Thermal behavior of the transmission loss of PDMS waveguide layer

5. Production technology

The described fabrication process developed in laboratory scale at the University of Dortmund now is transferred to an industrial production line (format 460 × 305mm2) within the framework of the BMBF-founded research project “ProSPeoS” [18]. In Fig. 8 a schematic configuration of the basic elements of the production line is shown. In a first attempt the line is conceived in a way that the samples pass through several times according to the sequence of the production steps. A mobile stacker is placed in front and at the end of the line for easy sample handling and transportation. The samples (14 samples at once) are stored in the stacker after one production cycle and inserted at the beginning again. The production unit consists of three main elements: A spray coater, a blading unit and a curing oven. In between there is space for manual operations like sample handling and retooling works.
The first unit is a spray coater (Systronic/ Mühlbauer) where the moulds are coated with PDMS and adhesion promoter, respectively. The automated blading unit is specially developed by ASEM GmbH, Dresden, in close cooperation with the University of Dortmund. Here the core material is applied by a peristaltic delivery, followed by blading and carrier lamination. In the curing oven the polymers are cross linked. Alternatively to inline curing the whole stacker could be placed into a fan oven. For producing the complete optical layer four cycles through the basic line of Fig. 8 are necessary. In order to be processable by the shown processing techniques the basic PDMS materials had to be modified. To enable spray coating, the cladding material was blended by silicone oil to lower the viscosity to values < 1000mPa s. By spray coating PDMS layer thicknesses between 20 and 200µm could be achieved. To extend the pot life of the

processable PDMS materials from a few hours to some days inhibitors have been used. A critical point in using PDMS materials in EOCBs is the realization of a mechanically stable interface between the optical PDMS layer and the adjacent PCB materials like FR4 or Kapton. Substantial work has been invested in the development of suitable surface treatments of the carriers and high-efficient adhesion promoters

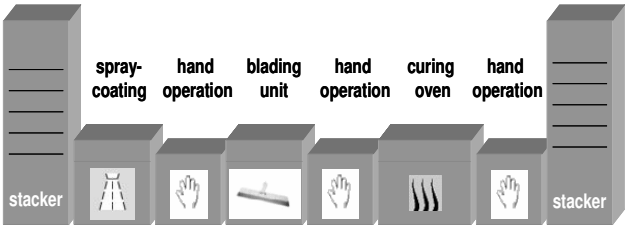


Fig. 8: ProSPeoS production line for optical waveguide layers

6. Conclusion

For polymer waveguide fabrication intended for optical interconnects at $\lambda = 850$nm, a variety of high performance polymer material systems are commercially available: epoxies, acrylates, and siloxanes showing low optical loss figures (<0,1 dB/cm) and good thermal stability (> 200°C). Furthemore, it has been demonstrated, that the developed PDMS waveguide technology is compatible with industrial printed circuit board production technology and is based on low cost polymers.The produced waveguide layers exhibit low optical loss (< 0.05 dB/cm) and high-temperature stability (> 260 ◦C).

Acknowledgements

The close and fruitful cooperation with Wacker Chemie, Burghausen, in the field of materials development is gratefully acknowledged as well as the collaboration with Dr. Heise from ISAS, Dortmund, in the field of optical materials characterization. Part of this work has been supported by the BMBF under the framework of "Research for the production of tomorrow", Project ProSPeoS.
.

References

1 J.Moisel, Information Technology, no. 45, p.72, 2003
2 Uhlig S at al., J. Lightwave Technol., no 24, p. 1710, 2006
3 G.L.Bona et al., Proc. of SPIE Micro-Optics, VCSELs, and Photonic Interconnects, no. 5453, p. 134, 2004.
4 http://www.microresist.de
5 Schröder, H. et al., Tagungsband der GMM/DVS-Tagung Elektrische Baugruppen, Aufbau und Fertigungstechnik, Fellbach, Deutschland, 2006.
6 http://opticalcrosslinks.com
7 Eldada, L., Proc. of Lasers and Electro-Optics Society, p. 361, 2005
8 http://www.exxelis.com/products/truemode
9 Bosman, E. et al. Proc. of SPIE, no. 6185, p. 60, 2006
10 DeGroot, J.V. et al, Proc. of the OFC 2005, paper OFD6
11 Su, K. et al, Proc. of SPIE, no. 6029, , p. 318, 2006
12 Moynihan, M. et al, Proc. of SPIE, no. 5212, p.50, 2003
13 Bona, G. L. et al, Proc. of SPIE, vol. 5453, p. 134, 2004
14 Lehmacher, S. et al, Electron. Lett., no. 36, p. 1052, 2000
15 Krabe, D. et al, Proc. of 49th ECTC, p.1164, 1999
16 Neyer, A. et al, Proc 55th ECTC, p. 246, 2005
17 Kopetz, S. at al, Electronics Letters, no 42, p. 634, 2006
18 http://www.prospeos.de

Bends in Polymeric Multimode Waveguides

Henry Kelderman, Mart B.J. Diemeer, Lucy T.H. Hilderink, and Alfred Driessen
University of Twente, Integrated Optical MicroSystems (IOMS) h.kelderman@ewi.utwente.nl

Abstract: *We developed photodefined, multimode-fiber compatible waveguides based on epoxies. The waveguides showed losses < 0.06 dB/cm at 832 nm and 633 nm. Propagation and bending losses are calculated and experimentally verified. The minimum allowable radius that can be connected to a straight waveguides are modeled and experimentally verified.*

Introduction

The continuous increase of the microprocessor clock-rate (expected clockfrequency $\sim 10^{10}$ Hz in 2011), in addition to the continuous increase of data rates in optical transmission systems, has created a bottleneck in high- end systems like servers, and telecom switches, at the interconnect between cards over their PCB (Printed Circuit Board) backplane. In those systems, aggregate data rates of multiple Tbps have to be transported via the backplanes over a typical distance of about 0.5 m. With such bandwidth-distance products, electrical data transmission through a copper line is touching its fundamental limit around 20 Gbps.
Optical transmission via waveguides offers the potential of a much larger capacity. Therefore, there is worldwide an intense research activity ongoing to realize Optical Backplanes. These are backplanes with an embedded multimode polymeric optical waveguide layer, equipped with in- and output couplers, fabricated with PCB compatible, low-cost fabrication techniques [1]. In [2] we reported on a photodefinable epoxy formulation with attractive properties for Optical Backplane applications. This paper shows propagation losses obtained from spiral structures and bending losses from U-shaped bends.

Waveguide Definition and Cross Section

The core of the waveguides presented in this paper is about $45 \times 45\ \mu m$. The core material used in the spirals was spun directly on the Pyrex substrate. This simplifies processing, but also introduces an asymmetry in the index below and surrounding the other sidewalls of the core. For the U-bends a bottom cladding was applied, resulting in a more symmetrical modal profile -as far as we can speak of modal profile in these highly multimodal waveguides- and subsequently a lower refractive index contrast can be used. Figure 1 shows a cross section of the several waveguides used in the U-bends.
For the U-bends the refractive index in the cladding is 1.514 and the core is 1.528 leading to an index contrast of 0.014. In the spirals a higher index contrast of 0.03 was used.

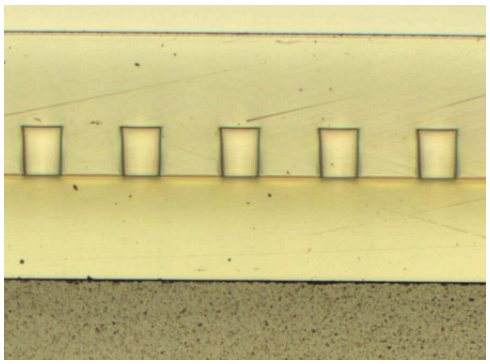


Fig. 1: Cross section of 5 waveguides used in U-bends.

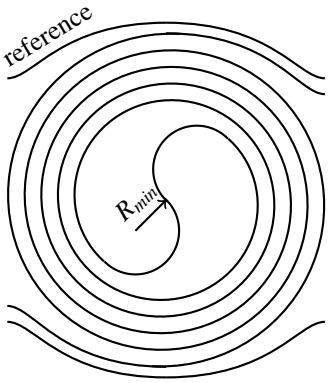


Fig. 2: Schematic layout of an Archimedean spiral with two reference waveguides.

Archimedean Spiral

Propagation losses in the order of 0.1 dB/cm are difficult to measure by cut-back measurements. Since differences in chiplength are typically centimeters, the differences in loss are in the same order as the fiber-chip coupling variation.
Therefore, we decided to create a waveguide of significantly longer length by curling it up in a spiral and comparing its losses to an on-chip shorter reference waveguide. The contribution of the bending loss will be limited when the curvature of the spiral and especially the S-bend in the middle is chosen appropriately i.e., the radius of curvature chosen large enough. The smallest radius will be found in the s-bend.
The mismatch of modes from connecting different curved waveguides e.g., in the center of the s-bend has been disregarded since improving it by adiabatically connecting different curvatures will result in a larger overall structure for which there was no space. The following section will show that this presumption did not introduce significant additional losses, which is a

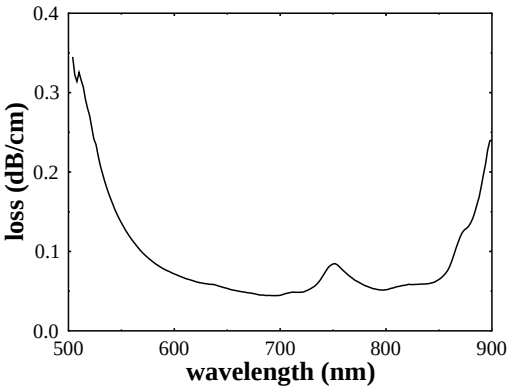


Fig. 3: Spectral dependence of propagation loss observed in spiral waveguide

result of the relatively high contrast used and the relatively large core dimensions.
An Archimedean spiral is defined by:

$$r = a\theta^{1/p} \tag{1}$$

We have set $a = 1.0$ and $p = 1.1$, and scaling appropriately to obtain more or less equidistant windings. The minimum radius used in the s-bend also defines the minimum radius in the spiral ($2R_{min}$). We have set R_{min} to $15mm$ leading to an approximate single winding length of $2 \times 2\pi R_{min} \sim 188mm$, where the pitch from winding to winding has been disregarded.
Equation 1 has been discretisized in θ leading to an array of points (r, θ). After transforming these to cartesian coordinates, these points have been connected by pieces of straight waveguides. Thus the curvature has been approximated by segmented lines. If the stepsize $\Delta\theta$ is chosen small enough this will be barely noticeable in the photomask.
The low contrast used ($NA = 0.2$) also allowed to use in-house laser beam written masks that typically have an edge roughness of ~150 nm. Propagation losses depicted here include scattering losses and an easy, albeit costly, improvement could be to use e-beam written photomasks.

Propagation Loss

To allow for accurate propagation loss measurements, a very long (103.6 cm) coiled up waveguide, combined with a short (7.2 cm) reference waveguide was made on a 4" Pyrex wafer. The long waveguide is an Archimedean spiral as shown in Figure 2.
Figure 3 shows the spectral dependance of the propagation loss in the spiral by subtracting the insertion loss for the reference waveguide and the spiral and accounting for the difference in propagation length.
To verify these losses we took a picture of a part of the spiral as shown in Figure 4. By integrating the intensity of the pixels over a small rectangle that captures just one waveguide, an estimate for the local power is

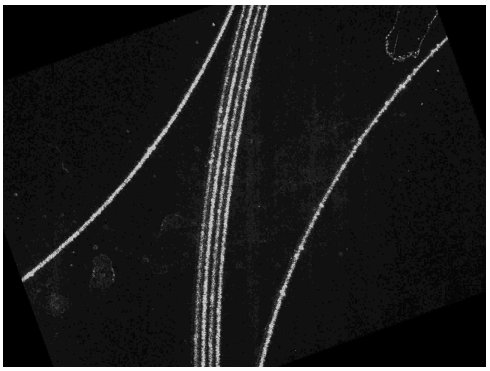


Fig. 4: Scattered light as observed from the top at 633 nm

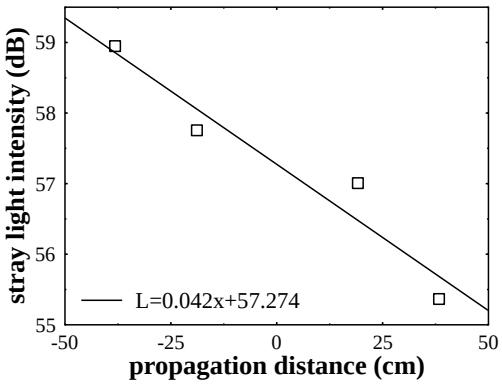


Fig. 5: Observed local intensity as function of propagated length in spiral.

obtained. This is done for the four waveguides that are close together and represent the four windings of the spiral. Since it is known how far the light propagated from one winding to the next, also accounting for the S-bend in the center, the intensity of each local area containing one waveguide can be set out versus its relative propagation length. Figure 5 shows the local scattered intensity versus the relative propagation length in the spiral, from that we can determine the propagation loss at 633 nm to be about 0.04 dB/cm. Which compares well to the values we found earlier.

Bend loss

The size of a spiral is determined by the radius of the arc used in the S-bend in the middle of the spiral where the losses are still acceptable. In order to find that 'cut-off' radius a sample has been made with varying radii. As depicted schematically in Figure 6 we choose a U-shaped bend where the total angle traveled is 360°. Note that the vertical section on the right hand side has been prolonged. This served two goals. Firstly it creates an offset between the input and the output. Secondly it was used to make the total propagation length in all U-bends exactly the same. Note that although in

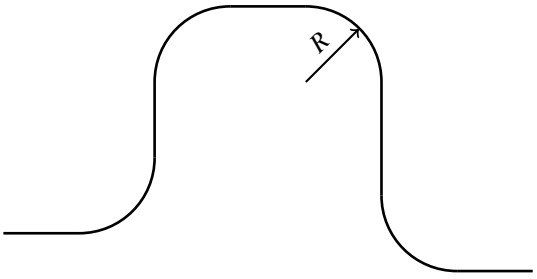


Fig. 6: Schematic 'U'-shaped bend

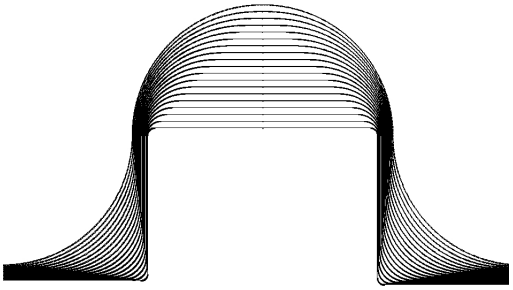


Fig. 7: Mask design showing multiple U-bends with varying radii.

Figure 6 only one U-bend has been shown, the radius has been varied from 1 to 19 mm in steps of 1 mm. See Figure 7 for resulting mask layout.

To determine the propagation loss, six straight reference waveguides have been placed on the same sample. The difference in length between U-bend and reference is 40 mm, which is expected to lead to an difference is loss of about 0.4 dB.

Figure 8 shows the insertion loss of the U-bends minus the loss found in the reference waveguide as function of the radius. Note that this introduces a systematic error of about 0.4 dB at wavelengths larger than 600 nm.

Reducing the bend radius gradually increases losses, until a certain cut-off is met, where losses increase rapidly. The transmission in the waveguides with the smallest radii seems to increase. This is an artifact that can be explained as follows; the light lost in the bend is not absorbed, and hence will find its way to the backside of the sample, leading to a background level of intensity. Especially in smaller radii where more light is lost, this effect is more predominant and makes alignment hard. The higher loss at 532 nm can partially be explained by the higher losses at that wavelength (cf. Figure 3).

The modeled response in Figure 8 can be calculated from [3]:

$$L = 10 \cdot^{10} \log\left(1 - \frac{t}{2R} - \frac{t^2}{2R^2} - \frac{t^3}{2R^3} - \frac{t^4}{2R^4}\right) \quad (2)$$

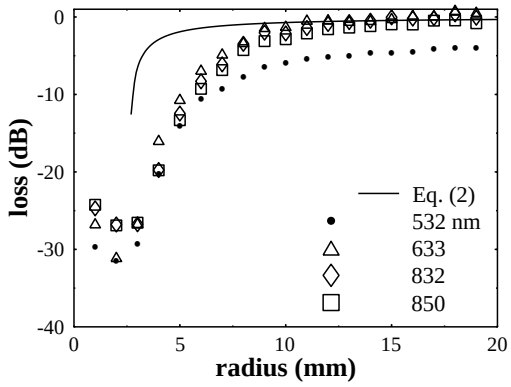


Fig. 8: Observed losses in 'U'-shaped bends at four different wavelengths.

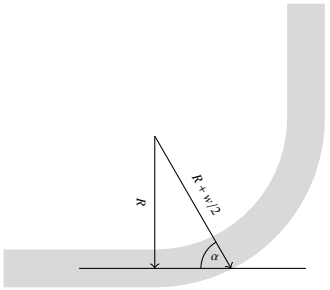


Fig. 9: A ray traveling in the middle of the waveguide coming from the right, would strike the normal to the tangent of the outer perimeter of the bend at an angle α.

where $t = (n_{core}^2 w)/(NA)^2$, w is the width of the waveguide and NA is the Numerical Aperture. The model fails when $t/R < 0.5$, but adequately describes the experimental results as shown in [4]. The offset in the cut-off region in our experimental data can be explained by the fact that in the U-bend eight straight-bend coupling areas are introduced, and the model includes only the effects of a circular bend.

Further inspection revealed that light is escaping the bend predominantly in the first part of the curved section, and not continuously over the entire bend as might have been suspected.

This can partially be explained by the angle at which a ray strikes the outer perimeter of the bend as shown in Figure 9. Suppose we were to look at a ray traveling in the middle of the straight waveguide. It would strike the outer perimeter at an angle α to the normal of the tangent described by:

$$\alpha = \arcsin\left(\frac{R}{R + w/2}\right) \quad (3)$$

If we use this angle in the Fresnel equation for s-

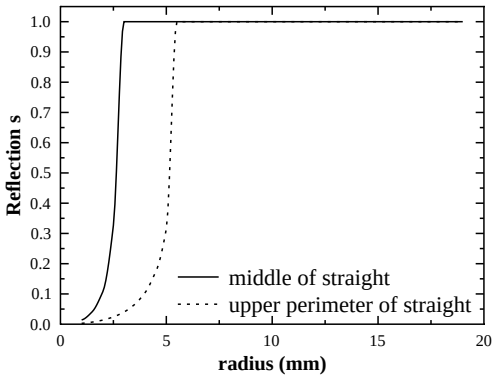


Fig. 10: Reflection coefficient from a ray travelling in the middle of the straight waveguide striking the outer perimeter of the curved section as function of the radius. Also shown is the reflection of a ray traveling along the upper boundary of the straight waveguide.

polarisation:

$$R_s = \frac{n_{core}\sin\alpha - n_{cladding}\sin\theta_2}{n_{core}\sin\alpha - n_{cladding}\sin\theta_2} \qquad (4)$$

where θ_2 can be obtained from Snell's law of refraction. we obtain Figure 10. Although not shown here, p-polarisation will result in almost the same fraction of light reflected. Without taking into account that the actual angles of the rays will vary, this simple description accurately estimates the minimum radius that can be connected without loss to a straight waveguide.
This argument does not directly explain the non-continuous loss through the bend. If we were to consider a ray traveling along the tangent of the inner perimeter of the bend, which is the ray that has the smallest angle to the normal and hence experience the lowest reflection. This specific ray would have been reflected at an earlier point in the bend at the same angle, therefore its power would have been reduced significantly upon the first reflection, provided the angle is sufficiently small.

Conclusion

We have presented multimode photodefinable waveguides for Optical Backplane applications. A propagation loss of <0.06 dB/cm at 850 and 633 nm has been measured in spirals using two methods; 1) from the difference in length and the obtained insertion loss thereof and 2) from analysis of the scattered light of different locations in the spiral. For a refractive index contrast of 0.014 (NA=0.2) we experimentally found that the minimum usable radius is 10 mm and verified this by simple calculation of Fresnel reflection and also compared this to a model by Israel et al. It has been shown that within the wavelength region measured (530-850 nm) the loss in bends as function of radius is independent of wavelength.

Acknowledgments

The authors acknowledge the financial support of Dutch Foundation STW (project TOE 6986) and wish to thank Anton J.F. Hollink for his support.

References

[1] C. Berger, R. Beyeler, G.-L. Bona, R. Dangel, L. Dellmann, P. Dill, F. Horst, M. Kossel, C. Menolfi, T. Morf, B. J. Offrein, M. L. Schmatz, T. Toifl, and J. Weiss, "Optical links for printed circuit boards," in 16th Ann. Meeting of IEEE Lasers & Electro-Optics Soc., October 26-30, Tucson, AZ, USA, 2003.

[2] Mart Diemeer, Lucie Hilderink, Ronald Dekker and Alfred Driessen, "Low-cost and low-loss multimode waveguides of photodefinable epoxy", IEEE Photon. Technol. Lett., vol. 18, no. 15, pp. 1624-1626, 2006.

[3] D. Israel, R. Baets, N. Shaw, and M.J. Goodwin, Techn. Digest MOC/GRIN, 1993.

[4] Sami Musa, Albert Borreman, A.A.M Kok, M.B.J. Diemeer, and Alfred Driessen, "Experimental study of multimode optical waveguides", Appl. Optics, vol. 43 no. 40, October 2004.

Polymer Optical Motherboard Technology

N. Keil, H. H. Yao, C. Zawadzki, W. Schlaak, M. Möhrle, N. Grote
Fraunhofer-Institute for Telecommunications Heinrich-Hertz-Institut, Einsteinufer 37,
D-10587 Berlin, Germany, keil@hhi.fraunhofer.de

Abstract: *Using polymer optical motherboard technology, an optical transceiver and a minispectrometer integrating an optical demultiplexer with optoelectronic devices are described. Main issues including coupling from waveguide to photodiode, laser to waveguide, bonding, and fibre to motherboard coupling are discussed.*

1. Introduction

Integration and miniaturization have always been the dream for engineers. They offer the path to low cost, high reliability and modularized products. Optical integration has not progressed as fast as electronic integration in the past years. One of the main reasons is that for integrated optics it is difficult to use only one material system to fabricate optimal devices with a wide range of functions.

Polymer waveguide devices are attractive because they offer the potential of fairly simple and low cost fabrication based on low-temperature processes and low cost packaging based on passive alignment [1-3]. The optical loss of optical polymers has been reduced to less than 0.1dB/cm recently [4]. Polymer optical waveguide device can provide a convenient integration platform including optical waveguide devices and optoelectronic chips.

In this paper, a PLC based optical transceiver and a minispectrometer are addressed. The transceiver is shown schematically in Fig. 1. The coupling from the polymer waveguide to the photodiode (PD) as well as from the laser diode (LD) to the polymer waveguide is accomplishhed via a 45° mirror (vertical coupling). The light from the LD can also be coupled to polymer waveguide by butt-joint coupling. For reducing cost, passive alignment of fibre-chip coupling is possible by U-grooves. These main issues will be discussed.

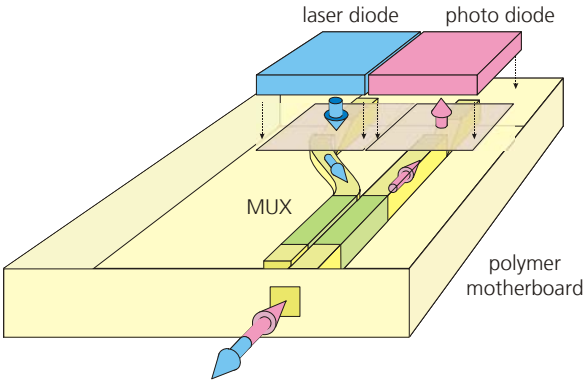


Fig. 1: Optical transceiver in polymer optical motherboard technology.

2. Optical transceiver

Fig. 2 shows a photo of the polymer optical motherboard of a PLC transceiver chip, Fig. 3 shows the chip layout.

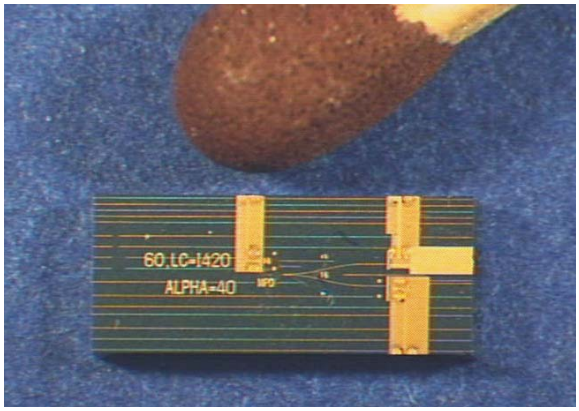


Fig. 2: Polymer optical motherboard of a PLC transceiver.

For achieving a high coupling efficency between the laser diode and the polymer waveguide, a polymer waveguide with a super-high refractive index contrast of $\Delta n=0.020$ and a dimension of 2.5 µm x 2.5 µm was used. The small waveguide dimension renders the waveguide to satisfy the strict single-mode conditions.

A directional coupler (DC) is used as a wavelength multiplexer. The DC is designed to have a bar-state at the 1310 nm upstream channel, and a cross-state at the 1490 nm downstream channel. The DC has a very compact size with a length of the coupling reagion of only 1.4 mm. A LD, a PD and a monitor photodiode (MD) are hybridly integrated on the polymer motherboard. The coupling from the polymer waveguides to the PDs as well as from to the LD to the polymer waveguide is accomplished via 45° mirrors. The chip size is only 3 mm x 7 mm.

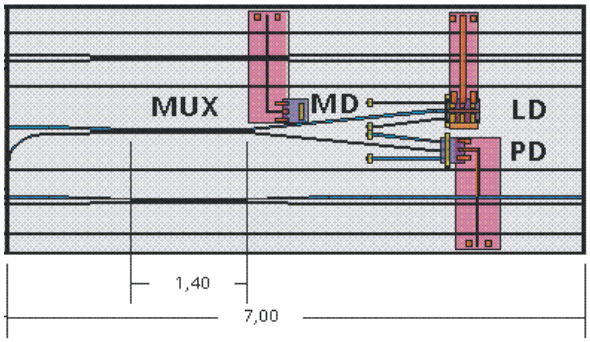


Fig. 3: Chip layout of a PLC transceiver.

3. Coupling of photo diodes (PD)

The downstream light at 1490 nm is coupled to the PD via a 45° mirror [5]. Fig. 4 shows the cross-section of a schematic picture of this coupling concept. The spot size of the above polymer waveguide is only 1.92 µm. This spot size will be expanded after propagating a distance in the mirror space. Fig. 5 shows the calculated beam size. It can be seen that even after 100 µm, the beam size is still less than 25 µm in the free space region at the mirror. If the mirror space is filled with polymer, the beam size reduces to about 15 µm. In our design, the propagation distance is less than 20 µm, resulting in a beam diameter of less than 10 µm, which is smaller than the active diameter of a PD used for 10 Gbit/s reception.

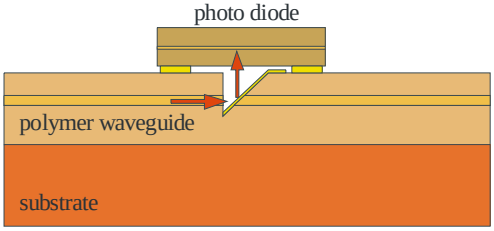


Fig. 4: Vertical coupling between waveguide and PD.

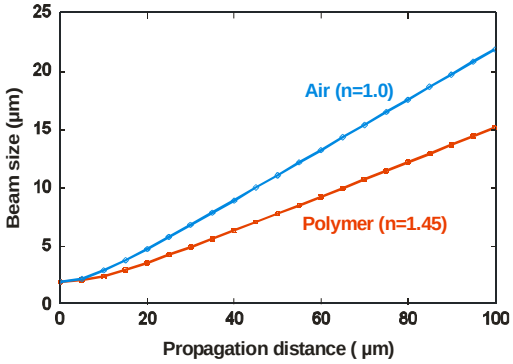


Fig. 5: Beam size of polymer waveguide after propagating a distance in the free space region at the mirror.

This vertical coupling concept has also been used in a miniature optical spectrometer. The spectrometer consists of a polymer arrayed-waveguide grating (AWG) that is fabricated on a polymer substrate, and an array of InP photo detectors (PD) that are hybridly integrated as shown in Fig. 6. The output beams of the AWG are vertically coupled to the PD array via a 45° mirror. Fig. 6 shows microscopic pictures of three detectors of the PD array and the cross-section of a 45° mirror for vertical coupling.

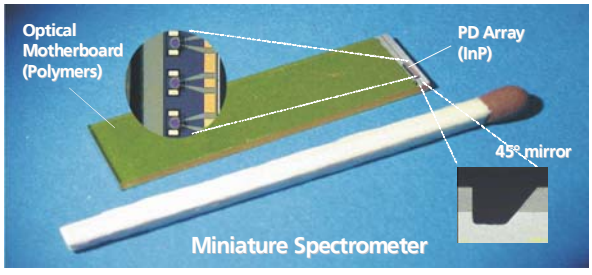


Fig. 6: Miniature optical spectrometer.

This miniature spectrometer can find wide applications as optical channel performance monitor in WDM (wavelength division multiplexing) networks, as wavelength meter and sensors in IR instruments.

4. Coupling of laser diodes (LD)

For an efficient coupling between a Gaussian beam of a LD and a polymer single-mode waveguide, the optical mode profiles of the LD and the polymer waveguide should be overlapped as much as possible [6]. The coupling can be accomplished by vertical scheme or butt-joint coupling.

4.1 Vertical coupling scheme

The main advantage of this scheme is easy adjustment of the laser diode because it avoids the adjustment in the vertical direction allowing automatic assemble using pick and placer. Fig. 7 shows the cross-section of the coupling scheme.

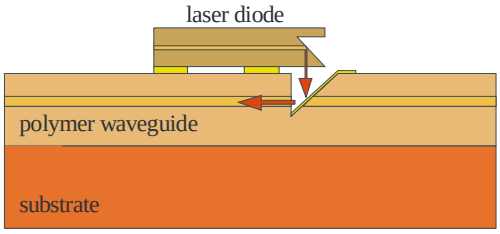


Fig. 7: Vertical coupling between waveguide and LD.

As it can been seen from Fig. 7, the laser beam has to travel a distance before entering the waveguide. For effective coupling this distance should be as small as possible. In our design, it was chosen to be ~ 15 µm. Fig. 8 shows the calculated coupling loss vs. the mirror deepness when the gap in the mirror is filled with polymer. The coupling loss depends strongly on the type of LD used. A typical ordinary LD has a far-field angle (FWHM: full width at half maximum) of about 32° in the lateral and 39° in the longitudinal direction. A tapered LD has divergence angles of 15° in the lateral and 20° in the longitudinal directions, respectively. The coupling loss of ordinary LDs is very high. Thus, a low-loss transceiver must use LDs with narrow divergence angles. If the space in the mirror is filled with air, the coupling loss is about 1-2 dB higher. From above discussion, a tapered LD and a polymer waveguide with $\Delta n = 0.020$, W=d= 2.5µm was chosen in our design of a low-loss transceiver.

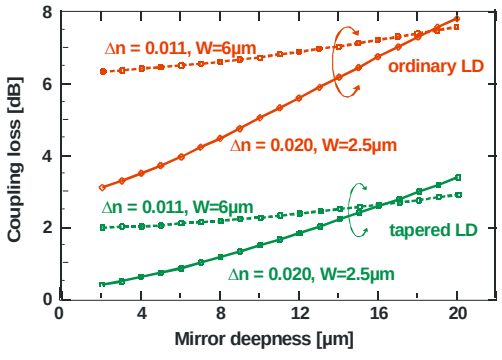


Fig. 8: Calculated coupling loss vs. mirror deepness for different LDs and polymer waveguides.

4.2 Butt-joint coupling

Fig. 9 shows the simplest approach of LD to single-mode fibre (SMF) coupling by butting a fibre to LD, which has a high coupling loss of 7 to 10 dB. For reducing this loss, different methods such as lenses and tapered fibre have been be used. In principle, such means serve as spot-size converter.

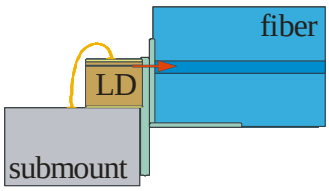


Fig. 9: Butt-joint coupling between a LD and a SMF.

A piece of polymer waveguide can be used as a spot-size converter as depicted in Fig. 10. From calculation, the coupling loss between a LD with far field angles of 27° in lateral direction and 47° in longitudinal direction to SMF is 9.7 dB. However, if this LD is coupled via a polymer waveguide the coupling loss amounts to about 3.5 dB only.

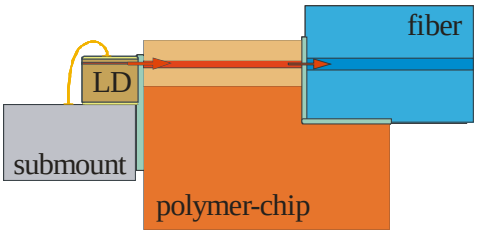


Fig. 10: Butt-joint coupling between a LD and a SMF via a polymer waveguide serving as a spot size converter.

Fig. 11 shows the calculated coupling loss between polymer waveguide with a high index contrast and LDs of different beam divergences. The allowed lateral mismatch for 1 dB tolerance is about 1 µm.

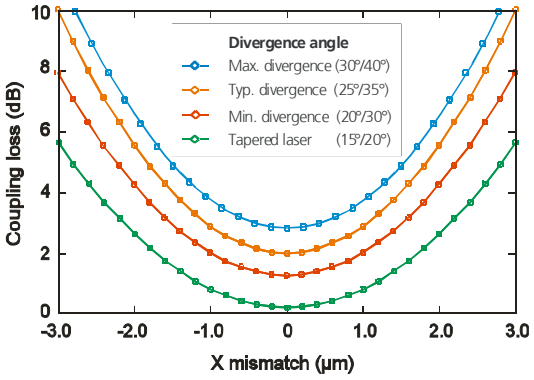


Fig. 11: Calculated coupling loss between LDs and polymer waveguide vs. lateral off-set.

For polymer waveguides with a refractive index difference of $\Delta n = 0.020$, the fibre-to-chip coupling loss is about 1.6 dB at 1.49 µm and 2 dB at 1.31 µm wavelength, respectively. In order to further reduce this coupling loss, a laterally tapered waveguide can be incorporated. The coupling loss depends strongly on the taper width (see Fig. 12). The loss can be reduced to only 0.25 dB at λ=1.49 µm if the width of the taper is only 1 µm. For λ=1.31 µm, the width of the waveguide taper should be reduced to 0.8 µm for obtaining a coupling loss of 0.25 dB [7].

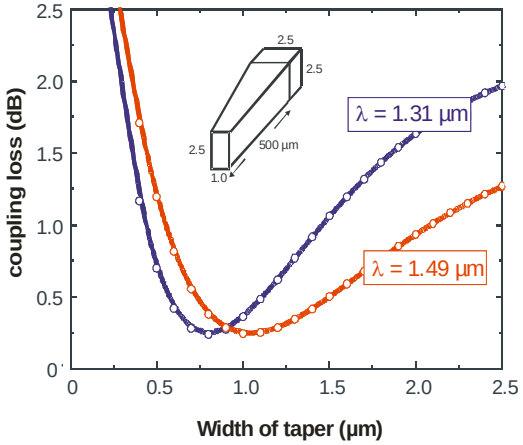


Fig. 12: Calculated coupling loss between SMF and polymer waveguide vs. width of taper.

These calculated values agree well with experimental results. Fig. 13 shows the photo of a LD with 27°/47° divergence angles coupled to a polymer waveguide. The measured coupling loss between LD and fibre was only 4.0 dB, which is close to the calculated value of 3.5 dB. For a LD with 20°/40° divergence angles the calculated loss value is 3.2 dB, and the measured one is 3.5 dB.

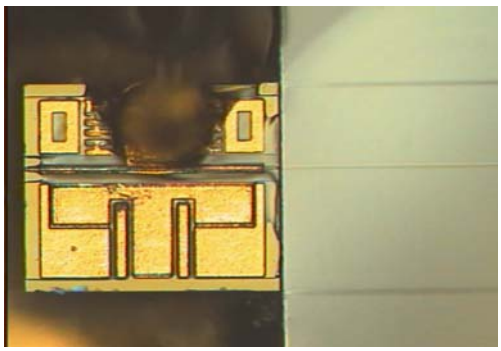


Fig. 13: A LD chip is coupled to a polymer waveguide.

5. Bonding

Fig. 14 shows a wire bond between a polymer chip and a submount using ultrasonic bonding. Pull tests show that the bond meets the MIL standard.

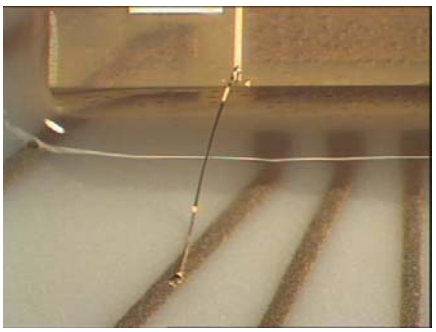


Fig. 14: Wire bonding.

6. Fibre/chip coupling

6.1 Fibre-array with polymer substrate

As we demonstrated earlier, the wavelength tuning behaviour of a polymer arrayed-waveguide grating (AWG) can be adjusted by choosing a suitable combination of TO (thermo-optic) coefficient of the polymer waveguide and the CTE (coefficient of thermal expansion) of the polymer substrate. It is possible to realize negative, positive and athermal tuning behaviour. An athermal AWG has been realized using this all-polymer approach at HHI [8], which also helps to control the polarization behaviour [8].

When an AWG on a polymer substrate is connected to a commercial silicon-based fibre-array, the mismatch between the CTE values of polymer and silicon may additional loss. Therefore, a fibre-array with polymer substrate was developed. Fig. 15 shows a photo of a all-polymer fibre-array with eight fibres.

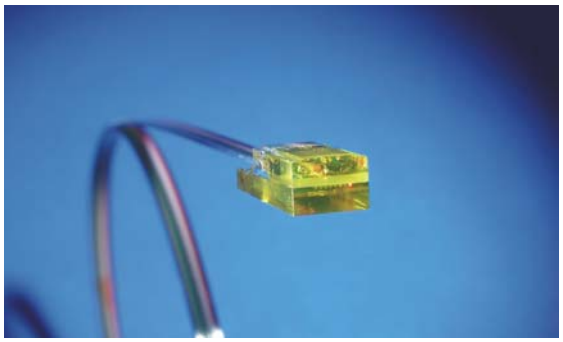


Fig.15: All-polymer fibre-array.

The fibres are inserted and guided in V-grooves that are fabricated by micro machining the polymer substrate, as shown in Fig. 16. This simple fabrication procedure allows for very low manufacturing costs. The core-to-core pitch is 250 µm. The cover plate is also made of polymer material. The end face of the fibre-array was polished to ensure low-insertion loss. The CTE of the fibre-array can be perfectly matched to the CTE of polymer waveguide devices if the same polymer substrate is used. Therefore, this all-polymer fibre-array is useful for packaging waveguide devices with polymer substrates.

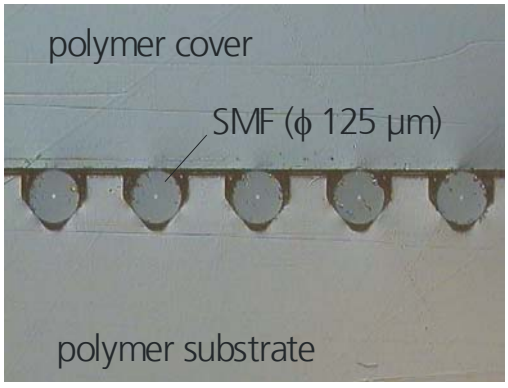


Fig.16: All polymer fibre-array.

6.2 Passive alignment

By using an alignment-free coupling scheme (called passive alignment), the cost of coupling optical SMF to polymer motherboard may be significantly reduced. Fig. 16 shows conceptiually how a U-groove may be formed in the same substrate as the polymer motherboard for aligning and fixing the fiber.

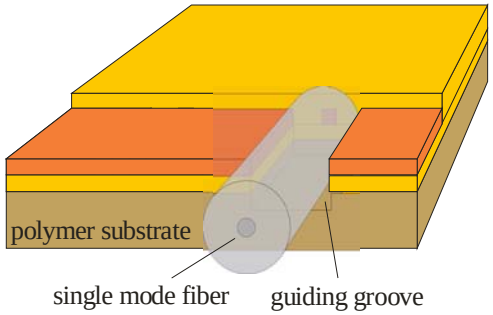


Fig.17: Sketch of a single-mode fibre coupled to a polymer waveguide using a guiding groove structure.

Conclusions

Polymer optical motherboards integrating polymer planar light wave circuits and optoelectronics devices such as laser diodes and photo diodes have been investigated. Good coupling efficiency between optical polymer waveguide and the optoelectronics devices were demonstrated. Simple alignment using a vertical coupling scheme or butt-joint coupling and passive alignment for fibre-chip coupling are possible.

Polymer motherboards may also be made incorporating thin-film filters (TFF), Bragg gratings, or many other features to produce hybrid integrated devices to be used as optical transmitter, receiver including D(Q)PSK receiver, optical transceiver, OTDR, etc..

Acknowledgments

Part of this work was financed by Future Funds of the state of Berlin, Germany.

References

1 S. Lehmacher et al, Electron. Lett., no. 12, p. 1052, 2000.

2 A. Rogner et al, OFC, Paper FB1, pp. 279, 1994.

3 J. T. Kim et al, ECOC Paper Th1.4.2, p. 806, 2004.

4 A. Yeniay et al, J. Lightwave Technol., no. 1, p. 154, 2004.

5 J.-W. Park et al, Photonic Techn. Lett., no. 4, p.807, 2005

6 M. Saruwatari et al, Applied Optics, no.11, p.1847, 1978.

7 T. Mizuno et al, J. Lightwave Technol., no. 3, p. 833, 2004.

8 N. Keil et al, ECOC Paper Tu3.5.3, p. 252, 2003.

UV Light Induced Single Mode Waveguides in Polymer for Visible Range Applications

Uwe Hollenbach, Hans-Jürgen Böhm, Jürgen Mohr (1)
Ludwig Ross, Dirk Samiec (2)
1) Forschungszentrum Karlsruhe GmbH, Karlsruhe, Germany, hollenbach@imt.fzk.de
2) Ingenieurgesellschaft Optische Technologien mbH, Waghäusel, Germany, ross@iotech-gmbh.de

Abstract: *In this paper we describe the fabrication of single mode waveguides in standard polymer substrates by a deep UV lithography technique. With regard to commercial applications the waveguides are designed to be used in the visible range. The paper shows the first results of the manufacturing process used to increase the refractive index for strip waveguide channels in the polymer substrate and the technique to cover the surface structures by a top layer to get buried waveguides. First results of refractive index step measurements as a function on the UV light exposure dose are discussed. Simulated mode profiles are compared with measured near field intensity distributions.*

Introduction

For the use in optical applications, low cost standard polymer substrates (PMMA) are available from many manufacturers. Material quality with respect to transparency, homogeneity and surface flatness is good enough also for waveguide manufacturing by standard UV lithography. Single mode applications in the NIR range from 1300 nm up to 1550 nm have been reported within the last years [1-5], whereas less publications can be found for applications in the VIS range, especially for RGB data signal applications.

In our work a simple UV lithography technique with structured slit masks is used to modify and adjust the refractive index of the polymer to fabricate single mode stripe waveguides for light in the VIS range from 400 nm up to 650 nm. The width of the slits varies around the order of some microns. To increase the refractive index by deep UV absorption the exposure time was optimized in the range of some minutes. In a first step we realised surface waveguides and in a second step we covered the substrate surface with a polymer substrate to get buried strip waveguides (Fig.1). An adapted index glue was used to connect the polymer substrate with the cover.

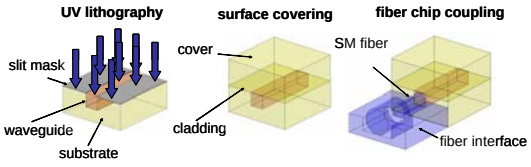


Fig. 1: Schematic picture of the manufacturing process for buried strip waveguides in polymer substrate.

Index profile discussion

To define the index profile distribution m-line spectroscopy and the index profile calculation (IWKB-method [6, 7]) is used after preparing unstructured film waveguides in polymer substrates. Therefore, the exposure doses are varied up tot values to get also multimode waveguides. The m-line spectroscopy with an Abbe refractometer was done at different wavelengths: a) 405 nm, b) 532 nm and c) 633 nm. Fig. 2 shows the normalized measured mode indices as a function of the substrate depth. The different markers represent the different wavelength. For this UV exposure dose 4-7 modes can be activated for the named wavelength. In a good approximation all markers follow a fitted exponential curve which decreases to a 1/e-value at a depth of app. 4.5 µm. We deduce that the UV light intensity absorption process is free from any important surface degradation for the exposure doses.

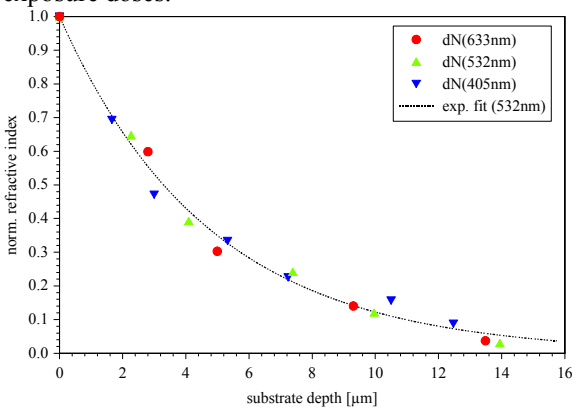


Fig.2: Normalized refractive mode indices of film waveguides as a function of the substrate depth for different wavelength.

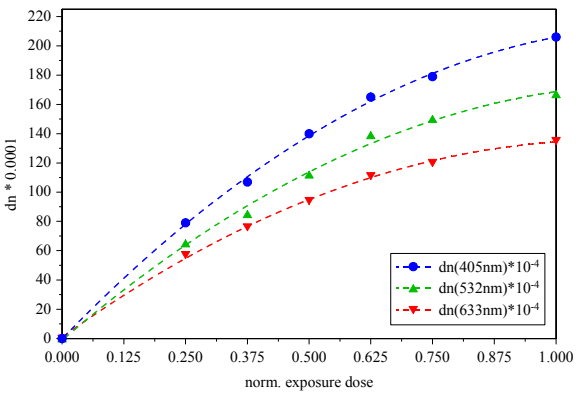


Fig. 3: Surface index change of film waveguides in polymer as a function of the exposure dose for different wavelength.

The maximum values of the refractive index change of the film waveguides at the surface of the polymer substrate are shown in Fig. 3. The index changes in units of 10^{-4} for different values of the UV exposure dose are significantly different for the measurement wavelengths. By these curves the index change for single mode waveguides can be fitted for any dose values within this range. The index profile can be written as

$$n(\lambda, y) = n_{sub}(\lambda) + dn(\lambda) * e^{(-y/\alpha)} \qquad (1)$$

with a decay constant α = 4.5 µm at the 1/e point, given from Fig 2. For small values of the normalized UV exposure doses the measured index change dn(λ)/[1*J/cm^2] can be linearised (see Fig. 3) for different wavelengths of 405 nm / 532 nm / 635 nm. The calculations of the index profiles for e. g. a normalized exposure dose of 0.0625 are shown in Fig. 4 for some specified wavelengths.

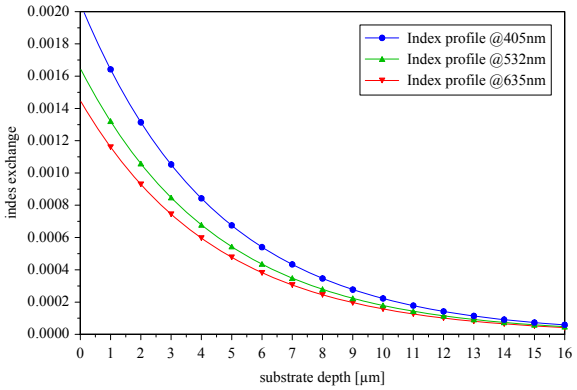


Fig. 4: Calculated index profiles for polymer waveguides for specified wavelengths.

Effective mode index calculation

The well known index profile function is necessary for index simulation by standard BPM methods for structured single mode strip waveguides. The effective mode index curves for the first and second TE mode are plotted in Fig. 5 for a wavelength of 405 nm. A single mode waveguide can be obtained up to a normalized exposure dose of app. 0.1. The basic parameters for the presented calculation are a mask slit width of a few microns, the cladding index above the surface strip waveguide is equal to the substrate index, a layer thickness of 10 µm has been assumed.

If the refractive index for the cladding above the structured waveguide matches not exactly the substrate index then the mode index decreases to lower values and the single mode range becomes smaller. Therefore, a good index matching of the cladding glue is necessary. Unfortunately such glue is not always available from stock.

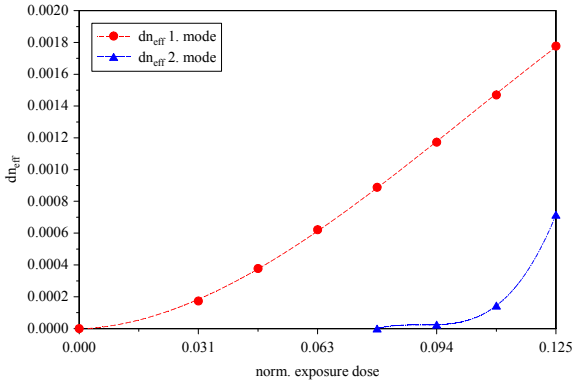


Fig. 5: Effective TE-Mode index distribution as a function of the UV exposure dose for strip waveguides in polymer operating at 405 nm.

Calculation of the mode field distribution

The standard BeamProp software from RSoft presents a tool for a full vector calculation of the TE/TM mode field distributions. Our interests are on single modes behaviour within the VIS range especially the RGB signal performance. The conditions for the calculation are the same as described in the last chapter.

Field distributions for buried single mode strip waveguides in polymer are presented in Fig. 6-8. The small Box in the figures marked the area of the index change between –x/2…+x/2 and y_0…$y_{1/e}$ wheras x is the slit width of the mask. At the waveguide entrance a Gaussian field was launched. The relative mode intensity becomes stable in values of 79 % / 82 % / 73 % compared to the launched intensity after a propagation lengths of app. 300 µm / 800 µm / 1800 µm at 405 nm / 532 nm / 635 nm wavelengths respectively. Thus, app. 20 % to 25 % of the launched intensity is lost due to mode mismatch between the Gausssian field and the mode filed in the waveguide.

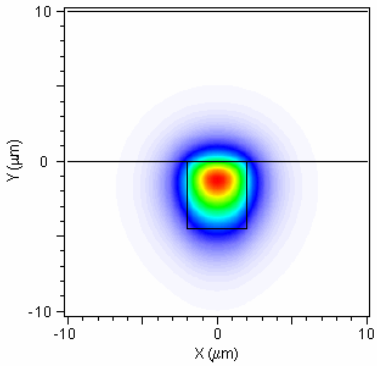


Fig. 6: Calculated transversal TE-Mode field distribution for 405 nm with a mode index step of dn_{eff} = 0.0012.

On one hand a normalized UV exposure dose of app. 0.1 gives a smaller mode field dimension for the blue light and the mode propagation is stronger with an effective mode index step of dn_{eff} = 0.0012 compared to green and red light (see Fig. 6-8). On the other hand a better mode propagation for the red light by

increasing the exposure dose resulting in an increased index change would result in a more instable light propagation in the blue because for this wavelength the second mode comes up.

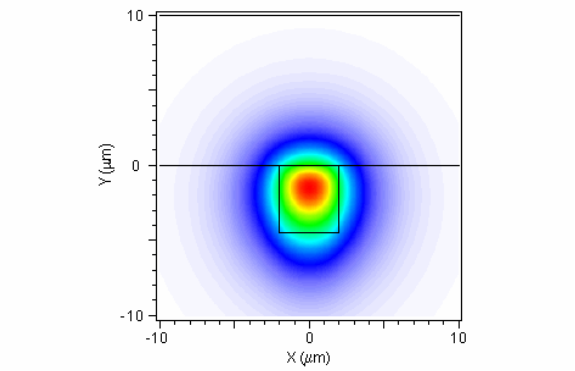


Fig. 7: Calculated transversal TE-Mode field distribution for 532 nm with a mode index step of $dn_{eff} = 0.0006$.

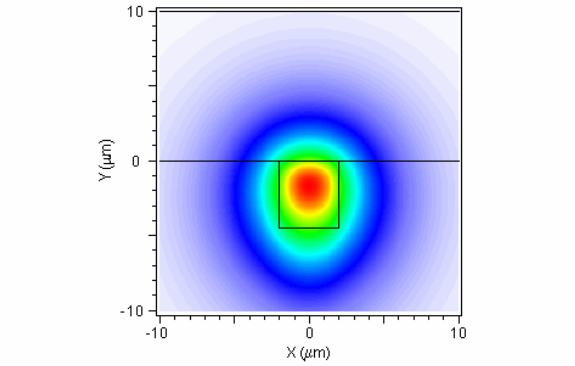


Fig. 8: Calculated transversal TE-Mode field distribution for 635 nm with a mode index step of $dn_{eff} = 0.0003$.

Measurement of the mode field distribution

The first interest is the quality of single mode surface waveguides without any cover material. For better understanding first we compare the well known measurement results of mode field distribution in the range of 850 nm down to 635 nm. In this range the waveguides show losses of app. 0.15 dB/cm. Fig. 9 shows three mode field measurement results for surface waveguides at wavelengths of 808 nm, 635 nm and 407 nm. For 808 nm and 635 nm the mode field distribution compares to fibre. In case of 407 nm the exposure dose has not yet been optimized resulting in a much broader mode distribution.

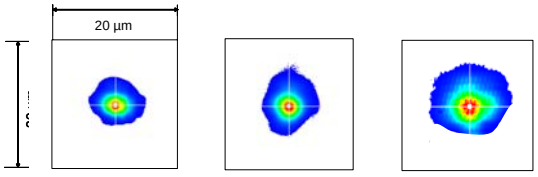


Fig. 9: Measured mode field distributions of surface waveguides for 808 nm / 635 nm and 407 nm wavelengths from left to right.

Fig. 10 shows a CCD picture from a part of the end face of a fabricated buried waveguide package realised with a cladding layer between two polymer substrates. The whole thickness is about 1 mm which can be compared by the scaling of the painted frame. To get this picture, the endface is illuminated from outside by a white light lamp. On the left side near the centre within the frame an arrow marked the light spot of the single mode waveguide. The laser power @ 407nm is reduced (LED mode) for better visibility of the whole picture.

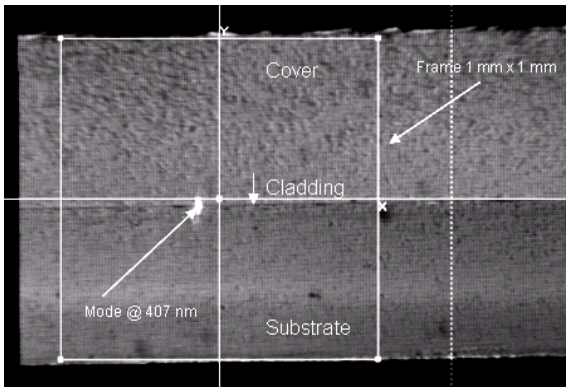


Fig. 10: CCD picture from the end face of a covered substrate with structured single mode waveguides. The light output of a guided mode is marked.

The cladding between substrate (down side) and the cover (top side) is a 10 µm thick layer of glue which looks free from any light propagation. The fine structure over the end face comes from the sawing process.

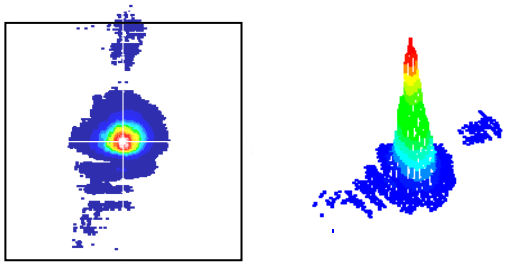


Fig. 11: Measured near field pattern of the light intensity distribution at the end face output of a buried single mode waveguide in a polymer substrate @ 407nm. The frame dimension in the left picture is about 20 x 20 μm^2.

The near field measurement from such a buried single mode waveguide @ 407nm laser wavelength is shown in Fig. 11. At present the fabricated waveguides are with some small imperfections at the adjusted UV exposure dose and the mask slit width. The imaged output intensity distribution in the left side picture of Fig. 11 is in a good agreement with the calculated mode pattern (see Fig. 6) if we consider the opposite orientation (y axis) of the sample in the measurement.

Sometimes, more or less irregularities in the intensity distribution are obtained in the substrate or in the cladding layer. This can be seen in Fig. 12 which gives the intensity distribution along the cross sections of the axis. The x-cut figure is more symmetric than the other and follows approximately a Gaussian curve. The anomaly of a Gauss profile along the (y)-cut profile could have been generated from an index mismatch of the cladding glue. In this example we use a cladding glue with an index difference of n_{sub} - n_{cla} = 0.0200. The cursors along the x-profile mark the width of the mask slit and in the y-profile the distance from the intensity maximum to the noise level in direction of the cladding.

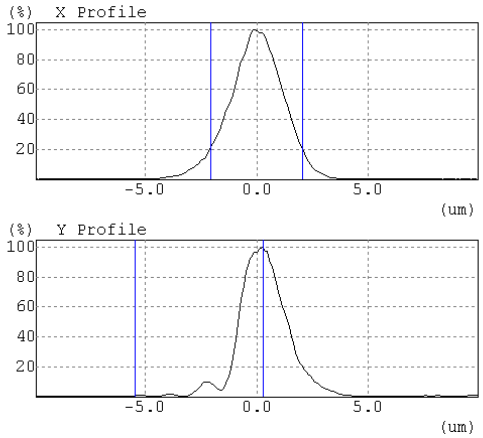


Fig. 12: Measured intensity distribution along the cross sections of the x and y axis.

Conclusions

In this paper we have presented the results of the development of single mode waveguides in a standard polymer substrate for applications in the visible range. The fabrication process for a reasonable index change by a simple UV lithography technique using a metallic evaporated slit mask could be demonstrated resulting in single mode waveguides down to wavelength of 400 nm. The exposure time is on the order of some minutes.

We discussed the wavelengths dependent results for the index change using effective mode index measurements. Based on the results of uncovered multimode film waveguides the index distribution was described by a general equation which can be used to re-calculate the exponential index profiles and the maximum surface index change as a function of the UV exposure dose.

In good agreement between calculated and measured mode profiles we presented results for the intensity distribution of uncovered and covered (buried) single mode waveguides between 400 nm and 635 nm.

In the future we will optimize the single mode propagation of visible light under the aspects of cladding glue index matching, the structure geometry for curved waveguides (S-bands, splitters, couplers), the insertion loss, the polarization depended loss and the optical damage in the case of high power application.

Furthermore the fibre-chip-coupling should be studied under the aspects of the best core diameter, the kind of fibre interface and the long time stability of the hybrid components.

Acknowledgments

We thank the Institute of Physics, Wroclaw University of Technology, Poland for the helpful discussions and measurement results on mode field propagation under conditions of birefringence. This cooperation was done under the NEMO-project (Network of Excellence on Micro-Optics, contract No. 003887) sponsored by the European Commission (www.micro-optics.org).

References

[1] P. Henzi, K. Bade, D. G. Rabus, J. Mohr, “Modification of Polymethylmethacrylate by Deep UV Radiation and Bromination for Photonic Applications,” J. Vac. Sci. Technol. B, vol. 24(4), pp. 1755–1761, August 2006.

[2] Y. Ichihashi, P. Henzi, M. Bruendel, D. G. Rabus, J. Mohr, “Material Investigation of Alicyclic Methacrylate Copolymer for Polymer Waveguide Fabrication,” Jpn. J. Appl. Phys., vol. 45, pp. 2572–2575, 2006.

[3] Y. Ichihashi, P. Henzi, M. Bruendel, D. G. Rabus, J. Mohr, “Influence of the Exposure Spectra on the Optical Properties of Alicyclic Methacrylate Copolymers Waveguides fabricated by Deep UV Exposure,” Jpn. J. Appl. Phys., vol. 45, pp. 6654–6657, 2006.

[4] D. G. Rabus, P. Henzi, J. Mohr, “Photonic Integrated Circuits by DUV induced Modification of Polymers,” IEEE Photon. Technol. Lett., vol.17, no. 3, pp. 591–593, 2005.

[5] Y. Ichihashi, P. Henzi, M. Bruendel, D. G. Rabus, J. Mohr, “Fabrication of Novel Polymer Waveguides Consisting of Alicyclic Methacrylate Copolymers by deep UV Exposure, Proc. of 11th Microoptics Conf. Tokyo, Japan, 131-132, 2005.

[6] J. M. White, P. F. Heidrich, “Optical waveguide refractive index profiles determined from measurement of mode indices: a simple analysis” Applied Optics, Jan. 1976, vol. 15, no. 1, pp.151-155.

[7] K. S. Chiang, “Construction of refractive index profiles of planar dielectric waveguides from the distribution of effective index”, J. of Lightwave Techn., Apr. 1985, vol. LD-3, no. 2, pp. 385-391.

RF Over Fibre Systems

Alwyn Seeds (1), Chin-Pang Liu (1) and Tabassam Ismail (1)
1) Department of Electronic and Electrical Engineering, University College London, Torrington Place, London, WC1E 7JE, England. a.seeds@ee.ucl.ac.uk

Abstract: *The expansion in mobile working has led to increased demand for wireless services, such as cellular radio and Wireless Local Area Networks (WLAN). The proliferation of such services and rapid evolution in coding and modulation standards has increased interest in Radio Frequency (RF) over fibre systems which distribute such services in their final modulated RF carrier form from a central site over optical fibre to antenna units which then convert the signal back to the RF domain. This paper reviews evolving technologies for such systems.*

Introduction

Development of the core optical communications network through dense wavelength division multiplex technology has led to massively increased transmission capacity, while increased interest in broadband applications, such as interactive video, has increased interest in broadband end to end capability. However the provision of fixed broadband (> 2 Mb/s bi-derectional) access has been relatively slow and expensive. Broadband wireless access through IEEE standards 802.11a/b/g and 802.16 has shown rapid growth in both private and public ("hot-spot") networks and is seen as a route to push forward broadband deployment. Such networks have been created by adding wireless transceivers to ethernet or similar wired networks. Changes in standards require corresponding changes in fielded transceivers.

Distributing broadband wireless signals over optical fibre has a number of advantages relative to traditional copper cabling. Because of the low transmission loss of optical fibre, the antenna units (AUs) can be located where coverage is required and remotely connected to the RF generation and detection hardware, which is centralised along with other telecommunications and network hardware in a single equipment room. In this case, the AU function can be simplified to just RF radiation/reception and electrical/optical conversion. Such a system can be made modulation format agnostic and therefore future-proof. When new standards and services are introduced, upgrades are only required to the centralised hardware in the equipment room, but not to the fibre infrastructure or AU. The wide bandwidth of optical fibre further allows different services such as Gigabit Ethernet, IEEE802.11a/g, 802.16, GSM and 3G to share the same infrastructure, making the wireless over fibre approach a truly multi-operator and multi-service technology.

In this paper the main technologies used for RF over fibre systems will be reviewed and promising approaches for future systems identified.

Passive Picocells

The concept of Passive Picocells was first proposed in 1997 by Wake *et al* [1] at BT Laboratories, who demonstrated that an unbiased waveguide electroabsorption modulator (EAM) would have sufficient performance to function as both optical modulator and photodetector simultaneously. When attached to an antenna, the EAM serves as a passive transceiver at the AU. An experiment was carried out in which the EAM was attached to an 8 dBi gain bow-tie type antenna and was placed in a Picocell (a 3m x 6m office). A 2.5 GHz commercial wireless LAN access point (AP) was located in the central station (CS) and after detaching its own antennas, the electrical input and output ports of this AP were converted to optical connections using a separate photodiode and a directly modulated laser. The AP in the CS was connected to the EAM transceiver in the Picocell with two optical fibres, one for the downlink direction (CS to AU) and one for the uplink direction (Picocell to AU) as shown in Fig. 1. To show that the EAM was functioning correctly as a remote Picocell transceiver, a notebook computer equipped with a wireless LAN adapter was brought to the Picocell office and a 3Mbit/s half-duplex network connection was successfully established between the computer and the EAM transceiver via a 2.5 GHz radio link, and thence via the two optical fibres to the AP in the CS.

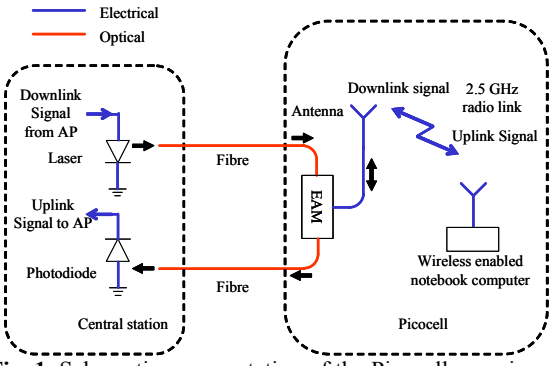


Fig. 1: Schematic representation of the Picocell experiment using a waveguide type EAM transceiver by Wake *et al*.

At UCL we have been investigating a different type of electroabsorption modulator for Picocell or broadband wireless over fibre applications. The modulator is an Asymmetric Fabry-Perot Modulator (AFPM) with an InGaAsP/InGaAsP Multiple Quantum Well (MQW) electroabsorbing region [2,3]. One key difference from the original passive picocell work is that the AFPM is a reflective device with a single optical window. The downlink optical signal is incident on the AFPM within the optical window.

The uplink optical signal on the other hand is simply the AFPM modulated reflection of the residual downlink optical signal through the same optical window. Because of the reflective nature of the AFPM, only one fibre is required for carrying both downlink and uplink optical signals. Compared to the waveguide type EAM, the AFPM also has a number of attractive features. Being a vertically addressed optical intensity modulator, the AFPM is polarisation insensitive because the electric field of the input optical signal is always in the plane of the MQW layers. Thus polarisation control is not required, in contrast to the waveguide type EAM. The optical insertion loss for the AFPM can be as low as 4 dB because of a relatively large (≈20μm in diameter) optical window which eases coupling to optical fibre compared to the typically small cross-sectional area of 1μm × 0.26μm of the waveguide InGaAsP/InGaAsP MQW EAM [4]. At UCL, a reliable air-bridge process has been developed which allows low-capacitance (< 270 fF) AFPMs to be fabricated. In this section, details of the application of the AFPM in RF over fibre systems and its characteristics are described.

Like the waveguide type EAM, the AFPM can be employed at the BS and function as a combined optical modulator and photodetector in a single device. Fig. 2 illustrates the role of an AFPM in a simplified wireless over fibre system.

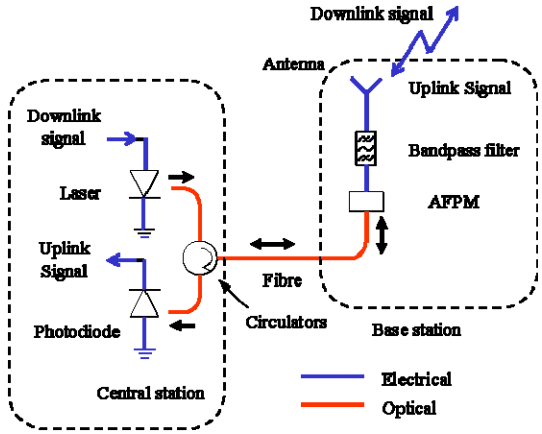


Fig. 2: A simplified wireless over fibre system concept involving an AFPM at the AU performing photo-detection for the downlink path and optical modulation for the uplink path.

The downlink signal is detected by the AFPM and radiated by the antenna. The radio uplink signal received by the antenna is fed to the AFPM which in turn modulates the residual light left from the downlink direction. This residual light, now carrying the up-link signal, is reflected by the AFPM back to the central station.

Fig. 3 shows a micrograph of the air-bridged AFPM developed and fabricated at UCL.

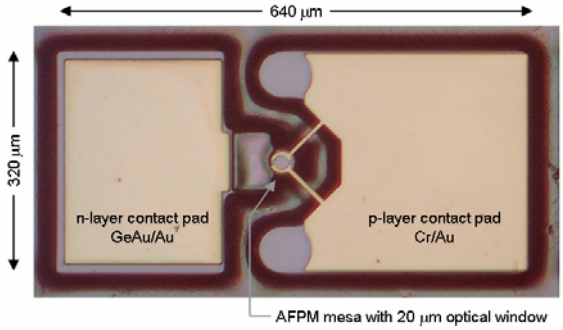


Fig. 3: Top microscopic view of a fabricated air-bridged AFPM.

The AFPM has a −3 dB modulation bandwidth of about 15 GHz which is more than sufficient for carrying the IEEE802.11a/b/g broadband wireless data as well as the cellular GSM and UMTS signals. This is the fastest long (1,550 nm) wavelength InGaAsP/InGaAsP MQW AFPM reported to date. Higher operation speeds have been reported for AFPMs using other material systems [5,6].

Bi-directional 5.2 GHz broadband 68 Mbit/s Differential Phase Shift Keying (DPSK) modulated wireless data transmission over a 12.6 km fibre has been demonstrated using an AFPM alternately as a modulator and a photodetector while keeping the device and experiment parameters same. Full details of the experiment can be found in [7].

Optical Analogue Link Performance Enhancing Techniques

Instead of employing an AFPM at the AU as a single electrical/optical transducer as in Fig. 2, the more traditional method would be to use separately a photodiode for the downlink and a directly modulated laser diode for the uplink. The BS can receive simultaneously both high- and low-power radio signals from nearby and distant users, respectively. Any non-linear components in the fibre-optic link such as a directly modulated laser can cause spectral re-growth (or broadening) of a strong input signal, interfering with any weak neighbouring channel. When a diode laser is directly modulated with two high-power modulated channels, strong inter-channel distortion products are also generated which can degrade a third neighbouring weaker channel or even render it undetectable.

At UCL a microwave frequency feed-forward linearisation scheme has been developed for directly modulated lasers [8,9]. It will be shown in this section that with such a linearisation scheme, the inter-channel distortion generated in the laser diode when driven by two high-power 11 Mega Symbols per Second (Msymb/s) Quadrature Phase-shift Keying (QPSK) modulated signals can be suppressed by at least 11 dB and a neighbouring low-power channel, which would otherwise have been buried

under such distortion, can be recovered and detected successfully.

Fig. 4 shows the implementation of the feed-forward linearisation [10] and the experimental arrangement for triple QPSK modulated wireless signal transmission over fibre.

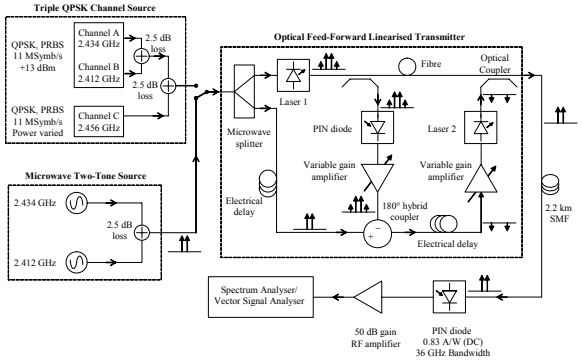


Fig. 4: Experimental arrangement for feed-forward linearisation and triple QPSK modulated wireless signal over fibre transmission.

Laser 1 had a wavelength of 1550 nm and was a commercially available fibre-pigtailed Distributed Feedback (DFB) diode laser. When directly modulated with two microwave tones, the non-linearity of Laser 1 caused third and higher order intermodulation distortion products as well as harmonic components of the two carriers to appear in the output optical intensity modulation spectrum. The detailed working principle of the feed-forward linearisation has been previously reported [11]. The key point is that the optical output of Laser 2 of 1570 nm wavelength replicates the distortion products generated by Laser 1 in anti-phase and without the main microwave tones. Therefore when the outputs from Lasers 1 and 2 are detected by the PIN type photodiode, the distortion products are cancelled, leaving only the linearised signal from Laser 1. The same principle applies when Laser 1 is directly modulated with two high-power QPSK channels. In the experiment the feed-forward could be enabled or disabled by simply connecting or disconnecting Laser 2 output from the optical coupler. The output from the optical feed-forward transmitter was transported over a representative 2.2 km length of Single Mode Fibre (SMF). Finally the linearised signal at the output of the photodiode was amplified and detected using a spectrum analyser and a Vector Signal Analyser (VSA).

A Vector Signal Generator (VSG) was used to provide two 11 Msymb/s QPSK modulated signals at 2.434 GHz (Channel A) and at 2.412 GHz (Channel B). Both Channels A and B had a fixed power level at +13 dBm throughout and were internally filtered with a root raised cosine function having a roll-off factor of 0.5 for reducing the occupied bandwidth. Another VSG provided Channel C which was an 11 Msymb/s QPSK modulated signal at 2.456 GHz. Channel C was internally filtered with a root Nyquist function having a roll-off factor of 0.5. A number of measurements were conducted with different Channel C power levels. All three QPSK channels were first combined using microwave combiners as illustrated in Fig. 4 before being fed to the optical feed-forward linearised transmitter.

With Channel C set at –23 dBm, the transmitted RF spectra with the feed-forward disabled and enabled were measured with a spectrum analyser and are shown in Fig. 5.

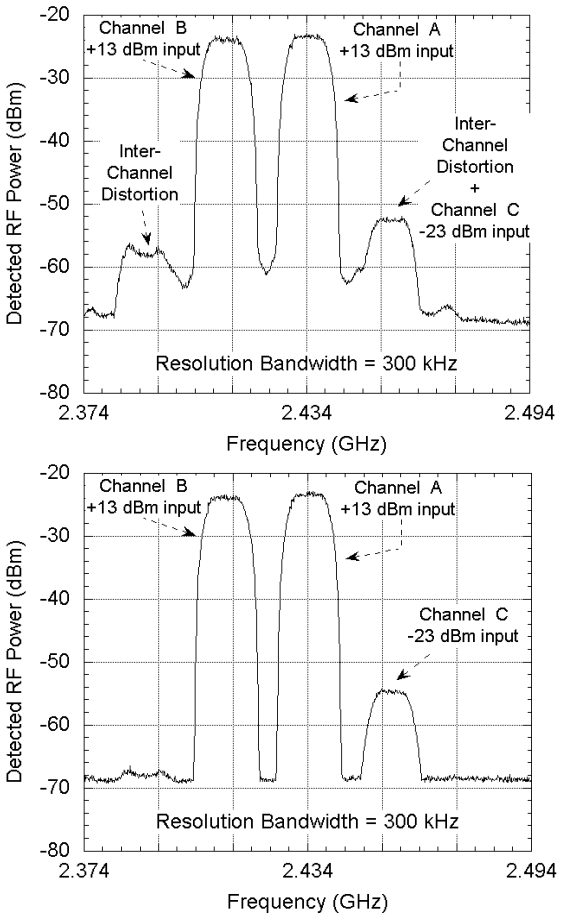


Fig. 5: Detected RF spectra of the three QPSK channels with feed-forward linearisation disabled (top) and enabled (bottom).

Under such a high-power input, particularly from Channels A and B, Laser 1 in Fig. 4 generated a significant level of inter-channel distortion as identified in Fig. 5 (upper plot) in the non-linearised case. The weaker Channel C was effectively buried under and could not be readily distinguished from such distortion products in the RF spectrum. With the feed-forward enabled, the inter-channel distortion was reduced by at least 11 dB and the spectrum of Channel C could then be clearly seen as in Fig. 5 (lower plot).

To assess further the impact of the inter-channel

distortion on the weaker Channel C in the time domain and the effectiveness of the feed-forward linearisation, a VSA was used to measure the eye-diagram, the error-vector magnitude (EVM) and the signal-to-noise ratio (SNR) for Channel C. With the VSA tuned to the centre frequency of Channel C at 2.456 GHz and set to a 20 MHz channel filter bandwidth, the eye-diagrams with feed-forward disabled and enabled were measured and are shown in Fig. 6.

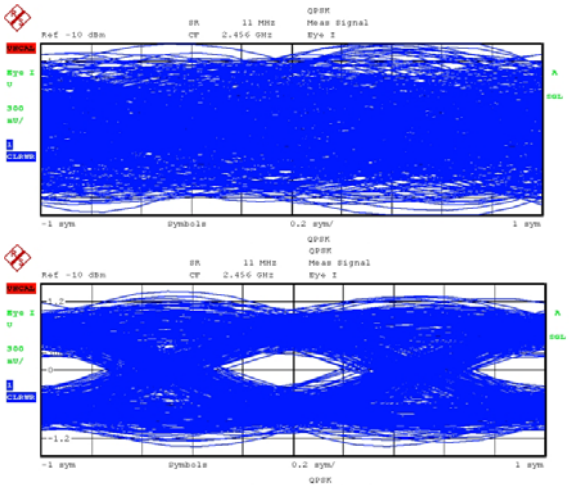


Fig. 6: Detected -23 dBm Channel C in-phase eye-diagrams with feed-forward disabled (upper) and enabled (lower). Channel filter bandwidth: 20 MHz.

When the feed-forward was disabled, no eye-diagram could be detected which suggests that the inter-channel distortion products from Channels A and B completely overwhelmed the weaker Channel C. When the feed-forward was enabled, a clear, widely open eye-diagram was obtained for Channel C. Such a dramatic difference in the quality of the received eye-diagrams illustrates how effective the feed-forward linearisation technique is in suppressing inter-channel distortion. In Fig. 6, only the in-phase eye-diagrams are shown since the corresponding quadrature-phase ones were very similar.

Finally the EVM and SNR for Channel C were measured as a function of channel input power and the results are plotted in Fig. 7.

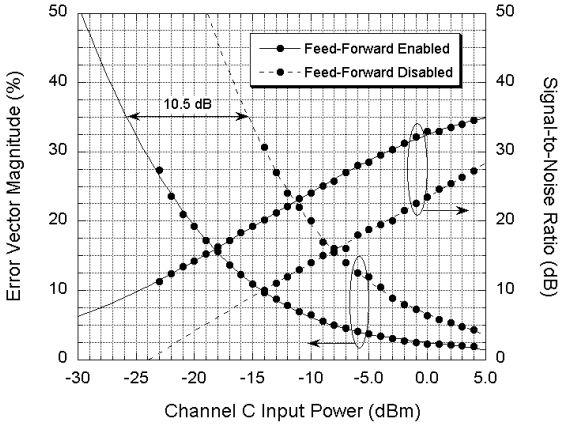


Fig. 7: EVM and SNR vs. Channel C input power. Channel filter bandwidth: 20 MHz.

The EVM decreased and SNR increased with increasing Channel C input power. At –14 dBm input power, the feed-forward linearisation reduced the EVM from 31 % to 10 % and increased the SNR from 10 dB to 20 dB. The IEEE 802.11b standard requires that the EVM not exceed 35 % and it can be seen in Fig. 7 that without feed-forward, Channel C would not be able to comply with this requirement for input levels below –15.5 dBm, whereas with feed-forward the specification is met for Channel C levels as low as –26 dBm, a power advantage of 10.5 dB.

Other researchers have also reported different analogue link performance enhancing techniques. Ackerman et al. [12] demonstrated an optical analogue link with RF noise figures ≤ 15 dB over the frequency range from 1.0 to 9.5 GHz with a laser RIN suppression technique which is illustrated in Fig. 8.

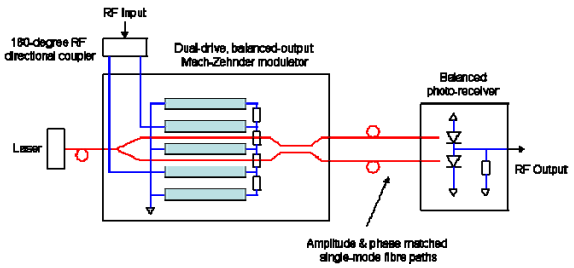


Fig. 8: Analogue optical link employing dual-drive Mach-Zehnder modulator and balanced photo-receiver for laser RIN suppression.

The key components in the optical link are the dual-drive Mach-Zehnder modulator (MZM) with balanced outputs and the balanced photo-receiver. The laser source is first split in two parts which are externally modulated in the two separate arms of the dual-drive MZM. Because of the 180-degree RF directional coupler, the modulation outputs from the MZM are in anti-phase. The two modulated optical signals are then transported to the balanced photo-receiver through two identical optical fibres having

matched amplitude and phase response. The balanced photo-receiver produces an RF output which is the difference between the two photodetected signals. Since the two modulated signals are out of phase by 180 degrees, the original RF input signal is enhanced and delivered to the RF output. On the other hand, since the RIN is the same in two fibres both in amplitude and phase, it is suppressed by the balanced photo-receiver.

Darcie et al. [13] realised that the problems associated with the shot noise and the laser intensity noise in an analogue optical link are caused by the presence of a large DC optical power level in the transmission system. They demonstrated a technique for decreasing the DC optical power level, hence reducing the shot noise and laser intensity noise, by using two MZMs set up in a Class AB configuration analogous to that in transistor amplifier circuits. Fig. 9 shows the simplified experimental arrangement for this Class AB analogue optical link.

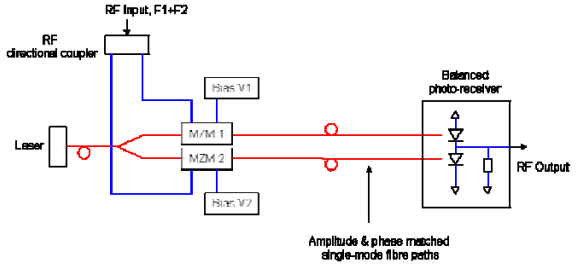


Fig. 9: Simplified experimental arrangement for the Class AB analogue optical link.

The key feature of this Class AB configuration is that the two MZMs are biased at $\pm V_{\pi}/6$ from the zero transmission, respectively. Therefore one of the MZMs is mostly transmitting in one half of the input signal circle and the other MZM mostly transmitting in the other half of the signal circle forming a Class AB configuration similar to that of a transistor amplifier circuit. The next effect is that the amount of average optical power reaching the balanced photo-receiver is reduced, lowering the effects of the shot noise and the laser intensity noise. Darcie demonstrated that the Class AB optical link shows a 5.7 dB reduction in shot noise compared to that achieved with a MZM conventionally biased at quadrature (50% transmission).

Wireless over Multi-Mode Fibre Systems

The work described so far has used single mode optical fibre which is invariably employed in long haul optical transmission systems. Most modern commercial buildings already have a multi-mode optical fibre (MMF) infrastructure for carrying Ethernet data. To provide cost-effective and reliable indoor cellular and WLAN coverage without dependence on the radio penetration from outside BSs, it is highly desirable that the same MMF infrastructure be used to carry these additional services between the equipment room and the remote AUs around the building.

MMFs were not previously regarded as being suitable for carrying modulated signals at microwave frequencies because they suffer from modal dispersion, limiting their bandwidth-distance products to between 500 MHz.km and 1 GHz.km at 1,300 nm wavelength. For cellular GSM1800 and UMTS systems, this would mean a maximum fibre length of around 500m while for IEEE 802.11a WLAN operating in the 5 GHz band, the maximum length is further reduced to less than 200m, which is not sufficient for large in-building installations. Commercial products for transporting cellular signals over fibre do exist which either transmit the signal over single mode fibre at the original RF, or transmit the signal over the MMF at a down-converted IF which is selected to be within the 3-dB bandwidth of the MMF. To provide in-building cellular coverage, the former method requires specialist and expensive fibre and component installation, because most installed fibres within buildings are MMF. The latter method requires complicated hardware, especially for the remote AUs since up-conversion from the IF to the original RF is necessary.

It was shown in 1998 by Raddatz *et al* [14] that transmission over MMF is possible over narrow bands of frequencies beyond the 3-dB bandwidth limit and this is because the impulse response of MMF contains a series of delta functions with different arrival times, which gives rise to high frequency components with considerable amplitude in the frequency domain.

UCL in collaboration with the University of Cambridge have investigated the transmission of cellular and broadband wireless IEEE 802.11b/g signals over MMF and the results so far are encouraging, sufficiently so that the work is now being exploited commercially [15]

To demonstrate that good quality broadband wireless signal transmission over multi-mode fibre can be obtained, experiments [16] experiments using 32-QAM modulation and demodulation were carried out. This complex digital modulation scheme requires a signal to noise ratio of more than 25 dB and is therefore a good test of the fibre performance. In the experiments a carrier frequency of 2 GHz and a symbol rate of 2 Ms/s were chosen, which corresponds to a transmission bit rate of 10 Mb/s.

Fig. 10 shows the constellation and eye diagrams for 32-QAM transmission. The left hand plots show results for a short coaxial cable link as reference and the right hand plots shows results for transmission over a 1km MMF (50 micron core and 125 micron cladding) with a specified bandwidth of 500 MHz. Comparable results were obtained using other similar

fibre reels. It is clear that transmission over multimode fibre, at least up to a length of l km is not significantly degraded compared to the short coaxial cable reference.

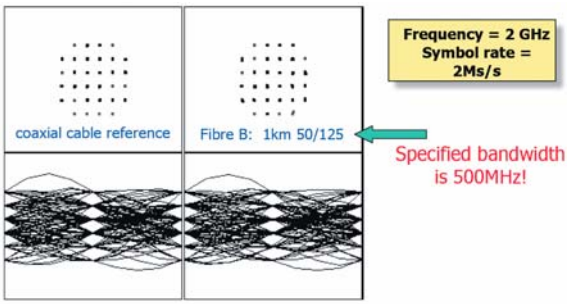


Fig. 10: Constellation and eye diagram for 32-QAM transmission at 2 GHz and 2 Ms/s. Left is coaxial cable (reference) and right is fibre reel B

To reduce the cost of in-building broadband wireless over fibre deployment even further, the use of uncooled, directly modulated lasers is highly desired. Transmission experiments using IEEE 802.11a/b signals over MMF have been performed using an uncooled 1,300 nm directly modulated laser [17]. Initially, the transmission performance of IEEE 802.11a/b wireless LAN signals over MMF was assessed using a VSA to determine the likely system performance. The received 11Mb/s 802.11b Complementary Code Keying (CCK) (similar to QPSK) constellation for a 2.41 GHz carrier frequency after 1km was clear with a measured error vector magnitude (EVM) of 1.21 %. The received 54Mb/s 802.11a 64-QAM constellation for a 5.35 GHz carrier frequency after 1km was also well defined with a measured EVM of 2.19 %. These are well within the maximum EVM specifications of 35 % for 802.11b and 5.6 % for 802.11a signals.

Conclusions

We have in this paper described a number of research projects which are relevant to broadband access using RF over fibre techniques, including using an AFPM as a single optical/electrical transducer for Picocell and wireline/wireless access applications, the feed-forward linearisation of directly modulated lasers, microwave signal transmission over low-cost multi-mode fibre and direct modulation of uncooled lasers.

Our experience has been that the take-up of such technologies is strongly dependent on applications drive. Specifically, we expect that ubiquitous in-building broadband wireless LAN (WLAN) coverage will be regarded as being as essential as coverage for the cellular systems such as GSM and 3G, and will be increasingly so when more and more people use their wireless enabled notebook computers or their handheld personal digital assistants (PDAs) not just for data applications but also for voice conversation instead of using the conventional mobile phone. Voice over IP (VOIP) is attractive as it allows people to make cheap (if not free) device to device or device to telephone calls conveniently and Skype, a piece of free software, has helped fuel the popularity of VOIP. As explained above, most commercial buildings have existing MMF infrastructure for carrying Ethernet traffic. It is also technically feasible to use MMF to carry other microwave signals beyond its 3-dB bandwidth limit. Therefore a strong case can be made that the existing MMF infrastructure be used for carrying a number of services, including WLAN, GSM, UMTS, TETRA and DECT etc. To provide such multi-service in-building coverage, the optoelectronic components involved must have high enough linearity, otherwise distortion products generated in them will degrade the system performance or even render one or more of the services unusable. In-building fibre infrastructure invariably uses direct modulation of semiconductor lasers to achieve the most cost-effective solution compared to other approaches such as external modulation. Although linearisation techniques for direct modulation lasers provide significant performance gains they require a number of extra components and are not sufficiently stable over time to be practical. We therefore expect that low-cost high-linearity direct modulation lasers will be the key to the success of future multi-service and multi-operator in-building wireless access networks. Given the difficulty in providing high data rate in-building coverage from outside the building, coupled with the need for comprehensive, rather than hot-spot WLAN coverage, to support VOIP we expect strong growth in the deployment of in-building wireless over fibre.

In conclusion, it is envisaged that the future of broadband wireless networks will depend on their ability to provide comprehensive multi-service and multi-operator coverage for buildings. Simple, practical and cost-effective technologies will be the key to success for suppliers to this market and there remains much scope for research on new devices and system architectures to assist this.

References

[1] D. Wake, D. Johansson and D. G. Moodie, "Passive picocell: a new concept in wireless network infrastructure," *Electron. Lett.*, Vol. 33, No. 5, pp. 404-409, Feb. 1997.

[2] C. P. Liu, A. J. Seeds, J. S. Chadha, P. N. Starvinou, G. Parry, M. Whitehead, A. Krysa and J. S. Roberts, "Normal-Incidence 1.56-µm MQW Asymmetric Fabry-Perot Modulator (AFPM) for Passive Picocells, " International Topical Meeting on Microwave Photonics 2002, pp. 49-52, Awaji, Japan, November 2002.

[3] C. P. Liu, A. J. Seeds, J. S. Chadha, P. N. Starvinou, G. Parry, M. Whitehead, A. Krysa and J. S. Roberts, "Design, fabrication and characterisation of normal-incidence 1.56-µm

multiple-quantum-well asymmetric Fabry-Perot modulators for passive picocells", IEICE Trans on Electronics, VOL.E86-C, NO.7, July 2003.

[4] D. G. Moodie, M. J. Harlow, M. J. Guy, S. D. Perrin, C. W. Ford and M. J. Robertson, "Discrete electroabsorption modulators with enhanced modulation depth," JLT, vol. 14, no. 9, pp. 2035-2043, 1996.

[5] C. C. Barron, C. J. Mahon, B. J. Thibeault, G. Wang, W. Jiang, L. A. Coldren and J. E. Bowers, "Millimeter-wave asymmetric Fabry-Perot modulators," IEEE Journal of Quantum Electronics, vol. 31, no. 8 pp. 1484-1493, August 1995.

[6] J. J. Huang, T. Chung, M. Lerttamrab, S. L. Chuang and M. Feng, "1.55-μm asymmetric Fabry-Perot modulator (AFPM) for high-speed applications," IEEE Photon. Technol. Lett., vol. 14, no. 12, pp. 1689-1691, December 2002.

[7] C. P. Liu, A. J. Seeds, J. S. Chadha, P. N. Starvinou, G. Parry, M. Whitehead, A. Krysa and J. S. Roberts, "Bi-Directional Transmission of Broadband 5.2 GHz Wireless Signals Over Fibre Using a Multiple-Quantum-Well Asymmetric Fabry-Perot Modulator/Photodetector", OFC 2003, vol. 2, pp. 738-740, Atlanta, March 2003.

[8] T. Ismail, C.P. Liu and A.J. Seeds, "Uncooled directly modulated high dynamic range source for IEEE802.11a wireless over fibre LAN applications," Optical Fiber Communications 2004 (OFC 2004), paper no. FE3 (no page no. assigned), February 22-27, 2004, Los Angeles Convention Center, Los Angeles, California, USA

[9] T. Ismail, C.P. Liu, J. Mitchell, A.J. Seeds, "Multichannel broadband wireless transmission over fibre using feed-forward linearised uncooled DFB laser," 30th European Conference on Optical Communication ECOC 2004, pt. 2, vol. 2 pp. 208-209.

[10] T. Ismail, C.P. Liu, J.E. Mitchell, A.J. Seeds, "Interchannel distortion suppression for broadband wireless over fibre transmission using feed-forward linearised DFB laser," 2004 IEEE International Topical Meeting on Microwave Photonics, 2004. MWP'04, pp. 229-232, 4-6 Oct. 2004.

[11] T. Ismail, C. P. Liu and A. J. Seeds, "Uncooled Directly Modulated High Dynamic Range Source for IEEE802.11a Wireless over Fibre LAN Applications," OFC 2004, FE3, 2004.

[12] E. Ackerman, G. Betts, W. Burns, J. Prince, M. Regan, H. Roussell and C. Cox, "Low noise figure, wide bandwidth analog optical link," 2005 IEEE International Topical Meeting on Microwave Photonics, pp. 325-328, Octovber, Korea 2005.

[13] T.E. Darcie, A. Moye, P.F. Driessen, J. D. Bull, H. Kato, and N. A. F. Jaeger, "Noise reduction in Class-AF microwave-photonic links," 2005 IEEE International Topical Meeting on Microwave Photonics, pp. 329-332, Octovber, Korea 2005.

[14] L. Raddatz, D. Hardacre and S.Y. Wang, 'High bandwidth data transmission in multimode fibre links using subcarrier multiplexing with VCSELs', Electron. Lett., 1998. 34, pp. 686-688

[15] http://www.zinwave.com

[16] D. Wake, S. Dupont, J.-P.Vilcot, A.J. Seeds, "32-QAM radio transmission over multimode fibre beyond the fibre bandwidth," 2001 International Topical Meeting on Microwave Photonics. Post Deadline Papers. MWP'01 (Cat. No.01EX476), 2001, pt. , p 4 pp. suppl.

[17] P. Hartmann, M. Webster, A. Wonfor, J. D. Ingham, R. V. Penty, I. H. White, D. Wake and A. J. Seeds, "Low-Cost Multimode Fibre-Based Wireless LAN Distribution System using Uncooled, Directly Modulated DBF Laser Diodes," ECOC-IOOC 2003, vol. 3, pp. 804-805, 2003

Waveguide Quantum Memory

W. Tittel (1), M. Afzelius (2), P. Baldi (3), N. Gisin (2), R. Ricken (4), S. Hastings-Simon (2), V. Scarani (2), H. Suche (4), W. Sohler (4), and M. Staudt (2)

1) Institute for Quantum Information Science, University of Calgary, Canada
2) Group of Applied Physics, University of Geneva, Switzerland
3) Laboratoire de Physique de la Matière Condensée, University of Nice-Sophia Antipolis & CNRS, France
4) Angewandte Physik, University of Paderborn, Germany

Abstract: *We study Erbium doped $LiNbO_3$ waveguides for their suitability to store quantum information encoded into single photons, as required for a quantum repeater. Specifically, we perform stimulated photon-echo experiments for storage and readout of (classical) light pulses, which yield important information about the storage of single photon states. Furthermore, we investigate Stark-shift based line-shifts of the 1.53 μm transition, as required for a highly efficient quantum state storage protocol. Our findings demonstrate the potential of Er:$LiNbO_3$ waveguides for quantum state storage.*

Introduction

The last years have seen a remarkable advance of experimental quantum communication, in particular of quantum cryptography that promises information-theoretic secure communication [1]. Yet, many problems still have to be overcome before a quantum secured communication network will be available. A major challenge concerns the increase of the transmission distance, which is, among others, limited through the combination of absorption in the transmission channel and detector noise. In contrast to classical telecommunications, a direct amplification of a single-photon quantum state is impossible. The concept of a quantum repeater [2] is based on several key elements, which are the creation and distribution of entangled pairs of photons over sub-sections of the complete link, swapping to extend the entanglement over the whole channel, and quantum memories that allow increasing the efficiency of the overall process. The entanglement can then be used for any kind of quantum communication task, for instance for quantum cryptography.

Many schemes for storage of non-classical light have been proposed. However, only a few experiments can be mentioned in the context of quantum memory [3], and efficient, reversible transfer of quantum information between different species has not yet been accomplished. An original protocol for a quantum, as well as classical, memory in solid state material is based on controlled reversible inhomogeneous broadening (CRIB) of a single atomic absorption line [4]. It requires an atomic ensemble with a large optical depth and a long optical coherence time. It also relies on the possibilities to prepare, through optical pumping, a narrow absorption line on a non-absorbing background, to broaden this line in a controlled and reversible way, and to apply a position dependent phase shift.

Erbium doped crystalline waveguides are interesting candidates for the realization of CRIB, as interaction lengths of many centimeters can be achieved, allowing for large absorption even at low doping concenration. In addition, the 1.53 μm, $^4I_{15/2} \rightarrow {}^4I_{13/2}$ transition in Erbium can feature coherence times in the ms range [5], and is well matched to standard telecommunication fibre, which allows future interfacing of such a memory with the standard telecommunication fibre network.

In this paper we report on the storage, recall and measurement of classical optical pulses via stimulated photon echoes [6], which provides an important test-bed for future quantum state storage based on CRIB. Furthermore, we present investigations of the linear dc-Stark effect for controlled broadening [7]. The experiments took advantage of Er^{3+} doped $LiNbO_3$ crystals with waveguiding structures, cooled to a temperature of around 3.5 Kelvin. While $LiNbO_3$ waveguides are extensively used in integrated optics, these are, to the best of our knowledge, the first studies in the context of all-optical data storage.

Photon-echo based storage of classical light pulses

A common approach to storage and retrieval of light is based on three-pulse photon echo (3PE), also known as stimulated photon echo [6]. In this process a first, strong, optical *write* pulse excites the medium, creating an atomic coherence. The *data* pulses, a sequence of pulses encoding the information to be stored, are sent into the medium some time after the write pulse, which transfer the coherence into a frequency-dependent population grating in the ground and excited states. In order to retrieve the information, a third, strong, *read* pulse is used, which scatters off the grating and causes a photon echo to be emitted a time after the read pulse, which is equal to the time separation between write and data pulse [8]. If certain conditions for excitation energy and absorption depths are met, the echo is, to a high degree, an amplitude and phase replica of the stored data pulses.

Now, consider a data field consisting of two pulses (D1 and D2) with an amplitude ratio R and relative phase φ (see Fig. 1). The 3PEs appear at times $t_e = t_r + t_{Di} - t_w$ (i = 1, 2), where t_r is the arrival time of the readout, t_{Di} the arrival time of data pulse Di (i = 1, 2), and t_w the arrival time of the write pulse. The echoes will thus be $dt = t_{D2} - t_{D1}$ apart.

Because the efficiency of the 3PE is at best a few percent [9], much of the frequency-dependent popu-

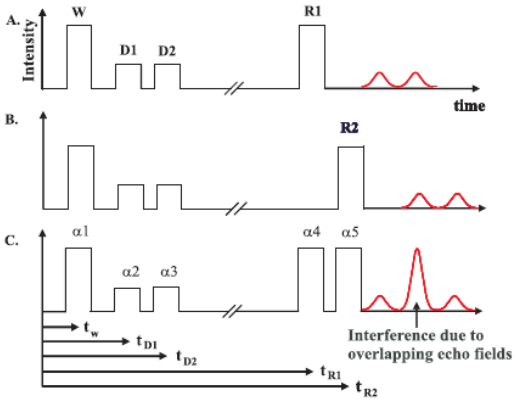


Fig. 1: Illustration of the sequence of pulses for the interference of photon echoes. The data is read out twice and the phase between the data (or read) pulses is changed to produce interference in the central time bin.

lation grating is preserved in the atomic ensemble after the read pulse. Therefore more echoes can be produced by sending in several read pulses. In our experiment, two subsequent read pulses were used to produce two copies of the data pulse. If we chose the distance between the read pulses to be dt, the same as the distance between the two data pulses D1 and D2, the echo of the second data pulse read out by the first read pulse (D2|R1), and the echo of the first data pulse read out by the second read pulse (D1|R2), will overlap and interfere (Fig. 1 c). The intensity of the echo in the central time interval (time-bin) is thus controlled by the phases of the write, the data and the read pulses, i.e. α1, α2/3, and α4/5, respectively. This is true provided that the phase coherence or amplitude ratio is not perturbed partially or totally during storage and retrieval.

The sequence of two data pulses above is related to what is known in quantum communication as a time-bin qubit [10]. A time-bin qubit is a coherent superposition of a photon being in two time-bins, separated by a time difference long compared to the coherence time of the photon. It can be written as:

$$|\psi\rangle = c_0\,|1,0\rangle + c_1 e^{i\varphi}\,|0,1\rangle, \qquad (1)$$

where $|1,0\rangle$ ($|0,1\rangle$) represents a photon in the first (the second, respectively) time-bin, and $\varphi=\alpha 2-\alpha 3$ denotes their relative phase.

In the present experiment, classical (strong) coherent pulses were used, with width smaller than the temporal spacing dt between the two pulses; the state of light is thus described by a Poisson distribution of photons ($n\sim10^8$), each of which is in the state described by Eq.1. Note that one could also describe our experiment as a setup containing two interferometers, as used for phase-coding quantum cryptography [1]: one interferometer prepares the time-bin qubits, i.e. here our two data pulses, while the second allows the projection measurement, i.e. our two read pulses.

Let us now describe the experimental setup. The output from an external-cavity cw diode laser was gated by a combined phase and intensity modulator, followed by an intensity modulator (both fibre optic). The first modulator was used to create the five excitation pulses and to apply phase shifts to some of the pulses, depending on the particular experiment. The second modulator was synchronized to the first one and used to improve the peak-to-background intensity ratio. The pulses were then amplified by an Erbium Doped Fiber Amplifier (EDFA). In order to obtain a good background suppression (>70 dB), the EDFA was followed by an acousto-optical modulator, which opened only for the series of pulses and suppressed light for all other times. The resulting pulses had durations of t_{pulse}=15 ns, with peak powers of around 5 mW for the write pulses, and around 1 mW for the other pulses. The first data pulse was created at t_{D1} = 0.6μs, the time between the data pulses was typically dt = 60ns and the read-out pulses were delayed with respect to the data pulses by 1 to 2 μs. The light was then coupled into an Er^{3+}-doped $LiNbO_3$ crystal (with waveguide, see below), which was cooled to 3.4 K by means of a pulse tube cooler. A magnetic field of about 0.2 Tesla was applied parallel to the C_3 axis. This reduces decoherence due to spectral diffusion [11], resulting in a coherence time T_2 of about 6 μs. Finally, the photon echoes were detected by a fast photo detector and displayed on an oscilloscope. The clock frequency was of 30 Hz, which ensured that most atomic excitations (featurig radiative a lifetime of 10 ms) had decayed between two subsequent storage/recall sequences.

The z-cut $LiNbO_3$ crystal was Erbium doped over a length of 10 mm by indiffusion of an evaporated 8 nm thick Er-layer at 1130°C for 150 h, leading to a Gaussian concentration profile of 8,2 μm 1/e penetration depth and $3.6\text{x}10^{19}\text{cm}^{-3}$ surface concentration. The guiding channel was fabricated by indiffusion of a 7 μm wide, 98 nm thick Titanium-stripe at 1060°C for 8.5 h, resulting in a mono-mode guide with a mode size of 4.5x 3 μm FWHM intensity distribution [12]. The light was injected and collected with stan-

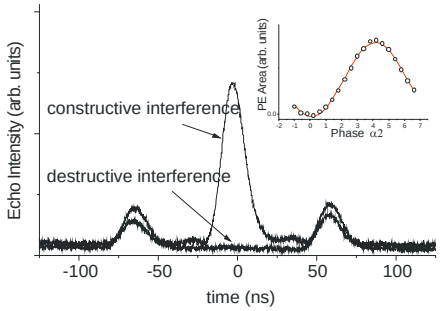


Fig. 2: Photon echo signals showing constructive and destructive interference. Inset: Central echo area as a function of phase.

dard optical fibers, which were butt coupled to the input and output of the waveguide.

In a first experiment, we varied the phase difference between the two data pulses. Figure 2 shows observed photon echoes in the case of constructive and destructive interference in the central time-bin, and the inset depicts the background subtracted area under the peak in the central bin as a function of the phase difference. Note that the background was of purely electronic origin and that no coherent or incoherent back- ground light was interfering with the echoes.

Figure 3 shows similar sinusoidal fringes, however, this time obtained through a phase change of the second read pulse. While this phase is scanned, the phase $\alpha 3$ of the second data pulse is kept constant at: 0, $\pi/2$, π, and $3\pi/2$, and all other phases are kept at zero. We observed an average visibility of 100% (within the experimental error). This experiment is conceptually analogous to preparing four different time-bin qubit states, which form two maximally conjugate bases, as is widely used in quantum cryptography in the so-called BB84 or four state protocol [13]. However, while in quantum cryptography setups the projection measurement is done with a widely unbalanced interferometer [1], we project the state with photon echoes using two read pulses. The photon echo process thus serves two purposes: storage/retrieval, and analysis of the state.

To further test the analogy between our photon-echo based interference scheme and a purely optical scheme, we measured the visibility V=(Max-Min)/(Max+Min) of the interference fringes for various ratios R of data pulse intensities. Note that the read pulses remained unchanged at equal intensity. In case of a purely optical measurement, the visibility of the interference should depend on R through

$$V = 2\sqrt{R}/(1+R). \qquad (2)$$

As depicted in Figure 4, the visibility in the photon-echo based read out reproduces indeed, within experimental error, the predictions for the optical setup.

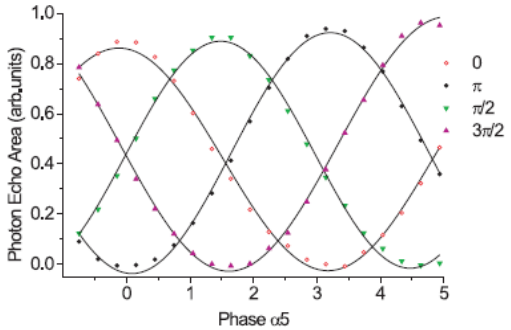


Fig. 3: Area under the central echo as function of the phase of the second read pulse. All four classical states, analogous to the quantum states used in the four-state quantum cryptography protocol, are stored, retrieved and analyzed with close to 100% fidelity.

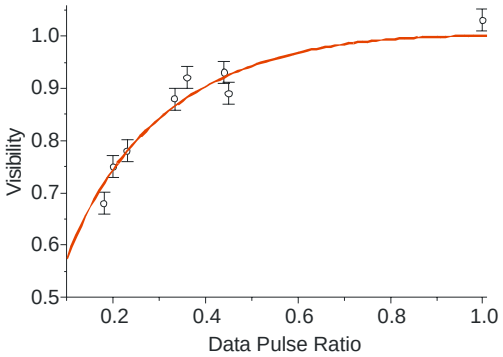


Fig. 4: Visibility as a function of the ratio of the data pulse intensities. Experimental points are in good agreement with the theoretical prediction, which contains no free parameter.

We thus find that stimulated photon echoes do not only allow all-optical storage and readout, but also projection onto various bases, thereby replacing standard interferometric setups. The outstanding visibilities obtained in our measurements paired with the ease to extend our scheme to more than two read pulses (equivalent to more than two arms in an interferometer), or read pulses with different intensities (i.e. beam-splitters with variable splitting ratios) makes it a very interesting approach to storage (and readout) of quantum information. While our experiments have been performed with classical pulses and (low efficient) traditional photon echoes, we believe that our scheme can be extended to highly efficient quantum state storage based on CRIB.

Controlled broadening based on Stark shifts

While photon-echo technology allows demonstrating and testing of key features required for quantum state storage, its limited efficiency of a few percent impacts on the use in quantum repeaters. A more efficient approach takes advantage of controlled reversible inhomogeneous broadening (CRIB) of a single absorption line [4].

A promising way to create controlled reversible broadening is based on the use of electric fields. In the presence of an external dc electric field, the energy levels of an atom with a permanent dipole moment are shifted; the linear dc-Stark effect. If the dipole moments are different for different electronic levels, this shift leads to a displacement of the associated optical transition frequency ω:

$$\Delta\omega\hbar = \Delta\mu_e \chi E \cos\theta \qquad (3)$$

Here $\Delta\mu_e$ is the difference between the permanent electric dipole moments of the two states connected by the transition, E is the applied dc electric field, $\chi=(\varepsilon+2)/3$ is the Lorentz correction factor, ε is the dielectric constant of the sample, and θ is the angle

between the vectors $\Delta\mu_e$ and E. The linear dc-Stark effect can and has been observed in RE doped crystals through shifts of spectral holes [7,14], where the dipole moment in the ion is induced by local electric fields. However, no measurements have been reported on RE doped waveguides, neither crystalline nor amorphous.

In a crystal, because of the ordered structure of the crystalline lattice, the dipole moments are aligned along a set of one or more well defined directions. The symmetry of the crystal along with the site symmetry at the rare-earth-ion position determines the number of directions. All ions with vector $\Delta\mu_e$ aligned along the same direction experience the same shift in their resonance frequency with an applied electric field and thus the application of a DC electric field leads to a shift or splitting of the spectral hole, depending on the number of possible directions. The projection of $\Delta\mu_e$ between the two states, along the direction of the applied electric field, can be determined by measuring the shift of a spectral hole as a function of the electric field, as given by equation 3.

In our investigation we used a monochromatic laser to excite Er^{3+} ions from the lowest crystal field level of the $^4I_{15/2}$ ground state to the lowest crystal field level of the $^4I_{13/2}$ excited state, thereby creating a spectral hole at the frequency of the laser. We then decreased the laser intensity and scanned the frequency around the initial burning frequency three times while measuring the transmitted light as a function of time. Together with an independent time-to-frequency calibration of the laser scan, this yields three spectral hole profiles. During the first scan there was no applied electric field, for the second scan we applied an electric field across the sample, and for the third scan, we switched off the electric field to demonstrate the reversibility of the Stark induced line shift. See figure 5 for a graphical representation of the measurement sequence.

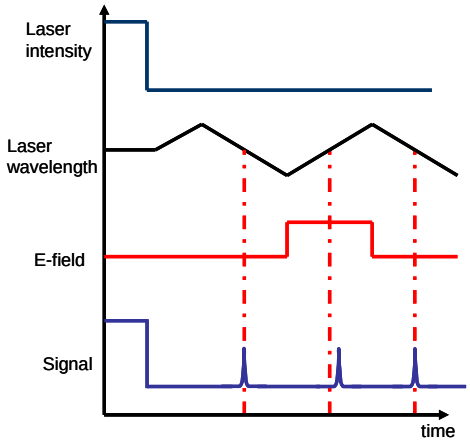


Fig. 5: Measurment sequence to assess magnitude and reversibility of the dc Stark shift.

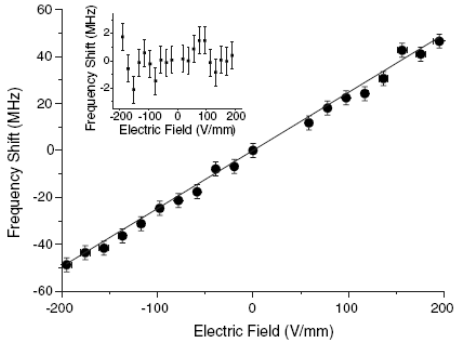


Fig. 6: Shift (and return) of the spectral hole's central frequency as a function of the electric field in the Erbium doped $LiNbO_3$ waveguide.

The sample used in this investigation was a single domain, z-cut, $LiNbO_3$ crystal,1 mm thick, 6 mm long, and 6 mm wide, doped with Er^{3+} (0.5 at %), and MgO (5 mol %) and featuring single mode waveguides fabricated via proton-exchange. The sample was mounted between two metal electrodes spaced by 1 mm and cooled to 3.8 K. Light, linearly polarized along the crystal C_3 symmetry axis, was injected and collected with standard optical fibers. The C_3 symmetry axis was oriented parallel to the applied electric field and perpendicular to the light propagation direction. The inhomogeneous broadening in the sample is of around 250 GHz. We applied a magnetic field of approximately 0.7 T, parallel to the C_3 symmetry axis, to reduce the width of the spectral hole [11] by a factor of 5, yielding a hole width of 47 MHz, FWHM, which was largely dominated by power broadening. Note that the position of the spectral hole, which is the relevant parameter in our investigation, could be determined within a precision of ±3 MHz. We performed hole burning experiments as described above, with applied voltages ranging from -200 to 200 V, using a scannable cw external cavity diode laser at a wavelength of 1531.00 nm. To measure the spectral hole we scanned the laser over 1.2 GHz in 500 μs and measured the transmitted light with a photo detector.

The frequency shift of the spectral hole, relative to the zero field position, as a function of electric field is plotted in Fig. 6. The line is a linear fit to the data which passes through the point (0, 0). The dipole moment difference can be calculated from the slope of the line according to Eq. (3). We find an effective dipole moment difference $(\Delta\mu_e\ \chi)/(h)=25\ \pm1$kHz/(V cm^{-1}). The inset in Fig. 6 shows the position of the spectral hole measured after switching off the electric field for each applied field; the spectral hole returns to the initial zero field position. This, plus the opposite directional shifts that were observed with positive and negative voltages, confirms the reversibility of the Stark effect.

Conclusions

Our findings show that the relative phase and amplitude ratio of data pulses can be preserved during storage in the optical memory, and that storage can be combined with projection measurments, as required in quantum communication and computation schemes. While this result is based on experiments with classical pulses containing many photons, we expect that it can be extended to a more efficient approach to storage based on CRIB. Furthermore, we demonstrated the possibility to use the dc-Stark effect for controlled inhomogeneous broadening, which is key to quantum state storage based on CRIB. While more work is required, in particular concerning the preparation of a single, isolated absorption line on a non-absorbing background, our findings demonstrate the potential of Er:$LiNbO_3$ waveguides for quantum state storage compatible with the requirements of a telecommunication (quantum) network.

Acknowledgments

We gratefully acknowledge support by, or discussions with, C. Barreiro, J.-D. Gauthier, D. Jaccard, and M. Nilsson. This work was supported by the Swiss NCCR Quantum Photonics and the European Commission's Integrated Project Qubit Applications (QAP), Contract Number 015848. M.A. acknowledges financial support from the Swedish Research Council, and W. T. by iCORE and General Dynamics Canada.

References

1 N. Gisin, G. Ribordy, W. Tittel, and H. Zbinden, Rev. Mod. Phys. **74**, 145 (2002).

2 H.J. Briege, W. Dürr, J.I. Cirac, and P. Zoller, Phys. Rev. Lett. **81**, 5932 (1998) .

3 B. Juulsgard *et al*., Nature **432**, 482 (2004), T. Chanelière *et al*., Nature **438**, 833 (2005), M.D. Eisaman *et al*., Nature **438**, 837 (2005).

4 M. Nilsson and S. Kröll, Optics Communications **247**, 393 (2005), B. Kraus *et al*, Phys. Rev. A **73**, 020302(R), A. Alexander *et al*, Phys. Rev. Lett. **96**, 043602 (2006), N. Sanguard *et al*., quant-ph/0611165.

5 T. Böttger, C.W. Thiel, Y. Sun, and R.L. Cone, Phys. Rev. B **73**, 075101 (2006).

6 T.W. Mossberg, Opt. Lett. 7, **77** (1982), M. Mitsunaga, Opt.and Quant. Electr. **25**, 1137 (1992), M. Staudt *et al*., quant-ph/0609201 (to be published in Phys. Rev. Lett).

7 S. Hastings-Simon *et al*, Opt. Comm. **266**, 716 (2006).

8 This simplified picture of a population grating is sufficient to describe our experiment, although remaining atomic coherences were a source of additional 2-pulse echoes. However, these echoes appear at different times compared to the 3PE and could be discarded via time-resolved detection.

9 T. Wang, C. Greiner, J. R. Bochinski, and T. W. Mossberg, Phys. Rev. A **60**, 757 (R) (1999).

10 J. Brendel, N. Gisin, W. Tittel, and H. Zbinden, Phys. Rev. Lett. **82**, 2594 (1999), W. Tittel and G. Weihs, Quant. Inf. Comp. **1**, 3 (2001).

11 Y. Sun et al, J. Lumin. **98**, 281 (2002).

12 I. Baumann *et al*., Appl. Phys. A **164**, 33 (1997) .

13 C.H. Bennett and G. Brassard, in Proceedings of the IEEE International Conference on Computers, Systems and Signal Processing, Bangalore, India (IEEE, New York, 1984), p. 175.

14 K. Polgar, A.P. Skvortsov, Opt. Spectrosc. (USA) **58**, 140 (1985), A. Skvortsov, K. Polgar, L. Jastrabik, Radiat. Eff. Defect. Solid. **150**, 287 (1999).

Generation of Polarization-Entangled Twin Photons by Type-II QPM Waveguide NLO Device

Toshiaki Suhara, Hiroaki Okabe and Masatoshi Fujimura
Department of Electrical, Electronic and Information Engineering, Graduate School of Engineering,
Osaka University suhara@eei.eng.osaka-u.ac.jp

Abstract: *A cross-polarized twin photon generation device was implemented with Ti-indiffused $LiNbO_3$ waveguides and domain-inverted gratings for Type-II (TE→TE+TM) quasi-phase matching. Generation of polarization-entangled twin-photon beams by a simple system using the fabricated device is demonstrated through quantum interference and photon polarization measurement experiments.*

Introduction

There has been increasing research interest in quasi-phase-matched (QPM) waveguide nonlinear-optic (NLO) devices for applications to quantum information processing[1-6]. An important element for quantum information technique is twin photons including photons of quantum entangled states, which offer a variety of possibilities such as quantum teleportation, quantum cryptography and quantum interface[7]. The authors are working on theoretical[8,9] and experimental[10,11] studies of waveguide QPM-NLO twin photon generation devices. Recently, we demonstrated implementation of a waveguide cross-polarized twin photon generation device based upon the Type-II QPM in a $LiNbO_3$ waveguide[11]. Cross-polarized twin photons can easily be split into each photon by a polarization beam splitter without loss and spurious photon.

In this paper, we demonstrate generation of polarization entangled states by the Type-II QPM waveguide NLO device, and report the results of quantum interference experiments.

Type-II QPM waveguide NLO device

The Type-II QPM waveguide twin photon generation device configuration is shown in Fig.1. The device consists of a channel waveguide and a ferroelectric domain-inverted grating for QPM in a z-cut $LiNbO_3$ crystal. Twin photon generation is based on parametric fluorescence due to the NLO tensor element $d_{24}(=d_{31})$, and the phase matching is accomplished by the Type-II (TE→TE+TM) QPM. As annealed proton-exchanged waveguides often used for NLO devices support the extraordinary mode only, a Ti-indiffused waveguide capable of guiding both polarization modes was adopted in this work. Devices of the interaction length L=30mm and the QPM grating periods around Λ=9.2μm were fabricated for generation of (nearly-) wavelength-degenerate twin photons in the 1.55μm band.

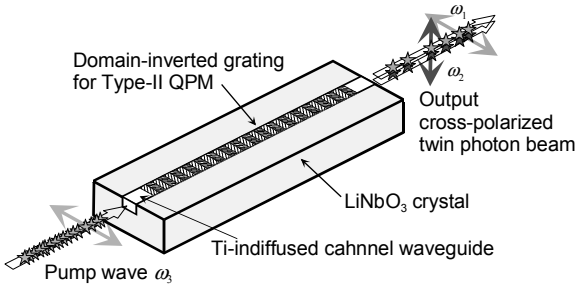


Fig. 1: Configuration of Type-II QPM waveguide NLO cross-polarized twin photon generation device.

The fabrication process was presented in detail in ref.11. At first Ti film of thickenss~100nm of stripe pattern with 7.0μm width was deposited on the $-z$ surface of a congruent $LiNbO_3$ crystal of 0.5mm thickness. The Ti film was indiffused by heat treatment at 1060°C for 7.5h, to obtain single-mode (at λ~1.55μm) channel waveguides. Then the unwanted domain-inverted layer induced on the $+z$ surface was removed by polishing to enable the QPM grating formation[12]. The QPM grating was then fabricated by two steps: uniform domain inversion over the whole crystal was first made to have the waveguides on the new $+z$ surface, and then a domain-inverted grating was formed by applying a voltage pulse (~9kV) through a periodic electrode.

Generation of cross-polarized twin photons

The basic characteristics of cross-polarized twin

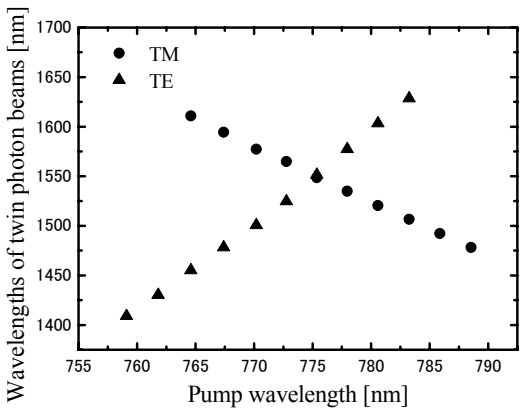


Fig. 2: Measured dependence of the twin-photon wavelengths on the pump wavelength.

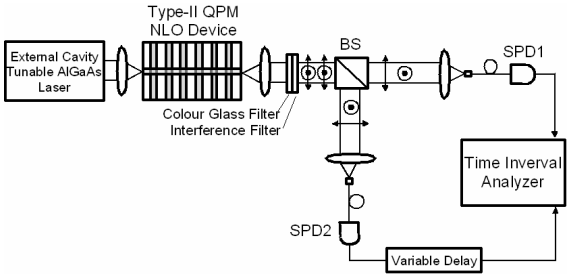


Fig. 3: Setup for measuring the time correlation of the cross-polarized twin photons.

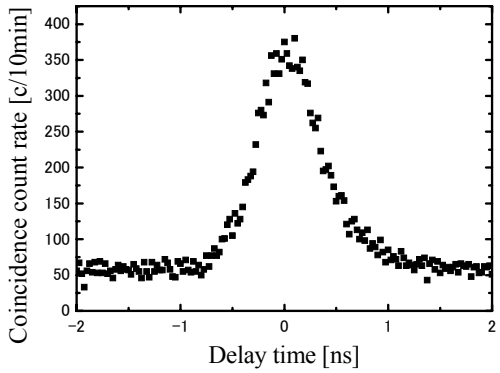


Fig. 4: Correlation of the cross-polarized twin photons.

photon generation were examined by using an external-cavity tunable AlGaAs laser as a pump source. The pump TE mode was excited by end-fire coupling, and the transmitted pump wave was cut by colour-glass and interference filters. Figure 2 shows the dependence of the twin photon wavelengths upon the pump wavelength, measured at room temperature for a typical device of a QPM grating period Λ=9.1μm. The result agrees well with the prediction[8,11] calculated by approximating the mode indexes with ordinary and extraordinary indexes of congruent bulk $LiNbO_3$ crystal. There was an evidence of slight drift of the wavelength-degenerate point due to the photorefractive damage. Therefore, the further experiments were carried out with the device temperature maintained at 90±0.1˚C. At this temperature, the wavelength-degenerate twin photons of wavelength $\lambda_1=\lambda_2$=1559.8nm were generated in a device of a QPM grating period Λ=9.3μm pumped at wavelength λ_3=779.9nm.

The wavelength bandwidths (FWHM) of the degenerate twin-photons, measured by using a monochromator of 0.9nm resolution, were 1.7nm and 1.8nm for the TE and TM photons, respectively, which were consistent with the theoretical prediction of 1.0nm for both polarizations. The output powers P_1, P_2 of the twin beams, separated by a polarization beam splitter, were measured using InGaAs PIN photodiodes and a lock-in amplifier, and the pump power P_3 was measured at the waveguide output end. The twin photon generation efficiency were $P_1/P_3=1.9\times10^{-10}$ for TE photons and $P_2/P_3=2.3\times10^{-10}$ for TM photons, which were of the same order of magnitude as $P_1/P_3=P_2/P_3=5.3\times10^{-10}$, theoretically predicted[8] by using the coupling coefficient $\kappa_3=0.12\mathrm{W}^{-1/2}\mathrm{cm}^{-1}$ determined from the result $\eta_{SHG}=\kappa_3^2L^2=13\%/\mathrm{W}$ of a Type-II QPM second-harmonic generation efficiency measurement.

The time correlation of the generated twin photons was examined by separating the QPM device output into two beams and detecting them by two single photon detectors (SPD's) using Giger-mode InGaAs/InP APDs and analyzing the photon detection signal by using a time interval analyzer (TIA), as shown in Fig.3. The obtained histogram of the coincidence counting rate dependent on the delay time is shown in Fig.4. The result clearly indicates the photon correlation peak at zero delay time with the resolution~1ns reflecting the jitter of the SPD and the TIA.

Generation of polarization entangled states

Theoretical description:

The wavelength-degenerate twin photon beams generated by the Type-II QPM NLO device can readily be converted into polarization-entangled twin photons by splitting the output beam into two beams by using a beam splitter (BS).

Although the multi-mode-pair model must be used for full description of the state of the twin photons generated by the parametric fluorescence, in the single-mode-pair model the quantum state of the QPM device output may simply be described as[8]

$$|\psi\rangle\approx|0\rangle+r|\mathrm{H,V}\rangle, \quad (1)$$

where $|0\rangle$ denotes the vacuum state, and $|\mathrm{H,V}\rangle$ the state of twin photons consisting of a horizontally (H) polarized photon and a vertically (V) polarized photon, and r is a constant depending upon the pump power, the device parameters and the deviation from the exact QPM condition. The output twin photon power is calculated by integrating $|r|^2$ over the QPM bandwidth[8,9]. By omitting the vacuum state term which has no effect on the photon detection and renormalizing the state, the output quantum state can be represented simply by $|\mathrm{H,V}\rangle$.

Consider a beam splitter (BS) of a polarization independent power splitting ratio of 1:1. The amplitude operators for the horizontal (x) and vertical (y) components of the fields in the output ports 1 and 2, a_{1x}, a_{2x}, a_{1y}, a_{2y}, can be correlated with those for the input ports 1 and 2, $a_{\mathrm{in}1x}$, $a_{\mathrm{in}2x}$, $a_{\mathrm{in}1y}$, $a_{\mathrm{in}2y}$, by

$$a_{1x}=\sqrt{1/2}\,(a_{\mathrm{in}1x}+ia_{\mathrm{in}2x}),\ a_{2x}=\sqrt{1/2}\,(ia_{\mathrm{in}1x}+a_{\mathrm{in}2x}), \quad (2a)$$

$$a_{1y}=\sqrt{1/2}\,(a_{\mathrm{in}1y}-ia_{\mathrm{in}2y}),\ a_{2y}=\sqrt{1/2}\,(-ia_{\mathrm{in}1y}+a_{\mathrm{in}2y}). \quad (2b)$$

The state generated by the QPM-NLO device and fed into the BS input port 1 can be written as

$$|\psi\rangle=|\mathrm{H,V}\rangle=a_{\mathrm{in}1x}^{\dagger}a_{\mathrm{in}1y}^{\dagger}|0\rangle, \quad (3)$$

where $a_{\mathrm{in}1x}^{\dagger}$ and $a_{\mathrm{in}1y}^{\dagger}$ are the creation operators. Therefore, the state in the BS output ports is

$$\begin{aligned}|\psi\rangle&=a_{\mathrm{in}1x}^{\dagger}a_{\mathrm{in}1y}^{\dagger}|0\rangle\\&=(1/2)(a_{1x}^{\dagger}+ia_{2x}^{\dagger})(a_{1y}^{\dagger}-ia_{2y}^{\dagger})|0\rangle\\&=(1/2)\{|xy;0\rangle-i|x;y\rangle+i|y;x\rangle+|0;xy\rangle\}. \quad (4)\end{aligned}$$

The states where the cross-polarized twin photon appears together in output port 1 or 2, denoted by $|xy;0\rangle$ and $|0;xy\rangle$, can be omitted since they do not affect the photon coincidence counting. Then after renormalization, we have

$$|\psi\rangle=\sqrt{1/2}\ \{|x;y\rangle-|y;x\rangle\}$$
$$=\sqrt{1/2}\ \{|\mathrm{H};\mathrm{V}\rangle-|\mathrm{V};\mathrm{H}\rangle\}, \quad (5)$$

where $|x;y\rangle=|\mathrm{H};\mathrm{V}\rangle$ denotes the state where a horizontally-(*x*-)polarized photon appears in the output port 1 and a vertically-(*y*-)polarized photon appears in the output port 2, and $|y;x\rangle=|\mathrm{V};\mathrm{H}\rangle$ the state where a vertically-(*y*-)polarized photon appears in the output port 1 and a horizontally-(*x*-)polarized photon appears in the output port 2.

If a polarization-selective phase shifter, which gives a differential phase shift $\Delta\Phi$ to the vertically-polarized component only, is inserted in the output port 1, the output state is given by

$$|\psi\rangle=\sqrt{1/2}\ \{|\mathrm{H};\mathrm{V}\rangle-\exp(i\Delta\Phi)|\mathrm{V};\mathrm{H}\rangle\}. \quad (6)$$

Thus the two of the four maximally-entangled Bell states, $|\psi^{+}\rangle$ and $|\psi^{-}\rangle$, can be generated by setting as $\Delta\Phi=\pi$ and $\Delta\Phi=0$ respectively. The time lag between the V and H photons due to the difference in the transit time in the $LiNbO_3$ waveguide QPM-NLO device can be compensated for by inserting a $LiNbO_3$ crystal (quantum eraser) of a length $L/2$, corresponding to the half of QPM-NLO device, with the crystallographic orientation 90° rotated with respect to that of the QPM-NLO device[8,13].

Generation of the entangled states can be examined by a photon coincidence counting experiment with polarizers inserted with the axis oriented at 45° angle in the two output ports of the BS (see Fig.5). Let *XY* be coordinate axes rotated 45° with respect to the *xy* axes (HV axes) for each output port. Then, using the relation between the amplitude operators for the *x* and *y* components, and *X* and *Y* components, we can rewrite (6) into an expression in *XY* basis. Omitting the terms which do not affect the coincidence detection, we obtain an expression for the terms which give rise to the coincidence detection through the 45° polarizers

$$|\psi\rangle=(1/2)^{3/2}\{1-\exp(i\Delta\Phi)\}|X;X\rangle. \quad (7)$$

Therefore, it is expected that, when $\Delta\Phi$ is changed, intensity interference of the photons, characterized by the modulation of the coincidence counting rate in proportion to $|1-\exp(i\Delta\Phi)|^2$, is observed as a result of the interference of the two terms of the rhs of (6).

Experiment:

Figure 5 shows the experimental setup for the entangled state generation and the photon intensity interference measurement. The output of the QPM-NLO device was split into two beams by a BS. Colour-glass and interference filters were inserted to cut the pump wave, and a tunable filter of 0.9nm FWHM bandwidth was inserted to transmit the wavelength-degenerate twin photons. As the quantum erasers, $LiNbO_3$ crystals of a length of $L/2$ =15mm were inserted in both output ports of the BS

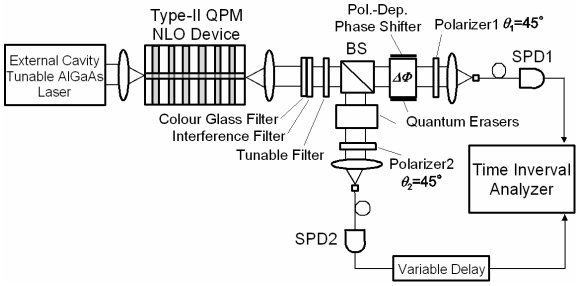


Fig. 5: Setup for polarization entangled state generation and measurement.

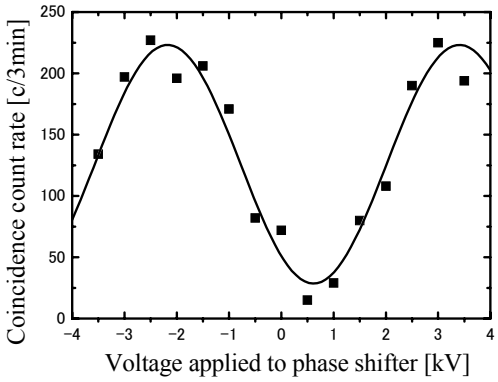


Fig. 6: Experimentally observed photon intensity interference.

with 90°-rotated orientation. Planar electrodes were attached to the *z* faces of one of the quantum eraser crystals, and DC voltage was applied to them to use the crystal also as an electrooptic polarization-dependent phase shifter for giving $\Delta\Phi$. The half wavelength voltage was V_π=2.8kV. Photon coincidence counting was performed through 45° polarizers for BS outputs by using two SPDs and a TIA. The pump wavelength was carefully adjusted to the wavelength-degenerate point, by monitoring the dependence of the photon counts on the filter tuning.

Figure 6 shows the measured coincidence counting rate (for time window of 2ns) dependent upon the voltage applied to the phase shifter. The accidental coincidence counting rate (smaller than 10% of the maximum coincidence counting rate) was subtracted from the measured rate. Clear periodic modulation in the coincidence counting rate with a period of 5.6kV (=$2V_\pi$), consistent with the theoretical prediction, was observed. The obtained modulation visibility was V=0.87. Similar quantum interference was observed even when the tunable filter of 0.9nm bandwidth was removed, although the visibility slightly degraded to V~0.6. These results indicate that the polarization entangled states of (6) were generated.

Entangled photon polarization measurement

It can readily be shown that the polarization entangled state given by (5) is invariant with respect to rotation of the polarization measurement basis.

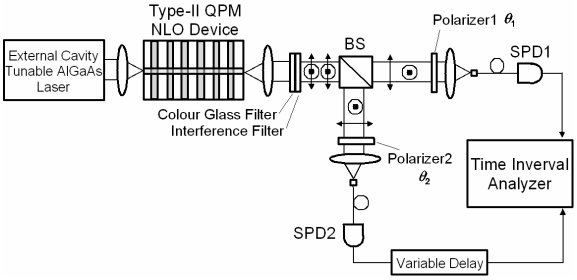


Fig. 7: Setup for twin photon polarization measurement.

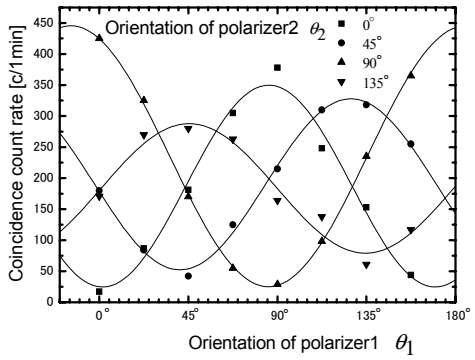


Fig. 8: Coincidence count rate dependent on polarizer orientation.

Let XY be basis axes rotated by an angle θ with respect to the xy (HV) basis axes. Then the invariance can be described as

$$|\psi\rangle=\sqrt{1/2}\ \{|x,y\rangle-|y,x\rangle\}$$
$$=\sqrt{1/2}\ \{|X,Y\rangle-|Y,X\rangle\}, \quad (8)$$

and it reflects the non-deterministic and non-local nature of the polarizations of entangled photons. Such a nature can be examined by a polarization-selective photon coincident counting experiment. Let θ_1 and θ_2 be the angles of the basis rotation for the output port 1 and 2, respectively. Then a simple theoretical calculation for the state (8) shows that the rate of coincidence counting for X polarized photons in each port is proportional to

$$P_{XX}=\langle\psi|a_{1X}^{\dagger}a_{2X}^{\dagger}a_{2X}a_{1X}|\psi\rangle=(1/2)\sin^2(\theta_1-\theta_2). \quad (9)$$

Figure 7 shows the setup for the polarization-selective photon coincident counting experiment. Polarizers were inserted in front of the two SPDs, and the coincidence counting rate (for time window of 2ns) was measured by using a TIA. Figure 8 shows the measured dependence of the coincidence counting rate on the orientation θ_1 of the polarizer 1 for a few fixed angles θ_2 of the polarizer 2. The result shows the periodic modulations consistent with the theoretical prediction given by (9), although the modulation visibility is not same for different θ_2. The deviation of the experimental result from (9) would be due to the difference in the detector quantum efficiency and optical coupling efficiency between the output port 1 and 2, and the spurious reflection at the quantum eraser crystal surfaces. The result, however, clearly demonstrates the non-deterministic and non-local nature of the polarizations of entangled photons, since the result can not be explained by the classic model.

Conclusion

We demonstrated generation of polarization entangled twin photon beams in a simple and efficient system using a Type-II QPM waveguide NLO device. Future work includes solution of the photorefractive-damage problem using $MgO:LiNbO_3$ crystal, and demonstration of the violation of the Bell's inequality.

Acknowledgments

This work was supported by Grant-In-Aid for Scientific Research on Priority Areas from Ministry of Education, Culture, Sports, Science and Technology (MEXT).

References

1 K.Sanaka, K.Kawahara and T.Kuga, Phys. Rev. Lett., vol.86, no.24, pp.5620-5623, 2001.

2 S.Tanzilli, W.Tittel, H.De Riedmatten, H.Zbinden, P. Baldi, M.De Micheli, D.B.Ostrowsky and N.Gisin, Eur. Phys. J. D, vol.18, pp.155-160, 2002.

3 T.Suhara, Europ. Conf. Integrated Optics (ECIO'03), Prague, April 1-4, ThP1, pp.73-84, 2003.

4 T.Suhara and M.Fujimura, *Waveguide Nonlinear-Optic Devices*, Springer, 2003.

5 A.Yoshizawa, R.Kaji and H.Tsuchida, Electron. Lett., vol.39, no.7, pp.621-622, 2003.

6 S.Tanzilli, W.Tittel, M.Halder, O.Alibart, P.Baldi, N.Gisin and H.Zbinden, Nature, 437, pp.116-120, 2005.

7 D.Bouwmeester, A.Ekert , and A.Zeilinger, Eds., *The Physics of Quantum Information.* Springer, 2000.

8 T.Suhara and H.Kintaka, IEEE J. Quantum Electron., vol.41, pp.1203-1212, 2005.

9 T.Suhara and T.Nosaka, IEEE J. Quantum Electron., vol.42, pp.777-784, 2006.

10 H.Kintaka and T.Suhara, Jpn. J. Appl. Phys., vol.43, no.5A, pp.2545-2546, 2004.

11 T.Nosaka, B.K.Das, M.Fujimura and T.Suhara, IEEE Photon. Tech. Lett., vol.18, pp.124-126, 2006.

12 D.Hofmann, G.Schreiber, C.Haase, H.Herman, W.Grundkotter, R.Rcken and W.Sohler, Opt. Lett., vol.24, no.13, pp.896-898, 1999.

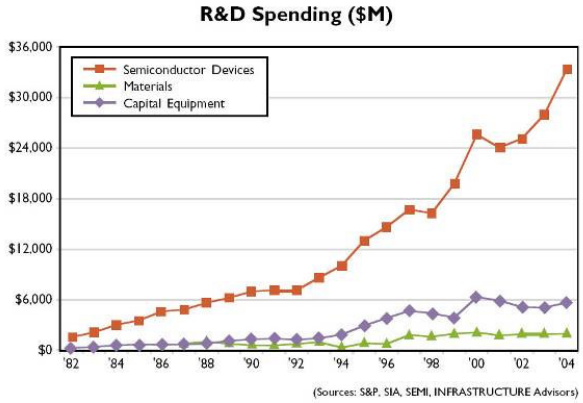
13 Y.Shih, IEEE J. Selected Topics Quantum Electron., vol.9, no.6, pp.1455-1467, 2003.

Trends in Silicon Photonics

T.L. Koch
Center for Optical Technologies, Lehigh University, Bethlehem, PA Email: tlkoch@lehigh.edu

Abstract: *Silicon photonics offers a compelling manufacturing and design platform to address today's imperatives for reducing the size, power, and cost of optical solutions. In addition to applications in telecom, the ability to provide low-cost photonics with integrated electronics may be enabling to many new applications in sensors and signal processing. This talk explores progress and potential in leveraging massive world-wide investments in silicon R&D into photonics applications, and examines outstanding challenges..*

As mainstream CMOS technology contemplates 450mm wafers and ever-smaller feature sizes, the requisite R&D expenditures for process technology provide major challenges for silicon chip vendors. However, as seen in Fig. 1, even in 2004 the R&D expenditures for the silicon devices, materials and capital equipment exceeded $40B annually.



© R. Leckie, Infrastructure Advisors – for download of white paper, see http://www.infras-advisors.com/whitepaper.html

Figure 1. Annual R&D spend for devices, materials, and capital equipment in the silicon microelectronics industry. Even back in 2004 this had reached a level of over $41B per year.

These investments offer an enticing opportunity for leveraging into photonics applications and markets. Key elements include (a) unprecedented film dimensional and compositional uniformity and reproducibility, (b) ultra-high resolution production lithography, (c) precision etch technology, and (d) exotic multi-layer metallization and other auxiallary features. These are all achieved without substantial optics-specific R&D, and immediately provide a pathway to high-volume manufacturing if designs can be realized that are compatible with mainstream electronics processing. From an optics perspective, silicon-on-insulator (SOI) in particular provides many attractive design attributes for photonic circuits. Inherent physical benefits include a very high index contrast, enabling ultra-small bend radius index-guided circuits and devices[1], and a variety of high-performance photonic crystal concepts[2]. Examples of this are illustrated in Fig. 2 and Fig. 3 below, showing the work of Vlasov and co-workers at IBM[1].

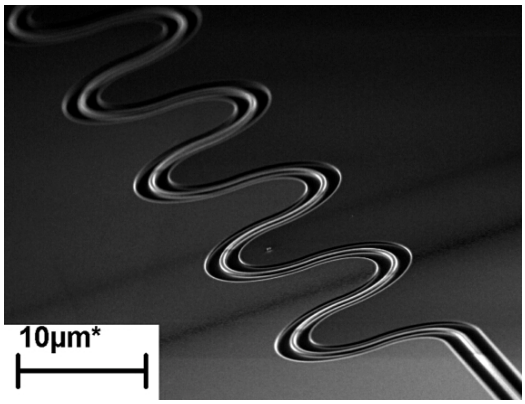


Figure 2. Figure 2. Demonstration of negligible bending losses in ultra-tight confinement SOI waveguides. Losses of 0.0043dB per turn were measured through a sequence of 200 turns with 6 μm radius[1].

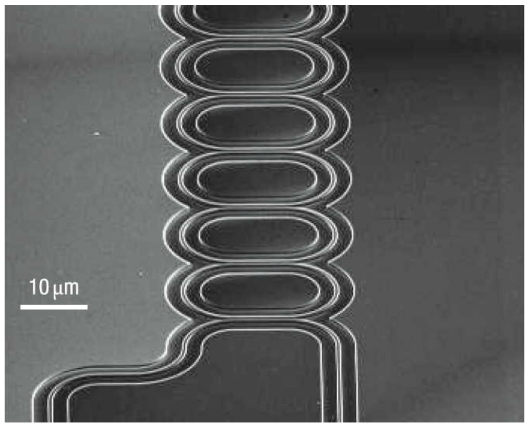


Figure 3. Ultracompact cascaded-ring slow-wave structure enabled by low-loss high-index contrast waveguide technology[1].

While silicon has historically not been viewed as a high-performance *active* optical material, recent work has now demonstrated that devices based upon plasma index mechanisms[3] can be quite efficient in field-effect configurations, effectively bypassing the previous bandwidth limitations of thermo-optic devices or forward-injection designs. Two designs have been explored, with results presented in the literature and recented conferences, and are

illustrated schematically below. The first utilizes reverse-biased P-N junctions, sweeping carriers in and out of the optical mode as the depletion region is minimized and maximized, while the second utilizes carrier accumulation (or depletion) in FET channels, which can be viewed simply as charge build-up at the gate oxide.

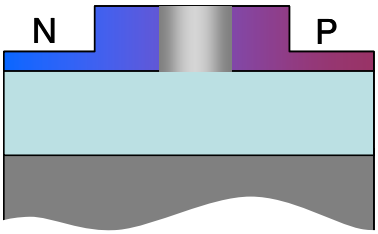


Fig. 4. Lateral P-N junction depletion-based modulator concept.

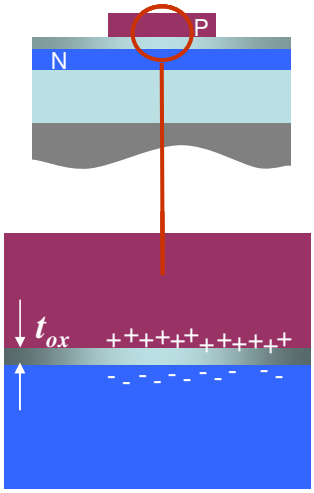


Fig. 5. Carrier accumulation at gate oxide.

Recent results on optical modulators include mm-scale Mach-Zehnder configurations from Intel[7] and Luxtera[6] with 10 Gb/s performance, and even 20 Gb/s devices from SiOptical[8]. With proper device design these modulators can be further reduced in size, but another path to small-area designs is through resonant enhancement[9]. Fig. 6 below shows an example of a highly compact ring configuration from Luxtera with sufficient modulation bandwidth for 10 Gb/s operation, while Fig. 7 illustrates a 20Gb/s Mach-Zehnder result from SiOptical, Inc.

Another promising Si-compatible modulation technology was recently demonstrated using the Quantum-Confined Stark Effect (QCSE) in Ge/SiGe quantum wells on silicon. InGaAsP QCSE electroabsorption modulators are a mainstay of today's telecom industry in the form of integrated laser modulators. As shown in Fig. 8, the performance of the Ge/SiGe device on silicon was comparable with standard InGaAsP designs, suggesting that waveguide modulators with 100 µm scale lengths should be readily achievable.

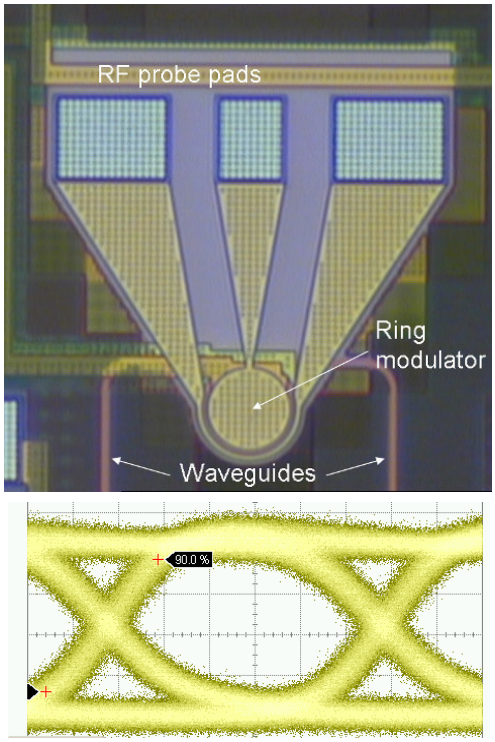


Fig. 6. Top: Compact resonant ring modulator from Luxtera[6] exhibiting open eye diagrams at 10 Gb/s (Bottom)

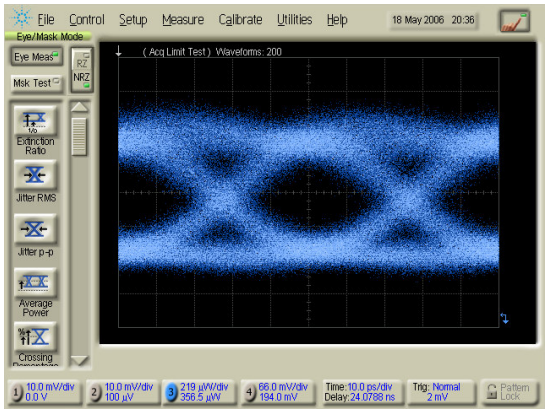


Fig. 7. 20 Gb/s eye diagram from SiOptical Mach-Zehnder modulator

Ge-based detectors, implemented with SiGe VLSI epitaxy technologies, have demonstrated high-performance waveguide designs and suggest that integration of photodetector function is not a major barrier.

The result of these studies is a nearly full suite of active and passive photonics devices that can be implemented with very high density and yield using commercial CMOS foundry technologies, with well-documented low costs per unit wafer area. In

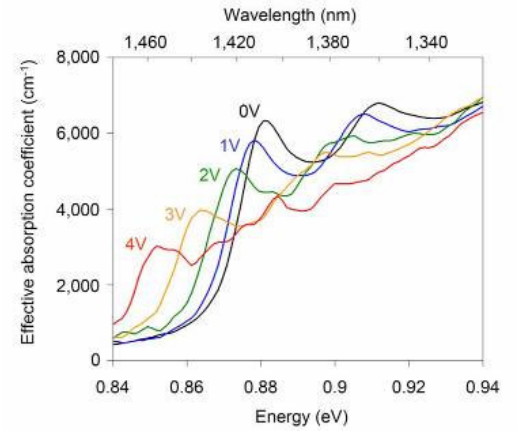


Fig. 8. QCSE modulation in Ge/SiGe quantum wells on silicon[9]

addition to broad progress in the international research community, there has been significant recent acceleration enabled by DARPA's EPIC program[5,6], as well as impressive advances from start-up companies pursuing product development or deployments in concert with major silicon foundry partners.

In addition to low cost, silicon photonics also offers potential for much lower electrical power consumption for optical links and interconnections. This results in part from the inherent voltage scaling that can be achieved through reduced dimensions in field-effect devices. An obvious benefit of designing into a CMOS foundry is the ability to integrate optical functions with standard VLSI circuitry functions on a single silicon chip. For example, Luxtera has demonstrated Mach-Zehnder modulators with integrated on-chip drivers at 10 Gb/s[6]. This integration can improve impedance issues compared to conventional multi-chip configurations for further potential power reduction. This is important especially in high-density array configurations, where additional power savings may be realized through sharing a single laser source for multiple communications ports.

Silicon photonics also offers promise for markets outside of telecom and data links, including sensors and signal processing applications, where the ability to integrate optical functions with advanced preamplification, DSP, and controller functions on a single low-cost chip could be dramatically enabling.

While these applications can and will proceed using off-chip optical sources, one outstanding challenge is a silicon-compatible electrically-pumped laser. This shortcoming will continue to make large-scale InP-based integration dominant for the highest performance core-network WDM-based applications[11]. However, recent progress has been demonstrated in hybrid integration, both in the form of sophisticated flip-chip grating-based coupling of III-V lasers on silicon photonic chips, as well as more intimate wafer-bonded hybrid integration where the laser utilizes a predominantly silicon waveguide. This talk will review recent work towards silicon-compatible lasers, including intrinsic, extrinsic, and hybrid materials technologies.

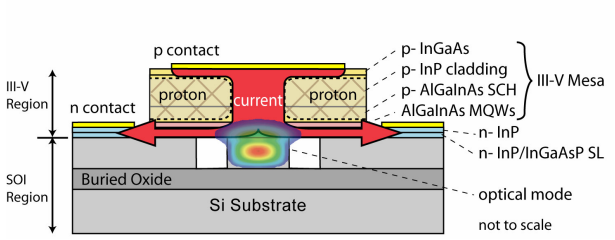


Fig. 9. Hybrid wafer-bonded III-V/Si laser demonstrating room-temperature, CW operation with 1.8 mW of fiber-coupled output power [12]

Acknowledgments

The author would like to thank his colleagues for generously providing figures and data that illustrate their work. The author would also like to acknowledge the support in silicon photonics from NSF National Science Foundation Grant ECS-0335067, Pennsylvania BFTDA Grant ME#21-116- 0014, and the Army Research Laboratory Cooperative Agreement W911NF-04-2-0015.

References:

[1] Y. Vlasov, private communication
[2] Noda et al, Nature, 425 (2003) 905 and also Nature Materials, 4 (2005) 207
[3] R. A. Soref, B. R. Bennett, IEEE J. Quantum Electron. QE-23, January 1987, pp. 123-129.
[4] L. Shares, et al, OFC/NFOEC 2006, Post-Deadline Paper PDP27, Long Beach, March 2006.
[5] L. Kimerling, et al, Paper 6125-2, Photonics West, San Jose, January 2006, *Proceedings of SPIE* Vol. #6125
[6] C. Gunn, Paper 6125-1, Photonics West, San Jose, January 2006, *Proceedings of SPIE* Vol. #6125
[7] L. Liao, et al, Optics Express Vol. 13, No. 8, p.3129 (2005).
[8] SiOptical, Inc. – Private communication
[9] Q. Xu, B. Schmidt, S. Pradhan, M. Lipson, Nature 435, 325-327 (2005).
[10] Y.-H. Kuo, et al, Nature 437**,** 1334-1336 (2005).
[11] R. Nagarajan, C. Joyner, R. Schneider, et al., IEEE JSTQE, Vol. 11, No. 1 (Jan/Feb 2005)
[12] A. Fang, et al, Paper TuC1, 2007 IEEE LEOS Annual Meeting, Montreal

.

Frequency Response of Slow and Fast Light in Integrated Semiconductor Waveguide Amplifiers and Absorbers

Filip Öhman and Jesper Mørk
COM•DTU Department of Communications, Optics & Materials, NanoDTU, Technical University of Denmark, Building 343, DK-2800 Kgs. Lyngby, Denmark, fo@com.dtu.dk.

Abstract: *We have investigated slow and fast light in a semiconductor waveguide device with concatenated gain and absorber sections for applications within microwave photonics. A phase shift of 110 degrees and a true-time delay of 150 ps at GHz-frequencies are demonstrated experimentally and investigated theoretically.*

Introduction

The possibility of controlling the propagation speed of light has received a lot of attention lately [1-11]. The effect has been demonstrated using electromagnetically induced transparency (EIT) in ultracold atomic gases [1] as well as coherent population oscillation (CPO) in a ruby crystal [2] and semiconductor structures [3]-[7]. It has been shown that the slow-down of light in saturable absorbers as used in [3]-[7] can also be described by time-dependent absorption saturation [5], [6]. Slow light effects have been demonstrated both using pulses [1], [6] and sine-modulated signals [2], [4], [5], [7], and are envisioned to have applications within several different areas. One of the more spectacular applications is the possibility to store optical pulses in an all-optical buffer. Theoretical predictions [5], [8], however, point toward a finite delay-bandwidth product for these effects, which limits the number of bits that can be stored to just a few. A less demanding, but very relevant, application is the control of optical microwave signals, where a phase delay of the signal is needed in for example optically fed phased array antennas and optical microwave signal processing [9].

Earlier experiments [5] have demonstrated an electrically and optically controllable delay in a single waveguide electro absorber (EA) at high modulation frequency. The EA acts as a saturable absorber and slow light is achieved by CPO, which in this case can also be described by a time varying absorption induced by the intensity modulated signal [5]. The maximum achievable delay is thus limited by the carrier lifetime, and the large residual absorption in the device further limits the achievable delay and introduces substantial losses to the signal. While the existence of a fundamental limitation in terms of a finite delay-bandwidth product is common for both CPO [5, 8] and EIT [8], the loss-limitation of the CPO effect is a main issue that may limit applications. In order to solve these problems we have recently shown that it is possible to utilize a waveguide device with several alternating sections of semiconductor optical amplifiers (SOA) and electro-absorbers (EA) for enhancing the delay and simultaneously achieving optical gain [7]. This also provides the possibility of independent control of the timing and amplitude of the signal. Furthermore, by concatenating several SOA-EA pairs an increase of the absolute value of the controllable time or phase delay is achieved. While the counteraction of the loss using an amplifier seems a trivial solution, the effect on the delay is not. It has been shown that an SOA introduces an advancement of the phase, corresponding to the effect of fast light [5, 10], thus counteracting the effect of the EA. The achievement of a net, sizable, phase change thus relies on a careful choice of the operating conditions of the SOA and the EA. We show below that this is indeed possible and besides resulting in net gain it also allows control of the amplitude of the output signal. In addition, the waveguide device is very compact and is easily integrated into arrays including a light source, modulator and detectors for a complete optical system. We believe this device structure represents a viable route for the use of slow-light effects for a number of practical applications, such as phased-array antennas and microwave filters, while benefiting from standard semiconductor fabrication technology.

In this paper we compare experimental results with an analytical model and investigate the interplay between the amplifying and absorbing sections, including the frequency dependence and true time delay.

The device and experimental setup

The fabricated device, shown in Fig. 1, employs an optical ridge waveguide structure that is angled 7 degrees relative to the cleaved facets, which are also anti reflection coated to further reduce reflections into the waveguide. The electrode on top of the waveguide is divided into sections. The length of the SOA and EA sections are 545 and 120 μm, respectively. Re-growth has been used to realize different active material in the amplifier and absorber sections, respectively. The amplifiers consist of five 7 nm thick, compressively strained, InGaAsP quantum wells, in a strain compensated structure and the absorbers have fifteen 10 nm thick wells. Experiments are made on two different devices, one as shown in Fig. 1 with two SOA-EA pairs and one device with a single pair.

The experiments are performed by sending a sinusoidal intensity modulated light signal through the device under test and measuring the phase and ampli tude of the modulated signal relative to a reference beam using a network analyzer. The reference beam

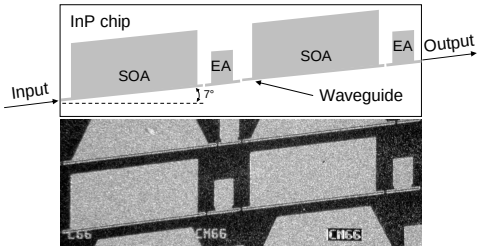


Fig. 1 Photo and schematic of the investigated device. The SOAs and EAs are 545 and 120 µm long, respectively.

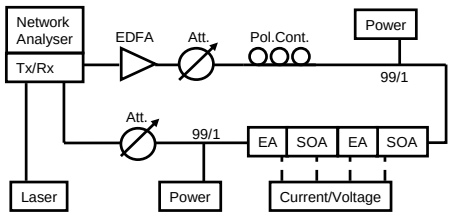


Fig. 2 The experimental setup used in the experiments.

has traversed the same path with the device operated at the desired reference point. For example, the background refractive index can be achived by biasing the device at transparency. The setup is shown in Fig. 2 and more details are given in [5] and [7]. The signal power at the input is controlled by an erbium doped fiber amplifier and a variable attenuator. The devices are not optimized for polarization independent operation and thus a polarization controller is used. The power at the input and output of the device is measured using 1% splitters and power meters.

The model

The model used in this paper for simulating the device is derived by using a wave mixing description [5]. A double-sideband modulated signal, as used in the experiments for validating the model, can be considered as a strong pump signal at the optical carrier angular frequency (ω_0) and a weak probe signal at the modulation sideband $\omega_1 = \omega_0 \pm \Omega$, where Ω is the modulation angular frequency. In order to compare the calculations to experiments the phase change of the modulated signal is calculated using

$$\Delta\varphi_{\mathrm{mod}} = \Omega \Delta t_{\mathrm{mod}} = \Omega \frac{L}{c}\left(\bar{n}_{\mathrm{mod}} - n_{gb}\right), \qquad (1)$$

where L is the length of the section, c is the speed of light in vacuum and n_{gb} is the background group index. The modulation index taking both sidebands into consideration and averaged over the length of the section is [5]

$$\bar{n}_{\mathrm{mod}} = n_{gb} - \frac{c}{L}\frac{1}{\Omega}\mathrm{Arctan}\left\{\frac{\Omega\tau_s (T_{sat}-1)P(0)/P_{sat}}{(\Omega\tau_s)^2 + 1 + (T_{sat}+1)P(0)/P_{sat} + T_{sat}(P(0)/P_{sat})^2}\right\}, \qquad (2)$$

where τ_s is the effective carrier lifetime, P_{sat} is the saturation power and $P(0)$ is the power at the input of the section. The saturated intensity transmission is given by the implicit expression

$$\ln(T_{sat}) + (T_{sat}-1)\frac{P(0)}{P_{sat}} = \Gamma g_0 L, \qquad (3)$$

where g_0 is the unsaturated gain and Γ is the confinement factor.

The parameters for the absorber sections depend on the reverse bias voltage. These effects are accounted for in a phenomenological way by introducing the following dependencies on reverse bias voltage, V:

$$g_0 = -a_V\left(V - V_{on}\right)^2, \qquad (4)$$

$$\tau_s = \tau_{s0}\exp(-V/V_{ref}), \qquad (5)$$

$$P_{sat} = P_{sat,0}\exp(V/V_{ref}), \qquad (6)$$

where a_V, V_{on}, τ_{s0}, $P_{sat,0}$ and V_{ref} are constants. These approximations are only valid for a limited range of reverse bias voltages. The amplifier sections are described by constant g_0, P_{sat} and τ_s, corresponding to a constant bias current.

More details of the model for a single EA section are presented in [5] and for this work we have extended the model to include multiple sections with absorption or gain. The gain sections model is derived using the same general assumptions as for the absorbers and the main difference is the choice of parameter values.

Results

In Fig. 3 the measured frequency response of the phase shift in two SOA-EA pairs is displayed. The reference phase is measured at an EA bias of 0 V, input power of 5.3 dBm and SOA bias current of 120 mA to each section. During the measurement the power and SOA bias is kept constant while the bias voltage to the two absorber sections is varied. An adjustable phase shift relative to the reference of up to 110 degrees is measured around 4 GHz. At higher frequencies the limited response time of the device due to a finite carrier lifetime results in smaller phase shifts. At large reverse bias the net absorption is high and detector noise becomes detrimental to the signal.

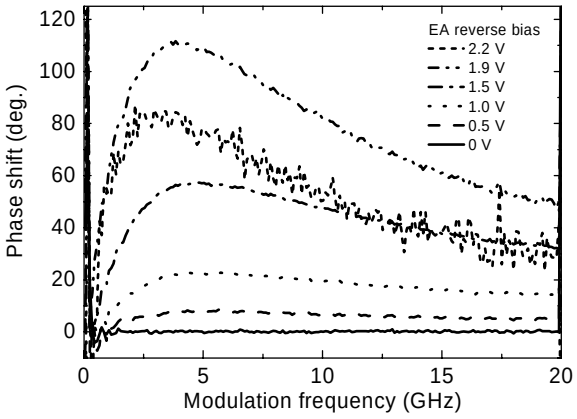


Fig. 3 Measured phase shift for different bias voltages to the two EAs, relative to an EA bias of 0 V. The input power was 5.3 dBm and the bias current 120 mA to each SOA section.

For applications in microwave photonics and in particular phased arrayed antennas it is important to have a phase shift which depends on modulation frequency as $\Delta\phi(\Omega) = \Delta\phi_0\Omega/\Omega_c$ [9], where Ω_c

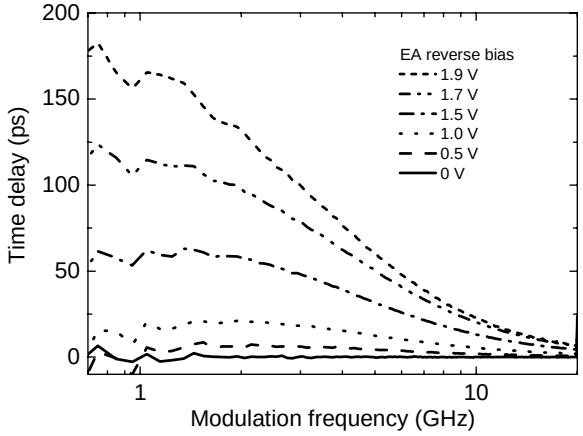


Fig. 4 Measured time delays as function of modulation frequency for different bias voltages to the two EAs.

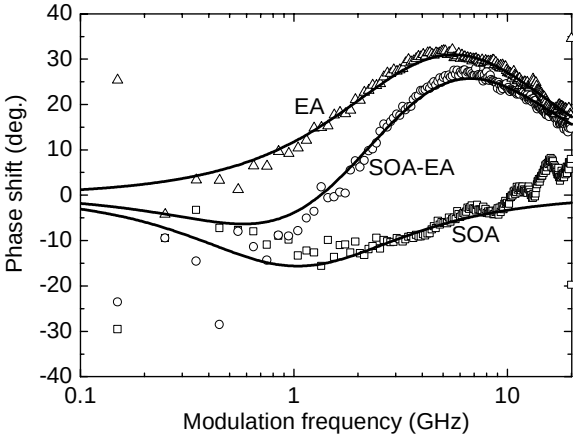


Fig. 5 Measured and calculated phase shift relative the background group index for a SOA-EA pair compared to a single SOA and a single EA. The SOA bias is 120 mA, the EA reverse bias is 0.7 V and the input power is 5.3 dBm.

is the microwave carrier frequency and $\Delta\phi_0$ is the phase shift achieved at this frequency. This translates into a so-called true-time delay which is constant, $\Delta t=\Delta\phi/\Omega$, for the whole signal bandwidth. The true-time delay corresponding to the measured phase shift is plotted in Fig. 4. A maximum time delay of 165 ps is measured at low modulation frequency. The time delay falls off rather quickly with modulation frequency resulting in a bandwidth of a few GHz.

The interplay between the delays in the SOA and the EA in dependence of the modulation frequency is investigated in Fig. 5. The phase shift in one SOA-EA pair as function of modulation frequency is compared to that of an EA section and that of an SOA section. For the measurements on the SOA-EA pair the phase shift is measured with reference to the background group index achieved by biasing the whole device at transparency. When measuring the single SOA the bias to the EA is kept at transparency and the bias to the SOA was 120 mA. When measuring the single EA the reference measurement was made with the SOA biased at 120 mA and the EA at transparency. The input power to the SOA was in all cases 5.3 dBm.

The results in Fig. 5 demonstrate that the gain and absorber sections have opposite responses for the induced microwave phase shift. In the absorber the signal is delayed due to a slowing down of the group velocity, while in the amplifier the group velocity is increased. The two opposite responses can however be separated by utilizing the fact that the fast sweep-out time of the carriers in the EA results in a phase shift that reaches maximum at higher frequencies in the EA than in the SOA, which has a longer carrier lifetime. This combined with an input saturation power in the EA that is lower than the output saturation power of the SOA results in a dominating slow light response from the EA in the component, especially at high frequencies, as seen in Fig. 5.

In the experiments in Fig. 3 the reference is chosen at a high input power, large SOA bias current and zero bias voltage to the EAs. The result is a push-pull effect where the reference is chosen at an operation point where the fast light effect in the SOAs is large and the slow light effect in the EAs is low. As the bias to the EAs is increased the slow light effect is enhanced while the higher absorption leads to lower input power to the second SOA and hence a smaller fast light effect. In total this gives a relative phase shift in the same direction in both EAs and the second SOA, leading to a larger delay relative to the reference. This operation mode also removes the fast light effect at low modulation frequencies, seen in Fig. 5 and results in a constant true-time delay as seen in Fig. 4.

In the model the EA and SOA parameters are chosen to give a good fit of the measured phase shift (Fig. 5) and gain (Fig. 6) of the SOA and EA. The input power to the SOA is 5.3 dBm and coupling losses are estimated to 3 dB. The background group index is n_{gb}=3.4 and for the SOAs Γ=0.065, g_0= 700 cm^{-1}, τ_s= 250 ps and P_{sat}= 7 mW. The EA parameter values are Γ=0.2, a_V= 8.5×10^4 V^{-2}m^{-1}, V_{on}= -0.9 V, V_{ref}= 2 V, τ_{s0}= 110 ps and $P_{sat,0}$= 1.5 mW. The model shows good agreement with the experiments in Fig. 5. However, when calculating the phase shift for the same conditions as in Fig. 3 only a qualitative agreement is achieved, as seen in Fig. 7. The model does not quite reproduce the maximum phase shift obtained experimentally and the maximum phase shift is achieved at a lower bias voltage. Furthermore the model displays a somewhat larger change in the position of the maximum phase shift towards lower modulation frequencies as the bias voltage is increased.

In the model, saturation effects due to the amplified spontaneous emission from the SOAs is not included and neither is the finite reflections at the facets. The model for the EAM is, as mentioned before, based on phenomenological assumptions that do not hold well for large reverse bias, which can be seen in Fig. 6 where the gain of the fitted model is compared to the experiments. At reverse biases of more than about 1 V the quadratic dependence of the absorption on the

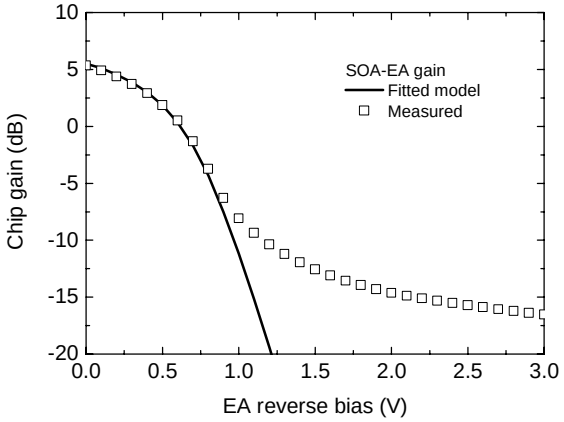


Fig. 6 Measured and calculated chip gain of the SOA-EA device. The SOA bias is 120 mA and the EA reverse bias is 0.7 V.

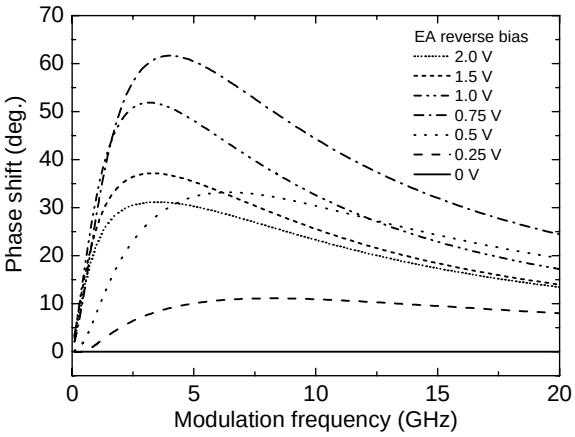


Fig. 7 Calculated phase shift (relative to an EA bias of 0 V) for different values of the bias voltage to the two EAs. The input power was 5.3 dBm.

bias in the EA model results in far too large absorption. This could to some degree account for the discrepancies between the model and experiments. In addition to the absorption, the voltage dependence of the sweep-out time and saturation power could also benefit from a more detailed model and potentially give a better quantitative agreement.

Conclusions

We have performed experiments and developed a theoretical model to investigate the frequency dependence of slow light in a semiconductor wave guide with alternating gain and absorber sections. The model agrees qualitatively with the experimental results but a more detailed model is required for better quantitative agreement. The investigations demonstrate the feasibility of achieving large true-time delay by cascading several sections and operating in a push-pull mode. The use of alternating gain and absorber sections also give the potential for simultaneous control of the modulation amplitude as well as tailoring of the frequency response. The device thus demonstrates good potential for applications within microwave photonics.

Acknowledgments

This work was supported by the Danish Research Council for Technology and Production Sciences.

References

1 L. V. Hau, S. E. Harris, Z. Dutton and C. H. Behroozi, “Light speed reduction to 17 meters per second in an ultracold atomic gas.” Nature 397, 594—598 (1999).

2 M. S. Bigelow, N. N. Lepeshkin and R. W. Boyd, “Observation of ultraslow light propagation in a ruby crystal at room temperature.” Phys. Rev. Lett. 90, 113903-1-4 (2003).

3 J. C. Chang-Hasnain, P.-C. Ku, J. Kim and S.-L. Chuang, “Variable optical buffer using slow-light in semiconductor nanostructures.” Proc. IEEE 91, 1884 (2003).

4 P. Palinginis, S. Crankshaw and F. Sedgwick, “Ultra-slow light (<200 m/s) propagation in a semiconductor nanostructure. Appl. Phys. Lett. 87, 171102 (2005).

5 J. Mørk, R. Kjær, M. van der Poel and K. Yvind, “Slow light in a semiconductor waveguide at gigahertz frequencies.” Opt. Express 13, 8136-8145 (2005).

6 M. v.d. Poel, J. Mørk and J. M. Hvam, “Controllable delay of ultrashort optical pulses in a semiconductor quantum dot amplifier.” Opt. Express 13, 8032-8037 (2005).

7 Filip Öhman, Kresten Yvind, and Jesper Mørk, “Voltage-controlled slow light in an integrated semiconductor structure with net gain”, Opt. Express, Vol. 14, Issue 21, pp. 9955-9962, (2006).

8 R. S. Tucker, P.-C. Ku and C. J. Chang-Hasnain, “Slow-light optical buffers: capabilities and fundamental limitations.” J. Lightwave Technol. B, 4046 (2005).

9 I. Frigyes and A. J. Seeds, “Optically Generated True-Time Delay in Phased-Array Antennas” Trans. Microwave Theory and Techniques, Vol. 43 pp. 2378-2386 (1995).

10 M. S. Bigelow, N. N.Lepeshkin and R. W. Boyd, “Superluminal and Slow Light Propagation in a Room-Temperature Solid.” Science 301, 200-202 (2003).

11 H. Su and S. L. “Chuang Room temperature slow and fast light in quantum-dot semiconductor optical amplifiers” App. Phys. Lett., Vol 88, 061102 (2006)

Realization of Polarization based Integration Scheme (POLIS) for Active and Passive Components

U. Khalique[1], J.J.G.M. van der Tol[1], F. H. Groen[1], F. Karouta[1], P. J. van Veldhoven[1], M.K Smit[1], M. van de Moosdijk[2], W. de Laat[2], K. Simon[2]

[1] COBRA Research Institute, Technische Universiteit Eindhoven,
Postbus 513, 5600 MB Eindhoven, The Netherlands
U.Khalique@tue.nl

[2] ASML De Run 6501, 5504 DR Veldhoven, The Netherlands

Abstact: *Polarization based integration scheme (POLIS) combines active and passive components on the same material, using polarization properties of compressively strained InGaAs/InP quantum wells. A first integrated circuit with detectors, polarization converters and waveguides has been fabricated, characterized and reasonable performances have been observed.*

Introduction

The evolution of information transport over optical networks is one of the drivers behind the upcoming information society. This development results in increasing demand for more complex optical functionality at ever-lower prices. The monolithic integration of these functions in an optical integrated chip (IC) opens the possibility for mass production, which will be able to fulfill this demand.

Essential to the success of mass production of these circuits is a cheap, flexible and efficient integration technique. An optical IC will contain a variety of components, such as optical waveguides, light sources, detectors, optical switches etc. These functions put different requirements on the material system used, e.g. waveguides require transparent materials to keep the attenuation low, while on the other hand detectors need absorption of the light. Several solutions have been proposed and demonstrated to reconcile these conflicting requirements. They all have however the disadvantage that additional processing steps are needed, e.g. applying extra material through a regrowth proces.

Here we report the idea of POLIS (POLarization based Integration Scheme) together with experimental results. It is based on the fact that properties of an optical IC are dependent on the polarization state of the signal. In general this is a severe problem, but here we use it to advantage. It is possible to design a layer structure on a substrate of indium phosphide (InP), which can guide light with one polarization, but absorbs light with the opposite polarization. This creates the possibility to integrate lasers and detectors together with waveguides, switches and demultiplexers on one material. The polarization is in this case a parameter that determines the material properties. Thus instead of changing the material via regrowth, the polarization state of the signal is changed to realize active and passive components. With polarization converters it is possible to obtain the required polarization, transparent or absorbing, in each component of the optical circuit.

Previously we have reported [1] that it is possible to realize active (detectors) and passive (waveguides) components on the same layer stack, with efficient device performance. However to integrate active and passive components an additional component, to rotate one polarization to another, is required. An efficient, short polarization converters on a wafer of indium phosphide has also been realized [2,3,4]. For them TE-TM polarization conversion efficiency was more than 95% and the insertion loss was about 1 dB for entire structure of length 125 μm.

Concept

As mentioned earlier, polarization for TE or TM, is the parameter that defines the active or passive part of the circuit. Therefore transparency for one polarization and absorption for the other is required at the same wavelength. This can be achieved through bandgap modification: strain in the quantum well splits the heavy hole and the light hole in the valence bandedge, and thus the two transitions give absorption at different wavelengths. At a single wavelength one polarization gives absorption while

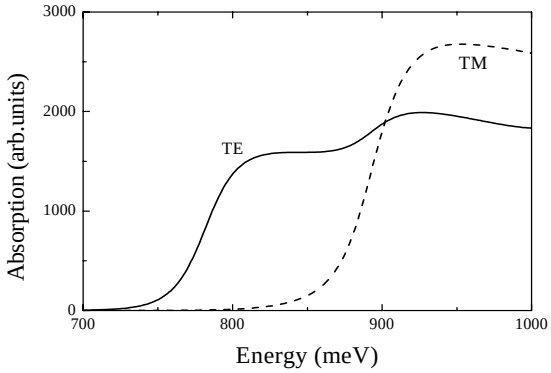


Fig. 1: Calculated absorption spectrum of a 4 nm compressively strained $In_{65}Ga_{35}As$ quantum well with InGaAsP barriers

the other is transparent. Compressive strain, which moves the heavy hole (TE-transition) up in the valence band and light hole (dominantly TM-transition) down, can serve our purpose. For higher strain, the separation between the heavy-hole and light-hole valence bands increases, resulting in an increased wavelength separation between the bandgap for TE and TM polarization. Calculations [5] showed that 4 nm thick $In_{0.65}Ga_{0.35}As$ compressively strained quantum wells have both TE absorption and TM transparency at 1550 nm wavelength as shown in the Fig 1.

Realization

Our material system contains InGaAs compressively strained quantum wells sandwiched between InGaAsP on a semi insulating InP substrate. The designed layer structure consists of a 300 nm $In_{73}Ga_{27}As_{59}P_{0.41}$, a 3 nm compressively stained quantum well of $In_{64}Ga_{36}As$ and again 300 nm $In_{0.73}Ga_{0.27}As_{0.59}P_{0.41}$ as a waveguide layer. The thickness of the quantum well is reduced w.r.t. the calculations, because our first realizations [1] showed POLIS-behaviour at too high wavelengths. A layer of 505 nm InP as a cladding layer and finally a contact layer of 100 nm $In_{0.53}Ga_{0.47}As$ are needed. A layer stack according to this design was grown by MOVPE.

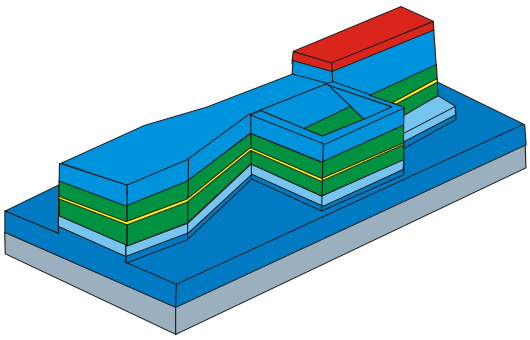
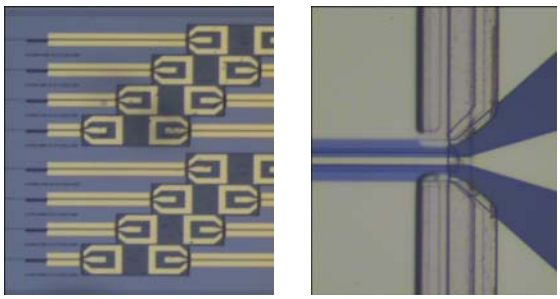


Fig. 2: Integrated waveguide and detector within POLIS (before metal contacts are applied). Form left to right the input waveguide, a taper, the polarization converter (with the sloped side inside a wall that defines the wet etch region) and the detector are shown.

The integrated circuits of input waveguide of 3 μm width, connected to the polarization converter of 0.9 μm width via taper and a small width waveguide of 1.5 μm. Detector is butt coupled to the other end of the polarization converter. Detector with length variations of 250 μm to 2000 μm in steps of 250 μm, for a width of 6 um are implemented. For polarization converter length is 150 um. However highest conversion efficiency of 90% is found for 137 μm. Schematic is shown in Fig. 2.

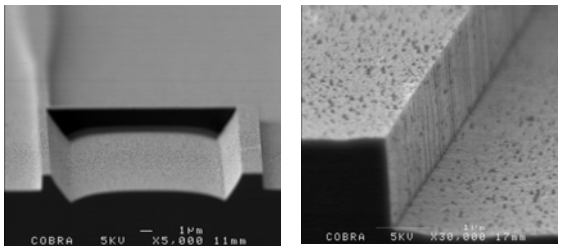
Polarization converter is relatively sensitive to fabrication errors. It needs at least three lithographic steps in order to define the width of the waveguide, then to form the vertical wall and in the end slanted side. The submicron width of the converter with a tolerance of 100 nm is difficult to realize with standard contact optical lithography. Alignment accuracy of protection masks to realize the vertical and slanted sides is also critical. So for these critical exposures high resolution optical lithography was used instead of contact optical lithography. An optical the critical component due 5x reduction wafer stepper is used. It is an ASML PAS5500/100D i-line tool with a variable numerical aperture (NA=0.48-0.60), overlay-accuracy of ≤ 60 nm (99.7% 2-point global alignment) and specified resolution 0.4 μm. Light of wavelength 365 nm is used to expose the wafer through a projection lens. Basically it is a step and repeat system for multiple exposures on four to eight inch wafers. However, we used a quarter of a two-inch wafer. To align and expose on the PAS5500/100D, a special mounting technique is developed. To align the quarters on this system phase grating alignment marks designed by ASML were made with standard optical contact lithography. Detector and waveguides ridges are processed together with the converter.

The vertical wall of the converter, the waveguides and the tapers are deeply etched by reactive ion etching. The slanted wall is realized by non-selective wet chemical etching with bromine methanol. SiN_x and Ti are used as masking materials. Metal pattern for top p-contact and side n-contacts are defined by evaporation and lift off techniques. SiNx is used for passivation of the active structures and for planarization polyimide is used. The top view of these integrated devices are shown in Fig. 3 (a), whereas in (b) the zoom in view of the end of the detector is presented, with 4 μm wide p top contact and 50 μm side n-contacts. Cross- sectional view of converter section and waveguide are shown in Fig. 4.



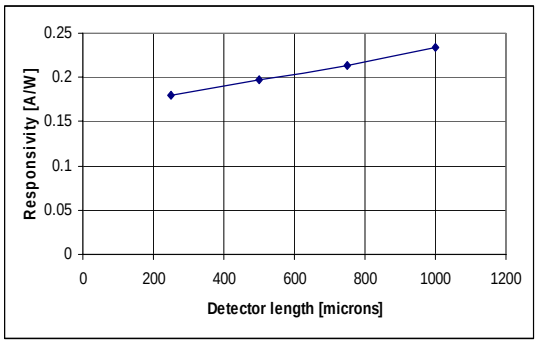
(a) (b)

Fig. 3: Integrated circuits after complete fabrication are shown, from left to right 3 μm input waveguide of 500 μm length, converter section of 150 μm length, then detectors with varying lengths (a), the edge of the detector is shown in (b).



(a) (b)

Fig. 4: Cross sectional of polarization converter (a) and waveguide (b) are shown.



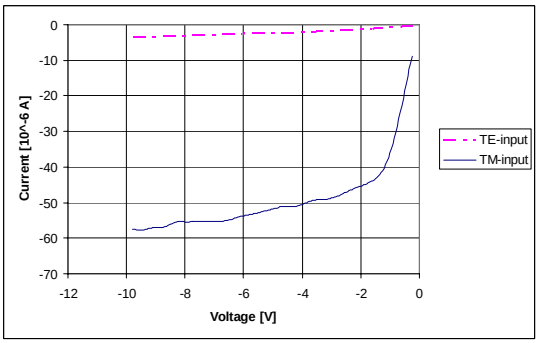


Fig. 5: Experimental results for the integrated waveguide-detector. Top: IV-curve of a 1 mm long detector with -6.1 dBm input power in TE and TM polarization. Bottom: Responsivity as a function of detector length, for TM polarized input power

Results and Discussion

The results are shown in Fig. 6. An external response of 0.234 A/W is measured, corresponding to an external quantum efficiency of 20%. These numbers are uncorrected for coupling losses, around 5 dB, into the waveguide and losses in the structure. Due to an accidental pollution (see fig 4b) high contact resistance was obtained. Therefore not all the photogenerated carriers are collected, as is evident from the linear increase of photocurrent with voltage and with length (which means linear decrease of contact resistance). This implies that much higher responsivities can be expected if both the contact resistance and the coupling losses can be reduced. The dark current is very low, in the order of a few nanoamperes. Because of the high contact resistance high frequency measurements are not relevant. The absorption length is however below 230 μm, which is short enough to allow detection at frequencies above 10 GHz with usual contact resistances. From the response to both the TM- and the TE-input an estimate of the polarization conversion can be made. The polarization converter in this circuit shows around 70% conversion, and the passive waveguide loss is less than 0.5 dB for 1 mm length.

Conclusions

The polarization based integration scheme (POLIS) opens up the possibility to integrate active and passive circuitry without regrowth. It is a simple technique to implement based on the fact that compressively strained quantum well increases the separation between the heavy-hole and light-hole valence bands, resulting in an increased wavelength separation between the bandgap for TE and TM polarization. Experimental results show quite good performance for the first integration of a waveguide with a detector and a compact polarization converter.

Acknowledgement

This work is carried out under the financial support of Dutch Technology Foundation (STW). Special thanks to the technical stuff for their valuable suggestions during the tedious task of processing. Among those are B. Smalbrugge, E.J. Geluk, T. de Vries and K. Sanders.

References

[1] U. Khalique et al., “Polarization based integration scheme (POLIS) for active and passive components”. *Proc. 11th European*

Conference on Integrated Optics, ECIO'03. 1, pp. 137-140.

[2] U. Khalique et al., ``Ultrashort polarization converter on InP/InGaAsP fabricated by optical lithography," in *Technical Digest Integr. Photon. Res. (IPR '05)*. April 2005, p. IWA3, San Diego, USA.

[3] F.H. Groen et al., "Compact polarization converter on InGaAsP/InP using an asymmetrical waveguide ", in Proceedings of the 11th European Conference on Integrated Optics, 2003, pp. 141-144.

[4] Y.C. Zhu et al., “Single-section Polarization Converter on InP/InGaAsP using asymmetrical waveguide”, Benelux IEEE-LEOS symposium, Brussels (Belgium), December 3, 2001, pp. 209-211.

[5] J.J.G.M. van der Tol et al., “A novel polarization based integration technique for photonic circuits: POLIS”, Benelux IEEE-LEOS symposium, Mons (Belgium), November 15, 1999, pp. 139-142.

Comparison of optical passive integrated devices based on three materials for optical clock distribution

B.Han[1], R.Orobtchouk[1], T.Benyattou[1], P.R.A. Binetti[2], S. Jeannot[3], J. M. Fedeli[4], X.J.M. Leijtens[2]

[1]Laboratoire de Physique de la Matière, Institut National des Sciences Appliquées de Lyon,
Bât. Blaise Pascal , 7 avenue Jean Capelle 69621 Villeurbanne cedex
[2]COBRA Research Institute, Technische Universiteit Eindhoven,
Postbus 513, 5600 MB Eindhoven, The Netherlands
[3]STMicroelectronics, 850 rue Jean Monnet, 38921 Crolles, France
[4]CEA-DRT/LETI, 17 rue des Martyrs, 38054 Grenoble Cedex 9, France

Abstract: *We report different passive integrated devices characterization based on three materials (SOI, a-Si:H and SiNx) for the realization of an optical compact link compatible with CMOS technology. The low level of losses obtained on the passive elementary components for the optical link (strip guides, micro bend and MMI beam splitter) shows the feasibility of photonic integration on silicon using amorphous silicon.*

Introduction

With the increasing demand for high frequency operation and the size reduction of the integrated circuits, the ITRS predicts that the evolution of microelectronic technologies will meet important difficulties in the future [1]. One of the major limitations will come from the metallic interconnections due to delay of the signalling and high power consumption. One solution could be the use of optical interconnects for clock signal distributions [2]. First, different approaches used for the integration of an optical link are presented in this paper as well as material issues. The fabrication and measurement of the device are presented. Then, we give the results of the characterizations of the elementary components (strip guides, micro bend and MMI beam splitter). Finally summarize of this study will be done.

Different materials for optical interconnect

The integration of new optical functionality in a microelectronic process must be compatible with CMOS technology, which leads to two possible approaches of integration with specific advantages [3-4]. With the first approach (Frond-end), the passive optical components are fabricated at the same level than the transistors at the beginning of the IC process (figure 1). To meet integrated circuit performance requirements, Silicon-on-Insulator (SOI) substrates are now more and more used in microelectronics industry. It also is a powerful candidate for photonic integrated circuit. SOI is made of a thin silicon layer separated from the silicon substrate by a buried oxide layer (BOX). The large difference of refractive index (~2) between silicon and buried silica makes it possible to guide the light in silicon layer and to reduce the dimension of the integrated optical components to submicronic sizes compatible with the dimensions of the integrated circuits.

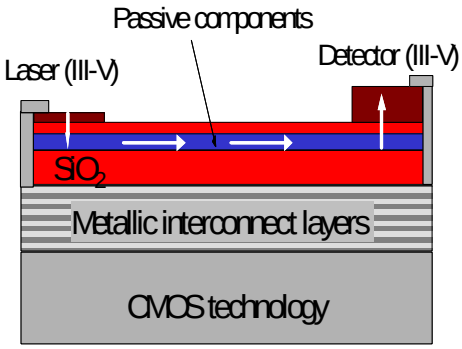


Figure 1 Diagram of integration of an optical link. The optical components are fabricated either on the top of the metal layers (Above IC approach), or at the level of components CMOS (Front end approach).

Using Front-end approach, the realization of various process steps is possible, but it requires an important modification at the level of the electronic design. So an alternative approach (above IC) can be envisioned, which consists in depositing a photonic layer above the integrated circuits at the end of the fabricating process (back end). Among the dielectric materials available in CMOS industry, Silicon nitride has the highest index of refraction that takes a better compromise between the density of the components and the design of the optical distribution. Also, it was grown by Plasma Enhanced Chemical Vapour Deposition (PECVD) at low temperature, that it makes it a good candidate for the integration of an optical link. In addition, in order to improve the compacity further, amorphous silicon (a-Si:H) photonical layer is studied whose index of refraction is larger than that of silicon nitride. The parameters of low temperature (<400°C) PECVD process were optimized to obtain photonic layer having possible higher index of refraction and lower level of losses of propagation losses in the infra-red domain.

Design, fabrication and measurement

Full vectorial mode solver [5] with transparent boundary condition [6] is used to perform the design

of the waveguide. This solver gives the propagation constant of the guided modes and it is also used to calculate the propagation losses due to leakage in silicon substrat. The modelling of 90° microbend is also simulated by Full vectorial mode solver with the conformal mapping method [7] to mimics the curvature of the waveguide. Geometries of the MMI splitters are evaluated by a 2D FDTD method coupled with the effective index method [8]. This method is less consuming in time and memory than a 3D FDTD and leads to the same results as regards with the devices optimization. The 3D FDTD is only used for results validation and for the computation of the losses of the devices.

All components are fabricated at CEA/LETI plan based on a standard CMOS technology with 8" wafer. TEOS was used as a precursor for oxide deposition. We manufactured the components with Deep UV (248nm) lithography and RIE etching (HBr) process for the realization of the strip waveguide. A cap layer of silica is added by PECVD process to encapsulate the optical circuit. An example of realization of strip waveguide of SiNx material is given on figure 2. In order to measure the index of refraction and intrinsic optical guided losses of the materials during process, a prism coupling technique (METRICON) is used. The characteristics of materials are summarized in table 1.

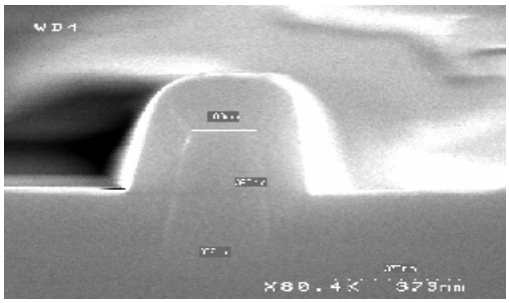


Figure 2 Cross-section of a strip guide of material SiN_x.

	SOI	a-Si:H	SiNx
Index at 1.3µm	3.505	3.4	2.1
Losses (dB/cm)	Non measurable	0.5	0.5

Table 1 The index of refraction and the intrinsic losses of planar waveguide for the 3 different materials that are investigated. The depths of the cord layer are respectively of 200 nm for the SOI and the a-Si:H, and of 400nm for the SiNx.

In order to have the spectral response of the devices in a strip waveguide configuration, light of 4 SLED sources is injected on the test devices by a butt coupling method with a tapered fiber and a linear polariser in line to get TE or TM like polarization. Manual 3D nanoactuators control the fiber alignment. The spectral response is collected by an output tapered fibre coupled with a spectrum analyser. A linear infrared camera is used to observe the light which is diffracted at the rough side wall of the waveguide.

Characterization of the elementary components

In order to evaluate the propagation losses of strip waveguides, as well as the losses of the 90° microbends and the MMI beam splitter for a wavelength range wavelength from 1.25µm to 1.65µm, we study a serie of devices shown in figure 3. They present 2 arms at the output: the first arm being a reference waveguide and the second arm include the elementary component to be studied. The losses measurements are presented in figures 4,5and 6 respectively for the strip waveguide, the microbend and the beam splitter MMI.

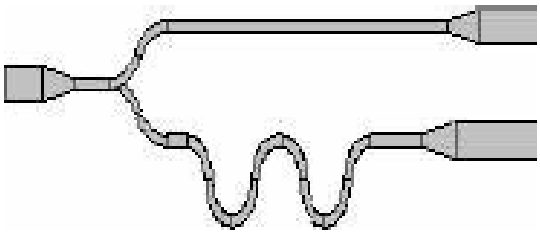


Figure 3 Devices for propagation losses measurements of waveguides and with the testing apparatuses.

For the sake of keeping the single mode condition in the components, we optimize the dimension of waveguide profile to $0.5*0.2\mu m^2$, $0.5*0.2\mu m^2$, $0.8*0.4\mu m^2$ for SOI, a-Si:H, SiNx. The losses at 1.3µm and 1.55µm are summarized in table 2. We report that the SOI and SiNx waveguides have weak losses of 2.9dB/cm and 2.2dB/cm at the wavelength of 1.5µm and 1.3µm respectively, which represents lowest level of propagation losses for strip waveguide encapsulated with PECVD silicon oxide [9] (see figure4). The losses of the a-Si:H waveguide are close to those of SOI crystalline material except for 1.375µm where the curve presents an absorption peak related to the SiOH bond in material. An annealing at low temperature (350°C) in the flow of hydrogen during 6 hours makes it possible to reduce considerably the influence of this absoption peak [10].

	SOI	a-Si:H	SiNx
1.3µm (dB/cm)	5.5	5.5	2.2
1.55µm (dB/cm)	4	4.5	6

Table 2 The propagation losses of strip waveguide for the three different materials at the wavelength of 1.3µm and 1.55µm.

We have tested the 90° microbends with different radii for SOI (2, 5, 10µm), a-Si:H (2, 5, 10µm) and SiNx (10, 15, 30µm). It is well know that the microbend losses decrease when the radius increase.

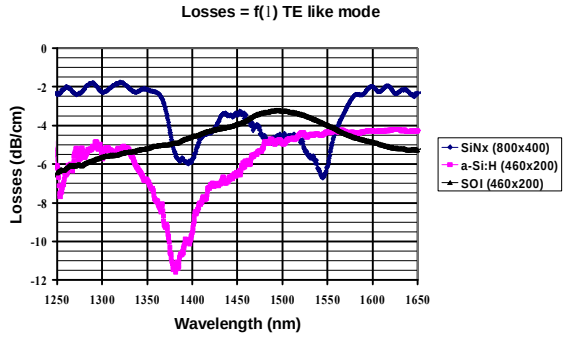


Figure 4 Evolution of the losses versus the wavelength for the strip waveguide.

An upper value of 0.15dB/bend has been taken, leading to a good compromise between the losses and the requirement of integration. We found an optimum radii value of 5µm for SOI and a-Si:H bends, and 15µm for SiNx (see figure5).

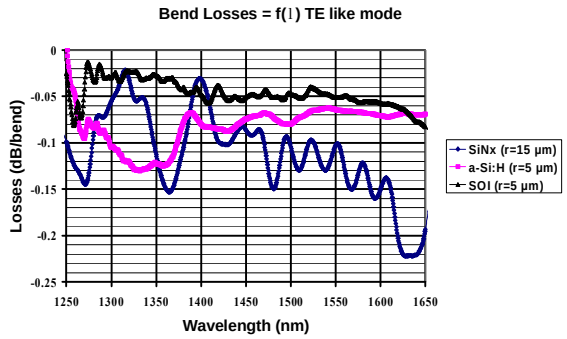


Figure 5 Evolution of the losses versus the wavelength for the microbends.

The characterizations of MMI beam splitter were realized with the same type of test device. The sizes are $2*5.4\mu m^2$ (SOI and a-Si:H) and $2.5*5.5\mu m^2$ (SiNx) and the excessive losses of MMI are 0.2dB, 1.3dB and 0.7dB for SOI, s-Si:H and SiNx respectively at the wavelength 1.3µm that is used for the design. The 3dB spectral ranges are 500nm for the SOI, a-Si:H device and are 250nm for SiNx device.

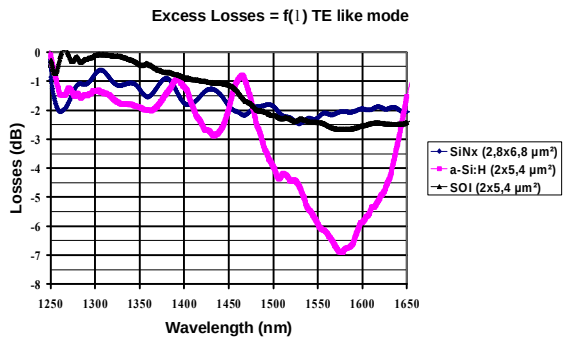


Figure 6 Evolution of the losses versus the wavelength for 1 by 2 MMI beam splitter.

According to the measurement of the elementary components, the passive optical distribution using different materials are realized. An example of a distribution from 1 entry to 8 exit including 7 MMI and 28 microbends for 1cm propagation distance is given on figure 7. The excessive losses for each branch are 6.28dB, 10dB, 4.66dB for SOI, a-Si:H, SiNx respectively. At the same time, the unbalance of each branch is ±0.5dB for the spectral range of the wavelength from 1300nm to 1600nm (figure 8).

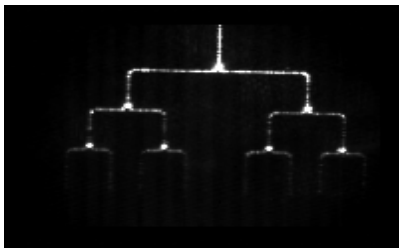


Figure 7 Optical distribution devices with measurements of spectral response of the elementary components.

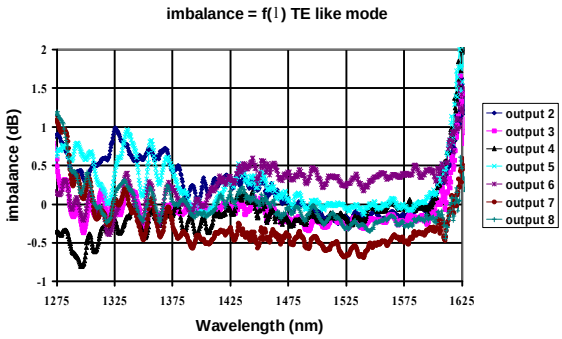


Figure 8 Unbalance of 8 exits in optical distribution.

Conclusion

In this paper we have studied three material approaches to optical interconnect: SOI, a-Si:H and SiNx. We have obtained results at the international state of the art on SOI devices (5dB/cm losses for $0.5*0.2\mu m^2$ waveguide at 1.3µm). Concerning a-Si:H and SiNx results, the value obtained (5.5 and 2.2 dB/cm) make them very attractive for photonic application. Particular a-Si:H that is studied for the first time. In our case, amorphous silicon has the same performances as SOI material but at a lower cost. It is also possible to design multilevel structures using this material, paving the way to 3D optical integration.

Aknowledgment

This work is financially supported by European Community through the STREP PICMOS program.

References

1 International Technology Roadmap for Semiconductor: Interconnect. http://public.itrs.net.
2 P.Kapur et al, Proceedings of IEEE International

IITC, pp.89-91, 2002.
3 R.Orobchouk et al, Proceedings of IEEE International IITC, pp.83-85, 2002
4 S.Jeannot et al., Proceedings of IEEE International IITC, pp.248-250, 2004.
5 P. Lusse et al, J.Lightwave.Techol. Vol. 12, 1994 pp. 487-494.
6 G.R. Hadley et al, , J.Lightwave.Techol. Vol. 13, 1995 pp. 465-469.
7 M. Heiblum et al, J. Quantum. Electronic. Vol. 11, 1975 pp. 75-83.
8 R.K. Varshney et al, J. Lightwave. Techol. Vol.6, 1988 pp. 601-606.
9 M. Melchiorri et al, Applied Physics Letter, Vol.86, 2005 pp. 121111.
10 R. Orobchouk et al, Proceedings of Europe Photonic, 2006, Vol.6183.

Evanescent-wave fluorescence excitation in aqueous solutions using symmetric planar waveguides

K. Leosson (1,2), M.H. Sørensen (3), T. Nikolajsen (3), M. Hansen (4), and S.I. Bozhevolnyi (5)
1) Science Institute, University of Iceland, IS-107 Reykjavik, Iceland, k.leosson@raunvis.hi.is
2) Lumiscence A/S, c/o CAT Science Parks, Postboks 30, DK-4000 Roskilde, Denmark
3) Crystal Fibre A/S, Blokken 84, DK-3460 Birkerød, Denmark
4) CAPRES A/S, DTU building 373, DK-2800 Kgs. Lyngby, Denmark
5) Dept. of Physics and Nanotechnology, University of Aalborg, Skjernvej 4A, DK-9220 Aalborg Ø, Denmark

Abstract: *We describe a method of delivering light to biological samples using a planar waveguide structure with a symmetric cladding environment. The symmetry of the waveguiding structure allows the penetration depth of the evanescent field to be tuned over a wide range by varying the thickness and/or refractive index of the waveguide. Furthermore, the symmetrical structure facilitates efficient excitation of waveguide modes using, e.g., optical fibers. We have performed fluorescence excitation experiments using of dielectric as well as metallic (surface plasmon) waveguides. The method is well suited for evanescent wave microscopy of biological samples, surface sensing and other applications that require illumination spread over macroscopic areas but confined to penetration depths ranging from 100 nm up to several μm.*

Introduction

Fluorescence microscopy (FM) can be regarded as one of the most important characterization techniques within cell biology, molecular biology and related fields [1]. Although most FM studies are carried out using conventional epi-fluorescence microscopes, there exists a wide range of more specialized techniques, including confocal laser scanning microscopy, two-photon absorption, resonance energy transfer and total internal reflection fluorescence microscopy (TIR-FM). In TIR-FM, the excitation light is usually incident on the sample from a substrate with higher refractive index (e.g. a thin glass slide) under an angle large enough for it to undergo total internal reflection at the substrate-sample interface. Fluorescence in the sample is therefore excited only within the penetration depth of the exponentially decaying evanescent field associated with the total internal reflection, typically extending approximately 100 nm into the low-index medium. A review of TIR-FM can be found in Ref. [2].

Fluorescence excitation by an evanescent field can also be accomplished using a planar waveguiding structure, where the sample (typically an aqueous solution) forms one of the waveguide cladding layers. The penetration depth of the evanescent field into the sample in this case is defined by the relationship between the refractive index of the sample, substrate and waveguide materials, as well as the thickness of the waveguide layer.

In this paper, we will present a new type of planar waveguide structure developed specifically for fluorescence microscopy applications [3], where the cladding material is chosen to match the refractive index of the sample. We discuss the special features of this waveguiding geometry and present experimental results obtained on samples containing fluorescent beads. In particular, we will focus on surface-plasmon excited fluorescence which currently attracts considerable interest in biological research [4].

Waveguide-excitation fluorescence microscopy

The use of planar waveguide structures for fluorescence excitation and microscopy has been previously reported in the literature [5]. The waveguide structure consisted of a glass substrate coated with a high-index thin film supporting a guided mode with 100–200 nm penetration depth of the evanescent field. A similar waveguide configuration was used to realize two-photon fluorescence excitation over a macroscopic surface area [6]. Conversely, Horváth et al. [7] developed a so-called "reverse-symmetry" waveguide sensor using nanoporous silica (n=1.2) as bottom cladding in order to greatly increase the penetration depth of the guided mode into the sample. This type of sensor geometry has been used to monitor cell attachment and spreading [8] but, to our knowledge, it has not been used for FM applications.

In the abovementioned experiments, light was coupled into the waveguides using surface gratings illuminated by light incident under a specific resonance angle that depends on the grating period, effective waveguide index and the excitation wavelength. Due to the asymmetry in the refractive index of the top and bottom cladding layers, the waveguides have a cut-off thickness below which no guided mode is supported by the structure, limiting the range of possible penetration depths.

The symmetric waveguide structures demonstrated in the present paper provide several advantages over previous designs. The penetration depth of the symmetric mode can be tuned over a wide range without cut-off. The guided mode can be efficiently excited directly from an optical fiber, eliminating the need for patterning of gratings and resonance-angle excitation. This also implies that the sample can be excited with multiple wavelengths through the same fiber. Aside from the fiber-coupled light source, the necessary components are no more than a few millimeters in height, meaning that a standard light microscope (normal or inverted) can be configured to deliver TIR-FM performance.

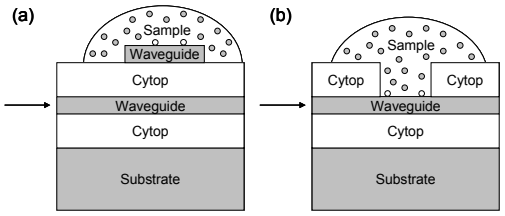


Fig. 1: Waveguide configurations used in the present study. (a) Coupled-waveguide structure using a buried "feeding core" waveguide and a surface "sensing" waveguide. (b) Single-waveguide structure with a sample well exposing part of the waveguide. Samples consisted of fluorescent beads in solution. Fluorescence is excited at the waveguide surface as indicated by the white beads.

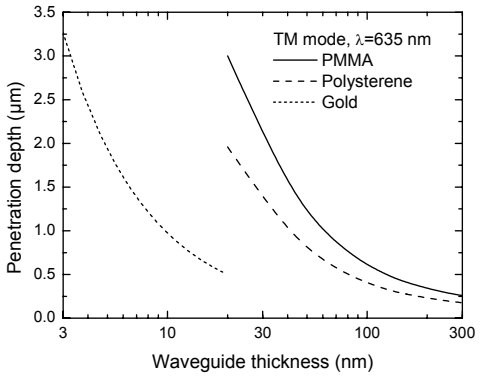


Fig. 2: Calculated $1/e^2$ penetration depth of the excitation field intensity into a sample with refractive index n=1.34.

Waveguide fabrication and system set-up

Planar waveguide structures were fabricated by spin-coating on silicon or glass substrates. Two excitation geometries were used, as shown in Fig. 1. For the bottom cladding layer we used Cytop (Asahi Glass Co.), an amorphous fluoropolymer closely index-matched to water. Waveguide layers with a wide range of thicknesses were fabricated using PMMA (n=1.49) or polystyrene (n=1.59). The waveguide film was covered with a second layer of Cytop. The area of sample excitation was defined by patterning a second waveguide layer (dielectric or metallic) on top of the cladding layer (Fig. 1a) or by making a hole through the top cladding (Fig. 1b) using reactive-ion etching. The substrates were cut into individual chips using a dicing saw.

Light at different wavelengths was coupled directly into the waveguide through the end facet using a fiber-coupled diode laser or diode-pumped solid state lasers (635 nm, 532 nm or 473 nm). Fiber-to-chip alignment was carried out by using translation stages or a specially constructed chip holder [9] while monitoring the light transmitted through the planar waveguide. A solution containing fluorescent probes (e.g. TransFluoSpheres® from Molecular Probes) was dispensed onto the waveguide chip. The fluorescence signal was collected with an Olympus BX51 research microscope and recorded with a Hamamatsu C8484 digital camera.

Mode analysis

In order to estimate the penetration depth of the excitation light into the sample, we calculated the vertical mode profile for planar dielectric waveguides of different thicknesses. Furthermore, we made similar calculations for surface plasmon polariton (SPP) waves propagating along thin gold films sandwiched between a Cytop substrate and an aqueous sample. Thin metal films in a substantially symmetric cladding environment support the propagation of so-called long-range surface plasmon polariton (LRSPP) waves, corresponding to a coupled mode of two SPP waves propagating along the top and bottom surfaces of the metal film [10]. Fig. 2 shows the penetration depth of the evanescent field into the sample for conventional dielectric waveguides as well as metallic LRSPP waveguides. The penetration depth in this case is defined as the distance where the field intensity has reached $1/e^2$ of the intensity at the surface. The LRSPP waveguide only supports a propagating TM mode whereas the dielectric waveguides also support a TE mode with a slightly shorter penetration depth (not shown).

The geometry shown in Fig. 1a supports two coupled (symmetric and antisymmetric) modes in the region of the sensing waveguide. Both modes are excited by the incoming light and interference between them results in a transfer of optical power between the "feeding core" and the surface waveguide. Similarly, efficient coupling can be achieved between a dielectric waveguide and a thin metal waveguide by matching their propagation constants. One such condition is shown in Fig. 3, where the embedded waveguide consists of a 49 nm layer of PMMA and the surface waveguide is an 8 nm gold film. The strength of the coupling between the two planar waveguides can be adjusted by tuning the thickness of the intermediate cladding layer. For the structure shown in Fig. 3, the coupling length (full power transfer from one waveguide to the other) is approximately 350 µm.

Experimental results

Microscope images of fluorescence from a solution containing 100-nm TransFluoSpheres® (T8878, 633nm/720nm) are shown in Fig. 4. The waveguide structure consists of an embedded PMMA waveguide and a gold surface waveguide with a closely matched propagation constant. Excitation light (635 nm) is incident from the left side through the embedded waveguide. Very little fluorescence is recorded in the left half of the image, where no gold film is present. The power transfer between the two waveguides is clearly seen in the fluorescence intensity. The confinement of the excitation light was confirmed by collecting images with and without filtering of the excitation wavelength (Fig. 4, left and right, respec-

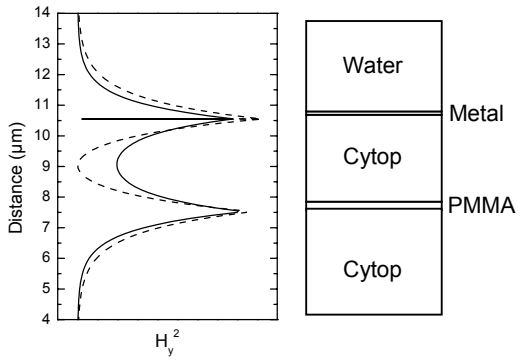


Fig. 3: Vertical mode profiles (solid line: symmetric, dashed line: antisymmetric) of a structure shown on the right, consisting of a 49 nm PMMA "feeding core," a 3.0 μm intermediate cladding layer and an 8 nm gold film surface waveguide.

tively), keeping the same camera settings. In the right image, some scattering from imperfections in the waveguides is observed but otherwise the images are very similar, confirming that fluorescence is excited primarily by light propagating in the plane of the surface.

The surface-bound nature of the excitation was also checked by observing scattering of the excitation light from gold nanoparticles. Particles in suspension appeared and disappeared as they moved randomly in and out of the excitation field. If the diffusion constant of the particles is known, the signal from a collection of particles can be used to estimate the penetration depth of the evanescent field [11].

The observed fluorescence signal in Fig. 4 decreases exponentially over a lateral distance of about 1 mm, due to absorption of the excitation light by the metal waveguide. In general, the propagation loss associated with LRSPP waveguides limits their applicability in transmitting light signals over longer distances, especially for shorter wavelengths. In order to extend the illumination range, we detuned the propagation constant by changing slightly the thickness of the embedded waveguide layer. The resulting structure supported two coupled modes, one confined mostly to the metal film and another confined mainly to the buried waveguide. Fig. 5 demonstrates how fairly uniform excitation can be obtained across a 5 mm gold film in such a structure. The signal intensity is reduced, compared to Fig. 4, because a smaller portion of the total incident power is contained within the evanescent tail.

Conclusions

We have demonstrated the applicability of symmetric planar waveguide structures to fluorescence microscopy of aqueous samples. We have also successfully carried out fluorescence imaging of live cells using the same method which will be the subject of a future publication. We believe that microscope slides using integrated optics for illumination have the potential

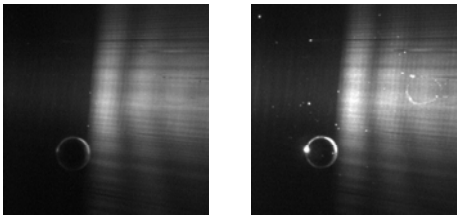


Fig. 4: Fluorescence induced on a waveguide chip with a metallic surface waveguide covering the chip in the right half of the images, with (left image) and without (right image) filtering of the excitation wavelength. The images are 1 mm across and light is incident from the left side.

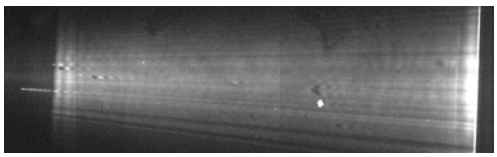


Fig. 5: Fluorescence excitation over a 5-mm wide gold film. The propagating mode is confined mainly to the dielectric feeding core. Initial beating with the rapidly decaying mode confined mainly to the metal film can be observed at the left side of the film.

to complement advanced characterization techniques in fluorescence microscopy in the future.

Acknowledgments

The authors thank Dr. T. Søndergaard at the University of Aalborg, Denmark and Dr. M. Hammer at the University of Twente, the Netherlands, for providing mode solver software. KL acknowledges support from the University of Iceland Research Fund and the Selma & Kaj Langvad Memorial Fund.

References

1 For a recent review of fluorescence microscopy techniques, see *Nature Methods*, Vol. 2, No. 12 (2005).
2 D. Axelrod, E.H. Hellen, R.M. Fulbright: Total internal reflection fluorescence. In J.R. Lakowicz, ed.: *Topics in Fluorescence Spectroscopy, Volume 3: Biochemical Applications*. New York, Plenum Press, pp. 289-343, 1992.
3 Lumiscence A/S, patent pending, PCT Publication No. WO/2005/052557.
4 J.R. Lakowicz, *Plasmonics* **1**, 5 (2006).
5 H.M. Grandin et al., *Biosensors and Bioelectronics* **21**, 1476 (2006).
6 G.L. Duveneck et al., *Biosensors and Bioelectronics* **18**, 503 (2003).
7 R. Horvath, H.C. Pedersen, N.B. Larsen, *Appl. Phys. Lett.* **81**, 2166 (2002).
8 R. Horvath et al., Appl. Phys. Lett. **86**, 071101 (2005).
9 Chip holder constructed by Lumiscence A/S.
10 D. Sarid, *Phys. Rev. Lett*. **47**, 1927 (1981).
11 Harlepp et al., *Appl. Phys. Lett.* **85**, 3917 (2004).

Planar photonic crystal waveguide biosensor

Nina Skivesen (1), Amélie Têtu (1), Martin Kristensen (1), Jørgen Kjems (2), Lars. H. Frandsen (3), and Peter I. Borel (3)

1) Department of Physics and Astronomy and iNANO, University of Aarhus, Denmark, skivesen@inano.dk, atetu@inano.dk, mk@inano.dk

2) Department of Molecular Biology and iNANO, University of Aarhus, Denmark, jk@mb.au.dk

3) COM•DTU, Department of Communications, Optics & Materials, Nano•DTU Technical University of Denmark, Denmark, lhf@com.dtu.dk, pib@com.dtu.dk

Abstract: *We present protein detection using a planar photonic crystal waveguide sensor. Experimental results of refractive index measurements show good agreement with simulations. The sensor has been used for protein detection and showed successful detection with excellent signal to noise ratio of proteins with concentrations around 10 µg/ml (0.15µMolar).*

Introduction

In the past 20 years, the research within biosensing has experienced increased intrest. Biosensing is a wide term that includes areas like fast and effective recognition of DNA/RNA, proteins or other biological molecules, recognition of chemical reactions for diagnoses of diseases, discovery of new drugs, and environmental control. In connection with biosensing, increased focus has been on the development of integrated optical biosensors, as they have the potential to be made compact with high sensitivity, and to be easily fabricated and integrated with other optical or electrical components.

The research in integrated optical biosensors has resulted in a wide range of devices and still new ones are suggested, especially those requiring easier fabrication methods. Amongst the well-proven methods suggested for biosensors, a few wide-known methods can be mentioned: optical waveguides, SPR-devices, resonant mirrors, interferometers, cantilevers and optical fiber-based devices.

We present a biosensor based on a planar photonic crystal. The advantages of the device we suggest are that it is realized in silicon and can be integrated on a SOI-wafer (silicon-on-insulator) along with other electronic and optical devices. Thus, the fabrication technology used for the sensor is the same used for CMOS electronic devices.

The suggested planar photonic crystal waveguide (PC-WG) sensor has been tested for both refractive index (RI) measurements and protein detection. The PC-WG can be made very compact and the sample volume to be analyzed can also be reduced considerably compared to the earlier suggested devices mentioned above.

Photonic crystal waveguide sensor

The basic property of a PC-WG is that a given bandwidth of light can be guided in the waveguide as the light is confined laterally by the band-gap of the photonic crystal (PhC) and vertically by total internal reflection (TIR), akin to conventional waveguide structures. Fig. 1(A) shows the experimental setup and a top-view of the configuration of the PC-WG sensor is illustrated in Fig. 1(B).

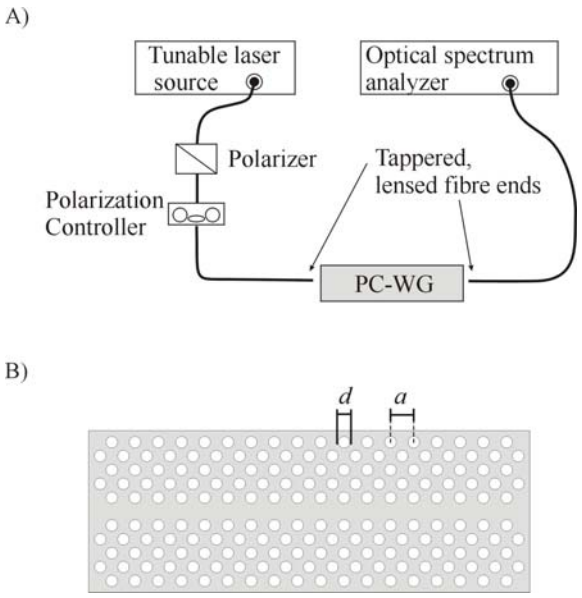


Fig. 1: A) Experimental setup. B) Top-view of the photonic-crystal waveguide configuration.

The properties of the PC-WG are highly influenced by changes in RI at the silicon surface, both on the top of the layered structure but also at the sidewalls of the holes due to the field distribution, which is decaying fast into the cover medium. This can be an advantage in biosensing as it will typically involve an aqueous cover medium containing biological molecules. The detection of specific biological molecules

is primarily done by immobilizing molecules at the surface, resulting in a RI change exactly where the evanescent field is strongest leading to a high detection efficiency. The penetration depth of the field into the holes depends on the wavelength and distance of the hole from the waveguide defect. Based on finite-difference time-domain (FDTD) simulation of this structure and SNOM measurements on a similar structure the penetration depth of the tested sensor can be approximated to 100 nm.

The band-gap of the PhC is the interesting property for sensor application. A sudden drop in the transmission spectra vs. wavelength is observed where the transmission of the fundamental photonic band-gap (PBG) defect mode is no longer possible. The change in wavelength position of this transmission drop is used for detection of RI changes in the cover medium of the sensor, as the wavelength position increases with an increase in RI of the cover medium.

Refractive index measurements

We tested the fabricated sensor and compared the results with 3D FDTD simulations for different homogeneous cover solutions. In Fig. 2(A) the resulting changes in wavelength position vs. changes in cover RI are shown for both the measured and calculated transmission curves. These results show that the method for applying the different solutions, the detection, and the reading of the signals give very reliable results.

Protein detection

Protein detection was successfully achieved with the fabricated sensor. A solution of 1 mg bovine serum albumin (BSA) and 1 mL MilliQ water was used for one experiment (a concentration of 15µMolar). In Fig. 2(B) steady response spectra for a solution of pure MilliQ water and the BSA solution are shown. A shift in cutoff wavelength of 0.6 nm is observed between the steady response for MilliQ water and the BSA solution, respectively. Before terminating the experiment the cover solution is changed back to MilliQ water and no shift in cutoff wavelength is observed, indicating that the BSA proteins have adsorbed onto the sensor surface. In addition we performed ellipsometry measurements on a silicon surface for the same concentration, which resulted in a protein layer thickness of 3.6 nm.

An estimate of the sensor response based on the change in wavelength position of the measured transmission signals is consistent with calculations and ellipsometry measurements of protein adsorption on the sensor surface. Furthermore, the estimate shows that the PC-WG sensor has a very high spatial sensitivity in the close vicinity of the sensor surface.

Protein concentrations down to 10 µg/mL have been detected with excellent signal to noise ratio and these results will be presented. However, even this low concentration does not express the lower sensitivity limit for the sensor, as the presented sensor is not optimized for biosening and can be improved in numerous places. Firstly, smaller changes in the cutoff wavelength should be possible to detect with acceptable signal-to-noise ratio. The sensitivity may also be increased by improvements of the sensor setup such as introducing temperature and coupling stabilization, continuous measurements of a reference waveguide and balanced bridge detection techniques.

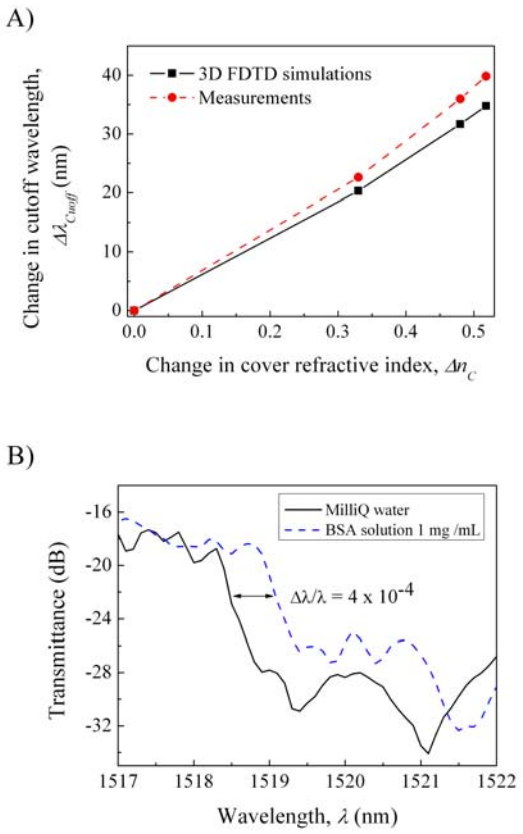


Fig. 2: (A) Curves showing the experimental (circles, dashed line) and simulated (squares, solid line) changes in wavelength position of the band-gap edge vs. changes in cover RI. (B) Measured curves before (solid line) and after (dashed line) protein adsorption on the sensor surface.

Conclusion

We present a photonic-crystal waveguide used for RI measurements and protein detection fabricated on a commercial SOI wafer using conventional CMOS fabrication procedures. A good sensitivity is demonstrated although the sensor is not yet optimized for biosensing application. A significant sensitivity-enhancement is therefore realistic.

Acknowledgments

The research was supported by the Carlsberg Foundation, PIPE and NEDO grants.

Waveguide grating spectral phase-shifter for temporal femtosecond pulse splitting

D. Pietroy, A.V. Tishchenko, M. Flury, R. Stoian, O. Parriaux
Laboratoire Hubert Curien (formerly TSI laboratory), UMR CNRS 5516, 18 rue Benoît Lauras, 42000 Saint-Etienne, France
email : olivier.parriaux@univ-st-etienne.fr

Abstract
A waveguide grating based on a mirror causes a 2π phaseshift of controllable slope in the spectrum of a femtosecond pulse giving rise to an adjustable, lossless temporal pulse splitting. A representation of resonant reflection based on phenomenological parameters enables the designer to achieve the synthesis of the mirrored waveguide grating structure exhibiting the desired temporal pulse shape. The example of a temporal beam splitter under fabrication is presented. Experimental results will be presented at the conference.

1. Introduction

The present paper concerns the technique of temporal femtosecond pulse shaping by acting on the spectral phase of the pulse by means of a waveguide grating mirror. The desired wavelength-dependent phaseshift Φ(λ) is imprinted on the spectrum of a pulse by a resonant grating composed of a slab waveguide of corrugated surface exhibiting the effect of 100% resonant reflection [1]. Usually this wavelength, angularly and polarization selective effect is used for its sharp high reflection peak. The sudden phase change associated with the reflection modulus peak is generally discarded except in [2] where it is shown that the phase variation is of utmost importance when such resonant mirror is associated with another element or inserted into a system. This is precisely the case in the present application where the spectral phase only, not the modulus, is the matter of concern. We propose here a lossless pulse shaping element using a mirror-based waveguide grating as a phase-only modulator. The experimental test of the element under fabrication will be reported at the conference.

2. The spectral phase of resonant reflection and its temporal transform

The temporal profile $f_i(t)$ of a pulse of initial spectrum $F_i(\nu)$, after experiencing a lossless frequency dependent phaseshift $\varphi(\nu)$, is given by the Fourier transform of the product $F_i(\nu)\exp[j\varphi(\nu)]$. It will be shown hereunder that the spectral phase of the resonant reflection from a mirrored slab waveguide grating is simply and remarkably given by an arctangent function of 2π amplitude :

$$\varphi(\nu) = -2\arctan\left(b\left(\nu-\nu_0\right)\right) \qquad (1)$$

where ν is the optical frequency, ν_0 is the optical frequency for synchronous waveguide excitation, $b = \frac{2\pi \sin\theta_i}{c\alpha}$ is the phase slope coefficient, θ_i is the incidence angle on the corrugated slab and α is the radiation coefficient [3]. Calculating the inverse Fourier transform of the product of a Gaussian initial pulse of half-width duration Δt by the spectral phase of expression (1) yields the temporal shape of the reflected pulse analytically :

$$f_f(t) = \frac{\sqrt{2\pi^3}\Delta t}{\sqrt{\ln 2}\,b} e^{\left(\frac{\pi\Delta t}{\sqrt{2\ln 2}\,b}\right)^2} e^{-\frac{2\pi}{b}t}\left[1+erf\left(\frac{\sqrt{2\ln 2}}{\Delta t}t-\frac{\pi\Delta t}{\sqrt{2\ln 2}\,b}\right)\right] - e^{-\frac{2\ln 2}{\Delta t^2}t^2} \qquad (2)$$

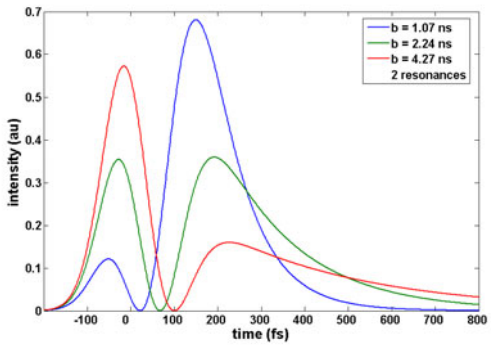


Fig. 1: Examples of temporal profiles obtained by introducing an arctangent phase in the spectrum of a 130 fs input pulse for different values of phase slope b.

Figure 1 illustrates the temporal shape of the output pulse obtained with the analytical expression (2) assuming a Gaussian input pulse of 130 fs half-width. The initial pulse is split into two subpulses. ν_0 sets the location of the phase change in the spectrum of the pulse. The slope b which depends on the resonance width defines the balance between the two subpulses. For instance, for a femtosecond pulse centered at 800 nm wavelength, the dimensionless ratio b/Δt should be comprised between essentially 6 and 55 to ensure a 10 % minimal subpulse intensity ratio. The temporal spacing between the two subpulses is mainly determined by the amplitude of the phase jump. It is an intrinsic limitation of resonant grating waveguide reflection to exhibit no more than 2π phase shift. However, there are ways to increase it by tailoring the dispersion of the slab waveguide for instance; this is beyond the scope of the present paper.

3. Modulus and phase of the reflection of a grating waveguide

A vivid representation of the reflection across a waveguide mode resonance will now be presented to give some insight into the operation of the element.

Figure 2 is the sketch of a waveguide grating slab propagating a guided mode excited contra-directionally by a femtosecond beam by means of the -1st order of the grating. Under collinear incidence and θ_i incidence angle, the resonance condition is $k_0 n^* + \beta = K_g$ where $k_0 n^* = k_0 \sin\theta_i$, $\beta = n_e k_0$ and $K_g = 2\pi/\Lambda$ where Λ is the grating period. The excitation of the waveguide mode is made collinearly via the -1st diffraction order for sake of preventing radiation losses via other orders. n_e is the effective index of the excited mode.

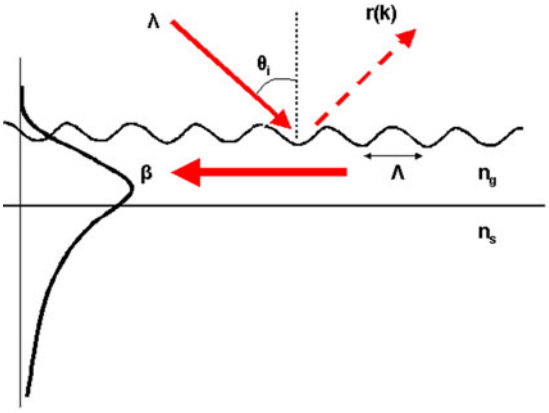


Fig. 2: Contradirectional coupling configuration of a plane wave under incidence angle θ_i into a grating waveguide via the -1st order. n_s and n_g are the refractive indices of the substrate and the waveguide media respectively.

In the inhomogeneous problem representation the occurrence of grating mode excitation is expressed as a pole of the reflection function. The reflection around the resonance can be expressed as the sum of two terms : an essentially constant regular term r_0 and a term r_g resulting from the presence of the pole in the k-vector space [4] :

$$r(k) = r_0 + r_g(k) \qquad (3)$$

$r_g(k)$ is the part of the reflection due to the re-radiated guided-wave :

$$r_g(k) = \frac{a_p}{(k-\beta) - j\alpha} \qquad (4)$$

where a_p is a complex constant.

The reflection coefficient r(k) is a complex function of the real variable k expressed as $k_0 n^* - K_g$. The scan of k will be made experimentally on the real axis by varying the incidence angle or the period.

$r_g(k)$ is a complex function having a first order pole. Interestingly, the locus of $r_g(k)$ in the complex plane upon the scan of k on the real axis is a circle as illustrated in Figure 3.

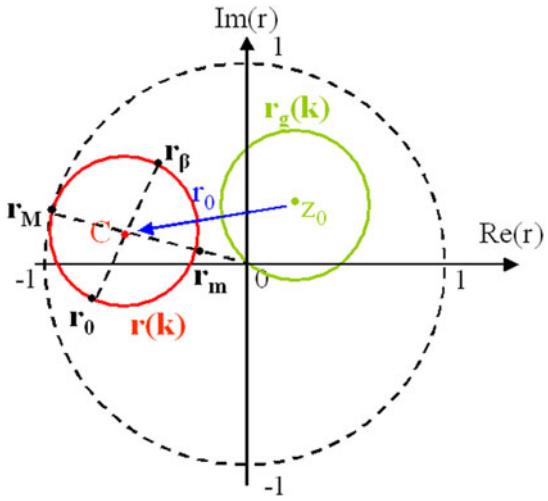


Fig. 3: Representation of the reflection coefficient r(k) in the complex plane.

The circle $r_g(k)$ is centered at complex point $z_0 = ja_p/2\alpha$ and its radius is $|a_p|/2\alpha$. The origin is on the circle since $r_g(k)$ is zero far from the resonance. Upon a scan along k from $-\infty$ to $+\infty$, the r_g apex describes one turn in the clockwise direction.

r(k) is the sum of the regular part r_0 and the resonant part $r_g(k)$. This just amounts to translating the described circle by the complex quantity r_0. Knowing that the reflection modulus is 1 at the condition of resonant reflection $r_M = r(k_M)$, the r(k) circle is tangent at this point to the circle of radius 1 centered at the origin of the complex plane. Therefore, the origin, the r(k) circle center C and the complex unit reflection point r_M are on the same straight line. On the same straight line is also the point of minimum reflection r_m. The r(k) circle is thus centered at point :

$$C = r_0 + j\frac{a_p}{2\alpha} \qquad (5)$$

and its radius is still $R = \frac{|a_p|}{2\alpha}$.

4. The phase of reflection in a mirror based resonant grating

The results of the last section are the basis for the design of the present spectral phase shifter for femtosecond pulses. The aim in the present temporal shaping operation is to have the whole spectrum reflected with the phaseshift somewhere in the middle. This condition can simply be achieved by placing the grating waveguide on top of a background mirror with sufficient distance between the waveguide and the mirror to electromagnetically isolate the modal field from the mirror. A thick low index buffer layer will thus be inserted between the waveguide slab and the mirror as sketched in Figure 4.

The change which the base mirror brings in the complex representation of the reflection is strikingly illustrated in Figure 4. The lossless mirror imposes

the reflection coefficient modulus to always be 1. Thus the reflectivity circle is the unity circle with its center at the origin of the complex plane. Consequently, setting expression (5) to 0 gives a simple expression for a_p :

$$a_p = 2j\alpha r_0 \qquad (6)$$

Then, using the above expression in the polar function (3) of the reflection coefficient gives :

$$r(k) = r_0\left(1 + \frac{2j\alpha}{(k-\beta) - j\alpha}\right). \qquad (7)$$

Expression (6) is a key result as it relates the unknown constant a_p of the algebraic expression (3) of r(k) to the phenomenological grating waveguide parameter α, and to an experimentally measurable quantity, r_0. As the modulus of r(k), therefore of r_0 is 1, the final expression for r(k) can be written as a phase function :

$$r(k) = -r_0\left(\frac{(\alpha - j(k-\beta))^2}{(k-\beta)^2 + \alpha^2}\right) = e^{j\left(\pi + \varphi_0 - 2\arctan\left(\frac{k-\beta}{\alpha}\right)\right)}$$

where φ_0 is the phase of the reflection coefficient off-resonance. Thus, the phase dependence of the reflection on a mirror-based resonant grating is now simply given by :

$$\varphi(k) = \pi + \varphi_0 - 2\arctan\left(\frac{k-\beta}{\alpha}\right) \qquad (8)$$

$$\varphi(\lambda) \simeq \pi + \varphi_0 + 2\arctan\left(\frac{2\pi \sin\theta_i}{\alpha\lambda_0^{\,2}}(\lambda - \lambda_0)\right) \qquad (9)$$

The phase of r(k) is now fully defined as a function of the opto-geometrical and phenomenological parameters in the case of a mirror based structure. This is the result expressed in (1) in term of the optical frequency ν which is at the basis of the temporal transform established in section 2.

5. Example of a pulse splitting monolith

An example of waveguide grating structure which is under fabrication is given in figure 4. It consists of an alternation of high index HfO_2 (n_h = 2.06) and low index SiO_2 (n_b = 1.46) layers. The mirror is composed of a gold substrate on which a 6-λ/4-layer dielectric mirror is deposited to increase the total efficiency. Minimizing the modal field at the metallic interface by inserting a low index buffer layer permits to decrease losses in the neighbourhood of the resonance. A 400 nm pitch grating of 60 nm depth will be etched in the last high index layer.

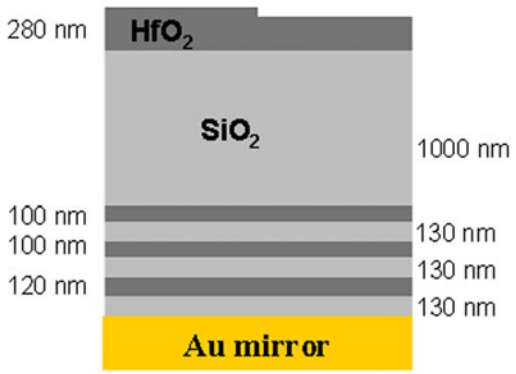


Fig. 4: Structure under fabrication.

Experimentally, the femtosecond incident beam at 800 nm wavelength is polarized horizontally. Therefore the structure is optimised to be excited by a TM polarized beam. Numerical simulations giving the spectral phase and the temporal profile of the output pulse are presented in figure 5 and figure 6. A first 105 fs width pulse containing 30% of the output energy is expected to be followed by a 225 fs pulse containing 70% of the energy.

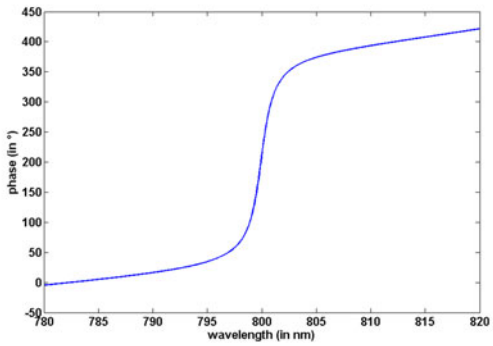


Fig. 5: Spectral phase induced by the model structure.

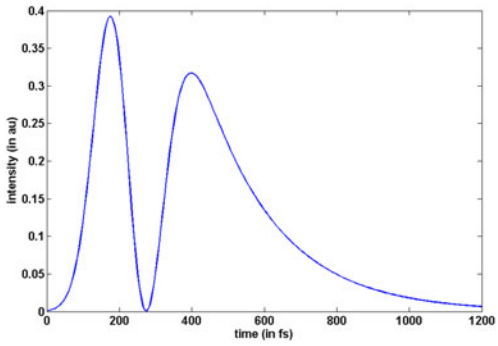


Fig. 6: Temporal profile of the output pulse after reflection of a 130 fs gaussian pulse on the resonant grating.

The multilayer structure has been fabricated on top of a gold mirror. The 400 nm period corrugation grating is under printing, and RIBE transfer in the last HfO_2 layer will be shortly performed. The functional demonstration under femtosecond pulse incidence will be reported at the conference.

7. Conclusion

A graphic representation of resonant reflection from a waveguide grating gives a vivid physical insight in the operation of a monolithic spectral phase modulator allowing the temporal shaping of femtosecond pulses. The association of a resonant waveguide grating mirror with a high reflectivity wide band mirror next to the latter represents a pure phaseshifting element where all spectral components of the pulse experience 100% reflection in modulus. The resulting 2π phase shift in the form of an arctangent function of the optical frequency gives rise to an effect of temporal pulse splitting. The relative amplitude of the subpulses can be chosen by adjusting the radiation coefficient α of the grating waveguide which determines the slope of the phase variation. This effect can be used in diverse laser machining applications as well as, if the temporal spacing between subpulses can somehow be increased and adjusted, to time resolved spectroscopic applications. Femtosecond pulse splitting using this element, which is now at the final fabrication stage, will be reported at the conference.

8. Acknowledgements

The authors want to thank Dr. N. Huot and Prof. E. Audouard, Hubert Curien Laboratory, for useful discussions related with femtosecond laser machining. LETI, CEA Grenoble, is gratefully acknowledged for the fabrication of the gold based multilayer. This work is related with WP2 on waveguide measurement in Network of Excellence NEMO.

References

[1] G.A. Golubenko et al, Sov. J. Quantum Electron., vol. 15, p. 886, 1985.
[2] B.A. Usievich et al, Opt. Quant. Elec., vol. 36, p. 109, 2004.
[3] V.A. Sychugov et al, Sens. Act. B, vol. 38-39, p. 360, 1997.
[4] M. Neviere et al, J. Opt., vol. 8, p. 231, 1977.

Low-Loss, High-Uniformity 1x2, 1x4 and 1x8 Polymer Multimode Y-Splitters Enabling Radio-over-Fibre Multicasting Applications

N. Bamiedakis, J. Beals, F. Yang, A. Wonfor, R. V. Penty, I. H. White (1) J. V. DeGroot Jr., T. V. Clapp (2)
(1) Electrical Engineering Division, University of Cambridge, 9 JJ Thomson Avenue, Cambridge, CB3 0FA, UK,
nb301@cam.ac.uk
(2) Dow Corning Corporation, 2200 W. Salzburg Rd, Midland, Michigan 48686, USA

Abstract: *Novel low-loss, high-uniformity polymer multimode Y-splitters/combiners are presented. Excess losses of 2 dB and a splitting uniformity as good as 1.2 dB are obtained for an eight-way Y-splitter. The multimode aspect of the devices allows signal combining without the fundamental loss of 3 dB per split associated with the reciprocal use of single mode devices. A total insertion loss of 4 dB for an 8x1 combiner is recorded. By way of example, the asymmetrical behaviour of the device, when used for splitting as opposed to combining, is shown to, provide system advantage in a radio-over-fibre network. Here radio-over-fibre multicasting is demonstrated achieving a 2% EVM for IEEE 802.11g transmission in an 8-way 150 m range MMF network.*

1. Introduction

Polymer multimode waveguides that can be integrated on printed circuit boards (PCBs) have been of particular interest recently as they offer a low cost and highly efficient solution for high speed interconnects [1,2]. Siloxane materials have been studied for such applications as they have high-reliability with excellent mechanical and thermal properties, so that they can withstand temperatures in excess of 250°C needed for soldering [3]. Due to their relaxed alignment tolerances, multimode waveguides allow for reduced cost connectorisation. Yet further cost advantages could be achieved if added functionality is attained by forming components in the polymer guides. In this paper therefore we report the fabrication and characterisation of novel low-loss high-uniformity multimode polymer 1x2, 1x4 and 1x8 Y-shaped splitters and combiners. Despite their low potential cost, good performance is achieved, while the multimode aspect of the devices additionally allows signal combining without the 3 dB penalty/split normally observed in single mode devices. This gives enhanced performance for optical systems requiring such combining and hence this paper demonstrates the use of the devices in enabling multicasting in radio-over-fibre systems.

2. Device design and fabrication

The siloxane polymers, used for the proof-of-principle demonstration of the devices, are spun in resin form directly onto a silicon substrate and patterned by conventional photolithographic techniques. All devices have a waveguide cross-section of 50x20 μm. The splitter output arms are separated by 250 μm to match conventional ribbon fibre, VCSEL and photodiode array spacing (Fig. 1). The 1x2 Y-splitters consist of the input arm, a broadening taper region and two s-bends to achieve the required pitch for the output arms. The taper angle and s-bend length are chosen so as to create an adiabatic change of the structure [4]. The 1x4 and 1x8 splitters consist of cascaded 1x2 splitters with s-bend lengths modified to yield a similar minimum radius of curvature for the curved sections. The total device length, including a 1mm long input arm, is approximately 8.5 mm, 16 mm and 30 mm for the 1x2, 1x4 and 1x8 devices respectively (Fig. 2). Sets of devices are separated using a Disco 321 dicing saw. As control samples, straight waveguides are fabricated which exhibit intrinsic losses of 0.03-0.05 dB/cm at 850 nm. Samples fabricated on FR4 substrates yield identical results, indicating that the cladding material sufficiently masks the roughness of the FR4 substrate.

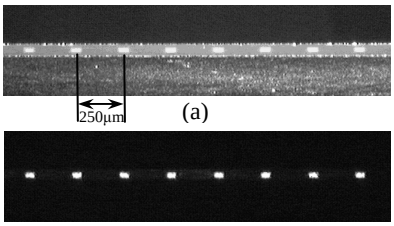


Fig. 1: Output facet of a 1x8 splitter (a) photograph (b) IR image with an 850 nm input.

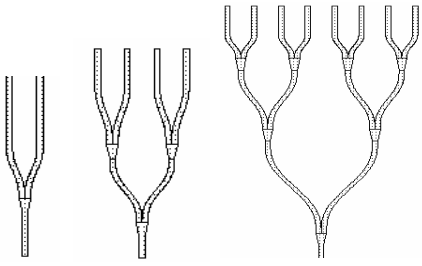


Fig. 2: Schematic of polymer Y-splitters.

3. Characterisation studies

The power transmission characteristics of the devices used as both splitters and combiners are investigated for different input conditions. An 850 nm VCSEL source is used as a transmitter. Two forms of launch have been studied. Firstly fibre launch has been employed where the input fibre can be offset in the horizontal direction to investigate the impact of input misalignment on overall power transmission as well as power imbalance between the output arms of the

device. Secondly a free space launch utilising two 10x objective lenses and an unpackaged VCSEL source is also examined as this gives higher coupling efficiency. In both cases, a 62.5/125 µm cleaved multimode fibre (MMF) collects the light at each output arm of the device and delivers it to an optical power meter.

With a SMF, 50 µm MMF and 62.5 µm MMF input the excess losses recorded for the 1x2 Y-splitters are as low as 0.5 dB, 2 dB and 2.7 dB, and for the 1x8 splitter 1 dB, 2 dB and 3.5 dB, respectively, indicating the relative coupling efficiency of the different launches. It should be noted that the MM fibre cores are larger than the device guides leading to imperfect coupling efficiencies. This is expected to be removed following waveguide redesign.

Owing to the multimode aspect of the devices, splitting uniformity strongly depends on the mode power distribution at the input of the device. Figure 3 shows the maximum recorded power imbalance for the various input conditions and devices. The power difference between the output arms is below 0.5 dB, 1 dB and 1.2 dB for the 1x2, 1x4 and 1x8 Y-splitters for an MMF input. Multimode launches typically allow lower power imbalances as more modes are excited and power is more uniformly distributed within the devices (Fig. 4).

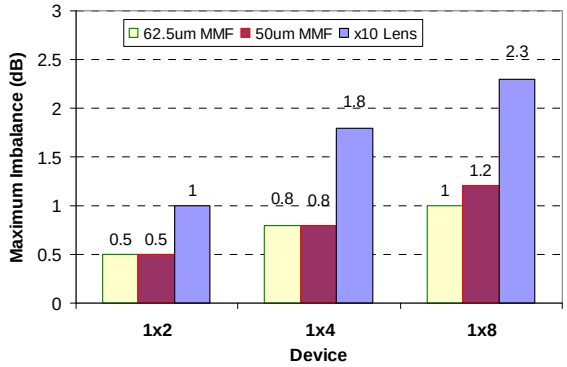
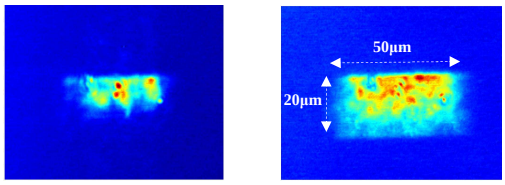


Fig. 3: Maximum imbalance between output arms of the 1x2, 1x4 and 1x8 Y-splitter for the various input conditions.



(a) (b)

Fig. 4: Near field images of an output arm of a 1x2 Y-splitter for a (a) restricted launch (SMF) (b) overfilled launch (MMF).

Figure 5 shows the variation of the maximum power imbalance between the output arms for a 1x8 Y-splitter with two different MMF launches as the input fibre is offset in the lateral direction. High splitting uniformity is achieved for all input fibre positions.

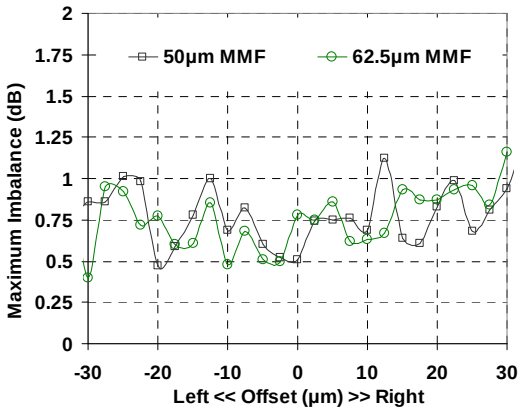


Fig. 5: Maximum imbalance between output arms of 1x8 Y-splitter for MMF inputs (waveguide core within ±25µm).

The devices are also studied under operation as combiners. The advantage of multimode combiners over single mode devices lies in the fact that there is no fundamental power loss associated with reciprocal use of the device (3 dB for a 1x2 device). Using a SMF or a lens input system to maximise coupling efficiency and achieve a restricted launch into the waveguides, the total insertion loss for a 1x2 combiner is 1.3 dB and for a 1x8 combiner is as low as 4 dB. Hence, the power difference between the two configurations (splitter and combiner) is 2 dB and 6 dB respectively for the 1x2 and 1x8 devices (Fig. 6). This asymmetric behaviour is particularly important in multicast antenna remoting or MMF PON applications where uplinks are limited by noise and hence power combining losses should be minimised. All arms of the combiner display high uniformity as well, exhibiting a power loss variation of less than 0.3 dB.

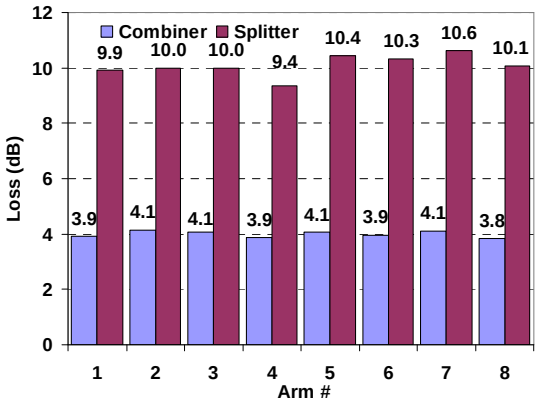


Fig. 6: Insertion loss of a 1x8 device used as a splitter and a combiner with a free space input.

A study of the causes of excess loss in the devices is currently in progress. The multimode launches that are used are overfilled and hence introduce additional loss, particularly in the combiners owing to the down-tapered region where higher order modes are susceptible to coupling to radiation modes. Optimisation of the launch is thus expected to lead to

improved performance. Table 1 summarises the results obtained for the 1x2, 1x4 and 1x8 devices when operating as a splitter and a combiner for the various input configurations. Total insertion losses include coupling, splitting and propagation losses.

Table 1: Total insertion loss (including splitting losses) (dB) for the 1x2, 1x4 and 1x8 devices with different inputs when used as a (a) splitter (b) combiner.

(a)

Input	Splitter		
	1x2	1x4	1x8
SMF	3.4	6.6	10
50µm MMF	5	7.8	11
62.5µm MMF	5.7	9	12.5

(b)

Input	Combiner		
	1x2	1x4	1x8
SMF	0.9	1.5	4
50µm MMF	4	5.1	7
62.5µm MMF	4.7	6	9

4. Radio-over-fibre multicasting

To demonstrate the potential of these low cost devices, multicasting is studied in a radio-over-fibre system (RoF). The 1x2 and 1x8 devices are used both in a splitter and a combiner configuration to account for the downlink and uplink components of the system thus exploiting the devices' asymmetrical splitter/combiner performance.

A wireless LAN IEEE-802.11g signal (64-QAM, 54Mbps) at a carrier frequency of 2.412GHz (channel 1) is generated by a Rohde & Schwarz SMIQ vector signal generator and directly modulates the VCSEL source. The optical signal is transmitted though the 1x2 or 1x8 devices and a 62.5/125 µm multimode fibre link with lengths of 150 m and 300 m. A photodiode converts the received optical signal to an electrical one which is then demodulated by a Rohde & Schwarz vector signal analyser (Fig. 7).

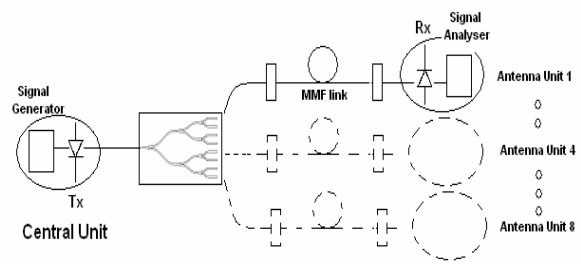
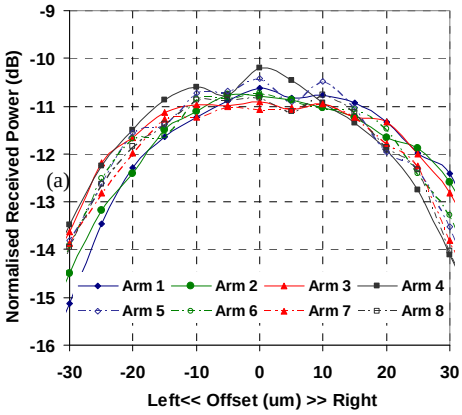


Fig. 7: Schematic of radio-over-fibre downlink.

The root-mean-square (rms) error-vector-magnitude (EVM) of the received electrical signal in all output channels is measured and plotted as a function of the fibre input misalignment and for the different link lengths of MMF. The received optical power in each arm is also recorded for every position of the input to verify uniform power splitting. Figure 8 shows the EVM and normalised received power in each output arm versus input offset for a downlink system with a 50 µm MM input fibre, a 1x8 splitter and a 150 m MMF link. EVM rms values are around 2% while the output power imbalance is less than 1.2 dB and the device excess loss is 1.5 dB. The additional 0.5 dB MM fibre link loss results in a total optical link loss of approximately 11 dB per channel. For the corresponding uplink a similar EVM value of 2% is recorded while the total loss is 7 dB, demonstrating the advantage of the splitter/combiner asymmetry. Using a SMF or free space input will yield a 4 dB total loss without any EVM degradation. Thus, the uplink noise performance is improved significantly. Table 2 summarises the results obtained for the RoF system under the conditions described above.

(a)



(b)

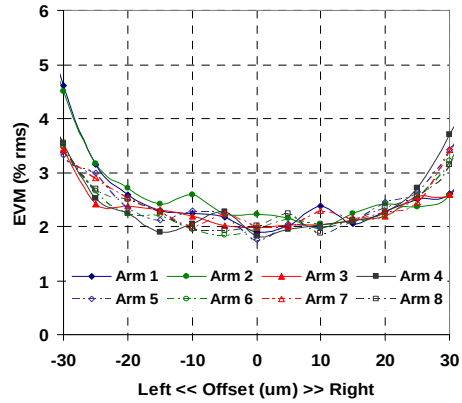


Fig. 8: 1x8 Y-Splitter performance for a 150 m MMF link: (a) Normalised received power (b) EVM versus input offset for all arms.

Table 2: EVM values of (a) 1x2 and (b) 1x8 devices for a 50 µm MMF input and different MMF link lengths.

(a)

Device	Y 1x2 – EVM (% rms)	
Link Length	Splitter	Combiner
0 m	1.3	1.2
150 m	1.5	1.5
300 m	2.3	2.3

(b)

Device	Y 1x8 – EVM (% rms)	
Link Length	Splitter	Combiner
0 m	1.5	1.5
150 m	2	2.2
300 m	3.2	3.5

5. Conclusions

Multimode polymer 1x2, 1x4 and 1x8 Y-splitters have been fabricated exhibiting high output uniformity and an excess loss as low as 2 dB for the 1x8 splitter. The devices exhibit differing behaviours when used as a splitter or as a combiner leading to a 6 dB power difference for the 1x8 device. Multicasting in a radio-over-fibre system is enabled for both the downlink and uplink directions. Exploiting the splitter/combiner asymmetry, a clear power advantage for the uplink is shown and similar EVM values as low as 2% are achieved for IEEE 802.11g transmission in both directions for an 8-way 150 m range MMF network.

6. References

[1] R. T. Chen, et al., “Fully embedded board-level guided-wave optoelectronic interconnects,” in Proc. IEEE, vol. 88, pp. 780–793, June 2000.

[2] C. Berger, et al., “Optical links for printed circuit boards,” in IEEE Lasers and Electro-Optics Society, 2003 vol. 1, Oct. 2003, pp 61-62.

[3] J. D. Ingham, et al., "Multimode siloxane polymer waveguides for robust high-speed interconnects," in Proc. Conference on Lasers and Electro-Optics 2006, paper CThS4 (2006).

[4] W.K. Burns, A. F. Milton, *Guided Wave Optoelectronics* (Springer-Verlag 1988), Chap. 3.

Optimized Deep UV hardbake process for metal-free dry-etching of integrated optical devices

Gabriel Sengo, Henk A.G.M. van Wolferen, Kerstin Wörhoff and Alfred Driessen
Integrated Optical Micro Systems, MESA+ Research Institute; University of Twente
P.O. Box 217, 7500 AE Enschede, The Netherlands, E-mail: g.sengo@utwente.nl

Abstract: *Photostabilization is a widely used post lithographic resist treatment process, which allows hardening the resist profile in order to maintain critical dimensions and to increase selectivity in subsequent process steps such as reactive ion etching. In this paper we present the optimization of Deep UV-curing of 0,3-3.5 μm thick positive resist profiles followed by heat treatment up to 280 ^{0}C. The effectiveness of this resist treatment allows for metal mask free reactive ion etching with selectivity up to 6 for silicon structures, thermal silicon oxide and silicon oxynitride. A number of experimental results on integrated optics structures are presented that demonstrate the improved etch profiles obtained with this approach.*

Introduction

Positive photo resist is not only widely used as a mask for patterning structures in the semiconductor industry but also for manufacturing of a wide range of optical devices. In contrast to electronic devices, where many patterning steps involve small lateral dimensions in combination with a small step height, the main challenge in the patterning of optical devices consists in the high lateral resolution together with often a large step height. In our research group a large variety of optical devices based on Si, Si_3N_4, SiO_2 and SiO_xN_y waveguides have been designed, realized and tested.[1,2] For optical waveguide fabrication, the majority of those applications require a steep, vertical step which can be up to several microns high. In order to realize low-loss optical waveguides, side walls with low roughness are crucial. When applying reactive ion etching (RIE) on standard processed resist structures, the imposed ion bombardment often causes damage to the resist profile resulting in increased sidewall roughness. In addition, when exceeding the glass transition temperature (Tg) of the resist; re-flown masking material will inhibit the maintenance of dimensions.

Although process optimization was shown to result in well-defined, high quality waveguides, the processing and design windows become rather limited. Therefore in many fabrication schemes an additional metal hard mask was introduced, which solved the selectivity problem on one hand, but yielded new problems on the other side. In addition to loss-increasing metal contamination and rough side-walls, mask material erosion and redeposition causes the formation of "spikes"[2] (see Fig. 1) which also contribute to increased losses.

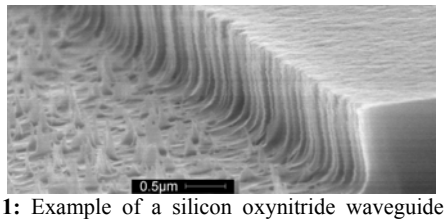


Fig. 1: Example of a silicon oxynitride waveguide with large side-wall roughness and spikes, typically obtained with an Ni hard mask in combination with RIE

Therefore, the application of metal hard masks should be avoided in low-loss optical waveguide fabrication and the feasibility of special resist treatment should be explored. The use of non-treated resist provides, however, also no solution, since most positive resist consist of novolac resins that begin to flow, depending on the manufacturer, at temperatures around 120^{0}C resulting in loss of critical dimension.
In order to make the resist structure thermally stable and strong so that it can withstand high temperatures which occur during the RIE and Ion Implantation, several resist treatment methods have been proposed. These include Deep UV (DUV) hardening followed by -or in combination with heating[3,4,5], plasma resist stabilization technique[6], and photoresist polymerization through pulsed photomagnetic curing[7]. In addition, hard baking of the resist structure at high temperature is also necessary to increase the resist selectivity during RIE.
Of the proposed resist treatment methods, DUV-curing and thermal heating is a widely used post lithographic process, to harden the resist profile in order to maintain critical dimensions and increase the resist selectivity necessary during the subsequent process steps such as RIE and ion implantation. In the following we apply this method to several integrated optics structures with critical dimensions.

Experiments

The experiments were carried out on various layer structures as used in integrated optics applications. The layers include blank silicon wafers, SiO_2 obtained by wet oxidization of Si-wafers or by plasma enhanced chemical vapor deposition (PECVD), low pressure CVD of Si_3N_4 and PECVD silicon oxynitride (SiON) of various thicknesses. The resist types used were the positive resist OIR 907/12, OIR 907/17 and OIR 908/35 of Arch Chemicals. After standard cleaning and resist spinning, the wafers were exposed with the Electronic Visions EV620 Mask aligner with a 12 mW/mm^2 conventional G-line (436 nm) light source. Different laser written masks were used with amongst others

waveguide structures of various dimensions, ranging from 0.9 to 4 μm. For the photonic crystals and gratings OIR 907/12 was diluted to obtain a thickness of 300 nm. The resist was then single exposed by a Laser Interference Lithography (LIL) system (λ=266 nm) for the gratings and double exposed for the photonic pillars. The grating period was about 500 nm.
For microring resonators OIR 907/12 was diluted to obtain thickness of 500nm.
After development, the wafers were, in contrast to the standard DUV-curing process carried out mostly in nitrogen or oxygen atmosphere[8], first intensely irradiated in an air filled chamber after which they were baked at temperatures of 180-280 ^{0}C for 1-3 hours.
After DUV-curing and a hardbake step, the structures were etched in Elektrotech Twin System PF 340 Reactive Ion Etching, Plasmatherm 790 parallel plate Reactive Ion Etching or Alcatel Adixen DE Inductive Coupled Plasma machines. The profiles were measured with a Dektak 8 of the Digital Instrument Veeco Metrology Group and examined with the Scanning Electron Microscope of JEOL, type JSM-5610/5610LV.

Results and discussion
The success of the photostabilization process strongly depends on the optimization of the two decisive processing steps, namely the heating and irradiation. It is believed that upon intense irradiation, a cross-linked outer skin of 100-200 nm with a higher degree of polymerization is formed. This skin should be strong enough to prevent the deformation of the resist profile even when hardbaked at elevated temperature far beyond the T_g of the resist. [3]
If the irradiation is not performed well, the internal stress due to heating or softening of the material above T_g might cause the deformation of the resist profile. On the other hand if the heating process is not carried out properly or too fast, the core of the resist profile will not have enough time to outgas and to harden resulting in deformation of the structure.

1. Process optimization for resist 907/17
In Fig. 2 the process optimization is presented for resist 907/17, spun at 6000 rpm, which gives a thickness of 1.2 μm.

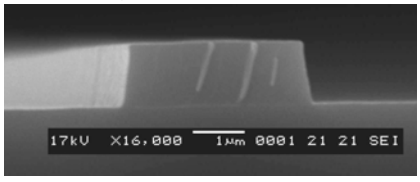


Fig. 2 (a): A typical resist profile after development in the OPD4262 positive resist developer.

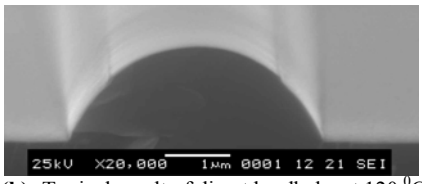


Fig 2 (b): Typical result of direct hardbake at 120 ^{0}C for 30 minutes without DUV irradiation. The T_g of the resist is exceeded causing severe reflow of the profile.

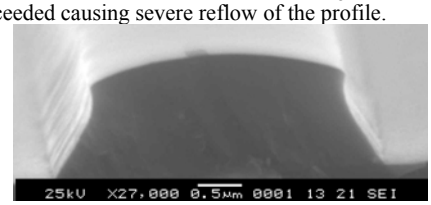


Fig. 2 (c): Not-optimized DUV-curing and direct hardbake at120 ^{0}C for 30 minutes. The outer-skin is too weak to withstand the internal stress.

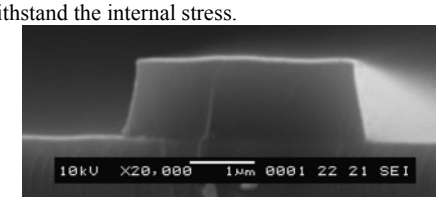


Fig. 2 (d): Optimized DUV-curing by applying proper irradiation time, followed by optimized hardbake with a final step at 120^{0}C for 30 minutes.

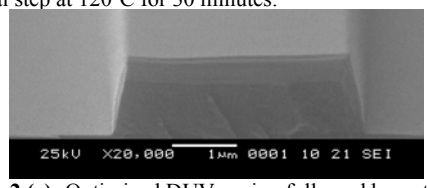


Fig. 2 (e): Optimized DUV-curing followed by optimized hardbake at 250^{0}C for 2 hours

The optimization of DUV- curing is obtained by the variation of irradiation time and optimization of the hardbake. The latter is done by performing bake steps with increasing temperature and by variation of the duration of those steps.

Starting with Fig. 2 (a), a typical resist structure after lithography without heat treatment is given. Fig. 2 (b) shows the result of hardbaking without applying DUV- curing. Fig. 2 (c) shows the importance of both the proper irradiation and gradual temperature rise in several steps. The irradiation is too short to form a strong cross-linked outer-skin to withstand elevated temperatures above T_g, resulting in the reflow of the profile. The next figures show the result of optimized temperature and irradiation. After achieving the optimized resist profile of Fig. (d), the result of (e) was obtained by further hardbaking steps up to 280^{0}C with an additional temperature optimization.

2. Process optimization for resist 908/35
In Fig. 3 the process optimization is presented for resist 908/35, spun at 4000 rpm, which gives a thickness of 3.5 μm.

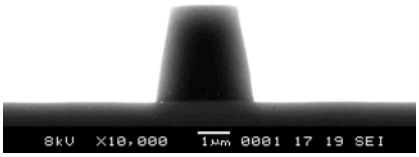


Fig. 3 (a): Typical resist profile after development.

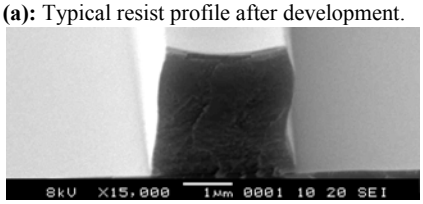


Fig. 3 (b): Similar resist profile with optimized DUV-curing followed by rampant heating from 25-180 ^{0}C for 3 hours.

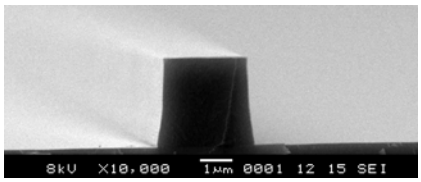


Fig. 3 (c): Optimized DUV-curing followed by optimized hardbake at 180 ^{0}C for 2 hours for the same profile.

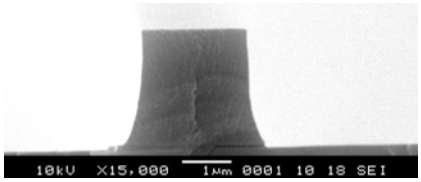


Fig. 3 (d): Optimized DUV-curing followed by optimized hardbake at 280 ^{0}C for 1 hour.

The set of figures show clearly the importance of controlled hardbake. If, after development (Fig. 3 (a)) the hardbake is carried out too fast, the internal stress will increase, resulting in the forming of the "wave" pattern of Fig. 3 (b). However, due to optimized DUV- irradiation, in analogy to Fig. 2, the cross-linked outer-skin prevents the reflow of the resist profile, see Fig. 3 (c).
After the optimization of both, the hardbake and DUV- irradiation, the resist has been baked up to 280 ^{0}C. As can be seen from Fig. 3 (d), the integrity of the profile is still well maintained, although the forming of the so-called "foot" is clearly present. This behavior was also observed by resist 907/12 and 907/17 baked at 280^{0}C. It appears that the bottom of the profile is slightly broader than the top which is of course partly inherent to the lithographic process, as can be seen in Figs. 2 (a) and 3 (a). The difference between the width at the top and bottom is varying from 0,15- 0.8 µm. The behavior of the "foot" is also clearly observed by I. Pollentier et al.[9]
To avoid the forming of the "foot", it is necessary to apply the hardbake below 280^{0}C. For our applications, the resist structures were used after an optimized hardbake at 180^{0}C for 2 hours.
The hardbake should be carried out step by step to the final temperature of 180^{0}C or higher in order to maintain the integrity of the resist profile.
Obviously the thicker the resist, the longer the irradiation and also a proper optimization is required. Characterizing and determining the proper sequence of DUV exposure and thermal rise to a final temperature are paramount to the success of photostabilization[8].

3. Diluted resist: nanostructures

For nanostructures as for example gratings, photonic pillars and microring resonators[10], thin resist is required to achieve high resolution in lithography. For this purpose resist 907/12 was diluted to obtain the thickness of 300 and 500 nm.

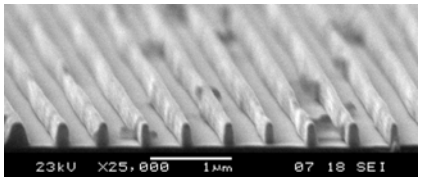


Fig. 4 (a): 300 nm optimized DUV-cured resist profile followed by optimized hardbake at 180^{0}C for 2 hours. This kind of resist structures has been used to etch gratings and photonic pillars.

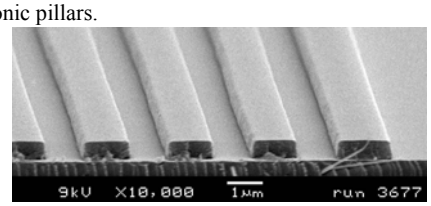


Fig. 4 (b): 500 nm optimized DUV-cured resist profile followed by optimized hardbake at 180^{0}C for 2 hours used for etching of microring resonators with a gap of 0,6 µm.

Figs. 4 (a) and (b) are typical resist structures used for etching of nanostructures in materials such as SiON, SiO2, Si3N4 and Si.
Compared to the resist structures of Figs. 2 and 3, the structures of figure 4 are obviously much shorter irradiated, because the thinner the resist, the shorter the irradiation time. The optimized hardbake was in all cases the same.

4. Etch selectivity

Experiments have been carried out with resist baked at 180 and 280^{0}C to investigate the etch selectivity. There was no noticeable difference measured between resist baked at these two temperatures. Therefore, for the further experiments, the resist profiles had an optimized hardbake with a final temperature step at 180^{0}C for 2 hours.
For PECVD SiON layers of 1.5 -2.5 µm deposited on silicon and etched in the Plasmatherm 790 dry etching machine, a selectivity of 5 was obtained. For layers of 1.5 -2.5 µm SiON deposited on 8 µm thermal oxide a selectivity of 6 was obtained. For silicon a selectivity of 4-5 is obtained for etching controlled structures of 200 - 1000 nm in the PF 340 Reactive Ion Etching twin system. For oxide, a

selectivity of 4 was obtained in the Plasmatherm 790 and a selectivity of 6 was obtained in the Alcatel Adixen DE Inductive Coupled Plasma etching machine. In addition, the silicon nitride selectivity never has been a problem; it is quite high.

5. Optical structures

Initial experiments have been carried out with PECVD SiON layers ranging from 1.0- 2.5 µm, because from the lithographic point of view, SiON is the most difficult material in achieving high resolution and high etching steps. If the photostabilisation process could be optimized for SiON, other materials like oxide, nitride and silicon would form no problem.

Under specific conditions it is possible for conventional contact mask lithography with a source wavelength of 436 nm, to open gaps of 600 nm, for example between a waveguide and a laterally coupled microring resonator.

In figure 5 some examples of these critical optical structures are presented.

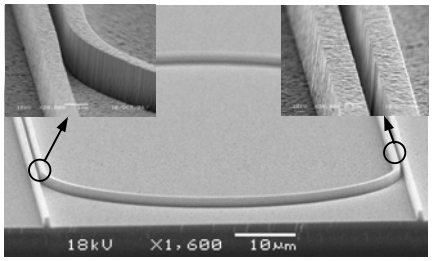


Fig. 5 (a): Microring resonator with a gap of 600 nm between the waveguide and the ring. The height is 1.7 µm etched in SiON layer of 2,5 µm deposited on 8 µm thermal oxide wafer.

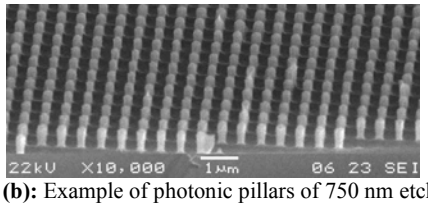


Fig. 5 (b): Example of photonic pillars of 750 nm etched in silicon using diluted resist of 300 nm obtained by LIL.

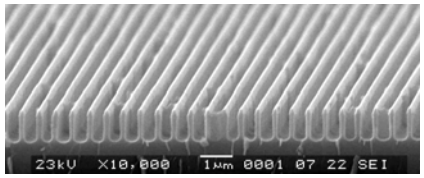


Fig. 5 (c): Example of gratings of 750 nm etched in silicon obtained by LIL using diluted resist of 300 nm.

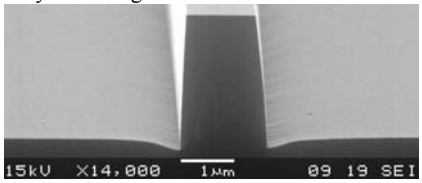


Fig. 5 (d): Waveguide of 2.3 µm height etched in thermal silicon oxide.

Fig. 5 (a) is a typical example of a microring resonator used for telecom applications obtained by SiON- technology using resist structures of Fig. 4 (b). Figs. 5 (b) and (c) are examples of respectively photonic pillars and gratings of 750 nm height etched in silicon using 300 nm hardbaked resist of Fig. 4 (a). Fig. 5 (d) is a typical example of a waveguide etched in thermal silicon oxide, with a sidewall angle of 85^0, obtained by Alcatel Inductive Plasma Coupled etching machine. With one micron harbaked resist, around 6 micron oxide can be etched.

Conclusion

It has been demonstrated that the use of the photostabilization process makes the resist strong and robust to withstand the subsequent process steps with minimum loss of critical dimension. The method is safe, clean, reliable, easy to apply and can be used for the production of wide range of critical optical devices in silicon, thermal silicon oxide, nitride and silicon oxynitride. In addition, the use of metal masks, causing a lot of problems in optical applications, for subsequent process steps can be avoided.

Acknowledgment

This work is partly funded by the Dutch National Broadband Photonics Access project.

References

1 K. Wörhoff et al., Electrochem. Soc. Proc., Vol. 2002-4, pp. 279-312, 2002
2 C. Roeloffzen, Ph.D. thesis, Enschede, 2002.
3 R. Allen et al., J. for Electrochem. Soc. vol. 129, pp. 1380, 1982.
4 R. Mohondro et al., Future Fab International, Vol. 3, pp. 235-247, 1997.
5 G. Jordhamo et al., International Society for Optical Engineering, Vol. 2724, pp. 588-600, 1996
6 W.H.L. Ma, International Society for Optical Engineering, Vol. 333, pp. 19-23, 1982.
7 Paul A. Ruggerio, Solid State Techn. Vol. March 1984, pp. 165-169, 1984
8 R. Mohondro, Solid State Techn. Vol. February 2003, 2003
9 I. Pollentier et al., Future Fab International, Vol. 12, 2002
10 D.J.W. Klunder et al., Appl. Phys. B, Vol. 73, pp.603-608, 2001

Waveguide grating for microchip-laser polarization control

Florent Pigeon (1), Marwan Abdou Ahmed (2), Olivier Parriaux (1), Svetlen Tonchev (3), Nicolas Landru (4) and Jean-Philippe Fève (5)
(1) Laboratoire Hubert Curien (formerly TSI) UMR CNRS 5516, 18 Rue B. Lauras, F-42000 Saint-Etienne
(2) Institut für Strahwerkzeuge (IFSW), Stuttgart University, Pffafenwaldring 43, D-70569 Stuttgart
(3) on leave from the ISSP, Sofia, Bulgaria
(4) Teem Photonics, 61 Ch. du Vieux Chêne, 38246 Meylan, Franc
(5) JDSU Laser Products Group, 430 North McCarthy Blvd., Milpitas CA 95035, USA
parriaux@univ-st-etienne.fr

Abstract: *A slab waveguide grating submirror monolithically associated with a standard multilayer submirror represents a laser output coupler which polarizes the emission of a passively Q-switched Nd:YAG microchip laser over its full emission bandwidth by intra-mirror destructive interference for the undesired polarization. A polarization extinction ratio of more than 25 dB is obtained up to 6.1μJ pulse energy. Linearly polarized emission shows no loss penalty.*

Introduction

In most applications of surface emitting lasers such as disk and microchip lasers or VCSELs, there is a need for an integrated element which controls the emitted polarization. The planar geometry of such lasers forbids the use of a Brewster element. Since the discovery [1] and analysis [2] of the effect of zeroth order resonant reflection from a grating slab waveguide, it is possible to achieve the polarization control of laser emission by highly polarization selective reflection as first demonstrated by Sychugov at al [3] in the case of a semiconductor laser with external cavity mirror. Zeroth-order resonant reflection can theoretically reach 100% for one polarization [4].

The present paper demonstrates a laser polarizing mirror solution which takes the best of two mirror technologies: the well established non-selective multilayer technology which ensures most of the needed reflection, and the corrugated slab technology which does not reflect much light but essentially produces the polarization selectivity. Stimulated emission does the rest by amplifying the sole polarization which experiences the larger reflection coefficient. The specific feature in the present combination of the multilayer and resonant submirrors is the destructive interference condition between fields which each submirror reflects which implies that it is the polarization which experiences resonant reflection which is filtered out.

This is not the only approach for monolithically polarizing laser emission by means of a periodic structure: the combination between each submirror can have a constructive character and lead to the lasing of the polarization experiencing waveguide coupling and resonant reflection [5]; there are important differences in terms of bandwidth and power flux resistance. There are other polarizing mechanisms as well: a deep binary grating etched into a thick high index layer can exhibit 100% reflectivity for the TM polarization according to the GIRO mirror scheme [6]. A shallow grating of relatively large period can also induce a reflection differential as demonstrated in VCSELs [7]; such an approach is however risky as a large period gives rise to propagating diffraction orders or couples the emitted wave to unforeseeable guided modes of the multilayer whose density may be large. Another, more predictive approach, uses deep trenches into the multilayer with the objective of giving rise to photonic crystal effects [8]; the risk here is the scattering losses associated with an imperfect trench pattern of very high index contrast. The present approach excites a well identified mode of the multilayer without losing power in radiated diffraction orders and it is much less traumatic than a photonic crystal to the mirror and photon generation process, since it is a soft post-process on top of an essentially standard multilayer.

Associating multilayer and resonant submirrors

The multilayer submirror ensures a low-loss, high-reflection pedestal, whereas the resonant mirror adds its polarization selectivity to the smaller part of the reflection it provides. The reflection pedestal provided by the multilayer submirror is set at the reflection level needed for laser operation of the desired polarization whereas the reflection dip due to waveguide coupling and resonant reflection must have a depth below threshold to prevent the amplification of the undesired polarization. The

sketch of the superposition of the two submirrors is shown in Fig. 1.

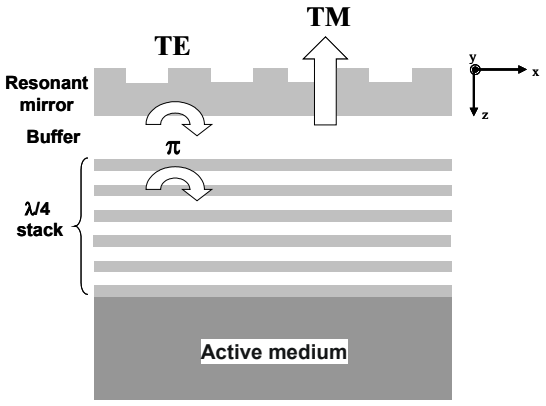


Fig. 1: Destructive interference polarizing mechanism resulting from the association of a multilayer submirror and a polarization selective resonant submirror.

The two submirrors are separated by a low-index buffer, whose thickness w_b is adjusted on the basis of the following criteria: first, the buffer layer thickness dictates the phase shift $\Delta\phi$ between the field reflected by the multilayer and that reflected by the resonant grating. If the grating is made at the cover side of the mirror (usually at the air side), $\Delta\phi$ is given by

$$\Delta\phi = 2\, k_0\, (n_b w_b + n_w w_w) + \pi \qquad (1)$$

where $k_0 = 2\pi/\lambda$ is the wave number in the cover (here considered as air), n_b and n_w are the refractive index of the buffer and waveguide slab layers of thickness w_b and w_w respectively. The last term of expression (1) is the phaseshift upon resonant reflection known to be π [4]. In the present case $\Delta\phi$ must be close to π modulo 2π for destructive interference between the multilayer and resonant submirror reflected fields as illustrated in Fig. 1: the polarization which is coupled to the slab waveguide does not lase since its reflection coefficient is decreased by destructive interference.

Design of the polarization selective mirror

As a practical example for the implementation of such a device, the polarizing function will be monolithically integrated into the multilayer mirror of a passively Q-switched microchip laser (Nd:YAG as the gain medium, bonded to a Cr:YAG saturable absorber).

The incidence is from the substrate side as suggested in Fig. 1. The substrate index at the emission wavelength of 1064 nm is $n_s = 1.82$. The multilayer mirror technology is HfO_2/SiO_2 ion plating with assumed layer refractive indices of 2.10/1.48. The targeted reflection coefficient of the laser output coupler for the lasing polarization, i.e. the multilayer pedestal, is set at about 85%, whereas the polarization selective resonant dip is set at 60% reflection at most to prevent the lasing of the undesired polarization.

An approximate design essentially defined by expression (1) is fed into a grating optimization code based on the modal method which searches for the desired dichroic properties of the polarization filter.

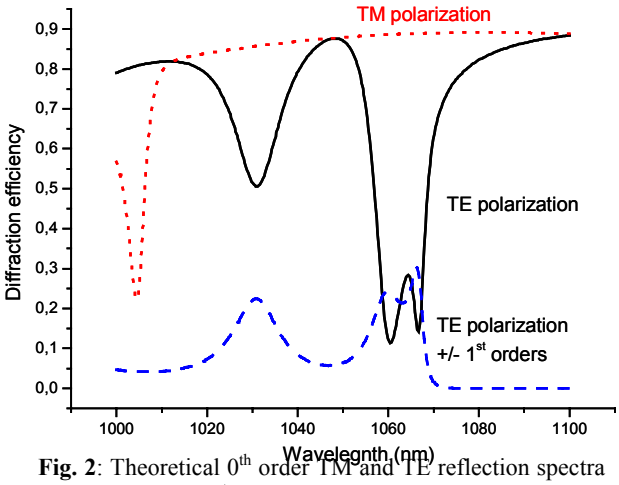


Fig. 2: Theoretical 0th order TM and TE reflection spectra and reflected ± 1st order TE diffraction efficiency with excitation from the substrate side.

Figure 2 gives the TE and TM reflection spectra of the optimized resonant grating multilayer. The grating is a binary corrugation of 605 nm period, 145 nm depth and 1/1 line/space ratio. The optimised thickness of the low index SiO_2 buffer is 400 nm. Figure 2 gives the theoretically expected TM and TE reflection spectra as well as the $\pm 1^{st}$ order TE reflection into the active substrate with incidence from the active substrate side. As expected, it has been possible to bring two neighbouring TE modes close to 1064 nm which permits to considerably broaden the tolerances. Their effective index is $n_e = \lambda/\Lambda = 1.776$ and 1.767. Plotting the electric field of these two modes reveals that the dominant modal field ($n_e = 1.776$) has no zero crossing and is the fundamental mode of the whole structure. The closely neighbouring mode with $n_e = 1.767$ with its single zero crossing is the TE_1 mode.

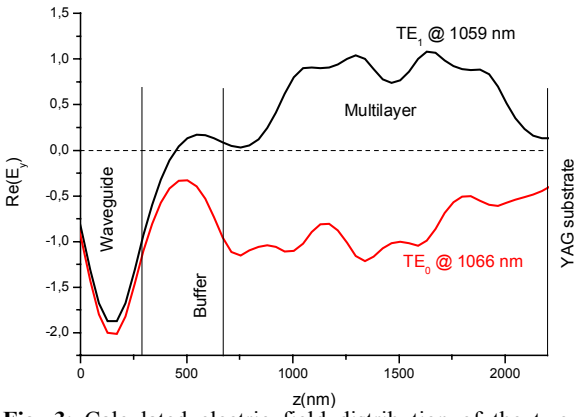


Fig. 3: Calculated electric field distribution of the two neighboring lowest order TE modes of the optimized structure giving rise to the spectra of Fig. 2.

Figure 3 illustrates the electric field profile of these two modes at their resonance wavelength. As intended from the start, both fields exhibit a strong maximum in the high index waveguiding layer and a slow decrease at the substrate side. One understands now why it was possible to bring the effective index of these two modes close to each other: thanks to the wide low index buffer layer the structure is equivalent for the two first order modes to a directional coupler with its two supermodes of neighbouring effective index, the first waveguide being the last high index waveguiding layer, the second waveguide being the rest of the multilayer.

Fabrication of the grating multilayer.

The prescribed SiO_2/HfO_2 multilayer was deposited onto 12.5 mm diameter, 1.23 mm thick Nd:YAG wafers bonded to a 0.33 mm thick Cr:YAG saturable absorber. The resist-coated wafers were exposed according to the design to a 605 nm period interferogram at 442 nm wavelength. The physical transfer was made by a RIBE process using a 60% CF_4 and 40% argon ion beam.

The corrugated multilayer was submitted to the incidence of a polarized microchip Nd:YAG laser beam at 1064 nm wavelength in the neighbourhood of normal incidence with incidence from the air side. Figure 4 gives the reflected power measured for both polarizations upon a variation of the incidence angle. As expected the reflected TM polarization exhibits a monotonic angular dependence since there is no TM resonance in this region. The TE polarization shows a pronounced reflection fall in the form of one wide dip at either side of the normal. As a whole there is a polarization eye between the TE and TM polarizations exhibiting a TE reflection coefficient at least 20% smaller than the TM's over a full angular range $\Delta\theta$ of about 3.4 degrees. Under close to normal incidence, and neglecting the wavelength dependence of the effective index, this corresponds to a wavelength range $\Delta\lambda = \Lambda\Delta\theta$ = 18 nm which covers well over the Nd:YAG gain bandwidth which is about 0.6 nm.

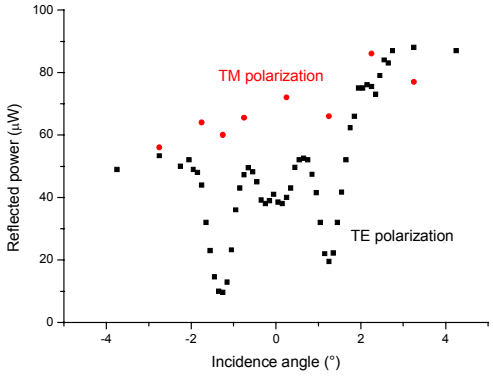


Fig. 4: TE and TM reflected power at 1064nm versus incidence angle measured upon incidence from the air side.

The wafer scale uniformity was tested by AFM scans made at 5 different places: the grating depth is 143 nm within 5 nm, and the line/space ratio is 1.0 ± 0.1. Systematic but low sensitivity scattering measurements have been performed on such a device by directing the collimated beam of a filtered white light source onto the grating region from the substrate side. The scattering level is evaluated on the reflected beam by repeatedly moving the grating area into and outside the beam cross section. The results reveal that the scattering level on the reflected TE polarization (that which couples the guided mode) is at most 0.6%, the scattering measurement being made outside the reflection dip at 1056 nm wavelength, and that the scattering of the reflected TM polarization (the lasing polarization) is at most 0.14%, the scattering measurement being made at the wavelength of the TE reflection dip.

Laser experiments

Pumping was achieved with a multimode diode at 808nm (1*100µm emitter, linear horizontal polarization). The pump power incident on the laser cavity was 0.8 W, focused by a gradient-index lens into a beam size of 60µm. Before etching the grating, the repetition rate was 10.4 kHz, the pulse energy 5.9 µJ, and the pulse duration 0.59 ns. After processing the grating, the frequency was 11.16 kHz and the

pulse energy 6.1µJ. This shows that the process did not degrade the multilayer coating. This is also highly consistent with the above scattering measurements: in the considered Nd:YAG microlasers, the loss penalty due to the grating itself is at least two orders of magnitude lower compared with the other passive losses of the laser cavity (output coupling and non-saturable absorption of the passive Q-switch). As a consequence, this additional loss does not play any noticeable role on the laser performance.

We measured the polarization of the 1064 nm output beam before etching the grating. The output polarization was partially linear, and we rotated the wafer to maximize the polarization extinction ratio (PER), which corresponds to the preferred orientation always horizontal, similar to the pump. We marked this preferred axis on the wafer as a guide for the alignment of the grating. Without grating, the PER was very inhomogeneous throughout the surface of the wafer, ranging from 4 dB to 34 dB; at the center of the wafer, measurements on four wafers varied from 11 dB to 33 dB. These huge variations confirm that an external mean is needed to obtain reproducible controlled output polarized beam from a microlaser.

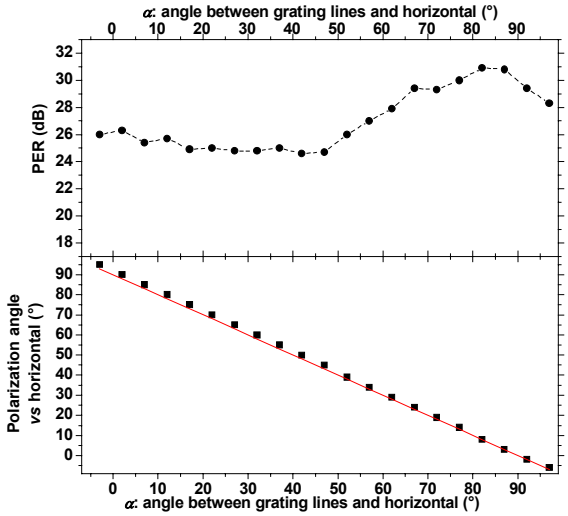


Fig. 5: Bottom curve: direction of polarization (measured from horizontal) vs angle α between the grating lines and the horizontal. The top curve represents the corresponding variation of the PER.

Figure 5 shows the polarization data measured at the center of the wafer after etching the grating. First, the PER is larger than 25 dB whatever the angle α between the grating and the horizontal axis (i.e. orientation of grating lines with respect to the polarization of the pump diode). Second, the polarization of the output beam is at 90° from the lines of the grating for every orientation of the wafer. These data clearly demonstrate that the grating ensures an efficient control of the polarization of the laser beam.

Conclusion

This paper reports on the demonstration of the monolithic control of the polarization emitted by a microchip laser by means of a waveguide grating effect suppressing the emission of the undesired polarization. An appropriate division of functions between a standard multilayer submirror and a post-processed two-layer waveguide submirror combines the low-loss feature of laser mirror technology and the polarization selectivity of resonant reflection, the latter causing the destructive interference of the two submirror reflected fields. The power flux resistance of the microchip laser is hardly affected by the action of the resonant grating since the latter only acts on the non-lasing polarization. For the same reason, grating scattering affects the lasing polarization only marginally.

Acknowledgement

The authors thank J.Cl. Pommier and S. Reynaud for performing the RIB-etching and the AFM scans. The support of the RMNT under the Micropack project is gratefully acknowledged.

References

1 V. N. Bel'tyugov et al., Proc. SPIE, vol. 1782, p. 206, 1992.

2 L. Mashev et al., Opt. Commun., vol. 55, p. 377, 1985.

3 G. A. Golubenko et al, Sov. J. Quantum Electron., vol. 15, p. 886, 1985.

4 I. A. Avrutsky et al., J. Mod. Opt., vol. 36, p. 1527, 1989.

5 J.-F. Bisson et al., Appl. Phys. B: Lasers and Optics, vol. 85, p. 519, 2006.

6. S. Goeman et al., IEEE Photon. Technol. Lett., vol. 10, p. 1205, 1998.

7. J. M. Ostermann, et al., IEEE Photon. Technol. Lett., vol. 17, 2505, 2005.

8. Dae-Sung Song et al., Appl. Phys. Lett., vol. 82, p. 3182, 2003.

18GHz Fabry-Pérot integrated extended cavity passively modelocked lasers

Y. Barbarin[1], E.A.J.M. Bente[1], M.J.R. Heck[1], J. Pozo[2], J.M. Rorison[2], Y.S. Oei[1], R. Nötzel[1] and M.K. Smit[1]
1) COBRA Research Institute, TU Eindhoven, e.a.j.m.bente@tue.nl
2) University of Bristol, jose.pozo@bristol.ac.uk

Abstract: *Integrated modelocked lasers producing pulses down to 2.1 ps were fabricated in bulk InGaAsP using butt-joint active-passive integration. It is demonstrated that good modelocked operation can be obtained in devices using this integration technology. Pulses obtained are close to transform limited and the dynamics outside the control parameter range for modelocked operating are reduced through the use of an extended cavity.*

Introduction

Modelocked lasers (MLL) are useful devices in optical telecommunications as transmitter sources and all-optical clock recovery devices [1]. When MMLs are realised in active-passive integration technology, they can be located anywhere on a larger chip containing other devices connected to the MLL. Also integrated extended cavity MLLs can have long cavities and therefor relatively low repetition rates which is usefull for many applications outside optical telecommunications. In this paper results from linear integrated extended cavity passively modelocked lasers (EC-MLL) are presented and comparisons are made with results obtained with all-active Fabry Perot MLLs (FPMLL). The active-passive wafer on which the EC-MLLs here were realized, is the one that showed very low butt-joint loss and reflections as presented in [2]. A number of 18 GHz self-colliding pulse modelocked lasers have been demonstrated. Pulses with a length of 2.1 ps and with a small pedestal have been observed. The linear lasers presented here demonstrate that butt-joint active-passive integration with sufficiently low junction reflectivity, as developed at COBRA can be utilized for integrated modelocked lasers. Moreover, the pulses obtained are close to transform limited [3,4] and the intensity modulations of the laser output in the range of the relaxation oscillation are significantly lower than the values observed in all-active FPMLLs [5].

Design and fabrication of the EC-MLL

A photograph of four fabricated 18 GHz EC-MLLs is presented in Fig. 1. The devices have been realized starting from extended cavity Fabry-Perot lasers that have been fabricated in active-passive integration technology at COBRA. A chip containing 12 lasers was cleaved at a length of 2.2 mm and no coating has been applied. One of the cleaves was made through the amplifier (active section). The other cleave went through the passive waveguides. The ridge waveguides are 2 µm wide. These are visible as dark lines in Fig. 1. The active regions are 30 µm wide, 750 µm long and are fully covered by the bright metal pads. The short SAs at the side of the FP cavity have been realized by electrically isolating a short section of the contact on the amplifier. This was done by using a Focused Ion Beam (FIB) machine at Bristol University within the COST 288 frame work to etch away the metal layer and highly doped top waveguide layers between two parts of the amplifier. By realizing the SA in this way, no extra mask was required and the SA lengths could be accurately controlled to vary from 5 to 17.5 µm. The electrical isolation sections that separate the SAs from the amplifiers are 15 µm long. With this method also part of

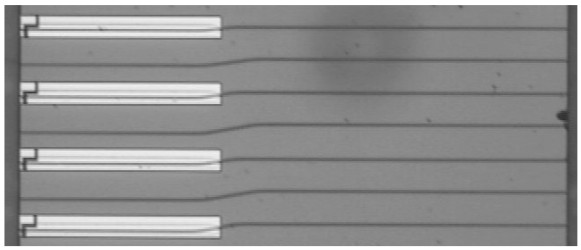


Fig. 1: Top view of four realized 18 GHz integrated extended cavity modelocked lasers. The active regions are covered by the bright metal pads. The short SAs at the left hand side of the FP cavity have been fabricated using a Focused Ion Beam (FIB) machine. One can see that the butt-joints are crossed at different angles.

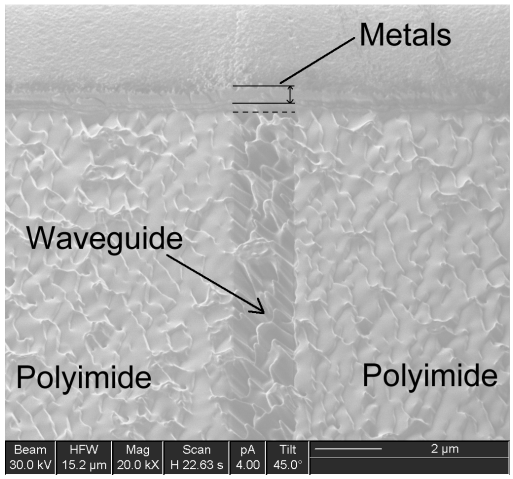


Fig. 2: Picture of a realized isolation between an amplifier and a saturable absorber, recorded with the Focused Ion Beam (FIB) machine. The metal layers of the electrical contact and part of the top cladding are etched away. Isolation obtained is >150 kKΩ.

Table 1: Characteristics of the extended cavity mode-locked lasers

SA length in µm	Butt-joint angle °	Reflectivity butt-joint (dB)	Mode-locked
5.0	15	-53	No
7.5	13	-51	No
10.0	11	-49	Yes
12.5	9	-47	Yes
15.0	7	-45	Limited
17.5	5	-43	No

the cladding (400 nm) has been removed during the etching processing (see Fig. 2). The electrical isolation obtained is 150 kΩ, which is more than sufficient. The waveguide in the EC-MLL contains adiabatic bends to make the crossing of the butt-joint in the cavity at varying angles. The original purpose of these devices was to study the effect of the different crossing angles [2]. The minimum radius of curvature of the bends in the waveguide is 250 µm. No offset between straight and curved waveguides is used.

18 GHz EC-MLL performance

The characteristic parameters of each laser are listed in Table 1. Modelocking has been observed for the devices with a 10 and a 12.5 µm long SA. The device with a 15 µm long SA has a very limited modelocking region. The devices with a 5 and a 7.5 µm long SA did not modelock. The absorption was too low, a higher reverse voltage than 3.0 V could have been applied but work on all-active MLLs has shown that the reverse current density (>20 kA/cm²) damages the SA. For the device with a 17.5 µm long SA no modelocking has been observed; the SA is too long or the laser suffers from internal reflections on the butt-joint which is the highest for this device (Table 1),

The ranges of the optical amplifier current and the saturable absorber voltage where modelocking occures, the modelocking region, have been determined for the 10 µm long SA device. It is modelocked continuously for a range of reverse bias voltages on the SA between 2.1 and 3.0 V and a range of amplifier currents between 144 and 162 mA. This device is discussed in more detail. First the operation outside the modelocked region is discussed. Two RF spectra of the laser output at current values outside the modelocking region are plotted in Fig. 3. Here the reverse bias voltage on the SA is fixed at 2.5V.

Just above threshold the laser is in a quasi-periodic state (Fig. 3.a). The RF peak at the fundamental frequency is 35 dB above the floor, but the laser behavior is dominated by strong amplitude modulation at frequencies below 1 GHz. It is

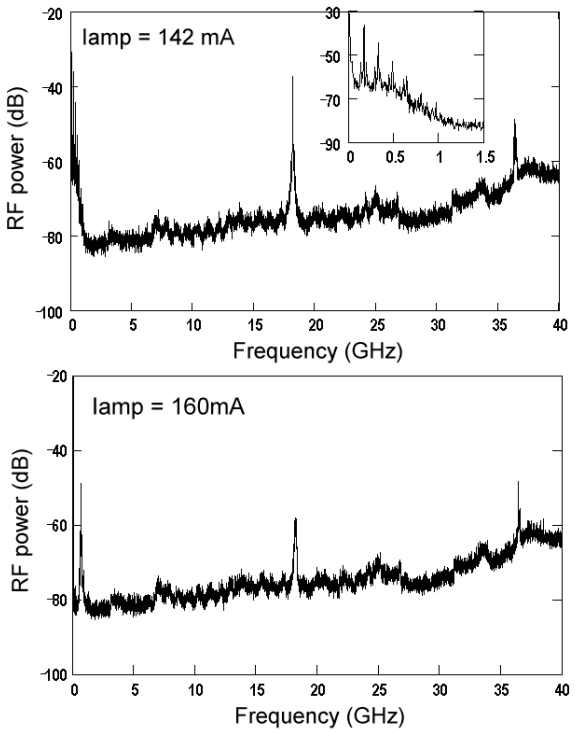


Fig. 3: Measured RF spectra of the passively modelocked laser output (L_{SA} = 10 µm, V_{SA} = – 2.5V) in:
a) a quasi-periodic state and
b) quasi-CW regime with few longitudinal modes beating

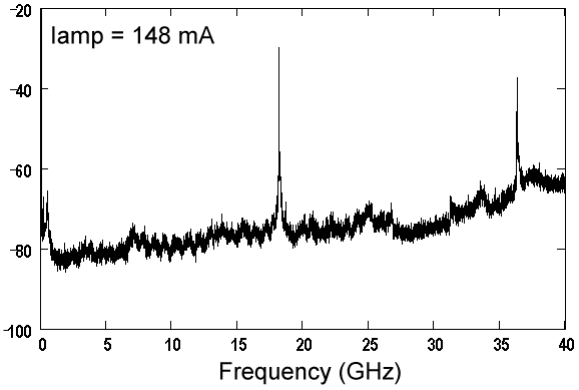


Fig. 4: Measured RF spectra of the passively modelocked laser output in modelocked state.
(L_{SA} = 10 µm, I_{amp} = 148 mA V_{SA} = – 2.5V)

interesting to compare those modulations to those at low frequency recorded from all-active FPMLL devices which have been realized by us in the same active layer-stack as the EC-MLLs here and have been reported upon earlier [5]. Just above threshold the EC-MLL shows pulsed modulation of the output at a frequency of ~150 MHz which is considerably lower than the 1 GHz pulsation observed for the all-active FPMLL output [5]. Another difference is that The intensity of the peak at the fundamental frequency of the EC-MLL output is already quite high (40 dB over the noise floor), close to the value in the modelocked state.

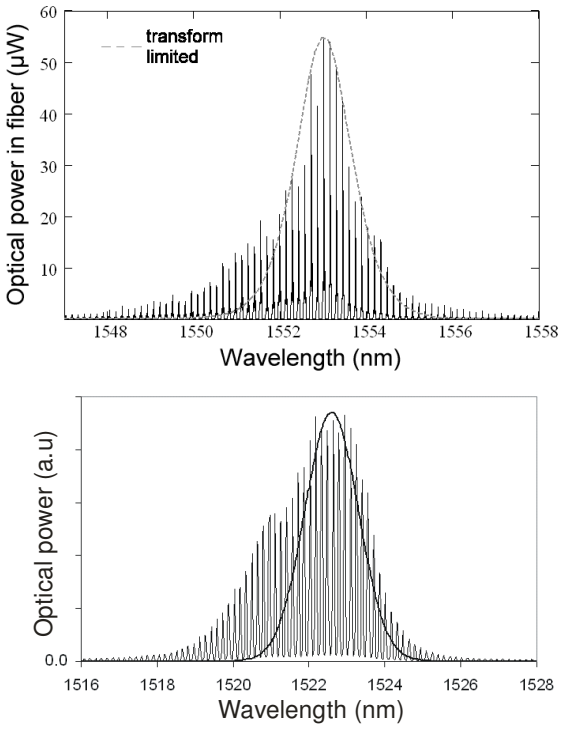


Fig. 5: Optical spectrum in linear scale of **a)** an extended cavity laser in a modelocked state for I_{amp} = 148 mA, L_{SA} = 10 µm, V_{SA} = – 2.5 V. **b)** a Fabry-Perot cavity laser in a modelocked state for I_{amp} = 121.7 mA and V_{SA} = – 1.9 V on the 10 µm long SA [5].

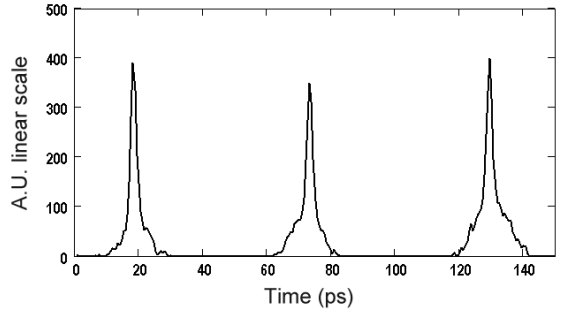


Fig. 6: Autocorrelator trace of an extended cavity modelocked laser for I_{amp} = 148 mA, L_{SA} = 10 µm, VSA = – 2.5 V.

For the EC-MLL, at current values higher than those for the modelocked state (Fig. 3.b), the main feature is a single low frequency component in the spectrum and two peaks separated by 150 MHz around the fundamental frequency. It corresponds to a quasi-CW regime with few longitudinal modes beating. Increasing the current further, the laser becomes more quiet. It demonstrates that the dynamics around the modelocking regime of the EC-MLL are reduced comparing to the all-active FPMLL [5] where at high current strong pulsations are observed at around 1.6 GHz. This reduction in oscillatory behavior is due to the smaller reservoir of carriers in the EC-MLL compared to the FPMLL. Fig. 4 shows the RF spectrum of an EC-MLL in a modelocked state. The peak at the fundamental frequency is 50 dB above the noise floor and 35 dB above the relaxation oscillation peak at ~800 MHz. The fundamental peak is 10 MHz wide (at -20 dB). The modelocked RF spectra are very similar to the ones of the all-active FPMLL [5].

In the modelocked state, differences between the output pulses and the optical spectra of the EC-MLL and the FPMLL are clearly visible. An optical spectrum of the EC-MLL output is plotted in Fig. 5a) for I_{amp} = 148 mA and V_{SA} = -2.5V; and in Fig 5b) for an FPMLL spectrum. Plotted in a linear scale, it reveals extra components at the blue side of the central longitudinal modes. The EC-MLL spectrum is approximately 1.6 nm wide (FWHM) but the shape of the wings of the spectrum is obviously not Gaussian or sech² like. The corresponding observed autocorrelation trace is plotted in Fig. 6. The autocorrelation shows pulses that are short with a considerable pedestal, but with a zero floor level between the pulses. In this condition, because of the pedestal, it is difficult to quantify with accuracy the length of the pulses from an autocorrelation. The estimated pulse length from the peak is ~2.1 ps FWHM. The time-bandwidth product for a transform limited pulse depends on the shape of the pulse (0.441 for a Gaussian pulse and 0.315 for sech² pulse). If it is assumed that the pulses from the laser are transform limited a pulse length and time-bandwidth product can be calculated from the observed optical spectrum. This time-bandwidth product is found to be ~0.33. Using the measured pulse width and spectral width leads to a time-bandwidth product of 0.39. Since these two values are close to each other the observed pulses are not far from being transform limited.

Conclusions

Experimental results from these EC-MLLs show that modelocked lasers can be realized using butt-joint active-passive integration. The intra-cavity reflections can be kept sufficiently low using a waveguide that crosses the butt-joint under an angle. The fabrication of SAs using a FIB did not create problems for the device. It allows for accurate control of the SA length and in the case of self-colliding pulse modelocked lasers the position of the SA in a cavity with cleaved mirrors. Comparing the experimental results of the EC-MLL with the all-active FPMLL devices [5], a smaller time-bandwidth product is observed from the EC-MLL [3,4]. Furthermore the dynamics outside the modelocking operating region are reduced. In fact, due to the shorter amplifier of the EC-MLL, it operates at one and a half to two times higher carrier density compared to the all-active FPMLL. Therefore, the effective differential gain [6] will be smaller and this leads to reduced Self-Phase Modulation (SPM).

Acknowledgments
This research was supported by the Towards Freeband Communication Impulse program of the Dutch Ministry of Economic Affairs, the NRC Photonics program and the COST 288 frame work.

References

1 K A Williams, M G Thompson and I H White, New Journal of Physics p. 179, Vol. 6 (2004)
2 Y. Barbarin et al,. Proc. IEEE LEOS Benelux 2005 Mons, Belgium, 2005
3 F. Camacho et al., IEEE Photon. Technol. Lett., no. 9, pp. 1208-1210, 1997
4 C. Ji et al., IEEE Photon. Technol. Lett., no. 18, pp. 625-627, 2006
5 Y. Barbarin et al., Proc. ECOC'05, Glasgow, Scotland, 2005.
6 Y. Barbarin et al. Applied Optics, No. 45, pp. 9007-9012, 2006

Low-loss and stable integrated optical Y-junction on lithium niobate modulators

N. Grossard, J. Hauden, H. Porte
Photline Technologies, 16 rue Auguste Jouchoux, 25000 Besançon, France.
nicolas.grossard@photline.com

Abstract: *We designed a new type of integrated optical Y-junction which can improve overall performances like optical losses, stability and geometrical dimensions. Optical simulations of the Y-junction on Ti:LiNbO3 waveguide and experimental results obtained confirm the predictions.*

Introduction

Single-mode Y-junctions play a key role in optical-waveguide circuits. These basic building blocks act as optical power divider-recombiner in devices like power splitters, modulators or switches. Actually, research in this field is still active [1] even if that type of fundamental element has been studied for many years [2]. These developments are motivated by the fact that little improvements on the design of the Y-junction can have a strong impact on more complicated integrated optical circuits with many cascaded Y-junctions: splitters, QPSK modulators...
Y-junction must generally meet a number of requirements which are summarized by the following points:

- low insertion loss;
- mode stability (low excitation of higher order modes);
- small longitudinal dimensions.

The main goal of optical designers is to propose the ideal scheme able to optimize these different points.
In this paper we present the development of a new Ti-indiffused LiNbO3 Y-junction and its application to the Mach-Zehnder intensity modulator.

Principle of the new design

Two-dimensional structures of the conventional Y-junction and the proposed Y-junction are depicted in Fig. 1.
The conventional single-mode Y-junction can be divided in three sections [3], the straight-guide section of width Wi, the tapered section where the width widens progressively from Wi to 2Wo+D and finally the branching section with half branching angle α and width Wo. Theoretically, the gap D between the arms tends towards zero but in practice the technological process limits it to a finite value to the order of the micrometer. This type of Y-junction suffers from instabilities due to the large taper width which can support higher order modes poorly recombined in the branches. Moreover, the truncation at the tip of size D can enhance the optical losses and the mode instabilities in a region particularly sensitive.
Taking into account the truncation, we have found a solution which bypass the problem: the single-mode Y-junction is split in two symmetric parts by a line of dimension to the order of the truncation [4]. We called this new structure the "Split-Y-junction". The Split-Y-junction can be described in two parts (Fig. 1): first the straight single-mode section with two little parallel waveguides of width Wi1 in close proximity D and after the branching section of angle 2α with the width varying from Wi1 to Wo. With a properly choice of parameters Wi1 and D, the straight single-mode waveguide can act as an efficient mode filter. Consequently, there is a better stability of the power splitting ratio. Moreover, as the truncation start from the beginning, no excess losses are generated at the transition between the straight section and the branching separation.

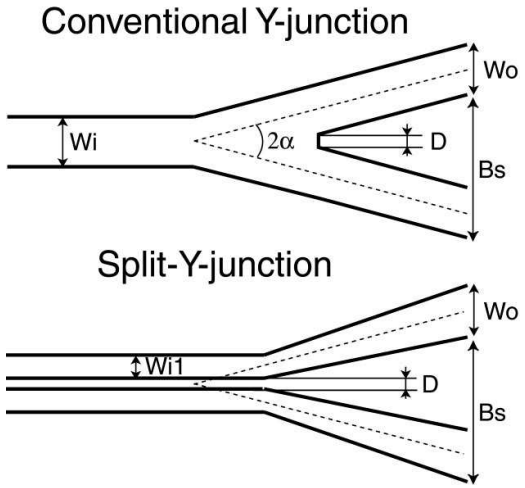


Fig. 1: schematic figure of the conventional Y-junction (up) and schematic figure of the proposed Y-junction (down).

Simulations and results

1. Geometrical dimensions

If we compare the size of each structure (Fig. 1), it seems evident that the Split-Y-junction is more compact than the conventional Y-junction. The length reduction Lr is calculated by the following formula:

$$Lr = \frac{D + Wi1}{Bs} \quad (1)$$

Graphical plots of the length reduction in percentage versus the branch separation are shown in Fig. 2. Whatever the input parameters D and Wi1 are, the gain in length is positive and rapidly increases when the branch separation decreases.

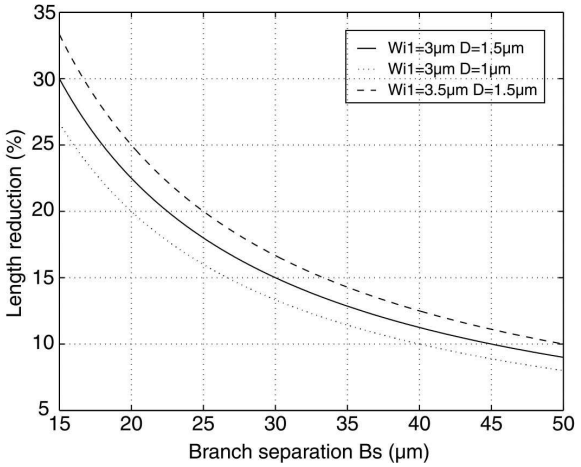


Fig. 2: Dependence of length reduction on branch separation.

For example, if D=1.5µm and Wi1=3µm, the length reduction can vary between 10% and 30% when the branch separation Bs is reduced from 50µm to 15µm.

2. Optical loss

The Y-junctions were modeled using the standard 2D finite-difference beam propagation method. Titanium in-diffused waveguides on X-cut lithium niobate were simulated at 1550nm. Typical dimensions of the Y-junctions are Bs=30µm, Wi=7µm, Wo=7µm, Wi1=3µm, D=1.5µm. The half branching angle α of each Y-junction was adapted to give the same longitudinal length L.

Table 1: Optical loss versus length of Y-junction.

L (µm)	Optical loss (dB) Conventional Y-junction	Optical loss (dB) Split-Y-junction
2000	0.99	0.58
4000	0.17	0.11
8000	0.13	0.02

Table 1 reports the calculated optical loss for three longitudinal dimensions. To give an idea, the corresponding half branching angles are around 0.4°, 0.2° and 0.1°. We note that in all cases the simulated optical losses are lower for the Split-Y-junction than for the conventional Y-junction.

3. Stability of the splitting ratio

Usually, Y-junctions are dependent to interferences effects of the fundamental mode with radiated modes or higher order modes (even or odd) which can come from distortions of the input field due to an imperfect alignment at the fiber-waveguide interface or after a curved waveguide. These effects induce a periodic variation of the splitting ratio at the end of the junction when the length of the straight section varies or when the wavelength changes. The goal of the designer is to model an Y-junction less sensible to these parasitic effects.

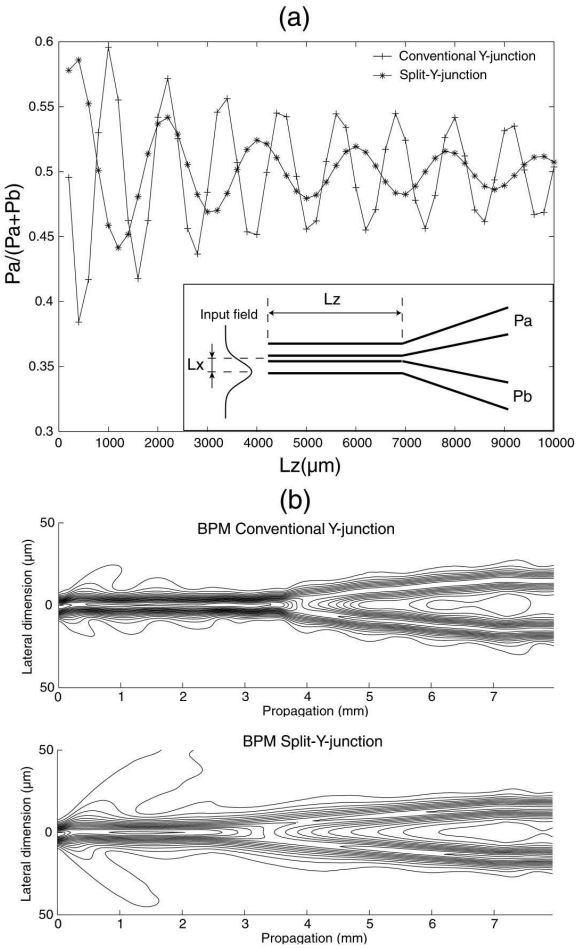


Fig. 2 a) evolution of the splitting ratio when the length Lz of the straight section varies. b) top view of the simulated optical field propagating through the two Y-junctions, Lz=2mm. In all simulations, the input field is a Gaussian mode of waist 10.5µm, the lateral displacement is Lx=1µm and longitudinal dimensions L of Y-junctions are the same.

To analyze the behavior of the Split-Y-junction, we simulated a lateral misalignment Lx (see Fig. 2) of the input field of a standard fiber and we observed the splitting ratio versus the propagation length Lz of the straight section [5].The splitting ratio is defined by the division between the output of one branch and the total output power: Pa/(Pa+Pb) or Pb/(Pa+Pb). Fig. 2 shows the results of the simulation. As stated before, we observe a periodic behavior of the splitting ratio around the symmetrical power splitting and decaying in amplitude with increasing length Lz. The new Y-junction presents superior performances with an amplitude oscillation always lower (around 50%) than the conventional one. One of the main reason is that the straight section of the new Y-Junction acts naturally as a high rejection mode filter because of its narrower equivalent width compared to the conventional Y-junction. In addition, there is no taper able to support higher order modes.

4. Experimental measurements

In order to verify the theoretical predictions, we decided to adapt the Split-Y-junction to the standard X-

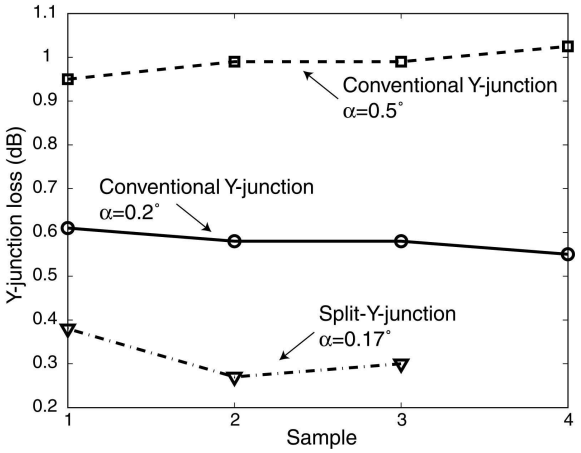


Fig. 3: Loss comparison between Y-junctions on different samples.

cut high speed lithium niobate intensity modulator [6]. Optical waveguides were formed by titanium diffusion. Each Y-junctions were implemented and the half branching angle was chosen to be the varying parameter. The other parameters were the same as those previously used in the simulations. The modulators were optically characterized at a wavelength of 1550nm using a polarization-maintaining fiber at the input and the output. Input light was TE polarized. The optical loss of each Y-junction was estimated by subtraction between a reference straight waveguide inserted on each chip and the Mach-Zehnder interferometer.

Fig. 3. shows the optical loss measured for different values of α. For the conventional Y-junction, the optical loss reduces from 1dB to 0.6dB when the half branching angle decreases from 0.5° to 0.2°. Concerning the Split-Y-junction, the half branching angle of 0.17° gives a value to the order of 0.3dB. If we compare the optical losses between the Split-Y-junction and the conventional Y-junction of the same longitudinal length (α=0.17° and α=0.2° respectively), we note an optical loss reduction of 0.3dB for the Split-Y-junction.

Consequently, we have experimentally demonstrated that, with equal dimensions, the Split-Y-junction exhibits a significant optical loss reduction when compared to the conventional Y-junction.

Conclusions

We have developed a new type of single-mode Y-junction which is better than the conventional Y-junction in terms of dimensions, optical loss and stability of the splitting ratio. X-cut LiNbO3 intensity modulators fabricated with this new design exhibited losses under 3dB including optical connectors and an extinction ratio better than 30dB without sacrificing initial longitudinal dimensions.

References

1 J. Gamet et al, IEEE Photon. Technol. Lett., no. 16, p. 2060, 2004.
2 H. Yajima, J. Quantum Electron., no. 14, p. 749, 1978.
3 M. Izutsu et al, Optics Letters, no. 7, p. 136, 1982.
4 N. Grossard et al, patent WO2006/129035.
5 A. Klekamp et al, J. Lightwave. Technol., no. 14, p. 2684, 1996.
6 E. Wooten et al, IEEE J. Select. Topics Quantum Electron., no. 6, p. 69, 2000.

Numerical Analysis of Picosecond Pulse Propagation in a Tensile-Strained Semiconductor Optical Amplifier with Parameter Extraction using Frequency Resolved Optical Gating

Michael J. Connelly (1), Aisling Clark (2) Prince M. Anandarajah (2) and Liam P. Barry (2)
1) Optical Communications Research Group, Dept. Electronic and Computer Engineering, University of Limerick, Limerick, Ireland, michael.connelly@ul.ie. 2) RINCE, School of Electronic Engineering, Dublin City University, Dublin 9, Ireland, liam.barry@dcu.ie.

Abstract: *A numerical model of picosecond pulse propagation in a tensile-strained bulk semiconductor optical amplifier is described. The phenomenological parameters were obtained using the Levenberg-Marquardt algorithm and experimental pulse amplitude and phase measurements obtained using frequency resolved optical gating.*

Introduction

Semiconductor Optical Amplifiers (SOAs) have attracted much interest in applications in all-optical signal processing such as clock recovery and optical time division demultiplexing (OTDM). In such applications SOAs are used to amplify high-energy optical pulses with pulse widths of the order of picoseconds. Common optical pulse sources used in ultrafast optical communications include mode-locked lasers, gain-switched lasers, and CW lasers followed by electro-absorption modulators. These sources can all generate high quality pulses that exhibit low chirp and jitter and high temporal and spectral purity. Commercial picosecond mode-locked lasers are now available that are suitable for use in ODTM systems.

It is of interest to model the propagation of such pulses through an SOA. Models can give greater insight into the physical processes occurring within SOAs and can also be used to design subsystems utilizing SOAs as active gain elements. Most pulse propagation models use a variant of a modified nonlinear Schrödinger equation (MSE) that includes the SOA non-linearities that are relevant to the pulse time scale [1]. Pulse propagation through an SOA is strongly dependent on the SOA pulse shape. Both the pulse intensity and phase must be considered. The MSE includes a number of phenomenological parameters, whose magnitude determines the influence the corresponding physical effect has on pulse propagation. The principle physical effects that influence pulse distortion in the 2 ps regime are non-linear gain saturation, carrier heating, due to the combined effects of stimulated emission, free-carrier absorption and two-photon absorption (TPA). The phenomenological parameters must be obtained by a comparison between model predictions and experiment.

The SOA modelled in this paper is a commercially available device manufactured by Kamelian. It has a tensile strained InGaAsP active region sandwiched between two InGaAsP separate-confinement heterostructure layers and operates in the 1.55 μm region. The device structure consists of central active region waveguide of width 1.1 μm, thickness 0.1 μm and length 840 μm. The active region narrows linearly as a lateral taper of length 80 μm to width 0.5 μm at each end. The tensile strain is used to compensate for the different TE and TM confinement factors in order to achieve polarization independent operation. In this paper we model the propagation of 2 ps mode-locked laser pulses using the MSE through this type of SOA. In the model, the spatial dependency of parameters such as the saturation energy is included. The MSE phenomenological parameters are obtained using the Levenberg-Marquardt technique and experimental measurements of the amplifier pulse amplitude and phase using the technique of Frequency Resolved Optical Gating (FROG). FROG can be used to overcome the limitations of traditional methods of pulse characterisation and provides complete characterization in the spectral and temporal domains with corresponding phase information.

Pulse propagation model

The MSE used to model the propagation in the SOA of an optical field with complex amplitude $V(z,\tau)$ is given by [1],

$$\left[\frac{\partial}{\partial z}+\frac{\gamma(\tau)}{2}+\left(\frac{\gamma_{2p}}{2}+ib_2\right)|V(z,\tau)|^2\right]V(z,\tau)=$$

$$\left\{\frac{1}{2}g_N(z,\tau)[1+i\alpha_N(z,\tau)]+\frac{1}{2}\Delta g_T(z,\tau)[1+i\alpha_T(z,\tau)]\right.$$

$$\left.-\frac{i}{2}\frac{\Gamma\partial g_m(z,\tau)}{\partial\omega}\bigg|_{\omega_0}\frac{\partial}{\partial\tau}-\frac{1}{4}\frac{\Gamma\partial^2 g_m(z,\tau)}{\partial^2\omega}\bigg|_{\omega_0}\frac{\partial^2}{\partial\tau^2}\right\}V(z,\tau)$$

where the local time $\tau=t-z/v_g$ (z is the propagation direction) and v_g is the group velocity. In the model we also take into account the spatial and time dependency of the attenuation coefficient $\gamma(\tau)$ and linewidth enhancement factors $\alpha_N(\tau)$ (due to carrier density changes) and $\alpha_T(\tau)$ (due to carrier heating). γ_2 is the TPA coefficient. b_2 represents self-phase modulation. The change in the dynamic gain due to carrier heating is given by

$$\Delta g_T(z,\tau) = -\int_{-\infty}^{\infty} U(s) e^{-s/\tau_{ch}} \begin{bmatrix} h_1 |V(\tau - s)|^2 \\ + h_2 |V(\tau - s)|^4 \end{bmatrix} ds$$

where h_1 is a phenomenological constant representing the contribution of SE and FCA to carrier heating and h_2 represents the contribution of TPA. $U(s)$ is the unit step function. The dynamic gain due to carrier density changes is given by

$$g_N(z,\tau) = \Gamma g_m(z) \exp\left[-\frac{1}{W_s(z)} \int_{-\infty}^{\tau} e^{-s/\tau_s} |V(s)|^2 ds \right]$$

where $g_m(z)$, $W_s(z)$ and τ_s are the unsaturated material gain coefficient, saturation energy and spontaneous lifetime respectively. $g_m(z)$ is determined, for a given bias current, using the steady-state model [2]. $W_s(z)$ is a function of *z* due to the spatial dependency of the optical confinement factor. Both g_m and W_s are also polarisation dependent and are shown in Fig. 1. The derivatives $\partial g_m(\tau,\omega)/\partial\omega\big|_{\omega_0}$ and $\partial^2 g_m(\tau,\omega)/\partial\omega^2\big|_{\omega_0}$ and the linewidth enhancement factors can also be determined from the steady-state model and are shown in Fig. 2 and Fig. 3 as a function of g_m.

Numerical solution and experiment

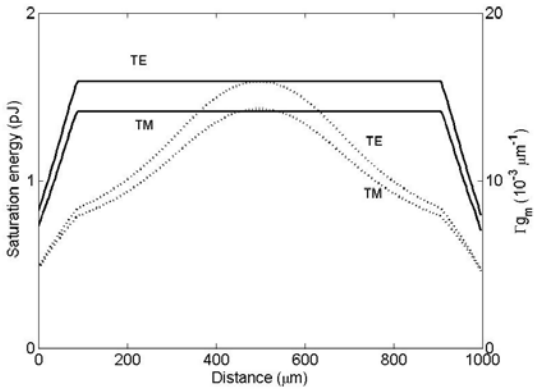


Fig. 1: Unsaturated TM polarisation dependent saturation energy (solid line) and material gain coefficient spatial distributions for a bias current of 200 mA, which corresponds to a fibre-to-fibre gain of 24 dB.

The MSE can be solved by using the finite-difference beam propagation method described in [3]. However in order to obtain good agreement between model predictions and experiment the phenomenological constants must be known. In this work we are particularly interested in the dynamics of the propagation of 2 ps mode-locked laser pulses. To determine the phenomenological constants, we first characterised the amplitude and phase of a 10 GHz repetition rate 2 ps pulsewidth commercial mode-locked laser. The pulses were then amplified and the amplified pulse stream also characterised using FROG [4]. It is well known that the distortion experienced by pulses amplified by an SOA is very sensitive to the input pulse shape. In this work we use the experimentally measured complex pulse amplitude as the model input. In order to determine the phenomenological contants h_1, h_2, γ_{2p} and τ_{ch} we use the pulse propagation model and the Levenberg-Marquardt technique to determine the values of the parameters that minimise the r.m.s. error between the normalised predicted and experimental amplified pulse power for

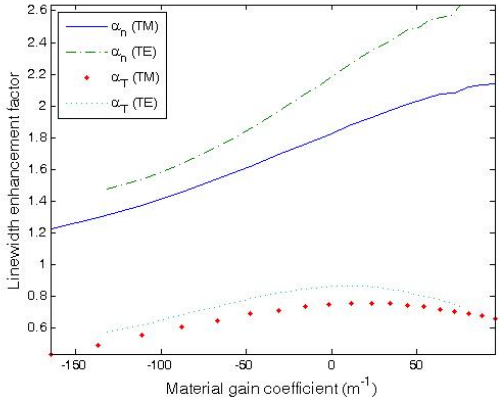


Fig. 2: Polarisation dependent linewidth enhancement factors versus corresponding polarisation dependent material gain coefficient.

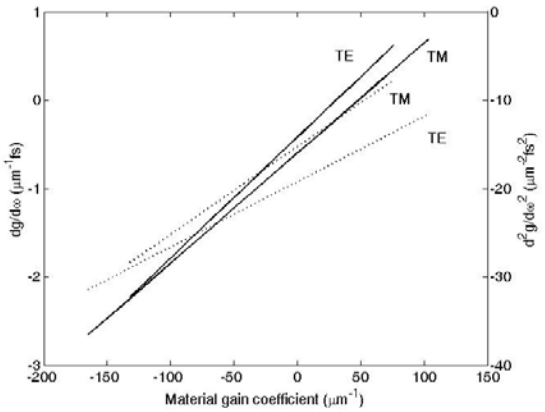


Fig. 3: First (solid line) and second order gain dispersion versus material gain.

three different input pulse peak powers ranging from low to high saturation. Once these values have been obtained, we then adjust the value of b_2 in order to obtain a reasonable match between the predicted and experimental frequency chirp of the amplified pulses. The normalised predicted and experimental input and amplified pulse power is shown in Fig. 4. The predicted and experimental pulse chirp is shown in Fig. 5. The agreement between experiment and the numerical model using the extracted parameters is good for the pulse power temporal profile. In the case of

the pulse chirp, although the magnitude of the predicted chirp and its slope is similar to the experimental results, the agreement is not as good. This is because the temporal distortions of the pulse power in the 2 ps regime are primarily due to the effects of the

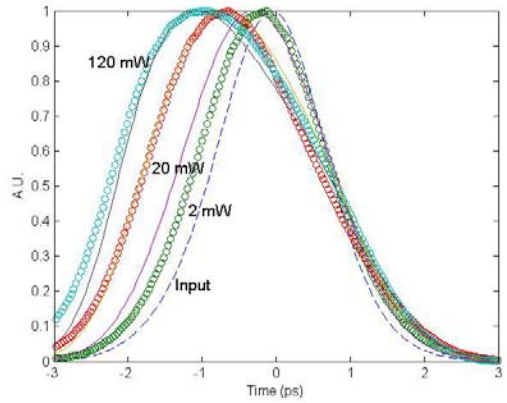


Fig. 4: Experimental ('o') and predicted (solid line) amplified pulse powers for TM polarisation at 1550 nm. The bias current is 200 mA and the parameter is the input pulse peak power.

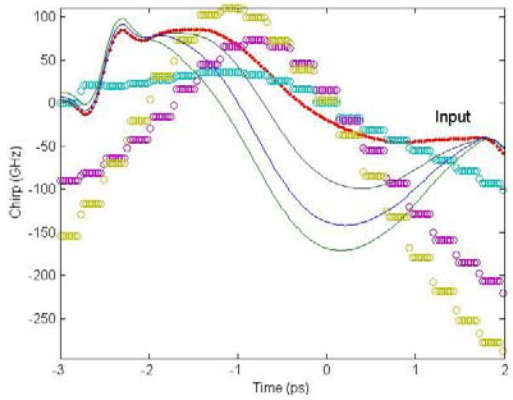


Fig. 5: Experimental ('o') and predicted (solid line) amplified pulse chirp for TM polarisation at 1550 nm for the pulses in Fig. 4. The chirp increases as the input power increases.

two types of gain saturation and the direct effect of TPA (i.e. the γ_2 term). However the phase evolution, and hence the chirp dynamics, is a result of a complicated addition of three types of self phase modulation, which are controlled by the changing pulse shape. It is also modified by the gain curvature and slope, which also depend on the pulse shape.

Conclusions

A numerical model for picosecond pulse propagation in tensile-strained SOAs has been developed. The phenomenological model parameters representing the various non-linear processes in the SOA are determined using a parameter extraction algorithm and experimental FROG measurements of amplified mode-locked laser pulses. There is good agreement between experiment and model predictions of the amplified pulse temporal power. However the amplified pulse chirp is more difficult to predict due to the complexity of the self-phase modulation processes in the SOA, and possibly requires the development of a more accurate propagation model.

Acknowledgments

This work was supported by Science Foundation Ireland Investigator Grant 02/IN1/I42. The author thanks A.E. Kelly of Amphotonix Ltd. for supplying the Kamelian SOA parameters and useful discussions.

References

1 M.Y. Hong et. al, IEEE J. Quantum Electron., no. 4, pp. 1122, 1994.
2 M.J. Connelly, IEEE J. Quantum Electron., no. 1, pp. 47, 2007.
3 N.K. Das, et al. IEEE J. Quantum Electron., no. 10, pp. 1184, 2000.
4 A.M Clarke et. al. IEEE Photon Tech. Lett., no. 9, pp. 1800, 2005.

Fully Tunable $LiNbO_3$ Ring Resonator Cavity for Frequency Comb Generator (FCG)

A. Kaplan, A. Greenblatt, G. Harston, P. S. Cho, Y. Achiam and I. Shpantzer
CeLight Inc. 12200 Tech Road, suite 200, Silver Spring, MD, 20904, akaplan@celight.com

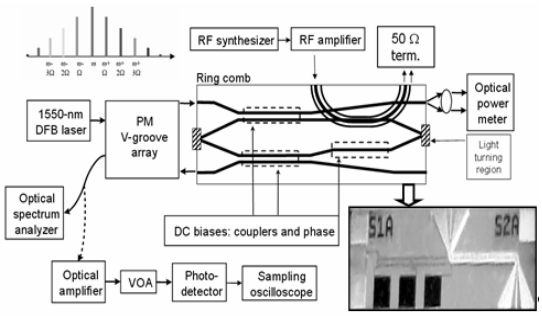


Fig. 1: Ring resonator optical comb schematic view and test setup. Inlay with actual device picture is shown.

Abstract: *A novel $LiNbO_3$ ring resonator cavity is developed for the tunable optical frequency comb generation. Such device enables a high frequency RF modulation of the optical field with independent tuning of the resonator add/drop coupling and phase. The modeling of the integrated ring FCG, fabrication and some experimental results are described.*

Introduction

Using an electro-optical phase modulator placed into a resonant cavity is the most direct method of producing a frequency comb that can be also viewed as an optical pulse generator for use, for example, in optical coherent sensing and tomography [1-2]. The modulation frequency should consist of a multiple number of the optical cavity FSR (an integer number of fringe separations) thus efficiently producing a comb by resonantly enhancing the modulation sidebands. High modulation frequency and electro-optical efficiency can provide a relatively broad resulting spectrum. The high bandwidth can be achieved by implementing traveling wave electrodes so that the electrical field co-propagates with the optical field in the $LiNbO_3$ substrate.

Integrated Ring FCG

In practice, a reliable wide spectral coverage (narrow pulse-train) requires high accuracy stable optical sources along with the well-controlled phase and cavity input/output coupling.

There are some drawbacks limiting the performance of the conventional FCG [3], such as suppression of the total sidebands power caused by increasing the mirror refractivity to increase the relative power transferred to the high order sidebands. By increasing the finesse (and/or modulating index) the pulse-width is narrowed while the peak power remains the same, thus decreasing the sidebands total power (average). Another difficulty is a small cavity size (1-2cm) (needed for a desired bandwidth) limits the modulating index and overall electro-optical design flexibility. With these issues in mind, a new type of ring-resonator FCG with tunable add/drop coupling was developed [3]. The problem of the high radiative bend losses associated with the weakly-guiding $LiNbO_3$ ring cavity was addressed by developing relatively low-loss light-reflective regions that helped to overcome the minimal limit for the cavity circumference needed for a reasonably large bandwidth. A schematic view of the ring-cavity OFG and photograph of the actual device are shown Fig. 1.

The analysis of the passive (without RF modulation) ring resonator with the tunable add/drop coupling is described elsewhere [4] for several types of couplers. It was shown that for a realistic lossy cavity the optimal, generally non-identical, add/drop coupling values can be defined and adjusted accordingly via the independent electro-optical perturbations of the couplers and resonator phase. Fig. 2 shows the quality/contrast optimization of such a tunable ring resonator.

3. Ring FCG experiment

The test setup is shown in Fig. 1. Two FCG cavity lengths of ~2.25 and ~4.5 cm were fabricated, both supporting ~6 and ~12 GHz modulating frequencies. An external 1550-nm DFB laser source was coupled into one of the bus waveguides of the ring resonator via a V-groove PM fiber array. The thru port of the comb output on the right side was directed to an optical power head using a focusing lens while the reflected port was fiber-coupled via the same V-groove array. RF and DC probes were applied to the traveling-wave, phase, and coupler electrodes of the device. Optical signal from the reflected port was monitored using an optical power meter, optical spectrum analyzer (OSA), and a 30-GHz sampling oscilloscope for

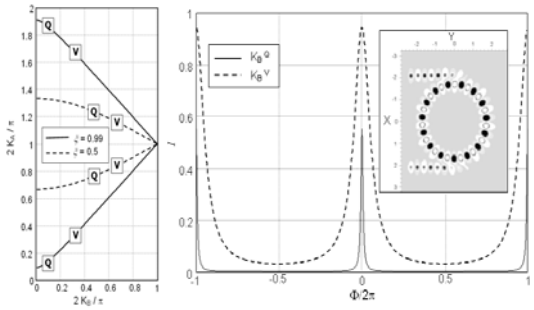


Fig. 2: a) Resonant coupling diagram. Marks indicate the coupling values for the maximum resonator quality Q or contrast V given for two values of cavity losses (1-ξ).
b) Q- and V- resonator response optimization by passive design or by an external tuning; for ξ=0.99.

monitoring of pulse train. RF signal was applied to the traveling-wave electrodes to produce phase-modulated output. Resonance of the comb was determined by an on-resonance (close to integer multiple of the FSR) and off-resonance RF drive frequency.

For high-resolution passive transmission spectrum extinction ratio measurement, the DFB laser was replaced with a wavelength-tunable laser and an optical power meter was used to measure the optical power at

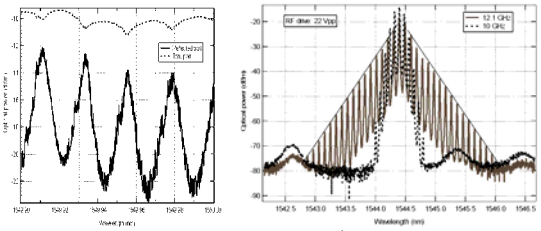


Fig. 3: a) Spectral scan of the reflected and thru ports of the ring OFG output. b) Optical spectrum of the reflected port with of 12.1GHz drive frequency (near resonance) and 10GHz (off-resonance). Resolution bandwidth: 0.01nm.

the reflected output port of the ring FCG device. The power (extinction) ratio recorded by the spectral scan is a function of the resonator finesse. Alternatively, a fixed wavelength laser can be used while the phase voltage of the comb device is swept to determine its spectral response. Fig. 3a shows a typical spectral scan for particular ring FCG. Both reflected and transmitted optical powers versus wavelength are shown. The measured FSR was about 2.84 GHz and the extinction ratio for the reflected port output is about 8dB.

Fig. 3b shows OSA spectral output from the reflected port of FCG driven at 12.1 and 10GHz (on- and off-resonance, respectively). The resolution bandwidth of the OSA was 0.01nm. The RF drive voltage was about 22 V peak-to-peak. The slope of the comb envelope was estimated to be about -0.28 dB/GHz at resonance. With off-resonance drive at 10 GHz the number of wavelengths reduced drastically. The temporal output of the ring comb device was monitored using a sampling oscilloscope as shown in Fig. 1. The repetition rate of the pulse train varies between 12.1 and 24.2 GHz (on- and off-resonance, respectively). An estimated finesse and modulation index was about 3.62 and 2.2, respectively. Several control loops for maintaining resonant FCG were suggested.

Active Control for FCG

One of the proposed control loops is based on a counter-propagating controlling laser, derived from the same external injected laser but launched counter-propagating to the RF traveling wave through the FCG as shown in Fig. 4. The clockwise-propagating control laser does not experience instantaneous phase modulation but only an average phase shift. The optical power of the control laser from the comb output can be used directly as a feedback signal to indicate whether or not the comb is in resonance. A device was tested using the counter-propagating configuration to check the residual phase modulation. The test setup is similar to that shown in Fig.1 except that the RF signal is applied to the other end of the traveling-wave electrode so that it travels opposite to the optical wave. Typical results are shown in Fig 5. RF peak-to-peak drive voltage was 8.69V at 12.1GHz. One can see that in either case the sideband-to-carrier power ratio is significantly reduced compared with the co-propagating case. The existence of sidebands at all in the counter-propagating case is likely due to reflections at the various waveguide interfaces. Due to multiple reflections a portion of the reflected control laser may co-propagate with the RF signal, experiencing instantaneous phase modulation, and later recombine with the counter-propagating laser.

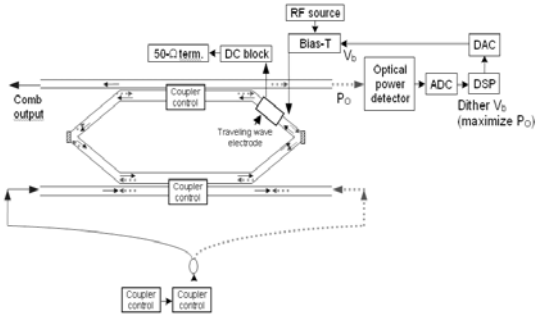


Fig. 4: Proposed resonant control for the ring comb based on monitoring of the output optical power of a clockwise laser shown in dashed line (feedback signal). The comb output is represented by the counter-clockwise arrow.

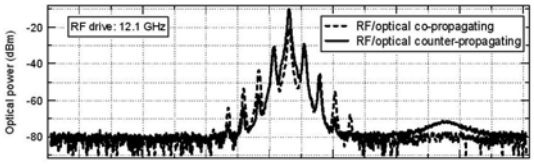
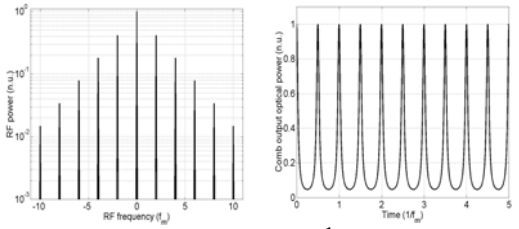


Fig. 5: FCG output spectra for 12.1GHz obtained with co- and counter-propagating optical and RF wave.

A feedback control loop based on monitoring the optical output of the comb device was also considered. When the comb device is driven by a sinusoidal RF signal at a modulation frequency of f_m an optical pulse train output with a repetition rate of $2f_m$ is expected when resonant conditions are met as shown in Fig. 6. This requires f_m to be precisely set according to the FSR of the comb resonator and also the injection laser optical frequency must be an integer multiple of the FSR or align to one of the resonant frequencies of the comb device.

One can obtain useful information on the operation status of the comb device by monitoring its output such as the average optical power (*Po*) and the RF power at *fm* (*VRF*) of the pulse train. The RF power of the pulse train can be obtained by using a photodetector with a bandwidth around *fm* followed by a RF detector to extract the RF power at *fm*.



a. b.

Fig. 6: a) Simulated pulse output of the optical comb biased at resonance. Note the pulse repetition rate is twice the modulation frequency, f_m. b) RF power spectrum of the pulse train shown on the left. Note the absence of odd harmonics of f_m.

Fig. 7 shows a typical plot of the calculated *Po* and *VRF* versus the comb phase bias based on a comb resonator model [2]. The comb phase bias changes the resonant frequencies which affects the resonant condition. In Fig. 7, resonance occurs at comb phase bias of 0 or integer multiples of p. Both *Po* and *VRF* approach to their respective minimum values at resonance. However, *Po* and *VRF* also reach minimum values at off-resonance (e.g., phase=π/2). Therefore, a resonance control algorithm based on minimizing *Po* and *VRF* may or may not converge to resonance depending on the initial phase bias. In order to ensure convergent to resonance regardless of the initial phase bias, the control algorithm must first adjust the comb bias to maximize *Po*.

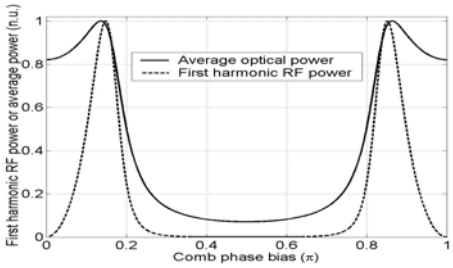
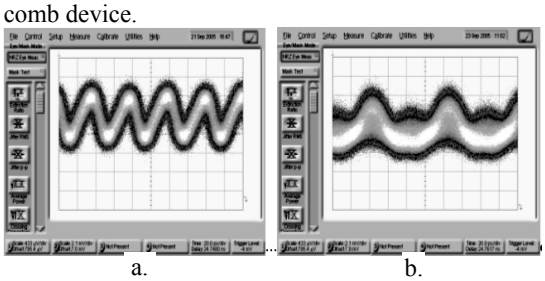


Fig. 7: Average optical power and RF power of the f_m first harmonic or V_{RF} versus phase bias. Resonance corresponds to comb phase bias of zero or integer multiples of π.

Once *Po* reaches maximum, the comb bias must be varied to minimize *VRF*. Note that if the modulation index is high, the relative phase bias position where maximum of *Po* and *VRF* are located may be interchanged. In this case, the algorithm should be modified so that *VRF* be maximized first followed by minimization of *Po*.

Experiments were conducted to verify the operation of the resonant control loop and also validate the performance of the variable ring comb. Fig. 8 shows the pulse waveforms of the ring comb output displayed on the sampling oscilloscope with and without the resonant control loop running. The sampling oscilloscope was set to infinite persistent mode so that drift and fluctuations of the comb output can be accumulated and recorded. Note that the pulse waveforms shown in the figures are limited by the detection bandwidth (40GHz) of the oscilloscope. With the control loop running, one can see from Fig. 8 that the ring comb device is maintained at resonance with a stable output pulse train at a repetition rate of about 24.4 GHz or 2*fm*. On the other hand, without the control loop the comb device seems to fluctuate randomly in and out of resonance causing the output pulse pattern to drift in time. As a result, no stable pulse train at 2*fm* was observed. The fluctuation can be attributed to variation of the injection laser optical frequency and environmental-induced perturbations on the refractive index of the LN waveguide of the comb device.



a. b.

Fig. 8: Pulse train of ring comb output with (a) and without (b) resonant control. Injection laser wavelength: 1544nm. The comb is driven at 12.2GHz. a)- pulse repetition rate is 24.4GHz. Detection bandwidth: 40GHz. Infinite persistent mode ~ 2 minutes. Horizontal scale: 20ps/div.

Conclusions

A novel fully tunable, $LiNbO_3$-integrated weak-guiding ring FCG device was developed. This device potentially overcomes the limitations of integrated $LiNbO_3$ Fabry-Perot cavities and existing ring cavities with limited coupling tunability. Preliminary experimental results are consistent with the simulation results. Current and future development includes the add/drop adjustment optimization, cavity losses minimization, and improved resonant control scheme that utilizes both available optical and electrical outputs for a more robust and stable performance.

$LiNbO_3$-based electro-optical ring resonators with autonomous input/output coupling ratios and phase tuning may become promising components for a variaty of applications such as FCG, channel add-drop filters, sensors, chromatic dispersion compensators, optical delay lines, and Er-doped cavities for loss compensation, to mention a few.

Acknowledgments

This work was partially supported by Contract DMEA H94003-04-D-0004.

References

1 M. Kourogi et al, IEEE J. Quantum Electron., vol.29, No.10, pp. 2693, 1993.

2 Fixed and Variable Optical Grid Comb Design Document, CeLight Inc., Technical Report Provided to Northrop Grumman for Secure Digital Coherent Optical Communications (SDCOC). Defense Microelectronics Activity (DMEA), 2005.

3 A. Kaplan et al., Coherent Optical Technologies and Application Topical Meeting, OSA Technical Digest, Whistler Canada, 2006, paper CFC3.

4 A. Kaplan, IEEE Selected Topics in Quantum Electronics, Vol.12, pp. 86-95, 2006.

Low-loss coupling technique between SOI waveguides and standard single-mode fibers

J. V. Galán (1), P. Sanchis (2) and J. Martí (3)
Valencia Nanophotonics Technology Center, 1) jogaco@ntc.upv.es, 2) .pabsanki@ntc.upv.es., 3) jmarti@ntc.upv.es

Abstract: *In this paper, an inverted taper-based technique for highly efficient coupling between SOI waveguides and standard single-mode fibers is reported. The coupling structure is polarization insensitive and it is based on the inverted taper coupled to a fiber-adapted waveguide. In this case, the fiber-adapted waveguide is made by using the SiO_2 layer under the Si waveguiding layer of the SOI wafer thus avoiding the use of extra materials such as polymers. The proposed coupling structure is aimed for being integrated with V-groove auto-alignment techniques. Coupling losses of 4.21dB and 4.5dB to 10µm mode field diameter standard single-mode fibers have been estimated for TE and TM polarizations respectively and 1550nm performance.*

Introduction

Efficient coupling between standard single-mode fibers and single-mode waveguides is a key point in silicon photonics. An optical integrated circuit is useless without an interface to the outside world. The small size of single-mode silicon-on-insulator (SOI) waveguides (typically 500nm width and around 200nm thickness) compared with the high diameter of a single-mode fiber (between 8-10µm) makes coupling inefficient. A direct end-fire coupling between a SOI single-mode waveguide and a standard single-mode optical fiber means around 20dB of coupling losses for TE polarization and 1550nm input signal wavelength. Three-dimensional (3D) tapers have been reported to achieve 3D spot-size conversion between the spot-sizes of the waveguide and the fiber [1]. More complex structures such as two different tapers formed at different levels have also been proposed [2]. However, the complexity of the fabrication significantly increases in 3D approaches and the coupling length is typically higher than 500µm. A more elegant and compact solution that is compatible with planar processing techniques is the use of two-dimensional (2D) inverted tapers to achieve 3D spot-size conversion [3-9]. In this case, the width of the taper is gradually decreased thus delocalizing the mode profile out of the waveguide core.

The tip of the inverted taper can be directly attached to the optical fiber [4,5]. However, in this case, very precise control on the chip facets position is required. Therefore, the mode out of the inverted taper is usually coupled into another fiber-adapted waveguide. This fiber-adapted waveguide is made of low index contrast polymer materials and it is placed on top of the inverted taper [6-9]. However, the inverted taper and the low-index contrast waveguide are optimized for low coupling losses into small core optical fibers with typically 3-4 µm mode field diameter (MFD). In this paper, a new coupling structure based on the inverted taper is proposed for low coupling losses between SOI waveguides and standard single-mode fibers with 10µm MFD. The proposed approach is polarization insensitive and it takes advantage of the SiO_2 layer under the Si waveguiding layer of the SOI wafer to obtain the fiber-adapted waveguide. Furthermore, the structure is designed with the aim of future integration with V-groove structures thus allowing passive alignment and easier packaging [10].

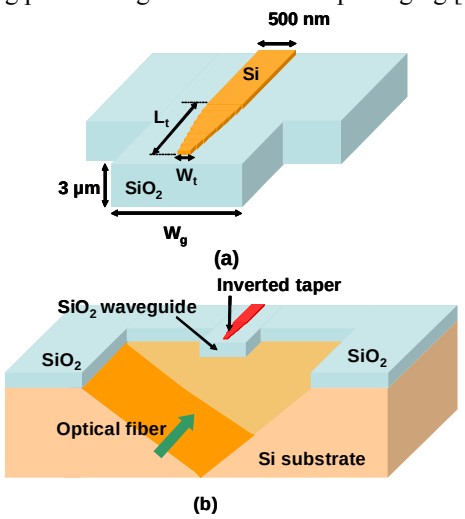


Fig. 1: (a) Proposed inverted taper-based structure and its main design parameters. (b) Detail of the integration of the proposed structure with the V-groove auto-alignment structure.

Proposed structure

The proposed inverted taper-based structure is shown in Fig. 1(a). The single-mode SOI waveguide is tapered down by the inverted taper. As SOI wafers of 205nm/3µm Si/SiO_2 layer thicknesses have been used, the Si waveguide width has to be around 500nm to achieve single-mode propagation. The main inverted taper design parameters are the inverted taper length (L_t) and the inverted taper tip width (W_t) both illustrated in Fig. 1(a). If the substrate of the SOI wafer is removed, it is possible to use the SiO_2 layer as the fiber-adapted waveguide, as shown in Fig. 1(a). Due to the SiO_2 SOI wafer layer thickness, the height of the SiO_2 waveguide is fixed to 3µm. The objective is to find the optimum SiO_2 waveguide width and the optimum inverted taper parameters to achieve the lowest coupling losses between the proposed structure and the standard single-mode fiber. Furthermore, the design is carried out to obtain a polarization insensitive structure. The most important application of the proposed structure is its

direct integration with V-groove auto-alignment structures as illustrated in Fig. 1(b). A step by step analysis of the proposed inverted taper-based structure is presented on the following sections. The analysis starts with the SiO_2 waveguide section parameters design in the fiber-SiO_2 waveguide interface to achieve the highest coupling efficiency to 10μm MFD standard single-mode fibers. Then, the optimum inverted taper tip width and length are designed.

SiO_2 waveguide width design

To find the optimum SiO_2 waveguide width to get the highest coupling efficiency between the SiO_2 waveguide and the fiber, a 3D overlap integral between fiber and waveguide fundamental mode profiles has been used. The fundamental mode profile of the SiO_2 waveguide has been obtained by a 3D mode solver based on the Beam Propagation Method (BPM). The fundamental mode profile of the fiber has been approximated by a Gaussian beam as a function of the fiber mode field diameter. The simulation results are shown in Fig. 2. The figure shows the estimated coupling efficiency between the SiO_2 waveguide and the fiber as a function of the fiber mode field diameter for different SiO_2 waveguide widths and a 1550nm input signal wavelength. A polarization insensitive behaviour of the coupling efficiency in the SiO_2 waveguide-fiber interface was observed, so results shown in Fig. 2 are valid for both TE and TM polarizations. As it is shown in Fig. 2, the estimated coupling losses for an 8μm width SiO_2 waveguide and a standard single-mode fiber (10μm mode field diameter) are around 4.2dB for both TE and TM polarizations and a 1550nm input signal wavelength. If the waveguide gets wider (e.g. 10μm width), the estimated coupling losses are only 0.4dB less than in the 8μm width SiO_2 waveguide case. Therefore, in order to minimize as much as possible the SiO_2 waveguide dimensions, the 8μm width SiO_2 waveguide case has been considered for the next inverted taper design parameters simulations.

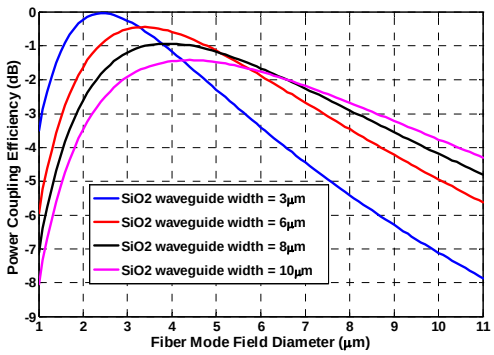


Fig. 2: Power coupling efficiency between the SiO_2 waveguide and the optical fiber as function of the fiber mode field diameter for different waveguide widths, λ=1550nm and both TE and TM polarizations.

Inverted taper tip width design

In order to find the optimum tip width of the inverted taper, it has been considered the inverted taper tip-SiO_2 waveguide interface of the proposed structure. It is possible to obtain the fundamental mode profiles of both the fiber-adapted SiO_2 waveguide with and without the inverted taper on top. These fundamental mode profiles have been obtained by a 3D mode solver based on the Beam Propagation Method (BPM). Evaluating the overlap integral of both fundamental mode profiles for different inverted taper tip widths, the final inverted taper tip width has been chosen the optimal one that results in the highest power coupling efficiency of the mentioned interface.

The simulation results are shown in Fig. 3. The figure shows the estimated coupling efficiency between the SiO_2 waveguide with and without the inverted taper tip on top, as a function of the inverted taper tip width for a 1550nm input signal wavelength and for both TE and TM polarizations. According to Fig. 3, almost negligible coupling losses are achieved in the taper tip interface for inverted taper tip widths lower than 200nm and for both TE and TM polarizations (around 0.01dB coupling losses for TE polarization and 0.3dB for TM polarization). Therefore, if a lower than 200nm inverted taper tip width is chosen, the proposed design is polarization insensitive in the considered interface. In order to maximize as much as possible the inverted taper tip width for an easier future fabrication, the 200 nm inverted taper tip width case has been chosen.

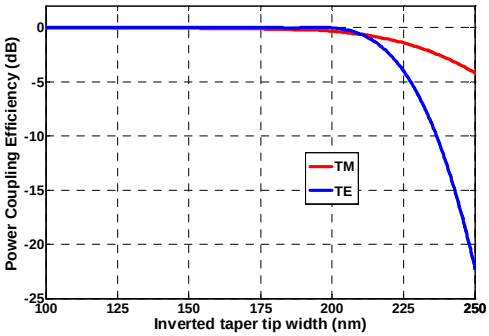


Fig. 3: Power coupling efficiency between the SiO2 waveguide with and without the inverted taper on the top, respectively, according to Fig. 3(b) as a function of the inverted taper tip width, λ=1550nm and for both TE and TM polarizations.

Inverted taper length design

The optimum inverted taper length has been designed by means of FDTD simulations using the inverted taper tip width (W_t=200nm) and the SiO_2 waveguide width (W_g=8μm) that were found to be the optimum ones in the previous sections. 3D FDTD simulations require very high computational memory because of the relative large taper length. So, the taper length effect has been simulated using 2D FDTD simulations. To take into account the neglected structure dimension in the 2D problem approximation, the

effective index method has been used. Two possibilities have been studied depending on the spatial perspective of the 2D structure approximation. It is possible to analyze the coupling structure according to a 2D top view or according to a 2D side view too. The used 2D FDTD simulations including these two 2D perspective views are shown in Fig. 4. In Fig. 4(a) the 2D top view FDTD structure simulation is illustrated while in Fig. 4(b) it is shown the 2D side view one. Basically, in the simulations in Fig. 4, the structure is excited by the SiO_2 slab waveguide fundamental mode at a 1550nm wavelength, and the Si waveguide coupled power is measured by a power monitor. As the schematics in Fig. 4 are being excited by the SiO_2 slab waveguide fundamental mode, the fiber-SiO_2 waveguide interface is not being considered. So, to obtain the total SOI waveguide-to-fiber coupling losses, the estimated coupling losses depending on the taper length have to be added to the estimated ones in the SiO_2 waveguide width design for the fiber-SiO_2 waveguide interface (4.2dB for a 10µm MFD standard single-mode fiber and both TE and TM polarizations).

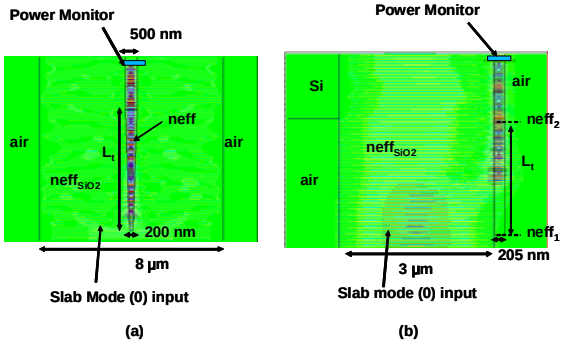


Fig. 4: Detail of the carried out 2D FDTD simulation to obtain the optimum inverted taper length. The effective index method has been used in both (a) 2D top view structure simulation, and (b) 2D side view structure simulation.

According to the 2D top view simulation in Fig. 4(a) and using the effective index method, the SiO_2 waveguide refraction index is replaced by an effective index ($neff_{SiO2}$ in Fig. 4(a)) for both TE and TM polarizations) to consider the 3µm thickness of the SiO_2 waveguide. In the same way, the Si waveguide and taper refractive index is replaced by other effective index (neff in Fig. 4(a)), considering the 205nm Si layer thickness. For the 2D side view simulation in Fig. 4(b), a similar procedure has been carried out. The SiO_2 waveguide refraction index is replaced by an effective index to consider the 8µm width of that SiO_2 waveguide ($neff_{SiO2}$ in Fig. 4(b)). About the inverted taper effective index, as the taper width is not constant along the propagation direction, and remembering that the structure is being analyzed according to its 2D side view, the linear variation of the taper width along the propagation direction is now transformed in an effective index linear variation as a function of the inverted taper width. At the 200nm width inverted taper tip, the effective index ($neff_1$ in Fig. 4(b)) considers the inverted taper tip width. That effective index increases along the propagation direction until the 500nm Si waveguide width corresponding effective index ($neff_2$ in Fig. 4(b)). The simulation results of both, 2D side view and 2D top view are shown in Fig. 5(a) for TE and in Fig. 5(b) for TM polarizations and for a 1550nm input signal wavelength.

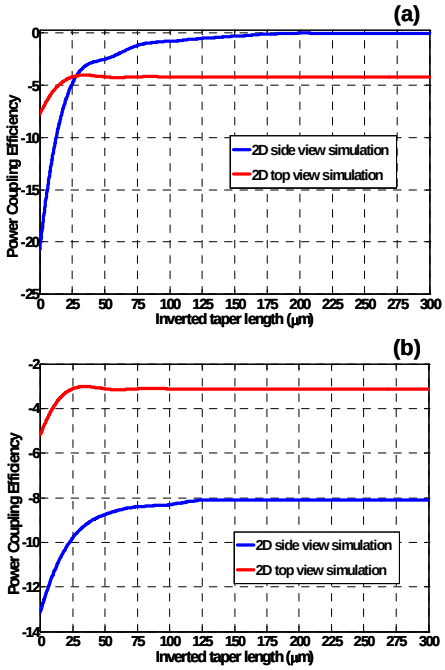


Fig. 5: Power coupling efficiency as a function of the inverted taper length for both 2D top and 2D side view FDTD simulations, 1550 nm input signal wavelength and for (a) TE and (b) TM polarizations.

Looking at Fig. 5(a) for TE polarization, it can be seen that the power coupling efficiency increases as the inverted taper gets longer due to the lower radiation losses. However, the 2D top view simulation in Fig. 5(a) does not behave just as the 2D side view one. In the 2D top view simulation, the obtained power coupling efficiency is maximum for a very low inverted taper length value which, in principle, does not seem realistic. Furthermore, in this case, it can be seen that the minimum coupling losses for the 2D top view simulation are not zero thus disagreeing with the 3D results shown in Fig. 3. This coupling losses value is due to the mode mismatch of the 2D approximation in the interface between the SiO_2 waveguide with and without the taper tip on top. 2D overlap integral between both the SiO_2 waveguide with and without the 200nm width taper tip on top confirmed the minimum coupling losses reached by the 2D FDTD simulations. For the 2D side view approximation, the minimum coupling losses calculated by the 2D overlap integral are very similar to the obtained value by means of the 3D overlap integral, which are around 0.01dB according to Fig. 3. So, it can be concluded that for TE polarization, the 2D side view simulation is a very good approximation of the 3D approach. The minimum inverted taper length to achieve negligible coupling losses is 200µm.

Taking a look in Fig. 5(b) for TM polarization, the same behavior than in the TE case is observed and the 2D side view simulation seems a better approximation than the 2D top view simulation. However, the minimum coupling losses obtained by means of the 2D side view simulation are not negligible. As for TE polarization, these coupling losses are due to the mode mismatch of the 2D approximation at the inverted taper tip-SiO_2 waveguide interface. Thereby, the 8dB minimum coupling losses were in agreement with the coupling losses obtained by means of a 2D overlap integral in the inverted taper tip-SiO_2 waveguide interface. So, these are the minimum coupling losses that the 2D approximation can reach according to the 2D side view simulation in Fig. 5(b). For a 125μm long inverted taper, the minimum coupling losses are reached and it corresponds to the mode mismatch in the inverted taper tip-SiO_2 waveguide interface, which were estimated in 0.3dB coupling losses by means of a 3D overlap integral according to Fig. 3 for TM polarization.

In order to have a similar behavior of the inverted taper for both TE and TM simulations, it has been chosen a 200μm long inverted taper. For a 200μm long inverted taper and for both TE and TM polarizations, the total SOI waveguide-to-fiber coupling losses are the sum of the fiber-SiO_2 waveguide interface coupling losses, which were estimated in 4.2dB, and the estimated coupling losses in the inverted taper tip-SiO_2 waveguide interface, which were estimated by means of the 3D overlap integral in 0.01dB and 0.3dB for TE and TM polarizations respectively, according to Fig. 3. It results in around 4.21dB and 4.5dB total coupling losses for TE and TM polarizations respectively.

Spectral response

Having obtained the most important inverted taper design parameters for a standard single-mode fiber efficient coupling and a 1550 nm input signal wavelength, a spectral analysis of the proposed structure has been carried out. Fig. 6 shows the simulation results for the inverted taper-based structure spectral response taking into account a 10μm MFD standard single-mode fiber.

It is observed an almost flat spectral response of the proposed inverted taper-based structure in the considered wavelengths range for both TE and TM polarizations. Coupling losses can be reduced by using fibers with a lower core diameter, as it can be seen in Fig. 2.

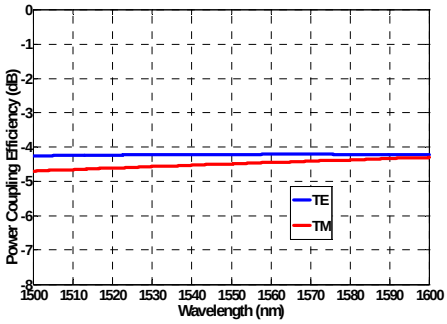


Fig. 6: Spectral response simulation results for the inverted taper-based structure and taking into account a 10μm MFD standard single-mode fiber.

Conclusions

In this paper, we report a polarization insensitive fiber-to-SOI waveguide efficient coupling technique using an inverted taper-based structure. The SiO_2 layer of the SOI wafer is considered to make the fiber-adapted waveguide thus avoiding the use of extra materials such as polymers. The proposed coupling structure is aimed for being integrated with V-groove auto-alignment techniques. Parameters have been designed to maximize the coupling efficiency to standard single-mode fibers (MFD=10μm). Two different techniques based on the effective index method have been evaluated to simulate the inverted taper performance by means of 2D FDD simulations. It has been obtained that 2D side view approach is a better approximation than the 2D top view approach. Coupling losses of 4.21 dB and 4.5dB for TE and TM polarizations respectively and 1550 nm input signal wavelength have been obtained using a 200μm long inverted taper. Furthermore, a flat spectral response is achieved because the coupling structure performance does not rely on any resonant effect.

Acknowledgments

Financial support by EC under project 017158-PHOLOGIC and Spanish MEC and EU-FEDER under contract TEC2005-07830 SILPHONICS is acknowledged. Authors also acknowledge financial support by Generalitat Valencia and Universidad Politécnica de Valencia.

References

1 A. Sure, et al, Opt. Express, 26, 3555-3561 (2003).
2 D. Dai, et al, IEEE JLT 24, 2418-2433 (2006).
3 T. Shoji, et al, EL, 38, 1669-1670 (2002).
4 L. Vivien, et al, IEEE JLT, 21, 1-5 (2003).
5 V. R. Almeida, et al, OL, 28, 1302-1304 (2003).
6 S. J. McNab, et al, OE, 11, 2927-2939 (2003).
7 K. Yamada, et al, IEICE TE, E87-C, 351-358 (2004).
8 K. K. Lee, et al, OL, 30, 498-500 (2005).
9 G. Roelkens, et al, PTL, 17, 2613-2615 (2005) .
10 S. Park, et al, IEEE PTL, 17, 1444-1446 (2005).

Metallo-Dielectric Multilayer Sensor for Hydrogen Detection in Exhaled Breath

N.Cioffi (4), D. de Ceglia (1)(2), M. De Sario (1), A. D'Orazio (1), V. Petruzzelli (1), F. Prudenzano (3), M. Scalora (2), S.Trevisi (1), M. A. Vincenti (1)

1) Dipartimento di Elettrotecnica ed Elettronica, Politecnico di Bari, Via Orabona 4, 70125, Bari, Italy, vincenti@deemail.poliba.it

2) Charles M. Bowden Research Center, AMSRD-AMR-WS-ST, Redstone Arsenal, AL 35898-5000, USA

3) Dipartimento di Ingegneria dell'Ambiente e per lo Sviluppo Sostenibile, Politecnico di Bari, Taranto, Via del Turismo 8, 74100, Italy

4) Dipartimento di Chimica, Università degli studi di Bari, Bari, via Orabona 4, 70125, Bari, Italy

Abstract: *A metallo-dielectric multilayer structure is proposed as a novel approach to the detection of hydrogen in the exhaled breath. Due to the bacterial overgrowth in the intestine, a spontaneous emission of H_2 is increased in the human breath when lactose intolerance occurs. By monitoring the changes in the optical properties of a multilayer palladium-polymeric structure one is able to detect a patient's disease and the level of lactose malabsorbtion.*

Introduction

The enhancement in expired hydrogen over the 20ppm baseline goes back to the fact that part of ingested carbohydrates and proteins is not absorbed or digested but is fermented to form hydrogen by bacteria settling either in the colon or, especially in the case of a bacterial overgrowth, also in the small intestine. Part of this hydrogen is dissolved in mucosal blood, transported to the lungs within few minutes and finally appears in the breath [1]. The most common test used to diagnose lactose malabsorption or other intestinal diseases is the hydrogen breath test. During this test, the patient ingests a large dose of lactose or other mixture, after which hydrogen levels in the breath are measured at regular intervals. A rise in hydrogen breath levels (>20 ppm over baseline) theoretically indicates increased gas production due to such a intestinal disease. Hence, by plotting the H_2-concentration in breath over time after the ingestion of the solution, one is able to reveal a malabsorption or an intolerance condition. In order to realize a high sensitive sensor for H_2 breath test clinical diagnosis, we underline the importance of the selectivity in hydrogen sensing. This issue arises from the fact that, in the majority of field applications, as well as in the breath exhaled, the hydrogen has to be detected at the presence of other gases, i.e. oxygen and nitrogen in the air. Moreover the breath of healthy people contains nitrogen, oxygen, carbon dioxide, water vapor and inert gases. The remainder of breath (<0.000001%) is a mixture of as many as 500 different compounds [2]. However pathologic conditions could alter the breath composition introducing other gases and substances that can modify the sensor response. As a consequence, the presence of some traps for organic species is essential to preserve the detection mechanism from external damaging agents. A large number of materials and devices operating on different principles has been exploited for hydrogen sensing [3], such as modified metal-oxide resistive gas sensor [4,5], pellistor [6] and ChemFET type [7] devices. Several solutions of hydrogen sensors based on palladium sensitive properties have been proposed. It has been demonstrated that thin palladium film can be deposited on an optical fiber to detect few hydrogen quantities [8,9]. The measure of hydrogen concentration by monitoring the reflectivity of a thin palladium film positioned on the tip of an optical fiber [10] or looking at the optical transmittance of a thin palladium film grown on a glass substrate [11] is also possible. Finally, more sensitive, but also more complex, is the monitoring of optical changes by surface plasmon resonance measurements [12] or interferometric ones [13].

In this paper we propose a novel approach to the inspection of hydrogen concentration that results in a new device useful for H_2-breath-test analysis. In fact, a palladium-dielectric multilayer structure reacts with small quantities of hydrogen in the human breath changing reversibly its transmission spectrum. The changes in the transmittivity involve certain wavelengths inside the spectrum and depends on the capability of the palladium films to absorb hydrogen particles, i.e. the change of dielectric constant. Metallo-dielectric structures allow to increase the total amount of sensitive metal within the structure improving their transmission properties and reaching high sensitivity values compared to other Pd-film-

based configurations.

Palladium-Hydrogen System

A lot of transition metals such as nickel, palladium and platinum absorb hydrogen spontaneously, changing their optical properties as a function of hydrogen concentration. In the latter part of the 19th century it was demonstrated that Palladium shows larger absorption of hydrogen compared to iron or platinum or other transition metals and that it is possible to store a high quantity of hydrogen in the Pd lattice [14]. Free electrons states of Pd are filled by free electrons of the absorbed hydrogen, modifying the Fermi level and changing reversibly the electrical [15] and optical [16] properties of Palladium. This causes both the real and the imaginary parts of the complex permittivity of palladium decrease [17]. It was demonstrated that the complex permittivity of the palladium hydride film ε_{PdH} could be expressed as:

$$\varepsilon_{PdH} = h \times \varepsilon_{Pd} \quad (1)$$

where ε_{Pd} is the complex permittivity of bare palladium and h is a nonlinear function that gets smaller as well as the hydrogen concentration is increased, having values between 0 and 1 [8]. It was also demonstrated that the Drude model could describe the hydride palladium optical properties as well [18]. The Palladium hydride is formed when palladium is exposed to hydrogen and an efficient dissociation rate occurs when hydrogen atoms are in contact with palladium surface. The palladium hydride film has different mechanical, electrical and optical properties than those of bare palladium. Moreover hydride palladium exhibits a different behavior depending on the value of the hydrogen concentration. The hydride palladium could be characterized by two different phases, the α phase and the β phase. The reversible α phase occurs at low hydrogen concentration and in the absence of hydrogen Pd is considered in the α phase as well. If the hydrogen concentration is increased, Pd is transformed in the β phase. The transition point does not depend only on the hydrogen concentration but also on the film thickness and temperature. The β phase is not reversible and introduces a hysteresis in the optical and mechanical parameters of the palladium film. The transition from α phase to β phase for a thin palladium film (10-100nm) crops up at wider hydrogen concentration values (more than 4%) [19]. For hydrogen sensing applications it is important to avoid the Palladium phase transition during the experiments. A H_2-breath-test is based on the detection of small quantities of hydrogen, ranging from 20 ppm for healthy conditions to 80 ppm or more for pathologic conditions. In the whole range of our investigation the palladium remains in the α phase, being reversible to repeat the measurements with the same device without any phenomena of hysteresis or structural variations.

Metallo-Dielectric Structure Theory

In recent years it has been demonstrated that it is possible to realize one-dimensional photonic band gap (PBG) structures, containing a few hundreds of nanometers of metals, relatively transparent to visible light and opaque for infrared and ultraviolet one [20]. This interesting property could be useful for many applications, such as the development of opto-electromechanical systems [21], or the enhancement of the quadratic and cubic nonlinearities of metal [22]. Propagation of light through thick metal layers arises from the resonance tunneling phenomenon. This feature takes place for many metals belonging to the transition metals class (ranging from group III to group XII). Some of noble metals, such as Au, Ag or Cu, are relatively transparent within a transmission window located at the beginning of the interband transition from d band to conduction band [22]. The most important objective of a metallo-dielectric, multi-layer structure is to enhance the transmitted field respect to the transmission through an equivalent amount of metal in a certain range of wavelengths. In this way, one is able to use a large quantity of metal, up to ten times more than the skin depth, maintaining losses exceptionally small. In fact, the concept of skin depth as the distance at which the field intensity is decreased to 1/e of its input value, looses its sense in the case of a periodic structure, due to the presence of spatial discontinuities, that drastically modifies the physical properties of the structure [20]. The bandwidth and the spectral position of the zero reflection condition, i.e. transparent metal regime, can be tuned by properly choosing the thickness of each layer. One or two anti-reflection coatings can be efficiently dimensioned by calculating the phase shift induced by the metal within the structure to improve the transmittance [23]. High values of transmittance and an high sensitivity to the presence of small quantity of the analyte, i.e. hydrogen, are reachable by using Pd, which is a transition metal, inside a periodic, metallo-dielectric structure. Several configurations for hydrogen sensing using Pd have been proposed embedding a thin film of metal between an isolating film and the tip of an optical fiber [23] or coating a piece of fiber with the sensitive material [24]. As suggested by the theory of metallo-dielectric multilayer structure, we can increase the overall thickness of Pd in the whole device, keeping the device transparent to the visible light.

Device Modeling

An efficient detection of hydrogen, operated by a multilayer structure, requires the use of a inert dielectric material that should be permeable to the hydro-

gen. Moreover, one of the most important issues leading to the transparent metal regime across the visible range is that the real part of the refractive indexes of the dielectric and palladium must be markedly different; While the majority of commercial polymers is characterized by a relatively low real part of the refractive index, reaching values lower than 1.8 [25], a high refractive index material has been recently proposed and realized. This material, known as EXP0454, is a titanium dioxide-rich polymer having refractive index values equal to 2 in the whole visible range. This material shows high transparency, resistance to chemical attack [26] being permeable to hydrogen. In fact, by properly alternating EXP0454 and Pd one is able to exploit the properties of a metallo-dielectric structure in order to realize a high sensitivity hydrogen sensor. Low values of hydrogen concentration, under the explosive limit of 4.65%, can be easily detected by the palladium/polymeric device if the optical properties of the hydride palladium are properly analyzed. If the surrounding mixture of gases is composed of oxygen (30%), nitrogen (70%) and hydrogen (few ppm) only, we can extract information about the optical properties of the Pd films, in order to relate a pathologic condition with an optical response for the sensitive metal. A malabsorption condition or intolerance results in an increase from a baseline value of 20ppm in the exhaled breath. This value remains constant during the test for healthy people, and change dramatically after few minutes for patients which suffers from lactose malabsorption or lactose intolerance. For medical purposes, we have to consider hydrogen values ranging from 20ppm to 100ppm, which are typical values for pathologic conditions of lactose malabsorption [27]. Several works report on changes of optical properties of thin film of hydride palladium absorbing different hydrogen concentration [16,17]. To take into account the dispersion properties of bare Pd we use the Drude model. One of the most important issues of the works mentioned above is that the Drude model still remains valid to describe the dielectric constant of palladium, even if the hydrogen concentration is increased [8]. In order to express the Drude parameters as a function of hydrogen concentration, the dielectric constant of bare Pd thin film has been measured using different substrates and comparing the results in terms of transmittance and reflectance [28]. Once the nonlinear function *h* (see eq.1) is evaluated, the Drude parameters and the dielectric constant are calculated for all hydrogen concentration under investigation. The use of the multilayer, metallo-dielectric structure allows to increase the total amount of the sensitive material, i.e. palladium, and, at the same time, improves the transmittivity. Moreover the sensitivity of the sensor is defined by the following expression:

$$S = \int_{H_2[ppm]} \frac{\Delta T_{peak}[\%]}{\Delta H_2[ppm]}, \quad H_2[ppm] = 20, \ldots 100 \text{ ppm} \qquad (2)$$

We have performed an optimization analysis of the key parameters of the structure, in particular the thicknesses of metal and polymer, in order to find a balance between the width of the whole structure and the transmission features, including the transmission peak bandwidth. Looking for a purposeful configuration, able to ensure good sensitivity in the whole range of investigation, we have analyzed different thickness values for polymer and for the metal. Among these values we found that the best compromise in terms of sensitivity, device compactness and linearity of the calibration curve is reached for a dielectric thickness equal to 110nm and metal thickness equal to 10nm. Therefore, the optimized multilayer structure is composed of five layers of 10nm of Pd alternated by 110nm of the EXP0454 polymer. This structure is embedded within two antireflection coatings of 60nm of the same polymer. The transmission spectrum of the structure is reported in Fig.1. It has been calculated using the standard transfer matrix method. Normal incidence, absorption and dipersion phenomena are considered in all the simulations. The transmission spectrum of the multilayer system experiences small changes as the H_2 concentration varies in the environment. For example, by increasing the concentration of hydrogen, transmittivity levels within the visible range increase. This phenomenon is strictly linked to the red shift of the plasma frequency and to the enhancement of the damping factor of the hydride palladium. We have evaluated an increase of 7,4% in terms of peak value when a malabsorption condition (the overtaking of the 20ppm baseline) is detected. Moreover, a total increase of about 15,6% of the transmission spectrum is revealed when the total amount of hydrogen in the environment grows from 20ppm to 100ppm (Fig. 2).

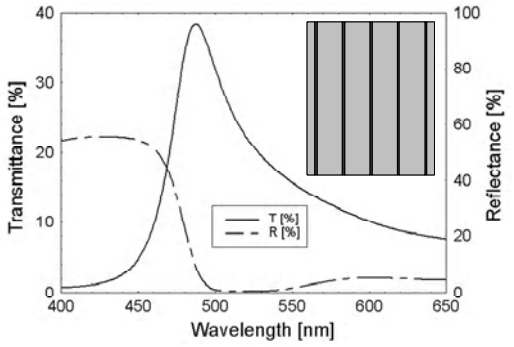


Fig.1: Sketch of transmission and reflection spectra for the multilayer structure. The inset shows the sensor structure: light grey regions are the dielectric layers (EXP0454) and dark grey regions are the metal layers (Pd).

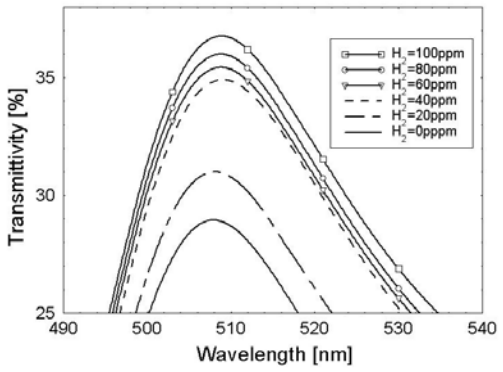


Fig.2: Transmission spectra for the optimized H_2 sensor: an increase of 7.4% in terms of transmittivity is noticed when a malabsorption condition occurs, i.e. the overtaking of the 20ppm baseline; the total increase of the transmittivity swelling the hydrogen concentration from 20ppm to 100ppm is about 15.6%.

Conclusions

We have proposed a novel approach to hydrogen sensing in order to realize a compact optical sensor suitable for the H_2-breath-test analysis. This kind of device is very useful for the detection of lactose malabsorption or intolerance condition, giving back a lucid information about the overtake of the healthy condition threshold. Moreover the proposed structure is appropriate to truthfully reveal the amount of hydrogen in the breath exhaled by unhealthy people, and can be proper to trace the relation between time and exhaled hydrogen.

Acknoledgments

This work was sponsored by the research contract PRIN 2005: “Photonic Band Gap Nanosensors”.

References

1. T.H.Vesa et al, J. Am. Coll. Nutr, vol. 19, pp. 165S -175S, 2000.
2. T. H. Risby, Conference on Lasers and Electro-Optics, vol.2, pp. 898-899, 2005.
3. P.T. Moseley et al, Philadelphia, PA: IOP, 1991.
4. K. Hara et al, Sens. and Act. B, vol. 65, pp. 366-370, 2000.
5. S. Basu et al, Sens. and Act. B, vol. 22, pp. 83-87, 1994.
6. V.R.Katti et al, Sens. and Act. B, vol. 84, pp. 219-225, 2002.
7. K. Domansky et al, Mater. Sci. Eng. B, vol.76, no.2 , pp. 116-121, 2000.
8. X. Bevenot et al, Sens. and Act. B, vol. 67, pp. 57-67, 2000.
9. J. Villatoro et al, Opt. Expr., vol. 13, no.13, pp.5087-5092, 2005.
10. M.A. Buttler, J. Electrochem. Soc., vol. 138, pp. 46-47, 1991.
11. Y. Oh et al, J. Ceram. Soc. Jpn., vol. 110, pp. 618-620, 1993.
12. B. Chadwick et al, Sens. Act. B, vol. 17, pp. 215-220, 1994.
13. A. Bearzotti et al, Sens. Act. B, vol. 7, pp. 685-688, 1992.
14. T. Graham, Phil. Trans. R. Soc. Lond., vol. 156, pp. 399-439, 1866.
15. J.C. Barton et al, Trans. Far. Soc., vol.62, pp. 960-970, 1966.
16. A. Mandelis et al, Sens. Act. B, vol. 49, pp. 258-267, 1998.
17. K. Wyrzykowski et al, J. Phys. Condens. Matt., vol. 1, pp. 2269-2982, 1999.
18. M.A. Ordal et al, Appl. Opt., vol. 22, pp. 1099-1120, 1983.
19. M. Tabib-Azar et al, Sens. Act. B, vol. 56, pp.158-163, 1999.
20. M. Scalora et al, Jour. App. Phys., vol. 83, pp. 2377-2383, 1998.
21. S. Baglio et al, IEEE Sens. Jour., vol.1, pp. 288-295, 2001.
22. N.N. Lepeshkin et al, Phys. Rev. Lett., vol. 93, 123902, 2004.
23. Y.K. Choi et al, Opt. Comm., vol. 230, pp. 239-243, 2004.
24. J. Villatoro et al, Opt. Expx., vol. 13, pp. 5087-5092, 2005.
25. N. Sadayori et al, Patent Application publication No. 20040158021A1, August 12, 2004.
26. Y. Wang et al, Proceedings of the SPIE, vol. 5724, pp. 42-49, 2005.
27. R.J. Vonk et al, Eur. Jour. Clin. Invest., vol. 33, pp. 70-75, 2003.
28. W.E. Vargas et al, Thin Sol. Films, vol. 496, pp. 189-196, 2006.

Segmented waveguide tapers for low insertion loss, high performance *SPE:LiNbO$_3$* integrated circuits

Davide Castaldini (1-2-3), Paolo Bassi (1-3), Guillaume Bertocchi (2),
Sorin Tascu (2), Pierre Aschieri (2), Marc De Micheli (2), Sebastien Tanzilli (2) and Pascal Baldi (2)
1) Dipartimento di Elettronica Informatica e Sistemistica, University of Bologna, Italy (e-mail: dcastaldini@deis.unibo.it)
2) Laboratoire de Physique de la Matière Condensée, University of Nice - Sophia Antipolis, France
3) also with MIST.E-R, Laboratory for MIcro and Submicro enabling Technologies of Emilia-Romagna

Abstract: *We present the results of an experimental study of waveguide tapers realized with segmented waveguides in $LiNbO_3$ substrates using the Soft Proton Exchange (SPE) technique. Measurements show that the tapers can be favorably introduced between the nonlinear or electro-optic part of the components, which requires strong mode confinement to increase efficiency, and the coupling section with a standard optical fiber, which requires low mode confinement, in order to have low coupling losses. These tapers allow almost lossless mode shape transformation with a reduction of the coupling losses up to* 0.7 *dB, thus proving the practical interest of the approach. As an example, the use of such tapers in a real integrated optical circuit is shown.*

Introduction

Insertion losses have always been a major problem in Integrated Optics (IO). Reducing the insertion losses is important for telecom and sensors applications and is mandatory in the case of Quantum Communication, where the information is carried by single photons and where amplifiers are not allowed. Losses are due to misalignments, Fresnel reflection and mode mismatch. Misalignments between fiber and IO device can be avoided using careful aligning procedures. Fresnel reflection losses, due to the different values of the refractive indices of the IO waveguide and the optical fiber, can be reduced using index matching fluids or antireflection coatings at the end-face of the sample. Mode mismatch losses are due to different mode sizes in the IO waveguide and the fiber. They are particularly important in the case of active electro-optic (EO) or nonlinear (NL) devices where the component efficiency is a growing function of the mode confinement. In these cases, designing the waveguide to optimize its coupling with low confinement telecom single mode fibers is far from being optimum, but is the more commonly used technique [1] since we are still missing a practical and cost effective solution allowing longitudinal variation of the transversal section of the waveguide mode. This mode size transformer (taper) should be adiabatic, as short as possible, in order to realize the best trade off between propagation losses and coupling efficiency. In the literature a lot of solutions for the design of a taper has been proposed [2, 3, 4, 5]. Among them, the segmented waveguide configuration seems the most suitable as it does not introduce additional steps in the fabrication process [6, 7, 8, 9, 10, 11].

In principle, this technique is rather general, and can be adapted to any material or waveguide fabrication technique. Nevertheless, as the excess losses induced by the segmentation depend very much on material and waveguide fabrication technique, each case has to be carefully studied experimentally. In this paper, we present a study devoted to waveguides realized in *Z-cut* wafers of $LiNbO_3$ that are commonly used for their good nonlinear properties, allowing for example the fabrication of efficient optical frequency converters and photon pair sources required for quantum communication at telecom wavelengths [12].
In order to realize optical waveguides in this substrate, various techniques have been proposed in the past: outdiffusion [13], titanium diffusion [14], ion implantation [15], proton exchange [16] and its different implementations (simple Proton Exchange [16], Annealed Proton Exchange, APE [17], Soft Proton Exchange, SPE [18]). Among the PE techniques, we choose the SPE process which does not perturb the crystalline structure of $LiNbO_3$ while other ones do [19, 20]. In particular, the ferroelectric domain inversion of PPLN devices used for photon pair generation remains intact after SPE [21]. The reported results show that when pushing the SPE parameters to obtain waveguides with the maximum Δn which allows maximum field confinement, tapers showing an overall reduction of the insertion losses with respect to the untapered waveguide can be successfully realized.
The paper is organized as follows. In the next section, the waveguide taper design and fabrication processes are described. In third section, the different characterization techniques used to evaluate the improvements of the taper are illustrated. In the fourth section, the experimental results obtained with different fabrication parameters of the taper are presented. In the fifth section, the use of the tapers in a real integrated circuit is shown and finally, conclusions are drawn.

Device fabrication

The tested devices are constituted by a taper that transforms the highly confined mode of a continuous waveguide (CWG) to a weakly confined one supported by a segmented waveguide (SWG) as shown in figure 1. To understand the features of the mode of such a waveguide, one should remind that, for wavelengths far away from the band gap, the SWG behavior can be described using the so called equivalent waveguide theorem for periodic structures [22, 23], which says

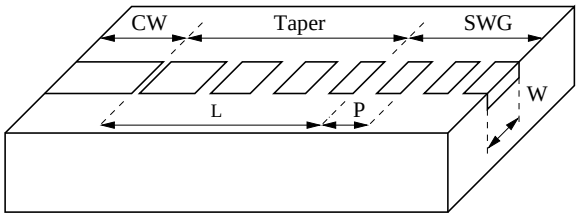


Fig. 1: Schematic of segmented waveguide taper.

that, in this case, a SWG is equivalent to a CWG with the same depth and width but with a surface index equal to:

$$n_{eq} = n_{sub} + \Delta n \cdot DC \tag{1}$$

where n_{sub} is the substrate index, Δn is the step index and DC is the duty cycle defined as the ratio between the length of the high index segment and the period. In the case of a taper, the DC varies from $DC = 1$ (continuous waveguide) to a smaller DC with constant period P so that the surface index of the equivalent waveguide is reduced as well as the mode confinement. Once the desired mode size is reached, the DC is kept constant down to the end of the sample to stabilize the mode size after the transformation in the taper.
Designing the taper one should fix its length (L), the segmentation period (P), the final duty cycle (DC) and the waveguide width (W). Tapers with 48 possible combinations of these parameters (listed in table 1) were first fabricated in order to find the best solution to adopt in the relay.

Table 1: Parameters used for the tapers present on the sample.

$P[\mu m]$	DC	$W[\mu m]$	$L[\mu m]$
15	0.5	5	100
25	0.6	7	600
	0.7		1000
			1400

In order to realize the optical waveguides in the *Z-cut* Lithium Niobate substrate, we have chosen the SPE process. The proton source used is the Benzoic acid with 2.8% of Lithium Benzoate, as this value has been previously shown to give the largest surface extraordinary index variation ($\Delta n = 0.03$ at $\lambda = 632.8nm$) while preserving the original nonlinear optical properties of Lithium Niobate.
The last fabrication step is the end-face polishing to allow end-fire coupling of the sample with the input and output fibers. A particular care is devoted to control the angle between the end-face and the waveguides. Such angle must be 90° in order to use the Fabry-Perot technique to measure the propagation losses [24].

Experimental setup
In this section we describe the experimental setup used to make all the characterizations. The laser source is a tunable external cavity laser emitting between 1.5 μm and 1.6 μm (NetTest Tunics Plus) with an automatic power control system and a narrow linewidth of 150 kHz. In order to control the field polarization state at the entrance of the sample, a monomode polarization maintaining (PM) fiber has been used to couple the source and the waveguides. A standard SMF-28 has then been used to collect the light at the output of the sample. An InGaAs detector allows measuring the light power. The input and output fibers are mounted on piezoelectric translation stages with 16 nm spatial resolution. All the setup is computer controlled via a GPIB interface. This system can be used not only to evaluate separately the IO waveguide propagation losses and the mode overlap integral but also their combined effect, comparing the overall coupling efficiencies using tapered and untapered structures.
The propagation losses are measured using the Fabry-Perot cavity technique [24]. Measuring the power transmitted through the system at different wavelengths, one obtains fringes whose contrast is directly related to the propagation losses. One of the most important advantages of this technique is that the measurement is independent of the coupling efficiency.
The mode mismatch losses can be evaluated via the measurement of the cross-correlation function between waveguide and fiber mode. Such a function is measured by exciting the waveguide under test with a constant power at a fixed wavelength and recording the power collected by the output fiber, while it scans, with 16 nm steps, a 25 $\mu m \times 25$ μm window centered on the waveguide output. Such measurement is similar to that described in [25] and provides many information. First of all we can quantify the tolerance of the fiber to waveguide alignment. A sharp cross-correlation function corresponds to high coupling losses for small alignment errors, while a smooth cross correlation function allows some alignment errors without dramatic impact on the coupling losses. Moreover, knowing the cross-correlation function and the fundamental mode pattern Ψ_f of the SFM-28 fiber, it is possible to reconstruct the waveguide mode field distribution Ψ_w through a simple deconvolution operation. The intensity overlap integral holds then:

$$I = \frac{\left|\iint \Psi_{SWG} \cdot \Psi_f^* dS\right|^2}{\iint |\Psi_{SWG}|^2 \, dS \cdot \iint \left|\Psi_f\right|^2 dS}. \tag{2}$$

Evaluating this integral for different tapers allows determining the combination of parameters which gives the better mode matching.
Finally, the overall coupling efficiency improvement, which depends on the combined effect of taper induced propagation losses and waveguide to fiber mode matching improvement can be evaluated comparing the maximum power transmitted through the different waveguides present on the sample under test. For each waveguide, the throughput power is measured optimiz-

ing contemporarily the positions of both input and output fibers with piezo-controlled stages.

Taper characterization

We have first characterized the sample with structures made by continuous waveguides and tapers in correspondence at one end-face. Figure 2 presents the mode size as a function of the *DC* of the SWG for $W = 5\ \mu m$ and a period $P = 15\ \mu m$. Note that for $DC = 1$, corresponding to a continuous waveguide, we found mode sizes smaller than the fiber mode size (dashed line). Reducing the *DC* the SWG mode size increases as expected. It is then possible to calculate the overlap integral between the fiber and the waveguide modes using the expression 2. The result is reported in figure 3. For

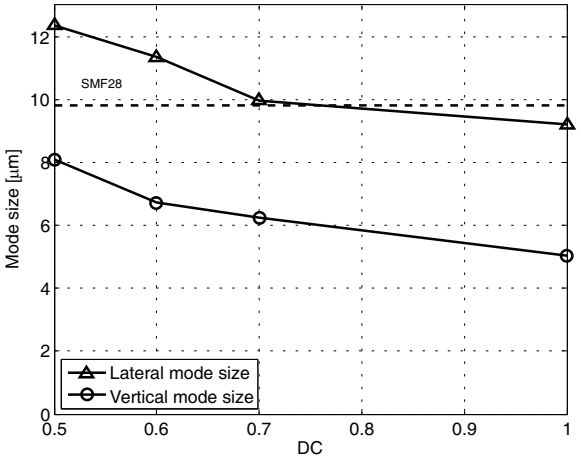


Fig. 2: Measurement of the lateral and vertical mode sizes (at $1/e$ of the field maximum) of SWGs as a function of *DC* with $W = 5\ \mu m$ and $P = 15\ \mu m$.

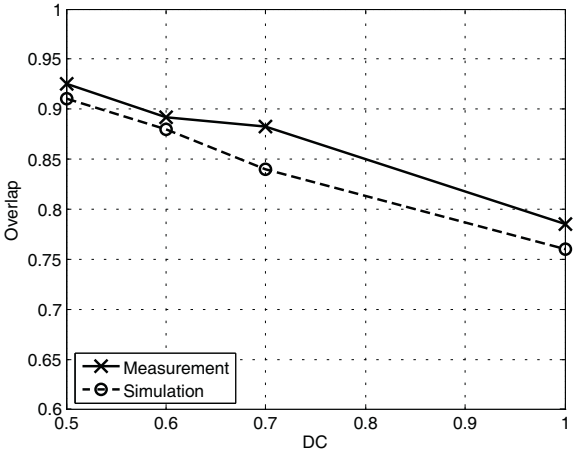


Fig. 3: Overlap between the segmented waveguide mode and the SMF-28 mode for different DC. Measurements (continuous line with crosses) are compared to simulation results (dashed line with circles).

the continuous waveguide we found that the overlap is 78% but the use of a segmented waveguide taper can improve it up to 92% for $DC = 0.5$ (continuous line). This corresponds to an improvement of 0.71 *dB* in logarithmic scale. This experimental result agrees with the numerical prediction obtained using a 3D BPM [26] (dashed line in figure 3). However, this result is not the real performance improvement, which can be obtained using tapered and segmented waveguides, as they induce extra propagation losses which are not taken into account in the overlap integral. These extra propagation losses are due to imperfect mode transformation and scattering losses at the segments edges. So, the use of a segmented waveguide taper becomes effective if the mode matching improvement is larger than the propagation loss increase. Using the Fabry-Perot cavity technique, illustrated in the previous section, we obtained the best result with a 1400 μm long taper associated to a 2600 μm long segmented waveguide, with $P = 15\ \mu m$, $W = 5\ \mu m$ and $DC = 0.5$. In this case we found a loss increase of only 0.04 *dB* with respect to the continuous waveguide. The total improvement obtained in terms of waveguide to fiber coupling is then $0.71 - 0.04 = 0.67\ dB$. The precision of this result is estimated to be around $\pm 0.2\ dB$.

The overall improvement was also measured evaluating the insertion losses difference between a tapered and an untapered waveguide. The results are reported in the table 2 where P_t and P_{CWG} are output powers measured at the end of the waveguides with and without taper respectively. Negative results correspond to the cases where the overlap improvement does not even compensate for the additional losses. The optimum length of the taper depends on the segmentation parameters. Table 2 reports the results for the lengths that provide the best performances.

Table 2: Insertion losses difference between tapered and an untapered waveguides for the different fabrication parameters.

$W[\mu m]$	$P[\mu m]$	$L[\mu m]$	DC	$10\log(P_t/P_{CWG})$ $[dB]$
5	15	1400	0.5	0.78
		1000	0.6	0.22
		600	0.7	0.19
	25	1400	0.5	-0.53
		1400	0.6	0.15
		600	0.7	0.51
7	15	1400	0.5	0.06
		1000	0.6	-0.25
		600	0.7	0.20
	25	1400	0.5	0.37
		1400	0.6	0.43
		600	0.7	0.47

In the case of the best result previously considered, we obtained an overall increase of 0.78 *dB* of the transmitted power with respect to the continuous waveguide. The precision of this measurement is around $\pm 0.1\ dB$. These two different measurements give re-

sults, which taking into account the uncertainties, are equal and confirm the practical interest of segmented waveguide tapers realized using the SPE process.

Integrated optical circuit with tapers

As an example of such practical interest, we now show the use of similar tapers in an integrated optical circuit specially developped for the realization of a quantum relay. The aim of such a device is to increase the achievable distance of quantum communications between two partners [27]. The scheme of the integrated realized device we tested is shown in figure 4.

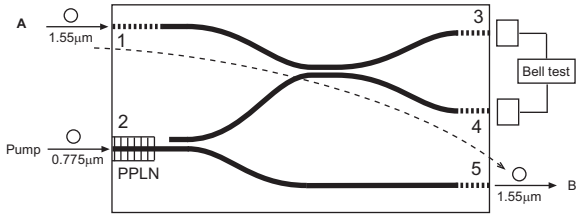


Fig. 4: Schematic of the quantum relay with tapers (dashed lines) at ports 1, 3, 4 and 5.

The performances of such an integrated quantum relay are extremely penalized by coupling losses as four of the five port interact with standard telecommunication fibers (ports 1, 3, 4, 5) at 1.55 μm. The presence of tapers to improve coupling efficiency is then of great interest.

In order to evaluate the insertion losses reduction induced by segmented waveguide tapers in quantum relay we have fabricated tapered and untapered structures on the same sample. The taper parameters correspond to the best result obtained with the previous study. The relay characterization consists of injecting a constant power in port 1 using a PM fiber and to measure the output powers P3 and P4 at port 3 & 4 using two SMF-28 fibers and a powermeter. The total output power (P3+P4) measured for relays that include tapers is 1.28 ± 0.5 dB higher than that obtained with bared ones. This means that each taper induces a coupling losses reduction of 0.64 ± 0.25 dB which is in agreement with the previously described results obtained for straight waveguides.

Conclusion

In this work we have presented experimental results concerning segmented waveguide tapers fabricated in $LiNbO_3$ by the SPE process. Such tapers have also been successfully introduced in an integrated optical circuit developed to realize an integrated optical quantum relay. We have found that, for each interconnection, the introduction of optimized tapers allows reducing by 0.64 dB the coupling losses between the relay and a standard SMF-28 fiber. This result will allow improving the performances of the relay and any other insertion-loss sensitive device.

Acknowledgments

Davide Castaldini gratefully acknowledges Università Italo Francese (http://www.universita-italo-francese.org) for providing him the PhD Vinci fellowship which allowed his participation to this project. This work was supported in part by the U.S. Department of Commerce under Grant BS123456, the Italian Ministry of Education, University and Research (MIUR) and Regione Emilia Romagna in the framework of the *MIST.E-R* Project.

References

[1] R. C. Alferness et al, IEEE J. Quant. Elect., vol. 18, p. 1807, 1982

[2] P. G. Suchoski et al, IEEE J. Lightwave Technol., vol. 5, p. 1246, 1987

[3] K. Kasaya et al, IEEE Photonics Tech. Lett., vol. 5, p. 345, 1993

[4] B. Luyssaert et al, IEEE J. Lightwave Technol., vol. 23, p. 2462, 2005

[5] F. Van Laere et al, ECOC, Paper Tu1.4.5, 2006

[6] M. H. Chou et al, Opt. Lett., vol. 21, p. 794, 1996

[7] F. Dorgeuille et al, Opt. Lett., vol. 20, p. 581, 1995

[8] M. M. Spuhler et al, IEEE J. Lightwave Technol., vol. 16, p. 1680, 1998

[9] Z. Weissman et al, Electr. lett., vol. 28, p. 1514, 1992

[10] Z. Weissman et al, IEEE J. Lightwave Technol., vol. 13, p. 2053, 1995

[11] M. Yanagisawa et al, IEEE Photonics Tech. Lett., vol. 4, p. 433, 1993

[12] O. Alibart et al, Opt. Lett., vol. 30, p. 1539, 2005

[13] J. R. Carruthers et al, App. Opt., vol. 13, p. 2333, 1974

[14] G. J. Griffiths et al, IEEE J. Quant. Elect., vol. 20, p. 149, 1984

[15] M. L. Shah, App. Phys. Lett, vol. 26, p. 652, 1975

[16] J. L. Jackel et al, App. Phys. Lett, vol. 41, p. 607, 1982

[17] M. L. Bortz et al, Opt. Lett., vol. 16, p. 1844, 1991

[18] L. Chanvillard et al, Appl. Phys. Lett., vol. 76, p. 1089, 2000

[19] Yu. N. Korkishko et al, IEEE J. Sel. Topics in Quant. Electr., vol. 2, p. 187, 1996

[20] C. Canali et al, J. Appl. Phys, vol. 59, p. 2643, 1986

[21] Yu. N. Korkishko et al, JOSA A, vol. 18, p. 1186, 2001

[22] Z. Weissman et al, IEEE J. Lightwave Technol., vol. 11, p. 1831, 1993

[23] P. Aschieri et al, App. Opt., vol. 38, p. 5734, 1999

[24] R. Regener et al, Appl. Phys B, vol. 36, p. 143, 1985

[25] D. Hannappe et al, Appl. Opt., vol. 35, p. 659, 1996

[26] F. Fogli et al, IEEE J. Lightwave Technol., vol. 17, p. 136, 1999

[27] D. Collins et al, J. Mod. Opt., vol. 52, p. 735, 2005

Er/Yb Waveguide Amplifiers in Novel Silicate Glasses

J. Jágerská (1), F. Ondráček (1), L. Salavcová (1,2), J. Špirková (2), M. Míka (3), and J. Čtyroký (1)
1) Institute of Photonics and Electronics AS CR, v.v.i., Chaberská 57, 182 51 Prague 8, Czech Republic, jagerska@ufe.cz
2) Department of Inorganic Chemistry, Institute of Chemical Technology,Technická 5, 166 28 Prague, Czech Republic, salavcol@vscht.cz
3) Department of Glass and Ceramics, Institute of Chemical Technology, Technická 5, 166 28 Prague, Czech Republic

Abstract: Novel type of ZnO:silica-based glasses co-doped with Er^{3+} and Yb^{3+} for optical waveguide amplifiers were designed. They are characterized by exceptionally low upconversion and essentially no evidence for Er-quenching at the Er-concentration of 0.6 at. %. In the reported glasses, straight channel waveguides with propagation loss as low as 0.18 dB/cm at 1600 nm were fabricated using $Ag^+ \Leftrightarrow Na^+$ and $K^+ \Leftrightarrow Na^+$ ion exchange. Net on-chip gain values of 6.3 dB and 6.6 dB @1537 nm were measured in waveguides pumped at 976 nm in 38-mm-long $Ag^+ \Leftrightarrow Na^+$ and $K^+ \Leftrightarrow Na^+$ waveguides, respectively. In the latter case, net fiber-to-fiber gain of 5 dB was achieved.

Introduction

Multicomponent silicate and phosphate glasses have proven their potential as outstanding substrate materials for realization of Er-doped waveguide lasers and amplifiers. Especially phosphate glasses are famous for dissolving high concentrations of rare-earth dopants, thus enabling to fabricate active devices of small-size and high gain up to 4.1 dB/cm [1]. On the other hand, silica-based glasses have an advantage of higher mechanical rigidity and chemical stability, lower cost and better compatibility with current commercial fiber technology.

As for silicate glasses, Al_2O_3 is typically used as a means to enhance the solubility and homogeneity of Er-dopants and reduce the rate of cluster and Er-pair formation [2]. Nevertheless, we have shown recently [3] that the presence of zinc oxide (ZnO) in the glass melt can also attribute for a substantial enhancement of rare-earth solubility. In this paper we present for the first time to authors' knowledge optical gain measurements on a Er-doped and Er/Yb co-doped Zn-silica-based material.

Spectroscopic and waveguide properties

Three different samples of Er-doped and Er/Yb-co-doped glass substrates differing in Yb concentration were prepared by standard melting technique from the following oxide constituents: SiO_2, Na_2O, ZnO, Al_2O_3, Er_2O_3 and Yb_2O_3. The exact chemical composition and the rare-earth doping concentrations, reported in Table 1, followed from a detailed optimization study. Special effort was made to increase the solubility and homogeneity of Er^{3+} and Yb^{3+} ions by means of the network intermediate ZnO. ZnO decreases the optical basicity of the glass, which was also proven to have a positive influence on the metastable level lifetime, luminescence bandwidth and absorption and emission cross-section spectra of the Er^{3+} ions [3].

Table 1: Concentration of the rare-earth ions [at/m^3]

	MM64 Er/Yb - 1:0	MM65 Er/Yb - 1:1	MM65 Er/Yb - 1:2
Er_2O_3	1.71×10^{26}	1.71×10^{26}	1.71×10^{26}
Yb_2O_3	–	1.70×10^{26}	3.40×10^{26}

All glass constituents were melted together for 4 h in a platinum crucible at the temperature of 1470 °C. Afterwards, the melt was quenched in a water bath and left to temper at 520 °C for another hour. The ready-made glass preform was cut into wafers and polished to dimensions of 40mm×20mm×2mm.

In the bulk glass substrates the waveguides were formed using the $K^+ \Leftrightarrow Na^+$ and $Ag^+ \Leftrightarrow Na^+$ ion exchange technique. This was feasible thanks to a large fraction of network modifier Na_2O contained in the glass matrix. Potassium and silver ion exchange waveguides differ actually a lot in both their fabrication conditions and waveguiding properties. While potassium channels exhibit lower propagation losses, the resulting refractive index contrast is low leading to large mode field area. Silver waveguides, on the contrary, can account for higher mode confinement; however, the inherent propagation loss is higher.

In order to define the waveguide boundaries, a standard optical contact lift-off lithography was used. The actual waveguide pattern consisted of a series of straight waveguide channels varying in width from 2 to 6.5 μm. One major advantage of this design was that regardless of small inaccuracy in the ion exchange condition settings, one could find a channel that exhibited a single mode performance at both pump (976 nm) and signal (1537 nm) wavelengths.

The process of ion exchange with K^+ ions was performed in a melt of pure potassium nitrate at 400°C for 1-2.5 h, depending on the exact Yb concentration. The Ag^+ ion exchange proceeded in eutectic $NaNO_3$-KNO_3 melt with addition of 3.6 wt.% of silver nitrate at 280 °C for 4-8 min.

The mode dimensions of potassium waveguides were measured to be 10×13 μm at 1550 nm and 7×11 μm at 980 nm. In the silver ion-exchange waveguides, the mode field dimensions were 6×7 μm and 3×5 μm at the wavelengths of 980 nm and 1550 nm, respectively. Although the large mode field area can ensure low coupling loss to single-mode fibers, it

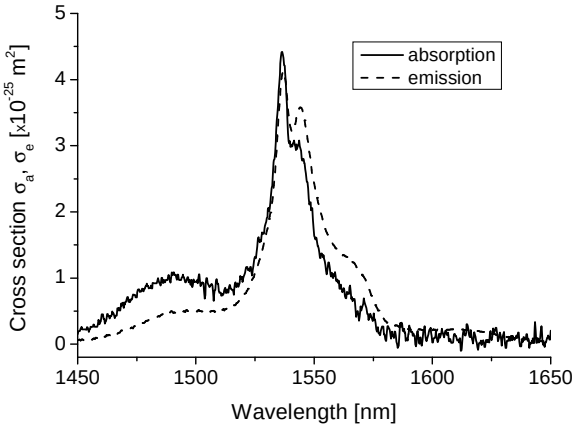


Fig. 1: Spectral dependency of the cross section of MM65 glass substrate

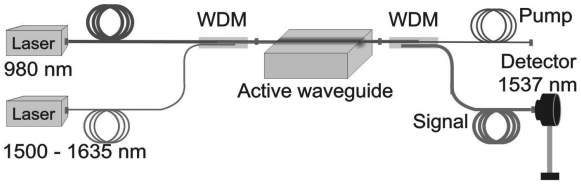


Fig. 2: Experimental setup for amplification measurement

naturally results in undesirably low pump efficiency. Higher confinement of intensity distribution and better overlap of pump and signal intensity profiles could be achieved if a more sophisticated technique (*e.g.*, a field assisted ion exchange burying the waveguide below the glass surface) were used.

The channel waveguide scattering loss was determined outside the Er absorption bands at 1600 nm using the Fabry-Perot resonator method [4]. Potassium waveguides exhibited losses as low as 0.18 dB/cm, while the loss of silver-exchanged channels read 0.8 to 0.9 dB/cm. In the latter case the loss could be reduced by about a half if annealed for 30 min at 300 °C, at the expense of considerable mode field expansion, however.

The relative absorption and emission cross section spectra at both pump and signal wavelengths were obtained from the bulk transmission and photoluminescence measurements and are presented in Figure 1. The relative absorption cross section spectrum was normalized by means of the measured waveguide transmission at the signal peak absorption wavelength. Using the known optical mode profile, waveguide transmission and the Er concentration of 1.72 at/m^3 (0.6 at.%) the peak absorption cross section at 1537 nm was calculated to be 4.42×10^{-25} m^2.

Absorption cross section of Er at the pump wavelength of 976 nm resulted in 1.25×10^{-25} m^2, while the absorption cross sections of ytterbium amounted to 8.4×10^{-25} m^2 in both MM65 and MM66 samples. Normalization constant for the emission cross section spectrum was calculated using the McCumber procedure [5]. The peak emission cross section at 1537 nm has the value of to 4.22×10^{-25} m^2 and the cross section of ytterbium at 976 nm equals 6.7×10^{25} m^2.

Finally, the metastable level lifetime of Er^{3+} was obtained from the photoluminescence decay measurement. The detected decay curve was single exponential with the time constant of 6.3 ms.

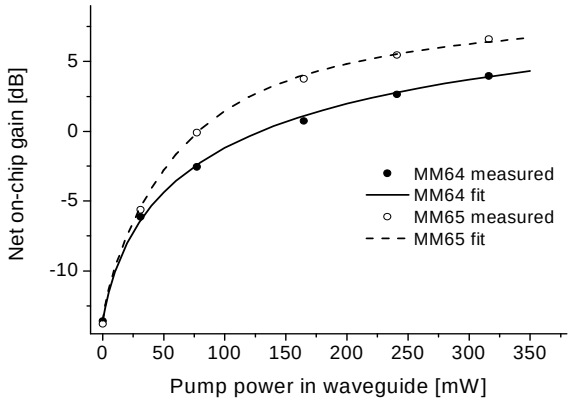


Fig. 3: Net on-chip gain vs. pump power: measured and simulated data for MM64 (Er) and MM65 (Er/Yb - 1:1) K^+ waveguides

Gain measurement and experimental results

Optical gain measurements were performed with 38-mm-long waveguide samples using the experimental setup depicted in Figure 2. A semiconductor laser diode of maximum optical power 375 mW emitting at 976 nm served as a pump source, and the signal light was provided by a highly monochromatic Agilent 81642B laser tunable in the wavelength range of 1495–1635 nm.

The signal and pump were combined by a 980/1550 nm fiber wavelength division multiplexer (WDM) and coupled into the waveguide using a SM 980 (4.5/125) fiber exhibiting singlemode performance at both signal and pump wavelengths. At the waveguide output the amplified signal was separated from the pump in second 980/1550 nm fiber WDM coupler and detected using InGaAs detector. At the waveguide input and output coupling gel was used to suppress Fresnel reflections and thus minimize the coupling losses. In potassium channel waveguides the resulting loss per an interface was estimated to be 0.8 and 0.85 dB at the signal and pump wavelengths, respectively. For silver waveguides with higher refractive index contrast and stronger mode field confinement the coupling loss was considerably higher counting approx. 1.8 dB.

First, the change in signal transmission as a function of pump power was measured at the central Er^{3+} emission wavelength of 1537 nm. Signal power at the waveguide input was set to 100 μW. The measured signal enhancement was converted to net optical gain by setting the gain at 1600 nm and zero pump power equal the waveguide scattering loss.

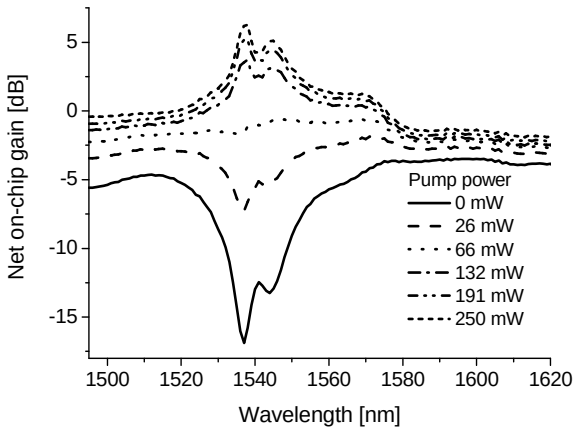


Fig. 4: Spectral dependency of the net on-chip gain of the MM66 (Er:Yb = 1:2) Ag^+ waveguide for several different pump powers (converted to input power in the waveguide).

Table 2: Maximum achievable net on-chip gain

	Net on-chip gain [dB per sample]	
	K^+ waveguide	Ag^+ waveguide
MM64	3.95	-
MM65	6.61	5.80
MM66	6.63*	6.31

* the length of the sample was only 34 mm

Figure 3 shows the measurements results on potassium channel waveguides fabricated in MM64 and MM65 substrates. In the purely Er-doped sample the net optical gain is reached at the pump power of 130 mW and upon pumping at 316 mW the positive on-chip gain achieves 4.0 dB. The performance of the Er/Yb-codoped sample is even better with the threshold pump power reduced to 80 mW and maximal achievable gain 6.6 dB. Thanks to low in/out coupling losses of potassium waveguides fiber-to-fiber gain as high as 4.9 dB was observed.
The optical gain measurement on silver channel waveguides was performed on MM65 and MM66 glass substrates. Due to higher waveguide scattering loss the maximum net gain amounted for 5.8 dB and 6.3 dB in MM65 and MM66 glasses, respectively. However, because of substantial coupling loss, fiber-to-fiber gain of only 2.6 dB was observed. All measurement results are summarized in Table 2.

The second part of the amplification measurement consisted in determining the amplifier bandwidth by measuring the spectral dependence of signal gain at several different pump powers. The input signal level was kept constant at P_s = 100 µW and the measurement was performed in the full achievable wavelength range from 1945 to 1635 nm. The gain spectrum of MM66 Ag^+ sample is depicted in Figure 4 and is characterized by a relatively narrow FWHM bandwidth of 15 nm, quite typical for ordinary silica-based glass materials [2].
Finally, spectral analysis of the amplified signal was performed and it showed that essentially no amplified spontaneous emission degrading the amplifier performance and contributing to noise figure was present.

Table 3 Model input data

Spectroscopic parameters		
Er^{3+} abs. cross section @ 1537 nm	$\sigma_{12}=4.42e^{-25}$ m^2	
Er^{3+} emis. cross section @ 1537 nm	$\sigma_{21}=4.22e^{-25}$ m^2	
Er^{3+} abs. cross section @ 976 nm	$\sigma_{13}=1.25e^{-25}$ m^2	
Yb^{3+} abs. cross section @ 976 nm	$\sigma_{56}=8.40e^{-25}$ m^2	
Yb^{3+} emis. cross section @ 976 nm	$\sigma_{65}=6.70e^{-25}$ m^2	
Er^{3+} metastable level lifetime	τ_{21}^{Er}=6.3 ms	
Yb^{3+} metastable level lifetime	τ_{65}^{Yb}=1.3 ms	
Er^{3+}-nonrad. lifetime of pump level	τ_{32}^{Er}=10 µs	
Up-Conversion coefficient	$C_{up}=1.1e^{-24}$ m^{3}s^{-1}	
Cross-relaxation coefficient	$C_{cr}=0.12e^{-22}$ m^{3}s^{-1}	
Waveguide parameters	K^+	Ag^+
Mode-field dimensions	9.6×12.9 µm	6.1×7.0 µm
Mode-field dimensions @ 980 nm	6.9×10.5 µm	3.2×4.8 µm
Scattering loss @ 1550 nm	0.18 dB/cm	0.85 dB/cm

Model Simulation and Discussion
A six-level numerical model of Er/Yb-co-doped active waveguide was formulated to fit the measured gain and analyze the amplifier performance. The model incorporates the Er/Yb rate and propagation equations on a 3-D grid to calculate the population inversion and the pump and signal evolution along the waveguide. It takes into account the cooperative upconversion as the most important quenching effect limiting the amplifier gain. Further, the Er-Yb cross-relaxation process as a mechanism of energy transfer between Er^{3+} and Yb^{3+} ions is considered [6].
All input data (Table 3) for the model calculations were taken from the previous measurements except for the nonradiative lifetimes and the Yb^{3+} metastable level lifetime that were found in literature [2], [7]. The up-conversion coefficient C_{up} and the cross relaxation coefficient C_{cr} constitute the unknown parameters to be found upon the fitting procedure.

First, the up-conversion coefficient C_{up} was determined from the measurement on purely Er-doped MM64 sample. The best fit of the measured data was found for the up-conversion coefficient $C_{up}=1.1\times10^{-24}$m^{3}s^{-1}. This is one of the lowest C_{up} values reported for a glass material with Er^{3+} concentration as high as 0.6 at. %. Low probability of the upconversion process can be also deduced from the fact that no visible green luminescence indicating the pump upconversion was present during the measurement.
Next, the cross-relaxation coefficient was obtained from fitting the data measured on MM65 and MM66 samples. The best fit shown in Figure 4 was achieved for $C_{cr} = 0.12^{-22}$m^{3}s^{-1}. The $Yb^{3+} – Er^{3+}$ energy transfer

efficiency can be estimated from the approximate equation for cross-relaxation quantum efficiency [8]:

$$\eta = \frac{C_{cr} N_{Er} \tau_{65}^{Yb}}{1 + C_{cr} N_{Er} \tau_{65}^{Yb} (1 + N_{Yb} \tau_{32}^{Er} / N_{Er} \tau_{65}^{Yb})} = 72\%$$

When fitting the cross-relaxation process we assumed the C_{up} coefficient keeps the unaltered value of $C_{up} = 1.10^{-24}\,m^3s^{-1}$. However, upon the measurement on MM65 and MM66 samples we did observe a certain amount of green luminescence, intensity of which grew with the Yb-doping concentration. Since Yb-codoping should not increase the upconversion probability, and moreover, no reduction of the metastable level lifetime of Er^{3+} as well as no degradation of amplifier gain was evident, we attributed the observation not to upconversion but to the presence of excited-state absorption facilitated by highly efficient Er-Yb energy transfer.

Finally, it should be noted that the 38-mm-length of the active waveguide samples is not optimum. In purely Er-doped MM64 substrate only a small portion of pump power (approx. 2 dB) is absorbed, which means that higher gain could be achieved in longer samples. The simulation results imply that a gain of 6.3 dB would be feasible in a 10-cm-long Er-doped waveguide. On the other hand, in MM66 samples, the full length of the waveguide is slightly underpumped due to strong absorption of pump power in Yb^{3+} ions.

Conclusions

Er doped and Er/Yb-codoped ZnO:silica-based waveguides were fabricated by standard ion exchange technique. A net on-chip gain values measured at the wavelength of 1537 nm were of 6.3 dB and 6.6 dB in 34 mm and 38 mm long Ag^+–Na^+ and K^+–Na^+ waveguides, respectively, when excited by a pump power of about 316 mW at the wavelength of 976 nm. The active waveguide substrates exhibit exceptionally low upconversion and essentially no evidence for Er-quenching at the Er-concentration of 0.6 at. %. The measurement results demonstrate a great potential of the reported silica-based glass as a substrate for up-to-date active devices.

Acknowledgments

This project was supported by the Grant Agency of the Czech Republic under projects No. 106/05/0706 and 102/05/0987.

References

1 Yan, Y. C., Faber, A. J., de Waal, H., Kik, P. G. Polman, A., *Appl. Phys. Lett.*, Vol. 71, pp.2922-2924, 1997.
2 Miniscalco W.J.: *J. Lightwave Technol*., vol. 9, pp 234, 1991.
3 M. Míka, O. Kolek, et al.: SPIE Vol. 5723, Optical Components and Materials II, Bellingham, WA, 2005
4 F. Ondráček, M. Skalský, J. Čtyroký: SPIE Vol. 6180 Photonics, Devices and Systems III, Bellingham, WA, 2006
5 Miniscalco,W. J., Quimby, R. S., *Opt. Lett.*, vol. 16, pp. 258-260, 1991.
6 J. Jágerská, Optical Waveguide Amplifiers in Er-doped Glass Substrates, Diploma Thesis, Czech Technical University, Prague, 2006
7 M.P. Hehlen, N.J. Cockroft, T.R Gosnell: *Phys. Rev.* B, Vol. 56, pp.9302-9318, 1997
8 D. L. Veasey, D. S. Funk, P. M. Peters, et al.: *J. Non-Cryst. Solids* vol. 263, pp. 369-381, 2000.

Polarization effects in gradient index MMI structures made by K^+-Na^+ ion exchange in glass

Damian Kasprzak, Marek Błahut*
Institute of Physics, Silesian University of Technology,
44-100 Gliwice ul. Krzywoustego 2, Poland, *e-mail: mblahut@ polsl.pl

Abstract
Experimental results obtained by visualization method of modal interference in MMI gradient structures, using fluorescence of the substance covering the MMI section, are presented. Experimental investigations are carried out for MMI structures made by K^+-Na^+ ion exchange process in glass. The investigations concern the self-imaging phenomena for symmetrical and paired interference for TE, TM and unpolarized light excitation. The comparisons between results obtained and BPM simulations are presented.

Introduction

Multimode interference (MMI) structures have been for a few years subject to intensive research studies [1]. A large majority of works on MMI concerned interference structures made on the base of step-index waveguides. In 2000 in the paper [2] was proposed for the first the application of MMI in graded-index structures. Gradient structures made by ion exchange in glass are particularly attractive for MMI technology. Ion exchange technique making use of multi-step diffusion processes, electrodiffusion, heating, diffusive and electrodiffusive burying allows modal properties of the waveguides obtained which decide on intermode interference effects to be easily changed. In work [3] is proposed the experimental method which allows visualization of effects of modal interference in MMI structures and some testing results for gradient index MMI structures made by K^+-Na^+ and Ag^+-Na^+ ion exchange in glass. The method uses fluorescence of the substance covering the MMI section. In this paper, using this method we show experimental dependence of light propagation on the window width, technological process parameters and the polarization of guided waves for structures made by K^+-Na^+ ion exchange.

Experimental method

Investigations of MMI structures are carried out in the arrangement described in the paper [3], shown in Fig.2. The MMI section in which the mode field's interference is observed excited from laser by the light of wavelength λ=0.63μm is covered with fluorescent substance by spin-coating.
This substance is the Nile Blue "A" perchlorate suspension in PMMA. Fluorescent substance produces lightening proportional to the energy of the excited mode. Recording of successive sequences of mode field interference patterns, by CCD camera on PC, makes it possible to find the propagation lengths for N-fold images.
Presented arrangement allows investigating MMI structures excited by polarized (TE or TM) field from laser trough the polarizer and un-polarized field from single-mode fibre.

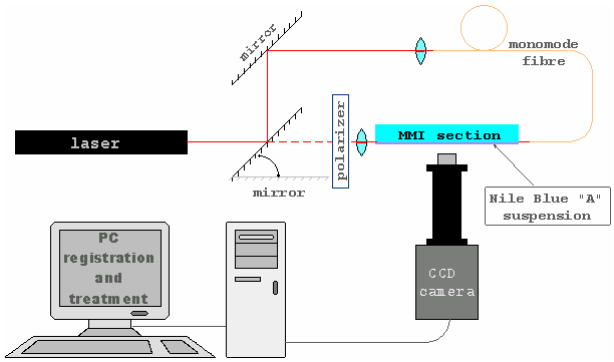


Fig.1 Experimental arrangement

That makes it possible to determine the dependence of propagation lengths for N-fold images on the window width, and the polarization of guided light.

Polarization effects in K^+-Na^+ ion exchanged waveguides

The investigated MMI sections are produced in the ion exchange process of in the time of 1h and temperature of 400°C in borosilicate glass. Diffusion is performed through the masks opening, in which, depending on the direction of excitation, symmetric or paired interference can be observed [1]. Widths W_M of the masks of MMI sections are 30, 39, 51, 60, 69 and 81 μm.
Experimental results are compared with BPM simulation. The distribution profile of refractive index of MMI section obtained in the diffusion process is calculated numerically from the nonlinear diffusion equation [4].

$$\frac{\partial C_K}{\partial t} = \nabla\left[\frac{D_K}{1-(1-m)\cdot C_K}\cdot\nabla C_K\right]$$

where C_K is the dopant K^+ ions concentration, proportional to the refractive index change. Material parameters of the technological process - self-diffusion coefficient of K^+ ions D_K, the mobility ratio m of the ions K^+ and Na^+, and the maximum of the refractive index change were determined by measurements of respective planar index profiles using IWKB method.

Fig.2 presents distribution profiles of the refractive index for the diffusion process of potassium ions at temperature 400°C and time 165h obtained by IWKB method [4]. The determined self-diffusion coefficient is equal 2.18 $\mu m^2/h$ for both profiles; whereas the distribution maxima on the surface are equal respectively 0.0095 and 0.0117. The observed differences in the distribution of the refractive index for both orthogonal polarizations result from the anisotropy of strains taking place during the technological process, and are of significant importance for performance characteristics of the MMI.

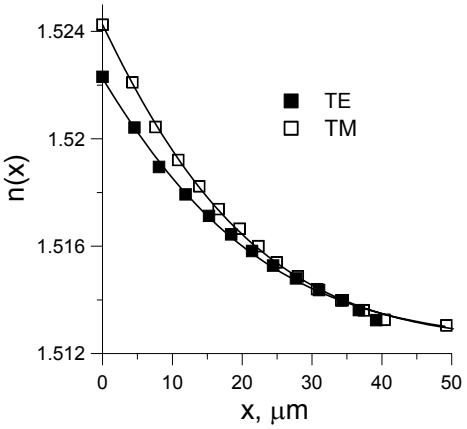


Fig.2. Profiles of refractive index for TE and TM waves in BK-7 glass, ■ - TM waves, □ - TE waves.

In Fig.3 are presented, for example, successive sequences of recorded mode field interference images for gradient index MMI section made by K^+-Na^+ ion exchange for the window width 60μm. The input field coming out from single-mode waveguide extends as a result of diffraction, achieving waveguide boundaries. Then, during successive reflections, the field matches to the mode structure and next interference patterns evolution along the propagation length is observed.

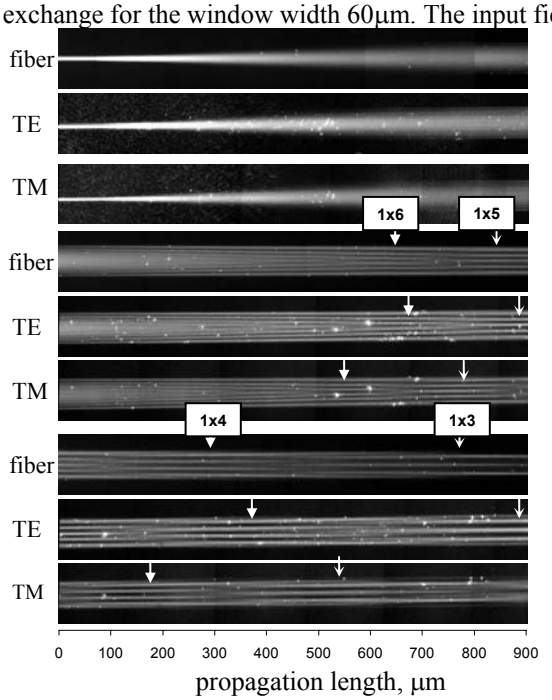


Fig.3 The successive sequences of recorded mode field interference images for MMI section of the width 60μm symmetrically excited (a)

Section is symmetrically excited and the effects of symmetric interference are observed. Distinctly visible are 1x6, 1x5, 1x4 and 1x3 N-fold images marked in the interference pattern. In wider section, observation of is also possible. The lengths of N-fold images depend of the polarization of guided light.

Interference images shown in Fig.4 for MMI sections of the width 60μm excited at 1/3rd of the section width are the examples of paired interference. We can distinguish here 1x5, 1x4, and 1 x 3 N-fold images. The images are not as clear as in the case of symmetrical interference. This can be explained by the effects of polarization, particularly important for asymmetrical excitation.

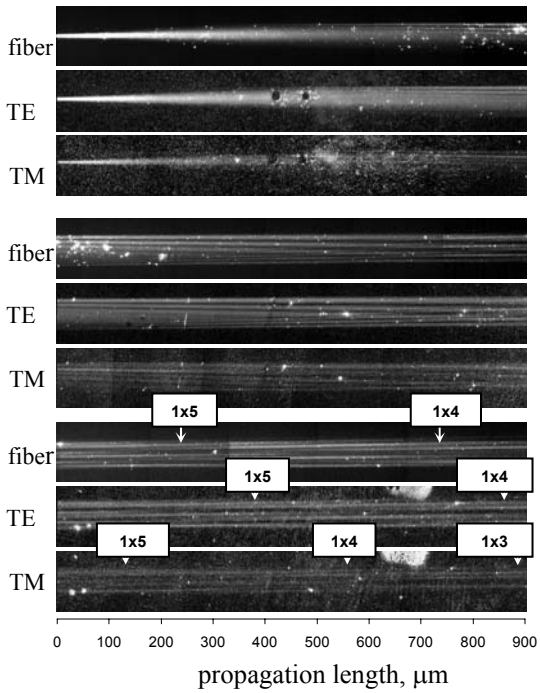
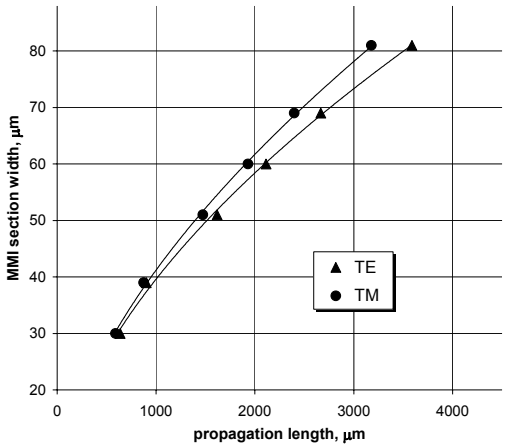


Fig.4 The successive sequences of recorded mode field interference images for MMI section of the width 60μm, excited at 1/3rd of the section width.

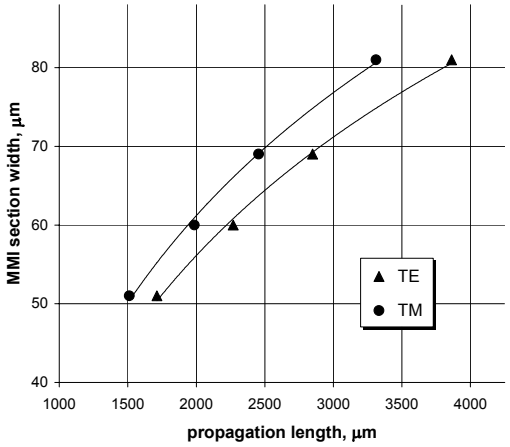
Analysis of experimental results

Analysis is carry out by reference of experimental results to the existed theory for step-index waveguides. On the base of the interference patterns analysis we determine dependences which describe light propagation in MMI gradient structures.

In Fig. 5 are presented dependences of length of N-fold images on the window width for symmetric (Fig. 5a) and paired (Fig. 5b) interference. Experimental dependences are compatible with equation for step-index waveguides of the refractive index n_r and the width W_e [1]: $L_z = \dfrac{\pi}{\beta_0 - \beta_1} \approx \dfrac{4 n_r W_e^2}{3\lambda}$



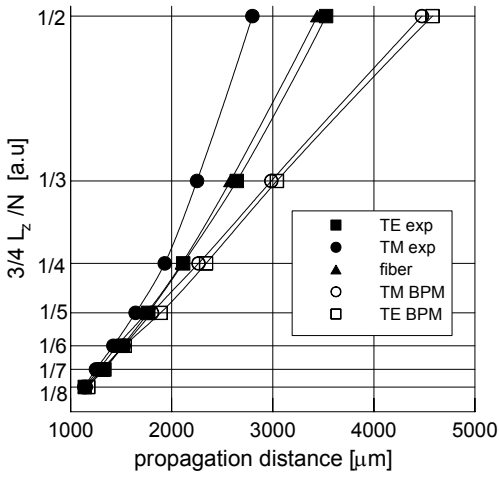
(a)



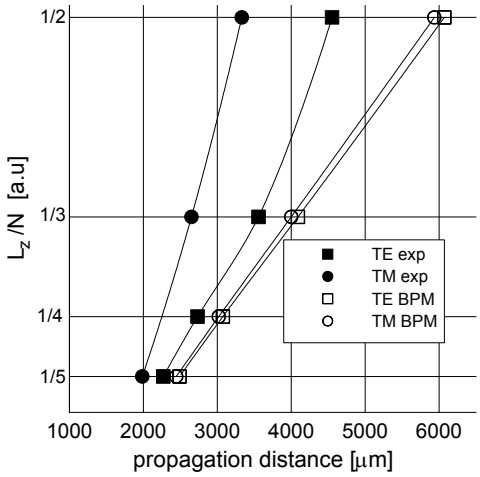
(b)

Fig.5 The dependence of length of N-fold images on the window width for MMI section made by K^+-Na^+ ion exchange; **a** - for symmetric interference, **b** - for paired interference.

which shows quadratic relation between the section width and self-imaging distance. On the base of the theory for step-index waveguides it is possible to predict the propagation lengths on which N-fold images should appear. Experimental results are compared with BPM simulations. Fig.6 shows comparison of experimental results with BPM simulations for MMI section of window width 60 μm for symmetric (Fig. 6a) and paired (Fig. 6b) interference. In both cases the propagation length for N-fold images decrease in comparison to numerical predictions, together with increase of the propagation distance. It can be noticed that the effect is bigger for TM polarization. The deviations can be probably explained by stresses. Participation of stresses in refractive index formation is important – in BK-7 glass it is 30% for TE and 40% for TM waves of the refractive index change [5]. Stresses depend on the time of the process and geometry of the waveguide. Therefore results obtained for strip waveguides



(a)



(b)

Fig.6 The comparison between experimental and theoretical dependences of lengths of N-fold images on propagation length; MMI section of the width 60μm, (a) – symmetric interference, (b) – paired interference.

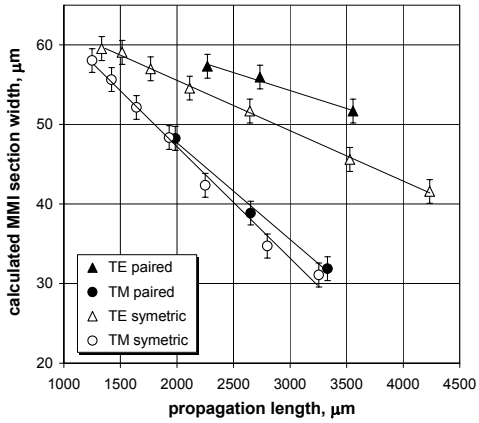


Fig.7 The dependence of calculated MMI section width on the propagation length for MMI section of the width 60μm.

produced in the time of 1h can differ from which determine self-imaging effects. numerical simulations based on the parameters obtained for the 1-D process in the time of 165h. It could be a reason of different

than quadratic dependence of propagation constants on mode number, which decide on self-imaging phenomena.
According to the theory for step-index waveguides, MMI section width can be determine from the transversal distance between images in each particular N-fold interference pattern. In Fig. 7 are presented dependences of calculated MMI section widths on propagation length. As we can see the calculated MMI section width decrease with the increasing of the propagation distance for both polarizations. The observed decrease of the transversal distance between images is stronger for TM modes. It is similar situation as in the case of the reducing of propagation lengths for N-fold images (Fig. 6).

Conclusions

In the paper experimental investigations of MMI structures produced by K^+-Na^+ ion-exchange are carried out. Investigations concern self-imaging phenomena of the input field for symmetrical and paired interference in dependence on polarization of guided light.
It can be confirmed that propagation length for N-fold image for symmetric and paired interference depends on MMI section width similarly as in the theory for step-index waveguides.
The propagation length for N-fold images decrease in comparison to numerical predictions, together with increase of the propagation distance. We also observe the decrease of the transversal distance between N-fold images of the input field. These effects results probably from stresses which are important for K^+-Na^+ ion exchange.

Literature

[1]L.B. Soldano, E.C.M Pennings, J.Lightwave Technol., LT-13 , 1995 , pp.615-627

[2]S.Das,D.Geraghty, S.Honkanen, N.Peyghambarian, Proc. SPIE **3936 (**2000), 239.

[3] M.Błahut, P.Karasiński, D.Kasprzak, R.Rogoziński, Opt. Comm. **214** (2002), 47.

[4] M.Błahut, A.Opilski, R.Rogoziński, Optica Applicata, v.22, No.3-4, pp.161-169, (1992)

[5] A. Brandenburg A., IEEE J. Lightwave Technol., vol.LT-4, No. 10, pp. 1580-1592 (1986).

Integrated electro-optic Mach-Zehnder modulators based on Zn-diffused $LiNbO_3$ waveguides

G. Lifante (1), P.L. Pernas (2), E. Cantelar (1), F. Cussó (1) and I. Suárez (1)
1) Departamento de Física de Materiales, C-IV. Universidad Autónoma de Madrid. 28049-Madrid (Spain)
2) Departamento de Física Aplicada, C-XII. Universidad Autónoma de Madrid. 28049-Madrid (Spain)
email: gines.lifante@uam.es

Abstract
Integrated Mach-Zehnder modulators fabricated on X- and Z-cut lithium niobate wafers are presented. The optical waveguides were fabricated by the Zn-diffusion method, which allows monomode TM-propagation at the wavelength of interest by choosing the channel waveguide width. The TM-mode is shown to be buried beneath the surface, which avoids the need of using a dielectric buffer to reduce propagation losses induced by the metallic electrodes to perform electro-optic modulation. A figure of merit of 9.2 V·cm has been obtained for the switching voltage-interaction length product in Z-cut modulators with CCS configuration, which is slightly higher that the calculated theoretical value using the overlap between the externally applied electrical field and the propagating optical field.

Introduction
The integrated Mach-Zehnder intensity modulator is perhaps the paradigm of integrated optical devices, and it has been succesfully used in optics communications technology [1], and to perform other different tasks, such as for the fabrication of integrated Q-switched lasers [2]. Due to its high electrooptic coefficients, $LiNbO_3$ crystals have been widely used to implement integrated electrooptic Mach-Zehnder modulators, either using Ti-diffusion or proton exchange technologies for fabricating the optical circuits. Although these techniques give rise to high quality low loss channel waveguides, each of them present some drawbacks, such as the high temperature processing in the case of Ti-diffusion, or the fact that proton exchange waveguides only support extraordinary polarized propagating modes. Recently, Zn-diffusion has been considered an alternative approach for fabricating optical waveguides in $LiNbO_3$ [3], either by the evaporation of a ZnO layer over a $LiNbO_3$ substrate [4], or by the direct Zn incorporation on a $LiNbO_3$ substrate from its metallic vapor phase, both followed by a thermal annealing. In fact, Zn-diffusion technology has been used to developed some interesting integrated optical devices, including active devices on rare earth doped $LiNbO_3$ [5], as well as functional devices [4] based on the electro-optical properties of the $LiNbO_3$ substrates. In this work, electrooptic integrated Mach-Zehnder modulators on X- and Z-cut $LiNbO_3$ substrates fabricated by vapor Zn diffusion are presented, showing a versatile design and low half-wave voltages.

Mach-Zehnder fabrication
The general design of the integrated Mach-Zehnder interferometer is schematically shown in figure 1, where the electrodes have been positioned for the case of Z-cut substrates. The two symmetric Y-junctions (input and output) are implemented by two-opposed 2º arcs of circles with a high curvature radius of 20.5 mm, choosen to minimize losses in the bends [6]. The upper and lower parallel arms of the interferometer have a length of 11 mm, and are separated a distance of 50 μm. Considering the input and output straight channel waveguides, the the device has a total length of 2 cm. The input and output straight channel waveguides, as well as the two arms, have been fabricating using masks of either 2 or 4 μm. These designs are transferred by UV photolithographic techniques using SiO_2 intermediate stopping-masks 0.5 μm thick on X- and Z-cut congruent $LiNbO_3$ wafer supplied.

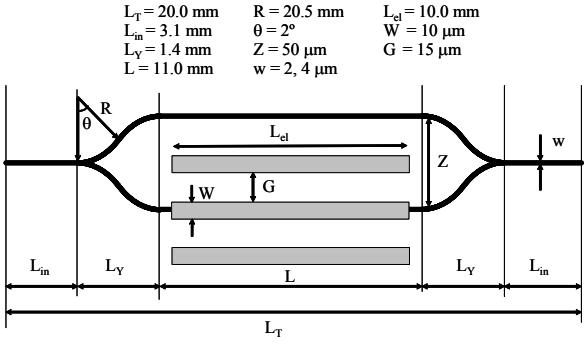


Fig.1. Integrated Mach-Zehnder interferometer design to fabricate electrooptic modulators. Electrodes are positioned for a Z-cut $LiNbO_3$ substrate.

After the lithography, waveguide fabrication was followed by the method described in reference [3], which consists on a vapor Zn diffusion at a temperature of 550 ºC during 2 hours followed by a thermal annealing in oxygen atmosphere: 850 ºC during 12 hours for the 2 μm channel width interferometer, and 900 ºC during 1 hour for the 4 μm wide channel waveguides. These parameters have been choosen to assure monomode behaviour at 1.55 μm wavelength. The optical characterization was performed by the end-fire-coupling technique at 0.633 μm and 1.55 μm, showing that the interferometers support both TE and TM propagation as expected, with a better guiding for TM polarization, and with no sign of

photorefractive damage even when using visible light. It has been also found that the extraordinary guides were buried some microns beneath the substrate surface, which can be the reason for the better guiding in this polarization as it has been discussed in [3]. The sizes of the fundamental modes for TM-propagation at 1.55 μm (measured at 1/e of the maximum) were 10.4x6.6 μm^2 and 10.6x7.3 μm^2, for the 2 μm and 4 μm wide channels, respectively, indicating some lateral diffusion of the Zn through the SiO_2 stopping mask during the annealing step.

Integrated electrooptic MZ modulators.

The next step in fabricating the integrated electrooptic modulators consists on depositing metallic electrodes along the arms of the interferometers. To use the highest electrooptic coefficient in $LiNbO_3$ (r_{33}), the externally applied electric field should be parallel to the Z-axis [7]. Therefore, in order to optimize the interaction between the electric field and the optical mode [8], in a Z-cut wafer the electrodes should be positioned on top of the waveguide arms (Fig. 2), while in an X-cut wafer the electrodes should be located on both sides of the branches. In these conditions the extraordinary index change by electro-optic effect in $LiNbO_3$ is given by [7]:

$$\Delta n_e = \frac{n_e \cdot r_{33}}{2} E_z \qquad (1)$$

where n_e is the extraordinary index, E_z the applied electric field and r_{33} the corresponding electro-optic coefficient (30.8 pm/V). As the r_{33} is three times higher that the r_{13} coefficient, the change on the ordinary index can be neglected. Following these considerations, the propagating light should be chosen TM-polarized in Z-cut substrates, and TE-polarized light when using X-cut wafers.

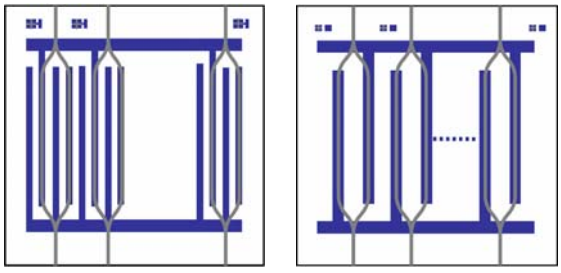


Fig. 2. Electrode mask alignement respect to the Mach-Zehnder interferometers on Z-cut substrates. Left: complementary coplanar stripline (CCS) Right: coplanar stripline (CS), forming a push-pull configuration. Note that the fourth electrode is initially not conected.

For Z-cut substrates the electrodes must be positioned on the top of the interferometric arms, while in X-cut substrates the electrodes lie besides the arms, in such a way that in both cases the major component of the electric field is along the crystal Z-axis. Also, the polarization chosen was the TM because it implies the higher electrooptic effect, and also it showed the better guiding as it has been discussed before.

Following this choice, 3000 Å thick and 10 μm wide aluminum electrodes were patterned by UV lithography on the position indicated in Figure 2, with a gap of 15 μm between electrodes and a length of 1 cm.

In other technologies, a buffer of SiO_2 must be placed between the waveguides and the metallic electrodes, in order to avoid the possible attenuation in the propagation mode. In our case, as the modes are buried some microns beneath the subtrate, the exponentially decay evanescent field of the mode does not reach the electrodes, and thus avoiding the need of using a dielectric intermediate buffer. Although the electrode mask was initially designed to work with Z-cut wafers, it is versatile enough to be used also with X-cut wafers, just by displacing laterally the electrode mask respect to the interferometer arms (see figure 3).

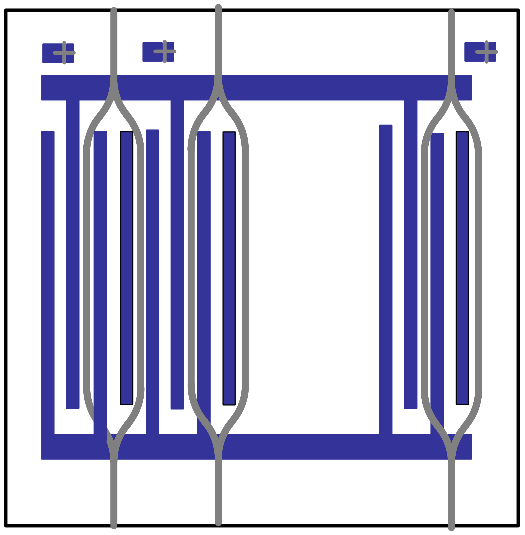


Fig. 3. Electrode mask alignement respect to the Mach-Zehnder interferometers on X-cut substrates. Let us note that the electrode mask is the same as that of figure 2 (left), showing the versatility of the mask design.

For this purpose, the electrode mask has several alignment motifs to be used for the different crystal cuts. Figure 4 shows an image of the left side of the EO-modulator, where it can be seen the channel waveguides, the metallic electrodes, as well as the alignement motifs.

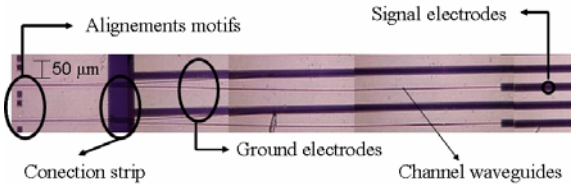


Fig. 4. Partial view of the integrated EO-modulator built into a Z-cut substrate.

The theoretical value for the half-wave voltage of the integrated electro-optic modulator can be calculated using the expression [9]:

$$V_\pi = \frac{\lambda\, g}{L\, n_e^3\, r_{33}\, \Gamma} \qquad (2)$$

where g is the gap between electrodes, L the electrode length and Γ a factor with relates the overlap between the applied electric field and the propagating modal field [10]:

$$\Gamma = \frac{\iint \varepsilon(x,y)\cdot E(x,y)\,dxdy}{\sqrt{\iint \varepsilon(x,y)^2\,dxdy}\cdot\sqrt{\iint E(x,y)^2\,dxdy}} \qquad (3)$$

where $\varepsilon(x,y)$ is the optical mode, and $E(x,y)$ the electric field produced by the metallic electrodes. Assuming an optical field intensity with dimensions of 10x9 μm^2 buried ~6 μm in the substrate and calculating the applied field with the mapping functions given in [7], an overlap factor of 0.48 is obtained. Using this value of Γ, and assuming that the electro-optic coefficient is not degraded by the Zn diffusion [4] a theoretical switching voltage of 6 volts is obtained for the configuration here designed.

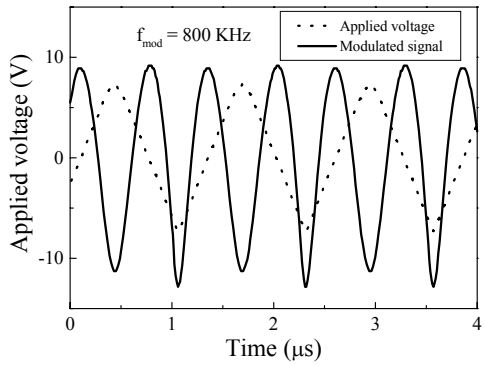


Fig. 5. Response of the integrated EO-modulator working at 800 KHz under a triangular electric signal, using a Z-cut substrate with CCS configuration.

To characterize the integrated electro-optic modulator, light from a polarized He-Ne laser is coupled into the interferometer input with the aid of a microscope objective, and a triangular wave coming from a HP-33120A wave-generator is applied to the modulator electrodes using gold wires. The modulated light at the interferometer output is collected and focused by means of a second microscope objective and detected by a S-20 photomultiplier ($\tau \sim 20$ ns). Both, applied voltage and modulated light intensity, were recorded by means of a 150 MHz digital oscilloscope Tektronics IX model TDS-420. Figure 5 shows the detected intensity (continuous line) when a triangular wave of 7.2 volts of amplitude (dashed line) is applied to the interferometer, at a frequency of 800 KHz. A plot of the modulated intensity versus the applied voltage gives the transfer function of the electro-optic modulator, where a half-wave voltage V_π of 9.2 V is obtained, and in consequence a voltage-length product of 9.2 V·cm, which is higher that the predicted theoretical value (6 V). This discrepancy between the theoretical and experimental V_π values can be attributed to an overestimation of the overlap factor given in equation (3).

Although no electro-optic modulation measurements have been taken at 1.55 μm, channel waveguides show monomode propagation at this wavelength when using a 2 μm width mask. The extrapolated half-wave voltage in this case using the relation (2) is 22.5 V, which is comparable with data reported by Twu et al. [4] using thermally evaporated Zn film to fabricate the channel waveguides, where they obtained a figure of merit of 9.6 V·cm using a push-pull MZ configuration, which reduces a half the switching-voltage.

The extintion ratios of the EO-modulators have been measured at 633 nm by comparing the maximum and minimum output intensity, using an oscilloscope working in DC mode. Figure 6 shows an example of these measurements, for a Z-cut modulator with CCS electrode structure, where a value of 7.6 dB has been obtained. Although this is not a very high value, it is expected that working at 1.55 μm the extintion ratio was superior, due to the monomode character of the channel waveguides at this wavelength.

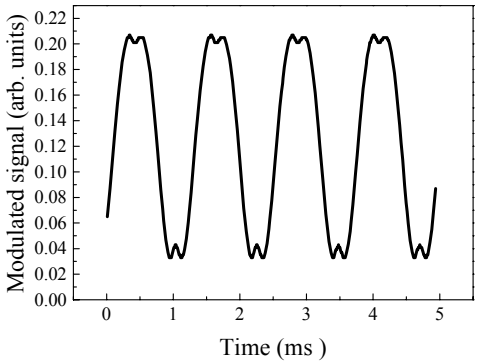


Fig. 6. Modulated signal, working on DC mode at the oscilloscope, for measuring the modulator extinction ratio.

Finally, the frequency response of the integrated EO-modulators has been obtained using the set-up previously described. Figure 7 shows the frequency behaviour, working under triangular wave, for 1 cm length electrode modulator. As it can be seen, the measured signal drops around 2 MHz. Unfortunately, this is the response limits of our measurement system (~20 ns), and thus this frequency represents a lower limit of the integrated EO-modulator. Theoretical estimations using the indicate a maximum frequency response of ~500 MHz

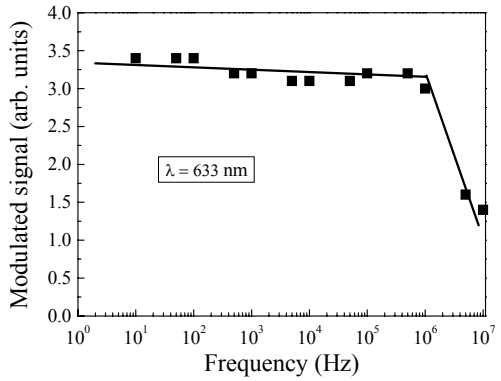


Fig. 7. Frequency response of the EO-modulator. The 2 MHz fall is just the limit of the measurement set-up, and thus indicates a lower limit for the frequency response of the modulator.

Conclusions

Integrated electro-optic modulators fabricated by the vapour Zn diffusion method in $LiNbO_3$ have been demonstrated. The design of the interferometric and electrodes masks is versatile in the sense that they can be used for X-cut wafers, just by shifting the electrodes respect to the waveguides. Also, the Zn diffusion technique for fabricating n_e guides has the advantage of avoiding the need of using a buffer to reduce propagation losses, as it is needed when using Ti diffusion technique. The electro-optic modulator shows a figure of merit of 9.2 V·cm, which is a little higher than the theoretical value, probably due to an overestimation of the overlap factor.

Acknowledgments

This work has been partially supported by the Ministerio de Ciencia y Tecnología and Comunidad de Madrid (Spain) under projects MOISES (MAT2005-05950) and MICROSERES (GR-MAT-0108-2004).
The authors acknowledge the technical support provided by Prof. W. Sohler group in the infrared interferometer characterization.

References

[1] K. Noguchi et al, Electronics Letters 28, p. 1759, 1992
[2] H. Suche et al, Electronics Letters 34, p. 1228, 1998
[3] I. Suárez et al, Optical Materials, 2006 (submitted).
[4] R. Twu et al, Microwave and Optical Technology Letters 43, p. 142, 2004.
[5] E. Cantelar et al, Applied Physics Letters 86, p. 161119, 2005
[6] L. Lerner, Electronics Letters 29, p. 733, 1993
[7] Ed. L. Wooten et al, IEEE J. Select. Topics in Quantum Electron. 6, p. 69, 2005
[8] O.G. Ramer, IEEE J. of Quantum Electron., 18, p. 386, 1981
[9] R.C. Alferness, IEEE Transactions on Microwave Theory and Techniques 30, p. 1121, 1982

High performance, single etch step MMI design on SOI

Robert Halir, Íñigo Molina Fernández, Alejandro Ortega Moñux, Juan Gonzalo Wangüemert Pérez, (1)
Dan-Xia Xu, Pavel Cheben and Siegfried Janz (2)
1) Departamento de Ingeniería de Comunicaciones, Universidad de Málaga, Spain, robert.halir@ic.uma.es
2) Institute for Microstructural Sciences, National Research Council, Canada, pavel.cheben@nrc-cnrc.gc.ca

Abstract: *We present a design criterion for high performance Silicon-on-Insulator (SOI) Multi-Mode Interference couplers (MMIs) based on single etch step rib waveguides. We design a shallowly etched* 2×2 *coupler with an excess loss of only* 0.1dB *and an imbalance of less than* 0.02dB *for both TE and TM polarizations.*

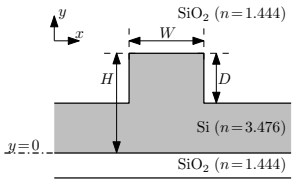
1 Introduction

Multimode inteference couplers (MMIs) [1] are commonly used in photonic integrated circuits (PICs) as power splitters, combiners and directional couplers, because of their ease of fabrication, high bandwidth, compactness and polarization insensitivity [2].

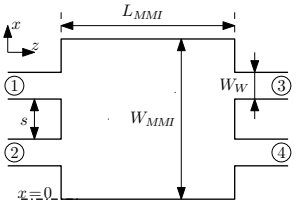
Silicon on Insulator (SOI) in turn has attracted a lot of attention in the last years since it offers a very high index contrast ($\Delta n \approx 2$) allowing for high light confinement and thus very compact devices. Other advantages of the SOI platform are its potential compatibility with CMOS technology [3], and the availability of high quality wafers, since they have been used for years in the CMOS industry.

The most commonly used waveguides on SOI are rib waveguides (see fig. 1(a)), as they can have a large cross section while still being practically single-moded [4][5]. The design of rib waveguide based MMIs on SOIs still poses some challenges: for the waveguide to be potentially single-moded, it has to be shallowly etched ($D \leq \frac{H}{2}$), but with this type of etching it seems to be difficult to achieve low excess loss and imbalance. For instance, even for relatively simple MMI configuration such as 1×2 splitter, a minimum imbalance of 0.28dB has been reported for a fabricated device in [6]. Simulations of a 1×4 splitter in [7] show an imbalance of 0.37dB and excess losses of 1.37dB. These relatively high losses are believed to be caused by imperfect imaging due to the shallow etching, which is why the authors of [7] propose a two etch step design, where both the access waveguides and the multimode section are deeply etched. While simulations show that such a design yields a nearly perfect imaging and very low losses, the fact that it requires two etching steps makes it more difficult and expensive to fabricate these devices. In fact, a fabricated MMI where only the multimode section is deeply etched is reported in [8], where a specific fabrication process is developed.

In this communication we show that by adequately designing the shallowly etched access waveguides it is possible to achieve high performance MMIs with a single etch step fabrication process. Our simulations of a 2×2 coupler show an excess loss of only 0.1dB and an imbalance of less than 0.02dB for both TE and TM polarizations. In the 1.5μm to 1.6μm bandwidth they remain lower than 0.6dB and 0.05dB, respectively.



(a)



(b)

Figure 1: (a) Rib waveguide cross sectional view and (b) MMI top view.

In section 2 we briefly review some basic MMI theory, which is further discussed for rib waveguides in section 3. From the spectral analysis of the fundamental mode of the rib access waveguides we derive, in section 4, a design criterion for these waveguides, which is applied to two 2×2 MMIs in section 5.

2 Idealized MMI imaging

Fig. 1(b) shows a schematic top view of a 2×2 MMI coupler. The access wave-guides are numbered from 1 to 4, and have a width of W_W, while the multi-mode (or imaging) region is L_{MMI} long and W_{MMI} wide. Light coming into the device through one of the waveguides excites several modes inside the multimode region which, after a certain distance, interfere to form self-images of the excitation. By placing the output waveguides in the position of these images the input power is divided between the output waveguides.

In the following we briefly review the basic MMI model established in [1], on which our further discussion will be based.

Under a 2D approximation, that is, ignoring the y dimension, the electromagnetic field of the access waveguide, $f(x)$, is completely expanded into the modes of the multimode section, i.e., $f(x) = \sum_m c_m \varphi_m(x)$, where $\varphi_m(x)$ may be approximated as

$$\varphi_m(x) = \sin\left(\frac{m\pi}{W_{MMI}} x\right), \; m = 1, 2, 3, ... \qquad (1)$$

The imaging then takes place at certain propagation

distances because the propagation constants β_m of the $\varphi_m(x)$ modes are related by a parabolic law, namely $\beta_m = \beta_1 - (m^2 - 1) \times const$. If this relationship is not fulfilled no perfect imaging is possible.
The excitation coefficients c_m are calculated by means of the overlap integral

$$c_m = \frac{2}{W_{MMI}} \int_0^{W_{MMI}} f(x) \sin\left(\frac{m\pi}{W_{MMI}} x\right) \mathrm{d}x \qquad (2)$$

Please note that, according to this definition, c_m are also the Fourier coefficients of $f(x)$.

3 MMI imaging in rib waveguides

In this section we will study to which extent the conditions for perfect imaging can be met in rib waveguides. In order to do so, we will study into which kind of modes of the multimode section the input field of the access waveguides can be expanded. We shall only consider imaging in the x direction, which is desired in most practical devices, as opposed to 3D imaging that also takes place in the y direction [9]. In the following we will use $\mathrm{TX}_{m,n}$ to refer to rib waveguide modes with m half cycles in the lateral direction and n half-cycles in the vertical direction of both TE and TM polarizations. Let us consider the two TE modes of a rib multimode section shown in fig. 2(a) and 2(b).
In a 2D approximation where the height of the device is "compressed" to zero, the TE_{41} mode in fig. 2(a) would be well approximated by a sine function like $\varphi_4(x)$ (see eq. 1). Obviously, the same is true for all $\mathrm{TX}_{m,1}$ modes, which means that their propagation constants will follow the parabolic law required for imaging. Thus, we will call such modes "imaging modes", because if only these modes were excited we would be in the same situation as in the 2D case (section 2), and imaging would be virtually perfect.
On the contrary, the TE_{12} mode in fig. 2(b) is a "non-imaging mode", because due to its two half-cycles in the y direction, its propagation constant cannot fit the parabolic law of the imaging modes. Consequently, if this mode were excited, it would propagate through the multi-mode region along with the imaging modes, but it would not properly contribute to image formation, thus deteriorating the image quality and the device's performance. Generally, any $\mathrm{TX}_{m,n}$ mode with $n \geq 2$ is a non-imaging mode.[1]
In conclusion, for imaging to work properly, we have to make sure that all the power of the input excitation is coupled into imaging modes, that is, guided modes with one half-cycle in the vertical direction. How the power of the input is distributed into the different modes of the imaging region depends on the shape of the input field, which will be analyzed in the next section.

4 Input mode field spectrum

We will now derive a criterion for the input waveguide dimensions which ensures that only imaging modes are excited in the multimode region. The input excitation is supposed to be the fundamental mode of the access waveguide. Fig. 2(c) shows the fundamental TE mode of single-mode rib waveguide (its dimensions fulfill Soref's condition [4]).
In order to find out what kind of modes this field excites inside the imaging region one option is to solve the discontinuity between the access waveguide and the imaging section. This can be done for example with a software like Fimmprop [2], but while this yields the rigorous result, it gives little insight into the problem. This is why we also use a second approach, based on an idealized (rectangular) imaging section of width W_{MMI} and height H that supports an infinite number of sine like modes

$$\varphi_{m,n}(x,y) = \sin\left(\frac{m\pi}{W_{MMI}} x\right) \sin\left(\frac{n\pi}{H} y\right),\ m,n = 1,2,3,... \qquad (3)$$

whose excitation coefficients are given by

$$c_{m,n} = \frac{4}{HW_{MMI}} \int_0^{W_{MMI}} \int_0^{H} E_d(x,y)\varphi_{m,n}(x,y) \mathrm{d}x\mathrm{d}y \qquad (4)$$

where E_d is the dominant field component of the mode, that is E_x for TE polarization and E_y for TM polarization. Note that eq. (3) and (4) are simply extension of eq. (1) and (2) and that $\varphi_{m,1}$ are the imaging modes. Since the $c_{m,n}$ coefficients can be interpreted as the (bidimensional) Fourier coefficients of E_d, the quantities

$$p_n = \frac{\sum_m |c_{m,n}|^2}{\sum_m \sum_n |c_{m,n}|^2} \times 100\% \qquad (5)$$

are the fraction of power of the input field that, in an idealized imaging region, would couple into all modes that have n half-cycles in the vertical direction. Particularly, the fraction of power that would couple into the imaging modes $\varphi_{m,1}$ is given by p_1.
If we analyze the mode of a typical single mode rib waveguide as the one in fig. 2(c) we get $p_1 = 93\%$, $p_2 = 6.6\%$, $p_3 = 0.1\%$. That means that even in a idealized imaging section only 93% of the power would couple into imaging modes so that a power loss of at least $-10\log_{10}(0.93) \approx 0.3$dB is to be expected. It is also very interesting to note that nearly all the remaining power couples into $\varphi_{m,2}$ modes, that is, modes of the same type as the one shown in fig. 2(b). This fact can be exploited to estimate more easily the fraction of power that couples into imaging modes. All the $\varphi_{m,n}$ modes with n odd are symmetrical with respect to $y = \frac{H}{2}$, whereas the modes with n even are antisymmetrical. Since virtually all the power that couples into symmetric modes couples into the imaging modes ($p_1 \gg p_3$), their power may be estimated as the power in the symmetric part of the input field:

$$p_{symm} = \frac{\iint_\Omega |E_d(x,y) + E_d(x,H-y)|^2 \,\mathrm{d}x\mathrm{d}y}{4 \iint_\Omega |E_d(x,y)|^2 \,\mathrm{d}x\mathrm{d}y} \times 100\% \qquad (6)$$

[1] This is only true when no 3D imaging is considered.

[2] Fimmprop is an eigenmode expansion based tool and is part of the Fimmwave package by Photon Design: `www.photond.com`

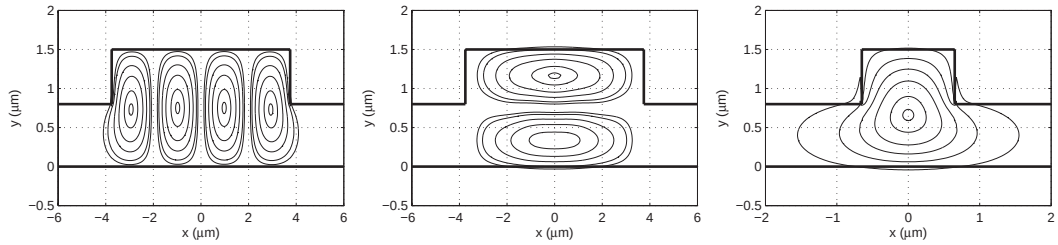


Figure 2: (a) and (b): Two modes of a shallowly etched multimode section ($W_{MMI} = 7.5\mu$m) (a) Example of an imaging mode (TE_{41}) (b) Example of a non-imaging mode (TE_{12}). (c): TE_{11} mode of a single mode access waveguide ($W_W = 1.3\mu$m); In all three figures $H = 1.5\mu$m, $D = 0.7\mu$m. .

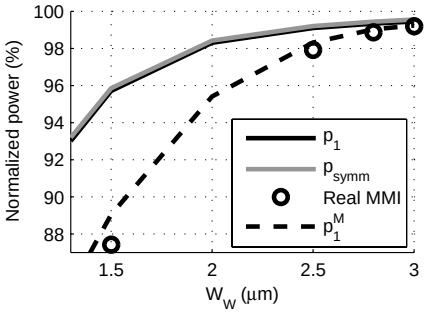


Figure 3: Fraction of power coupled from the TE_{11} mode of a rib waveguide into the imaging modes of a $W_{MMI} = 7.5\mu$m wide multimode section as a function of W_W ($H = 1.5\mu$m, $D = 0.7\mu$m.) .

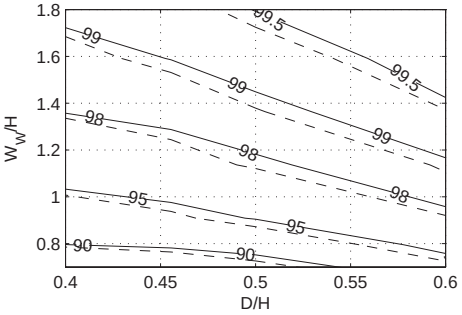


Figure 4: Symmetry factor p_{symm} [eq. (6)] as a function of the rib aspect ratios W_W/H and D/H (solid lines: $H = 1.5\mu$m, dashed lines: $H = 2.2\mu$m) .

where Ω is the waveguide's cross-section. This result is actually rather intuitive: since all the imaging modes are symmetric with respect to $y = \frac{H}{2}$, their superposition can only represent excitations with the same kind of symmetry. Fig. 3 illustrates how the fundamental mode of a shallowly etched rib waveguide becomes more symmetrical as the waveguide width (W_W) is increased, so that more power couples into the imaging modes of the idealized multimode section (curves p_{symm} and p_1). The data labeled "Real MMI" in fig. 3 represents the fraction of power coupled into the imaging modes of the real (rib) multimode section as simulated with Fimmprop. For small widths the real coupling is lower than predicted by the idealized model, but this is simply because the number of imaging modes supported by the rib structure is limited, so that its resolution is too low to completely represent the symmetric part of the input field. Actually, if we convert the rib multimode section into a slab waveguide using the effective index method, calculate the number of modes (M) it supports, and define $p_1^M = \sum_{m=1}^{M} |c_{m,n}|^2 / \sum_m \sum_n |c_{m,n}|^2 \times 100\%$, we obtain a much better agreement between the model and the simulated data (curve p_1^M in fig. 3). Anyhow, by the time the input fields becomes highly symmetric ($p_{symm} \geq 98\%$), it is also wide enough to be faithfully represented by the real imaging modes.

The conclusion of this section and one of the main points of this communication is thus that for imaging to work properly, the input waveguides have to be designed so that their fundamental TE and TM modes are highly symmetric in the vertical direction ($p_{symm} \rightarrow 100\%$) [eq. (6)].

5 Design

At this point we are ready to design two MMIs based on the criterion established in the previous section. We start by calculating the symmetry factor p_{symm} for a set of common rib aspect ratios and for two different substrate heights. From the results shown in fig. 4 it is clear that the symmetry is higher for wider waveguides (as already observed in fig. 3), but also for deeply etched waveguides, which explains the good performance of deeply etched MMIs. It is also noticeable that p_{symm} only weekly depends on the absolute substrate height H, so that the chart is probably also useful for other values of H. It has to be pointed out that the results are given only for the TE polarization, as we have found that the TM modes always have a slightly higher symmetry factor (probably because their confinement is better), so that the TE polarization is actually the worst case.

For our design we chose a substrate height of $H =$

Table 1: Dimensions of the optimized general and paired interference based MMIs (all values are in μm).

	W_{MMI}	L_{MMI}	W_W	s
General	7.5	274	2.8	1.5
Paired	12.8	256	2.8	1.5

1.5μm and an etching depth of $D = 0.7\mu$m, so that a waveguide with $W_W < 1.4\mu$m is single-moded [4]. While such a single mode waveguide is useful as in interconnecting waveguide within a larger circuit [10], it is not adequate as MMI access waveguide, because its fundamental mode has a low symmetry factor. Actually, according to fig. 4, since $D/H \approx 0.46$, to achieve $p_{symm} \geq 99\%$ one has to choose $W_W \geq 1.6 \times 1.5 \approx 2.4$. In order to make the design somewhat tolerant to etching depth fluctuations, we set $W_W = 2.8\mu$m, so that the required symmetry is maintained even if the etching depth were only $D = 0.6\mu$m. Obviously this requires an adiabatic taper between the interconnecting single mode waveguide and the MMI access waveguide; we intend to address this issue in the near future.

The next step in the design of the MMI is to determine the minimum separation between the access waveguides to avoid coupling between them. Using Fimmprop, we found that a separation of $s = 1.5\mu$m (see fig. 1(b)) yields satisfactory values.

We designed two 2×2 couplers, one based on general interference and another one based on paired interference [2], whose minimum widths are given by $W^G_{MMI} = 2W_W + s = 7.1\mu$m and $W^P_{MMI} = 3(W_W + s) = 12.9\mu$m. To numerically optimize the width and length of the devices, we have used the fact that length scans are very fast in Fimmprop so that the following procedure could be used:

1. For the initial width, find the optimum length of the device, in the sense of a tradeoff between minimum excess loss and minimum imbalance.

2. Decrease the width by 0.1μm and find the optimum length of the device. If the tradeoff between excess losses and imbalance is improved, repeat this step until no further improvement is achieved. If the performance is worse, increase the width.

Excess loss and imbalance are defined as usual, $\mathrm{EL} = -10\log_{10}\left(\frac{P_3+P_4}{P_1}\right)$ and $\mathrm{IB} = -10\log_{10}\left(\frac{P_3}{P_4}\right)$, where P_i denotes the power of the fundamental mode in access waveguide i (see fig. 1(b)), and the excitation was launched from waveguide 1.

The final dimensions of the devices are given in table 1 and their performance is shown in fig. 5. While both devices exhibit very low excess losses and imbalance for both polarizations, it can be seen that the general interference based MMI has slightly lower excess loss in the extremes of the bandwidth, whereas the paired interference based device offers a better imbalance.

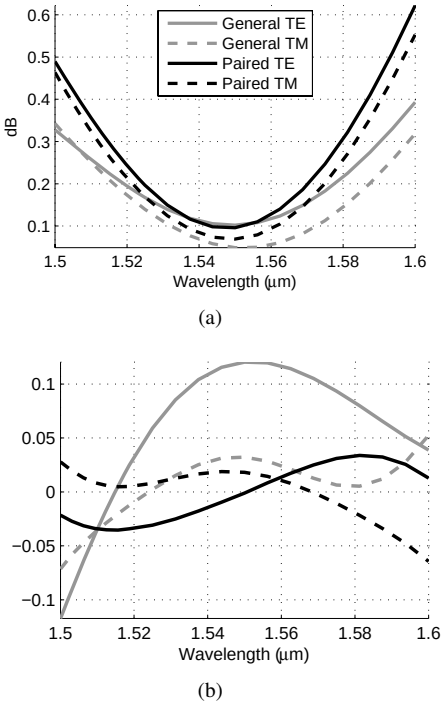


Figure 5: (a) Excess losses and (b) imbalance of the designed MMIs as a function of wavelength.

Conclusion

We have presented a design procedure for single etch step, high performance MMIs based on the symmetry factor of their access waveguides [eq. (6)]. Two devices with potentially single mode access waveguides have been designed, and optimized via simulations, yielding very promising values of excess loss and imbalance, which can easily compete with those reported for the two etch step design in [7].

Acknowledgments

This work was supported by the Spanish Ministerio de Educación y Ciencia under project TEC2006-02868.

References

[1] M. Bachmann et al, Applied Optics, no. 33, p. 3905, 1994

[2] L.B Soldano et al, J. Lightwave Tech., no. 13, p. 615, 1995

[3] B. Jalali et al, Sel. Topics Quantum Electronics, no. 4, p. 938, 1998

[4] R.A. Soref et al, J. Quantum Electronics, no. 27, p. 1971, 1991

[5] J. Lousteau et al., J. Lightwave Tech., no. 22, p. 1923, 2004

[6] H. Wei et al, Optics Letters, no. 12, p. 878, 2001

[7] D. Dai et al, Applied Optics, no. 24, p. 5036, 2005

[8] Y. Tang et al, Optical Engineering, no. 43, p. 2495, 2004

[9] M. Rajarajan et al, J. Lightwave Tech., no. 9, p. 2078, 1996

[10] R. Halir et al, J. Optical & Quantum Elec., to be published

High-temperature phases with increased refractive index in $H_xLi_{1-x}TaO_3$ waveguide layers

A.V. Tsarev, I.E. Kalabin, V.V. Atuchin

Laboratory of Optical Materials and Structures, Institute of Semiconductor Physics, SB RAS, Novosibirsk, 630090, Russia.

Abstract: *Optical properties and relaxation kinetics of high-temperature $H_xLi_{1-x}TaO_3$ phases have been investigated in proton exchanged waveguide layers. Temperature intervals and refractive index of high-temperature phases have been evaluated for concentration intervals of α′, α and δ-phases of $H_xLi_{1-x}TaO_3$ solid solutions. The decay of high-temperature phase in δ-phase $H_xLi_{1-x}TaO_3$ has been traced and life times of metastable states are estimated at T=20°C and 100°C. The nature of metastable states in $H_xLi_{1-x}TaO_3$ and $H_xLi_{1-x}NbO_3$ has been discussed.*

Introduction

Lithium tantalate (LT) is a well-known ferroelectric crystal widely used in integrated optics as a substrate material. One of the basic methods used for optical waveguide formation in LT is a proton exchange reaction. Proton exchanged layers in LT (H:LT) with chemical composition $H_xLi_{1-x}TaO_3$ are the promising waveguide mediums for electrooptical modulators, frequency converters and integrated lasers [1,2] because of apparent simplicity of their fabrication and relatively low temperature of ion exchange reaction, far below the Curie temperature of LT crystal. However, the applicability of H:LT waveguide layers in modern integrated optic devices is limited by noticeable refractive index instabilities [3-7]. Earlier, it has been supposed that the refractive index variation with time at room temperature can be related to relaxation of high temperature phases (HTP) to equilibrium phases at T=20°C [5]. More recently, this supposition has been confirmed for H:LT layers with low x values [8] but H:LT waveguides with high hydrogen concentrations, which are most valuable for present practical applications, were not investigated up to now. In this study the sources of refractive index instabilities in H:LT layers with high hydrogen contents have been revealed. To this aim the variation of refractive index in hydrogen doped layers was measured as a function of quenching temperature. Moreover, the evolution of refractive index due to HTP relaxation was traced for δ-phase of H:LT.

Experimental setup

H:LT waveguide layers were formed in Z-cut LT by ion exchange in pure benzoic acid at T=240°C. After this, annealings were applied to decrease the hydrogen concentration in the layer to the level that belongs to the composition range of desired equilibrium phase. As a criteria of phase assignment, the surface value of refractive index increase $\Delta n_e(0)$ was used. The intervals of $\Delta n_e(0)$ related to selected equilibrium phase at *T=20°C* were taken from [9]. To search for the HTP formation the quenching technique was applied. With this aim the samples were subjected to annealing for 10 min at different temperatures over the range 20°C< T<400°C. After this, two cooling regimes (α-H:LT) were applied: slow cooling for 2-3 hours together with the furnace or quick cooling for 5-7 minutes (quenching) by taking the samples out from the furnace to room. Waveguide mode effective indices N_m were measured by prism coupling method with possible error of ±0.0002 at wavelength λ=0.6328μm. Then, taking a set of N_m values as a basis, the profile of Δn_e over the waveguides depth was reconstructed by the inverse WKB method [10].

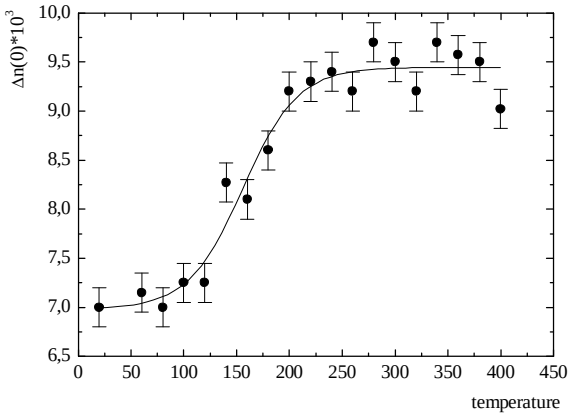


Fig.1: Refractive index on surface of waveguide layer vs. quenching temperature from near room to 400°C.

Results and discussion

Typical dependence of Δn(0) on quenching temperature is shown in Fig.1. As it is seen, the temperature interval of Δn(0) jump increase (ΔT=125-200°C) can be revealed. Those intervals are related to interphase transitions between the phase equilibrium at room conditions and the high temperature phase. It is principal that after short annealing at any particular temperature in the range up to 400°C and slow cooling the refractive index value returns to the initial value related to the equilibrium phase. This fact confirms the absence of noticeable hydrogen diffusion under the experimental conditions and allows to connect the

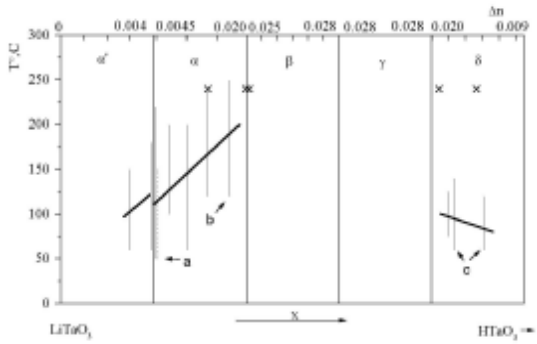


Fig.2: Phase diagram of $LiTaO_3$-$HTaO_3$ system, including HTP properties. Lines a, b, c are drawing using data from [11-13] correspondingly. Sign × mark Δn value where HTP formation were observed in [14], but no additional date was traced.

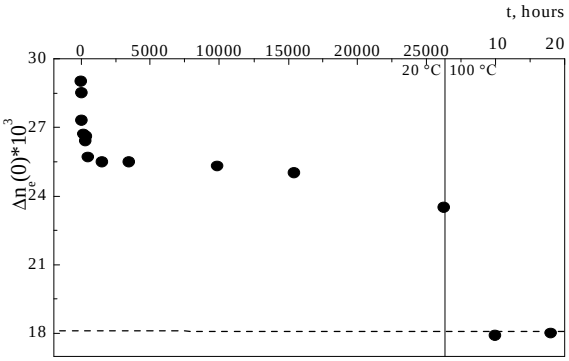


Fig.3: Refractive index evolution due HTP relaxation in concentration interval of δ-H:LT.

observed variations of Δn(0) with HTP formation. Thereby, the formation of HTP in H:LT compound is evident in Fig.1.

The quenching curves similar to that shown in Fig.1 were measured for a number of samples with different hydrogen content. The results were used as a basis for reconstruction of $LiTaO_3$-$HTaO_3$ phase diagram for the layers. The diagram accounting the HTP existence is presented in Fig.2. Here vertical segments show the temperature intervals of interphase transition between equilibrium and HTP and the hard dark lines, connecting the middles of vertical segments, depict the appropriate interphase boundaries. The existence of HTP was detected for a wide range of hydrogen concentration in H:LT system. Regrettably, the intervals of β- and γ-phases of $H_xLi_{1-x}TaO_3$ solutions were not investigated in this study because the Δn(0) value is not vary on x variation for the equilibrium phases and precise identification of equilibrium H:LT phase is not possible by waveguide mode spectroscopy. Observed HTP are metastable at room temperature and refractive indices variation for the states is induced by continuous transition to the relating equilibrium phase. When the temperature rises from T=20°C, the typical temperature of the interphase transition beginning is ~ 50-100°C. This is typical working temperature range for high frequency electrooptical modulators [15]. So, the HTP formation is possible by technological heat treatments during integrated device fabrication or due to device working temperature fluctuations and involves long time drift of optical characteristic.

To determine the life-time of HTP phases in H:LT the sample with Δn(0)=0.018, corresponding to concentration interval of δ-H:LT was subjected to quenching at 400°C, 10 min. The refractive index of HTP formed by this way was equal 0.029 and slowly decreases with time under room condition (Fig.3).

As one can see, the additional refractive index, induced by HTP formation on quenching, decreases by a half for ~26000 hours (~3 years). The function governing the evolution of refractive index can be written as $\Delta n_e = \Delta n_e(0) \cdot (e^{\frac{-0.693 \cdot t}{\tau_1}} + e^{\frac{-0.693 \cdot t}{\tau_2}})$ with two significantly different components, characterized by τ_1~100 hours, τ_2~70000 hours. Under the temperature ~100°C the process of HTP decay is faster and phase transition to an equilibrium state finishes during 20 hours.

In our resent investigations [16], we observed that the HTP decay in α-H:LT is a single process, and half-life period is ~1500 hours. Above this, the interphase transition in H:LN system is more quick, and totally finishs after ~250 hours at room conditions.

Taking into account the shape of functions of refractive index evolution the nature of high-temperature states in $H_xLi_{1-x}MO_3$ (M=Nb, Ta) can be suggested. The high-temperature phase formation could be related to the existence of several proton positions in crystal lattice. For $H_xLi_{1-x}NbO_3$ system in [17] the total energy of crystal was calculated as a function of the displacement of proton It was estimated, that the total energy structure of the hydrogen displacement along the O-O line has a double well energy structure. The one site is more stable by 0.27 eV then second site and these sites are separate by 0.9 Å in space. It may be supposed that the variations of refractive index during the high-temperature phase formation can be induced by partial displacement of hydrogens from stable site with low energy to metastable site with higher energy. Then, on the high-temperature phase relaxing, the protons returns back from metastable site to stable one. This is a single process, that's why the refractive index decreasing during the hightemperature phase relaxation in $H_xLi_{1-x}NbO_3$ is described by one exponent. Perhaps, in $H_xLi_{1-x}TaO_3$ the lattice energy dependence on the hydrogen displacement along the O-O bond line have a triple well energy structure, and the hydrogens redistribute between three nonequal sites when the high-temperature state formation takes place. In this case, on high-temperature phase relaxation, protons rmove to stable site from two metastable sites simultaneously but with different probability. It explains why the double exponent function of refractive index variation with time during high-temperature phase relaxation is observed. In this

function one exponent describes proton replacement from one metastable site to stable site, and second exponent - from another site.
However, this simple model is not able to describe existence more then one high-temperature phase, which is not in agreement with experimental data. Moreover, in [18] authors obtain the six nonequivalent positions of protons in $LiNbO_3$ crystal lattice. The six positions could explain formation of four high-temperature states, described in [16], and suggest undetected fifth phase.
Four mechanisms of refractive index variation are known. The absence of chemical composition under high-temperature phase formation-decay processes was shown in [8] and we can neglect by molar refraction changes. The spontaneous polarization change also unclear. It was shown using X-ray diffractometry [18] that one crystal cell parameter (c) changes under phase transition. Therefore, only the molar volume variation and elastooptic effect can be considered as causes for refractive index variation. Using experimental data from [18] ($\Delta n_e(0)^{room}$=0.1088, $\Delta n_e(0)^{hightemperature}$=0.1164 => $\delta\Delta n_e(0)$=0.0076, $\delta\Delta c$=0,26%), and using expression

$$\delta\Delta n_e^V = \frac{\delta\Delta c}{6\cdot n_e}\cdot(n_e^2+2)\cdot(n_e^2-1)$$

we get $\delta\Delta n_e(0)$=0.0060, which is in good enough agreement (23%) with experimental value.

Conclusions

The existence of high-temperature, metastable at room conditions phases in $H_xLi_{1-x}TaO_3$ waveguide layers was observed over wide range of hydrogen content. The refractive index jumps and temperature intervals of phase transitions between equilibrium and high-temperature states were traced. It was shown, that the relaxation of HTP in concentration interval of δ-H:LT occurs for a long time period. The nature of HTP in $H_xLi_{1-x}TaO_3$ and $H_xLi_{1-x}NbO_3$ is discussed.

References

1. T. Findakly, P. Suchoski and F. Leonberger, Optics Lett. 13 (1988), p. 797.
2. P. Baldi, M.P. De Micheli, K. El Hadi, S. Nouh, A.C. Cino, P. Aschieri and D.B. Ostrowsky, Opt. Eng. 37 (1998), p. 1193.
3. T. Maciak, Int. J. Optoelect. 7 (1992), p. 557.
4. P.J. Matthews and A.R. Mickelson, J. Appl. Phys. 71 (1992), p. 5310.
5. H. Åhlfeldt, J. Webjörn, F. Laurell, and G. Arvidsson, J. Appl. Phys. 75 (1994), p. 717.
6. H. Åhlfeldt and F. Laurell, Elec. Lett. 31 (1995), p. 750.
7. I. Savatinova, S. Tonchev, R. Todorov, M.N. Armenise, V.M.N. Passaro and C.C. Ziling, J. Lightwave Technol. 14 (1996), p. 403.
8. V.V. Atuchin, D. Dimova-Malinovska, T.I. Grigorieva, I.E. Kalabin, I. Savatinova, I. Savova, E.V. Spesivtsev, S. Tonchev, C.C. Ziling, Applied Physics B.73 (2001), pp. 559-563.
9. K. El Hadi, P. Baldi, M.P. De Micheli, D.B. Ostrowsky, Yu.N. Korkishko, V.A. Fedorov and A.V. Kondrat'ev, Opt. Commun. 140 (1997), p. 23.
10. V.G. Pankin, V.U. Pchelkin and V.V. Shashkin, Kvant. Elect. 4 (1977), p. 1497 (in Russian).
11. H. Ahlfeldt, J. Webjorn, F. Laurell, G. Arvidsson, J. Applied Physics 75, 2 (1994), pp. 717-727.
12. C.C. Ziling, V.V. Atuchin, I. Savatinova, S. Tonchev, M.N. Armenise, V.M.N. Passaro, J. of Physics D: Applied Physics 30 (1997), pp. 2698-2703.
13. V.V. Atuchin, I. Savatinova, C.C. Ziling, Material Letters 46 (2000), pp. 189-192.
14. I. Savatinova, S. Tonchev, R. Todorov, M.N. Armenise, V.M.N. Passaro, C.C. Ziling, J. Lightwave Technology 14, 3 (1996), pp. 403-409.
15. H. Nagata, IEEE Phot. Techn. Lett. 12 (2000), p. 386.
16. I.E. Kalabin, V.V. Atuchin, T.I. Grigorieva, Optical Materials, 23, 1-2 (2003), pp. 283-286.
17. H.H. Nahm, C.H. Park, Applied Physics Letters 78, 24 (2001), pp. 3812-3814.
18. I.E. Kalabin, D.I. Shevtsov, I.S. Azanova, I.F. Taysin, V.V. Atuchin, A.B. Volyntsev, A.N. Shilov, J. of Physisc.D: Applied Physics 37 (2004), pp. 1829-1833.

Energy deposition and heat diffusion in the process of chalcogenide glass modification by femtosecond laser pulses

Elena Romanova (1), Andrey Konyukhov (1), Sergey Muraviov (2), Grigory Gelikonov (2)
1) Saratov State University, Russia, romanova@optics.sgu.ru
2) Institute of Applied Physics of RAS, Nizhny Novgorod, Russia

Abstract: *The process of energy deposition in highly non-linear chalcogenide glasses by focused femtosecond pulses, heat diffusion and subsequent cooling of the illuminated volume are investigated in a theoretical model as well as in experiments.*

Introduction

Direct photo-fabrication of optical waveguides by femtosecond (fs) laser pulses in bulk materials enables the dawn of a new generation of optical devices, which are potentially cheap and allow for a dense integration due to the 3D character.

When a femtosecond pulse is tightly focused in a transparent material, the energy is deposited in a small volume around the focus due to multiphoton absorption. The photo-generated hot electron plasma rapidly transfers its energy to the lattice, giving rise to high temperatures and pressures. This produces, by a mechanism still under investigation, a local material densification with an increase or decrease of refractive index, depending on the glass composition. The unclear mechanism of refractive index variation is currently the main drawback in the theoretical treatment of the modifications of the optical properties of glasses via exposure to fs pulses. In [0] the glass modification was associated with the heating process. A thermal diffusion model accurately tracks the waveguide diameter. However theoretical model in [1] does not take into account pulse propagation dynamics and pulse nonlinear absorption. For proper description of the shape of the modified glass region the glass phase transition during the thermal diffusion should be considered also.

In this paper, we study the process of energy deposition into highly non-linear (chalcogenide) glass by focused fs pulse and subsequent heat diffusion outside the illuminated volume. The theoretical treatment is based on the model of fs pulse propagation in non-linear dielectric medium [2]. Spatiotemporal dynamics of the pulse is described by the 2D+T parabolic wave equation where we used the Pade approximation with respect to longitudinal coordinate to take into account wide-angle radiation of the tightly focused laser beam. In the model, we assume that permanent change of the refractive index is associated with heating of the glass sample up to the glass transition temperature T_g, subsequent cooling and solidification. After illumination, variation of the absolute temperature T with time is described by the heat diffusion equation with account of heat flow on the moving boundary between solid and liquid phases in a glass sample.

We are presenting also the experimental results of chalcogenide glass modification by fs pulses of 1.55 μm fibre laser (pulse duration 150 fs, repetition rate 25 MHz). The AsSe glass chemical composition has been tailored by doping with germanium or tellurium. For characterisation of the refractive index variation upon the glass modification, the optical coherent tomography has been used.

Non-linear absorption of focused fs pulses

Spatiotemporal dynamics of the pulse is described by the 2D+T parabolic wave equation for the slowly varying envelope $E(z,r,\tau)$ of electrical field:

$$\frac{\partial}{\partial z}\left(1+\frac{1}{2ik}\frac{\partial}{\partial z}\right)E+\frac{1}{2ik}\left(\nabla_{\perp}^{2}E-\frac{2}{u}\frac{\partial^{2}E}{\partial z\partial\tau}\right)= \\ =\left(iP_{\mathrm{nl}}-\frac{2}{\omega_0}\frac{\partial P_{\mathrm{nl}}}{\partial\tau}\right)-i\frac{\beta_2}{2}\frac{\partial^{2}E(z,r,\tau)}{\partial\tau^{2}}-j_{\mathrm{nl}}, \quad (1)$$

where we use the Pade approximation with respect to longitudinal coordinate. The second order derivative $\partial^2E/\partial z^2$ was included into the left-hand-side of Eq.(1) to prevent beam collapse due to Kerr self-focusing. In Eq. (1), $k=\omega_0/u$ is the mean wavenumber (u is the light velocity in glass, $\tau=t-z/u$ is the time in the moving coordinate system, ω_0 is the pulse carrier frequency), β_2 is the group-velocity dispersion. In the expression for the nonlinear polarization P_{nl}, we include the effects of the nonlinear refractive index change and energy deposition through formation of electron plasma density ρ:

$$P_{\mathrm{nl}}(z,r,\tau)=\gamma|E|^{2}E+i\frac{\alpha_p}{2}\left(\delta_1\rho+|E|^{2(p-1)}\right)E, \quad (2)$$

$\gamma = n_2\omega_0/c$, $n_2=1.8\times10^{-14}$ cm^2/W is the Kerr constant, α_p is the p-photon absorption coefficient. For chalcogenide glasses which have bandgap edge at 1.24 eV the major role in nonlinear absorption of λ=1.55 μm radiation plays the two-photon absorption (p=2, α_p=0.6 cm/GW).

The current density is defined by equation

$$\frac{\partial\rho(z,r,\tau)}{\partial\tau}=\delta_1\rho|E|^{2}+|E|^{2p}-\delta_2\rho^{2}, \quad (3)$$

where the first term on the right-hand-side describes growth of the electron plasma by cascade (avalanche) ionization, the second term is the contribution of multiphoton absorption, which acts both as a source for the cascade process and as a contributor to plasma

growth, and the third term describes the radiative electron recombination. Evolution of plasma in glass is described by the Drude model [3]:

$$j_{nl}(z,r,\tau) = i\frac{1}{L_{pl}}\left(1-\frac{i}{\omega_0\tau_c}\right)\left(E-\frac{\tau_c}{1-i\omega_0\tau_c}\frac{\partial E}{\partial \tau}\right)\rho, \qquad (4)$$

where τ_c is the electron-collision time ($\omega_0\tau_c$=5), L_{pl}=1 μm^{-1} is the plasma length. In Eq. (4), plasma diffusion is not taken into account because we consider here fs pulses with so short time scales that plasma diffusion (characteristic time ~1 μs) occurs after the pulse has left the region of focusing.

Heat diffusion in glass

Energy deposition into the glass sample by a fs pulse results in temperature increase inside the illuminated volume. To study the dynamics of glass heating upon a fs pulse irradiation, a model of thermal diffusion was used. After irradiation, spatial variation of the absolute temperature T with time t is described by the equation:

$$\left(c(T)+\Lambda\delta(T-T_g)\right)\frac{\partial T}{\partial t} = \frac{1}{r}\frac{\partial}{\partial r}\left(K(T)r\frac{\partial T}{\partial r}\right), \qquad (5)$$

where $c=\rho_g C$ is temperature-dependent coefficient, C is specific heat capacity, ρ_g is the glass density, Λ is enthalpy, $\delta(T-T_g)$ is the unit impulse function, K is temperature-dependent heat conductivity. The temperature dependency of the coefficients take into account glass phase change at $T=T_g$.

$$c(T) = \begin{cases} c_1, T < T_g \\ c_2, T > T_g \end{cases}, \quad K(T) = \begin{cases} K_1, T < T_g \\ K_2, T > T_g \end{cases}, \qquad (6)$$

where c_1=1.47 J·cm^{-3}·K^{-1}, c_2=1.76 J·cm^{-3}·K^{-1}, K_1=0.3×10^{-2} W·cm^{-1}K^{-1}, K_2=0.25×10^{-2} W·cm^{-1}K^{-1}, Λ=23.6 c_1. Stepwise function for $c(T)$ and $K(T)$ was used, because detailed information concerning thermal properties of chalcogenide glasses was not available. The initial temperature variation is defined as

$$\Delta T = W / c, \qquad (7)$$

where W is energy density of the heat source. The heat source due to a fs pulse irradiation can be considered as a delta function in time because the pulse duration is much less than the characteristic time of the heat diffusion (~1 μs).

In our model, we assume that permanent change of refractive index is associated with heating of the glass sample up to the glass transition temperature T_g due to the energy deposition by a fs pulse, subsequent cooling and solidification of the illuminated region.

Numerical results

In numerical simulations, non-stationary Gaussian beam (λ=1.55 μm) was focused at the depth 200 μm from the surface of bulk glass sample (focal spot dimension of low-intensity beam ~1 μm). Initial temporal distribution was taken *sech*-shaped with the half-width (pulse duration) 100 fs.

The energy deposition and spatial distribution of heat sources inside the irradiated volume depend mostly on a balance of self-focusing, multi-photon absorption and plasma defocusing. It doesn't depend significantly on splitting of the pulse at the focus resulting from the self-steepening and space-time focusing effects because energy of the heat sources is calculated by integration of pulse temporal envelope at each point of the illuminated volume.

Numerical results

Strong multiphoton absorption of the pulse energy arises before the focal plane (Fig.1, 180<z<200 μm). Full absorbed energy increases with initial pulse energy that fits the available experimental results [4]. The pulse energy absorption increased sufficiently when the beam becomes strongly self-focused (Fig.2).

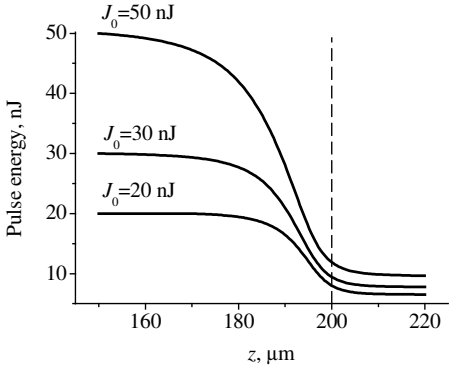


Fig.1: Pulse energy absorption. J_0 is the energy of input pulse. Vertical dashed line shows the focal plane inside the glass.

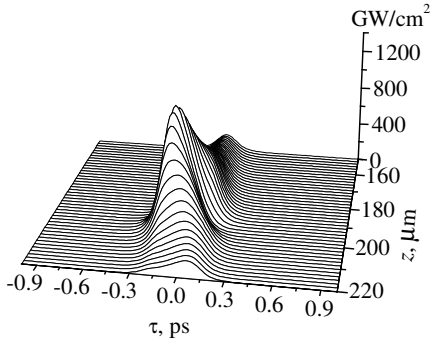


Fig.2: Intensity on the beam axis. Energy of input pulse is 50 nJ.

The multiphoton absorption, self-steepening and plasma formation lead to distortion of the pulse shape. In spite of the high intensity on the beam axis the propagation distance is not sufficiently large to obtain significant pulse spectral broadening due to self-phase modulation (Fig.3). After the focal plane (z>200 μm) the beam become strongly divergent and

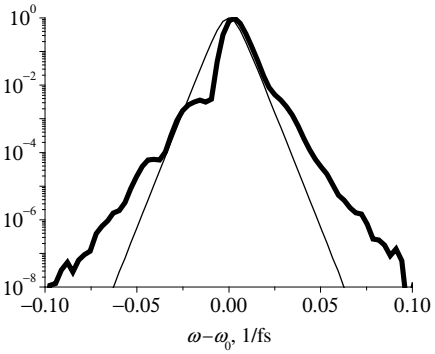


Fig.3: Spectral intensity on the beam axis. Initial pulse specrum (thin curve) and pulse spectrum after propagation distance 220 μm (thick curve). Energy of input pulse is 50 nJ.

local intensity rapidly decreases. As result the effect of the nonlinear processes become inappreciable. For considered pulse energies the pulse shape and pulse spectrum practically does not change after focal plane.

In Fig.4, contour lines correspond to T_g =180°C (chalcogenide glass) measured at some moments of time t after irradiation. At t=0, shape and dimensions of the initially melted region ($T>T_g$) can be tailored by enhancing or decreasing the self-focusing with respect to the plasma defocusing. The increase of the energy of input pulse shifts the region $T>T_g$ backward to the pulse source, because with the higher energy pulses the mulltiphoton absorption starts at the shorter propagation distances (Fig.1). For the pulse energy equal to 50 nJ the temperature is at a maximum at the point r=0, z=196 μm, while for pulse energy 20 nJ this point is r=0, z=197 μm.

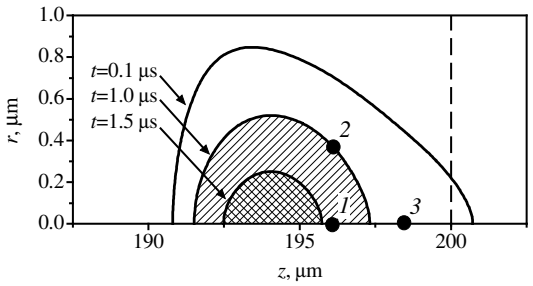


Fig.4: Contour lines $T=T_g$ at the different time after radiation by single 100 fs pulse. Initial pulse energy is 50 nJ. Vertical dashed line shows focal plane of the focusing lens. The temperature dynamics at three black points shown in the Fig.5.

Both the region restricted by the curve $T=T_g$ (t≤0.1 μs, Fig.4) and experimentally observed laser-induced refractive index change [1] have drop-like shape.

While glass is cooling, the T_g lines move inside the irradiated region (Fig.4). Structural changes upon transformation of hot viscous liquid into solid glass

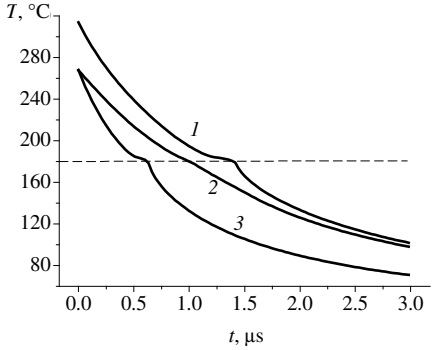


Fig.5: Temperature dynamics at the three different spatial points (see Fig.4). Dashed line shows $T=T_g$.

depend on the cooling rate. We show that the cooling rate is greater at the beam axis than at the periphery (Fig.5) that is associated with the ellipsoidal shape of the modified region (Fig.4). Due to the glass phase transition (6) the cooling rate at $T=T_g$ is slowed down (on-axis points *1* and *3*, Fig.5). The cooling rate can be also tailored by variation of the pulse energy and pulse repetition rate so that the motion of T_g lines can be managed to provide better cooling conditions.

Up to t=1.3 μs the length and radius of modified region decrease linearly (Fig.6). For t>1.3 μs r_m and z_m decrease rapidly to zero.

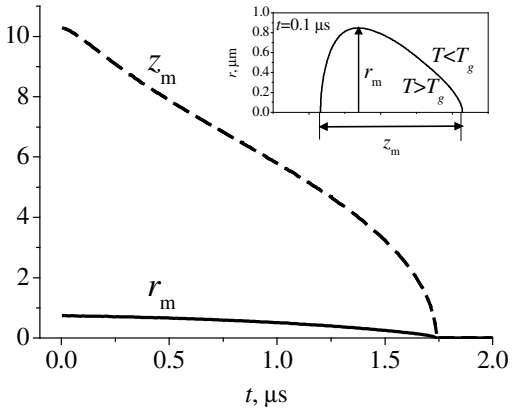


Fig.6: Radius r_m (solid curve) and length z_m (dashed curve) of modified region versus time. Inset show the method of determining r_m and z_m.

Experiments

In experiments (Fig.7), glass samples were locally illuminated by 150 fs laser pulses with mean wavelength at 1.55 μm.

Three kinds of glasses were used: E_g=1.72 eV, T_g=185°C ($As_{40}Se_{60}$, oxygen gettered glass), E_g=1.51 eV, T_g=205°C ($Ge_{17}As_{18}Se_{65}$ glass) and E_g=1.27 eV, T_g=265°C ($Ge_{17}As_{18}Se_{56}Te_9$ glass), where E_g is the band edge. Mean power of the Er^{3+} doped fibre laser was varied in the range 2.0−8.0 W.

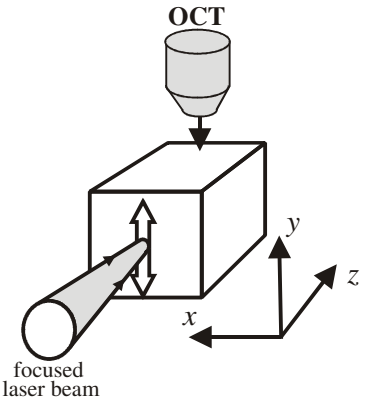


Fig.7: Experimental setup. The glass was modified inside the sample by focused laser pulses. The λ=1.55 μm radiation was focused by 60× microscope objective. During the glass modification process the glass sample was translated in *y*-direction. The change of refractive index was detected by optical coherent tomography (OCT).

Results of the illumination were characterised by the optical coherent tomography.

Behaviour of the illuminated regions inside glass demonstrated strong dependence on the glass composition. We have found thresholds for irreversible glass modifications which decrease significantly with linear bandgaps. For some range of powers below the bandgaps, reversible modifications have been found by observation of diffraction patterns on a screen. These diffraction patterns disappeared within few seconds. However for a range of powers above the bandgaps, the diffraction patterns were stable. Changes of the refractive index over the modified regions were observed (Fig.8) by optical coherent tomograph (3D spatial resolution 10 μm at wavelength 1.3 μm, scanning time 1 s, scanning depth 2-3 mm, sensitivity for refractive index changes 0.001).

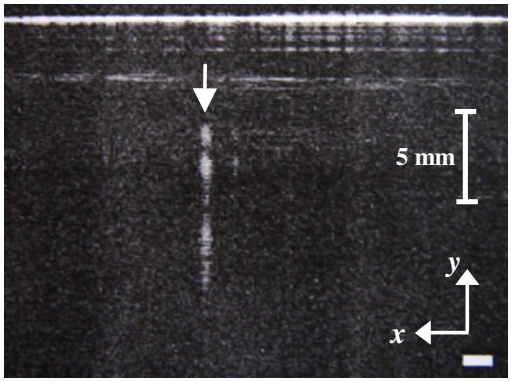


Fig.8: OCT image of a refractive index change. Laser direction is normal to page. Pointer shows the modified area.

Variations of the refractive index in the spots are due to variation of the focusing conditions during the sample illumination.

The threshold powers for irreversible modifications were found significantly lower for lower bandgap glasses (0.1−1 W). Increase of the power above the damage threshold resulted in ablation and glass evaporation. For $Ge_{17}As_{18}Se_{65}$ glass, the range of powers between the threshold for modification and ablation was extremely small (6-7 W).

Conclusions

In the paper, we have presented theoretical model for glass modification by fs laser pulses and applied this model to study energy deposition and heat diffusion in chalcogenide glasses. In parallel, we have studied the thresholds for chalcogenide glass modifications in experiments using Er^{3+} fibre laser and optical coherent tomograph.

The results demonstrated great flexibility of the technology that can be achieved by tailoring glass composition and illumination conditions. Temporal dependences of the glass cooling over the illuminated region provide insight into the photo-structural process and can be used together with Differential Thermal Analysis for better understanding of modification process in different glasses. The results obtained by optical coherent tomograh prove efficiency of this technique in characterisation of the complicated 3D structures for photonics.

Acknowledgments

The authors gratefully acknowledge Professor A. Seddon, Professor T. Benson and Dr. D. Furniss from the University of Nottingham for the glass samples which they kindly provided for the experiments, for helpful discussions and collaboration in this research field.

References

1 S. Eaton et al, Opt. Express, v. 13, no. 12, p. 4708, 2005
2 K. Moll, A. Gaeta, Opt. Lett., v. 29, p. 995, 2004
3 Q. Feng et al, IEEE J. of Quant. Electron, v. 33, no. 2, p.127, 1997
4 A. Alexandrov et al., Quant. Electron., v. 31, p. 398, 2001.

Deep etched DBR gratings in InP for photonic integrated circuits

B. Docter, E.J. Geluk, F. Karouta and M.K. Smit

COBRA Inter-University Research Institute on Communication Technology
Eindhoven University of Technology
Faculty of Electrical Engineering, Opto-Electronic Devices Group
P.O.Box 513, 5600 MB Eindhoven, The Netherlands
Email: b.docter@tue.nl

Abstract: *A novel fabrication process for the realization of deep-etched DBR gratings in InP is presented. It is shown that a combination of chromium and SiO_x provides a very resistant etching mask for Cl_2-based ICP etching. Both e-beam and optical lithography are used to limit e-beam writing time.*

Introduction

Deep etched distributed Bragg reflector (DBR) gratings are very promising devices for InP/InGaAsP-based photonic integrated circuits (PICs). In theory, a first order deep etched grating can achieve a reflectivity of more than 97%, within only a few grating periods [1]. The small size and high reflectivity makes the DBR grating an ideal building block for high-Q cavities [2]. These can be used to make ultra small, in-plane lasers that can be applied in photonic logical circuits.

The realization of these sub-micrometer scale structures is very challenging. Being able to integrate the DBR mirrors with other photonic components adds additional restrictions to the fabrication process. We present here first results of a technology for fabrication of high quality 3 µm deep DBR gratings, using electron beam lithography and inductively coupled plasma (ICP) etching, which is compatible with our conven-tional Active Passive integration Technology [3].

DBR grating design

The first order DBR gratings are schematically shown in fig. 1. The air gaps in the DBR sections are about 390 nm wide and the lines are about 120 nm wide. This corresponds to ¼ of the wavelength in each medium. The p-InP cladding layer is sufficiently thick to avoid optical loss from the InGaAsP contact layer, which is necessary to integrate semiconductor optical amplifiers (SOAs) and optical phase shifters in the same chip. Because the gratings should be etched through the waveguide layer, an etch depth of at least 3 µm is required. Furthermore, the sidewalls should be smooth and vertical.

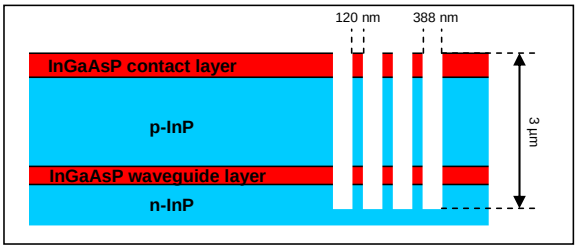


Fig. 1: *Schematic drawing of deep-etched DBR grating*

Fabrication process

To meet the above requirements a Cl_2:Ar:H_2 ICP process was used. This process has a high etch rate (~2.0 µm/min) and the addition of H_2 results in good passivation of the sidewalls. The selectivity towards a PECVD deposited SiO_x mask layer is about 20:1. However, because of faceting effects on the mask, which play a major role in the small DBR structures, this SiO_x layer needs to be at least 400 nm thick.

The grating structures are written using a Raith-150 electron beam lithography system, operating at 30 kV acceleration voltage. The typical thickness of common ZEP resist is 320 nm, which is not sufficient to accurately transfer a detailed pattern to the thick SiO_x layer, and therefore an extra 50 nm chromium mask layer was added.

The process flow is shown in fig. 2. The InP layerstack is covered by a 400 nm thick SiO_x layer by PECVD at 300 degrees. Subsequently a 50 nm thick chromium layer is evaporated and a 320 nm thick ZEP layer is spun on top. The ZEP resist is patterned using the e-beam lithography system. Usually a thin gold layer is deposited on top of the ZEP layer to avoid charging of the sample during e-beam patterning, but because of the chromium layer, this extra step is not necessary.

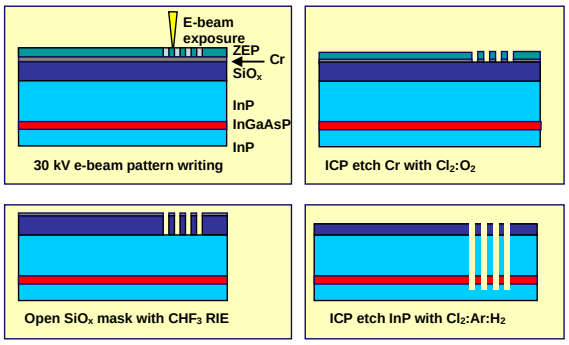


Fig. 2: *Process flow for the ICP deep etched DBR gratings*

After development of the ZEP pattern, the chromium is etched in an ICP system. A Cl_2:O_2-based process is used at intermediate ICP power and low RF power. This is a well known process that is also used for the fabrication of high quality photolithography masks [4]. The selectivity of the process is not extremely high (about 1:2 for Cr:ZEP), but it has a high uniformity, and since the chromium layer is very thin, this is an acceptable value.

Subsequently the chromium is used as an etching mask to open the SiO_x layer in a CHF_3 RIE process. The selectivity between chromium and SiO_x is approximately 1:17. This allows the thick-ness of the SiO_x layer to be well over 400 nm.

The high quality SiO_x pattern is used as a mask in a high power ICP etching process. The resulting DBR grating is shown in fig. 3. The ICP power was 1000 W and the RF power was 120 W. This gives very straight and smooth sidewalls. The roughness that is still visible on the DBR sections is caused by a sub-optimal proximity effect correction in the e-beam patterning.

Combination EBL - waveguide lithography

In the previous section a general process for fabricating deep-etched DBR gratings was presented. The process relies on EBL patterning of the full structure, and since ZEP is a positive e-beam resist, this requires writing the pattern around the DBR gratings and the waveguides. This means that if the DBRs are integrated in a bigger chip design, the total writing time becomes very long. Additionally, the proximity effect correction algorithm, which was originally developed for periodic photonic crystal structures, is not very suitable for these patterns. Therefore a more complex process was developed that enables us to define only the DBR sections by EBL and the rest of the waveguide structures by conventional lithography.

The process flow is schematically shown in figure 4. First the ZEP layer is patterned by EBL, defining the gaps between the DBR sections (fig 4a). The vertical lines are several microns wider than

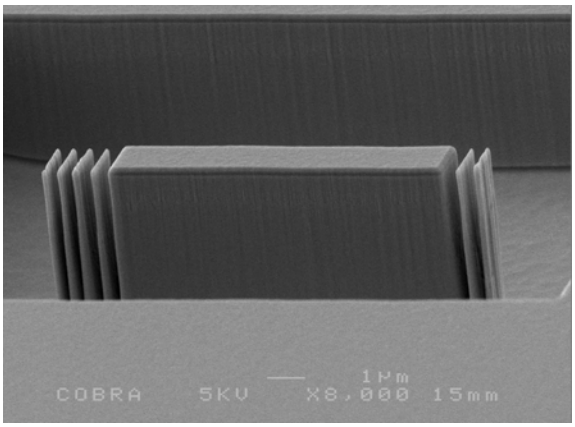


Fig. 3: *6 µm deep DBR gratings in InP*

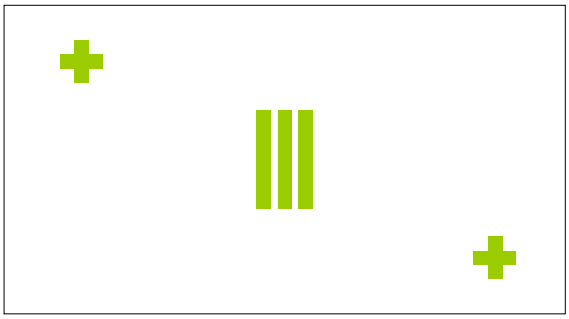


Fig. 4a: *EBL pattern*

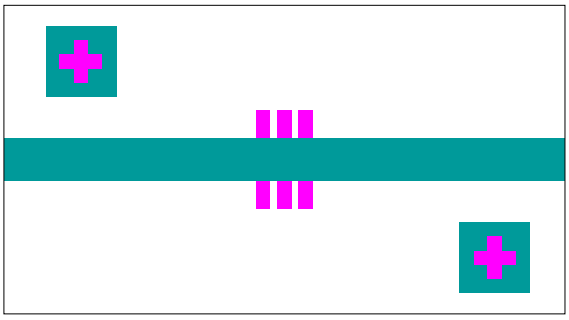


Fig. 4b: *Waveguide pattern aligned to EBL pattern*

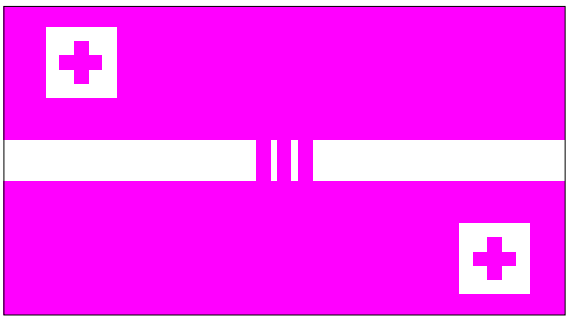


Fig. 4c: *Final chrome mask*

the waveguide, to compensate for lithography alignment errors. Together with the DBRs, alignment markers are written for the waveguide lithography step. Then the ZEP pattern is transferred into the chrome layer with the first ICP etch.

Next, the waveguides are defined by optical lithography (fig 4b). The pattern is aligned on the

markers defined in the chrome layer. A second chrome ICP etch is performed (fig 4c) after which the SiO_x etch and the InP etch are done.
This process has the advantage of being very accurate at the DBR sections, but requires less EBL writing time and is much more suitable for the proximity effect algorithm, since the EBL pattern is periodic. Also, the alignment of the two lithography steps is not very critical, because the DBR spaces can be made several micrometers wider that the waveguide.

Conclusion

We presented a novel fabrication process for deep etched DBR gratings in InP. The process is capable of realizing high quality deep etched structures with minimum EBL writing time. Furthermore, the technology is fully compatible with other processing steps and therefore enables the use of deep etched DBR gratings as building blocks in future advanced photonic integrated circuits. The first DBR gratings in passive waveguide structures are currently being realized using this new process technology.

References

[1] K.J. Kasunic, “Design Equations for the Reflectivity of Deep-Etch Distributed Bragg Reflector Gratings”, J. of Lightwave Techn., Vol. 18, No. 3, 2000

[2] T. Baba et al., “A Novel Short-Cavity Laser with Deep-Grating Distributed Bragg Reflectors”, Jpn. J. Appl. Phys., Vol. 35, 1996

[3] J.H. Den Besten et al. “An integrated 4x4-channel multi-wavelength laser on InP”, IEEE Phot. Techn. Lett., Vol. 15, nr. 3, 2003

[4] K.H. Smith et al. “Cr absorber etch process for extreme ultraviolet lithography mask fabrication”, J. Vac. Sci. Technol. B, Vol. 19, nr. 6, Nov/Dec 2001

Surface Modes in Antiresonant Reflecting Optical Waveguides with Rectangular Hollow Core

Federica Poli, Matteo Foroni, Simone Busanelli, Annamaria Cucinotta and Stefano Selleri
Information Engineering Department, University of Parma, e-mail: stefano.selleri@unipr.it

Abstract: *The guiding properties of antiresonant reflecting optical waveguides with rectangular hollow core have been deeply investigated. In particular, waveguides whose core is filled with water and ethylene glycol have been studied through a full-vector modal solver based on the finite element method, providing the dispersion and confinement loss curves in the wavelength range between 600 nm and 900 nm. Simulation results for both the considered waveguides have demonstrated the presence of anti-crossing points in the dispersion curves, which are associated with the transition from the guided mode to a surface one and, consequently, to high confinement loss values.*

Introduction

The idea of confining leaky modes in a low index core through cladding layers which alternate low and high refractive indices has been proposed for the first time in [1]. This principle is the basis of the so called Anti-Resonant Reflecting Optical Waveguides (ARROWs). Along with photonic crystal fibers [2], which exploit the photonic bandgap given by the periodic cladding material, ARROWs are the only structures which offer the possibility of light guiding in low index materials, such as air, liquid or gas [3, 4, 5, 6]. Moreover, these waveguides can be realized with the standard fabrication technology for integrated optical devices [3, 4, 6], thus providing advantages, such as compact size, planar geometry, potential for massively production, high level of chip integration. All these aspects fit well with the requirements for sensor design [7], from nano scale device [8] down to single molecule sensitivity [9] and can be exploited for many applications in different disciplines, including engineering, physics, biology and biochemistry.

So far, the analysis of hollow core ARROW has been limited only to few working wavelengths, fixed according to the particular gas or liquid filling the core [4, 5], and to the width of the cladding layers which assure the antiresonant effect. This approach allowed to successfully verify the light guiding in hollow cores, matching experimental results and theoretical expectations, but a general description of the waveguide behaviour in frequency and according to the material filling the core is still missing.

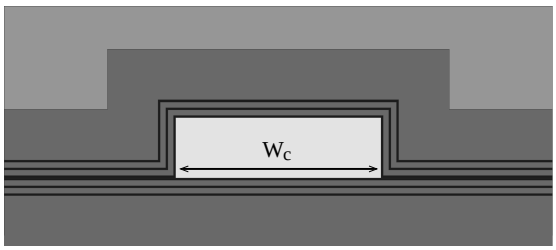


Fig. 1: Cross-section of the ARROW with rectangular hollow core. Three alternating layers of silicon nitride (black) and silicon oxide (dark grey) confine the light in the core region (light grey).

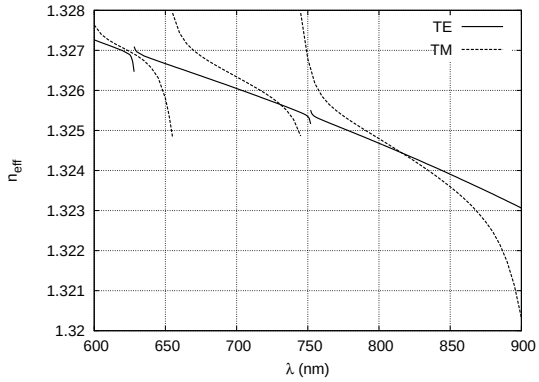


Fig. 2: Dispersion curves of the TE and TM polarizations of the fundamental mode for the ARROW with rectangular core of width $w_c = 12\ \mu m$, filled with water.

The present work provides an extensive spectral investigation of the ARROW properties with liquid-filled rectangular core. In particular, through a detailed analysis of the effective index, the confinement loss and the field distribution, the presence of surface modes have been demonstrated in these structures for the first time to the authors' knowledge. The appearance of these surface modes is quite similar to that of surface modes in hollow core photonic crystal fibers. In these fibers they are located in the thin silica layer surrounding the core [10] and are responsible of a strong reduction of the fiber transmission band [11]. In the same way, the surface modes considerably influence the ARROW performances, being responsible of the loss peaks which pollute the spectrum of the waveguides. Both TE and TM polarizations have been investigated in the wavelength range between 600 *nm* and 900 *nm*.

The present analysis has been performed by means of a full vector modal solver based on the Finite Element Method (FEM) [12], whose flexibility allows to describe any kind of cross-section and material, and guided as well as leaky modes. A complex formulation with the perfectly matched layers as boundary conditions [13] has been used. In particular, the FEM based

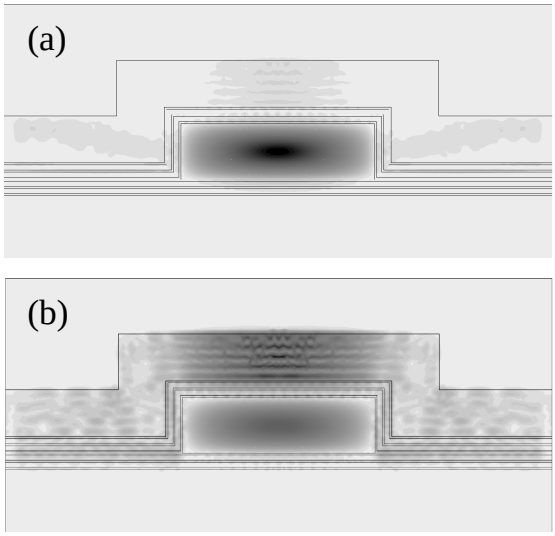


Fig. 3: Magnetic field modulus of the TE polarization of the fundamental mode at (a) $\lambda = 740$ *nm* and (b) $\lambda = 752$ *nm* for the ARROW with water-filled rectangular core of width $w_c = 12\ \mu m$.

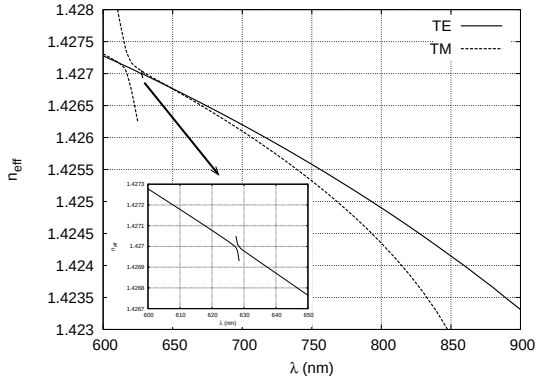


Fig. 4: Dispersion curves of the TE and TM polarizations of the fundamental mode for the ARROW with rectangular core of width $w_c = 12\ \mu m$, filled with ethylene glycol. Inset: particular of the anti-crossing point in the TE-polarized mode dispersion curve around 628 *nm*.

solver provides the field distribution and the complex propagation constant, that is the mode effective index n_{eff} and the attenuation constant α which yields the confinement loss due to the field leakage.

ARROW structure

The ARROW considered in the present work is the rectangular waveguide sketched in Fig. 1, optimized for a liquid-filled core. The guide has been previously designed and fabricated in [4]. The cladding is characterized by three periods of silicon nitride SiN and silicon oxide, or silica, SiO_2, whose refractive index is 2.1 and 1.46, respectively [4]. The thickness of the two layers, which is 126 *nm* for the SiN layer and 326 *nm* for the SiO_2 one, has been chosen in order to optimize the light guiding at 800 *nm* in a water-filled core with a refractive index of 1.33 [1, 4]. The height of the rectangular core is 3.5 μm, while its width w_c is equal to 12 μm [4]. The two layers at the top and at the bottom of the ARROW have been considered both made of SiO_2, while air covers the upper layers.

Core filled with water

The effective index n_{eff} of the TE and TM modes, computed for a water-filled rectangular core, are reported in Fig. 2. It is important to note that the dispersion curve for both the polarizations is broken in two points, called the anti-crossing points [10], which are around 627 *nm* and 752 *nm* for the TE fundamental mode, being significantly wider for the TM one. The presence of the surface modes is related to these discontinuities of the ARROW n_{eff} curves, as it happens for the hollow-core photonic crystal fibers, which support surface modes localized in the thin silica region surrounding the air-core [10, 11]. The magnetic field modulus of the TE fundamental mode is reported in Fig. 3 for two different wavelengths near the second anti-crossing point, that is 740 *nm* and 752 *nm*, clearly showing what happens to the ARROW fundamental mode. In fact, Fig. 3(a), at 740 *nm* the field is almost completely confined in the water-filled core, even if small components leak in the top and lateral regions of the waveguide. When the wavelength increases, the leaky components of the fundamental mode become stronger and stronger, and, at 752 *nm*, the TE-polarized fundamental mode is mainly confined in the layers surrounding the core, especially in the central region of the top silica layer, as shown in Fig. 3(b). The field maximum is no longer located in the hollow core. This guided mode change into a surface mode is described by a sharp decrease of the effective index curve. The field behaviour is specular as the wavelength decreases after the anti-crossing point on the other branch of the n_{eff} curve, passing from a surface configuration to a guided one. The same kind of transition can be observed also for the TM polarization.

Core filled with ethylene glycol

In order to analyze the influence of the liquid which fills the ARROW hollow core on the guiding properties, the same waveguide has been studied by considering the ethylene glycol as the core material. Ethylene glycol is characterized by a higher refractive index with respect to water, that is 1.43. This liquid has been often used instead of water for the experimental measurements reported in literature, since it evaporates more slowly than water, thus allowing for longer measurement times [4, 5, 6]. As reported in Fig. 4, the dispersion curves for the TE and TM polarizations present only one anti-crossing point in the short wavelength range.

With respect to the previous ARROW with a lower index core, the discontinuity is narrower for both polarizations, in particular for the TE one. As a conse-

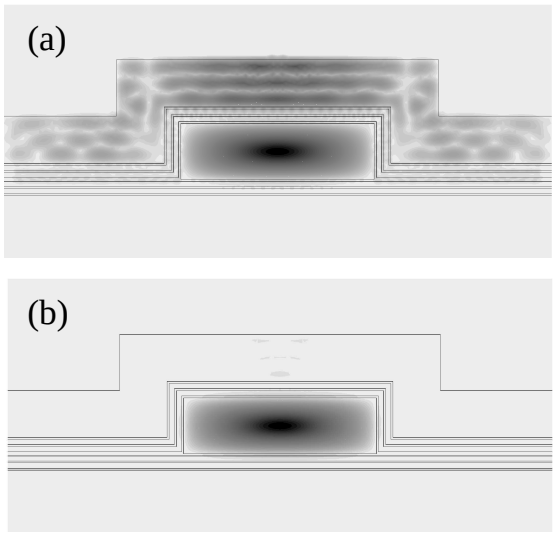


Fig. 5: Magnetic field modulus of the TE polarization of the fundamental mode at (a) $\lambda = 628$ *nm* and (b) $\lambda = 640$ *nm* for the ARROW with rectangular core of width $w_c = 12\ \mu m$, filled with ethylene glycol.

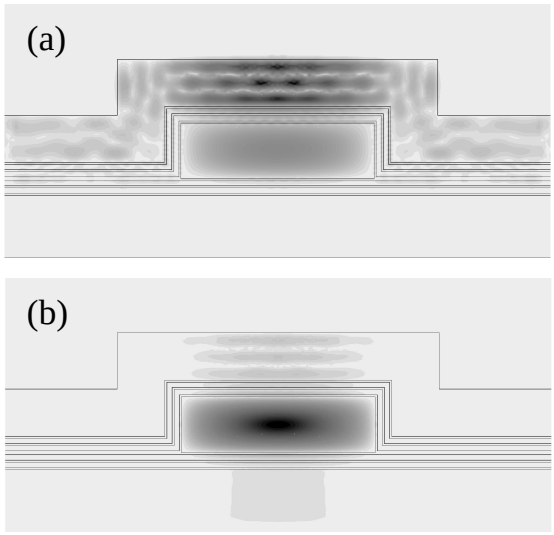


Fig. 6: Magnetic field modulus of the TM polarization of the fundamental mode at (a) $\lambda = 615$ *nm* and (b) $\lambda = 640$ *nm* for the ARROW with rectangular core of width $w_c = 12\ \mu m$, filled with ethylene glycol.

quence, the waveguide with the ethylene glycol-filled core can be used in a wider wavelength range, even around 750 *nm* where the water-filled core ARROW can sustain only a surface mode, instead of the one confined in the core for TE and TM polarizations.
Besides the wavelength shift and the narrower discontinuity, the qualitative behaviour is the same as the one described in the previous Section. In particular, Fig. 5 shows, for the TE polarization, the transition from surface to guided mode, when the wavelength increases from 628 *nm* to 640 *nm*, going away from the anti-crossing point.
In order to demonstrate the influence of the fundamental mode polarization on the surface mode behaviour, the distribution of the magnetic field modulus for the TM polarization is reported in Fig. 6 for two wavelength values similar to the previous ones. Being larger the discontinuity in the dispersion curve of the TM-polarized mode, and centered around a shorter wavelength, that is 620 *nm*, the field at 615 *nm* has been chosen in order to show the surface mode behaviour, while the wavelength has been kept fixed to 640 *nm* for the guided one. Notice that the field distribution for the surface mode with TM polarization, shown in Fig. 6(a), is similar to the one previously reported in Fig. 5(a) for the TE-polarized mode, so the change of the guided mode into the surface one occurs for both the fundamental mode polarizations. Moreover, it is interesting to compare the characteristics of the field of the guided mode for the two polarizations at the same wavelength of 640 *nm*, which is reported, respectively, in Fig. 5(b) and 6(b). While the TE-polarized field is completely confined in the ARROW liquid-filled core, some field components for the TM polarization leak into the higher refractive index layers at the top and the bottom of the rectangular core. This observation is also confirmed by the analysis of the confinement loss discussed in the next Section.

ARROW confinement loss
The Confinement Loss CL of the modes are deduced from the attenuation constant α as

$$CL = 20\alpha \cdot \log_{10} e \cdot \frac{1}{100} \simeq 0.087 \cdot \alpha \quad [dB/cm]\,, \quad (1)$$

and are reported in Fig. 7 in the wavelength range between 400 *nm* and 1000 *nm* for the TE-polarized fundamental mode, comparing the two hollow core ARROWs, filled with water and ethylene glycol. The wavelength range has been enlarged toward the lower wavelengths, in order to clearly observe the curve behaviour. Notice that the transmission spectrum of both the waveguides is abruptly interrupted by high CL peaks at the wavelengths corresponding to the anti-crossing points in the dispersion curves, due to the surface mode presence. Notice that two additional surface modes, one at about 466 *nm* for the ethylene glycol-filled core waveguide and one around 945 *nm* for the water-filled core one, have been demonstrated through this wider-band analysis of the confinement loss.
Looking at Fig. 7, it is important to underline that the liquid in the waveguide core strongly influences its confinement loss behaviour. In fact, both curves present a U-shaped profile with a minimum value, which is located around 780 *nm* when considering water and down shifts when filling the core with ethylene glycol. The CL levels provided by the two materials are, however, quite different. As can be expected, the refractive index of the ethylene glycol, higher than the water one, helps in focusing the field thus resulting in much lower losses. In particular, it is possible to

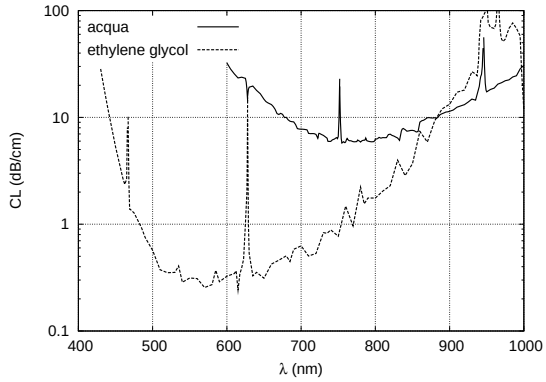


Fig. 7: Confinement loss versus the wavelength of the TE polarization of the fundamental mode for the ARROWs with rectangular core of width $w_c = 12\ \mu m$, filled with water and with ethylene glycol.

identify a spectral range of almost 300 *nm* where the guide presents CL lower than 1 dB/cm, even if broken off by the loss peak related to the anti-crossing point around 628 *nm*. The water core ARROW never reaches such CL values, being the minimum slightly lower than 6 dB/cm. This, however, does not prevent possible applications, for example in sensing systems, where typical waveguide lengths are of the order of few millimeters or few centimeters [4, 8]. The TM mode CL has been calculated as well for both the core liquids, showing, as expected, higher values with respect to the TE polarization. In particular, confinement loss higher than 3 dB/cm and 100 dB/cm has been obtained in all the considered wavelength range, respectively, for the ethylene glycol-filled and the water-filled ARROW. These high values render the TM polarization actually not guided in water-filled core ARROW, even for very short waveguides.

Conclusion

A detailed analysis of the guiding properties of ARROWs with a hollow core has been developed, for the first time to the authors' knowledge, in a wide wavelength range, between 600 *nm* and 900 *nm*. The field distribution, the dispersion curves and the confinement loss for both the TE and TM polarizations have been evaluated in water, as well as ethylene glycol filled rectangular core ARROW by applying a full-vector modal solver based on the FEM. Results have highlighted the differences due to the use of different liquid core material and allowed the transition from guided to surface mode in correspondence of the anti-crossing points of the dispersion curve to be described. The related confinement loss has been discussed as well, showing much lower CL levels for the ethylene glycol filled core and the TE polarization.

A further analysis on the effect of the core geometry, its dimension and the number of the cladding layers around the core will be done in future and also described at presentation time.

References

[1] M. A. Duguay et al, Applied Physics Letters, no. 1, p. 13, 1986.

[2] A. Bjarklev et al, Photonic Crystal Fibres, 1st ed., Kluwer Academic Publisher, 2003.

[3] D. Yin et al, Optics Express, no. 12, p. 2710, 2004.

[4] H. Schmidt et al, IEEE J. Selected Topics Quantum Electronics, no. 2, p. 519, 2005.

[5] D. Yin et al, Optics Express, no. 26, p. 10564, 2005.

[6] J. P. Barber et al, IEEE Photon. Technol. Letters, no. 6, p. 28, 2006.

[7] P. Measor et al, CLEO, Paper JThC89, 2006.

[8] R. Bernini et al, WFOPC, p. 254, 2005.

[9] D. Yin et al, CLEO, Paper CTuB1, 2006.

[10] J. A. West et al, Optics Express, no. 8, p. 1485, 2004.

[11] F. Poli et al, OFC, Paper OML8, 2007.

[12] A. Cucinotta et al, IEEE Photonics Technology Letters, no. 11, p. 1530, 2002.

[13] L. Vincetti et al, Optical and Quantum Electronics, 2006.

Silicon-on-Insulator Slot Waveguides for Integrated Optical Sensing

Francesco Dell'Olio and Vittorio M. N. Passaro
Politecnico di Bari, Dipartimento di Elettrotecnica ed Elettronica, via Edoardo Orabona n. 4, 70125 Bari, Italy
(e-mail: passaro@deemail.poliba.it)

Abstract: *Silicon-on-Insulator slot waveguides for highly sensitive and compact photonic integrated sensors are theoretically proposed and discussed in this paper. Slot guiding structure sensitivity has been investigated by 3D Finite Element Method and results are compared with those related to rib or wire sub-micrometer silicon waveguides.*

Introduction

In recent years, there is a growing interest for highly sensitive optical sensors in different areas such as process control, medical diagnostics, environmental monitoring and biotechnology. In this framework, integrated optical sensors have attracted considerable attention because of their immunity to electromagnetic interference, high sensitivity, good compactness and robustness and high compatibility with fiber networks [1].

Different kinds of guided-wave optical sensors have been proposed, such as those based on directional couplers [2], Mach-Zehnder interferometers [3], Bragg gratings [4], and microring resonators [5]. In these sensors the shift of a chemical/physical quantity to be sensed affects the propagating mode effective index, which is measured in different ways, according with sensor architecture. The effective index change is usually produced by a change of cover medium refractive index. Measurement sensitivity depends on the distribution of evanescent optical field in the cover medium, so one of the most important design task is the waveguide optimization in order to maximize its sensitivity.

CMOS-compatible technologies are widely used for fabrication of integrated optical sensors because of their low cost and possibility to monolithically integrate photonic and electronic devices. Recently sub-micrometer silicon wire waveguides [6], realized using Silicon-on-Insulator (SOI) technology, have been demonstrated as very attractive for evanescent field integrated optical sensors because they exhibit a sensitivity significantly greater than that assured by other kinds of guiding structures, such as rib waveguides in silicon oxinitride (SiON), polymeric materials or silica [7]. Adopting a Si-wire waveguide, a highly sensitive microring resonator-based ammonia optical sensor has been proposed [8].

When two Si-wires are very close to each other, it is possible to realize another kind of SOI nanometer guiding structure, usually indicated as SOI slot waveguide [9]. It enables to confine optical power in a narrow low-index gap region between the two high-index Si-wires. A great variety of optical devices can be realized by using slot waveguides, including microring resonators [9], optical modulators [10], electrically pumped light emitting devices [11], directional couplers [12], all-optical logic gates [13] and beam splitters [14]. A Finite Element Method (FEM)-based modal investigation devoted to study slot waveguide geometrical parameter influence on optical power fraction confined in the low-index gap region has been recently performed [15].

However, SOI slot waveguides for integrated optical sensors represent a quite unexplored research field.

In this paper, we demonstrate that SOI slot waveguides (see Fig. 1) exhibit a sensitivity significantly higher than that of other sub-micrometer SOI waveguides. Moreover, we have optimized the slot guiding structure geometrical parameters to maximize its sensitivity to changes of cover medium refractive index. As operating wavelength λ =1550 nm has been assumed.

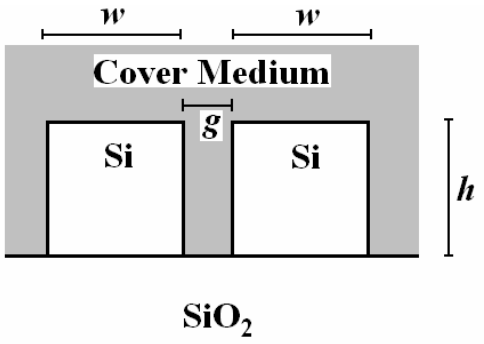


Fig. 1. SOI slot waveguide structure.

Sensitivity Calculation

Slot waveguides sensitivity to changes of cover medium refractive index can be expressed as:

$$S_w = \frac{\partial N}{\partial n_c} \tag{1}$$

where N is the effective index of mode propagating in the guiding structure and n_c is the cover medium refractive index.

According with variational theorem for dielectric waveguides, we can write:

$$S_w = \left.\frac{\partial N}{\partial n_c}\right|_{n_c = n_c^0} = 2c\, n_c^0 \iint_C |\mathbf{E}|^2 \, dxdy \tag{2}$$

where c is speed of light in vacuum, C indicates cover medium region, n_c^0 is the unperturbed value of cover medium refractive index and **E** is the normalized electric field of optical mode propagating

in the slot structure.

From Eq. (2), it is evident that waveguide sensitivity depends on the optical field confinement factor in the cover medium. As defined in Eq. (1), it can be numerically estimated by varying the cover medium refractive index n_c in a narrow range and finding the relevant change of effective index N. To determine effective index N, the rigorous numerical approach based on 3D full-vectorial FEM has been applied.

Slot waveguide sensitivity dependence on Si-wire width w has been investigated, for gap region width g equal to 50 nm, 100 nm and 200 nm and quasi-TE or quasi-TM modes (as in Fig. 2 and Fig. 3, respectively). The Si-wire height is h = 250 nm. As cover medium an aqueous solution containing a chemical substance (as, for example, glucose) whose concentration has to be measured, has been assumed. When analyte concentration in the solution changes, a shift of cover medium refractive index is induced. Cover medium refractive index unperturbed value n_c^0 has been fixed as equal to 1.33 (water), while cover medium variation range was between 1.333 and 1.335.

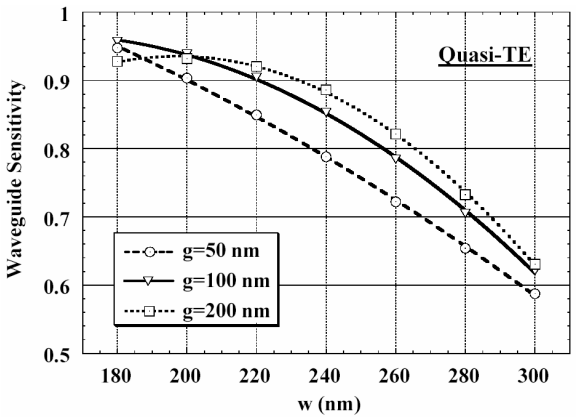


Fig. 2: Slot waveguide sensitivity dependence on w, for quasi-TE mode and g=50 nm, 100 nm and 150 nm (h=250 nm).

From data reported in Fig. 2 and 3, it is evident as quasi-TE mode is significantly more sensitive to cover medium refractive index changes than quasi-TM one. This difference is due to the fact that optical field confinement in the cover is larger for quasi-TE than for quasi-TM mode (see Fig. 4 and 5). For example, optical field confinement factor in the cover medium is equal to 67.31% for quasi-TE and 41.41% for quasi-TM mode, assuming a slot waveguide with h=250 nm, w= 250 nm and g=100 nm.

For quasi-TE mode, slot waveguide sensitivity decreases monotonically when w increases either for g=50 nm or g=100 nm, whereas sensitivity dependence on w exhibits a maximum (0.932, corresponding to w=200 nm) for g=200 nm. However, the maximum sensitivity (0.957) is obtained for g=100nm and w=180nm. For quasi-TM mode, sensitivity dependence on w is monotone for g=50 nm and g=200 nm and exhibits a maximum (corresponding to w=220 nm) for g=100 nm. Maximum value (0.518) is obtained for g=100 nm and w =220 nm.

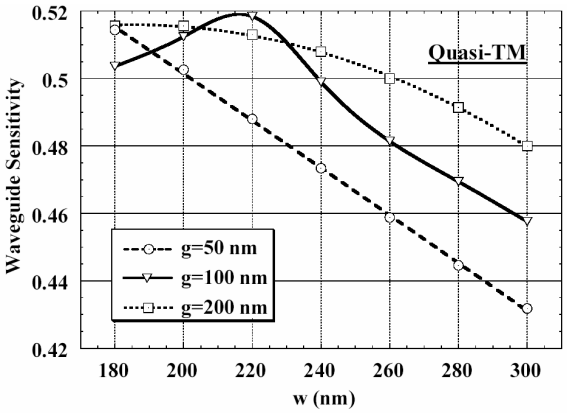


Fig. 3: Slot waveguide sensitivity dependence on w, for quasi-TM mode and g= 50 nm, 100 nm and 150 nm (h=250 nm).

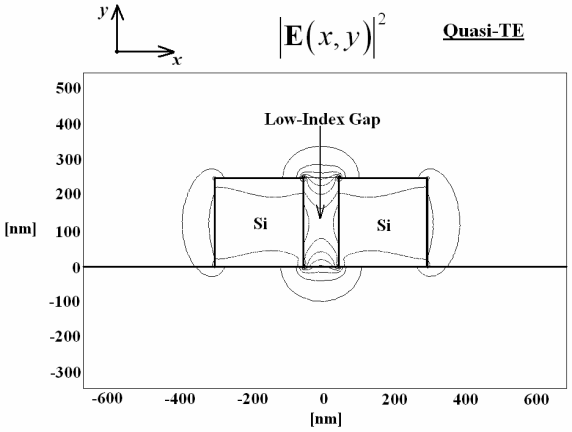


Fig. 4: Squared electric field module for quasi-TE mode (h=250 nm, w=250 nm, g=100 nm, n_c=1.333).

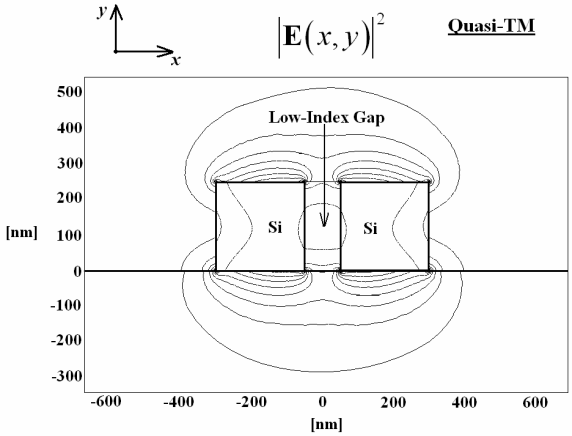


Fig. 5: Squared electric field module for quasi-TM mode (h=250 nm, w=250 nm, g=100 nm, n_c=1.333).

To compare slot waveguides sensitivity with that of other SOI sub-micrometer structures, sensitivity dependence on waveguide width for either SOI rib waveguide (Fig. 6) or Si-wire waveguide (Fig. 7) has been investigated. In both cases we assume a

waveguide height equal to 250 nm and an aqueous solution as cover medium (index 1.33). For SOI rib waveguide an etch depth d_{rib} =200 nm has been fixed. Results are shown in Fig. 8 and 9 considering both quasi-TE and quasi-TM modes.

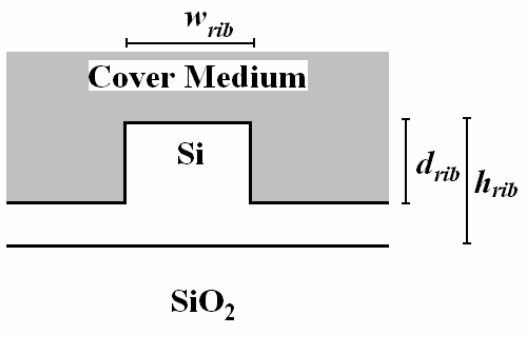


Fig. 6: SOI rib waveguide structure.

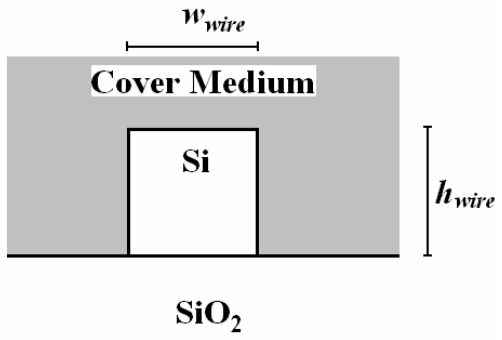


Fig. 7: Si-wire waveguide structure.

For SOI rib waveguide, quasi-TM mode assures a higher sensitivity than quasi-TE one, whereas for Si-wire waveguide, quasi-TM case is more sensitive than quasi-TE one only for w_{wire} >320 nm. Moreover, it is possible to notice that Si-wire waveguide exhibits a higher sensitivity with respect to SOI rib waveguides in all considered cases. Moreover, sensitivities for both SOI rib and Si-wire waveguides are always lower than that assured by a SOI slot waveguide when quasi-TE mode propagates.

To further maximize the SOI slot waveguide sensitivity, we have investigated the influence of *h*/*w* ratio. Assuming *g* = 100 nm, waveguide sensitivity has been calculated versus *h*/*w* varying in the range from 1.2 to 1.8, with *w* = 140 nm, 180 nm and 220 nm, respectively. Quasi-TE (in Fig. 10) and quasi-TM modes (Fig. 11) have been considered.

For quasi-TE mode, sensitivity monotonically increases by increasing *h*/*w,* but the relevant slope decreases when *w* increases. For *w*=180 nm and *h*/*w*=1.8 (i.e. *h*=324 nm), the maximum sensitivity has been obtained (S_w = 1.0076).

For quasi-TM mode and *w*=140 nm, sensitivity increases monotonically when *h*/*w* increases. For *w*=180 nm, sensitivity dependence on *h*/*w* exhibits a maximum for *h*/*w* =1.4. Finally, for *w*=220 nm, sensitivity monotonically decreases when *h*/*w* increases.

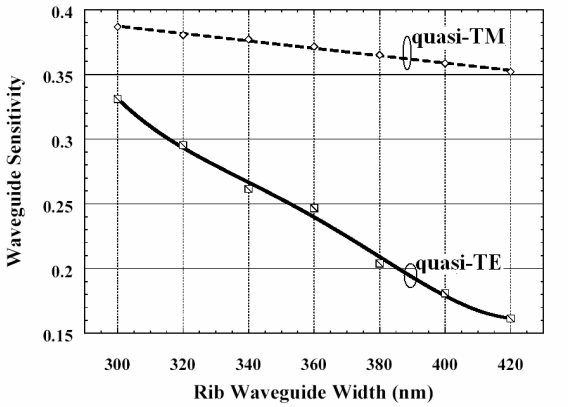


Fig. 8: SOI rib waveguide sensitivity dependence on w_{rib}, for quasi-TE and quasi-TM modes (h_{rib}=250 nm, d_{rib}=200 nm).

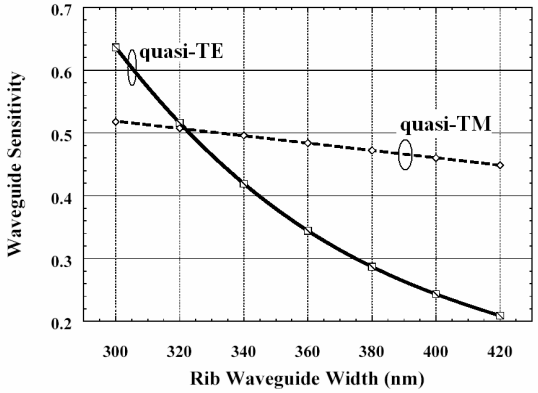


Fig. 9: Si-wire waveguide sensitivity dependence on w_{wire}, for quasi-TE and quasi-TM modes (h_{wire}= 250 nm).

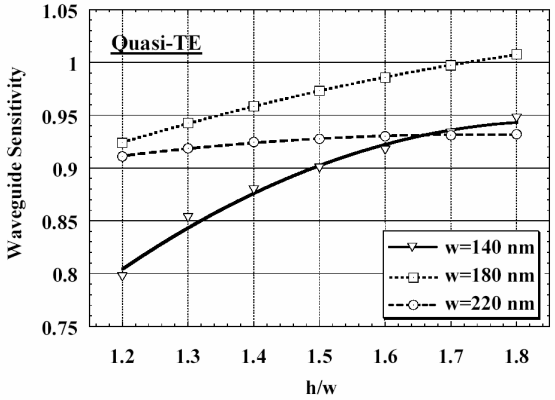


Fig. 10: SOI slot waveguide sensitivity dependence on *h*/*w*, for quasi-TE mode and *w*=140 nm, 180 nm and 220 nm (*g*=100 nm).

Slot waveguide sensitivity dependence on *h*/*w* can be expressed analytically by a quadratic polynomial. Thus we can write:

$$S_w = c_0 + c_1\left(\frac{h}{w}\right) + c_2\left(\frac{h}{w}\right)^2 \qquad (3)$$

where c_0, c_1 and c_2 are fitting parameters, whose values are reported in Table 1.

Finally, for *w*=180 nm, *h*=324 nm and quasi-TE mode, sensitivity dependence on *g* has been investigated (see Fig. 12). The maximum sensitivity

(1.0076) has been obtained exactly when g = 100 nm.

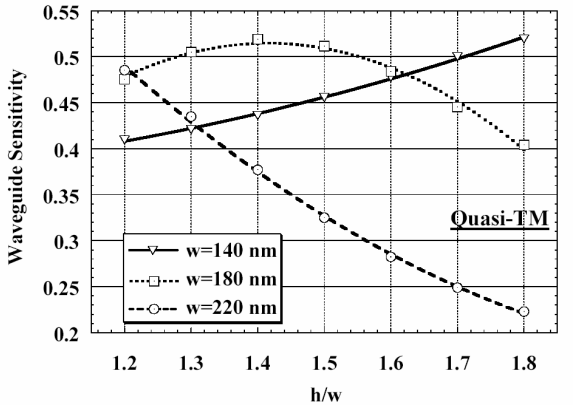


Fig. 11: SOI slot waveguide sensitivity dependence on h/w, for quasi-TM mode and w=140 nm, 180 nm and 220 nm (g=100 nm).

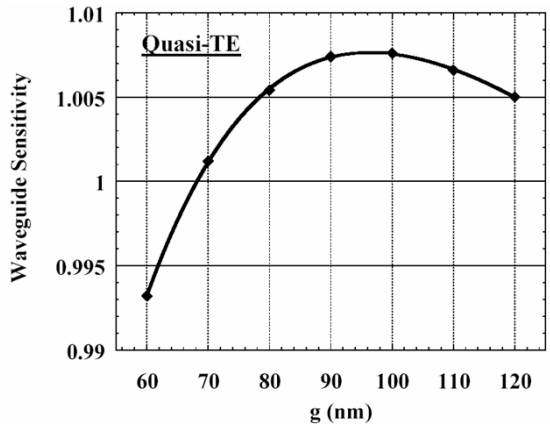


Fig. 12: SOI slot waveguide sensitivity dependence on g, for quasi-TE mode, w=180 nm and h = 324.

Table 1: Fitting parameters related to slot waveguide sensitivity dependence on h/w.

	w	c_0	c_1	c_2
TE	140	-0.161	1.186	-0.318
	180	0.584	0.380	-0.080
	220	0.719	0.244	-0.070
TM	140	0.390	-0.101	0.097
	180	-1.056	2.218	-0.783
	220	1.705	-1.390	0.314

The optimized SOI slot waveguide having h=324 nm, w=180 nm and g=100 nm has been investigated for n_c=1 (air as cover medium) and n_c=1.33 (water as cover medium). Effective index, birefringence, optical field confinement factor in the cover medium and effective index dispersion (defined as the derivative of effective index with respect to wavelength) have been calculated, either for quasi-TE or quasi-TM modes (see Table 2).

Conclusions

Sensitivity of SOI slot waveguide has been optimized in this paper. A set of geometrical parameters permitting to achieve a sensitivity value of 1.0076 has been found. This value is significantly larger (difference around 40%) than that obtainable adopting any Si-wire or SOI rib waveguide.

Moreover, has been proved that slot guiding structures are the most attractive for SOI technological platform in nanometer evanescent field photonic integrated sensors.

Table 2: Parameters of optimized SOI slot waveguide (h=324 nm, w=180 nm, g=100 nm).

Parameter	$n_c = 1$	$n_c = 1.33$
Effective index (TE)	1.252891	1.870414
Effective index (TM)	1.578634	1.989995
Birefringence (N_{TM} - N_{TE})	0.737	0.411
Effective index dispersion (TE) [nm^{-1}]	-8.02×10^{-4}	-7.81×10^{-4}
Effective index dispersion (TM) [nm^{-1}]	-1.38×10^{-3}	-1.19×10^{-3}
Confinement factor in cover medium (TE)	70.5%	76.4%
Confinement factor in cover medium (TM)	38.0%	41.2%
Waveguide sensitivity (TE)	-	1.0076
Waveguide sensitivity (TM)	-	0.4040

References

1 J. S. Wilkinson, Proc. ECIO, paper ThB3-1, 2005.
2 B. J. Luff et al., Opt. Lett., p. 618, 1996.
3 F. Prieto et al., Nanotechnology, p. 907, 2003.
4 W. C. L. Hopman et al., IEEE J. Sel. Top. in Quantum. Electron., p. 11, 2005.
5 C. Y. Chao et al., IEEE J. Sel. Top. in Quantum. Electron., p. 134, 2006.
6 H. Yamada et al., IEEE J. Sel. Top. in Quantum. Electron., p. 1371, 2006.
7 A. Densmore et al., IEEE Photon. Technol. Lett., p. 2520, 2006.
8 F. Dell'Olio et al., IMCS, Paper MO1.5.3#103, 2006.
9 Q. Xu et al., Opt. Lett., p. 1626, 2004.
10 T. Baehr-Jones et al., Opt. Express, p. 2516, 2005.
11 C. A. Barrios et al., Opt. Express, p. 10092, 2005.
12 T. Fujisawa et al., Opt. Lett., p. 56, 2006.
13 T. Fujisawa et al., J. Opt. Soc. Am. B, p. 684, 2006.
14 T. Fujisawa et al., IEEE Photon. Technol. Lett., p. 1246, 2006.
15 P. Müllner et al., IEEE Photon. Technol. Lett., p. 2557, 2006.
16 Comsol Multiphysics by COMSOL ©, ver. 3.2, single license, 2005.

Peculiarity of multi-reflector filtering technology

Andrei Tsarev

Laboratory of Optical Materials and Structures
Institute of Semiconductor Physics, Siberian Branch of Russian Academy of Science
Prospect Lavrenteva, 13, Novosibirsk, 630090, Russia
tsarev@isp.nsc.ru

Abstract: *Paper described recent results of numerical investigation by FDTD method of novel widely tunable TO and AO filters and reconfigurable optical add/drop multiplexers (ROADMs) employing multi-reflector beam expanders. A novel design of thin SOI ROADM structures that utilizes 2D-grating, nano-grooves, and double waveguides with p^+-doping regions to provide single mode behavior and better manufacturability is presented.*

Introduction

Reconfigurable optical add/drop multiplexers (ROADMs) are among the most demanded devices that can increase flexibility and capacity of wavelength-division-multiplexing (WDM) fiber optic networks. A great number of different technologies and device structures for ROADMs implementation has been already developed [1]. Although a great progress has been achieved in recent years, none of actual technologies could be regarded as ideal to substitute all the others in the near future.

The large part of current research activity is focused on further improvement of existing technologies as well as on the development of new emerging technologies, in order to develop better optical devices for WDM.

In order to reduce the cost per channel needed for the commercialization of WDM systems, tunable optical filters (TOFs) and ROADMs based on integrated optics and patented multi-reflector (MR) filtering technology have been already proposed [2-7]. This technology combines physical phenomena of wave-guiding, reflection and constructive interference in a novel way. The MR filtering technology accomplishes filtering operation by spatially expanding the optical beam through a patented MR-beam expander (BE) [8], then tuning and filtering the desired wavelength by an acousto-optic (AO) Bragg sell (see **Fig. 1**.) or by a set of tunable channel waveguides (see **Fig. 2**) and by constructive interference of multiple sub-beams, combined at the output channel waveguide by another beam expander. Multi-reflector technology provides the possibility of developing tunable devices (TOF and ROADM) on different materials (silicon, polymer, lithium niobate) [2-5], allowing partial reflector manufacturing, optical phase tunability and low optical losses in the single-mode waveguides. Nowadays, MR-filtering technology has not yet been studied experimentally and its theoretical study is not completed, containing a lot of unresolved aspects.

This paper described general peculiarity of milti-reflector filtering technology that is accompanied by a number of numerical simulations performed by finite difference time domain (FDTD) method in order to demonstrate the device proof-of-concept.

I. Multi-reflection technology in $LiNbO_3$

The origin of multi-reflector filtering technology comes from the research devoted to developing compact acousto-optic tunable filters (AOTF) with improved spectral resolution. This aim accomplished by implementing highly dispersive multi-reflector beam expanders (MR-BEs) (see **Fig. 1**) that evolve the fruitful conception of holographic grating beam expander. An MR-BE consists of a channel optical waveguide of chalcogenide As_2S_3 glass (on $LiNbO_3$ substrate) that is crossed by periodically spaced partial reflector strips.

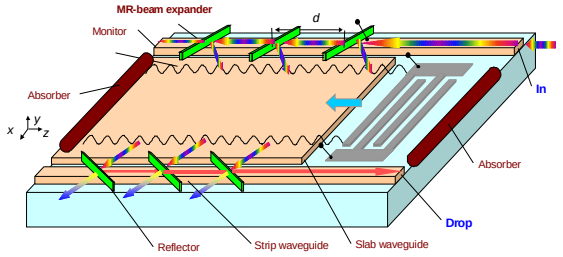


Fig.1: Noncollinear AOTF with MR beam expanders.

Quantitative description of MR-AOTF is very complicated and can be studied only numerically. Here we present the first simulation of device by FDTD method. To fasten simulations 3D structure has been replaced by 2D analogy using the effective index method (EIM) that decomposes 3D strip waveguide into two 2D slab waveguides. By this approach, we examine MR-AOTF by means of 2D FDTD method by software tool FullWAVE from RSoft Design Group, Inc. [9]. Practically, this 2D situation corresponds to the 3D-waveguide structure with reflectors whose area overlaps guided mode in transverse direction (Y).

Typical results of MR-AOTF simulation by the FDTD method is presented in **Fig**. **3**. Effect of phase grating induced by SAW is examined by static grating of refractive index with period around L = 1.2 μm, and aperture L = 50 μm. The beam expander splits input optical beam into 32 sub-beams that

interact with SAW. Note, that diffraction efficiency of expanded multi-beam light is equal to that of single optical beam with the same total aperture (150 μm). Diffracted beam enters the second beam expander and at particular optical wavelength it is effectively dropped and forwarded to the end of device. By changing the SAW wavelength (1.1μm<L<1.4 μm) one can change also filtered optical wavelength (see **Fig. 3**) within the large tunable range 98 nm to work with C- or L- bands.

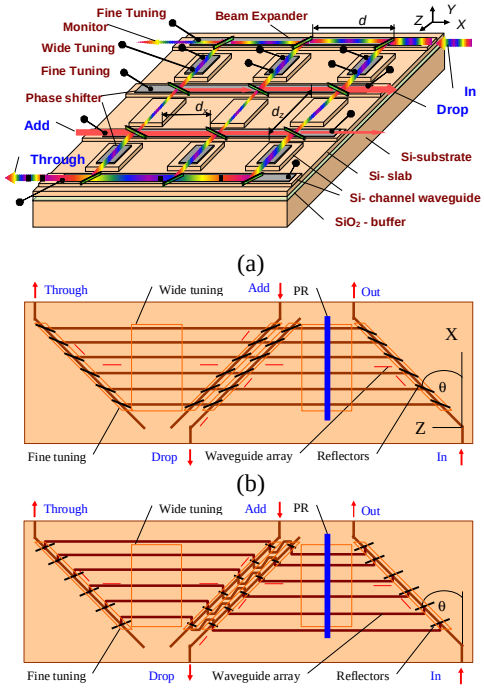


Fig. 2: General view of thermo-optic MR-ROADM with (a) rectangular; (b) slanted arrangement with large incident angle; (c) slanted arrangement with small incident angle.

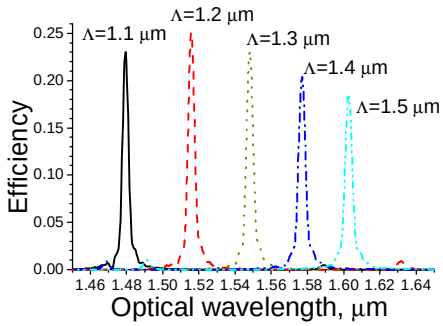


Fig. 3: The response of MR-tunable filter at different SAW wavelengths. FWHM = 4.5 nm.

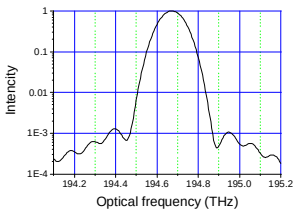


Fig. 4: Simulated response of MR-AOTF. SAW frequency 1227 MHz, aperture 0.58 cm, internal loss IL_D= -3.6 dB.

Current *3dB* linewidth (FWHM=*4.5* nm) is a result of small device dimensions *(150´70 mm²)* that can be analysed by FDTD due to limited memory and capacity of our computer. Our independent simulations taking into account spectrum approach [4] show that by some increase of device area (within 1 cm²) and by optimum choose of variable reflection coefficients of beam expander reflectors one can develop set of AO devices working with 25 GHz or smaller ITU grid (see **Fig. 4**).

II. Multi-reflection technology in SOI

The general view of MR-ROADM based on Silicon-on-Insulator (SOI) rib waveguides and thermo-optic phase shifters is shown in **Fig. 2**. Typical MR-ROADMs [3, 5] contain four multi-reflector beam expanders [8], constituted by the optical waveguide array crossed by periodically spaced partial reflector strips. SOI partial reflectors can be fabricated by etching a deep groove and filling it by a material with different optical properties. The technology of deep etching and filling is widely used for MEMS and Bragg reflectors.

The operation of thermo-optic MR-ROADM has a lot of common features with the AO counterpart. Optical signal that comes to the Drop and Through outputs strongly depend on the phase delay of every sub-beams that passes through the multiple partial reflectors along the optical waveguides. Condition of constructive and destructive interference for the particular filtering optical wavelength could be adjusted by thermo-optic phase shifters of fine and wide tuning, placed along the beam expanders and the connecting waveguides, respectively. Rectangular ROADM arrangement (see **Fig. 2a**) is more compact, but it is strong polarization dependent that need polarization diversity [5]. Slanted arrangement (see **Fig. 2b, c**) provides better tuning rate ($\partial l/\partial T$ up to 0.6 nm/°C) [2, 5] and could provide low polarization dependence (PDL and PDF) by inserting additional polyamide half-plate for polarization rotation (PR).

The typical simulation (by FDTD) of MR-ROADM is shown in **Fig. 5, 6.** It proves that device could realize Drop/Through function. Better performances provides by the device with the large number of reflectors with variable reflector coefficients (see **Fig. 7a**). Simulation of this device (see **Fig. 7b**) has been done by the ray model and taking into account phase delays of all reflected and transmitted sub-beams. It proves that MR-ROADM can be implemented for 25 GHz or smaller ITU grids.

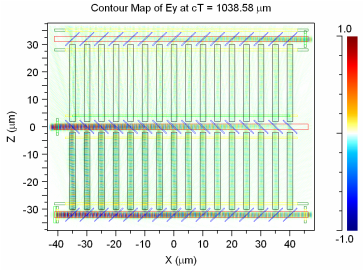


Fig. 5: Simulation of MR-ROADM at Drop wavelength.

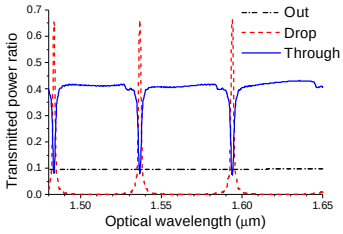
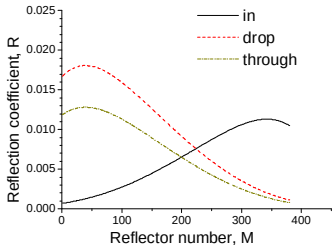
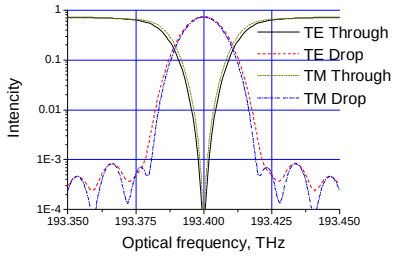


Fig. 6: Simulated frequency response of MR-OADM with 32 slanted reflectors (j = 45°). FWHM = 1.6 nm.



(a)



(b)

Fig. 7: Reflector coefficients apodization (a) and frequency response (b) of the 25 GHz slanted ROADM for two polarizations. Internal losses. TM: IL_D = –1.27 dB, IL_T = –1.31 dB; TE: are IL_D = –1.42 dB, IL_T = –1.46 dB.

III. Multi-reflection technology in thin SOI

Recently, two-dimensional grating [11] etched in a thin (220 nm) silicon-on-insulator waveguide had been used as a fiber-to-ridge waveguide coupler. This 2D grating is also perspective for multi-reflector technology as it provides additional possibility of polarization diversity without polarization rotators. This device is very compact and couples orthogonal modes from a single-mode optical fiber into two quasi-TE modes of two ridge waveguides that could be connected to the input/output of the photonic integrated circuit. The problem is that ridge waveguide has the dimension 220 nm by 10 μm that has multi-mode behavior which strongly disturbs device performances.

We propose new double waveguide design that is suitable for thin SOI devices. From the well-known paper by Soref et al. [12] one could derive simple relation between obtained changes in refractive index (Dn) and absorption ($\Delta\alpha$) at the wavelength of interest (λ_0=1.55 μm) due to presence of free electron (N_e) and hole concentration (N_h) in silicon:

$$\Delta\alpha_e = 0.12\times|\Delta n_e| \qquad (1)$$
$$\Delta\alpha_h = 0.16\times|\Delta n_h|^{5/4}$$

Thus total change of complex refractive index due to the charge effect is:

$$\Delta n=\Delta n + jn', \qquad (2)$$

where $n' = \Delta\alpha\lambda_0/(4\pi)$, $\Delta n=\Delta n_h+\Delta n_e$, $\Delta\alpha= \Delta\alpha_h + \Delta\alpha_e$. From equation (1) one can see that if $\Delta n<0.3$ then the hole doping is more preferable as it provides smaller optical losses at the same index change with quality factor $|\Delta n_h|^{1/4}$. Thus we use p^+ doping for all structures discussed below.

Multi-mode behavior of thin ridge waveguides could be compressed by manufacturing heavily doped p^+ regions Wg on both sides of the Si-ridge of width W. One can see from data of **Fig. 8** that fundamental mode of such double waveguide has negligible losses related to the losses of the high order modes. Heavily doped p^+ regions could be also used for manufacturing the slanted reflectors of MR-ROADM (see **Fig. 2b)**. Dependence of reflected and transmitted power for the incident angle 75^0 is shown in **Fig. 9**. Although the additional absorption losses are noticeable but they provides possibility to manufacture device with suitable performances.

Alternative method to manufacture partial reflectors for MR-ROADM design presented in **Fig. 2c** is based on the deep groove technology. For the case if quasi-TE mode incidents the reflector at close to the Brewster angle then reflective coefficient could be sufficiently small that will make possible to eliminate complex back filling of the groove by the material with appropriate refractive index. Results presented in **Fig. 10** shows for the case of nano-width groove the reflection coefficient could be variable in the appropriate range (see **Fig. 7a)** by changing the width and incline angle of the groove. One must mention that at Brewster angle the reflected filed is distorted and energy of fundamental mode is less than the total reflected power (due to the presence of high order modes). As it is shown on Fig.8 these modes decay due to the heavy doped regions of double waveguide.

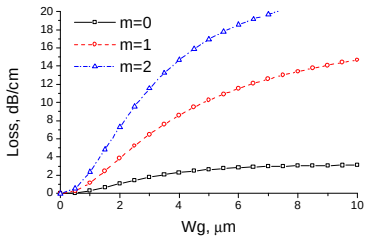


Fig. 8: Optical losses in double waveguide as a function of p^+-doped width Wg. Undoped width W=8, Dn_h=0.002.

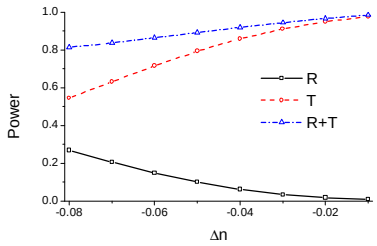


Fig. 9: Dependence of the power reflection and transmitting coefficients as a function of $\Delta n=\Delta n_h$.

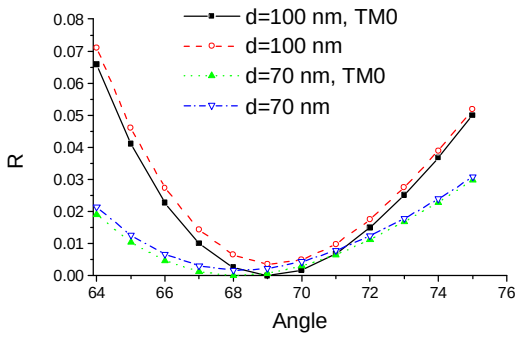


Fig. 10: Dependence of the power reflection as a function of the incident on the deep groove. Waveguide width 10 μm. Solid dots corresponds to the reflection to the fundamental TM_0 mode. 2D FDTD simulation.

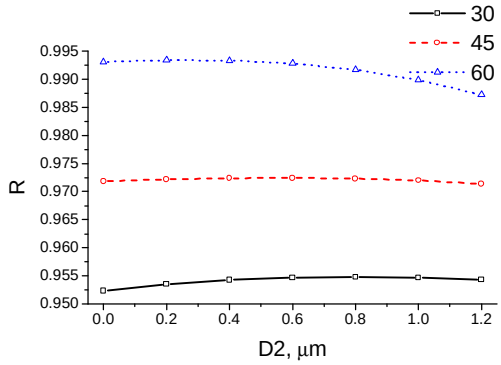


Fig. 11: Dependence of the corner reflection as a function of the waveguide shift (D2) at different incident angle.

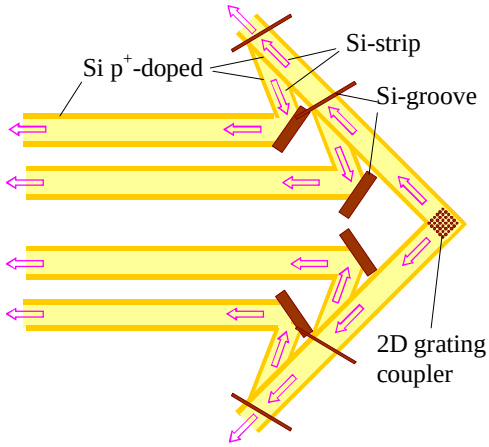


Fig. 12: General design of nono-scale SOI MR-ROADM.

MR-ROADM design presented on **Fig. 2c** needs implementation of small area bends. Deep grooves in double waveguide with heavy dopes sides provides very small optical losses for the large area of bend angles (see **Fig. 11).** All these provide the new designs of MR-ROADM that also utilize 2D-grating, heavy p^+-doping and nono-scale grooves. The part of this design is presented on **Fig. 12** and show the way to provide polarization diversity of the device.

Conclusions

The paper described recent results of theoretical investigation of the novel widely tunable reconfigurable optical add/drop multiplexers (ROADMs) and tunable filters employing multi-reflector beam expanders. It provides detailed description of devices based on Silicon-on-Insulator technology with thermo-optic tuning as well as the chalcogenide As_2S_3 glass on $LiNbO_3$ structures with acoustooptic tuning. A variety of different design architectures are described including a novel thin SOI double-waveguides for ROADM that utilizes nono-grooves and p^+-doping to provide better device manufacturability. Theoretical examination of multi-reflector filtering technology has been performed by appropriate application of finite difference time domain (FDTD) method, spectral approach and ray model (depending on the case study). Multiple numerical examples illustrate peculiarity of this new technology that provides wide tunability (within total C- or L-band) and remarkably high tuning rate (up to 0.6 nm/°C) without applying the Vernier principle. These kind of tunable filters and multiplexes are intended for flexible redirection of multi-hundred WDM wavelength channels in intelligence all optical networks with high dense ITU grid 25 GHz.

Acknowledgments

The author thanks Prof. Vittorio M. N. Passaro from the Politecnico di Bari, Italy, as well as Dr. E. Kolosovsky from the Institute of Semiconductor Physics, Novosibirsk, Russia for the fruitful cooperation and helpful discussions concerning muli-reflector filtering technology. He would like to thank Company RSoft Design Group, Inc.[9] that provides user licence and technical support for powerful Rsoft Photonic CAD Suite 7.0 including FDTD software.
This work is done under support by Grant No 05-02-08118-ofi-a from Russian Fund for Basic Research.

References

1 O.E.Naniy, Lightwave Russian edition, no 2, p. 47, 2004.
2 A.V.Tsarev et al, ECIO, p. 394, 2005.
3 V.M.N. Passaro, et al, *Optics Express*, vol. **13**, p. 3429, 2005
4 A.V.Tsarev et al, Optoelectronics, Instrumentation and Data Processing, No 6, p. 93, 2006.
5 A.V.Tsarev et al, in Silicon Photonics, Editor: Vittorio M N Passaro, Research Signpost, Trivandrum, Kerala, India: ISBN: 81-308-0077-2, chapter 3, p. 47-77, 2006.
6 A.V.Tsarev, USA Patent No 6,999,639, 2006.
7 A.V.Tsarev, USA Patent No 7,092,139, 2006.
8 A.V.Tsarev USA Patent No. 6,836,601, 2004.
9 www.rsoftdesign.com.
11 D. Taillaert et al, *IEEE Photon. Technol. Lett.*, no.9, p. 1249, 2003.
12 R.A.Soref et al, IEEE J. Quantum Electron., p.73, 1986.

Investigation of Silicon Slot-based Directional Couplers

Francesca Magno (1), Vittorio M. N. Passaro (1), Francesco Dell'Olio (1) and Francesco De Leonardis (2)
1) Dipartimento di Elettrotecnica ed Elettronica, Politecnico di Bari, *passaro@poliba.it*
2) Dipartimento di Ingegneria dell'Ambiente e per lo Sviluppo Sostenibile, Politecnico di Bari

Abstract: *A theoretical investigation of optical directional couplers based on silicon slot waveguides is carried out. The influence of various geometrical parameters on the coupling length is studied. A number of interpolation curves are extracted and presented for design purposes. Although the results are obtained for a specific technology, the theoretical approach is very general.*

Introduction

Silicon Photonics is increasingly important in integrated optics for technology and cost reasons. Silicon is transparent in the range of optical telecommunication wavelengths (1.3 and 1.55 μm) and is a well understood and robust material, available in large size, good quality and low price. Recently, several silicon based active and passive devices with high performance have been demonstrated.

Moreover, there is a current trend in silicon photonic circuits to move to smaller device dimensions for improved cost efficiency and device performance. In this scenario, very recently slot waveguides are attracting much attention [1].

A slot waveguide structure is based on a low index (air or SiO_2) sub-micrometer slot embedded between two silicon wire waveguides. In such waveguide geometry, the optical field in the low refractive index region is enhanced with respect to the silicon ones, because of the electric field discontinuity at the high index contrast interfaces.

Using slot waveguides, many optical devices have been already realized and proposed, including directional couplers [2], all-optical logic gates [3], beam splitters [4], ring resonators with high quality factor [5], optical modulators [6], light emitting devices with strong light confinement and enhanced emission properties [7]. A finite element method modal investigation has been performed [8] to show the possibility of confining more than 50% of optical power in the low-index gap region of a SOI slot waveguide, by optimizing its geometrical parameters.

Directional couplers are routinely used for a large variety of applications and functions related to lightwave technology. Directional couplers composed of two parallel slot waveguides have been experimentally demonstrated [9], but a detailed theoretical investigation on these devices has never been carried out.

In this paper, we use the Coupled Mode Theory (CMT) and the Finite Element Method (FEM) to investigate directional couplers based on slot waveguides. We have also compared our approach with simulation results obtained in other papers using different methods.

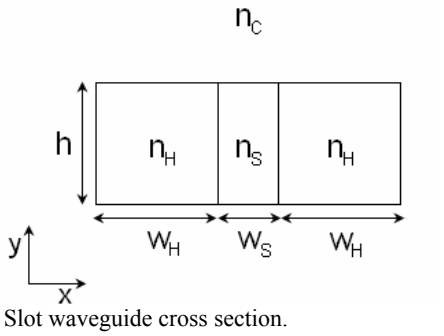


Fig. 1: Slot waveguide cross section.

Slot waveguide investigation

In this paper a horizontal slot waveguide geometry is assumed, in which the quasi-TE modes, polarized along *x* axis (see Fig. 1), are strongly confined in the slot region. The operating wavelength is 1550nm. There exist also quasi-TM modes, but they are not only confined in the slot region but mainly in the whole waveguide (including the two high index regions).

The slot waveguide is formed by a silicon oxide slot (n_S = 1.46) embedded by two silicon wires (n_H = 3.48). The whole waveguide is surrounded by silicon oxide (n_C = 1.46).

First, we have employed FEM [10] to study the birefringence of the slot waveguide in Fig. 1. Our analysis started with the following dimensions: waveguide height h = 250nm and high index region width w_H = 200nm. The slot width w_S has been varied from tens of nanometers to 200nm.

Fig. 2 shows a graph of the variation of the TE/TM fundamental mode effective index difference ($\Delta N = N_{TE} - N_{TM}$) versus the slot width for various waveguide heights, namely 250nm, 300nm and 350nm. In the first case, the slot width for zero birefringence (ZBR) is 75.2nm, in the second it is 17.7nm, and in the third case it is smaller than 10nm.

For larger values, the slot width has less influence on the mode birifrangence in all cases, especially for larger waveguide heights.

We have also evaluated the fraction of optical power confined in the slot (Fig. 3). For h = 250nm, the ZBR slot width provides also a good power confinement, close to the maximum (nearly 26%). Increasing the waveguide height, the maximum power confinement becomes higher, but the relevant slot widths are far from ZBR points.

Directional coupler investigation

We have investigated directional couplers formed by two parallel slot waveguides, as described above. We have denoted with d the distance between the centers

of the two slot waveguides. The theoretical approach is based on CMT and FEM.

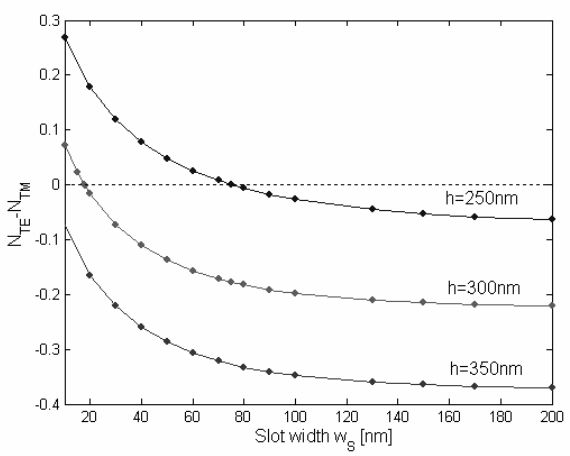


Fig. 2: Birefringence of slot waveguide for various slot heights and widths.

According to CMT, the coupling coefficient between two optical modes propagating in two adjacent optical waveguides can be expressed as

$$\kappa = \frac{1}{2}(\beta_s - \beta_a) \qquad (1)$$

where β_s and β_a are the propagation constants of symmetric and anti-symmetric modes within the directional coupler, respectively. Using 2D full-vectorial FEM to perform modal analysis of the coupler cross-section, it is possible to calculate β_s and β_a with great accuracy.

The coupling length L_C is related to coupling coefficient by the following formula:

$$L_C = \frac{\pi}{2\kappa} \qquad (2)$$

To validate our modeling, we have studied two couplers proposed in [2]. These couplers, having h=250 nm, w_H=200 nm, w_s=100 nm, d =1 μm and 1.5 μm, respectively, and n_C fixed to obtain polarization-independence, were investigated in [2] by full-vectorial FEM and beam propagation method. Coupling lenghts for quasi-TE and quasi-TM modes, calculated by our modeling and by the other method [2], are summarized in Table I. The comparison shows a very good agreement (maximum shift around 5%).

Therefore, our analysis started with height h = 250nm, slot width w_S=100nm, and high index regions width w_H=200nm. With these dimensions, we have investigated the dependence of the coupling length L_C on the separation distance d between the slots. Coupling coefficient κ is proportional to the overlapping of the electric fields in both slot waveguides, therefore it is related to the gap d as $\kappa(d) \propto \exp(-\gamma d)$, where γ is the decay rate of the optical field in the cladding region. As expected, we have obtained an exponential relationship between L_C and d, namely:

$$L_C^{TE} = 0.346 \times \exp(4.441d) \qquad (3)$$

$$L_C^{TM} = 0.236 \times \exp(4.58d) \qquad (4)$$

with d >0.7μm. These dependences are sketched in Fig. 4.

Table 1: Comparison for couplers designed in [2].

	Our method		Literature [2]	
	L_C (TE) [μm]	L_C (TM) [μm]	L_C (TE) [μm]	L_C (TM) [μm]
d = 1 μm n_C=1.30655	22.18	22.21	22.23	22.23
d = 1.5 μm n_C=1.41545	201.82	201.93	203.0	203.0

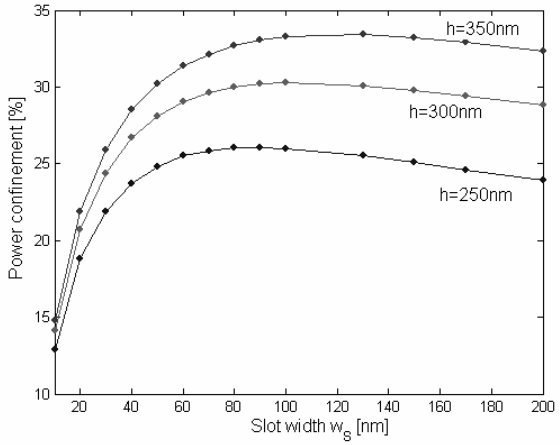


Fig. 3: Power confinement in the slot region.

All the successive calculations have been carried out for d = 1 μm, i.e. in the worst case.

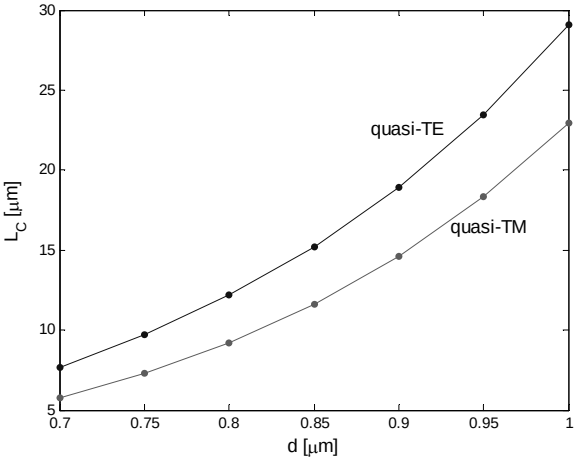


Fig. 4: Coupling length versus separation distance d.

We have analyzed the influence of height h of coupled waveguides on quasi-TE and quasi-TM coupling lengths. As it can be observed in Fig. 5, the former shows a linear dependence, while the latter has a fourth degree polynomial behavior. Thus, by increasing the waveguide height h, the coupling length for quasi-TM increases more rapidly than for quasi-TE polarization.

The two curves intersect at h=274 nm, providing the same coupling lengths for both polarizations.

For the same geometrical configuration, we have also evaluated the height h corresponding to the ZBR condition for quasi-TE and quasi-TM symmetric modes of directional coupler. This height is about 239.9 nm.

Then, we have studied the influence of high index symmetric region width on coupling length. We have performed the calculations for three waveguide heights, namely 250nm, 350nm and 400nm. The three corresponding graphs are sketched in Fig. 6,7,8.

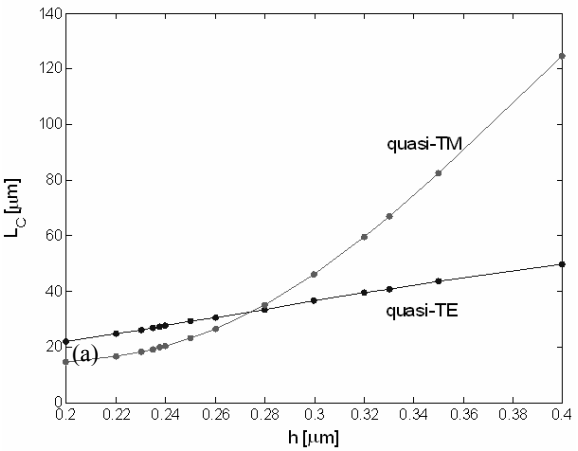


Fig. 5: Coupling length versus height h.

In the first case, for h=250nm (Fig. 6), the coupling lengths for both polarizations show a parabolic behavior. The two curves do not intersect for any value of the parameter w_H.

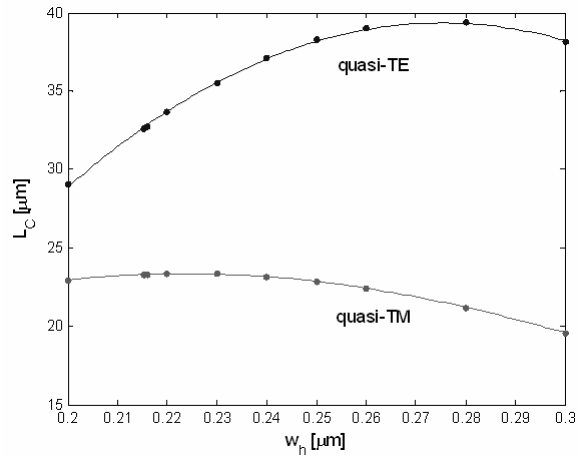


Fig. 6: Coupling length versus w_H for h = 250nm.

For this configuration, ZBR condition for quasi-TE and quasi-TM symmetric modes of directional coupler corresponds approximately to w_h = 215.5nm.

For larger h values, the situation changes significantly, as sketched in Fig. 7 and 8. The coupling lengths for quasi-TE and quasi-TM polarizations show a third order polynomial behavior, and it is possible to find a w_H value where the coupling lengths are the same for both polarizations. For h=350 nm and 400 nm, the intersection points are obtained for w_H=284 nm (L_C =55.61μm) and w_H=303 nm (L_C =59.03μm), respectively. Besides, for higher waveguide heights, coupling lengths for quasi-TM shows a stronger dependence on w_H with respect to those for quasi-TE polarization.

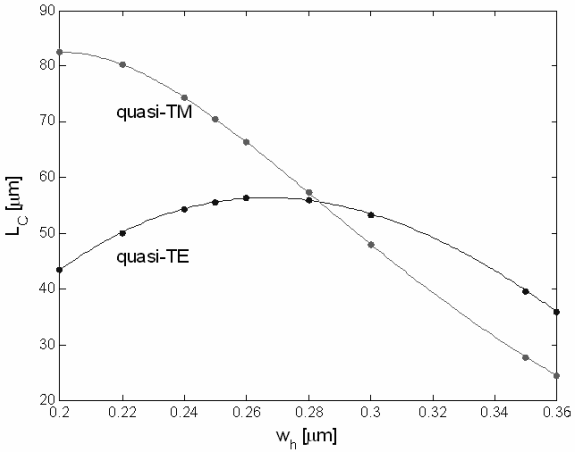


Fig. 7: Coupling length versus w_H for h = 350nm.

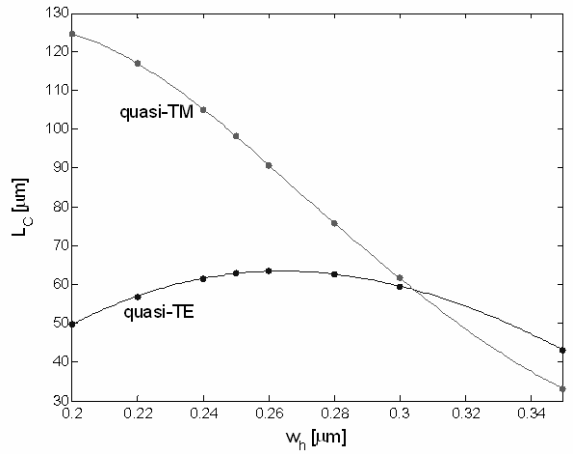


Fig. 8: Coupling length versus w_H for h = 400nm.

Either for quasi-TE or for quasi-TM modes, coupling length dependence on high index regions width can be expressed as:

$$L_c = p_0 + p_1 w_H + p_2 w_H^2 + p_3 w_H^3 \qquad (5)$$

where p_0, p_1, p_2 and p_3 are fitting parameters whose values are collected in Table 2, for considered values of h and both polarizations.

Conclusions

In this work, we have investigated directional

couplers formed by two parallel symmetrical silicon slot waveguides. The adopted modeling approach, validated by comparisons with other numerical results reported in literature, is based on Coupled Mode Theory and Finite Element Method, and results very fast and accurate. Our work is a starting point for future investigations and optimizations. Many devices can be realized based on slot waveguides and directional couplers, also employing different materials.

Table 2: Fitting parameters for coupling length.

h [nm]	Mode	p_3	p_2	p_1	p_0
250	TE	0	-1851	1019	-100.9
	TM	0	-639.3	285	-8.42
350	TE	3622	-5590	2208	-203.6
	TM	17020	-14880	3857	-229.7
400	TE	4056	-6309	2483	-227
	TM	25490	-21190	5115	-254.7

References

1 V. R. Almeida et al, Opt. Lett., no. 11, p. 1209, 2004.
2 T. Fujisawa et al, Opt. Lett., no. 1, p. 56, 2006.
3 T. Fujisawa et al, J. Opt. Soc. Am. B, p. 684, 2006.
4 T. Fujisawa et al, IEEE Photon. Technol. Lett., p. 1246, 2006.
5 T. Baehr-Jones et al, Appl. Phys. Lett., no. 86, p. 081101, 2006.
6 T. Baehr-Jones et al, Opt. Express, p. 2516, 2005.
7 M. Galli et al, Appl. Phys. Lett., no. 89, p. 241114, 2006.
8 P. Mullner et al, IEEE Photon. Technol. Lett., no. 24, p. 2557, 2006.
9 Q. Xu et al, Opt. Lett., no. 29, p. 1626, 2004.
10 Comsol Multiphysics by COMSOL ©, ver. 3.2, single license, 2005.

An optimal design strategy for MMI splitters

Kehinde Latunde-Dada (1) and Frank Payne (2)
1) Department of Engineering Science, Parks Road, University of Oxford, Oxford, OX1 3PJ, UK. e-mail: kehinde.latunde-dada@eng.ox.ac.uk, 2) Department of Engineering Science, Parks Road, University of Oxford, Oxford, OX1 3PJ, UK
frank.payne@eng.ox.ac.uk

Abstract: : *In this paper we design novel tapered 2x2 MMI splitters based on adiabatic tapered MMI sections which are both low loss and significantly more compact in length compared to their generic straight equivalents.*

Introduction

Multimode Interference (MMI) devices have gained in popularity due to their versatility for use in many optical circuits such as power splitters, power combiners, and Mach-Zehnder optical switches.
However, the large lengths associated with generic straight MMI structures leads to an undesirable demand on space in optical waveguide circuits. This has resulted in a variety of proposals and suggestions based on tapered designs for the MMI section which are aimed at reducing the length of MMI couplers [1-3]. In this paper we propose an entirely new tapered structure which is both compact and adiabatic, resulting in a minimum loss design. The adiabatic design of the device is achieved by ensuring there is minimal coupling between the modes in the tapered MMI section. This reduces the coupling losses incurred in the device and ensures near-perfect imaging. In addition we shall be comparing its performance to that of a parabolically tapered device.

Adiabatically Tapered 2x2 MMI Structures

In [4], we discussed the theory of an adiabatically tapered 1x2 MMI coupler. Here, we extend our results to the case of a 2x2 coupler.
In a straight multimode interference waveguide device, the formation of images is described by the self-imaging principle [4]. The straight waveguide section of the MMI can support a number of modes depending on its width. These modes propagate along the waveguide interfering destructively and constructively to form multiple images.
In a straight 2x2 3dB MMI coupler the double imaging length is given by [4]:

$$L = \frac{3}{8} L_\pi \tag{1}$$

where L_π is half the beat length between the two lowest order modes,

$$L_\pi = \frac{\pi}{\beta_0 - \beta_1} \simeq \frac{4 n_1 W_e^2}{3\lambda_0} \tag{2}$$

Hence the double imaging length L is given by

$$L = \frac{n_1 W_e^2}{2\lambda_0} \tag{3}$$

where n_1 is the refractive index of the MMI waveguide, λ_0 is the free space wavelength, $k_0 = 2\pi/\lambda_0$ and W_e is the effective width of the waveguide which takes into account the Goos-Hänchen shift at the waveguide boundaries.
In [1-4], it is shown that the length of an MMI can be significantly reduced by tapering the MMI section. However, for low loss the tapered section musy also be adiabatic.
It has been shown in [4] and [5] that the criterion which the sturcture must satisfy along its length to ensure adiabaticity and a more compact length is given by

$$\Omega << \rho(\beta_0 - \beta_1)/2\pi \tag{4}$$

where $\Omega(z)$ is the angle between the tangent to the waveguide boundary and the central waveguide axis as shown in Fig. 1 below and β_0 and β_1 are the propagation constants of the two lowest order modes excited in the waveguide.

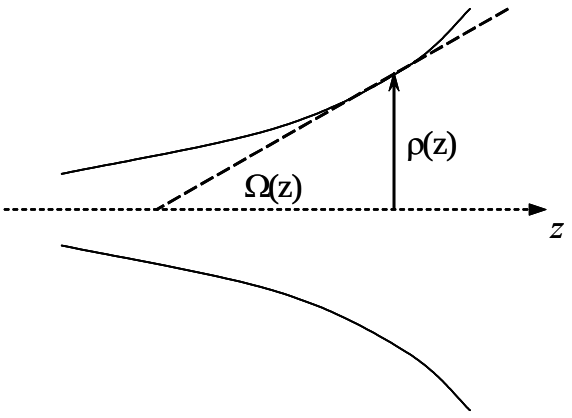


Fig. 1: Longitudinal section of tapered waveguide

Equation (4) defines the limit on the local taper angle as a function of z for an adiabatic taper. It has been shown that equation (4) provides a very good estimate for the adiabaticity of a tapered waveguide [5]. This means that the taper angle must be sufficiently small and also satisfy equation (4) at each position along the taper. The propagation constants, β_0 and β_1 depend on the local guide half-width $\rho(z)$, and thus the right hand side of equation (4) will vary with the degree of tapering.
The delineating limit, i.e. the boundary between the taper being approximately adiabatic and non-

adiabatic can therefore generated by equating the two sides of this equation:

$$\Omega = \rho(\beta_0 - \beta_1)/2\pi \qquad (5)$$

Device Design

The local delineating limit in the 2x2 splitter is derived from (2) and (5) as:

$$\Omega(z) = \frac{3\lambda_0}{16 n_1 w(z)} \approx \frac{\partial \rho}{\partial z} \qquad (6)$$

where w (z) is the local width of the MMI waveguide and $\frac{\partial \rho}{\partial z}$ is the local tangent and where we have ignored the Goos-Hänchen shift.

The shape profile of the adiabatic splitter can thus be derived by simply integrating equation (6). This will result in the width equation for one half of the 2x2 coupler, the other half is simply the mirror image.

$$w_{1/2} = \sqrt{\frac{3\lambda z}{4n_1} + w_1^2} \quad \text{for z >0}$$

and likewise for z<0

$$w_{-1/2} = \sqrt{-\frac{3\lambda z}{4n_1} + w_1^2} \qquad (7)$$

where w_1 is the width of the middle section as shown in the Fig. 2 below.

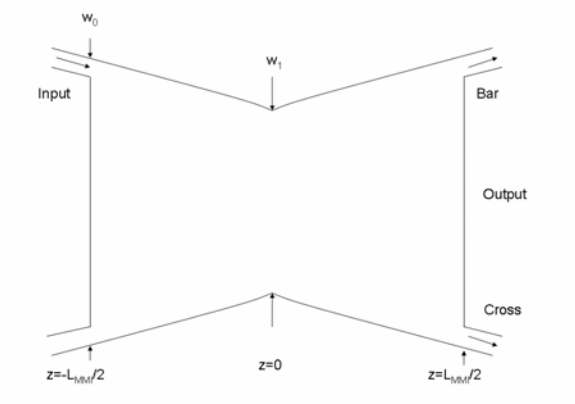


Fig. 2: 2x2 adiabatic MMI splitter showing the input and output waveguides

Simulation and Results

We have simulated the performance of the 2x2 adiabatic tapered MMI splitter using the BPM method. This was done using a BPM-CAD Waveguide Optics Modeling Software System by the Optiwave Corporation. Using waveguide parameters employed in [6], n_1 = 3.32517, n_2, the refractive index of the surronding cladding =3.17, λ_0 =1.507 µm, and w_1 = 2.46 µm. The evolution of the optical field through the MMI is shown in Figure 4 which was computed with a 4 µm long input waveguide of input width 1.1 µm and output waveguides of a similar 1.1 µm width. This simulation predicts a tapered MMI section length of 58 µm as shown in Figure 3. This is somewhat shorter than the length calculated for the straight waveguide, 82 µm.

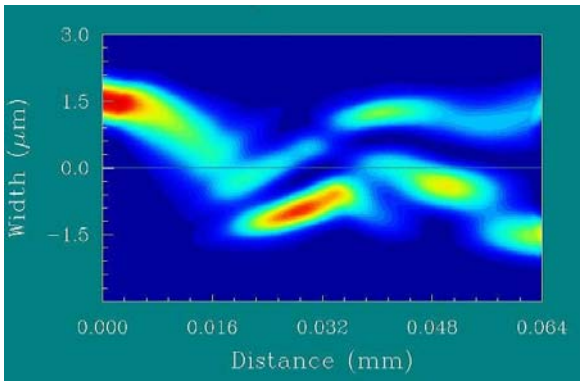


Fig. 3: BPM simulation of propagation through an adiabatically tapered 2x2 MMI splitter.

Simulations were also performed on quadratic tapered MMI splitters as shown in the Table 1 below.

Table 1: Comparison of output performance as measured in different couplers using BPM where n_1 = 3.32517, n_2 =3.17, λ_0 =1.507 µm.

	w_0	$d\Omega$	L_{MMI}	Loss(dB)	b%	c%
Straight	3.8	0	82	0.074	50	50
Adiabatic	4	0.4	58	1.27	40	60
Quadratic	4.1	0.4	50	0.52	46	54
Optquad	3.8	0.35	52	0.23	52	48

where w_0 is the initial and final width,

$d\Omega$ is the normalised width variation = $\frac{w_0 - w_1}{w_0}$,

L_{MMI} is the overall length of the MMI.

Loss is the output power loss measured in decibels and *b* and *c* are the proportion of power in both the bar and cross outputs respectively relative to the total power output. This defines coupler's the splitting ratio.

Looking at the results under the Adiabatic and Parabolic profiles in Table 1, with a similar $d\Omega$ of 0.4, one can see that the splitting is much more symmetric in the quadratic profile i.e. much more even. The total output power loss is also smaller. This can be

attributed to the phase changes which occur at the midplane of the adiabatic device as $\frac{dW}{dz} \neq 0$ at z = $L_{MMI}/2$ as can be seen in Figure 2 above. This leads a discontinuous change in the propagating wavefront and hence in poor imaging i.e. poor splitting ratio and lower power output level.

In order to correct the discontinuity problem incurred in the adiabatic tapered coupler, we introduce a design refinement to the middle portion of the MMI waveguide.

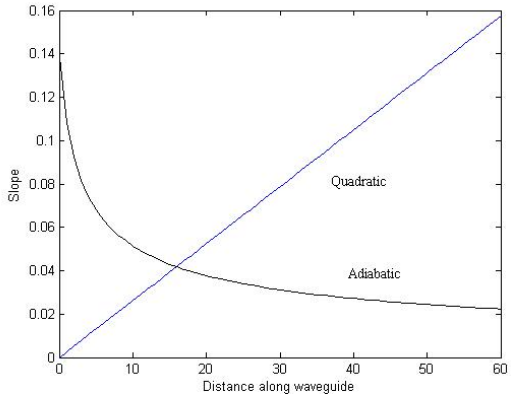


Fig. 4: Comparison of slopes of quadratic and adiabatic half-profiles where n_1 = 3.32517, n_2 =3.17, λ_0 =1.507

µm. Looking at Fig. 4, one can see that the half-quadratic profile obeys the angle criterion up until a length of about 12 µm when the slope exceeds the minimum allowable by the adiabatic criterion. However, one can create hybrid structure which includes a quadratic profile as proposed in [6] of full quadratic length 24 µm and thereafter a profile which follows the adiabatic criterion as shown in Fig. 5. Such a waveguide will combine the beneficial properties of both structures; the continuous change of width $\frac{dW}{dz} = 0$ in the quadratic section and the negligible coupling in the adiabatic tapered section.

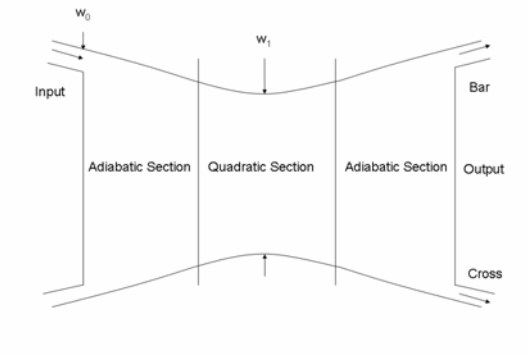


Fig. 5: 2x2 hybrid splitter showing the adiabatic and quadratic sections.

The hybrid structure was simulated using the parameters given above with the BPM-CAD program resulting in the results under the OptQuad profile in Table 1. One can see that the total output power loss is much less and the splitting ratio improved accompanied with an additional reduction in MMI length which is only 52 microns. The figure below shows the evolution of the optical field through the hybrid OptQuad MMI splitter.

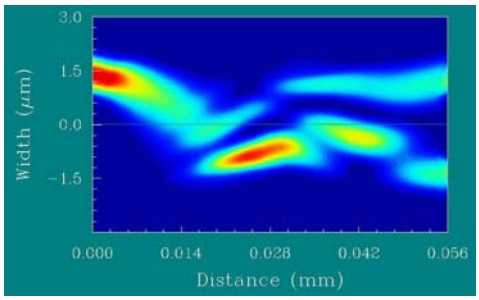


Fig. 3: BPM simulation of propagation through a hybrid tapered 2x2 MMI splitter.

Conclusions

In this paper we have presented the theory and design for adiabatic tapered 2x2 MMI splitters which are more compact than straight MMIs yet have comparable low loss. We have also considered the problem of discontinuity incurred in purely adiabatic splitters and proposed a hybrid structure which has a simulated loss which is much lower than that for quadratically tapered devices based on similar parameters. Although we have discussed the design of 2x2 3dB splitters in this paper, the theory presented here is easily extended to more general NxM devices.

References

1 H. Wei, J. Yu and X. Zhang, 'Compact 3-dB tapered multimode interference coupler in silicon-on-insulator, Optics Letters, Vol. 26, pp 878-880, 2001

2 W. Zhigang and U. Katsuyuki 'Study on Tapered Multimode Interference Coherent Lightwave Combiners', IEICE Transactions on Electronics , Vol. E88-C, pp. 1005-1012, 2005.

3 R.M. Lorenzo, C. Llorente, E.J. Abril and M. Lopez, 'Improved self-imaging characteristics in 1 x N multimode couplers', IEE Proceedings – Optoelectronics,, Vol. 145, pp.65-69, 1998.

4 K. Latunde-Dada and F. Payne, 'Design of Adiabatic Multimode Interference 3-dB Coupler', IEEE Journal of Lightwave Technology. To be published March 2007

5 J.D Love, 'Application of a low-loss criterion to optical waveguides and devices ', IEE Proceedings, Vol. 136, Pt. J, pp.225-228, 1989.

6. D.S. Levy, R. Scarmozzino. Y.M. Li, R.M. Osgood, 'A New Design for Ultracompact Multimode Interference-Based 2x2 Couplers', IEEE Photonics Technology Letters, Vol 10, No 1, pp. 96-98, 1998

Numerical Studies on Silica Wire Directional Couplers

Ziyang Zhang, Min Yan and Min Qiu
Laboratory of Optics, Photonics and Quantum Electronics, Department of Microelectronics and Applied Physics, Royal Institute of Technology (KTH), Electrum 229, 164 40 Kista, Sweden

Abstract: Directional couplers based on silica and silicon wires are studied numerically using 3D FDTD *method. With 6μm overlapping length, 80% power transfer is achieved at 1.54μm. Silica wires can also be used to generate slow light in photonic crystal slab waveguide by counter-directional coupling.*

Introduction

Silicon wire waveguides with cross-section around 250nm by 400nm have been widely used for modern photonic integrated circuits (PICs). However, it is challenging to couple light directly from a conventional single-mode fiber with core diameter ~6μm. The butt-coupled light-injecting method causes large insertion loss due to the small overlap of the mode profile and index mismatch. One solution is to use polymer inverse taper to increase the mode overlap [1-2]. However, this requires precise fabrication control to bring down the tip of the silicon wire to below 100nm. Another solution is to use in-plane gratings to couple light out-of-plane from fiber to silicon wire [3]. This method also involves additional fabrication steps.

In this work, we propose a coupler design based on evanescent directional coupling between suspended silica and silicon wires. The schematic is shown in Fig. 1. The diameter of the silica (index 1.5) wire ***R*** is 1μm. The details involving fabrication of such wires are described in Ref. [4]. The silicon (index 3.6) wire has a cross-section of 250nm by 400nm. Both silica and silicon wires remain single-mode at 1550nm wavelength region. The two wires go parallel and axis-aligned with an overlapping distance ***l***. Their vertical spacing is ***s***. To prevent light leakage into the silica substrate the beginning section of the silicon wire is also suspended in air. This can be done by selective wet-etching during fabrication. The finite-difference time-domain (FDTD) cell size is 25nm in all three dimensions.

Silica and silicon wire coupling

From coupled mode theory, the silica waveguide mode ***A*** and silicon waveguide mode ***B*** along ***x*** direction are related by [5]

$$\frac{dA}{dx} = -i\kappa B e^{-2i\delta x}, \qquad \frac{dB}{dx} = -i\kappa A e^{2i\delta x} \qquad (1)$$

where $\delta = \beta_b - \beta_a$ is the difference between the modified propagation constants of mode ***A*** and mode ***B*** in the coupled system. κ is the coupling coefficient. With initial condition $A(0)=A_0$ and $B(0)=0$, the power relation in the couple system becomes,

$$P_b(x) = P_0 \frac{\kappa^2}{\kappa^2+\delta^2}\sin^2[(\kappa^2+\delta^2)^{1/2}x] \qquad (2)$$

$$P_a(x) = P_0 - P_b(x)$$

To reach maximum power transfer from A to B, the overlapping distance ***l*** must satisfy

$$\sin^2[(\kappa^2+\delta^2)^{1/2}l] = 1. \qquad (3)$$

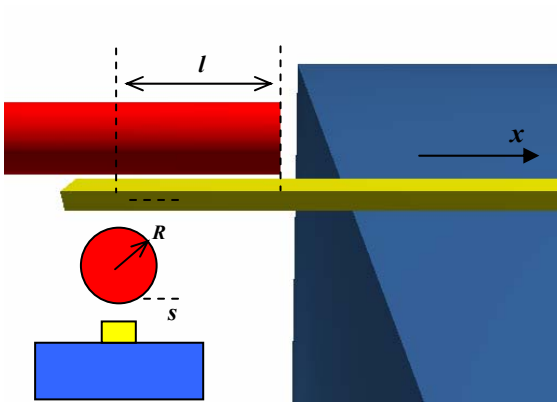


Fig. 1: schematic of silica and silicon wire coupler

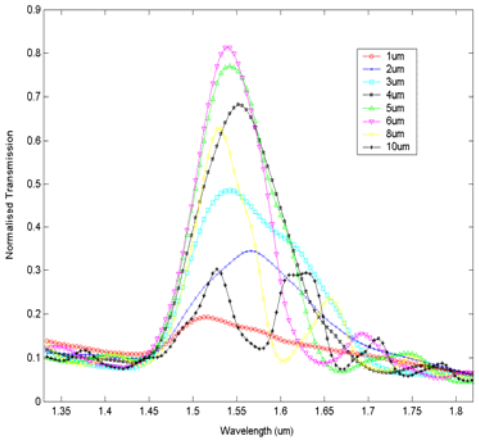


Fig. 2: Power transmission from silica to silicon wire at different overlapping distances.

In this system δ is not zero and from Eq. 2 light cannot be transferred completely from silica to silicon wire or vice versa. Nevertheless, if the coupling between the two modes is strong enough so that $\kappa >> \delta$, we can still have high power transfer.

In our FDTD simulations, we set ***s=0*** so that the two wires come into contact to improve their mode coupling. We vary the overlapping distance ***l*** in search for the maxmum power transfer. The results are

shown in Fig. 2.
It is seen that as ***l*** goes from 1μm to 6μm, the power transferred from silica to silicon wire increases. At overlapping distance 6μm, 81% of light transferrs from silica wire to silicon waveguide at 1.54μm with 3dB bandwidth of around 100nm. When ***l*** further increases, the peak transfer power starts to drop.

Silica wire and photonic crystal waveguide coupling

There has been extensive study of slow light properties in two-dimensional photonic crystal slab (2D PCS) waveguide. To couple slow light efficiently, a mode converter is usually needed between 2D PCS and silicon wire [6]. As an alternative, we investigate the evanescent directional coupling between silica wire and one-missing-row waveguide (W1PC) in 2D PCS and try to find a way to improve this coupling. The schematic is shown in Fig. 3.

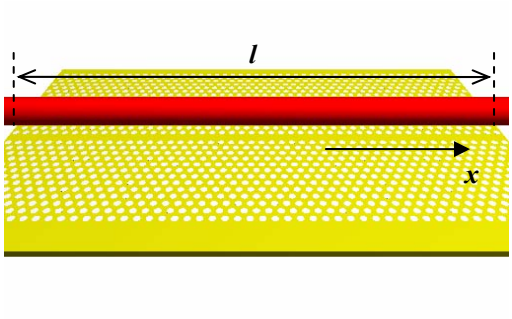


Fig. 3: Directional coupling of silica wire and 2D PCS waveguide (W1PC).

The silica wire diameter is 1μm and the W1PC waveguide goes parallel with their axis aligned. The silicon 2D PCS has index 3.6 and thickness 0.6***a***, where ***a*** is the lattice constant. The airhole diameter is 0.6***a***. As shown in Fig. 4, zero-order W1PC waveguide mode has a flat dispersion curve near the lower band edge and the group velocity is significantly reduced in this region. The silica waveguide mode on the other hand is approximately a straight line within a small frequency range. At cross point P, W1PC and silica waveguide mode share the same propagation constant. Considering the opposite slope sign of the two dispersion curves, the evanescent coupling between these two waveguides is counter-directional. The location of P can be varied by two methods, i.e., either changing the silica wire properties (refractive index or the diameter) to shift its propagation constant or modifying the geometry of W1PC to shift the dispersion curve of the zero-order guided modes. In this work, we choose to vary silica refractive index in our simulations. It is intented to demonstrate the feasibility of generating slow light when P moves to the flat band region. A more realistic way would be to modify W1PC structure and this will be done in our future work.
Assume the initial power in the silica wire is $P_A(0)$, the power variation of the system is,

$$P_A(x) = P_A(0)\frac{\cosh^2[\kappa(x-l)]}{\cosh^2(\kappa l)}$$
$$P_C(x) = P_A(0)\frac{\sinh^2[\kappa(x-l)]}{\cosh^2(\kappa l)} \qquad (4)$$

The coupling coefficient κ is determined by wire and W1PC spacing as well as their individual mode profile. When $x = l \to \infty$,

$$P_A(\infty) \to 0$$
$$P_C(\infty) \to 0 \qquad (5)$$
$$P_C(0) \to P_A(0)$$

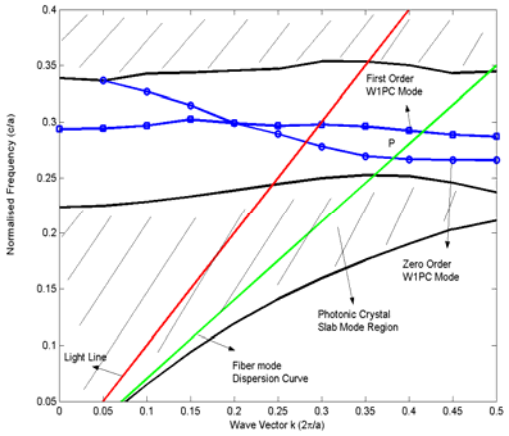


Fig. 4: Band diagram of 2D PCS and dispersion curve of W1PC waveguide modes.

From Eq. 5, complete power transfer from silica wire to W1PC waveguide is possible when their coupling distance ***l*** goes to infinity. In this case, their vertical spacing ***s*** can not be too small, as the close presence of silica wire modifies the 2D PCS band structure and seriously changes W1PC waveguide mode dispersion curve. ***s*** cannot be too large either, as it will-decrease coupling coefficient κ. In our simulations, we set ***s=500nm***.
We take ***a=420nm*** and the results are shown in Fig. 5. By increasing silica index, the cross point P moves toward W1PC flat band region (longer central wavelength). This increases the coupling between silica wire and W1PC and the power transfer becomes more efficient. As the overlapping length ***l*** increases from ***23a*** to ***59a***, the maximum power transfer increases by 10% for n_f***=1.92***, which agrees well from Eq. 4. For the best case, 87% power transfer takes place at 1.55μm.

Conclusions

We have numerically studied the directional coupling between silica wire and other photonic waveguides such as silicon wire and W1PC in 2D PCS. With 6μm overlapping distance, more thn 80% light is transferred from silica to silicon wire. The strong coupling provides an alternative to inject light into photonic integrated circuits. The counter-directional

coupling between silica wire and W1PC waveguide is a new method to generate slow light. This method involves careful W1PC band engineering so that the cross point of their dispersion curves stays in the slow light region. By changing the wire index, we have demonstrated the effectiveness of this coupling.

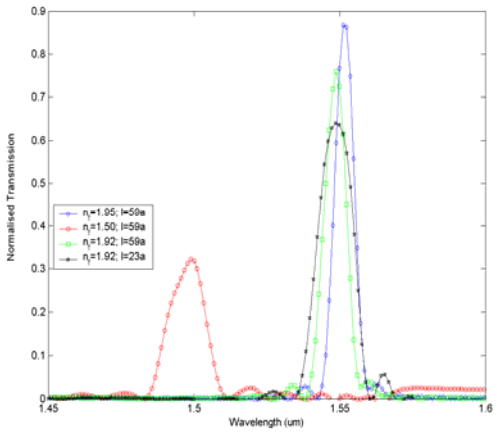


Fig. 5: Counter-directional power transfer from silica wire to W1PC waveguide at different index and overlapping lengths.

Acknowledgments

This work is supported by the Swedish Foundation for Strategic Research (SSF) through the INGVAR program, the SSF Strategic Research Center in Photonics, and the Swedish Research Council (VR).

References

1 T. Shoji et al, Electron. Lett. no. 38, p. 1669, 2002.
2 V.Almeida et al, J. Lightwave. Opt. Lett., no. 28, p. 1302, 2002.
3 D. Taillaert et al, Opt. Lett. No. 29, p. 2749, 2004.
4 L. M. Tong et al, Nature, no. 426, p. 816, 2003.
5 A. Yariv, "Optical Electronics in Modern Communications," 5th ed. Oxford University Press, New York 1997, chpt 13.
6 M. Povinelli et al, Opt. Express, no. 13, p. 7145, 2005.

The New Design and Numerical Simulation by 3D BPM of New Compact Polarisation Rotator in Anisotropic $LiNbO_3$ Graded Index Waveguide

Andrei Tsarev

Laboratory of Optical Materials and Structures
Institute of Semiconductor Physics, Siberian Branch of Russian Academy of Science
Prospect Lavrenteva, 13, Novosibirsk, 630090, Russia
tsarev@isp.nsc.ru

Abstract: *The new compact polarisation rotator in anisotropic graded index Ti:$LiNbO_3$ waveguide has been proposed and investigated by 3D beam propagation method (BPM) by the software tool BeamPROP from RSoft Design Group, Inc. The polarization conversion from quasi-TE to quasi-TM (and backwards) guided modes at the 8 mm waveguide length has been demonstrated. Device is intended for polarisation diversity of integrated optic elements based on $LiNbO_3$ structures.*

Introduction

Twenty years ago the great number of investigations had been devoted to the studding of anisotropic graded index waveguides in lithium niobate ($LiNbO_3$) substrate. It was shown that optical guided modes are strongly hybrid [1]. Besides at particular angle of propagation (that is not far from the crystallographic ***X*** axis) the guided quasi-TE and quasi-TM modes have the circular polarisation [2, 3] with opposite direction of rotation. Similar types of hybrid modes with the circular polarisation also exist in proper directed 3D channel waveguides based by Ti-diffusion into $LiNbO_3$. Thus the input linear polarisation could be rotated during the light propagation along the anisotropic channel waveguide by means of two hybrid modes that exited in the optical waveguide and that have different effective refractive indexes and opposite direction of rotation of their circular polarisation. This effect of polarisation conversion/rotation in anisotropic graded index waveguides has been studied in this paper for the first time by the full-vectorial 3D beam propagation method (BPM) by the software tool BeamPROP from RSoft Design Group, Inc. [4].

I. Simulated results and discussion

We have examined polarisation rotation at variable orientation of input liner polarisation for different direction q of the strip waveguide related to the crystallographic ***X*** axis of ***Y***-cut $LiNbO_3$. Typical waveguide width w is 8 μm, waveguide height h is 3.5 μm, maximum refractive index increment in the diffused waveguide dN is 0.03, substrate main refractive indexes are N_e = 2.138 and N_o = 2.212. All these parameters corresponds to the case of Ti-diffused $LiNbO_3$ waveguide at optical wavelength 1.55 μm, except that for simplicity we use the same value dN for both extraordinary and ordinary increment of refractive indexes. Graded index distribution of the refractive index across the waveguide depth is typical for diffusion model that is used by RSoft Design Group Inc. in the simulated example for $LiNbO_3$ case [4]. Namely, waveguide refractive index distribution is derived as [4]:

$$n(x,y) = n_0 + \left[\Delta n g(x) f(y)\right]^{\gamma}$$

$$g(x) = \frac{1}{2}\left\{ erf\left[\frac{\left(\frac{w}{2}+x\right)}{h_x}\right] + erf\left[\frac{\left(\frac{w}{2}-x\right)}{h_x}\right]\right\},$$

$$f(y) = e^{\left(-\frac{y^2}{h_y^2}\right)}.$$

In our case we use $h_x = h_y = h$, g = 1. Typical refractive index distribution is shown in **Fig**.1.

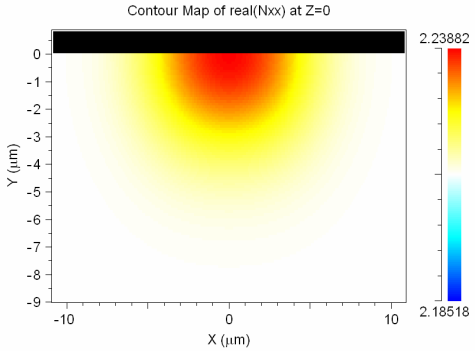


Fig. 1. Simulated distribution of refractive index in channel waveguide. w=8 μm, h=3.5 μm, dN=0.03.

Optical field distribution simulated by BPM for the major and minor components of optical wave are shown in **Fig**. 2 for the case of the waveguide orientation along the crystal axis ***X*** *(q=0).* In order to study effect of polarisation rotation in slanted *(q¹0)*

channel anisotropic waveguide we use this optical filed of quasi-TE polarisation as an input filed and then examine by BPM optical wave propagation by determination the overlap integral of the resulted field with the filed distribution of quasi-TE and quasi-TM modes determined for the case *(q=0).*

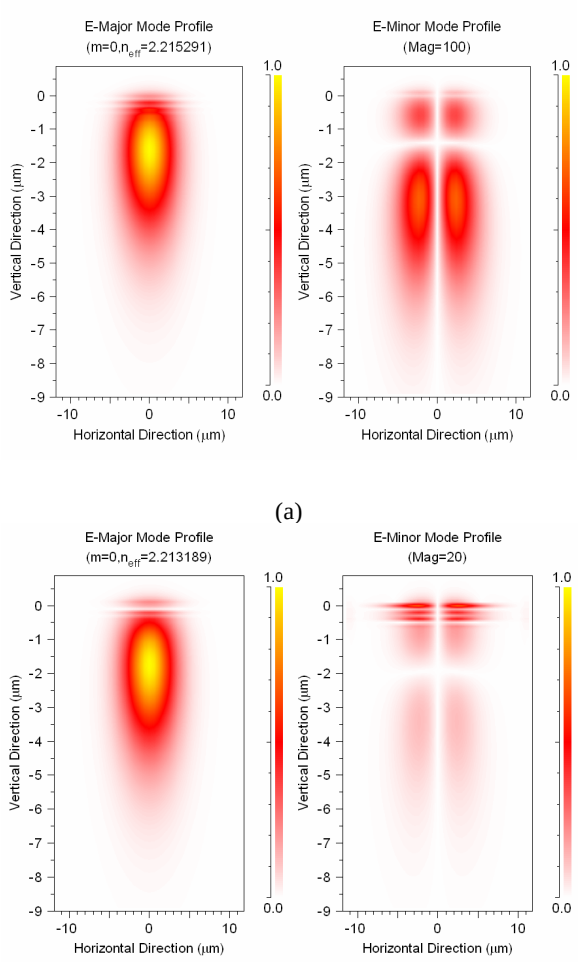


Fig. 2. Simulated distribution of optical filed of guided modes in diffused waveguide presented in **Fig**. 1.
(a) quasi-TE mode, (b) quasi-TM mode. *q=0.*

Typical behaviour of propagation of optical beam along diffused channel waveguide directed at angle 5.7^0 relative to ***X***-axis in ***Y***-cut Ti:$LiNbO_3$ is shown on **Fig**. 3 for the case of incidence of liner polarisation with 45 degree orientation related to the waveguide plate. One can see that incident optical beam is coupled into two hybrid guided modes of circular polarisation. Due to phase delay coursed by a small difference in the refractive index of these modes their superposition produces different polarisation of the resulted filed depending on the propagation length.
The measure of the polarisation rotation is the ratio of quasi-TE and quasi-TM modes. The left part of **Fig**.3 demonstrates propagation of quasi-TE mode. The right part of the **Fig**. 3 demonstrated behaviour of the power amplitude of both quasi-TE and quasi-TM guided modes.

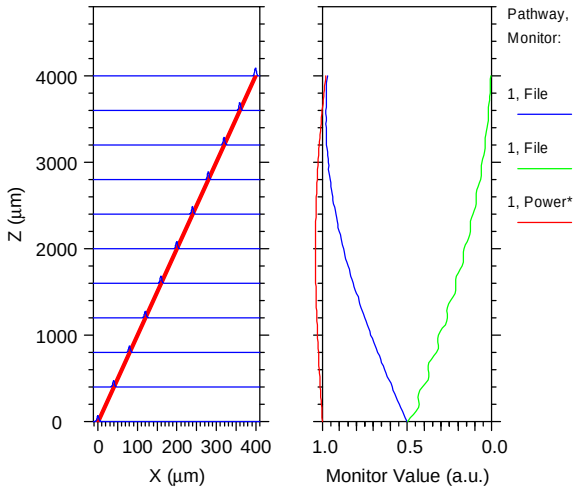


Fig. 3. 3D BPM simulation of polarisation conversion in anisotropic channel waveguide directed at angle $q=5.7^0$. Input polarisations: TE&TM.

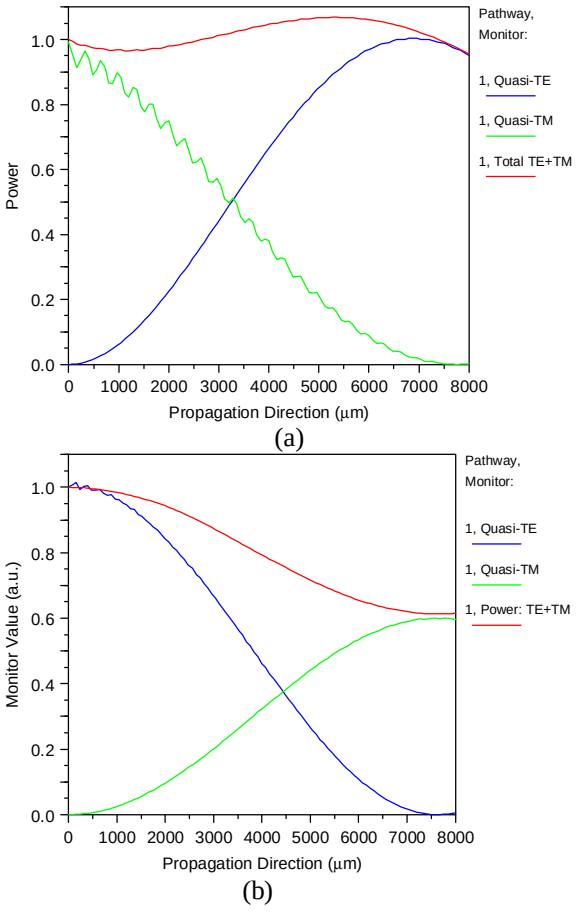


Fig. 4. 3D BPM simulation of polarisation conversion in anisotropic channel waveguide directed at angle at angle $q=5.7^0$. Input polarisations: (a) TM (b) TE.

It is easily seen that at the distance of 4 mm this anisotropic waveguide produce the 45-degree rotation of incident linear polarisation. By the double increase of the waveguide length this optical element

can be used as the 90-degree polarisation rotator and thus could transform incident polarisation from quasi-TE to quasi-TM (see **Fig**. 4a) or from quasi-TM to quasi-TE (see **Fig**. 4b). To measure the actual wait of different polarisation one has to normalize simulated results for quasi-TM and quasi-TE modes to the total power for both polarisations.

Note, that it was impossible to have the constant level of the signals due to simulation problems typical for the full-vectorial 3D beam propagation method that currently has a natural limitation to work only in paraxial approximation. Nevertheless for our particular waveguides with the small contrast this method could be also applied for the slanted waveguides ($q < 7^0$) but by some expense in the nonconstant level of the signals that can be compensated by the simple additional power normalisation procedure.

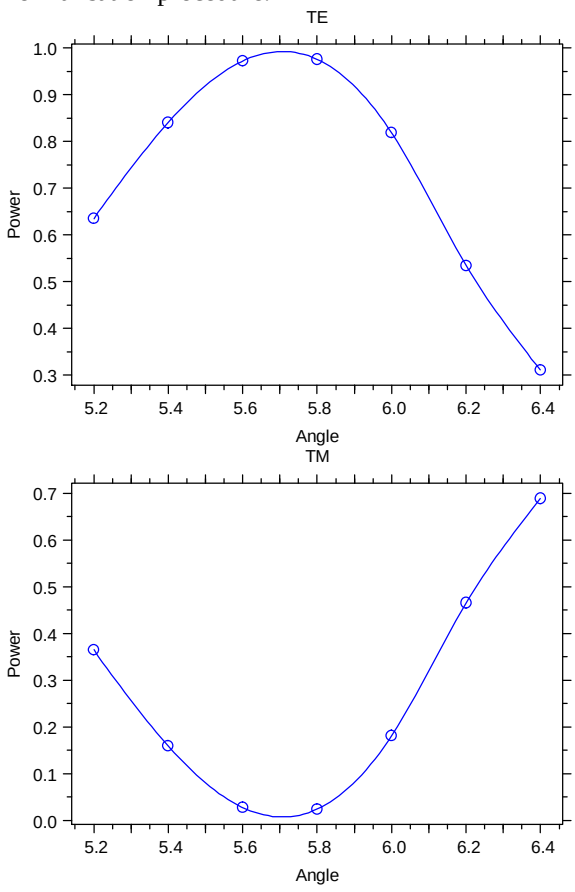


Fig. 5. 3D BPM simulation of polarisation conversion at different angle q relative to ***X***-axis in **Y**-cut Ti:$LiNbO_3$. Input polarisations: (a) TM (b) TE.

The definition of the optimum angle q_0 of the waveguide orientation have bean examined by the power transmittance analyse for quasi-TE and quasi-TM modes pass through the anisotropic waveguide of 4 mm length. This length is near the optimum for the 45-degree rotation thus the input polarisation has also chosen to have the 45-degree orientation. As a result at optimum direction q_0 of the strip waveguide we have the maximum power transmittance for quasi-TE mode and minimum transmittance for quasi-TM mode, respectively. Results of these simulations are presented in **Fig**.5. One can see that the anisotropic strip waveguide in $LiNbO_3$ is working as a good polarisation rotator only within small angle range $\Delta q \sim 0.2^0$ cantered around the angle $q_0 = 5.7^0$ related to the ***X*** axis. For the another waveguide parameters the optimal angle q_0 is differ from this one but the optimum range Δq is of the same order of magnitude. In general the larger difference between the effective refractive indexes for the fundamental quasi-TE and quasi-TM modes (measured along ***X*** axis) and the smaller anisotropy (*No-Ne*) of the crystal than the larger optimum value of the angle q_0. Proposed optical element has the high extinction ratio (larger then -20 dB) in a wide transmitting band (see **Fig**. 6) that is very important for the practical applications. For example, proposed polarisation rotator can be applied with the well known polarisation splitter [5] for the polarisation diversity of the multiple photonic devices that can be monolithically integrated in lithium niobate substrate.

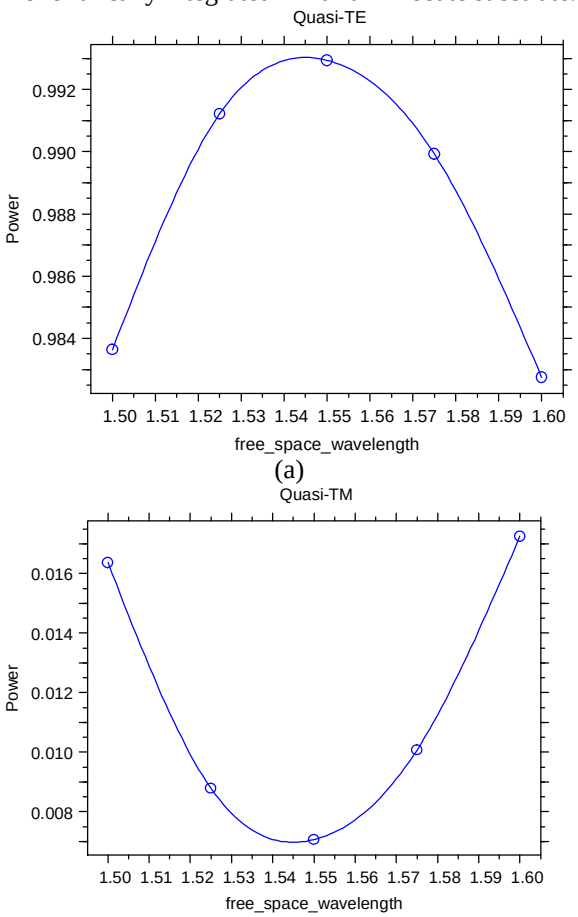


Fig. 6. 3D BPM simulation of polarisation conversion at different optical wavelengths in anisotropic channel waveguide directed at angle $q = 5.7^0$.
Input polarisations: (a) TM (b) TE.

Conclusions

The paper proposes and describes the results of theoretical investigation of the novel integrated optics polarization rotator based on the anisotropic graded index Ti-diffused waveguide in $LiNbO_3$ substrate. The work of the device is based on the hybrid nature of guided modes in 3D anisotropic waveguides. At particular direction of the waveguide relative to crystal axis the two basic fundamental modes could have the circular polarisation with the opposite direction of rotation. Thus linear polarisation has to be rotated during the propagation along the anisotropic channel waveguide by means of two hybrid modes with opposite direction of rotation. This effect of polarisation conversion/rotation in anisotropic graded index waveguides has been studied in this paper for the first time by full-vectorial 3D beam propagation method by the software tool BeamPROP from RSoft Design Group, Inc. [4]. We have examined polarisation rotation at different lunching polarisation for different waveguide orientations and waveguide parameters. It was found that at the particular waveguide direction (around 6 degrees related to ***X*** axis of ***Y***-cut $LiNbO_3$) one can find the condition of total polarisation conversion from quasi-TE to quasi-TM mode (and backwards) at the waveguide length about 8 mm. The half length 4 mm is enough for the 45-degree polarisation rotation. This optical element could find wide applications for the polarisation diversity of photonics devices monolithically integrated in the $LiNbO_3$ substrate.

Acknowledgments

The author thanks Company RSoft Design Group, Inc. [4] that provides user licence and technical support for powerful Rsoft Photonic CAD Suite 6.0 including BeamPROP software for BMP simulations.

References

1 J.Ctyroky, M.Cada, IEEE Journal of Quantum Electronics, vol. 17, p. 1064, 1981.
2 E.M.Zolotov et al, Quantum Electronics (in Russian), vol. **5**, p. 1379, 1978.
3 E.A.Kolosovsky et al, Optics Communications, vol. **43**, p. 21, 1982.
4 www.rsoftdesign.com.
5 L.Bersiner et al, J. Opt. Soc. Am. B, vol.8, p. 422, 1991.

A Semi-Analytical Propagation Equation Model for the Study of Signal Propagation in Kerr Nonlinear Nano-photonic Waveguides

Thomas Kamalakis, Thomas Sphicopoulos and Athanasios Theoharidis
Department of Informatics and Telecommunications, University of Athens Greece, (thkam@di.uoa.gr)

Abstract: A nonlinear propagation equation model is derived in the case of periodic nanophotonic waveguides using reciprocity relations. The frequency dependence of the Self Phase Modulation (SPM) coefficient is analyzed and higher order nonlinear terms are calculated in the middle and the edge of the guided band.

Introduction

Nanophotonic structures are constantly attracting increased attention for the realization of future optical integrated circuits with increased scale of integration. Particular attention is given to artificial periodic dielectric structures usually referred to as Photonic Crystals (PC) [1]. PCs can exhibit photonic badgaps, i.e. a range of frequencies where no guided mode exists. By introducing defects in a PC structure, one can form waveguides and cavities in which light is tightly confined. PC waveguides provide an efficient means of guiding light by allowing the realization of sharp optical bends. As in the case of optical fibers, signal processing could be accomplished in the nonlinear regime [2]. In another context, a large chain of coupled cavities can be thought of as a novel type of waveguide where light propagates through evanescent wave coupling from cavity to cavity. This new type of waveguide is called the Coupled Resonator Optical Waveguide (CROW) [3] and has many interesting properties. By appropriately positioning the resonators, it is possible to construct sharp, lossless and reflection-less bends throughout the entire CROW band. Another important property of the CROW is its ability to drastically slow down the optical wave (the slow light concept) which can find important applications in the realization of compact optical delay lines. The low group velocity and large optical field amplitudes of the localized modes lead to an enhancement of nonlinear effects which could potentially be useful for signal processing.

In this paper, we derive a propagation equation model to describe the pulse propagation inside a single mode nonlinear periodic nanophotonic waveguide which is very similar to the one used in conventional constant cross-section optical waveguides [4]. The derivation is based on a straight forward application of the reciprocity relations [5] in Maxwell's equations. The model provides an efficient means of simulating nonlinear behaviour while avoiding the computational complexity of more complex Finite Difference Time Domain (FDTD) method [6].

Envelope Functions of the Guided Mode

Assuming a single mode waveguide, the electric field **E** can be expressed as

$$\mathbf{E}(\mathbf{r},t) = \mathbf{E}_P(\mathbf{r},t) + c.c. \quad (1)$$

where

$$\mathbf{E}_P(\mathbf{r},t) = \int_P d\omega a(z,\omega)\mathbf{E}_\omega e^{-j\omega t} \quad (2)$$

where the spectrum of $\mathbf{E}_P$ has a bandiwdth of $\delta\omega$ and lies near a central frequency $\omega=\omega_0$ and $P=[\omega_0-½\delta\omega, \omega_0+½\delta\omega]$. The envelope functions $A(z,t)$ of the mode can be defined as

$$A(z,t) = \int_P d\omega a(z,\omega)e^{j\Delta\beta z - j\Delta\omega t} \quad (3)$$

where $\Delta\omega=\omega-\omega_0$. Using Bloch's theorem, the mode of the waveguide is written as

$$\mathbf{E}_\omega = \mathbf{e}_\omega e^{j\beta(\omega)z} \quad (4)$$

where $\mathbf{e}_\omega$ is the periodic vector function and $\beta(\omega)$ is the propagation constant of the mode. The guided mode obeys

$$\nabla\times\mathbf{H}_\omega = -j\omega\varepsilon_L\mathbf{E}_\omega,\ \nabla\times\mathbf{E}_\omega = j\omega\mu\mathbf{H}_\omega \quad (5)$$

and the mode is normalized so that:

$$N = \int_S dS(\mathbf{E}_\omega\times\mathbf{H}_\omega^* + \mathbf{H}_\omega\times\mathbf{E}_\omega^*)\cdot\mathbf{z} = 1 \quad (6)$$

where ε_L is the linear part of the dielectric constant.

Fig. 1 illustrates the dispersion relation of the guided mode of a CROW based on 2D photonic crystal defect cavities (see figure inset) calculated using the Plane Wave Expansion (PWE) method [7]. In this case the electric field is polarized along the y direction, i.e. $\mathbf{e}_{1,\omega}=\mathbf{y}e_y(x,z)$. The refractive index of the rods was taken n_a=3.4 while that of the surrounding medium was taken n_b=1.0. The PC lattice constant is taken a=0.6μm while the adjacent cavity spacing D and the rod radius r_a is $D=2a$ and $r_a=0.18a$ respectively. The guided mode band extends from 185.7THz to 204.8THz. Also shown in the same figure is the slow down factor S of the mode defined as $S=c/v_g$, where c is the speed of light in vacuum, while v_g is the group velocity of the mode. Near the band edges, S is large, implying larger

amplitudes for the modal fields and hence an enhancement of nonlinear effects. This is illustrated in Fig. 2 (a) and (b), where the normalized modal fields $e_y(x,z)$ are plotted assuming $\beta=½\pi/D$ (middle of the band) and $\beta=0.05\pi/D$ (near the band edge) respectively and it is deduced that the modal amplitude is stronger in the latter case. Fig. 2 illustrates the modal field distribution at $\beta=0.25\pi/D$ (middle of the guided band) and $\beta=0.05\pi/D$ (band edge). It is deduced that althought the shape of the main lobe of the mode does not change drastically, the modal amplitudes are significantly enhanced.

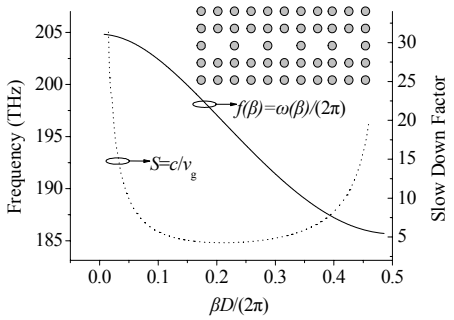


Fig. 1**:** The dispersion relation and slow down factor S of the guided mode of a coupled resonator optical waveguide (CROW) formed out of 2D photonic crystal defect cavities spaced $D=2a$ apart

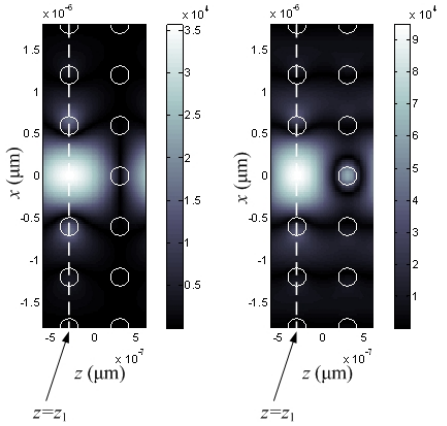


Fig. 2**:** a) and b) the modal field distribution of the electric field e_y of the modes inside the waveguide cell at $\beta=\pi/D/2$ and $\beta=0.05\pi/D/2$.

Expanding the modal field and the propagation constant around $\omega=\omega_0$,

$$\mathbf{e}_\omega = \sum_{n=0}^{\infty} \frac{\partial^n \mathbf{e}_{\omega_0}}{\partial \omega^n} \frac{\Delta\omega^n}{n!} \ , \ \beta(\omega) = \sum_{n=0}^{\infty} \beta_n \frac{\Delta\omega^n}{n!} \qquad (7)$$

with $\beta_n=\partial^n\beta(\omega_0)/\partial\omega^n$. Substituting (7) in (2) and using (3), one obtains:

$$\begin{aligned} \mathbf{E}(\mathbf{r},t) &= \sum_{n=0}^{\infty} \frac{\partial^n A(z,t)}{\partial t^n} \frac{\partial^n \mathbf{e}_{\omega_0}}{\partial \omega^n} \frac{j^n}{n!} e^{j\beta_0 z - j\omega_0 t} + c.c. \\ &\cong A(z,t)\mathbf{e}_{\omega_0} e^{j\beta_0 z - j\omega_0 t} + c.c. \end{aligned} \qquad (8)$$

where the second approximate equality is obtained by keeping only the first order terms. According to equation (8) the electric field is approximately written in terms of the Bloch function at $\omega=\omega_0$, modulated by the enveloppe fucntion $A(z,t)$. Differentiating with respect to z

$$\frac{\partial A(z,t)}{\partial z} = \int_P d\omega \left[\frac{\partial a}{\partial z} + j\Delta\beta a \right] e^{j\Delta\beta z - j\Delta\omega t} \qquad (9)$$

where $\Delta\beta=\beta(\omega)-\beta(\omega_0)$. Expanding $\Delta\beta$ around $\omega=\omega_0$, equation (9) is written as

$$\frac{\partial A(z,t)}{\partial z} = \int_P d\omega \frac{\partial a}{\partial z} e^{j\Delta\beta z - j\Delta\omega t} + \sum_{n=1}^{\infty} \frac{j^{n+1}\beta_n}{n!} \frac{\partial^n A}{\partial t^n} \qquad (10)$$

Equation (10) provides an evolution equation for the envelope function of the mode. In the next section the integral in the right hand side will be expressed in terms of the nonlinear contribution using the reciprocity relations.

Application of Reciprocity Relations

The total electromagnetic field (**E**,**H**) obeys the usual time dependent Maxwell's equations:

$$\nabla\times\mathbf{E} = -\mu\frac{\partial\mathbf{H}}{\partial t} \ , \nabla\times\mathbf{H} = \varepsilon\frac{\partial\mathbf{E}}{\partial t} \qquad (11)$$

where $\varepsilon=\varepsilon_L+\varepsilon_{NL}|\mathbf{E}|^2$ is the nonlinear dielectric constant of the waveguide. Setting $\mathbf{F} = \mathbf{E}\times\mathbf{H}^*_{\omega_0} + \mathbf{E}^*_{\omega_0}\times\mathbf{H}$ and applying Green's theorem one obtains:

$$\begin{aligned} &\frac{\partial}{\partial z}\int_S \mathbf{F}\cdot\mathbf{z}dS = -\int_S \left(\mu\mathbf{H}^*_{\omega_0}\cdot\frac{\partial\mathbf{H}}{\partial t} + \varepsilon\mathbf{E}^*_{\omega_0}\cdot\frac{\partial\mathbf{E}}{\partial t} \right) dS \\ &-j\omega_1\int_S \left(\varepsilon_L\mathbf{E}\cdot\mathbf{E}^*_{\omega_0} + \mu\mathbf{H}\cdot\mathbf{H}^*_{\omega_0} \right) dS \end{aligned} \qquad (12)$$

where S is any plane perpendicular to the propagation direction z. Using this equation, one obtains:

$$\frac{\partial}{\partial z}\int d\omega a R(\omega) e^{-j\omega t} = j\int d\omega a M(\omega) e^{-j\omega t} \qquad (13)$$

with

$$R(\omega) = \int_S dS \left(\mathbf{E}_\omega\times\mathbf{H}^*_{\omega_0} + \mathbf{E}^*_{\omega_0}\times\mathbf{H}_\omega \right)\mathbf{z} \qquad (14)$$

$$M(\omega) = \int_S dS \left\{ \mu\Delta\omega\mathbf{H}_\omega\mathbf{H}^*_{\omega_0} + \left(\omega\varepsilon - \omega_0\varepsilon_l\right)\mathbf{E}_\omega\mathbf{E}^*_{\omega_0} \right\} \qquad (15)$$

Setting $\mathbf{F}_1 = \mathbf{E}_\omega\times\mathbf{H}^*_{\omega_0} + \mathbf{E}^*_{\omega_0}\times\mathbf{H}_\omega$ and applying Green's divergence theorem, one obtains

$$\frac{\partial R}{\partial z} = j\Delta\omega\int_S \left[\mu\mathbf{H}^*_{\omega_0}\cdot\mathbf{H}_\omega + \varepsilon_L\mathbf{E}^*_{\omega_0}\cdot\mathbf{E}_\omega \right] dS \qquad (16)$$

Combining (16) and (13), the following equation is obtained:

$$\int d\omega \frac{\partial a}{\partial z} R(\omega) e^{j\Delta\beta z} e^{-j\omega t} = G(t) \qquad (17)$$

where the function $G(t)$ is

$$G(t) = j\int d\omega\omega a(z,\omega) e^{-j\omega t} \int_S dS \varepsilon_{NL} \left|\mathbf{E}\right|^2 \mathbf{e}_\omega \cdot \mathbf{e}^*_{\omega_0} \qquad (18)$$

Inverting the Fourier transform in (17) and re-integrating in P, equation (17) is written as

$$\int_P d\omega \frac{\partial a}{\partial z} e^{j\Delta\beta z} e^{-j\Delta\omega t} = \int_P \tilde{G}(\omega) R^{-1}(\omega) e^{-j\Delta\omega t} \qquad (19)$$

where Expanding R^{-1} around $\omega=\omega_0$, one obtains:

$$R^{-1}(\omega) = \sum_{r=0}^{\infty} R_n \frac{(\Delta\omega)^n}{n!} \qquad (20)$$

and using (20) in (19) along with (10), one obtains the following expression:

$$\frac{\partial A}{\partial z} = \sum_{r=0}^{\infty} \frac{j^r}{r!} R_r \frac{\partial^r G_P}{\partial t^r} + \sum_{n=1}^{\infty} \frac{j^{n+1}}{n!} \beta_n \frac{\partial^n A}{\partial t^n} \qquad (21)$$

where $\tilde{G}(\omega)$ is the spectrum of $G(t)$

$$G_P(t) = j\int_P d\omega\omega a e^{-j\Delta\omega t} \int_S dS \varepsilon_{NL} \left|\mathbf{E}\right|^2 \mathbf{e}_\omega \cdot \mathbf{e}^*_{\omega_0} \qquad (22)$$

In the next section G_P(t) will be expressed in terms of the enveloppe function A in order to complete the derivation.

Nonlinear Perturbation

To express $G_P(t)$ in terms of the envelope function of the guided mode, on makes use of the fact that

$$\left|\mathbf{E}\right|^2 = \mathbf{E}\cdot\mathbf{E} \cong 2\left|\mathbf{E}_P\right|^2 \qquad (23)$$

In (23), the terms oscillating around $\pm 2\omega_0$ are ignored. Using (2)

$$\left|\mathbf{E}\right|^2 \cong 2\left|\mathbf{E}_P\right|^2 = 2\int_P d\omega_1 a(z,\omega_1) \int_P d\omega_2 a^*(z,\omega_2) \times e^{j\Delta\beta_p z - j\Delta\omega_1 t - j\Delta\beta_q z + j\Delta\omega_2 t} \mathbf{e}_{\omega_1} \cdot \mathbf{e}^*_{\omega_2} \qquad (24)$$

Defining the function

$$T = 2\omega \int_S dS \varepsilon_{NL} \left(\mathbf{e}_{\omega_1} \cdot \mathbf{e}^*_{\omega_2}\right)\left(\mathbf{e}_\omega \cdot \mathbf{e}^*_{\omega_0}\right) \qquad (25)$$

and expanding around $\omega_1=\omega_2=\omega=\omega_0$,

$$T = \sum_{\mu\nu\kappa} T_{\mu\nu\kappa} \frac{(\Delta\omega)^\mu (\Delta\omega_1)^\nu (\Delta\omega_2)^\kappa}{\mu!\nu!\kappa!} \qquad (26)$$

and using (26) and (24) in (22), the nonlinear pertubation is written as:

$$Q_P = j\sum_{\mu\nu\kappa} \frac{j^{\mu+\nu-\kappa}}{\mu!\nu!\kappa!} T_{\mu\nu\kappa} \frac{\partial^\mu A}{\partial t^\mu} \frac{\partial^\kappa A^*}{\partial t^\kappa} \frac{\partial^\nu A}{\partial t^\nu} \qquad (27)$$

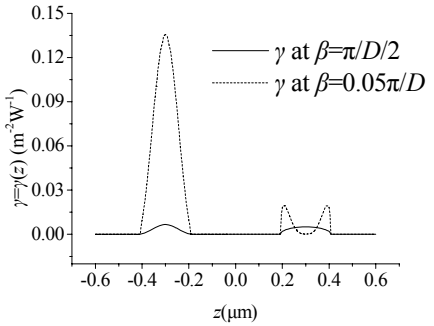


Fig. 3: The SPM coefficient for the CROW of Fig. 1 at the middle and the edge of the guided band.

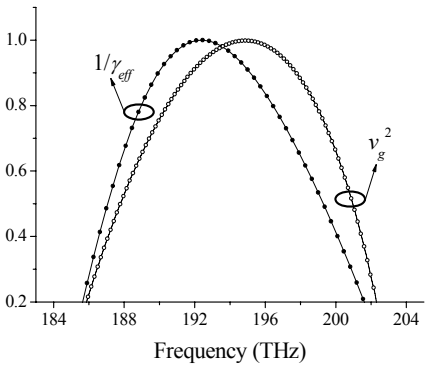


Fig. 4: Frequency dependence of $1/\gamma_{eff}$ and v_g^2

Propagation Equation

Using (27) and (21), one obtains the following propagation equation for the envelope function:

$$\frac{\partial A(z,t)}{\partial z} = \sum_{n=1}^{\infty} \frac{j^{n+1}}{n!} \beta_n \frac{\partial^n A(z,t)}{\partial t^n} + \sum_{r=0}^{\infty} \frac{j^{r+\mu+\nu-\kappa+1}}{r!\mu!\nu!\kappa!} U_r \frac{\partial^r}{\partial t^r}\left[T_{\mu\nu\kappa} \frac{\partial^\mu A}{\partial t^\mu} \frac{\partial^\kappa A^*}{\partial t^\kappa} \frac{\partial^\nu A}{\partial t^\nu}\right] \qquad (28)$$

Keeping the nonlinear terms up to first order:

$$\frac{\partial A}{\partial z} = \sum_n \frac{j^{n+1}\beta_n}{n!} \frac{\partial^n A}{\partial t^n} + j\gamma\left|A\right|^2 A + \delta_1 \frac{\partial}{\partial t}\left(\left|A\right|^2 A\right) - \left(\delta_2 + \delta_3\right)\left|A\right|^2 \frac{\partial A}{\partial t} + \delta_4 A^2 \frac{\partial A^*}{\partial t} \qquad (29)$$

where

$$\gamma = R_0 T_{000} = 2\omega_0 \int_S dS \varepsilon_{NL} \left|\mathbf{e}_{\omega_0}\right|^4 \qquad (30)$$

is the SPM coefficient. Fig. 3 illustrates the value of γ across the unit cell of the CROW considered in Fig. 1, in the case where $\beta=½\pi/D$ (middle of the band) and $\beta=0.05\pi/D$ (near the band edge). The nonlinear refractive index of the rods was taken $n_2=1.5\times10^{-17}\text{m}^2/\text{W}$. \Note that unlike conventional waveguides, the SPM coefficient is periodic and

varies along the propagation direction. Also, as explained before, near the band edge, the modal fields $\mathbf{e}_\omega$ are enhanced and hence the value of γ increases accordingly. The frequency dependence of the SPM coefficient is depicted in Fig. 5, where the normalized inverse of the effective SPM coefficient γ_{eff} is plotted and

$$\gamma_{eff} = \frac{1}{D}\int_{-D/2}^{D/2} \gamma(z)dz = \frac{2\omega_0}{D}\int_V dV\,\varepsilon_{NL}\left|\mathbf{e}_{\omega_0}\right|^4 \quad (31)$$

Also plotted in the figure is the normalized v_g^2. Comparing the two curves it is deduced that the SPM coefficient roughly exhibits a $1/v_g^2$ behavior.

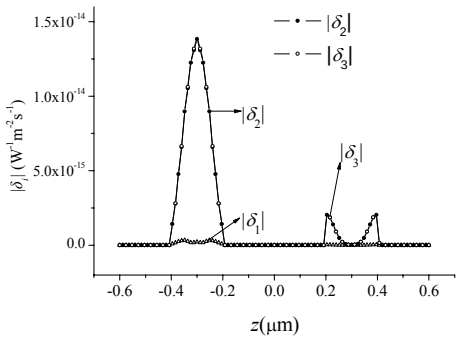


Fig. 5: Higher order nonlinear term coefficients for the CROW of Fig. 1 at $\beta=\pi/D/2$

The nonlinear term with coefficient δ_1 corresponds to r=1 and $\mu=\nu=\kappa=0$ in (28) and is given by

$$\delta_1 = -U_1 T_{000} = u_1\gamma \quad (32)$$

where $U_1=\partial(u^{-1})/\partial\omega=-u_1/u_0^2=-u_1$ and

$$u_1 = \int_S dS\left(\frac{\partial \mathbf{e}_{\omega_0}}{\partial\omega}\times\mathbf{h}^*_{\omega_0} + \mathbf{e}^*_{\omega_0}\times\frac{\partial\mathbf{h}_{\omega_0}}{\partial\omega}\right)\mathbf{z} \quad (33)$$

The term δ_2 is obtained for ν=1 and $r=\nu=\kappa=0$ in which case,

$$\delta_3 = 2\omega_0\int_S dS\,\varepsilon_{NL}\left|\mathbf{e}_{\omega_0}\right|^2\left(\frac{\partial\mathbf{e}_\omega}{\partial\omega}\cdot\mathbf{e}^*_{\omega_0}\right) \quad (34)$$

The term δ_3 corresponds to μ=1 and $r=\nu=\kappa=0$ and is given by

$$\delta_2 = 2\int_S dS\,\varepsilon_{NL}\left|\mathbf{e}_{\omega_0}\right|^2\frac{\partial}{\partial\omega}\left(\omega\mathbf{e}_\omega\cdot\mathbf{e}^*_{\omega_0}\right) = \frac{\gamma}{\omega_0}+\delta_3 \quad (35)$$

The last nonlinear term is obtained for κ=1 and $r=\nu=\mu=0$ and is written as

$$\delta_4 = 2\omega_0\int_S dS\,\varepsilon_{NL}\left|\mathbf{e}_{\omega_0}\right|^2\left(\frac{\partial\mathbf{e}^*_\omega}{\partial\omega}\cdot\mathbf{e}_{\omega_0}\right) = \delta_3^* \quad (36)$$

Inspecting equations (32)-(36), one deduces that, as expected the higher order nonlinear contributions arise from the frequency dependence of the Bloch function $\mathbf{e}_\omega$.

In Fig. 5, the value of the higher order nonlinear coefficients at the middle of the CROW band (β=½π/D) are plotted. The influence of the terms also depends on the magnitude of the derivatives of the envelope functions. Assuming Gaussian incident pulses $A(0,t)=\exp(-t^2/2T_0^2)$, these derivatives are proportional to $1/T_0$ and hence the magnitude of the terms is roughly δ_i/T_0. For 10ps pulses, $T_0=10^{-11}$s and hence the maximum of δ_2/T_0 will be of the order of 5×10^{-6}W^{-1}m^{-2} which is about three orders of magnitude less than the maximum of the SPM coefficient which is $\gamma_{max}=6\times10^{-3}$W^{-1}m^{-2} for β=½π/D. It is therefore reasonable to deduce that the higher order nonlinear terms will not significantly affect the pulse propagation. The value of the higher order nonlinear coefficients near the band edge (β=0.05π/D) are plotted in Fig. 5. For $T_0=10^{-11}$s, the maximum of δ_2/T_0 becomes 1.4×10^{-3}W^{-1}m^{-2}, which is now 2 order of magnitude less than $\gamma_{max}=1.3\times10^{-1}$W^{-1}m^{-2}. This means that the higher order terms have a more pronounced influence near the band edges and for pulse durations less than 10ps, they have to be included in the analysis.

References

1 J.D Joannopoulos, et al *Photonic Crystals, Molding the flow of Light*, Princeton University Press, 1995.

2 M. Solja˘cic´ et al, Nature, Vol. 3 pp. 211-218 (2004).

3 A. Yariv et al, Optics Letters, Vol. 24, pp. 711-713 (1999).

4 G.P. Agrawal, *Non-linear fiber optics*, Academic Press, 2001.

5 T. Kamalakis et al, IEEE J. Quant. Elect. Vol. 42 , pp. 827-837 (2006).

6 A. Tafflove et al *Computational Electrodynamics: the finite difference time-domain method*, Artech House Publishers, 2000.

7 K. Sakoda, *Optical Properties of Photonic Crystals*, Springer-Verlag Berlin, 2001.

Design of photonic crystal directional couplers for electro-optical wavelength switching

Eric Cassan, Damien Bernier, Guillaume Maire, Delphine Marris-Morini, Laurent Vivien
Institut d'Electronique Fondamentale, UMR 8622, Bât. 220, Université Paris Sud, 91405 Orsay Cedex, France
corresponding author: eric.cassan@ief.u-psud.fr

Abstract:
Photonic crystal directional couplers are designed for the realization of compact electro-optical wavelength switches in SOI technology. Influence of group velocity dispersion properties of slow Bloch modes involved in the device operation is studied and switching devices' performances are evaluated as a function of refractive index variations induced by carrier plasma effect in a wide range.

Introduction

Silicon nanophotonics has received a growing interest from several years. Integration of optics within the mainstream silicon technology is expected to enable the realization of dense and complex photonic integrated circuits and the design of new on-chip applications. In this context, implementation of optical wavelength division multiplexing (WDM) communications is viewed as an important step to enable high bandpass aggregate data transfers [1]. Elements to be considered in WDM communications are optical multiplexers/demultiplexers, selective filters, and wavelength switches.

This work is focused on the design of electro-optical wavelength switches in silicon on insulator (SOI) technology. Resonators have been mainly considered for channel dropping devices. Although ring resonators between two optical waveguides provide an ideal basic structure for removal of a wavelength channel from an input bus, it was shown that surface roughness in this kind of devices adversely affects performances by the coupling between counterpropagating optical waves. For this reason, the use of other optical resonators was proposed. It was theoretically shown that 100% efficiency selective dropping is possible provided that very well defined conditions are fulfilled to achieve the desired transfer characteristics [2,3]. The used resonator should have two degenerate modes that possess appropriate symmetries with respect to resonator symmetry planes and coupling rates between these modes and the two device ports should be properly balanced. The possible combination of this approach in photonic crystal (PC) compact structures was theoretically shown. In spite of excellent predicted performances, this approach raises very challenging issues from the technological point of view as mode forced degeneracy is obtained using very fine tuning of device parameters such as individual hole diameters and positions.

On the other hand, simpler approaches based on traditional integrated optics have been proposed in planar PC configurations [4]. These approaches basically rely on a directional coupler configuration without any kind of mediating structure between coupled waveguides. Strongly corrugated PC waveguides are then essential to allow high phase mismatch between coupled supermodes, so that overall structures can be designed with only few-wavelength sizes.

Starting from a directional coupler configuration, active switching can be obtained. In ref [4], an electro-optical switch implemented in coupled PC waveguides was proposed. Short coupling lengths (< 10λ) were demonstrated but it was shown that electrical conductivity induced by carrier plasma effect as high as 10 Ω^{-1} cm^{-1} was necessary in planar silicon air-hole PC waveguides corresponding to carrier concentrations in excess than 10^{20} cm^{-3}. Structural modifications of the directional coupler geometry have been proposed in ref [5] to allow small switching length and wide bandwidth, but no study was made on device performances as a function of refractive index variations practically reachable in the silicon technology, as well as on the possible influence of group velocity dispersion (GVD) effects of the slow Bloch supermodes sustaining the device principle of operation.

Photonic crystal directional couplers

In this work, simple design PC directional couplers allowing a continuous tuning of GVD effects is studied for the realization of wavelength electro-optical switches. Refractive index in silicon induced by carrier plasma effect is considered. Active coupling lengths are evaluated as a function of carrier injection level in selected configurations, and electro-optical switch device design is proposed for working wavelengths around λ=1.55µm.

The investigated structure is based on a 2D PC formed by a triangular lattice with lattice parameter a=400nm, and hole diameter 2r =240nm (r/a = 0.3), respectively. Refractive index of slab regions is 2.872, while hole refractive index is 1.45. These values correspond to the effective index of a 240 nm thick SOI slab waveguide at λ=1.55µm and to silicon oxide, respectively. PC band diagram has been calculated with the MIT plane wave software [6] in TE polarization and a frequency bandgap was found extending from band 1 at $\omega_r = a/\lambda = 0.2463$ to band 2 at ω_r=0.2802. From this starting point, symmetric photonic crystal directional couplers can be obtained by removing two rows of holes. Two W1 PC waveguides can be coupled through three rows of holes. The two coupled PC waveguides then give rise to the appearance of two guided supermode bands, with even and odd symetries with respect to the directional coupler mirror plane.

An even supermode is then carefully prepared to present a flat band in the wide normalized wavevector range [5]. Due to this particular feature, even low refractive variations that only slightly shifts photonic bands can induce a strong varation between the even and odd wavectors at a given frequency. Contrary to previous approaches based on both hole size tuning and shift of multiple holes, design strategy was simplified to the variation of only one parameter.

Figure 1 shows the studied directional coupler configuration, as well as the obtained even and odd supermode photonic bands as a function of normalized wavevector along the propagation direction. Hole radius of the central row was varied from r/a=0.39 to r/a=0.43 to allow some tuning of the even supermode properties. It can be seen in figure 1 that a continuous change of the even-mode frequency slope can be obtained by this simple design strategy. Either positive or negative light group velocities can be obtained in a limited range of wavector values around k_R=0.37 and perfectly flat even supermode band can be ideally designed for r/a~0.42.

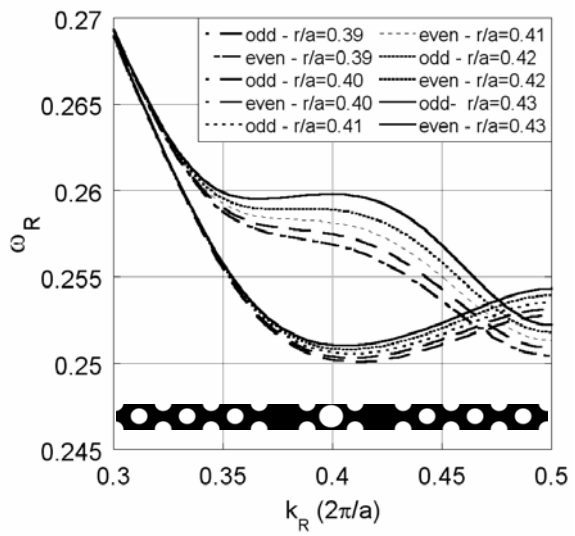


Fig. 1: Dispersion characteristics of the two even and odd supermode photonic bands of the studied photonic crystal directional coupler configuration

Influence of group velocity dispersion (GVD) on device properties

Although design of ideally flat even supermode band is desirable for the realization of compact PC directional coupler swiching devices, it is to be verified that compactness and sensitivity to refractive index variations is not allowed at the expense of a huge level of group velocity dispersion (GVD) that can be responsible for strong temporal deformations of optical pulse propagating in the device.

Group velocity v_{GR} and GVD coefficient D_λ of even supermodes obtained for r/a ranging from 0.39 to 0.43 have been calculated. D_λ was estimated as:

$$D_\lambda = -\frac{2\pi c}{\lambda^2}\frac{d^2k}{d\omega^2} = \frac{a}{c\lambda^2}\frac{1}{{v_{GR}}^3}\frac{dv_{GR}}{dk_R} \qquad (1)$$

, with a the lattice parameter and $c=3.10^8$ ms^{-1}.

To ensure negligeable temporal distorsions of τ=100ps width optical pulses after a propagating length L_{Device} of 300µm, a practical limit of $D_\lambda \approx 10^5$ ps/(nm.cm) is found according to:

$$D_\lambda << \frac{2\pi c}{\lambda^2}\frac{\tau^2}{L_{Device}} \qquad (2)$$

Figure 2 and figure 3 show the evolutions of the even supermode v_{GR} and D_λ parameters as a function of normalized wavevector k_R, respectively.

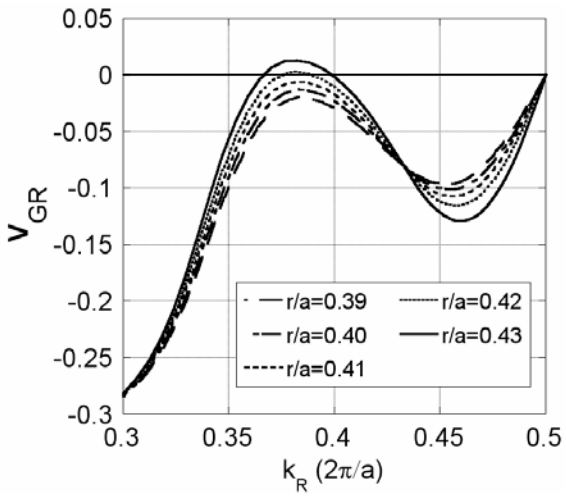


Fig. 2: Influence of the hole radius of the central row holes on the even supermode group velocity

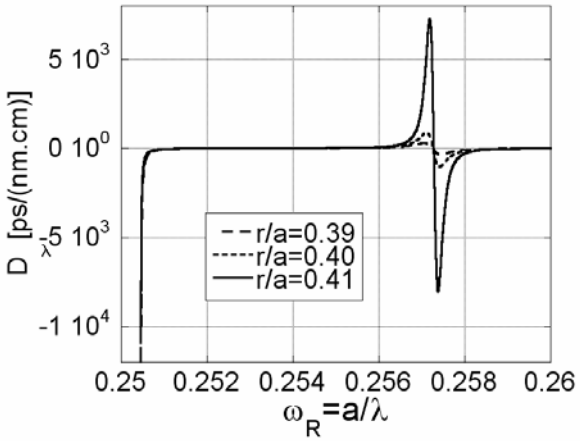


Fig. 3: Group velocity dispersion coefficient of the even supermode for several values of the hole radius in the central row of the symmetric directional coupler

It can be seen that two zero group velocity points are obtained for r/a values above 0.41, while non-zero v_{GR} slopes are found at this particular points. According to relationship (1), it turns that infinite values of D_λ are then reached, which is not desirable from a practical point of view. For this reason, values of r/a leading to the flattest even band (r/a~0.42) have to be removed due to GVD-induced pulse distorsions. At the same time, Figure 3 shows that r/a values around 0.41 lead to a good compromise, with peak D_λ values

near the frequency operating point ($\omega_R \approx 0.257$) around 8.10^3 ps/(nm.cm).

Design of electro-optical wavelength switch

Electro-optical wavelength switch has been further designed with a hole radius in directional coupler central row r/a of 0.41.

Figure 4 shows a schematic of the complete device.

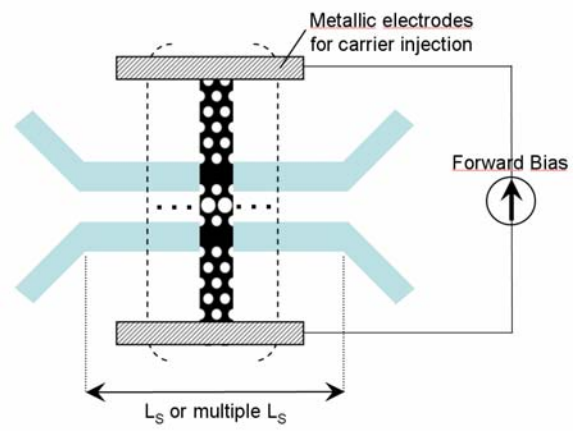


Fig. 4: Schematics of the studied device configuration

Static coupling length L_S is define as the required size to ensure a π phase shift between the even and odd supermode in absence of free carrier injection:

$$L_S(\omega_r) = \frac{\pi}{k_e(n,\omega_r) - k_o(n,\omega_r)} \qquad (3)$$

Active coupling length L_A from one output port to the other then results from from refractive index variation -Δn and was estimated as:

$$L_A(\omega_r) = \frac{\pi}{\left[k_e(n-\Delta n,\omega_r) - k_e(n,\omega_r)\right] - \left[k_o(n-\Delta n,\omega_r) - k_o(n,\omega_r)\right]} \qquad (4)$$

, with $k_e=k_e(n,\omega_r)$ and $k_o=k_o(n,\omega_r)$ the even and odd dispersion relationships.

L_A can be viewed as the required length to ensure an additional π phase shift between both supermodes for a given level of refractive index decrease -Δn at a given normalized frequency.

Figure 5 shows the obtained static and active coupling lengths L_S and L_A as a function of refractive index variation Δn ranging from -10^{-4} to -2.10^{-3}. This value range corresponds to layer refractive index variations pratically reachable using plasma dispersion effect in silicon.

It can be observed that low active coupling length values are obtained for frequency around $\omega_r=0.258$. This corresponds to the condition of flat even supermode photonic band. The higher Δn the lower L_A. It is also visible that the region with lowest values of static coupling length ($\omega_r<0.2577$) is not the best operating configuration. This is due to the fact that extremely low L_S values (~3µm) are obtained in this condition due to to strong mismatch between ke and ko, but sensitivity of (ke-ko) to index variation is then relatively poor. For this reason, the optimization procedure is first made on the criterium of low active coupling length. This allows the choice of operating normalized frequency. Static length is then deduced from the knowledge of ω_r.

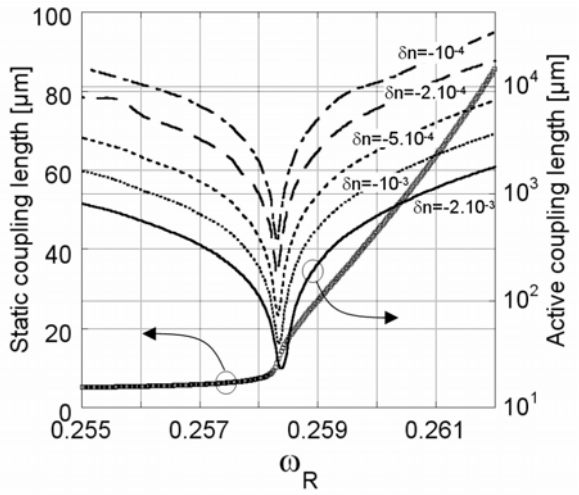


Fig. 5: Static coupling length and active coupling length obtained for several values of refractive index variation

Table 1 shows the minimum values of L_A as a function of Δn obtained around $\omega_r=0.258$ ($\lambda \approx 1550$nm for lattice parameter a equal to 400nm as previsouly stated).

-Δn	L_A (µm)	L_S (µm)
10^{-4}	139.5	4.5
2×10^{-4}	70.5	4.55
5×10^{-4}	29.7	5.0
10^{-3}	16.0	5.2
2×10^{-3}	9.5	5.8

Table 1: Minimum active coupling lengths and associated static coupling lengths

It is shown that reasonable active coupling length are obtained (< 140µm) even for low refractive index variation ($\Delta n = -10^{-4}$).

Extremely low active coupling length (~16µm) is obtained for a refractive index variation of 10^{-3}. According to the plasma dispersion relationship in silicon given by:

$$\Delta n = -8{,}8.10^{-22}\Delta N - 8{,}5.10^{-18}\Delta P^{0,8} \text{ at } \lambda = 1.55\mu m$$

, this correspond to a carrier injection level ΔN (electrons) or ΔP (holes) around 5.10^{17} cm^{-3}.

A possible implementation to realize an electro-optic wavelength switch at λ=1550nm is shown in figure 6. A static coupling length of 20.8µm ($L_S=4\times5.2$ µm) is chosen so that even and odd supermodes are phase-matched ($\Delta\varphi=4\pi$) after propagating through the whole device in absence of free carrier injection. Light injected in input port n°1 is thus to be collected

at output port n°1 (‘bar’ state). A limited area of 16µm length is chosen for carrier injection with electrode and silicon doping level engineered to ensure $\delta n=-10^{-3}$ in the ‘cross’ state (light collection at output port n°2 in case of injection into input port n°1). Bandpass of the device was also estimated to around 1 nm in the studied conditions.
Considering a possible chirp of lattice parameter a, it is envisioned that similar electro-optic wavelength switch could be designed in a wavelength wide range around 1.55 µm.

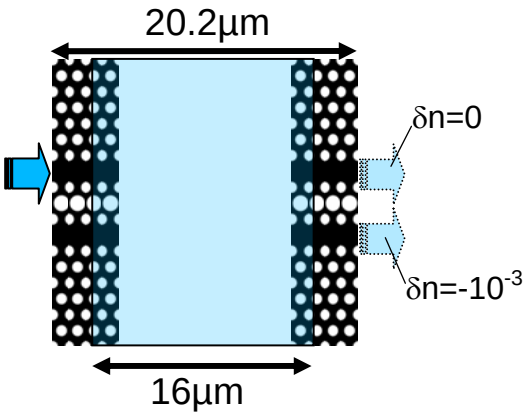


Fig. 6: Design of a 16µm long PC wavelength directional coupler for wavelength switching around λ=1.55µm

Conclusions

This work reports the study of a wavelength-sensitive switch based on a optimized PC SOI directional coupler configuration. Previous approaches have been simplified to limit the number of tuned technological parameters to only one to obtain the required Bloch mode slow light properties.
Influence of GVD in the studied configuration is studied for the first time. It is shown that the most desirable configuration with respect to flat bland condition and device compactness are not desirable due to temporal pulse deformations induced by GVD.
Cross-bar active coupling length is estimated as a function of refractive index variations pratically reachable in silicon with plasma dispersion effect.
It is shown that device length only around 10λ can be obtained provided that index variation around 10^{-3} is induced which corresponds to free carrier injection concentration about 5.10^{17} cm^{-3} in silicon.
Studied optoelectronic devices exhibit bandpass around 1 nm at λ=1.55µm and can be designed for operation in a wide wavelength range around this central wavelength.

Acknowledgments

The authors would like to aknowledge Suzanne Laval for fruitful discusssions.

References

1 M. Haurylau et al, IEEE Group IV Photonics conference, n°10.1109/Group4.2005.1516388, p. 17, 2005.
2 S. Fan et al, Physical Review Letters, n°80(5). p. 960, 1998.
3 S. Fan et al, Optics Express, n°3(1). p. 4, 1998.
4 A. Sharkawy et al, Optics Express, n°10(20). p. 1048, 2002.
5 N. Yamamoto et al., Optics Express, n°14(3). p. 1223, 2006.
6 MIT photonic band (MPB) available at: http://ab-initio.mit.edu/photons/

Photonic crystals in diamond: Cavity Q – Mode volume influence on the design

Igal Bayn (1) and Joseph Salzman (2)
1), 2) Department of Electrical Engineering and Microelectronics Research Center, Technion Haifa, 32000, Israel,
eebayn@techunix.technion.ac.il

Abstract: We present a qualitative analysis of the influence of the mode volume on a planar photonic crystal (PC) cavity quality factor (Q) in diamond. Optimal waveguide based cavity geometry with minimized vertical losses is considered. The mode width and slab thickness are varied to provide maximum Q. The results are compared to the similar designs in silicon. The optimal geometric parameters for diamond cavities are derived. These results are supported by 3D Finite Difference Time Domain (FDTD) calculations on double heterostructures (DHs) cavities. The highest $Q\approx135,000$ is demonstrated.

Introduction

2D Photonic Crystal Structures in diamond are being considered as an attractive architecture for the control and manipulation of atom-photon dressed states [1]. Several designs for the high-Q cavities on diamond were recently reported [2, 3], while the best result of $Q\approx70,000$ is obtained for the DH cavity design [3]. This result is more than one order of magnitude lower than similar designs in silicon [4, 5]. This major discrepancy rises the question of the physical mechanism responsible for the dielectric constant influence on photonic crystal cavity Q. Here, we discuss the difference between quality factors in high-ε (silicon) and low-ε (diamond) slab PC cavity designs.

The considered PC cavities consists of a membrane suspended in air and periodically modulated by a triangular array of air holes. The design resonances are TE-like modes located at the 1st bandgap.

Qualitative approach

The cavity mode is confined laterally by the Bragg reflection and vertically by total internal reflection. Therefore, the quality factor (Q) can be divided into two major components, for the lateral (Q_l) and the vertical (Q_v) losses [5]. Since Q_l is determined by the number of PC periods around the cavity, by embedding the cavity in a sufficiently large PC, the value of Q_l can be made arbitrarily large. Therefore, $Q=Q_v$ is assumed.

We discuss the cavities formed as spatial modulation of a PC waveguide, providing mode localization, that demonstrated the best Q values in both silicon [4, 5] and diamond [3]. The PC waveguide is defined by a linear defect into the PC slab in the ΓJ direction, with one filled row of holes (see Fig. 1). The cavity design is based on the lowest waveguide mode.

The vertical power losses (P_v) in a cavity are proportional to the integral of the Fourier Transform (FT) squared - $|FT(H_y)|^2$ (H_y - magnetic field in y direction) in the light cone area, i.e. in $k_l<k_0$, where $k_l=(k_x,k_z)$ and $k_0=2\pi/\lambda_0$. Following the inverse problem approach [5], the cavity mode is represented as a product of waveguide field and a slowly varying envelope function. In order to minimize P_v an ideal Gaussian envelope function is assumed [5]:

$$FT_2\left(H_y\right)= \sum_{k_{x0},k_{z0}} sign\left(k_{x_0}\right)\exp\left(-\left(k_x-k_{x_0}\right)\frac{\sigma_x}{\sqrt{2}}\right)^2\exp\left(-\left(k_z-k_{z_0}\right)\frac{\sigma_z}{\sqrt{2}}\right)^2 \quad (1)$$

where: σ_x and σ_z are the modal widths in real space in x and z directions respectively, and $(\pm k_{x0} \pm k_{z0})$ are the J points.

We assume that cavity resonance is close to the waveguide one, i.e. $\omega_0\approx\omega_w$. Since silicon dielectric constant is higher than that of diamond, the PC

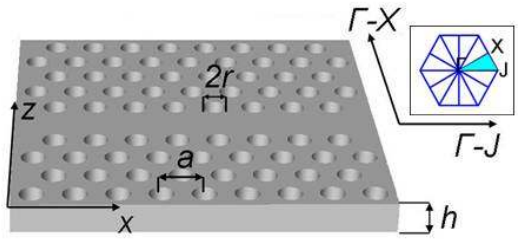


Fig. 1: The notation of PC waveguide. In the inset the 1st Brillouin zone of the triangular lattice with high symmetry points are depicted.

waveguide mode frequency in silicon is lower than that of diamond ($\omega_{wSi}<\omega_{wD}$). Consequently, cavity mode frequencies satisfy $\omega_{0Si}<\omega_{0D}$. This difference in the resonant frequency is responsible for the different light cones, thus resulting in exponentially different Q_v in silicon and diamond [3].

In Fig. 2(a) the ratio between the vertical quality factors (Q_{vSi}/Q_{vD}) as a function of modal width in x direction (σ_x) for the ideal envelope cavities (Eq. 1) is depicted. Note, that $\sigma_{xD}=\sigma_{xSi}$ is assumed. The mode widths in the z direction are defined by the bandgap confinement, and obtained from the fit to DHs in [3] and [4]. From the figure Q_{vSi}/Q_{vD} exponentially increases with σ_x, since the vertical losses (P_v) in silicon and diamond light cones are exponentially different.

The exponential dependence of Q_v on σ_x suggests that higher P_v in diamond can be compensated by an increased σ_{xD}, thus improving $|FT(H_y)|^2$ localization. In Fig. 2(b) σ_{xD}, vs. σ_{xSi} values leading to $Q_{vSi}=Q_{vD}$

are plotted. There is an accurate fit to σ_{xD}: $\sigma_{xD}=[A+B(\sigma_{xSi}-C)^2]^{1/2}$, while for $\sigma_{xSi}>0.9a$, it may be approximated by a linear relation. A general expression for $\sigma_x(\varepsilon_1)$ vs. $\sigma_x(\varepsilon_2)$, where ε_1, ε_2 are respective slab dielectric constants, will be presented.

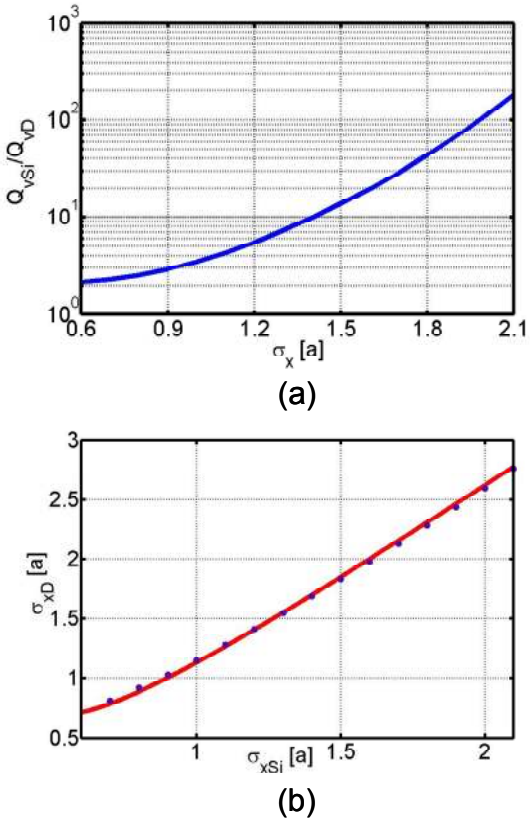


Fig. 2: (a) Q_{vSi}/Q_{vD} vs. σ_x. (b) σ_{xD} (that provides $Q_{vSi}/Q_{vD}=1$) vs. σ_{xSi} . In blue σ_{xD} is shown. In red the fit to $\sigma_{xD}=[A+B(\sigma_{xSi}-C)^2]^{1/2}$.

In the following the influence of slab thickness (h) on the vertical quality factor (Q_v) is discussed. Although the analysis given here treats the diamond cavities with a Gaussian envelope, it can be extended to other materials and to any PC waveguide based design, including DH cavities. Here, we assume that the cavity resonance frequency is close to the waveguide one, i.e. $\omega_0 \approx \omega_w$. As one can observe from Fig. 3(a), the mode's k decreases with an increase in the slab height. This k decrease in the light cone radius results in a subsequent decrease of vertical power losses, thus significantly improving the Q_v.

In Fig. 3(b, c) we present the Q_v behavior in two diamond Gaussian envelope cavities with different mode widths in x direction (σ_x) as a function of the slab thickness. We can see that the increase in the slab thickness from *0.6a* to *0.9a* increases the Q_v by the factor that varies from *3.45* for the $\sigma_x=1.5a$ to *13* for $\sigma_x=2.6a$. Note that slab thickness increase is bounded by a subsequent decrease in the bandgap, which sustains lateral confinement of cavity mode. Therefore, slab thickness increase is limited by the photonic bandgap existence condition.

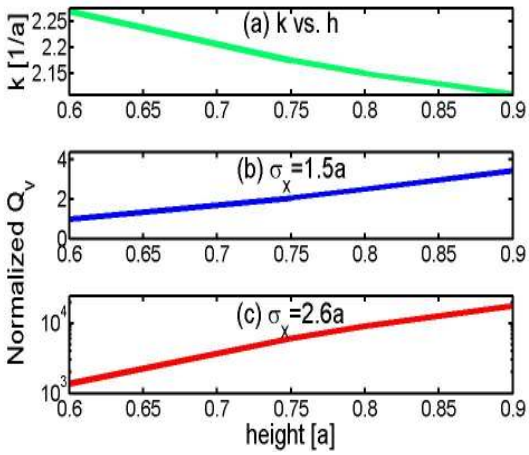


Fig. 3: Slab height influence on Q_v. (a) Diamond light cone radius k vs. h in waveguide based cavities. (b) Q_v vs. h for $\sigma_x=1.5a$. (c) Q_v vs. h for $\sigma_x=2.6a$. All quality factors are normalized to the cavity with $h=0.6a$ and $\sigma_x=1.6a$.

DH Analysis

These qualitative results are checked for the diamond modified double heterostructure (DH)] cavities [4] with 3D FDTD calculations. In this structure the confinement in x direction is formed by two different layers of elongated photonic crystals: a_1, a_{21} ($a_2>a_{21}>a_1$), while the confinement in z (lateral) direction is supported by the band gap (see Fig. 3(a)). When the number of a_{21} periods is increased from *0* to *3*, σ_{xD} increases from *1.93a* to *2.08a*, resulting in Q_v increase from *67,000* to *135,000*. Although DH is not an ideal Gaussian, still Q_v vs. σ_x is nearly exponential. The H_y profile is shown in Fig. 3(b). Note that the increase in slab thickness in DH

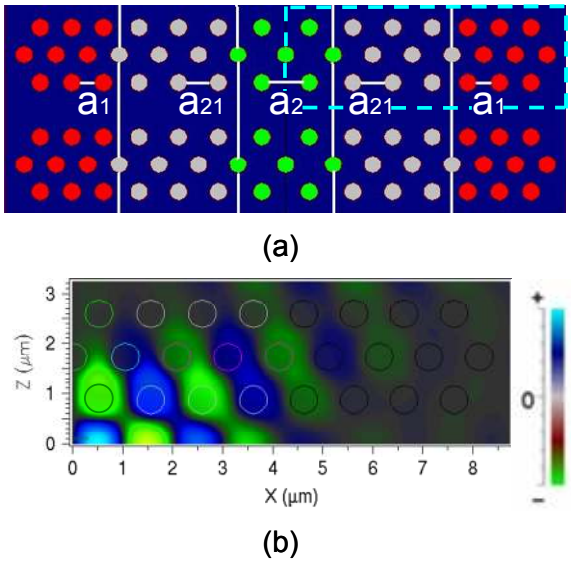


Fig. 3: (a) Modified DH with $3a_{21}$ periods. (b) The H_y profile in the 1st quarter of the DH at $y=0$ plane.

increases Q_v from 37,000 to 67,000 [3]. This can be easily explained by the decrease in the vertical power losses. In a DH cavity, the resonant mode frequency is found between the 1st waveguide mode and the

dielectric band edge, while the dielectric band edge dependence on a slab thickness is similar to that of the waveguide one. Therefore, similar decrease in the light cone radius (k) as the slab thickness increases, is expected.

Conclusions

We studied how the modal width and slab thickness increase can significantly improve the cavity Q. Moreover, for the QED application, since Q dependence on σ_x is exponential, while mode volume V dependence is linear, it is worth to compensate high vertical losses with increased mode width. The slab thickness increase in the waveguide based cavity designs improves the Q_v by decreasing the light cone. In the diamond cavity studied here an optimal cavity thickness of $0.9a$ is obtained. Similar behavior is observed at diamond modified DH cavities, where the increase in σ_x results in $Q_v=135,000$.

Acknowledgments

This research was partially supported by the fund of Promotion Research in the Technion.

References

1 A.D. Greentre, J. Salzman, S. Prawer, and L.C. Hollenberg, Phys. Rev. A73, 013818 (2006).
2 S. Tomljenovic-Hanic, M. J. Steel, C. M. de Sterke and J. Salzman, Optics Express 14, 3556 (2006).
3 I. Bayn and J. Salzman, Eur. Phys. J. Appl. Phys. (2006), DOI: 10.1051/epjap:2006131,
4 B. Song, S. Noda, T. Asano and Y. Akahane Nature, Vol.4, March 2005.
5 D. Englund, I. Fushman, J Vuckovic, Optics Express 12, 5961 (2005).

Excitation of Leaky modes in the System of Coupled Waveguides

Boris Usievich, Jamil Nurligareev, Vladimir Sychugov (1) and Konstantin Golant (2)
1) General Physics Institute, Moscow, Russia e-mail: borisu@kapella.gpi.ru
2) Fiber Optic Research Center, Moscow, Russia e-mail: golant@fo.gpi.ru

Abstract: *In this paper we study a system of coupled waveguides where the number of guided modes M is less than number of individual waveguides N. We study in details leaky modes in this system both theoretically and experimentally. In particular we show that leaky modes are excited from the side of the waveguide system at the same time when the reflection coefficient for the exciting beam goes to zero.*

Introduction

Uniform system of coupled waveguides is a group of equidistantly placed identical waveguides. It could be a multilayer dielectric mirror or a group of channel waveguides in the dielectric layer on top of lower index substrate. Recently this kind of waveguide systems attracted attention due to possiblity of creation of high-power lasers [1]. Earlier we studied the process of light propagation in a uniform system of coupled waveguides [2-3]. It was noted that the Bragg diffraction process in this system is of particular interest [4]. I this paper we are trying to examine the Bragg diffraction process in details for both edge and side incidence of the exciting light on the system of coupled waveguides.

Theory

It was shown earlier [2] that number of modes in a system of coupled waveguides depends on number of waveguides N and the refractive indices of guides and gaps. I this paper we study the system with the following parameters: number of waveguides N=50; waveguide layers n_f=1.465, h=1.1mkm; gaps n_s=1.46, s=1.3; cover and substrate also have refractive index 1.46 [6]. In the case of weak waveguides number of guided modes M is less than number of waveguides N. For this particular system we have M=34 and the rest of the modes are leaky. Figure 1 present the dependence of the effective refractive indices of modes n^* on the mode order m. Leaky modes exhibit light radiation into the adjacent media during the propagation along the system. Angle of propagation through the side surfaces of the system is given by following equation:

$$\cos\theta = \frac{n^*}{n_s} \qquad (1)$$

Figure 2 presents the dependence of this angle on the mode order for modes m = 35 … 50 (curve 1) [5].

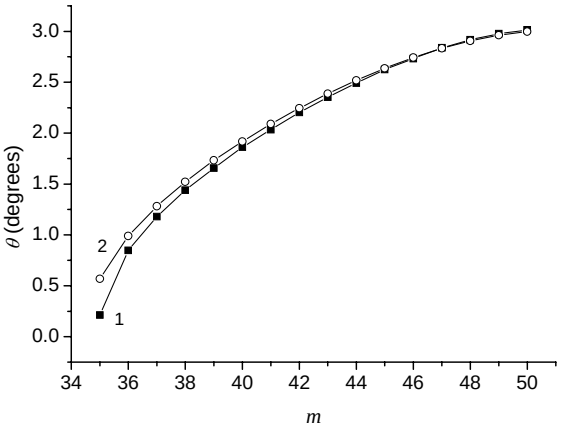


Fig. 2: Leak angles for different modes

Leaky modes in the system can be excited by the light beam incident on the side surface of the system. As our system is periodic it exhibit well known Bragg reflection. First we calculated the dependence of the reflection coefficient for side incident beam. Figure 3 presents these results.

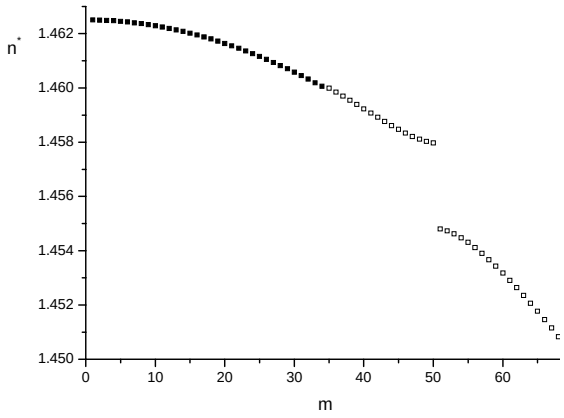


Fig. 1: Effective refractive indices of modes

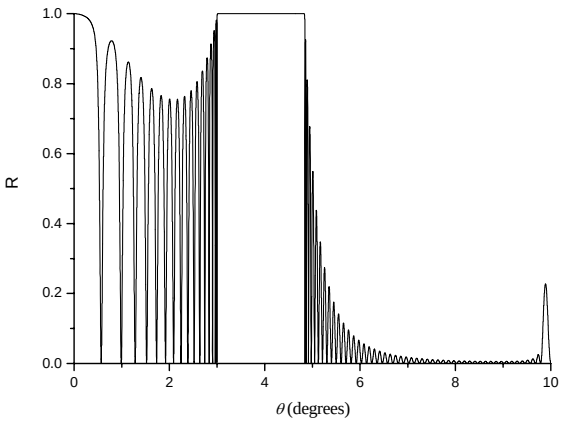


Fig. 3: Reflection coefficient for side-incident beam

One should note that in the range of incidence angles from 0 to 3º there are peaks and dips and the number of dips is equal to the number of leaky modes of the waveguide system in the first permitted band: $N - M = 16$. Then we compared the positions of these minima (fig.2 curve 2) with the dependence of leak angle for modes calculated earlier and that they are in good agreement. These two things led us to conclusion that leaky modes are excited when the angle of incidence coincides with the minimum of the reflection curve $R(\theta)$.

Treating our waveguide system as a photonic crystal it is convenient to present a field inside the system as a combination of Floquet-Bloch waves with the Bloch wavevector K_b given by the following formulas [7]:

$$\cos K_b\Lambda = \cos\kappa_f h \cdot \cos\kappa_s s - \frac{1}{2}\left(\frac{\kappa_s}{\kappa_f} + \frac{\kappa_f}{\kappa_s}\right)\cdot \sin\kappa_f h \cdot \sin\kappa_s s \qquad (2)$$

where $\kappa_f = k\sqrt{n_f^2 - n^{*2}}$, $\kappa_s = k\sqrt{n_s^2 - n^{*2}}$ are transverse components of plane wave wavevectors in guiding and intermediate layers respectively, $k = 2\pi/\lambda$, λ is wavelength of light on free space. According to [7] the reflection coefficient $R(\theta)$ can be calculated as follows:

$$R(\theta) = \frac{|C|^2}{|C|^2 + \left(\sin K_b\Lambda / \sin NK_b\Lambda\right)^2} \qquad (3)$$

and is mainly determined by rapidly changing term $\sin K_b\Lambda / \sin NK_b\Lambda$. Coefficient $|C|^2$ is a structure factor and is given by

$$|C|^2 = \frac{1}{4}\left(\frac{\kappa_f}{\kappa_s} - \frac{\kappa_s}{\kappa_f}\right)^2 \cdot \sin^2\kappa_f h \qquad (4)$$

It slowly changes with the variation of incidence angle. In the case of non-zero $|C|^2$ the condition

$$\frac{\sin NK_b\Lambda}{\sin K_b\Lambda} = 0 \qquad (5)$$

is actually the dispersion relation for leaky modes of the system.

We calculated the field inside the system when it is illuminated by side-incident beam. It was found that the minima of reflection correspond to the maxima of energy accumulation in the system that means that leaky modes are excited. Distribution of field in that case corresponds to the calculated earlier mode profile of leaky modes. For angles corresponding to the maxima of the reflection energy accumulation is practically absent. This behaviour is analogous to widely used Fabry-Perot interferometer where the energy is also accumulated in the minima of transmission.

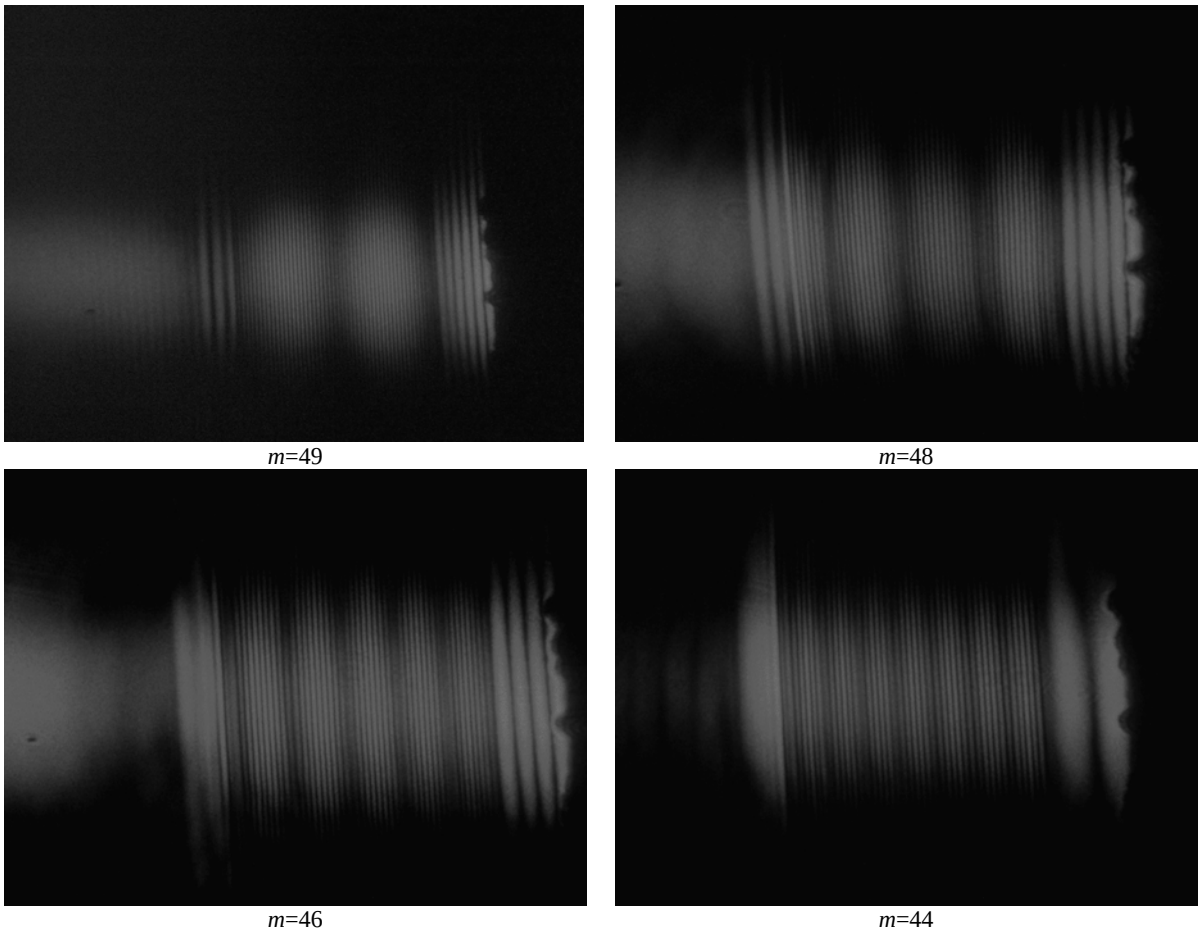


Fig. 4: Leaky modes field at the output edge of the waveguide system

Experiment

We observed the excitation of leaky modes with the side-incident beam first in [8]. In this paper we want to study this phenomenon in more details. We used the setup shown in figure 5. Transmitted and reflected beams were observed on the screen put at 2.5m distance. For observation of the intensity distribution at the output edge of the system its image was created on the screen using micro-objective with a magnification factor M=300. Light beam falls onto the edge of the sample in the buffer layer area, refracts on the air-subratate interface and then drop onto the side surface of the waveguide system (see fig.7).

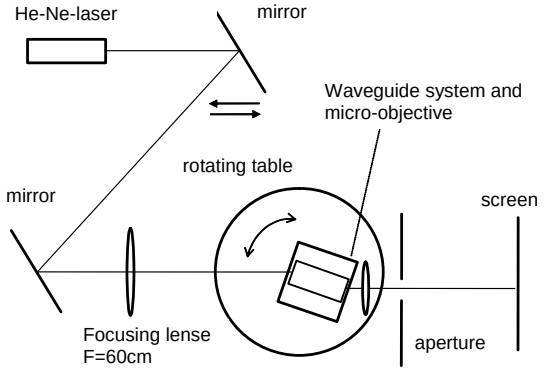


Fig 5: Experimental setup

For angles $3 < \theta < 4.8^{\circ}$ corresponding to the photon forbidden band of the system we observed bright reflection spot and the intensity of the transmitted wave was practically zero. For angles below 3° we observed several dark stripes in the reflected beam and the matching bright stripes in the transmitted beam. Each of these stripes corresponds to one of leaky modes propagating in the waveguide system. For modes close to the forbidden band angular distance between modes was about 0.1° that is several times less that the angular aperture of the exciting beam incident on the side surface of the system that was about 0.6° for the beam having 50 μm diameter. That is why we observed simultaneous excitation of several (3-4) leaky modes. For angles in the middle of the allowed band ($\theta \sim 1-2^{\circ}$) we observed excitation of 1-2 modes as the distance between modes is larger. We also observed the same behaviour for angles in the second allowed band $4.8 < \theta < 9.9^{\circ}$.

Figure 4 presents images of output edge of the system excited by a 230μm beam incident on its side. Shown photographs correspond to the 2nd, 3rd, 5th and 7th dips in the reflection counting from the forbidden band. This means that they are present the 49th, 48th, 46th and 44th modes respectively. The 50th mode that is closest to the forbidden band has the lowest losses and the narrowest resonance. It is difficult to excite it efficiently that is why we do now show its image. One can see that that envelope of the mode fields has periodicity depending on the detuning from the band edge that is in full coincidence with the calculation results.

For incidence angles inside the photonic forbidden band $3 < \theta < 4.8^{\circ}$, modes of waveguide system, can not be excited by a side-incident beam. However the edge-incident beam under the Bragg angle

$$\varphi_{Br} = \arcsin\frac{\lambda}{2\Lambda} \qquad (6)$$

excites both low-loss Bragg modes [6] that can be seen at figure 6. This figure presents the power that was registered at the output edge of the waveguide system (collecting lense and the photodetector were used in this experiment instead of screen). It is important that both Bragg modes are excited simultaneously and are leaky modes in our case. The observed peak clearly shows that the Bragg modes have the lowest losses among other leaky modes and thus could potentially be used for mode selection in lasers. We should note one interesting fact (see Figure 7). If we we use the refraction law and recalculate the edges of forbidden band into angles in air (4.38º-7.02º) then we found that the Bragg angle φ_{Br} = 7.58º lies outside the range calculated from the reflection

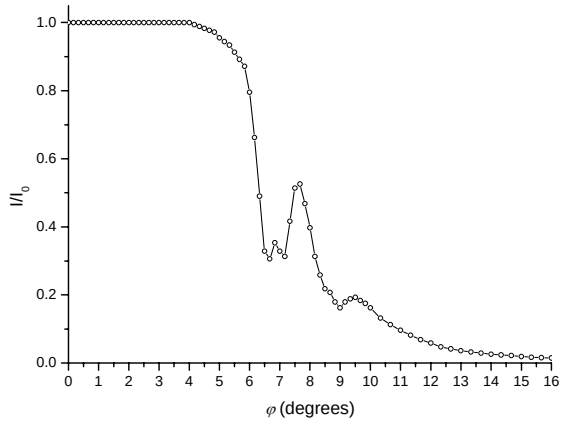


Fig. 6: Waveguide system transmittion for edge excitation

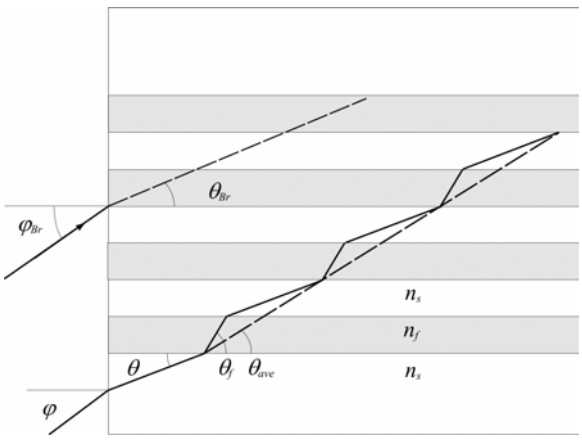


Fig.7: Scheme explaining the geometry of propagation in the multilayer structure

curve $R(\theta)$. At first sight it contradicts to the common sense, but there is very simple explanation. Angle of light propagation in the guiding layers θ_f differs significantly from θ despite the low refractive index difference ($n_s \cos\theta = n_f \cos\theta_f$). Average angle of light propagation through the system can be determined from simple geometrical consideration and appears to be in 3.81º-5.53º range ($(h+s)\,\mathrm{ctg}\,\theta_{ave} = h\,\mathrm{ctg}\,\theta_f + s\,\mathrm{ctg}\,\theta$). If we recalculate the Bragg angle into the waveguide system using the averaged refractive index we get 5.17º. Thus there is no contradiction and the Bragg angle lies inside the forbidden band as it should. One should note that the averaged refractive index calculated from the formula $n_{ave}\cos\theta_{ave} = n_s \cos\theta$ depends not only the layers parameters but also on the incidence angle.

Conclusions

Thus or study of Bragg diffraction in the system of coupled waveguides and examination of light reflection from the side surface of the system complement each other and as a whole give us the total understanding of the processes taking place in the system. In particular for the system having number of guided modes *M* smaller than the number of waveguides *N* it was found that leaky modes can be excited by a side-incident beam and there are *N*-*M* of them. It was shown that leaky modes are excited from the side of the waveguide system at the same time when the reflection coefficient for the exciting beam goes to zero. It was verified experimentally that the Bragg modes have the lowest losses among leaky modes that can be used for mode selection in lasers

References

1. R.J. Beach et al, JOSA B, v.19, no.7, p.1521, 2006
2. B.A. Usievich et al, Optics and Spectroscopy, v.101, no.5, p.999, 2006
3. A.A. Goncharov et al, Quantum Electronics, v.33 no.4, p.342, 2003
4. A.A. Goncharov et al, Laser Physycs, v.13, no.8, p.1017, 2003
5. E. Anemogiannis et al, IEEE J. of Lightwave Technology, v.17, no.5, p.929, 1999
6. J.Kh. Nurligareev et al, Quantum Electronics, v.36, no.7, p.653, 2006
7. A. Yariv, P. Yeh, Optical waves in crystals, John Wiley & Sons Inc, 1984
8. B.A. Usievich et al, Quantum Electronics, v.35, no.6, p.554, 2005

Band Structure and Coupled Surface Plasmons in one dimensional Photonic Crystals

Michael Bergmair (1) and Kurt Hingerl (2)
1) Christian Doppler Labor für Oberflächenoptische Methoden, Institut für Halbleiter- und Festkörperphysik, Universität Linz, A-4040 Linz, Austria; michael.bergmair@jku.at
2) Christian Doppler Labor für Oberflächenoptische Methoden, Institut für Halbleiter- und Festkörperphysik, Universität Linz, A-4040 Linz, Austria; kh@jku.at

Abstract: *In the last two decades photonic crystals (PC) have been studied in one, two and three dimensions. Recently metallic two and three dimensional PCs were investigated with the focus on using such structures in incandescent lightning and thermal photovoltaic applications. These structures exhibit a metallic band gap below a certain threshold frequency as well as structural band gaps. The PC can be designed that the metallic band gap allows to block the infrared transmission respectively emission. We will show that also the simpler one dimensional system has the same features, namely a metallic band gap which is furthermore omni directional for all angles of incidence. For one dimensional PCs consisting of polaritonic materials the dispersion exhibits also an additional band gap next to structural band gaps. This polaritonic band gap is also complete. In the last part of this article we show the dispersion relation of surface plasmons and polaritons by studying grazing incidence parallel to the layers. These surface states extend over adjacent layers. It is shown that propagating states must lie within the Wiener bounds.*

Introduction

Planck's derivation of thermal radiation has led to quantum mechanics but is also extremely important for applications as lightning and sensing. Recently, thermal radiation from three dimensional metallic photonic crystals (MPC) has attracted a lot of attention because it was proposed that thermal radiation from these structures might even exceed the radiation of a black body[1]. However, an ab-initio calculation of the equilibrium thermal emission properties of a photonic crystal assuming Kirchoff's law has shown that thermal radiation from photonic crystals in equilibrium can exceed only that of a black-body by means of fluctuations (which vanish by averaging)[2].

The physics of surface plasmons (SPL) and surface polaritons (SPO) are investigated since long time ([3],[4]) and SPLs have highly interesting sensor applications [5] or enhance the efficiency of light emission[6].

Photonic crystals with a real dielectric constant are well known and have been investigated since the end of the 80s. The periodicity in these structures leads to forbidden frequency bands which can be used to filter or to guide waves with a certain energy.

Kuzmiak *et al.*[7] were one of the first authors who treated MPC characterized by a frequency dependent and complex dielectric function. For the MPC this frequency dependence is assumed to be Drude[7] like. To our knowledge Rung[8] and co-workers were the first authors who treated a polaritonic material in a photonic crystal (PPC).

Further we will investigate one dimensional (1D) MPC and PPC for all angles of incidence and especially the behavior of the metallic and polaritonic band gap. The main focus of our work is dedicated to propagation parallel to the sheets and therefore on the modified dispersion of surface states due to the coupling over adjacent layers. Additionally the damping normal and parallel to the sheets is studied.

Theoretical description

Decoupling Maxwell's equations leads to the well known wave equation

$$\frac{1}{\varepsilon(\vec{r})}\nabla\times\nabla\times\vec{E}(\vec{r},t) = \frac{1}{c^2}\frac{\partial^2\vec{E}(\vec{r},t)}{\partial t^2} \quad (1)$$

$$\nabla\times\frac{1}{\varepsilon(\vec{r})}\nabla\times\vec{H}(\vec{r},t) = \frac{1}{c^2}\frac{\partial^2\vec{H}(\vec{r},t)}{\partial t^2} \quad (2)$$

which formally is an eigenvalue problem. $\varepsilon(\vec{r})$ denotes the dielectric function at position $\vec{r}$ which is in the 1D case only a function of the variable z. For a complex dielectric function $\varepsilon(\vec{r},\omega)$ the solution of the new nonlinear eigenvalue equation yields either a complex frequency ω (interpreted as lifetime) or a complex wave vector k (interpreted as spatial damping). Kuzmiak presented two techniques to calculate the band structure: With plane wave expansion (PWE) the band structure $\omega(k)$ and the electric $\vec{E}$ and magnetic $\vec{H}$ field for 1D,2D,3D MPCs can be numerically determined; with a Kronig Penney (KP) like description $k(\omega)$ is calculated, but with the exception of special arrangements[9], only for 1D PCs. The results given below are obtained with KP because this method is exact whereas for the PWE only a finite number of Fourier coefficients can be taken into account. Furthermore PWE resulted in an higher computational load. Therefore we obtain the dispersion $k_z(\omega)$, i.e. for an arbitrary frequency we obtain the complex wave vector. The band structure solutions were also correlated with transmission matrix calculations.

Using the fact that the electric field and its derivative have to be continuous at the surface and also fulfil the Bloch condition one obtains an equation in the frame of the KP-model[10] which reads

$$\cos(k_z L) = \cos(k_1 a_1)\cos(k_2 a_2) \quad (3)$$

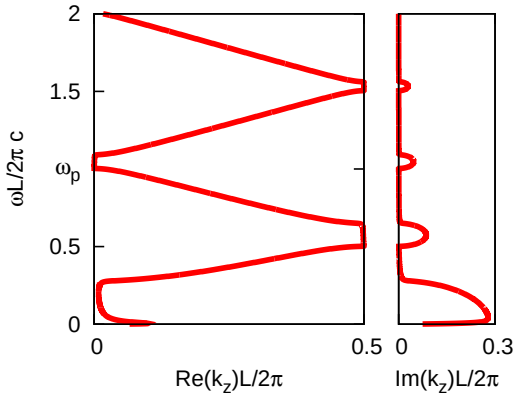


Fig. 1: Band structure for normal incidence on a MPC with $f = 0.1$ and $\gamma = 0.01\omega_p$. The imaginary part corresponds to damping. The metallic band gap extends between zero and $\omega \sim 0.3\omega_p$.

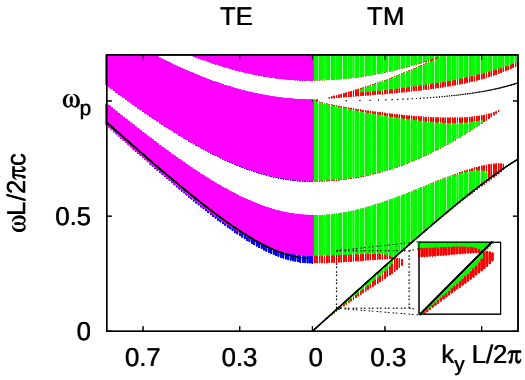


Fig. 2: Band structure and allowed states for oblique incidence. In blue (TE) and red (TM) solutions with $\Im(k_z)L/2\pi < 0.01$; in magenta (TE) and green (TM) solutions with $\Im(k_z)L/2\pi < 0.005$ are presented. Wiener bounds are marked by black lines.

$$-\frac{1}{2}N \sin(k_1 a_1) \sin(k_2 a_2)$$

with $k_1 = \sqrt{\left(\frac{n_i \omega}{c}\right)^2 - k_y^2}$. $n_i = \sqrt{\varepsilon_i}$ denotes the refractive index and a_i the width of the layer with indices $i = 1, 2$ describing either the background material or the metal/polaritonic layer. The metallic or ionic layers are orientated in the x-y plane and separated by a background material (i.e. air) which has the dielectric constant value ε_b.

For oblique incidence the degeneracy between TE (electric field parallel to the layers) and TM (magnetic field parallel) is lifted. For TE polarization the factor N reads $N_{TE} = (n_1^2+n_2^2)/(n_1 n_2)$ whereas for TM polarized light this factor reads $N_{TM} = n_1^2 k_2/n_2^2 k_1 + n_2^2 k_1/n_1^2 k_2$.

By changing the value of the parallel part of the wave vector k_y one can treat the different angles of incidence with the special case $k_y = 0$ for perpendicular propagation.

Metallic Photonic Crystal

A simplified model for a metal is the Drude approximation where the opaque behavior of the metal below the plasma frequency ω_p is described by a negative real part and a large imaginary part of $\varepsilon(\omega)$. The dielectric function of the MPC is

$$\varepsilon(\omega, z) = \begin{cases} \varepsilon_\infty \left(1 - \frac{\omega_p}{\omega(\omega+i\gamma)}\right) & \text{in metal} \\ \varepsilon_b & \text{background} \end{cases} \quad (4)$$

The damping factor γ, the plasma frequency and the constant value of the dielectric function for large frequencies ε_∞ are chosen typical for some metals (e.g. Ag). The plasma frequency is $\omega_p = 10^{15}\text{s}^{-1}$, $\varepsilon_\infty = 1$ and $\gamma = 0.01\omega_p$.

In this article we use dimensionless variables $\omega' = \omega L/2\pi c$ and $k' = kL/2\pi$ and choose the thickness of the metallic/polaritonic sheets to be ten percent of a period, i.e. the filling factor is $f = 0.1$. In this section of MPC we normalize ω_p to be one in dimensionless variables; this means we assign the period to be equal to the free space wavelength of the plasma frequency.

In Fig. 1 we see the band structure for normal incidence onto a 1D MPC. On the right hand side we plot the imaginary part of k_z which indicates band gaps: One notices that between zero and a certain threshold frequency ($\sim 0.3\omega_p$) the value of $\Im(k_z')$ is quite large which yields the metallic band gap. Furthermore band gaps occur around $\omega' \sim 0.5, \omega_p, 1.5$; these are the structural band gaps. Already previous authors [7],[11] have observed these remarkable effects: Propagation through such *infinite* structures becomes allowed even much below ω_p and there is a clear distinction between structural and metallic band gaps because the penetration depth in the metallic band gap is about 2-3 periods and much less than in the structural band gaps. These results suggests that 1D MPC structures can be used to filter infrared light in optical applications. Can such a filter characteristics be extended to off-axis propagation, too, for obtaining an omni directional band gap[12],[13]?

To answer this question we calculated the band structure of a 1D MPC for non-normal incidence for TE and TM polarized waves by varying the parallel component of the wave vector.

In Fig. 2 we present the band structure for increasing values of k_y which is not limited as we do not have periodicity in this direction. The shaded regions in the plot are projected solutions (the k_z axis is normal to the plotting plane) and one can only see propagating solutions ($\Im(k_z') < 0.01$ for the blue and red regions and $\Im(k_z') < 0.005$ for the magenta and green shaded areas). The right side is for TE polarized incident, the left part for TM polarized light.

One can clearly see that the metallic band gap is complete except for solutions in the TM regime. By decreasing the cut-off limit $\Im(k_z)$ these states vanish and only modes on the black line will remain. The black

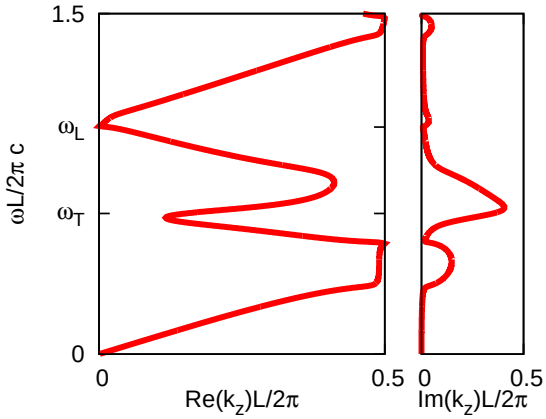


Fig. 3: Normal incidence band structure for $f = 0.1$ for $\varepsilon_0 = 7.75$, $\omega_T L/2\pi c = 0.62$ and a damping factor of $\gamma = 0.132\omega_T$

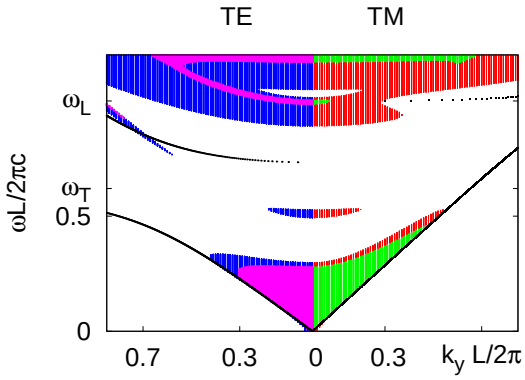


Fig. 4: Band structure for polaritonic PCs. In blue(TE) and red (TM) solutions with $\Im(k)L/2\pi < 0.03$; in magenta (TE) and green (TM) solutions with $\Im(k)L/2\pi < 0.01$ are presented. Wiener bounds are marked in black.

line indicates the Wiener bounds [14],[15] which are upper and lower limits for the effective dielectric function of a composite with a given volume fraction, irrespective of micro-structure. In the model of Wiener these bounds indicate maximum (TM) and minimum screening (TE) of the electric field.

The states which remain in the metallic band gap for TM polarized light are surface states, i.e. their real k_z component is zero. Therefore no propagating states along z-direction are located in the metallic band gap.

Polaritonic Photonic Crystal

In this part we will substitute the metallic sheets with layers made of a ionic crystal and calculate the optical response in the infrared (Reststrahlenbereich). The polaritonic dielectric function for such a material reads

$$\varepsilon(\omega) = \varepsilon_\infty + \left(\frac{(\varepsilon_0 - \varepsilon_\infty)\omega_T^2}{\omega_T^2 - \omega^2 - \imath\omega\gamma} \right) \tag{5}$$

For a bulk material this dielectric function yields a band gap between the transversal optical frequency ω_T and the longitudinal frequency ω_L which is the node of $\varepsilon(\omega)$. These two frequencies are related to the ratio of the dielectric function for zero frequency ε_0 and ε_∞; this is the famous Lyddane-Sachs-Teller relation.

In the following we will consider a PPC with a filling factor $f = 0.1$.The material parameter are chosen to describe $\varepsilon(\omega)$ for BeO, i.e. $\hbar\omega_T = 87$ meV, $\varepsilon_0 = 7.75, \varepsilon_\infty = 2.99$ and the damping $\gamma = 0.132\omega_T$. Again, we choose the period to be equal to the free space wavelength of ω_L, so we normalize the longitudinal frequency to one.

The dispersion for normal incidence (Fig. 3) provides the same features as we have observed for the MPC: The imaginary part of $\varepsilon(\omega)$ becomes large in the vicinity of ω_T and therefore we obtain an additional band gap in this frequency region, the polaritonic band gap. Furthermore the PPC already becomes transparent below ω_L ($\Im(k_z')$ is small). As the polaritonic band gap is correlated to ω_T we can shift this forbidden frequency region and can either merge or separate the polaritonic and structural band gaps.

By considering Fig. 4 one may note how the band structure changes in case of oblique incidence. We again see the projected band structure where different colors indicate different cut-off limits for the imaginary part of k_z. The polaritonic band gap is omni directional and again, no propagating states exist below the Wiener bounds.

Surface states

As mentioned above in this section we are interested in states which only propagate parallel to the layers in the PC. These states only occur for TM polarization and their real normal component of the wave vector k_z is zero. This gives rise to the conclusion that these states are somehow related to surface plasmons (SP) as they appear on a single metal-air (polaritonic-air) interface as well. On a single interface one can calculate the dispersion of SP by using the continuity conditions of the components of the electric and displacement field as it is done in [16]. One finds

$$k_y = \frac{\omega}{c}\sqrt{\frac{\varepsilon(\omega)}{\varepsilon(\omega) + \varepsilon_b}} \tag{6}$$

where the dielectric function can either be Drude or polaritonic like.

Comparing this dispersion with the solutions obtained from the KP eq. 3 which have ($\Re(k_z) = 0$) one finds a quite similar solution. The dispersion of SP in a MPC is presented in Fig. 5 and one can see that the curve approaches $\omega = \omega_p/\sqrt{2}$ for large values of k_y (for $\varepsilon_\infty = \varepsilon_b = 1$). The only difference in the dispersion relation is that in the long wave length limit the solutions have a different slope. For the MPC the filling factor enters the slope [17]: The dashed line in Fig. 5 is described by

$$\omega = \frac{ck_y}{\varepsilon_b}\sqrt{1 - f} \tag{7}$$

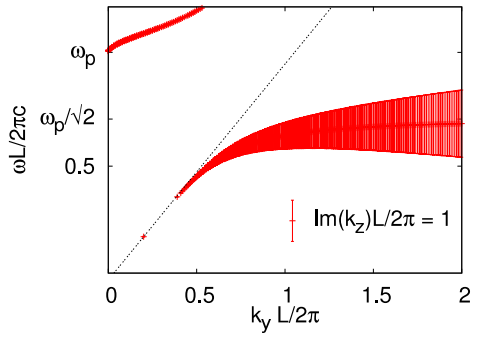


Fig. 5: Dispersion of *pure* surface plasmons in red ($\Re(k_z) = 0$). The vertical bars indicate the damping, norm given by the red bar. The black dotted line indicates the modified light line.

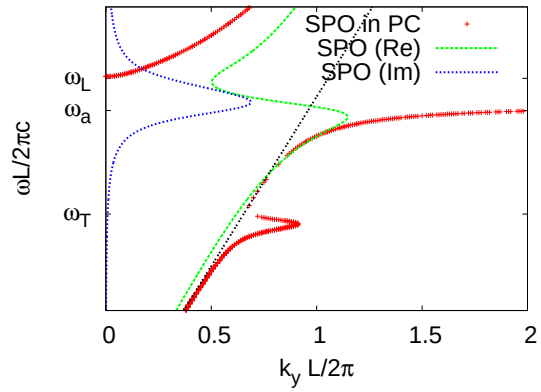


Fig. 6: Dispersion of SPO on a single surface in green (real) and blue (imaginary) and in a PPC (thicker red dotted line).

which means that the SP are coupled over adjacent layers. The vertical bars indicate the value of the imaginary part of k_z which is large ($\sim$ factor 100-1000) compared to $\Im(k_y)$. This means that SP in a MPC are hardly damped in y-direction whereas they decay rapidly normal to the sheets.

It is remarkable that the dispersion relations for surface polaritons (SPO) on a single interface and in a PPC are quite different (see Fig. 6). Due to the imaginary part of eq. 5 the dispersion is bent back: On the single surface (dispersion is presented by the green (real) and blue (imaginary) part) this occurs above the limiting frequency where $\varepsilon(\omega) = -\varepsilon_b \Rightarrow \omega'_a \sim 0.9$ and in the PPC (the dotted red line) around the transversal frequency ω_T. Despite negative and infinite group velocities this back bending is not unphysical [18]. The dotted line indicates again the modified slope of the linear part of the dispersion for small values of k_y. For small values of the frequency and in the back bended region around ω_T the damping $\sim \Im(k_y)$ of SPO in a PPC is smaller than the damping in normal direction and orders of magnitude smaller than its real part.

Conclusion

In this article we considered a 1D PC which consists of layers with a frequency dependent and complex dielectric function. With the help of a KP like description we derived the band structure for normal, oblique and parallel incidence. Previous authors have already found that additional band gaps occur in frequency regions where the absorption is large. These band gaps remain complete for all angles of incidence except excitations which propagate parallel to the layers. These surface states occur only for one polarization and are coupled over adjacent layers.

Acknowledgments

The authors are grateful for a grant from the European community (N2T2) and the Linz supercomputer center (Johann Messner).

References

[1] P. Weiss, see article on http://www.sciencenews.org/articles/20031004/bob9.asp,2003

[2] C. Luo et al, Physical Review Letters, vol. 93, p. 213905, 2004.

[3] H. Raether, Surface Plasmons on Smooth and Rough Surfaces and on Grantings, Springer Berlin, 1988

[4] V. Agranovich, Surface polaritons, North-Holland Amsterdam 1982

[5] A. Stepanov et al, Optics-Letters, vol. 30, p. 893, 2005

[6] R.Pariella, Applied Physics Letters, vol. 87, p. 111104, 2005

[7] V. Kuzmiak et al, Physical Review B, vol. 55, p. 7427, 1997

[8] A. Rung et al, Physical Review Letters, vol. 92, p. 123901, 2004

[9] S. Kawakami, Journal of Lightwave Technology, vol. 20, p. 1644, 2002

[10] P. Yeh, Optical waves in layered media, Wiley, New Jersey, 1988

[11] X. Xu et al, Applied Physics Letters, vol. 86, p. 091112, 2005

[12] D. Chigrin et al, Journal of Lightwave Technology, vol. 17, p. 2018, 1999

[13] J.N. Winn et al, Optics Letters, vol. 23, p. 1573, 1998

[14] D. Aspnes, Physical Review B, vol. 25, p. 1358, 1982

[15] O. Wiener, Abh. Math-Phys. Kl.Königl.Saechs. Ges., vol. 32, p. 509, 1912

[16] K. Sakoda, Optical Properties of Photonic Crystals, Springer Berlin, 2004

[17] M. Bergmair et al, Applied Physics Letters, vol. 89, p. 081907, 2006

[18] E. Bolda et al, Physical Review A, vol. 48, p. 3890, 1993

A Semi-analytical Model for Estimation of the Transfer Function of a Coupled Resonator Optical Waveguide Based on Coupled Mode Theory

Nikolaos Avaritsiotis, Thomas Kamalakis and Thomas Sphicopoulos
Department of Informatics and Telecommunications, University of Athens, Greece (nickava@di.uoa.gr)

Abstract: *Coupled Resonator Optical Waveguides (CROWs) are receiving increased attention for the realization of future nanophotonic waveguiding devices. In this paper a detailed analysis is provided in order to study the frequency response of finite CROWs including the input/output waveguide-cavity coupling. A semi-analytical model is obtained based on the application of reciprocity relations on Maxwell's equations and can also include the coupling between non adjacent cavities and handle CROWs of arbitrary long length. The model is verified by comparing its results to the Finite Difference Time Domain (FDTD) method.*

Introduction

Coupled resonator optical waveguides (CROWs) present a new type of light-waveguiding by propagation through coupling between adjacent unit cells of a nanophotonic optical integrated circuit [1]. Such devices are currently a topic of intense research due to their potential applications in optical filtering, dispersion compensation, optical buffering, nonlinear optics, etc [2]-[6]. One possible realization of a CROW is a sequence of coupled defect cavities embedded in a two-dimensional periodic photonic crystal structure. These defect cavities are designed such that their resonant frequency falls within the forbidden gap of the surrounding 2D photonic crystal structure and thus permitting coupling due to the evanescent Bloch waves [4].

The frequency response of the CROW also depends on how light is coupled into the structure. Figure 1 illustrates one possible arrangement where light propagating in a waveguide is side coupled to the first cavity of the CROW and another waveguide collects the light from the last cavity. Such structures can be analysed either with the finite difference time domain method (FDTD) using direct numerical solution of Maxwell's equations. However, as the number of cavities becomes larger, FDTD simulations eventually become impractical due to the large computational time required. In addition FDTD simulations usually do not provide any useful physical insight. To properly engineer a CROW, one rather needs a fast analytical or semi-analytical model. Such models already exist based on the tight binding approximation, for both finite and infinite CROWs but without taking into account the coupling between the cavities and the input/output waveguides. One can use coupled mode theory (CMT) to extend the model in order to include the influence of the waveguides.

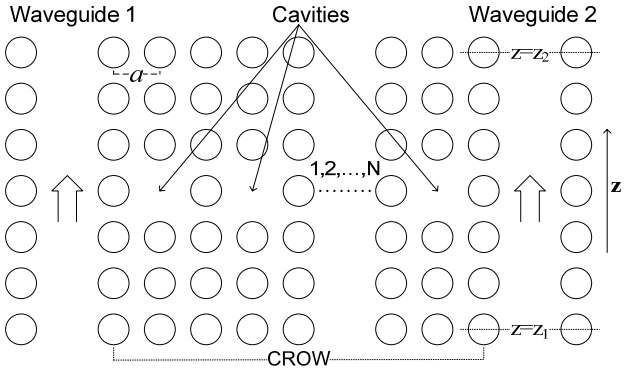


Figure 1: CROW device containing input waveguide 1 and output waveguide 2 and *N* cavities.

In this paper a detailed derivation of the coupled mode equations relating the amplitudes of the cavity and waveguide modes is given for the CROW/waveguide system starting from Maxwell's equations and using the reciprocity relations. This provides a useful, semi analytical model for the efficient estimation of the transfer function of a device with an arbitrary number of cavities. The results of the model are compared with the results of the FDTD method and good agreement is observed.

Field Expansion

In the spirit of the tight binding approximation, in the frequency domain one may expand the total electric and magnetic field **E** and **H** inside the CROW in terms of the modes of the input/output waveguide and the isolated cavities, i.e.

$$\mathbf{E} = \sum_n a_n \mathbf{E}_n + \sum_l a_{fl} \mathbf{E}_{fl} + \sum_l a_{bl} \mathbf{E}_{bl} \qquad (1)$$

$$\mathbf{H} = \sum_n a_n \mathbf{H}_n + \sum_l a_{fl} \mathbf{H}_{fl} + \sum_l a_{bl} \mathbf{H}_{bl} \qquad (2)$$

where $\mathbf{E}_n$, $\mathbf{H}_n$ are the electric and magnetic modal fields of the nth isolated cavity modes ($1 \le n \le N$), ($\mathbf{E}_{fl}$, $\mathbf{H}_{fl}$) and ($\mathbf{E}_{bl}$, $\mathbf{H}_{bl}$) are the forward and backward propagating modes of the lth waveguide. In addition a_n, a_{fl} and a_{bl} denote the excitation coefficients of the nth cavity mode and the forward and backward isolated propagating mode of the lth waveguide respectively. Assuming that z is the propagation direction of the forward waveguide modes, a_{fl} and a_{bl} are considered z-dependent, while the cavity mode amplitudes

a_n are assumed not to depend on z [7]. One may use Bloch's theorem in order to express the waveguide mode fields as:

$$\mathbf{E}_{ml}(\mathbf{r}) = \mathbf{e}_{ml}(\mathbf{r})e^{j\beta_{ml}z} \quad (3)$$

$$\mathbf{H}_{ml}(\mathbf{r}) = \mathbf{h}_{ml}(\mathbf{r})e^{j\beta_{ml}z} \quad (4)$$

where assuming an exp(-$j\omega t$) dependence, the propagation constant β_{ml} is positive for the forward (m=f) and negative for the backward (m=b) propagating mode while $\mathbf{e}_{ml}$ and $\mathbf{h}_{ml}$ are periodic vector functions with the same periodicity a as the input/output waveguides. In addition forward and backward modes fulfill certain symmetry relations as shown in [1]. The isolated waveguide modes obey Maxwell's equation in the frequency domain

$$\nabla \times \mathbf{E}_{ml} = j\omega\mu \mathbf{H}_{ml} \quad (5)$$

$$\nabla \times \mathbf{H}_{ml} = -j\omega\varepsilon_l(\mathbf{r})\mathbf{E}_{ml} \quad (6)$$

where $\varepsilon_l(\mathbf{r})$ is the dielectric constant of the lth waveguide alone. The waveguide modes are assumed normalized so that

$$\eta_m = \int_S (\mathbf{E}^*_{ml} \times \mathbf{H}_{ml} + \mathbf{E}_{ml} \times \mathbf{H}^*_{ml}) \mathbf{z}\, dS = \pm 1 \quad (7)$$

where η_m=1 for the forward propagating mode (m=f) and η_m=-1 for the backward propagating mode (m=b). In addition the forward and backward propagating modes of each waveguide obey the following orthogonality relations,

$$\int_S (\mathbf{E}^*_{fl} \times \mathbf{H}_{bl} + \mathbf{E}_{bl} \times \mathbf{H}^*_{fl}) \mathbf{z}\, dS = 0 \quad (8)$$

The cavity modes obey a similar set of equations,

$$\nabla \times \mathbf{E}_n = j\omega_o \mu \mathbf{H}_n \quad (9)$$

$$\nabla \times \mathbf{H}_n = -j\omega_o \varepsilon_{cn} \mathbf{E}_n \quad (10)$$

where $\varepsilon_{cn}(\mathbf{r})$ is the dielectric constant of nth cavity alone and ω_0 is the mode resonant frequency. For the cavity modes, the electric fields can be chosen purely real $\mathbf{E}_{rn}{}^* = \mathbf{E}_{rn}$ resulting in a purely imaginary magnetic field, $\mathbf{H}_{rn}{}^* = -\mathbf{H}_{rn}$.

Waveguide amplitude equations

In this section using the reciprocity relations outlined in [1] and the field equations presented in the previous section, we derive the amplitude equations for the forward and backward propagation modes of the waveguides. Although one could assume that the waveguides interact only with their adjacent cavities such an approximation will not be used in the derivation in order to obtain a model as general as possible. To apply the reciprocity relations, we first define the vector functions

$$\mathbf{F}_{ml} = \mathbf{E} \times \mathbf{H}^*_{ml} + \mathbf{E}^*_{ml} \times \mathbf{H} \quad (11)$$

Using the 2D form of Green's theorem as in [1], one obtains

$$\frac{\partial}{\partial z}\int_S \mathbf{F}_{ml}\mathbf{z}\, dS = j\omega \int_S (\varepsilon - \varepsilon_l)\mathbf{E}^*_{ml}\mathbf{E}\, dS \quad (12)$$

where the surface S is any plane perpendicular to the z axis. Substituting (1) and (2) in (12) and neglecting the self coupling of the waveguide modes as in [1], leads to the following system of equations for the forward waveguide amplitudes

$$\frac{\partial a_{fl}}{\partial z} = j\mathbf{k}_{fl} \cdot \mathbf{a} \quad (13)$$

where $\mathbf{a}$=(a_1,…,a_N) and the vector $\mathbf{k}_{fl}$ contains the coupling coefficients of the cavity and waveguide modes, given by

$$k_{fl,n} = \int_S (\omega\varepsilon - \omega_o\varepsilon_{cn})\mathbf{E}^*_{fi}\mathbf{E}_{rn}dS + \mu(\omega - \omega_o)\int_S \mathbf{H}^*_{fi}\mathbf{H}_{rn}dS \quad (14)$$

Using similar arguments one may also derive a system of equations for the backward amplitudes,

$$\frac{\partial a_{bl}}{\partial z} = -j\mathbf{k}_{bl} \cdot \mathbf{a} \quad (15)$$

where

$$k_{bl,n} = \int_S (\omega\varepsilon - \omega_o\varepsilon_{cn})\mathbf{E}^*_{bl}\mathbf{E}_n dS + \mu(\omega - \omega_o)\int_S \mathbf{H}^*_{bl}\mathbf{H}_n dS \quad (16)$$

These equations relate the rate of change of the waveguide mode excitation coefficients to the cavity amplitudes and will be used to derive simpler relations between the cavity amplitudes and the waveguide excitation coefficients.

Cavity amplitude equations

The derivation of the cavity amplitude equation is similar to the one used above for the waveguides. The vector functions defined are:

$$\mathbf{F}_n = \mathbf{E} \times \mathbf{H}^*_n + \mathbf{E}^*_n \times \mathbf{H} \quad (17)$$

and from applying the 3D version of Green's theorem and taking into account that the cavity modal fields vanish at infinity, we obtain

$$j\mu(\omega - \omega_o)\int_V \mathbf{H}^*_n\mathbf{H}\, dV + j(\omega\varepsilon - \omega_o\varepsilon_{cn})\int_V \mathbf{E}^*_n\mathbf{E}dV = 0 \quad (18)$$

After substituting the total field expressions from (1) and (2) we obtain the coupled mode equation for the amplitudes of the cavities

$$j\int_{z_1}^{z_2}\mathbf{k}_{fl}^{*}\cdot\mathbf{a}\,dz+j\int_{z_1}^{z_2}\mathbf{k}_{bl,n}^{*}\cdot\mathbf{a}\,dz+j\boldsymbol{K}\mathbf{a}=0 \qquad (19)$$

where the elements of the cavity mode coupling matrix are given by

$$K_{pq}=\int_V\mu(\omega-\omega_o)\mathbf{H}_p^{*}\mathbf{H}_q dV+\int_V(\omega\varepsilon-\omega_o\varepsilon_p)\mathbf{E}_p^{*}\mathbf{E}_q dV \qquad (20)$$

Assuming that the cavity modes are normalized to have unity energy, the diagonal elements of $\boldsymbol{K}$ which represent the self coupling coefficients can be simplified by neglecting the cavity mode self coupling in the waveguides and thus obtaining $K_{mm}=\omega-\omega_0$. Applying integration by parts, transforms equation (19) to

$$\sum_l a_{fl}(z_1)\mathbf{K}_{fl}+\sum_l a_{bl}(z_2)\mathbf{K}_{bl}+\boldsymbol{J}\mathbf{a}+j\boldsymbol{K}\mathbf{a}=0 \qquad (21)$$

where

$$J_{nl}=\int_{z_1}^{z_2}(k_{fl,n}\Lambda_{fl,n}^{*}-k_{bl,n}\Lambda_{bl,n}^{*})dz \qquad (22)$$

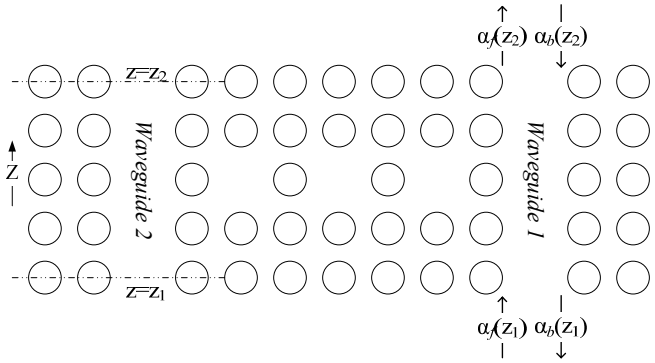


Figure 2: Simplified 3-cavity and 2-waveguide CROW device.

where $\Lambda_{ml,n}$ and are given by

$$\Lambda_{ml,n}=\int_{z_1}^{z_2}k_{ml,n}dz \qquad (23)$$

and $\mathbf{K}_{fl}$ and $\mathbf{K}_{bl}$ are equal to $-j\Lambda_{fl}^{*}(-l)$ and $j\Lambda_{bl}^{*}(l)$ respectively.

Transfer Function Calculation

In order to obtain the transmission transfer function $H(\omega)$ of the CROW, one can use equation (21) combined with equation (13). Alternatively the reflection transfer function can be obtained using (21) and (15). Assuming waveguide 1 is the input waveguide then

$$H(\omega)=\frac{a_{f1}(z_2)}{a_{f1}(z_1)}e^{j\beta L} \qquad (24)$$

where $L=z_2-z_1$. Assuming no backward propagating modes at both waveguides at $z=z_2$ and no forward propagating mode at waveguide 2 at $z=z_1$ then (21) yields

$$\mathbf{a}=-\left[(\boldsymbol{J}+j\boldsymbol{K})^{-1}\mathbf{K}_{f1}\right]a_{f1}(z_1) \qquad (25)$$

Using (13), one obtains

$$\frac{\partial a_{f1}}{\partial z}=-ja_{f1}(z_1)\int_{z_1}^{z_2}\mathbf{k}_{f1}(z)\left[(\boldsymbol{J}+j\boldsymbol{K})^{-1}\mathbf{K}_{f1}\right]dz \qquad (26)$$

Integrating with respect to z and using (24),

$$H(\omega)=\left(1-\left[(\boldsymbol{J}+j\boldsymbol{K})^{-1}\mathbf{K}_{f1}\right]\mathbf{K}_{f1}\right)e^{j\beta L} \qquad (27)$$

Equation (27), relates the transfer function of the CROW to the coupling coefficients of the cavities and the input/output waveguides which can be computed using numerical integration. In the following subsection the semi-analytical model for the estimation of the transfer function based on (27), will be compared to FDTD simulations in the case of a finite CROW.

Simulation Results

To test the validity of the model, the finite CROW presented in Figure 2 was considered, consisting of three 2D photonic crystal defect cavities and two photonic crystal waveguides. The center to center distance between the lattice rods is r_a=0.6μm while their radius is r=0.18r_a. The refractive index of rods equals n_{rods}=3.4 and that of the surrounding medium is n_{air}=1.0. The cavity mode resonant frequency calculated by the plane wave expantion (PWE) was near f_o=195.75THz that corresponds to a resonant wavelength of 1.532μm.

Both the cavity and waveguide mode field distributions were calculated using the PWE method. The cavity mode is normalized so as to have unit total electromagnetic energy while the waveguide mode is normalized according to (7).

Using (27) one can obtain the transfer function for the transmission of waveguide 1. Figure 3 depicts the power transfer function $T=|H|^2$ of the transmission of waveguide 1. The three peaks of T are due to the resonant frequencies of the three cavity system. Furthermore the amplitude of the power transfer function reaches approximately the value 0.25 at the resonant frequencies. In order to test the validity of our results an FDTD simulation with the same parameters was performed and the resulting power transfer function

of the transmission of waveguide 1 was calculated. This result is depicted in Figure 4. As expected there still exist three peeks for the tranfer function due to the cavity modes, however one notices a small difference of the order of 1%-2% in the resonant frequencies computed by the two methods. This slight disagreement maybe due to the inherent inaccuracies of the plane wave expansion method used to calculate the modal fields as well as the coupling coefficients

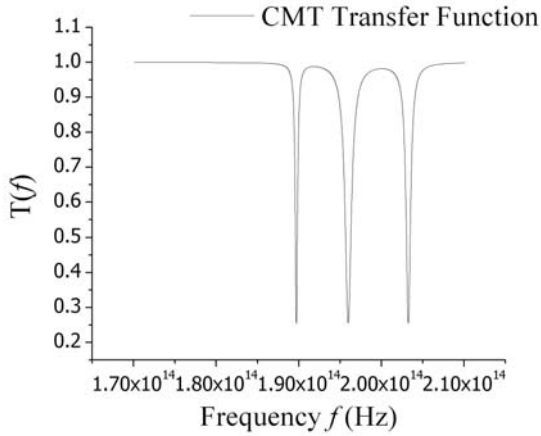


Figure 3: Power tranfer function of the 3-cavity CROW calculated using equation(25).

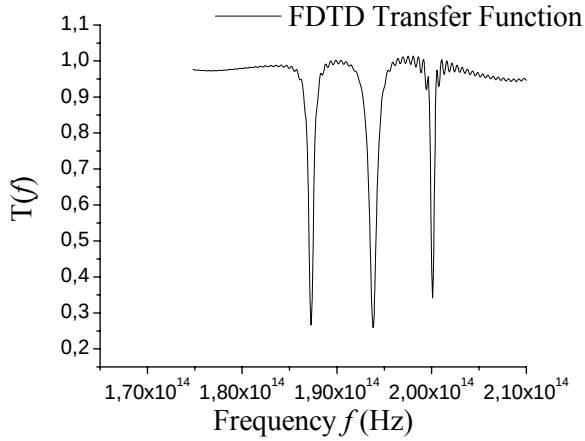


Figure 4: Power tranfer function using FDTD simulations for the 3-cavity CROW.

in (27) and the FDTD methods.

Finally both the FDTD and CMT power transfer functions are plotted in Figure 5 shifted so that the first resonant frequency is the same. One notices good agreement of the amplitude of the first two peeks as well as for their 3dB half-width. A small disagreement is observed for the third peek as a result of possible inaccurancies of the FDTD simulations or the PWE calculations.

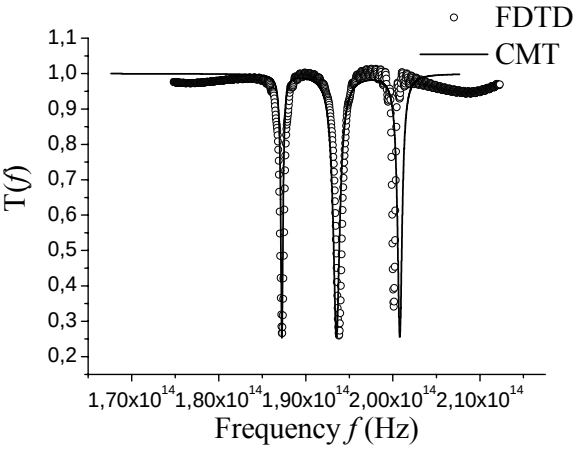


Figure 5: Comparison of FDTD and CMT amplitude power tranfer functions.

Conclusions

This paper presented an analysis for the derivation of a semianalytical model for the estimation of the frequency response of finite CROW devices. Using the reciprocity relations on Maxwell's equations the cavity/waveguide and cavity/cavity coupling coefficients were theoretically calculated. The model was verified using FDTD simulations. The results showed good agreement, however a small difference in the resonant frequencies was detected.

References

[1] T.Kamalakis, T. Sphicopoulos, IEEE Journal Quant. Elec., vol. 42, no 8, 2006.

[2] F. Xia, L. Sekaric, M. O'Boyle, Y. Vlasov, Appl. Phys. Lett. 89, 2006.

[3] B.E. Little, S. T. Chu, W. Pan, D. Ripin, T. Kokubun, and E. Ippen, IEEE Photonics Technol. Lett. 11, 215 1999.

[4] A. Yariv, Y. Xu, R. K. Lee, A. Scherer, Opt. Lett., vol. 24, no 11, 1999.

[5] Mookherjea and A. Yariv, Phys. Rev. E 65, 056601 2002.

[6] Mookherjea and A. Yariv, Phys. Rev. E 66, 046610 2002.

[7] A. W. Snyder, J. D. Love, Optical Waveguide Theory. Chapman and Hall, 1983.

Light propagation in a highly birefringent photonic crystal fiber infiltrated with a nematic liquid crystal

K.A. Rutkowska, T.R. Wolinski, P. Lesiak, A. Czapla, S. Ertman, K. Nowecka
Faculty of Physics, Warsaw Univ. of Technology, Koszykowa 75, 00-662, Warsaw, Poland, kasia@if.pw.edu.pl

Abstract: *Theoretical analyses as well as experimental results of light propagation in a new microstructured photonic liquid crystal fiber (PLCF) are presented. The analyzed PLCF was composed of a commercially available highly birefringent (HB) photonic crystal fiber (PCF) infiltrated with a low-birefringence nematic liquid crystal (LC) introduced into the selected micro-holes by the capillary effect.*

Introduction

For more than last twenty years the anisotropic optical fibers exhibiting particular polarization properties have been extensively investigated [1] including also the fibers with the liquid crystal cores [2]. Recently, a really great interest in the photonic crystals fibers and particularly in the photonic liquid crystal fibers [3-6] is observed. The latter, consisting of a PCF structure infiltrated with a LC, possess the unique and uncommon propagation and polarization properties as a result of the combination of a passive PCF host structure and an active LC guest material.

In the last ten years the photonic crystal fibers have become the subject of the intensive investigations and the great number of scientific publications [7,8]. This new class of optical fibers is typically composed of the large number of air micro-holes placed in the silica cladding. The change of the both location and the size of the holes allows for the designing and creating of the optical fibers with required properties for the particular practical applications. Recently, the particular attention has been devoted to the possibility of infiltration of the air holes with the different materials. This fact leads to the possibility of the bandgap tuning, as well as of the switching between two different waveguiding mechanisms – Total Internal Reflection (TIR) and Photonic Band Gap (PBG) [4,5]. Moreover, depending on the infiltrating material, some of the infused PCFs enable new applications in the area of the temperature and electrical controlled sensing, as well as in the all-optical information processing.

Modal analysis of HB PLCF

In this paper the custom software (i.e. the vectorial mode solver) was used. It is based on the full-vector wave equation, where two transverse components of the electric field intensity E_x and E_y are given in the following form [9]:

$$\begin{bmatrix} P_{xx} & P_{xy} \\ P_{yx} & P_{yy} \end{bmatrix} \begin{bmatrix} E_x \\ E_y \end{bmatrix} = k^2 N_{eff}^2 \begin{bmatrix} E_x \\ E_y \end{bmatrix} \quad (1)$$

where:

$$P_{xx}E_x = \frac{\partial}{\partial x}\left[\frac{1}{n^2}\frac{\partial\left(n^2 E_x\right)}{\partial x}\right] + \frac{\partial^2 E_x}{\partial y^2} + n^2 k^2 E_x,$$

$$P_{yy}E_y = \frac{\partial}{\partial y}\left[\frac{1}{n^2}\frac{\partial\left(n^2 E_y\right)}{\partial y}\right] + \frac{\partial^2 E_y}{\partial x^2} + n^2 k^2 E_y,$$

$$P_{xy}E_y = \frac{\partial}{\partial x}\left[\frac{1}{n^2}\frac{\partial n^2 E_x}{\partial y}\right] - \frac{\partial^2 E_y}{\partial x \partial y},$$

$$P_{yx}E_x = \frac{\partial}{\partial y}\left[\frac{1}{n^2}\frac{\partial n^2 E_y}{\partial x}\right] - \frac{\partial^2 E_x}{\partial y \partial x}$$

and k is wavevector, N_{eff} is effective refractive index of the resultant mode, n is refractive index distribution in the fiber cross section.

As one can see, the equation (1) is a full-vector eigenvalue equation, which describes the modes that propagates in the analyzed structure. For its discretization a finite-difference technique was used. In this way the partial-differential equation was translated into an equivalent matrix eigenvalue equation, which was solved by implementing of the Matlab library.

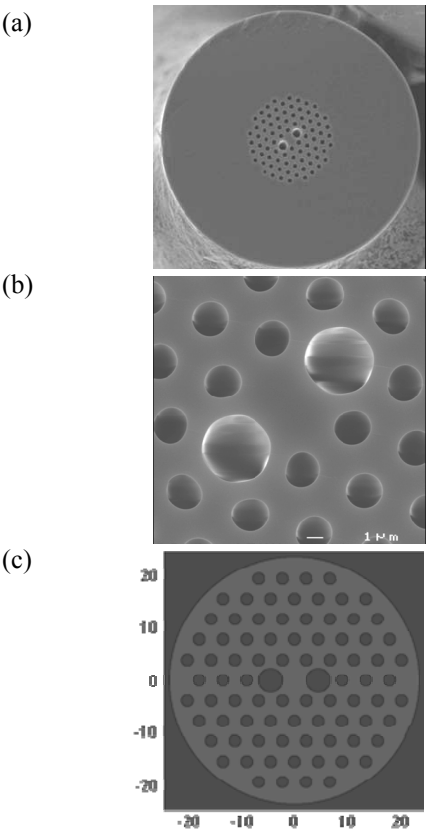


Fig. 1: The photos of the cross sections of the analyzed PM-1550-01 *Blazephotonics* PCF (a-b) and the calculating window (axis labels in micrometers) used for the numerical simulations (c).

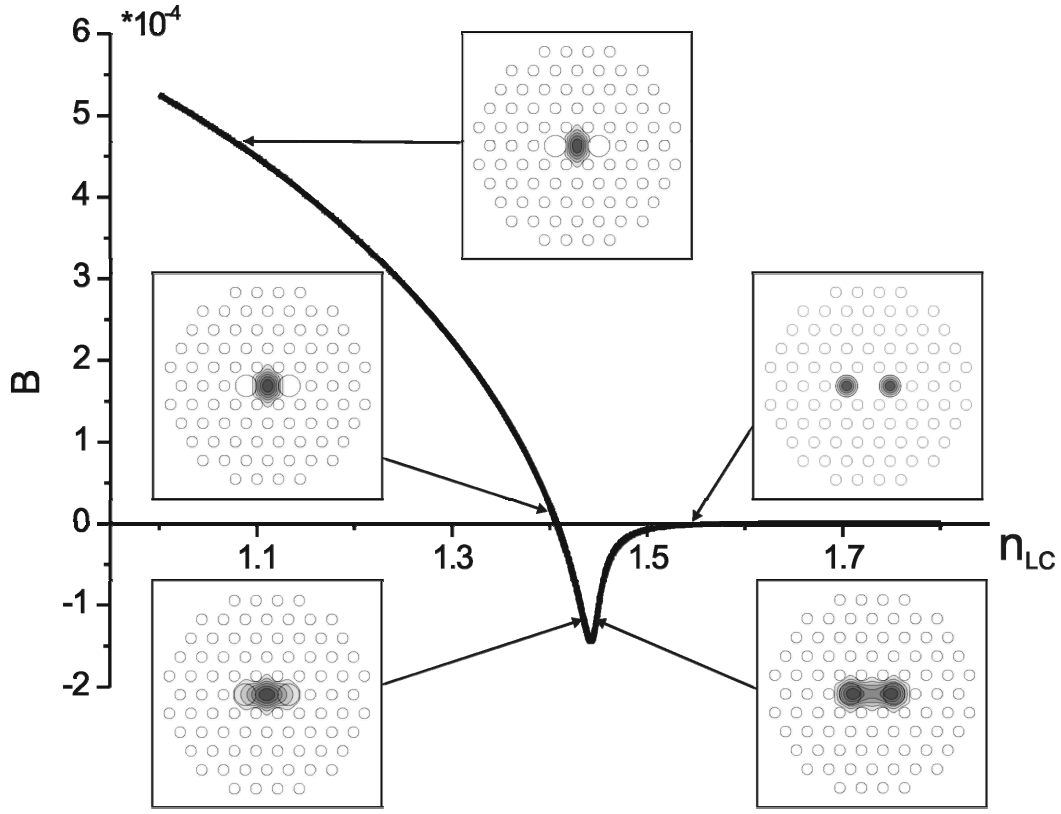


Fig. 2: Modal birefringence B for the fundamental mode (LP_{01}) as a function of the refractive index of NLC (n_{LC}) infiltrating the region of the large holes. The examples of the modal light intensity distributions for the different values of n_{LC} are also presented.

The investigated structure was based on the commercially available highly birefringent PCF fabricated by *Blazephotonics* (UK) (Fig. 1a-b) with only two large holes infiltrated with LC. The geometrical parameters of such a fiber are as follows: pitch (spacing between adjusted holes) Λ=4.4μm, large hole diameter d_H=4.5μm, small hole diameter d=2.2μm, diameter of the holey region D=40μm. In the numerical simulations the grid period was taken as 0.1μm in both x and y direction within the calculating window of the size of 48.4μm x 48.4μm (all holey region) (Fig. 1c). The value of the refractive index of the glass cladding was taken as 1.444 at the wavelength of 1550nm.

Any change in the value of the refractive index of the LC (which can be easily realized by the temperature tuning) within the large holes allows for magnificent changes in the modal field and therefore also in the optical properties of the fiber. As it is shown in Fig. 2 by the increasing the value of the LC refractive index the transition from the single to the double core (when the refractive index of LC is above the refractive index of silica glass) propagation is possible. In the case of double core propagation the modal birefringence B of the fundamental mode reaches the zero value.

Results and discussion

Preliminary experimental results confirmed that if the refractive index of the LC infiltrating the PCF holes increases over the refractive index of the fused silica two-core propagation is possible. In the unfilled PCF, the mode profile is located in the silica core of the fiber (Fig. 3a.), but after the infiltration of the large holes with the low-birefringence nematic LC mixture, cat. number 1550 (manufactured at the Military Univ. of Technology, Poland and described elsewhere [6]) the shape of the propagating field confined in the core was changed. Assuming that the predominant planar LC molecular alignment within the holes is obtained, only the changes of the ordinary refractive index of LC mixture affect the modal structure of the propagating electromagnetic field. If the refractive index in the holes is equal or higher than the refractive index of the fused silica (for 1550 LC mixture it is truth for the temperatures below 40°C) the propagating field distributed between the fused silica solid core and two liquid crystal cores (Fig. 3b) was obtained. For temperatures above 40°C the light propagation in the infiltrated holes disappears (refractive index in the holes is lower than the refractive index of the fused silica) and in consequence, the mode is again located mainly in the solid core. Hence the switching between single-core and two-core propagation was obtained.

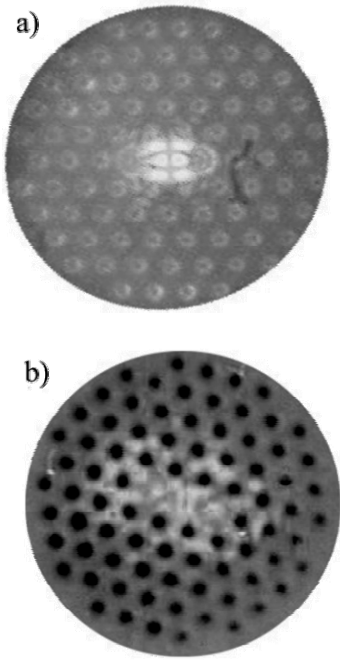


Fig. 3: Experimental observation of the end face of the unfiltrated PCF (a) and PLCF (b) for λ= 633 nm.

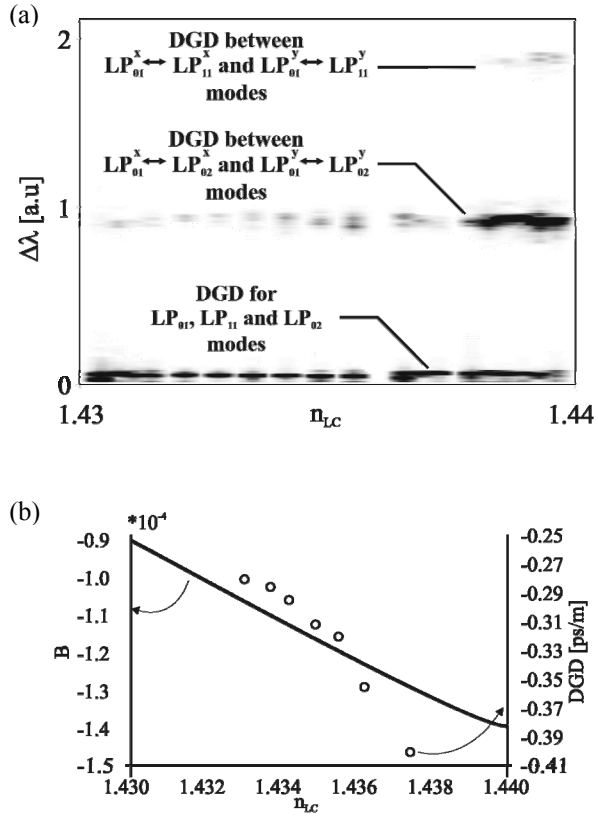


Fig. 4: Intermodal Δλ for PLCF filled with 1550 LC (a) and DGD changes in PLCF filled with 1550 LC (open circles) in comparison to the numerical calculations of modal birefringence (line) (b).

The group birefringence is the difference in the group indices for both orthogonal polarization modes. It contributes to the polarization mode dispersion (PMD) of the anisotropic fiber. In the wavelength sweeping method, the group birefringence can be calculated by counting maxima of the light intensity after analyzer as a function of the wavelength and by averaging their period of repetition over the total scanned wavelength spectrum [10]:

$$B_g = \frac{\lambda_1 \lambda_2}{L \Delta\lambda},$$

where: λ_1 and λ_2 are the wavelengths (maxima) that contribute with the same states of polarization and $\Delta\lambda = \lambda_2 - \lambda_1$ is a period of the polarization state repeatability and L is the length of tested PLCF. Hence, the differential group delay (DGD) in the measured fiber, defined as a difference in the velocities between two orthogonal modes of the fundamental mode can be described by the following formula:

$$DGD = \frac{\lambda_1 \lambda_2}{c \Delta\lambda}.$$

The maxima shown in Fig. 4a are responsible for differential group delays (DGDs) between first three modes (i.e. LP_{01}, LP_{02} and LP_{11}) that can propagate in the HB *Blazephotonics* PCF infiltrated with 1550 LC mixture [11]. Precise measurements of DGD between polarization modes LP_{01}^{x} and LP_{01}^{y} clearly demonstrate that the birefringence of the fundamental LP_{01} mode decreases to the negative value of the birefringence (Fig. 4b). Results obtained fully confirm numerical simulations shown in Fig. 2.

Conclusions

In this paper light propagation in a highly birefringent photonic crystal fiber infiltrated with a nematic liquid crystal was analyzed. It has been demonstrated that such a photonic structure exhibits an unusual propagation properties. The experimental results confirm the numerical simulations predictions and in particular the switching between single-core and two-core propagation was observed. Moreover by using the 1550 LC mixture the temperature-induced changes in DGD, switching between fundamental and higher order mode propagation in the PLCF was possible. Obtained results hold the great potential for both fiber-optic sensing and in-fiber polarization mode dispersion control and compensation.

Acknowledgments

The work was supported by the Polish Ministry of Science and Education under the grant 3T10C 016 28 and also partially by European Network of Excellence on Micro Optics (NEMO).

The authors are very grateful to Prof. Roman Dabrowski and Dr. Edward Nowinowski-Kruszelnicki from Military University of Technology, Poland for fruitful collaboration.

References

1. T.R.Wolinski, in Encyclopedia of Optical Engineering, R. G. Diggers, ed., (M. Dekker, New York), 2150-2175, 2003.
2. T.R.Wolinski P. Lesiak, R. Dabrowski, J. Kedzierski, E. Nowinowski, Mol. Cryst. Liq. Cryst. 421, 175-186, 2004.
3. T.T. Larsen, A. Bjarklev, D.S. Hermann, J. Broeng, Opt. Exp. 11, 2589-2596, 2003,
4. T.R. Wolinski, K. Szaniawska, K. Bondarczuk, P. Lesiak, A.W. Domanski, R. Dabrowski, E. Nowinowski-Kruszelnicki, J. Wojcik, Opto-Electr. Review 13(2), 59-64, 2005.
5. T.R Wolinski, K. Szaniawska, S. Ertman, P. Lesiak, A.W. Domanski, R. Dabrowski, E. Nowinowski-Kruszelnicki, J. Wojcik, Meas. Sci. Technol., 17, 985-991, 2006.
6. T.R. Wolinski, P. Lesiak, A.W. Domanski, K. Szaniawska, S. Ertman, R. Dabrowski, J. Wojcik, Mol. Cryst. Liq. Cryst. 454, 333-350 (2006).
7. J.C. Knight, Nature 424, 847-851 (2003).
8. J.C. Knight, T. Birks, B. Mangan, P. Russell, Opt. & Photon. News 30, 26-30 (2002).
9. C.L. Xu, W.P. Huang, M.S. Stern, S.K. Chaudhuri. IEEE Proc. Opt. 141(5), 281–286 (1994).
10. K. Kikuchi, T. Okoshi, Opt. Lett. 8, 122-124 (1983).
11. P. Lesiak, T.R. Wolinski, K. Brzdakiewicz, K. Nowecka, S. Ertman, M. Karpierz, A.W. Domanski and R. Dabrowski, Opto-Electronics Rev. 15 (1), 27-31 (2007).

Finite-element analysis of Λ-wedge plasmon polariton guide

Min Yan and Min Qiu
Department of Microelectronics and Applied Physics, Royal Institute of Technology
Electrum 229, 164 40 Kista, Stockholm, Sweden
min@kth.se (M.Q.)

Abstract: *The Λ-wedge plasmon polariton waveguide is analysed using a vector finite-element method. The mode appreance, propagation loss, and geometric dispersion of such waveguide are studied at both visible and near infrared wavelenghts. No modal cutoff is seen for increasing wedge angle at any wavelength.*

Introduction

A straight Λ-shaped metal corner [Fig. 1(a)] is able to guide plasmon polariton waves (so-called wedge plasmon polaritons, or WPPs) [1]. Using some noble metals (e.g. gold and silver) the guided mode can be at the near infrared and even visible light wavelength range. The electromagnetic field of the mode is coupled with the oscillating electrons in the metal and therefore is highly localized to the metal surface (laterally at Λ tip for the problem at hand). Such non-diffraction-limited wave guidance in (better yet) such a simple structure can be a very promising candidate for both optical integration as well as sensing applications.

Previous theoretical analysis was limited to the finite-difference time-domain (FDTD) method [1]. The traditional FDTD method interprets material interfaces (where mode field is at its maximum for plasmon polariton waveguides) cruelly owing to its use of orthogonal mesh. In this paper, we use a vector finite-element method (FEM) to study this class of waveguides. The FEM is based on the wave equation governing the transverse magnetic field. The Gauss's law for magnetic field, $\nabla \cdot \mathbf{H} = 0$, is explictly imposed for eliminating spurious modes [2]. Abilities in accurately defining material interfaces as well as in adaptive mesh resolution make FEM especially advantageous for deriving surface plasmon polariton (SPP) modes (a WPP is nothing but coupled SPPs). Second-order shape function is used for accelerating numerical convergence. At the same time, formulation in second-order shape function makes the computed mode field twice differentiable, which in turn allows us to derive the rest four field components (i.e. H_z, E_x, E_y, E_z fields). For certain waveguide structures, a triangle edge size as small as 2nm at the Λ tip is used to achieve convergence [Fig. 1(b)].

The studied Λ metal wedges are assumed to have infinite side walls. This is to mitigate the influence of other metal corners formed when the height of the wedge is finite. Numerically we enlarge the computation domain (around the wedge tip) until field amplitude decays by 30dB at the computational boundary. We point out that the field tends to be singular at a sharp wedge tip, a feature that is also present in pure-dielectric waveguides. Such field singularity in dielectric waveguides usually does not prevent a numerical method from converging. It however significantly affects the propagation constant of a mode guided by a metal corner (including the V-shaped channel plasmon polariton waveguide) when the numerical resolution is further refined. For this reason, all Λ corners are rounded with an arc of 10nm in radius in the current analysis.

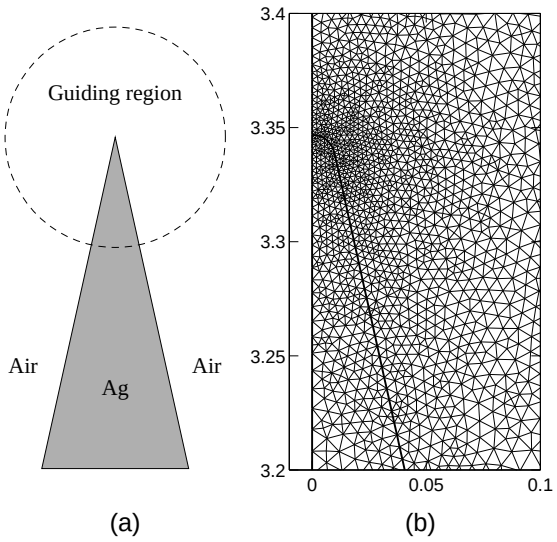


Fig. 1: (a) Schematic diagram of a metal wedge plasmon polariton waveguide. (b) Finite-element mesh of a metal wedge guide with Λ angle at 25 degree. Only half of the waveguide is used by using perfect magnetic conductor (PMC) condition at its symmetry line ($x = 0$). The tip is rounded with an arc with 10nm radius. Axis unit: μm.

FEM analysis

Our study concentrates on silver-air structure. The dielectric constant of silver is described in Drude model as $\epsilon = \epsilon_\infty - \frac{(\epsilon_0 - \epsilon_\infty)\omega_p^2}{\omega^2 + i\omega\gamma}$, with $\epsilon_\infty = 4.017$, $\epsilon_0 = 4.896$, $\omega_p = 1.419 \times 10^{16}$rad/s, and $\gamma = 1.117 \times 10^{14}$rad/s. This drude model is fitted according to the measured data from Palik's handbook [3]. In Fig. 2(a), we show the dispersion curve of the guided WPP mode as the Λ angle is varied, at 633nm and 1550nm wavelengths. The effective index value (related to propagation constant as $n_{\text{eff}} = \beta/k_0$) decreases as the angle increases, and it asymptotically approaches to the value corresponding to the SPP mode guided by a single Ag-air interface. It is obvious to see that such waveguide in general does not experience a cutoff as the Λ angle in-

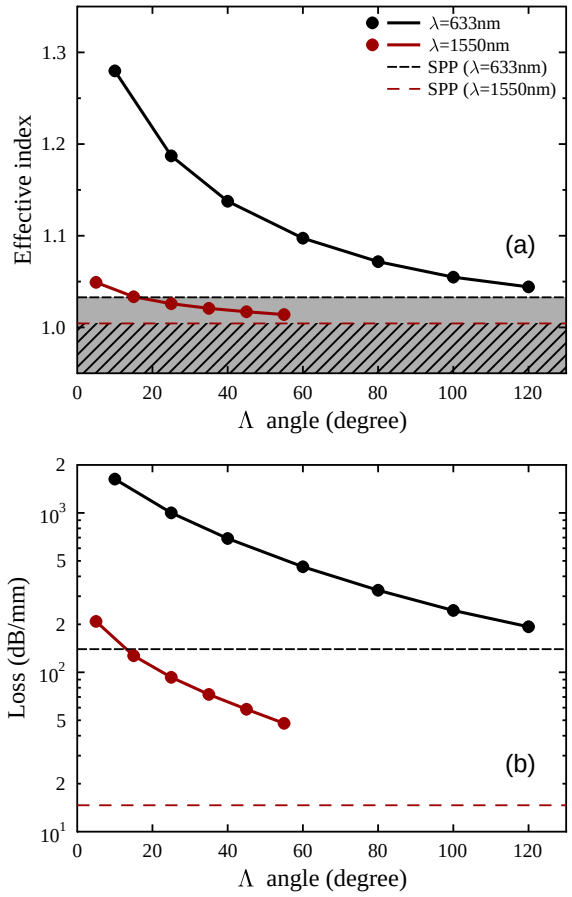


Fig. 2: (Color online) Dispersion (a) and loss (b) curves of the guided WPP mode as Λ angle changes. Gray (line-shaded) region in (a) is the allowed states by an Ag-air interface at $\lambda = 633$nm (1550nm).

creases, opposed to what was concluded in [1]. At a small angle, the mode field highly concentrates at the Λ tip. At larger angles, the field extends further away from the tip. Eventually, when the Λ angle is infinitesimally close to 180° (the Λ wedge becomes almost a flat surface), the mode will extend for the whole Ag-air interface, and becomes a SPP mode.

The transverse decay constant of the overall mode field along the surface and in the air can be estimated using

$$k_t^s = k_0 \sqrt{n_{\text{eff}}^2 - n_{\text{SPP}}^2}, \quad (1)$$

$$k_t^a = k_0 \sqrt{n_{\text{eff}}^2 - n_{\text{air}}^2}, \quad (2)$$

respetively. As n_{SPP} is always larger than n_{air}, field tends to strech longer along the two side interfaces. Note that the decay is highly polarization-dependent at the metal interface. Figure 3 shows the mode guided by a wedge with a 25° angle. Notice the Ag-air interfaces at two sides are close to vertical. As the x-component of the magnetic field [Fig. 3(a)] is not supported by a vertical Ag-air surface, it decays more quickly along the side interfaces, compared to the y field component [Fig. 3(b)]. The maximum of H_x is at the tip top, where, if examined in great detail, the field is parallel to the Ag-air interface. In contrast, the y component tends to extend more along the two side interfaces. And it is anti-symmetric about the $x = 0$ symmetry line. Notice at a very large Λ angle, the opposite attenuation behaviors along side interfaces are expected for the two polarizations. The maximum of the y component is not at the tip top, but at two sides near to the top. The H_y fields at two sides of the tip are coupled through the metal. The H_z field component [Fig. 3(c)] has a very similar appearance as compared to the H_y field component. This is due to the two fields are both parallel to (or close parallel to) the metal surface.

The propagation loss of the guided mode is shown in Fig. 2(b). In general, the mode experiences a higher loss at a smaller Λ angle, and at a smaller wavelength. A smaller angle induces stronger field coupling, and therefore a larger percent of the field is located in the metal, which results in higher loss. At a longer wavelength, silver has a larger negative dielectric constant (a more perfect conductor), therefore field tends to be expelled out of metal region. The loss value is close to that of the SPP mode as the Λ angle is approaching to 180°.

Discussion and Conclusion

Two points should be addressed for better understanding such metal wedge waveguide. First, although group theory allows a mode with symmetric reflection symmetry (whose transverse magnetic field is parallel to y axis at $x = 0$ symmetry line), it however has a n_{eff} value in the shaded region in Fig. 2(a), and therefore will radiate away. Due to this fact, we have only used the PMC condition on the $x = 0$ symmetry line. Second, the physical problem is divergent with respect to sharpness of the Λ tip. Field tends to be more trapped into the corner if the tip becomes sharper (smaller curvature radius there). And correspondingly, the propagation constant becomes larger. This peculiar property of WPP waveguides though imposes great difficulties for theoreticians, it, however, indicates that we can achieve better confinement (and therefore denser integration) with sharper wedges. On the other hand, we should also expect that sharp irregularities on fabricated waveguides involving metals would affect the waveguides' performance greatly.

In conclusion, using the finite-element method, we have studied the modal properties of plasmon polariton modes guided by Λ-shaped metal wedges. Such waveguides are promising for nanoscaled integrated optical circuits and sensing applications. At the same time, such metal corners are most often present in other plasmon polariton waveguides (e.g. metal strip waveguides, and V-shaped channel waveguides), therefore knowing the modal behavior of such Λ-wedge waveguide is important for designing more complex waveguides.

Acknowledgments

This work is supported by the Swedish Foundation for Strategic Research (SSF) through the INGVAR program, the SSF Strategic Research Center in Photonics, and the Swedish Research Council (VR).

References

[1] D. F. P. Pile, T. Ogawa, D. K. Gramotnev, T. Okamoto, M. Haraguchi, M. Fukui, and S. Matsuo, "Theoretical and experimental investigation of strongly localized plasmons on triangular metal wedges for subwavelength waveguiding," Appl. Phy. Lett. **87**, 061,106 (2005).

[2] H. E. Hernández-Figueroa, F. A. Fernández, Y. Lu, and J. B. Davies, "Vectorial finite element modelling of 2D leaky waveguides," IEEE Trans. Magn. **31**(3), 1710–1713 (1995).

[3] E. D. Palik, *Handbook of Optical Constants of Solids*, chap. Part II, Subpart 1 (Academic Press, 1985).

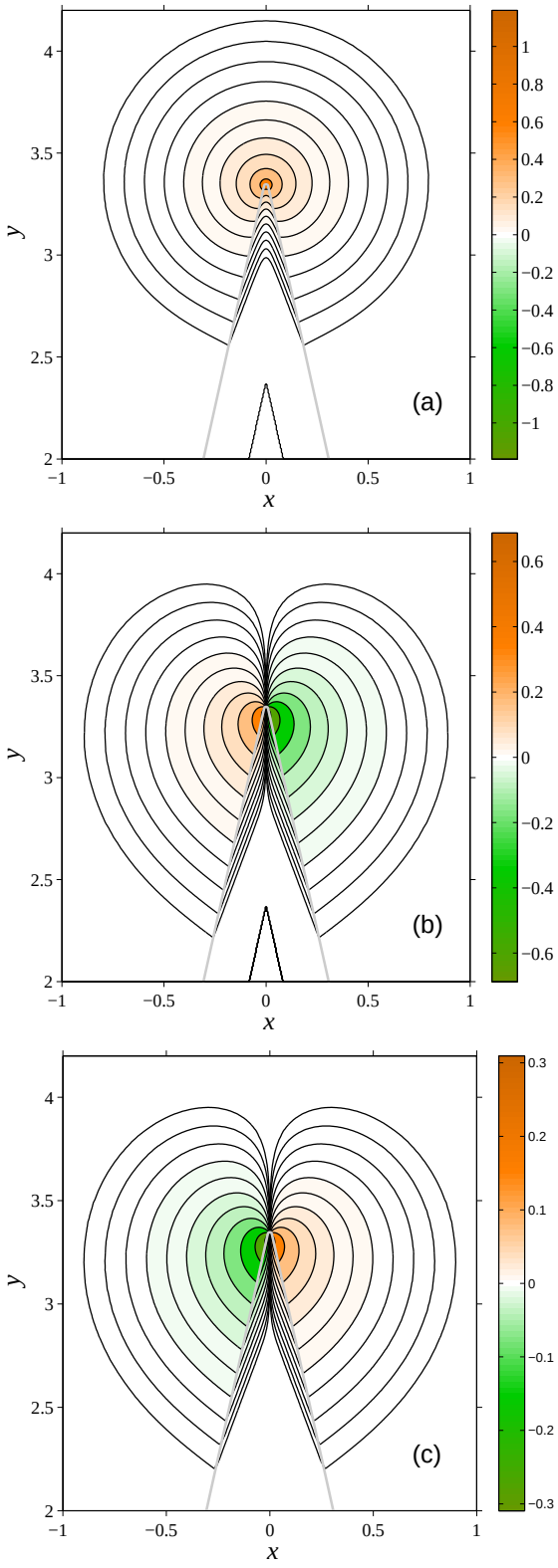


Fig. 3: (Color online) H field components of a mode guided by a wedge with a 25° angle. (a) H_x component; (b) H_y component; (c) H_z component. Orange for positive, and green for negativ. Contour lines (except the first one, which is at 90% of the maximum value) are in 3dB separation. The void regions within the metal wedge as appeared in (a) and (b) are not computed as the field there can be safely treated as zero.

Whispering Gallery Mode for Second-Harmonic Generation in Microresonators

G. Kozyreff (1,2), J.L. Dominguez Juarez (1), **and Jordi Martorell (1,3)**

1) ICFO-Institut de Ciencies Fotoniques, 08860 Castelldefels (Barcelona), Spain

2) ONT, Université Libre de Bruxelles, Campus Plaine CP231, Bruxelles, Belgium

3) Departament de Fisica i Enginyeria Nuclear, Universitat Politecnica de Catalunya, 08222 Terrassa, Spain
Gregory.Kozyreff@icfo.es , luis.domingues@icfo.es and jordi.martorell@icfo.es

Abstract: *We study theoretically surface second harmonic generation in microsphere using whispering gallery modes. Coupled-mode theory is derived. Conditions for double-resonance and phase matching are discussed. An experimental realization using a silica microsphere pumped with a tapered fiber is considered.*

Introduction

Since the demonstration that with the use of spherical microresonators one could couple the evanescent field of a single photon with a single atom,[i] it became clear the relevance that such type of resonators could have for the detection of very small concentrations of un-marked chemical or biological compounds. The high sensitivity of devices based on such type of microresonators resides on the high value of the quality factor for the cavity ($Q\sim10^8$) and on an evanescent field that penetrates the surrounding medium.[ii] The presence of an external agent on the outside surface of the microcavity produces a change in the evanescent wave, which translates into a detectable change in the light that propagates within the sphere in a whispering gallery mode (WGM).

The measurable changes come either from a change in the mass of the region where the evanescent wave propagates or from a change in the refractive index. To date, such microresonators have been used as biochemical sensors, where a change in the position of the resonance could be attributed to a change in the concentration of glucose,[iii] to quantify unmarked DNA,[iv] to detect the presence of certain proteins after a displacement of the resonance,[v] and to detect the presence of highly volatile organic compounds such as, for instance, toluene or nitrobenzene.[vi]

The performance of such micro resonators as sensors could be enhanced if the molecule to be detected played a direct role in the light generation process, or in a less favorable case, if the species to detect sat very close to the material that was used to generate the light.

In a process such as surface second harmonic generation in total internal reflection geometry, not only the propagation but also the light generation within the micro-resonator is directly related to the chemical composition of the surface. Although to reach a non-vanishing second order nonlinear process there are very strict requirements one must set on the parameters of the sphere, it has been proven, very recently, that it is possible to fabricate micro resonators of nonlinear material where the quadratic nonlinear interaction is efficient.[vii] However, the challenge to experimentally demonstrate a second harmonic interaction coupling the evanescent field with the radiation from a nonlinear dipole on the surface of the sphere remains.

Second Harmonic Generation in the WGM

We consider second harmonic generation in the WGM of a dielectric microsphere. On the surface of the sphere, inversion symmetry is broken, allowing the existence of a local second-order susceptibility.

We thus analyze the generation due to a surface nonlinearity.

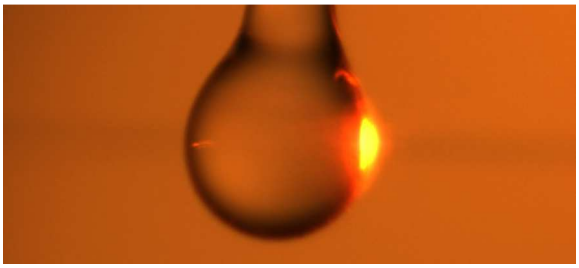


Fig. 1: Signature of fundamental WGM excitation. As the pump tapered fiber (shadow in the background) touches the sphere, an intense field is suddenly radiated at the rim of the sphere. Sphere diameter: 113 μm; wavelength: 0.8 μm.

A natural way to treat second harmonic generation is through a coupled-mode theory. We assume the electric field to be essentially described by two

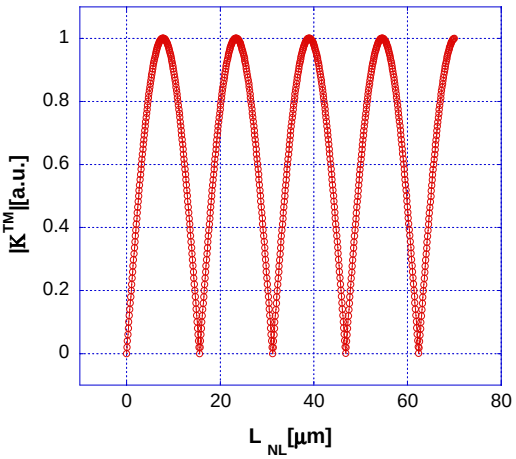


Fig. 2: Absolute value of nonlinear coupling, $|K^{TM}|$ as a function of the nonlinear coating length along the equator ($\mathbf{L_{NL}}$). Sphere radius R= 83 µm.

resonant modes of the sphere as

$$\mathbf{E} = \alpha_1(t)\mathbf{E}_{\omega_1}(\mathbf{r})e^{-i\omega_1 t} + \alpha_2(t)\mathbf{E}_{\omega_2}(\mathbf{r})e^{-i\omega_2 t} + c.c.,$$

where ω_1, ω_2 are resonant frequencies such that ω_1 is close to the pump frequency and $\omega_2 \approx 2\omega_1$. The resonant modes of the sphere $\mathbf{E}_{\omega_{j1}}(\mathbf{r})$ are given by the vector spherical harmonic solutions of Maxwell's equation. When the orbital number ℓ and the azimutal number *m* of such a solution are both large, this solution describes a Whispering Gallery Mode (WGM) of the cavity.

Such modes are typically excited by pumping light in the cavity with a tapered optical fiber, as shown in Figure 1. For a pump wavelength around 800 *nm* and a sphere radius larger than 30 μm, we have $\ell >> 1$ and the resonant frequencies are accurately given by asymptotic formulas[viii] . It is important to note that the spherical modes, being spherical waves away from the resonator, have an infinite energy (just as plane waves do). The amplitudes $\alpha_1(t)$ and $\alpha_2(t)$ are therefore normalized such that $|\alpha_j(t)|^2$ be the power (in watts) radiated by the jth mode. Bearing this normalization in mind, we thus seek to derive a set of coupled-mode equations of the form

$$\frac{d\alpha_1}{dt} + \Gamma_1\alpha_1 = \Gamma_1\sqrt{P}e^{-i\Delta_1 t} + i\kappa^*\alpha_2\alpha_1^* e^{i(\Delta_2 - 2\Delta_1)t},$$

$$\frac{d\alpha_2}{dt} + \Gamma_2\alpha_2 = i\kappa\alpha_1^2 e^{-i\Delta_2 t}.$$

In these equations, P is the power that would be radiated by the fundamental mode in the absence of nonlinear conversion, taking into account the injection efficiency and the various losses suffered by that mode. On the other hand Δ_1, Δ_2 are the detuning between the injection frequency and the fundamental mode and the detuning between fundamental and second harmonic, respectively. Finally, Γ_j are the amplitude decay rates of the WGM. These are not only due to radiation, but also absorption and scatterin by surface impuritites.[ix] The purpose here is to derive the coupling strength κ between the two modes. Note that TM and TE WGM have very distinct electric field distribution in this limit and we must consider both cases separately.

Coupling strength and phase matching

The usual ray picture of a WGM suggests to understand phase matching in terms of two nearly-plane waves circulating along the equator of the sphere. This is however misleading. Indeed, WGM are cavity modes, i.e. they are confined to a closed geometry, which is quite distinct from free propagation. To demonstrate this point, we derive a coupled-mode theory from Maxwell's equation. We thus show that the coupling coefficient between a TM fundamental mode and a TM second harmonic with quantum numbers L and M obeys

$$\kappa^{TM} \propto \iint \chi^{(2)}_{s,\perp\perp\perp} Y^*_{LM} Y^2_{\ell m} \sin\theta d\theta d\varphi .$$

In this expression, $\chi^{(2)}_{s,\perp\perp\perp}$ is the appropriate component of the nonlinear susceptibility tensor. For a uniform nonlinear susceptibility, this integral will vanishes unless the quantum mechanical rules for angular momentum composition are satisfied. In a spherical cavity, therefore, phase matching corresponds to

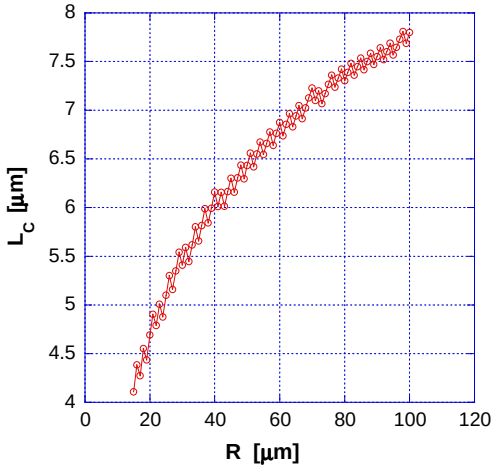


Fig. 3: Coherent Length ($\mathbf{L_C}$) for Second Harmonic Generation as function of the radio (**R**) of sphere.

conservation of angular momentum, instead of linear momentum for plane waves.

Furthermore, we show that TE fundamental modes are much more efficient to generate second harmonics. Indeed, we find that

$$\left|\kappa^{TE}\right| \sim \ell^2 \left|\kappa^{TM}\right|.$$

Except under the special favourable circunstance discussed above, the integral in κ^{TM} will vanish. A quasi-phase matching strategy is, therefore, to cover the surface of the sphere only over a distance L_{NL} along the equator. To determinate the coherent length of the sphere, let us suppose that:

$$\chi^{(2)}_{s\perp\perp\perp} = \begin{cases} \chi^{(2)}_s & \text{for} \quad 0 < \varphi < L_{NL}/R, \\ 0 & \text{otherwise,} \end{cases}$$

R being the radius of the sphere and φ the azimutal angle. One obtains the periodic dependence $\kappa^{TM}(L_{NL})$ depicted in Figure 2. The coherence lengh L_C is thus defined as half the speration between two maxima of $\left|\kappa^{TM}\right|$.[x] In Figure 3, we plot the coherent length L_C as a function of R. Note that the coherence length is not constant as the sphere radius varies, due to the index modal dispersion of the WGM. The discontinuous character of the curve results from jumps in the values of ℓ and L corresponding to the most resonant fundamental and second harmonic modes as R is varied. The same approach can of course be followed for more realistic nonlinear coatings, e.g. spherical caps of varying diameter L_{NL}.

Conclusion

We have discussed the possibility of second harmonic generation (SHG) in a microsphere due to a surface nonlinearity. This system, apart from fundamental interest, has promising applications in sensor technology. To describe SHG, a coupled-mode theory based on Whispering Gallery Modes is derived, for which the main result is an analytical expression for the coupling strength between fundamental and second harmonic modes. Phase- and quasi-phase matching is still possible in this system, but as the expression for the coupling constant clearly indicates, frequency mixing now requires conservation of angular momentum. Furthermore, nonlinear generation is ℓ^2 times more efficient with a TE fundamental mode than with a TM fundamental mode. Finally, the concept of coherence length was revisited and discussed for the spherical geometry.

Silica microspheres of the adequate diameter have been prepared to demonstrate such predictions of the coupled-mode theory. We have shown that it is possible to cover the surface of the sphere with a layer of nonlinear material. We also present the realization of the experimental setup to measure second harmonic generation in the Whispering Gallery Modes of the spherical resonator.

References

[i] D. W. Vernooy et al. Phys. Rev. A, Vol. **57**, R2293 (1998).

[ii] K. J. Vahala, "Optical Microcavities", *Nature*, Vol. **424**, pp. 839-846, 2003.

[iii] Chung-Yen Chao and L. Jay Guo, Appl. Phys. Lett., Vol. **83**, 1527 (2003).

[iv] F. Vollmer et al., Biophysical Journal, Vol. **85**, 1974 (2003).

[v] F. Vollmer et al., Appl. Phys. Lett., Vol. **80**, 4057 (2002).

[vi] W. Fang et al. Appl. Phys. Lett., Vol. **85**, 3666 (2004).

[vii] V. S. Ilchenko et al., Phys. Rev. Lett., Vol. **92**, 043903 (2004).

[viii] C.C. Lang, P.T. Leung, and K. Young, J. Opt. Soc. Am. B, Vol. **9**, 1585 (1992).

[ix] M.L. Gorodetsky, A.A. Savchenkov, and V.S. Ilchenko, Opt. Lett., Vol. **21**, 453 (1996).

[x] M. M. Fejer, G. A. Magel, D. H. Jundt, and R. L. Byer. IEEE J. Quantum Electron., Vol. **28,** 2631–2654 (1992).

Lab-on-a-Chip Systems with Integrated Optics for Biochemical Applications

Klaus B. Mogensen, Detlef Snakenborg, Ómar Gústafsson, Pedro S. Nunes and Jörg P. Kutter
MIC – Dept. of Micro and Nanotechnology, Technical University of Denmark, 2800 Kgs. Lyngby, Denmark
jku@mic.dtu.dk

Abstract: *The challenges and possibilities of integrating optical elements with fludic channels for applications in miniaturized biochemical devices are discussed with the help of examples from our lab.*

Introduction

Over the past 15 years, a new field of research has emerged at the junction between chemistry, physics, biology and engineering. The objects of interest in this field are either referred to as micro-Total Analysis Systems (μ-TAS) or Lab-on-a-Chip Systems (LOC) [1,2]. Both build upon the ideas of gaining advantages by miniaturizing and integrating all functions necessary to perform a given (bio)chemical analysis and utilizing the particular features of fluids confined in micrometer-sized geometries (microfluidics). At these length scales, liquid flows are very well behaved, allowing to easily create laminae flowing alongside each other, which can then be used to control location, and perform flow sorting and other fluidic handling steps. Transport of chemical species across these laminae is mostly relying on diffusion, which, in most cases, is a fast enough process on small length scales, and thus another reason to miniaturize.

LOCs are being designed for applications in chemistry, biology and medicine, where often investigations have to be performed on very small amounts but at the same time on a large number of different samples. Here, the reduced consumption of chemicals and the improved performance in terms of time and efficiency are the main motivations to invoke miniaturization and microfluidics.

Traditionally, the design and fabrication of these devices has relied on techniques inherited from microelectronics and micromechanics. Thus, silicon and glass have been the preferred materials for realizing LOCs. However, in recent years, the focus has shifted towards polymer substrates, since these materials are potentially both better suited and cheaper for one of the main applications of LOCs, namely as one-time use diagnostic devices. For this to be successful, a range of new fabrication approaches and techniques had to be developed and tested. New designs making use of the special properties of polymers while considering their individual restrictions are continuously being developed.

All LOCs are made up of a number of functional elements, which are necessary for a given task. These typically include fluidic handling elements (channels, valves, pumps, …) and detection elements (electrodes, optical elements, sensors, …). Also here, the integration of several of these functional elements on a planar substrate in a miniaturized format can lead to performance improvements and, in fact, to new, hitherto unseen functionalities as compared to more conventional setups.

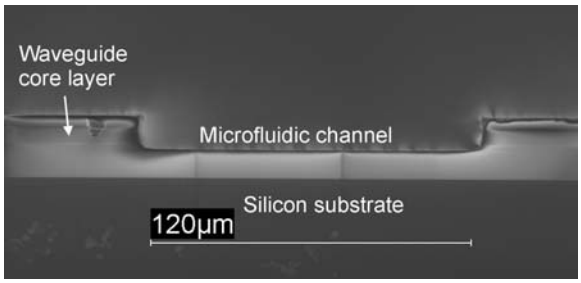


Fig. 1: Cross-sectional view of a fluidic channel with waveguides. The waveguides structure consists of three layers: a buffer layer of silicon oxide, a core layer of doped silicon oxide and a cladding layer of silicon oxide again. Note, no cover lid has yet been bonded to the structure.

In our lab, for a number of years now we have been working with integration of fluidic and optical elements, in an effort to steer away from bulk optics, which apart from taking up too much space, requires alignment before every new measurement and is not considered conducive to portable, hand-held devices. The central element in this effort was and is the waveguide, very well suited for the quasi 2D nature of planar microfluidic devices.

Nitrogen-doped and pure silica waveguides

To present on-chip alternatives to fluorescence detection and the often required labeling, sensitive absorbance detection on a chip is an option. Here, light is shone through the sample and the reduction of the measured light intensity is related to the concentration of analyte molecules present in the sample volume. While fluorescence can be very selective, absorbance (especially when including the UV portion of the optical spectrum) is almost universal, i.e., many different types of molecules can be directly detected without having to modify them prior to the detection. The main drawback is a drastically reduced sensitivity when compared to fluorescence detection, and – at first glance – implementing this technique in microsystems seems to be the wrong strategy. The measured absorbance, A, is, according to Beer's law, directly proportional to the optical path length, d:

$$A = \varepsilon c d$$

with c: concentration and ε: molar extinction coefficient. Without invoking more advanced machining, bulk optics approaches can only exploit the channel

depth as the optical path length, which in many cases is smaller than the channel width. Using

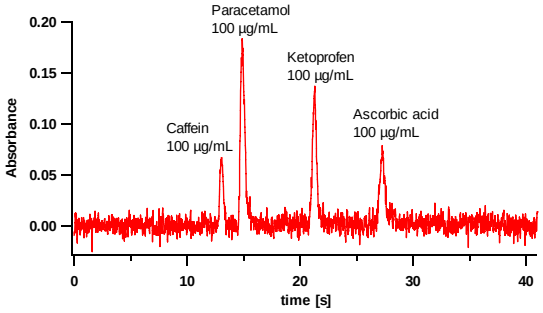


Fig. 2: Electrophoretic separation of four components in a microfluidic chip using UV-absorbance detection at 254 nm. The detection cell was the 750 um long lower part of a U-shaped channel probed by UV-transparent waveguides [6].

planar waveguides monolithically integrated with the fluidic channels, light can be brought in from the side thereby using the width of the channel as optical path length. Furthermore, U- and Z-cells can now be designed featuring even longer optical path lengths.

At MIC we have developed and fabricated UV-transparent waveguides using silica-on-silicon technology (see Figs. 1, 4). Changing the traditionally used germanium as core dopant material to nitrogen, waveguides with transmission down to about 210 nm were realized [3]. More recently, pure silica waveguides have been realized that show very low propagation losses down to 200 nm [4]. Using such waveguides microchips for capillary electrophoretic separation and UV-absorbance detection were realized – a typical separation is shown in Fig. 2 [5, 6] One of the practical challenges is still the optical connection to the macro-world, which is done via optical fibers. Since the cross-sections of fibers and waveguides differ, there is always the threat of stray light, i.e., light coming out of the fiber and propagating unguided through the buffer or cladding layer of the waveguide structure. Such light can reach the detector without interacting with any sample solution thereby limiting the performance of the detection set-up. Special care has to be taken in the design of the waveguides to avoid influences from stray light. This is also illustrated in the next example.

Polymer waveguides

With standard cleanroom technology silica-on-silicon waveguides can be fabricated with great accuracy and excellent optical qualities. However, some of the processes involved are rather time-consuming, making these waveguides more expensive and the turn-around time longer. Along with the generally increased interest in low-cost polymer fluidic devices there is a demand for waveguides and other optical elements made from polymeric materials as well. One polymer that is being used extensively in microsystems already is SU-8, which can be structured in a photolithographic process. Since it also has a sufficiently high refractive index, it is at the same time suitable as a waveguide. When using air as the cladding material at both sides it is possible to reduce the fabrication effort to just one mask step, and yet allowing the realization of fluidic channels, waveguides and fiber couplers (for easier connection

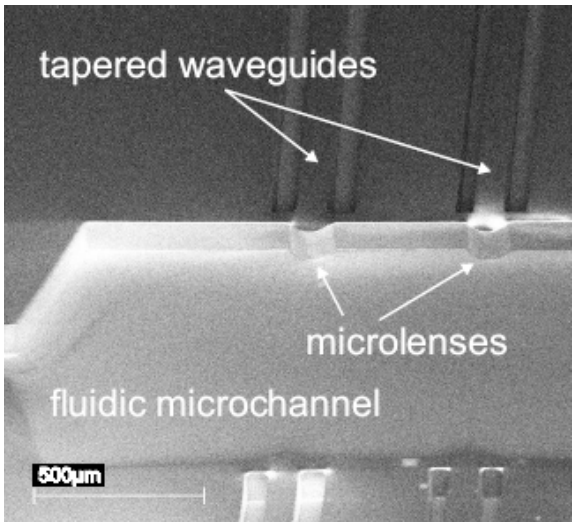


Fig. 3: Microfluidic channel with tapered waveguides and microlenses at the interface between channel and waveguides. All elements are defined in a single mask and realized using SU-8 lithography.

to the macro-world) at the same time [7]. It should, however, be noted that SU-8 has different optical properties than silica. It is only transparent down to around 580 nm, and is therefore preferably operated with red laser light. Using special detection geometries, optical path lengths of up to 1000 µm are employed, again in order to improve the detection sensitivity. However, this detection path length cannot be made arbitrarily long, as the signal-to-noise level deteriorates with a decreasing signal. It is therefore more important to ensure that as much as possible of the optical power delivered by the waveguide is used to interact with the molecules in the detection zone. In other words, the spreading of the (unguided) light within the channel has to be reduced. This can be achieved by shaping the beam as it exits the waveguide endface. SU-8 proves here to be a flexible material to work with, as it allows to taper the waveguides and even makes it possible to define lens structures at the interface between the waveguide and the fluidic channel (see Fig. 3) [8].

While working with SU-8 allows faster turnaround times and easier prototyping than working with silicon and glass, it is still a photolithographic process, which has only limited applicability for production of large numbers of replicas. Recently, micro-milling and casting processes have been employed to realize chips including waveguides in a potentially mass-producible way. Here, polymethylmethacrylate (PMMA) is used as the base polymer, whereas the higher refractive index necessary for waveguiding is ensured by a spun-on or cast PMMA layer, which is

doped with a different polymer to adjust its refractive index and subsequently structured to define the waveguides [9].

Fig. 4 presents an overview of the spectrally resolved propagation loss of all the different waveguides developed and tested in our lab over the past couple of years. Note, that the micro-milled waveguides have very acceptable propagation losses over a wide region of wavelengths.

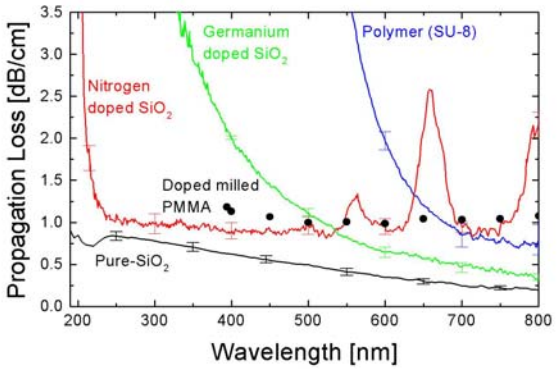


Fig. 4: Comparison of the wavelength-resolved propagation losses of a number of different waveguides fabricated and tested at MIC over the past several years.

Applications

As already mentioned, waveguides are combined with fluidic channels as detecting elements in separation systems (see Fig. 2). Here, one input and one output waveguide are typically sufficient. In principle, it is just as difficult to fabricate one waveguide as it is to fabricate an array of waveguides. With more than one waveguide, a number of applications can be realized, such as, e.g., velocity measurements on fluorescently labeled particles or cells. There exists a variety of detection principles, which can favorably be implemented on microchips with integrated waveguides, since this assures a high degree of accuracy in geometry and alignment. One such technique is known as Shah Convolution Fourier Transform detection (SCOFT). It was previously demonstrated on microchips using slitmasks and bulk optics [10,11], while the realization with waveguides is conceptually much more elegant and promises improved performance [12]. Figure 5 shows the layout of a chip developed for SCOFT including beamsplitters and an array of 32 waveguides (designs with up to 128 waveguides were tested). The goal of this layout was to achieve equally-spaced illumination of the fluidic channel.

Using such waveguide arrays velocities of particles and cells can be measured even when there is a continuous influx of particles in the detection area and also when ensembles of particles with different velocities are present at the same time. The velocity information is extracted from the recorded signal trace after a Fourier transform operation, which yields a frequency that is directly related to the velocity of the particles [12].

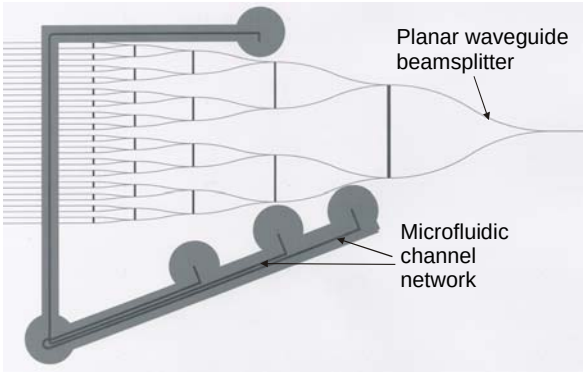


Fig. 5: A fluidic structure combined with an array of waveguides for periodic illumination of the channel, as used for the determination of the velocities of particles moving through the channel. The structures in between the split pairs of waveguides are stray-light rejection elements.

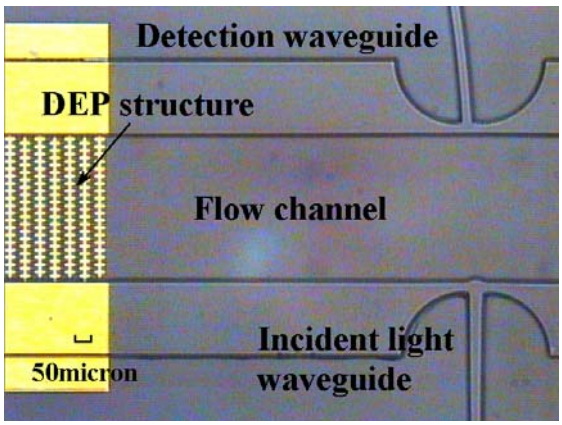


Fig. 6: A waveguide-based flow cytometer down-stream from a dielectrophoretic cell trap. Note the beam-shaping lens at the end of the incident light waveguide ensuring light to be focused in the path of the cells [14].

Waveguides can also be used in connection with fluidic channels to efficiently monitor passage of cells in these channels (flow cytometry) and even get further information on the cells or particles (such as size, viability etc.) using scattered light measurements [13]. Such measurements have been employed to gauge and better understand the function and efficiency of an on-chip dielectrophoretic (DEP) cell trap. By using a waveguide-based flow cytometer both upstream and downstream from the trap, its efficiency under different conditions can be monitored counting the cells passing each of the detection regions. Fig 6 shows the waveguide arrangement downstream from a DEP trap in a microfluidic channel [14].

Integration of light sources and detectors

Our efforts in fabricating waveguides to control where light is delivered and collected on a microfluidic chip were recently combined with other research

efforts going on at MIC. There has been work on the integration of photodiodes with particular emphasis on the connection and packaging issue when combining photodiodes and fluidic structures for aqueous chemistry. Also, there have been recent efforts to realize fluidic dye lasers on microchips at MIC. Here, a laser cavity was defined by SU-8 microstructures and rhodamine dye was percolated through the cavity while an Excimer laser acted as optical pump source. The combination of such a dye laser with waveguides, fluidic channels and photodiodes represents a highly integrated microsystem for biochemical applications. Figure 7 shows a picture of such a device and the layout beneath. The mixing device allows two chemicals to be mixed and the subsequent reaction can then be monitored by any or all of the waveguides spanning the fluidic channel at different positions along the flow direction [15].

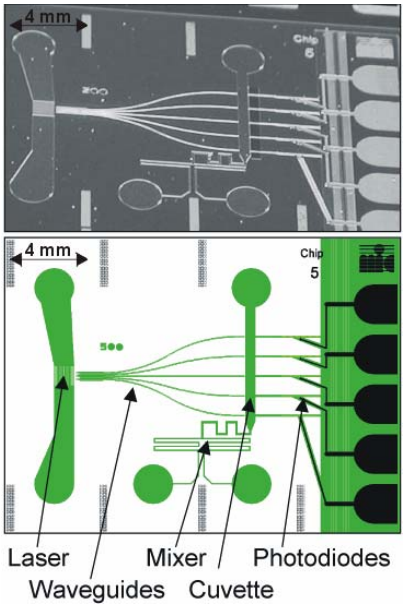


Fig. 7: Photograph (above) and layout (below) of a chip including fluidic channels, a fluidic dye laser, waveguides, and photodiodes as well as metallic pads for electrical connections [15].

Trends - Optofluidics

Optofluidics is an emerging field where nanophotonics and microfluidics meet. At MIC, we are developing microfluidic systems containing micro- or nanomachined elements that can fulfil both fluidic (chemical) functions as well as optical functions. Fig. 8 shows a chip containing a regular arrangement of pillars in a channel. This arrangement provides the function to separate complex mixtures of chemicals as they flow along the channel. At the same time, the arrangement constitutes an inverse photonic band gap structure and can thus be exploited for a number of different detection purposes. Light is coupled in perpendicularly to the flow direction using waveguides. Pick-up waveguides are also placed on the opposite side of the channel. With such an arrangement, detection can be performed at various stages along the flow direction, thus also allowing the dynamics of a separation or a reaction to be monitored. It is expected that this and similar structures will introduce new detection schemes for LOCs.

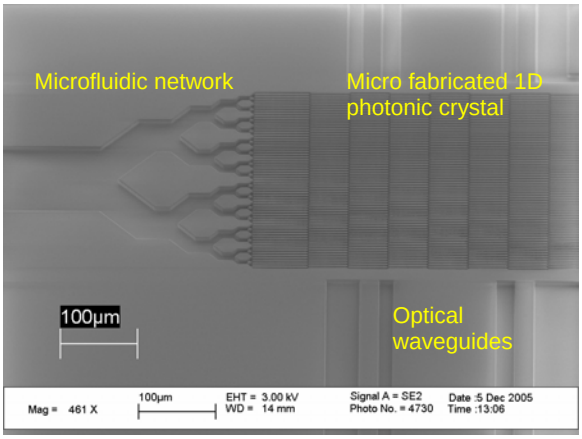


Fig. 8: Micrograph of a fluidic structure with a regular array of pillars, which at the same time can fulfil fluidic and optical functions.

Conclusions

Integration of optics and fluidics offers a range of possibilities for new and improved tools for applications in the life sciences.

Acknowledgments

Anders Kristensen, N. Asger Mortensen, Anders Wolff and their groups are acknowledged for collaborations. Funding comes from the Danish National Research Council and the European Community.

References

[1] Reyes, D. R. et al., *Anal. Chem.* **2002**, *74*, 2623-2636.
[2] Auroux, P.-A.et al., *Anal. Chem.* **2002**, *74*, 2637-2652.
[3] Mogensen, K. B. et al., *Opt. Lett.* **2001**, *26*, 716-718.
[4] Mogensen, K. B. et al., *Electrophoresis* **2004**, *25*, 3788-3795.
[5] Mogensen, K. B. et al., *Electrophoresis* **2001**, *22*, 3930-3938.
[6] Petersen, N. J. et al., *Electrophoresis* **2002**, *23*, 3528-3536.
[7] Mogensen, K. B. et al., *Appl. Optics* **2003**, *42*, 4072-4079.
[8] Snakenborg, D. et al., *Proc. of Micro-TAS 2003*, 2003; 841-844.
[9] Snakenborg, D. et al., *J. Micromech. Microeng.* **2006**, *16*, 375-381.
[10] Crabtree, H. J. et al., *Anal. Chem.* **1999**, *71*, 2130-2138.
[11] Kwok, Y. C.; Manz, A. *Analyst* **2001**, *126*, 1640-1644.
[12] Mogensen, K. B. et al., *Anal. Chem.* **2003**, *75*, 4931-4936.
[13] Wang, Z. et al., *Lab Chip* **2004**, *4*, 372-377.
[14] Wang, Z. et al., *Electrophoresis* **2006**, *27*, 5051-5058.
[15] Balslev, S. et al., *Lab Chip* **2006**, *6*, 213-217.

New frontiers in optical biosensing

Laura M. Lechuga
Biosensors Group. Centro Nacional de Microelectrónica (IMM-CNM). CSIC. Laura@imm.cnm.csic.es

Abstract: *The technology of optical biosensors has reached a high degree of maturity and several commercial products are on the market. But problems of stability, sensitivity and size have prevented the general use of optical biosensors for real field applications. Our last developments to solve such drawbacks will be showed, mainly related to the development of portable and highly sensitive photonic sensing platforms.*

Introduction

The progressive demand for the rapid and precise detection of any type of substances has speed-up the development of a large variety of biosensors. For most of the applications it is desirable to have a compact biosensor of high sensitivity, fast response and able to perform real-time analysis. These requirements can be achieved mainly with optical sensors, due to the own nature of the optical measurements that endow a great number of different techniques as emission, absorption, fluorescence, refractometry or polarimetry[1]. Among them, photonic biosensors based on evanescent wave detection have demonstrated its outstanding properties as an extreme high sensitivity method for the direct measurement of biomolecular interactions in real time and in label-free schemes[2].

In the evanescent wave detection, a receptor layer is immobilized onto the waveguide; the exposure of such a surface to the partner analyte molecules produces a biochemical interaction, which induces a change in its optical properties. This change is detected by the evanescent wave. The extent of the optical change will depend on the concentration of the analyte and on the affinity constant of the interaction, obtaining a quantitative signal of the interaction. The evanescent wave decays exponentially as it penetrates the outer medium and, therefore, only detects changes taking place on the surface of the waveguide. For that reason, it is not necessary to carry out a prior separation of non-specific components (as in conventional analysis) because any change in the bulk solution will hardly affect the sensor response. In this way, evanescent wave sensors are selective and sensitive devices for the detection of very low levels of chemicals and biological substances and for the measurement of molecular interactions in-situ and in real time[3].

The advantages of the optical sensing are significantly improved when this approach is used within an integrated optics context[4]. Integrated optics technology allows the integration of passive and active optical components (including fibres, emitters, detectors, waveguides and related devices) onto the same substrate, allowing the flexible development of miniaturised compact sensing devices, with the additional possibility to fabricate multiple sensors on a single chip. The integration offers additional advantages such as miniaturization, robustness, reliability, potential for mass production with consequent reduction of production costs, low energy consumption and simplicity in the alignment of the individual optical elements[4].

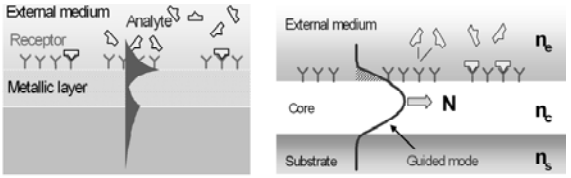


Fig. 1. Evanescent field sensors. Evanescent field detection of biomolecules with (a) SPR sensor and (b) planar waveguides sensors.

Nowadays most of the optical biosensors are based on optical fibers, Surface Plasmon Resonance (SPR) or integrated optics (as interferometers, grating couplers, etc..). Table I details most of the existing optical biosensors.

Table 1. OPTICAL BIOSENSORS

Optical Fibers
Surface Plasmon Resonance Sensors (SPR)
Integrated Interferometers (Mach-Zehnder, Young, Michelson, difference)
Resonant Mirror
Grating Couplers
Ring Resonators, Fabry-Perot Resonators
Photonic Crystals
Localised Surface Plasmon Resonance

With the emergence of nanotechnology new photonic structures has been suggested. A scaling down of the photonic biosensors towards nanometer-size structures could allow a significant increase of their sensitivity[5]. Several transducers as photonic crystals[6], ring resonators[7], porous silicon[8] or nanoparticles for localised surface plasmon resonance (LSPR)[9,10] has been proposed. But the biosensing demonstration using such structures is scarce and their experimental sensitivity is worse than the sensitivity showed by the standard optical biosensors (as surface plasmon resonance or interferometers).

In the following, we will give an overview of the most prominent developments in optical biosensors and the future lines of research which are being investigating in our laboratory.

Plasmonics based biosensors

SPR biosensing has focused a strong effort since the technique was first applied in 1983 and has become one of the most successful label-free and commercially accepted optical biosensor[11]. This technique has been employed in biomolecular engineering, drug design, monoclonal antibody characterization, epitope mapping, phage display libraries, virus-protein interaction, environmental pollutants detection, among other interesting problems[2].

SPR is the predominant optical technology and besides the new developments is SPR, the focus is pointed out in the applications. We will show the applicability of our SPR device in the following fields:

(1) Our sensor is the first SPR-based immunosensor applied to the detection and validation of three relevant pesticides (DDT, chlorpyrifos and carbaryl) with higher sensitivity than other immunochemical systems (e.g. ELISA)[12,13].



Fig 2. Portable SPR platform, including sensor, optics, electronics and flow delivery system.

Measurements of the pollutants are carried out using inhibition binding assays with sensitivity at ppt level. Although the SPR system has only two channels, we have implemented a new procedure for simultaneous multi-analyte determination. Environmental real water samples has been analysed and we have demonstrated that our level of detection accomplishes the EU legislation[14].

(2) The SPR sensor can also be used as an on-line immunoanalytical method for the evaluation of pesticide metabolites which can be present in the human body. We have detected the metabolite from chlorpyrifos pesticide (3,5,6-trichloro-2-Pyridinol (TCP)) from its primary via of elimination (urine). The immunoassay format allows a highly sensitive detection of TCP in human urine without the need of previous clean-up and preparation of samples. The comparison between TCP limits of detection in urine and assay buffer used as control showed similar sensitivity values and a limit of detection of 0.1 μg L^{-1} was obtained for TCP urinary determinations[15].

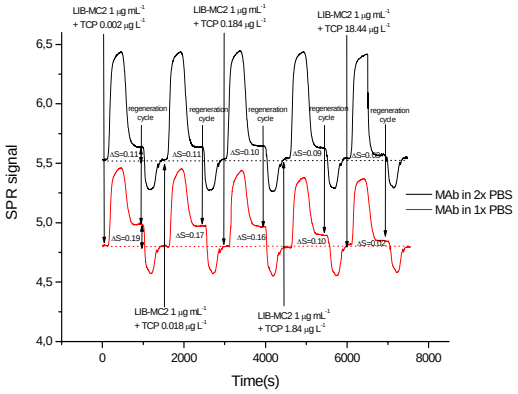


Fig 3. SPR detection of TCP in human urine. A regeneration cycle is applied after each determination. A limit of detection of 0.1 μg L^{-1} was obtained.

(3) The SPR technique has been also applied to the real-time and label-free detection of DNA hybridization and single point mutations. We have studied the mutations at gene BRCA-1 related to the predisposition in women to develop an inherited breast cancer. The SPR sensor has successfully discriminated between normal and mutant sequences with a limit of detection of only 100 nM. The device could be employed for the analysis of point mutations in the DNA samples of patients.

For many applications, improvement in the sensitivity of the SPR sensors is an important issue, and several alternative configurations have been suggested as Localised Surface Plasmon Resonance (LSPR) based on nanoparticles or Magnetooptical Surface Plasmon Resonance sensor (MOSPR).

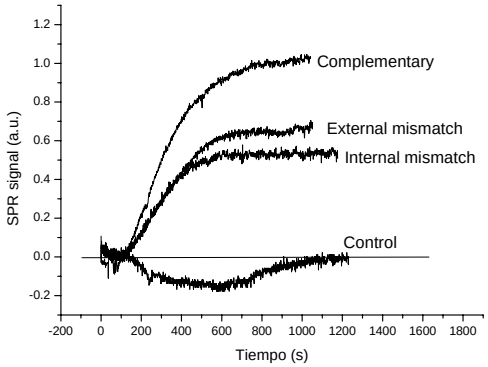


Fig.4. SPR direct discrimination between fully complementary and mismatches DNA probes. It can be observed: (i) hybridisation of fully complementary DNA strand to the immobilised probe (ii) hybridisation of DNA strand with an internal mismatch (iii) hybridisation of DNA strand with an external mismatch (iv) control signal (no hybridisation).

Magnetooptical Surface Plasmon Resonance Sensor

We have recently developed a novel Magnetooptical Surface Plasmon Resonance (MOSPR) Sensor which can improve the sensitivity of the conventional Surface Plasmon Resonance (SPR) sensors[16]. This MOSPR sensor arises from the combination of the Surface Plasmon Resonance in thin metallic layers and the magneto-optic (MO) activity of ferromagnetic metallic materials. Such combination generates a large enhancement of the MO effects closely localized at the surface plasmon resonance.
The sensor uses Co/Au multilayers of nanometric thicknesses as transducers, a prism-coupling configuration and p-polarized light to excite the surface plasmon, rotating magnets or magnetic coils to apply a modulating magnetic field, and detects the magnetooptic effects of the reflected light as a function of the angle of incidence. A large and sharp enhancement of the MO effect is produced at the angle of incidence in which SPR is excited and, likewise the conventional SPR sensors, the enhancement shifts to higher (lower) angles when the refraction index of the adjacent dielectric medium increases (decreases). Therefore, the local variations of refractive index produced within the evanescent field of the surface plasmon can be detected measuring, in real time, the changes of the MO effects of the reflected light.
The experimental characterization of the MOSPR sensor has shown an increase in the limit of detection in a factor of three in changes of refractive index and in the adsorption of biomolecules as compared to the standard SPR sensors. An improvement of the limit of detection up to one order of magnitude could be achieved by an adequate combination of the magnetic-metallic layers and by decreasing the noise of the experimental set-up.
In a further innovation, the thin layer of the magneto-optic transducer could be composed by magnetic nanostructures (2D or 3D) embedded in a noble metal matrix. The incorporation of magneto-optical elements tailored on the nanometer scale into the nanooptical structures can even improve the sensitivity limit due to the localisation of the magnetoplasmonic effect.

Integrated Optics based biosensors

Evanescent wave photonic biosensor devices based on standard microelectronics and related micro/nanotechnologies are providing an integrated technological solution for achieving high sensitive arrays of biosensing devices. But problems of stability, sensitivity and size have prevented the general use of integrated optical biosensors for real field applications.
In order to solve the above drawbacks, we work on the development of ultrasensitive and miniaturised photonic silicon sensors able to be integrated in a "lab-on-a-chip" microsystem platform. As sensors we use integrated Mach-Zehnder interferometer based on TIR waveguides ($Si/SiO_2/Si_3N_4$) of micro/nanodimensions[17] as it is shown on figure 5.

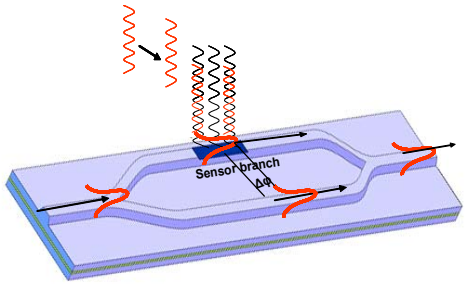


Fig 5. Mach- Zehnder interferometer configuration

For biosensing applications, the optical waveguides of the MZI should have a high surface sensitivity and single mode behaviour. The highest surface sensitivity is obtained in waveguides with a high contrast of refractive index between the core and the substrate [10]. For that reason, we have chosen Si_3N_4 core layers (n_c = 2.00) over a SiO_2 substrate (n_s = 1.46). In this waveguide configuration (and for λ in the visible range), the single mode behaviour is obtained for core thickness below 300 nm, and rib depths below 5 nm, when the rib width is 4 μm. Our modelling shows that the maximum surface sensitivity is obtained for core thicknesses about 150 nm and 75 nm for the TM and TE polarizations, respectively[17]. Figure 6 shows a scheme of the waveguide configuration.

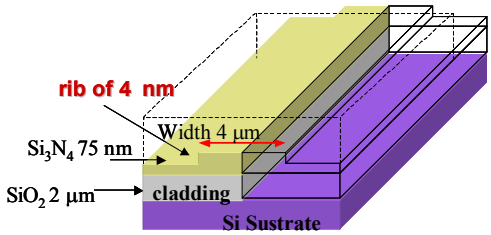


Fig.6. Cross-section scheme of the TIR waveguides employed in the integrated MZI device

The devices are fabricated in our Clean Room facilities. The evaluation was performed in an optical bench where polarized light from a He-Ne laser (λ=0.633 μm) was end-fire coupled to the sensor. The light coming out the interferometer is collected by a single-mode fiber, which is pigtailed to a photodiode. The signal is amplified, digitalized and processed. Precise translation stages are used for the accurate alignment of all the components.
Propagation losses of the waveguides were measured by the Fabry-Perot resonance technique and optical coupling losses were calculated by the cut-back method. Propagation losses vary between 0.13 and 0.15 dB/cm for TE polarization and between 0.27 and 0.30 dB/cm for TM polarization. The fiber-waveguide insertion loss measurements were 5.84 dB

for TM polarization and 3.12 dB for TE polarization and low losses were assured with couplers designed with circular arms of R = 80 mm. The final device has a length of 3 cm and the sensor area is 1.5 cm long and 50 μm wide.

The sensitivity of the sensor for both polarizations was evaluated in the same way as in previous reports[17]. The evaluation was done flowing solutions of water and ethanol of varying concentration (refractive index steps of 10^{-3}), and measuring the output signal in real time. With these measurements, a calibrating curve was obtained. The standard deviations (σ_v) and thermal drifts of the experimental set-up were evaluated in maximum condition of stability and considering the case in which the interferometric devices were located in the quadrature point. Under these conditions, the lowest detection limit in the phase change was calculated assuming the $3\cdot\sigma_v$ criterion, resulting in a value of $\Delta\varphi=1.6x10^{-4}x2\pi$ rads for TM polarization. Taking account the signal-to-noise ratio of this configuration, the lowest detection limit in the variation of the refractive index was found to be (for TM polarization) $\Delta n_{0,\,min} = 1 \cdot 10^{-7}$ ($\Delta N_{eff,\,min} = 6.4 \cdot 10^{-8}$).

As a proof of the utility of MZI technology towards the detection of ultrasensitive biomolecular interaction, we have applied the sensor in the Genomics field. The MZI device has been used for the direct detection of DNA hybridization and for the detection of single nucleotide polymorphisms at the BRCA-1 gene, involved in breast cancer development, without target labeling.

The oligonucleotide probe is immobilized by covalent attachment to the sensor surface through silanization procedures. A silane (3-mercaptopropyltrimethoxysilane) with a thiol group at the free end was employed for the chemical modification of the surface. The thiol-derivatized oligonucleotides (28 mer) used as receptors can bind to the silanized Si_3N_4 surface through a disulphide bond. The DNA probe has also a 15-T tail which is employed as a vertical spacer chain to increase the accessibility to the complementary DNA to the sensor surface.

After DNA immobilization, complementary oligonucleotides (58 mer) were flowing in the sensor for hybridization experiments. The hybridization was performed for different DNA target concentrations from 1 pM to 1 μM. Non-complementary oligonucleotides did not show any significant signal. Regeneration after each hybridization was achieved flowing HCl 3.2 mM.

The calibration curve can be observed in Figure 7. 10 pM of complementary non–labeled DNA in buffer solution was the lowest hybridization limit achieved and means an average DNA growth layer of $1 \cdot 10^{-4}$ nm and an estimation of $2 \cdot 10^{5}$ DNA molecules/cm^2 hybridized on the sensor area of the MZI.

Additionally, we have detected the hybridization of 100 nM DNA target with two mismatching bases corresponding to a mutation of the BRCA-1 gene.

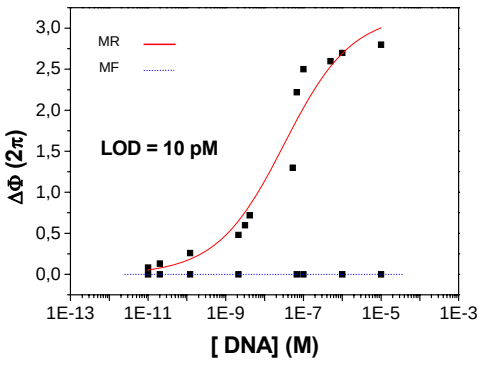


Fig. 7. Calibration curve of the DNA hybridisation evaluated in real-time by the MZI device.

Most of the studies related to the detection of DNA hybridizations in real-time and label free with optical biosensors have been performed using SPR biosensors. The limit of detection of the hybridization with SPR is above 10 nM, three orders of magnitude lower from the MZI hybridization detection limit.

Lab-on-a-chip integration

For the development of a complete lab-on-a-chip microsystem device based on integrated MZI, several units must be incorporated on the same platform: (i) the micro/nanodevices, (ii) the flow cells and the flow delivery system, (iii) a phase modulation system to convert the periodic interferometric signals in direct phase measurements, (iv) integration of the light sources and the photodetectors (v) CMOS processing electronics. For achieving this goal, our first step has been the development of a novel low temperature (100 ºC) CMOS compatible microfluidic technology to create 3D embedded interconnected microfluidic channels made of polymer SU-8[18]. The microfluidic channels have a height from 40 to 60 μm and a width between 100 to 250 μm. In Figure 8 a photograph of the cross section of the channels onto the sensing area of a MZI device can be observed[18].

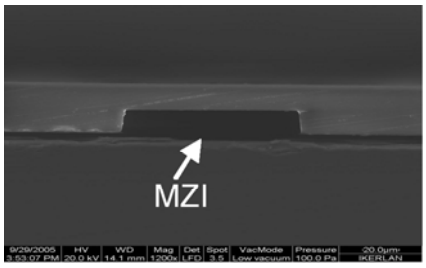


Fig. 8. SEM photograph of the cross section of the polymer microfluidic channel over the MZI sensing area.

Nanomechanical optical biosensors

Microcantilever biosensors came from the microcantilevers used in atomic force microscopy. The principle of their operation is based on the bending induced in the cantilever when a biomolecular interaction takes place on one of its surfaces. In this way, microcantilevers translate the molecular reaction into a nanomechanical motion, which is commonly detected using optical or piezoresistive read-out[19] (see Figure 9). In order to achieve highly integrated microsystem with microcantilever transducers, we have recently introduced a new type of read-out technique. The technique is represented by a new generic sensing probe based on microcantilevers acting as optical waveguides operated in visible range[20,21]. The principle of operation is based on the sensitivity of energy transfer between two butt coupled waveguides to their misalignment with respect to each other as it is represented in Figure 10.

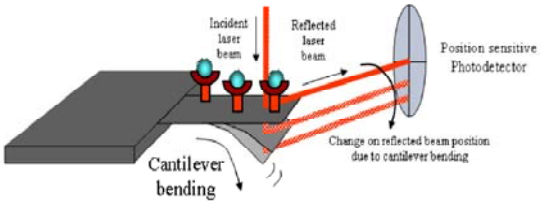


Fig. 9. Principle of working of nanomechanical biosensors with an optical read-out.

This new technique can be considered as an alternative to the known optical methods used for read-out of nanomechanical response of microcantilevers. With the proposed method, sub-nanometer displacement of cantilever free end can be registered with a conventional photodetector. Real-time parallel monitoring of several channels can be realized because no preliminary alignment or adjustment, except for light coupling, is required.

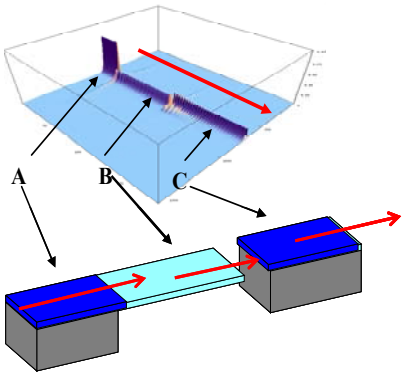


Fig. 10. Principle of working of the waveguided microcantilever sensor and theoretical modelling.

The design of the sensor is shown in Fig. 10 and can be operated both in visible and in infrared ranges. The cantilever is located in a cavity and is a symmetrical waveguide butt coupled with an output waveguide, called receptor, through a short gap.

We have fabricated arrays of 20 optical microcantilevers. Each of them is 200 μm long, 40 μm wide, and 500 nm thick with a spring constant of 0.050 N/m. Fabrication of the sensor was done using standard microelectronic technology. The cantilevers are made of thermal silicon dioxide, transparent in visible range. Input and output waveguides are made of silicon nitride and were 140 nm thick. Coupling of the light in the cantilever is achieved through the evanescent filed of the input waveguide. Both the cantilevers and the waveguides were 40 μm wide. The cantilever has low stress gradient and is practically flat, the misalignment between the output waveguide and the cantilever free end is around 1 μm. Some photographs of the fabricated devices are shown in Figure 11.

The experimental characterization has demonstrated that a subnanometer resolution in the cantilever deflection can be achieved. This new device has shown good performances for biosensing and offers an interesting approach for further integration in lab-on-a-chip microsystems.

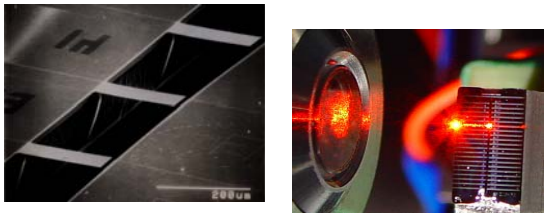


Fig. 11. Photographs of: *(left)* the optical cantilevers and *(right)* coupling of the light inside the device.

Conclusions

The technology of optical biosensors is a powerful one for the high sensitive, label-free and real-time detection of biomolecular interactions. Our last developments in this field, mainly related to the development of portable and highly sensitive photonic sensing platforms, have been shown. Plasmonics and integrated optics approaches look as the most promising ones for achieving devices which could fulfil most of the requirements in order to be transfer in commercial products in the near future.

Acknowledgments

Authors would like to thank the financial support of the Spanish Ministry of Education and Science (project TEC2005-13604) and M. Botín Foundation.

References

1 L.M. Lechuga, in Biosensors and Modern Biospecific Analytical Techniques, edited by Ed. L. Gorton. Comprehensive Analytical Chemistry Series, Elsevier Science BV, Ch. 5. 2005

2 F.S. Ligler and C. Rowe Taitt (Eds.), Optical Biosensors: Present and future. Elsevier, Amsterdam, 2002.

3 L.M. Lechuga, F. Prieto and B. Sepulveda, In: R.

Narayanaswamy and O.S. Wolfbeis (Eds.), Optical Sensors. Industrial, Environmental and DiagnosticApplications. Springer, Heidelberg, 2003
4 C. Dominguez, L.M. Lechuga and J.A. Rodriguez, In: S. Alegret (Ed.), Integrated Analytical Systems. Elsevier, Amsterdam, 2003
5 L.M. Lechuga et al., In Nanodevices for Life Sciences. Book Series on Nanotechnology for Life Sciences, Vol 4, p 317, Ed. Challa S.S. R. Kumar, Wiley-VCH Verlag GmbH&Co.KgaA, 2006
6 G. W. Burr et al, Nanophotonics for Information Systems, paper NPIS-ThC4
7 Ksendzov et al, Optics Letters no. 30, p. 3344 2005.
8 H. Ouyang et al, Analytical Chemistry no.79, p. 1502, 2007.
9 J. Zhao et al, Nanomedicine no. 1, p. 219, 2006.
10 Haes et al, J. Phys. Chem. B no.108, p. 109, 2004.
11 J. Homola, Anal. Bioanal. Chem., no.377, p. 528, 2003.
12 E. Mauriz et al, Biosens Bioelectron, no.21, p. 2129, 2006.
13 E. Mauriz E et al, Biosens Bioelectron, no. 22, p.1410, 2007.
14 E. Mauriz et al, Anal. Chim. Acta, no. 561, p. 40, 2006.
15 E. Mauriz et al, Anal. Bioanal. Chem. DOI 10.1007/s00216-007 (in press)
16 B. Sepúlveda et al, Optics Letters, no. 31, p. 1085, 2006.
17 F. Prieto, et al. Nanotechnology no. 14, p.907, 2003.
18 F. J. Blanco et al, J. Micromech. Microeng., no. 16, p.1006, 2006.
19 L.G. Carrascosa et al, Trends in Analytical Chemistry, no. 25, p. 196, 2006.
20 L.M. Lechuga et. al, Sens. Actuators B, no. 118, p. 2, 2006.
21 K. Zinoviev et al, J. Lightwave Technol., no. 24, p. 2132, 2006.

Slow light - perspective and applications

Thomas F. Krauss
SUPA, School of Physics & Astronomy, University of St Andrews,
North Haugh, St Andrews, Fife, KY16 9SS, United Kingdom
tfk@st-and.ac.uk

The phenomenon of slow light is discussed, with a focus on slow light structures based on photonic crystals. Slow light offers field enhancement for increased nonlinear interaction, phase enhancement in devices such as Mach-Zehnder modulators and the possibility of controllable delay time. We believe that bandwidth is a key parameter and have now demonstrated a slow light structure that can accommodate 2.5 THz of bandwidth. Furthermore, slow light can only be useful if it is not compromised by losses. Due to recent improvements in our technology, we can now achieve losses of order 4 dB/cm, which is amongst the best reported for single mode photonic crystal waveguides.

Keywords: Slow light, photonic crystals, optical waveguides

Introduction

The phenomenon of slow light has captured the imagination of many researchers in the last few years because it offers an important level of control over light-matter interactions. So far, the slowdown of light has mainly been pursued in atomic media, most notably via electromagnetically induced transparency (EIT), but also in semiconductors featuring population oscillations, nonlinear gain and loss characteristics as well as in fibres. More recently, slow light has also been demonstrated in dielectric structures, especially coupled ring resonators [1,2] and photonic crystals [3] and it is the latter that this paper is focused on.

The keen interest in slow light in dielectrics is motivated by the fact that slow light adds functionality to a material by structuring alone. This is of great interest, as it allows the enhancement of the typically weak light-matter interaction in optical materials. Linear effects such as gain, thermo-optic and electro-optic interaction scale with the slowdown factor, whereas nonlinear effects may scale with its square [4]. An alternative to the slow light approach is to use cavities for such increased light-matter interaction, a topic that is widely studied in the photonic crystal community. In comparison to cavities, slow light structures offer additional control over the spectral bandwidth of the light-matter interaction and the phase change achievable in a device. This phase argument is explained in fig. 1 below.

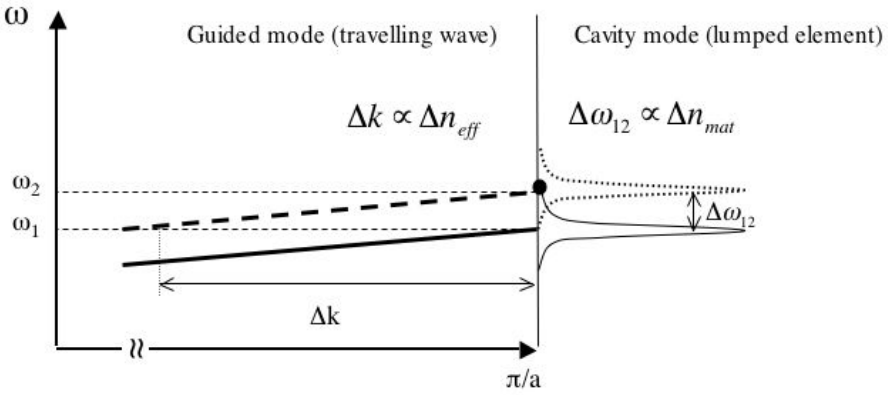


Figure 1. Idealised dispersion curve of a waveguide in the slow light regime. The solid curve represents the original dispersion curve, whereas the dashed line represents the same curve after application of a refractive index change Δn_{mat}.

The phase change in an interferometric device, such as a Mach-Zehnder interferometer, is enhanced in the slow light regime because the Mach-Zehnder response depends on Δk, i.e. the change in effective index Δn_{eff}, not just the material refractive index change Δn_{mat}. If a refractive index change is applied to the device, the dispersion curve shifts correspondingly. In the cavity, the same shift in material index corresponds to a shift in the resonance, as illustrated by the two resonance curves on the right of the figure. Because of the small slope of the curve, i.e. its low group velocity, a small Δn_{mat} results in a large Δk. Therefore, even devices that operate on a phase change can benefit from a low group velocity.

Bandwidth

While slow light in photonic crystals has already been observed several years ago [5], the operating point is typically on a near-parabolic dispersion curve near the edge of the Brillouin zone. Therefore, slow light in photonic crystals tends to coincide with high dispersion, which removes most of the advantages of operating in the slow light regime and severely limits the bandwidth that can be utilised. This is not an intrinsic property of the structure, however, but subject to design. As shown recently [6,7], the appropriate choice of structure and careful design allow us to design structures with moderate slowdown factor (group indices in the range between 10-100) and bandwidths of several nanometres in wavelength at 1550 nm, corresponding to a THz or more. Although higher slowdown factors have already been demonstrated [3], the corresponding penalty is a reduction in bandwidth. For applications in all-optical signal processing, bandwidth is a key concern, as this is the main advantage of Optics over Electronics. Designing optical structures that limit the bandwidth to the MHz or low GHz regime, such as very high Q cavities, therefore does not seem to be advisable.

Losses

Losses are another critical issue. It is essential to build slow light devices on the basis of very low loss devices; otherwise, any benefit deriving from the slow light operation may be lost. It is therefore remarkable that photonic crystal waveguides exhibiting losses in the few dB/cm range have now been demonstrated, which is close to the values reported for photonic wires.

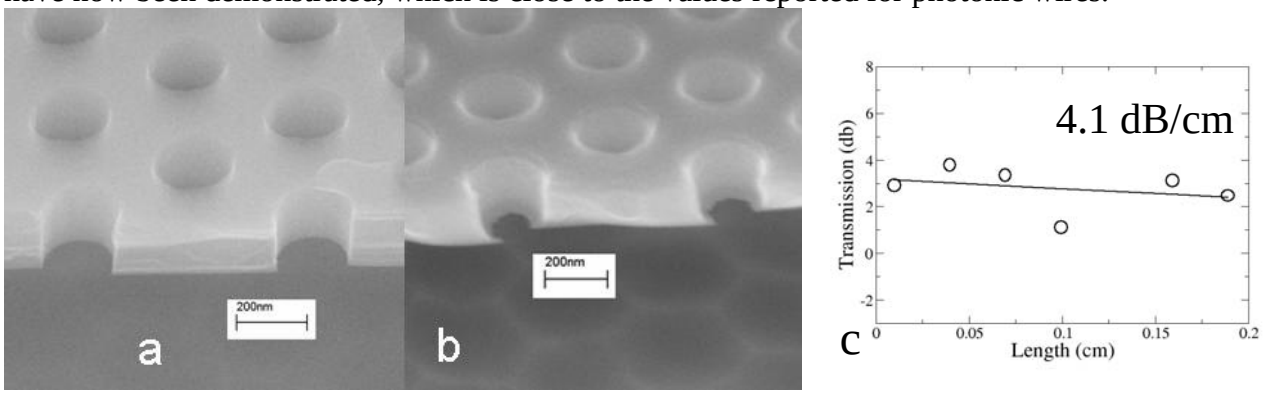


Figure 2. Cross-section of a Si airbridge after etching, highlighting the sidewall profile of the photonic crystal holes. a) Etching quality of very low loss waveguides (<10db/cm), b) Etching quality of higher loss (here: 105 db/cm) waveguides, featuring small rims at the bottom of the hole - the etch depth being fractionally too small. This results in the formation of a lip or rim at the bottom of the hole, which scatters light very strongly. In addition, such defects are also prone to large variations from hole to hole, which causes disorder, further increasing the scattering loss. c)

Transmission versus W1 waveguide length at a wavelength of 1.52 μm. The slope is 4.1± 0.9 db/cm [8] which is near the best value reported worldwide [9].

The next question is how losses scale with the slowdown factor. There have been suggestions that there is a square dependence of the loss on the slowdown factor, i.e. losses scales as $1/n_g^2$ [9]. While this is certainly the case for the type of waveguide with a pararabolic dispersion curve operating near the band-edge as discussed earlier, there are indications that a slow light design operating away from the bandedge has a more favourable dependence [7].

Discussion and Conclusion

In a photonic crystal, the phenomenon of slow light is created by the resonant interaction of the guided mode with the periodic lattice, resulting in the formation of a slow moving interference pattern (the "slow mode"). By controlling this interaction between the incoming mode and the lattice, it is possible to control the resulting slowdown factor and the bandwidth over which it occurs to the extent that slow light devices with THz bandwidth have now been demonstrated. Any all-optical device has to accommodate a sizeable bandwidth in order to compete with the electronic approach The typical bandwidth achieved with photonic crystals, namely 100's of GHz or even THz, is therefore an essential requirement, compared e.g. to slow light based on atomic resonances as in electromagnetically-induced transparency [10]. Hence, we believe that broadband and slow light enhanced all-optical functions such as switches and modulators are the most likely outcomes of this research. Optical memory, which is another function proposed for slow light devices, is more difficult to achieve, since even with the losses of order few dB/cm discussed above, storage times in the nanosecond regime are difficult, which would allow the storage of a few bits of information only. Such storage would also require tunability of the slowdown factor, which is more difficult to achieve in photonic crystal-based devices than, for example, in EIT or in systems based on semiconductor optical amplifiers (SOAs).

References

[1] A. Melloni, F. Morichetti and M. Martinelli, "Linear and nonlinear pulse propagation in coupled resonator slow-wave optical structures," *Opt. Quantum Electron.* **35**, 365-379 (2003).
[2] F. Xia, L. Sekaric and Y. Vlasov, "Ultracompact optical buffers on a silicon chip", *Nature Photonics* **1**, 65-71, 2007.
[3] H. Gersen, T.J. Karle, R.J.P. Engelen, W. Bogaerts, J.P. Korterik, N.F. van Hulst, T.F. Krauss and L. Kuipers, "Real-Space Observation of Ultraslow Light in Photonic Crystal Waveguides," *Phys. Rev. Lett.* **94**, 073903 (2005).
[4] M. Soljacic and J.D. Joannopoulos, "Enhancement of nonlinear effects using photonic crystals," *Nature Materials* **3,** 211-219 (2004).
[5] M. Notomi, K. Yamada, A. Shinya, J. Takahashi, C. Takahashi and I. Yokohama, "Extremely large group-velocity dispersion of line-defect waveguides in photonic crystal slabs", *Phys. Rev. Lett.* **87**, 253902 (2001).
[6] L.H. Frandsen, A.V. Lavrinenko, J. Fage-Pedersen and P.I. Borel, "Photonic crystal waveguides with semi-slow light and tailored dispersion properties", *Opt. Express* **14**, 9444-9450 (2006).
[7] M.D. Settle, R.J.P. Engelen, M. Salib, A. Michaeli, L. Kuipers and T.F. Krauss, "Flatband slow light in photonic crystals featuring spatial pulse compression and terahertz bandwidth", *Optics Express* **15**, 219-226 (2007).
[8] L. O'Faolain, X. Yuan, D. McIntyre, S. Thoms, H. Chong, R. De La Rue and T.F. Krauss, "Low loss propagation in photonic crystal waveguides" *Electron Lett.* **42**, 1454-1456 (2006).
[9] E. Kuramochi, M. Notomi, S. Hughes, A. Shinya, T. Watanabe and L. Ramunno, "Disorder-induced scattering loss of line-defect waveguides in photonic crystal slabs", *Phys. Rev. B* **72**, 161318 (2005).
[10] L.V. Hau, S.E. Harris, Z. Dutton and C.H. Behroozim "Light speed reduction to 17 m/s in an ultracold atomic gas" *Nature* **397** 594-598 (1999)

Focused Ion Beam Milling Strategies of Photonic Crystal Structures in Silicon

Wico C.L. Hopman (1), Feridun Ay (1), Wenbin Hu (1), Vishwas J. Gadgil (1),
Laurens Kuipers (2), Markus Pollnau (1), René M. de Ridder (1)
1) MESA+ Institute for Nanotechnology, University of Twente, P.O. Box 217, 7500 AE Enschede, The Netherlands,
W.C.L.Hopman@utwente.nl, F.Ay@utwente.nl, R.M.deRidder@utwente.nl
2) FOM Institute for Atomic and Molecular Physics (AMOLF), Kruislaan 407, 1098 SJ Amsterdam, The Netherlands

Abstract: *We report on optimisation of the side wall angle of focused ion beam (FIB) fabricated sub-micron diameter holes in silicon. Two optimisation steps were performed. First, we compare two different FIB scanning procedures and show the advantages of using a spiral scanning method for the definition of holes in photonic crystal slab structures. Secondly, we investigate the effect on the geometry, of parameters such as dwell time, loop number, and ion dose, to determine the optimum FIB milling parameters for reducing the tapering effect. Furthermore, we report on the initial results regarding effects of Ga^+ ion implantation during FIB milling on optical losses, both before and after an annealing step, showing over a decade reduction of optical loss.*

Introduction

Photonic crystal slabs (PCS) have recently received much attention as an attractive technology promising an increase of photonic integration density by several orders of magnitude [1, 2]. In a typical PCS, in-plane light confinement is realised by the photonic bandgap effect, while the vertical confinement is a result of refractive index guiding. A high-refractive index layer (e.g. Si) perforated with a 2-D periodic lattice of air holes constitutes a characteristic PCS structure, having structural detail in the sub-micrometre range.

For fabrication of the PCS structures small photonic crystal elements requiring sub-10 nm resolution have to be aligned with relatively large-sized features like access waveguides for interfacing with the outside world. Focused ion beam (FIB) milling is a very interesting tool for achieving both of these requirements simultaneously. FIB processing is a well-established technique with unique capabilities to locally sputter-etch, ion-implant, and deposit metals and insulators with a feature size in the order of nanometres, without the need of a mask [3, 4].

Despite the maturity of this method for e.g. semiconductor chip repair, the realisation of photonic components with desired characteristics is still challenging. In particular, fabricating sub-micron holes in silicon with perfectly vertical side-walls by FIB milling is nearly impossible due to the redeposition effect [5]. In addition, the losses induced by ion bombardment and implantation of for example gallium ions in the sample, causing modifications of the crystalline Si, are still too high to fabricate practical PCS devices [6]. These issues are addressed in the following sections.

Experimental

The FIB experiments presented in this paper were conducted on the dual-beam Nova 600 FIB machine from FEI company. The advantage of this machine is that it contains both an electron and ion beam in a single vacuum chamber. Therefore, nanostructuring by FIB milling and inspection by SEM can be done in a single session. The machine uses a liquid gallium source to generate a Ga^+ ion beam. The stitching-error-free writing field of the FIB is divided in 4096 by 4096 pixels. The actual size of the writing field depends on the selected magnification (compared to the size on the monitor). In the experiments reported here, we fixed the magnification to 5000 times, resulting in a writing field of about 25x25 μm and a grid spacing of 6.2 nm. This writing field size is well suited for definition of PCS devices on top of larger structures like waveguides which can be defined using conventional UV lithography. The machine allows for a number of currents to be selected, ranging from 1.5 pA to several nanoamperes. However switching between currents requires time-consuming switching of apertures and refocusing. Therefore the milling current was fixed at 48 pA and the acceleration voltage was set to 30 kV. The minimum obtainable beam spot-size is determined by the milling current. At 48 pA the 1/e spot size was estimated to be 18 nm. The ion beam can be controlled by a so-called stream-file containing the sequential coordinates defining the scan path, and the dwell time at each of these coordinates. The structures were defined such that the 1/e ion beam spot size was maintained at approximately 1.5 times the inter-pixel distance.

Cross-sectioning

FIB nanostructuring was mainly investigated by analysing cross-sections of the various structures. These cross-sections were also realised using the FIB. We tried several cross-sectioning techniques, milling of a hole with a sloped milling depth, line by line polishing and combinations. In the optimised method the first step is to locally deposit a layer of Pt using the FIB, in order to prevent redeposition. Secondly, a hole is milled with a sloped angle to avoid long milling times. Finally, a line-by-line scan (termed cleaning cross-section) is applied at a lower current (28 pA) to establish a high contrast image, as depicted in Fig. 1.

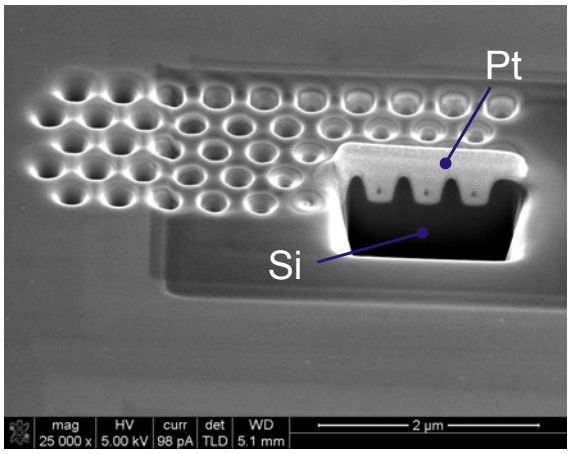
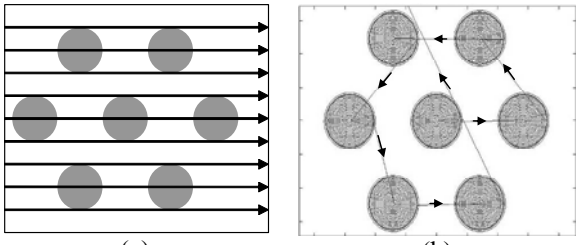


Fig. 1: Optimised cross-sectioning method used for investigation of the milled structures.

Since the electron-beam and the ion-beam columns have a fixed relative angle of 52°, angled SEM photos of the cross-section can be taken without rotating the stage. By tilting the substrate, the ion beam angle can be reduced for minimising the milling time of deep holes. Since the SEM photos are taken at an angle, the horizontal scale bar can not be applied to the vertical direction. The length of the image in vertical direction has to be scaled by 1/sin(angle).

Scanning procedures

In general, the first step in any FIB milling experiment is preparation of a mask file (stream file). This file contains all the information required by the machine in order to mill the desired geometry. Namely, the file contains series of pixels that define the structure and the milling time information for each pixel. The major difference between different scanning procedures is the sequence of each pixel, i.e. the order by which each pixel is milled. In a conventional raster scanning procedure, the ion beam sweeps the observed area line by line, as depicted in Fig. 2 (a) [7]. The ion beam is ideally turned on only on the pixel on which the geometry is defined and is off elsewhere. In practice, however, it is not completely off outside the desired areas, which in turn results in inter-hole milling. For the special case when the milled geometry has a circular cross section a spiral scanning routine may avoid the above mentioned shortcoming to a large degree. A schematic drawing of the spiral scanning procedure is given in Fig. 2 (b).

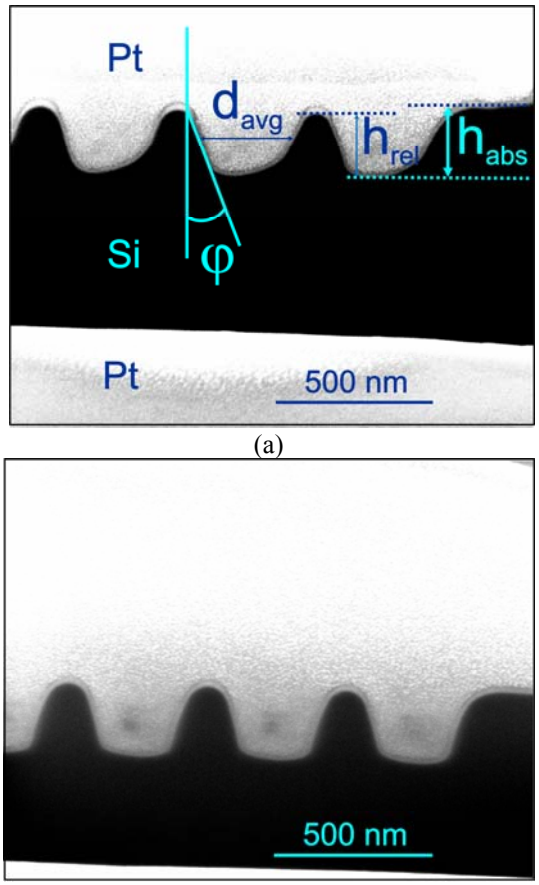


(a) (b)

Fig. 2: Schematic representation of the raster (a) and spiral (b) scanning methods. The beam is moving inside out in case of the spiral scan.

In order to compare the two types of the scanning procedures we have performed a series of experiments on Si. The sample was mounted on a holder by silver glue to ensure a conductive connection between the two. Two different stream files were designed for FIB milling. The common structure to be milled was chosen to be a 50-hole array with periodicity of 440 nm and hole diameter of 250 nm. There was a small difference in the number of pixels in the stream files due to the different file generation methods, which also caused minor difference in dose per hole for the two structures. Using a loop number of 12 for each method a milling depth of about 250 nm was obtained.

The results of the milling procedures using raster and spiral scanning are given in Fig. 3 (a) and (b), respectively. In order to be able to compare the two methods, we define two additional parameters, absolute height h_{abs} and relative height h_{rel}. The first one corresponds to the total height from the bottom of the hole to the surrounding silicon, while h_{rel} stands for the height difference between the bottom of the hole and the inter-hole sidewall. The side-wall angle φ is defined by the angle between the normal to the surface and the sloped side-wall around $h_{rel}/2$. The height of $h_{rel}/2$ of is also used as the reference point in the definition of the average hole diameter.



(a)

(b)

Fig. 3: Patterns milled at 48 pA using 12 loops and a dwell time per pixel of 0.1 ms. (a) Raster scan (b) Spiral scan.

Comparison of the cross-section profiles given in Fig. 3 clearly suggests that the holes are better defined by the spiral scanning method. It is evident that the absolute and relative heights in the two methods are different as expected from the different scanning strategies where in the raster scan method the side-walls are scanned many more times than in spiral scanning. A further important difference between the structures fabricated by using the two methods is the difference between the side-wall angles in the case of raster scanning. This also results in an asymmetric cross-section of the holes. This effect is probably due to the redeposition effect that becomes significant when the beam is scanned in one direction. It is not observed in the case of spiral scanning which follows a more symmetric route, therefore minimizing the effects of redeposition.

As a result, in the course of FIB milling the spiral scan method reduces the amount of inter-hole milling significantly and results in better side-wall angles by reducing the effects of redeposition.

Dwell time variation

The redeposition can be influenced by changing not only the scan routine as shown in the previous section, but also by modifying the dwell-time parameters. Changing the dwell time in a scan pattern, leads to a change in required loop number to achieve similar milling depths.

We have performed two different studies in order to analyze this effect. In the first set of experiments the dwell time was kept constant at 0.1 ms while the loop number was steadily increased, resulting also in an increase of the dose per hole. The parameters are summarized in Table 1 and the analysis of sidewall angle variation with dose per hole used in the definition of the structure is plotted in Fig.4. The increase in the number of loops as the dwell time is increased also corresponds to increase in the ion dose per hole. It is evident from the figure that as dose per hole is increased in this case, the sidewall angle is reduced as desired.

To find the side-wall angle dependence on the dwell time, we kept the total dose applied to each hole constant. In this way the influence of the dose on the side-wall angle is separated from the dwell time dependency.

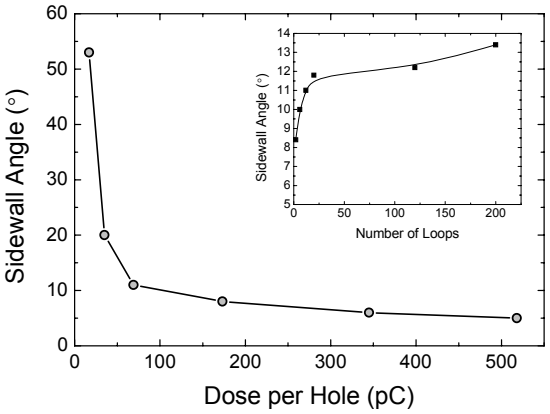


Fig. 4: Variation of the sidewall angle of hole structures as a function of number of loops

The dose can be kept constant by changing also the loop number when varying the dwell-time, i.e. keeping the product dwell time and the number of loops constant. The sidewall angle variation as a function of increasing number of loops is depicted in the inset of Fig. 4. Here, the increase in the loop number also corresponds to shorter dwell times. As a result, we can state that in order to obtain as small sidewall angles as possible one should choose a higher dose in combination with longer dwell time. However, this cannot be generalized for hole-sizes and doses other than studied here, because the geometry of the hole will specify the redeposition function and consequently the hole geometry.

Investigation of Gallium ion implantation

It is well known that ion beam milling in silicon can result in structures having high optical loss because of modifications of the crystalline Si induced by ion bombardment and implantation of for example Gallium ions within the sample. A possible route for achieving lower loss is by high temperature annealing. We have performed a preliminary investigation of the effect of Gallium ion implantation on optical loss of single-mode SOI channel waveguides. For that purpose we have exposed straight optical waveguides to the ion beam at six different doses between 5×10^{14} and 2×10^{17} ions/cm^2.

Table 1: Results of dwell time variation experiments.

Number of loops	Dose per hole (pC)	Absolute Depth, h_{abs} ±3% (nm)	Relative depth, h_{rel} ±3% (nm)	Average diameter, d_{avg} ±5% (nm)	Sidewall angle, ±5% (°)
3	17	83	68	310	53
6	35	160	141	290	20
12	69	320	292	261	11
30	173	872	766	220	8
60	345	1168	1065	222	6
90	518	1312	1224	217	5

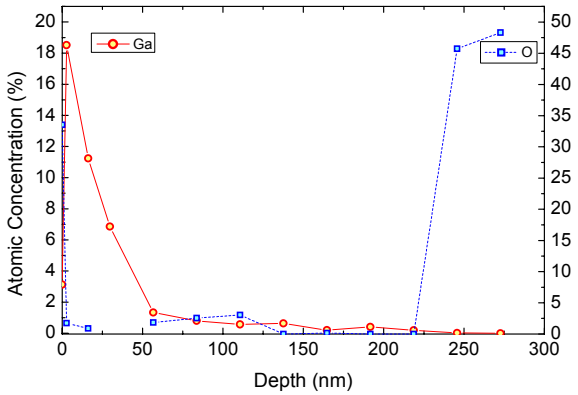


Fig. 5: Depth variation of gallium and oxygen atomic concentrations through SOI as measured by XPS.

For the smallest dose, the volume of the Si increases due to implantation; at higher doses we observe also Si removal by sputtering. The incorporation of Ga^+ ions in Si was analyzed by depth profiled XPS. A representative implantation profile is as given in Fig. 5. For a dose of 1×10^{17} ions/cm^2 we observe that almost all the gallium is within the first 50 nm of Si. We also observe the lower cladding's oxygen atoms as expected for the used SOI structure.

The optical losses were measured by using a customized setup that involves analysis of the scattered light with a linear infrared camera at a wavelength of 1.55 μm. A thermal annealing process was used in order to possibly reduce the optical losses. The preliminary results are plotted in Fig. 6.

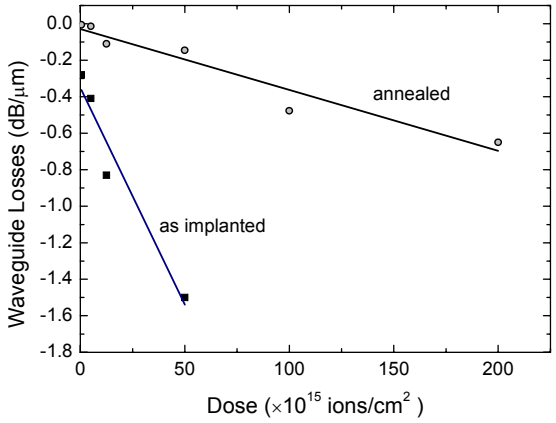


Fig. 6: Variation of measured waveguide losses with Ga ion implantation dose for both as-implanted and annealed single mode SOI waveguides.

For the as-implanted waveguides the optical losses are significantly higher and for the highest two doses there was no detectable propagation at all. As the samples were annealed at 800 °C for 60 minutes, light propagation improved by more than an order of magnitude.

The initial results discussed above suggest that further improvement is possible. The study towards minimization or elimination of the optical losses caused by gallium ion implantation while performing FIB milling is still ongoing.

Conclusions

We have investigated the technological difficulties in fabrication of sub-micron holes in silicon by using focused ion beam milling. Namely, we compared two FIB scanning procedures and showed the advantages of using a spiral scanning method for definition of holes in PCS structures. By investigating the parameters such as dwell time, loop number, and ion dose we determined the optimum FIB milling parameters. Furthermore, we reported on the initial results on the effects of Ga^+ implantation during FIB milling on optical losses. We were able to reduce the propagation losses by more than an order of magnitude by thermally annealing the SOI waveguides.

Acknowledgments

This research was supported by NanoNed, a national nanotechnology program coordinated by the Dutch ministry of Economic Affairs, and was also supported by the European Network of Excellence ePIXnet.

References

1 Y. Akahane et al., Nature 425, p. 944, 2003.
2 Y.A. Vlasov et al., Nature 438, p. 65, 2005.
3 S. Reyntjens et al., J. Micromech. Microeng. 11, p. 287, 2001.
4 A.A. Tseng et al., Small 1, p. 924, 2005.
5 Y.K. Kim et al., IEEE J. Sel. Top. Quantum Electron. 11, p. 1292, 2005.
6 M.J. Cryan et al., IEEE J. Sel. Top. Quantum Electron 11, p. 1266, 2005.
7 Y.Q. Fu et al., Int. J. Adv. Manuf. Technol. 16, p. 877, 2000.

Efficient coupling to W1 Photonic crystal waveguide on InP membrane through thinly supported access guides

A.Talneau, K.H.Lee, S.Guilet and I.Sagnes
CNRS/ Laboratoire de Photonique et de Nanostructures, Route de Nozay, F-91460 Marcoussis
anne.talneau@lpn.cnrs.fr

Abstract : Thinly supported access ridges have been designed in order to improve the coupling efficiency into W1 Photonic crystal –PhC- waveguides on InP membrane. This integration allows to control the termination of the W1 PhC guide. Low propagation losses have been measured for these thinly supported guides.

Introduction

InP-based Photonic Crystal –PhC– membranes are attractive because they can combine the advantage of operating PhC guides (mainly W1) below the air light-line [1], so theoretically in a lossless regime, with the possibility of including emitters such as quantum boxes emitting at 1.55µm. The theoretical lossless regime can be reached in the case of a perfect system. Part of the imperfections comes from e-beam lithography [2] and part comes from holes etching.

We have investigated here an ICP-RIE process leading to very smooth etched surfaces. Previous work had implemented a Cl2/Ar-based processes for deep etching. But, we were not able to suppress some residual roughness [3]. In the case of a membrane, deep etching is no more an issue, since the membrane thickness does not exceed 350-400nm (λ/4) in order to operate in a monomode regime. But the etched surfaces have to be very smooth, because any additional roughness will produce scattering, thus increasing propagation losses. We have developed a process including N2 in the gas mixture, as already proposed by P.Strasser et al [4], and discussed in [5].

Injecting light in a strongly confined PhC guide is still difficult due to the strong modal mismatch. Also, the role of the termination of the W1 guide has been evidenced to play a crucial role [6]. We propose here a new type of access guide, thinly supported access guides that are realized during the same technological steps than the holes. They allow to control the final termination of the PhC guide. relative position of the injected power. We fabricated W1 PhC guides on a 340nm thick InP membrane. A 770nm sacrificial GaInAs layer is selectively etched away to produce the membrane. Different lengths of W1 are fabricated in order to obtain the propagation losses through the Fabry-Perot oscillation method. The PhC triangular matrix has a 420nm period. The air-filling factor is close to 30%. These PhC parameters allow to cross the air light-line in a wavelength domain close to 1500nm. Due to the strong effect of termination [6], the reasonably low propagation losses found here are a first estimate, and have to be confirmed.

PhC technology

PhC holes are defined by e-beam lithography in a PMMA resist layer, and then transferred with a CHF_3-based RIE process in a SiO_2 250nm-thick underlying layer deposited on the semiconductor material. After removing the PMMA resist, this SiO_2 layer is used as a mask for ICP etching. ICP etching is performed in a Sentech SI500 system. We first investigated different Cl_2/N2 ratio , while keeping a low Cl_2 fraction in order to avoid a too large chemical contribution. This two-gas mixture does not allow the obtainment a smooth and simultaneously vertical surface: the surface passivation is always too large, and lead to closed holes as visible on the SEM picture (cross section) of fig.1-a. The non-verticality of the holes is detrimental for propagation because it produces additional losses. In order to keep the advantage of surface passivation through N2, and

simultaneously improve the verticality of the etched profile, we have added BCl3 in the Cl2/N2 gas mixture. In the presence of the electronegative N2 molecule, the extremely electron-deficient compound BCl3 is dissociated and then contributes to the chemical part of the etching. BCl3 is also ionized, and the heavier ions (versus those produced through Cl2) contribute to a stronger physical component of the etching process, and as a consequence a more vertical profile. The advantage of BCl3 is clearly visible on Fig 1-B. The ICP source power is set to 1000W, the DC-bias is set to -200V in order to limit the mask etching rate.

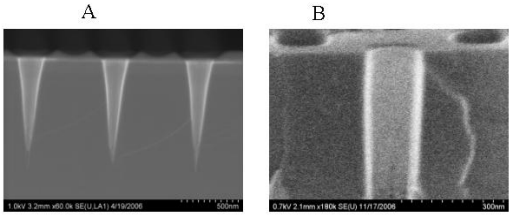


Figure 1. SEM cross section view of etched holes using A-Cl2/N2 process B- Cl2 / N2 / BCl3 process

W1 PhC guides are fabricated on a 340nm thick InP membrane. A 770nm sacrificial GaInAs layer is selectively etched away to produce the membrane (fig.2). Different lengths of W1 are fabricated in order to obtain the propagation losses through the Fabry-Perot oscillation method. The PhC triangular matrix has a 420nm period. The air-filling factor is close to 30%. These PhC parameters allow to cross the air light-line in a wavelength domain close to 1500nm.

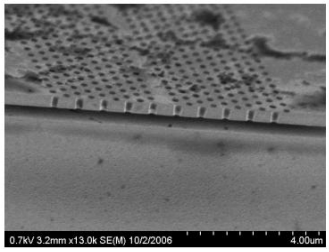


Figure 2. InP membrane after selective etching

W1 PhC guide on InP membrane

The spectrally resolved transmission of a 450µm long W1 measured using the end-fire method is plotted in Fig.3, also with the related dispersion curve: we can follow the even mode crossing the air light line (point A), then the transmission is reduced due to the high losses experienced by the odd mode, especially close to its cut-off (point B or/and B'), then the transmission is ensured by the even mode alone down to its cut-off (point C). Coupling to the odd mode is possible because the position of the external fiber cannot be perfectly centered on the W1 axis. An access guide would prevent this from happening. Losses measured using the Fabry-Perot resonance technique in the reduced frequency window centered at λ=1490nm [7] reach 35dB/cm. This value represents the overall losses, including the perturbation due to the odd mode. Also, additional uncertainty comes from the different termination for all the different guides measured. The very large dispersion at longer wavelength (λ=1540nm) prevents the loss calculation using the same method.

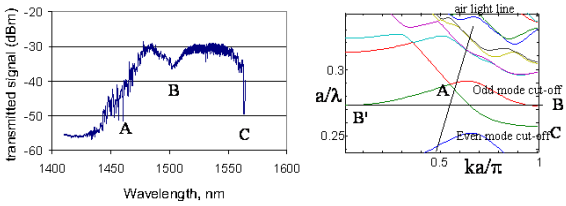


Fig 3. Spectrally resolved transmission of a 450µm long W1 and the related dispersion curve

Thinly supported guides

Thinly supported access guides have been designed in order to produce a perfectly centered optical injection in the W1, and also to control the termination of W1. These guides are written during the same e-beam lithography, thus ensuring a perfect alignment of the axis guide with the W1 axis, and also etched during the same step. Fig.4-a shows a perspective SEM view of a thinly supported guides, with 10µm long sections and 0.15µm wide supporting fins. These fins do not affect the transmission of the guide: fig.4-b displays a detail of the transmission spectrum measured on a 210nm wavelength span (1410nm-1620nm) for 461µm long guide, demonstrating a 4dB contrast fringe contrast, the propagation losses of these guides are 16dB/cm. The Fourier transform spectra on 12 windows (fig.4-c) show no dispersion on this very large spectral range.

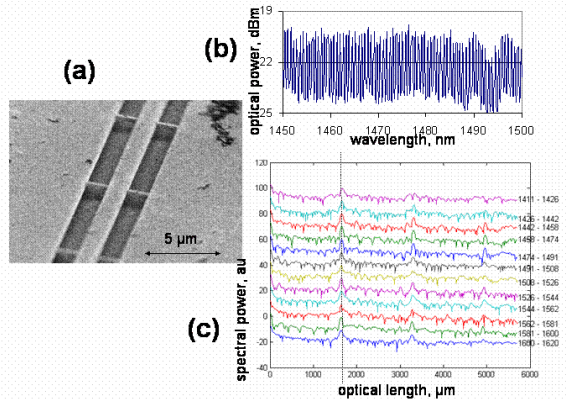


Fig.4 (a) SEM view of a thinly supported guide
(b)Detail of the spectrally resolved transmission
(c)Fourier transformed spectra of this transmission

W1 PhC guides with thinly supported access guides

W1 PhC have been fabricated in between these access guides. Three different lengths have been fabricated : 210µm, 420µm and 630µm, to allow the loss measurement through the Fabry-Perot method. A resolved spectrum of a 420µm long W1 is plotted on Fig.5 : the dip due to the coupling to the even mode is still visible. We can then conclude that, in spite of an on-axis optical injection from the access guide the odd mode is excited. Fabrication imperfection, mainly e-beam lithography are responsible for this optical power transfer from the even mode to the odd mode. We also see that in the spectral region of the single even mode, the transmission is larger than the one in the case of the W1 alone by a few dB (-27.5 instead of -30 dB in Fig. 4, a trend systematically observed) : the thinly supported guides improve the transmission.

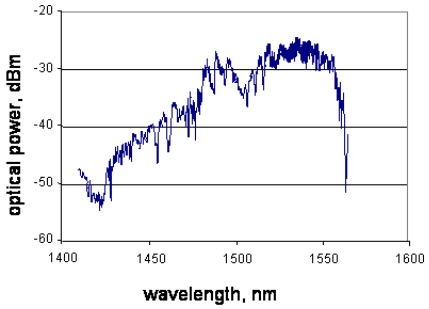


Fig.5 : Spectrally resolved transmission of a 420µm long in between access guides

.

These very first results have to be comforted by additional characterization in progress.

Conclusion

Propagation losses have been measured on W1 Photonic Crystal waveguides etched using an N2-based ICP process on InP membranes and operating below the light line. The W1 PhC guide has been designed to support one even and also one odd mode in the spectral domain investigated. The cut-off of the odd mode is in this case a clear signature of the even/odd coupling produced, either by an imperfect injection, or by an imperfect fabrication, or by both. We have proposed the new design of a thinly supported access guide to produce a correctly centered injection. The still observed cut-off of the odd mode in the case of a W1 with these access guides indicates that fabrication imperfections are still present. The design is however validated by an observed better coupling.

References

[1] D.Gerace et al, Optics Express, 13, 4939 (2005)
[2] E.Kuramochi et al., Phys.Rev.B, 72, 161318® (2005)
[3] K.H.Lee et al. IPRM'06
[4] P.Strasser et al., 17th IPRM, May 2005
[5] Y.Suzuki et al., Applied Surface Science 162 (2000)
[6] P.Sanchis et al., IEEE J. Quant. Electron., 40, 541 (2004)
[7] A.Talneau et al., Appl. Phys. Lett., 82,2577 (2003)

Self-collimated superprism effect using a photonic crystal with parallelogram lattice

Damien Bernier, Eric Cassan, Guillaume Maire, Delphine Marris-Morini, Laurent Vivien
Institut d'Electronique Fondamentale, UMR 8622, Bât. 220, Université Paris Sud, 91405 Orsay Cedex, France
Corresponding author: damien.bernier@ief.u-psud.fr

Abstract: *A photonic crystal with parallelogram lattice exhibiting both self collimation and superprism effect for a limited frequency range is studied. The input Gaussian beam shape broadening is limited so that division of a few wavelengths can be achieved without diffraction compensation. Simulations show that a good transmission is obtained without matching stages at the photonic crystal's interface.*

Introduction

Photonic crystals (PC) have attracted much interest for their optical tunable properties in both propagating and bandgap domains. In particular, two-dimensional (2D) slab PCs have been widely investigated for their diffraction properties outside of the photonic bandgap. The band engineering of those PCs has lead to the demonstration of structures allowing collimation, focusing or strong wavelength-dependant dispersion [1-5].

Wavelength division using high dispersion has been generally studied for the triangular and square lattice [6]. One of the key problems when using very strong superprism effect is the beam broadening that generally occurs in the same time [7]. Focusing has been proposed to overcome the angular spreading by adding a negative diffration effect, thus leading to structures with small PC area [8]. A preconditionned region of diffraction compensation is however needed when using this effect. The preconditionned region can be a homogeneous medium if the PC has negative diffraction, but the area needed in this case is large. A second PC with strong diffraction might also be used to obtain a smaller whole structure.

In the present work, another approach is studied to contole the beam quality profile in strong superprism dispersive configurations. To avoid beam broadening, PCs bands simultaneously presenting strong dispersion with collimation effect have been investigated.

Such regions are present in square PC lattice geometries. By changing the lattice into a parallelogram one, those regions can be extended and excited by a smaller incident angle. This paper is organized as follows. The diffraction properties of a parallelogram lattice PC are first presented. Beam propagation has then been studied by an effective index propagation method and by Finite-Difference Time-Domain (FDTD) calculations to evaluate the structure resolution and transmission.

Diffraction properties of parallelogram lattice PC

Figure 1 shows the considered photonic crystal. It consists of a parallelogram lattice (a=300 nm) of air holes etched within a 220 nm thick dielectric silicon film, with a buried silicon oxide layer of 1 µm and air as top cladding. The lattice vectors have an equal length and are angularly spaced by 105°. The radius r of the holes is 0.3a. The interface between the homogeneous medium and the PC is along a lattice vector direction of the crystal.

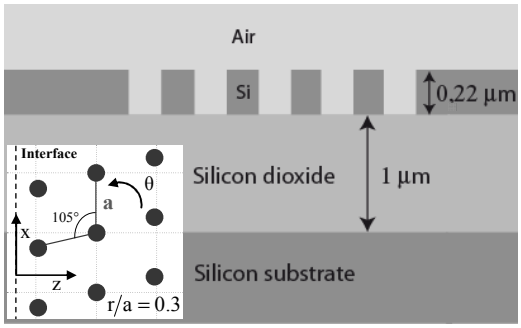


Fig. 1: Considered photonic crystal and interface orientation and SOI slab waveguide structure.

Three-dimensional plane wave (3D-PWM) calculations with a supercell in the vertical direction have been performed using the MIT program [9] to obtain the band structure of the PC. The considered silicon and silica indices at λ=1520 nm are 3.478 and 1.444, respectively. Figure 2 shows the first band equi-frequency curves of the PC. Wavevectors $k_{||}$ and k_z are the tangential and normal components with respect to the PC interface. Shaded regions are added to exhibit the zones of the reciprocal space with low beam broadening (light gray) and high dispersion (medium gray). Regions presenting both high dispersion and low beam broadening are reported in dark gray. Those zones have been delimited using the divergence p and dispersion q factors previously introduced by Baba et al. to evaluate the superprism resolution [7]. These factors correspond to the variations of the refraction angle with the incident angle and with the normalized frequency, respectively: $p = \partial\theta_R / \partial\theta_{IN}$ and $q = \partial\theta_R / \partial(a/\lambda)$

Shaded low beam broadening regions correspond to |p|<2 and strong dispersion areas have been chosen to correspond to |q|>35. For both cases, only modes that propagate within the PC are considered ($|\theta_R|$<90°). The θ_{IN}=-50° equi-frequency curve is reported in figure 2. For this incidence angle, a frequency domain is found to have low beam broadening and strong dispersion.

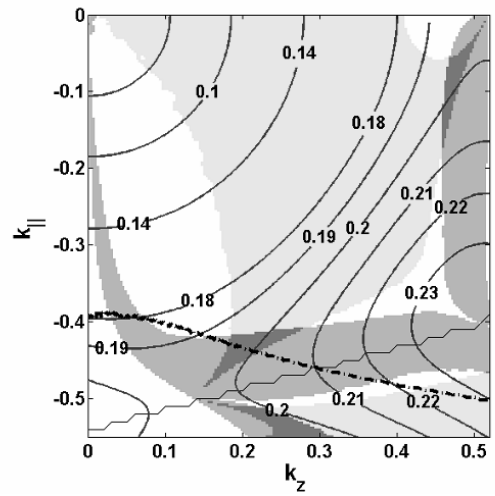


Fig. 2: First band equi-frequency curves of the PC. Equi-incident angle curve for θ_{IN} = -50° (thick dashed line). Low beam broadening regions (soft gray), strong dispersion regions (medium gray) and areas with both properties are reported (dark gray).

Figure 3 shows the |p| (circle markers) and q (plain square markers) factors along the -50° equi-frequency curve as a function of the wavelength. The p factor value is less than 1 for a 23 nm wavelength range. This corresponds to a beam spreading lower than the one of the homogeneous slab waveguide. Collimation (p=0) occurs for λ=1510 nm with a q factor of 65 that corresponds to 0.49°/nm. The p factor is positive for wavelengths above λ=1510 nm and negative below.

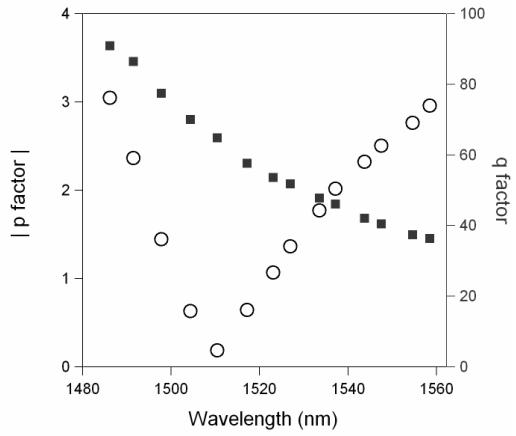


Fig. 3: p (circle markers) and q (square markers) factors around the collimation point for the θ_{in} = -50° equi-frequency curve.

Propagation results

To study the PC demultiplexing efficiency, beam propagation method using a method of effective index model has been used [10]. The equi-frequency curves of the planar waveguide and PC have been approximated by second order polynomial functions. The input Gaussian beam has been expanded in plane waves by Fourier transforming along a wavevector

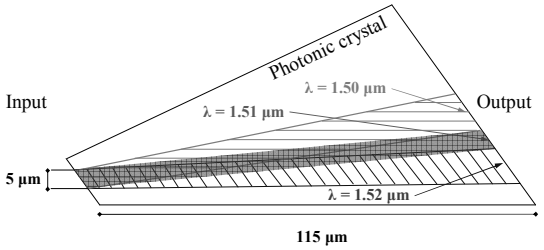


Fig. 4: Gaussian beam propagation using effective index model for λ = 1.50 µm, 1.51 µm and 1.52 µm with 5 µm wide input beams.

axis parallel to the PC interfaces. The spatial beam shape at a given propagation length has then been calculated by propagating the plane waves using the approximated equi-frequency curves and by inverse Fourier transform, i.e. the high spatial frequency modulation induced by PC holes is not considered.

Starting with a gaussian beam 5 µm wide (field 1/e width), the length of PC needed to separate beams of Δλ=10 nm around λ=1.51 µm has been evaluated. Figure 4 shows the beam width within the PC for λ=1.50 µm, λ=1.51 µm, and λ=1.52 µm. The three beams are separated with a PC propagation length around 115 µm, leading to a PC area less than 2500 µm².

In order to evaluate the diffraction properties and transmission of the structure, 3D-FDTD simulations have been performed using crystalwave software [11]. The PC being too large to be entirely simulated, only 40 µm of PC has been considered. The PC's output interface with the slab planar waveguide has been taken parallel to the input interface. A Gaussian excitor is placed in the silicon film 8 µm before the PC interface, and parallel sensors are placed in the homogeneous silicon film before and after the PC. The last one is placed 57 µm after the Gaussian excitor so that the beam experiences a 17 µm long propagation in the homogeneous medium. Figure 5 shows the simulation settings and beam intensity for λ =1.51 µm.

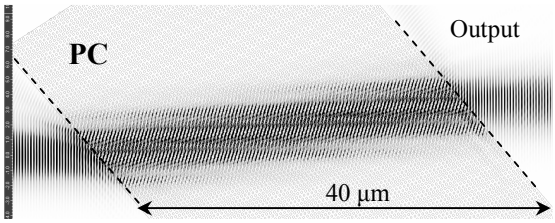


Fig. 5: Beam intensity of 3D-FDTD simulation for λ=1.51 µm and an initial beam width of 5 µm.

The transmission and beam width at the output sensor $W_{FDTD\ OUT}$ are resumed on table 1 for λ=1.50 µm, 1.51 µm and 1.52 µm. The output beam shapes being very close to Gaussian curves, their widths have been obtained by Gaussian fitting. The theorical beam width after propagation within 57 µm in the Si slab waveguide W_{SLAB} is given for comparison (effective

Table 1: FDTD output beam widths and transmissions after a 57 µm propagation (with 40 µm of PC) of a 5 µm input Gaussian beam. Refraction angle θ_R within PC. Theorical beam width for the homogeneous slab waveguide W_{SLAB}.

	Wavelength		
	1500 nm	1510 nm	1520 nm
$W_{FDTD\ OUT}$	5.10 µm	6.24 µm	7.66 µm
Transmission	75.4%	83.9%	90.1%
W_{SLAB}	9.11 µm	9.16 µm	9.22 µm
θ_R	39.51°	44.40°	48.62°

index: 2.854 at λ=1.51 µm). For the considered wavelengths, the beam width with the PC wavelength-dispersive region is narrower than the width of the beams propagated in the slab homogeneous medium. For λ=1.50 µm, the output beam is 5.10 µm wide that is almost equal to the initial 5.0 µm width. For this wavelength, the beam propagates within the PC with a negative p value that compensates the broadening of the beam within the 17 µm long homogeneous slab. The collimation wavelength found by FDTD calculations is close to 1505 nm, i.e. close to 1510 nm expected from plane wave method calculations.

The dispersion has also been evaluated by FDTD using the central beam position at the output sensor. The refraction angles are 39.51°, 44.40° and 48.62° for λ=1.50 µm, 1.51 µm and 1.52 µm, respectively. The dispersion at the FDTD collimation point (λ=1505 nm) is then 0.49°/nm that agrees with the q factor given by plane wave expansion calculations at collimation point.

The transmission of the PC has been evaluated using the positive flux recorded by sensors before and after the PC, both normal to the beam's direction of propagation. A transmission from 75.4 % to 90.1% is found as the wavelength goes from 1500 nm to 1520 nm. Losses are mainly due to the input and output interface mismatching and increases as the wavelength shorten. Losses for wavelengths below 1500 nm become important as the excited Bloch waves are close to the edge of the first Brillouin zone.

Given the high dispersion parameter for wavelength above 1520 nm and below 1500 nm, this structure can be used to divise other wavelengths provided the enlargement of the wavelength channel spacing. To keep a Δλ at 10 nm for a larger wavelength range, a precompensation PC that has an opposite wavelength dependant p factor might be used to to keep the beam width at its minimum along the output interface.

Conclusion

A photonic crystal exhibiting both strong dispersion and collimation effect has been studied. Simulations showed low beam distorsion for Gaussian beams 5 µm wide with a mean transmission around 83% without matching stages at the PC interfaces. This single PC structure can divise three wavelengths spaced by 10 nm using an area lower than 2500 µm² without beam preconditioning regions. The PC structure might be further optimized to enlarge the wavelength range of low beam broadening.

Acknowledgments

The authors would like to aknowledge Suzanne Laval for fruitful discusssions.

References

1 T. Matsumoto et al, Optics Express 13, 10768-10766 (2005).
2 H. Kosaka et al, J. Lightwave Technol, vol. 17, no. 11, 2032-2038, November 1999.
3 L. Wu et al, IEEE J. Quantum Electron., 38, 915-918 (2002).
4 S.N. Tandon et al, Photonic and Nanostructures, Fundamentals and Applications 3 (2005) 10–18
5 A. Lupu et al, Optics Express **12**, 5690-5696 (2004).
6 B. Momeni et al, J. Select. Areas Commun. **23**, 1355-1364 (2005).
7 T. Baba et al, Appl. Phys. Lett. 81, 2325-2327 (2002).
8 B. Momeni et al, Optics Express **14** No 6, 2413-2422 (2006).
9 MIT photonic band (MPB) available at: http://ab-initio.mit.edu/photons/
10 B. Momeni et al, J. Lightwave Technol., vol. 23, no. 3, pp. 1522–1532, Mar. 2005.
11 Lavrinenko et al, "CrystalWave", Photon Design, www.photond.com

Mapping the field distribution of a resonator in a photonic crystal slab, using transmission SNOM

René M. de Ridder, Wico C.L. Hopman, R. Stoffer, and Kees O. van der Werf
University of Twente, MESA+ Institute for Nanotechnology, Enschede, The Netherlands
R.M.deRidder@utwente.nl

Abstract: *Transmission scanning near-field optical microscopy (T-SNOM) is a recently introduced method for imaging optical intensity distributions in dielectric waveguiding structures, with a resolution below the diffraction limit. It is in particular suitable for mapping out standing-wave patterns in resonators. Application of the method to a Fabry-Perot-like cavity in a line-defect waveguide in a photonic crystal slab is demonstrated. Two different two-dimensional models have been used to verify that the T-SNOM image is a good representation of the optical intensity distribution in the resonator.*

Introduction

Scanning near-field optical microscopy (SNOM) methods [1], can provide the resolution below the diffraction limit that is required for measuring the field distribution in high-refractive-index microcavities, e.g. in photonic crystals. The interpretation of images obtained by such methods may be challenging because the probe that is used for local light collection and/or illumination also perturbs the optical structure under investigation. Although probe tips can have diameters below 100 nm, their effect can certainly not be neglected when small high-Q resonators are to be characterised. Especially metal-clad tips, that provide the best spatial resolution, may strongly affect the optical field, thus making the interpretation of such measurements difficult. In particular, this can be a problem with high-Q resonators which can be considerably detuned by the presence of a nano-sized probe [2, 3, 4]. The perturbation of the field by the probe is essential for obtaining resolution below the diffraction limit by converting part of the evanescent field to radiation. Recently we [4] and others [5] have demonstrated a related method, now called transmission scanning near-field optical microscopy (T-SNOM), where the functions of light collection and illumination on the one hand are separated from the function of perturbation on the other hand. The effect of this perturbation of the field by a dielectric or metallic probe is measured through the light that is transmitted through (or back-reflected from) the structure. The method is especially useful for mapping out standing-wave patterns. Although other SNOM types, like photon scanning tunnelling microscopy (PSTM) have a broader field of applicability (not requiring transmitted or back-reflected light to be available for analysis), T-SNOM has several advantages compared to PSTM. The scanning tip can be significantly smaller (potentially increasing the resolution) without necessarily decreasing the sensitivity; there is a large freedom in choosing the tip material, allowing to select the strength of the mechano-optical interaction; the availability of a larger optical signal improves the signal-to-noise ratio, thus allowing less complicated detectors and signal processing electronics. In this paper we will explain the method, show some results for a Fabry-Perot-like cavity resonator in a photonic crystal slab, discuss the interpretation of the results, and show through simulations that the T-SNOM image indeed closely resembles the intensity distribution in the unperturbed resonator.

T-SNOM operation

The principle of the set-up is shown in Fig. 1. The tip of an atomic force microscope (AFM) probe is scanned over the surface of the photonic structure, while the light transmission through the structure is recorded for each tip position. The strongest interaction can be expected at those positions where the optical field has the largest intensity, so that the optical field distribution is effectively mapped out. The AFM probe can be scanned across the device either in contact mode or in tapping mode. In contact mode the highest sensitivity and resolution can be expected, but damage to the tip or the structure may easily occur. In tapping mode, damage is much less likely to occur, but resolution and sensitivity may be less because of the reduced optical intensity in the evanescent field compared to that of the diffraction limited radiation field. However, as was recently pointed out by Li et al. [6], this height-dependent differential sensitivity may be exploited for discriminating between the evanescent field and the radiation field by using the tapping mode with a suitable signal processing method.

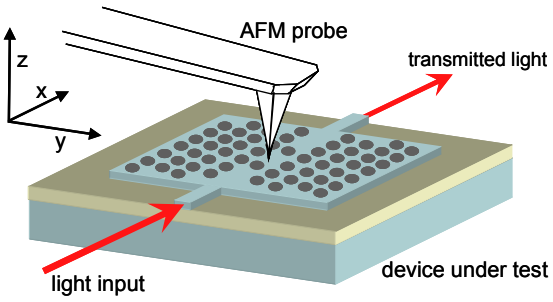
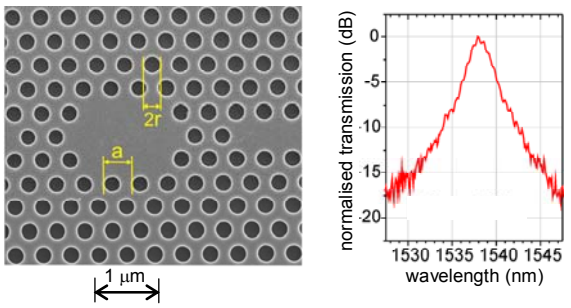


Fig. 1: T-SNOM set-up. Light from a tuneable laser is coupled into the device under test using a microscope objective. The transmitted light is collected on a photodetector, and the transmission is recorded for each position of the scanning AFM tip.



(a) (b)

Fig. 2: Device under test. a) SEM image of the structure, a Fabry-Perot-type cavity formed between extra holes in a W1 waveguide in a photonic crystal slab. b) Transmission spectrum of the undisturbed device around a resonance wavelength. The quality factor $Q \cong 650$.

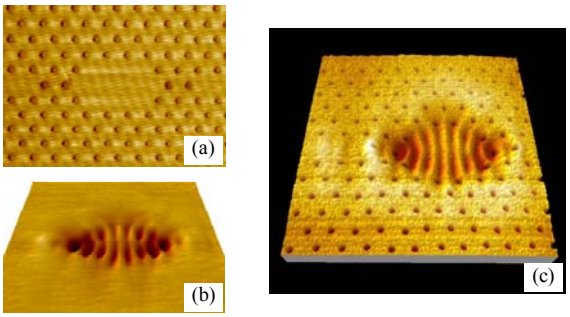


Fig. 3: Image formed by scanning an AFM tip over the top surface of the resonator structure. a) Height data (conventional AFM image). b). Optical transmission versus AFM tip position (T-SNOM image). c) Superposition of images a) and b), showing the location of interaction maxima relative to the structural device features (hole boundaries enhanced for clarity).

In Fig. 2a we show a SEM picture of a resonator in a silicon-on-insulator photonic crystal slab. The top silicon layer is 220 nm thick, the lattice parameter $a = 440$ nm, and the hole radius $r = 270$ nm. The fabrication process was described in [7].

Figure 3 shows that the combination of the height mapping (conventional AFM image, Fig. 3a) with the optical transmission mapping, Fig. 3b, results in a map, Fig. 3c, of the locations of maximum probe interaction with respect to the resonator topography. In this experiment we used a silicon nitride AFM tip with approximately 10 nm radius.

Modelling T-SNOM

As we demonstrated before [4], the presence of an AFM tip in the near field of a microcavity resonator may affect the losses (scattering, absorbing or guiding away part of the light) and the tuning (local increase of the average refractive index). The resulting change in Q-factor or resonance wavelength will affect the measured transmission through the device under test. Intuitively, this effect is expected to be maximum at locations of intensity maxima and to vanish at locations where the optical field is negligible. We investigated the validity of this assumption by modelling the optical microcavity in the photonic crystal and its interaction with a dielectric AFM probe tip. Since the problem is essentially three-dimensional, the model should be 3-D in principle. However, for practical reasons of computing resources, we have chosen to test two different 2-D models in two cross-sectional planes of the composite resonator-probe structure.

The first model, illustrated by Fig. 4, is in the x-z plane, c.f. Fig. 1. This model translates our problem into a cavity between two short grating sections. The AFM-probe is modelled here as a semi-infinite 50 nm thick silicon slab in the y-z-plane. Using a quadridirectional eigenmode propagator (QUEP) [8], the power transmission T and reflection R are calculated, and, assuming no absorption, the loss due to scattering S is found from the energy balance $T + R + S = 1$. Figure 5 shows the spectra obtained for the unperturbed resonator (without AFM tip). Next, the wavelength is fixed at $\lambda_r = 1.5388$ nm, (resonance), and the tip is scanned along the x-direction, while being in contact with the top surface of the resonator. The resulting variation of T with the probe position is shown in Fig. 6. Assuming that the main effect of the probe is a detuning of the resonator, the T-curve in Fig. 5 is used for calculating a wavelength shift that is equivalent to the change in T. The assumption of detuning only is not completely valid, but the consequences of the resulting error are small as will be reported elsewhere [9]. Finally, this calculated wavelength shift is shown in Fig. 7, together with the intensity distribution in the unperturbed resonator. The horizontal position scale for both curves is identical, and the vertical intensity scale is matched to the wavelength shift scale for maximum visual correspondence. It can be seen that the AFM-probe induced wavelength shift matches the intensity distribution of the undisturbed resonator quite well.

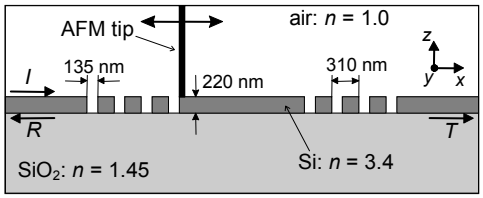


Fig. 4: Model used for simulating AFM-tip interaction with optical field in photonic-crystal microresonator.

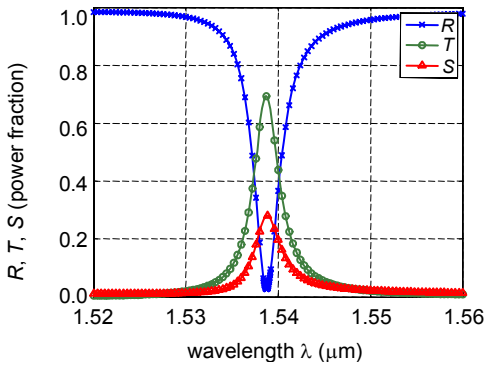


Fig. 5: Calculated transmission (T), reflection (R) and scattering ($S = 1 - T - R$) spectra of the unperturbed resonator.

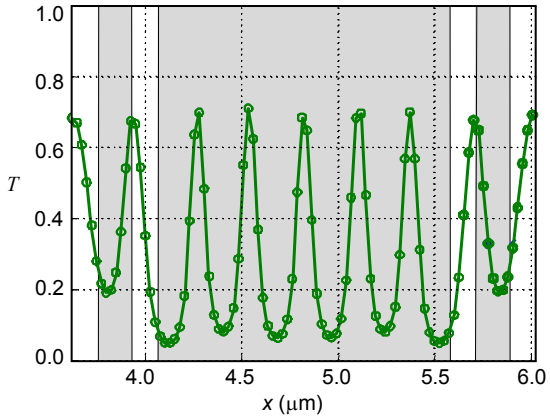


Fig. 6: Calculated transmission (T) through the resonator, versus the x-position (see Fig. 4) of an infinitively long, 50 nm wide silicon AFM tip. The white vertical bands indicate the hole locations. The calculation was done at the resonance wavelength of the unperturbed resonator.

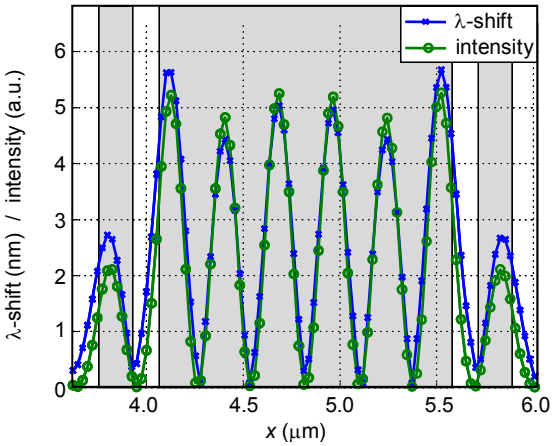


Fig. 7: Equivalent wavelength shift due to *local perturbation* by AFM tip, (calculated from Fig. 6, using Fig. 5), and calculated intensity distribution in the *unperturbed* device.

The second model maps the resonator and AFM probe on the x-y-plane, parallel to the photonic crystal slab. The photonic crystal structure is "flattened" using a kind of effective index approach. The refractive index values (n_{slab} = 2.9 and n_{hole} = 1) to be used in the simulation were chosen such that the calculated standing wave pattern in the undisturbed structure matched the experimental observation. Figure 8 shows this intensity distribution at resonance, calculated using a finite-difference time-domain (FDTD) method. The effect of the AFM-probe is modelled by introducing a small square (120 nm on a side) with a slightly increased refractive index superimposed on the refractive-index pattern of the resonator. The model was then recalculated many times, each time shifting the square representing the tip to a new position on a 40 nm grid overlaying the structure, thus mapping the power transmission versus probe position. The relatively large size of the square and the grid were chosen for keeping the computational effort within reasonable bounds. As this purely 2D model cannot account for out-of-plane scattering, it models just the detuning effect of the AFM tip.

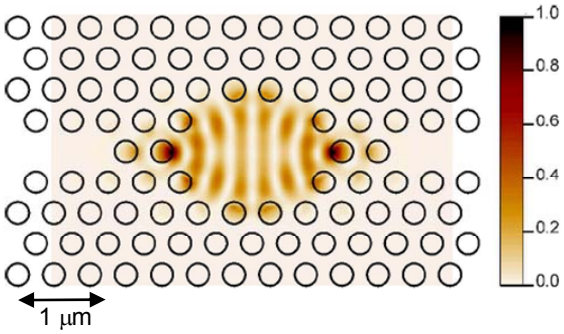


Fig. 8: Computed optical intensity distribution of the undisturbed resonant mode (2D FDTD).

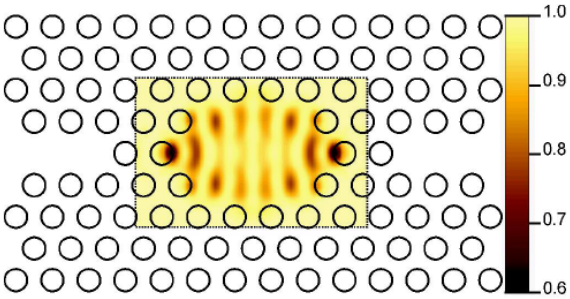


Fig. 9: Simulated T-SNOM image obtained by calculating (using 2D FDTD) the transmission through the resonator versus the position in the resonator plane of a small (120 nm x 120 nm) region of slightly increased refractive index (Δn = 0.2) representing the local effect of the AFM tip.

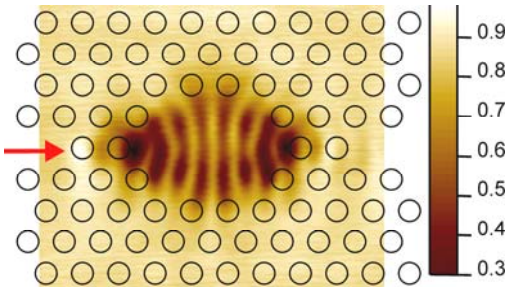


Fig. 10: Measured T-SNOM image, taken at the undisturbed resonance wavelength, using a silicon nitride AFM tip in contact mode.

The transmission value at each position of the square is converted to a colour of a pixel that is plotted at that position in a map of the structure. Figure 9 shows the result of such a sequence of calculations which simulates the scanning of the AFM tip over the resonator surface. Finally, Fig. 10 shows a T-SNOM measurement of the standing-wave pattern at resonance, at the surface of a photonic-crystal microcavity. Figures 9, 10 and 11 have been reproduced at the same scale in order to facilitate the comparison between the calculated intensity pattern, the simulation, and the measurement. A good agreement between these results can be seen, indicating that a T-SNOM mapping can give a good representation of the intensity distribution in a cavity. A more detailed account of these modelling methods and results will be published elsewhere [9].

The measurements presented here do not show the limits of resolution that can be obtained with T-SNOM. Of course, the demonstrated resolution (here about 100 nm) cannot be better than the finest detail in the intensity distribution that is mapped. Experiments at shorter wavelengths and with cavities in different materials are needed to explore the limit of resolution of this method.

Conclusions

Transmission scanning near-field optical microscopy (T-SNOM) was found to be a useful and convenient tool for mapping out the intensity distribution of a standing-wave pattern in an optical microcavity in a photonic crystal slab. Calculations using 2D models in cross-section and "top view", simulating T-SNOM operation demonstrate that the obtained image is a good representation of the intensity distribution. The simulated pattern matched the actually measured data rather well. We believe that this method has a wider range of applicability.

Acknowledgments

We thank Anton Hollink for his invaluable help with realising the measurement set-up, and Wim Bogaerts for coordinating the fabrication of our resonator samples. This work was supported by NanoNed, a national nanotechnology program coordinated by the Dutch ministry of Economic Affairs, and was also supported by the European Network of Excellence ePIXnet.

References

1. D. Courjon et al., Rep. Prog. Phys. 57, p. 989, 1994.
2. A.F. Koenderink et al., Phys. Rev. Lett. 95, 153904, 2005.
3. I. Märki et al., Opt. Express 14, p. 2969, 2006.
4. W.C.L. Hopman, et al., Opt. Express, 14, p. 8745, 2006.
5. J.T. Robinson et al., Opt. Express, 14, p. 10588, 2006.
6. Y. Li et al., Opt. Commun. 258, p. 275, 2006.
7. W. Bogaerts et al., J. Lightwave Technol. 23, p. 401, 2005.
8. M. Hammer, Opt. Commun. 235, p. 285, 2004.
9. W.C.L. Hopman et al., *submitted*, 2007.

Ultra High-speed Photodetectors and Photoreceivers for Telecom and Datacom also Aiming at THz Applications

Heinz-Gunter Bach
Fraunhofer Institute for Telecommunications, Heinrich-Hertz-Institut, Einsteinufer 37,
D-10587 Berlin, Germany, Phone: ++49(0)30 31002-503, Fax: ++49(0)30 31002-558,
e-mail: bach@hhi.fraunhofer.de

Abstract: *Ultra-high speed photodetectors and receivers based on advanced waveguide-integrated photodiodes are presented. Main applications are the up-coming 100 G Ethernet and optical free space communications. The waveguide-integrated InP-based detectors are monolithically integrated with HEMTs, employing semi-insulating optical waveguides on a semi-insulating InP:Fe substrate, leading to 80/85 Gbit/s photoreceivers. For serving the emerging THz sensor and security application fields, a monolithic integration of a micro-pin photodiode with a circularly-toothed planar logarithmic-periodic antenna is presented and analysed in the 100 GHz range.*

Introduction

Leading system providers upgrade their long-haul optical communication systems for single channel bit rates of 40 Gbit/s, aiming to exploit the transport capacities of the single-mode fiber (SMF) of exceeding 10 Tbit/s by joint progress in combining time division multiplexing (TDM) and wavelength division multiplexing (WDM) techniques. System developers push experiments employing 80/85 Gbit/s data rates with the aim to proceed towards serial PHY 100 G Ethernet solutions and to support optical data transmission rates even at e.g. 160 Gbit/s and higher [1], to serve the steadily increasing data traffic (Fig. 1).

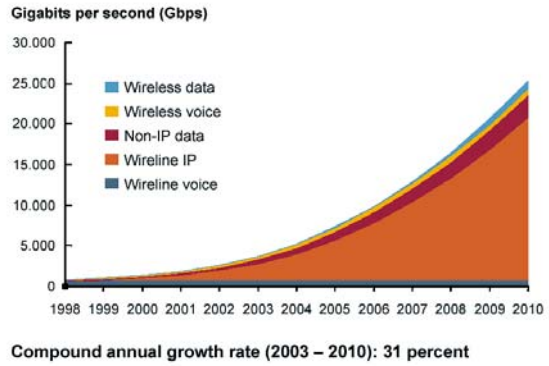


Fig. 1: Ever increasing data traffic;
source: IST Concertation Meeting September 2004.

FhG-HHI developed a family of 40 to 160 Gbit/s photodetectors and receivers, focussed on various high-power waveguide-integrated photodiodes, including those of special structure (twin-type, balanced or traveling wave) and InP-based monolithically integrated pinTWA photoreceivers (OEIC receiver) for 40/43 and 80/85 Gbit/s data rates [2, 3]. Those developments are based on a flexible integration concept, using semi-insulating substrates and semi-insulating optical waveguide layer stacks. Based on the waveguide-integrated concept, in section 1 high-power ultra-broadband photodetectors approaching a 3 dB cut-off frequency of 110 GHz are presented including their packaging into pig-tailed modules. In section 2 photoreceiver concepts are discussed, leading to the distributed amplifier type for achieving highest speed in electronic amplification. The receiver integration concept will be explained, which allows the monolithic integration of waveguides, MMI splitters, evanescently coupled pin photodiodes, HEMTs and distributed amplifiers. An advanced ultra-broadband pinTWA receiver OEIC for 80/85 Gbit/s detection is presented. The detectors and photoreceivers described are suitable for electrical TDM (ETDM) with high data rates (actually up to 160 Gbit/s in case of the detectors) within the single channel as well as for even higher data rates in transmission schemes employing optical TDM (OTDM) techniques. In section 3 the waveguide-integrated photodiodes are miniaturized into micro-pin photodiodes. These are then monolithically integrated with a circularly-toothed planar logarithmic-periodic antenna to represent a transmitter chip, aiming at THz applications.

1. Photodiodes and Modules for 100 G Ethernet

Side-illuminated photodetectors show an improved high-power behaviour, because the absorption is distributed laterally into a larger length of a thinner absorption layer in a controlled manner, compared to perpendicular illuminated detectors. Our waveguide-integrated photodiode employs a rib-waveguide, the light from which is coupled evanescently from the lower side into the small-gap absorption layer. This type of detector comprises also a monolithic taper at its input waveguide facet.

The recently fabricated photodetector chips are based on InP and comprise an evanescently coupled mesa photodiode of 5x20 μm^2 size, a spot-size converter for increased fiber alignment tolerances, a biasing network and a 50 Ω matching resistor. An optimized impedance line connecting the p-mesa to the electrical output line of the detector leads to an increase of the cut-off frequency up to 110 GHz [4].

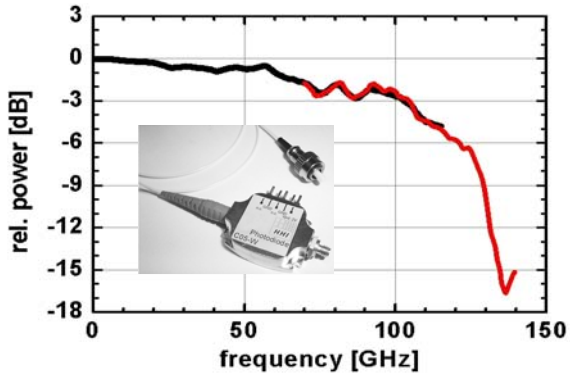


Fig. 2: Relative frequency response of the PD module (+2.3 dBm optical input power) measured with hp437B (black) and PM3 (red) , inset: photograph of the PD module.

The chip is assembled into a housing equipped with a 1 mm coaxial output connector and a fiber pigtail (Fig. 2, inset). A cleaved fiber is fixed directly at the chip's antireflection-coated waveguide facet. A responsivity of 0.73 A/W with a polarization dependent loss (PDL) of only 0.4 dB at 1.55 µm wavelength was obtained. The electrical output signal is provided by a short coplanar waveguide (CPW) which is connected by multiple short bonding wires to a following low-loss CPW on quartz substrate leading to the output connector. All fabricated modules are routinely tested for robustness against vibration (10 min, 60 g, 50 Hz) and thermal cycling from 10°C to 50°C and showed no degradation. The frequency characteristic of the photodetector (PD) module was determined by an optical heterodyne measurement setup employing a fixed and a tunable laser around 1.55 µm. The RF signal was measured by a power meter (hp437B) with three different power sensors for the respective RF bands 0-50 GHz, V- and W-band. In the F-band (90-140 GHz) we used a high-frequency power meter (PM3 Erickson Instr.). An excellent agreement of the measured characteristics was observed in the overlapping frequency ranges. Fig. 2 shows the calibrated frequency response of the photodetector module at 2 V reverse bias (V_{bias}). A -3 dB bandwidth of 100 GHz is obtained. At 120 GHz signal frequency the response has decreased by 6 dB. The dip around 135 GHz can be attributed to a higher order mode arising in the coaxial connector, which limits the performance of the 1 mm coaxial interface.
Mounting alternatives comprising flip-chip technology led to similar good broadband properties.
The PD modules have been evaluated in several back-to-back OTDM transmission experiments.
Fig. 3 shows the received electrical 80 Gbit/s RZ eye patterns at different optical input power levels using the setup described in [5]. All measured eye patterns are opened widely with a peak voltage up to 0.6 V revealing only negligible saturation effects at +12 dBm.

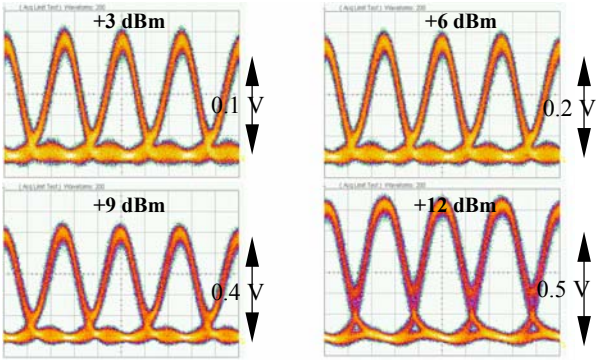


Fig. 3 Electrical 80 Gbit/s RZ eye pattern at 3, 6, 9 and 12 dBm optical input power detected by the detector module at -2.5 V bias (x: 5ps/div).

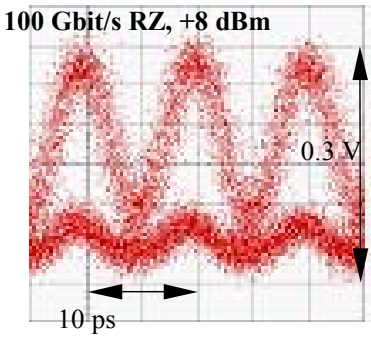


Fig. 4 100 Gbit/s RZ eye pattern at +8 dBm input power, V_{bias}: -2 V, 2^{20}-1 PRBS (courtesy of L. Moeller, Lucent Techn., USA).

Measurements at 100 Gbit/s RZ were performed using a 100 GHz sampling scope (LeCroy SDA with SE-100 standard time base) demonstrating the highest available bit rate with RZ modulation format at which o/e conversion could be performed without any reduction of the modulation depth (Fig. 4).
Fig. 5 shows the detected 160 Gbit/s RZ data stream at +12 dBm optical input power. Due to the insufficient bandwidth of the sampling head (70 GHz, Agilent 86118A) and the PD module we observe an RZ-to-NRZ conversion. Nevertheless, the eye amplitude is still remarkable and the inner eye opening reaches 160 mV.

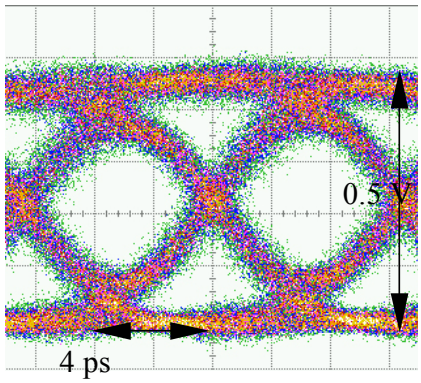


Fig. 5 Detected eye pattern under 160 Gbit/s RZ excitation, V_{bias} = -2.5 V.

2. Photoreceivers for 80/85 Gbit/s Applications

The concept of combining a waveguide-integrated photodiode with a spot-size converter and a HEMT-based amplifier and allowing the independent optimization of each of the components has been widely discussed in earlier publications [6, 7]. For 80/85 Gbit/s system applications a circuit design has

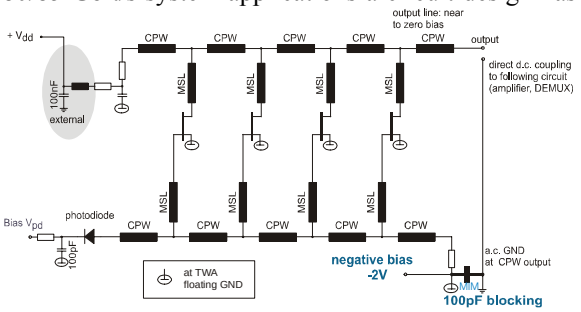


Fig. 6 Circuit diagram of the photoreceiver with negative bias and GND-isolated output port.

been developed, using HEMTs with modified layer structures and shorter gate lengths. The biasing configuration is accomplished with a negative bias supply at the common source electrode blocked with an MIM capacitor [8]. The circuit diagram of the photoreceiver with a negative bias and ground (GND)-isolated output port is depicted in Fig. 6.

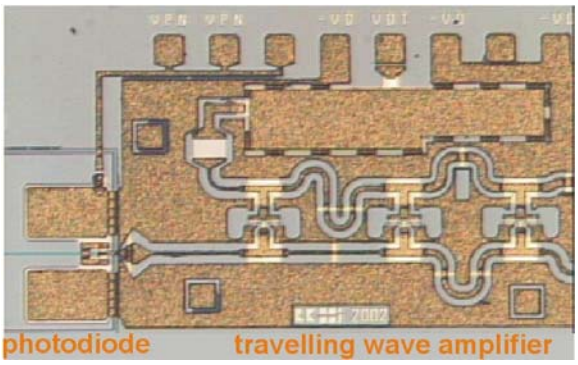


Fig. 7 Partial view of the integrated photoreceiver OEIC.

The amplifier's DC current is fed into the terminal V_{dd}. The HEMTs with 0.18 µm gate length, exhibit cut-off frequencies f_T/f_{max} of typically 140/300 GHz. The complete circuit was designed applying the ADS simulation tool, revealing a minimum 3-dB bandwidth of 65 GHz and transimpedance (Z_T) of 40 dBΩ. The reflection coefficient S_{22} is less than 10 dB over almost the whole frequency range up to 80 GHz. A partial view of the chip is given in Fig. 7, which shows the photodiode at the left being connected to the input of the traveling wave amplifier via an air bridge. The amplifier characteristics defined by the transimpedance (Z_T) is derived from the measured S-parameters. The transimpedance amounts to 39 dBΩ (71Ω) and has a bandwidth of 72 GHz. The packaged photoreceiver is shown in the inset of Fig. 8, with 1 mm RF output, a DC supply and an optical input. The frequency characteristic of the module is given in Fig. 8. The 3 dB bandwidth exceeds 70 GHz, which is comparable to the OEIC characteristics and proves a high quality RF

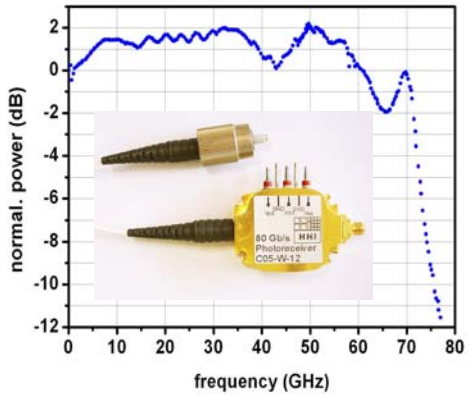


Fig. 8 Opto-electronic frequency response of the pinTWA photoreceiver module: inset: photograph of a pig-tailed OEIC module with 1mm RF output.

packaging. The overall conversion gain of the photoreceiver module is 45.4 V/W, which is high enough for 80 Gbit/s ETDM systems as well as a high frequency measurement equipment. Time domain measurements with the module demonstrated

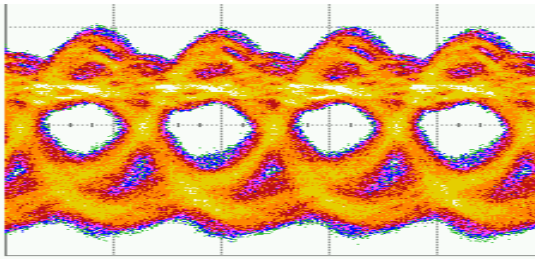


Fig. 9 85 Gbit/s NRZ eye pattern at +7 dBm optical input power detected by the pinTWA receiver module, Alcatel SEL AG, Stuttgart [10], x: 10 ps/div, y: 100 mV/div.

well opened 80 Gbit/s RZ and 85 Gbit/s NRZ eye patterns at 7 dBm optical input power [9, 10]. The back-to-back 85 Gbit/s NRZ eye pattern measurement (Fig. 12) was achieved at +7 dBm optical input power in an ETDM very short range transmission setup at Alcatel SEL AG [10].

3. Transmitter Chip Aiming at THz Applications

Photomixing has proved to be a versatile and convenient measurement technique in the THz frequency range, appropriate to different THz sensor and security applications. The present work focusses on the realisation of an optical-waveguide coupled p-i-n photomixer integrated with a broad-band THz antenna in a single chip, Fig. 10. The broad-band logarithmic-periodic circularly-toothed planar antenna

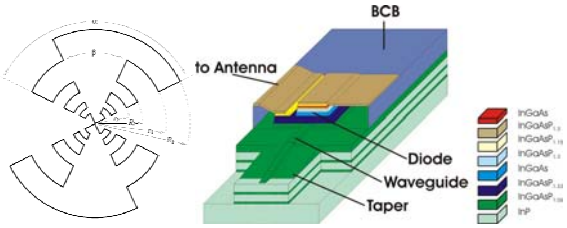


Fig. 10 Components of the photonic mixer: left: logarithmic-periodic circularly-toothed planar antenna, right: schematic view of the waveguide integrated micro-pin photodiode of 5x7 µm^2 size with spot size converter.

allows to cover a wide frequency range from 0.1 to 1.5 THz with a single chip [11]. The optical-waveguide taper implemented in our chip relaxes the tolerances for fibre-coupling by an order of magnitude compared to edge-coupled photodiodes and improves the quantum efficiency of the photomixer by an order of magnitude compared to the back-illuminated THz photodiodes. The transmitter chip was fabricated on InP:Fe substrate employing a metal-organic vapour phase epitaxy (MOVPE) epi-

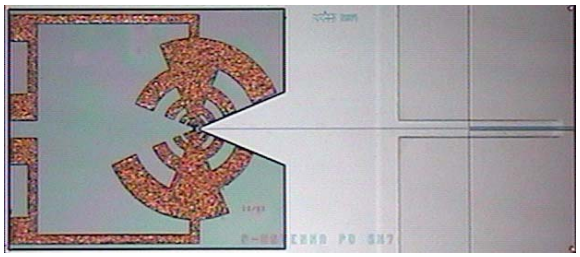


Fig. 11 Photograph of the complete photomixer chip with dimensions 2.75 x 1.4 mm²; illumination is from the right.

taxial approach for the layer stacks of the waveguide-integrated PD. It comprises a spot-size converter, an optical waveguide, a micro p-i-n mesa PD of 5-µm

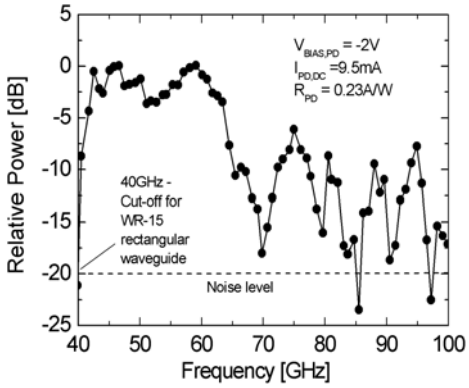


Fig. 12 Heterodyne measured AC characteristics: relative radiated RF output power vs. frequency.

width and 7-µm length [12], and the antenna structure on a BCB layer, cf. to Fig. 11 [13]. The THz signal radiated from the transmitter is received by a special feed horn antenna after free space transfer in a distance of 3 cm above the chip planar side. The detector can transform signals in the frequency range between 10 GHz and 120 GHz. The electrical output signal is measured by a microwave power meter up to –23 dBm. In Fig. 12 the relative power of the electrical signal is plotted versus the beat frequency of the injected optical signal with a power of 15 dBm at a wavelength λ_0 of 1.55 µm. Radiated power measurements applying a lens on the substrate, collecting a quite larger amount of radiated power will be published elsewere.

Conclusions

A highly efficient 100 GHz photodetector module for the detection of single channel bit rates up to 160 Gbit/s RZ has been reported. The detected eye diagrams are well opened with sufficient peak voltages to drive any available demux electronics directly. PinTWA photoreceivers were demonstrated for O/E conversion of 80/85 Gbit/s data rates, applying the RZ/NRZ modulation formats. A prototype of an InP-based integrated THz emitter comprises a micro p-i-n PD with a nominal cut-off frequency of 120 GHz operating as a photonic mixer which determines the maximum frequency of about 100 GHz measured with a feed horn antenna in air above the chips planar side. These results demonstrate the potential of the integration concept of evanescently coupled pin photodiodes for the use in RF microwave links and ultra high-speed systems up to data rates of 160 Gbit/s.

Acknowledgments

The author gratefully acknowledges contributions from his colleagues A. Beling (now ab3pj@virginia.edu), G.G. Mekonnen, R. Gibis, D. Schmidt, R. Kunkel, T. Eckhardt, C. Schubert, W. Ebert, and A. Seeger at the FhI Heinrich-Hertz-Institut, Berlin. Further he acknowledges the cooperation with Alcatel SEL AG, Stuttgart (E. Lach, K. Schuh) and TU Darmstadt (C. Sydlo, P. Meisner). This work was financed partly by the MultiTeraNet program of the German Federal Ministry of Education and Research.

References

1 Y. Muramoto et al, Electron. Lett., 40 (6), pp. 378-379, 2004.
2 A. Beling et al, in Tech. Digest Optical Fiber Communication (OFC 2002), pp. 274–275.
3 A. Beling et al, Electron. Lett., 39 (16), pp. 1204-1205, 2003.
4 H.-G. Bach et al, IEEE JSTQE, Vol. 10, no.4, pp. 668-672, 2004.
5 A. Beling et al, in Tech. Digest Optical Fiber Communication (OFC 2005), paper OFM1.
6 H.-G. Bach et al, Special Issue of IEEE JSTQE, Vol. 2, No. 2, 1996, pp. 418 – 423.
7 W. Schlaak et al, Technical Digest, OFC 2001, Mar 17-22, 2001, Anaheim, CA, USA, paper WQ4, pp. 1-3.
8 G. G. Mekonnen et al, 14th Intern. Conf. on InP and Related Materials (IPRM 2002), May 12-16, 2002, Stockholm, Sweden, paper A8-1.
9 G. G. Mekonnen et al, IEEE JSTQE, Vol. 11, Issue 2, 2005, pp. 356-360.
10 E. Lach et al, 32nd European Conference on Optical Communication (ECOC), 24th-28th September 2006, WP 144.
11 C. Sydlo et al, FREQUENZ, 59, pp. 207-210, 2004.
12 A. Beling et al, IEEE JSTQE, special issue on High-Speed Photonic integration, Vol. 13, No. 1 (2007), pp. 15-21.
13 R. Kunkel et al, Optical Terahertz Science and Technology (OTST), March 18-21, 2007, Orlando, Florida, TuC5.

Controlling Modes using VCSEL-Based Photonic Crystal Heterostructures

L. D. A. Lundeberg and E. Kapon
Ecole Polytechnique Fédérale de Lausanne (EPFL), Laboratory of Physics of Nanostructures,
CH-1015 Lausanne, Switzerland
lars.lundeberg@epfl.ch

Abstract: *Photonic crystal heterostructures can be used to tailor the optical supermodes in arrays of vertical-cavity surface emitting lasers. Merging mode confinement effects with active control of the photonic properties opens up the way for new optical switching devices utilizing wide-area coherent light sources.*

Introduction

One of the advantages of vertical-cavity surface-emitting lasers (VCSELs) is the ability to couple several lasers together in two-dimensional (2D) arrays. Such arrays may lase in a phase-locked mode providing wide-area coherent light with laser emission contained in diffraction limited far-field pattern [1]. Along with the appealing possibilities for novel photonic devices, two-dimensional arrays of VCSELs can be regarded as a model photonic lattice [2-4], and the concept of photonic crystals (PhC) has successfully been applied for the study of photonic disorder [5] and photonic band structure [6] in this type of arrays. Furthermore, concatenating VCSEL-arrays with different dispersion properties can yield PhC heterostructures (PhCHs), with which the photonic envelope functions can be controlled using PhC heterojunctions [7-9]. In particular, such PhCHs can confine the photonic states in a 2D "island" domain of low photonic band-gap material surrounded by a "sea" of higher photonic band-gap (Fig 1). In this way, it is possible to tailor the distribution of the transverse lasing mode, which should find applications in novel optical switches and routers.

In this work, we combine photonic envelope function confinement with active control of the gain distribution in VCSEL-based PhCHs. Tweaking PhCH domains in and out of coupling significantly alters the far-field pattern, which make possible active beam switching and wavelength tuning with wide-area VCSEL-arrays

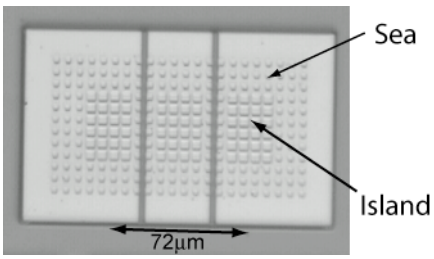


Fig. 1: Optical micrograph (top view) of a PhCH containing three 4x6 photonic islands defined on a VCSEL wafer.

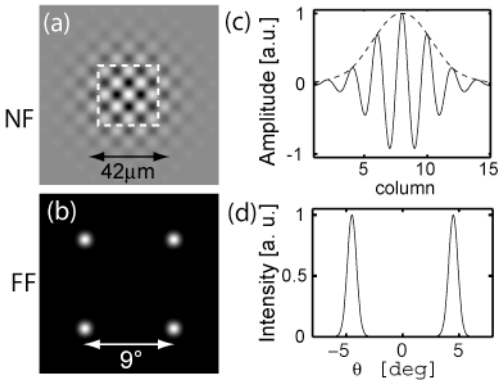


Fig. 2: (a) Calculated near and far-field (b) patterns of 5×5 photonic island (dashed square). (c) Near field line scan across the center of (a). (d) Far-field line scan across the main lobes. λ=940 nm, Λ=6 μm, Au pixel size 4.9×4.9μm^2, (island), 3×3μm^2 (sea).

Coupled Heterostructures

Figure 2 illustrates confinement of the envelope function in a single photonic island [8]. The PhCH consists of an island comprising 5×5 high reflectivity Au pixels (4.9×4.9μm^2 on a 6μm pitch) surrounded by a low reflectivity Cr grid, deposited on a conventional InGaAs/GaAs/AlGaAs VCSEL wafer [1] emitting at 943nm wavelength. The island is surrounded by a sea of the same square lattice structure but of smaller Au pixel size (3×3μm^2). The lowest loss supermode maintains the out-of-phase modulation across the heterojunction and the resulting far-field pattern exhibits four main far-field lobes.

As a natural extension to the single photonic island system, we consider two embedded PhC islands in a PhC sea and study the coupling between them. Following the analogy with semiconductor heterostructures, the system of two separated PhC domains can be regarded as two coupled photonic wells. As such, two equal-sized photonic islands of identical crystal structure are expected to couple, forming symmetric and anti-symmetric photonic envelope function states.

Numerical simulations demonstrate splitting of the out-of-phase lowest loss supermode of a single island into bonding and antibonding states with envelope functions confined in both islands [Fig. 3(a)]. The envelope function of the antibonding state exhibits a node at the center of the heterobarrier, whereas the bonding state does not vanish there. The difference in relative phase of the envelope functions of the bonding and antibonding states at the islands is

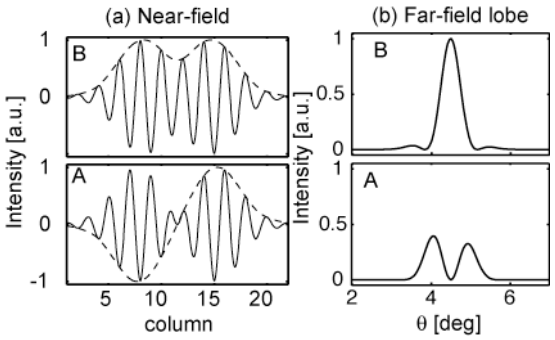


Fig. 3: (a) Calculated near and far-field (b) line scans of the bonding (B) and anti-bonding (A) modes of two 5×5 photonic island separated by 2 lattice periods. Other parameters are as for Fig. 2.

manifested by different characteristic far-field patterns [Fig. 3(b)]. It can be seen that the interference of the emission from the coupled islands produces additional features in the main far-field lobes obtained for an individual island [compare Fig 2(b,d)]. In the bonding state, the two envelope functions of the islands are in phase, producing a bright intensity fringe at the center of each lobe. Conversely, for the antibonding state the envelope function at the two islands is out-of-phase, resulting in a dark fringe at the center of the lobes.

The system of two closely placed photonic islands is an example of a lattice where an additional periodicity is superimposed on the heterostructure scale. In fact, a PhCH superlattice (SL) can be formed by constructing an array of coupled islands, for which the island supermodes would split in a PhCH SL miniband. Figure 4 illustrates this for three coupled photonic islands. As in the case of two photonic islands, the lowest loss mode maintains the out-of-phase relationship between adjacent lattice sites. This is because the higher order modes have envelope functions that exhibit nodes within the array. This either forces the amplitude of a column to vanish or renders two columns in phase, which in both cases increases the modal losses.

The difference in envelope functions of the three modes is manifested by different characteristic far-field patterns [Fig 4(b)]. The fine structure of the main far-field lobe now shows a splitting into additional fringes, as compared to the single and two-island far-field lobes. These characteristic signatures of the lowest loss modes make it possible to experimentally distinguish between the modes.

Tuning of two photonic islands

In the case of two-coupled islands, lasing on the bonding envelope-function mode was observed as the system was driven by a single electrical contact [9]. However, the fabrication of identical photonic islands is limited by the resolution of the lithography technique and by nonuniformities of the VCSEL wafer. There are thus inadvertent differences between

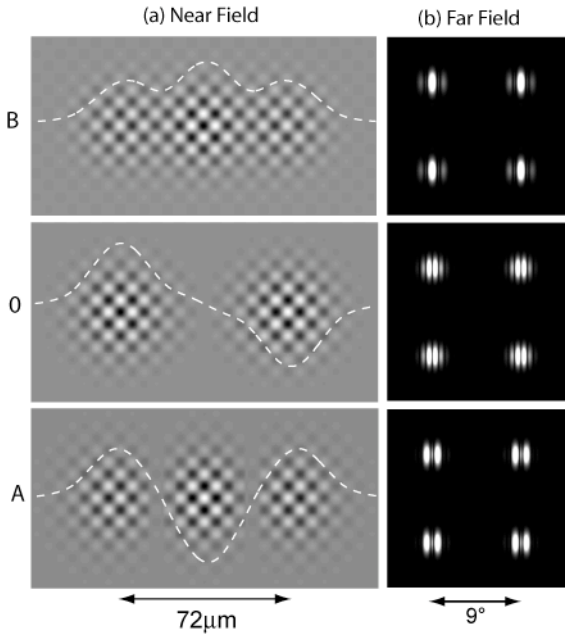


Fig. 4: (a) Calculated near and far-field (b) pattern of the "bonding" (B), "zeroth" (0) and "anti-bonding" (A) modes of three 5x5 photonic island, each separated by 2 lattice periods. The dashed curve is the slowly varying envelope function along the center of the array. All other parameters are as for Fig. 2.

the islands, resulting in weaker effective coupling between them and, in turn, to localization of the envelope function at either island. The dissimilarities between the islands can be compensated for by modifying the gain at each island, which may be achieved by injecting different currents into separated parts of the array. Separate contacting can thus be useful in bringing the two islands into resonance and inducing efficient coupling. Alternatively, current control of the coupling may be used to change the localization of the photonic mode, which can yield beam switching.

We have fabricated separate-contact coupled islands such that two different currents can be fed into each island while avoiding significant changes in the mirror reflectivity pattern across the PhCH. In order to keep the periodic reflectivity pattern, the two contact pads were aligned with the lattice defining the PhC. Removing the Cr grid between two pixel columns in the barrier between the islands separated the two contacts, Fig.1. The locally removed Cr grid slightly perturbs the periodic reflectivity pattern. In order to minimize this perturbation, the unpatterned top distributed Bragg reflector separating the two contacts was etched such as to imitate the reflectivity of the missing Cr patterned grid.

Figure 5 demonstrates the lasing characteristics of such VCSEL-based PhCH system incorporating two 4×5 photonic islands using two separated contact pads. The VCSEL-based PhCH was pulse-driven, with a repetition rate of 100kHz and 50 ns wide

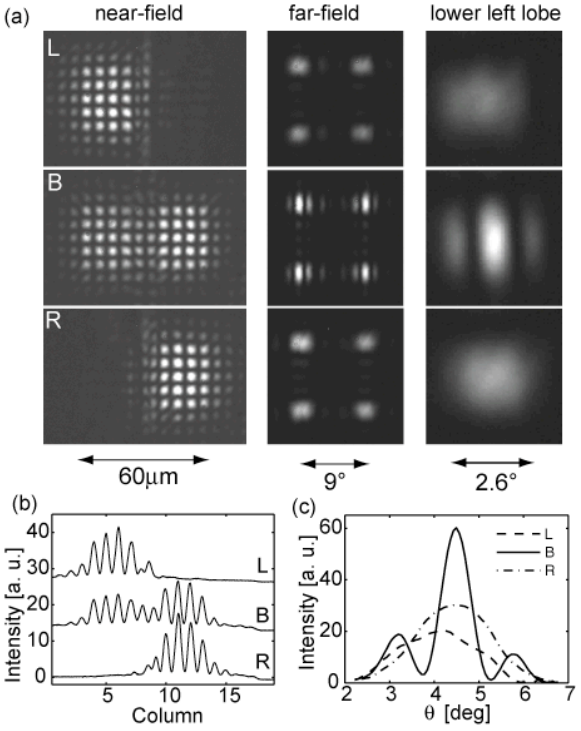


Fig. 5: Emission characteristics of separate-contact PhCHs incorporating two 4×5 coupled islands separated by 2 lattice periods. (a) Near-field patterns corresponding to current injection in the left (L), right (R) and both of the photonic islands (B) and corresponding far-field patterns (The light from the "sea" domain was blocked). (b) Average line scans across the near-field patterns of (a). (c) Average line scans of the lower left far-field lobes in (a).

pulses. Injection into the left side of the array (L) leads to photonic envelope function localization in the island situated there. Switching the current to the right contact yields switching of the envelope function to the right island. Coupling between the islands was achieved by synchronizing the electrical pulses in time and adjusting their relative magnitudes. In this way, we achieved lasing at both islands with preserved periodicity of the optical mode across the entire array, [Fig 5(a,b), B].

The switching between coupled and uncoupled coupling PhCH islands is corroborated by the measured far field patterns shown in Fig 5(a). For single island operation, the PhCH lases on the lowest loss out-of-phase supermode with a characteristic four-lobe far-field pattern, indicating a π phase shift between neighboring lattice sites. The mutual coherence between the coupled islands is manifested by the fine structure splitting of the main far-field lobes. In particular, the occurrence of a bright fringe at the center of each main lobe evidences lasing on the bonding state, as predicted by the calculations presented above. Of special interest is also the far-field position where the beam of the coupled structure exhibits a null, since bringing the islands in and out of coupling modulates the optical field there with high modulation contrast.

The coupling of the envelope functions of the two islands is also characterized by "wavelength alignment" among the array element, as shown by the measured, spectrally resolved near-field patterns in Fig. 6(a). These patterns were generated by focusing one row in the center of the PhCH onto the input slit of a spectrometer. For individual operation of the islands, each island lases generally at a different wavelength. The elements within each array side are however locked to the same wavelength. By proper adjustment of the two currents, the wavelength of the resulting coherent supermode could be locked into a single spectral line [see Fig.6(a,b)]. The wavelength of the coupled system is red-shifted with respect to the lasing wavelengths of the solitary islands. Thus, the emission wavelength of the coupled structure can be electrically tuned by changing the two injected currents.

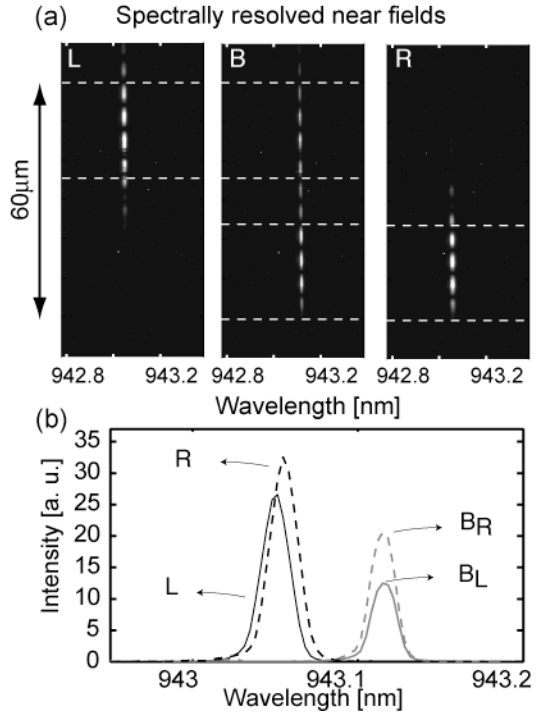


Fig. 6: (a) Spectrally resolved near-field of one row of the coupled PhCH islands of Fig. 5 corresponding to current injection in the left (L), right (R) and both (B) photonic island(s). (b) Line scans across the spectra (averaged between the white dashed lines) in (a). The index notation B_L and B_R relates to the spatial positions corresponding to the left and right islands, respectively.

Photonic Superlattices

In addition to the system of two photonic islands, we have fabricated arrays incorporating three, separately contacted photonic islands, [see Fig. 1]. As in the case of the double-contact structures, control of the gain distribution was achieved by adjusting the currents injected into each island. By proper adjustment of the currents, the PhCH SL can be brought to lase at mainly one SL mode where the separated islands are mutually coherent. Small

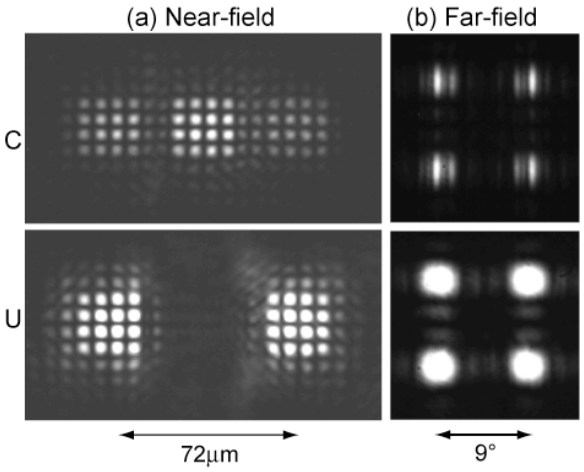


Fig. 7: Measured near (a) and far-field (b) patterns of coupled (C) and uncoupled (U) PhC SLs. I_L=690 mA, I_R=700 mA, I_M=0 mA (U) and I_M=380mA (C).

changes in the currents can break the coupling, with a subsequent significant change in the near and far-field pattern.

Figure 7 depicts the measured near and far-field patterns of the PhCH SL as it is brought in and out of coupling by adjusting the current I_C through the center island. For I_C=0 and I_L=690 mA, I_R=700 mA (pulsed conditions), the left and right islands lase independently, and the far-field pattern shows the expected four-lobe pattern due to diffraction at each island. (The light from the "sea" domain was blocked in order to increase the lobe width). For I_C= 380 mA, the center island lases as well, and each far-field lobe splits into several narrow peaks. Comparison of the measured and calculated far-field profiles, (Fig. 8), shows that lasing under these conditions is mainly on the bonding SL mode, with weaker contributions from the A and 0 SL modes.

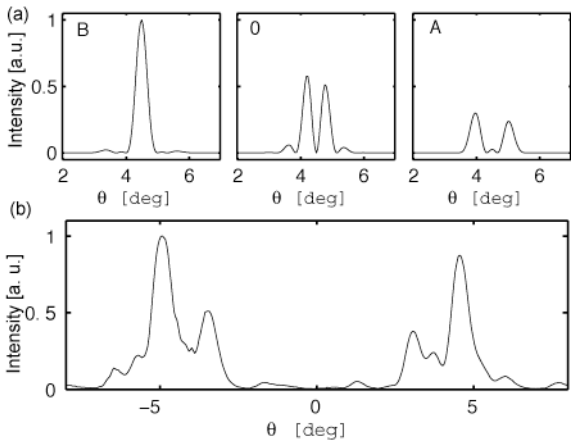


Fig. 8: (a) Calculated far-field line scans across the major lobes of the 3 lowest loss modes (B, 0, A) of Fig 4. (b) Measured line scan across the lower far-field lobes of Fig 7 in the coupled case.

Conclusion

Combining photonic envelope function confinement effects with active control of the gain distribution in VCSEL-based photonic crystal heterostructures brings about beam switching due to envelope function coupling and localization. We demonstrate coherent coupling of multiple heterostructure domains, resulting in significant modifications of the near-and far-field patterns. Controlling the envelope function modes in photonic crystal heterostructures and superlattices might be useful for applications such as optical beam steering and routing.

References

1 M. Orenstein, E. Kapon, N. G. Stoffel, J. P. Harbison, L. T. Fiorez, and J. Wullert, Appl. Phys. Lett, **58**, 804 (1991).
2 H. Pier, E. Kapon, and M. Moser, Nature **407**, 880 (2000).
3 L.J. Mawst, IEEE Circuits Devices Mag. **19**, 34 (2003)
4 M. Dabbicco, T. Maggipinto, and M. Brambilla, Appl. Phys. **86**, 021116 (2005).
5 A. Golshani, H. Pier, E. Kapon, and M. Moser, J. Appl. Phys. **85**, 2454 (1999).
6 D. L. Boiko, G. Guerrero, and E. Kapon, Optics Express, **12**, 2597 (2004).
7 C.-A. Berseth, G. Guerrero, E. Kapon, M. Moser, and R. Hövel, Conference on Lasers and Electro-Optics (CLEO), San Francisco, 7-12 May 2000, (Optical Society of America, Washington, D.C., 2000), pp 171-172.
8 G. Guerrero, D. L. Boiko, and E. Kapon, Optics Express, **12**, 4922, (2004).
9 L.D.A. Lundeberg, D.L. Boiko, and E. Kapon, Appl. Phys. Lett. **87**, 241120 (2005)

Detailed investigation of spontaneous emission decay rates of self-assembled InAs quantum dots

Toke Lund-Hansen, Jeppe Johansen, Søren Stobbe, Jørn M. Hvam, and Peter Lodahl
COM•DTU, Technical University of Denmark, Kgs. Lyngby, Denmark, toke@com.dtu.dk

Abstract
We present detailed measurements of time-resolved spontaneous emission from self-assembled InAs quantum dots (QDs). From the decay rates measured at different emission energies, we find that the decay of the QD ground state can be modelled well by Fermi's Golden Rule. This indicates a high quantum efficiency of the ground state. In contrast, the excited states are shown to have a significant non-radiative decay rate. To investigate the efficiency of the ground states quantitatively, we have furthermore measured the spontaneous emission decay rates in media where the local density of optical states (LDOS) is modified in a controlled way. Hereby the quantum efficiency and dipole moment of the QDs are determined, without introducing any adjustable parameters.

Introduction
Self-assembled QDs are highly interesting light sources for fundamental experiments in quantum optics, a candidate for scalable solid-state quantum information devices, and utilized for nanophotonics devices such as low-threshold lasers. In many applications and experiments, control of spontaneous emission from an excited emitter is central. Such control is mediated by the number of available optical modes at the position of the emitter: the LDOS. Significant recent experiments include the demonstration of strong coupling between a single QD and an optical cavity mode [1,2], and the control of spontaneous emission decay rates by the modified LDOS in a photonic crystal [3].

However, a number of fundamental properties of QDs have not yet been rigorously studied, and precise measurements of important parameters have been lacking. Thus, a detailed study of the dependence of spontaneous emission decay rate on the emission energy, and the associated interpretation of the measurements using Fermi's Golden Rule have to our knowledge not been carried out. Moreover, excitons confined in QDs can decay through non-radiative processes such as Auger emission. As the non-radiative decay rate is unaffected by a modification of the LDOS, quantum optics experiments employing a modified LDOS require a high internal quantum efficiency of the emitter, which should be measured carefully. Another key parameter is the transition dipole moment of the QDs, which determines the coupling strength between the QD and the electromagnetic vacuum field that drives spontaneous emission of light.

Here we present a series of detailed measurements of time-resolved spontaneous emission from ensembles of QDs and interpret the results using the appropriate theory. The paper is divided in three sections. Section I describes experiments on InAs QDs embedded in GaAs. We find that the ground state decay is well-described by Fermi's Golden Rule using the LDOS for a homogeneous medium. The excited states decay faster than predicted by the radiative decay rate, which shows that a significant non-radiative contribution is present. Section II describes quantitative measurements of the radiative and non-radiative decay rates, the quantum efficiency and the dipole moment of InAs QDs using samples where the LDOS is modified in a controlled way. In Section III we conclude and comment on the suitability of InAs self-assembled QDs as emitters for solid-state quantum optics experiments.

Section I: Energy dependence of the decay rates in InAs quantum dot ensembles.
QDs were grown by molecular beam epitaxy (MBE) using the Stranski-Krastranov (SK) growth technique. A suitable GaAs buffer layer was grown on a GaAs (100) substrate, followed by 1.7 monolayer of InAs grown at 594 °C. A 30 s growth interrupt was introduced in order to allow the surface to reconfigure into suitable QDs. Finally the structure was capped with 300 nm of GaAs.

The sample was cooled in a He cryostat operating down to 10 K. For excitation a mode-locked Ti:Sapphire laser with a pulse width of ~120 fs and a repetition rate of 75 MHz was used. For the measurements presented here the laser was operating at 750 nm, which corresponds to an excitation energy of 1.65 eV. The excitation beam was incident with an angle of approximately 60° relative to the sample normal, and the photoluminescence was collected perpendicular to the sample surface. Hereby scattered light from the excitation source was eliminated. All measurements presented here were ensemble measurements using an excitation spot size of 40x80 μm, thus typically probing 10^6 QDs.

The photoluminescence was collected and spatially filtered, and optionally spectrally filtered to remove multiply scattered light from the excitation source. The collected emission was dispersed by a spectrometer with a CCD for time-integrated spectra. For

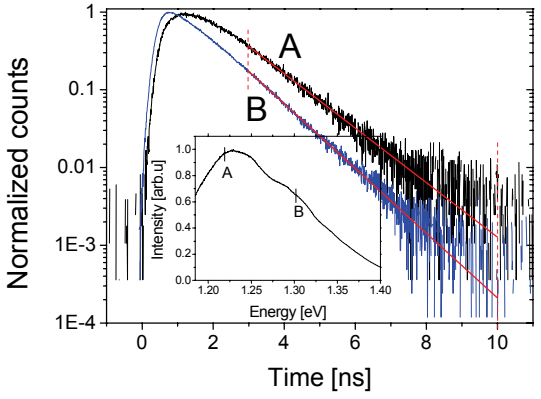


Fig. 1: Two decay curves for different QD emission energies. The specific energies are indicated in the inset, in which the full spontaneous emission spectrum is shown. Pronounced variation of the decay rate with energy is observed.

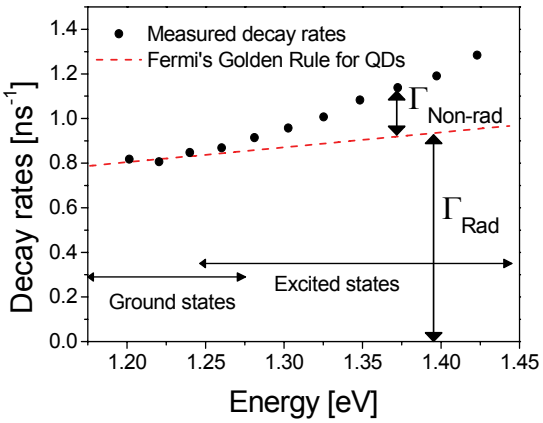


Fig. 2: The measured decay rates (solid symbols) and the theoretical rate of radiative decay (dashed line).

time-resolved measurements a second exit from the spectrometer was used, where a single photon counting avalanche photodiode (APD) was mounted. Time-resolved detection of the emitted photons was accomplished by correlating the detection of a photon in the APD with the synchronization pulse from the laser. In this way the time-delay between the excitation of the QDs and the detection of a photon can be determined. The resolution of the measurements is limited by the instrument response function, which was 300 ps (FWHM) and was limited by the time response of the APD.

Two representative spontaneous emission decay curves at fixed temperature (T=10 K) and pump density, but for two different QD energies corresponding to the ground state and excited state transitions, are shown in Fig. 1. The inset shows the full emission spectrum on which the two specific energies are indicated. We find that the decay curves are very well modelled by a single exponential decay (red solid lines in Fig. 1). This implies that the decay rate of the QDs is constant over the integration time of the measurements, and that different QDs emitting light at the same frequency also decay with the same rate. This clearly indicates the high optical quality of the QD ensemble. Furthermore, a clear difference in the decay rates for the ground state and excited state transition is observed, thus the excited state decays significantly faster than the ground state.

Fig. 2 shows the spectrally resolved decay rates measured over a broad energy range covering the inhomogeneously broadened ground state and excited state. A pronounced increase in the measured decay rate is observed with increasing emission energy. The decay of an excited QD can take place through both radiative as well as non-radiative decay channels. The radiative decay rate for a QD in a homogeneous medium can be calculated from Fermi's Golden Rule employed to an exciton in the strong confinement regime

$$\Gamma_{rad-\mathrm{hom}} = \frac{d^2 n \omega_{bulk}^2 \omega}{3\hbar\varepsilon_0 \pi c^3} \qquad (1)$$

Here d is the transition dipole moment, n the refractive index, ω_{bulk} the frequency of the band gap for the bulk semiconductor, and ω the frequency of the QD transition. The radiative decay rate is found to scale linearly with the transition frequency, as opposed to the case of an atom in vacuum where the radiative decay rate scales with the transition frequency cubed [4]. The dashed line in Fig. 2 corresponds to the theoretical values for the radiative decay calculated by Fermi's Golden Rule for a dipole moment of 1×10^{-28} C m. The ground state decay rates can be satisfactorily modelled by Fermi's Golden Rule and hence as a pure radiative decay. The steeper slope of the decay rates of the excited states cannot be accounted for using Eq. (1) as the line must intersect the origin. We therefore conclude that the excited states of the QDs have significant non-radiative decay contributions.

Section II: Radiative and non-radiative decay rates of QD ground state excitons

A quantitative study of the dynamics of spontaneous emission can be undertaken measuring decay rates of QDs in media with a modified LDOS. The simplest structure with a modified LDOS is an interface between a high-refractive material and a low-refractive material, where Fresnel reflection at the interface is responsible for the LDOS changes that can be calculated exactly. By placing QDs in different distances from an interface, the radiative and non-radiative contributions to the decay rate can be separated since only the radiative decay rate varies with distance. This provides a way of accurately measuring the quantum efficiency and transition dipole moment of QDs.

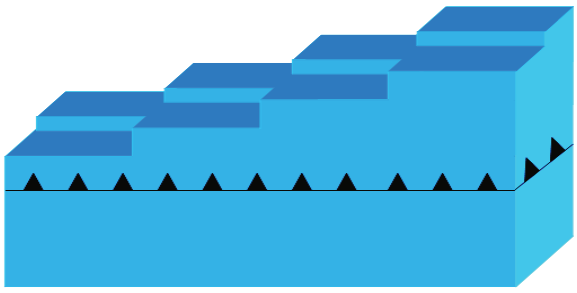


Fig. 3: Schematic layout of the investigated sample. The surface of the wafer is etched into different heights so that the QDs (black triangles) experience a different vacuum field due to the reflection at the GaAs/air interface.

We fabricated 32 samples from a GaAs wafer containing self-assembled InAs QDs grown by MBE using the SK growth mode on a (100) GaAs substrate. The growth sequence was as described in the previous section except for the InAs QD layer, which was 2.0 monolayer thick and grown at 620 °C. The wafer was processed by standard UV-lithography following five topologically orthogonal masks and wet chemical etching in order to obtain the 32 samples with varying distances from QDs to the GaAs/air interface as shown schematically in Fig. 3. For the wet etching, mixtures of H_3PO_4, H_2O_2 and DI H_2O were employed to yield smooth surfaces while keeping the etch rates low so that the step heights were ~10 nm. The etch depth was measured by a Dektak surface profiler and/or atomic force microscopy. The exact distance from the wafer surface to the QD layer was measured using secondary ion mass spectroscopy.

Due to interference between the electromagnetic field and its reflection from the air-GaAs interface the local density of optical states (LDOS) oscillates as the distance to the interface is varied. This oscillation is directly observed in the measured decay rates (Fig. 4, solid dots) as the radiative decay rate is directly proportional to the LDOS. The data shown in Figure 4 are taken at the energy corresponding to the ground state transition of the QDs. The non-radiative decay rate is unaffected by the LDOS and therefore provides a constant background in Figure 4. The measured decay rate can be expressed as

$$\Gamma_{tot}(\omega,r) = \Gamma_{rad-\mathrm{hom}}(\omega)\frac{\rho(\omega,r)}{\rho_{\mathrm{hom}}(\omega)} + \Gamma_{non-rad}(\omega), \qquad (2)$$

where $\Gamma_{\text{rad-hom}}(\omega)$ is the radiative decay rate in a homogeneous medium, $\rho(\omega,r)/\rho_{\text{hom}}(\omega)$ is the position dependent LDOS at the distance r from the interface, normalized to the LDOS in a homogeneous medium. $\Gamma_{\text{non-rad}}(\omega)$ is the non-radiative decay rate. By modelling the experimental data with the expression in Eq. (2) (Fig. 4, solid line), we deduce a radiative decay rate of $\Gamma_{\text{rad-hom}} = 0.85\pm0.08$ ns^{-1}, corresponding to a dipole moment d = 9.7x10^{-29}C m. The non-radiative decay rate is $\Gamma_{\text{non-rad}} = 0.25\pm0.08$ ns^{-1}. From these numbers we obtain the quantum efficiency for the ground state of 77%. The observed modification of

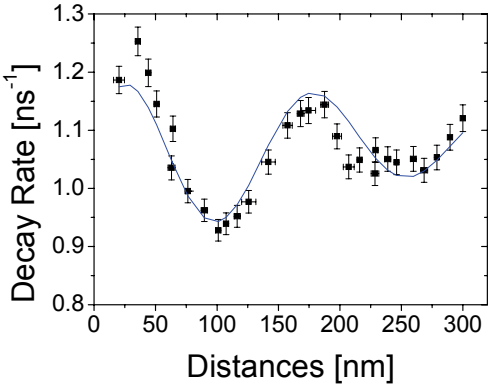


Fig. 4: Measured decay rates of spontaneous emission from QDs for different distances to the air-GaAs interface (solid dots). The solid line is the theoretical decay rate calculated using the deduced radiative and non-radiative decay rates.

the decay rates is very well described by theory assuming that the dipoles are oriented parallel to the interface. This is in agreement with results obtained from absorption measurements where the ground state is found to be primarily TE polarized [5].

Section III: Conclusion

We have presented detailed measurements of the radiative decay of self-assembled InAs QDs both as a function of emission energy and in the presence of a modified LDOS. The measurements show that the QDs decay exponentially in time indicating that there is no variation of the quantum efficiency of QDs of the same size. The energy-dependent decay rates show that the quantum efficiency of the ground states of self-assembled InAs QDs is high, whereas a significant non-radiative decay rate is found for the excited states. Furthermore, we have measured decay rates of QDs subject to a modified LDOS, which is obtained by deliberately placing the QDs at known distances to a GaAs/air interface. In this way a high quantum efficiency of 77% of the exciton ground state was measured. The dipole moment of the dots was also extracted, and the value found is in agreement with the value obtained by modelling the energy dependent decay rate of the ground states by Fermi's Golden Rule. Our detailed understanding of a simple model system provides an important fundament for future quantum optics experiments on photonic crystals and nano-cavities. Hereby a quantitative assessment of the potential of such nano-photonics structures is within reach.

References

[1] J.P. Reithmaier, G. Sek, A. Löffler, C. Hofmann, S. Kuhn, S. Reitzenstein, L.V. Keldysh, V.D. Kulakovskii, T.L. Reinecke, and A. Forchel, *Strong coupling in a single quantum dot − semiconductor microcavity system*, Nature **432**, 197 (2004).

[2] T. Yoshie, A. Scherer, J. Hendrickson, G. Khitrova, H. M. Gibbs, G. Rupper, C. Ell, O. B.

Shchekin, and D. G. Deppe, *Vacuum Rabi splitting with a single quantum dot in a photonic crystal nanocavity*, Nature, **432**, 200 (2004).
[3] P. Lodahl, A.F. van Driel, I.S. Nikolaev, A. Irman, K. Overgaag, D. Vanmaekelbergh, and W.L. Vos, *Controlling the dynamics of spontaneous emission from quantum dots by photonic crystals*, Nature **430**, 654 (2004).
[4] A.F. van Driel, G. Allan, C. Delerue, P. Lodahl, W.L. Vos, and D. Vanmaekelbergh, *Frequency-dependent spontaneous emission from CdSe and CdTe nanocrystals: Influence of dark states*, Phys. Rev. Lett. **95**, 236804 (2005).
[5] S. Cortez, O. Krebs, P. Voisin, and J.M. Gerard, *Polarization of the interband optical dipole in InAs/GaAs self-organized quantum dots*, Phys. Rev. B **63**, 233306 (2001).

Surface acoustic wave driven light modulation

Mike van der Poel (1), Markus Beck (2), Maria B. Dühring (3), Maurício M. de Lima (4), Lars H. Frandsen (1), Christophe Peucheret (1), Ole Sigmund (3), Uwe Jahn (2), Jørn M. Hvam (1), and Paulo Santos (2)
1) COM-DTU, NanoDTU, Technical University of Denmark, DK-2800 Kgs. Lyngby, Denmark 2) Paul-Drude Institut für Festkörperfysik, D-10117 Berlin, Germany, 3) Department of Mechanical Engineering, NanoDTU, Technical University of Denmark, DK-2800 Kgs. Lyngby, Denmark, 4) Material Science Institute, University of Valencia, 46071 Valencia, Spain

Abstract: *Si and GaAs Mach-Zehnder type light modulators with surface acoustic wave (SAW) excitation are demonstrated. Relative modulation depths of 40% at 950 nm and 5% at 1550 nm in the GaAs and Si samples respectively are achieved at SAW frequency around 600 MHz. Active area dimensions are down to 20 x 20 μm.*

Introduction

Compact, integrated light modulation devices are essential components in many photonic applications and have received large attention in recent years [1-4]. Of particular interest is the realization of modulation functionality in the Si material system [3-5] as this has the potential for seamless integration with electronics.

An important class of light modulators work by achieving uneven phase shifting of the light in the two arms of a Mazh-Zehnder interferometer (MZI). The change in relative phase and resulting constructive or destructive interference of the light waves at the exit port is the mechanism behind the light modulation. The principle of the phase change can be based upon shifting of the modal index of the guided wave by utilizing e.g. the thermo-optic [2], the electro-optical effect [3] or the Kerr effect [4].

In this paper we present light modulation in compact Si and GaAs [1] MZI devices with phase shifting resulting from surface acoustic wave (SAW) modulation of the waveguides.

SAW modulator

A SAW consists of a strain field propagating along the surface of a solid. The field strength decays towards the bulk with the wavelength as the characteristic decay length. The SAW field can be excited by applying an electrical RF field to an interdigital transducer (IDT) on a piezo electric material. The SAW strain field results in a periodic refractive index modulation $\Delta n \sin(\omega_{SAW} t)$ in the material, where ω_{SAW} is the SAW angular frequency. This is the primary

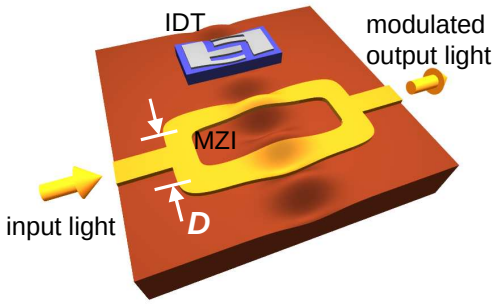


Fig. 1: Schematic representation of an MZI device with SAW modulation. Separation of the MZI arms, *D*, is an odd number of half SAW wavelenghts, so that tbhe SAW field modulates the two arms in opposite phase.

mechanism behind the optical phase change $\Delta\phi_1$ and $\Delta\phi_2$ in arm 1 and 2 of a SAW based MZI modulator respectively. For an interaction length L, the light waves of common angular frequency ω in arm 1 and 2 of the MZI undergo a harmonic phase shift of magnitude $\Delta\phi_{1,2} = \omega\Delta n_{1,2}L/c$, where c is the speed of light in vacuum. The index change is proportional to the strength of the SAW strain field and thus changes sign during a SAW cycle. We note that it follows from this, that the induced phase shift is proportional to the square root of the SAW power.

In the experiments reported here, we use a SAW propagating perpendicularly to a MZI with arm spacing D corresponding to an odd number of half SAW waves (fig. 1). In this configuration, the SAW results in a modal index variation of opposite phase in the two arms thus increasing the phase difference of the two light waves when combined at the exit port of the MZI device. Besides the acoustic phase moulation, the light field at the exit port also dependends on the static phase difference $\Delta\phi_s$ between the two interferometer arms. A path-length difference in the two arms of Δx results in a static phase difference $\Delta\phi_s = \omega n\Delta x/c$, where n is the modal index of the guided light. We write the electrical field E_{out} of the light at the exit port as

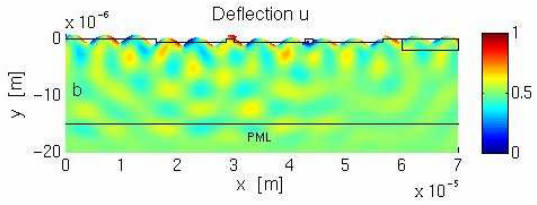


Fig. 2: SAW propagating in the MZI from the left to the right. The colorbar indicates the deflections in the x-direction.

$$E_{out} = \frac{E_0}{2}\{\sin[\omega t - \Delta\phi_1 \sin(\omega_{SAW} t)] + \sin[\omega t - \Delta\phi_2 \sin(\omega_{SAW} t - \pi/2) - \Delta\phi_s]\}, \quad (1)$$

where E_0 is the electrical field amplitude at the MZI input.

The light modulation in a MZI device as described above [1] depends strongly on the static phase difference between the two interferometer arms. For a small amplitude of the phase modulation $\Delta\phi_{1,2}$, for instance, the maximum modulation at the SAW frequency is achieved with a static phase difference $\Delta\phi_s = \pi/2$, while $\Delta\phi_s = 0$ or π results in no modulation at the SAW frequency and instead a modulation at twice the SAW frequency.

SAW modelling

To understand and improve the interaction of the SAW elastic field with the optical field in the waveguides a numerical model of the MZI is made. The SAW generation by IDTs is modeled using a 2D finite-element model of a piezoelectric, inhomogeneous material implemented in the high-level programming language 'Comsol Multiphysics'. To prevent unwanted reflections of the SAW from the boundaries of the calculation domain perfectly matched layers [6] are employed to absorb the elastic and electric field at the sides and at the bottom of the domain. The solution of this model gives the stresses in the material introduced by the SAW, from which the associated change in refractive index in the two wave guides can be calculated. This model is successively coupled to an optical model where the time independent wave equation is solved as an eigenvalue problem giving the effective refractive index of the fundamental mode in the waveguides.

With this numerical model the propagation of the SAW in the MZI can be studied. In fig. 2, a SAW is generated at the left part of the surface and propagating in the right direction through a GaAs MZI. It is observed that a part of the SAW propagates through the MZI and another part is redirected into the bulk substrate because of the disturbance at the surface caused by the wave guides. Figure 3 shows the

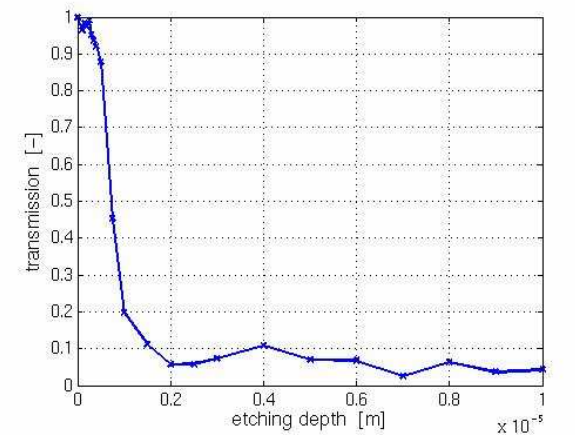


Fig. 3: The transmission of the SAW as function of the etching depth.

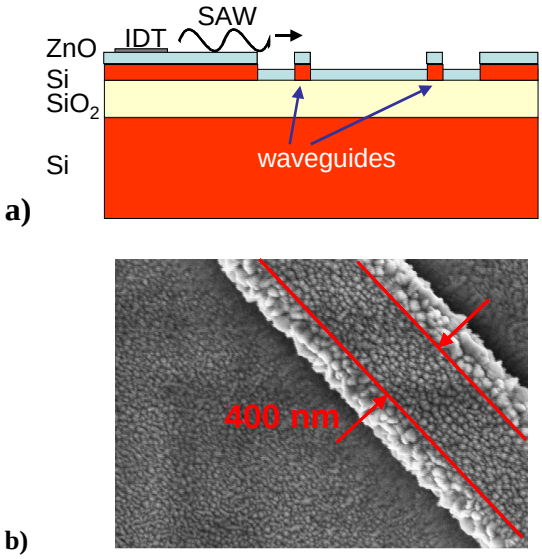


Fig. 4: a) Schematic edge view of SOI wafer with waveguides. b) SEM micrograph with top view of 400 nm ridge waveguide covered with ZnO.

transmission of the SAW (calculated as the part of the deflections in the x-direction that reaches the marked rectangle in the right corner of the domain in fig. 1) as function of the etching depth. It is seen that for small etching depths almost the entire SAW is transmitted, but for larger depths most of the SAW energy will be reflected back or disappear into the bulk substrate.

This model can be used to simulate the acousto-optical interaction in the MZI from the experiments and by a parameter study of the geometry it can be determined how the geometry should be changed in order to improve the optical modulation.

Devices

Devices based upon the Si and GaAs material system have been fabricated.

The GaAs MZI devices were fabricated on a (Al,Ga)As waveguide structure grown by molecular beam epitaxy on a GaAs (100) wafer. The waveguide core consists of a 300-nm-thick GaAs core grown on a 1500-nm-thick $Al_{0.2}Ga_{0.8}As$ cladding layer. The acoustic waves were generated by a split-finger IDT with an aperture of 120 µm and operating at an acoustic wavelength λ_{SAW}=5.6 µm. The waveguides were fabricated by combining contact optical lithography with plasma etching. Further details of the fabrication process can be found in Ref. [1].

The Si based samples were made on a Si-on-insulator (SOI) wafer with a top 340 nm thick Si layer. 400 nm wide single-mode ridge waveguides were defined by electron-beam lithography (fig. 4a). Si itself is not a piezo electrical material: for the electric SAW excitation, the sample is covered with a 500 nm layer of piezoelectric ZnO before IDT deposition. Scanning electron microscopy (SEM) of the sample after ZnO deposition (fig. 4b) shows a corrugated surface with ZnO crystallites grown from all surfaces. This is ex-

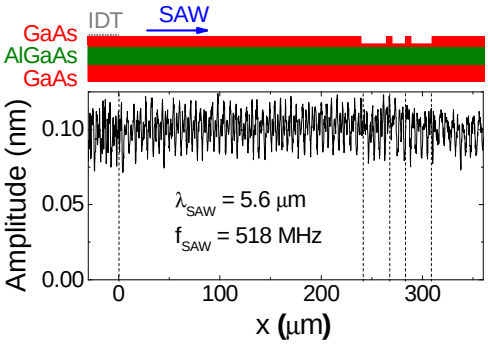


Fig. 5: Transmission of a SAW across the GaAs MZI structure.

pected to lead to the undesirable effect of increased 1) optical waveguide losses and 2) scattering of the SAW wave at Si etch steps. The former is discussed in a section below. To investigate the latter, we perform interferometric measurements of sample surface displacement. Fig. 5 shows interferometric measurements of the amplitude of the acoustic wave normal to the surface in similar structures on a GaAs/AlGaAs sample. Consistent with the calculations discussed above, the reflections of the wave at the grooves and ridges of the structure are small. In the SOI structures, we observe considerably stronger reflections.

Modulation experiments

The optical properties of the GaAs MZI devices were measured by coupling light to the cleaved edge of the waveguides using a tapered fiber and collecting the transmitted light using a microscope objective. As a light source, we used a CW superluminescence diode with peak emission at 950 nm and full width of half maximum of approx. 50 nm. The transmitted intensity was detected with a time resolution of 300 ps using a Si avalanche photodiode. Fig. 6 compares the time dependence of the transmitted intensity (normal-

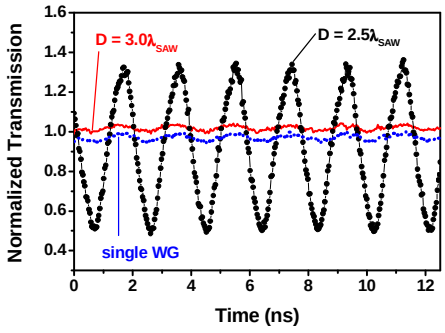


Fig. 6: Transmission of MZI devices with waveguide separation D = 3 λ_{SAW} (solid line) and 2.5 λ_{SAW} (dots). The dotted line shows the transmission in a control structure where the MZI arms have been replaced by a single waveguide. All measurements were carried out by coupling an RF-power P_{IDT}=60 mW to the IDTs.

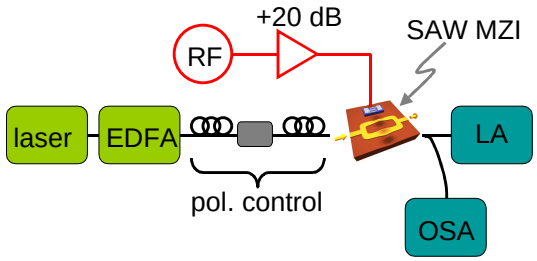


Fig.7: Experimental setup for characterizing SOI modulator.

ized to the transmission in the absence of acoustic excitation) of devices with distances *D* between the MZI arms of 3 λ_{SAW} (solid line) and 2.5 λ_{SAW} (dots). All measurements were carried out by coupling an rf-power P_{IDT}=60 mW to the IDTs. For the devices with 3 λ_{SAW}, as well as in control structures where the MZI arms have been replaced by a single waveguide (dotted line in fig. 6), the relative modulation does not exceed 2 %. In devices with D = 2.5 $\lambda_{SAW,}$ where the MZI arms are excited with opposite acoustic phases, the relative modulation reaches 40 %. These results demonstrate the large modulation performance achieved by the simultaneous out-of-phase modulation of the MZI arms. By employing focusing IDTs, we were able to further increase the performance and to reduce the length of the MZI arms down to approx. 15 µm. [1].

The experimental setup of the modulation experiments carried out on the SOI devices can be summarized as follows (fig. 7): A fiber-coupled, tunable CW laser and Er doped fiber amplifier (EDFA) was used as light source in the wavelength range 1530-1580 nm. A polarization controller was used to achieve transverse-electric (TE) polarized light before using a tapered fiber to couple the light into the MZI device under test. Modulation properties of the light output from the MZI were then analyzed using a lightwave analyzer (LA).

The MZI were deliberately made with a path length difference in the two interferometer arms of 34 µm so as to have a wavelength-dependent static phase

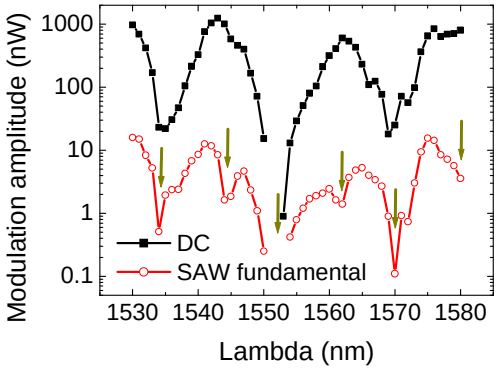


Fig. 8: Transmission (black line, filled symbols) and modulation (red line, open symbols) spectrum of SOI MZI with arm separation of *D*=4.5λ_{SAW}. RF power to IDTs P_{RF}= 50 mW.

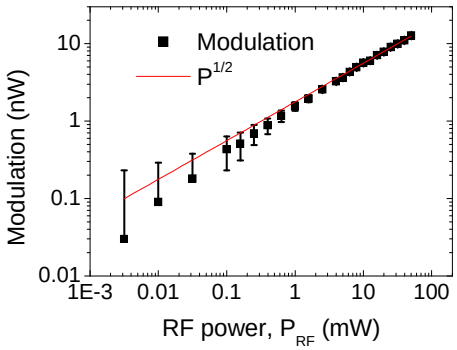


Fig. 9: Modulationamplitude at SAW frequency vs. RF power to the IDT, P_{RF}.

$\Delta\phi_s = \omega n \Delta x/c$ as mentioned above. This results in a sinusoidally varying DC transmission spectrum of the device (fig. 8). The overall transmission of the device at constructive interference at the exit port was about –20 dB. This poor performance is primarily ascribed to the two T-splitters in the MZI. These topology-optimized ridge-waveguide splitters [7] were designed without ZnO coverage in mind. We also believe that the deviations from a sinusoidal transmission spectrum are due to the T-splitters.

The MZI had an arm separation of D=4.5λ_{SAW} corresponding to an out-of-phase phase-change in the two interferometer arms when SAW modulation is applied to the device. It follows from eq. 1 that the modulation spectrum at the SAW frequency will display minima at both the DC transmission maxima and minima in agreement with fig. 8 (minima marked with arrows). Furthermore it is concluded from eq. 1, that the observed modulation at the SAW fundamental frequency is consistent with a refractive change of 2.3×10^{-5}. This value is also consistent with the absence of measurable higher harmonics in the modulated light at all wavelengths. The relative modulation in the investigated wavelength range varied from 0% to 8%. Finally, we mention that the modulation amplitude vs. RF power was measured, and a reasonable agreement with the expected $P_{SAW}^{1/2}$ dependency, as demonstrated in fig. 9.

Conclusion

SAW-driven MZI is a promising technology for compact light modulators in integrated semiconductor platforms such as Si and GaAs.

Acknowledgments

This project is supported by the EU network of excellence ePIXnet. Mike van der Poel acknowledges support from the Danish Research Council.

References

1 M. M. de Lima, Jr., M. Beck, R. Hey, and P. V. Santos, Appl. Phys. Lett., vol. 89, p. 121104, 2006.
2 E. A. Camargo, H. M. H. Chong, and R. M. De La Rue, Opt. Express, vol. 12, p. 588, 2004.
3 R. S. Jacobsen et al., Nature, vol. 44, p. 199, 2006.
4 M. Hochberg et al., Nature Mater., vol. 5, p. 703, 2006.
5 M. Lipson, J. Lightwave Techn., vol. 23, p. 4222, 2005.
6 U. Basu and A. K. Chopra,, Comput. Methods Appl. Mech. Engrg., vol. 192, p. 1337 (2003).
7 L. H. Frandsen, paper CMV4, Conference of Lasers and Electro-Optics (CLEO), 2006.

Different-Guided-Mode-Coupling DBR for WDM Optical Interconnection Board Using Channel Waveguides

Kenji Kintaka (1), Junji Nishii (1), Satoshi Yamaguchi (2), Takayuki Kobayashi (2) and Shogo Ura (2)
1) National Institute of Advanced Industrial Science and Technology, Osaka 563-8577 JAPAN, kintaka.kenji@aist.go.jp
2) Kyoto Institute of Technology, Kyoto 606-8585 JAPAN, ura@kit.ac.jp

Abstract: *A distributed Bragg reflector (DBR) coupling TE_0 and TE_1 guided modes was designed and fabricated for constructing an intra-board chip-to-chip optical interconnection with wavelength-division multiplexing. Coupling efficiency of 97% and wavelength selectivity of 2 nm were predicted for interaction length of 0.3 mm. Preliminary experimental results were also reported.*

Introduction

Intra-board chip-to-chip optical interconnection is one of strong candidates for solving the so-called pin-bottleneck problem in constructing future ultra-high-speed signal-processing units [1]. Recently, optical interconnect configurations using multimode waveguides as optical signal paths have been investigated extensively because of their high compatibility with printed circuit boards and large fabrication tolerance with low insertion loss [2-7]. As another approach, optical interconnect configurations using free space as optical signal path have been proposed and demonstrated in order to realize two-dimensional (2-D) parallel transmission of optical signals from a 2-D array of vertical cavity surface emitting lasers (VCSELs) to a 2-D array of photodiodes (PDs) so far [8-12]. Most of these techniques have utilized micro-optic components such as micro-mirrors and micro-prisms.

On the other hand, we have proposed and investigated an integrated-optic configuration using a thin-film waveguide as optical signal paths [13-20]. The integrated-optic configuration utilizes wavelength-division multiplexing (WDM) technique with free-space-wave add-drop multiplexers consisting of focusing grating couplers (FGCs) and distributed Bragg reflectors (DBRs). The proposed configuration has advantage in compatibility with printed circuit boards, compactness, and 2-D parallel signal transmission. However, the width of each guided wave should be determined by waveguide length, namely, signal transmission length, due to diffraction. Therefore, wiring density is limited down to several channels per millimeter for 10-mm transmission length.

In order to improve the wiring density, we have proposed and investigated a new integrated-optic configuration using channel waveguides [21, 22]. The proposed interconnection device consists of vertically Y-branched mode splitters/combiners and different-guided-mode-coupling (DGM) DBRs which couple fundamental and 1st-order modes contra-directionally in order to realize wavelength add-drop multiplexing. The new configuration can have higher wiring density and larger tolerances in input coupling than our previous configuration. In this paper, we report design, fabrication and characterization of a proto-type 2-D DGM-DBR for the first time.

Configuration of intra-board optical interconnection

Cross-sectional configuration of a single waveguide channel of the proposed optical interconnection is illustrated in Fig. 1. Only two WDM signal channels are shown for simplicity. Optoelectronic interposers integrating VCSELs or PDs are surface-mounted with LSI chips on a board. The optical interconnect device in the board consists of two vertically stacked waveguides with different refractive indices. Add/drop and transmission cores are contacted in multiplexing region, while they are separated by a splitting layer in input/output region. The multiplexing and input/output regions are connected with vertical Y-branch region. Both waveguides can guide only fundamental mode in the input/output region. Fundamental TE-like mode of signal transmission waveguide (E_{00}^{T} mode) in input/output region is coupled to fundamental TE-like (E_{00}^{M}) mode in the multiplexing region, and fundamental TE-like mode of add/drop waveguide ($E_{00}^{A/D}$ mode) in input/output region is coupled to 1st-order TE-like (E_{01}^{M}) mode in the multiplexing region. DGM-DBRs are integrated

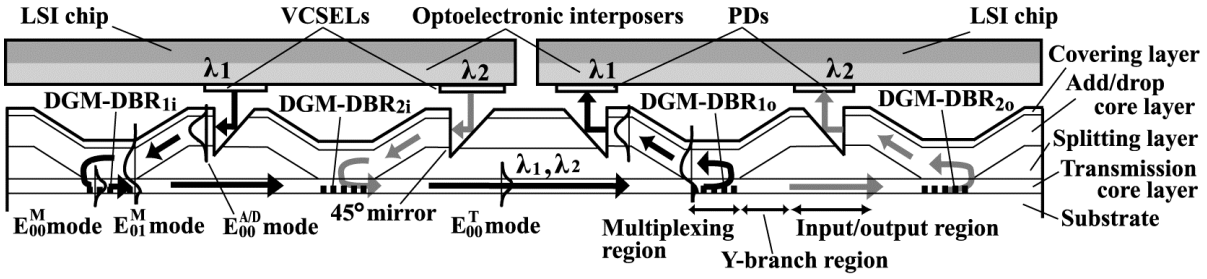


Fig. 1: Schematic view of the optical interconnect configuration

for contra-directionally coupling of E_{00}^{M} and E_{01}^{M} modes in the multiplexing region. 45° mirrors are integrated in the input/output regions for input/output coupling of free-space and $E_{00}^{A/D}$ guided waves.

A free-space wave of wavelength λ_1 from a VCSEL is coupled to $E_{00}^{A/D}$ mode by a 45° mirror. The $E_{00}^{A/D}$ mode passes through an add/drop waveguide and an upper branch in Y-branch, and becomes E_{01}^{M} mode in the multiplexing region. The E_{01}^{M} mode is contra-directionally coupled to E_{00}^{M} mode by DGM-DBR_{1i}. The E_{00}^{M} mode propagates in a lower branch in Y-branch and signal transmission waveguide as E_{00}^{T} mode, and passes through DGM-DBR_{2i}. The propagated E_{00}^{T} mode becomes E_{00}^{M} mode, and is contra-directionally coupled to E_{01}^{M} mode by DGM-DBR_{1o}. The E_{01}^{M} mode passes through an upper branch in Y branch and propagates in an add/drop waveguide as $E_{00}^{A/D}$ mode. The $E_{00}^{A/D}$ mode is coupled out to a free-space wave, and reflected to a PD by a 45° mirror. In the same way, a free-space wave of wavelength λ_2 from another VCSEL is transmitted and detected by another PD.

Design of 2-D DGM-DBR

We designed a 2-D DGM-DBR at operating wavelength of 850-nm band. Figure 2 illustrates a cross-sectional structure and a refractive index profile of the designed 2-D waveguide. The thickness and refractive index of add/drop core layer were set to 4 μm and 1.47, respectively, so that the guided-mode profile coincides to beam profile from a single-mode VCSEL. The thickness and refractive index of transmission core layer were set to 0.8 μm and 1.54, respectively. DBR grating was formed by patterning Si-N layer of refractive index of 2.01 and embedded in the bottom of the transmission core layer. The thickness and refractive index of covering layer were set to 1 μm and 1.46, respectively.

The device characteristics were calculated by conventional coupled-mode analysis. Calculated mode profiles of TE_0^M and TE_1^M modes are also shown in Fig. 2. A coupling coefficient of DGM-DBR between TE_0^M and TE_1^M modes was calculated to be 8.3 mm^{-1} with grating groove depth of 0.03 μm. Figure 3 shows the calculated wavelength dependence of coupling efficiency for interaction length of 0.3 mm. A maximum coupling efficiency and full-width at half maximum (FWHM) wavelength-selectivity were calculated to be 97% and 2 nm, respectively. The period Λ of DGM-DBR is given by,

$$\Lambda = \lambda/(N_0^M+N_1^M), \qquad (1)$$

where λ is the coupling wavelength, N_0^M and N_1^M are effective refractive indices of TE_0^M and TE_1^M modes, respectively. The effective refractive indices of TE_0^M and TE_1^M modes were calculated to be 1.515 and 1.468, respectively, in the grating area. The grating period was calculated to be 283.27 nm for operating wavelength of 845 nm.

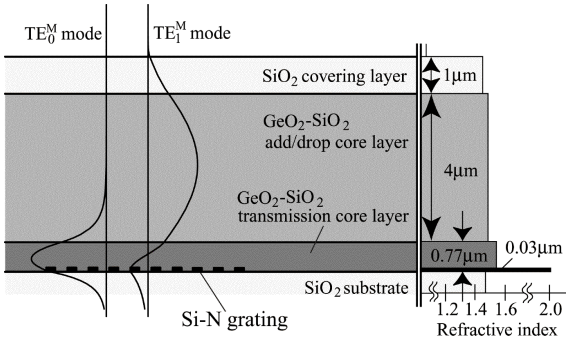


Fig. 2: Cross-sectional structure and refractive index profile of the designed DGM-DBR

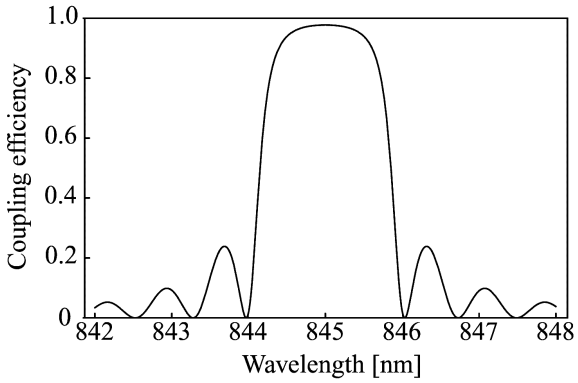


Fig. 3: Calculated wavelength dependence of coupling efficiency

Fabrication

A fabrication process is illustrated in Fig. 4. An election-beam (EB) resist of 0.4-μm thickness was spin-coated on a SiO_2 substrate, and DGM-DBR area of 0.3 mm × 0.5 mm was patterned by EB direct writing and developing. A Si-N film with thickness of 30 nm and refractive index of 2.01 was deposited by reactive DC sputtering followed by lift-off. An EB resist of 0.3-μm thickness was spin-coated, and DGM-DBR pattern with 283.27-nm period was written by EB direct writing. After developing, the grating pattern was transferred to the Si-N film by reactive ion etching (RIE) using C_3F_8 gas. Figure 5 shows an optical microscopic and a scanning electron microscope (SEM) photographs of the fabricated Si-N grating.

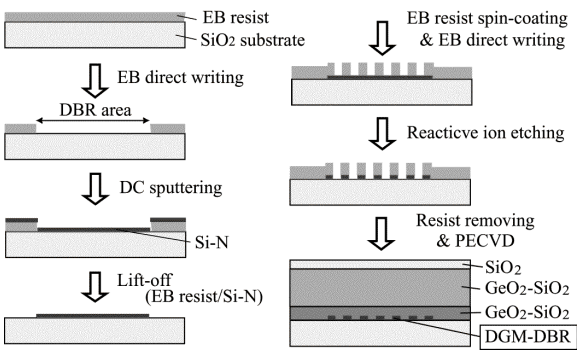


Fig. 4: Fabrication process

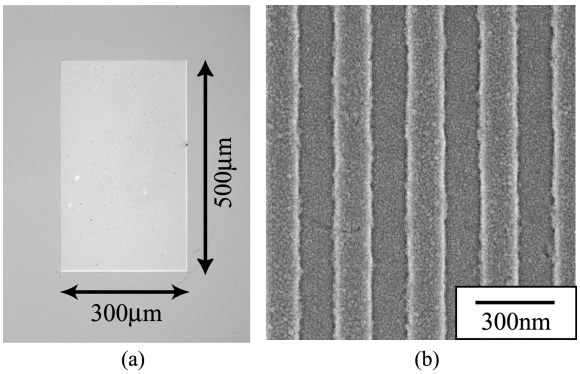


Fig. 5: Microscopic photographs of the fabricated Si-N grating; (a) the whole and (b) part

The grating with line/space ratio of 1:1 could be obtained. A GeO_2-SiO_2 transmission core layer with refractive index of 1.54 and thickness of 0.8 μm, a GeO_2-SiO_2 add/drop core layer with refractive index of 1.47 and thickness of 4.0 μm, and a SiO_2 covering layer with refractive index of 1.46 and thickness of 0.5 μm were sequentially deposited by plasma-enhanced chemical vapor deposition (PECVD) using $Si(OC_2H_5)_4$ and $Ge(OCH_3)_4$ as precursors. A grating coupler (GC) of 1.3-μm period, 0.3-μm depth, and 0.5 mm × 0.3 mm aperture was fabricated by EB direct writing and RIE for exciting TE_1^M mode in the waveguide. The reason why the thickness of the covering layer was thinner than the designed value was that the TE_1^M mode was excited by the GC with high efficiency. The waveguide ends were fabricated by cleaving after notching backside surface of the substrate. The distance between the GC and DGM-DBR was 10 mm, and the distances between the DGM-DBR and waveguide ends were 20 mm both.

Experimental results

A experimental setup is illustrated in Fig. 6. A tunable laser diode (LD) was used as a light source, and TE_1^M mode was excited in the waveguide by the GC. Effective refractive index of TE_1^M mode in the GC area was measured to be 1.462 from the incidence angle. Transmitted power as TE_1^M mode and reflected power as TE_0^M mode were measured at waveguide ends by optical power meter through an objective lens. Figure 7 shows the measured wavelength dependence of the transmitted and reflected power. Open and solid circles show output power of transmitted (TE_1^M) and reflected (TE_0^M) modes, respectively. A maximum efficiency of 51% was obtained

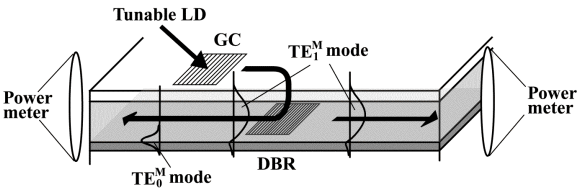


Fig. 6: Experimental setup

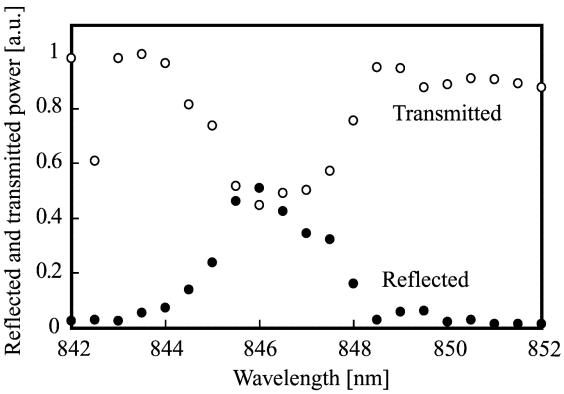


Fig. 7: Wavelength dependence of the fabricated DGM-DBR

at wavelength of 846 nm. FWHM of wavelength selectivity was measured to be 3 nm. The discrepancy between the predicted and measured values in coupling wavelength would be caused primarily by fabrication errors in refractive index and thickness of the fabricated waveguide. The reason for lower reflection efficiency and wider FWHM of wavelength selectivity than the predicted values are currently under study.

Conclusions

We designed and fabricated a DGM-DBR which couples TE_0^M and TE_1^M modes contra-directionally. Coupling efficiency and wavelength selectivity were theoretically predicted to be 97% and 2 nm, respectively, with interaction length of 0.3 mm at wavelength of 850 nm. Wavelength selectivity of the fabricated DGM-DBR was confirmed experimentally, and the maximum coupling efficiency of 51% was obtained. Experimental work is being continued to improve the coupling efficiency and wavelength selectivity. Application of the DGM-DBR to the proposed add-drop multiplexers is also investigated in order to construct the proposed WDM optical interconnection.

References

1 N. Savage, IEEE Spectrum, vol. 39, p. 32, 2002.
2 H. Takahara, IEEE J. Select. Topics. Quantum. Electron., vol. 9, p. 443, 2003.
3 L. Schares *et al.*, IEEE J. Sel. Top. Quantum Electron., vol. 12, p. 1032, 2006.
4 M. Karppinen *et al.*, ECTC, Paper 18-7, 2006.
5 H. Schröder et al., ECTC, p. 1053, 2003.
6 C. Berger *et al.*, Proc. SPIE, vol. 4942, p. 222, 2003.
7 S. Hiramatsu *et al.* : J. Lightwave Technol. vol. 24, p. 927, 2006.
8 S. Voigt *et al.*, IEEE Photon. Technol. Lett., vol. 14, p. 1484, 2002.
9 M. Chateauneuf *et al.*, Appl. Opt., vol. 43, p. 463, 2004.
10 C. Debaes *et al.*, IEEE J. Sel. Top. Quantum.

Electron., vol. 9, p. 518, 2003.
11 H. Sasaki *et al.*, Appl. Opt., vol. 40, p. 1843, 2001.
12 M. Gruber, Appl. Opt., vol. 43, p. 463, 2004.
13 S. Ura, Proc. SPIE, vol. 4652, p. 86, 2002.
14 K. Kintaka *et al.*, IEEE Photon. Technol. Lett., vol. 16, p. 512, 2004.
15 K. Kintaka *et al.*, Optics Express, vol. 12, p. 3072, 2004.
16 J. Ohmori *et al.*, Jpn. J. Appl. Phys., vol. 44, p. 7987, 2005.
17 S. Ura *et al.*, Appl. Opt., vol. 45, p. 22, 2006.
18 S. Ura *et al.*, Optics Express, vol 14, p. 7057, 2006.
19 A. Horii *et al.*, CLEO-PR, Paper CWK1-4, 2005.
20 K. Kintaka *et al.*, IEEE Photonics Technol. Lett., vol. 18, p. 2299, 2006.
21 K. Kintaka *et al.*, ODF, Paper 7S2-04, 2006.
22 S. Yamaguchi *et al.*, MOC, Paper F-5, 2006.

SOI grating structure for perfectly vertical fiber coupling

Günther Roelkens (1), Dries Van Thourhout (2), Roel Baets (3)
1) Photonics Research Group, Ghent University-IMEC, Sint-Pietersnieuwstraat 41, B-9000 Ghent,
gunther.roelkens@intec.ugent.be
2) Photonics Research Group, Ghent University-IMEC, Sint-Pietersnieuwstraat 41, B-9000 Ghent,
dries.vanthourhout@intec.ugent.be
3) Photonics Research Group, Ghent University-IMEC, Sint-Pietersnieuwstraat 41, B-9000 Ghent,
roel.baets@intec.ugent.be

Abstract: *We present the design of a grating coupler structure allowing efficient coupling to a perfectly vertically positioned single mode fiber. This design no longer implies tilting of the fiber to avoid a large second order reflection, reducing the cost of packaging. By incorporating a slight asymmetry in the grating structure design, a grating fiber coupling efficiency of 50% to single mode fiber and 65% to high numerical aperture fiber can be obtained, with a 3dB bandwidth of 55nm. Constraints in the design are related to the manufacturability using 248nm deep UV lithography. The fabrication tolerance of the device is assessed, which is compatible with the state-of-the-art Silicon processing techniques.*

Introduction

Silicon-on-Insulator (SOI) is emerging as the platform for large scale integration of optical functions due the high omni-directional refractive index contrast between the Silicon core (n_{Si}=3.476) and the SiO_2 cladding (n_{SiO2}=1.447). Moreover, standard CMOS technology can be used to fabricate these photonic integrated circuits, increasing the reproducibility and yield, and lowering the cost of fabrication due to the economy of scale [1]. An inherent drawback of the high omni-directional refractive index contrast is however the large mismatch in mode size between the SOI waveguide and the single mode fiber, making efficient optical coupling to the photonic integrated circuit a non-trivial task. A promising approach is the use of a grating structure to couple the light from a single mode fiber into the photonic integrated circuit. This approach allows wafer scale testing of the integrated circuit as no polished facet is required for coupling [2]. Although one-dimensional grating structures behave very differently for TE and TM polarization, two-dimensional grating structures can be used to tackle this problem by using a polarization diversity approach [3]. Several grating designs are described in literature, both based on vertically etched slits in the Silicon waveguide layer [2] as on slanted grating structures [4]. While the latter directly enable the use of a perfectly vertically oriented optical fiber, the definition of the angled slits is not compatible with standard CMOS processing. Recently, we showed that high coupling efficiency to optical fiber can be obtained using vertically etched slits by optimizing the grating design [5]. A uniform grating structure exhibiting a fiber coupling efficiency of 66% was designed, while using a non-uniform grating structure 78% coupling efficiency could be obtained. The coupling efficiency was in this case dramatically improved by locally adding a Silicon epitaxial layer on top of the 220nm thick single mode Silicon waveguide layer prior to grating etching. However, these designs relied on slightly tilting the optical fiber with respect to the vertical axis (typically 10 degrees off vertical). This was required to avoid a large second order Bragg reflection back into the SOI waveguide in the case of perfectly vertical coupling, which dramatically reduces the fiber coupling efficiency. This can also be understood from symmetry considerations, as equal coupling efficiency in both exit waveguides of the grating structure is obtained when perfectly vertically illuminating a uniform grating structure, resulting in an absolute maximal fiber coupling efficiency of 50%. The requirement of the slight tilting of the optical fiber has important consequences for practical applications, which would require angled polishing of the fiber ferrule and mounting of the ferrule under an angle with respect to the photonic integrated circuit normal direction [6]. In order to avoid this costly complication in the packaging of the photonic integrated circuit, the possibility for perfectly vertical coupling in an efficient way is assessed here, by designing an asymmetric grating structure in order to avoid the large second order Bragg reflection. The grating structure can be made asymmetric by tailoring the width and pitch of the individual grating teeth. This is however not interesting from a fabrication point of view, as the practical realization of these type of structures is hampered by the different etch rate for slits with a different width and optical proximity effects in the lithographic definition of the non-uniform grating structure. In this paper, we will combine the previously mentioned approach of locally adding a Silicon epitaxial layer to improve the fiber coupling efficiency and incorporating an asymmetry in the grating coupler structure to avoid the large second order Bragg reflection, while maintaining a uniform grating structure in which all slits are identical in width and etch depth.

Proposed device structure

The structure we propose to allow efficient vertical fiber coupling is schematically depicted in figure 1. A 220nm Silicon waveguide core layer on top of a 2μm buried SiO_2 layer is assumed. Locally, a Silicon epitaxial layer of thickness *t* is grown in order to in-

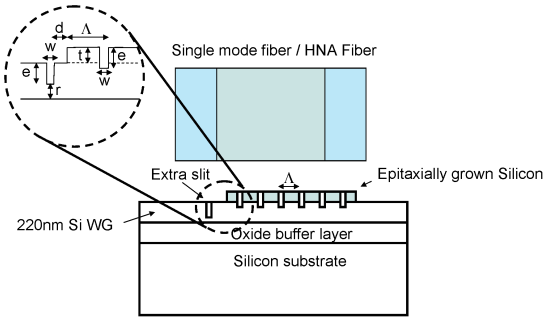


Fig. 1: Layout of the proposed fiber coupler structure together with a definition of the different parameters of the design

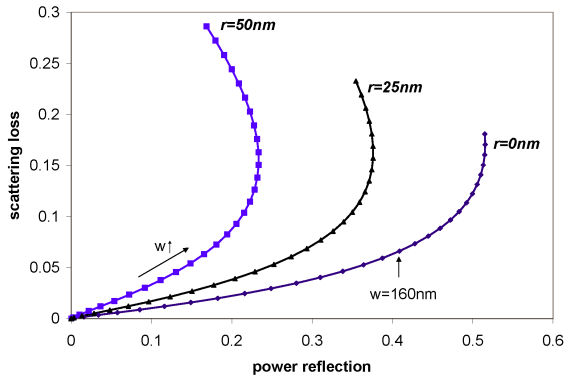


Fig. 2: Scattering loss of a single slit in a 220nm SOI waveguide as a function of the power reflection for various slit widths and etch depths

crease the directionality of the grating (being the ratio of the upwards diffracted optical power to the total diffracted power) as explained in [5]. The asymmetry in the grating structure is created by etching one additional slit in the 220nm thick Silicon waveguide layer instead of in the thicker epitaxial layer stack. This slit will function as a partially reflecting mirror to achieve destructive interference of the second order Bragg reflection from the uniform grating structure.

Optimization of the device structure

The grating structure was optimized using CAMFR [7], a two-dimensional fully vectorial eigenmode expansion tool. A wavelength of 1.55µm and TE polarization is assumed. As mentioned before, these grating structures are very polarization dependent, a problem that can be circumvented using a two-dimensional grating for polarization diversity operation [3]. Therefore, we will only discuss the results for TE polarization here. An analogous approach can be followed for two-dimensional grating structures. The behaviour of the etched slit in the 220nm thick Silicon waveguide layer as a partially reflecting mirror was assessed by calculating power reflection and scattered optical power as a function of the slit etch depth, using the slit width w as a parameter. Results are shown in figure 2 for three different etch depths, corresponding to r=0 (etched through the Silicon waveguide layer), r=25nm and r=50nm. From this simulation it is clear that the completely etched

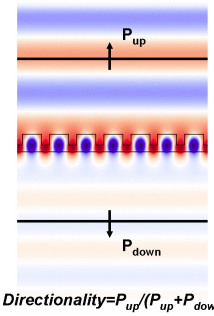


Fig. 3: Electric field of the vertically leaky Bloch mode with optimized directionality

through slit offers the largest reflection for a given acceptable scattering loss. Therefore, in the subsequent analysis, the slit is assumed to be etched completely through the 220nm Silicon waveguide layer. This assumption also fixes the slit etch depth in the uniform grating structure to 220nm, for ease of fabrication as explained above. In order to keep the scattering losses low while maintaining a sufficient reflection, the minimum definable slit width using 248nm deep UV lithography of 160nm was chosen for the design. This then also fixes the slit width w of the diffractive grating structure in the thick Silicon layer stack to 160nm. In a second step of the optimization, the thickness of the epitaxially grown Silicon t and the period of the grating structure Λ were optimized to achieve diffraction in the vertical direction at 1.55µm while maximizing the directionality (the ratio of upwards diffracted optical power to the total diffracted power) of the grating at this wavelength. This can be done by evaluating the Bloch modes at the Γ-point supported by the periodic grating structure and assessing the directionality of these leaky modes. Optimal directionality and vertical coupling at 1.55µm was obtained for a Silicon epitaxial layer thickness t of 150nm and a grating period Λ of 560nm. The electric field of this TE Bloch mode is plotted in figure 3. The directionality of the optimized grating structure is higher than 80%. In order to appreciate the influence of the additional slit on the fiber coupling efficiency, the symmetric grating structure without the additional slit was simulated first. The fundamental TE mode at 1.55µm was launched in the SOI waveguide and the scattering by the grating structure was evaluated. In order to obtain the coupling efficiency to a single mode optical fiber, the electric field $\mathbf{E}_{scat}$ at a certain distance above the grating structure was evaluated and the overlap integral of $\mathbf{E}_{scat}$ and a Gaussian beam, with its mode field diameter ($1/e^2$ intensity width) as a parameter, was evaluated. This was done for various center positions of the Gaussian beam profile, thereby obtaining the optimal position of the optical fiber, the optimal mode field diameter and the maximum achievable fiber coupling efficiency. For the uniform grating structure without the additional slit and the parameters mentioned above, a fiber coupling efficiency of 33% and 26% is obtained for a mode field diameter

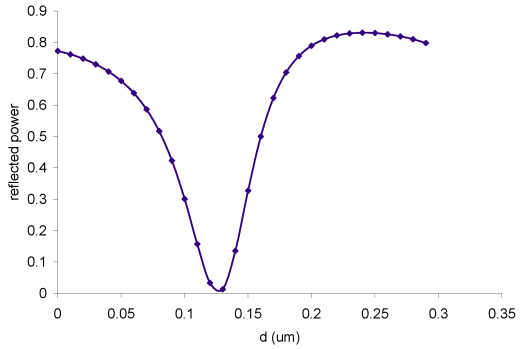


Fig. 4: Influence of the extra slit distance *d* on the power reflection in the SOI waveguide

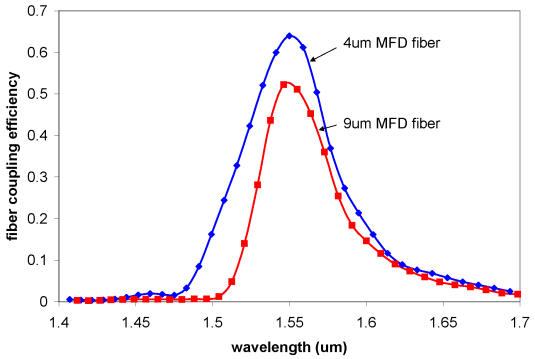


Fig. 5: Optimized fiber coupling efficiency as a function of wavelength for a 4µm and 9µm mode field diameter fiber

of 4µm and 9µm respectively. Reduced mode field-diameters can be obtained by splicing a high numerical aperture fiber to a single mode fiber with low optical loss at the splice [8]. This low coupling efficiency is, as mentioned above, due to the large second order Bragg reflection (55% in this case). In order to achieve destructive interference of this reflection in the proposed design, the distance *d* between the slit and the edge of the thickened layer stack needs to be optimized. The power reflection as a function of the distance *d*, for the parameters mentioned above, is plotted in figure 4. This simulation shows that nearly perfect destructive interference can be obtained by choosing an optimal distance *d* of 0.13µm. Using this optimal set of parameters, the coupling efficiency can be reassessed. The wavelength dependence of the fiber coupling efficiency is plotted in figure 5 for the case of a 4µm and 9µm mode field diameter fiber, showing that a fiber coupling efficiency of 65% and 50% can be obtained respectively, with a 3dB bandwidth of approximately 55nm, while the 1dB bandwidth is about 35nm. This implies a 3dB improvement in coupling efficiency over the symmetric grating structure. A field plot of the optimized structure, when illuminated by the 4µm diameter high numerical aperture fiber is shown in figure 6.

Fabrication tolerance analysis

In order to assess the manufacturability of the device using standard 248nm deep UV lithography, the

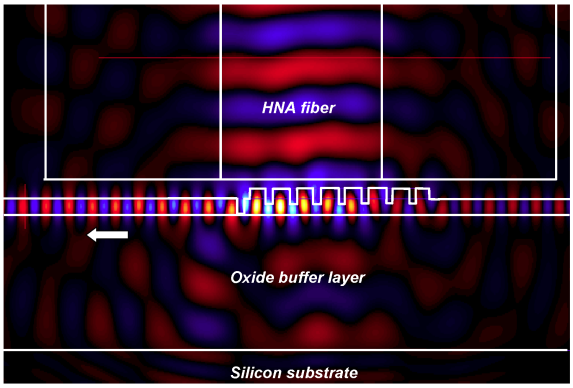


Fig. 6: Electric field plot of the optimized structure for a 4µm mode field diameter fiber

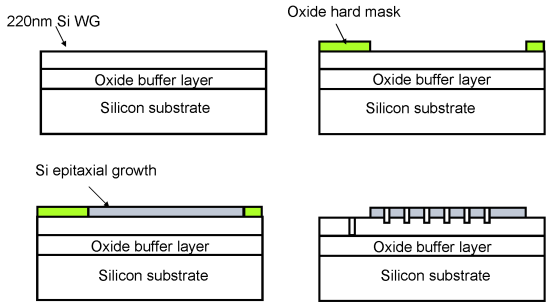


Fig. 7: Proposed processing sequence for the device

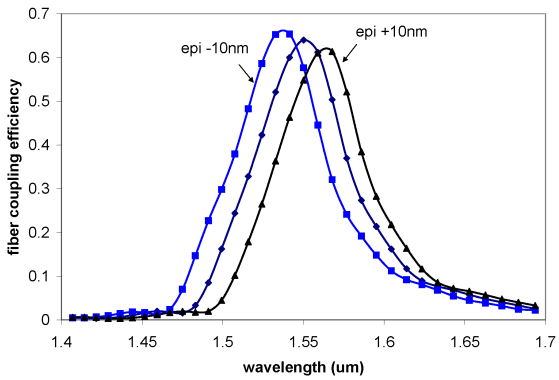


Fig. 8: Influence of a +/-10nm error of the epitaxial layer thickness on the fiber coupling efficiency spectrum (4µm mode field diameter fiber)

influence of deviations from the optimized design on the fiber coupling efficiency spectrum was evaluated. To see where deviations can originate from, an overview of the proposed processing scheme for the device is shown in figure 7. After deposition of an SiO_2 hard mask, Silicon is epitaxially grown in an opened window. After epitaxial growth, the grating structure is lithographically patterned in a photoresist layer and etched into the Silicon. By optimizing the exposure dose and applying a proximity correction to the grating structure on the mask, the dimensions of the fabricated slits can approach the optimal values. The epitaxial growth and the etching process are time based processes and a typical deviation of +/- 10nm from the targeted values can be expected. Moreover, the alignment of the grating with respect to the

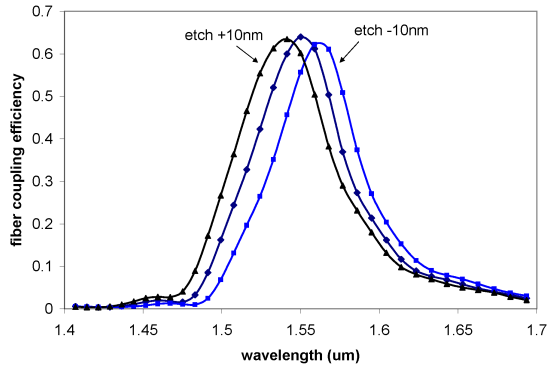


Fig. 9: Influence of a +/-10nm error of the slit etch depth on the fiber coupling efficiency spectrum (4µm mode field diameter fiber)

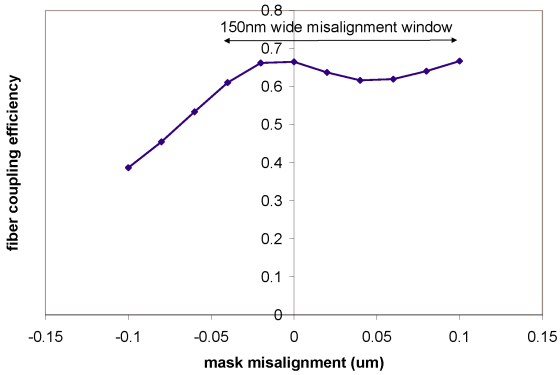


Fig. 10: Influence of the mask misalignment on the obtainable fiber coupling efficiency for a 4µm mode field diameter fiber

window of epitaxially grown Silicon can vary. Typically, an alignment accurary of +/-50nm can be obtained. Finally, a non-optimal position of the optical fiber results in a decrease in fiber coupling efficiency. The influence of a +/- 10nm variation on the epitaxial Silicon thickness *t* and the grating etch depth *e* is plotted in figure 8 and 9 respectively. As the additional slit is etched completely through the Silicon waveguide layer, reaching the SiO_2 etch stop layer, this additional slit cannot be overetched. From these simulations we can conclude that these deviations mainly result in a shift in the wavelength spectrum. In figure 10, the influence of misalignment of the epitaxial Silicon window and the grating structure on the fiber coupling efficiency at 1.55µm is plotted. From this simulation it is clear that there is a sufficiently large window for high efficiency coupling. The influence of the position of the optical fiber on the fiber coupling efficiency is plotted in figure 11. Although a higher coupling efficiency can be obtained for the reduced mode field diameter fiber, alignment tolerances are stricter in this case.

Conclusions

In this paper we developed a Silicon-on-Insulator grating structure for efficient coupling to a vertically positioned optical fiber. A 3dB improvement over a symmetric structure is obtained. While this improvement can decrease the cost of packaging of a

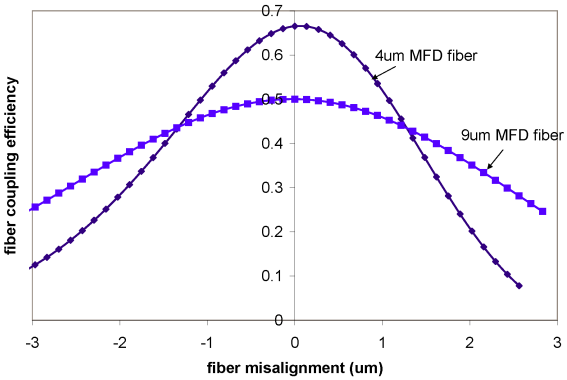


Fig. 11: Influence of a fiber misalignment on the obtainable fiber coupling efficiency for a 4µm and 9µm mode field diameter fiber

photonic integrated SOI circuit, it can also be used for other purposes, for example to efficiently couple light from a flip-chipped VCSEL into an SOI waveguide circuit, using the same grating. While this paper deals with the optimization of a one-dimensional grating structure, the same principle can be used in two-dimensional grating structures for polarization diversity.

References

1 W. Bogaerts et al, J. Lightwave. Techol., no. 23, p. 401, 2005.
2 D. Taillaert et al, J. Quant. Electron., no. 38, p. 949, 2002.
3 D. Taillaert et al, Photon. Techn. Lett., no. 15, p. 1249, 2003.
4 B. Wang et al, Photon. Technol. Lett., no. 17, p. 1884, 2005.
5 G. Roelkens et al, Optics Express, no. 24, p. 11622, 2006.
6 P. Dumon et al. Optics Express, no. 14, p. 664, 2006.
7 P. Bienstman et al., IEE Proc.-Optoelectron., no. 149, p. 161, 2002.
8 J. Harper et al., Electron. Lett., no. 24, p.245, 1988.

Spatial and Spectral Distributed Multi Population Rate Equations Model for Quantum Dot Superluminescent Diodes

Mariangela Gioannini, Ivo Montrosset
Dipartimento di Elettronica, Politecnico di Torino, mariangela.gioannini@polito.it

Abstract: *We present a spectral model of the emission characteristics of quantum dot superluminescent diodes including the influence of residual facet reflectivity. We analyze the transition from the amplified spontaneous emission to lasing regime and the characteristics of multi-section devices with improved performance.*

Introduction

Superluminescent light emitting diodes (SLD) offer the prospect of high power and wide bandwidth sources for various sensing and spectroscopy applications and in particular for optical coherent tomography, where it is required broad band and very bright light sources with a short temporal coherence. In the last years the Quantum Dot (QD) semiconductor materials have been promising used for the realization of QD-SLD [1,2], thanks to the possibility of tailoring the optical gain bandwidth with a proper engineering of the QD size and composition. Very recently multi-section QD-SLDs [3] have been proposed as a viable solution for the realization of devices with very high power and simultaneously broad band emission. A detailed numerical model for the analysis and the design of bulk SLD has been recently presented in [4], but to our knowledge only simple models have been reported for the case of QD semiconductor material [1].

The model we present in this work takes into account all the peculiar characteristics of the QD material and allows simulating the non-idealities of the device. From the material point of view we include the non-homogeneous distribution of the dot size (inhomogeneous gain broadening) and the presence of other states (wetting layer and SCH states) besides the states confined in the QDs (ground state, GS, and excited state, ES) to calculate the spectral characteristics of the emitted photons. From the device point of view we take into account the longitudinal spatial hole burning effect that is particularly strong in SLD and the effect of non zero reflectivity at the facets. We can therefore predict the amount of ripple in the output spectrum and the condition at which the transition from the SLD to the laser behavior occurs. A proper SLD model has therefore to be able to simulate the effect of the unwanted facet reflectivity and to calculate the output spectrum and the power versus current characteristics including the longitudinal spatial hole burning and the spectral hole burning effects caused by finite carrier capture/escape times in/from the various QDs of different size.

The paper is organized as follow: we will briefly describe the numerical model used and then we will validate it in a test case, comparing the characteristics of an ideal SLD (zero-facet reflectivity) with those of a laser (as cleaved facet reflectivity). We will then show how the model can be used to analyze some SLD realistic structure. In particular we will analyze the effect of residual facet reflectivity due to non-ideal anti-reflection coating and we will give two examples of analysis of multi-section SLDs.

Numerical model

The numerical model is based on a traveling power approach: the device is divided in several sections whose photon densities are obtained from the propagation of the forward and backward photons of the two nearest sections. Given the importance of the SLD emission spectra in practical applications, the model is also based on a spectral slicing approach [5]. In each longitudinal section of the device the model calculate the local true spontaneous emission (TSE) and the gain spectra solving a Multi Population Rate Equation system [6]. With this modeling the non-uniform QD ensemble is represented by several sub-groups of QDs, coupled through the wetting layer via the carrier capture and escape process. Each *n*-th QD group has different GS and ES energies (E_n) and its carrier density is depleted by the stimulated emission of the photons of that section (spatial hole burning). The various QD sub-groups are also coupled together via the homogeneous broadening of the emitted photons (spectral hole burning) that appear in the stimulated emission term. The TSE obtained by the carrier occupation of the various states is then sliced in several energy intervals with sampling step ΔE. In equation (1) we report the expression of the TSE emission rate at the central energy E_k of the *k*-th energy interval evaluated in the *z* section of the device:

$$R_{sp}(z,E_k)=\sum_{GS,ES}\mu_{GS,ES}N_D n_L C_{spon}\sum_n f^2_{n_{GS,ES}}(z)\cdot\rho_{opt}(E_n)\cdot G_n\cdot L(E_n-E_k) \quad (1)$$

where $\mu_{GS,ES}$ is the state degeneracy, N_D is the QD density per layer, n_L the number of QD layers, C_{spon} is a coefficient [6], $\rho_{opt}(E_n)$ is the density of the optical modes, $f^2_{n,ES,GS}$ is the occupation probability of the GS/ES of n-th QD population in the *z* section and is obtained solving the MPRE system [6]. In expression (1) G_n is the existence probability of the n-th QD population that accounts for the inhomogeneous QD distribution and $L(E_n-E_k)$ is the homogeneous

broadening function.
The photon density in the forward (S_f) and reverse (S_r) direction are then given by:

$$S_{f,r}(z,E_k) = S_{f,r}(z,E_k)\cdot\exp(g(z,E_k)\cdot\Delta z) + 0.5\cdot\beta_{sp}\cdot\frac{\Delta z^2}{v_g}\cdot R_{sp}(z,E_k)\cdot\Delta E_k$$

Where $g(E_K)$ is the gain spectrum calculated in [6], Δz is the sampling step in the longitudinal direction, v_g is the group velocity and β_{sp} is the amount of TSE coupled with the guided mode. In the first and last section of the device we add to the term reported above also the contribution of the reverse/forward fields reflected back in the cavity.
Solving the MPRE model in each z section we therefore account for the spatial hole burning effect in the longitudinal direction of the SLD and we can calculate how much the carrier population in the GS and ES are depleted by the propagating photons in the various sections.

Numerical results

The numerical model presented above has been validated analyzing first two test structures with the purpose of showing how the model can simulated a device with any value of end facet reflectivity and therefore account of both amplified spontaneous emission and lasing regimes. At this purpose we have considered a device with as cleaved facet reflectivity (laser, LD, behavior) and a device with zero facet reflectivity (ideal SLD behavior).

Comparison between laser and SLD behavior

We consider for the comparison two InAs/GaAs 4.5 mm long QD devices. We compare in the inset of Fig.1a the calculated output power versus current characteristics while in Fig.s 1a and 1b are reported the output emission spectra for the two cases at various level of current injection. The spectrum at the highest current in Fig.1, just above LD GS threshold, clearly shows a sharp peak around the GS emission while the SLD spectrum shows a dominant GS emission. The cavity gain in Fig. 2 (a- for the LD and b- for the SLD) helps in this interpretation because the modal gain around the GS emission is clamped in the LD case whereas, in the SLD case, it presents a maximum. Increasing the current (Fig.s 1b and 2a) the LD spectrum broadens and then also the ES start lasing. On the contrary, for the SLD the ES emission becomes first equal to GS emission and than dominates since the GS starts saturating. This behavior has been measured in actual SLD and LD. Fig. 3 reports the calculated normalized longitudinal photon density distribution at the wavelengths corresponding to the GS (dashed line) and ES (solid line) output power spectral peak wavelengths. The strong longitudinal field variation in the SLD case justify the need to use a longitudinally discretized model to correctly represent the high injection regime, whereas, as it is well known, this is not strictly necessary in a laser except when the ratio of the two reflectivity is high.

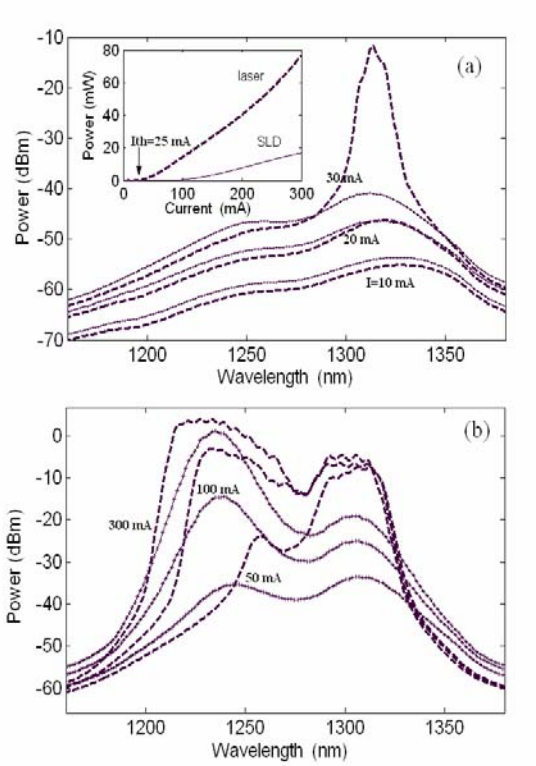


Fig. 1: P-I (a) and the spectral (a and b) characteristic of a SLD with zero (continuous lines) and with cleaved (dashed lines) facets reflectivity.

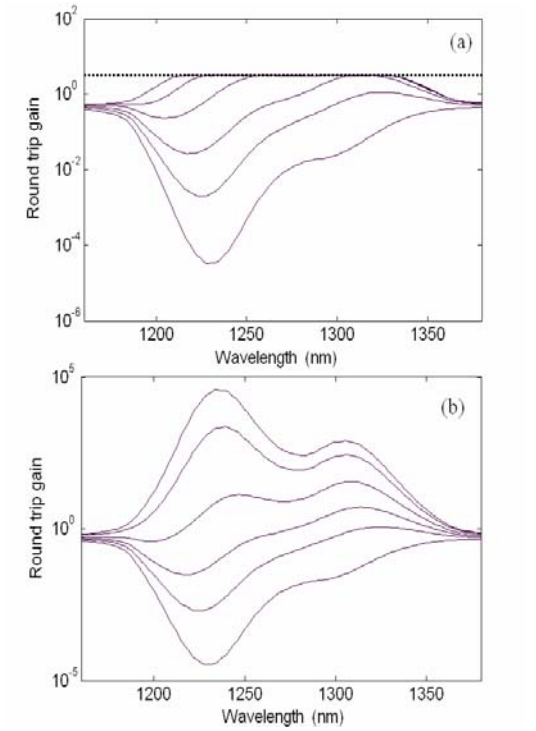


Fig. 2: Device round trip gain for the two cases of Fig.1. (a) cleaved FP cavity and (b) ideal SLD. The current levels of each curve are the same of Fig.1.

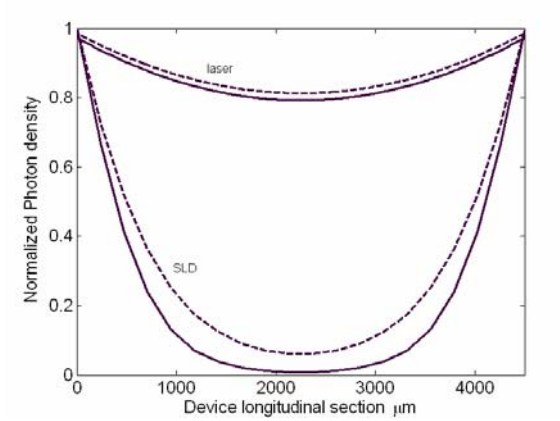


Fig. 3: Normalized longitudinal photon distribution at the peak emission wavelengths (GS – dashed and ES- continuous lines) for the ideal SLD and for the FP LD.

SLD with non-zero facet reflectivity

In this section we report an example of simulation results of a SLD with non-zero facet reflectivity. We assume that the two facets have a residual reflectivity of $3 \cdot 10^{-4}$ due to the non-ideal anti-reflection coating. In Fig. 4 we report the calculated power versus current curve and the maximum ripple of the output spectrum evaluated at the peak of the GS and ES emission. The figure shows that the ripple remains low for the GS because the GS gain saturates at quite low values (see Fig. 2b), but it significantly increases for the ES emission. The strong ES ripple at I=150 mA evidence that the ES is getting close to the threshold condition. This result shows that if low ripple values are required (e.g. < 3dB), the SLD output power is significantly reduced.

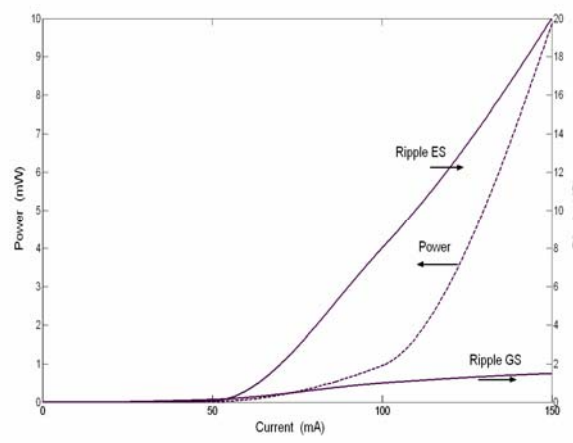


Fig. 4: Power versus current characteristic and maximum ripple in the output spectrum at the GS and ES peak emission wavelength. The residual reflectivity of the SLD is set to $3 \cdot 10^{-4}$

Analysis of multi-section SLD

The present model has therefore been used to analyze from a theoretical point of view various solutions presented in the literature to suppress the residual reflectivity [3,7] and/or increase the output power and emission bandwidth [3]. In all the cases the SLD is divided in two or more sections injected with different current levels.

In this section we analyze two examples of two sections SLD: in the first example we study a SLD with an active plus an absorber section, in the second example we analyze a SLD with two active sections pumped with different current.

The addition of the saturable absorber section was proposed several years ago [7] to suppress the lasing in bulk SLD and applied to the QD case in [3]. The purpose of this example is to show that, in the QD case, when the power in the active section increases, the absorber, being optically pumped by the generated photons, has first a reduction of the absorption and then a transition to a gain condition. In this example we consider a 3 mm long active section followed by 1.5 mm absorber with zero injected current. The facets are as cleaved. We ran several simulations keeping null the current injected in the absorber section and varying the current injected in the active section. We have observed that the many photons emitted by the ES in the active section pump first the carriers in the ES of the absorber; then these carriers relax in the GS giving an increasing of the GS carrier density. The consequence of this behavior is shown in Fig. 5, where we report the average gain of the absorber at the various current injected in the active section. The figure demonstrates that both GS and ES absorption gets smaller and smaller. However, differently from quantum well and bulk saturable absorbers, the GS absorption is not clamped to transparency, but, being refilled from the ES, it can reach a positive gain condition. As a consequence the suppression of the facet reflectivity is reduced more and more and eventually the device starts lasing first from the GS and then also from the ES.

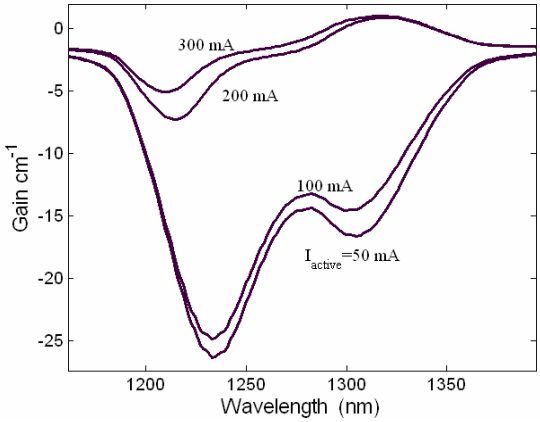


Fig. 5: Average gain in the absorber section as function of the current injected in the active section.

In the second example we analyze the output characteristics of a SLD divided in two active sections in-

jected with different currents and with ideally zero facet reflectivity. In this case the first section (1.5 mm with 20 mA current injection) provides the GS power; the second section (3 mm with 450 mA injection) amplifies the GS emission provided by the first section and also generates the ES power. In Fig. 6 we compare the output spectrum of the two section SLD with the one of a 3 mm uniform SLD obtained injecting the same current density. In the two sections case the GS power is suppressed of only 3.7 dB, whereas in the one section design the GS output power is suppressed of more than 9 dB. This example shows that the multi-section SLD design is a viable solution for optimizing the emission bandwidth and output power of these devices.

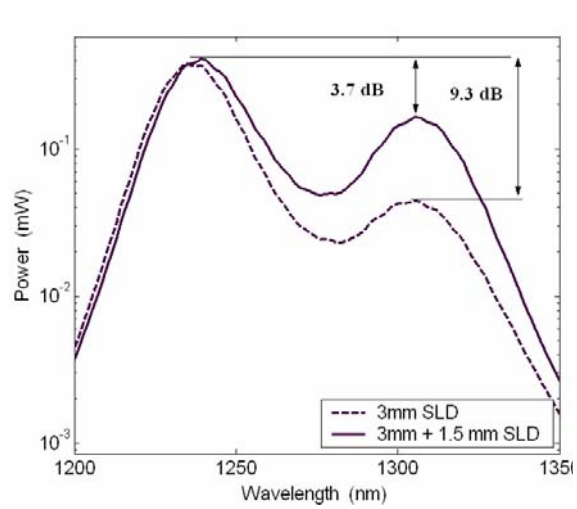


Fig. 6: Comparison between the output spectra of one section SLD (dashed line) and two section SLD (solid line).

Conclusion

We have presented a numerical model for the analysis of QD-SLD. The model includes the inhomogeneous gain broadening due to the QD material, the spectral and spatial hole burning effect and the influence of non null end facet reflectivity. We have demonstrated that the model can account for the transition from the amplified spontaneous emission regime to the lasing regime and it can be used to predict the amount of ripple in the SLD output spectrum. We have also given two examples of analysis of multi-section SLD showing that the present model could be used to test the viability of new design solution of SLD with improved spectral performance.

Acknowledgments

The author acknowledge the support of the EC IST-NMP-3 STREP project NANO UB-SOURCES.

References

1 M. Rossetti, A. Markus, A. Fiore, L. Occhi, C. Velez, "*Quantum dot superluminescent diodes emitting at 1.3 μm*", IEEE Photon. Tech. Lett., no. 3, pp. 540-542, 2005.

2 S.K. Ray, K.M.Groom, H.Y. Liu, M. Hopkison, R.A. Hogg, "*High poer 1.3 μm quantum dot superluminescent diodes*", Photonics West, January 2006.

2 S.K. Ray, K.M.Groom, H.Y. Liu, M. Hopkison, R.A. Hogg, "*High power 1.3 μm quantum dot superluminescent diodes*", Photonics West, January 2006.

3 Y.C. Xin, A. Martinez, T. Saiz, T.A. Nilsen, A-Moscho, Y. Li, A.L. Gray, A. Vahktin, L.F. Lester, *"Novel quantum dot 3-section superluminescent diode",* International Conference on Solid State Devices and Materials, Paper B-6-3, Yokohama (Japan), 2006

4 J. Park, X. Li, *"Theoretical and numerical analysis of superluminescent diodes",* IEEE J. Light. Tech., no. 6, pp. 2473-2479, 2006.

5 J. Park, X. Li, W.P. Huang, *"Comparative study of mixed frequency-time domain models of semiconductor optical amplifiers",* IEE Proc. Optoelectron., no. 3, pp. 151-159, 2006.

6 M. Gioannini, A. Sevega, I. Montrosset, *"Simulation of differential and linewidth enhancement factor of quantum dot semiconductor lasers"*, Springer Optical and Quantum Electronics, no. 4-6, pp. 381-394, 2006.

7 N.S.K. Kwong, K.Y. Lau, N. Bar-Chaim, *"High power high efficiency GaAlAs superluminescent diodes with an internal absorber for lasing suppression"*, IEEE J. Quantum Electron. , no. 4, pp. 696-704, 1989.

Full-vectorial time-domain modelling of photonic crystal semiconductor lasers

Wolfram H.P. Pernice (1), Dominic F.G. Gallagher (2) and Frank P. Payne (1)
1) Oxford University, Department of Engineering Science, Parks Road,Oxford, OX1 3PJ, UK,
wolfram.pernice@eng.ox.ac.uk
2) Photon Design, 34 Leopold Street, Oxford, OX4 1TW, UK

Abstract: *We present a novel numerical scheme for the simulation of photonic crystal lasers with nonlinear response. The gain of the lasing material is closely modelled over a large wavelength range. High computational efficiency is achieved by using refined meshes and implementing the method for distributed computing.*

Introduction

Photonic crystals show promise for shaping the optical properties of semiconductor lasers. They are for example used to optimise beam quality of VCSEL lasers [1] and to achieve low-threshold [2] or ultrafast lasers [3]. However, the design of such structures provides serious challenges to numerical methods available to date. For one, the material properties of the lasing material have to be described accordingly in the algorithm. In addition, the structural size of the device under consideration often overextends the computational hardware available in standard research facilities.

We present an efficient numerical solution to these challenges. We use the finite-difference time-domain (FDTD) method [4] due to its flexibility to handle complex geometric and material systems. Material gain is included into the standard FDTD algorithm by linking the gain to a frequency dependent conductivity. Because data for material gain in a quantum well structure is readily available [5], we choose to incorporate active material behaviour using the conductivity, which can be expressed in terms of the material gain and therefore allows us to describe complex vertical layer structures. Using a semi-deterministic fitting algorithm, the gain function can be cast into a suitable mathematical form that can be used in the FDTD method, while preserving causality in the time domain. Our fitting routine yields accurate results for a large wavelength range. Similarly, we achieve high accuracy for modelling the dielectric function of the metal grating used in the validation of the algorithm.

The hardware limitations are overcome by using a non-uniform meshing algorithm, yielding higher mesh densities for areas with small geometrical features. A new interpolation method is used in order to reduce spurious reflections from mesh boundaries. The algorithm is also developed for use on parallel computers making it possible to fit large structures into distributed memory.

We validate our algorithm by simulating different photonic crystal laser structures. We consider a PC membrane laser, a high-Q cavity laser and a polymer laser based on a metallic nano-particle grating.

Extended Maxwell's equations and FDTD formulation

For an adequate representation of the material gain we need to consider both the frequency dependent behaviour of the lasing material and fluctuations of the carrier density due to spatial hole burning and carrier depletion. As shown by [6], the material gain can be linked to a frequency dependent conductivity J_t, which we include in the standard set of Maxwell's equations as

$$\varepsilon \frac{\partial E}{\partial t} = \nabla \times H - J_t \qquad \mu \frac{\partial H}{\partial t} = -\nabla \times E \tag{1}$$

J_t can be a single Lorentzian or as in this paper a sum of N individual Lorentzian poles. By using a multipole formulation the fit to the material gain yields much more accurate results than alternative formulations [7]. Each single Lorentzian pole yields a second order differential equation in the time domain as

$$T_k^2 \frac{\partial^2 J_k}{\partial t^2} + 2T_k \frac{\partial J_k}{\partial t} + (1+\omega_k^2 T_k^2) J_k = \frac{\sigma_k}{1+I/I_S}\left(E + T_k \frac{\partial E}{\partial t}\right) \tag{2}$$

where I denotes the optical intensity and I_S the saturation intensity. The coefficients T_k, ω_k and σ_k for each pole are dependent on the carrier density and denote the relaxation time, the resonant frequency and the peak gain, respectively. The non-linear dependence of the gain saturation on the optical intensity, which is determined by the spectral hole-burning and/or hot carrier effects, is included in our gain model by the factor $(1+I/I_S)^{-1}$. As given by [8] the carrier density is linked to the electric field and the current density as

$$\frac{\partial N}{\partial t} = \frac{2}{\hbar\omega_0} E \sum_{k=1}^{N} J_k - \frac{N}{\tau} + W_P \tag{3}$$

where τ is the carrier lifetime, ω_0 is the frequency of the gain peak and W_P the electrical pump rate. The above equations provide the complete updating scheme that is discretized using centred finite differences in both space and time as shown by [4]. It is, however, important to make sure that fields on the left- and right-hand side of the equations are centred on equivalent time-steps, as failing to do so leads to numerical instability [7]. We therefore apply a semi-implicit discretization scheme, which is solved to yield explicit updating equations for all fields.

Semideterministic fitting routine

In order to include the material gain in our algorithm, we need to obtain the Lorentzian parameters in equation 2 as a function of carrier density. The fitting routine therefore needs to obtain a set of parameters for each of the material gain sets. We use the commercial product Harold [5] to obtain material gain data for our quantum-well gain structure. The fitting routine is performed before the actual FDTD algorithm is started. It is important to control the fitting routine such that the fitted parameters vary smoothly with increasing carrier density. Therefore we apply a semi-deterministic fitting routine as shown schematically in figure 1, using an adaptive non-linear least-squares algorithm as described in detail in [9]. We fit each individual gain curve with a set of four Lorentzians. Each pole corresponds to a determined

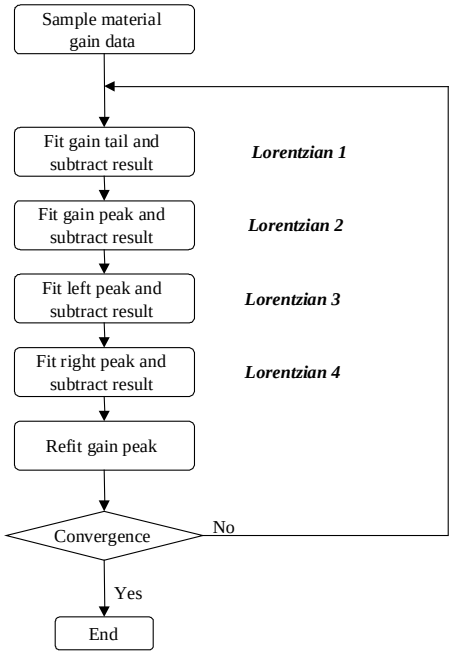


Fig. 1: Flow chart for the fitting routine for gain materials.

spectral position in order to fit the gain peak, curvature and absorption in the vicinity of the peak with high accuracy. We fit one pole at a time and then subsequently subtract the fitted result from the original data. This way dominant resonance peaks in the gain spectrum are individually removed. We first fit the absorption tail of the gain curve, followed by the gain peak. Subsequently spurious resonances to the left and right of the peak are removed with one additional pole each. Because the sum of these four Lorentzians might not represent the peak gain well, we refit the gain peak. This cycle of fitting can be applied repeatedly. We find that the algorithm converges very quickly to the local optimum in only one or two iterations. Representative results from our algorithm are shown in figure 2. As required, the fitting algorithm yields a close match to the gain

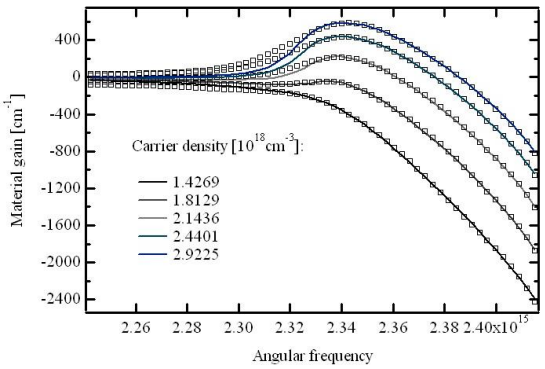


Fig. 2: Fitted gain curves for varying carrier density. Each fit is composed of four Lorentzian resonances that preserve gain peak and curvature as well as long-wavelength absorption.

peak, curvature and long-wavelength absorption tail. We note that a better fit to the left side of the peak could be obtained by selecting a greater number of poles. However, this increases the computational burden of the FDTD algorithm and also worsens the trajectory of the Lorentzian parameters. In figure 3 we show the trajectories for the peak Lorentzian as a function of carrier density. In order to facilitate evaluation in the FDTD updating scheme, we approximate the trajectory with a polynomial, fitted

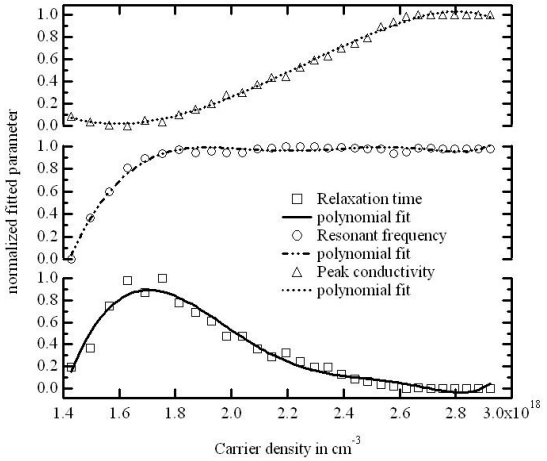


Fig. 3: The trajectory of the parameters of the peak Lorentzian with varying carrier density. Shown is also a polynomial fit of fifth order.

also in a least-squares sense. Because the parameters vary without major jumps, a polynomial of fifth order is sufficient to represent the trajectory. Polynomials can be evaluated at minimal costs and are therefore ideally suited for a fast FDTD algorithm.

Mesh refinement and distributed computing

As suggested by [4], the FDTD algorithm requires a spatial resolution of roughly 20 grid points per wavelength in order to yield a numerical accuracy of 1 %. Because this criterion is dependent on the refractive index of individual geometrical features, small shapes with high refractive index impose an unnecessary stringent grid resolution for the computational domain. We therefore implement a mesh refinement scheme, which provides higher resolution

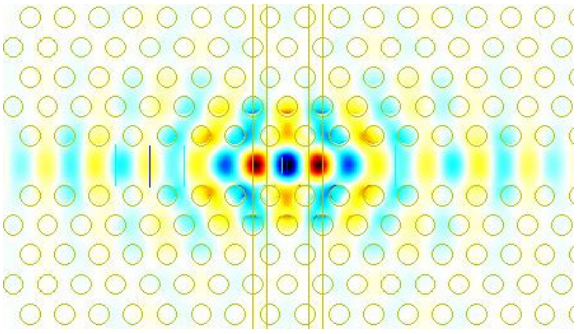


Fig. 4: Lasing mode at steady state for the high Q laser.

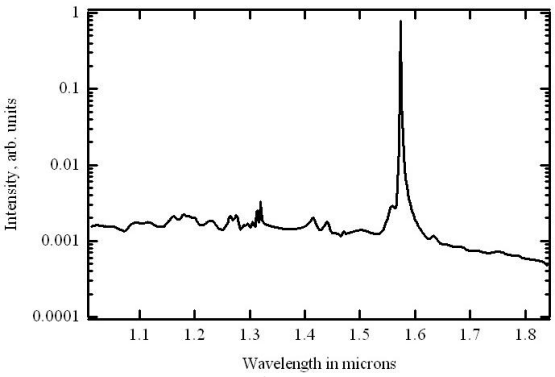


Fig. 5: Spectral response of the nano-cavity laser. The lasing peak is positioned at the resonance frequency of the cavity at 1.574 microns.

in areas with high refractive index, such as metallic particles. We choose a refinement factor of two. This refinement scheme can however by recursively applied to yield smaller grid steps. A factor of two is chosen because higher refinement steps yield higher reflections from refinement boundaries. A further reduction in reflection can be obtained by using a parabolic interpolation scheme in order to obtain boundary points for the refined region.

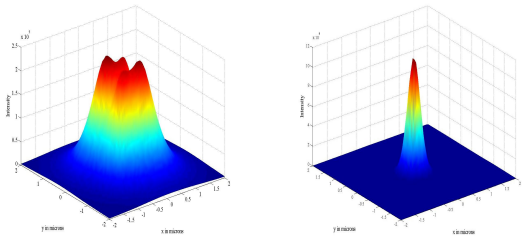
Though the use of non-uniform meshes reduces memory requirements significantly, three-dimensional problems still challenge computational hardware. Because many research facilities do not have access to supercomputing equipment, it is convenient to use in-house cluster systems formed by linking personal computers to a distributed environment. We split the computational domain into regions that fit into the memory of each machine. An mpi-based message passing system is employed to make sure that neighbouring domains have access to required information. The distributed version of the software not only allows us to reduce calculation time, but more importantly increases the size of problems that can be treated by the FDTD.

Numerical experiments

In order to evaluate the proposed algorithm we numerically investigate several photonic crystal laser geometries.

Ultra-high Q cavity laser

In a first example we compute the lasing spectrum for a nano-cavity membrane laser. The nano-cavity is designed as described by [10]. Nano-cavity lasers have attracted interest in recent years due to low threshold and fast tuning speeds. The ultra-high Q cavity provides a nice way to realize a laser, because the optical pumping can be provided through the waveguide channel in the photonic crystal lattice. The cavity is composed of a hetero photonic crystal lattice with lattice constants I=410 nm and lattice constant II=420 nm. The membrane thickness was set to 287 nm. This cavity design shows a resonance peak at 1.574 microns. The high quality factor of the cavity results from the dual lattice nature of the structure. Wavelengths are allowed in the region with larger lattice constant that cannot propagate in the regions with smaller lattice constant. When the waveguide in photonic crystal II is short enough, the frequencies that photons are allowed in this region become quantized - similar to the situation for electrons in a semiconductor quantum structure. We apply our algorithm to this particular structure. We choose a grid spacing of 25 nm and propagate the fields for 5 ps to ensure that the laser has reached steady state. The lasing output is recorded in the air space above the membrane. In figure 4 we show the



a) **b)**

Fig. 6 a) Far field obtained for a single defect cavity. **b)** Far field for 7 coupled nanocavities.

lasing mode once the laser has reached steady state. The cavity mode is clearly visible for the resonant frequency of 190.5 THz. The spectral response of the laser reveals a central peak at 1.574 microns as shown in figure 5.

Nano-cavity array membrane laser

In a second example we consider the beam characteristics of coupled nano-cavity lasers. Such membrane laser arrays have can provide ultra-fast modulation speeds [3]. Here we consider a thin membrane of 280 nm thickness. A hexagonal photonic lattice with lattice constant 365 nm is inscribed into the membrane, where the hole diameter is set to 175 nm. InP is chosen as a material system with 4 quantum wells included in the membrane to yield a peak gain around 1.25 microns. Cavities are generated in the membrane by removing a single hole from the lattice. Choosing only one defect atom allows us to preserve the symmetry of the lattice and therefore obtain better mode shaping properties. In this experiment we study the far field behaviour of single and coupled cavities. As shown

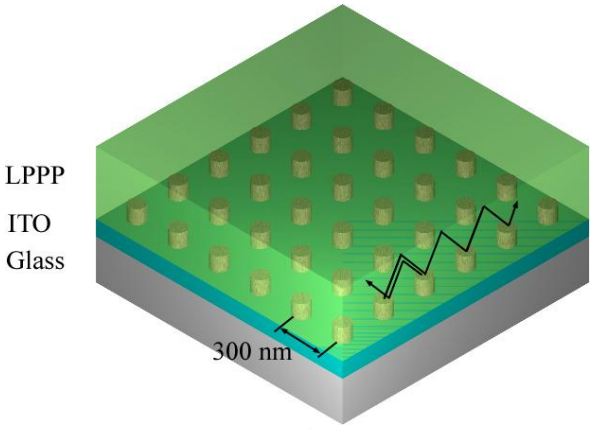


Fig. 7: Geometrical structure of the polymer PC laser. Optical feedback is provided through second-order Bragg scattering as indicated by the black arrows.

in figure 6a), a single cavity does not result in a directional output beam. However, by coupling 7 cavities a supermode exists in the photonic crystal lattice that does yield a directional output, as demonstrated in figure 6b). Furthermore, the output intensity is increased by a factor of approximately 4.8. The simulation confirms therefore the possibility to improve the output characteristics of coupled cavity lasers with numerical techniques.

Polymer laser with a metallic nano-particle grating

In the last numerical example we investigate lasing behaviour in a polymer laser. Since the demonstration of stimulated emission in organic semiconductors this field of research has attracted increasing interest. In this study we employ the optical feedback mechanism described by Stehr et al. [2] consisting of a grating of gold nano-discs. The simulated structure is shown in figure 7. A 110 nm thin layer of indium tin oxide (ITO) on a glass substrate is used as the substrate for the metal grating. The gold discs of diameter 110 nm and 30 nm height form a two-dimensional photonic crystal lattice with a lattice constant of 300 nm. The grating provides feedback through second order Bragg scattering. A thin methyl-substituted ladder-type poly(para phylene) (LPPP) layer of 460 nm thickness is chosen as a gain medium with an emission peak at 490 nm. We consider six rows of photonic crystals in this investigation. The global grid resolution is set to 20 nm. In order to achieve high accuracy for the metal disks, we enclose them in a subgridding region of refinement factor 4, meaning that we use a mesh density that is four times higher than in the global grid. The computational domain is terminated with uniaxial perfectly matched layers in order to absorb reflections from the grating structure. The total simulation time is set to 5 pico-seconds and the lasing output is recorded above the LPPP layer in air. In figure 8 we show the spectral response of the polymer laser. A clear peak is visible at 476 nm in the blue visible range. This peak corresponds to the Bragg wavelength of the grating in second order mode. The lasing output is coupled out of the LPPP layer

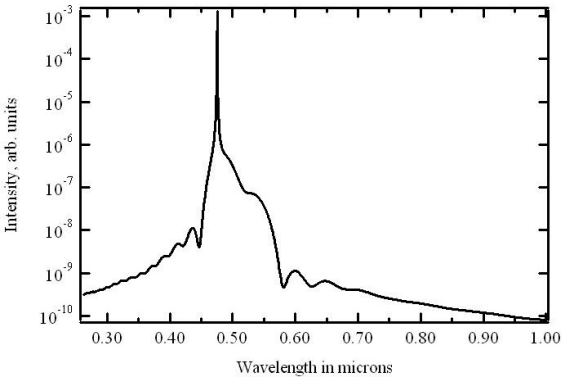


Fig. 8: Spectral response of the polymer PC laser.

through the first order mode as shown in [2].

Conclusions

We have presented a novel flexible FDTD algorithm that is capable of simulating lasing in complex material systems in three dimensions. We fit the gain material to a multi-pole Lorentzian model using a semi-deterministic fitting algorithm providing accuracy over a wide spectrum. Saturation effects and spatial hole burning are included through rate equations and a non-linear saturation model. The algorithm uses mesh refinement techniques and is developed for use in a distributed cluster system thus allowing for numerical investigation of large devices. The validity of the approach was demonstrated by simulating a variety of photonic crystal laser structures. We investigated lasing in nano-cavity membrane lasers and polymer based lasers with a gold nano-particle grating.

Acknowledgements

Wolfram H.P. Pernice would like to thank Photon Design for funding a DPhil. Research studentship.

References

1 N. Yokouchi et al., IEEE Sel.Top. Quantum Electr., vol. 9, no. 5, pp. 1439-1445, 2003.
2 J. Stehr et al., Advanced Materials, vol. 15, p. 1726, 2003.
3 H. Altuc et al., Nature Physics, vol. 2, pp. 484-489, 2006.
4 A. Taflove and S. C. Hagness, "Computational Electrodynamics: The Finite-Difference Time-Domain Method", Boston: Artech House, 2005.
5 Harold, Photon Design, 34 Leopold Street, OX4 1TW Oxford, U.K.
6 S. C. Hagness et al., Radio Sci., vol. 31, no. 4, pp. 931-941, 1996.
7 M. Bahl et al., IEEE Journal of Quantum Electronics, vol. 41, no. 10, pp. 1244-1252, 2005.
8 A. E. Siegman, Lasers. Mills Valley, CA: Univ. Sci. Books, 1986.
9 J. E. Dennis et al., ACM Trans. Math. Softw, vol. 7, no. 3, pp. 348-368, Sept. 1981.
10 B-S. Song et al., Nature Materials, vol. 4, pp. 2007-2010, 2005.

Direct Experimental Observation of Pulse Temporal Behavior in Integrated-Optical Ring-Resonator with Negative Group Velocity

H. P. Uranus, L. Zhuang, C.G.H. Roeloffzen, and H.J.W.M. Hoekstra
Dept. of Electrical Engineering, University of Twente, P.O. Box 217, 7500 AE Enschede, The Netherlands.
e-mail: h.p.uranus@ewi.utwente.nl, l.zhuang@ewi.utwente.nl

Abstract: *We report a direct experimental observation of pulse temporal behavior in an integrated optical two-port ring-resonator circuit as a function of coupling strength, including the transition across the critical coupling point. We demonstrate the observation of pulse 'advancement' in the negative v_g regime and pulse delay in the positive v_g regime. We also observed a smooth transition of the pulse shape from highly negative to highly positive v_g (or vice versa) through a pulse splitting phenomenon. The observed phenomena agree well to theoretical simulations.*

Introduction

The possibility to control the light group velocity (v_g) is currently an interesting research topic [1-6]. The capability to make light to travel with low v_g (e.g. much lower than light velocity in vacuum c in a so called slow-light phenomenon [1]), has raised many prospects in application areas of optical signal processing, light sources, optical sensing, etc. Besides, light can also be forced to travel with large v_g (e.g. larger than c), or even with negative v_g [1-6] either by engineering the material dispersion of the medium [2, 3] or the waveguide dispersion of the structure [4]. Although the phenomenon of negative v_g seems to be counter-intuitive as the peak of the output pulse appears earlier than the peak of the input pulse, its consistency with the causality principle has been experimentally verified [5].

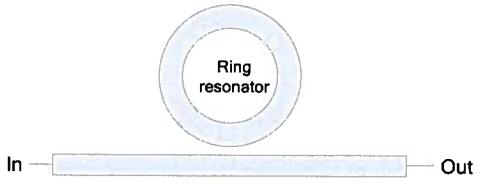


Fig. 1: A two-port ring-resonator circuit

It is well known that in lossy two-port ring-resonator (TPRR) circuits as shown in Fig. 1, in the under-coupling condition, light can have a negative group velocity [7] as shown in Fig. 2. Experimental [8] and theoretical [4, 6] studies on such a phenomenon has also been carried out. However, since it is understood that there will be no true negative delay (or 'advancement') in such a phenomenon (hence not so useful for signal processing applications), there is not much attention paid on experimental aspects for this phenomenon, compared to works on the same phenomenon using e.g. atomic gases [2] or fibers [3]. In fact, experiments using an integrated optical chip can be more handy and within the reach of many research groups. Also, we have theoretically showed [6] that such phenomenon has similar enhancing light-matter-interaction feature, like its slow-light counterpart, and therefore will be useful for applications like integrated-optical sensing. Consequently, further study and better understanding on such phenomenon from experimental aspect, are indispensable.

In this paper, we report the first direct experimental observation of pulse temporal behavior at the output of such a resonator for the regimes of negative and positive v_g, and transition between them across critical coupling point.

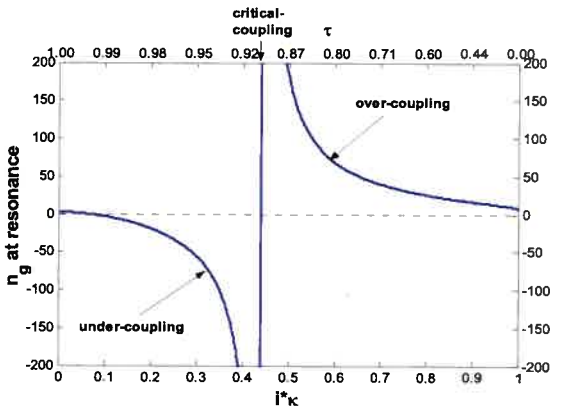


Fig. 2: The group index ($n_g \equiv c/v_g$) at resonant wavelength of a two-port ring-resonator circuit with parameters taken from the device under test discussed in this paper.

Experimental Set-up

For this experiment, we chose a TPRR which was originally designed for a delay line for optical beamforming applications [9]. The TPRR, which was designed and fabricated by Lionix BV [10], The Netherlands, has a controllable coupling constant and resonant wavelength through a thermo-optical mechanism. This Si_3N_4 based TPRR has a geometric ring round-trip length of 11916.4μm and supports a single q-TE mode with n_{eff} and $dn_{eff}/d\lambda$ (as calculated by a vectorial mode solver) of 1.6499 and $-0.1029\mu m^{-1}$, respectively. For a detailed description

of the TPRR, please see the respective publication [9].

The experimental set-up is shown in Fig. 3. The measurement of pulse temporal behavior is basically carried out by sending a light pulse through the TPRR and recording its output pulse shape detected by an optical receiver using a fast oscilloscope (Agilent 54854A).

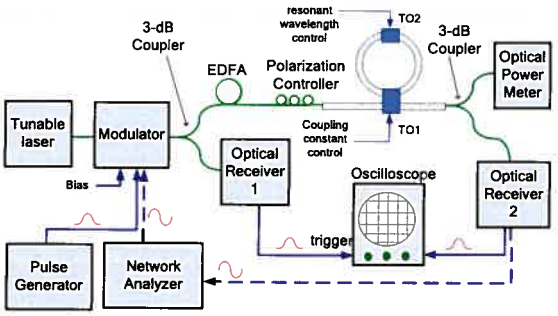


Fig. 3: The experimental set-up

For comparison between results of various settings of the TPRR, we need a reference time, which is measured at a well defined condition. For this purpose, we first tuned the laser to the resonant wavelength of the TPRR, and intensity modulated the light by a smooth pulse generated by a pulse generator, which has an internal electronic pulse shaper to control its rise and fall time. The pulse width is selected to be sufficiently small to be able to observe the phenomenon discussed in a later section. Then, we tuned the thermo-optical modulator TO1 (which controls the coupling constant) such that the output pulse amplitude (as detected by Optical Receiver2 and observed by the oscilloscope) is the lowest. Such condition is associated to a well defined critical coupling condition [6]. We then tuned TO2 (which controls the resonant wavelength) such that the ring is in an anti-resonant condition (a condition in the middle between two consecutive resonances). In such condition, the effect of the ring is minimal, and the delay is approximately the same as the one contributed by a similar circuit without the ring. We took this condition as a reference condition and refer to such fictitious ringless structure as the reference structure.

The output pulse shapes for various values of control to TO1 were recorded with TO2 set back to the TPRR resonant condition. Note that during these measurements, the oscilloscope was triggered by pulses detected by Optical Receiver1. Such triggering condition was kept the same during the whole measurements. Also note that an EDFA was inserted in the measurement set-up to compensate the loss of power in the set-up in order to capture a well detectable signal, while the polarization controller was used to condition the light to TE polarization before launched into the TPRR.

For the purpose of comparing the measurement results with theory, we also recorded the transmission spectra and the relative group delay spectra for each associated setting of TO1, and used these curves to retrieve the value of the coupling constants and ring loss through a curve fitting procedure. The transmission curves were measured by reading the output power while sweeping the tunable laser across the resonant wavelength. The relative group delay curves were measured by measuring the delay of the optical envelope signal using a modulation phase shift method [11, 12] while scanning the wavelength of the tunable laser. For this purpose, the pulse generator was disconnected and a vector network analyzer was introduced into the set-up (see the dashed-lines signal path in Fig. 3). In this set-up, the light was intensity modulated by a sine signal with modulation frequency of 50MHz with a bias and level set to produce undistorted output signal from Optical Receiver2. The vector network analyzer measured the delay between the sine signal it sent out to the modulator and the one it received from the Optical Receiver2, relative to a similar delay of the reference condition, which was measured earlier.

Results and Discussions

Fig. 4 shows the measured pulse temporal behavior for various values of coupling constant as set through TO1. For clarity, we also overlaid the picture with a pulse shape measured at the reference condition and draw a vertical dotted line to indicate its peak position which is referred to as $t = 0$. Since this reference condition approximately represents a condition for the reference ringless structure, the measured signal relative temporal position represents the 'advancement' or delay contributed by the ring resonator.

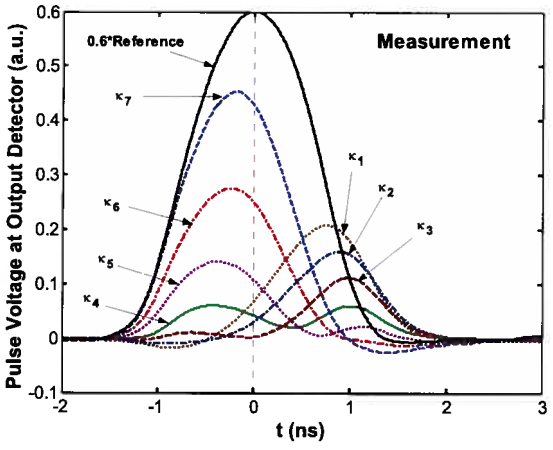


Fig. 4: The measured pulse temporal behaviour of the TPRR working in the positive and negative group velocity regime.

Fig. 4 clearly shows that at cross coupling constant values of κ_5, κ_6, and κ_7 (which were set through

TO1), the (main) peak of the output pulses of the TPRR comes out earlier than the peak of similar pulse for the reference structure. Such a pulse 'advancement' phenomenon is associated with a negative v_g condition. Inversely, for coupling constants of κ_1, κ_2, and κ_3, the (main) peak of the output pulses of the TPRR comes out later than the peak of similar pulse for the reference structure. Such pulse delay is associated with a positive v_g condition. Note that the higher the 'advancement' or delay, the smaller the pulse amplitude (or in other words, the larger the loss), indicating the more intense light-matter interaction in the ring. Hence, a highly negative v_g is in fact as potential as the positive one for applications that exploit light-matter interaction mechanism like optical sensing [6]. Fig. 4 also shows that the leading edge of the reference output pulse always appears before the peak of the weak output pulse of the TPRR, implying that the energy velocity contributed by the ring-resonator is always positive even in the negative v_g regime. Hence, there is no violation to the causality principles [1, 5].

The measured smallest output amplitude happens at a coupling constant of κ_4. This condition is associated with a critical coupling condition [6]. Fig. 4 shows that at this condition, the output pulse is highly distorted and split into two sub pulses, one with delay, and the other with 'advancement'. These two sub pulses represent the largest delay and 'advancement' achievable in the corresponding TPRR. We observed experimentally that the transition from the highly 'advancement' in the undercoupling condition to the highly delay in the over coupling condition acrossing this critical coupling point evolves in a very smooth manner, regardless on the fact that the group index at their resonant frequency changes abruptly as shown in Fig. 2. This smooth transition is due to the fact that the light is not single frequency anymore as a result of the modulation, and its Fourier spectrum is wide enough to cover the sharp feature in the ring response spectra. Experiencing such highly dispersive condition, makes the relative temporal positions of the frequency components of the signal to realign, change their superposed peak position, and split into two peaks at the extreme condition of the critical coupling. Such pulse splitting phenomenon suggests that there is a maximum achievable pulse delay and 'advancement' contributed by a single ring-resonator, bringing up the necessity of employing multiple cascaded ring-resonators for a time delay application [9] with relatively large delay. For the particular TPRR under test in this measurement, the maximum delay and 'advancement' deduced from Fig. 4 are 1.01 ns and 0.43 ns, respectively. The maximum achievable delay is always larger than the maximum achievable 'advancement' due to the fact that the group delay spectra corresponding to the undercoupling condition consists of both negative and positive group delay (see below) components, while for the overcoupling condition, such spectra only consists of positive delay. We should note that the pulse splitting condition could not be observed for a wide pulse which has Fourier spectrum of sufficiently narrow to avoid such highly dispersive condition. However, the delay and 'advancement' become not so pronounced anymore in such situation.

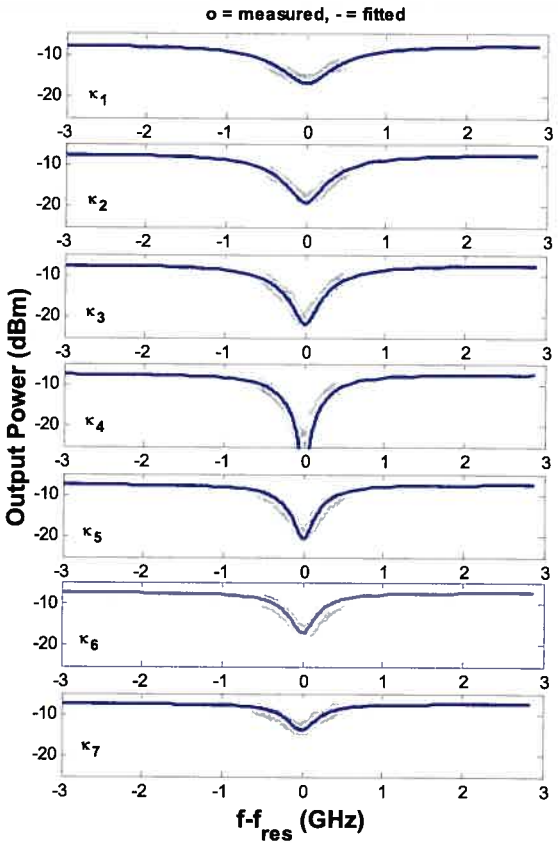


Fig.5: The measured output power (circles) and their best fit theoretical curves (solid lines).

Fig. 5 and 6 show the measured transmission spectrum and the relative group delay, together with their best fit theoretical curves that give minimum least squares error. In this fitting, the curves are treated altogether. Since there is limitation of the modulation phase shift method [12] and the wavelength scanning mechanism to capture extremely sharp features in the neighborhood of the critical coupling point, the measured data for this condition (κ_4) are excluded in the fitting for accuracy reasons. The measurement result for this coupling constant is assumed to be as the one of the critical coupling simply based on the fact that in the temporal measurement (Fig. 4) it exhibited the maximum loss. The best fit values of the structure parameters for κ_1, κ_2, κ_3, κ_5, κ_6, κ_7, and ring attenuation constant α are -0.5984i, -0.5542i, -0.5223i, -0.3581i, -0.3196i, -0.2695i, and 0.7842dB/cm, respectively. The

coupling constant for critical coupling as calculated from α and ring round trip length is -0.44i.

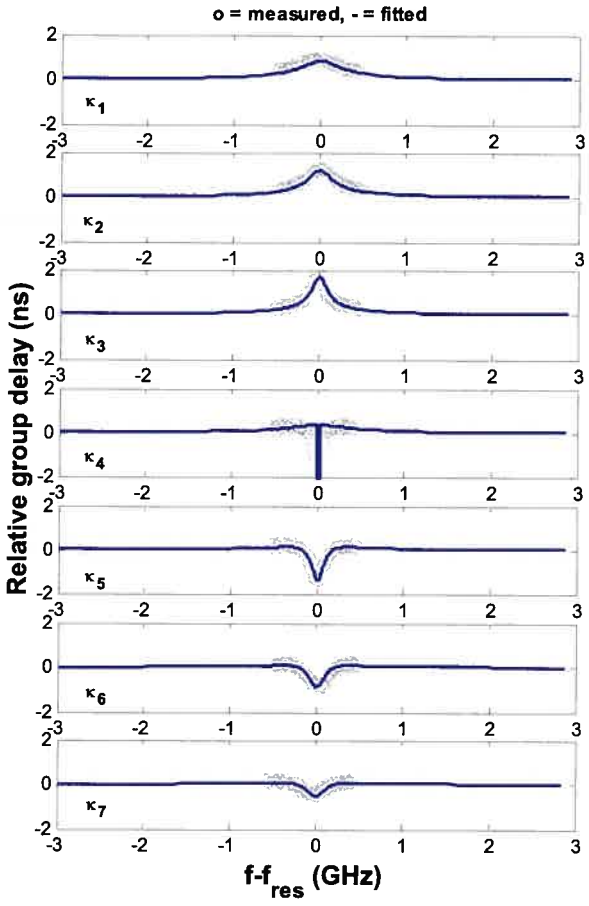


Fig.6: The measured relative group delay (circles) and their best fit theoretical curves (solid lines).

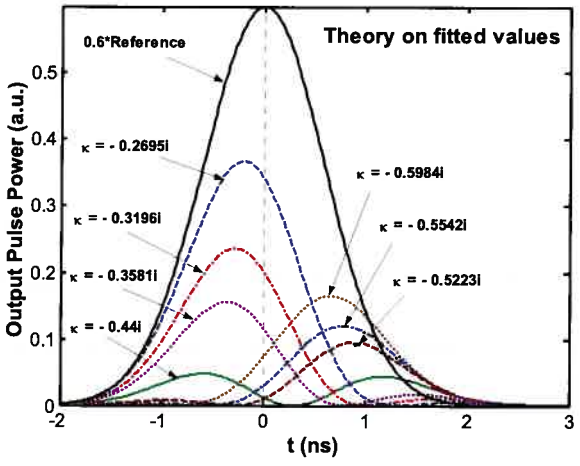


Fig. 7: The simulated pulse temporal behavior of the TPRR using the best fit values of the coupling constants and ring attenuation constant.

Using Fourier transform and the TPRR transfer function [6], we simulate the pulse temporal behavior in TPRR with the above mentioned best fit structure parameters. For this purpose, we took an input pulse with Gaussian amplitude which has a normalized power (or square of amplitude) profile that best fit to the measured reference pulse. Fig. 7 shows the simulated theoretical pulse temporal behavior on the fitted coupling constants and ring loss. These results show a good qualitative agreement between the observed and simulated pulse temporal behavior in the TPRR, including the pulse 'advancement', pulse delay, and pulse splitting phenomena.

Conclusions

We report a direct measurement of the pulse temporal behavior in a two-port ring-resonator circuit. We demonstrate the observation of the pulse 'advancement' under negative v_g and pulse delay under positive v_g conditions. We also observed that at the critical coupling point, the pulse is split into two sub pulses. We show that such a pulse splitting phenomenon facilitates a smooth transition between the high 'advancement' and the high delay condition acrossing the critical coupling point.

Acknowledgments

HU and HH acknowledge the support from STW Technology Foundation through Project TOE6596. LZ and CR acknowledge the support from Dutch Ministry of Economic Affairs under SenterNovem project IS052081.

References

1. R. W. Boyd and D. J. Gauthier, in Prog. in Optics 43, ed. E. Wolf, p. 497, 2002.
2. L. J. Wang, A. Kuzmich, and A. Dogariu, Nature 406, p. 277, 2000.
3. K. Y. Song, M. G. Herráez, and L. Thévenaz, Opt. Express 13, p. 82, 2005.
4. J. E. Heebner and R. W. Boyd, J. Modern Opt. 49, p. 2629, 2002.
5. M. D. Stenner, D. J. Gauthier, and M. A. Niefeld, Nature 425, p. 695, 2003.
6. H. P. Uranus and H. J. W. M. Hoekstra, "Modeling of loss-induced superluminal and negative group velocity in two-port ring-resonator circuits," submitted for publication.
7. C. K. Madsen and J. H. Zhao, Optical filter design and analysis: a signal processing approach, John Wiley and Sons, Inc., New York, 1999.
8. H. Takahashi et al., Photon. Technol. Lett. 16, p. 2063, 2004.
9. L. Zhuang et al., Proc. 11th IEEE/LEOS Symp. Benelux, Eindhoven, the Netherlands, pp. 7, 30 Nov. 2006.
10. http://www.lionixbv.nl/
11. B. Costa et al., Trans. Microwave Theory and Techniques MTT-30, p. 1497, 1982.
12. T. Niemi, M. Uusimaa, and H. Ludvigsen, Photon. Technol. Lett. 13, p. 1334, 2001.

2 bit Continuously Tunable Slow Wave Delay Line at 2.5 Gbit/s

A. Melloni[1], F. Morichetti[1,2], C. Canavesi[2], A. Breda[1], C. Ferrari[1], R. Costa[2] and M. Martinelli[1,2]
1) *Dipartimento di Elettronica e Informazione, Politecnico di Milano,*
Via Ponzio 34/5, 20133 Milano – Italy, melloni@elet.polimi.it
2) *CoreCom, Via G. Colombo 81, 20133 Milano, Italy*

Abstract: A continuously tunable time delay from zero to 800ps has been experimentally achieved on a 2.5Gbit/s signal with a Slow Wave Delay Line realized with coupled ring resonators is Silicon Oxinitride technology. The overall insertion loss is 8 dB and the footprint is less than 2.9 mm^2.

Summary

In this contribution we report both the spectral and time domain characterization of tunable slow wave delay lines (SWDL) realized with directly-coupled ring-resonators in SiON (Silicon Oxinitride) technology. We claim that the presented experimental results represent the state of the art of tunable delay in optical domain. A continuously tunable delay from zero to 800ps has been achieved on a 2.5 Gbit/s NRZ signal, corresponding to a fractional delay of 2 bit.

The architecture of the delay line is shown in Fig. 1. It comprises two ring-based cascaded structures coupled to the same bus.

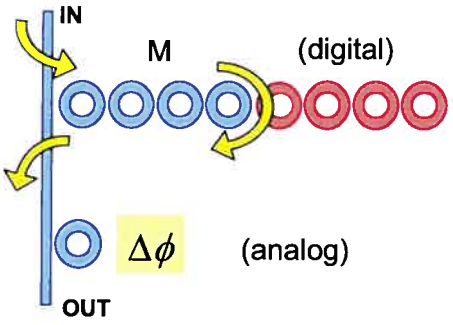


Fig. 1: Scheme of a continuously tunable delay line including a 'digital' or discrete tunable section and an 'analog' or continuously tunable delay.

The input signal enters the first structure and propagates along the ring chain until an out-of-resonance ring is found. At this point the light is reflected and propagates backward to the bus where it arrives from with a delay $T_d=2M/\pi B$, where B is the bandwidth of the structure and M is the number of rings tuned at resonance. The folded layout allows an easy and complete reconfiguration of the delay line as well as a reduction of the overall dimensions. This chain induces a 'digital' or discrete delay with a resolution equal to the time delay induced by the single ring ($2/\pi B$). The second structure is simply a ring phase shifter that induces a continuously variable delay ('analog') depending on the detuning between the signal and its resonant frequency. The two cascaded structures can therefore induce a continuously variable delay from zero to the maximum value.

Fig. 2 is a photograph of the initial section of an integrated realized SWDL.



Fig. 2: Photograph of the first rings of a slow wave delay line realized with directly coupled ring resonators. The diameter of the rings is approximately 1.24 mm, corresponding to a FSR=50GHz.

The input waveguide is on the top left and the output port on the bottom right of the photograph. The different shape of the first rings is because of the apodization of the coupling coefficients of the directional couplers, in order to achieve a flat intensity spectral response as well as a ripple free group delay characteristic. All the rings have the same nominal resonance. An heater is placed on each ring to control the resonant frequency and the electric pads are clearly visible the middle of the rings. The delay line can be reconfigured at the typical velocity of a thermocontroller, that is well below 1 ms, simply by changing the voltage applied to the heater.

A 2.2 by 2.2μm square waveguide in SiON with 4.4% index contrast has been employed to realize the devices. These waveguides can be easily coupled with small core optical fibers with an insertion loss of 0.2dB per facet. The present waveguide attenuation is 0.35dB/cm but an attenuation of 0.15dB/cm has been recently achieved at 1550nm. The 4.4% index contrast guarantees a minimum bending radius of 300 μm with negligible radiation losses, corresponding to ring resonators with a FSR of 100 GHz. This is a limitation only to the minimum achievable footprint and does not limit neither the group delay per ring (equal to $2/\pi B$) nor the insertion loss per ring (equal to $IL_r=c\alpha/\pi Bn_g$, being n_g the group index of the waveguide).

Fig. 3 shows both the intensity and delay spectral responses of a SWDL with FSR=50 GHz, useful bandwidth of 2.5 GHz and finesse 16 (slowing ratio S=10). Continuous lines refer to experimental measurements whereas dashed lines are the simulated responses of the nominal structure.

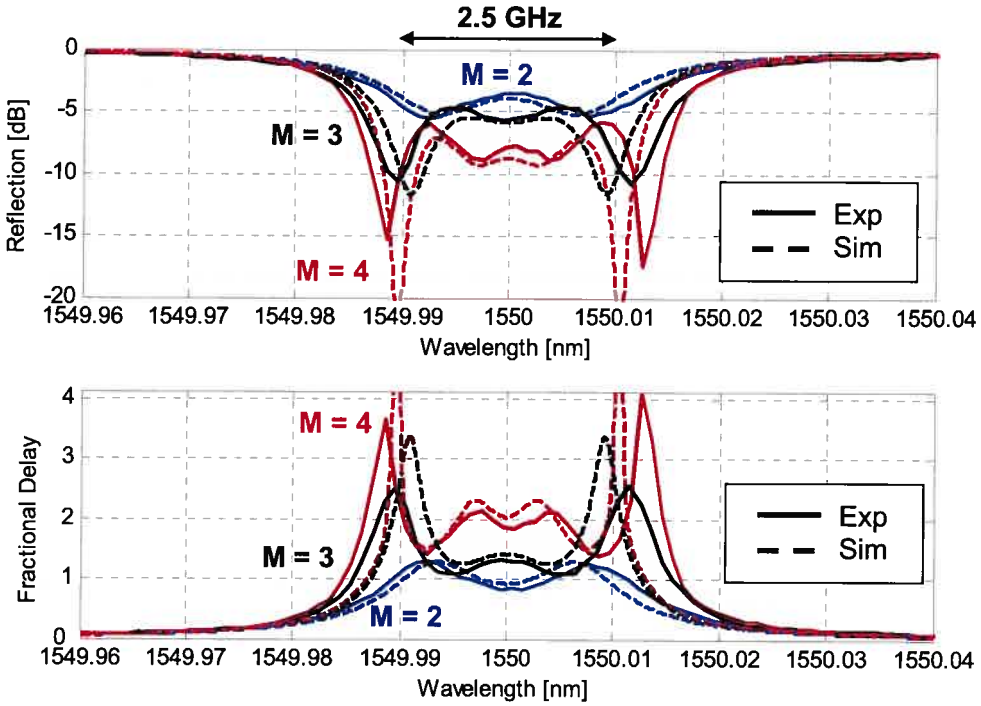


Fig. 3: Spectral intensity and group delay characteristic of a SWDL with M=2, 3, 4 tuned rings. The delay is normalized to 2.5Gbit/s NRZ pulse width.

The agreement is excellent, apart the peaks at the edges of the passing bands that are very critical with respect to the coupling coefficients and to the detuning. These, however, do not impact on the pulse shape because are outside the used band. The group delay is normalized to the NRZ 2.5Gbit/s pulse width. Our folded SWDL with four rings in resonance induces a delay equal to 2 bit lengths (800 ps) with an insertion loss lower than 8 dB, one of the best experimental results to author knowledge [1], [2], [3]. As figure of merit, the usually used group delay to insertion loss ratio results to be 100 ps/dB, achieved in a structure with a footprint of 2.9 mm^2, that is 276 ps/mm^2.

Note that the theoretical limit on the insertion loss per unit delay is $IL/T_d=c\alpha/n_g=7dB/ns$, not very far from the measured result (10dB/ns).

In Ref. [2] Vlasov presents a fractional delay of 1.7 bit at 3 Gbit/s with negligible distortion and longer delays but with noticeable distortion. However, these delays are obtained with another ring based architecture (APF) that is not fully tunable. In Ref.[3], instead, a CROW with 12 rings is presented but the induced delay is 110ps over a bandwith of 17 GHz and the figure of merit is only 2.5 ps/dB.

By increasing the number M of tuned rings, both the delay and the insertion loss increase but the intensity spectral shape remains roughly the same obtained with four rings.

The spectral characteristic shown in Fig. 3 has been achieved by tuning the various ring separately. A Peltier was inserted below the chip and the small thermal crosstalk between the rings compensated during the reconfiguration of the structure. To investigate the impact in the time domain of the frequency misalignments we have measured the induced time delay and the pulse distortion on a 2.5 Gbit/s NRZ data stream. To this end a SWDL with FSR=50GHz and bandwidth B=6.25 GHz, that is a finesse equal to 8 (slowing ration S=5) was used.

The measured eye diagrams at the output of the SWDL are shown in Fig. 4 for a delay line with 0, 1, 2 and 3 tuned rings, respectively.

The input signal is rather sharp and can be described with a supergaussian of order 5, that is a pulse with a bandwidth much larger than the useful bandwidth of the delay line. Despite the distortion of the leading and trailing pulse edges clearly visible in Fig. 4, the eye remains well open, with a small intersymbol interference and only slightly attenuated (the scale of the pictures are identical). These distortions will almost disappear if a smoother input pulse is used, as an example by filtering the electric signal sent to the electro-optical modulator. Simulations, not shown here for brevity, are in perfect agreement with time domain measurements.

The best way to tune the various rings to the correct position is in the time domain by maximizing the eye opening rather than impose a flat intensity spectral response. In this way also the group delay characteristic is optimized and the pulse shape well preserved.

The continuous delay is achieved with a single phase shifter with a FSR of 50 GHz. By changing the signal to ring resonance detuning the delay is varied from

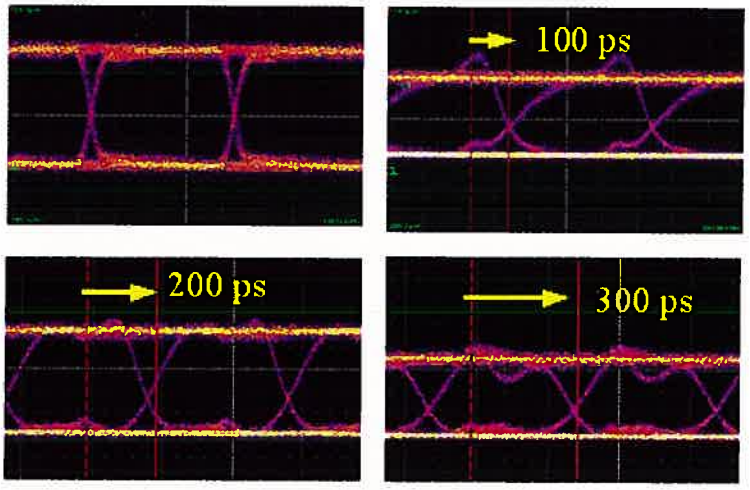


Fig. 4: 2.5Gbit/s eye pattern delayed by a SWDL with *M* rings tuned to resonance. A total delay of 300 ps is induced without significant pulse distortion.

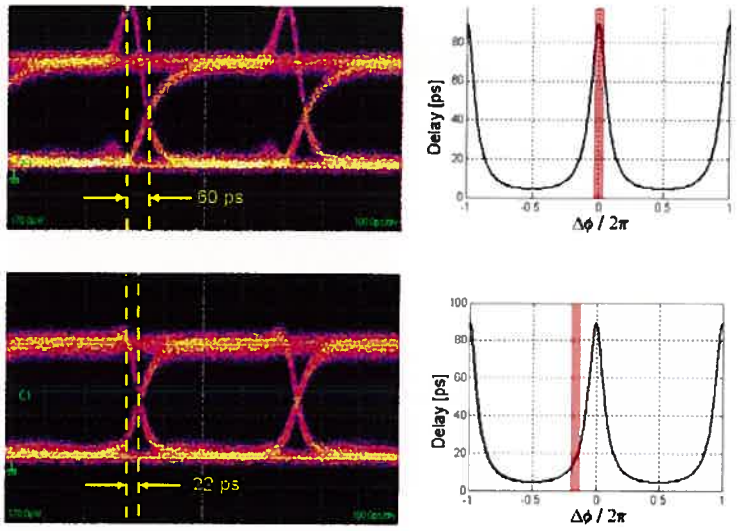


Fig. 5: 2.5Gbit/s eye pattern delayed by a single ring phase shifter tuned at resonance and detuned by 0.2 FSR.

zero to the roundtrip time delay of the ring. Fig. 5 shows a 2.5 Gbit/s pulse that undergo a delay of 60 ps, obtained close to the resonance and of 22 ps, when detuned by 0.2 FSR. The distortion of the trailing edge is evident but the eye aperture remains unaffected. Clearly this overshoot disappears with smoother pulse shapes.

In conclusion, we have shown the potentialities of a fully tunable delay line realized with large rings in glass material. Although the footprint of structures realized with such a technology is far away to be comparable with Silicon based SWDLs [2], the weak attenuation, the easy tuneability and their simplicity and flexibility appoint these structure as very promising for the implementation of reasonable delays with acceptable insertion losses.

Acknowledgments

Authors would tank the European project SPLASH (6th FP) for the partial financial support.

References

1 F. Morichetti et al., "Tunable Slow wave Optical Delay Lines", OSA Topical Meeting on Slow and Fast Light, paper MB2, July 2006.

2 F. Xia, L. Sekaric and Y. Vlasov, "Ultracompact optical buffers on a silicon chip", Nature Photonics 1, 65-71, 2006.

3 J.K. Poon, L.Z. Zhu, G.A. DeRose, A. Yariv, "Transmission and group delay of microring coupled-resonator optical waveguide", Optics Letters, 31, 4, 456,2006..4 R.G.Heideman et al, Photonic West, 2006.

Probing the local density of optical states in 2D-photonic crystal membranes

B. Julsgaard, S. Stobbe, J. Johansen, T. Stolberg-Rohr and P. Lodahl (1),
T. Sünner, M. Kamp, and A. Forchel (2).
1) COM•DTU, Danmarks Tekniske Universitet, Ørsteds Plads 345, 2800 Kgs. Lyngby, Denmark.
2) Technische Physik, Universität Würzburg, Am Hubland, D-97074 Würzburg, Germany.

Abstract: *Time-resolved spectroscopy is performed on ensembles of InAs/GaAs self-assembled quantum dots in photonic crystal membranes. The spatial distribution of the quantum dots in the photonic crystal gives rise to a distribution of the local density of optical states and hence a distribution of radiative decay rates. Accordingly, a non-single-exponential decay curve is expected and measured. However, the multi-level structure of each quantum dot adds to the complexity of the decay curves. Enhancement and inhibition of spontaneous emission are observed and compared to theoretical calculations.*

Introduction

Photonic crystal structures are interesting because of their ability to affect the dynamics of light/matter-interactions. The radiative lifetime of internal light sources can be modified [1], and also the spatial spontaneous emission pattern can be controlled [2]. These effects open up the possibility of constructing more efficient and compact devices such as LEDs [3], and the implementation of quantum information protocols in solid-state systems becomes more attractive [4].

The primary motivation for our research is to improve the basic understanding of the interaction between the quantum dots and the radiation field in the presence of a photonic crystal. In order to study the impact of the photonic structure, we have fabricated a number of photonic crystal membranes while systematically varying the geometry. We optically excite quantum dots within the membranes and detect the time-resolved luminescence decay.

It is a major challenge to deduce the physical understanding from such decay curves, which we observe to be non-single-exponential. This is a signature of the local density of optical states (LDOS), which varies for quantum dots at different positions inside the photonic crystal. Hence, we probe the luminescence decay from an ensemble of quantum dots with varying radiative lifetime, and our experiments present a systematic study of LDOS effects in 2D photonic crystal membranes. Also, the emission pattern is different for different positions inside the photonic crystal, and the fact that our experimental setup selects a certain detection solid angle may play a role in the detailed understanding of the decay curve. Many of these effects have been calculated theoretically in [5] by Koenderink *et al.*, and we will compare our experimental observations with these theoretical results. In addition to the above points, the internal structure of each quantum dot leads to bi-exponential decay curves in absence of the photonic crystal, and the understanding hereof is necessary to obtain the complete picture.

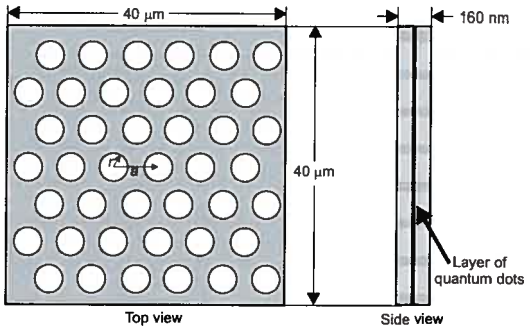


Fig. 1: Schematic view of a membrane (the size of the holes is exaggerated), defining the hole radius, r, and the lattice constant, a. The quantum dots are embedded in a central layer within the 160 nm thick membrane.

Fabrication of quantum dots and photonic crystal membranes

A schematic view of a photonic crystal membrane is shown in Fig. 1. The membranes are made from GaAs, and the dimension of each membrane is $40 \times 40\ \mu m^2$ with thickness 160 nm. Centered within the membrane is a layer of InAs quantum dots grown by molecular beam epitaxy. We observe the fluorescence from the lowest exciton state in the quantum dots, which is polarized in-plane with the membrane. The photonic crystal is made by etching a triangular hole structure with hole radius, r, and hole spacing, a. For all membranes in this experiment we have $r/a = 0.313 \pm 0.006$.

Experimental results

The photonic crystal samples are mounted inside a closed-cycle cryostat operated at $\approx$14 K. The optical setup is shown in Fig. 2. The time-resolved luminescence decay is measured for lattice constants, $a = 180, \ldots, 470$ nm in steps of 10 nm. All of these decay curves are shown together in Fig. 3.

Decay curves measured in absence of the photonic crystal structure are in general bi-exponential (we attribute this effect to the non-radiating dark exciton states, which populate the radiating bright exciton state by a spin flip). The decay curves shown in Fig. 3 are clearly non-single-exponential. This is an effect of probing ensembles of quantum dots with varying LDOS [6]. Separating out the pure LDOS effect from the internal structure of the quantum dots (and possibly

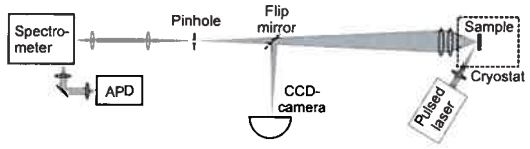


Fig. 2: The experimental setup. A Coherent Mira 900 ti:sapphire femto-second laser, running at wavelength $\lambda_{ex} = 757$ nm, is focused on a single photonic crystal membrane and excites a number of electron-hole pairs in the GaAs layer. These relax into bound exciton states inside the quantum dots, and the luminescence from the radiative recombination of the exciton ground state is detected at $\lambda_{em} = 983$ nm. A pinhole images the fluorescence from a 25 μm diameter circular disk of the central part of the $40 \times 40\,\mu m^2$ membrane onto the spectrometer and further on to an avalanche photo diode (APD). A CCD-camera is used for proper alignment and focusing.

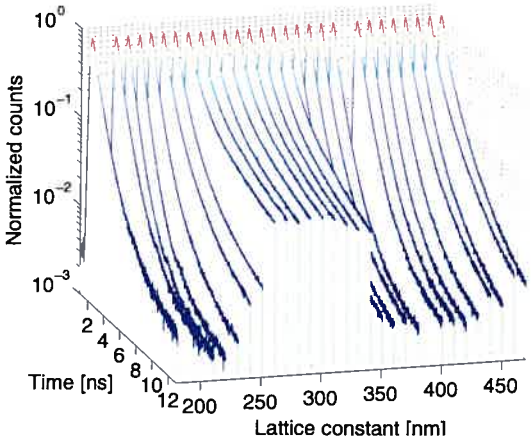


Fig. 3: All measured decay curves with background subtraction and normalized to the same initial value of unity. In the range $a = 270$ nm to 350 nm, the decay clearly extends to longer times compared to the remaining cases.

other effects) is a challenge and a topic of our current research. Hence, we will not attempt to explain the detailed shape of the decay curves here but instead treat a few pronounced features.

For each curve in Fig. 3, we extract the fastest and slowest decay rate by fitting the first and last part, respectively, to a straight line on the log-scale. The results are shown in Fig. 4 and we see a clear feature of the 2D photonic bandgap for lattice constants in the range $0.265 \leq a/\lambda_{em} \leq 0.345$. For the fastest rates, we compare the results to a reference value measured in absence of the photonic crystal (the blue line in Fig. 4). The fast decay rate inside the bandgap is below 70% of the reference value, and outside the gap it may be 30% higher than the reference value. The slowest decay rates (marked with red squares in Fig. 4) also show a pronounced bandgap feature.

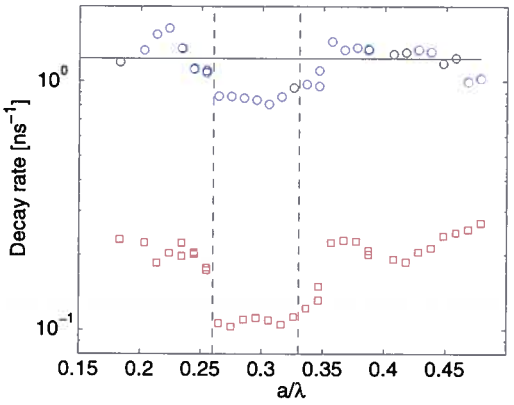


Fig. 4: The fastest (blue circles) and slowest (red squares) decay rates found by fitting the first and last parts of all decay curves shown in Fig. 3. On the horizontal axis is the lattice constant, a, normalized to the emission wavelength, $\lambda_{em} = 983$ nm. The blue line represents the fast decay rate in absence of the photonic crystal structure. The vertical dashed lines mark the bandgap edges predicted in [5].

We may compare these experimental observations with theoretical results derived in [5], where calculations are given for membranes with $r/a = 0.3$ and thickness 250 nm (compared to our values $r/a = 0.313$ and thickness 160 nm).

First of all, the photonic bandgap edges for in-plane polarized emission is calculated in [5] to be positioned at $a/\lambda = 0.26$ and 0.33. These limits are marked in Fig. 4 with vertical dashed lines and are seen to almost coincide with our experimental observations.

We may also compare the enhancement and inhibition of the decay curves. Inside the 2D band gap, the fastest rate is predicted to be less than 50% of the reference value. Outside the gap, the enhancement is predicted to be up to five times faster than the reference value. These predictions are more pronounced than our experimental observations. The reason for this is unknown at the moment, but it seems obvious that if the quality of the photonic crystal is non-perfect, radiation modes will be affected less and the emission properties of the quantum dots should be closer to the case of an isotropic medium. Note that simulated decay curves can be found in [5].

Conclusion

In conclusion, we have studied the effect of a photonic crystal structure on the fluorescence emission from quantum dots in thin membranes. The observed time-resolved luminescence decay curves show clear features of a 2D photonic bandgap, and the results are in general in agreement with predictions by Koenderink *et al.* [5], although the observed effects on the magnitude of the decay rates are less pronounced than expected. However, many quantitative details are still to

be understood and present a challenge for future work.

Acknowledgments
We thank Femius Koenderink for generously sharing his LDOS calculations. We gratefully acknowledge financial support from the Danish Research Council (division FNU). The work is part of the EU project "QPhoton". B. Julsgaard is supported by the Carlsberg Foundation.

References

[1] P. Lodahl *et al.*, Nature, vol. 430, p. 654, 2004.

[2] M. Fujita *et al.*, Science, vol. 308, p. 1296, 2005.

[3] K. J. Vahala, Nature, vol. 424, p. 839, 2003.

[4] C. Simon *et al.*, Phys. Rev. B, vol. 75, art. 081302(R), 2007.

[5] A. F. Koenderink *et al.*, J. Opt. Soc. Am. B, vol. 23, p. 1196, 2006.

[6] I. S. Nikolaev *et al.*, Phys. Rev. B, vol. 75, art. 115302, 2007.

An Optical Interconnect Layer on Silicon

P.R.A. Binetti (1), J. van Campenhout (4), X.J.M. Leijtens (1), M. Nikoufard (1), T. de Vries (1), Y.S. Oei (1), L. Di Cioccio (2), J.-M. Fedeli (2), C. Lagahe (3), R. Orobtchouk (5), X. Letartre (5), P. Regreny (5), P. Rojo-Romeo (5), C. Seassal (5), P.J. van Veldhoven (1), R. Nötzel (1), D. Van Thourhout (4), R. Baets (4) and M.K. Smit (1)

1) COBRA Research Institute, Technische Universiteit Eindhoven, Postbus 513, 5600 MB Eindhoven, The Netherlands.
2) CEA-Léti, Minatec, France. 3) TRACIT Technologies, France. 4) UGent, Belgium.
5) INL, Université de Lyon, France.
p.r.a.binetti@tue.nl

Abstract: *We demonstrate an optical interconnection link on silicon. Compact InP-based micro-disk lasers and photodetectors (PDs) are connected via Si photonic waveguides on top of a Si wafer. The photonic devices are fabricated in a way compatible with wafer scale processing steps, guaranteeing compatibility towards future generation electronic IC processing. Device design, fabrication, integration scheme and preliminary measurements of the full optical link are described in this paper.*

Introduction

For future generation electronic ICs, a bottleneck is expected at the interconnect level. The integration of optical sources, waveguides and detectors forming a photonic interconnect layer on top of the CMOS circuitry is a promising solution, providing bandwidth increase, immunity to EM noise and reduction in power consumption [7, 6, 1]. This solution is investigated within the European project PICMOS[1]. In that context, an interconnect layer is built as a passive Si photonic waveguide layer and InP-based photonic sources and detectors are fabricated with wafer scale processing steps. A possible integration technique that is investigated here assures compatibility towards future generation electronic ICs and is based on a die-to-wafer bonding technology [2]. In this paper we present compact laser and photodetector structures that can be used for the above mentioned optical interconnections. The design, fabrication, and characterization of the optical link are described.

Design

In our approach, light from an electrically driven InP-based micro-disk laser is coupled into the Si waveguide in the interconnection layer. The optical power is carried by the Si waveguide over the link (6-7 mm) and is coupled into a detector structure by means of an InP membrane coupler. As shown in Fig. 1, two types of link were implemented: laser-to-detector point-to-point (P2P) links and broadcast links. A schematic draw of the micro-disk laser-to-detector P2P link is shown in Fig. 2. Grating fiber couplers were designed in the Si photonic waveguide layer to allow characterization of lasers and detectors without the need of a full optical link manufacture. Such gratings are described more in detail in [4].

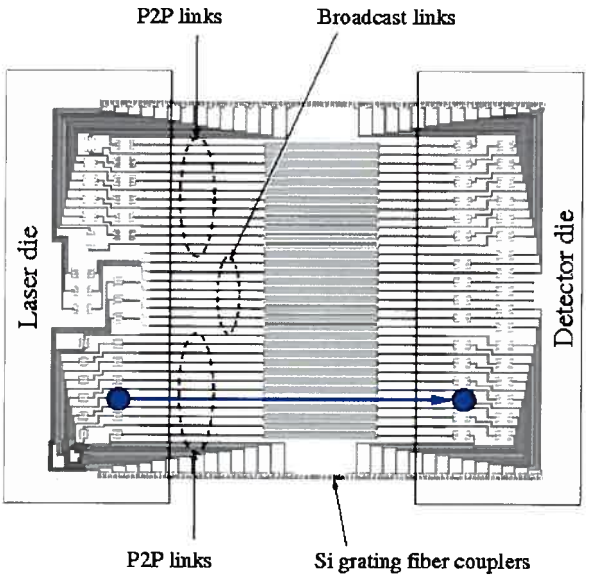


Fig. 1: Optical link scheme. On the left (right) the position of the source (detector) die is drawn. Micro-disk lasers are connected to detectors via point-to-point and broadcast links. The Si photonic waveguide pattern is shown in the scheme background. The point-to-point link schematically drawn in Fig. 2 is indicated.

The micro-disk laser is built as a InAsP multi-quantum well active layer in the n.i.d. InGaAsP structure core, which is sandwiched by highly n- and p-doped InP contact layers. We refer to [5] for more details about the source design. The PD structure is built as an n.i.d. 700 nm InGaAs absorption layer sandwiched between a highly p-doped 50 nm InGaAs contact layer and a highly n-doped 250 nm InP layer, which is also used for realizing a membrane waveguide acting as a coupling structure. The detector mesa footprint is $5 \times 10\,\mu m^2$. Source and detector layer stack were chosen to reach a trade-off between the ease of integration (see [5]) and device performance. More details about the detector structure design can be found in [9].

[1] Photonic Interconnect Layer on CMOS by Wafer-Scale Integration (PICMOS), http://picmos.intec.ugent.be

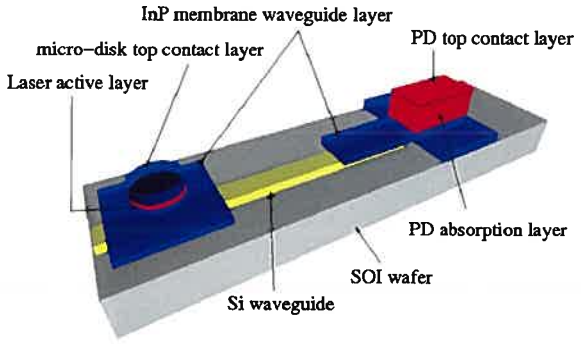


Fig. 2: Schematic diagram of a point-to-point photonic link. Electrically pumped micro-disk laser (left) launches an optical signal into the Si waveguide. Light is collected by the detector structure (right).

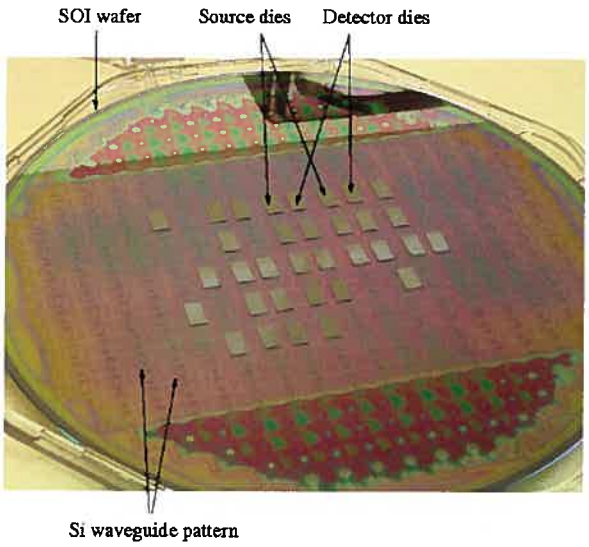


Fig. 3: Source and detector InP-based dies bonded on an SOI wafer.

Fabrication

Two InP-based 2 inch wafers with the laser and the PD layer stacks were epitaxially grown by Solid Source MBE and by MOVPE, respectively. The wafers were diced in 9×7 mm^2 pieces, which were then bonded upside down on an SOI wafer (see Fig. 3), in which the Si waveguide pattern had been defined. A SiO_2 layer was grown on top of the SOI and InP wafers to provide a silica-to-silica interface for the molecular bonding. We refer to [2] for the details about such bonding technique, while details about design and fabrication of the Si photonic waveguides are extensively presented in [8]. Afterwards, the die substrate was wet-chemically removed and lasers and PDs pattern was defined by e-beam lithography and transferred to a 150 nm thick SiO_2 hard mask. The SOI wafer was sawn into samples containing both source and PD dies and test samples with only the source or the detector die. We proceeded with the serial processing of the sources and of

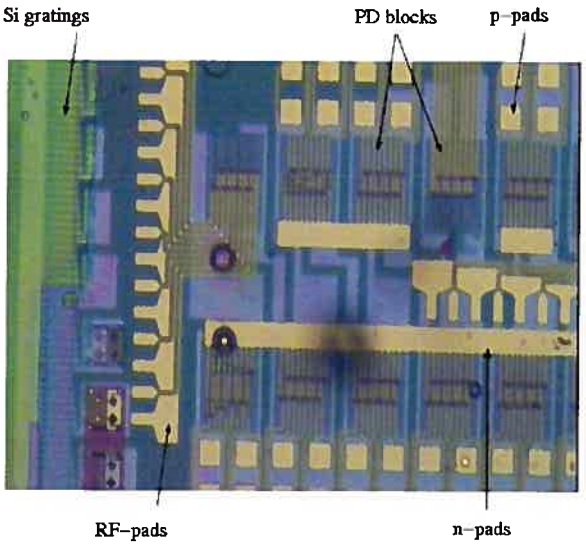


Fig. 4: Picture of the fabricated chip. Ten PD blocks (8 devices/block) are shown in this picture. DC and RF p- and n-contact pads are also visible, as well as the Si grating couplers (on the very left).

the detectors, by covering with thick protective photoresist one die while processing the other. The SiO_2 hard mask was used to dry-etch the microdisks in the laser die, while in the PD die it masked the dry-etch of the membrane waveguides and of the PD bottom contact areas, which share the same n-InP layer. The silica mask on top of the detectors was then dry-etched away and the mesas were wet-chemically etched. The following common processing steps were finally done to complete the chip. A benzocyclobutene (BCB) layer was deposited to planarize the chip surface and provide electrical isolation. Device top- and side-contact windows were opened by a combination of O_2 plasma-etch and RIE, and metal was evaporated and patterned by lift-off. Top and bottom PD contacts were metallized with a Ti/Pt/Au layer stack, as well as the bottom laser contacts, while a Ti/Au layer stack was used for sources top contacts. Fig. 4 shows a picture of the fabricated devices.

Measurement Results

We performed preliminary measurements of the P2P full optical link. The characterization was done by electrically biasing the micro-disk laser in pulsed regime while recording the detector generated photocurrent through a Keithley read-out unit, which was also used to provide reverse bias voltage to the PD. The laser output power was monitored by coupling the emitted signal into an optical fiber aligned over the Si grating and connected to an optical spectrum analyzer (OSA). We registered a laser average output power of tens of nW, depending on the driving current and the emitted pulses parameters. We measured optical links at different pulsed working regimes, as can be seen in Fig. 5. The detector generated photocurrent measured

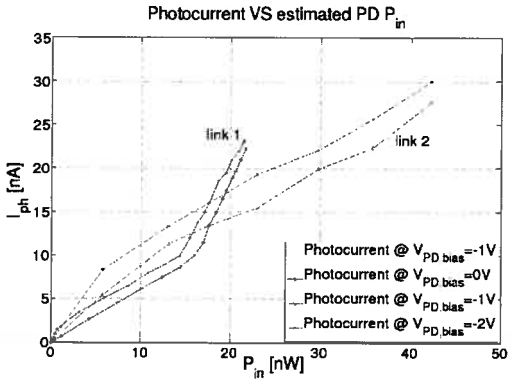


Fig. 5: Detector average photocurrent measured in CW for two different links as a function of the estimated power in the Si waveguide at the PD input. In link 1 (link 2), the laser emits 125 ns (45 ns) wide pulses with a duty cycle of 2.5% (4.5%).

in CW is plotted in the figure, for two different links. In link1 (link2) the laser emits 125 ns (45 ns) wide pulses with a duty cycle of 2.5% (4.5%), while the PD is biased at 0 V and -1 V (-1 V and -2V). When the laser is OFF, a dark current of 10-13 nA flows through the photodiode when biased at -1 V. When the laser is ON, an average photocurrent of up to 22 nA (30 nA) is measured.

Conclusions

We demonstrated a photonic interconnection layer on silicon. The InP membrane-based micro-disk lasers and photodetectors were manufactured. Device design, integration scheme and fabrication were described. First measurements performed with electrically driven lasers working in pulsed regime and detectors working in CW demonstrate working optical link.

Acknowledgments

We acknowledge the support by the EU through the IST-PICMOS project.

References

[1] D.A.B. Miller, "Optical interconnects to Si", IEEE JSTQE, Vol. 6, No. 6, November/December 2000.

[2] L. Di Cioccio et al., "Recent results on advanced molecular wafer bonding technology for 3D integration on Silicon", Wafer Bonding Conference, Quebec, 2005.

[3] B. Han et al., "Comparison of optical passive integrated devices based on three materials for optical clock distribution", accepted, ECIO 2007, Copenhagen, Denmark, 2007.

[4] D. Taillaert et al., "An Out-of-Plane Grating Coupler for Efficient Butt-Coupling Between Compact Planar Waveguides and Single-Mode Fibers", IEEE JQE, Vol. 38, No. 7, July 2002.

[5] P. Rojo Romeo et al., "Heterogeneous integration of electrically driven microdisk based laser sources for optical interconnects and photonic ICs", Optics Express, Vol. 14, No. 9, pp. 3864-3871, 1 May 2006.

[6] C. Piguet et al., "Extremely low-power logic", Proc.of the Design, Automation and Test in Europe Conference and Exhibition (DATE'04), vol. 1, pp. 656-661, Feb. 16-20 2004.

[7] *International Technology Roadmap for Semiconductors (ITRS)*. http://public.itrs.net.

[8] D.V. Thourhout et al., "Recent progress in SOI nanophotonics waveguides", Proc. 31st Eur. Conf. on Opt. Comm. (ECOC '05), pp. 241-244, Glasgow, Scotland, Sep. 25-29 2005.

[9] P.R.A. Binetti et al., "A compact detector for use in photonic interconnections on CMOS ICs", Proc. 2005 Symposium IEEE/LEOS Benelux Chapter, pp. 233-236, Mons, Belgium, 2005.

[10] P.R.A. Binetti et al., "Membrane couplers and photodetectors for optical interconnections on CMOS ICs", Proc. 2006 Symposium IEEE/LEOS Benelux Chapter, pp. 237-240, Eindhoven, The Netherlands, 2006.

Transition Matrix Methods

David Yevick (1) and Michael Reimer (2)

1) Department of Physics, University of Waterloo, Waterloo, ON N2L 3G1, Canada, yevick@uwaterloo.ca 2) Department of Physics, University of Waterloo, Waterloo, ON N2L 3G1, Canada, mareimer@sympatico.ca

Abstract: *The transition matrix describes the probabilities of transitions of a system between different sets of states. In this presentation, we demonstrate that techniques similar to the multicanonical method can be employed to find the elements of the transition matrix between pairs of highly unlikely states in an optical communication system. This result is then applied to determine the probability distribution of outage times resulting from polarization mode delay (PMD).*

Introduction

While biased sampling procedures, most notably the multicanonical or importance sampling techniques, are now frequently employed to investigate static system quantities such as the probability distribution functions (pdf) of the differential group delay (DGD) or of the eye opening penalty.[1-4], these methods have not been applied to dynamic system behavior such as the average time spent in an outage. Here we adapt the transition matrix methods of statistical mechanics[5-7] to dynamic communications problems (it should be noted that a transition matrix approach was earlier applied to analyze the error of static PMD calculations in [8]).

Multicanonical Method

Since our transition matrix discussion generalizes our previous work on biased sampling methods, we first review the foundations of the multicanonical method. A randomly fluctuating physical system can generally be described by a vector of N_e system observables, $\mathbf{E}$, each of which is affected by N_a stochastically varying parameters $\mathbf{a}$. For example, in this paper $\mathbf{E}$ are suitably defined moments of a pulse that has passed through a series of polarization controllers to which fluctuating voltages specified by $\mathbf{a}$, are applied. Typically, the average value of a function $p(\mathbf{E})$ in regions of sample space with an extremely small probability of occurrence must be determined without recourse to an unrealistically large number of samples, $\mathbf{a}_i$.

Accordingly, the multicanonical method biases the sample space. in such a manner that, if $p(\mathbf{E})$ represents the pdf of $\mathbf{E}$, the sampling probability after many iterations coincides with the inverse of the pdf and the sampling becomes uniform in the system observables $\mathbf{E}$. In the standard implementation, the physically accessible region of $\mathbf{E}$ is partitioned into N histogram bins centered at $\mathbf{E}_m$ with $m = 1, 2, \ldots N$. Next, the elements of a histogram that will store the unnormalized pdf, $p^0(\mathbf{E}_m)$, and a second histogram that holds temporary values, $H(\mathbf{E}_m)$, are both initialized to unity. The starting value of $\mathbf{E}$ is computed from a randomly chosen set of system variables $\mathbf{a}^{cur}$. These system variables are then randomly perturbed according to $\mathbf{a}^{new} = \mathbf{a}^{cur} + \delta\mathbf{a}$, leading to new observables $\mathbf{E}^{new}$. To insure that the computation spends more time in states with small values of $p(\mathbf{E})$, this transition is accepted with probability $\min(1, p^0(\mathbf{E}^{cur})/p^0(\mathbf{E}^{new}))$, in which case $\mathbf{a}^{cur}$ is set to $\mathbf{a}^{new}$; otherwise $\mathbf{a}^{cur}$ is unchanged for the following iteration. In either case, the histogram element, $H(\mathbf{E}_m)$, for the new value of $\mathbf{E}^{cur}$ is incremented by unity. After this process is repeated M times, an improved estimate, $p^1(\mathbf{E})$, of $p(\mathbf{E})$ is obtained after the bias in the system variables during the iteration is removed according to $p^1(\mathbf{E}) = cp^0(\mathbf{E})$ $H(\mathbf{E})$. In the following iteration $p^1(\mathbf{E})$ replaces $p^0(\mathbf{E})$, $H(\mathbf{E})$ is reset to unity and the above process is repeated.

Transition Matrices

The multicanonical method can be employed to determine the relative probability for transitions between each pair of system variables even for highly unlikely pairs of states. In particular, for every accepted or rejected transition from a state in the n:th to a state in the m:th histogram bin obtained during a multicanonical calculation, the corresponding element, $\mathcal{T}_{nm}$, of an *unbiased* but *unnormalized transition matrix*, $\mathcal{T}$, is incremented by unity. At any point in the calculation, the rows of $\mathcal{T}_{nm}$ can be normalized to unity, yielding an estimate of the standard *transition matrix T*. We can also construct a *biased multicanonical transition matrix*, B, such that B_{nm} gives the likelihood of a transition from the n:th to the m:th state in the multicanonical procedure.. Here T_{nm}, typically at the end of the last iteration, is multiplied by the multicanonical acceptance probability, $\min(1, p^L(\mathbf{E}_n)/p^L(\mathbf{E}_m))$ after which each row of this matrix is normalized to unity. A further matrix R, with $R_{nm} = T_{nm}/B_{nm}$, can be constructed that specifies the ratio of the probability of an unbiased transition from state n to state m to the probability of this transition transition probability in the multicanonical method.

An alternative method for biasing transitions is to formulate the acceptance rule directly from an estimate of $\mathcal{T}$ that is dynamically updated as the calculation step.[6] Here, starting from initial values $\mathcal{T}_{nm}=1$, transitions between two states $\mathbf{E}_m^{new}$ and $\mathbf{E}_n^{cur}$ generated by $\mathbf{a}^{new} = \mathbf{a}^{cur} + \delta\mathbf{a}$, are accepted with probability $\min(1, \mathcal{T}_{nm}/\mathcal{T}_{nn})$ while again incrementing

$\mathcal{T}_{nm}$ or $\mathcal{T}_{nn}$ by unity for accepted and rejected transitions, respectively. We have slightly modified this technique by fixing our estimate of the transition matrix after every M transitions and employing this estimate for the next M transitions; since this ensures that for most transitions, the detailed balance condition, $P(\mathbf{E}_n)\ T_{nm} = P(\mathbf{E}_m)\ T_{mn}$ for each n and m, where $P(\mathbf{E}_n)$ denotes the probability of finding the system in the n:th histogram bin, is satisfied. However, we still impose detailed balance at the end of the calculation to avoid unphysical complex eigenvalues of the transition matrix. Since $P(\mathbf{E})$ is identified below with the eigenvector of the transition matrix with unit eigenvalue., we compute the $P^{(0)}(\mathbf{E}_n)$ associated with the transition matrix $T^{(0)} \equiv T$ and iteratively improve T according to $T_{nm}^{(i+1)} = (P^{(i)}(\mathbf{E}_m)T_{mn}^{(i)} + P^{(i)}(\mathbf{E}_n)T_{nm}^{(i)}) \,/\, 2P^{(i)}(\mathbf{E}_n)$.

Time-Dependent Problems

Time-dependent systems can be simulated in a similar manner to time-independent systems if the magnitude of the random perturbation, $\delta\mathbf{a}$, is adjusted such that the average change in the observables, $|\mathbf{E}^{new} - \mathbf{E}^{cur}|$, coincides with a measured change over some time interval, Δt.

To sample transitions between physically unlikely states, paths can be composed of randomly generated transitions between states that observe the transition probabilities stored in the biased transition matrix or, equivalently, the multicanonical acceptance rule can be applied in conjunction with the unbiased transition matrix probabilities. In either case, repeated evaluation of the system observables from the system parameters is avoided. Each path from the state m to the state n over the intermediate states 1, 2, ... k must however be assigned the weight $w = R_{m1}R_{12}...R_{kn}$ in the resulting histogram.. Of course, the unbiased transition matrix can be employed directly if only the high probability region of the sample space is of interest.

The time evolution of a system property can also be derived from the eigenvalues and eigenvectors of T. The eigenvector with unit eigenvalue here yields the probability distribution function for finding the system in a given state while the distribution functions associated with the other eigenvectors instead decay with time constants proportional to their eigenvalues as the system tends towards its equilibrium distribution..

Outage Times

To illustrate the above considerations, we compute the pdf of the PMD-induced outage durations in a single mode optical fiber system. Our calculation employs a fiber model consisting of 100 concatenated birefringent fiber segments each of which poseses a DGD of 2.17ps. These are separated by polarization rotators that can be adjusted to generate any desired rotation of the incoming polarization vector $\mathbf{\Omega}_i$ on the Poincaré sphere. For certain mutual orientations of these polarization vectors, the ratio of the emulator DGD to the average DGD of the fiber segment will exceed a certain value associated with a system outage.. The time interval over which the DGD exceeds this value is termed the outage time.

Identifying the vector of system variables $\mathbf{a}$ with the $2l$-dimensional relative angles between the birefringence vectors of successive sections, and the system observables, $\mathbf{E}$, with the DGD, the outage time distribution is normally determined by performing many time steps $\mathbf{a}^{new}=\mathbf{a}^{cur} + \delta\mathbf{a}$, and recording the length of time for which the system remains in the outage region for each outage. However, in our calculations, the Markov chain can be directly modeled by sampling transitions according to the probabilities stored in the unbiased or biased transition matrices (in the latter case, however, the histogram for the time duration of each system path must be incremented by an appropriate weighting factor).

Alternatively, we can take as the initial state of the system a distribution equal to $P(\mathbf{E}_n)$ for n in the in non-outage region and zero elsewhere, corresponding to the average distribution of states that have not yet entered the outage region. The time evolution of this state is then modeled by repeatedly multiplying by the transition matrix. After the k:th step, the sum of the histogram values that fall outside the outage region can be identified with the probability that the system returns to a non-outage state within the time interval $(k\text{-}1)\Delta t<t<k\Delta t$ The values of the system vector in the non-outage region are then set to zero before the $(k+1)$:st time step. The time evolution can also be determined by noting that since the state vector of paths that are restricted to the outage region is repeatedly multiplied by the submatrix formed from the matrix entries for the outage states, the eigenvalues of this submatrix yield the decay rates corresponding to the distributions given by the associated eigenvectors. The desired outage time distributions can therefore be found through projection of the distribution after one time step onto these states.

Numerical Results

To illustrate the above methods, in Fig. 1 we show the pdf of the outage times, for both DGD>$2\tau_{avg}$ and DGD>$3\tau_{avg}$ outage conditions. The circles in this figure refer to an unbiased Markov chain calculation that recorded the outage times observed during 10^9 time steps (fewer than 10,000 samples were recorded in the outage region for the $3\tau_{avg}$. outage condition). The solid line displays the result after constructing an unbiased transition matrix from the accepted and rejected transitions of three $5\text{x}10^6$ sample multican-

onical iterations and then generating a biased Markov chain from the the multicanonical acceptance rule together with appropriate weight factors for the paths. Replacing the multicanonical acceptance rule by a rule derived from the ratio of transition matrix elements was found to decrease the sampling of the tail of the pdf for a fixed number of realizations. Finally, successive multiplications of the initial state vector by the unbiased transition matrix obtained after two $2x10^5$ sample multicanonical iterations yielded the dashed line; as was also computed from the eigenvalues and eigenfunctions of the outage state submatrix. Although the biased transition matrix clearly samples a far wider range of states than the standard procedure, some accuracy is necessarily sacrificed since the standard method preserves all information about the system variable correlations in different regions of the system state space.

Finally, Fig. 2 displays the eigenvectors corresponding to the three largest eigenvalues of the transition matrix determined with three $5x10^6$ multicanonical iterations. The insert contains the magnitude of the 50 largest eigenvalues. Note that the eigenvector with unit eigenvalue (solid line) yields the pdf of the DGD for infinitely long fiber samples while the other eigenvectors can be used to compute the DGD at finite fiber lengths.

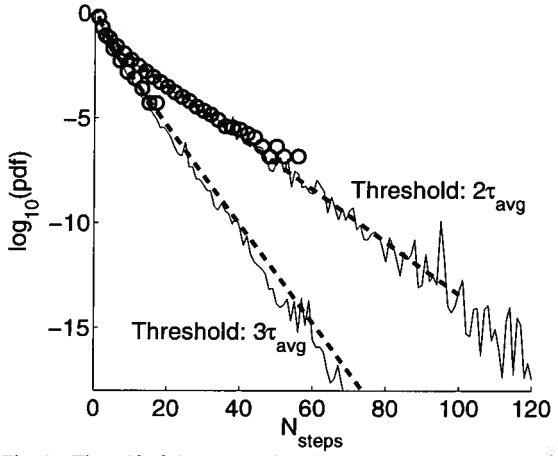


Fig. 1. The pdf of the outage durations associated with an optical fiber emulator for thresholds of $2\tau_{avg}$ and $3\tau_{avg}$. The results of the standard method with 10^9 samples, the multicanonical reweighing method with 3 iterations of $5x10^6$ samples and repeated multiplication of the initial state vector by an unbiased transition matrix obtained after two $2x10^5$ sample multicanonical iterations. are denoted by circles, solid and dashed lines, respectively.

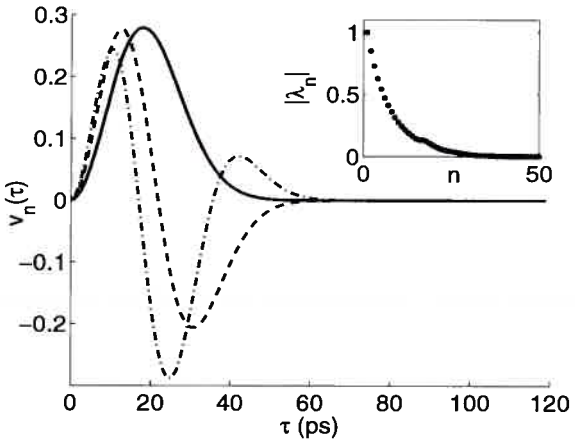


Fig. 2. The first three (solid, dashed and dashed-dotted lines, respectively) transition matrix eigenvector computed after 3 multicanonical iterations of $5x10^6$ samples. The inset contains the magnitude of the first 50 eigenvalues.

Conclusions

That time-dependent effects in communication and other physical systems can be rapidly and accurately modeled, even in very low probability regions by transition matrix methods can significantly impact future communication system simulations. We therefore hope to shortly extend our results to several challenging system calculations.

Acknowledgments

This work was supported in part by the National Sciences and Engineering Research Council of Canada (NSERC), the Canadian Institute for Photonic Innovation (CIPI), Nortel and the Ontario Research and Development Challenge Fund (ORDCF).

References

1. B. Berg and T. Neuhaus:,Phys. Lett. B, V. 267, p. 24, 1991
2. D. Yevick: IEEE Photon. Technol. Lett., vol. 15, pp. 224-226, 2003
3. T. Lu, D. Yevick, B. Hamilton, D. Dumas and M. Reimer, IEEE Photon. Technol. Lett., vol. 17, p. 2583, 2005
4. T. Lu, W. Huang, D. Yevick, M. O'Sullivan and M. Reimer,, J. Opt. Soc. Am. A vol. 22, p. 2804, 2005.
5. G. Smith and A. Bruce, J. Phys. A: Math. Gen. vol. 28, p. 6623 (1995)
6. J-S Wang and R. Swendsen, J. Stat. Phys. vol. 106, p. 245 (2002)
7. M. Fitzgerald, R. Picard and R. Silver, J. Stat. Phys. vol. 98, p. 321 (2000)
8. A. Lima, I. Lima, and C. Menyuk, J. Light. Technol. vol. 23, p. 3781 (2005)